

GLOBCER'23

Global Conference on Engineering Research

13-16 September 2023

3rd GLOBAL CONFERENCE on ENGINEERING RESEARCH

Proceedings Book

ISBN: 978-605-73639-8-5

PROCEEDINGS BOOK

3rd GLOBAL CONFERENCE on ENGINEERING RESEARCH

13-16 September 2023

3rd GLOBAL CONFERENCE ON ENGINEERING RESEARCH (GLOBCER'23)

13-16 September 2023

ISBN: 978-605-73639-8-5

3rd Global Conference on Engineering Research (GLOBCER'23)

13-16 September 2023

Organizing Board

Dr. M. Nuri SEYMAN
Dr. Adem DALCALI

Scientific Board

Dr. Ahmed Kadhim HUSSEIN
Dr. Alexandre Jean Rene SERRES
Dr. Degan ZHANG
Dr. Feyzullah TEMURTAŞ
Dr. Goran PUTNIK
Dr. Hui CHEN
Dr. İbrahim DEVELİ
Dr. Jianjun WANG
Dr. Jue-Sam CHOU
Dr. Ke-Lin DU
Dr. Lianggui LIU
Dr. Mehmet TEKTAŞ
Dr. Miladin STEFANOVIĆ
Dr. Mustafa GÜNAY
Dr. Necmi TAŞPINAR
Dr. Paweł LULA
Dr. Recep ÇALIN
Dr. Zitaun CAI
Dr. R. Gökhan TÜRECİ
Dr. Mahmut BÖYÜKATA
Dr. Gökçe NUR YILMAZ
Dr. Abdullah YEŞİL
Dr. M. Nuri SEYMAN
Dr. Bülent BÜYÜK
Dr. Emre ÇELİK
Dr. Fahmina TARANUM
Dr. Filmor MURILLO
Dr. H.Oktay ERKOL
Dr. Halit ÖZTEKİN
Dr. Héctor F. MIGALLON
Dr. M. Hanefi CALP
Dr. Muharrem PUL
Dr. Neelamadhab PADHY
Dr. Ning CAI
Dr. Harun ÖZBAY
Dr. Adem DALCALI

Dr. İsmail KOÇAK
Dr. Oye Nathaniel DAVID
Dr. Hayri YAMAN
Dr. Alican KARACA
Dr. Sasmita MOHAPATRA
Dr. Selim ÖNCÜ
Dr. Serhat DUMAN
Dr. Ziyodulla YUSUPOV
Dr. Onur ÜLKER
Dr. Oytun Emre SAKICI
Dr. Hasan ŞAHİN
Dr. Serhat Berat EFE
Dr. Oğuz Akın DÜZGÜN
Dr. Ahmet AKKÖSE
Dr. Serkan ŞENOCAK
Dr. Semet ÇELİK
Dr. İlyas ÖZER
Dr. Abdullah ELEN
Dr. Zafer ÜNAL
Dr. Rıdvan KOÇYİĞİT
Dr. Abdollah Doosti-AREF
Dr. Abdul QAYYUM
Dr. Akif KARAFİL
Dr. Alex Michailovic ASAVIN
Dr. Kadir İLERİ
Dr. Asit Kumar GAIN
Dr. Behnaz HASSANSHAHI
Dr. Charles Z. LIU
Dr. Diego Real MAÑEZ
Dr. Evren İŞEN
Dr. Igor Simplice MOKEM FOKOU
Dr. Kamarulzaman KAMARUDIN
Dr. M.M. KARMRUZZAMAN
Dr. Mahmut ÜNVER
Dr. Marlon Mauricio Hernandez CELY
Dr. Maxim A. DULEBENETS
Dr. Mehmet Metin ÖZGÜVEN
Dr. Minh Trong HOANG
Dr. Mohammed Hassan DIGHIRI
Dr. Mustafa EKER
Dr. Onursal ÇETİN
Dr. Radu Emanuil PETRUSE
Dr. Rahim DEHKHARGHANI
Dr. Semih KORKMAZ
Dr. Tingting ZHAO
Dr. Yifang WEI
Dr. Yuan TIAN
Dr. Farooque Hassan KUMBHAR
Dr. Mingxiong ZHAO
Dr. Quang Ngoc NGUYEN
Dr. Vandana ROY
Dr. Farzin ASADI
Dr. Nesli AYDIN
Dr. Volodymyr Gennadievich SKOBELEV

İÇİNDEKİLER/TABLE OF CONTENTS

Tree Density in Floodplains on Stage-Discharge in Meandering Compound Channels 1

Wear Mechanisms on Turning of Nimonic C-263 Under Cryogenic Conditions 6

Flow and Heat Transfer Analysis of Obstacles with Different Geometries in a Rectangular Grooved Channel 14

Sürtünme Karıştırma Kaynağında Üretime Bağlı Sorunlar, Nedenleri ve Çözüm Önerileri 25

Comparison of Cooling Efficiency of Conventional and Conformal Cooling Channels in Plastic Injection Cycle 36

DIN 1.2312 Çeliklerde Farklı Kesme Parametrelerine Bağlı AlTiCrN Kaplamalı Tungsten Karbür Takım Ömrünün İncelenmesi 43

An Investigation on Formability of Metallic Bipolar Plate Micro Channels Under Different Material Models 49

Vision-Based Gas Pipe Inspection for Domestic Hobs 58

Classification of Spherical Graphite Cast Iron Images by Using Machine Learning Techniques 65

Awareness Level of Rural Enterprises on Agricultural Supports 74

Prophet Modeli ile Ürün Talep Tahmini 84

Enjeksiyonla Kalıplanmış Polilaktik Asit Parçaların Farklı Tavlama Ortamı ile Mekanik Özelliklerinin Geliştirilmesi 91

Debriyaj Diskindeki SAE 1010 Malzeme Disk Kapağının Temperleme Isıl İşlemi ile Renklendirilmesinin Parçanın Mekanik Özellikleri Üzerine Etkisinin İncelenmesi 98

Debriyaj Kafesi Tasarım Optimizasyonu ve Validasyonu 107

Debriyaj Rulmanının Taşıyıcı Parçasında Sıvama Bölgesinde Yapılan Tasarım Farklılığının Çekme Kuvvetine Etkisinin İncelenmesi 121

Tasarım Optimizasyonu ile DMF Ağırlık Azaltma Çalışması 129

Application of Metal-Organic Frameworks (MOFs) in Pipette-Tip Solid-Phase Extraction: A Mini Literature Review 138

UV-VIS Detection of Algae Based Gold Nanoparticles: A Mini-Review 143

Enerji Verimliliğini Arttırarak Sürdürülebilirliği Sağlayan Merkezi Hidrolik Güç Ünitesi 148

Prediction of Diabetes Mellitus Using Tree-Based Machine Learning Algorithms: A Comparative Analysis 158

Kazık Gruplarının Oturması 163

Etkileşimli Oyunlaştırılmış Fizyoterapi Uygulaması Örneği: Therapinno 169

Tuning of the Controller Parameters Based on Equilibrium Optimizer Algorithm for Two Input Two Output Systems 179

Effect of Additional Wire on Microstructure and Mechanical Properties of Weld Joints in Laser Welding 189

Farklı Sinterleme Parametrelerinin Monolitik Alüminanın Yoğunluğuna Etkisinin İncelenmesi 196

A Practical Implementation of Measurement System for QTF Sensing Applications 209

Polyamid Fırçalarda Biriken Tozların Elimine Edilebilmesi İçin Gerekli Ekipmanin Tasarım ve Analizi 220

A Multi-Scale Convolutional Neural Network and Empirical Mode Decomposition-Based Model for Electricity Price Forecasting 231

Enhancing Technical Drawing Education in Industrial Engineering through Architectural Approaches:An Educational Study 240

Design of a Novel Bubble Column Photobioreactor and Circular Illumination System for Microalgae Cultivation 251

EAF Slag Detection System Development and Software 259

Realistic Robot Arm Energy Optimization with Using Torsional Springs 264

YOLOv5 Deep Learning Model Approach for the Detection and Classification of Gunshot Residue Images 279

Effect of CNT distribution on the dynamic behavior of carbon nanotube reinforced FGM shells 289

A Case Study: Metallurgical Examination of Material Technical Requirements for M-50 Bearings in the Aerospace Industry 300

Evaluating the Influence of Concrete Class on the Performance of Reinforced Concrete Structures through Incremental Dynamic Analysis 309

Hybrid Approach for Link Prediction in The Networks Created from Turkish Literature 315

Thermal And Forced Vibration of a Carbon Nanotube Incorporated in An Elastic Medium 325

Classification Of Vocal Cord Diseases Using Wavelet Transforms in Multi-Class 335

Sualtı Teknolojileri ile Elde Edilen Sonar Verilerine Dayalı Derin Öğrenme Tabanlı Mayın ve Kaya Ayırımının Tespiti 347

Effect of Gelatin, Nano Gelatin, and Lyophilized Nano Gelatin on Swelling and Water Solubility Properties of Sodium Alginate Composite Film 355

A Review on Image Captioning Using Deep Learning Methodologies: Limitations, Datasets, Metrics, and Recommendations 364

Çok Kullanımlık Çantaların Üretiminde Verimlilik Artışını Sağlayan Bir Sistem 378

Sesaltı Rüzgar Tünelinde Naca0015 Kanat Profilinin Kuvvet Ve Akış Görüntüleme Yöntemi ile Analizi 385

Internet of Things Technology Combination with Smart Cities - Solution to Public Transportation 393

Investigation of the Effects of Changes in Battery Components on Battery Performance Using Design of Experiments Approach 401

Süreksiz Kolonlara Sahip Betonarme Binalarda Sehimlerin Analiz Yaklaşımlarına Göre İncelenmesi 408

The Investigation of The Effect of T6I6 Interrupted Aging on The Mechanical Properties of AA7075 Aluminum Alloy 416

Detection of COVID-19 in X-Ray Images Using Image Processing and Machine Learning Methods 424

Van İli Kuraklığının Yağış Anomali İndeksi (RAI) Yöntemi ile Belirlenmesi 436

Evaluation of Recent Developments in Thermoelectric Generators 447

Farklı çeliklerin Çift Taraflı TIG Kaynaklı birleşim özelliklerinin incelenmesi 460

Diagnosis of Coconut Tree Leaf and Bud Diseases using Deep Learning 466

Experimental Investigation of Mechanical Behavior of Household Gas Hob Glasses 476

Fun Letters Collage from Music Notes with GAN Algorithm 477

Effects of First Thinning on Stratification and Health in Sessile Oak 478

Adsorption Properties of Red Mud, Bauxite and Red Soils in Seydişehir (Konya)-Akseki (Antalya) Region 480

Rare Earth Element Contents of Bauxites in Seydişehir (Konya) Region 482

Recovery of Lanthanum (La) from A Bauxide Residue (Red Mud) Solution by Sorption Process with A Strong Acid Cation Exchange Resin and A Microcapsule 483

Recovery Of Lanthanum (La) From A Bauxide Solution by Sorption Process with A Weak Acid Cation Exchange Resin and A Microcapsule 484

Investigation Of Roasting Parameters on Rare Earth Elements Recovery from Bauxite 485

Rare Earth Elements Recovery from Red Mud with Hydrochloric Acid Using Taguchi Method 486

Application Of Hybrid Particle Swarm Optimization for Energy Demand Prediction in Türkiye 487

Drone Arm Optimization Using Genetic Algorithm 488

A Software System Design for Data-Driven Automotive Spare Parts Management 489

Firefly and Artificial Bee Colony Metaheuristic Algorithms for Enhanced Neural Network Prediction Modeling of Sediment Load in Çoruh River 490

Fabrication Of Graded Al2O3-SiC Composites by Spark Plasma Sintering 491

Modelling and Analyses of Collection Process of an Insurance Company via "Business Process Modelling and Simulation" 492

Derin Öğrenme Algoritmalarının Gelecekteki Potansiyel Gelişme Alanlarının Değerlendirilmesi 493

Investigation The Utilization of Rice Husk Ash in The Production of Ceramic Coating Materials 495

Establishing an Urban Mobility Index within the Scope of Sustainable and Smart Mobility 496

Banka Müşterilerinin Dijital Bankacılığa İlişkin Yaklaşımlarının Veri Madenciliği Teknikleri ile İncelenmesi 497

An Experimental Investigation of a New Tensile Strength Test Method for Concrete 499

Synthesis And Piezoresistive Characterization Of Pressure-Sensitive MWCNTS Decorated Electrospun MWCNTS/TPU Nanofibrous Structures 501

Reversing Process of Zoning's Plan The 18th Article Implementation Which is Annulment by a Justice Decision 502

Pervious Concrete - Sustainable Solution for Low Traffic Areas 504

Effect of Construction and Demolition Waste Substitution on the Compressive Strength of Cement Mortars 505

High Strength Special Octagon Profile Production 507

Silajlık Mısır Tarımı ve Sürdürülebilirlik: Kiraz/İzmir Örneği 508

Eczacıbaşı Yapı Gereçleri Sipariş Verileri ile Birliktelik Kuralı Analizi 510

Dye Sensitive Solar Cells and Their Applications 512

Investigation of different Structures of Perovskites as the Absorber layers in the Solar Cells from the Perspective of COMSOL Simulation 513

PV Sistemler için Artan İletkenlik ve Değiştir-Gözle Yöntemlerinin Yapay Sinir Ağı ve PID Kontrolör Kullanılarak İyileştirilmesi 514

Characterization of Hydrochar Product from Pistachio Shell 516

Convertible Wheel/Track Design for Robots 517

Calculation of bulk modulus as a function of pressure in a perovskite-like framework of $[(C_3H_7)_4N]$ $[Mn(N(CN)_2)_3]$ 519

Örnek Bir Bina İçin Yapısal Performans ile Maliyet Arasındaki İlişkinin İncelenmesi 520

Evaluation of Critical Factors in Mechanically Extrusion Based Syringe Driver System Design for 3D Bioprinters 522

Possible Problems with Multi-DOF Force/Torque Sensor Designed and Built Using Cost-Effective Load Cells 524

Evaluation of Liquefaction Potential of Alluvial Deposits in Canakkale Settlement Area by using Shear Wave Velocity 526

Multiple Sclerosis Lesion Prediction using CNN-LSTM 527

The Usability of Hazelnut Shell Agricultural Waste as Filler in Polymer Composites.....528

Arbitrary Amplitude Dust-Acoustic Solitary Structures in Thermally Degenerate Plasmas 529

Self-Gravitational Potential Structures in Dusty Quantum Plasmas.....530

Investigation of Practical Use of Infill Walls with Flexible Connections 531

Investigating The Effects of Chemical Waterproofing Agent Application Techniques on The Permeability of Concrete Specimens.....532

Lung Tumor Detection and Localization on CT scans Using a Deep Learning Algorithm.....533

Examining The Effects of Centrifugal Fan Body Design Changes on Air Flow Rate and Pressure Through Computational Fluid Dynamics 534

Tree Density in Floodplains on Stage-Discharge in Meandering Compound Channels

Amir Ghaderi[1], Mirali Mohammadi[*2], Zeyneb Kılıç[3]

[*]m.mohammadi@urmia.ac.ir, ORCID: 0000-0002-8664-6302
[1] *Department of Civil Eng., Faculty of Eng., Urmia University, Urmia, Iran,*
[2] *Department of Civil Eng., Faculty of Eng., Urmia University, Urmia, Iran,*
[3] *Department of Civil Eng., Faculty of Eng., Adiyaman University, Adiyaman, Turkey*

Abstract: In this study, numerically investigate to understanding how and why trees and tree densities can affect the flow conveyance in the main channel and floodplain? A numerical simulation was done using computational fluid dynamics techniques and FLOW-3D software. To investigate the flow field in the meandering compound channel and the effect of the density of trees and their distribution on the floodplains, the smooth meandering compound channel of Liu et al. (2014) was used. Effects of emergent floodplain tree density on flow phenomena in meandering compound channels has not yet been understood and indeed it requires accurate modelling. Numerically investigated to understanding how and why trees and tree densities can affect the flow conveyance in the main channel and floodplain.

It was shown that, the main channel was more efficient for conveying water when the floodplain was covered with trees compared to the smooth floodplain. This led to a decrease in the conveyance capability in the main channel and an increase in a depth-ratio (Dr) in both channels. The depth ratios in the floodplain with trees are greater than those in the smooth floodplain. For the treed floodplain, the conveying water from the main channel increased by 37% compared to the smooth floodplain. For a given depth ratio, as the density of the floodplain blocks increases, the ratio of the main channel discharge to the total discharge increased, and the discharge conveyance capacity of the floodplains was reduced.

Keywords: *Compound Channel, Depth Ratio, Flood Flow, Stage-Discharge Relationship, Tree Density.*

I. INTRODUCTION

To regulate the slope of the energy line, rivers rarely flow in a straight path and usually have a curved path, which is called as a meandering river. During a flood, the water level exceeds the main channel section of the river and enters its floodplains. Floodplain flows in meandering compound channels influence the main channel flow field and the conveyance of the channels. As most floodplains are roughened to some degree by vegetation or other obstacles, there have been some studies with floodplain roughness elements in meandering compound channels.

In this research, numerically investigate to understanding how and why trees and tree densities can affect the flow conveyance in the main channel and floodplain. As a result of this study, the main channel was more efficient for conveying water when the floodplain was covered with trees compared to the smooth floodplain. The present research work explored the effect of treed floodplains with different tree densities on the channel conveyance capacity. It was shown that, the main channel was more efficient for conveying water when the floodplain was covered with trees compared to the smooth floodplain. This led to a decrease in the conveyance capability in the main channel and an increase in a depth-ratio (Dr) in both channels.

II. MANUSCRIPT CONTENT

A numerical simulation was done using computational fluid dynamics techniques and FLOW-3D software. FLOW-3D software solves the Navier-Stokes–Reynolds equations for the three-dimensional flow of an incompressible fluid using the volume of fluid (VOF) on a gridded domain. To investigate the flow field in the meandering compound channel and the effect of the density of trees and their distribution on the floodplains, the smooth meandering compound channel of Liu et al. (2014) was used. The dimensions of the channel and the data collection areas in the numerical models are the same as those of the laboratory model (see more details, Liu et al. 2014). The three main densities for floodplains were considered sparse, average, and dense scenarios (Figure 1). The sparse scenario in the numerical simulation is like the sparse mangrove cases in practice. The presence of mangrove trees in numerical models was estimated based on the "solid volume fraction" of mangroves. The solid volume fraction per volume unit for cylinders in a mangrove tree association can be estimated using the following equation:

$$\phi = N \times (\pi \times d^2 / 4) \tag{1}$$

where d is the stem diameter and N is the density of mangrove trees. Considering the diameter of 0.05 meters for non-submerged cylinders, the density of a cylindrical arrangement based on the solid volume fraction per square meter for sparse, average, and dense scenarios was obtained as 25, 50, and 100, respectively. 0.049, 0.098, and 0.196 are obtained. The meshing and boundary conditions applied in the domain are shown in Figure (2).

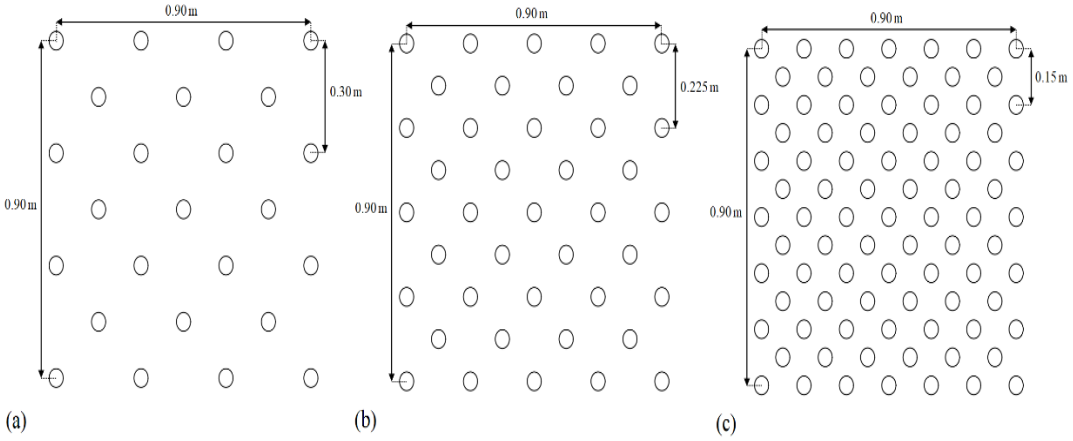


Fig. 1. Distribution of non-submerged cylinders in the density scenarios of the present research
a: Sparse b: Average c: Dense

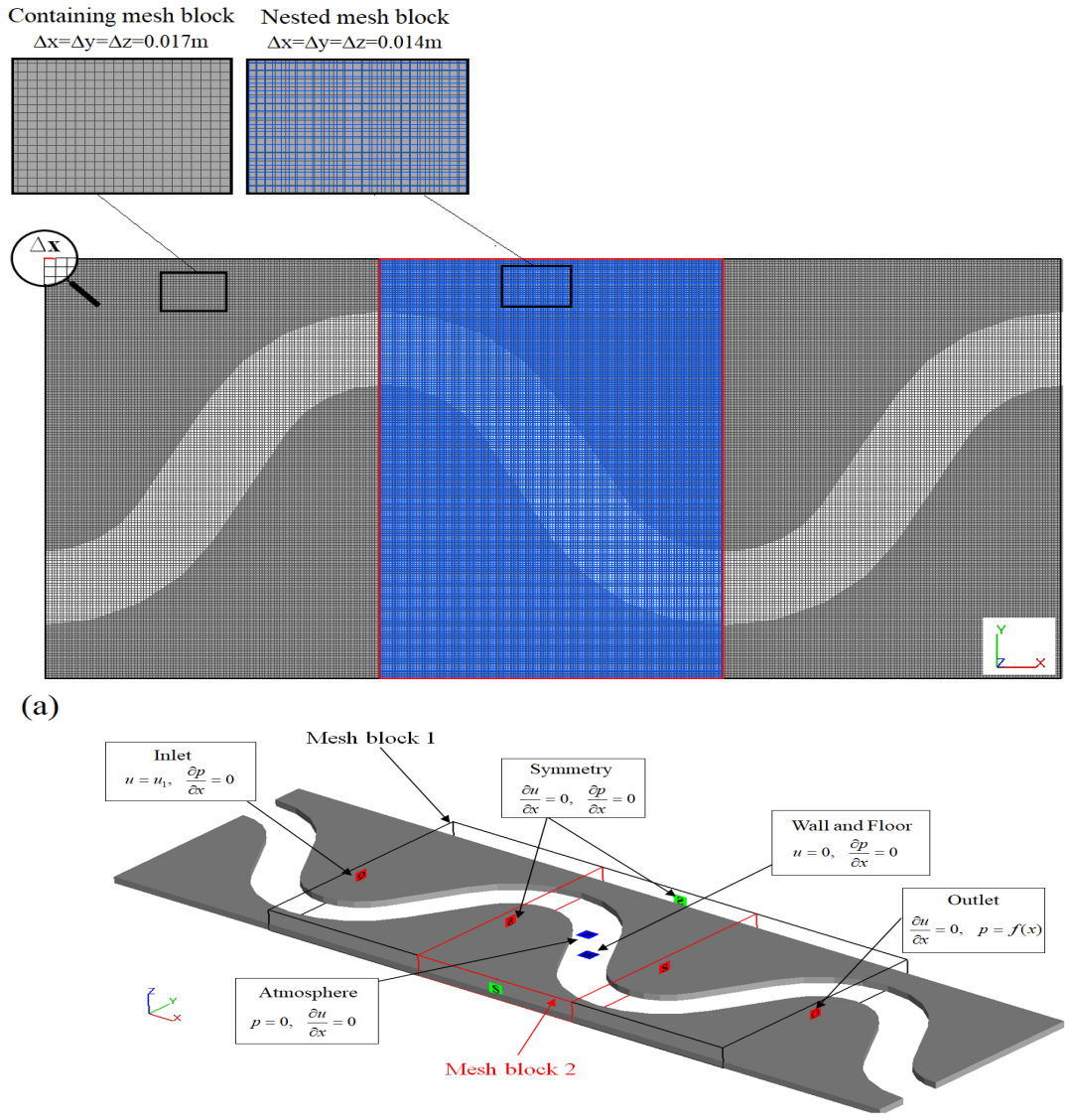


Fig. 2. The solution area in the numerical model a: Meshing b: Boundary conditions

III. RESULT AND DISCUSSION

The determination of stage-discharge curves is critical for flood forecasting in meandering, compound rivers. Figure (3) illustrates the stage-discharge curve for channels with and without trees at three different densities. As shown, the discharge increases with the increase in flow depth in both channels. For a given discharge, trees in the floodplains increase the flow depth. With the increase in tree density, the flow depth increased compared to a smooth floodplain. Dr values in the floodplain with trees are higher than those in the smooth floodplain for a given discharge. With the increase in the density of the trees, Dr values increased by 24% compared to the smooth floodplain, on average.

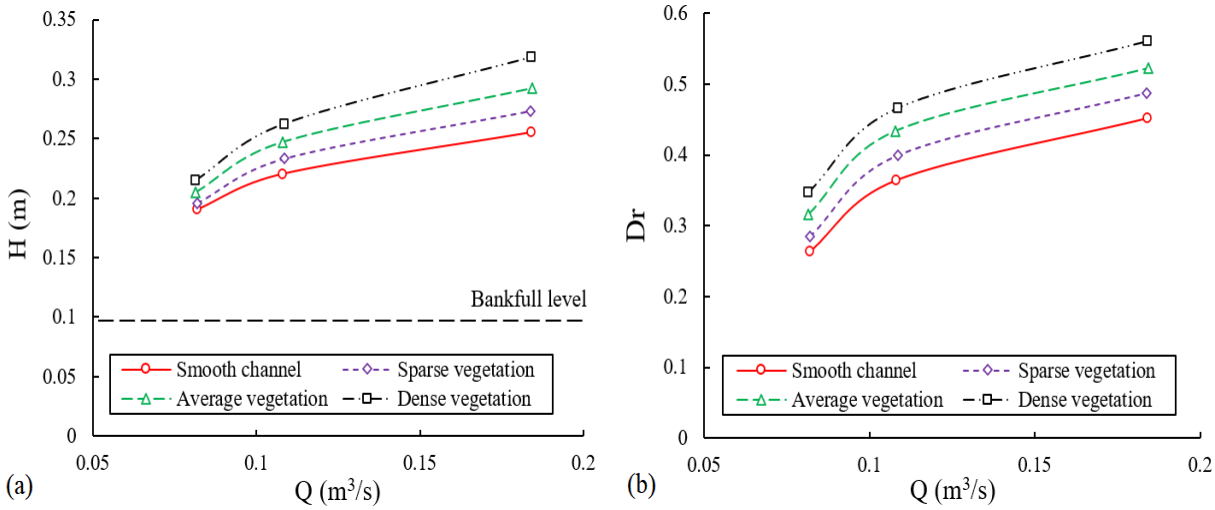


Fig. 3. Stage-discharge curves and discharge variation against depth ratio (a): Q vs H (b): Q vs Dr

The separation of sub-area discharge capacity in the main channel and floodplains reflects the effect of vegetation or trees on the conveyance efficiency. Figure (4) shows the ratio of main channel discharge (Q_{mc}) and floodplain discharge (Q_{fp}) to total discharge (Q_{total}) for the cases of floodplain with and without trees. Under the same conditions, as the total discharge increased, the conveying water in the main channel decreased and the conveying water through the floodplain increased. As tree density increased, the difference was greater. For a given total discharge, the main channel was more efficient for conveying water when the floodplain was covered with trees, compared to the smooth floodplain.

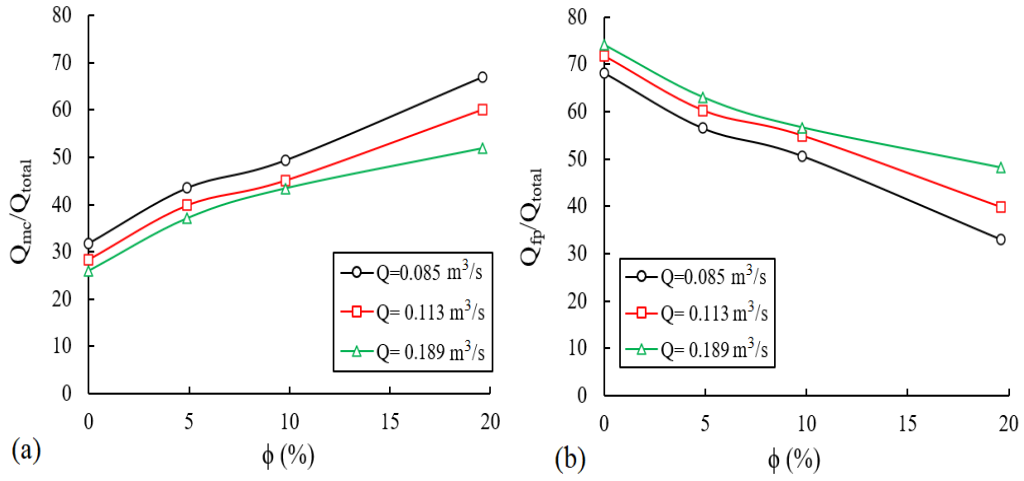


Fig. 4. The effect of tree density on the channel capacity. a: Main channel b: Floodplain

Figure (5) indicates the Q_{mc}/Q_{total} ratio for different sections of both smooth and treed meander channels. It can be observed that, at a given depth ratio (Dr), the existence of trees has increased the conveying of water in the main channel in all sections CS1 to CS7. In addition, the conveying water in the main channel was higher than in the smooth channel due to the high tree density and varied between 30.6 and 36.8%. The conveyance capability in the main channel decreased while Dr increased in both channels.

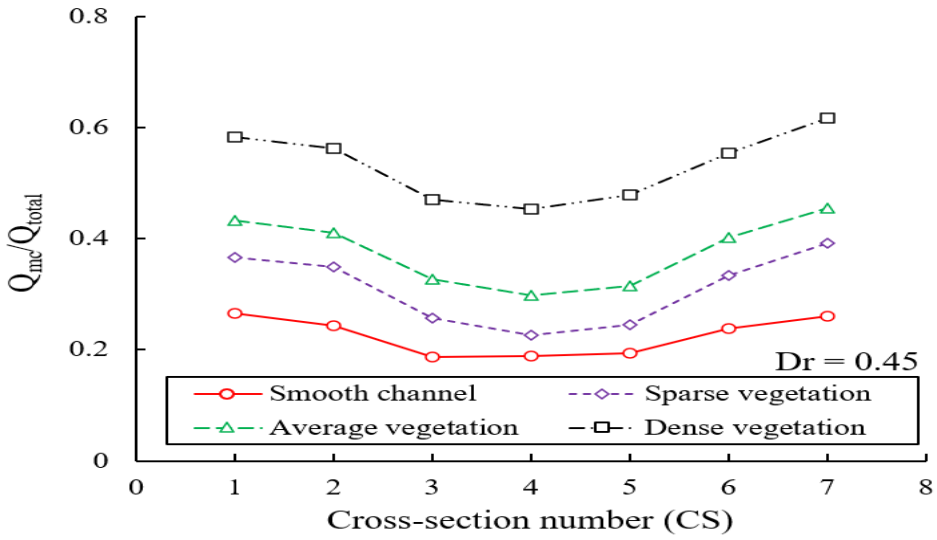


Fig. 5. The ratio of main channel discharge (Q_{mc}) and total discharge (Q_{total})

IV. CONCLUSION

In conclusion, the key findings from this study are as follows:

The depth ratios in the floodplain with trees are greater than those in the smooth floodplain. As the density of the trees increased, Dr increased by 24% on average if compared to the smooth floodplain.

For the treed floodplain, the conveying water from the main channel increased by 37% compared to the smooth floodplain. In addition, the capacity of the meandering compound channel is controlled through the main channel.

For a given depth ratio, as the density of the floodplain blocks increases, the ratio of the main channel discharge (Q_{mc}) to the total discharge (Q_{total}) increased, and the discharge conveyance capacity of the floodplains was reduced. The increase in depth ratio from 0.26 to 0.45 (i.e., low to high value) decreased the capacity of the main channel by 6.9 and 13% for smooth and treed floodplains, respectively.

REFERENCES

[1] Liu, C. Wright, N. Liu, X. and Yang, K. An analytical model for lateral depth-averaged velocity distributions along a meander in curved compound channels, *Advances in Water Resources*, 74, 26-43, 2014.

[2] Pan, Y. Li, Z. Yang, K. and Jia, D. Velocity distribution characteristics in meandering compound channels with one-sided vegetated floodplains. *Journal of Hydrology*, 578, 2019.

[3] Sanjou, M., and Nezu, I. Large eddy simulation of compound open-channel flows with emergent vegetation near the floodplain edge. *Journal of Hydrodynamics*, Ser. B, 22(5), 582-586, 2010.

[4] Naghavi, M., Mohammadi, M., and Mahtabi, G. An Experimental Evaluation of the Blocks in Floodplain on Hydraulics Characteristics of Flow in a Meandering Compound Channel. *Journal of Hydrology*, 127-976, 2022.

[5] Naghavi, M., Mohammadi, M., Mahtabi, G., and Abraham, J. Experimental assessment of velocity and bed shear stress in the main channel of a meandering compound channel with one-sided blocks in floodplain. *Journal of Hydrology*, 129073, 2023.

Wear Mechanisms on Turning of Nimonic C-263 Under Cryogenic Conditions

Muhammad Ikhwan Roslim, Mohamad Ridzuan Jamli, Mohd Amri Sulaiman

*ikhwanroslim@gmail.com, ORCID: 0000-0002-1071-7107
[123]*Faculty of Manufacturing Engineering, Universiti Teknikal Malaysia Melaka, Melaka, Malaysia*

Abstract: In machining, tool wear is a constant factor in failure. Dimensional accuracy and surface finish are significantly influenced by the degree of tool wear. The flank face, rake face and cutting edge of a cutting tool are the three key areas where the tool gradually wears out. Abrasive wear, adhesion wear, diffusion wear, fatigue wear and oxidation wear are some of the wear mechanisms that result in tool wear. Therefore, the present work is carried out to comprehensively investigate the type of wear mechanism present during the turning process of Nimonic C-263 alloy under cryogenic cooling conditions. Cryogenic cooling, employing liquid carbon dioxide as a coolant, offers a promising solution to enhance the machining performance of Nimonic C-263. Nimonic C-263, a superalloy with remarkable strength and low heat conductivity, poses substantial challenges in conventional machining. Conventional machining techniques cause rapid tool wear, lowering the quality of the machined surface. This study uses PVD-coated carbide inserts as the cutting tool during the machining process. The tool wear mechanism on the flank face of the PVD-coated carbide insert is observed using the optical microscope and is analysed using Field Emission Scanning Electron Microscopy (FESEM). The cutting parameters, including cutting speed, feed rate and depth of cut, are designed based on the Design of Experiment and Box Behnken method. Tool wear mechanism is investigated at various cutting parameter combinations. The FESEM analysis reveals that adhesion wear predominantly governs the tool wear mechanism on the flank face of the PVD-coated carbide insert during the machining of Nimonic C-263. Additionally, the presence of Ni, Cr, Mo, and Co on the surface of the carbide inserts signifies the occurrence of diffusion wear. This research emphasises the complexity of wear phenomena and the significance of considering wear mechanisms when developing strategies for improving machining performance in difficult materials like Nimonic C-263.

Keywords: *Tool wear mechanism, Adhesion, Nimonic C-263, Cryogenic*

I. INTRODUCTION

NICKEL- based superalloys are high-performance alloys that are used in a variety of industrial applications due to their excellent mechanical properties. These alloys are composed of nickel and other alloying elements such as chromium, cobalt, molybdenum, and tungsten [1]. Due to their numerous applications in a variety of industries, including the chemical, nuclear, aerospace, and marine industries, nickel-based superalloys have grown in significance during the past several years. These alloys are strong, have great resistance to corrosion and thermal shocks, and have superior mechanical and chemical properties at high temperatures[2]. One of the properties that affects tool wear in Nimonic C-263 is its hot strength. This alloy exhibits excellent hot strength, allowing it to withstand high temperatures without significant deformation. However, Nimonic C-263 is a nickel-based superalloy, however it is difficult to machine because of its poor thermal conductivity, low hot strength, propensity to work harden, and propensity for tool wear. These characteristics speed up tool

wear in cutting zones with high temperatures [3]. Additionally, Nimonic C-263 has a tendency to work harden during machining. Work hardening occurs when a material becomes harder and more resistant to further deformation as it is subjected to mechanical stress. This property makes it challenging to achieve efficient material removal and contributes to increased tool wear [4]. Furthermore, Nimonic C-263 has a high affinity for tool wear due to its composition and properties. The combination of high temperatures, low thermal conductivity, and work hardening tendency accelerates the wear of cutting tools, resulting in rapid tool wear in high-temperature cutting zones [5].

Researchers have investigated a number of strategies to alleviate the difficulties caused by rapid tool wear in high-temperature cutting zones when machining Nimonic C-263. Cryogenic cooling is one method for lowering the cutting zone's temperature. Cryogenic cooling includes cooling the cutting zone with liquid nitrogen or carbon dioxide to lower the temperature and lessen the impact of high-temperature cutting zones on tool wear.

The use of cryogen-like liquefied Nitrogen and Carbon Dioxide as a coolant during metal removal operation is termed as cryogenic machining [6]. Cryogenic machining requires the use of cryogenic coolant directly in the cutting zone to reject heat, hence reducing tool wear and improving surface integrity. A study investigated the cooling capability of liquid nitrogen and carbon dioxide in cryogenic milling. They found that liquid nitrogen was more effective in reducing the temperature at the cutting edge and improving the surface finish [7]. The application of Cryogenic LN2 coolant in turning AISI 1045 steel reduced the cutting temperature to an extent of about 9–34% and 3–17% when compared to wet and CO2 machining conditions, respectively [8]. A study on comparison in carbon dioxide-assisted, MQL and carbon dioxide-assisted, and liquid nitrogen-assisted cryogenic machining in the turning process of AISI 4140 found that liquid nitrogen-assisted cryogenic machining results in a better reduction of tool wear, including flank and nose wear [9]. Hence, in this study, wear mechanisms at the cutting tool face were investigated in turning of Nimonic C-263 under cryogenic condition. One of the objectives of this study was to investigate the wear mechanism of the PVD-coated carbide in turning of Nimonic C-263 under different cutting parameters. A field emission scanning electron microscope was used to detect the tool wear and energy dispersive X-ray spectroscopy technique was employed to study the wear mechanism.

II. METHODOLOGY

The workpiece material chosen for this machining operation was Nimonic C-263 Alloy. The workpiece material had a diameter of 90mm and a length of 150mm and came in a cylindrical shape. The experimental study aims to investigate the turning/lathe operation of Nimonic C-263 using a CNC Lathe Haas ST-20 with a three-axis axis as shown in Fig. 1 The lathe machine has a continuously variable spindle speed, which is a crucial feature in turning operations. Turning machines are commonly used to machine cylindrical workpieces, and cutting tools are used to reduce the diameter of the workpiece.

A cryogenic cooling machine was used to reduce the temperature of the cutting zone in this study investigation. The cryogenic carbon dioxide cooling system was built using a number of tools, including a CO_2 gas tank, a pressure gauge, a pipe and a nozzle. A CO_2 tank with a capacity of 50 litres is employed in this research. Fig. 2 depicts the cryogenic CO_2 setup for the experiment. A steel pipe connects the CO_2 tank to the CO_2 pressure gauge in this experiment. In this experiment, two CO_2 pressure gauges are used; one measures the pressure of CO_2 in the tank, while the other controls the output pressure of CO_2. The cylinder tank holds the CO_2 gas. The CO_2 gas automatically exits the tank as a result of the air pressure inside. In order to limit the uses of the CO_2 gas, the pressure for cryogenic CO_2 was controlled and set at 20 psi. Carbon dioxide CO2 gas was conveyed directly from the tank through a hose.

In the turning experiments, the cutting tools used were PVD-coated (AlTiN) carbide inserts.

These cutting tools had a rhombic shape and included a chip breaker and ISO code (CNGG 120408-SGF 1105) for carbide tips. The cutting tool holder was based on the DCLNR 2020K12 specification.

Utilising the Hitachi SU5000 Field Emission Scanning Electron Microscope (FESEM), the forms of wear and the mechanisms that cause each type of wear were observed in detail as shown in Fig. 3.The FESEM analysis was performed in order to investigate the wear mechanism that influencing tool wear. The SU5000 FESEM is capable to explore the intricate details of wear phenomena, including abrasive wear, adhesive wear, fatigue wear and diffusion wear. In order to ensure that the sample is clean throughout the observation, it is crucial to clean it. The cutting tool PVD-coated carbide was immersed in ethanol for a cleaning procedure employing an ultrasonic bath with high vibration and a 30-minute soak time. A range between 100X and 500X was chosen for the FESEM micrograph's magnification.



Fig. 1. CNC Haas Lathe Machine

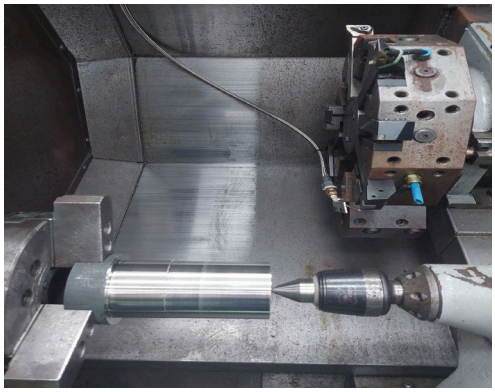


Fig. 2. Cryogenic Cooling Setup



Fig. 3 Hitachi SU5000 Field Emission Scanning Electron Microscope (FESEM)

III. RESULT AND DISCUSSION

The wear mechanism of the cutting tool during machining is an important factor that affects the machining performance and tool life. The most common wear mechanisms that occur during machining are abrasive wear, adhesive wear, diffusion wear, and plastic deformation [10]. These wear mechanisms occur due to mechanical contact between the tool and the workpiece. Abrasive wear occurs when hard particles in the workpiece material scratch the tool surface, causing material removal. Diffusion wear occurs when the workpiece material diffuses into the tool material, causing changes in the tool microstructure and subsequent tool wear. Plastic deformation occurs when the workpiece material deforms the tool surface, causing material removal. These wear mechanisms can significantly affect the tool life and machining performance.

In this study, two different cutting parameter combinations were analyzed using FESEM to observe the adhesion phenomenon on the cutting tools. Fig. 4 (a) illustrates a cutting tool with a cutting speed of 120 mm/s, a feed rate of 0.15 mm/rev, and a cutting depth of 0.4 mm. On the other hand, Fig. 4 (b) depicts a cutting tool with a cutting speed of 60 mm/s, a feed rate of 0.1 mm/rev, and a cutting depth of 0.5 mm.

Adhesion occurs due to molecular attractions between the workpiece material and the cutting tool surface. Various forces and mechanisms, such as intermolecular forces, chemical adhesion, and micromechanical adhesion, contribute to this phenomenon. One critical factor influencing adhesion is the high temperature at the cutting zone, which promotes material transfer and adhesion on the tool surface. FESEM analysis of both cutting tool samples revealed the presence of adhesion on their surfaces. Adhesion wear was evident in the form of material transfer and accumulation on the cutting tools. However, a notable difference in adhesion severity was observed between Fig. 4 (a) and Fig. 4 (b) configurations. Fig. 4 (a) with a higher cutting speed and feed rate demonstrated less severe adhesion compared to Fig. 4 (b), which had lower cutting speed and feed rate. The reduction in cutting speed and feed rate in Fig. 4 (b) resulted in prolonged contact time between the workpiece and the tool surface, facilitating greater material transfer and adhesion. Consequently, the combination of low cutting speed and feed rate leads to an increased total machining time, which can adversely affect the overall machining efficiency. The FESEM analysis presented in this study provides valuable insights into the influence of cutting parameters on adhesion wear in machining processes. The results suggest that optimizing cutting speeds and feed rates can help mitigate adhesion effects on cutting tools, thereby improving their tool life and overall productivity. Additionally, controlling the cutting temperature through proper cooling methods can play a vital role in reducing adhesion-related issues.

Nimonic C-263 exhibits a distinctive characteristic of low thermal conductivity, leading to concentrated heat at the cutting tool chip contact. This concentrated heat causes elevated temperatures and pressures, providing a favorable environment for the diffusion wear mechanism to manifest. Diffusion wear involves a chemical reaction between the Nimonic C-263 and the carbide insert at high temperatures and pressures. The result of this reaction is the gradual diffusion of the tool material into the workpiece material, leading to a loss of material from the cutting tool surface.

The study indicates that at higher cutting speeds, diffusion wear emerges as the primary cause of flank wear. The intensified cutting speeds generate elevated temperatures within the cutting area, exacerbating the conditions conducive to diffusion wear. The FESEM analysis, represented in Fig. 5 and Fig. 6, substantiates the presence of Nickel (Ni), Chromium (Cr), Carbon (C), and Cobalt (Co) on the flank surface of the cutting tool, providing tangible evidence of diffusion wear. The findings of this study align with research by Hoier et al. [11], who investigated diffusion wear during the machining of Inconel 718 and Waspaloy at higher cutting speeds. Their study, similar to ours, revealed diffusion wear as the primary contributor to flank wear. Additionally, Watson et al. [12], conducted a comprehensive examination of

diffusion wear mechanisms in WC-10%Co carbide tools during the dry machining of titanium alloys. Their research also confirmed the dominance of diffusion wear, particularly for uncoated inserts. The consequences of diffusion wear are detrimental to cutting tool performance. As the diffusion process weakens the surface structure of the cutting tool, it ultimately leads to tool failure, negatively impacting machining productivity and product quality.

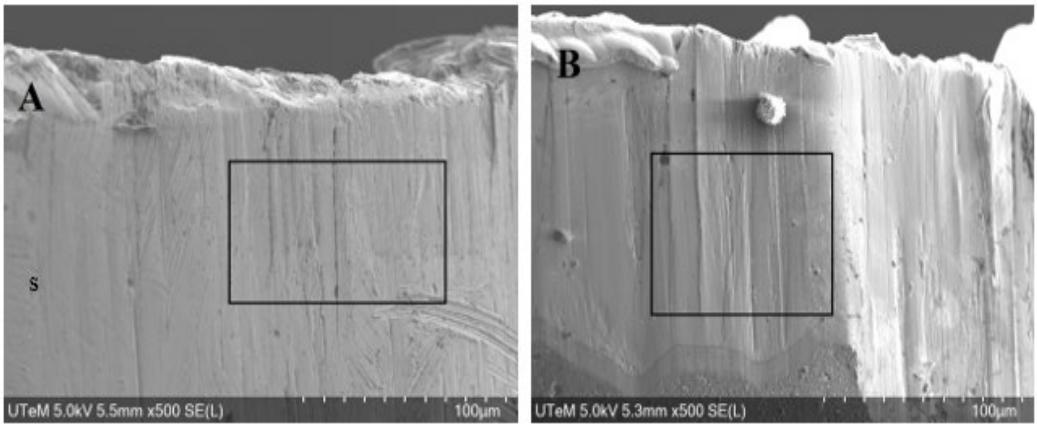
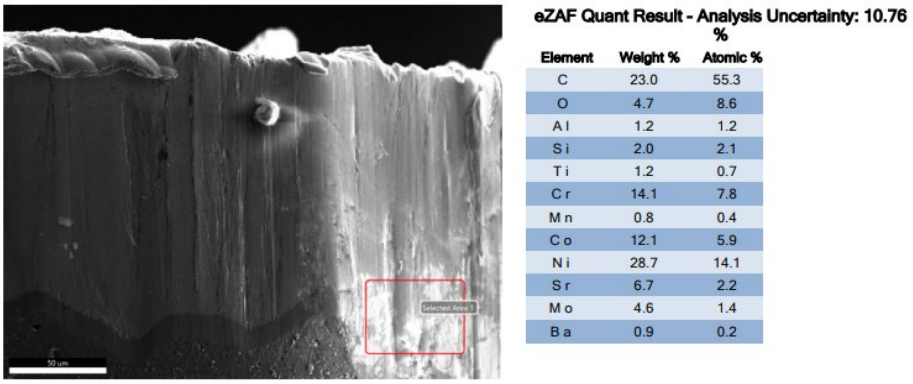


Fig. 4. (a) Cutting Speed: 120 mm/s, Feed Rate: 0.15 mm/rev, Depth of Cut: 0.4 mm (b) Cutting Speed: 60 mm/s, Feed Rate: 0.1 mm/rev, Depth of Cut: 0.5 mm



eZAF Quant Result - Analysis Uncertainty: 10.76 %

Element	Weight %	Atomic %
C	23.0	55.3
O	4.7	8.6
Al	1.2	1.2
Si	2.0	2.1
Ti	1.2	0.7
Cr	14.1	7.8
Mn	0.8	0.4
Co	12.1	5.9
Ni	28.7	14.1
Sr	6.7	2.2
Mo	4.6	1.4
Ba	0.9	0.2

Fig. 5. Element Composition from EDS Analysis

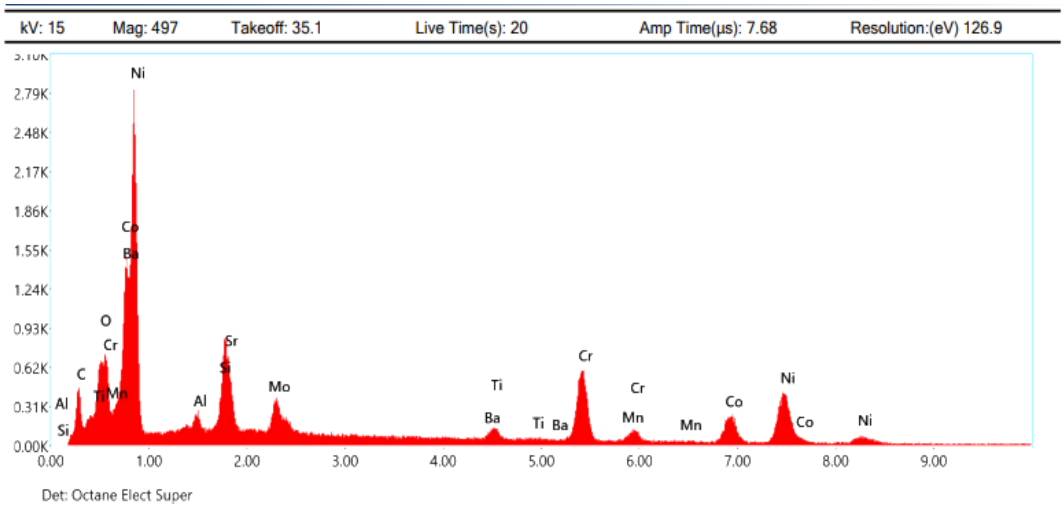


Fig. 6. Element Composition Spectrum

Fracture wear occurs due to the formation of cracks in the cutting insert's material as a result of high stresses and strains during the cutting process. The extreme mechanical and thermal loads experienced by the cutting tool can lead to microcrack initiation and propagation,

ultimately resulting in fracture wear. The study identifies the typical wear pattern observed on the cutting insert as consistent with fracture wear.

Fig. 7 displays the results of FESEM analysis, which provides a detailed examination of the fracture wear pattern on the cutting insert. The observed characteristics align with the typical features of fracture wear, confirming the prevalence of this wear mechanism during the machining process.

To establish the significance of fracture wear in cutting inserts, a study by electron microscopy on tool wear evaluation [13] was referenced. The investigation explored the wear patterns of selected inserts after turning, and the findings indicated that fracture wear is one of the primary wear types observed on cutting inserts. This corroborates our study's findings and highlights the importance of understanding fracture wear for optimizing machining performance.

To gain deeper insights into the fracture wear mechanism, EDS analysis was performed on the fracture area of the cutting insert, as illustrated in Fig. 8 and Fig. 9. The elemental composition revealed the presence of Tungsten (W) in the fracture region, which is a primary element in the composition of cutting tools. The presence of Tungsten supports the notion that the fracture originated from within the tool material itself.

Fracture wear poses significant challenges to cutting tool durability and machining efficiency. Cracks and material loss on cutting inserts can lead to tool failure, necessitating frequent replacements and interruptions in production. Understanding the factors that contribute to fracture wear, such as cutting parameters, tool material properties, and machining conditions, is essential for devising effective mitigation strategies.

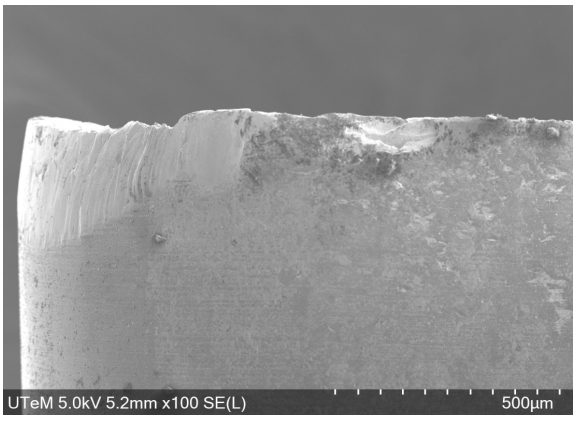
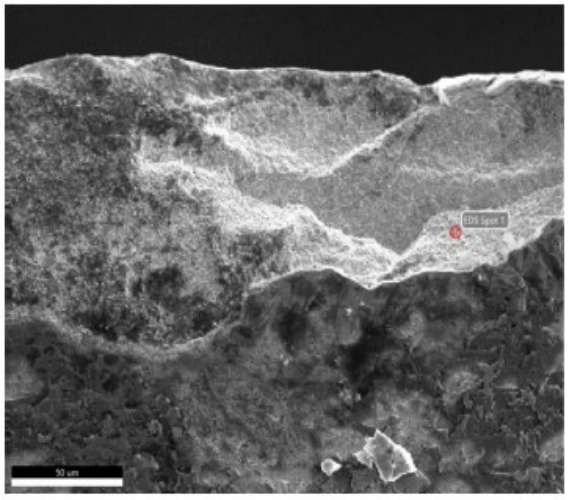


Fig. 7. FESEM Analysis



eZAF Quant Result - Analysis Uncertainty: 11.27 %

Element	Weight %	Atomic %
C	36.6	77.7
O	6.2	10.0
Cr	2.8	1.4
Co	6.3	2.7
Ni	5.1	2.2
W	42.9	6.0

Fig. 8. Element Composition from EDS Analysis

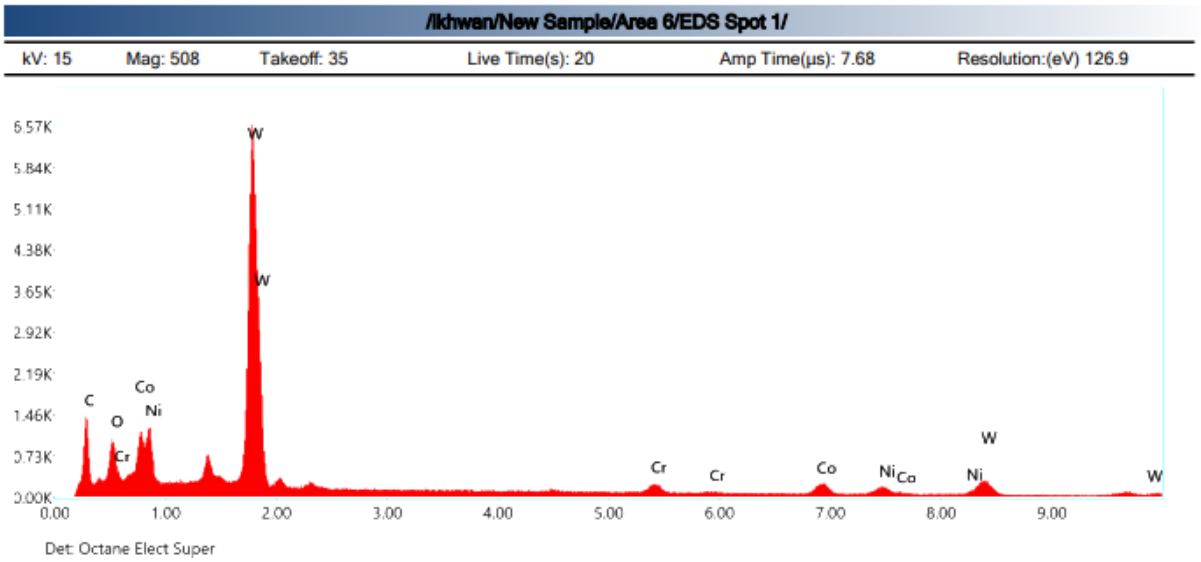


Fig. 9. Element Composition Spectrum

IV. CONCLUSION

The results show that during the machining of Nimonic C-263, adhesion wear dominates the tool wear mechanism on the side face of the PVD-coated carbide insert. Furthermore, the presence of Ni, Cr, Mo, and Co on the carbide inserts' surface suggests that diffusion wear has occurred. This study underlines the complexity of wear phenomena and the significance of taking wear mechanisms into account when formulating plans to enhance machining performance in difficult materials like Nimonic C-263.

The research advances knowledge of the mechanics underlying tool wear during the machining of Nimonic C-263 and sheds light on the efficiency of cryogenic cooling in improving machining performance. The cutting zone temperature can be lowered and the impact of high temperature cutting zones on tool wear can be mitigated using cryogenic cooling, which uses liquid carbon dioxide as a coolant. Cryogenic cooling may enhance dimensional accuracy and surface polish while cutting Nimonic C-263 by minimizing tool wear.

ACKNOWLEDGMENT

The Author would like to thank the Research Management Centre, Universiti Teknikal Malaysia Melaka for funding the publication of this article. This research is supported by the Fundamental Research Grant Scheme, FRGS/1/2020/FKP-COSSID/F00455.

REFERENCES

[1] R. C. Reed and C. M. F. Rae, *Physical Metallurgy of the Nickel-Based Superalloys*, Fifth Edit., vol. 1. Elsevier B.V., 2014.

[2] H. S. Mali and D. R. Unune, *Machinability of Nickel-Based Superalloys: An Overview*. Elsevier Ltd., 2017.

[3] K. Mouralova *et al.*, "Precision machining of nimonic C 263 super alloyusing WEDM," *Coatings*, vol. 10, no. 6, pp. 1–20, 2020, doi: 10.3390/coatings10060590.

[4] C. Ezilarasan, V. S. Senthil Kumar, and A. Velayudham, "Theoretical predictions and experimental validations on machining the Nimonic C-263 super alloy," *Simul. Model. Pract. Theory*, vol. 40, pp. 192–207, 2014, doi: 10.1016/j.simpat.2013.09.008.

[5] B. Koyilada, S. Gangopadhyay, and A. Thakur, "Comparative evaluation of machinability characteristics of Nimonic C-263 using CVD and PVD coated tools,"

Meas. J. Int. Meas. Confed., vol. 85, pp. 152–163, 2016, doi: 10.1016/j.measurement.2016.02.023.

[6] Y. V. Deshpande, A. B. Andhare, and P. M. Padole, "How cryogenic techniques help in machining of nickel alloys? A review," *Mach. Sci. Technol.*, vol. 22, no. 4, pp. 543–584, 2018, doi: 10.1080/10910344.2017.1382512.

[7] F. Pu, D. Grgura, M. Koch, and P. Krajnik, "Cooling capability of liquid nitrogen and carbon dioxide in cryogenic milling Citation for the original published paper (version of record): CIRP Annals - Manufacturing Technology Cooling capability of liquid nitrogen and carbon dioxide in cryogenic mil," vol. 68, pp. 73–76, 2019, doi: 10.1016/j.cirp.2019.03.016.

[8] B. D. Jerold and M. P. Kumar, "Machining of AISI 316 stainless steel under carbon-di-oxide cooling," *Mater. Manuf. Process.*, vol. 27, no. 10, pp. 1059–1065, 2012, doi: 10.1080/10426914.2011.654153.

[9] Y. Kaynak and A. Gharibi, "Progressive tool wear in cryogenic machining: The effect of liquid nitrogen and carbon dioxide," *J. Manuf. Mater. Process.*, vol. 2, no. 2, 2018, doi: 10.3390/jmmp2020031.

[10] R. Wang, D. Yang, W. Wang, F. Wei, Y. Lu, and Y. Li, "Tool Wear in Nickel-Based Superalloy Machining: An Overview," *Processes*, vol. 10, no. 11, 2022, doi: 10.3390/pr10112380.

[11] P. Hoier, K. B. Surreddi, and U. Klement, "Tool wear by dissolution during machining of alloy 718 and Waspaloy: a comparative study using diffusion couples," *Int. J. Adv. Manuf. Technol.*, vol. 106, no. 3–4, pp. 1431–1440, 2020, doi: 10.1007/s00170-019-04805-9.

[12] H. Watson *et al.*, "Author ' s Accepted Manuscript Author ' s Accepted Manuscript," *Prostaglandins, Leukot. Essent. Fat. Acids*, vol. 115, pp. 60–66, 2016, doi: 10.1097/JU.0000000000002945.

[13] N. Nàprstkovà, J. Cais, P. Kraus, and T. N. Van, "Tool Wear Evaluation of Selected Inserts after Turning by Electron Microscopy," *Manuf. Technol.*, vol. 16, no. 5, pp. 74–75, 2016, doi: 10.21062/UJEP/X.2016/A/1213-2489/MT/16/5/1068.

Flow and Heat Transfer Analysis of Obstacles with Different Geometries in a Rectangular Grooved Channel

Selma AKÇAY

selmaakcay@karatekin.edu.tr, ORCID: 0000-0003-2654-0702
Department of Mechanical Engineering, Çankırı Karatekin University, Çankırı, Turkey

Abstract: This study numerically examined the effects of obstacles with different geometries on flow and heat transfer in a rectangular grooved channel. Numerical study was carried out with the help of the ANSYS Fluent commercial program, and the equations were solved using the standard k-ε turbulence model. In the study, the obstacles with three different geometries as square, deltoid and circular were placed in the rectangular grooved channel. The obstacles were positioned in the middle of the rectangular expanding sections of the channel. The results were compared to the grooved channel without obstacles. The surfaces of the grooved channel were maintained at a constant temperature of T_w = 350 K. The working fluid is air. Reynolds number used in the range of 2000 ≤ Re ≤ 10000. Nusselt number (Nu), thermal enhancement (η), friction factor (f), relative friction factor (f_{rel}), and performance factor (PF) were calculated for these parameters. The numerical results were validated with previous study results. To observe the effects of the obstacles on flow and thermal fields, the velocity and temperature distributions were obtained. The results of the simulations demonstrated that the flow and heat transfer were significantly affected by inlet velocity of the channel, the geometries of the obstacles and the channel. According to the findings, while the lowest friction factor occurred in the circular obstacle case, the highest Nusselt number was obtained in the deltoid obstacle case. The heat transfer enhanced 1.83 times in the deltoid obstacle case and at Re = 2000 compared to the channel without obstacles. For all the obstacle cases, the Nusselt number and the pressure drops increased with increasing Reynolds number. The pressure drop for the square and deltoid obstacles was quite close to each other, but quite high compared to the circular obstacle case. Performance factor (PF) dramatically decreased with increasing Reynolds numbers due to the increase in pressure drop.

Keywords: *Rectangular Trough Channel, Circular Obstacle, Square Obstacle, Deltoid Obstacle, Heat Transfer, Turbulent Flow*

I. INTRODUCTION

PASSIVE heat transfer improvement methods have been a research area of interest for a long time. Since these methods do not require additional energy, they are both inexpensive and safe. For this reason, it is widely preferred in heat transfer applications such as, solar air ducts, heating/cooling, heat exchangers, and chemistry processes [1-4]. One of the widely used passive heat transfer enhancement methods is the use of corrugated or grooved channels with different geometries. Many numerical and experimental studies investigated flow and heat transfer in corrugated channels with different geometries [5-10]. The results of these works indicated that corrugated surfaces provide higher thermal performance than straight channels.

Ahmet et al. [11] carried out a numerical work studying the flow and heat transfer in sinusoidal, trapezoidal, and triangular corrugated channels. The highest heat transfer and pressure drop were found the trapezoidal corrugated channels. Zhang and Che [12] investigated

the thermohydraulic performance in different grooved channels (trapezoidal, sinusoidal, triangular, rectangular, and elliptical) and declared that trapezoidal wave profile provide higher heat transfer and friction factor than other channels. Salami et al. [13] found the highest heat transfer in the trapezoidal corrugated channel, while the best thermohydraulic performance was provided in the sinusoidal wavy channel. Ameur and Sahel [14] noticed that heat transfer, and pressure drop decreased in rectangular, triangular, and semicircular wavy channels, respectively. Shahsavar et al. [15] studied the thermal performance of nanofluids in different wavy channels (triangular, trapezoidal, and sinusoidal), and reported that higher heat transfer was obtained in the sinusoidal wave profile. Togun et al. [16] numerically investigated the heat transfer of hybrid nanofluids in a semicircular grooved channel for different modifications of ribs at $10000 \leq Re \leq 25000$. They indicated that the heat transfer increased as the Reynolds number increased, and the highest heat transfer was achieved at $\varphi = 0.02$ particle volume fraction for $Re = 25000$.

Another passive heat transfer enhancement method is the use of elongated surfaces and obstacles added to the channels. The primary purpose of these modifications is to change the flow direction of the fluid, and to increase the heat transfer area [17, 18]. The use of only corrugated surface geometries to increase the heat transfer is very limited. Higher heat transfer rate can be provided by using more than one passive method together. For this reason, obstacles or baffles in different configurations are added to corrugated channels. Although the use of obstacles increases heat transfer, it will increase pumping power due to the blocking in the flow area. The effect of the obstacles added into the channel on the flow and heat transfer have been investigated by many researchers. The study results indicated that the obstacles provide important enhancement in heat transfer along with an increase in pressure drop [19, 20]. Handoyo and Ichsani [21] investigated the effects of delta obstacles on flow and heat transfer in V-type wavy solar air ducts in a numerical study. They examined four different ratios of obstacles (S/H: 0.5, 1, 1.5, 2) using the turbulence model. The obstacles placed in a small spacing (S/H) increased heat transfer and pressure drop. The heat transfer improved from 27.2 when no obstacle used to 94.2 when obstacles added with $S/H = 0.5$. The friction factor increased from 0.0316 at no obstacle to 0.628 at ratio $S/H = 0.5$. Selimefendigil and Öztop [22] carried out a numerical study examining heat transfer under nanofluid flow over a backward facing step with a corrugated bottom wall in the presence of different obstacles placed behind the step was performed. Heat transfer enhanced of 6.66% for the diamond shaped obstacle compared to the corrugated duct without obstacles. Pattanayak et al. [23] investigated the dynamics effects of Brownian particles in obstacle arrays and corrugated ducts. Menni et al. [24] presented a review study investigating improvement of convective heat transfer in smooth air ducts with wall-mounted obstacles in the flow path. Abdelmalek et al. [25] numerically discussed the drag and lift forces on uniformly heated square cylinder in a magnetized corrugated duct. It was reported that the drag force of uniformly heated square cylinder is an increasing function of magnetic field parameter. Alnak [26] numerically analyzed the impacts of the baffle angles on the flow and heat transfer at $1000 \leq Re \leq 6000$ in a duct with V-shaped corrugated lower wall and a flat top surface. It was declared that for $Re = 6000$, the heat transfer at $\alpha = 90^o$ baffle angle was 52.8% higher than at $\alpha=60^o$ baffle angle. Koca [27] numerically examined the heat transfer at different Reynolds numbers in a backward step combined with a triangular wavy surface and found that the highest Nusselt number was obtained on the 5 mm triangular surface at $Re = 20000$. Feng et al. [28] investigated the heat transfer of triangular channel flow with trapezoidal baffles in different arrangements. They noticed that the Nu and friction factor increased by 1.7 times and 3.5 times, and the performance factor by 30% in the trapezoidal baffles, compared to the channel without baffles.

The purpose of the above studies is to design the channel geometry that provides the highest thermal performance while keeping pressure drop to a minimum. Due to the large number of

investigated parameters, new studies are needed. Therefore, this study numerically investigated the flow and heat transfer of obstacles with different geometries (square, deltoid and circular) in a rectangular corrugated channel.

II. NUMERICAL STUDY

A. Geometry of Numerical Model

Fig. 1 shows two dimensional geometric schemes of rectangular grooved channels with details of the obstacles. The maximum and minimum height of the channels are H_1 = 40mm and H_2 = 30mm, respectively. There is an adiabatic straight section of $L_1 = 10H_1$ and $L_3 = 5H_1$ at the inlet and outlet of the channels, respectively. The total length of the grooved section of the channel is L_2 = 500mm. The lengths a and b of the rectangular grooved parts are 20 and 60 mm, respectively. Size of the obstacles is d=15 mm. The channel contains a total of 6 groove sections.

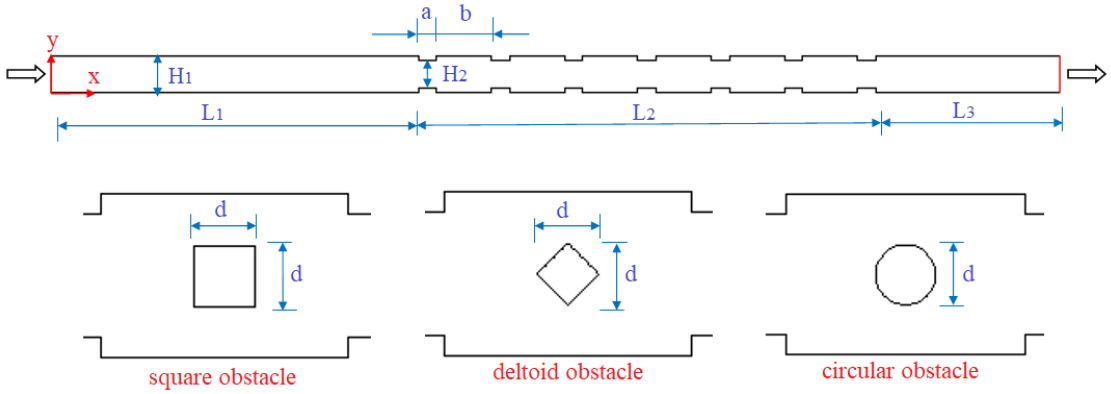


Fig.1. Geometry of the numerical model with details.

B. Governing Equations

In the numerical study, the working fluid is air. The fluid is single-phase, incompressible, and Newtonian type. The flow model is turbulence regime at steady conditions. Fluid properties are constant. Gravity effects and heat transfer with radiation are neglected. According to these assumptions, the governing equations for standard k-ε turbulence model are written by:

$$\frac{\partial}{\partial x_i}(\rho \bar{u}_i) = 0 \quad (1)$$

$$\frac{\partial}{\partial t}(\rho \bar{u}_i) + \frac{\partial}{\partial x_j}(\rho \bar{u}_i \bar{u}_j) = -\frac{\partial \bar{p}}{\partial x_i} + \frac{\partial}{\partial x_j}\left[(\mu + \mu_t)\left(\frac{\partial \bar{u}_i}{\partial x_j} + \frac{\partial \bar{u}_j}{\partial x_i}\right)\right] - \rho\overline{u_i' u_j'} \quad (2)$$

$$\frac{\partial}{\partial t}(\rho c \bar{T}) + \frac{\partial}{\partial x_j}(\rho \bar{u}_i \bar{T}) = \frac{\partial}{\partial x_j}\left[(\Gamma + \Gamma_t)\left(\frac{\partial \bar{T}}{\partial x_j}\right)\right] \quad (3)$$

$$-\rho\overline{u_i' u_j'} = (\mu_t)\left(\frac{\partial u_i}{\partial x_j} + \frac{\partial u_j}{\partial x_i}\right) \quad (4)$$

$$\frac{\partial}{\partial t}(\rho k) + \frac{\partial}{\partial x_i}(\rho k \bar{u}_i) = \frac{\partial}{\partial x_j}\left[\left(\mu + \frac{\mu_t}{\sigma_k}\right)\frac{\partial k}{\partial x_j}\right] + G_k - \rho\varepsilon \quad (5)$$

$$\frac{\partial}{\partial t}(\rho\varepsilon) + \frac{\partial}{\partial x_i}(\rho\varepsilon\bar{u}_i) = \frac{\partial}{\partial x_j}\left[\left(\mu + \frac{\mu_t}{\sigma_\varepsilon}\right)\frac{\partial\varepsilon}{\partial x_j}\right] + C_{1\varepsilon}\frac{\varepsilon}{k}G_k - C_{2\varepsilon}\rho\frac{\varepsilon^2}{k} \quad (6)$$

In this study, flow and heat transfer in the rectangular grooved channel with different obstacle cases were studied for varying Reynolds numbers ($2000 \leq Re \leq 10000$).

Reynolds number (Re) is given by:

$$Re = \frac{\rho u_o D_h}{\mu} \quad (7)$$

where, D_h is hydraulic diameter, ρ is the fluid density, μ is the dynamic viscosity, and u_o is the mean velocity.

The average Nusselt number (Nu) is calculated by:

$$Nu = \frac{h\,D_h}{k_f} \quad (8)$$

where, k_f is the thermal conductivity and h is the heat transfer coefficient.

The convection heat transfer coefficient (h) is calculated by:

$$h = \frac{q''}{\Delta T_{lm}} \quad (9)$$

here q" represents the heat flux and ΔT_{lm} indicates the logarithmic temperature difference.

The thermal enhancement (η) is defined as the ratio of the Nusselt number (Nu_t) in the rectangular grooved channel with obstacles to the Nusselt number (Nu_s) in the rectangular grooved channel without obstacles and is given as:

$$\eta = \frac{Nu_t}{Nu_s} \quad (10)$$

The friction factor (f) calculated based on the pressure difference (ΔP) between the channel inlet and outlet is defined by:

$$f = \frac{2\Delta P D_h}{\rho L u_o^2} \quad (11)$$

The relative friction factor (f_{rel}) is calculated by:

$$f_{rel} = \frac{f_t}{f_s} \quad (12)$$

where, f_s and f_t are the friction factor for grooved channel flow without obstacles and grooved channel with obstacles, respectively.

The performance criteria (PC) can be calculated by:

$$PC = \frac{Nu_t/Nu_s}{(f_t/f_s)^{1/3}} \quad (13)$$

C. Numerical Procedure

The numerical simulations were performed with Ansys Fluent software [29]. The convection parameters were discretized using a second-order upwind scheme. The governing equations

were solved by a segregated implicit iterative scheme. The iterations for the velocity-pressure coupling were solved with the SIMPLE (semi-implicit pressure-linked equation) algorithm. The convergence criterion for energy equations was 10^{-7}, for other residuals was 10^{-5}. As a result of the mesh independence test, it was decided that the 111958 (for the rectangular grooved channel with square obstacle), 115548 (for the rectangular grooved channel with deltoid obstacle) and 101254 (for the rectangular grooved channel with circular obstacle) element numbers are sufficient for the calculations.

D. Boundary Conditions and Validation

The fluid enters the channel at a temperature of $T_i = 300K$ with an average velocity u_o and the inlet velocity is considered uniform. At the exit of the channel, the pressure outlet boundary condition is defined. The straight sections (L_1 and L_3) are described as adiabatic. The rectangular grooved walls of the channel (L_2) are maintained constant at $T_w = 350$ K. The all obstacles have adiabatic and non-slip boundary conditions. In addition, the non-slip boundary condition is defined for all wall surfaces of the channel.

The numerical results of the present study, [30]'s experimental and numerical results were compared. The agreement between the results of this study and the result of the previous study was indicated in Figure 2.

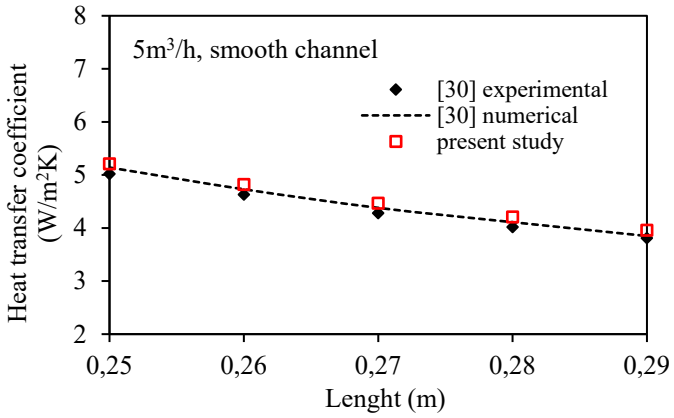


Fig.2. Validation of the numerical study.

III. RESULTS AND DISCUSSION

In this study, the velocity and temperature distributions were obtained in the rectangular grooved channel at varying Reynolds numbers to observe the effect of different obstacles on the flow and thermal fields.

Fig. 3 showed velocity contours for all channel flows at Re = 2000 (Fig. 3a) and Re = 10000 (Fig. 3b). It was observed that the channel geometry, the geometries of the obstacles and the Reynolds number significantly affected the flow fields. It was seen that the flow velocity increased in the sections where the cross-sectional area narrows in the channel flow without obstacles. The velocity of the fluid passing through the narrowing channel section increased and the main flow was divided into two branches due to obstacles. Due to the obstacles, the fluid was directed towards the hot channel surfaces. The contact of the colder fluid with the hot grooved surfaces was ensured. It was seen that the flow rejoins after each obstacle (Fig. 3a). With increasing Reynolds number, momentum and mass transfer in the channel increased and hot grooved surfaces encountered more fluid (Fig.3b). At Re = 10000, it is observed that the stagnant fluid region behind the obstacles is larger than Re = 2000.

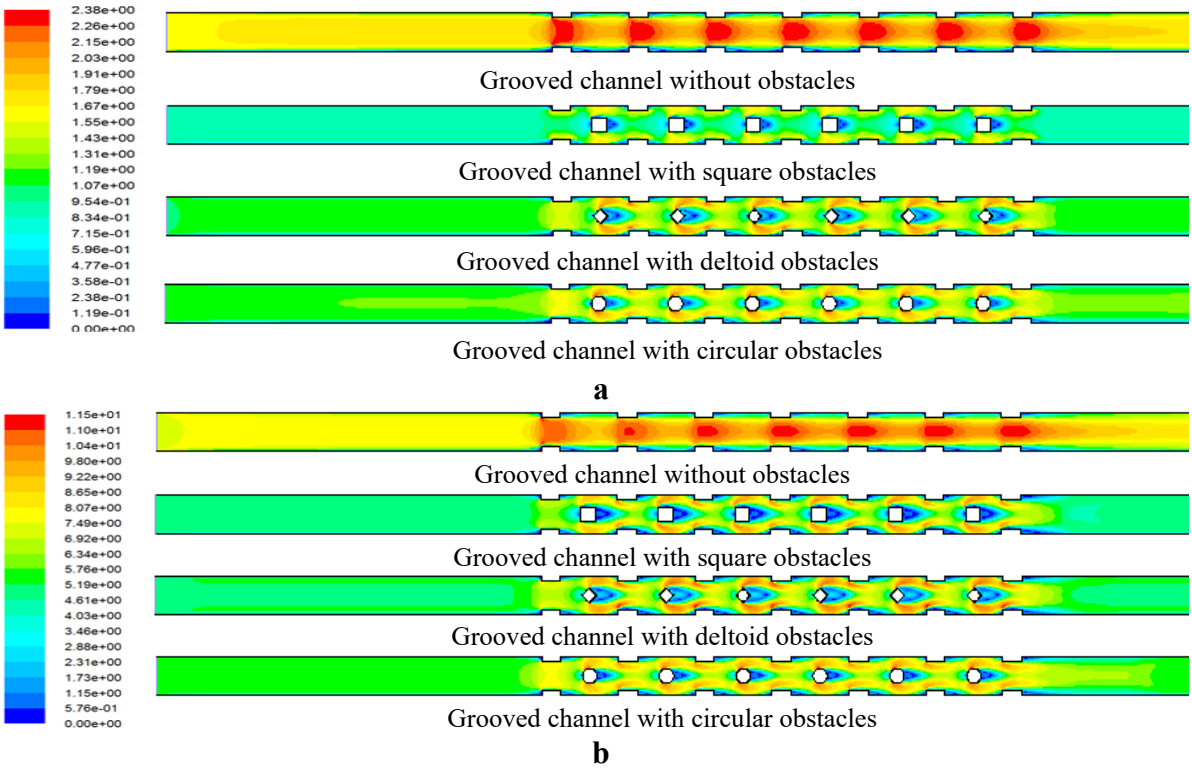


Fig. 3. Velocity contours, a-Re=2000, b- Re=10000.

Fig. 4 indicated the temperature fields for all channel flows at Re = 2000 (Fig. 4a) and Re = 10000 (Fig. 4b). The temperature fields were affected by the channel geometry, the geometries of the obstacles and the Reynolds numbers. At Re = 2000, the temperature gradient is quite high in all channels. It was seen that the temperature gradient decreased highly at Re = 10000. Increasing Re allowed more cold fluid to contact the grooved channel surfaces. The obstacles directing the fluid to the grooved surfaces contributed to the reduction of surface temperature of the channel.

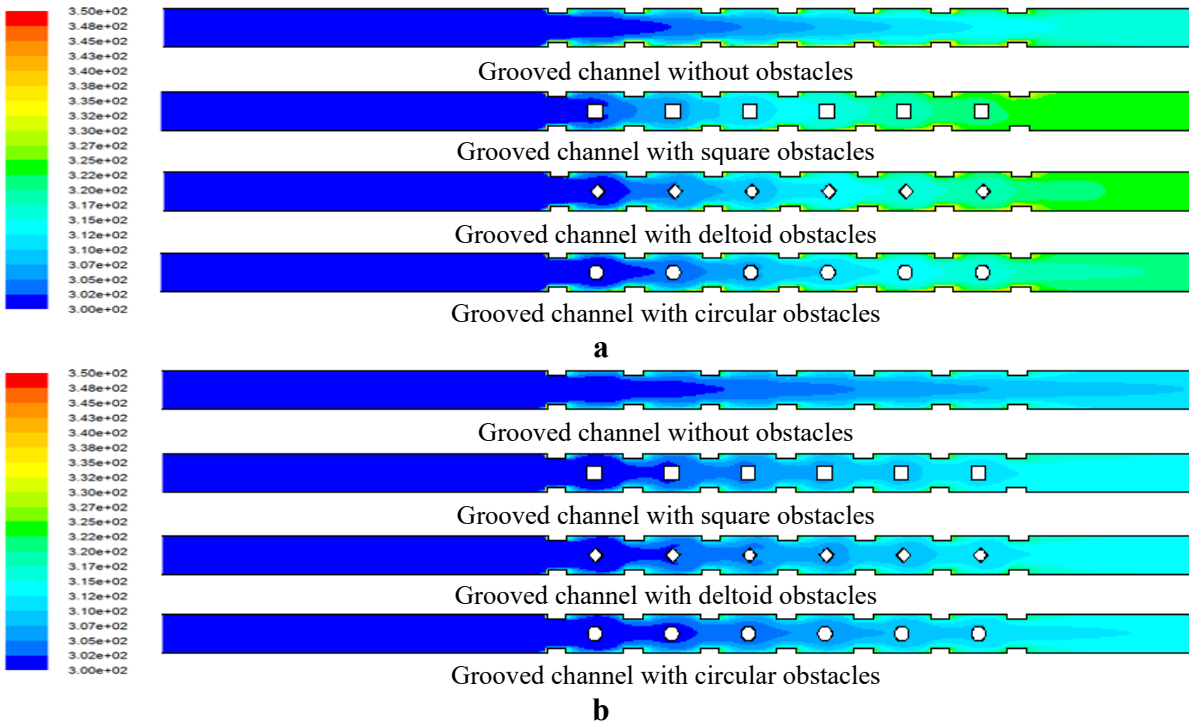
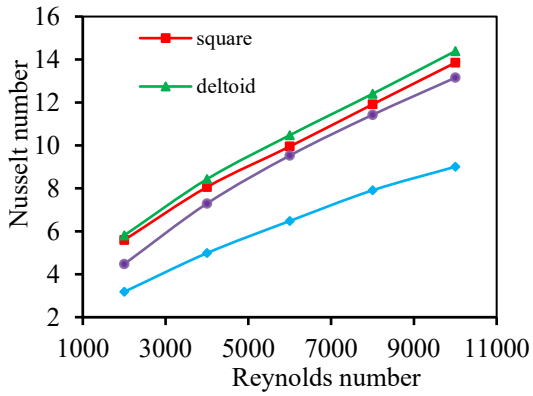


Fig. 4. Temperature contours, a-Re=2000, b-Re=10000.

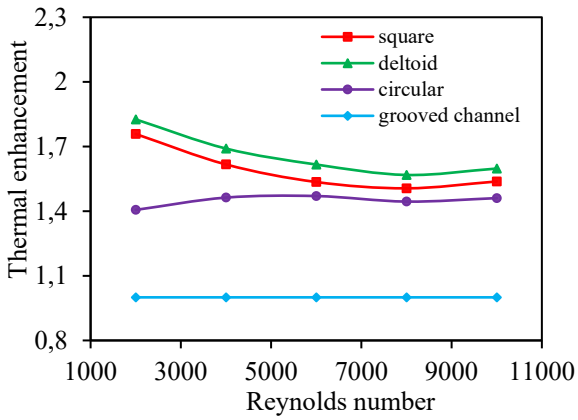
Fig. 5a shows the variation of the Nu with the Re for all channel flows. As the Re increases, the Nu increases. It is seen that the Nusselt number significantly increase in all obstacle cases compared to channels without obstacles. It is observed that the highest Nusselt number is obtained in the deltoid obstacle, followed by the square and circular obstacles, respectively. At Re = 10000, the highest Nu was found to be Nu = 14.39 in the channel with the deltoid obstacle and the lowest Nu was obtained to be Nu = 9 in the channel without obstacle.

Fig. 5b presents the variation of thermal enhancement with the Re. The Nu obtained in the channel flow without obstacles (named grooved channel) is accepted as a reference. Thermal enhancement is obtained by the ratio of Nusselt numbers obtained from the grooved channel with obstacles to grooved channel without obstacles. The thermal enhancement in three obstacle cases was found to be higher than the non-obstacle case. However, in the deltoid obstacle case, this enhancement appears to be greater, and the highest thermal enhancement was obtained to be 1.82 at Re = 2000.

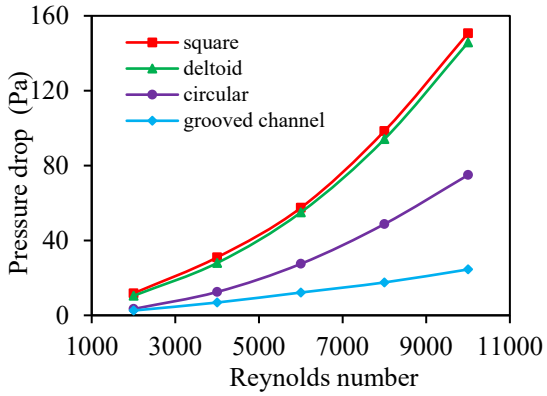
Fig. 5c gives the pressure drop versus Re for all channel flows. It is seen that the pressure drop increases with the Reynolds number because the obstacles in the channel prevent the flow. The highest-pressure drop occurred in the square obstacle case, followed by the deltoid and circular obstacles, respectively. The pressure drop of circular obstacle case is much less than square and deltoid obstacles. At Re = 10000, the highest-pressure drop was 150.68 Pa in the square obstacle case.



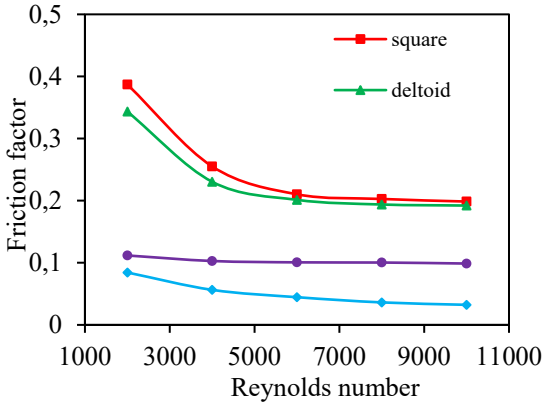
a



b



c



d

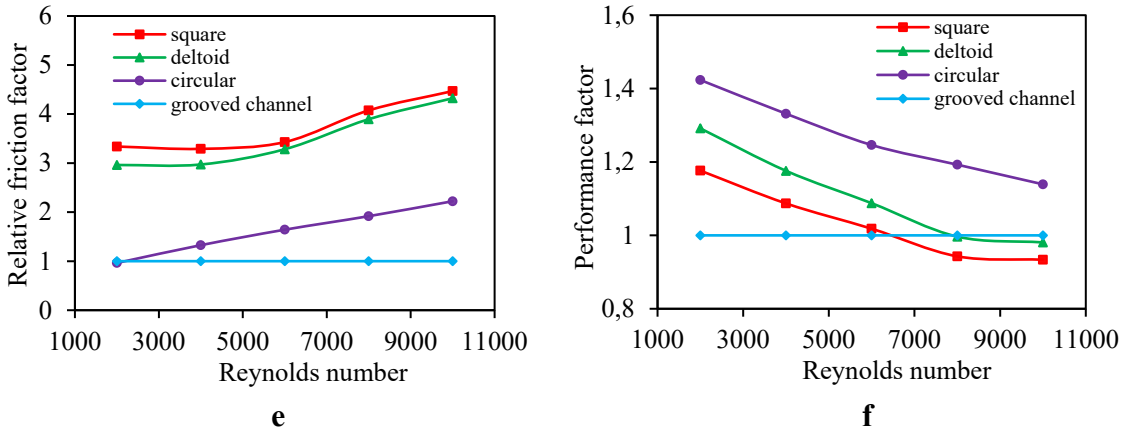


Fig. 5. a- Nusselt number, b- Thermal enhancement, c- Pressure drop, d- Friction factor, e- Relative friction factor, f- Performance factor versus Reynolds number.

The variation of the friction factor calculated according to the pressure drop with the Reynolds number in all channel flows is given in Figure 5d. As the Re increases, the friction factor decreases. The friction factor of circular obstacle case is much less than square and deltoid obstacles. At high Reynolds numbers (Re≥6000), the friction factor obtained for square and deltoid obstacles was found to be quite close to each other.

Fig. 5e presents the variation of the relative friction factor with the Reynolds number in all channel flows. The grooved channel without obstacles was taken as reference. The relative friction factor of circular obstacle case is much less than square and deltoid obstacles. The highest-relative friction factor was found in the square obstacle case.

Fig. 5f indicates the variation of the performance factor with the Reynolds number. The grooved channel without obstacles was considered as reference. As the Re increases, the performance factor decreases. Although obstacles increased the heat transfer, they also caused an increase in pressure drop in the channel. The best performance factor was achieved in the duct with circular obstacles. Because the pressure loss in the case of circular obstacle is lower than the deltoid and square obstacles. In the case of square and deltoid obstacles, the performance factor fell below the reference value at high Reynolds numbers (Re ≥ 8000). The highest performance factor was obtained as 1.42 in the circular obstacle case at Re = 2000.

IV. CONCLUSION

The present study numerically analyzed the effects of obstacles with different geometries on the flow and heat transfer in a rectangular corrugated channel. Simulations were carried out in the range of Reynolds numbers 2000 ≤ Re ≤ 10000. The velocity and temperature contours were obtained in the rectangular corrugated channel to observe the effects of the obstacles with different geometries. The important findings obtained in the study were listed below:

- The flow and temperature contours indicated that the channel geometry, the geometries of the obstacles and the Reynolds number significantly affected the flow and thermal fields.
- For all channel flows, as the Reynolds number increased, the Nusselt number increased. The highest Nusselt number was obtained to be Nu = 14.39 the channel with the deltoid obstacle at Re = 10000.
- The highest thermal enhancement was obtained to be 1.82 in the deltoid obstacle case at Re = 2000.
- The pressure drop of circular obstacle case is much less than square and deltoid obstacles. The highest-pressure drop occurred 150.68 Pa in the square obstacle case at Re = 10000.

- For all channel flows, as the Re increased, the friction factor decreased. The friction factor of the circular obstacle case is much less than square and deltoid obstacles.
- The highest-relative friction factor was found in the square obstacle case compared to the grooved channel without obstacles.
- For all channel flows, as the Re increased, the performance factor decreased. The best performance factor was achieved as PF = 1.42 in the circular obstacle case at Re = 2000.

This study showed that obstacles added in a grooved channel can increase heat transfer with an increase in pressure drop. In future studies, the flow and heat transfer behavior can be investigated by changing the geometry of the obstacles and their placement in the channel by using different grooved channel geometry and the optimum parameters that provide high performance value can be searched.

REFERENCES

[1] T. Alam, R.P. Saini, and J.S. Saini, "Use of turbulators for heat transfer augmentation in an air duct–A Review," Renewable Energy, vol. 62, pp. 689-715, February 2014.

[2] H. Ameur, D. Sahel, and Y. Menni, "Numerical investigation of the performance of perforated baffles in a plate-fin heat exchanger," Thermal Science, vol. 25, no. 5B, pp. 3629–3641.2021.

[3] S.S.M. Ajarostaghi, M. Zaboli, H. Javadi, B. Badenes, and J.F. Urchueguia, "A review of recent passive heat transfer enhancement methods," Energies, vol. 15, pp. 986, 2022.

[4] S. Akcay, "Numerical analysis of hydraulic and thermal performance of Al_2O_3-water nanofluid in a zigzag channel with central winglets," Gazi University Journal of Science, vol. 36, no. 1, pp. 383-397. 2023.

[5] N. Kurtulmus, and B. Sahin, "A review of hydrodynamics and heat transfer through corrugated channels," International Communications in Heat and Mass Transfer, vol. 108, pp. 104307, 2019.

[6] S.R. Nfawa, A.R. Abu-Talib, S.U. Masuri, A.A. Basri, and H. Hasini, "Heat transfer enhancement in a corrugated-trapezoidal channel using winglet vortex generators," CFD Letter, vol. 11, pp. 69-80, 2021.

[7] H. Zontul, H. Hamzah, N. Kurtulmuş, and B. Şahin, "Investigation of convective heat transfer and flow hydrodynamics in rectangular grooved channels," International Communications in Heat and Mass Transfer, vol. 126, pp. 105366, 2021.

[8] E.N. Krishnan, H. Ramin, A. Guruabalan, and C.J. Simonson, "Experimental investigation on thermo-hydraulic performance of triangular cross-corrugated flow passages," International Communications in Heat and Mass Transfer, vol. 122, pp. 105160, 2021.

[9] M.A. Alfellag, H.E. Ahmed, M.G. Jehad, and A.A. Farhan, "The hydrothermal performance enhancement techniques of corrugated channels: A review," Journal of Thermal Analysis and Calorimetry, vol. 147, pp. 10177-10206, 2022.

[10] S. Akcay, "Numerical analysis of heat transfer improvement for pulsating flow in a periodic corrugated channel with discrete V-type winglets," International Communications in Heat Mass Transfer, vol. 134, pp. 105991, March 2022.

[11] M. Ahmed, M. Yusoff, K. Ng, and N. Shuaib, "Effect of corrugation profile on the thermal–hydraulic performance of corrugated channels using CuO–water nanofluid," Case Studies in Thermal Engineering, vol. 4, pp. 65-75, 2014.

[12] L. Zhang, and D. Che, "Turbulence models for fluid flow and heat transfer between cross corrugated plates," Numerical Heat Transfer, Part A: Applications, vol. 60, pp. 410–440, 2011.

[13] M. Salami, M. Khoshvaght-Aliabadi, and A. Feizabadi, "Investigation of corrugated channel performance with different wave shapes," Journal of Thermal Analysis and Calorimetry, vol. 138, pp. 3159-3174, 2019.

[14] H. Ameur, and D. Sahel, "Effect of some parameters on the thermo-hydraulic characteristics of a channel heat exchanger with corrugated walls," Journal of Mechanical and Energy Engineering, vol. 3, pp. 53-60, 2019.

[15] A. Shahsavar, S.S. Alimohammadi, I.B. Askari, and H.M. Ali, "Numerical investigation of the effect of corrugation profile on the hydrothermal characteristics and entropy generation behavior of laminar forced convection of non-Newtonian water/CMC-CuO nanofluid flow inside a wavy channel," Int. Commun. Heat and Mass Transfer, vol. 121, pp. 105117, 2021.

[16] H. Togun, R.Z. Homod, Z.M. Yaseen, A.M. Abed, J.M. Dhabab, R.K. Ibrahem, S. Dhahbi, M.M. Rashidi, G., W. Ahmadi Yaïci, and J.M. Mahdi, "Efficient heat transfer augmentation in channels with semicircle ribs and hybrid Al2O3-Cu/water nanofluids," Nanomaterials, vol. 12, no. 15, pp. 2720, 2022.

[17] Z-X. Li, S-Q. Sung, C. Wang, C-H. Liang, S. Zeng, T. Zhong, W-P. Hud, and C-N. Feng, "The effect of trapezoidal baffles on heat and flow characteristics of a cross-corrugated triangular duct," Case Studies in Thermal Engineering, vol. 33, pp. 101903, May 2022.

[18] S. Akcay, and U. Akdag, "Heat Transfer Enhancement in a Channel with Inclined Baffles under Pulsating Flow: A CFD Study," Journal of Enhanced Heat Transfer, vol. 30, no.5, pp. 61-79, 2023.

[19] C.E. Bensaci, A. Moummi, F.J. Sanchez de la Flor, E.A. Rodriguez Jara, A. Rincon-Casado, and A. Ruiz-Pardo, "Numerical and experimental study of the heat transfer and hydraulic performance of solar air heaters with different baffle positions," Renew Energy, vol. 155, pp. 1231–1244, 2020.

[20] A.T. Inan, H. Koten, and M.K. Kartal, "Experimental comparison and CFD analysis of conventional shell and tube heat exchanger with new design geometry at different baffle intervals," Numerical Heat Transfer, Part A: Applications, 28 Jul 2022.

[21] E.A. Handoyo, and D. Ichsani, "Numerical studies on the effect of delta-shaped obstacles' spacing on the heat transfer and pressure drop in V-corrugated channel of solar air heater," Solar Energy, vol. 131, pp. 47-60, 2016.

[22] F. Selimefendigil, and H.F. Öztop. "Numerical study of forced convection of nanofluid flow over a backward facing step with a corrugated bottom wall in the presence of different shaped obstacles," Heat Transfer Engineering, vol. 37, no.15, pp. 1280-1292, 2016.

[23] S. Pattanayak, R. Das, M. Kumar, and S. Mishra, "Enhanced dynamics of active Brownian particles in periodic obstacle arrays and corrugated channels," The European Physical Journal E, vol. 42, pp. 1-7, 2019.

[24] Y. Menni, A. Azzi, and A. Chamkha, "Enhancement of convective heat transfer in smooth air channels with wall-mounted obstacles in the flow path: a review," Journal of Thermal Analysis and Calorimetry, vol. 135, pp. 1951-1976, 2019.

[25] Z. Abdelmalek, K.U. Rehman, and I. Tlili, "Finite element analysis on uniformly heated square cylinder in a magnetized corrugated channel," Case Studies in Thermal Engineering, vol. 20, pp. 100637, 2020.

[26] D.E. Alnak, "Thermo hydraulic performance study of different square baffle angles in cross-corrugated channel," Journal of Energy Storage, vol. 28, pp. 101295, April 2020.

[27] F. Koca, "Numerical investigation of corrugated channel with backward-facing step in terms of fluid flow and heat transfer," Journal of Engineering Thermophysics, vol 31, no:1, pp. 187-199. 2022.

[28] C-N. Feng, C-H. Liang, and Z-X. Li, "Friction factor and heat transfer evaluation of cross-corrugated triangular flow channels with trapezoidal baffles," Energy & Buildings, vol, 257, pp. 111816, 2022.
[29] ANSYS Inc., ANSYS Fluent User Guide & Theory Guide- Release 15.0, USA, 2015.
[30] Z. Brodniansk´a, S. Kotˇsmíd, "Heat transfer enhancement in the novel wavy shaped heat exchanger channel with cylindrical vortex generators," Applied Thermal Engineering, vol. 220, pp. 119720, 2023.

Sürtünme Karıştırma Kaynağında Üretime Bağlı Sorunlar, Nedenleri ve Çözüm Önerileri

Production-Based Problems, Causes, and Solution Suggestions in Friction Stir Welding

Bekir ÇEVİK

bekircevik@duzce.edu.tr, ORCID: 0000-0002-1209-5364
Biyosistem Mühendisliği Bölümü, Ziraat Fakültesi, Düzce Üniversitesi, Düzce, Türkiye

Özet: Sürtünme karıştırma kaynağının son 30 yılda özellikle metal ve alaşımlarına uygulanabilirliği konusunda yoğun çalışmalar yapılmıştır. Yöntem, otomotiv, makine imalat, yat yapımı, havacılık ve uzay endüstrilerinde gelecek vadetmektedir. Özellikle havacılık endüstrisinde kullanılan birçok yapısal parçanın sürtünme karıştırma kaynağı ile birleştirilmesi konusunda yapılan çalışmalar her geçen gün artmaktadır. Ancak, sürtünme karıştırma kaynağında yanlış takım tasarımı, malzeme türü ve kalınlığı, uyumsuz kaynak parametrelerinin seçimi kaynaklı birleştirmelerde kusurların oluşmasına neden olmaktadır. Bu konuda yoğun çalışmalar yapılmasına rağmen sürtünme karıştırma kaynağında karşılaşılan sorunlara tam olarak çözüm getirememiştir. Bu çalışmada sürtünme karıştırma kaynağı ile birleştirilmesinde karşılaşılan üretime bağlı sorunlar, nedenleri ve çözüm önerileri irdelenmiştir.

Anahtar kelimeler: *Sürtünme karıştırma kaynağı, üretim, kaynak sorunları, çözüm önerileri*

Abstract: In the last 30 years, intensive studies have been carried out on the applicability of friction stir welding, especially to metals and their alloys. The method is promising in the automotive, machine building, yacht building, aircraft, and aerospace industries. Studies on the joining of many structural parts used in the aircraft industry with friction stir welding are increasing day by day. However, in friction stir welding, incorrect tool design, material type, thickness, and the selection of incompatible welding parameters cause defects in welded joints. Despite intensive studies on this subject, it has not been able to provide a complete solution to the problems encountered in friction stir welding. In this study, production-related problems, causes, and solution suggestions encountered in joining with friction stir welding are examined.

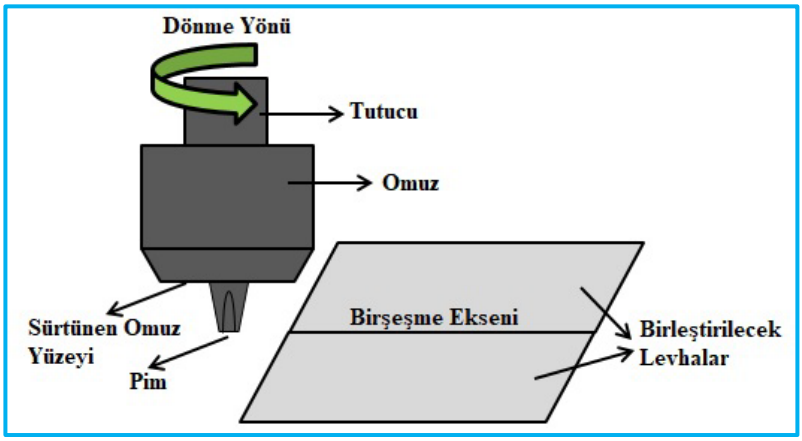
Keywords: *Friction stir welding, production, welding problems, solutions*

I. GİRİŞ

Sürtünme karıştırma kaynak (SKK) yöntemi, İngiliz Kaynak Enstütüsü'nde (The Welding Institute-TWI) 1991 yılında Wayne Thomas tarafından geliştirilmiş ve patenti alınmıştır [1]. Bir katı hal kaynak yöntemi olan SKK, öncelikle alüminyum alaşımlarının ergitmeli kaynak yöntemleriyle birleştirilmesinde karşılaşılan mekanik ve metalürjik özelliklerindeki sorunları geliştirmek amacıyla geliştirilmiştir [2]. Bu yöntemde, kaynak işlemi karıştırıcı uç ve/veya takım olarak isimlendirilen bir eleman ile yapılmaktadır. Karıştırıcı uç omuz ve pim olarak isimlendirilen iki kısımdan oluşur [2,3]. Karıştırıcı ucun pim kısmı kaynak yapılmak üzere alın alına getirilmiş malzemelere daldığında omuz kısmı bu malzemelerin üzerinde çapı genişliğinde yüksek devirde sürtünmekte ve eksenel olarak belirli bir hızda ilerletilmektedir

[4]. Karıştırıcı takımın omuz kısmının levhalara yüksek devirde sürtünmesi esnasında sürtünen yüzeyler arasında ısı meydana gelmektedir. Bu ısı sebebiyle levhalarda özellikle omuzun sürtündüğü çap genişliğinde bir bölgede malzemelerde akma dayanımının düşmesiyle birlikte yumuşama meydana gelmektedir [3-5]. Pim ise malzemedeki yumuşayan bu kısmı yüksek devirde karıştırarak ilerlemesi ile kaynak işlemini gerçekleştirir. Bu işlem esnasında omuz kısmı karıştırılan bölgeye yüksek devirde dönerek baskı oluşturması nedeniyle karıştırılan malzeme kaynak bölgesinde sıkıştırılır [1,2,6].

SKK'da kullanılan karıştırıcı takımlar birleştirilecek malzemelerin türüne ve kalınlığına bağlı olarak yüksek mukavemetli ve yüksek tokluk özelliklerine sahip çeliklerden yapılmaktadır [1,2,6,7]. Genel olarak bu işlem için takım çelikleri tercih edilmekte ve karıştırıcı takım üretimi sonrasında ısıl işlem ile sertlik değerleri yükseltilmektedir [5,6]. Literatürde, bu yöntemde kaynak işlemi için ideal bir sürtünme ısısı oluşturabilmek için karıştırıcı ucun omuz/pim çapı oranının en az üç (3) olması gerektiği ifade edilmektedir [7]. Yöntem ilk uygulanmaya başladığında vida görünümlü uçlar geliştirilmiş ve kullanılmış ancak daha sonra üçgen, vidalı üçgen, kare, düz silindir, düz konik, dişli konik uçlar, dişli konik ve ters kanallı uçlar geliştirilmiş ve denenmiştir [1,2]. Ayrıca pim boyu sabit veya pim boyu kaynak yapılacak malzeme kalınlığına göre ayarlanabilen karıştırıcı takımlar da tasarlanmış ve başarılı bir şekilde denenmiştir [1,2,8-10]. Dolayısıyla bu yöntemde kaynak işleminin başarısı ilk önce birleştirilecek malzemelere uygun bir malzemeden karıştırıcı takım tasarlamak ve üretmektir. Şekil 1'de karıştırıcı takımın şematik resmi verilmiştir.



Şekil 1. Karıştırıcı takımın şematik görüntüsü [11]

Sürtünme karıştırma kaynak yöntemi ile yapılan kaynaklı birleştirmelerin özelliklerini etkileyen birçok faktör ya da kaynak parametresi vardır. Bunlar; karıştırıcı takımın malzeme türü, sertliği ve sürtünme katsayısı, karıştırıcı takımın tasarım özellikleri (omuz çapı, omuzun geometrik özellikleri, pim çapı, pim yüksekliği, pimin geometrik özellikleri), karıştırıcı takımın dönme yönü, karıştırıcı takımın baskı kuvveti, seçilen devir sayısı, karıştırıcı uç ilerleme hızı ve birleştirilecek malzemenin kimyasal ve fiziksel özellikleridir [2,8-12]. Karıştırıcı takımın malzeme türü sürtünme katsayısına dolayısıyla sürtünme ısısına etki etmektedir [8]. Pimin geometrik özellikleri veya uç profili, birleşme bölgesindeki malzemelerin karışma kabiliyetlerini doğrudan etkilemektedir. Bu durumda, malzemelerin plastik deformasyonla karıştırılması ve malzeme akışı, mekanik özellikler üzerinde önemli sonuçlar doğurmaktadır [1,2,5,6,8,9]. Karıştırıcı ucun devir sayısı ve ilerleme hızının her ikisi de kaynağın sürtünme sıcaklığını etkilemekte ve böylece kaynak bölgesinin metalurjik özelliklerinin değişmesine yol açmaktadır [11-15]. Dolayısıyla, sürtünme karıştırma kaynağı ile yapılan birleştirmenin kalitesine birçok faktör etki etmekte ve birleştirilecek malzemelerin türüne ve kalınlığına bağlı olarak seçilen optimum kaynak parametreleri ile başarılı kaynaklı birleştirmeler elde edilebilmektedir.

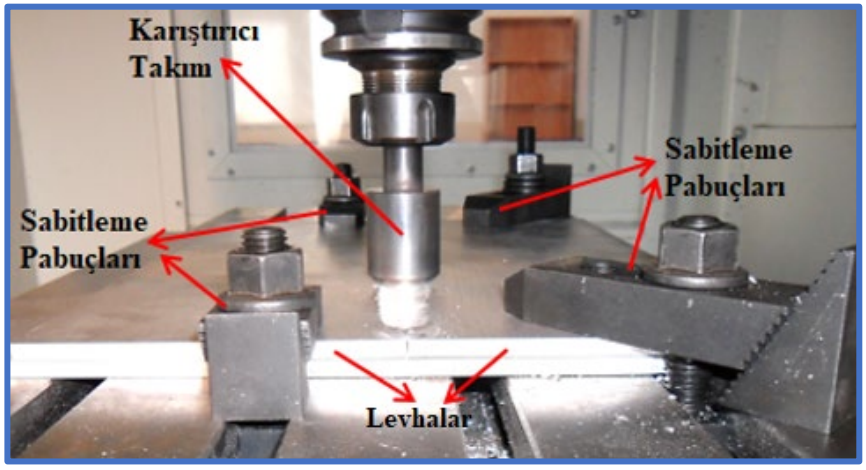
Bu çalışmada, sürtünme karıştırma kaynak yöntemi ile yapılan birleştirmelerde üretime bağlı oluşan kaynak sorunları, nedenleri ve çözüm önerileri araştırılmıştır.

II. SKK'DA ÜRETİME BAĞLI SORUNLAR

SKK işleminde birçok kaynak parametresi kaynak dikişinin kalitesine etki etmektedir. Bu nedenle, her malzemeye ve her kesit kalınlığına uygun kaynak parametrelerini belirlemek zor bir işlemdir. SKK yöntemi ile kaynak işlemi yapılmadan önce bu kaynak parametrelerini ve bu parametrelerin etkilerini çok iyi bilmek gerekir. Aksi takdirde, kaynak parametrelerinin çokluğu kaynaklı üretime bağlı sorunların oluşmasını beraberinde getirmektedir. Kaynak parametrelerindeki uyumsuzluk, karıştırıcı takım tasarımındaki ve üretimindeki hatalar, birleştirilecek malzeme türüne ve kalınlığına uygun seçilmeyen karıştırıcı takım SKK işlemi ile birleştirmede hem birçok yüzeysel makro hatalarına hem de kaynak bölgesinde mikro hatalara neden olmaktadır. Bu hataların oluşması malzeme ve enerji kaybı başta olmak üzere işçilik ve zaman kayıplarına da sebep olmaktadır. Hammadde kaynaklarının hızla tükendiği, enerji ve işçilik maliyetlerinin sürekli arttığı günümüzde üretimden kaynaklanan kayıplar olmadan üretimin sürdürülebilirliği daha da fazla önem arz etmektedir [5-10].

A. Karıştırıcı takımın/pimin kırılması

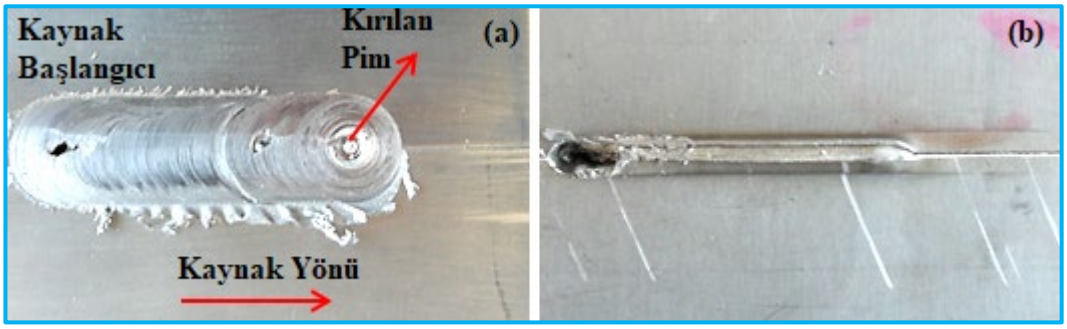
SKK işlemi bir karıştırıcı takım kullanılarak yapılır. Kaynak işlemi esnasında karıştırıcı takım hem burulma momenti hem de eğilme yüklerine maruz kalır. Karıştırıcı takımın omuz kısmı yüksek devirde dönerek sürtünme ısısı oluştururken bu esnada pim kısmı da ısınma nedeniyle yumuşayan metali karıştırma işlevi görür [1,2,8-14]. Şekil 2'de SKK işlemi görülmektedir.



Şekil 2. SKK işlemi

SKK yönteminde ısı girdisine birçok farklı faktör etki eder. Karıştırıcı takımın omuz genişliği, devir sayısı, karıştırıcı takım ilerleme hızı ısı girdisine etki eden en temel faktörlerdir [5-9]. Bunların haricinde karıştırıcı takımın malzeme türü, sertliği, ısı iletim kabiliyeti ve sürtünme katsayısı ile birleştirilecek parçaların türü, ısı iletim kabiliyeti ve sürtünme katsayısı da ısı girdisine etki etmektedir [1,8-11]. Kaynak bölgesinde oluşan ısı girdisi malzemelerin akma dayanımını düşürerek yumuşama meydana getirir. Bu yumuşama ile birlikte karıştırıcı takımın pim kısmı levhalarda yüksek devirde karıştırma yaparak malzeme transferini gerçekleştirir. Bu karıştırma işlemi ile aynı zamanda karıştırıcı takımın ileri hareketi de söz konusu olduğu için kaynak dikişi oluşmaktadır [14-18]. Bu faktörlerdeki uyumsuzluk kaynak yapılacak malzemelerde yeterli yumuşamayı yapamadığında karıştırıcı takım ve pim üzerinde hem burulma momenti hem de eğilme yükleri artar [1,19,20]. Yükleme esnasında pimin kesit alanı karıştırıcı takımın omuz kısmından daha küçük olduğu için kaynak işlemi

tamamlanmadan pim kırılıp kaynak dikişi içerisinde kalabilmektedir. Bununla birlikte kaynak işlemi esnasında karıştırıcı takımın pim kısmının kırılmasına pim boyu uzunluğu da neden olabilmektedir. Şekil 3'te SKK işlemi sırasında karıştırıcı takımın/pimin kırılması sonucu oluşan kaynak kusuru verilmiştir. SKK işleminde çok kalın parçaların tek taraftan kaynak edilmesi sırasında pim boyunun uzunluğu daha fazla eğilme yükleri nedeniyle pimin kırılmasına neden olabilmektedir. Dolayısıyla çok kalın parçaları çift taraftan kaynak yapmak karıştırıcı takımın hasara uğramadan işlevini yerine getirmesi bakımından önem arz etmektedir. Diğer taraftan karıştırıcı takım pim profili de kaynak işlemi esnasında pim kısmının kırılmasına etki edebilmektedir. Diş açılmış pimlerde diş dipleri çentik etkisi yaparak eğilme yükleri altında pimin kırılmasına neden olabilmektedir. Bu durumda hem karıştırıcı takım hasar görür hem de kaynak yapılan parçalar kullanılamaz duruma gelir. Dolayısıyla tüm bu faktörler göz önüne alınarak karıştırıcı takım ve pim kısmı tasarlanmalıdır. Ayrıca, birleştirilecek levhalarda yumuşamaya sebep olabilecek şekilde birbiri ile uyumlu devir sayısı ve karıştırıcı takım ilerleme hızı belirmeli ve karıştırıcı takımın omuz genişliği/pim çapı oranı uygun bir oranda tasarlanıp üretilmelidir.

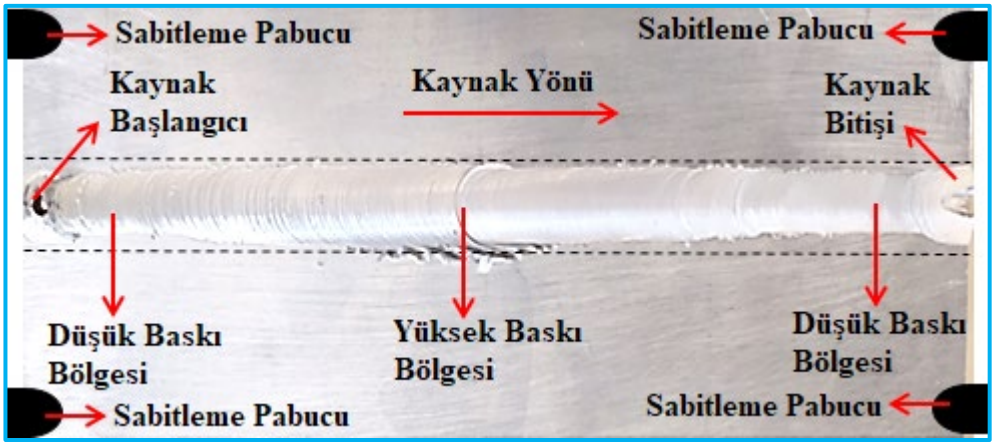


Şekil 3. Karıştırıcı takımın/pimin kırılması, a) Kaynak üst yüzeyi, b) Kaynak alt yüzeyi

B. Levhaların sabitlenme işleminden kaynaklanan problemler

Sürtünme karıştırma kaynak işleminde karıştırıcı takımın yüksek devirde dönmesi ve ilerlemesi nedeniyle birleştirilecek olan levhaların sıkı bir şekilde sabitlenmesi gerekmektedir [1,2]. Aksi takdirde alın alına veya bindirme biçiminde üst üste getirilen parçaların kaynak eksenleri karıştırıcı takımın yüksek devirde dönme ve ilerleme hareketiyle bozulmaktadır. Sıkı bir şekilde sabitlenmeyen levhalarda kaynak işlemi esnasında levhalar arasında açılma meydana gelmektedir [1,5,6]. Bu durumda da hem kaynaklı levhanın ölçü toleranslarında bozulmaya hem de kaynak dikişinin ilerleyen kısımlarında yetersiz birleşmeye neden olmaktadır. Diğer taraftan, sıkı bir şekilde dört tarafından sabitlenen levhaların orta kısmında sehim oluşabilmektedir. Şekil 4'te levhaların sabitlenmesi sırasında orta kısımda oluşan sehimin kaynağa etkisi görülmektedir. Oluşan bu sehim ilk bakışta tespit edilememektedir. Kaynak işleminden önce tüm kaynak parametreleri CNC programına girilmekte ve sabitlenmektedir. Bu parametrelerden bir tanesi de karıştırıcı takımın batma derinliğidir. Karıştırıcı takımın batma derinliği sürtünme esnasında takımın levhaların üstüne sabit bir sürtünme kuvveti oluşturması bakımından önemlidir [1,2,9-13]. Diğer bir deyişle, karıştırıcı takımın batma derinliği kaynak dikişi boyunca değişecek olursa levhalara uygulanan baskı kuvveti de değişecektir. Bu durumda sürtünme ısısı oluşumunun kaynak dikişi boyunca homojen olmasını olumsuz etkileyecektir. Sürtünme ısısının kaynak dikişi boyunca homojen olmaması birleştirilen levhaların mekanik ve metalürjik özelliklerinin lokal olarak değişmesine neden olur. Isı girdisinin artması kaynak bölgesinde mikro tanelerin kabalaşmasına ve ısıdan etkilenen bölgenin genişliğinin artmasına neden olurken, birleştirilen levhaların daha önceki işlemlerinden (yaşlandırma ısıl işlemi, deformasyon sertleşmesi v.s) kazandıkları mekanik özelliklerin de azalmasına neden olmaktadır [9,11,12,14,15]. Bu nedenle ideal bir kaynak dikişinin her tarafında aynı veya birbirine yakın mekanik ve metalürjik özelliklerin olması beklenir. Ancak, sabitleme esnasında levhaların orta kısmında çok az bir sehim oluştuğunda

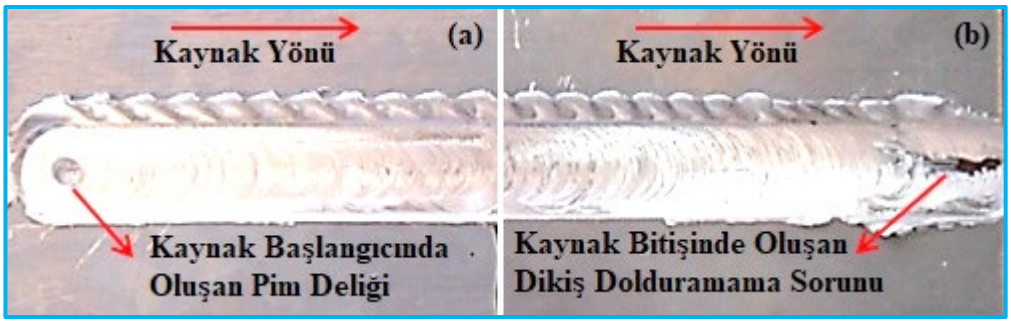
karıştırıcı takım o bölgede daha fazla derine dalacak ve hem sürtünme ısısı oluşumu arttıracak hem de karıştırıcı takımın omuz kısmı daha fazla yumuşayan malzemeyi yan tarafa yığarak ondüle (çapak) oluşumuna neden olacaktır. Diğer taraftan karıştırıcı takım, kaynak dikişinin başlangıç ve bitiş bölgelerinde ise daha az derine batacağından dolayı bu bölgelerde daha düşük sürtünme ısısı oluşacak ve daha az metal yığılması meydana gelecektir. Dolayısıyla, SKK işleminde levhaların sabitlenmesi kaliteli kaynak dikişleri yapabilmek için dikkat edilmesi gereken kaynak süreçlerinden birisidir.



Şekil 4. Levhaların sabitlenmesi sırasında orta kısımda oluşan sehimin kaynağa etkisi

C. Kaynak dikişi başlangıç ve bitiş bölgesinde oluşan problemler

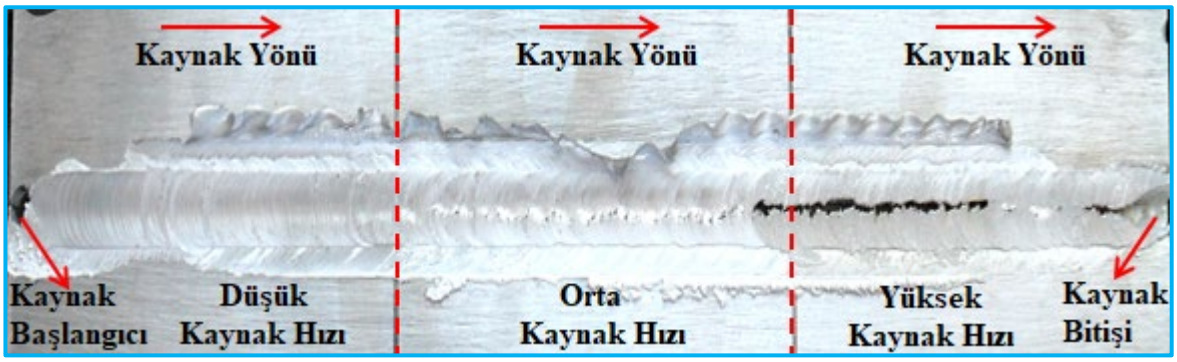
SKK işleminde kaynak dikişinin başlangıç ve bitiş bölgeleri kritik öneme sahiptir. Bu yöntemde ergiyen bir dolgu metali olmadığından dolayı kaynağın başlangıç ve bitiş kısımlarında problemler ortaya çıkmaktadır [1]. Kaynak işlemi daha ön kısımdan başka bir metal üzerinde başlatılıp, bitiş kısmının arkasına konulan bir metal parça üzerinde bitirilebilir ancak bu durum uygulama da her zaman mümkün değildir. Karıştırıcı takımın pim kısmı, kaynak dikişinin başlangıç kısmında pim omuz yarıçapı kadar daha ileride levhalara batar. Bu durumda da omuz yarıçapı kadar olan ön kısımda birleşmeyen bölge kalır. Ayrıca, pimin ilk battığı yerde pim çapı kadar bir delik ya da oyuk kalabilmektedir. Kaynak dikişinin sonuna yaklaşıldığında ise pim karıştırma esnasında son kısımdan transfer edecek yeterli malzeme bulamadığından bu kısımda da eksik kaynak dikişi ya da yığılan metal sorunu oluşur [1,6-13]. Şekil 5'te SKK işleminde kaynak başlangıç ve bitiş bölgelerinde oluşan kusurlar gösterilmiştir. Dolayısıyla, SKK işleminde kaynak dikişinin başlangıç ve bitiş kısımlarında kaynak hataları olarak kabul edilmektedir. Bu kısımların kesilerek çıkarılması kaynak kalitesi bakımından önem arz etmektedir. Ancak bu durumda, kaynaklı birleştirmelerde malzeme israfına, hurda kaybına ve malzeme maliyetlerinin artmasına neden olur. SKK işleminde karıştırıcı takım tasarımı ve üretimi konusunda yoğun çalışmalar olmasına rağmen bu sorun tam olarak çözülememiştir.



Şekil 5. Kaynak başlangıç ve bitiş bölgeleri kusurları, a) Başlangıç bölgesi, b) Bitiş bölgesi

D. Karıştırıcı takım ilerleme hızına bağlı oluşan problemler

SKK işleminde karıştırıcı takım yüksek devirde dönerken belirli bir hızda ileri gitme hareketi yapar. Karıştırıcı takımın yüksek dönme devri ile sürtünen lokal bölgede ısı girdisi oluşur, ilerleme hareketiyle ise lokal bölgede oluşan sürtünme ısısı takımın ilerlediği yön doğrultusunda homojen bir şekilde oluşmasını ve dağılmasını sağlar [11-14,17,18]. Ayrıca, dönme ve ilerleme hareketleri sırasında karıştırıcı takım alın alına getirilen levhalarda malzeme transferini yaparak birleştirme gerçekleşir. Dolayısıyl,a SKK işleminde kaynak doğrultusu boyunca birleşme bölgelerinin yumuşamasına imkan sağlayacak bir dönme devri seçilmelidir. Bununla birlikte seçilen dönme devri ile uyumlu bir karıştırıcı takım ilerleme hızı seçmek de önem arz etmektedir [12,14].

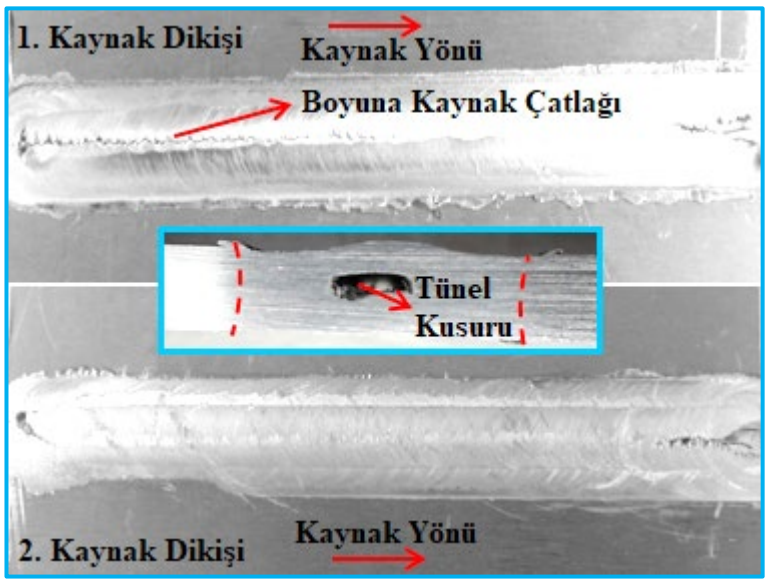


Şekil 6. Karıştırıcı takım ilerleme hızına bağlı oluşan problemler

Şekil 6'da sağ helis vida pim uca sahip karıştırıcı takım ile yapılan birleştirmede artan ilerleme hızına bağlı oluşan üst yüzey kaynak kusurları gösterilmiştir. Düşük karıştırıcı takım ilerleme hızı ile SKK işlemi yapıldığında kaynak dikiş yüzeyinde homojen bir karışmanın olduğu görülmektedir. Karıştırıcı takım ilerleme hızı arttırıldığında kaynak dikiş yüzeyinde gözenekler oluşmuştur. Karıştırıcı takımın ilerleme hızı yüksek olduğunda ise pim kısmı kaynak bölgesinde homojen bir karıştırma ve doldurma işlemi yapamamaktadır. Bu durumda da kaynak dikişi yüzeyinde birleşme boşlukları, makro ve mikro gözenekler oluşmaktadır. Ayrıca, kaynak dikişi içerisinde de mikro ve makro gözenekler, tünel kusurları ve birleşme hataları oluşmaktadır. Dolayısıyla karıştırıcı takım ilerleme hızına bağlı kaynak kusurlarının oluşmaması için devir sayısı ile birlikte karıştırıcı takım ilerleme hızı birleştirilecek parçanın türü, sertliği ve kalınlığı dikkate alınarak seçilmelidir.

E. Çift taraftan yapılan kaynak işleminde oluşan problemler

SKK işleminde kaynak esnasında bir ilave metal kaynak bölgesine gönderilmemektedir. Bu nedenle ergiyerek ve ergiterek kaynak bölgesine dolgu yapılması söz konusu değildir. Kaynak işlemi esnasında karıştırıcı takımın pim kısmı alın alına getirilen levhalara batar, omuz kısmı ise levhaların yüzeyine sürtünür [1-3,5-9]. Pim kısmı geometrik özelliklerine göre farklı malzeme transfer davranışları gösterir. Sağ helis vida profilli pimin saat ibresi yönüne yüksek devirde (soldan sağa doğru) dönüşü esnasında pimin dişleri malzemeleri alt ve yan kısımlardan alarak omuzun sürtünen kısmına ve yanlara doğru taşır ve sıkıştırır [1,2]. Bu durumda levhaların alt kısmını doldurucu bir hareket söz konusu olmadığı için kaynak dikişinin alt kısmında tünel kusuru oluşur [12,20]. Bu kusuru minimize etmek için alın alına getirilen levhalara çift taraftan kaynak yapmak gerekir. Ancak bu durumda da sağ helis vida pim dönme esnasında kesit içerisindeki transfer ettiği malzemeleri sürtündükleri yüzeylere doğru transfer ederek sıkıştırır. Bu durumda da kaynak dikişinin orta kısmında tünel kusuru oluşur. Ayrıca ilk kaynak işleminden sonra levhaya diğer tarafından ikinci kaynak dikişi çekildiğinde karıştırıcı takımın pim kısmının karıştırma hareketi ve baskısı nedeniyle kaynak dikişinden boylamasına çatlağın oluşabilmektedir.

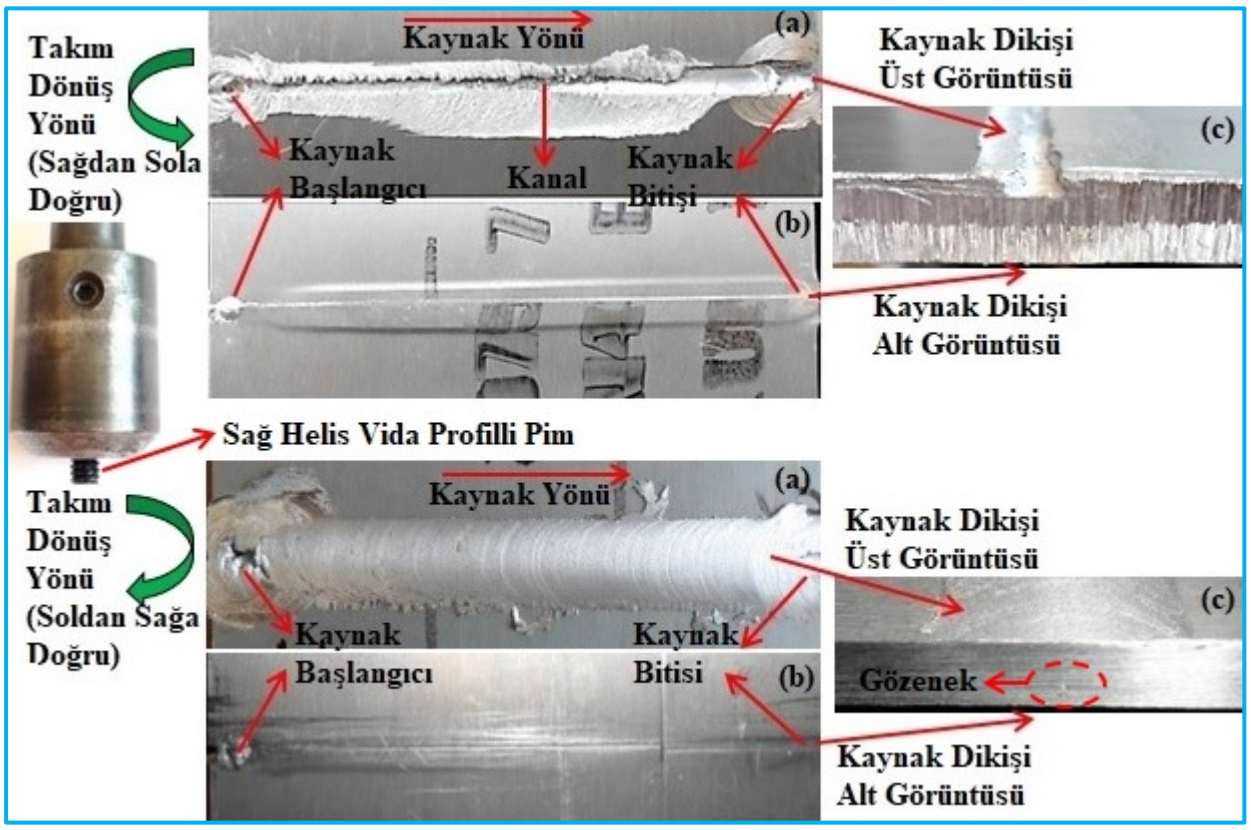


Şekil 7. Çift taraftan yapılan kaynak işleminde oluşan problemler

Şekil 7'de çift taraftan yapılan kaynak dikişinde oluşan tünel kusuru ve boyuna çatlak gösterilmiştir. Levhaların diğer yüzeyinden kaynak yaparken karıştırıcı takımın pim kısmımım ilk kaynağa baskı uygulaması nedeniyle boyuna kaynak çatlağı oluşmuştur. Bu sorunu minimize etmek amacıyla pim profili konusunda yoğun çalışmalar yapılmıştır. SKK işlemi sırasında levhaların alt kısmından üst kısmına doğru malzeme transferini azaltacak pim tasarımları yapılmış ve bazı malzemelerde ve belirli kalınlıklarda başarılı sonuçlar vermiştir [1,14-23]. Özellikle diş derinliği azaltılmış konik vidalı uçlar kaynak dikişinde tünel oluşumunu azaltıcı etkisi görüldüğünde, bu tip pimlerin tasarımları geliştirilmiştir [1]. Whorl™ olarak isimlendirilen ve adını aynı biçimli bir deniz canlısı kabuğundan alan bu karıştırıcı pimler kesik koni biçimli olup plastik akışa uğrayan metali aşağıya doğru yönlendirmek için helisel vida dişleri ihtiva etmektedir [1,2]. Bu pimler konik vida diş formunun yanında iki veya üç kanallı şekilde de üretilmiş ve bu uçlarla malzeme transferi azaltılmıştır. Bununla birlikte, malzeme transferini azaltmak amacıyla MX Triflute™ olarak isimlendirilen pim formları da üretilmiştir. Yapılan araştırmalarda, MX Triflute™ karıştırıcı pimlerin aynı çaptaki alışılmış vida profilli silindirik karıştırıcı pime göre daha az malzemeyi yer değiştirdiği belirlenmiştir. MX Triflute™ karıştırıcı pimlerin konik vida açılmış dişlere ters yönde açılan kanallarla malzeme transferini azaltması sağlanmıştır. Whorl™ türü karıştırıcı pimlerde yer değiştiren malzeme hacmi % 60, MX Triflute™ takımda ise % 70 oranında azaldığı görülmüştür [1]. Bu da tünel kusuru oluşumunu engellemektedir.

F. Karıştırıcı takım dönme yönüne bağlı oluşan problemler

SKK işleminde karıştırıcı takımın dönme yönü sağdan sola doğru (saat ibresi ters yönü) veya soldan sağa doğru (saat ibresi yönü) olmak üzere iki farklı şekilde uygulanabilmektedir [1]. Karıştırıcı takımın dönme yönü omuz kısmının sürtünme ısısı oluşturmasına herhangi bir etkisi olmamasına rağmen özellikle vida dişli silindirik ve konik pimlerin bulunduğu karıştırıcı takımlarda malzeme transfer yönüne etki ettiği için önem arz etmektedir [1,2,21-25]. Şekil 8'de sağ helis vida pime sahip karıştırıcı takım ile yapılan birleştirmede dönme yönüne bağlı oluşan kaynak kusurları gösterilmiştir.



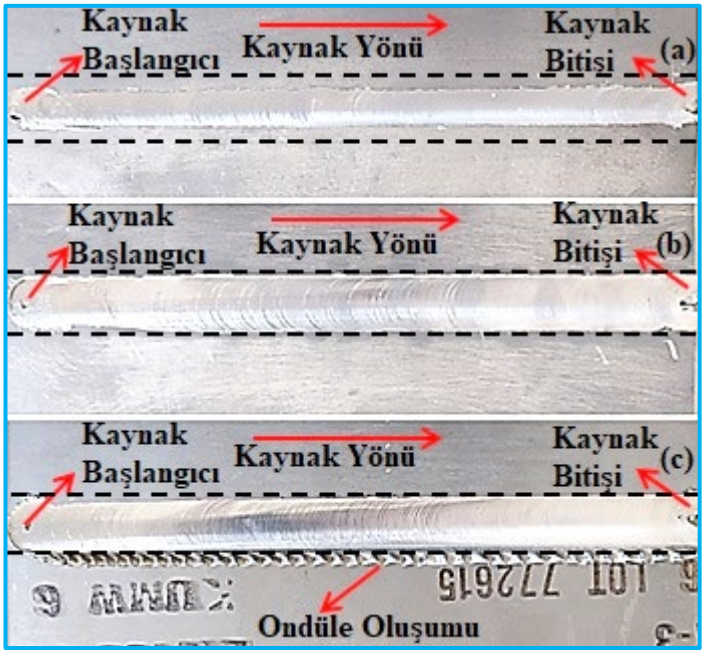
Şekil 8. Karıştırıcı takım dönme yönüne bağlı oluşan problemler, a)üst görünüş, b) alt görünüş, kesit görünüşü

Sağ helis vida pime sahip karıştırıcı takım kullanılarak alın alına sabitlenen levhaların birleştirilmesinde sağdan sola doğru (saat ibresi ters yönü) dönme yönü nedeniyle vida dişli pim levhaların üst tarafından alt tarafına doğru malzeme transferi ve sıkıştırılması yapmaktadır. Bu durumda levhaların üst tarafında ve omuzun sürtündüğü kısımdaki malzeme alt kısımlara doğru taşındığı için pimin hareket ettiği doğrultu boyunca kanal meydana gelir. Ancak, sağ helis vida pim karıştırma sırasında malzemeyi aşağı kısımlara transfer edip sıkıştırması ile kaynak dikişinin alt kısmında tünel kusuru oluşmaz. Ayrıca, karıştırıcı takımın omuz kısmı altına doğru malzeme transferi olmadığı için omuzun yüksek devirde dönerek sürtünmesi ile o bölgede malzeme sıvanması meydana gelmez. Sağ helis vida pime sahip karıştırıcı takım SKK işlemi sırasında soldan sağa doğru (saat ibresi yönü) döndürüldüğünde ise vida dişli pimin malzeme transferi ve sıkıştırması levhaların altı kısmından üst kısmına doğru olur. Bu durumda kaynak dikişlerinin alt kısmında tünel kusuru, mikro ve makro gözeneklerin oluşmasına neden olur. Ayrıca, karıştırılan malzeme levhaların alt kısmından sürtünen karıştırıcı takımın omuz kısmının altına doğru taşındığından dolayı omuz kısmı bu malzemeyi birleştirme bölgesine sıvar ve kaynak dikişini oluşturur. Dolayısıyla, SKK işleminde karıştırıcı takımın dönme yönü, pimin vida dişlerinin helis özelliklerine de bağlı olarak kaynak gölgesinin özelliklerine etki eden önemli bir kaynak parametresidir. Bu nedenle, SKK işleminde takım dönme yönü seçimi karıştırıcı takımın pim profili ve vida diş helis yönü dikkate alınarak uygulanmalıdır.

G. Karıştırıcı takımın basma kuvvetinin neden olduğu problemler

SKK işleminde karıştırma ile birleşmenin gerçekleşmesi için kaynak bölgesindeki malzemelerin yumuşamasına ihtiyaç vardır. Bu yumuşamayı sağlayan etken de ısı girdisidir. SKK işleminde dışarıdan bir ısı verilmediği gibi ark ile de ısıtma söz konusu değildir. Kaynak işlemi için gerekli ısı girdisi karıştırıcı takımın omuz kısmının birleştirilecek levhalara sürtünmesi elde edilir [19,20]. Bu yöntemde ısı girdisine devir sayısı, karıştırıcı takım ilerleme hızı, karıştırıcı takım omuz çapı, karıştırıcı takımın malzeme türü, sertliği, sürtünme katsayısı,

pim profili, karıştırıcı takımın levhalara uyguladığı basma kuvveti ve birleştirilen malzemelerin sürtünme katsayısı ve ısı iletkenlik özellikleri etki etmektedir [24-28]. Bu parametrelerden karıştırıcı takımın basma kuvveti hem ısı girdisine etki eder hem de karıştırma sırasında levhaların yüzeyine transfer edilen malzemeyi omuz kısmının alt yüzeyi ile sıvayarak kaynak dikişini oluşturur [15-22]. Başka bir deyişle, karıştırıcı takımın alın alına sabitlenen levhaların yüzeyinde sürtünme ısısı oluşturabilmesi için uygun bir basma kuvvetinin (ya da batma derinliği) uygulanması gerekir. Şekil 9'da 20 mm omuz genişliğine sahip karıştırıcı takım ile düşük, orta ve yüksek basma kuvveti uygulanarak yapılan kaynak dikişlerinin görüntüsü verilmiştir. Basma kuvveti düşük tutulduğunda düşük sürtünme ısısı oluşur. Bu durum kaynak bölgesindeki malzemenin yeterli seviyede yumuşamasını engeller. Birleştirilecek malzemelerde yeterli yumuşama olmadığında karıştırıcı takımın pim kısmı daha fazla moment ve eğilme yüklerine maruz kalır. Bu durumda pim kısmının kırılmasına neden olur. Pimde kırılma olmadığında ise hareket ettiği doğrultudaki yeterli yumuşama olmamış malzemeyi keserek sıkıştırır ancak homojen bir karıştırma olmadığı için kaynak dikişi kusurlar barındırır. Ayrıca, karıştırıcı takım levhalar üzerine düşük baskı kuvveti yaptığında ya da düşük dalma derinliği ile kaynak yapıldığında kaynak dikişinin üst tarafına omuz yeterli sürtünmeyi yapamadığı için genişliği omuz genişliği kadar bir sıvama işlemi gerçekleşmez (Şekil 9.a). Birleştirilecek malzemelere uygun seçilen bir karıştırıcı takım baskı kuvveti uygulandığında ise düzgün görüntülü kaynak dikişleri elde etmek mümkündür. Bu durumda, omuzun sürtündüğü bölgede sürtünme ile kenara yığılan malzeme miktarı da az olur. Dolayısıyla kaynak bölgesinde malzeme kaybından dolayı kesit incelmesi meydana gelmez (Şekil 9.b). Ancak, karıştırıcı takıma yüksek bir baskı kuvveti uygulandığında karıştırıcı takımın dalma derinliği de artacağından dolayı omuz kısmının altına transfer edilen malzeme daha çok omuzun kenarından kaynak dikişinin yan bölgesine doğru yığılır (Şekil 9.c). Bu duruma ondüle (çapak) oluşumu denir [1-3]. Ondüle oluşumu ne kadar fazla olursa kaynak dikişi yüzeyinden o kadar çok miktarda malzemenin yan tarafa yığılması durumu söz konusudur. Bu durumda da kaynak dikişinin kesitinde çevre bölgelere göre azalmalar meydana gelir ve mekanik özellikleri olumsuz etkiler.



Şekil 9. Karıştırıcı takım baskı kuvvetinin neden olduğu problemler, a) düşük basma kuvveti, b) orta basma kuvveti, c) yüksek basma kuvveti

III. SONUÇLAR

SKK işlemi, özellikle ergitmeli kaynağı zor olan aynı tür veya farklı tür malzemelerin birleştirilmesi için gelecek vadeden bir kaynak yöntemidir. Tüm parametrelerin önceden belirlenip sabitlenebilmesi ve CNC olarak kontrol edilebilmesi operatör/insan kaynaklı sorunların önüne geçmesine imkan tanımaktadır. Ancak, SKK işlemindeki parametrelerin çokluğu bu yöntem ile yapılan kaynak işleminde optimum parametrelerin belirlenmesi ve kullanılmasını gerekli kılmaktadır. Dolayısıyla, kaynaklı birleştirme yaparken oluşan sorunlara tek bir parametrenin etki ettiği söylenemez. Çünkü kaynak işleminde oluşan soruna bir çok parametre birden katkı sağlayabilmektedir. Bu nedenle, SKK işleminde karşılaşılan problemler ve bu problemlere neden olan etkenler iyi bir şekilde bilinmesi gerekir.

KAYNAKLAR

[1] E. Kaluç, E. Taban, "Sürtünen Eleman ile Kaynak (FSW) Yöntemi", TMMOB Makine Mühendisleri Odası Yayınları, Ankara, 2007, pp. 1-86.

[2] N. Kahraman, B. Gülenç, "Modern Kaynak Teknolojisi", Epa-Mat Basım Yayın Ltd Şti, Ankara, 2009, pp. 46-51.

[3] A. Kurt, M. Boz, M. Özdemir, "Sürtünme karıştırma kaynağında kaynak hızının birleşebilirliğe etkisi", Gazi Üniversitesi Mühendislik Mimarlık Fakültesi Dergisi, 19(2), pp. 191-197, 2004.

[4] C. Meran, "Sürtünme karıştırma kaynağı için takım tutucu tasarımı", Gazi Üniversitesi Mühendislik Mimarlık Fakültesi Dergisi, 23(3), pp. 671-679, 2008.

[5] A. Hasçalık, U. Çaydaş, E. Ünal, F. Karaca, "AA5251 alaşımının sürtünme karıştırma kaynağı ile birleştirilebilirliğine uç geometrisinin etkisi", Makine Teknolojileri Elektronik Dergisi, 4, pp. 1-7, 2007.

[6] S. Dalkılıç, "Sürtünme karıştırma kaynağı ve havacılık ve uzay endüstrisindeki uygulama alanları", Havacılık ve Uzay Teknolojileri Dergisi, 5(4), pp. 25-33, 2012.

[7] W. Deqing, L. Shuhua, C. Zhaoxia, "Study of friction stir welding of aluminum", Journal of Materials Science, 39(5), pp. 1689-1693, 2004.

[8] S. Rajakumar, C. Muralidharan, V. Balasubramanian, "Influence of friction stir welding process and tool parameters on strength properties of AA7075-T6 aluminium alloy joints", Materials and Design, 32, pp. 535–549, 2011.

[9] B. Çevik, Y. Özçatalbaş, B. Gülenç, "Effect of tool material on microstructure and mechanical properties of friction stir welding", Materials Testing, 58,3pp. 6–42, 2016.

[10] D. Chouhan, S.K. Pal, S. Garg, "Experimental study on the effect of welding parameters and tool pin profiles on mechanical properties of the FSW joints", Journal of Engineering Research and Applications, 3, pp. 1972-1978, 2013.

[11] A. Yürük, B. Çevik, N. Kahraman, "The design of fatigue test machine and the analysis of fatigue behavior of FSWed dissimilar aluminum alloys. Experimental Techiques, 47, pp. 591-601, (2023).

[12] T. Azimzadegan, S. Serajzadeh, "An investigation into microstructures and mechanical properties of AA7075-T6 during friction stir welding at relatively high rotational speeds", Journal of Materials Engineering and Performance, 19, 1256–1263, 2010.

[13] Z.Y. Ma, A.H. Feng, D.L. Chen, J. Shen, "Recent advances in friction stir welding/processing of aluminum alloys: microstructural evolution and mechanical properties", Critical Reviews in Solid State and Materials Sciences, 43, pp. 269-333. 2018.

[14] B. Çevik, Y. Özçatalbaş, B. Gülenç, "Friction stir welding of7075-T651 aluminium alloy", Practical Metallography, 53, pp. 6–23, 2016.

[15] A. Yürük, B. Çevik, N. Kahraman, "Microstructure and mechanical properties of friction stir welded dissimilar 5754-H111-6013-T6 aluminum alloy joints", Materials Testing, 61, pp. 941-946, 2019.

[16] G. Çam, S. Mıstıkoğlu, "Recent developments in friction stir welding of Al-alloys", Journal of Materials Engineering and Performance, 23, pp. 1936-1953, 2014.
[17] A. Özer, A. Şık, B. Çevik, M. Özer, "The effect of friction stir welding parameters on microstructure and fatigue strength of CuZn37 brass alloys" Kovove Materialy, 55, pp. 107-114, 2017.
[18] B. Çevik, Y. Özçatalbaş, B. Gülenç, "Effect of welding speed on the mechanical properties and weld defects of 7075 Al alloy joined by FSW", Kovove Materialy, 54, pp. 241-247, 2016.
[19] D. Trimble, J. Monaghan, G.E. O'Donnell, "Force generation during friction stir welding of AA2024-T3", CIRP Annals, 61, pp. 9-12, 2012.
[20] K.J. Quintana, J.L.L. Silveira, "Analysis for the forces in FSW for aluminum alloy considering tool geometry and process velocities", Journal of the Brazilian Society of Mechanical Sciences and Engineering, 40, pp. 229, 2018.
[21] B. Çevik, Y. Özçatalbaş, İ. Uygur, "7075 alüminyum alaşımının sürtünme karıştırma kaynağı ile birleştirilmesi", 2.International Conference on Welding Technologies and Exhibition (ICWET'12), 369-376, 23-25 May 2012, Ankara, 2012.
[22] B. Çevik, Y. Özçatalbaş, B. Gülenç, "SKK ile birleştirilen 7075-T651 Al alaşımının mikroyapı ve mekanik özelliklerine devir sayısının etkisi", 3.International Conference on Welding Technologies and Exhibition (ICWET'14), 658-668, May 2014, Manisa.
[23] W. Li, Q. Yang, Z. Zhang, D. Gao, "Effect of weld curvature radius and tool rotation direction on joint microstructure in friction stir welding casting alloys", Materials & Design, 53, pp. 124-128, 2014.
[24] S.M. Chowdhury, D.L. Chen, S.D. Bhole, X. Cao, "Effect of pin tool thread orientation on fatigue strength of friction stir welded AZ31B-H24 Mg butt joints", Procedia Engineering, 2, pp. 825-833, 2010.
[25] A.K. Jassim, D.Ch. Ali, A. Barak, "Effect of tool rotational direction and welding speed on the quality of friction stir welded Al-Mg alloy 5052-O". Journal of Engineering and Applied Sciences, 13, pp.2352-2358, 2018.
[26] C.S. Terra, J.L.L. Silveira, "Models for FSW forces using a square pin profile tool", Journal of Manufacturing Processes, 68, pp.1395-1404, 2021.
[27] S. Memon, D. Fydrych, A.C. Fernandez, H.A. Derazkola, H.A. Derazkola, "Effects of FSW tool plunge depth on properties of an Al-Mg-Si alloy T-joint: thermomechanical modeling and experimental evaluation", Materials, 14(16), pp. 4754, 2021.
[28] D.G. Hattingh, C. Blignault, T.I. van Niekerk, M.N. James, "Characterization of the influences of FSW tool geometry on welding forces and weld tensile strength using an instrumented tool", Journal of Materials Processing Technology, 203, pp. 46-57, 2008.

Comparison of Cooling Efficiency of Conventional and Conformal Cooling Channels in Plastic Injection Cycle

Burak Erkan[1*], İbrahim Özkul[1], F. Deniz Beliç[1*], Ezginaz Karamahmutoğlu[1]

[*]deniz.belic@karelkalip.com.tr, ORCID: 0000-0001-7003-3682
[1]*Karel Kalıp Sanayi A.Ş., İstanbul, Türkiye*

Abstract: Plastic materials are used in almost all areas of daily life due to their advantages such as being cheap and easy to process, low density, low thermal and electrical conductivity, transparency, wide color options, corrosion resistance and being reprocess able. Since plastics can become fluid with heat, they are suitable materials for mass production. Mass production techniques can be counted as plastic injection molding, extrusion molding, blow molding and vacuum molding. The injection molding process is known as forcing the plastic material into the mold cavity in the form of the part to be produced. After the cavity is filled with molten plastic, it cools and solidifies, and then the mold is opened, and the plastic part is taken out. Optimum properties of plastic parts can be obtained with the right mold temperature and efficient use of the cooling system. The cooling step can make up 80% of the total cycle of an injection molding process. Productivity will increase by cooling the mold to the expected temperature because of efficient cooling. On the other hand, defects such as slump marks, differential shrinkage, internal thermal residual stress and distortion can be reduced by balanced cooling. In the study, the cooling cycle in the plastic injection cycle of a sample cover piece with a shaped surface and deep rib structure designed to represent complex shaped geometries used in the automotive or white goods industry was simulated by Autodesk Moldflow Insight software.

Keywords: *Plastic injection, Conventional cooling system, Conformal cooling system*

I. INTRODUCTION

Plastic materials are used in almost all areas of daily life due to their advantages such as being cheap and easy to process, low density, low thermal and electrical conductivity, transparency, wide color options, corrosion resistance and being reprocess able. Since plastics can become fluid with heat, they are suitable materials for mass production. Mass production techniques can be counted as plastic injection molding, extrusion molding, blow molding and vacuum molding [1].

The injection molding process is known as forcing the molten plastic material into the mold cavity in the form of the part to be produced, as seen in Figure 1. After the cavity is filled with molten plastic, it cools and solidifies, and then the mold is opened, and the plastic part is taken out. It is a popular process for the manufacture of plastic products today, as many parts can be easily produced with injection molding. Products throughout the process are highly reproducible, require very little finishing, and have very low labor costs compared to the cost of parts [3].

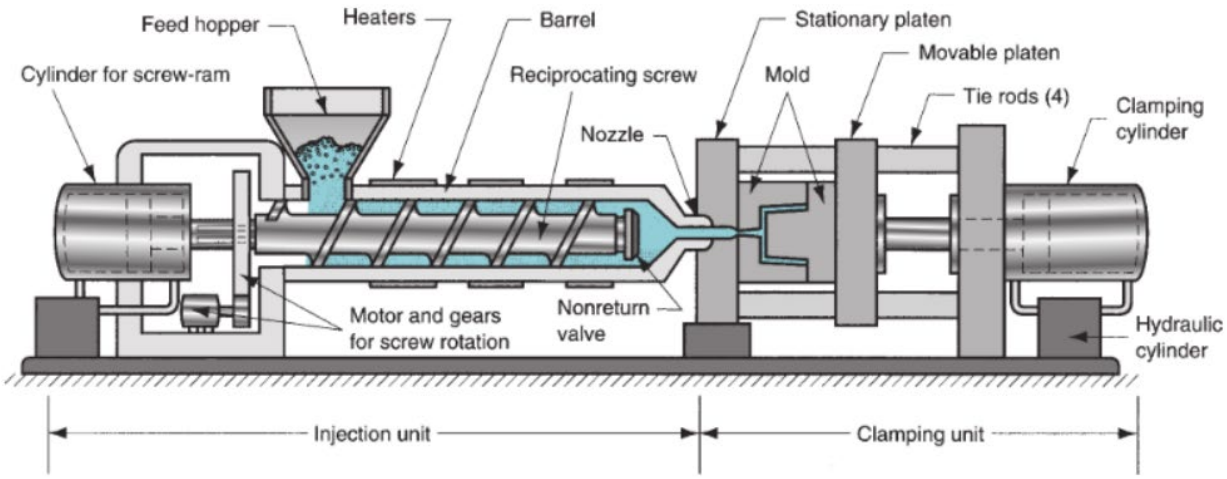


Figure 1. A section view of plastic injection molding machine [2].

Production with plastic injection requires the use of molds. These molds are one of the most important components in the production of a plastic part because they directly affect the cycle time and product quality. Optimum properties of plastic parts can be obtained with the right mold temperature and efficient use of the cooling system [4].

The cooling process plays an important role in determining both productivity and part quality. The cooling stage can make up 80% of the total cycle of an injection molding process. Productivity will increase by cooling the mold to the expected temperature because of efficient cooling. On the other hand, defects such as flow marks, differential shrinkage, internal thermal residual stress and distortion can be reduced by balanced cooling [5].

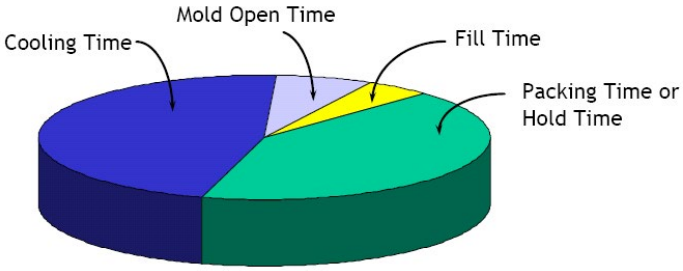


Figure 2. Time allocation in one cycle of injection molding [3]

The cooling of plastic injection molds is done by passing cold water through the channels passing around the mold cavity and removing the heat on the mold. The most common method for cooling the mold plates is to drill the mold plates to form a closed water circuit. This method is preferred because it is cheap and practical. Unnecessary hole outlets are closed with plugs after drilling. There are two types of connection methods of cooling channels used for cooling the planar mold plates. In the serial connection, the water entering from a single inlet follows a single flow path to the outlet. In this connection type, pressure losses increase due to the lengthening of the total flow path. In the parallel connection type, the water entering from a single inlet is divided into multiple flow branches within the channels. In parallel connection type, pressure losses are lower along the flow.

In the cooling process, it is desired that all parts of the plastic material cool with an equal cooling rate. The fact that the solidification rate is variable in different regions causes shrinkage and distortion on the plastic part. The cooling phase is very critical as it directly affects the production speed and product quality by influencing the cycle time.

The commonly used cooling process is provided by cooling channels obtained by perforating

the mold plate close to the mold cavity. Although this method is suitable for linear mold cavity surfaces, it does not provide regular and homogeneous cooling to parts with complex surfaces. A cooling system with a short cooling time in which the uniform temperature distribution is not good or a cooling process with a good uniform temperature distribution but taking a long time are not preferred. The fact that the distance between the mold cavity and the cooling channel changes according to the regions causes the heat transfer to be different in different regions. In order to increase the cooling efficiency, conformal cooling channels that follow the cavity in harmony with the cooling channels are another preferred channel type [6].

Cooling channels in line with the development of additive manufacturing technology mean that the coolant flow can follow the geometry of the molded part, thereby efficiently transferring heat from the mold cavity to the cooling channel. Another additional advantage of conformal cooling channels is the reduction of cooling time as well as the improvement of the surface temperature distribution of the part. Efficiency in the cooling process is then achieved by designing an optimum channel system that maximizes the thermal exchange process between the part and the coolant flow [4].

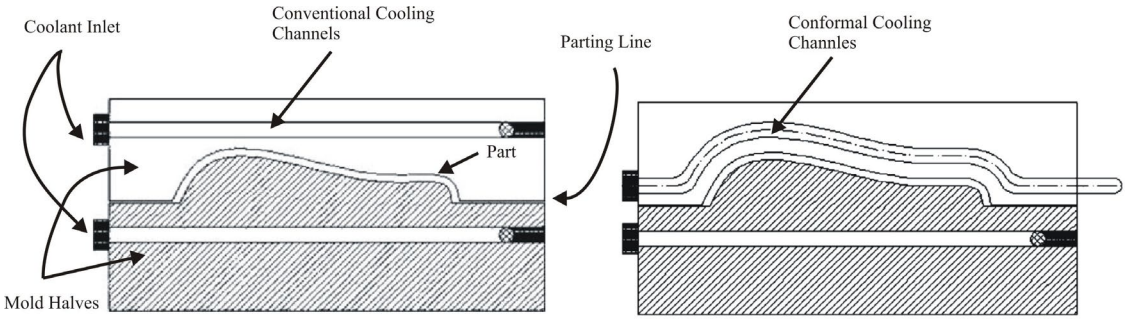


Figure 3. Configuration of conventional cooling channel design and Conformal cooling channel design [3]

Commercial software packages such as MOLDFLOW can perform cooling simulation to help evaluate the performance of the specified cooling system design, including cooling channel design and process condition selection.

In plastic injection molding, the standard deviation of the mold surface temperature distribution in the equation below is aimed to be minimum. Here, x is the geometric position of the mold surface, S is the area of the mold surface, and $\bar{T}(x)$ is the mean mold surface temperature.

$$f(x) = \frac{1}{S}\int_S^1 (T(x) - \bar{T}(x))^2 dS \quad (1)$$

Here, the mean mold surface temperature $\bar{T}(x)$ is defined as,

$$\bar{T}(x) = \frac{1}{S} T(x) dS \quad (2)$$

In Equation 1, when the lower and upper surface area of the mold (A_{Cavity}, A_{Core}) are separately evaluated in the equation and the equation is rewritten with numerical method for each finite element, the following equation is obtained.

$$f(x) = \frac{1}{A_{Cavity} + A_{Core}} \sum_{i=1}^{2N} A_i (T_i(x) - \bar{T}(x))^2 \quad (3)$$

Here N represents the finite number of elements defined in the model, and i represents each finite element. When the equation is rearranged for the mean mold surface temperature, the following equation is obtained.

$$\bar{T}(x) = \frac{1}{A_{Cavity} + A_{Core}} \sum_{i=1}^{2N} A_i \, T_i(x) \tag{4}$$

The temperature heat field is expressed by the Laplace equation as follows. X, y and z represent the geometric position of the mold, A represent the total surface area of the mold and ∇ the Laplace operator. Here p represents a point within area A.

$$\left(\frac{\partial^2 T}{\partial x^2}\right) + \left(\frac{\partial^2 T}{\partial y^2}\right) + \left(\frac{\partial^2 T}{\partial z^2}\right) = \nabla^2 T = 0; p \in \mathrm{A} \tag{5}$$

The representation of the heat flux (q) is as follows. k represents the thermal conductivity of the material, $\bar{h}$ the equivalent heat transfer coefficient, n the finite elements in the model.

$$q = -\mathrm{k} \frac{\partial \mathrm{T}}{\partial \mathrm{n}} = \bar{\mathrm{h}} \, (T - T_\infty); p \in S \tag{6}$$

II. METHOD

In the study, the cooling circulation in the plastic injection cycle of a sample cover part with shaped surface and deep rib structure in Figure 4, which is designed to represent complex shaped geometries used in the automotive or white goods industry, was simulated by Autodesk Moldflow Insight software.

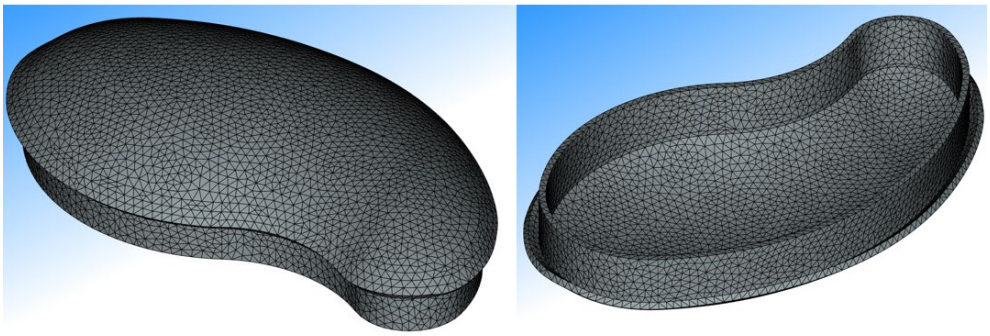


Figure 4. Isometric views of the cover part designed for the study.

Heat transfer between steel and plastic is used to cool the plastic in the mold. Consequently, the mold steel must be cooled with cooling channels. A total of three cases were analyzed, consisting of the cooling of the mold steels with the two conventional methods widely used in the sector and the complex cooling channel geometry cycle formed by the additive manufacturing method called conformal cooling. Additive-free polypropylene Sabic QR6711K raw material was chosen as plastic raw material and water was chosen as the cooling liquid. The first of the conventional cooling channels (Figure 5A) with straight channels following the part surface; The second (Figure 5B) is the design with baffles, which is used to cool the deep regions and follows the part form. These two designs can be created by machining into steel on standard drill or gun drill machines. The third design (Figure 5C) is a conformal cooling design, which can be manufactured by additive manufacturing method, completely following the part surface.

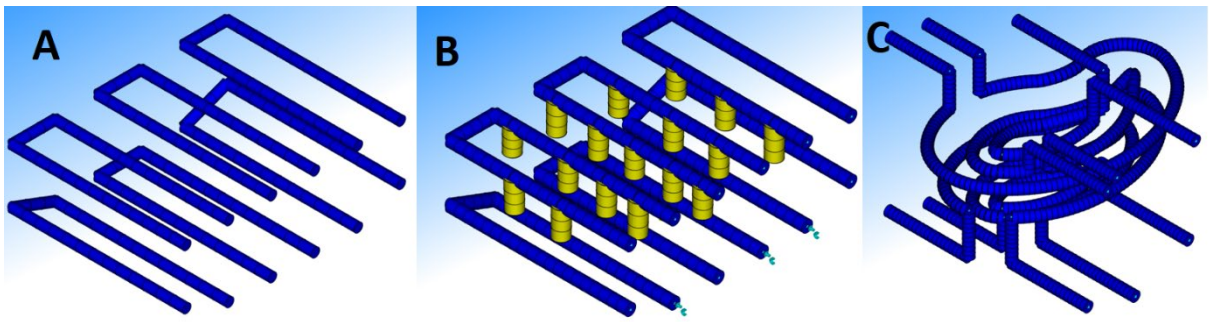


Figure 5. Model A, Model B and Model C which are different cooling channel designs.

In the study, these three designs were compared in terms of the heat flux from the part to the steel, the minimum time the part can be removed from the mold, and the plastic and mold steel interface temperature. DIN 1.2312 tool steel was chosen as the mold steel, the water inlet was provided at 20ºC temperature and 10 bar pressure. The melt plastic temperature was determined as 220ºC. In the finite element method used, the maximum number of iterations was determined as 50 and a termination interval of 0.1ºC. The friction losses in the cooling channels are solved with the Cole-Brook equation, the cooling channels are modeled with 1-dimensional beams and the part is modeled with 2-dimensional surface mesh.

III. RESULTS

In Table 1, the analysis results are examined with maximum values. It is observed that the heat flux in the Model A is lower than the other designs, therefore the mold temperature and cycle time are higher. In the Model C, the highest value for heat flux was obtained, and the mold temperature was 35% lower than the Model A and 27% lower than the Model B. A mold temperature of 58.61ºC was observed in the Model B, which can be produced by conventional methods. It was observed that the maximum heat flux was 3% higher than the Model A and the time to reach ejection temperature was 12.15 s.

Table 1. Comparison of the analysis results.

Model	Maximum Heat Flux (W/m^2)	Maximum Mold Surface Temperature (ºC)	Maximum Time to Reach Ejection Temperature (s)
A	18702	65.65	12.67
B	19256	58.61	12.15
C	19267	42.99	11.27

In Figure 6, while the maximum heat flux was on the outer surface of the rib in Model A and Model B, it was observed on both the inner and outer surfaces of the rib of Model C.

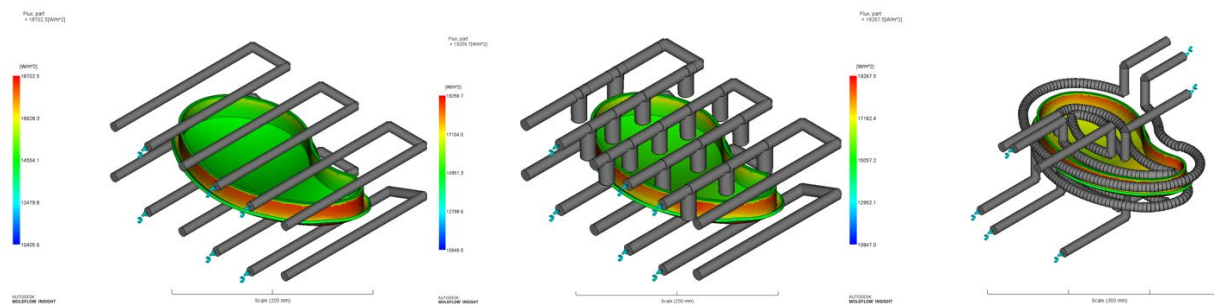


Figure 6. Comparison of the heat flux from the part surface to the mold.

The demolding time was determined as the time for the finite element in the relevant mesh to reach a temperature of 124oC. This value is the recommended temperature value for

polypropylene raw material [8]. In Figure 7, the times at which the part can be removed from the mold are 12.67 s, 12.15 s and 11.37 s for the A, B and C models, respectively. It can be said that conformal cooling provides a 7% cycle time reduction compared to the best conventional method.

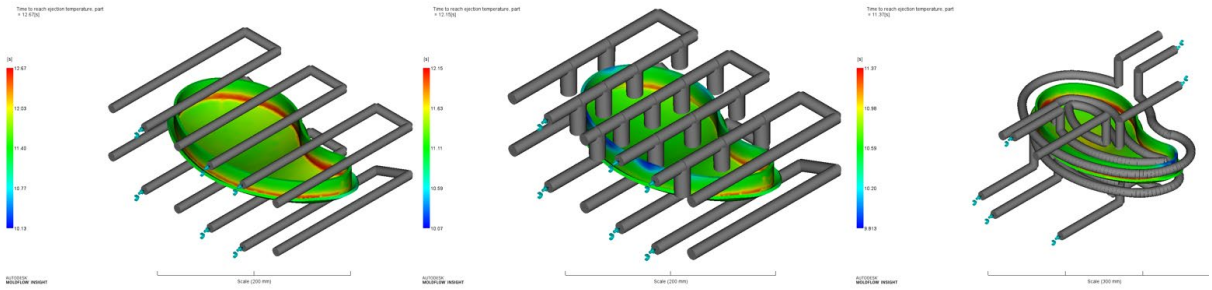


Figure 7. Comparison of times to reach ejection temperature.

In Figure 8, for Model A and Model C, the highest mold temperature was observed both on the shaped surface of the part and on the surface where the shaped surface and the rib intersect, while in Model B, it was observed only on the surface where the shaped surface and the rib intersect.

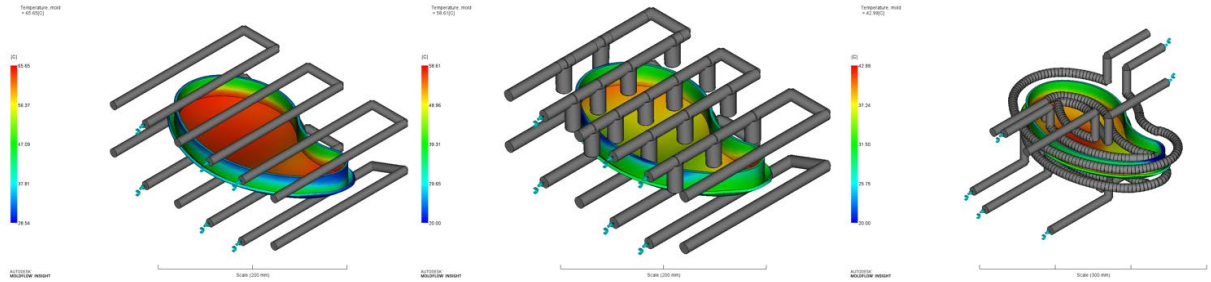


Figure 8. Comparison of mold surface temperatures.

In order to minimize the cycle time, conformal cooling design with the lowest mold temperature and the shortest time to reach ejection temperature should be preferred. However, manufacturing a mold core with the additive manufacturing method is more costly than the conventional method. According to the analysis results, cooling channels should be designed by adding baffles in molds manufactured by conventional method. Failure to control the mold surface temperature may cause problems such as warpage, increasing of production cycle time, and ejector marks on the cosmetic surface. In order to reduce the 58.6ºC temperature at the bottom of the ribs, nitrogenous thermal pins can be added to the areas where the ribs and shaped surface intersect, and the cooling efficiency can be improved with the conventional method.

REFERENCES

[1] Güllü A., Jain R. and Yalçınkaya S, "Teknolojik gelişmeler ve mühendislik uygulamaları," pp. 1-321, 2022.
[2] Groover, M. P. (2020). Fundamentals of modern manufacturing: materials, processes, and systems. John Wiley & Sons.
[3] Özmen M.E., "Part cooling analysis by conformal cooling channels in injection molding," pp. 1-128, Middle East Technical University, 2007.
[4] Dağlı M., "Kalın cidarlı HDPE (YYPE) malzemelerin plastik enjeksiyon yöntemiyle kalıplanmasında soğutma parametrelerinin parça kalitesine etkilerinin incelenmesi," pp. 1-76, Sakarya Uygulamalı Bilimler Üniversitesi, 2021.
[5] Lam Y.C., Zhai L. Y., Tai K. and Fok S. C., An "Evolutionary approach for cooling system optimization in plastic injection moulding," 42(10), pp. 2047-2061, International Journal of Production Research, Taylor & Francis, 2007.
[6] Kulcu S., "Plastik enjeksiyon kalıpçılığında konformal soğutma kanal tasarımı," T.C.

Bursa Uludağ Üniversitesi Fen Bilimleri Enstitüsü, pp. 1-109, 2002.
[7] SABIC, "Polyproplene random copolymer for injection molding," SABIC® PP QR6711K datasheet, May 2017.
[8] Reddy K.P. and Panitapu B., "High termal conductivity mould insert materials for cooling time reduction in thermoplastic injection moulds," pp. 519-526, ICMPC 2016, Materials Today: 4, 2017.

DIN 1.2312 Çeliklerde Farklı Kesme Parametrelerine Bağlı AlTiCrN Kaplamalı Tungsten Karbür Takım Ömrünün İncelenmesi

Investigation of AlTiCrN Coated Tungsten Carbide Tool Life Depending on Different Cutting Parameters in DIN 1.2312 Steels

Burak Erkan[1*], F. Deniz Beliç[1*], Ezginaz Karamahmutoğlu[1]
[*]deniz.belic@karelkalip.com.tr, ORCID: 0000-0001-7003-3682
[1] *Karel Kalıp Sanayi A.Ş., İstanbul, Türkiye*

Özet: Teknolojik gelişmeler doğrultusunda son yıllarda talaşlı imalat sektöründe kesici takım malzemeleri ve takım tezgâhları gelişmiş ve yüksek hızda üretim teknikleri ile proses süreleri azaltılmış ve bunların sonucu olarak üretim maliyetlerinin azaltılmasıyla ilgili çalışmalar öne çıkmıştır. Bu gelişmeler, talaşlı imalat yöntemleri ve kesici takımların önem kazanmasını beraberinde getirmiştir. Üretim esnasında, takımlarda oluşan kırılma, aşınma gibi durumlar yenisi ile değiştirme veya bileme işlemleri ile giderilmektedir. Takımın belirli bir aşınma miktarına veya tam aşınarak kesememesine kadar geçen süre takım ömrü olarak bilinmektedir. Başarı elde edebilmek için takımda oluşan aşınma mekanizmaları ve sebepleri, işlem esnasında oluşan problemlerin bilinmesi ve önlemlerin alınması önem taşımaktadır. Talaşlı imalat esnasında takım çok yüksek sıcaklıklar ve gerilmeler altında kaldığı için şekil değişimleri oluşmakta ve aşınma ile bu durum talaş kaldırma işlemini olumsuz olarak etkilemektedir. Takımda oluşan deformasyonlar parça yüzey kalitesini bozmakta, takım tezgahındaki titreşimin artarak enerji sarfiyatını ve dolayısıyla maliyeti artırmaktadır. Bu olumsuzluklar takım ömrünü azaltarak maliyet artışına neden olmaktadır. Takım ömrünün incelenmesi çalışmasında gerçekleştirilen deneyler, 21 mm çaplı ve 1 mm köşe radyusa sahip Tungsten Karbür AlTiCrN kaplamalı Moncarb firmasının 3 takma uçlu DCHW 070210 model takımlarıyla gerçekleştirilmiştir. İşlenen numunelerde takım ömrünün tamamlanma kriteri olarak 0.03 mm aşınma kabul edilmiştir. Takımlar 0.025 mm aşınmaya kadar her 30 dakikada bir, 0.025 aşınmadan sonra 3 dakikada bir ölçülerek değerlendirilmiştir.

Anahtar Kelimeler: *AlTiCrN kaplamalı tungsten karbür; DIN 1.2312 çelikler; Takım ömrü; Taguchi; Taylor*

Abstract: In line with technological developments, cutting tool materials and machine tools have been developed in the machining sector in recent years, and process times have been reduced with high-speed production techniques, and as a result, studies on reducing production costs have come to the fore. These developments have brought about the importance of machining methods and cutting tools. During production, situations such as breakage and wear in the tools are eliminated by replacing them with new ones or by grinding processes. The time it takes for the tool to reach a certain amount of wear or not be able to cut completely is known as tool life. In order to achieve success, it is important to know the wear mechanisms and causes of the tool, the problems that occur during the process and to take precautions. Since the tool is under very high temperatures and stresses during machining, deformations occur, and this situation negatively affects the chip removal process with wear. Deformations in the tool deteriorate the surface quality of the part, increase the vibration on the machine tool and

increase the energy consumption and therefore the cost. These negativities cause cost increase by reducing tool life. The experiments carried out in the study of examining the tool life were carried out with Moncarb company DCHW 070210 model tools with 3 inserts, with a 21 mm diameter and 1 mm corner radius, with Tungsten Carbide AlTiCrN coating. In the machined samples, 0.03 mm of wear was accepted as the completion criterion for the tool life. Tools were evaluated by measuring every 30 minutes up to 0.025 mm wear and every 3 minutes after 0.025 wear.

Keywords: *AlTiCrN coated tungsten carbide; DIN 1.2312 steels; Tool life; Taguchi; Taylor*

I. GİRİŞ

Sektörler arası rekabetin arttığı günümüz küreselleşen dünyasında, üretici firmaların faaliyetlerini sürdürdükleri en-düstri alanlarında rekabet edebilme yetenekleri ve konumlarını koruyabilmeleri mali güçleri ile ilişkilidir.

Günümüz endüstrisinde mekanik işlemler, metalik parçalara nihai şekillerinin verilip kullanılabilir hale getirilmesi için uygulanmakta ve bu mekanik işlemlerin tamamı talaşlı imalat yöntemlerini gerektirmektedir. Teknolojik gelişmeler doğrultusunda son yıllarda talaşlı imalat sektöründe kesici takım malzemeleri ve takım tezgâhları gelişmiş ve yüksek hızda üretim teknikleri ile proses süreleri azaltılmış ve bunların sonucu olarak üretim artışı sağlanmıştır. Bu gelişmeler, talaşlı imalat yöntemleri ve kesici takımların önem kazanmasını beraberinde getirmiştir.

Endüstrinin büyük bir kısmında kullanılan kesici takımlar son derece büyük kapasiteli firmalar için daimî bir gider bölümünü oluşturmaktadır. Üretim esnasında, takımlarda oluşan kırılma, aşınma gibi durumlar yenisi ile değiştirme veya bileme işlemleri ile giderilmektedir.

Takımın belirli bir aşınma miktarına veya tam aşınarak kesememesine kadar geçen süre takım ömrü olarak bilin-mektedir. Takım geometrisinin yanı sıra talaş kesiti ve kesme hızı tarafından belirlenen takım ömrü büyük oranda kesme hızından etkilenmektedir. Bu nedenle diğer parametreler çoğunlukla kesme hızına göre belirlenmektedir.

Takımların ömrünü belirleyen iki etken;

- Takım ömrünün, parçanın istenen tolerans sınırları içinde üretilmesi
- Parçanın yüzey kalitesinin istenen sınırlar içinde tutulması

Bu koşullarda başarı elde edebilmek için takımda oluşan aşınma mekanizmaları ve sebepleri, işlem esnasında oluşan problemlerin bilinmesi ve önlemlerin alınması önem taşımaktadır.

Talaşlı imalat esnasında takım çok yüksek sıcaklıklar ve gerilmeler altında kaldığı için şekil değişimleri oluşmakta ve aşınma ile bu durum talaş kaldırma işlemini olumsuz olarak etkilemektedir. Takımda oluşan deformasyonlar parça yüzey kalitesini bozmakta, takım tezgahındaki titreşimin artarak enerji sarfiyatını ve dolayısıyla maliyeti artırmaktadır. Bu olumsuzluklar takım ömrünü azaltarak maliyet artışına neden olmaktadır.

Takım ömrünün takibi için direkt ve indirekt olmak üzere iki tür yöntem kullanılmaktadır. Talaş kaldırma işleminin durdurularak takım üzerinde oluşan aşınmaların çeşitli tekniklerle ölçülmesi direkt yöntem olarak bilinmektedir. Aksine, talaşlı imalatın durdurulmadan tespit edilen titreşim, gürültü, güç, kesme kuvveti, iş mili hızı değişimi, parça yüzey kalitesi ve boyutlarındaki değişimin ölçümü gibi sinyaller aşınma durumu ile ilgili bilgi vermektedir ve bu yöntem indirekt yöntem olarak bilinmektedir.

F.W. Taylor tarafından formüle edilen Takım Ömrü Beklentisi için Taylor denklemi, değişen kesme hızı v_c için takım ömrüne iyi bir yaklaşım sağlamaktadır. Taylor denklemi;

$$v_c \,.\, T^m = C_T \tag{1}$$

Bu denklemde, v_c kesme hızı, T beklenen takım ömrü, m ve C_T analitik olarak ölçülen

verilerden türetilen veya en küçük kareler yöntemi kullanılarak eğri uydurma ile hesaplanan sabitlerdir.

Belirli bir metal kesme işlemi için takım aşınmasını incelerken, hız en etkili faktör olurken, uygulanan ilerleme f, takım ömrü için daha az önemli olacaktır. Yük, takımın daha büyük bir kısmına dağıldığından, ancak birim uzunluk başına yük yaklaşık olarak aynı olacağından, a_p kesme derinliği takım aşınmasında yalnızca küçük bir rol oynayacaktır. Daha iyi bir takım ömrü tahmini için Taylor denkleminin birkaç versiyonu yayınlanmıştır.

Bunlardan en sık kullanılan genişletilmiş Taylor denklemlerinden biri;

$$v_c \, . f^p \, . a_p^q \, . T^m = \, C_T \tag{2}$$

Değişen eşdeğer talaş kalınlığını (h_e veya ilerleme hızı f) ve kesme derinliği a_p hesaba katılarak iki sabit p ve q eklenmiş denklem yukarıdaki gibidir. [1,2,3]

II. YÖNTEM

Deneyler 21 mm çaplı ve 1 mm köşe radyusa sahip Tungsten Karbür AlTiCrN kaplamalı Moncarb firmasının 3 takma uçlu DCHW 070210 model takımlarıyla gerçekleştirilmiştir. Takım tezgâhı olarak DMG Mori DMU 75 model CNC freze kullanılmıştır. DIN 1.2312 (40CrMnMoS8-6) takım çeliğiyle yapılan deneylerdeki numune sertliği Şekil1'de gösterildiği üzere 27 HRC olarak ölçülmüştür. İşlenen numunelerde takım ömrünün tamamlanma kriteri olarak 0.03 mm aşınma kabul edilmiştir.



Şekil 1. Deney numunesinin sertliğinin ölçülmesi.

Şekil 2'de gösterilen kesici takımlar 0.025 mm aşınmaya kadar her 30 dakikada bir, 0.025 aşınmadan sonra 3 dakikada bir ölçülerek değerlendirilmiştir. Deneyler Taguchi L9 [4] ile oluşturulmuş ve ANOVA üzerinden parametrelerin takım ömrüne etkileri incelenmiştir. Deneylerde soğutucu kesme sıvısı olarak Gemaoil Duramet 1100 %5 emülsiyon metal işleme sıvısı kullanılmıştır. Deneylerde takım dönme hızı 4000 dev/dk 4800 dev/dk ve 5400 dev/dk olarak belirlenmiş; takım ucu başına ilerleme 0.15, 0.18 ve 0.21 mm/dev olarak seçilmiştir. Kesme derinlikleri 0.15, 0.18 ve 0.21 mm olarak tanımlanmıştır. Kesme hızı Denklem 3 ile hesaplanarak istatistiksel analiz yapılmıştır.



Şekil 2. Deneyde kullanılan kesici takım.

Deney sonuçları incelenirken tezgâha girdi olarak verilen takım dönme hızının kesme hızına dönüştürülmesi için; D, takım çapı; n, takım dönme hızı olmak üzere:

$$V = \frac{\pi D n}{1000} \tag{3}$$

Eşitliği kullanılmıştır.

Tablo 1. Takım dönme hızına karşılık gelen kesme hızları

Takım Dönme Hızı (dev/dk)	Kesme Hızı (m/dk)
4000	263.89
4800	316.67
5400	369.45

III. SONUÇLAR

Kesme Hızı (m/dk)	İlerleme (mm/devir)	Kesme Derinliği (mm)	Takım Ömrü (dk)
263.89	0.15	0.15	1122
263.89	0.18	0.18	969
263.89	0.21	0.21	732
316.67	0.15	0.18	579
316.67	0.18	0.21	387
316.67	0.21	0.15	432
369.45	0.15	0.21	390
369.45	0.18	0.15	369
369.45	0.21	0.18	291

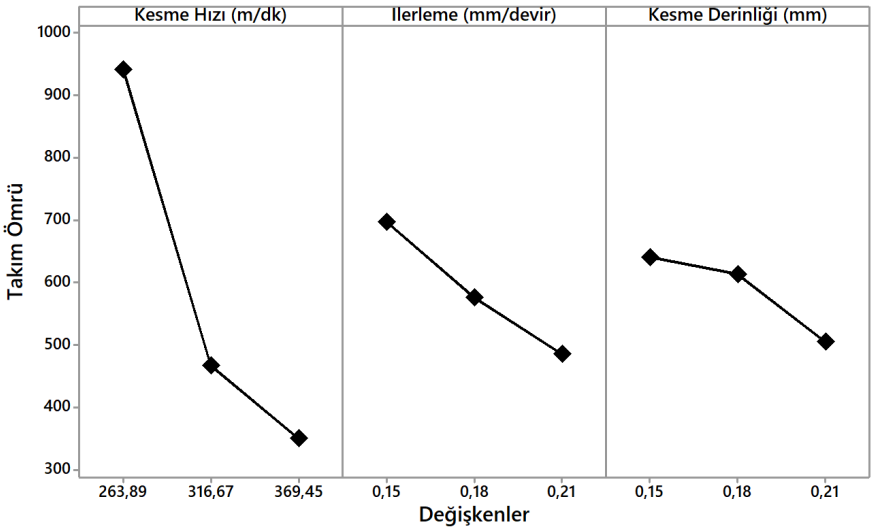
Tablo 2. Deney sonuçları

Deney sonuçları (Tablo 2) Minitab ile analiz edilerek istatistiki olarak incelenmiştir. Parametrelerin takım ömrüne olan etkilerinin p değerleri Tablo 3'te gösterilmiştir. %95 güven aralığı için yapılan analizde kesme hızı ile ilerlemenin Takım ömrü üzerinde doğrudan etkisinin olduğu izlenirken, kesme derinliğinin dolaylı etkisi olduğu gözlenmiştir.

Parametre	p-Değeri
Kesme Hızı (m/dk)	0.005
İlerleme (mm/devir)	0.041
Kesme Derinliği (mm)	0.085

Tablo 3. ANOVA sonucu parametrelerin takım ömrüne etkisi

Tüm parametrelerin artışı takım ömrünün kısalmasına neden olmaktadır. Ana etki grafiğinde 263,89 m/dk ile 316.67 m/dk arasında takım ömrü hızlı bir şekilde düşüş gösterirken; 316.67 m/dk'den 369.45 m/dk'ye artan kesme hızının takım ömrüne olan etkisinin eğiminde düşüş izlenmiştir. Aynı etki 0.15 mm/devir ilerleme ile 0.21 mm/devir ilerleme arasında da görülmüştür. Kesme derinliğinde ise 0.18 mm'ye kadar olan düşüş takım ömrüne daha kısıtlı bir negatif etki gösterirken; 0.21 mm'ye olan kesme derinliği artışı takım ömrünü daha yüksek bir eğim ile düşürmüştür.



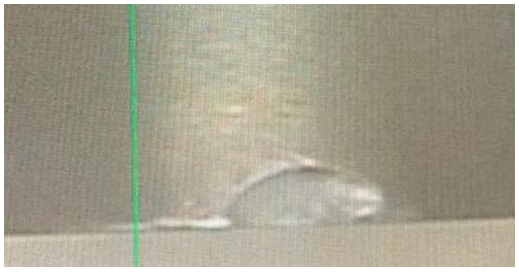
Şekil 3. Parametrelerin takım ömrüne etkilerinin ana etki grafiğinde değerlendirilmesi

Yapılan deneyler neticesinde geliştirilmiş Taylor denklemi için kesme hızı, ilerleme ve kesme derinliğine bağlı denklemin katsayılarının hesaplanmasıyla, DIN 1.2312 çeliğinin AlTiCrN kaplamalı 21 mm çaplı ve 2 mm uç radyuslu takım için takım ömrü Denklem 4 ile ifade edilir.

V, kesme hızı; d, kesme derinliği; f ilerleme; T, takım ömrü ve 1699.4 takım ömrüne bağlı bir katsayı olmak üzere:

Denklem 4: Geliştirilmiş Taylor takım ömrü denkleminin oluşturulması.

$$VT^{0.85}d^{2.1}f^{0.1} = 1699.4 \quad (4)$$



Şekil 4. Takımdaki uç aşınmasının mikroskop altında incelenmesi

Çalışmada ifade edilen çelik, takım ve şartlar için, takım ömrünün kesme parametreleriyle olan ilişkisi ve takım aşınmasının zamana bağlı ilerlemesi incelenmiştir. Çalışmada; kesme hızı ve ilerlemenin artışının takım ömrünü azaltmada anlamlı negatif etkisi olduğu, kesme derinliğinin ise dolaylı negatif etkisinin olduğu gözlenmiştir. Deney sonuçlarına göre yapılacak bir çalışma ile; makine-saat maliyetleri ve takım maliyetleri optimize edilerek maliyet iyileştirme sağlanabilir. Deneyler sonucunda geliştirilmiş Taylor takım ömrü denklemi katsayıları bulunmuş ayrıca kesme parametrelerinin takım ömrüne olan etkileri ayrı ayrı incelenmiştir.

TEŞEKKÜR

Çalışmada katkıları bulunan Ümit Selam ve Moncarb Kesici Takımlar'a teşekkürlerimizi sunarız.

REFERANSLAR

[1] Özdemir K., "İlk aşınma bölgesinde takım aşınmasını etkileyen parametrelerin deneysel analizi," Uludağ Üniversitesi Fen Bilimleri Enstitüsü, pp.1-82, 2008.
[2] Beköz Üllen N., "Tornalama işlemlerinde çeşitli kesici takım uçlarının hasar

mekanizmaları," 2nd International Eurasian Conference on Science, Engineering and Technology, pp. 655-661, 2020.
[3] Johansson, D., Hägglund, S., Bushlya, V., & Ståhl, J. E., "Assessment of commonly used tool life models in metal cutting," Procedia Manufacturing, 11, pp. 602-609, 2017. https://doi.org/10.1016/j.promfg.2017.07.154
[4] Aveiro, P., "Design of experiments in production engineering," J. P. Davim (Ed.). Basel, Switzerland: Springer International Publishing, 2016.

An Investigation on Formability of Metallic Bipolar Plate Micro Channels Under Different Material Models

Mahmut Caner Acar[*,1], Habip Gökay Korkmaz[1], Serkan Toros[1]

[*]mahmutcaneracar@ohu.edu.tr, ORCID: 0000-0002-6206-5374
[1]*Mechanical Engineering Department, Nigde Omer Halisdemir University, Nigde, Türkiye*

Abstract: Because of their superior properties, metallic materials have been extensively investigated as bipolar plates in polymer electrolyte membrane (PEM) fuel cells. However, the micro formability of metallic materials is still regarded as an issue, and numerous research efforts have been carried out on this subject. In this study, the hydroforming of 0.1 mm thick Ti6Al4V alloy is numerically analyzed by using three different material models of "3 - Parameter Barlat" (MAT 36), "Transversely Anisotropic Elastic Plastic" (MAT 37) and "Kinematic Hardening Transversely Anisotropic" (MAT 125). The finite element method (FEM) is used to evaluate the influence of various material models on metallic bipolar plate fracture, wrinkle, thinning, and channel depth. The spring-back effect of each model is also taken into consideration during the numerical studies. Without any cracking, highest channel depths are obtained with MAT 37, whereas the lowest channel depths are obtained with MAT 36. Thickness reductions are especially visible in the channel corners for each material model, and MAT 37 has the greatest thinning. Three material models exhibit noticeable wrinkles on the formed Ti6Al4V. According to the results, fractures can be seen in the early stages of the MAT 36 model, which means that the MAT 36 is most susceptible to fracture occurrences. For each material model, spring-backs are observed in both upward and downward directions.

Keywords: *Metallic Bipolar Plate, PEM Fuel Cell, Hydroforming, FEM*

I. INTRODUCTION

Duo to the negative effects of conventional fossil fuel consumption on the environment and rising energy demand in parallel with the human population, the requirement for environmentally friendly power generation systems has grown significantly in recent years. Fuel cells have been considered as one of the most promising energy conversion technologies, and researchers have conducted a number of studies on these systems. Between them PEM fuel cells have outstanding features such as lower operating temperature, higher power density and quite operation. Therefore, PEM fuel cells can be used in a wide range of applications, including automotive, transportation, unmanned aerial vehicles, submarines, space and military applications.

PEM fuel cells convert the chemical energy of hydrogen gases into electrical energy via electrochemical reactions within the stack. Generally, a PEM fuel cell unit consists of a polymer electrolyte membrane, anode and cathode electrolytes, anode and cathode gas diffusion layers and anode and cathode bipolar plates. Bipolar plates provide multiple functions, including the circulation of reactants, water and coolant through flow channels, support of the fuel cell, and transport of electrons from the anode to the cathode [1,2]. The bipolar plates constitute 60-80% by weight and about 80% by volume of a PEM fuel cell [3–5]. Thus, bipolar plates are one of the most critical components of a PEM fuel cell stack, and the type of microchannel formation technique would have a significant impact on system costs. Bipolar plates are classified into three types based on their material: graphite, metal, and

composite bipolar plates [6]. Especially in the automotive sector, many studies are carried out to research and develop metal bipolar plates. Stainless steel, titanium, nickel, aluminum, copper, and their alloys have been extensively investigated as metal bipolar plate materials.

Delivery of H_2 and O_2 gases to the electrodes, removal of unreacted gases and water released as a result of reactions from the cell are provided by micro channels formed on the metallic bipolar plates. There are several micro channel forming methods, and the most researched are stamping [7], hydroforming [8] and roll forming techniques [9]. Table I shows the advantageous and disadvantageous of these plastic forming methods.

Table I. Advantageous And Disadvantageous Of Plastic Forming Methods [10]

Forming method	Advantageous	Disadvantageous
Hydroforming	- High repeatability, - The manufactured bipolar plate has higher strength.	- High requirements for forming equipment.
Stamping	- Lower cost of stamping process, - High production rate, - Long life molds.	- The performance and quality of bipolar plates is relatively poor.
Roll forming	- Low cost, - Suitable for mass production.	- Cannot produce bipolar plates with complex flow channels.

Both experimental and numerical studies on metallic bipolar plate forming process have been performed by researchers in the literature. Zhang et al. [11] experimentally studied the fracture initiation of SS 316L by stamping method. They stated that the material fracture and thinning can be seen at the contact location of dies and sheets. A 2D finite element analysis of stamping process was also performed in the study and a good agreement between the experiment and numerical model was achieved. Modanloo et al. [12] conducted a numerical investigation on the fracture prediction of 0.1 mm thick pure titanium utilizing three ductile fracture models from Ayada, Brozzo, and Rice-Tracey, as well as an improved model based on the material size effect. According to the model results, the Brozzo model predicted the fracture in stamped titanium more accurately. The impact of grain size effects on the formability of a copper metallic bipolar plate during the hydroforming process was investigated by Xu et al. [13]. They found that as the grain size approaches the plate thickness, the pressure and maximum height at which failure occurs decrease. Mohammadtabar et al. [8] used a two-step hydroforming procedure to address the formability issues of a metallic bipolar plate with interdigitated flow field. It was discovered that two-step hydroforming improves the micro formability of bipolar plates even for flow channels that have higher geometrical complexity. Bauer et al. [14] investigated the suitability of the roll forming technique for the formation of micro flow channels on SS 316L bipolar plate. The findings of the experiments revealed favorable results in terms of forming accuracy and channel cross-section shape. They also employed a calibrated model to improve the forming process based on material deformation and wrinkles.

This study involves a three-dimensional formability analysis of a 0.1 mm thick Ti6Al4V titanium alloy using various material models including MAT 36, MAT 37, and MAT 125. In this context, the hydroforming method is selected as the forming method, and the effects of different material models on thinning, fracture, wrinkles, spring-back, and flow channel depth are numerically investigated.

II. METHODOLOGY

The Ti6Al4V titanium alloy sheet with 0.1 mm thickness is considered in this study. The

mechanical properties and chemical composition of the Ti6Al4V are shown in Table II and Table III, respectively.

Table II. Mechanical Properties Of Ti6Al4V Titanium Alloy

Density (kg/m^3)	Poisson's ratio	Young's modulus (MPa)
4430	0.34	1.1×10^5

Table III. Chemical Composition Of Ti6Al4V Titanium Alloy

Chemical composition (%)							
Ti	Fe	C	N	O	H	Al	V
89.6	0.049	0.01	0.011	0.044	0.0089	6.15	4.15

Fig. 1 shows the geometry of hydroforming die and its channels used in numerical study. Four micro channels are considered in the forming process of metallic bipolar plate. The width and length of the metallic sheet are 20 mm and 23 mm, respectively. The die, blank, and binder all have a zero-thickness shell surface, and each part was meshed as the shell elements in Dynaform commercial software program. A forming limit diagram (FLD) included in the software is used for analyzing the deformations that occur on the bipolar plate after the hydroforming process.

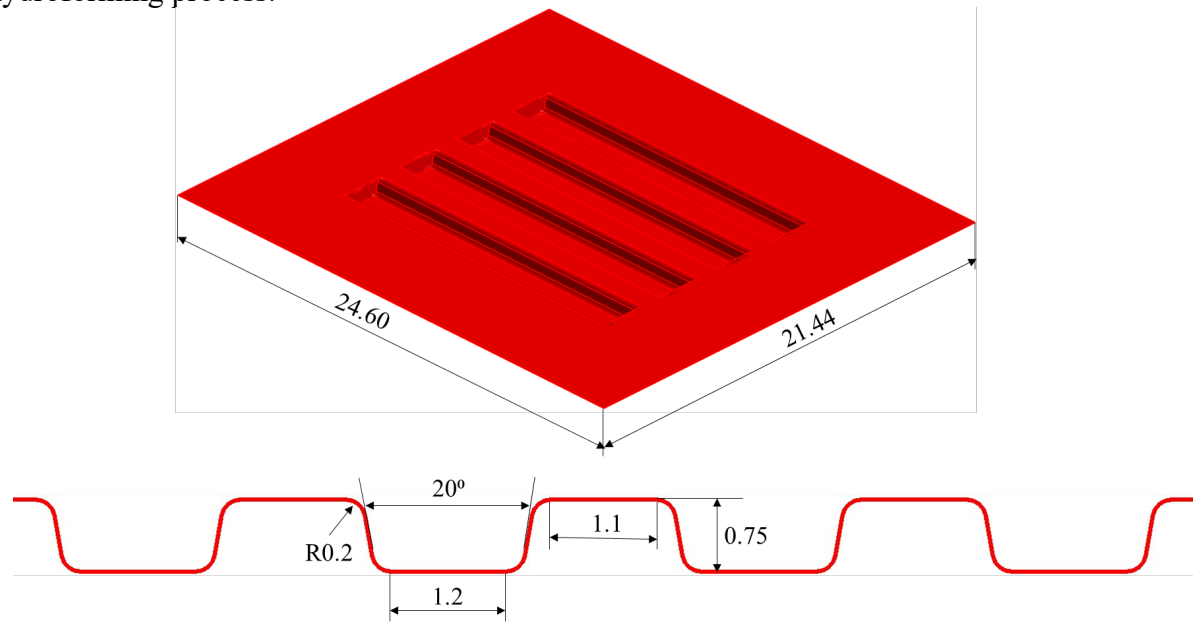


Fig. 1. Model geometry and channel dimensions of the hydroforming die (unit: mm).

The commercial Dynaform finite element software is used for the hydroforming process of Ti6Al4V metallic sheet. A linear pressure profile as given in Equation (1) is employed to the program as the hydroforming pressure.

$$P = 10^4 t \tag{1}$$

where P represents the applied pressure (MPa) and t represents the time (s). The applied pressure ranges from 0 to 100 MPa with a 10 MPa increment. The friction coefficient of 0.125 is used during the simulation process of each material model. The die is assumed to be stationary, and a constant force of 2,000 kN is applied on the binder surface.

The element size on the blank is meshed to be 0.05 mm. The total number of elements in the

system is 196,404. The analyses are carried out utilizing three different material models, namely MAT 36, MAT 37, and MAT 125, all of which are available in Dynaform's material library. After the forming process, a spring-back analysis is run to ensure that the part became final. Forming analyzes are run as explicit and spring-back analyzes are run as Implicit. Parameters of MAT 36, MAT 37 and MAT 125 material models used in the analyzes are given in Table IV, Table V and Table VI, respectively.

Table IV. Mat 36 Model Parameters Of Ti6Al4V Material

K	n	R0	R45	R90
1389.7	0.0859	0.9730	2.0433	1.1707

Table V. Mat 37 Model Parameters Of Ti6Al4V Material

σ_y	H	R
925	1917.5	1.5576

Table VI. Mat 125 Model Parameters Of Ti6Al4V Material

Y	c	B	Rsat	b	h	k	Ea	ξ	C_1	C_2
960	7.382	1100	1066	89.982	0.95	37.384	62980	1.9314	1.9578	0.0895

III. RESULTS AND DISCUSSION

Fig. 2 shows the FLD of shaped Ti6Al4V plate after the hydroforming process for three different material models of MAT 36, MAT 37 and MAT 125. Cracking occurs particularly in the channel corners where the plate and die come into contact. When MAT 36 is used as the material model, more crack and wrinkle locations occur, and tearing are seen in the middle channels. The formation of cracks and wrinkles is at a minimal level in the case of MAT 37 material model.

The FLD of shaped Ti6Al4V titanium alloy just before cracking occurs for various material models are illustrated in Fig. 3. As can be seen from the figure that two inner channels are in safe region while the wrinkle tendencies are observed at two outer channels. The wrinkles occur especially on both edges of the formed plates that are parallel to the flow channels. The formed plate modeled with MAT 37 has the highest possibility of crack zones, whereas the formed plate modeled with MAT 125 has the lowest.

The flow channel depth of PEM fuel cells should be as high as possible for maximum system efficiency. Fig. 4 depicts the channel depths of formed Ti6Al4V plate before cracking occurs for three different models. For each material model, symmetrical channel depth distributions are observed. Since the material flow is greater in locations near the outer channels, the depths are higher in these channels. The MAT 37 has the maximum channel depth while the MAT 36 has the minimum. This is due to the increased and decreased responses of the plate to cracking when the MAT 37 and MAT 36 material models are employed, respectively.

The thickness distribution of the formed plate (before cracking) along the centerline perpendicular to the flow field is seen in Fig. 5. As expected, the thinning is seen mostly in the locations where the plate and the die come into contact. Because the MAT 37 has the greatest channel depth until the crack begins, a maximum thinning of 9% is observed with this model. The MAT 36 has the smallest thickness reduction among the different material models.

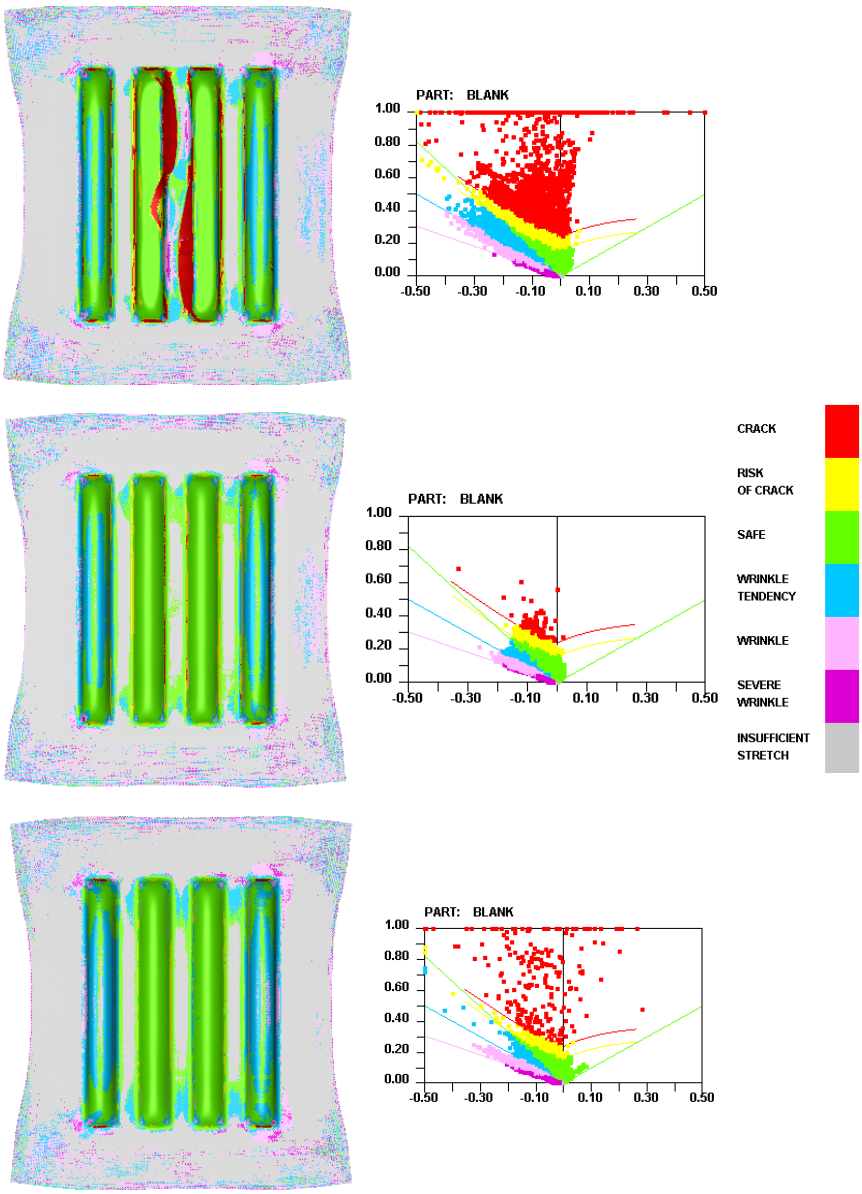


Fig. 2. FLD of Ti6Al4V for (a) MAT 36, (b) MAT 37 and (c) MAT 125.

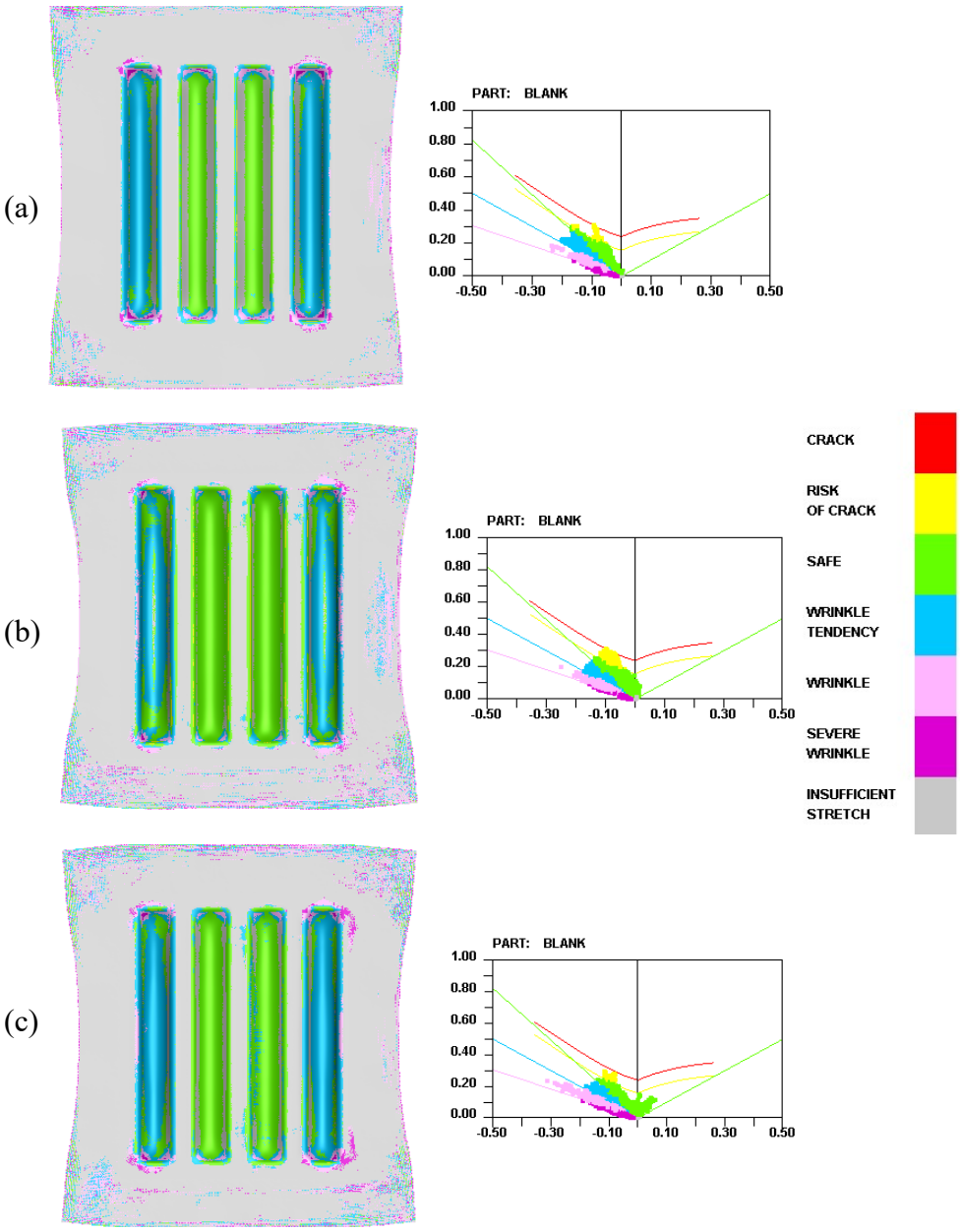


Fig. 3. FLD of Ti6Al4V for (a) MAT 36, (b) MAT 37 and (c) MAT 125.

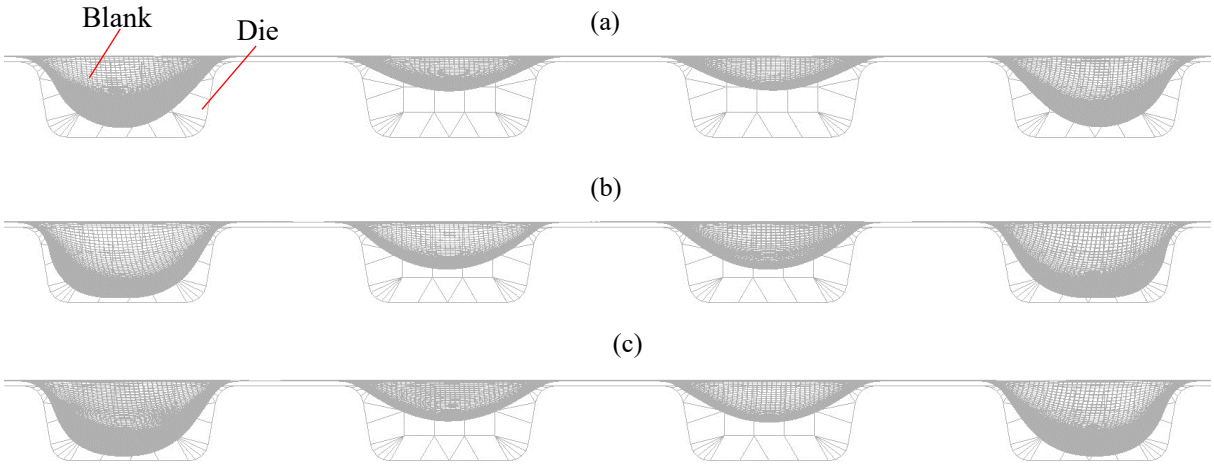


Fig. 4. Channel depths of Ti6Al4V for (a) MAT 36, (b) MAT 37 and (c) MAT 125.

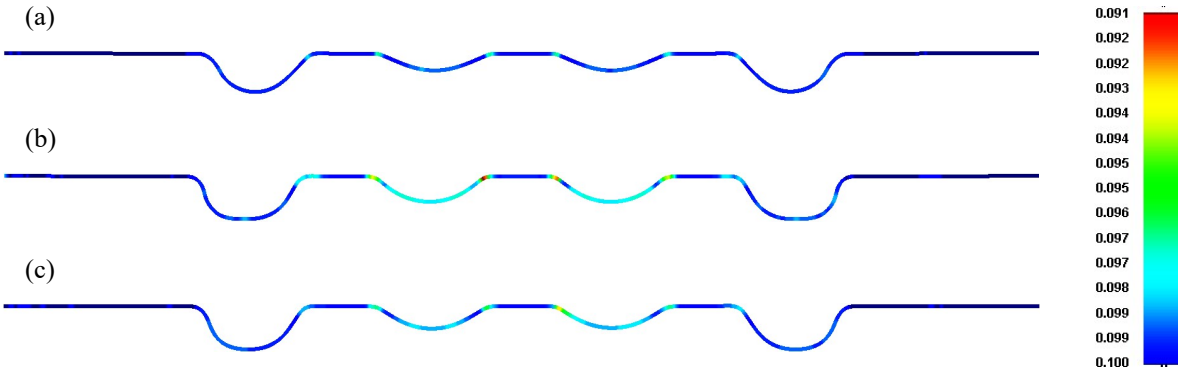


Fig. 5. Thickness distribution along the formed plate for (a) MAT 36, (b) MAT 37 and (c) MAT 125.

The effect of spring-back should be taken into consideration to get more reliable results from the numerical model. As shown in Fig. 6, a spring-back analysis is performed on formed Ti6Al4V plates for different material models. The red and green colors represent the states before and after the spring-back analysis, respectively. As illustrated by the figure, notable spring-backs can occur at the end of formation and should not be neglected. Both upward and downward spring-backs are observed in all three material models. In the MAT 125, the upward spring-back is dominant, whereas the upward and downward spring-backs are almost the same in the MAT 36 and MAT 37 models.

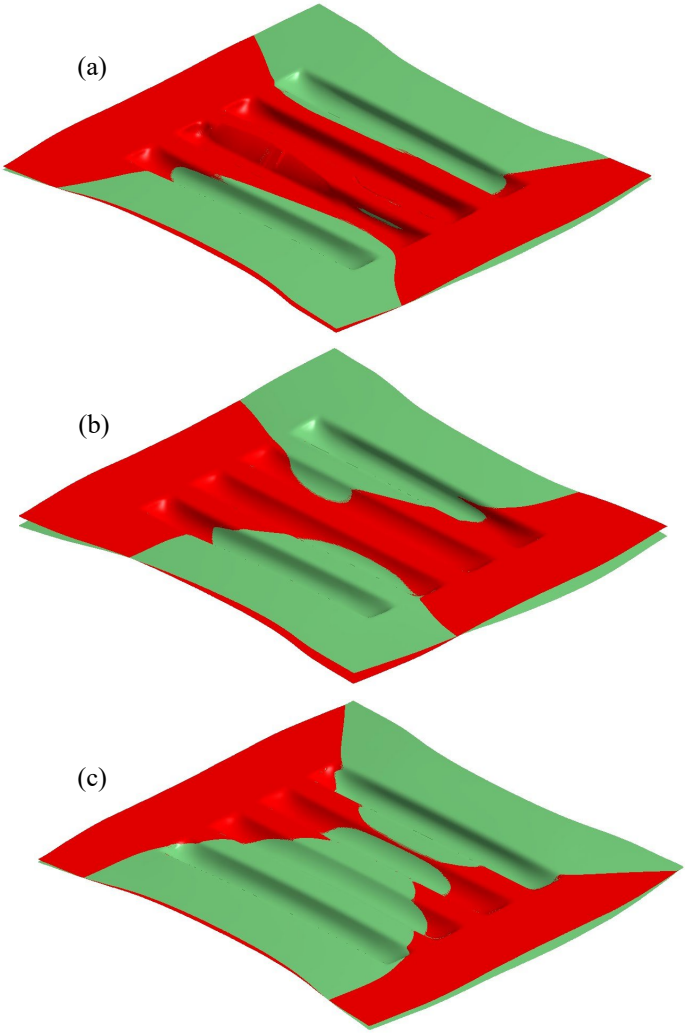


Fig. 6. Spring-back results for (a) MAT 36, (b) MAT 37 and (c) MAT 125.

IV. CONCLUSION

A hydroforming study for 0.1 mm thick Ti6Al4V titanium alloy, which is regarded as an ideal candidate for the PEM fuel cell bipolar plate, is carried out using three material models: MAT 36, MAT 37, and MAT 125. The effects of various material models on metallic plate fracture, wrinkles, thinning, and channel depth are numerically investigated using FEM. During the hydroforming process, a linear pressure profile is applied from 10 MPa to 100 MPa with a 10 MPa increment. The following are the conclusions of this study:

1. The FLD analysis shows that selecting MAT 36 as the material model results in more crack locations than MAT 37 and MAT 125, and the MAT 37 can be considered the safest model. The FLD analysis, which is performed prior to the cracking process, reveals that the two inner channels are safer than the two outer channels. In addition, the outer channels tend to wrinkle more.
2. The highest and lowest channel depths just before cracking are reached with the MAT 37 and MAT 36 material models, respectively.
3. Greater thickness losses are observed in the contact regions of the die and plate. Since the use of MAT 37 as the material model results in the maximum channel depth, this model exhibits the most thinning.
4. Spring-backs occur in both the upward and downward directions for all three material models.

REFERENCES

[1] M. Li, S. Luo, C. Zeng, J. Shen, H. Lin, C. Cao, Corrosion behavior of TiN coated type 316 stainless steel in simulated PEMFC environments, Corros. Sci. 46 (2004) 1369–1380. https://doi.org/10.1016/S0010-938X(03)00187-2.

[2] R.F. Silva, D. Franchi, A. Leone, L. Pilloni, A. Masci, A. Pozio, Surface conductivity and stability of metallic bipolar plate materials for polymer electrolyte fuel cells, Electrochim. Acta. 51 (2006) 3592–3598. https://doi.org/10.1016/j.electacta.2005.10.015.

[3] C. Zhang, J. Ma, X. Liang, F. Luo, R. Cheng, F. Gong, Fabrication of metallic bipolar plate for proton exchange membrane fuel cells by using polymer powder medium based flexible forming, J. Mater. Process. Technol. 262 (2018) 32–40. https://doi.org/10.1016/j.jmatprotec .2018.06.014.

[4] M. Elyasi, F.A. Khatir, M. Hosseinzadeh, Manufacturing metallic bipolar plate fuel cells through rubber pad forming process, Int. J. Adv. Manuf. Technol. 89 (2017) 3257–3269. https://doi.org/10.1007/s00170-016-9297-6.

[5] Y. Liu, L. Hua, Fabrication of metallic bipolar plate for proton exchange membrane fuel cells by rubber pad forming, J. Power Sources. 195 (2010) 3529–3535. https://doi.org/ 10.1016/j.jpowsour.2009.12.046.

[6] R. K. Gautam, S. Banerjee, K. K. Kar, Bipolar Plate Materials for Proton Exchange Membrane Fuel Cell Application, Recent Patents Mater. Sci. 8 (2015) 15–45. https://doi.org /10.2174/1874464808666150306223104.

[7] D. Qiu, L. Peng, P. Yi, X. Lai, W. Lehnert, Flow channel design for metallic bipolar plates in proton exchange membrane fuel cells: Experiments, Energy Convers. Manag. 174 (2018) 814–823. https://doi.org/10.1016/j.enconman.2018.08.070.

[8] N. Mohammadtabar, M. Bakhshi-Jooybari, S.J. Hosseinipour, A.H. Gorji, Feasibility study of a double-step hydroforming process for fabrication of fuel cell bipolar plates with slotted interdigitated serpentine flow field, Int. J. Adv. Manuf. Technol. 85 (2016) 765–777. https:// doi.org/10.1007/s00170-015-7960-y.

[9] B. Abeyrathna, P. Zhang, M.P. Pereira, D. Wilkosz, M. Weiss, Micro-roll forming of stainless steel bipolar plates for fuel cells, Int. J. Hydrogen Energy. 44 (2019) 3861–

3875. https://doi.org/10.1016/j.ijhydene.2018.12.013.
[10] K. Xiong, W. Wu, S. Wang, L. Zhang, Modeling, design, materials and fabrication of bipolar plates for proton exchange membrane fuel cell: A review, Appl. Energy. 301 (2021). https://doi.org/10.1016/j.apenergy.2021.117443.
[11] P. Zhang, M.P. Pereira, B.F. Rolfe, D.E. Wilkosz, P. Hodgson, M. Weiss, Investigation of material failure in micro-stamping of metallic bipolar plates, J. Manuf. Process. 73 (2022) 54–66. https://doi.org/10.1016/j.jmapro.2021.10.044.
[12] V. Modanloo, H. Talebi-Ghadikolaee, V. Alimirzaloo, M. Elyasi, Fracture prediction in the stamping of titanium bipolar plate for PEM fuel cells, Int. J. Hydrogen Energy. 46 (2021) 5729–5739. https://doi.org/10.1016/j.ijhydene.2020.11.088.
[13] Z. Xu, L. Peng, P. Yi, X. Lai, An investigation on the formability of sheet metals in the micro/meso scale hydroforming process, Int. J. Mech. Sci. 150 (2019) 265–276. https://doi.org/10.1016/j.ijmecsci.2018.10.033.
[14] A. Bauer, S. Härtel, B. Awiszus, Manufacturing of metallic bipolar plate channels by rolling, J. Manuf. Mater. Process. 3 (2019) 1–12. https://doi.org/10.3390/jmmp3020048.

Vision-Based Gas Pipe Inspection for Domestic Hobs

Mehmet Kayğusuz[*,1], Barış Öz[1,2], Ayberk Çelik[2,3], Sultan Sancar[1], Ebru Gezgin Sarıgüzel[1,2]
Gözde Şimşek[1,2]

[*] mehmet.kaygusuz@mamurtech.com, ORCID: 0000-0003-2188-8582
[1]*Ar-Ge Merkezi, Mamur Teknoloji Sistemleri, Istanbul, Turkey*
[2]*Graduate School of Science and Engineering, Yildiz Technical University, Istanbul, Turkey*
[3]*Graduate School of Science and Engineering, Kocaeli University, Kocaeli, Turkey*

Abstract: Machine vision applications are widely used in industrial white goods production facilities to determine product quality. In the assembly of products containing flammable or toxic substances in industry, determination of product dimensions is critical for the safety. These dimensions determine the safety limit range of the product. The dimensions of the product are determined by manual and computer-aided measurement methods. Computer-aided measurement is often preferred because manual measurement takes a long time and the accuracy of the measurement depends on the person taking the measurement. Safe gas distribution pipes are used for gas cookers. These pipes are produced in two different forms, blow-moulding and countersinking. The dimensions of the forms are taken from two views, one from top and one from the side. In the top view, the diameter values of the pipe are determined, and in the side view, the measurement values of the blow-moulding and the flare structure are determined. In this study, the top dimensions of the gas distribution pipe were extracted using the Hough transform and line scanning method, and the side dimensions were extracted using the reference-based point distance method by extracting perpendicular lines. The setting of a reference point improves the accuracy of the control, while the line scan method reduces the cost of calculation. As a result of the study, the visual inspection system was integrated into the production line. Based on our tests with 500 products, the inspection system is able to measure the product to an accuracy of 0.1 mm.

Keywords: *Machine vision, Pipe Inspection, Image Processing*

I. INTRODUCTION

Aluminium is a material that is used in large quantities in manufacturing plants due to its high strength to weight ratio and low cost. Aluminium pipes for gas cookers, a product of the white goods industry, are designed and used for the passage of gas. As a result, the gas cookers produced are light and durable.

For aluminium pipes used in gas cookers, compliance with standards is an important criterion. Pipes can be manually or visually inspected for compliance with standards. The aluminium pipes in gas cookers have two types of joint: blow-moulding and countersinking. Quality control of these pipes involves checking measurements such as inside and outside diameter values, distance from the blow-moulding point to the pipe end and blow-moulding length. During manual quality control, diameter and distance measurements are made using traditional methods such as pass-through gauge and caliper. Nowadays, image-based product quality inspection methods offer high accuracy and time savings compared to manual quality control methods. For this reason, the use of vision-based product quality inspection approaches in manufacturing facilities continues to grow. Conventional methods are based on sampling. As a result, the entire production process cannot be controlled. However, the solution, which is integrated into the automation system using machine vision, allows the quality control of all

products to be measured quickly and stably.

Kim, H.S. [1] used the images analysed from the top and side angles according to the product position for measurement extraction. In the top position-based images, the outer diameter was extracted using the maximum points of the contour obtained, while the inner diameter was obtained using the average of the lines scanned from the centre. In the lateral position based images, the slope in the regions of interest was calculated at different locations depending on the reference point obtained based on the pipe position. Gaohua, L. [2] proposed a threshold segmentation algorithm for crack detection on a series of high-gloss ceramic tubes. The reflected light from the ceramic creates small grey areas in the defective areas. The signals obtained from the grey areas are used to calculate the average defect rate, and a threshold value is determined as a function of product availability. Jiming, S. [3] investigated three parameters to achieve defect detection in corrugated pipes in an image: extraction of pipe body lines, burr control and extraction of the number of holes in perforated pipe types. These parameters were analysed by extracting the edge images of the desired region at different thresholds in binary images. Yaoheng, F. [4] performed a measurement by applying an optimised Hough transform to the image matrix to which a Sobel filter was applied to measure the liquid level in the image. In their study, they defined the measurement region to be obtained as the region closest to the centre. Thus, the circle diameter closest to the centre formed the result of the measurements. In the experimental verification, a product size of 808 mm was measured with an error of 2.99 mm. Raisa B. R. [5] implemented differential measurement considering time-varying object size variation. In his study to extract diameter measurements from randomly moving fuel drop images, he performed gradient estimation using the first derivative of the image matrix to extract diameter size and direction information. By supporting this estimation with boundary point optimisation, he was able to find the optimum circle region and measurements with an accuracy of 0.2mm. Kim, H.S. [6] proposed a computer vision based tube inspection algorithm by obtaining front and side view tube images using CCD cameras. To reduce the processing time in his algorithm, he applied an improved Hough transform based on calculating the geometry of straight line segments. He also calculated the centre points of the inner and outer diameters using the line scan method. They developed a method to improve sensitivity by using a line equation with an average parameter. The system they developed detects whether the pipe is faulty or not and separates the faulty pipes from the driving machine.

In this study, an image control system was developed for the aluminium form structure required for the gas cooker. From the top view of the aluminium tubes, diameter values were obtained using the Hough and line scanning methods, and from the side view, structural measurement values of blow-moulding and flare were obtained using the point distance method by subtracting the vertical lines and reference points.

II. TUBE GEOMETRICAL MEASUREMENT ALGORITHM

In this section an algorithm is developed to check the dimensions of aluminium tubes to ensure safe gas passage in gas cookers. Two images, one from the top and one from the side, have been taken for each of the blow-moulding and countersinking connection models, whose mechanical design is shown in Figure 1. The aim is to extract the control dimensions from the four different images obtained and to produce these dimensions within the tolerances (0.1 mm) defined for quality and safety.

Each desired measurement parameter has different illumination and position values. Therefore, different image pre-processing is required for each measurement parameter. In the general algorithm, images taken from the top angle are used to calculate the inner and outer diameters. The Hough transform method is used to measure the outside diameter. With this method, pixel transitions can be clearly captured and the low noise level provides ideal results for outside diameter measurement. When measuring the inside diameter, different reflection

angles depending on the pipe size cause noise. This noise prevents the extraction of the diameter with high accuracy. For the inner diameter, the line scanning method is applied at different angles from the centre of the outer circle obtained by the Hough transform method and in the direction of the outer diameter. This set of points is used to calculate the internal diameter.

An adaptive ROI is first applied to the images obtained from the side angle. Adaptive ROI is applied due to the deviations that can occur in the point plane image acquisition point of different types of pipes. An adaptive region of interest is defined for each pipe in order to reach the desired areas of the pipes to be analysed. Vertical and horizontal lines (with slopes of 0° and 90°) are extracted from the overall image using morphological operations. The final image is used for line extraction with Hough transform and to create a point set. The values obtained from the point set are used for distance measurement.

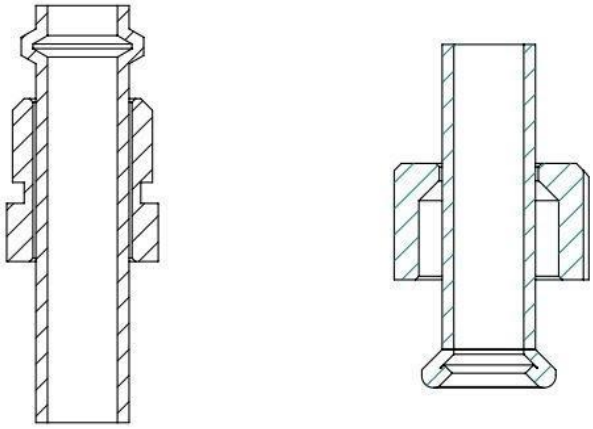


Fig 1. Tube Mechanical Drawing

III. OVERALL OF PIPE ANALYSIS ALGORITHM

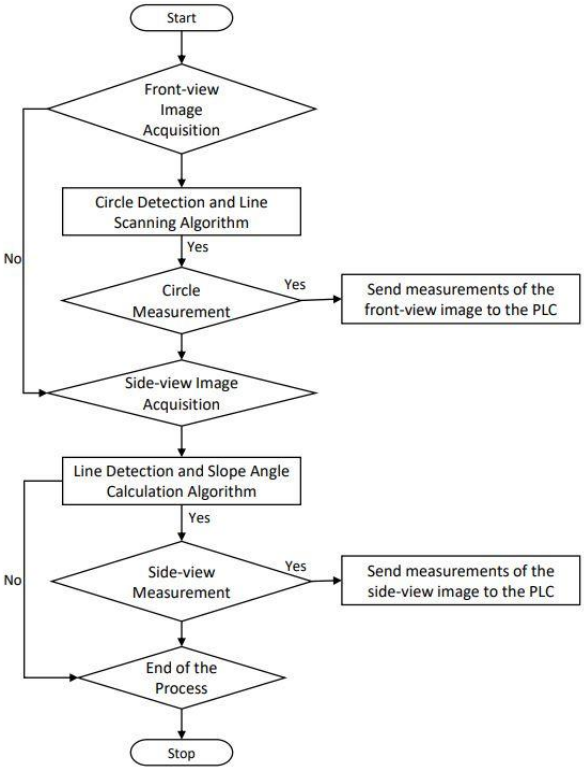


Fig 2. Flowchart of Tube Automation

A. Front-view Analysis

The outside diameter of the aluminium pipe was determined by taking an image from above. A shadowless square light was used to capture the image of the pipe from all angles. This lighting provided clear black and white transitions in the image. In addition, the lighting conditions were not affected by changes in product focus due to production. As a result, the lighting accuracy remained constant even as the dimensions changed. The methods used to detect the dimensions on the image matrix are as follows.

Front-view Circle Detection

The image matrix obtained from the top angle contains two pieces of information as outer and inner diameters. For the outer diameter measurement of the pipes, a 3x3 median filter was applied to the image pixels (1920x1390) to reduce the distortion effects caused by the environment. A binary thresholded image was then obtained using the binary thresholding method. This provided the image area needed to extract the geometric features of the product. The resulting image is shown in Figure 3 a. The aim is to obtain the outer diameter of the product by clearly extracting the product edge lines. For this reason, the pixel density of the product was increased by applying a reconstruction matrix to the image. The result of the application is shown in b. The product diameter was extracted by applying the edge detection algorithm on image b. The image with diameter information is as in c.

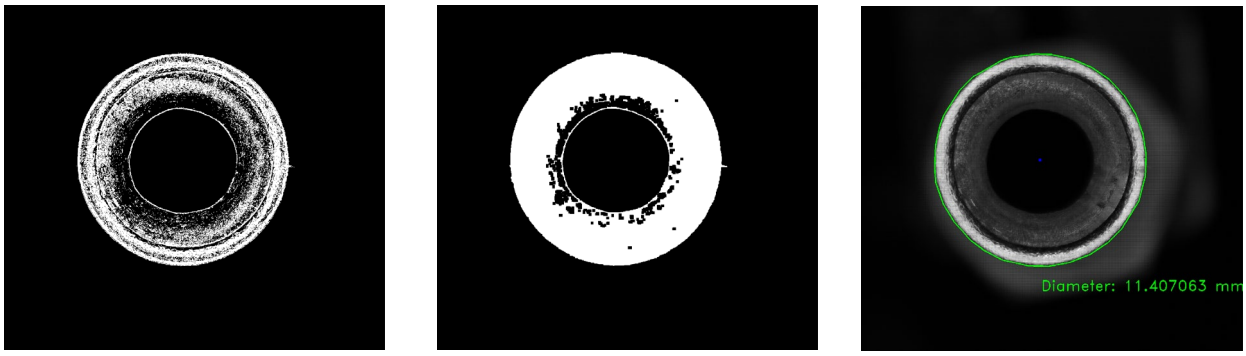


Fig 3. Pipe outer diameter measurement (a- Threshold image, b- structural operation, c- result)

The second feature to be obtained is the inner diameter of the pipe. The inner diameter is the boundary region of the dense black area from the grey region shown in Figure 4 a. The thresholded image of the boundary region is shown in b. In this case, the fact that the boundary transition is a diffuse feature made it possible to calculate the result statistically. For this purpose, angular scans were performed on the thresholded image from the centre to the region of interest at 15° intervals. The first and last quartile values of the scan lines were eliminated and the average of the remaining values was taken as the diameter value. As a result of the analysis, the scan lines are displayed in green and the average diameter information is displayed in red. The average diameter output is shown in equation 1. In the equation, n is the total number of scans, q is the scan order of the first and last quadrants.

$$mean = (1 / (n - 2 * q)) * sum(data[q + 1 : n - q - 1]) \quad (1)$$

The $sum(data[q+1:n-q-1])$ expression calculates the sum of the data in the specified range.$(1 / (n - 2 * q))$ is the normalisation function that reduces the expression to the mean.

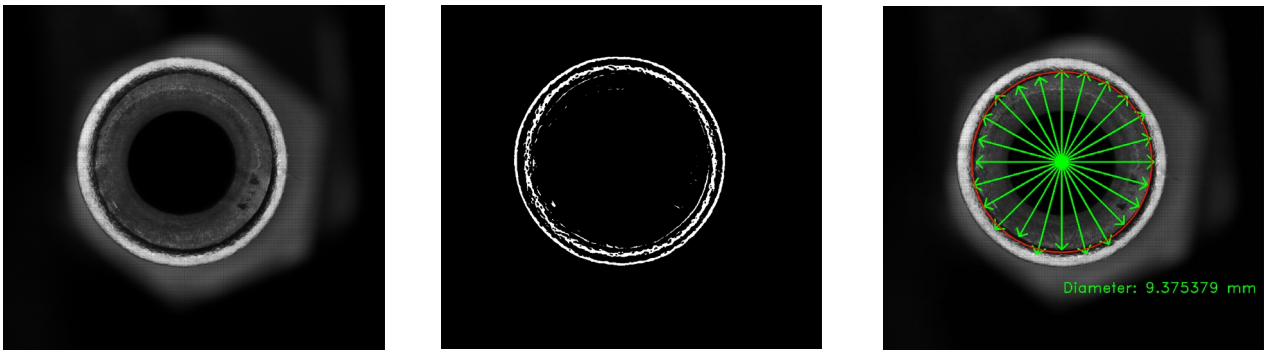
B. Side-View Analysis

The blow-molding length and the distance from the blow-molding point to the end of the pipe are calculated from a side view of the pipe. Aluminium pipes were held by a 6-axis robot and brought to the image acquisition point. As the pixel value of the pipe end distance is an important reference distance for the values to be obtained from the side image, it must be unambiguously determined. Therefore, to avoid image loss and to obtain an accurate measurement, it is necessary to take an image section that can change according to the pipe position. The extraction of the image region of interest is determined according to the distance between the pipe ends.

Figure 5 shows the resulting Canny Edge Detection image. The first step is to obtain the centre distance by scanning from a fixed point line along the line in the edge image. Then the end point of the product was detected by scanning along the column. The point obtained as a result of the average of the y-coordinate values of these two points, shown in blue in Figure 5, and the column scan was set as the pipe end point.

The perpendicular regions shown as green circles in Figure 5a are used to obtain the distance between the blow-moulding zone and the pipe end. By using the areas perpendicular to the pipe surface in these areas, the distance between a point obtained from this area and the point obtained from the pipe end position is given as the desired measurement value.

A 3x3, [-1, 0, 1] matrix was used to extract vertical lines from the image. To filter the vertical lines, lines with a horizontal threshold of 1 pixel and a minimum vertical pixel threshold were defined as the desired regions, and a set of points in the desired region was obtained by applying the Hough transform to the pixels. The Hough transform in polar coordinates is given by equation 2, where (x, y) are points in the central coordinate system and (θ, p) are polar coordinate points. θ is the angle between the start and end points of the line and p is the distance from the centre of the line to the end point [10]. The result was a set of line points in the desired region.



$$r = x * \cos\theta + y * \sin\theta \quad (2)$$

Fig 4. Pipe inner diameter measurement (a- Test image, b- Threshold image, c- result)

The difference between a point taken from the point set of vertically valued line pixels and the starting point defined as the region of interest at the horizontal position of the pipe gives the desired tip size. In the blow-moulding section, horizontal lines were extracted to find the blow-

moulding length in the image obtained from the side angle, and other data was eliminated by leaving it below the threshold. The largest horizontal line starts at the end of the blow-moulding and continues along the pipe. This starting point represents the end point of the blow-moulding section. The first point of the blow-moulding section is represented by the vertical lines obtained in the previous



algorithm. The difference between these two points is the blow-moulding length. Figure 5 b shows the pipe end length and c shows the pipe blow-moulding dimension.

Fig5. Pipe Side-view diameter measurement (a- Threshold image with reference points set, b- Pipe end zone dimension, c- Pipe blow-moulding dimension)

IV. CONCLUSION AND DISCUSSION

In this study, a production integrated vision system was developed for the production of tubes in the internal mechanism of a gas cooker. The system developed measures product dimensions with an accuracy of 0.1 mm. The control system ensures that the product dimensions are within a certain precision range and gives feedback to the control system for products outside this precision range. Defective products are removed from production by a robot while production of the correct parts continues. In addition, images and log files of faulty products are stored for system maintenance and root cause analysis.

In the study that was developed, it was found that the Hough method was not able to provide a sufficient level of precision. The reason for this is that the manufactured product contains a wide range of dimensional changes. The Hough method produces accurate values in a limited range. However, there is a wide range of product variation in production systems. In this case, the Hough method produces incorrect analysis regions or cannot produce accurate values over a large analysis scale. For this reason, point scale analysis with line scanning and contour based area analysis have been preferred. The boundaries obtained by line scanning determine the accuracy of the product measurement. Filtering operations are then applied for accurate background extraction and contour regions are used for product analysis. This method was found to give more accurate results in systems with a wide variety of products.

REFERENCES

[1] K. Hyoung-seok, L. Byung-ryong, K. Rak-jin, "Development of Computer-Vision-Based Pipe Inspection System," International Forum on Strategic Technology, February 2007.

[2] L. Gaohua, L. Mouyou, X. Junmei, "A Machine Vision Approach for Small Ceramic Tubes Detection," International Conference on Intelligent Computation Technology and Automation, October 2009.

[3] S. Jimming, Z. Jiahui, C. Shuo, Y. Feng and A. Yilun, "Research on Corrugated Pipe Defect Detection Based on Digital Image Processing," IEEE Advanced Information

Management,Communicates,Electronic and Automation Control Conference, May 2018.

[4] F. Yaoheng, P. Yongqing, L. Peng, and W. Weiku, "Research on Image Liquid Level Measurement Technology Based on Hough Transform," International Conference on Pattern Recognition and Machine Learning, August 2021.

[5] R. Raisa, A. Thomas, X. Yuhao, H. Michael and R. Anthony, "Dynamic Differential Image Circle Diameter Measurement Precision Assessment: Application to Burning Droplets," IEEE Transactions on Pattern Analysis and Machine Intelligence, May 2022.

[6] K. Hyoung-Seok, N. Erdensuren, A. Sheikh, B. Yong-Hwan and L. Byung-Ryong, "Real-time forming error inspection system using computer vision for small-sized tubes," ICCAS-SICE, August 2009.

[7] R. Malik, Z. Chen, B. Mike, N. Gunther, "Imaging sensor and imaging algorithms for quality inspection of flexible materials," IEEE Sensors Applications Symposium (SAS), April 2016.

[8] V. Yüksel, Y.E. Tetik, M. Yılmaz, Ö.C. Özdemir, "Automated Pipe Inspection Based on Image Processing," 47th Annual Conference of the IEEE Industrial Electronics Society (IECON), October 2021.

Classification of Spherical Graphite Cast Iron Images by Using Machine Learning Techniques

Samuel A. OYEWOADE[*,1], Ayşe E. CANBİLEN[1], Mehmet Ş. ATAŞ[2], Mehmet YILDIRIM[2]

[*]f181202097@ktun.edu.tr, ORCID: 0009-0007-4244-8021
[1]*Department of Electrical-Electronics Engineering, Konya Technical University, Konya, TURKEY*
[2]*Department of Metallurgy and Materials Engineering, Konya Technical University, Konya, TURKEY*

Abstract: In the casting industry, productions can be made in quite different qualities and standards based on the nature of the current need. Accurate classification of the samples is essential, as even minor changes in grain size and boundaries, as well as particle orientation can result in significant variations in how a metal responds to stress and deformation. In addition to that, accurate detection of the quality of the samples during the production and control stages is crucial to speed up all related processes. Thus, the prediction success of the microstructure classes can increase automation and productivity of a manufacturer that uses iron as a raw material. Considering that, in this study, it is intended to present a computer-aided decision support system for the casting industry. Specifically, a total of 1230 microstructure images belonging four different often preferred types of spherical graphite cast iron (SGCI) in this industry are classified by using a variety of machine learning (ML) techniques, namely linear support vector (SV), *k*-nearest neighbor (KNN), Naïve Bayes and random forest classifiers. The RGB image data set was converted to grayscale image before extracting several statistical features, which are then used in the training of the models. The efficacy of these ML models was evaluated in terms of accuracy, specificity, sensitivity, precision and F1 score. Also, a comparison based on the time it takes to train and test for each model was observed. When the classification performances are compared, it is observed that the best results are obtained with the KNN classifier.

Keywords: *Image Classification, Machine Learning, Spherical Graphite Cast Iron*

I. INTRODUCTION

Casting is one of the most important production processes of metal and alloy fabrication. Nowadays, spherical graphite cast iron (SGCI) is popular as the preferred type of cast iron thanks to its advantages [1]. Therefore, although experiments involving the conversion of the graphite matrix into spherical form have been carried out since the late 1940s, their importance is increasing day by day. Indeed, SGCI is an alternative to commercial carbon steel due to its similar mechanical properties and lower production cost compared to steel [2], [3]. It has good machinability and is about 10% lighter than steel. Besides, the production cost of SGCI is between 20% to 40% more affordable than commercial steel according to the literature [4], [5].

In the meantime, many studies have been carried out on the control of the composition of SGCI, which is also called ductile iron. In nodular cast iron, various trace elements such as lead, antimony, titanium, etc. are kept as low as possible for a good graphite structure, and a small amount of cerium is added to the casting to end the undesirable effects of the raw material. On the other hand, some certain elements come to the fore in SGCI, such as carbon, silicon, magnesium, etc. [6]. It is worth noting here that magnesium is the most popular element in the industry, due to its effectiveness in spheroidizing the ductile cast iron. However, this element is exceedingly difficult to put in cast iron. Therefore, many processes aimed at solving

this problem have been developed [7].

In addition to that, minor differences in microstructures of metals can indeed matter significantly, especially in various engineering and material science applications. For instance, as GGG 40 refers to iron with minimum tensile strength of 400 MPa and GGG 70 refers to iron with minimum tensile strength of 700 MPa, using a GGG 70 iron where GGG 40 ought to be used may not only be ineffective but also unsuitable in the areas of impact resistance, wear properties, machinability etc. Therefore, the importance of the classification is to eliminate the chance of over-engineering.

By the advent of computer vision (CV) and machine learning (ML) technologies, it has been possible to analyze materials by quantitatively correlating microstructure with composition, and processing properties [8]. Thus, several studies used CV and ML approaches to automate the measurement of the area fraction of graphite particles in the microstructure of the SGCI [8], [9].

Considering the above-mentioned points, four most preferred types of SGCI are classified in this study by using various ML techniques with the aim of proposing a decision support system to define quality of ductile iron and make more fast and accurate decisions based on the microstructure images. The support vector (SV), *k*-nearest neighbor (KNN), Naive Bayes and random forest classifiers are used for the classification process, which also supplies an idea on the tensile strength of the samples. The performances of the suggested classifiers are evaluated by using accuracy, specificity, sensitivity, precision and F1 score parameters.

II. MATERIALS AND METHODS

In this section, first, we mention the SGCI data set used in this study, and then explain the preprocessing and feature extraction steps. Following that, the utilized classification approaches are detailed, respectively. Lastly, the comparison criteria are given.

A. Spheroidal Graphite Cast Iron (SGCI) Data Set

The most preferred ductile iron castings according to the microstructure in the sector are GGG 40, GGG 50, GGG 60, and GGG 70, respectively, which are also used in this study and given in Table 1 according to the microstructure properties [1], [5]. In order to visualize the SGCI microstructures, Fig.1 is provided with sample images representing the related classes.

Table I . Sgci Types According To Microstructure

Samples	GGG40	GGG50	GGG60	GGG70
Microstructures	Ferritic	←→		Pearlitic

The samples used in this study were obtained from various companies operating in Konya City industry. A total of 1230 images were taken from four different samples at 100X magnification. Among them, 315 images were labeled as GGG 40, 307 of them labeled as GGG 50, 299 of them labeled as GGG 60 and 309 of them labeled as GGG 70. For the metallographic investigation, samples were mounted in Bakelite at 180°C, ground with Silicon-Carbide (SiC) papers from 180 to 2000 grit, and then, mechanically polished with 1 and 0.3µm alumina solution. Finally, samples were etched with a 5% Nital solution for up to 20 seconds, depending on the aging condition. The graphite of the samples was examined by Nikon Eclipse MA100 model inverted optical microscope.

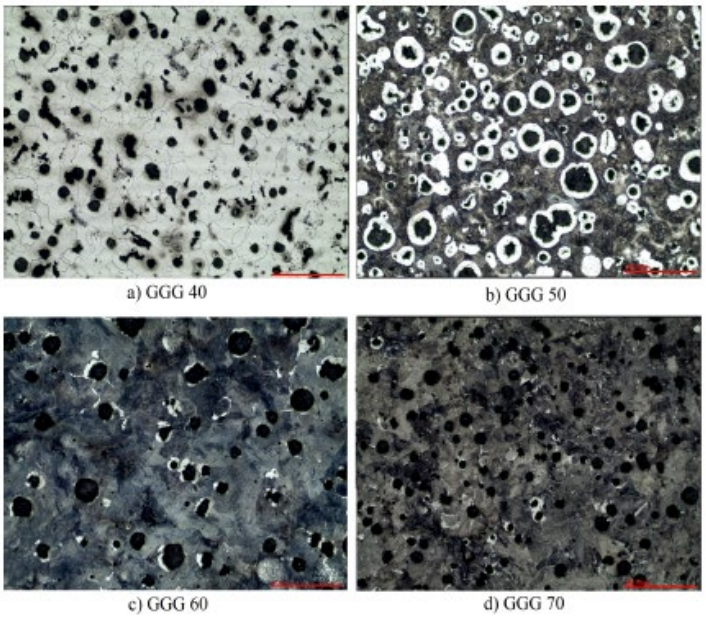


Fig. 1. Sample images from the SGCI data set.

B. Preprocessing and Feature Extraction

The utilized dataset contains 1230 SGCI microstructure images. Among them, we used 984 of them (80% of the total image samples) as a training data set and 246 of them (20% of the total image samples) as a test data set. The total data set contains 315, 307, 299 and 309 labeled images for GGG40, GGG50, GGG60, and GGG70, respectively. With the aim of reducing the complexity related to computational requirements, we convert the RGB images to gray-scale images. Using the matrix of the gray levels, we calculate the following statistical features as shown in Fig. 2:

- *Mean:* The average value of all pixel intensities in an image.
- *Median:* The middle value when all pixel intensities are sorted in order.
- *Sum:* The total number of all pixel values. It exhibits a correlation with image contrast.
- *Standard Deviation:* A measure of the amount of variation in pixel intensities. A higher standard deviation indicates greater variation.

	Mean	Standard Dev	Median	Sum(x10^6)	Class
0	159.358200	64.564932	190.0	501.297552	40
1	98.011959	67.337531	120.0	308.318963	40
2	93.496218	67.789256	112.0	294.113670	40
3	90.677685	67.730805	105.0	285.247334	40
4	91.855244	67.018895	103.0	288.951614	40
...	...	...	...	...	...
1225	82.413814	41.338208	86.0	259.251443	70
1226	82.950492	41.566694	86.0	260.939686	70
1227	80.420264	41.034509	83.0	252.980275	70
1228	81.092177	40.944398	84.0	255.093932	70
1229	65.964829	39.887673	67.0	207.507411	70

Independent variables

Dependent variables

1230 rows × 5 columns

Fig. 2. The statistical features used for the SGCI data set.

In order to create a model that generalizes all the cases well, the entire dataset is randomly shuffled before splitting the data into training and test set. Additionally, it is observed that certain models perform better when the independent variables are normalized. Therefore, a normalization process is applied to the entire dataset. The independent and dependent variables from the training set shown in Fig. 2 are utilized to feed the ML models for training. The evaluation metrics are calculated based on the predictions generated from the test dataset.

C. Machine Learning (ML) Techniques

In this section, the ML techniques utilized to classify the SGCI images are introduced in subheadings, respectively.

1) SV Classifier (SVC): SV machine (SVM) is one of the most popular ML algorithms [10]. Although it was initially proposed for solving binary classification problems, SVC has been optimized to also solve regression and multi-class classification problems in later times [11], [12]. This ML algorithm works by drawing a separator, which is a point for one dimensional (1D), a line for two dimensional (2D) and a plane for more than 2D input data. The point, line or plane are referred to as hyperplane. A sample SVM diagram indicating the hyperplane and SVs is shown in Fig. 3. Indeed, the goal of this classifier is not only to draw any hyperplane, but also to draw one with widest distance margin. This leads to SVC being referred to also as maximum margin classifier. The data variables closest to the gutter's outward are referred to as SVs. Technically, there cannot be SVs within the margin as their weights will be zero. The farther the SV, the lesser its weight. If the input data can be separated by straight lines, the data is linearly separable, otherwise it is non-linearly separable. To be able to solve non-linearly separable data problems, it is essential to apply a technique called kernel trick. By using kernel trick, the data sets, which are not linearly separable, are transformed to a higher dimension.

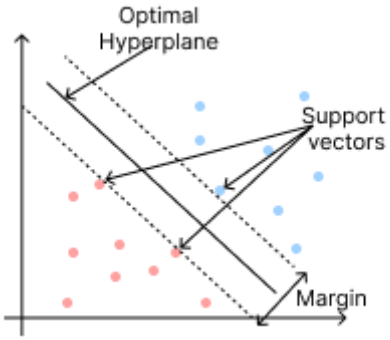


Fig. 3. A sample SVM diagram indicating the hyperplane and SVs.

2) KNN Classifier: This is another form of supervised ML algorithms that makes prediction by considering k amount of nearest data as its name implies [13]. Two most common ways of finding k are given as: *i)* taking the square root of the total number of training datasets, and *ii)* plotting either the accuracy or error of the various samples of k over k. The algorithm makes prediction by collecting the nearest k samples based on the distance -in our case the Euclidean distance-, and the prediction will be made as the sample with the mode. KNN is a lazy algorithm as all it does during the training is store the data, and computation is done on run time, once there is need to test or predict [14]. It is crucial for k to be an odd number for a binary classification problem, while it should not be a multiple of the number of classes for a multi-class classification problem. We assumed $k = 3$ for this study, and a sample KNN diagram is given in Fig. 4.

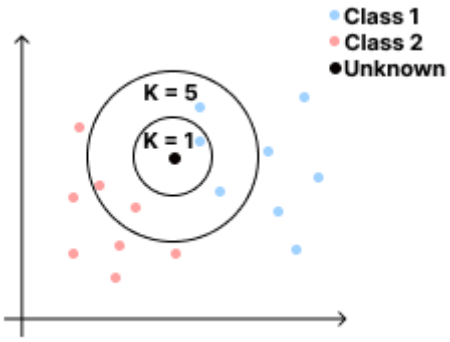


Fig. 4. A sample KNN diagram.

3) Naive Bayes Classifier: The algorithm of this classifier is dependent on the Bayes theorem, which states that given series of events X = {X1, X2, ..., Xn}, the probability of events Y = {Y1, Y2, ..., Yn} can be calculated from

$$P(Y/X_1, X_2, \dots, X_n) = \frac{P(X_1, X_2, \dots, X_n\ /Y)P(Y)}{P(X_1, X_2, \dots,\ X_n)} \quad (1)$$

where $P(X_1, X_2, \dots, X_n\ /Y)$ denotes the probability of events X occurring on the condition that Y is given, while $P(Y)$ and $P(X_1, X_2, \dots, X_n)$ are representing the marginal probabilities of observing Y and X, respectively.

The value of the probability given in (1) is then normalized, compared and the argmax is returned as the target class. Naive Bayes algorithms often thought to assume that features are independent of one another, which has, however, been proven otherwise by its performance on functionally dependent features [15]. Naive Bayes classifier is a good fit for a situation where there is less training data or outlier [16]. It is also known to be fast [17].

4) Random Forest Classifier: Random forest classifier is the application of ensemble method on tree-structured classifiers, which aims to eliminate the fitting problems that often come with single decision tree [18]. It works by bootstrapping the N number of decision trees and then calculating the information gained on each leaf node, which is a deterministic factor for the classification process. Random forest is a solution to the poor generalization problem of decision tree classification method. Unlike other algorithms, increase in model complexity do not directly lead to over-training. In other words, random forest provides increased generalization accuracy without compromising on training accuracy [19]. A sample random forest diagram can be seen in Fig. 5.

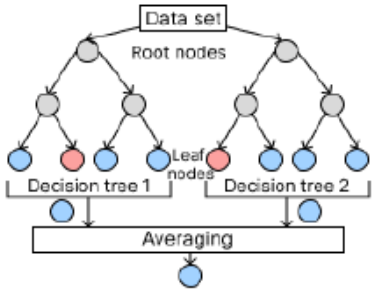


Fig. 5. A sample random forest diagram.

D. Comparison Criteria

In this section, the comparison criteria used for evaluating and comparing the SGCI microstructure classification performances of the above-mentioned ML techniques are presented. All the metrics provided here can be obtained by using a confusion matrix as given in Fig. 6, and also can be calculated as follows.

i) Accuracy: This is the ratio of the total number of right predictions to the total prediction that can be calculated as

$$acc = \sum_{i=1}^{n} \frac{TP_i+TN_i}{TP_i+TN_i+FP_i+FN_i}, \quad (2)$$

where *n* represents the number of classes, while *TP, TN, FP,* and *FN* denote true positive, true negative, false positive and false negative cases, respectively.

ii) Sensitivity: This is the measure of positive class that is correctly classified as positive. It is also known as recall, recall of positive class, or true positive rate. Sensitivity is given by

$$sn = \sum_{i=1}^{n} \frac{TP_i}{TP_i+FN_i}. \quad (3)$$

iii) Specificity: This is the measure of negative classes that are correctly classified as negative. Specificity is also known as the recall of negative class or true negative rate. It can be calculated from

$$sp = \sum_{i=1}^{n} \frac{TN_i}{TN_i+FP_i}. \quad (4)$$

iv) Precision: It measures the effectiveness of a model's positive prediction. Precision can be obtained as the ratio of TP over the total number of positive predictions as follows

$$pr = \sum_{i=1}^{n} \frac{TP_i}{TP_i+FP_i} \quad (5)$$

v) F1 score: It gives the harmonic mean of recall and precision that can be calculated from

$$F1 = 2(pr \times sn) / (pr + sn). \quad (6)$$

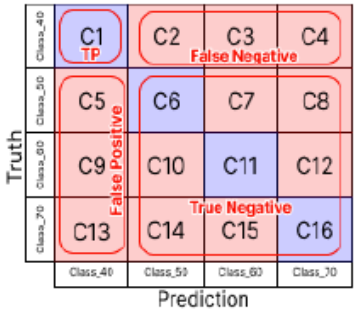


Fig. 6. Confusion matrix for a multi-class classification using cell C1 as case study.

III. EXPERIMENTAL RESULT

In this section, the details of both the simulations realized for the classification of the SGCI images and the obtained results are presented.

As the first step, a preprocessing procedure is realized, and followed by statistical feature extraction. Specifically, the SGCI microstructure images data set is converted into grayscale and then the mean, standard deviation, median and sum parameters are computed. After that, the calculated parameters are normalized to extract trainable features. By using the normalized statistical features of the images as the input for the ML algorithms, classification procedure is realized with 5-fold cross validation through the proposed classifiers, respectively, and the evaluation metrics are computed. The results are obtained by utilizing the one-vs-rest strategy with macro averaging and presented in Table II. From this table, it can be easily concluded that the KNN method provides the best results, while Naive Bayes gives the worst. To give more details on misclassifications, confusion matrices are provided for each method in Figs. 7-10, in

which 0, 1, 2 and 3 represent GGG 40, GGG 50, GGG 60 and GGG 70, respectively.

In addition to that, average training and test execution times are calculated for each classifier and given in Table III. Since the execution time may vary on consecutive runs, the average and median of processing time for 21 runs are calculated. We take the outlying feature of the first run into consideration when collecting the time data. According to Table III, the fastest training and test procedures are realized with KNN and Naive Bayes, respectively, while random forest classifications are quite slow compared to the others.

Table II. Comparison Of Evaluation Metrics

Model	*Accuracy*	*Specificity*	*Sensitivity*	*Precision*	*F1 Score*
Linear SVC	0.9919	0.9945	0.9835	0.9843	0.9838
KNN	1.0	1.0	1.0	1.0	1.0
Naïve Bayes	0.9451	0.9635	0.8918	0.9019	0.8940
Random Forest	0.9939	0.9960	0.9877	0.9878	0.9877

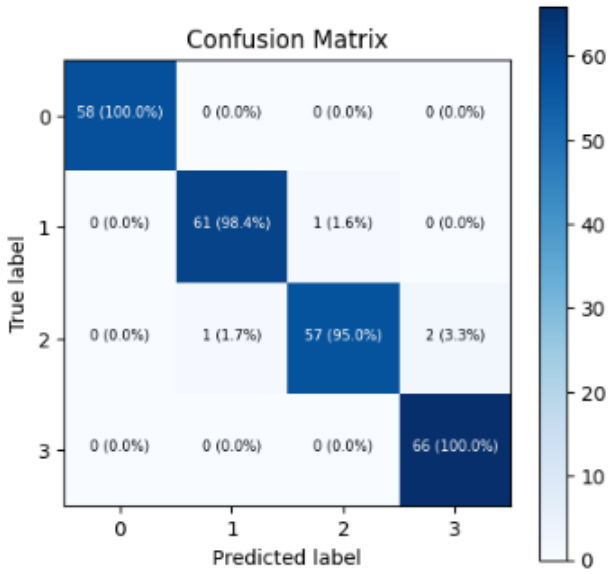


Fig. 7. Confusion matrix of linear SVC.

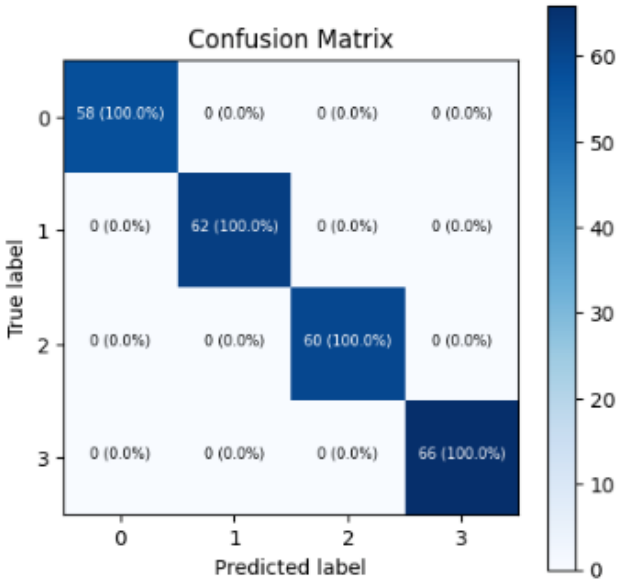


Fig. 8. Confusion matrix of KNN classifier.

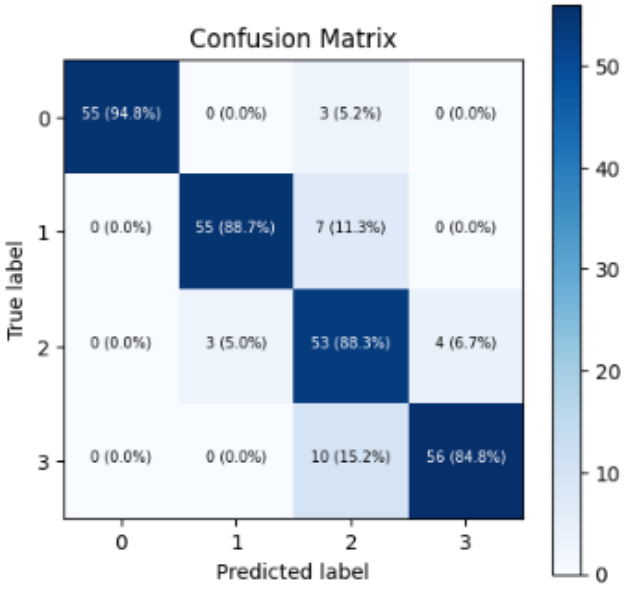


Fig. 9. Confusion matrix of Naive Bayes classifier.

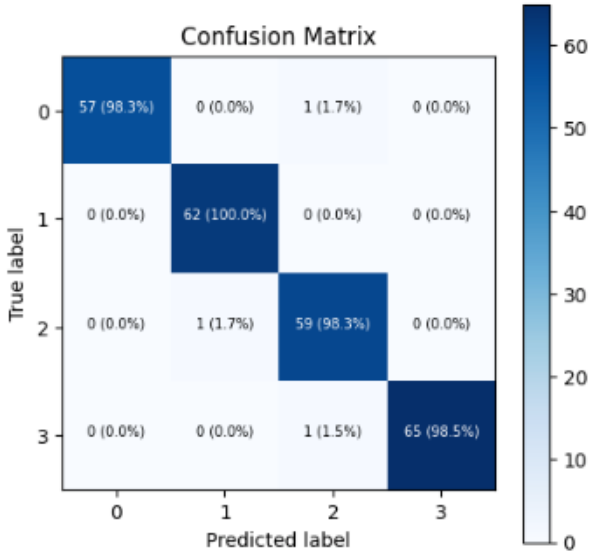


Fig. 10. Confusion matrix of random forest classifier.

Table III. Average Training And Test Execution Times

Model	*Training*		*Test*	
	Average	**Median**	**Average**	**Median**
Linear SVC	45.18 ms	42.70 ms	4.19 ms	3.95 ms
KNN	1.14 ms	1.15 ms	9.28 ms	9.71 ms
Naïve Bayes	1.22 ms	1.24 ms	0.68 ms	0.65 ms
Random Forest	292.61 ms	287.0 ms	16.84 ms	14.80 ms

IV. CONCLUSION

In this study, a computer-aided decision support system, which automatically defines quality of ductile iron and gives an idea on the tensile strength of the samples is introduced. The proposed system makes faster and more accurate decisions based on the microstructure images. Comparing five different evaluation metrics, it is concluded that the KNN is the most appropriate method for classifying the SGCI data set. The KNN classifier has the fastest training speed since it performs a few operations during the training stage. Naive Bayes classifier is clearly the fastest for testing at the expense of efficiency because all its operations

are basic arithmetic.

It is worth noting that the advent of using ML is to seek for a new way of classifying that saves time and cost with increased automation and scalability without compromising on accuracy. Using nodularity and sphericity characteristics of the SGCI microstructures as input parameters of the ML algorithms can provide more practical evaluations in future studies.

REFERENCES

[1] C. S. Çetinarslan and S. K. Genç, "Study in the variation of mechanical properties of nodular cast iron depending upon section thickness," Materialwissenschaft und Werkstofftechnik, vol. 45, no. 2, pp. 106–113, 2014.

[2] B. Karaca and M. ¸Sim¸sir, "The effects of heat treatment on the tensile properties of camshaft made of GGG70 series spherical graphite cast iron," Acta Physica Polonica A, vol. 135, no. 4, pp. 811–818, 2019.

[3] A. Al-Ghonamy et al., "Effect of graphite nodularity on mechanical properties of ductile iron for waterworks fittings and accessories," Int. J. Civil & Environmental Engineering, vol. 10, no. 3, pp. 1–4, 2010.

[4] J. Kohout, "A simple relation for deviation of grey and nodular cast irons from hooke's law," Materials Science and Engineering: A, vol. 313, no. 1, pp. 16–23, 2001.

[5] D. O. Fernandes et al., "Nodular cast iron GGG40, 60, 70 mechanical characterization from bars and blocks obtained from brazilian foundry," Metals, vol. 12, no. 7, 2022.

[6] M. M. Henderson, Cooperation, convertibility, and compatibility among information systems. National Bureau of Standards Miscallaneous Publication, 1966.

[7] H. O. Gekonde, "Material characterization of ductile irons for industrial applications," master's thesis, University of Nairobi, 1989.

[8] K. Alrfou et al., "Synergy of unsupervised and supervised machine learning methods for the segmentation of the graphite particles in the microstructure of ductile iron," Materials Today Communications, vol. 30, p. 103174, 2022.

[9] E. A. Holm et al., "Overview: Computer vision and machine learning for microstructural characterization and analysis," Metallurgical and Materials Trans. A, vol. 51, p. pages5985–5999, 2020.

[10] C. Cortes and V. Vapnik, "Support-vector networks," Machine Learning, vol. 20, pp. 273–297, 1995.

[11] V. Vapnik, S. Golowich, and A. Smola, "Support vector method for function approximation, regression estimation and signal processing," Advances in Neural Information Process. Syst., vol. 9, 1996.

[12] J. Weston and C. Watkins, "Multi-class support vector machines," Citeseer, Tech. Rep., 1998.

[13] T. Cover and P. Hart, "Nearest neighbor pattern classification," IEEE Trans. Information Theory, vol. 13, no. 1, pp. 21–27, 1967.

[14] P. Cunningham and S. J. Delany, "k-nearest neighbour classifiers-a tutorial," ACM computing surveys (CSUR), vol. 54, no. 6, pp. 1–25, 2021.

[15] I. Rish et al., "An empirical study of the naive bayes classifier," in IJCAI Workshop on Empirical Methods in Artificial Intelligence, vol. 3, no. 22, 2001, pp. 41–46.

[16] G. I. Webb, E. Keogh, and R. Miikkulainen, "Naïve bayes." Encyclopedia of Machine Learning, vol. 15, pp. 713–714, 2010.

[17] J. Ren et al., "Naive bayes classification of uncertain data," in Int. Conf. Data Mining, 2009, pp. 944–949.

[18] L. Breiman, "Random forests," Machine Learning, vol. 45, pp. 5–32, 2001.

[19] T. K. Ho, "Random decision forests," in Int. Conf. Document Analysis and Recognition, vol. 1, 1995, pp. 278–282.

Awareness Level of Rural Enterprises on Agricultural Supports

Yavuz Taşcıoğlu[*,1], Cengiz Sayın[1]

[*] ytascioglu@akdeniz.edu.tr, ORCID: 0000-0002-8989-3145
[1]*Department of Agricultural Economics, Akdeniz University, Antalya, Türkiye*

Abstract: Countries make various regulations to reach the level of economic development and to improve the living conditions of the society. The main purpose of these regulations is to ensure development. Development is a phenomenon that includes changes in economic structure and social structure. This process, which starts with economic change, continues with changes in social, cultural, and political structure. For development to be balanced, it is necessary to ensure harmony between population dynamics, natural resources, economic activities, technological developments, social and cultural structures, and to analyze planning and policy development processes well. To achieve development goals, one of the most important objectives should be to improve the qualifications of the society in terms of education, health, and manpower, which are the most basic needs of the society, to raise the standard of living of the society and to eliminate interregional differences. The rapid cycle of industrialization in the world, the concentration of the sector in urban areas has made urban areas the focal points of development. Rural areas, on the other hand, have not benefited sufficiently from development processes. In line with the principles of development, public policies and practices directed towards rural areas for the elimination of interregional distinctions and differences for social change constitute the basis of the rural development process. In this direction, the focus is on evaluating and developing the existing potential of rural areas around the world. In this study, the level of awareness of the agricultural enterprises in the area towards the practice of supporting rural development investments in the target group approach in Turkey was investigated. In the study, micro data obtained by face-to-face survey method from 96 enterprises benefiting from the support program in the Western Mediterranean Region were used. Simple descriptive statistics were used in the analysis and evaluation of the data. According to the results obtained, a close relationship was found between the field of activity of the enterprises and the level of awareness. This result requires target group-oriented differentiation in support tools and components for rural areas.

Keywords: *Development; Rural area; Support; Business; Awareness*

I. INTRODUCTION

Development is the advancement of human life in the economic and social spheres and the increase in welfare. Harris (1992) defines development as the growth of the economy, changes in its structure and improvements in the political and cultural spheres by improving the distribution of income [1]. Ensuring people's access to living conditions, improving the distribution of national income by increasing their incomes, and ensuring improvements in social and cultural areas are among the priorities of development. The basic principle is that these priorities should be compatible with the local structure and transfer natural resources to future generations. In addition to this, development is the reduction of human deficiencies that arise in countries to a great extent and the increase of their material welfare and the mobilization of their potentials. In this respect, development is not only the

increase in the income of individuals in economic terms, but also social and cultural developments. For development to be balanced, it is necessary to analyze the available resources well and reflect them to the society by using them in the most effective way. Reflection processes should be ensured within the framework of national and international policies. Achieving development goals is only possible by improving the quality and quantity of the basic needs of society such as education, health, and infrastructure. For development to be balanced, existing resources should be analyzed well and reflected to the society by using them in the most effective way. Reflection processes should be ensured within the framework of national and international policies. Achieving development goals is possible by improving the quality and quantity of the basic needs of society such as education, health, and infrastructure. In order to achieve the goals in development initiatives, it is desirable to organize them by considering social, regional, etc. structure and differences. However, the developments and changes that started with industrialization have led to the idea that industrialization is the main element of development, and as a result, a process to the detriment of rural areas [2]. For many years, it has been accepted that urban areas are the focal points of development and progress. However, in many countries, especially in recent years, this idea has started to change with the demonstration that there is no distinction between urban and rural areas for social development. It has been recognized that national development cannot be successful without putting mental and physical effort into the development of rural areas. This situation has increased the responsibilities of policy makers working on rural development policies and made it obligatory to realize the practices for rural areas and rural society urgently [3].

In recent years, developed and developing countries have increased the importance they attach to rural development. For this reason, countries make legal arrangements to create policies for rural development. Rural development policies created for this purpose are the policies created to reveal the efforts made throughout the country in order to improve the economic, social, social, and cultural opportunities of the communities living in rural areas, to increase their quality of life and to support them to participate in national development [4]. Countries around the world implement rural development policies for many reasons. The most important of these reasons is that a significant portion of the world's population lives in rural areas and that these communities make their livelihoods through the agricultural sector, which is essential for human nutrition.

In Turkey, rural development activities started in the early years of the republic and continue today. In addition to many public institutions and organizations in Turkey, professional organizations, foundations, cooperatives, unions, private organizations, and universities carry out studies on rural areas in various aspects [5].

Along with national and regional activities for rural development in Turkey, various development-oriented programs are also carried out. One of these programs is the " Rural Development Investment Support Program (RDISP)", which was established according to the principles set out in the National Rural Development Strategy (NRDS) and put into practice after being published in the Official Journal No. 26131 dated 06.04.2006. The program aims to increase the income level of the communities living in rural areas by protecting the environment and natural resources, improving the infrastructure of rural areas, ensuring the integration of agriculture and industry sectors, strengthening food security, creating alternative sources of income in rural areas, increasing the effectiveness of the rural development activities being carried out, increasing the level of public services and creating a certain capacity in rural society [6].

To realize means to see, select, discriminate, understand, intuit. Awareness is defined as the state of being aware [7]. In addition, awareness can be described as a mental state obtained through observing one's own thoughts, emotions, and body [8]. If the phenomenon of awareness is tried to be expressed in the form of customer orientation in which the continuity

of enterprises in the competitive environment is in question; it is the perception, thinking and evaluation of the enterprises of which individuals are customers [9]. In terms of enterprises interested in agriculture in rural areas, awareness is considered as knowing and perceiving the rural area, having information about the support elements, learning, or knowing the existing potential of the rural area, expanding existing investments in accordance with the existing potential of the rural area, making new investments, evaluating the agricultural sector and the national economy on a national and regional scale.

In this study, the level of awareness of agricultural enterprises in the region regarding the practice of supporting rural development investments in Turkey with a target group approach was investigated. In addition, the awareness levels of the enterprises benefiting from the current support towards the rural area; the structure of the countryside, the region and the national economy, the sources of information about the support program and participation in the courses were revealed and the extent to which the awareness levels are effective in improving the goals and activities of the enterprises was examined.

II. MATERIALS AND METHODS

The research was conducted with original data obtained from the target group through a face-to-face interview-based survey, supported by secondary data based on literature research.

A "field research" was conducted in the area called TR61 according to the Classification of Statistical Regional Units (IBBS) Level 2, which includes the provinces in the Western Mediterranean Region (Antalya, Burdur and Isparta), covering the enterprises benefiting from the Rural Development Investments Support Program. In the study, a survey was conducted with 47 enterprises in Antalya province, 26 enterprises in Burdur province and 23 enterprises in Isparta province benefiting from the Rural Development Investments Support Program. Information on these enterprises was obtained from the Support Branches of the relevant Provincial Directorates of Agriculture.

Simple descriptive statistics and a five-point Likert scale were used to analyze the data. In Likert scale, the scale was determined and applied as 1. strongly disagree; 2. disagree; 3. undecided; 4. agree; 5. strongly agree. In the ranking according to the degree of importance, the first three preferences of the business owners/managers according to the topics were taken into consideration and the first preference was multiplied by 3 points, the second preference by 2 points and the third preference by 1 point. The results obtained were taken as a general total and the prioritization ranks for the topics were formed.

III. RESULTS

In the Western Mediterranean Region, the highest number of enterprises benefiting from the program was in Antalya province. Although the region is located in the same geography, there are differences in climate conditions and soil fertility. While Antalya experiences the typical climatic conditions of the Mediterranean Region, Burdur and Isparta provinces show the common characteristics of the Mediterranean and continental climate zones. This situation also affects the agricultural sector and agriculture-based industry. In addition, due to the entrepreneurial characteristics of Antalya province and the closer relationship of individuals with agricultural organizations, they have more information about such supports. On the other hand, in Burdur and Isparta provinces, the need for agriculture-based industry differs due to the nature of the investments made, and this is also reflected.

Among the types of enterprises benefiting from the support program in the Western Mediterranean Region, it was observed that more than half of the total economic investment (56%) was used by companies. After companies, development and irrigation cooperatives and unions (22%) and Village Service Provision Unions (VSPU) (19%) received the most support from the program. Individuals or bilateral partnerships benefited the least from the program (3%). 80.9% of the enterprises benefiting from the program in Antalya province and 52.2% in

Isparta province are companies in terms of their legal structure. In Burdur province, Village Service Provision Unions (approximately 60%) were the most beneficiary enterprises.

Within the scope of the program, enterprises in the region that determined their own field of activity benefited from grant support for processing, packaging, and storage (61.5%). This situation is the same in all three provinces in the region. Business owners applied and benefited from the program by evaluating the deficiencies in the post-production activities of fruit and vegetable production, which is the potential of the region. The program has been an opportunity for the enterprises in the region and the need for processing and packaging of agricultural products produced in the region has been met to a certain extent. In addition, the need for storage of agricultural products produced in the region was met through the support program. In this respect, it has been observed that the support program has benefited the rural area of the Western Mediterranean Region.

Sources from which enterprises get information about the program;

When the information sources of the enterprises benefiting from the program were examined, it was seen that the information sources of the enterprises were different, since the phenomenon of awareness is to access information and evaluate that information.

Enterprises gave more than one answer about the sources of information. Accordingly, the meetings held by the provincial organization of the Ministry of Agriculture and Forestry (61%) were the most important source of information about the program. The other important source of information about the program is the governorships of the provinces in question. Within the framework of the cooperation between institutions, the governorships in the region informed the institutions and organizations in the provinces and districts about the program with official letters. As a result of this information, all VSPU operating under the governorship and district governorships received information about the program. These sources of information were followed by friends, electronic media, relevant websites, press releases, chambers of commerce and industry operating in the region, and the Official Journal (Figure 1).

The enterprises benefiting from RDISP in the Western Mediterranean Region generally obtained information about the program from the meetings held by the provincial directorates of agriculture, which are the provincial organizations of the Ministry of Agriculture and Forestry. However, since approximately 60% of the projects that applied to the program and were accepted in Burdur province were implemented by KHGBs, the information sources of these unions were also through the provincial governorships.

Participation of the interviewees in courses for rural areas;

When the participation in the courses that are seen as educational activities for the development and change of the rural area within the framework of the awareness of the entrepreneurs interviewed in the enterprises benefiting from the program and the trainings they received in these courses are examined, 40.9% of the entrepreneurs attended courses on animal breeding, 18.2% on preparing the projects they will prepare for their investments in rural areas, 13.6% on fruit growing, 9.1% on marketing management, 9.1% on milk processing techniques and the remaining 9.1% on various subjects.

Since animal husbandry activities are more intensive in Burdur and Isparta provinces of the Western Mediterranean Region compared to Antalya province, this is also reflected in the courses opened in these regions. While business owners/managers attended courses on animal husbandry in Burdur and Isparta provinces, it was observed that none of the interviewees in Antalya province, which is different from the existing provinces in terms of climate and production type, attended any courses in this field.

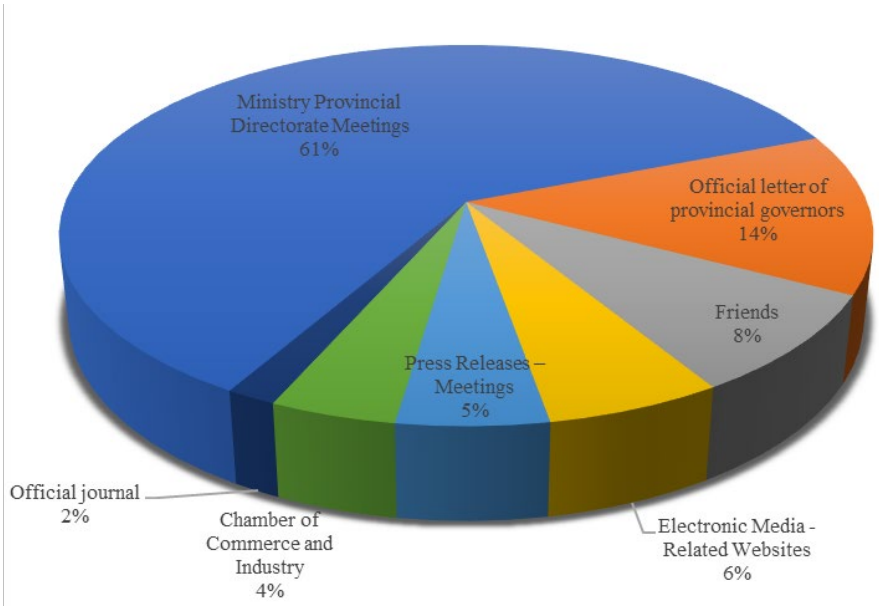


Fig 1. Sources of information of enterprises about grant support (* More than one answer was given.)

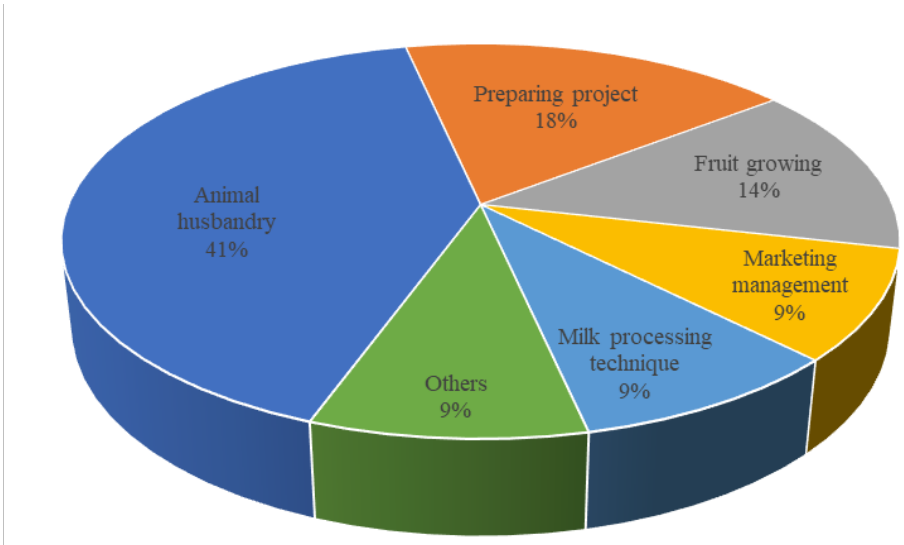


Fig 2. Subjects of the course attended by the enterprise owner's/manager's for rural areas

A significant portion (63.7%) of the courses attended by rural business owners/managers were organized by the provincial organization of the Ministry of Agriculture and Forestry. This situation also shows the degree of impact of the courses organized by the provincial organization in reaching the entrepreneurs in the region. Each course, seminar, etc. to be opened for rural areas will benefit the development of the region. For this purpose, especially the provincial organization of the Ministry of Agriculture and Forestry, other public institutions, and non-governmental organizations, etc., which are effective in rural areas, should take part in such activities.

Entrepreneurs' opinions about rural areas;

Within the framework of the level of awareness, having information about the region and local structure to be invested in is important for the enterprises that will invest. The fact that the support program is provided entirely for rural areas is a situation related to having knowledge about rural areas.

TABLE I

ENTERPRISE OWNER'S/MANAGER'S THOUGHTS ABOUT THE RURAL AREA OF THE REGION

	Thoughts on the Rural Area	Importance levels					Mean[1]	SD[2]	Var[3]
		1	2	3	4	5			
1	Rural areas must be protected	-	-	4	49	43	4.41	0.57	0.33
2	Increased use of technology in rural areas	1	-	4	61	30	4.24	0.63	0.4
3	Support is beneficial for the region	-	1	-	75	20	4.19	0.47	0.22
4	The project benefited the rural community	1	2	19	44	30	4.04	0.83	0.69
5	Rural areas are at the forefront of support	-	6	16	45	29	4.01	0.85	0.73
6	Services that could not be done by the public were done	2	7	6	72	9	3.82	0.78	0.61
7	Eliminated low production and productivity in rural areas	-	5	37	30	24	3.76	0.89	0.80
8	Increased ability to deliver services to the people of the region	-	11	24	47	14	3.67	0.87	0.75
9	The project met the needs of the people of the region	1	26	17	36	16	3.42	1.09	1.19
10	Lack of knowledge in rural areas addressed	1	34	15	44	2	3.13	0.97	0.93
11	Deficiencies of the rural area were eliminated	1	34	29	26	6	3.02	0.96	0.93
12	Changes in the way of life in rural areas	4	32	23	37		2.97	0.95	0.89
13	Idle investments in the region were utilized	27	15	24	6	24	2.84	1.53	2.34

1. strongly disagree; 2. disagree; 3. undecided; 4. agree; 5. strongly agree
[1] Mean: Average; [2] SD: Standard Deviation; [3] Var: Variance

Enterprises attach great importance to the protection of rural areas. For this purpose, the most preferred of their thoughts about the rural area is the protection of the rural area. In rural development studies and within the scope of the current program, it is essential that the applications to be made for rural areas are carried out by protecting nature. For this reason, it has been observed that the enterprises comply with the principle of transferring the rural area to future generations without harming the environment and nature. In addition, it has been observed that the use of technology in rural areas has increased with the investments made and that they agree with the idea that the support provided is beneficial for the region. Entrepreneurs are also of the opinion that the investments and projects have left positive traces in the rural community and are beneficial. However, the enterprises disagree with the idea that the program makes use of idle and unused investments in the rural areas of the region. Entrepreneurs are of the opinion that new investments or existing investments are evaluated within the scope of the program. In addition, the enterprises stated that there was no change in the way of life in the rural areas of the region with the program (Table 1).

Entrepreneurs' opinions on the economic structure of the country and the region;

Within the scope of awareness level, it is as important for enterprises to have information about the economic structure of the country and the region as it is to have information about the rural structure. It is expected that investment ideas will be formed according to the advantages or disadvantages of the economic structure. The opinions of the entrepreneurs about the economic structure of the country and the Western Mediterranean Region are given in Table 3.

Entrepreneurs agree with the idea that the supports provided within the scope of the program are an opportunity for the enterprises in the region, and therefore they would like to benefit from such supports again. However, it is seen that they agree with the opinion that projects that enable the development of the rural areas of the region should be supported in such supports, and that the enterprises established with the program will contribute to the national economy. In addition, the enterprises do not agree with the idea that the public burden has decreased in the investments made in the region. As a matter of fact, the opinion that the public sector should assume a leading role in the development of rural areas and guide the private sector is adopted by the entrepreneurs. Another important emphasis made by the entrepreneurs is that with the implementation of the program, there has been an increase in public services in the rural areas of the region and they do not agree with the view that the resources are used effectively in rural areas with the projects carried out by the entrepreneurs.

TABLE II

ENTERPRISE OWNER'S/MANAGER'S THOUGHTS ON THE ECONOMIC STRUCTURE

	Thoughts on the Economic Structure of Turkey and the Region	Importance levels					Mean[1]	SD[2]	Var[3]
		1	2	3	4	5			
1	Support is an investment opportunity for business	-	-	1	40	55	4.56	0.52	0.27
2	I would benefit from such support again	-	3	2	39	52	4.46	0.70	0.48
3	Projects that enable development should be supported	-	-	4	53	39	4.36	0.56	0.32
4	The project contributed to the national economy	-	-	1	60	35	4.35	0.50	0.25
5	The program allowed for such projects in the future	-	-	5	62	29	4.25	0.54	0.30
6	Projects that will enable local participation should be supported	-	5	2	57	32	4.21	0.72	0.53
7	Support has had an economic impact on communities in the region	-	4	27	31	34	3.99	0.90	0.81
8	Support boosted economic revival in the region	3	2	13	58	20	3.94	0.84	0.71
9	Increased emphasis on rural development in the region	-	5	21	47	23	3.92	0.82	0.67
10	Agricultural products find markets in the region	3	10	18	27	38	3.91	1.13	1.29
11	Created alternative sources of income in the region	-	7	24	52	13	3.74	0.79	0.62
12	Support boosted private sector services in the region	1	17	10	48	20	3.72	1.02	1.05
13	The activity carries risk	5	6	25	38	22	3.69	1.06	1.12
14	Support increased entrepreneurship capacity in the region	-	7	29	55	5	3.6	0.70	0.49
15	Investments increased in the region with support	-	13	31	34	18	3.59	0.95	0.90
16	Industry's demand for raw materials met in the region	4	3	44	27	18	3.54	0.97	0.95
17	Without support, the business would not be able to operate	2	27	22	25	20	3.35	1.16	1.35
18	Provided alternative job opportunities to the region with support	-	18	41	31	6	3.26	0.84	0.70
19	Sectors other than agriculture expanded in rural areas	9	28	25	29	5	2.93	1.09	1.18
20	Resources were used effectively in rural areas	16	18	33	19	10	2.89	1.21	1.47
21	Support has increased public services in the region	16	26	26	1	17	2.86	1.33	1.76
22	Reduced public burden with the project	28	14	24	21	9	2.68	1.35	1.82

1. strongly disagree; 2. disagree; 3. undecided; 4. agree; 5. strongly agree

[1] Mean: Average; [2] SD: Standard Deviation; [3] Var: Variance

The entrepreneurs strongly disagreed with the idea that the public burden decreased with the program and the projects they carried out, and strongly agreed with the idea that the support had an economic impact on the community in the region, that there was a market for agricultural products in the region and that they would benefit from such support again.

Objectives of the enterprises related to the project;

Within the framework of awareness, individuals are expected to reflect this awareness to their business life and set goals for awareness. Apart from the reasons for receiving grants under the program, the goals that the enterprises want to achieve are also different. Enterprises preferred the utilization of agricultural products produced by themselves and other enterprise owner's/manager's in the region as the most important goal they want to achieve. Enterprises have a common opinion on the evaluation of fruit, vegetable and animal products produced in the region within the region, and the production of added value through elements such as processing, packaging, and storage. Utilization of resources such as products and employment in the region is seen as the second important target for enterprises. It is expected to be beneficial for the development of the region not only on the basis of production but also with all the elements after production. The need of the region for such enterprises, increasing the capacities that are not sufficient to a certain extent, protecting water resources, the need for existing established enterprises, contributing to the development of the region, increasing the efficiency of existing enterprises, meeting the needs of enterprise owner's/manager's, saving labor, renewing technology, exporting and promoting the region are seen as the goals that enterprises want to achieve in the projects they submitted to the program (Table 3).

TABLE III
OBJECTIVES THAT ENTERPRISES WANT TO ACHIEVE WITH THE PROJECT

Issues related to the objectives to be achieved by the project	Number of persons (A)	1st preference (B=A.3p)	Number of persons (C)	2nd preference (D=C.2p)	Number of persons (E)	3rd preference (F=E.1p)	Total (B+D+F)	Order of Importance
Evaluating products	21	63	10	20	2	2	85	1
To evaluate the existing resources of the region	18	54	1	2	1	1	57	2
The need of the region	9	27	11	22	5	5	54	3
Capacity expansion	17	51	1	2	-	-	53	4
Protecting water resources	9	27	3	6	9	9	42	5
The need of the business	5	15	7	14	-	-	29	6
Contributing to the development of the region	6	18	5	10	-	-	28	7
Increasing yield	3	9	9	18	-	-	27	8
Meeting the needs of the enterprise owner's/manager's	7	21	2	4	-	-	25	9
Saving labor	-	-	7	14	2	2	16	10
Technology innovation	1	3	5	10	-	-	13	11
Exporting	-	-	1	2	-	-	2	12

Enterprises' thoughts on increasing capacity;

Within the scope of the awareness level, when the status of the enterprises that have a certain idea about the existing structure of the rural area is examined, their thoughts about increasing the capacity of their enterprises in the future years after the grant aid are different. While 63.5% of the enterprises think of increasing their business capacities in the following years, 36.5% of them do not want to increase their capacities due to the current production of their enterprises and because they think that the region does not need it. 48.9% of the enterprises in Antalya province, 34.8% of the enterprises in Isparta province and only 15.4% of the enterprises in Burdur province think of increasing their capacities in the future. In addition, 59.4% of the enterprises are planning to invest in their regions in the coming years. The remaining 40.6% of the enterprises do not plan to make any further investments in the region. On a provincial basis, 68.1% and 69.6% of the enterprises in Antalya and Isparta, respectively, are planning to invest in their regions, while this rate is 34.6% in Burdur.

IV. CONCLUSION

Development is defined as "the process of increasing people's access to humane living conditions, improving income distribution, increasing income level, ensuring localized developments in social and cultural areas, protecting and utilizing natural resources and reflecting the wealth to the lives of individuals". Development is a goal that countries want to achieve and a series of developing movements. In order for development to be balanced, it is necessary to ensure harmony between population dynamics, natural resources, economic activities, technological developments, social and cultural structures, and to analyze planning and policy development processes well.

The Program for Supporting Rural Development Investments for rural development in Turkey is a program that has prioritized the aim of revealing and supporting the existing potential of rural areas in recent years. Within the scope of the program, 96 enterprises benefited from the program in the Western Mediterranean Region, and the level of awareness of these enterprises about the support policies in rural areas was investigated. According to this

The information sources of the enterprises about the program are mostly the Ministry of Agriculture and Forestry and its provincial organizations. The relevant ministry provides

supports at different scales for rural areas within the scope of rural development activities. It is desirable that these supports find their effect in rural areas. The basis of such programs is the efficiency of rural development activities in rural areas. In this context, in order to make rural development activities more active in the relevant ministry, meetings, etc. are held to inform the enterprises in the region or the enterprises that will be newly established with support programs to benefit from such supports. In the Western Mediterranean Region, meetings, etc. organized by the relevant ministry have been important in terms of providing information to the enterprises benefiting from the support programs. It has been observed that having information and creating awareness about the support elements are effective in achieving the purpose of the support program. Another element is the provision of information to producer organizations through the governorships, which is also important for the effectiveness of rural areas and rural development studies for this type of support.

The definition of development includes the phenomenon of unlocking people's potential. The most effective way to reveal the existing potential of people is through education. Education is an important tool in revealing the potential of human beings. All types of educational activities are used to reveal human potential. Elements that provide information to people such as meetings and seminars are part of education, and it is possible to see this element in the support program. It has been observed that enterprises benefiting from the quality support program participate in courses for rural areas in order to benefit from the existing structure of the rural area. These courses and meetings provide enterprises with foresight for such support in the future and encourage them to benefit from it. The effects of such meetings and courses on the rural area in improving the level of awareness have also been seen with the sample support program.

In the phenomenon of awareness, there is knowledge about the existing structure. Realizing and turning this difference into action is an expected situation. Both in rural areas and in development processes, both in people, societies, and countries, it is necessary to achieve certain goals and realize these goals. Noticing and awareness is a structure that should be considered in determining the direction of the paths followed to achieve these goals. Achieving current goals is important in this respect. In the current support program, targets have been set in line with the objectives given. Achieving these targets is important in terms of raising awareness in rural areas and development efforts in rural areas. In this framework, these support programs provide gains to business owners/managers as an opportunity that should be used in order to benefit from the potential of the rural area. It has been observed that RDISP has also contributed to the rural development efforts in the Western Mediterranean Region in terms of achieving the targets on an entrepreneur basis.

Enterprises show a structure that prefers to increase their existing investments in order to reach their targets. This situation is also seen in the enterprises benefiting from the support program. It has been observed that enterprises are willing to increase capacity within the framework of awareness level by recognizing the existing structure of the rural area. Enterprises that have information about the existence of the potential of the rural area think of increasing capacity thanks to the support policies.

The fact that enterprises have information about the area in which they will operate can be measured by the level of awareness about this area. When the level of awareness about the rural area is examined in the enterprises benefiting from the support, they are of the opinion that the sustainability of the work they will do in the rural area should be ensured by protecting the existing structure of the rural area. A significant portion of the enterprises benefiting from the support in the region benefited from the support for the purpose of processing, storing, and packaging the products produced in the region. Other enterprises benefiting from the support benefited from the support program for irrigation, which is necessary for agricultural production. The fact that the region is a region where herbal and animal agricultural production activities are carried out efficiently and intensively indirectly explains the desire of the enterprises to prevent product losses in the supply chain with rural protection. In addition, it

has been observed that the level of technology required in the evaluation processes of the products after agricultural production is met with the support program and this situation is beneficial for the development of the region.

The economic structure of the country and the region directly affects the investment of enterprises. The positive impact of the national economy will increase the existing investment capacity. The level of awareness of enterprises towards the economic structure of the country and the region increases the willingness of enterprises to invest more with the support elements. The enterprises in the region want to benefit from the support program again with the positive situation in the economic structure. In addition, enterprises find it important in terms of contributing to the development of rural areas and adding value to the national economy.

The main purpose of support policies is to direct the production of agricultural products in rural areas, to enable enterprises to make investments that they cannot make due to lack of capital and to protect the supply-demand balance in the national economy. As can be seen in this support application given by provinces, the fact that the entrepreneurs who want to invest in rural areas have information about the rural area, the region and the national economic structure will increase their level of awareness, and a high level of awareness will enable such support policies to achieve their objectives and increase the effectiveness of rural development activities.

ACKNOWLEDGMENT

We would like to thank Akdeniz University Scientific Research Projects Coordination Unit for their financial support.

REFERENCES

[1] Harris, J. 1992. Rural Development, Routledhe, London, 15-37.
[2] Van Den Bor, W., Bryden, J. and Fuller, A.M. "Rethinking rural human resource management: the impact of globalization and rural restructuring on rural education and training in Western Europe", Mansholt Studies, Wageningen, The Netherlands, pp. 18 . 1997.
[3] Taşcıoğlu, Y., Mencet, M.N. and Sayın, C. 2008. "Investigation of Turkey's legal and institutional compliance with European Union rural development policies", Turkey VIII. Agricultural Economics Congress, 25-27 June, Bursa.
[4] SPO 2000. Rural development specialization commission reports, Republic of Turkey Prime Ministry State Planning Organization, VIII. Development Plan, Ankara, pp. 73.
[5] Bakırcı, M. "Rural Türkiye; historical development, problems and rural development approaches", Istanbul University, Journal of Geography, 2003. pp. 11, İstanbul.
[6] OJ, 06.04.2006 date and 26131 number Republic of Turkey Prime Ministry Offical Journal
[7] TLA, 2023, Dictionaries of Turkish Language Association https://sozluk.gov.tr/
[8] Anonymous, 2023 http://www.farkindalik.info/farkindalik_nedir.asp
[9] Portakalcı, M. "Companies' level of awareness of customer-oriented understanding in their marketing activities". Journal of Awareness, 2(Special 3), 2018, pp. 21-28.

Prophet Modeli ile Ürün Talep Tahmini

Product Demand Forecasting with the Prophet Model

Serkan KARTAL

skartal@cu.edu.tr, ORCID: 0000-0001-9801-8986
Department of Computer Engineering, Cukurova University, Adana, Turkey

Özet: Günümüzün dinamik iş dünyasında, perakende ve e-ticaret sektörleri gibi satış odaklı endüstriler, gelecekteki talebi tahmin etme yeteneğini artırmaya yönelik sürekli bir çaba içerisindedirler. Literatürde, talep tahmini genellikle ARIMA gibi geleneksel zaman serisi yöntemleriyle ele alınmakta, ancak problemin hem dış hem de iç faktörlerden etkilenen karmaşık bir problem olması nedeniyle, daha iyi yöntem arayışı sürekli olarak devam etmektedir. Bu bağlamda, yapay zeka (YZ) teknolojilerinin gelişimi, işletmelere büyük miktarda veriyi analiz etme ve bu verileri kullanarak gelecekteki talepleri daha hassas ve doğru bir biçimde tahmin etme potansiyeli sunmaktadır. Bu çalışmada da stok tahmin işlemi için, sezonsal trendleri yakalamada başarılı ve uzun zamanlı tahmin işlemi yapabilen Prophet modeli kullanılmıştır. Bu model, Facebook'un veri bilimi ekibi tarafından 2017 yılında geliştirilen açık kaynak kodlu bir araç olup, özellikle geleneksel yöntemlerin sınırlamalarıyla karşılaşan işletmelere değerli bir çözüm sunmaktadır. Modelin eğitim ve test işlemi için 10 farklı mağazaya ait 50 farklı ürünün beş yıllık satış değerlerinden oluşan bir veri seti kullanılmıştır. Veri zaman serisi verisi olduğundan model ilk dört yıllık eğitim verisi ile eğitilip, başarısı bir yıllık test verisinin günlük, haftalık ve aylık periyodlarda tahminleri üzerinde değerlendirilmiştir. Sonuçlar, Prophet modelinin MOYH metriğine göre günlük satış tahminlerinde %14.42, haftalık tahminlerde %6.65 ve aylık tahminlerde %5.78 hata oranlarıyla tahminler yapabildiğini göstermektedir. Bu durum, modelin stok satış değeri örüntülerini anlayarak uzun ve kısa vadeli tahminler yapma konusunda son derece etkili olduğunu göstermektedir. Elde edilen bu sonuçlara göre, perakende sektöründe rekabet avantajı elde etmek isteyen işletmelerin, üretim planlaması ve insan kaynakları yönetimi konularında kararlar alırken Prophet modelinin tahminlerinden faydalanabilecekleri görülmektedir.

Anahtar Kelimeler: *Yapay Zeka, Stok Tahmini, Prophet, LSTM*

Abstract: In today's dynamic business world, sales-focused industries such as retail and e-commerce are constantly striving to enhance their ability to forecast future demand. In the literature, demand forecasting is often addressed using traditional time series methods like ARIMA. However, due to the complexity of the problem, influenced by both external and internal factors, the search for better methods continues. In this context, the advancement of Artificial Intelligence (AI) technologies offers the potential to analyse vast amounts of data and make more accurate and precise forecasting of future demands. In this study, the Prophet model, which is successful in capturing seasonal trends and making long-term forecasting, is used for stock forecasting. Developed by Facebook's data science team in 2017, this open-source tool provides a valuable solution, particularly for businesses encountering limitations with traditional methods. During the training and testing process of the model, a dataset consisting of five years of sales data of 50 different products in 10 different stores is used. As the data is in the form of a time series, the model is trained on the first four years of data, and its performance is evaluated on one year of test data, making daily, weekly, and monthly forecasting. The results indicate that the Prophet model can make daily sales forecasts with an

error rate of 14.42%, weekly forecasts with 6.65%, and monthly forecasts with 5.78% error rate, according to the MAPE metric. This demonstrates the model's effectiveness in learning stock sales patterns and making both long and short-term forecasts. Based on these findings, it is evident that businesses aiming to gain a competitive advantage in the retail sector can benefit from the forecasting provided by the Prophet model when making decisions related to production planning and human resource management.

Keywords: *Artificial Intelligence, Stock Forecasting, Prophet, LSTM*

I. GİRİŞ

Perakende sektörü, sürekli değişen tüketici taleplerine ve pazar dinamiklerine uyum sağlama zorluğuyla karşı karşıyadır. Bu sektörde başarılı bir şekilde rekabet edebilmek ve karlılık sağlayabilmek için doğru ürün satış tahminleri yapabilmek kritik öneme sahiptir [1, 2]. Bazı endüstrilerde üretim planlaması, yeterli insan gücü seviyesini belirleme, üretim biriminin genişletilmesi veya daraltılması gibi firmanın kârlılığını etkileyen birçok operasyon ve iş planının karar aşamasında talep tahmin işlemi sonuçları kritik veri olarak göz önünde bulundurulmaktadır [3]. Geleneksel ürün satışı tahmin yöntemleri tipik olarak geçmiş verilere dayanmakta ve piyasa değişkenliklerini ve tüketici davranışlarını yakalamakta yetersiz kalabilmektedirler. Bu nedenle, günümüzde kullanımı hızlı bir şekilde yaygınlaşan yapay zeka (YZ) gibi daha güçlü ve esnek tahmin modelleri gereklidir. Bu teknolojilerin gelişimi, ürün satış tahminlerini optimize etme ve işletmelerin verimliliğini artırmada yeni bir yol sunmaktadır.

Literatürde, satış ve talep tahmini genellikle ARIMA ve SARIMA gibi geleneksel zaman serisi yöntemleriyle ele alınmıştır. Ancak satış tahmini karmaşık bir problemdir ve hem dış hem de iç faktörlerden etkilenir [4]. Diğer yandan günümüzde yeni YZ tabanlı yöntemler, tahmine dayalı performansı geliştirme ve doğrusal olmayan örüntüleri modelleme yetenekleri nedeniyle ilgi kazanmışlardır [5]. Bu algoritmalar hava durumu ve sıcaklık tahminlerinden, borsa tahminlerine, ürün hasat miktarı tahminlerinden araç satış tahminlerine kadar birçok farklı alanda kullanılmaktadırlar [6, 7, 8]. Özellikle makine öğrenmesi (MÖ) modelleri, verilerdeki örüntüleri tespit etmedeki esneklikleri nedeniyle iş dünyası problemlerini çözmede yaygın olarak kullanılmaya başlanmışlardır [9]. Haselbeck ve ark. [10] satış tahmininde makine öğrenmesi (MÖ) modellerinin klasik istatistiksel modellerden daha iyi sonuç verip vermediğini araştırmak için dokuz farklı MÖ modelini üç klasik tahminleme modeli ile karşılaştırmıştır. Sonuçlar MÖ modellerinin tüm testlerde klasik modellerden daha iyi sonuçlar verdiğini göstermiştir. Fantazzini ve ark. [11] Google verilerini kullanarak Almanya'daki otomobil satışlarını tahmin etmede kullanılan çok değişkenli yeni modeller önermiştir. X. Yua ve ark. [12] dergi ve gazete satış tahmini için destek vektörü regresyonunu kullanmışlardır. Bazı diğer çalışmalarda ise tahmin performansını arttırmak için fuzzy neural networks ve radial basis function neural network kullanılmıştır [13, 14].

Sonuç olarak, YZ tabanlı ürün satış tahminleri, perakende sektöründe rekabet avantajı sağlamak isteyen işletmeler için önemli bir araç haline gelmiştir. Bu teknolojilerin doğru bir şekilde uygulanması, işletmelere daha iyi stok yönetimi, müşteri memnuniyeti ve karlılık sağlama fırsatı sunabilmektedir. Literatürdeki çalışmalar, YZ tekniklerinin daha kesin, hızlı ve öngörülü tahminler elde etmek amacıyla kullanımının yaygınlaştığını ve sürekli yeni YZ modellerinin ortaya çıktığını göstermektedir. Bu bağlamda 2017 yılında Facebook tarafından eksik ve aykırı verilerden çok etkilenmeyen, trendlerdeki sezonsal değişkenlik örüntülerini kolayca öğrenebilen ve tahmin yapmak için çok fazla zaman serisi verisine ihtiyaç duymayan Prophet modeli sunulmuştur. Bu model bayes modelindeki eğri uydurma tekniğine dayanmaktadır ve LSTM gibi sadece birkaç adım ötesini tahmin edebilen algoritmalara kıyasla çok daha uzun süreli tahminler yapabilmeyi sağlamaktadır. Bu çalışmada da ileri tarihli ve

uzun süreli tahmin yapmak amacıyla Facebook tarafından geliştirilen Prophet modeli kullanılmıştır.

II. VERİ SETİ

Çalışmada, Kaggle web sitesi üzerinden sunulmuş, 10 farklı mağaza için 01-01-2013 ve 31-12-2017 tarih aralığına ait 50 farklı ürünün mağaza-ürün satış verilerinin bulunduğu açık kaynak veri seti kullanılmıştır [15]. Veri setine ait örnek birkaç veri Tablo 1'de verilmiştir. Veri seti toplam 913000 kayıttan (satırdan) ve her kayda ait dört adet özellikten (tarih, mağaza id, ürün id, satış miktarı) oluşmaktadır. Bu verilerin %80'i Prophet modelinin eğitimi, %20'si ise modelin başarısının değerlendirilmesi için kullanılmıştır. Veri zaman serisi verisi olduğundan, ürünlere ait ilk dört yıllık veriler eğitim ve geçerlilik verisi, son bir yıllık veriler ise test verisi olarak kullanılmıştır.

Tablo 1. Veri setine ait örnek veriler

Tarih	Mağaza	Ürün	Satış Miktarı
01-01-13	1	1	13
02-01-13	1	1	11
03-01-13	1	1	14
04-01-13	1	1	13
05-01-13	1	1	10

III. YÖNTEM

Çalışmada stok tahmini yapmak için Facebook tarafından geliştirilen Prophet modeli kullanılmıştır [16]. Prophet modeli, zaman serisi verilerindeki genel eğilimleri, mevsimsel desenleri ve özel etkileri bir araya getirerek tahminler yapmaktadır. Modelin açık ve sezgisel kullanımı, hiperparametre ayarlarının basitliği ve tatmin edici sonuçları, özellikle iş dünyasında stok tahmini gibi uygulamalarda popüler hale gelmesini sağlamıştır. Geliştirilen model açık kaynak kodlu olup Facebook'un veri bilimi ekibi tarafından yayınlanmıştır. Modelin temel formülü aşağıdaki gibidir:

$$y(t) = g(t) + s(t) + h(t) + \in_t \quad (1)$$

Burada: $y(t)$ zaman serisi verilerini, $g(t)$ genel trendi, $s(t)$ mevsimsel (haftalık, aylık) etkileri, $h(t)$ tatil günlerini veya özel etkileri, $\in_t$ hata terimini temsil etmektedir.

Model, zaman içindeki genel büyüme veya düşme eğilimini yakalamak için $g(t)$ genel trend bileşenini kullanır. Bu bileşen, verinin genel eğilimini yansıtarak zaman içindeki uzun vadeli değişimleri yakalar. Haftalık, aylık veya yıllık periyotlarda tekrarlanan örüntüleri yakalamak için ise $s(t)$ fonksiyonu kullanılır. $h(t)$ Fonksiyonu tatil günleri veya özel olaylar gibi belirli tarih aralıklarındaki etkileri temsil eder. Örneğin, tatil günlerinde veya büyük indirim etkinliklerinde stok talebinde artışlar olabileceği düşünülerek bu bileşen kullanılır. Hata Terimi ise modelin tahmin ettiği değerler ile gerçek değerler arasındaki farkı temsil eder. Bu hata terimi, modelin doğru tahminler yapamayabileceği faktörleri yakalamaya yardımcı olur.

IV. PERFORMANS DEĞERLENDİRME METRİKLERİ

Modellerin performansını değerlendirmek için iyi bilinen üç değerlendirme ölçütü, Karesel Ortalama Hata (KOH), Ortalama Mutlak Hata (OMH) ve Ortalama Mutlak Yüzde Hata (OMYH) kullanılmıştır. Metriklerin denklemleri aşağıda verilmiştir.

$$KOH = \sqrt{\frac{1}{n}\sum_{i=1}^{n}(y_i - \hat{y}_i)^2} \quad (2)$$

$$OMH = \frac{1}{n}\sum_{i=1}^{n}|y_i - \hat{y}_i| \quad (3)$$

$$OMYH = \frac{1}{n}\sum_{i=1}^{n}\left|\frac{y_i - \hat{y}_i}{y_i}\right| \times 100 \quad (4)$$

Burada y_i ve $\hat{y}_i$, sırasıyla veri setindeki *i*'inci gerçek değeri ve *i*'inci tahmin edilen değeri göstermektedir.

V. TARTIŞMA

Çalışmada Prophet modeli kullanılmıştır. Bu modelin seçilmesindeki temel motivasyon ise, uzun kısa süreli bellek (LSTM) modeli gibi zaman serisi verileri üzerinde tahmin yapmak için kullanılan modellerin, bir ya da birkaç adım ileriyi tahmin etmede başarılı sonuçlar üretirken, daha ileriki adımları tahmin etmede yetersiz kalmalarıdır. Bu modeller ileriki adımları tahmin ederken modellerin daha önceki adımlarda tahmin ettikleri değerleri kullanmakta ve buda modellerin uzun vadeli tahminlerindeki hata oranını arttırmaktadır. Örneğin bir günlük verilerle bir gün ilerisini tahmin etmek için eğitilen bir LSTM modeli ile birinci günü mevcut veriler ile tahmin edebilirken, ikinci günü tahmin etmek için birinci güne ait tahmin verilerini, üçüncü günü tahmin etmek için ise ilk iki güne ait tahmin verilerini kullanmak, yani ileri günlerin tahminin yaparken tahmin verilerini iteratif olarak kullanmak gerekmektedir. Dolayısıyla bu verileri kullanarak başka bir tahmin işlemi yapmak, var olan hatanın da üzerine ekleyerek devam etmesine, yani hata miktarının artmasına neden olmaktadır.

Çalışmada kullanılan Prophet modelinin performansını değerlendirebilmek için model dört yıllık veriler ile eğitilerek, beşinci yıla ait veriler günlük, haftalık ve aylık periyotlarda tahmin işlemlerinde kullanılmıştır. Buna göre günlük tahmin modeli bir sonraki yıla ait günlük satış verilerini, aylık tahmin modeli ise 12 aya ait ortalama satış verilerini tahmin etmekte kullanılmıştır. Modelin günlük, haftalık ve aylık tahmin değerlerinin OMH, OMYH ve KOH ölçeklerine göre elde ettikleri hata değeri Tablo 2'de verilmiştir.

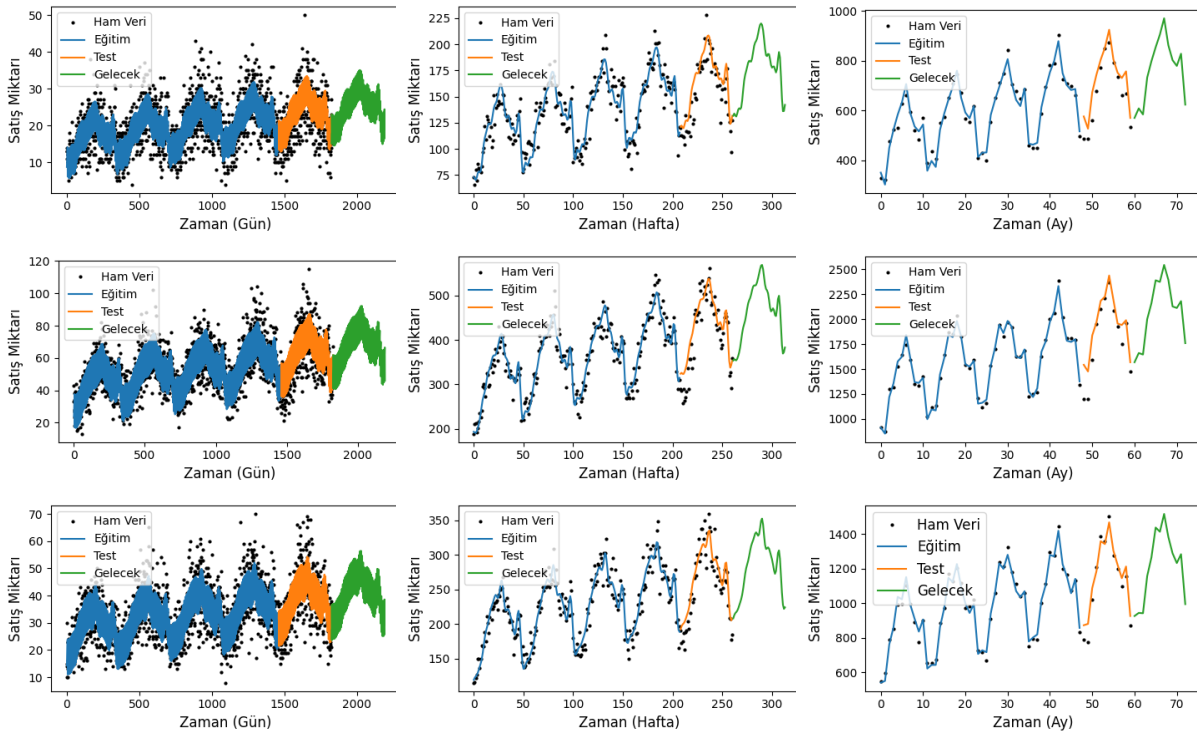
Tablo 2. Prophet modelinin günlük, haftalık ve yıllık zaman periyotları için bir yıllık satış tahminlerinin ortalama hata miktarları.

	OMH	OMYH	KOH
Günlük	6.8	14.42	8.46
Haftalık	23.36	6.65	28.59
Aylık	88.03	5.78	106.81

Tabloya göre model günlük satış değeri tahmininde OMH ve KOH ölçeklerine göre sırasıyla 6.8 ve 8.46 büyüklüğünde ortalama hataya sahiptir. Ancak bu hata değerlerinin haftalık bazda günlük hata değerine göre daha yüksek, aylık bazda ise en yüksek değerlere ulaştığı görülmektedir. Bunun nedeni ürünlerin günlük satış değerleri arasındaki değersel farkın düşük iken, haftalık ve aylık farkların daha da yüksek olmasıdır.

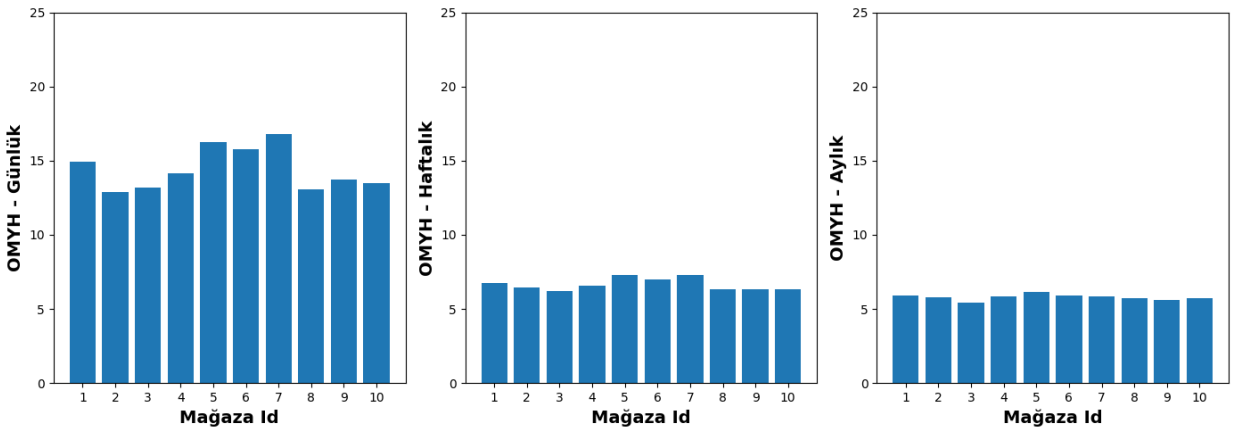
Şekil 1'de bir numaralı mağazada satılan ilk üç ürüne ait günlük haftalık ve aylık satış değerleri ile Prophet modelinin eğitim (mavi) ve test (turuncu) verileri için yaptıkları tahminler ve bir sene ilerisi için yaptığı tahmin grafiği (yeşil) verilmiştir. Diğer taraftan günlük değer dalgalanmalarını yakalamak zor iken, haftalık ve aylık ortalama satış değerlerindeki sapmalar daha yumuşak olacağından, haftalık ve aylık zamansal ürün satış değeri örüntülerini yakalamak ve oransal olarak (OMYH ölçeğinde) daha düşük hatalı tahminler yapmak mümkündür. Dolayısıyla Tablodaki OMYH günlük hata değeri 14.42 iken bu değer haftalık bazda 6.65'e aylık bazda ise 5.78'e gerilemiştir. Bu sonuçlar bize modelinde genel olarak ürünlerin satış örüntülerin yakalamakta başarılı olduğunu göstermektedir. Benzer sonuçları Şekil 1'de verilen görseller üzerinden okumak mümkündür. Bu şekillerden de anlaşılabildiği gibi, Prophet modeli

satış örüntülerini ve genel trendi yakalamakta tatmin edici ölçüde başarılı iken, model öğrendiği örüntüye bağlı olarak grafikte verilenden çok daha uzun vadeli tahminler yapabilme yeteneğine de sahiptir.

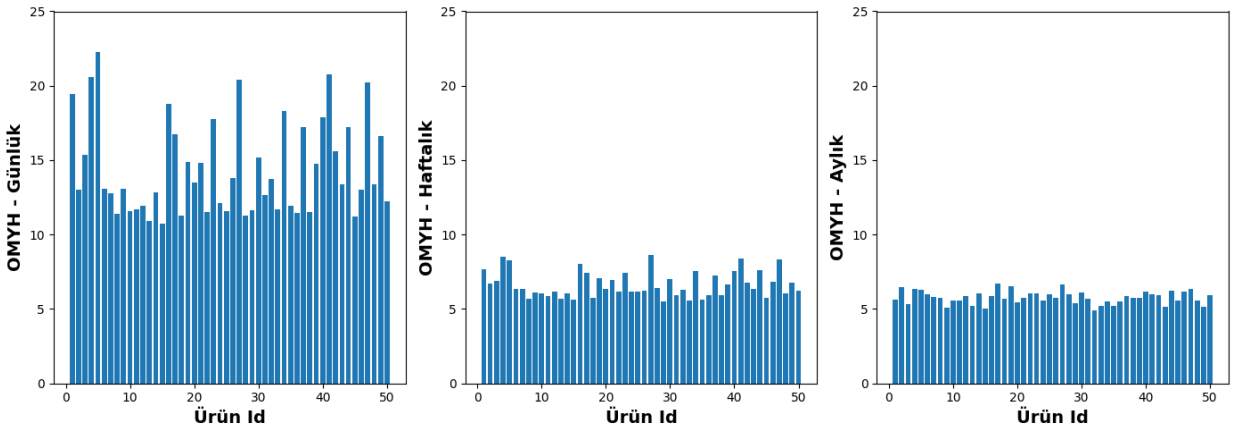


Şekil 1. Veri setindeki birinci mağazaya ait ilk üç ürünün günlük, haftalık ve aylık gerçek satış değerleri ile modelin eğitim verisi, test verisi ve gelecek bir sene için yapmış olduğu tahminler.

Yapılan tahminleri daha detaylı analiz edebilmek için mağaza ve ürün bazında OMYH ölçeğine göre yapılan hata miktarları sırasıyla Şekil 2 ve Şekil 3'te verilmiştir. Bu grafiklere göre, özellikle haftalık ve aylık bazda mağaza bazında yüzdesel hata (OMYH) değerlerinin birbirlerine yakın olduğu görülmektedir. Ürün bazında ise hata oranları her ne kadar yakın olsa dahi, bazı ürünlerin OMYH hata değerlerinin diğerlerine göre daha fazla olduğu, ancak zamansal periyod büyüdükçe bu hatanın da azaldığı görülmektedir. Bu grafiklere bakarak bu ürünlerin günlük satış değerlerinde görece büyük farklılıklar olduğunu, dolayısıyla bir sonraki günlük satış değerini tahmin etmenin görece zor olduğunu, ancak periyod büyüdükçe bu ani dalgalanmaların ortadan kalktığını ve zamansal örüntünün otaya çıkmasıyla bu ürünlerin satış değerlerinin de daha doğru bir şekilde tahmin edilebildiğini söyleyebiliriz.



Şekil 2. Mağaza bazında günlük, haftalık ve aylık satış tahminleri için elde edilen OMYH hata miktarları.



Şekil 3. Ürün bazında günlük, haftalık ve aylık satış tahminleri için elde edilen OMYH hata miktarları.

VI. SONUÇLAR

Çalışmada Prophet modeli kullanılarak 10 farklı mağazanın 50 farklı ürün için günlük haftalık ve aylık periyotlarda bir yıllık satış tahmini yapılmıştır. Model dört yıllık mağaza-ürün satış verileri ile eğitilmiştir. Sonuçlar Prophet modelinin haftalık 6.65, aylık ise 5.78 OMYH oranları ile başarılı tahminler yaptığını, yani modelin ürün satış örüntülerini öğrenebildiğini göstermektedir. Ayrıca model LSTM gibi zaman serisi verilerinin tahmini için kullanılan algoritmalara kıyasla uzun vadeli tahinlerde yapabilmektedir. Tüm bu sonuçlar göz önünde bulundurulduğunda perakende sektöründe rekabet avantajı sağlamak isteyen işletmelerin üretim planlaması ve yeterli insan gücü seviyesini belirlemek için karar alırken Prophet modelinden faydalanabilecekleri görülmektedir.

KAYNAKÇA

[1] Makridakis, S. (1996). Forecasting: its role and value for planning and strategy. International journal of forecasting, 12(4), 513-537.

[2] Nguyen, H. D., Tran, K. P., Thomassey, S., & Hamad, M. (2021). Forecasting and Anomaly Detection approaches using LSTM and LSTM Autoencoder techniques with the applications in supply chain management. International Journal of Information Management, 57, 102282.

[3] Sa-Ngasoongsong, A., Bukkapatnam, S. T., Kim, J., Iyer, P. S., & Suresh, R. P. (2012). Multi-step sales forecasting in automotive industry based on structural relationship identification. International Journal of Production Economics, 140(2), 875-887.

[4] Chatfield, C., & Weigend, A. S. (1994). Time series prediction: Forecasting the future and understanding the past: Neil A. Gershenfeld and Andreas S. Weigend, 1994,'The future of time series', in: AS Weigend and NA Gershenfeld, eds.,(Addison-Wesley, Reading, MA), 1-70. International Journal of forecasting, 10(1), 161-163.

[5] Karmy, J. P., & Maldonado, S. (2019). Hierarchical time series forecasting via support vector regression in the European travel retail industry. Expert Systems with Applications, 137, 59-73.

[6] Kartal, S. (2023). Assessment of the spatiotemporal prediction capabilities of machine learning algorithms on Sea Surface Temperature data: A comprehensive study. Engineering Applications of Artificial Intelligence, 118, 105675.

[7] Kartal, S., & Sekertekin, A. (2022). Prediction of MODIS land surface temperature using new hybrid models based on spatial interpolation techniques and deep learning models. Environmental Science and Pollution Research, 29(44), 67115-67134.

[8] Parmar, I., Agarwal, N., Saxena, S., Arora, R., Gupta, S., Dhiman, H., & Chouhan, L. (2018, December). Stock market prediction using machine learning. In 2018 first

international conference on secure cyber computing and communication (ICSCCC) (pp. 574-576). IEEE.

[9] Tkáč, M., & Verner, R. (2016). Artificial neural networks in business: Two decades of research. Applied Soft Computing, 38, 788-804.

[10] Haselbeck, F., Killinger, J., Menrad, K., Hannus, T., & Grimm, D. G. (2022). Machine learning outperforms classical forecasting on horticultural sales predictions. Machine Learning with Applications, 7, 100239.

[11] Fantazzini, D., & Toktamysova, Z. (2015). Forecasting German car sales using Google data and multivariate models. International Journal of Production Economics, 170, 97-135.

[12] Yu, X., Qi, Z., & Zhao, Y. (2013). Support vector regression for newspaper/magazine sales forecasting. Procedia Computer Science, 17, 1055-1062.

[13] Kuo, R. J., Hu, T. L., & Chen, Z. Y. (2009, February). Application of radial basis function neural network for sales forecasting. In 2009 International Asia Conference on Informatics in Control, Automation and Robotics (pp. 325-328). IEEE.

[14] Chang, P. C., & Wang, Y. W. (2006). Fuzzy Delphi and back-propagation model for sales forecasting in PCB industry. Expert systems with applications, 30(4), 715-726.

[15] Inversion, 2018. Store item demand forecasting challenge. URL: https://kaggle.com/competitions/demand-forecasting-kernels-only.

[16] Taylor, S. J., & Letham, B. Forecasting at scale. PeerJ Preprints 5: e3190v2 (2017).

Enjeksiyonla Kalıplanmış Polilaktik Asit Parçaların Farklı Tavlama Ortamı ile Mekanik Özelliklerinin Geliştirilmesi

Improvement of Mechanical Properties of Injection Moulded Polylactic Acid Parts with Different Annealing Media

Fatih Huzeyfe Öztürk*, Özkan Öz

*fhozturk@karabuk.edu.tr, ORCID: 0000-0001-8025-8236
Industrial Design Engineering Department, Karabük University, Karabük, Turkey

Özet: Polilaktik asit (PLA), petrol bazlı polimerlerin aksine geri dönüştürülebilir özelliği nedeniyle endüstri uygulamalarında sıklıkla kullanılmaktadır. PLA, yüksek elastisite modülüne, rijitliğe ve dayanımına rağmen, yavaş kristallenme hızına sahip olduğu için enjeksiyonla kalıplama uygulamalarında ticari kullanımı sınırlıdır. Bununla birlikte, PLA rijit yapısından dolayı düşük şekil değiştirme kabiliyeti göstermektedir. Bu nedenle, enjeksiyonla kalıplanmış PLA parçaların üretim hızından etkilenmeden (enjeksiyon kalıbının soğutma hızının yavaş olması) mekanik özelliklerinin geliştirilmesi gerekmektedir. Bu nedenle bu çalışmada, enjeksiyon kalıplama yöntemi ile üretilen PLA parçaların mekanik özelliklerini geliştirmek için termal tavlama işlemi uygulanmıştır. İki farklı ortamda (vakumlu ve vakumsuz) konveksiyonel fırın kullanılarak numuneler tavlanmıştır. Tavlama ortamının PLA'nın mekanik özelliklere etkisi incelenmiştir. PLA, 90°C'de 8 saat sürede tavlanmıştır. Tavlamanın mekanik özelliklere etkisi çekme testi ile belirlenmiştir. Çekme testi sonrası sonuçlar, tavlama işleminin PLA parçaların çekme dayanımını, elastisite modülünü ve yüzde uzamasını artırdığını göstermiştir. En yüksek artış vakum ortamı ile tavlanan numunelerde görülmüştür. Bu artış elastisite modülü için %12.05, maksimum çekme dayanımında %5.48 ve yüzde uzamada %131.11 olarak hesaplanmıştır. Vakumlu ve vakumsuz ortamın kullanılmasının mekanik özelliklerde en düşük farkı %0.06 ile maksimum çekme dayanımında ve en yüksek farkı %13.26 ile yüzde uzamada olduğu görülmüştür. Sonuç olarak, düşük işlem maliyetli tavlama işleminin enjeksiyonla kalıplanmış yarı kristal polimerlerin mekanik özelliklerininin geliştirilmesi amacıyla kullanılabileceği görülmüştür.

Anahtar kelimeler: *Polilaktik asit, Tavlama, Enjeksiyon kalıplama*

Abstract: Polylactic acid (PLA) is frequently used in industrial applications due to its recyclable properties, unlike petroleum-based polymers. Despite its high modulus of elasticity, stiffness and strength, PLA has a slow crystallisation rate, which limits its commercial use in injection moulding applications. However, PLA shows low strain capability due to its rigid structure. Therefore, it is necessary to improve the mechanical properties of injection moulded PLA parts without being affected by the production speed (slow cooling rate of the injection mould). Therefore, in this study, thermal annealing process was applied to improve the mechanical properties of PLA parts produced by injection moulding method. Samples were annealed in two different media (vacuum and non-vacuum) using a convection oven. The effect of annealing media on the mechanical properties of PLA was investigated. PLA was annealed at 90°C for 8 hours. The effect of annealing on mechanical properties was determined by tensile test. The results after tensile test showed that the annealing process increased the tensile

strength, modulus of elasticity and percentage elongation of PLA parts. The highest increase was observed in the samples annealed with vacuum media. This increase was calculated as 12.05% for modulus of elasticity, 5.48% for maximum tensile strength and 131.11% for percentage elongation. The lowest difference in mechanical properties between vacuum and non-vacuum media was 0.06% for maximum tensile strength and the highest difference was 13.26% for percentage elongation. As a result, it has been seen that the low-cost annealing process can be used to improve the mechanical properties of injection molded semi-crystalline polymers.

Keywords: *Polylactic acid, Annealing, Injection molding.*

I. GİRİŞ

PLA, mısır, nişasta ve şeker pancarı gibi yenilenebilir kaynaklardan üretilen doğal, biyolojik olarak parçalanabilen termoplastik polimerdir [1,2]. Literatürde otomotiv endüstrisi gibi yapısal parçalar için enjeksiyonla kalıplanmış PLA ile ilgili sınırlı araştırma bulunmaktadır [3]. PLA iyi mekanik özelliklere sahiptir ancak, sıkı kullanılan tolerans uygulamalarında, darbe dayanımı veya yüksek dayanım gerektiren uygulamalarda yetersiz kalmaktadır. PLA'nın kompostlanabilirliği korunarak mekanik özelliklerinin geliştirilmesi daha yaygın kullanımını sağlayabilir. PLA'nın yavaş kristallenme hızı nedeniyle enjeksiyonla kalıplama uygulamalarında yüksek kristalli parça imalatı zordur [4]. Polimerin kristalliği, malzemenin performansında önemli etkiye sahiptir. Kristallik oranındaki artış rijitlik, dayanım ve kimyasal dirençte artışa neden olabilmektedir [4,5].

Enjeksiyonla kalıplama uygulamalarında yüksek derecede kristallik ile özellik geliştirmeleri için, enjeksiyon kalıbının soğutma hızının yavaş olması veya enjeksiyon sonrası üretilmiş parçanın tavlanması gerekmektedir [4,6]. Tavlama işlemi, bütün numunelere aynı anda uygulanabilir ve kalıp soğutma süresi azalmadığı için üretim hızı etkilenmeden PLA parçaların uygun maaliyet ile performans geliştirmesi yapılabilir.

Goto vd. [6], tavlama işleminin enjeksiyonla kalıplanmış PLA'nın kırılma davranışı ve deformasyonu üzerindeki etkilerini incelemişlerdir. 120°C'de 5 dakika boyunca tavladıkları numunenin gevrek kırılma gösterdiğini, camsı geçiş sıcaklığı *(T_g)*'ye yakın sıcaklıkta ve 5 dakika boyunca tavlanan numunede akma sonrasında boyun gösterdiğini ve yaklaşık %100'e kadar uzama gerçekleştiğini bildirmişlerdir.

Li vd. [7], enjeksiyonla kalıplanmış PLA'yı farklı sıcaklıklarda (80,100 ve 120°C) ve sürelerde (0.5, 1, 1.5 ve 2 saat) tavlamışlardır. Tavlama sıcaklığı ve süredeki artışın, çekme dayanımı ve elastisite modülünü artırdığını ancak tokluğun farklı davranış gösterdiğini belirtmişlerdir. Ayrıca, saf PLA'ya göre kopma uzamasında 80°C tavlama sonrası 3 kat artış gözlemlemişlerdir.

Srithep vd. [8], tavlama süresi ve sıcaklığının enjeksiyonla kalıplanmış PLA üzerindeki etkilerini araştırmışlardır. 80°C tavlama sıcaklığında 30 dakikada ve 65°C'de 31 saatte, çekme dayanımında sırasıyla %17 ve %26 artış elde etmişlerdir.

Bu çalışmada, tavlama ortamının enjeksiyonla kalıplanmış PLA'nın mekanik özelliklerine etkisi çekme testi ile incelenmiştir. İki farklı ortam (vakumlu ve vakumsuz) kullanılmıştır. Numuneler 8 saat boyunca 90°C'de tavlanmıştır. Tavlama işlemi sonrası numuneler oda sıcaklığında soğumaya bırakılmıştır.

II. MATERYAL VE METOD

A. Numunelerin Üretimi

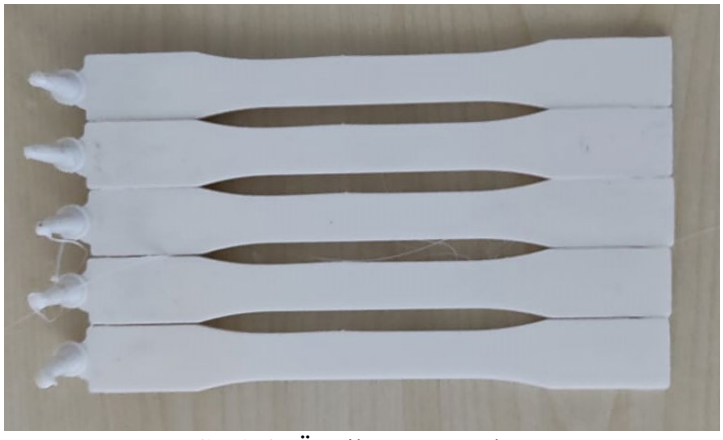
Parçaların üretilmesinde ticari olarak temin edilen Flashforge PLA filament kullanılmıştır. Kullanılan filament kırıcı yardımıyla granül hale getirilmiş ve fırında 4 saat boyunca 60 °C'de kurutulmuştur. PLA için önerilen sıcaklıklarda enjeksiyon makinesi kovan bölgeleri

ayarlanmıştır. Bu sıcaklıklar, boğaz bölgesi için 185° C, orta ve çıkış bölgesi için 210 °C olarak seçilmiştir (Şekil 1).



Şekil 1. Enjeksiyon kalıplama cihazı.

Enjeksiyon kalıplama ile, her parametre için 5 adet numune üretilmiştir. Üretilen numuneler Şekil 2'de ve numunelere verilen kısaltmalar Tablo 1'de gösterilmiştir.



Şekil 2. Üretilen numuneler.

TABLO I.NUMUNELERİN KISALTMASI

Kısaltma	Ortam	Sıcaklık	Süre
S	Tavlanmamış	-	-
V	Vakumlu Fırın	90 °C	8 saat
K	Vakumsuz Fırın		

Erime (T_m) ve camsı geçiş sıcaklığı (T_g) arasındaki tavlama daha etkili olduğundan [9,10], tavlama işlemi, 90°C'de (PLA için T_m=155-170 °C ve T_g ~ 55-60 °C) ve 8 saat sürede gerçekleştirilecektir. PLA'nın soğuk kristalizasyon sıcaklığı 110 °C'de başlamış ve 120 °C'de en yüksek değerine ulaşmıştır [11]. Tavlanan numunelerin nihai kristalliği, soğutma hızından etkilenmektedir. Daha yavaş soğutma hızı, numunede daha yüksek kristalliğe ve daha hızlı soğutma hızı, daha düşük kristalliğe yol açmaktadır [12]. Belirtilen süre boyunca sıcaklık sabit tutulduktan sonra, numuneler fırından oda sıcaklığına getirilmiş ve soğumaya bırakılmıştır. Çalışmada NÜVE EV018 vakumlu fırın Şekil 3.a ve NÜVE FN400 Şekil 3.b vakumsuz fırın kullanılmıştır. Vakumlu fırında numuneler-0.5 ATM basınçta tavlanmıştır.



(a) vakumlu fırın (b) vakumsuz fırın

Şekil 3. Kullanılan fırınlar.

B. Çekme Testi

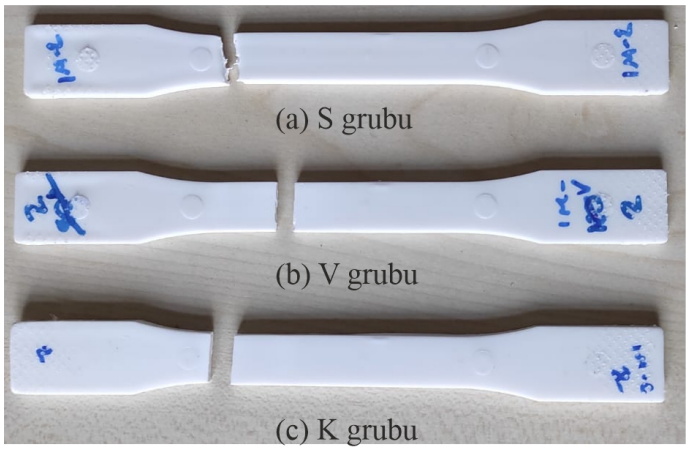
Enjeksiyonla kalıplanmış ve tavlanmış numunelere ASTM D638 Tip 1 standardına [13] göre çekme testi yapılmıştır. Elastisite modülü, maksimum çekme dayanımı ve yüzde uzaması, oda sıcaklığında (23 °C) ZWICK marka çekme test cihazında belirlenmiştir (Şekil 4). Numunelere hasara uğrayana kadar 5 mm/dk hız ile yük uygulanmıştır.



Şekil 4. Çekme testi.

III. DENEYSEL SONUÇ VE TARTIŞMA

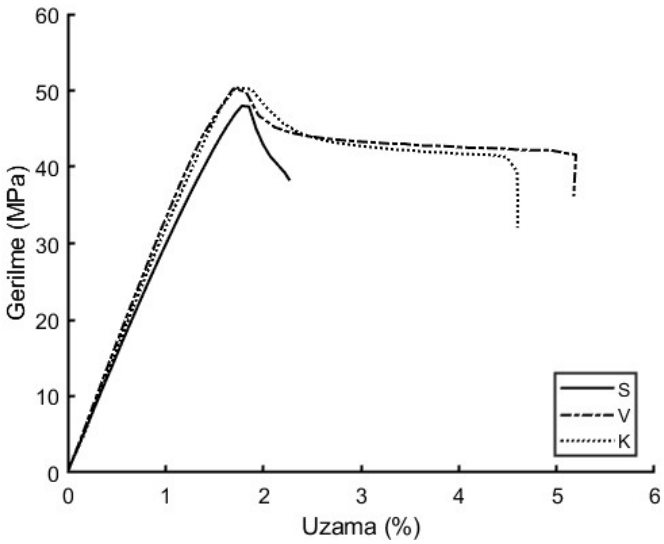
Şekil 5'te çekme test sonrası numunelerin hasarları görülmektedir.



Şekil 5. Çekme testi sonrası hasar yüzeyleri.

Şekil 5.a'ya göre, V ve K grubu numunelerde gevrek kırılma görülmüştür. [6]'ya göre yazarlar benzer şekilde tavlama işlemi sonrası işlem görmemiş PLA'ya göre gevrek kırılma gözlemlemişlerdir. Vakumlu ve vakumsuz fırın ile tavlamanın numunenin hasar yüzeyine etkisi görülmemiştir.

Şekil 6'da çekme testi sonrası elde edilen gerilme-uzama grafiği verilmiştir.



Şekil 6. Gerilme-uzama grafiği.

Şekil 6 incelendiğinde tavlanmış V ve K grubu numuneler, işlem görmemiş numuneye göre daha rijit davranış göstermiştir. [6,7]'de belirtildiği gibi tavlama işlemi sonrası numunelerin çekme dayanımı ve yüzde uzama değerleri artmıştır. Tablo 2'de çekme testi sonrası elde edilen mekanik özelliklere yer verilmiştir.

TABLO II. MEKANİK ÖZELLİKLER

Kısaltma	Maksimum çekme dayanımı (MPa)	Elastisite modülü (MPA)	Uzama (%)
S	48.70 ± 1.92	3112 ± 58.8	2.25 ± 0.21
V	51.37 ± 0.56	3487 ± 60.3	5.20 ± 0.71
K	51.34 ± 0.57	3409 ± 38	4.51 ± 0.07

Tavlama işlemi sonrası işlem görmemiş numuneye göre çekme dayanımındaki artış V ve K grubu için sırasıyla %5.48 ve %5.42 olmuştur. Elastisite modülünde bu artış sırasıyla %12.05 ve %9.54 olarak hesaplanmıştır. Yüzde uzama değerlerinde saf numuneye göre artış V grubu için %131.11 ve K grubu için %100.44 olmuştur. Yüzde uzama değerlerinde ki bu artış [6,7]'de bulunan çalışmalardaki artışlara benzer şekilde olmuştur. [14]'de yazarlar uzama değerlerindeki bu artışı, tavlama işleminden sonra küçük kristallerin oluşumundan dolayı olduğunu belirtmişlerdir. Ayrıca tavlama işlemi moleküler randomizasyon derecesini azalttığı için elastisite modülü ve çekme dayanımını geliştirmiştir [15].

IV. SONUÇ

Bu çalışmada, vakumlu ve vakumsuz fırınla tavlama işleminin enjeksiyonla kalıplanmış PLA parçaların dayanımı üzerindeki etkisi incelenmiştir. Numuneler 90°C'de 8 saat boyunca tavlanmıştır. Sonuçlar tavlama işleminin PLA parçaların çekme dayanımını, elastisite modülünü ve yüzde uzamasını artırdığı göstermiştir. En yüksek artış vakumlu fırın ile tavlanan

numunelerde elastisite modülü için %12.05, maksimum çekme dayanımında %5.48 ve yüzde uzamada %131.11 elde edilmiştir. Vakumlu ve vakumsuz fırın kullanılmasının mekanik özelliklerde belirgin farkı olmadığı görülmüştür. Tavlama işlemi, enjeksiyonla kalıplanmış yarı kristal polimerleri, uygun maliyetli mekanik özellikleri geliştirmek amacıyla kullanılabilir olduğu sonucuna varılmıştır.

KAYNAKLAR

[1] Farah, S., Anderson, D. G., and Langer, R. "Physical and Mechanical Properties of PLA, and Their Functions in Widespread Applications — A Comprehensive Review." *Advanced Drug Delivery Reviews*, Vol. 107, 2016, pp. 367–392. https://doi.org/10.1016/j.addr.2016.06.012.

[2] Vink, E. T. H., Rábago, K. R., Glassner, D. A., and Gruber, P. R. "Applications of Life Cycle Assessment to NatureWorks™ Polylactide (PLA) Production." *Polymer Degradation and Stability*, Vol. 80, No. 3, 2003, pp. 403–419. https://doi.org/10.1016/S0141-3910(02)00372-5.

[3] Sekito, T., Miyake, Y., and Matsuda, M. *Performance Improvement of Eco Plastics/Poly Lactic Acid*. Publication 2006-01–0335. SAE International, Warrendale, PA, 2006.

[4] Harris, A. M., and Lee, E. C. "Improving Mechanical Performance of Injection Molded PLA by Controlling Crystallinity." *Journal of Applied Polymer Science*, Vol. 107, No. 4, 2008, pp. 2246–2255. https://doi.org/10.1002/app.27261.

[5] Srithep, Y., Javadi, A., Pilla, S., Turng, L.-S., Gong, S., Clemons, C., and Peng, J. "Processing and Characterization of Recycled Poly(Ethylene Terephthalate) Blends with Chain Extenders, Thermoplastic Elastomer, and/or Poly(Butylene Adipate-Co-Terephthalate)." *Polymer Engineering & Science*, Vol. 51, No. 6, 2011, pp. 1023–1032. https://doi.org/10.1002/pen.21916.

[6] Goto, K., Nakano, S., and Kuriyama, T. "The Effects of Annealing on Deformation and Fracture Behavior of Injection Molded PLA." *Strength, Fracture and Complexity*, Vol. 4, No. 3, 2006, pp. 185–188.

[7] Li, G., Yang, B., Han, W., Li, H., Kang, Z., and Lin, J. "Tailoring the Thermal and Mechanical Properties of Injection-Molded Poly (Lactic Acid) Parts through Annealing." *Journal of Applied Polymer Science*, Vol. 138, No. 2, 2021, p. 49648. https://doi.org/10.1002/app.49648.

[8] Srithep, Y., Nealey, P., and Turng, L.-S. "Effects of Annealing Time and Temperature on the Crystallinity and Heat Resistance Behavior of Injection-Molded Poly(Lactic Acid)." *Polymer Engineering & Science*, Vol. 53, No. 3, 2013, pp. 580–588. https://doi.org/10.1002/pen.23304.

[9] Yeh, G. S. Y., Hosemann, R., Loboda-Čačković, J., and Čačković, H. "Annealing Effects of Polymers and Their Underlying Molecular Mechanisms." *Polymer*, Vol. 17, No. 4, 1976, pp. 309–318. https://doi.org/10.1016/0032-3861(76)90187-7.

[10] Viswanath, V., Maity, S., Bochinski, J. R., Clarke, L. I., and Gorga, R. E. "Thermal Annealing of Polymer Nanocomposites via Photothermal Heating: Effects on Crystallinity and Spherulite Morphology." *Macromolecules*, Vol. 46, No. 21, 2013, pp. 8596–8607. https://doi.org/10.1021/ma401855v.

[11] Barkhad, M. S., Abu-Jdayil, B., Mourad, A. H. I., and Iqbal, M. Z. "Thermal Insulation and Mechanical Properties of Polylactic Acid (PLA) at Different Processing Conditions." *Polymers*, Vol. 12, No. 9, 2020, p. 2091. https://doi.org/10.3390/polym12092091.

[12] Fischer, E. W., Sterzel, H. J., and Wegner, G. "Investigation of the Structure of Solution Grown Crystals of Lactide Copolymers by Means of Chemical Reactions." *Kolloid-*

Zeitschrift & Zeitschrift für Polymere, Vol. 251, No. 11, 1973, pp. 980–990. https://doi.org/10.1007/BF01498927.

[13] *ASTM D638-14: Standard Test Method for Tensile Properties of Plastics*. ASTM International, 2014.

[14] Wang, G., Zhang, D., Li, B., Wan, G., Zhao, G., and Zhang, A. "Strong and Thermal-Resistance Glass Fiber-Reinforced Polylactic Acid (PLA) Composites Enabled by Heat Treatment." *International Journal of Biological Macromolecules*, Vol. 129, 2019, pp. 448–459. https://doi.org/10.1016/j.ijbiomac.2019.02.020.

[15] Viswanath, V., Maity, S., Bochinski, J. R., Clarke, L. I., and Gorga, R. E. "Thermal Annealing of Polymer Nanocomposites via Photothermal Heating: Effects on Crystallinity and Spherulite Morphology." *Macromolecules*, Vol. 46, No. 21, 2013, pp. 8596–8607. https://doi.org/10.1021/ma401855v.

Debriyaj Diskindeki SAE 1010 Malzeme Disk Kapağının Temperleme Isıl İşlemi ile Renklendirilmesinin Parçanın Mekanik Özellikleri Üzerine Etkisinin İncelenmesi

Investigation of the Effect of Coloring of the SAE 1010 Material Disc Cover on the Clutch Disc by Tempering Heat Treatment on the Mechanical Properties of the Part

Ulaşcan KURT*[,1], Ceren ÇELİK[1,2], Caner EŞ[1], Ömer YILDIZ[1], Orhan KARABULUT[1,2]

*u.kurt@donmezdebriyaj.com.tr , ORCID: 0000-0002-1280-7210
[1]*Ar&Ge ve Test Validasyon Mühendisi, Dönmez Debriyaj Sanayi ve Ticaret AŞ., İzmir, Türkiye*
[2]*Makine Mühendisliği, Yüksek Lisans, İzmir Yüksek Teknoloji Enstitüsü, İzmir, Türkiye*

Özet: Günümüzde malzeme bilimi ve ısıl işlem koşulları her geçen gün gelişmektedir. Endüstrinin ihtiyacı ve yüksek mukavemetli çeliklere olan talep de bu gelişmelere bağlı olarak artmakta olup geniş çaplı bir rekabet ortaya çıkmaktadır. Otomotiv endüstrisinde büyük bir pazar payına sahip olan güç aktarma organları da bu değişimden etkilenmekte ve her geçen gün gelişmektedir. Taşıtlarda motor gücünü iletmesi ve gerekli durumlarda iletimini kesmesi sebebi ile debriyaj önemi yüksek bir aktarma organıdır. Bu çalışmada, debriyaj diskindeki helezon yayları tutan SAE 1010 malzemeden imal edilen alt ve üst kapağa farklı sıcaklıklarda ve farklı fırınlanma sürelerinde temperleme ısıl işlemi uygulanmıştır. SAE 1010 malzemeye uygulanan ısıl işlem sonucu meydana gelen renk değişimi gözlemlenmiştir. Sertlik ölçümü için HRN-15 cinsinden tahribatlı muayene ile sertlik değerleri elde edilerek verilerin sıcaklık ve zamana bağlı olarak değişimi incelenmiştir. Yapılan çalışmalar neticesinde farklı sıcaklıklarda uygulanan temperleme ısıl işlemi sonucunda sıcaklık artışı ile sertlik değerinin azaldığı ve mekanik özelliklerinin değiştiği gözlemlenmiştir.

Anahtar Kelimeler: *Debriyaj, Debriyaj Diski Kapağı, SAE 1010 Malzeme, Temperleme Isıl İşlemi, Renk Menevişi, Sertlik.*

Abstract: Nowadays material science and heat treatments conditions have been developing day by day. Industrial's need and demanding high strength steels are also growth depend on these developing. Under these conditions, there are created a wide competition. The powertrain, which has a large market share in the automotive industry, is also imposed by this change and is developing day by day. Clutch is a highly important powertrain as it transmits engine power in vehicles and interrupts transmission when necessary. In this study, the tempering heat treatment was applied to the upper and lower covers made of SAE 1010 material, which hold the helical springs in the clutch disc, at different temperatures and for different annealing durations. The color chancing formed as a result of the heat treatment applied to the SAE 1010 material was observed. Hardness values were obtained by destructive examination with HRN-15 for hardness measurement, and the changes in data were examined with respect to temperature and time. As a result of the studies, it was observed that the hardness value decreased, and the mechanical properties changed with the temperature increase consequently tempering heat treatment applied at different temperatures.
Keywords: *Clutch, Clutch Disc Cover, Material SAE 1010, Tempering Heat Treatment, Hardness.*

I. GİRİŞ

Otomotiv sanayi, motorlu taşıtların üretim ana sanayisi ve bu ana sanayinin taleplerine uygun orijinal veya eşdeğer aksam, parça, modül ve sistemler üreten yan sanayi sektörünün tamamını içeren büyük bir sanayi koludur [1]. Bu büyük sanayi kolunu besleyen sektörlerden biri çelik endüstri olarak adlandırılabilir. Otomotiv endüstrisinde yaygın olarak SAE 1010 ıslah çeliği kullanılmaktadır. Çelik malzemelerin mekanik özellikleri, mikro yapı ve kimyasal yapıya bağlı olarak üretim esnasında malzemeye farklı ısıl işlemler uygulanmasıyla değiştirilebilir. Uygulanacak ısıl işlem, malzemenin mikro yapısını iyileştirerek malzeme yüzeyine uygun özellikleri kazandırmalıdır.

Literatürde çelik malzemelerin ısıl işlemleri ilgili birçok çalışma bulunmaktadır. Bu çalışmalardan Saraç ve Özbek, AISI 4140 ıslah çeliğine su verme işlemi sonrasında temperleme ısıl işlemi uygulayarak, ısıl işlem sıcaklığının çeliğin mekanik özellikleri üzerindeki etkisini araştırmışlardır sıcaklık değişikliklerinin çeliğin mekanik özellikleri üzerindeki etkisini incelemiştir [2]. Güler ve Özcan, farklı sıcaklıklara ısıtılan yüksek karbonlu çelik malzemenin suda soğutma işleminin mekanik özelliklere etkisi incelenmiştir. Bu amaçla, gerçekleştirilen ısıl işlemlerden elde edilen bulgular yorumlanmıştır [3]. Demirezen ve ark., otomotiv endüstrisinde yaygın kullanım alanına sahip AISI 5140 ve AISI 4140 çeliklerini farklı sıcaklıklarda menevişleme işlemine tabi tutarak, ısıl işlemin mekanik özelliklere etkisini incelemiş; optimum ısıl işlem sıcaklığını belirlemişlerdir [4]. Tomita, yüksek karbonlu ve düşük alaşımlı çelikleri yağ ortamında soğutma işlemini gerçekleştirmiş ve bu prosesin mikro yapı üzerindeki etkilerini inceleyerek mekanik özelliklerini belirlemiştir [5]. Nayak ve ark., orta ve yüksek karbonlu çelik malzemelerin karbonca zenginleştirilmiş östenit oluşumunu ve su verme işlemini inceleyerek bu prosesin sertlik ve mikro yapı üzerindeki etkilerini araştırmıştır [6]. Literatür çalışmaları incelendiğinde, çelik malzemelerin kimyasal özelliklerini değiştirmeksizin, ısıl işlem uygulanarak malzemenin dayanımı, sünekliği ve sertliği değiştirilebilmektedir sonucuna varılmıştır. Çalışmalar, artan sıcaklıkla birlikte numunelerin çekme ve akma dayanımı değerlerinde azalma tespit edildiği şeklinde yorumlanabilir. Buna ek olarak bakıldığında en düşük temperleme sıcaklığında sertlik değerinin maksimuma ulaştığı gözlemlenmiştir. Bu çalışmada, seçilen SAE 1010 çelik malzemenin farklı sıcaklıklara ısıtılıp daha sonra havayla soğutma işlemi gerçekleştirilmiştir. İşlem sonrasında malzemenin mekanik özelliklerinin belirlenmesi amacıyla, her ısıl işlem sonrası Super Rockwell sertlik cihazında ölçümler gerçekleştirilerek ortaya çıkan renk değişimleri çelik renk skalası ile karşılaştırılmıştır.

A. Kuru Sürtünmeli Debriyaj Sistemleri

Taşıtlarda kullanılan debriyaj sistemi, motor çalışırken tekerleklerin hareket etmediği durumlarda veya hız değişikliklerinde motor gücünün vites kutusuna iletimini geçici olarak keserek vites değiştirme veya durma gibi işlemlerin yapılmasına olanak sağlayan aktarma organıdır. Motor ile vites kutusu arasında yer alan bu sistem, ilk hareket sırasında motorun hareketini tekerleklere ileterek aracın sarsıntısız olarak harekete geçmesini sağlar. Yukarıda bahsedildiği üzere debriyajın görevleri şu şekilde sıralanabilir; ilk hareket sırasında aracın titreşimsiz bir şekilde harekete geçmesini sağlamak ve motor düzensizliklerini sönümlemek için motor torkunu şanzımana iletmektir. Taşıt hareket halindeyken vites durumlarını değiştirmek için geçici bir şekilde motordan vites kutusuna hareket iletimini kesmektir ayrıca gerektiğinde motorla güç aktarma organları arasındaki bağlantıyı keserek aşırı torka maruz kalma durumlarında şanzımanı korumak da debriyajın önemli bir işlevidir. Bir debriyajın doğru şekilde çalışmaması durumunda güç aktarımı ve vites değiştirme oldukça zorlaşacaktır. Sürtünmeli debriyaj sistemleri, güç aktarımını sağlamak için sürtünme kuvvetini kullanan bir debriyaj türüdür. Sürtünmeli tip kavramalarda tork iletimi, düzgün işlenmiş iki yüzey ile bunların arasına sıkışmış bulunan balatalı disk arasındaki sürtünme kuvvetiyle olur. Çeşitli

uygulamalarda kullanılan farklı sürtünmeli debriyaj sistemleri vardır. Otomobillerde yaygın olarak kullanılan bir debriyaj türü olan kuru sürtünmeli debriyaj bunlardan birisidir. Kuru sürtünmeli debriyajda kavramayı ayırma işlemi sürücü alanında bulunan debriyaj pedalı ile başlar. Kavrama ayırmak istendiğinde debriyaj pedalına basılarak mekanik veya hidrolik aktüatör tarafından eksenel yönde baskı komplesi üzerindeki diyafram yayı üzerine kuvvet uygulanır. Bu uygulanan kuvvet neticesinde diyafram parmakları eksenel olarak hareket eder ve baskı plakası mesnet lamaları vasıtasıyla geriye çekilerek disk komplesi üzerinden tork aktarımı kesilir, ayrılma gerçekleşir. Debriyaj pedalından ayağınızı kaldırdığınızda ise mekanik veya hidrolik aktüatör tarafından eksenel yöndeki kuvvet geriye çekilir. Disk komplesi, baskı plakası ve volan arasında sıkışarak disk yüzeylerinde yer alan balatalar üzerinden kavrama gerçekleşir, bu sayede disk göbeği içinden geçen şanzıman miline tork aktarımı tekrar sağlanmış olur [7]. Disk komplesinde bulunan helezon yaylar, motordan gelen titreşimleri ve aşırı torkları sönümleyerek vites kutusuna iletilmesini engellerken, helezon yayların sıkışması sırasında bunlara mesnet görevi gören alt ve üst kapak torka maruz kalmaktadır. Torka maruz kalan bu alt parçalarda dayanımın artması için temperleme ısıl işlemi uygulanmaktadır.

B. Isıl İşlem

B.1. Karbon Emdirme

Demirin çeşitli oranlarda karbon ile alaşımlandığı bir malzeme olan çeliğe karbonun eklenmesi işlemi, genellikle çeliklerin düşük karbon içeriğine sahip olmaları durumunda uygulanır. Bu tür çelikler alaşımsız veya düşük alaşımlı çelikler olarak adlandırılır. Alaşımsız çeliklerde karbon içeriği genellikle %0,2'yi geçmez iken düşük alaşımlı çeliklerde karbon içeriği %0,2 ile %0,4 arasında değişebilir. Karbon emdirme, metal parçaların yüksek sıcaklıkta genellikle gaz veya sıvı halde olan bir ortamda yüzeylerine karbonun nüfuz etmesini sağlamak amacıyla uzun süre tutulmasıyla uygulanan bir ısıl işlem prosedürüdür. Karbonun yüzeyden iç kısma doğru nüfuz etmesi işlemidir. Bu işlem, çeliğin yüzey özelliklerini değiştirerek sertlik, aşınma direnci, yüzey pürüzlülüğü gibi özelliklerin iyileştirilmesini amaçlar. Ayrıca çelik yüzeyine nüfuz eden karbon sayesinde yüzey sertliği artarken, iç kısımda çeliğin süneklik ve tokluk özelliklerini korumasına yardımcı olabilir. Bu işlem, çeşitli endüstrilerde, özellikle otomotiv, makineler, aletler ve metal işleme sektörlerinde kullanılan önemli bir yüzey işlemidir [8].

B.2. Sertleştirme

Çelik parçanın östenit faz sıcaklığına ısıtılması ve hızlı bir şekilde soğutulmasıyla gerçekleşir. Bu yöntemle çelik cam gibi sert hale gelir ancak kırılganlık riski artar. Homojen bir yapı sağlamak için yeterli süre bekletilen çelik parça, hızlı soğutma ile ‘’martenzit’’ yapıya dönüşebilir. Ana amaç, minimum soğuma hızında tamamen martenzit elde etmektir ve bu hıza "kritik soğuma hızı" denir. Sertleştirme sonucunda mikroyapı, sertlik ve dayanım değerleri soğutma hızına bağlı olarak değişir. Çelik parça, kritik soğutma hızından daha hızlı soğutulursa yüksek sertlikte martenzit yapısı oluşurken, daha yavaş soğutma sonucu östenitin bir kısmı veya tamamı ferrit ve perlit yapısına dönüşerek sertliği düşürür. Soğuma hızı ile kritik soğuma hızı arasındaki fark arttıkça östenitin dönüşüm miktarı artar ve sertlik düşer. Sertleştirmede genellikle su ve yağ kullanılırken, bazı özel durumlarda hava da tercih edilir. Nitrürleme, yüzeye bor emdirme ve indüksiyon akımıyla sertleştirme gibi farklı yöntemler de bulunur.

B.3. Temperleme (Meneviş)

Sertleştirme işlemi sırasında oluşan fazlasıyla sert ve gevrek martenzit yapısının dezavantajlarını gidermek amacıyla kullanılır. Martenzit yapısı hızlı soğuma sonucu yüksek gerilimlere ve kırılganlığa yol açabilir. Menevişleme, su ile sertleştirilmiş çelikleri ötektoid

sıcaklığının altındaki belirli sıcaklıklarda ısıtarak iç gerilmeleri azaltmayı amaçlar. Bu işlem sırasında düşük sıcaklıklar gerilmeleri alırken, yüksek sıcaklıklar çeliğin sertliğini ve mukavemetini düşürüp daha tok ve sünek bir yapıya dönüştürür. Menevişleme esnasında meydana gelen mekanik özellik değişiklikleri, ısıtma sırasında mikroyapıda gerçekleşen olaylardan kaynaklanır. Sertleştirilmiş çelikler menevişlendikçe çekme dayanımı ve akma sınırı düşerken, kopma uzaması, kesit daralması ve çentik darbe dayanımı gibi şekil değişebilirlik karakteristikleri artar. Meneviş kırılganlığı gösteren çeliklerde, bu kırılganlığı gidermek için meneviş sıcaklığında tavlama veya yavaş soğutma gibi yöntemler kullanılabilir [9].

II. AMAÇ

Bu çalışmanın amacı, debriyaj diskindeki helezon yayları muhafaza eden SAE 1010 malzemeden imal edilen alt ve üst kapağın mekanik özellikleri sabit tutulurken farklı sıcaklıklarda ve fırınlanma sürelerinde uygulanan temperleme ısıl işlemi sonrasında ortaya çıkan renk değişimini gözlemlemektir. Ardından sertlik ölçümü için HRN-15 cinsinden tahribatlı muayene ile farklı renklere sahip alaşım çeliklerinin sertlik değerleri ölçülerek, verilerin sıcaklık ve zamana bağlı değişimini incelemektir. Yapılan çalışmalar sonrasında sıcaklığın renk değişimi ve sertlik değerleri üzerindeki etkisini gözlemlemektir.

III. MATERYAL VE METOT

Sanayide geniş kullanım alanına sahip olan çelikler, içerisindeki karbon miktarı nedeniyle sertleştirme işlemine uygun ve ısıl işlem uygulandıktan sonra belirli bir çekme dayanımına sahip yüksek tokluk özelliği gösteren makine imalat çelikleridir.

A. Materyal

Bu çalışmada incelenen %0,10 karbon içeriğine sahip düşük karbonlu bir çelik olan SAE 1010 ıslah çeliğinin kimyasal bileşimi SAE J403 standardına uygun olarak Tablo 1'de detaylı olarak görülmektedir.

TABLO I. SAE 1010 KALİTELİ ÇELİK MALZEMENİN KİMYASAL BİLEŞİMİ (%)

Element	Oranı
C	0.08 – 0.13
Mn	0.30-0.60
P	0.030 max.
S	0.050 max.

C =Karbon, Mn = Mangan, P = Fosfor, S = Kükürt [10].

B. Metot

Isıl işlem fırınları, malzemelerin sıcaklık değişikliklerine tabi tutularak mekanik veya yüzey özelliklerini değiştirmek amacıyla kullanılan endüstriyel fırın sistemleridir. Bu işlem, otomotiv ve diğer endüstrilerde yaygın olarak kullanılır.

Isıl işlem fırınları, malzemelerin mekanik özelliklerini, sertliğini, tokluğunu, dayanıklılığını ve diğer özelliklerini geliştirmek veya değiştirmek için kullanılır. Bu işlem, malzemelerin daha iyi performans göstermesini, uzun ömürlü olmasını veya belirli işlevlere daha uygun hale gelmesini sağlar. Isıl işlem fırınları sertleştirme, tavlama, çözelti İşlemi, östenitleştirme, yaşlandırma vb. olmak üzere çeşitli işlemler için kullanılabilir.

B.1. Uygulanan Isıl İşlem

Isıl işlem için kuyu tipi ısıl işlem fırını kullanılmış olup fırın görselleri Şekil 1'deki gibidir. Çelik numuneler üzerine karbonitrasyon işleminin ardından 225°C'de 60 dakika, 235°C'de 35 dakika ve 240°C'de 70 dakika süre ile temperleme ısıl işlemi uygulanmıştır.



Şekil 1. Temperleme Isıl İşlem Fırını.

Fırınlama operasyonunun ardından sertlik ölçüm cihazı ile parçaların sertlikleri ölçülmüştür.

B.2. Sertlik Ölçüm Cihazı

Farklı sıcaklıklarda temperleme işlemine tabi tutulan SAE 1010 ıslah çeliği numunelerin sertlik ölçümleri AFFRI VRSD 251 sertlik ölçüm cihazı ile gerçekleştirilmiş olup sertlik cihazı görseli Şekil 2'teki gibidir. Sertlik ölçümü ASTM E18 standardına göre HRN-15 cinsinden Elmas 120° uç ile tahribatlı muayyene aracılığıyla oda sıcaklığında yapılmıştır. Numunelerin ham sertliği 89.7 HRN-15'Tir.



Şekil 2. Super Rockwell Sertlik Ölçüm Cihazı.

B.3. Tuz Test Cihazı

Sertlik ölçümleri yapılan SAE 1010 çeliğin Salt Spray Chamber tuz test cihazı ile korozyon dirençleri ölçülmüştür. İşlem sırasında kullanılan korozyon tuz test cihazı Şekil 3'te görülmektedir.



Şekil 3. Tuz Testi Cihazı.

IV. DENEYSEL SONUÇLAR

A. Sertlik Ölçümü

Çeliklerde su verme sonrası oldukça sert ve gevrek olan martenzit yapısı oluşur. Dolayısıyla çalışma koşullarında kolayca çatlayarak hasara yol açabilir. Su verilmiş çeliklerde temperleme adı verilen bir ısıl işlemle çeliğin gevrekliği giderilebilir ve çeliğe tokluk kazandırılabilir.

SAE 1010 malzemeden imal edilen alt ve üst kapağa farklı sıcaklıklarda ve farklı fırınlanma sürelerinde uygulanan temperleme ısıl işlemi sonucunda ortaya çıkan renk değişimleri gözlemlenmiştir. HRN-15 cinsinden tahribatlı muayyene ile sertlik değerleri elde edilerek verilerin sıcaklık ve zamana bağlı olarak değişimi incelenmiştir. Numunelerin sertlik değerlerini temperleme sıcaklıklarına bağlı olarak gösteren veriler Tablo 2'de sunulmuştur. Tablo analiz edildiğinde; temperleme ısıl işlemi uygulanmamış numunenin en yüksek sertlik ve tokluk değerine sahip olduğu görülmektedir. 225 °C ile 240 °C sıcaklık arasında uygulanan temperleme sıcaklıklarıyla birlikte sertlik değerleri de düşmüştür. Temperleme uygulanmamış çelik numune 89.7 HRN-15 sertliğe sahip iken, 225°C sıcaklıkta 60 dakika boyunca temperlendiğinde sertliği %1,3 azalarak 88.5 HRN-15'e düşmüştür. Sıcaklık 235 °C'ye çıkarılarak 35 dakika boyunca temperlendiğinde ise sertlik değeri %2 oranda daha düşük olarak 87.9 HRN-15 değerinde ölçülmüştür. Son olarak 240°C sıcaklıkta temperlenmiş numunede 85.7 HRN-15 olarak en düşük sertlik değeri ölçülmüş ve azalma oranı %4.45'tir. 225°C ile 240 °C sıcaklık arasında uygulanan temperleme sıcaklıklarıyla birlikte SAE 1010 malzemede meydana gelen renk değişimleri numerik olarak Tablo 2'de yer almakta olup görsel hali Şekil 4'teki gibidir. Yapılan çalışmalar sonucunda, artan temperleme sıcaklığı ile sertlik değerlerinde genel olarak bir azalma gözlemlenmiş olmasına rağmen SAE 1010 çeliği istenilen yüzey sertliği aralığında kalmıştır. Bu durumda çalışma koşulları düşünüldüğünde sertlikte meydana gelen azalma göz ardı edilebilir aralıktadır. Düşük temperleme sıcaklıklarında çelik numunelerin mikroyapısında bulunan martenzit yapının artan temperleme sıcaklığıyla beynit ve perlit yapıya dönüşmesiyle ilişkili olduğu

düşünülmektedir. Ayrıca parçaların mekanik özelliklerinden olan tokluk ve süneklik değerlerinin arttığı gözlemlenmiştir.

TABLO I I . SAE 1010 ÇELİĞİNİN TEMPERLEME SICAKLIKLARINA BAĞLI SERTLİK DEĞİŞİMİ

Sıcaklık (°C)	Zaman (dakika)	Renk	Sertlik (HRN-15)
225	60	Sarı Metal/Pirinç	88.5
235	35	Mor	87.9
240	70	Mavi	85.7

°C= santigrat



Şekil 4. SAE 1010 Çeliğinin Temperleme sıcaklıklarına bağlı renk değişimi.

B. Renk Skalası

Çeliğin yüksek sıcaklıkta ısıtılması ve hızlı bir şekilde soğutulmasıyla çeliğin martenzite dönüşmesini sağlar. Ancak martenzit yapı genellikle çok sert ve kırılgan olduğundan çeliğin kullanımını olumsuz etkiler. Bu durumu önlemek için çeliklerde temperleme ısıl işlemi, ısıl işlem sonrası meydana gelen fazla mukavimliği ve kırılganlığı azaltmak amacıyla yapılmaktadır. Farklı sıcaklıklarda uygulanan temperleme sıcaklığına bağlı çelik malzemede meydana gelmesi beklenen renk skalası Tablo 3'te yer almaktadır. Bu tabloda sıcaklığın artmasıyla çeliklerde meydana gelen renk değişiminin siyahtan kırmızıya doğru olduğu görülmektedir.

TABLO III. ÇELİĞİN TEMPERLEME SICAKLIKLARINA BAĞLI RENK SKALASI DEĞİŞİMİ

Sıcaklık	Renk	Sıcaklık	Renk
199°C		302°C	
229°C		427°C	
241°C		538°C	
249°C		593°C	
260°C		649°C	
271°C		704°C	
282°C		760°C	

°C= santigrat

C. Tuz Testi

Malzemelerin korozyon direncini değerlendirmek için kullanılan yaygın bir test yöntemidir. Bu test, özellikle metal yüzeylerin tuzlu ortamlarda nasıl davrandığını anlamak için kullanılır. Test sürecinde malzeme numuneleri belirli bir süre boyunca tuz sisi cihazında

maruz bırakılır. Test sonucunda, malzemenin yüzeyinde oluşan korozyon ürünleri, paslanma, kabarma, bozulma gibi belirtiler gözlemlenir. Bu hasarlar genellikle standartlara veya spesifikasyonlara göre değerlendirilir.

Yapılan çalışma sonucunda, temperleme ısıl işlemi operasyonunun fosfat kaplama ile aynı mekanik özellikleri sağlamadığı gözlemlenmiştir. Şirket bünyesinde imal edilen SAE 1010 malzeme disk kapağına yapılan fosfat kaplama operasyonu kaldırılırsa, karbonitrasyon operasyonundan sonra yapılan temperleme ısıl işleminin korozyona yeterli direnci sağlayamayacağı gözlemlenmiştir. Bunun sebebi uygulanan temperleme ısıl işleminin malzemedeki korozyonu arttırmış olmasıdır. Korozyon tuz testine maruz bırakılan temperlenmiş ürün Şekil 4'te görülmektedir.



(a) (b)

Şekil 4. Temperlenmiş SAE 1010 Çeliğinin Tuz Testi; (a) Tuz Test öncesi, (b) Tuz Test sonrası.

V. SONUÇ VE DEĞERLENDIRME

Bu çalışmada, SAE 1010 çeliğine sertlik işleminden sonra, 225, 235 ve 240 °C olmak üzere farklı sıcaklıklarda temperleme ısıl işlemi uygulanmış ve numunelerin mekanik özelliklerindeki değişim incelenmiştir. İnceleme sonuçları aşağıdaki gibidir:

Temperlenmemiş numune ile 240 °C'de temperlenmiş numuneler arasında sertlik değerlerinde temperleme uygulanmamış numunelerin daha yüksek değerde olduğu görülmüştür, bunun sebebi olarak temperleme uygulanmamış numune iç yapısının martenzit yapıda olması ile alakalı olduğu düşünülmektedir.

Çalışma koşulları düşünüldüğünde, artan temperleme sıcaklığı ile numunelerin sertlik değerlerinde kabul edilebilir düzeyde azalma olurken, tokluk değerlerinde artış meydana geldiği gözlemlenmiştir. Bu gözlemin temperleme işlemi sonucunda AISI 4140 çeliğinin mikroyapısında meydana gelen faz dönüşümü ile ilgili olduğu düşünülmektedir. Faz dönüşümünde, martenzit yapıdaki taneler küreselleşerek homojen bir yapı ortaya çıkarmış olup, sonrasında daha yumuşak bir yapıya sahip olan beynit ve perlit yapının arttığı düşünülmektedir.

Bunlara ek olarak, temperleme operasyonunun fosfat kaplama ile aynı mekanik özellikleri sağlayamadığı gözlemlenmiştir. Karbonitrasyon operasyonundan sonra uygulanan temperleme ısıl işleminin korozyona yeterli direnci karşılayamadığı gözlemlenmiştir.

Yapılan çalışmalar sonucunda, SAE 1010 çeliğe farklı sıcaklıklarda uygulanan temperleme ısıl işlemi sonucunda bu sıcaklık aralıklarında çelikte elde edilen renk değişimleri literatüre kazandırılmıştır.

TEŞEKKÜR

Çalışmamızda emeği geçen ve desteklerini esirgemeyen Dönmez Debriyaj A.Ş AR-GE çalışanlarına teşekkürlerimizi sunarız.

REFERANSLAR

[1] Anonim, "Türkiye otomotiv sektörü strateji belgesi ve eylem planı," Sanayi ve Ticaret Bakanlığı Sanayi Genel Müdürlüğü, 2011–2014.
[2] E. Saraç, N.A. Özbek, ''Temperleme Isıl İşlem Sıcaklıklarının AISI 4140 Çeliğinin Mekanik Özellikleri Üzerine Etkilerinin Araştırılması,'' 2019.
[3] H. Güler, R. Özcan, ''Yüksek Karbonlu Çeliklere Su Verme İşleminin Mekanik Özelliklere Etkisinin İncelenmesi,'' Uludağ Üniversitesi Mühendislik Fakültesi Dergisi, Cilt 19, Sayı 2, 2014.
[4] M. Demirezen, M. Bayrak, ve F. Öztürk, ''DIN 41Cr4 ve DIN42CrCo4 Çeliklerde Isıl İşlemin Mekanik Özelliklere Etkisinin Araştırılması'', Teknoloji, 9 (2), 145-152, 2006.
[5] Y. Tomita, ''Development of mechanical properties of structural high-carbon low-alloy steels through modified heat treatment'', Journal of Materials Science, 24 (4), 1357-1362, 1989.
[6] S.S. Nayak, R. Anumolu, R.D.K. Misra, K.H. Kim, D.L. Lee, ''Microstructure-hardness relationship in quenched and partitioned medium-carbon and high-carbon steels containing silicon'', Materials Science and Engineering, A,498 (1-2), 442-456, 2008.
[7] A. Dündar, "Debriyaj Sistemlerinde Yastıklamalı Yay Üretim Prosesinin Araç Konforuna Etkisinin İncelenmesi," Bursa Uludağ Üniversitesi, 2022.
[8] https://www.anadoluinduksiyon.com.tr/kategoriler.php?kid=1606738887.
[9] U. Kınıt, ''30mnb4 Cıvata Malzemesinin Statik Dayanım Değerlerinin Değişik Isıl İşlem Türlerine Göre Deneysel İncelenmesi,'' İstanbul Teknik Üniversitesi Fen Bilimleri Enstitüsü, Haziran 2013.
[10] SAE J403: Chemical Compositions of SAE Carbon Steels,2014.

Debriyaj Kafesi Tasarım Optimizasyonu ve Validasyonu

Design Optimization and Validation Clutch Cover

Sadık ŞENOL[*,1], Ömer YILDIZ[1], Caner EŞ[1]

s.senol@donmezdebriyaj.com.tr, ORCID: 0009-0007-5762-2782

[1] *R&D Center, Dönmez Debriyaj San. Ve Tic. A.Ş., İzmir, Turkey*

Özet: İçten yanmalı motorlu araçlarda ve bazı makinelerde motor ve şanzıman arasında tork ve hareketi aktarma organı olarak debriyaj sistemleri kullanılmaktadır. Debriyaj sistemleri debriyaj diski, debriyaj baskısı ve debriyaj rulmanı olarak 3 ana bileşen, volan ve debriyaj çatalı olmak üzere 2 yardımcı bileşenden oluşmaktadır. Çalışmamızda debriyaj ana bileşenlerinden olan debriyaj baskısının alt parçalarından debriyaj kafesi konu alınmıştır. Debriyaj baskısı hareket aktarımı sırasında dönme momenti ve baskı kuvvetine maruz kalır. Dönmez Debriyaj A.Ş bünyesinde üretilen debriyaj kafesinin üretim aşaması ham madde olarak gelen parçanın lazer kesim operasyonu ile başlar. Ardından sıvama operasyonu yapılır. Bu operasyonu 1. kalibre, 2. kalibre ve 3. kalibre operasyonları takip eder. Daha sonra preste kesme ve delik delme operasyonları uygulanır. Son olarak havşa ve cnc torna operasyonları uygulanmaktadır. Bu konunun ele alınma sebebi maliyet azaltmayı ve üretim hızının arttırılmasının yapılabilirliğini incelemektir. Buradan yola çıkılarak çalışmada debriyaj kafesinin tasarımında kafes iç yüzeyinde dışa doğru radyus verilerek mesnet noktası oluşturulması planlanmıştır. Oluşacak bu mesnet noktasının mesnet halkası malzemesinin görevlerini tam anlamıyla karşılaması hedeflenmektedir. Buradan yola çıkarak yeni tasarım yapılması ve bu tasarımın eski tasarımla kıyaslanması hedeflenmiştir. Bunun sonucunda hedefimiz mesnet halkası parçasının üretimden kaldırılmasıdır. Çalışmamızda debriyaj kafesinin iç yüzeyindeki radyusun, diyafram yay, ayna ve debriyaj kafesi üzerindeki gerilmelere etkisi incelenmiştir. Mesnet halkalı ve Mesnet halkasız olarak iki farklı debriyaj kafesinin tasarımı ANSYS ticari yazılımı static structural modülünde gerçek çalışma şartları tanımlanıp simüle edilmiştir. Her iki tasarım üzerinden eşdeğer gerilmeler, asal gerilmeler, toplam deformasyon ve gerilme vektörleri sonuçları elde edilmiştir. İki tasarım arasında baskı kuvvetleri kıyaslanmıştır. Bu kıyaslamaya teorik olarak hesapladığımız baskı kuvveti de dahil edilmiştir. Çıkan sonuçlar yüzdelik olarak birbirleriyle kıyaslanmış ve ürünün tolerans değerleri arasında olup olmadığına bakılmıştır. Sonuçlara göre debriyaj kafesinin iç yüzeyinde radyus oluşturulması, mesnet halkası görevini üstleneceği kanıtlanmıştır. Böylece debriyaj baskı bileşenleri içinde olan mesnet halkasına ihtiyaç kalmamıştır. Böylece hedeflediğimiz mesnet halkasız debriyaj baskısı üretilebileceği kanıtlanmıştır.

Anahtar Kelimeler: *Debriyaj, Debriyaj Baskısı, Mesnet Halkası, Mesnet Noktası, Sonlu Elemanlar Analizi, Kavrama*

Abstract: In internal combustion engine vehicles and certain machines, clutch systems are used as the means of transmitting torque and motion between the engine and the transmission. Clutch systems consist of 3 main components as clutch disc, clutch cover assembly and clutch bearing, and 2 auxiliary components as flywheel and clutch fork. In this study, the focus is on the clutch cover, which is one of the main components of the cover assembly. The cover assembly undergoes torsional moments and pressure forces during power transmission. The clutch cover production process starts with the laser cutting of the part received as raw material at Dönmez Debriyaj A.Ş. Following this, the spinning operation is performed. This operation

is followed by the 1st calibration, 2nd calibration, and 3rd calibration operations. Subsequently, cutting and hole drilling operations are performed using a press. Finally, countersink and CNC turning operations are applied. The reason for this issue is to examine the feasibility of reducing costs and increasing production speed. Based on this, the study plans to create a support Point by giving an outward radius on the inner surface of the clutch cover during the cover's design phase. The aim is for this support Point to fully serve the functions of the fulcrum ring material. Based on this, it is aimed to make a new design and compared with the old design. As a result, our goal is to remove the fulcrum ring component from production. In this study, the impact of the radius on the inner surface of the clutch cover on the stresses on the diaphragm spring, pressure plate, and clutch cover is investigated. The design of two different clutch cover, one with a fulcrum ring and one without, is simulated under real working conditions using the ANSYS software's static structural module. Equivalent stresses, principal stresses, total deformation, and stress vectors are obtained for both designs. Compression forces were compared between the two designs. The pressure force that we calculated theoretically is also included in this comparison. The results are compared with each other as a percentage, and it was checked whether the product was within the tolerance values. According to the results, it has been proven that forming a radius on the inner surface of the clutch cover will act as a fulcrum ring. Thus, the need for a fulcrum ring, which is a component of the cover assembly, is removed. Consequently, it is demonstrated that a fulcrum ring-less cover assembly can be produced as intended.

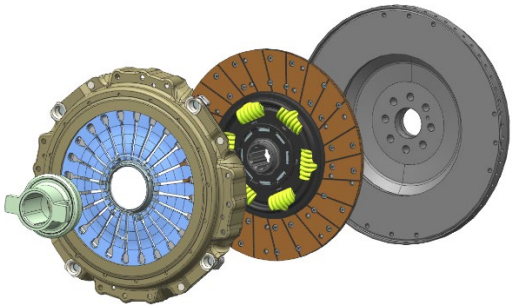
Keywords: *Friction Clutch, Clutch Cover Assembly, Fulcrum Ring, Support Point, Finite Element Analysis, Clutching*

I. GİRİŞ

Günümüzde otomotiv sektörünün ileri gelen firmalarının başlattığı 5S, Kaizen, yalın üretim gibi yöntemler fabrikalarda düzen, güvenlik ve sürekli iyileştirme konusunda gelişimler sağlamaktadır. Sürekli iyileştirme isteği ana sanayi otomotiv firmalarının tedarikçi firmalarından talep ettiği maddelerden biridir. Mühendisler ürün ve proses üzerinde iyileştirme çalışmaları yaparken bu durumdan hem kendileri hem firmaları kazanç sağlamaktadır. Tasarımsal iyileştirmeler ürüne ve prosese hafiflik, maliyet, montaj ve operasyon kolaylığı sağlarken aynı zamanda performans olarak da uygun kaliteyi sağlamalıdır. Çalışmamızda debriyaj baskısında tasarım optimizasyonu ile maliyet ve proseste geliştirme yapılmış, teorik olarak performansı incelenmiştir.

A. Debriyaj

Debriyaj, krank milinden gelen tork ve kuvveti priz direk miline aktarmak veya ayırmak için kullanılan bir makine elemanıdır. Debriyaj, motordan gelen hareket durmaksızın aktarım veya ayırma yapmayı sağlar [1].



Şekil 1 Debriyaj Seti

Debriyaj sistemi sade bir yapıya sahiptir, karmaşık değildir. 3 ana bileşen ve 2 yardımcı bileşenden oluşmaktadır. Bunlar,

- Debriyaj baskısı
- Debriyaj diski
- Debriyaj rulmanı
- Volan (Yardımcı)
- Çatal (Yardımcı)

B. Debriyaj Baskısı

Debriyaj baskısı; ayna, diyafram yay ve baskı kafesi gibi alt parçalardan oluşur. Sürekli dönen bir parça olan baskı volan yüzeyine diyafram yayın ön gerilmiş halde bağlanmasından kaynaklanan kuvvet ile disk parçasını sabitler. Diyafram yaydaki kuvvet ortadan kalktığında yani debriyaja pedalına basıldığında aradaki bağlantıyı kesen bir mekanizmadır.

C. Debriyaj Diski

Disk Balata, göbek, ana saç, yaprak yay gibi alt parçalardan oluşur. Volan ile ayna arasında kuru sürtünmeli çalışan bir kavrama elemanıdır. Ayna tarafından iletilen baskı kuvveti, sürtünen yüzey alanı ve sürtünme kuvveti ile ilişkilendirilen bir aktarma kapasitesine sahiptir. Ayrıca debriyaj diski sahip olduğu torsiyonel yaylar ile motordan gelen ani titreşim ve salınımları sönümlemede görev alır.

D. Debriyaj Rulmanı

Debriyaj rulmanı, debriyaj baskı komplesinin itmeli ya da çekmeli ayırma tipli olmasına göre, diyafram yayı ileri ya da geri hareket ettirir. Bu sayede vites geçişi ve hareket aktarımı sağlanır.

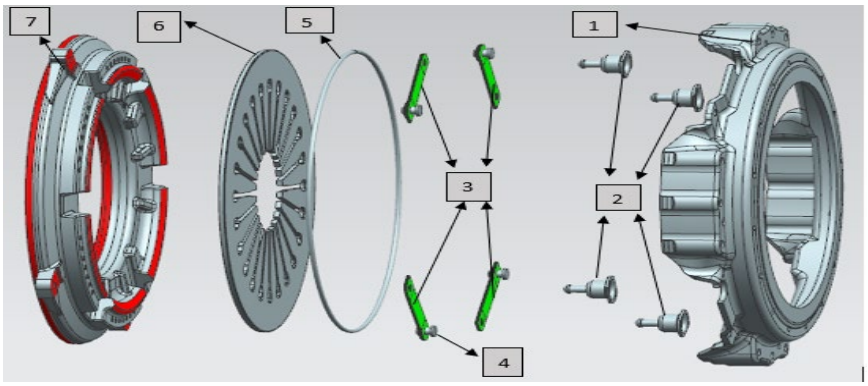
E. Yardımcı Elemanlar

Volan motor bütünün ana parçalarından olmasının yanında debriyaj sistemi için de önemli bir göreve sahiptir. Marş motorundan alınan ilk hareketi motora iletmesi ve debriyaj diskini baskı kuvveti etkisi ile ayna arasında sıkıştırılmasını ve hareketin iletilmesini sağlar. Çatal, debriyaj rulmanına uyguladığı eksenel hareket ile ayırmayı gerçekleştirir. Bu sayede vites geçişi yapılabilir [2].

II. DEBRİYAJ BASKISI

A. Debriyaj Baskısı

Debriyaj baskısı, uyguladığı kuvvet ile motordan gelen torkun kavrama diskine iletilmesini sağlar. Metal bir gövdeden oluşan debriyaj baskısı volana cıvata yardımı ile montajlanır. Motor devri volana aktarılır. Volan ile dönen baskının balansının olmaması gerekir. Ayrıca kavrama esnasında sürtünmeden dolayı açığa çıkan ısı baskı bileşenleri tarafından uzaklaştırılır [3].



Şekil 2 Baskı Seti

Kafes (1), tahdit perçini (2), Mesnet lamaları (3), Mesnet laması tespit perçini (4), Fulcrum ring (5), Diyafram yay (6) ve Ayna (7) oluşmaktadır.

Debriyaj araca bağlanırken, diyafram yay (6), kafes (1) ve fulcrum ring (5) arasına ön gerilmiş halde bağlanır. Tork iletimi esnasında, diyafram yay aynaya basmaktadır. Debriyaj pedalına basılmasıyla birlikte baskı rulmanının diyafram yayı esnemeye zorlamasıyla birlikte ayna (7) ile disk teması kesilir. Böylece ayırma gerçekleşir [4].

Ayna esneklik modülü düşük mesnet laması ile debriyaj kafesine bağlıdır. Ayna genellikle iyi aşınma ve ısı taşınım özelliklerine sahip olan gri dökme demirden yapılmaktadır. Kavrama için gerekli sürtünme yüzeyleri ayna ile diskteki balata arasında sağlanır. Debriyajın en önemli parçalarından diyafram yay, debriyaj kafesi içinde bulunur. Diyafram yay, kafesteki yuvaya yerleştirilmiş olup serbest halde bulunmaktadır. Düşük alaşımlı paslanmaz çelikler grubuna giren 50 CrV4 yüksek mukavemet ve yorulma dayanımları özellikleri sebebi ile diyafram yay malzemesi olarak kullanılmaktadır [5].

B. Diyafram Yay

V.B. Bhandari (2008), deneyinde Diyafram yayın düz, yay çeliğinden sıkıştırılmış bir disk olduğunu açıklamıştır. Kafes ile ayna arasında, rulman tarafından itildiğinde veya çekildiğinde ayırmayı gerçekleştiren elemandır. Diyafram yay, üzerine kuvvet uygulandığında tek bir ince metal levha gibidir. Kuvvet ortadan kalktığında diyafram yay orijinal şekline döner. Diyafram yayın orta kısmı yarıklıdır. Serbest bırakma kolları olarak işlev gören çok sayıda parmağa sahiptir. Sürücü debriyaj pedalına bastığında debriyaj rulmanı diyafram yaya itme veya çekme kuvveti uygular. Diyafram yay bu kuvvet sonrasında hareket eder ve baskı yüzeyi ile disk yüzeyinin temasını keser. Bu sayede sürücü vites değişikliğini kolayca yapabilmektedir. Sürücü debriyaj pedalını bıraktığında diyafram yay normal konumuna döner ve kavrama sağlanır [6].

III. AMAÇ

Debriyaj sistemlerinde diyafram yayın kuvvet iletiminde mesnet noktası oluşturmak için Fulcrum ring kullanılır. Fulcrum ring debriyaj üretiminde artı maliyet ve montaj aşamasında artı zaman kaybı getirir. Bunun için kafes üzerinde değişiklik yapılması kararlaştırılmıştır. Bu iyileştirmede fulcrum ring kullanılmadan kafes üzerinde değişiklik yapılması ve mesnet noktasını kafes üzerine taşınması planlanmıştır. Bu doğrultuda yeni bir kafes tasarımı yapılması planlanmıştır. Kafes'in Siemens NX unigraphics programında katı modellemesi yapılması planlanmıştır. Bu modelin diyafram yay ile çalışması ANSYS Mechanical modulünde sonlu elemanlar yöntemi ile analizi yapılması planlanmıştır.

IV. KAPSAM

A. Debriyaj Kafesi Gerilme ve Yük Analizi

Debriyaj, motordan gelen torku şanzımana iletmek ya da iletimi kesmek için kullanılan bir aktarma organıdır.. Nitin Panchal ve Prof. Ankit R. Patel araştırmasında debriyaj kafesini incelemiştir. Debriyaj kafesinden dolayı arıza oluştuğu tespit etmişlerdir. Bu sebeple yeni bir kafes tasarımı yapılmasını kararlaştırmışlardır. İlk olarak kafes tasarımın yük ve gerilme analizi yapmışlardır. Çelik ve alüminyum kafesler için karşılaştırmalı yük ve stres analizi ANSYS programını kullanarak yapmışlardır. Daha sonra CREO da modellemişlerdir.

TABLO 1

SINTERLENMİŞ DEMİR (SÜRTÜNME MALZEMESİ)

	Analitik Hesaplama	Yazılım Analizi
Toplam Deformasyon	0,393x10-4mm Or 3,93 x10-5 mm	0,5308x10-4 mm or 5,308 x 10-5mm
Gerilmeler	0,6237x10-4$\frac{N}{mm^2}$ 6,237x10-5Mpa	0,664

N=Newton, mm=milimetre, Mpa=Mega Pascal

Ansys programı yardımıyla eski tasarım ve yeni tasarım arasında kıyaslama yapılmıştır. Bu kıyaslama sonucunda yeni tasarımın çalışma koşullarına dayanabileceğini tespit etmişlerdir [7].

B. Aşınma Analizi

Birbirlerine temas halinde çalışan malzemeler arasında sürtünme kuvveti olur. Sürtünme kuvvetinden dolayı malzeme yüzeylerinde aşınma meydana gelir. Aşınma miktarı hem malzemelerin ömrünü azaltır hem de çalışma performanslarını önemli ölçüde etkilemektedir. Bu kaybı önlemek veya en aza indirmek için standart koşullar altında malzemelerin aşınma miktarının belirlenmesi gerekmektedir. Bu doğrultuda laboratuvar ortamında gerçekleştirilen aşınma testleri büyük önem kazanmıştır. Aşınma, hareket halinde çalışan sistemlerde son derece sıklıkla rastlanan bir hasar türüdür. Birden fazla farklı mekanizma ile gerçekleşebilir. Bunlar temel olarak adhesif aşınma, abrasif aşınma, yorulma aşınması ve korozif aşınma olarak sınıflandırılmaktadır. Aşınma olayını etkileyen birçok faktör bulunmaktadır. Temas halinde olan malzemelerin kristal kafes yapısı, sertliği, elastisite modülü, deformasyon sertleşme üssü (deformasyon davranışı), yüzey pürüzlülüğü sadece malzemeye bağlı faktörler olmak üzere ortam şartları (sıcaklık, nem vb.) da son derece etkilidir. Bunların yanı sıra malzemenin maruz kaldığı basınç, hareket hızı, kayma mesafesi de aşınma davranışlarını yakından etkileyen faktörler arasındadır. Tüm bunlar göz önünde bulundurulduğunda aşınma hasarının karmaşık yapısı daha iyi anlaşılmaktadır. Aşınma hasarının en aza indirgenebilmesi için aşınma davranışlarının dikkatlice incelenmesi gerekmektedir. Bunun için farklı deney düzenekleri kullanılmaktadır. Ancak en yaygın olanı pin-on-disk düzeneği ile dönerek hareket eden disk üzerinde sabit şekilde belirli bir kuvvet altında duran pinin (pim) veya bilyanın (ball) aşınması veya tam tersi diskin aşınması ile sürtünme katsayısının belirlenmesi yöntemidir. Bu yöntem ile aşınan disk veya pin/bilya üzerindeki aşınma izi ölçülerek aşınma kaybı (miktarı) belirlenmektedir. Bu deney farklı yükler altında, farklı kayma hızları ve mesafelerinde hatta farklı sıcaklıklarda da yapılabilmektedir. Canay DEMİR bu çalışmada malzemelerin sürtünmeden kaynaklı aşınmalarını incelemiştir. Bunun için bu formüllerden yardım almıştır.

$SÜRTÜNME\ KATSAYISI$:

$$\mu = F/N \tag{1}$$

$SÜRTÜNME\ YÜZEYİ(kontak\ yüzeyi)$:

$$(\pi D^2)/4 \tag{2}$$

$SÜRTÜNMEDEN\ KAYNAKLI\ HACİM\ DEĞİŞİKLİĞİ$:

$$W = Z\ Ps/H \tag{3}$$

W: Hacim kaybı P: yük s: kayma mesafesi H: malzemenin sertliği Z: atom numarası
Tüm yüzey sürtündüğünde (maksimum temas alanına ulaşıldığında):

$$\delta A = \pi a^2; = \delta W/H\ [8] \tag{4}$$

C. Kafes Optimizasyon Analizi

Haktanır M. ve Ark. yaptıkları çalışmada 430 mm çaplı debriyaj baskısının dış çap ölçüsünün tolerans değerleri dışına çıktığını gözlemlemişlerdir. Yaptıkları incelemede bu kaçıklığın tahdit yüzüklerinin baskı kafesine uyguladığı ekstra yük olduğunu gözlemlemişlerdir. Bu doğrultuda 6 mm sac kalınlığı olan kafesin rijitliğini arttırmak amacıyla kalınlığı arttırılmış ve 6,5 mm yapılmıştır. 6 mm sac kalınlığı olan kafes modeli ile 6.5 mm sac kalınlığı olan kafes Ansys Workbench programında analize tabi tutulmuştur.

TABLO 2

DD13 çeliğinin mekanik özellikleri:

σAKMA (MPa)		σÇEKME (MPa)	Yoğunluk (kg/m^3)	Elastisite Modülü (MPa)	Poisson Oranı
1,5≤d<2	2≤d<11	max.	ρ	ε	ν
170-330	170-310	400	7850	200000	0,3

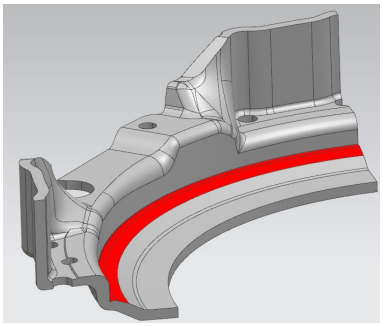
Yapılan kıyaslamada 6.5 mm kafesin çarpılması 6 mm'ye göre %12 daha az olduğu tespit etmişlerdir. Sonuç olarak mukavemeti yüksek ve kolay montajlana bilen bir kafes elde etmişlerdir. Ayrıca müşteri şikayetlerinin de önüne geçmişlerdir [9].

V. YÖNTEM

İncelediğimiz bildiri ve makaleler göz önünde bulundurularak tasarım optimizasyonu öncesi analiz ve hesaplamaların yapılması düşünülmüştür. Fulcrum ring ürünün baskı sisteminden kaldırılması sonucu yeni bir mesnet noktası gereksinimi ortaya çıkacaktır. Bu mesnet noktası kafes üzerinde yeni bir tasarım yapılarak sağlanması planlanmıştır. 3D modelleme Siemens Nx programında tasarlanmıştır. Bu tasarım sonlu elemanlar yöntemi kullanan bir yazılım olan Ansys Workbench programında analize tabi tutulmuştur.

VI. ANALİZ

Analiz için öncelikle hali hazırda üretimimizde olan bir baskı seçilmiştir.. Bu baskının 3D modeli üzerinde optimizasyon yapılmıştır.



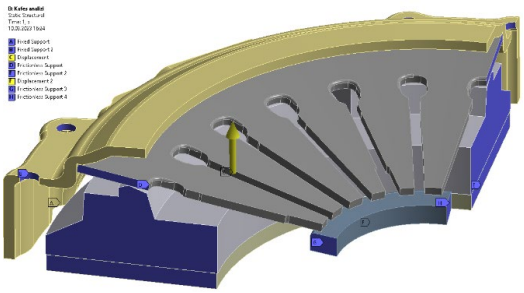
Şekil 3 Yeni Tasarım Mesnet Yüzeyi

3D tasarımın ¼ kesiti Ansys Workbench programına yüklenmiştir. Kafesin ¼ kesit olarak alınmasının sebebi analiz süresini azaltmak ve Ansys üzerinde çözüm kolaylığı sağlamaktır. Kafesin malzeme özellikleri Ansys programına girilmiştir.

Tablo 3

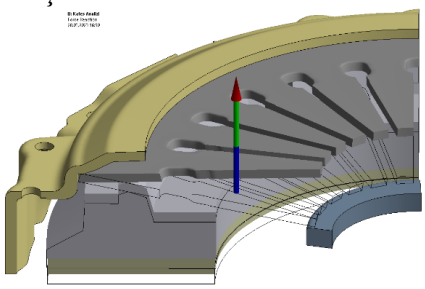
σAKMA (MPa)		σÇEKME (MPa)	Yoğunluk (kg/m^3)	Elastisite Modülü (MPa)	Poisson Oranı
1,5≤d<2	2≤d<11	max.	ρ	ε	ν
170 - 330	170 - 310	400	7850	200000	0,3

A. Analiz Kurgusu



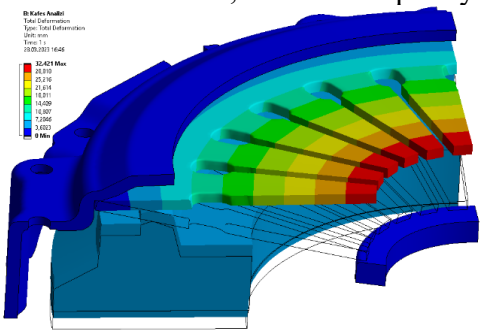
Şekil 4 Sınır Şartları ve Yüklemeler

Debriyaj baskıları serbest haldeyken şekli resimdeki gibidir. Ancak araç üzerine montajı sırasında kurulur ve diyafram yay düz konuma gelir. Bunu sağlamak amacıyla Ansys üzerinde ilk olarak volan bağlantı deliklerinden kafes fixlenmiştir (sabitlenmiştir). Daha sonra debriyajın kurulumunu simülasyon olarak gerçekleştirebilmek adına ayna parçasına displacement yani yer değiştirme verilmiştir. Ayna parçası yukarı yönlü hareket ederek diyafram yayı kafes ile ayna tepe noktası arasında sıkıştırmıştır. Bu sayede debriyaj kurulmuş ve araç üstündeki montajlanmış halini almıştır. Ayrıca model ¼ kesitte çalışıldığı için kesilen her iki yüzeye de frictionless support tanımlandı. Analiz 1. Saniyede kurulu konuma gelmesi, 2. Saniyede rulman diyafram yay konumuna gelecek şekilde ve 3. Saniyede ayrıma gerçekleşecek şekilde kurgulanmıştır.



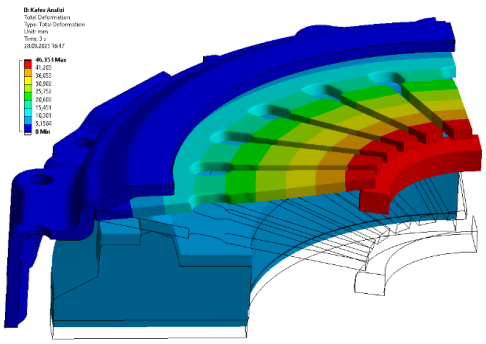
Şekil 5 Kafesin Kurulmuş Hali

Analiz 217.473 node ve 129.734 element ile 0,81 element quality ile gerçekleştirilmiştir.



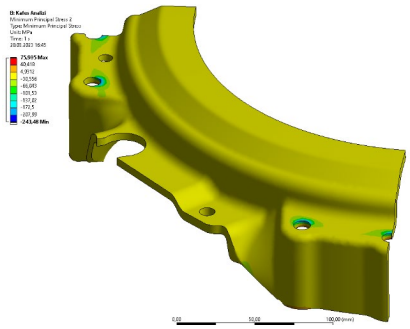
Şekil 6 Debriyaj Kuruluyken Yer Değiştirme

Debriyaj kurulu konumdayken "maximum total deformation" (yer değiştirme) diyafram yay parmaklarının ucundadır. Buradaki "total deformation" 32,421 mm'dir.



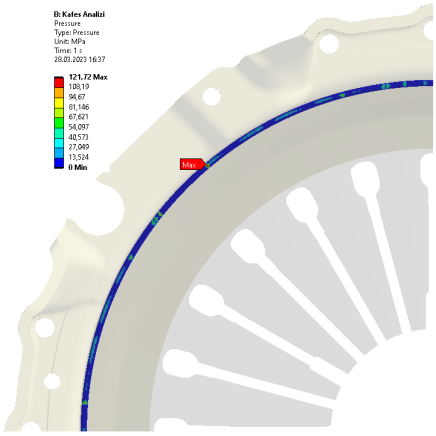
Şekil 7 Ayırma Anında Yer Değiştirme

Debriyajda ayrılma gerçekleştiğinde "total deformation" (yer değiştirme) 46,353 mm olur.

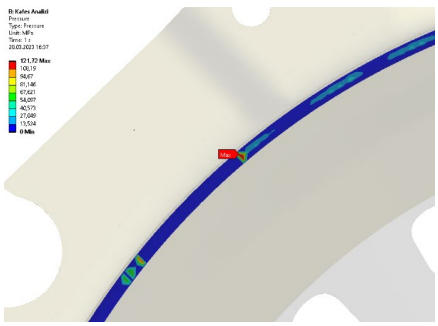


Şekil 8 Kafes Gerilme

Kafes üzerindeki maksimum gerilme volan bağlantı deliklerinde gelmektedir. Buradaki değer 243,48 Mpa'dir.



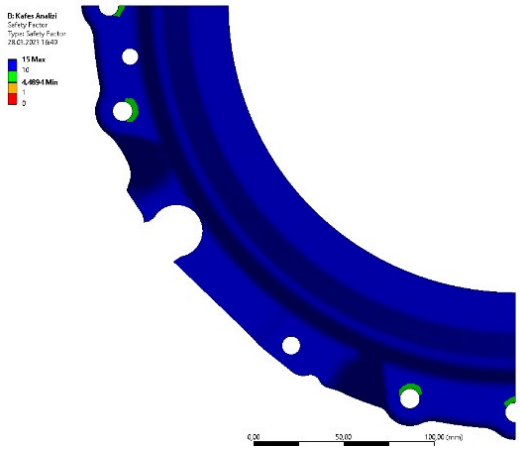
Şekil 9 Sürtünme Yüzeyi



Şekil 10 Sürtünme Yüzeyi Detay

Diyafram yaylarda iç bükeylik olduğu için düz konuma geldiğinde çok düşük düzeylerde kesitli temas gözükebilir. Ancak "contact pressure" (temas basıncı) düşük olduğu için aşınma

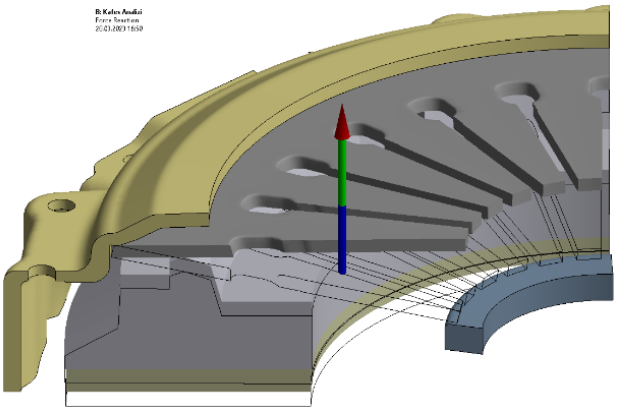
beklenmemektedir. Aşınmayı en çok "contact pressure" etkilemektedir. "Contact pressure" nin en yüksek olduğu zaman 1. saniye yani debriyajın kurulu olduğu andır.



Şekil 11 Güvenlik Katsayısı

Analiz sonucuna göre safety factor yani güvenlik katsayısı minimum 4,4894 gelmektedir. Standartlara göre 1,5 güvenlik katsayısının üstü kabul edilebilir değerdir.

VII. BASKI KUVVETİ



Şekil 12 Baskı Kuvveti

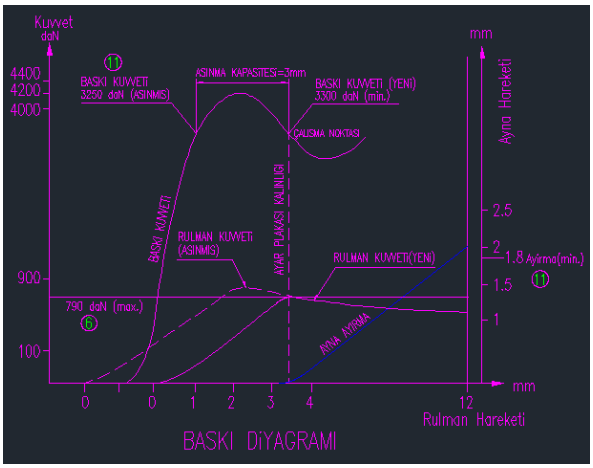
"Force reaction" da (Tepki kuvveti) her zaman diyafram yay kuvveti debriyajın kurulu olduğu zaman baz alınır. Analizimizde çeyrek model kullanıldığı için çıkan sonuç 4 ile çarpılacaktır. Çeyrek modelde çıkan force reaction 10.060 Newton'dur. Bu değeri 4 ile çarptığımızda 40240 Newton elde ederiz.
Ancak ürünün teknik resim verileri ve test cihazı sonucuna baktığımızda baskı kuvvetinde bir fark olduğu gözükmektedir. Referans alınan ürünün baskı performans test sonuçlarında baskı kuvveti 38.490 N olarak gelmektedir. Bunun sebebi analizde çözüm kolaylığı ve süre kazancı için analize dahil etmediğimiz diyafram yaya karşı kuvvet uygulayan mesnet lamasının kuvvetidir.

Mesnet laması: Debriyaj sisteminde 8 adet mesnet laması kullanılmaktadır. Çözüm kolaylığı ve zaman tasarrufu adına 2 adet mesnet laması üzerinden analiz yapılmıştır.

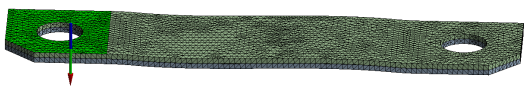
Mesnet lamasına yapılan analizlerde debriyajın kurulma anında 341.57 Newton force reaction görülmektedir. Debriyaj baskı setinde 8 adet mesnet laması bulunduğu için bu sonuç 4 ile çarpılacaktır.



Şekil 13 Baskı Performans Test Cihazı Test Sonucu



Şekil 14 Baskı Teknik Verisi



Şekil 15 Mesnet Laması

Tablo 4

Baskı Kuvvetleri	
Mesnet Lamasız Diyafram Force Reaction	40240 N
Mesnet Lamasının Force Reaction	-1366 N
Sonuç	38874 N
Test Ölçümü	-38490 N
Aradaki Fark	384 N

VIII. TEORİK HESAP

Teorik olarak Almen ve Laszlo'nun formülü kullanılmıştır.
Formül şu şekildedir:

$$F = \frac{4 \cdot E}{1 - v^2} \cdot \frac{t^4}{k_1 \cdot D_d^2} \cdot k_4^2 \cdot \frac{s}{t} \cdot \left[k_4^2 \cdot \left(\frac{h_0}{t} - \frac{s}{t}\right) \cdot \left(\frac{h_0}{t} - \frac{s}{2 \cdot t}\right) + 1\right] \tag{5}$$

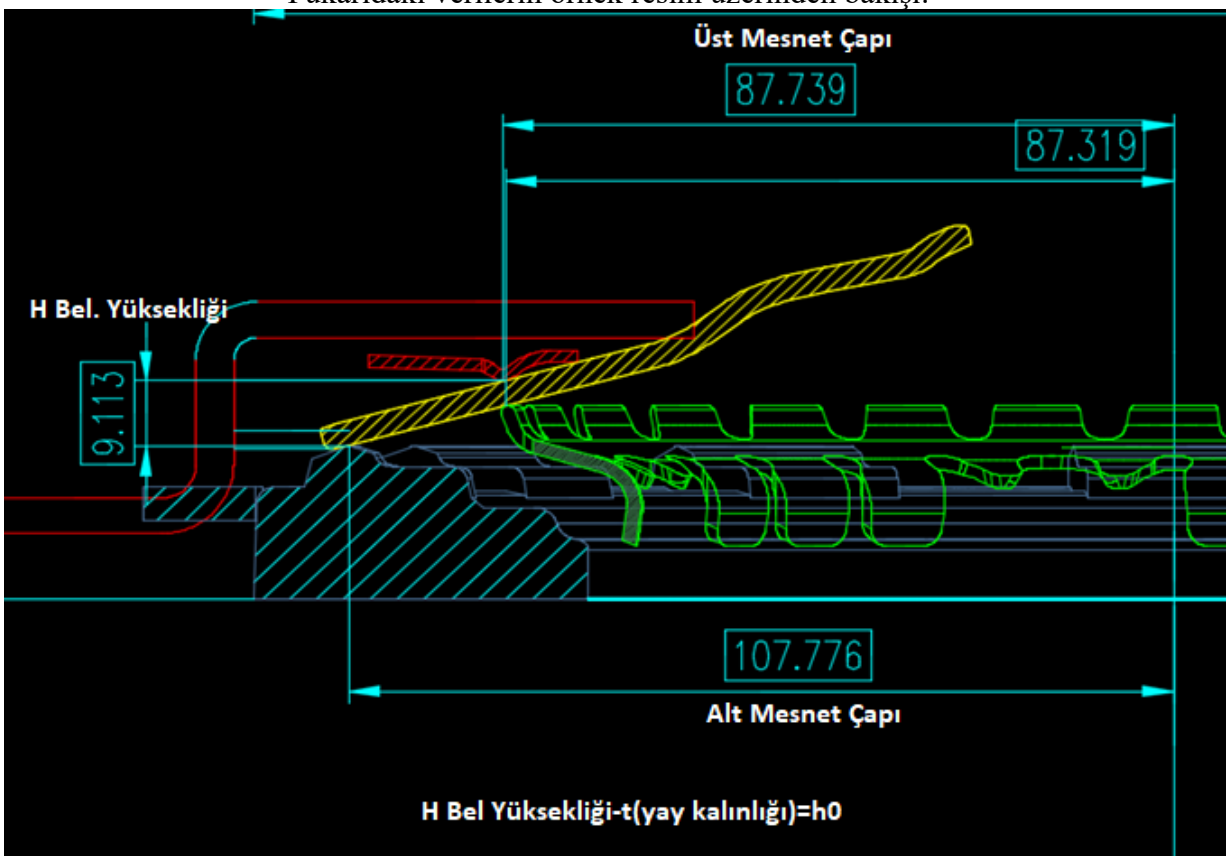
F: Bir yayı etkileyen kuvvet. Birimi Newton
S: Yaylama yolu. Birimi mm.
T: Yayın kalınlığı. Birimi mm.
k_1: Çaplar oranıyla değişen birinci 1. Yay faktörü
k_4: Grup 3 için dayanma faktörü, Grup 1 ve 2 için 1.
D_d: Yayın dış çapı. Birimi mm.
h_0:Tam yaylanma boyu. Birimi mm.

$$k_1 = \frac{1}{\pi} \cdot \frac{(\frac{\delta - 1}{\delta})^2}{\frac{\delta + 1}{\delta - 1} - \frac{2}{ln\delta}} \tag{6}$$

Tablo 5

Diyafram Yay Hesabı					
Alt Mesnet Çapı (d_1)	Deplasman	t	Üst Mesnet Çapı (d_2)	h_0	H Bel. Yüksekliği
391	1	5.45	333	10.55	16

Yukarıdaki verilerin örnek resim üzerinden bakışı:

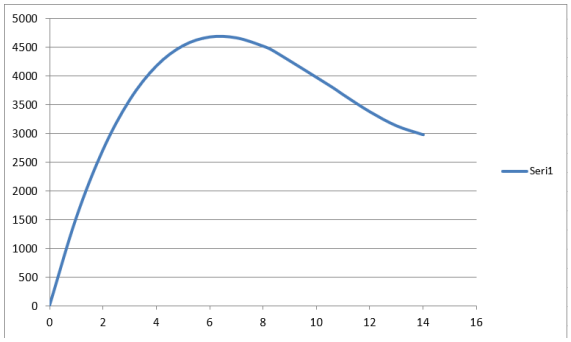


Şekil 16 Diyafram Yay Hesabı

h_0 Diyafram yay araç üzerindeki montajlı halidir. Yani diyafram yayın kurulması için gerekli mesafedir.

TABLO 6

	Baskı Kuvveti
0	0
1	1531,92 daN
2	2714,62 daN
3	3584,67 daN
4	4178,65 daN
5	4533,10 daN
6	4684,61 daN
7	4669,74 daN
8	4525,06 daN
8,4	4439,03 daN
10,55	3819,57 daN
11	3677,80 daN
12	3379,53 daN
13	3134,29 daN
14	2978,64 daN



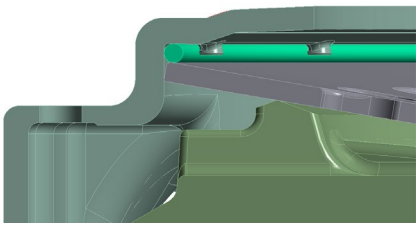
Şekil 17 Formüllerden çıkan sonuca göre oluşan excel grafiği

Diyafram yayın kurulu hale gelmesi için 10.55 mm yer değiştirme gereklidir. Bu yer değiştirme için gerekli kuvvetin teorik hesabı tablodaki gibidir. 10.55 değeri diyafram yayın slotunun serbest haldeki yüksekliğinden diyafram yay kalınlığı çıkarılarak bulunur.

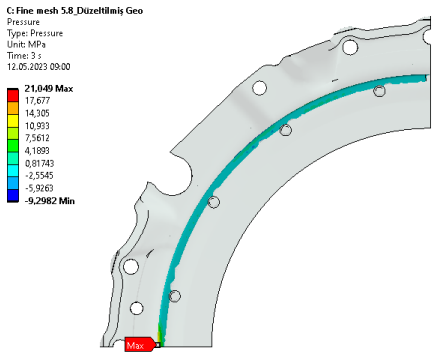
TABLO 7

Baskı Kuvvetleri		
Analiz Sonucu	Test Cihazı Sonucu	Teorik Hesap Sonucu
38874 N	38490 N	38195,7 N

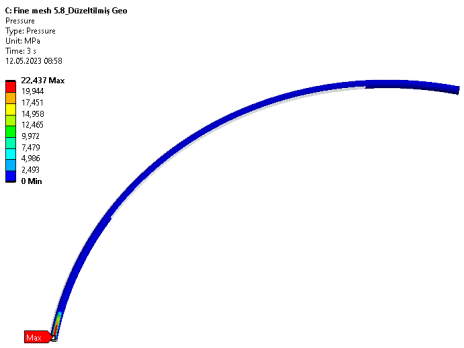
IX. FULCRUM RİNG İLE ÇALIŞAN BASKI ANALİZİ



Şekil 18 Mesnet Halkalı Baskı

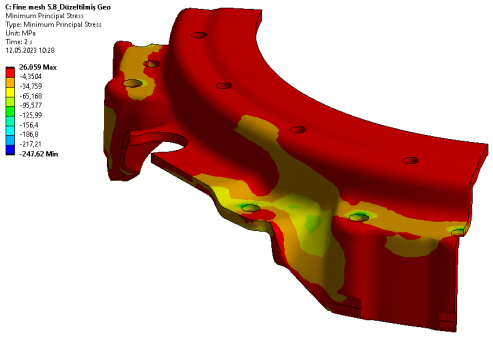


Şekil 19 Mesnet Halkası Temas Yüzeyi



Şekil 20 Mesnet Halkası

Fulcrum ringli baskı analizi sonucunda fulcrum ringin kafese temas ettiği yüzeydeki basınç maximum 21,049 Mpa olarak görülmüştür. Fulcrum ring üzerine gelen basınç ise 22,437 Mpa olarak görülmüştür.



Şekil 21 Kafes Üzerinde Gerilme

Kafes üzerindeki maksimum gerilme volan bağlantı deliklerinde gelmektedir. Buradaki değer 247,62 Mpa'dir. Bu sonuç fulcrum ring olmayan kafesin sonucuna çok yakındır. Aralarında yaklaşık olarak 4 Mpa fark vardır. Analiz sonucuna göre 36.806 Newton baskı kuvveti ortaya çıkmıştır.

TABLO 8

Baskı Kuvvetleri

Analiz Sonucu	Test Cihazı Sonucu	Teorik Hesap Sonucu	Mesnet Halkalı Analiz Sonucu
38.874 N	38.490 N	38.195,7 N	36.806 N

X. SONUÇ

Analiz sonucundan çıkan baskı kuvveti teorik hesabımızdan %1,77 daha fazla gelmektedir. Performans test sonucumuza göre ise %0,99 daha fazla gelmektedir. Fulcrum ring olan kafesin

analizine göre de %5,61 daha fazla gelmektedir. Bu sonuçlara göre debriyaj baskısının çalışma performansında bir değişim olmayacağı, yüzdelik olarak değişimlerin çalışma aralığında olduğu tespit edilmiştir. Dolayısıyla kafes optimizasyonu gerçekleştirilebilir olduğu kanıtlanmıştır. Fulcrum ring kaldırma sayesinde yılda %2 daha az maliyetle baskı üretimi gerçekleştirilecektir. Ayrıca montaj esnasında her baskıda 1 dk süre kazanımı olacaktır.

TEŞEKKÜR

Çalışmada emeği geçen Dönmez Debriyaj A.Ş Ar&Ge merkezi çalışanları ve yöneticilerine teşekkürlerimizi sunarız.

KAYNAKÇA

[1] (Rajesh Purohit et al. / Procedia Materials Science 6 (2014) 490 – 502)
[2] Cakmak, S., Yildiz, Ö., Kurt, İ. C. K. U., & Eş, C. (2022). Alternatif Polimer Esaslı Malzemelerin Debriyaj Diski Stoperine Entegrasyonu.
[3] Ordu, B. (2018). Debriyaj sisteminin dinamik analizi (Master's thesis, Uludağ Üniversitesi).
[4] Topaç, M.M., Hamurişçi, Y., Kuralay, N.S. 2009. Taşıt Kavraması Kapağında Pedal Kuvveti Altında Oluşan Elastik Şekil Değişiminin Sonlu Elemanlar Yöntemiyle Belirlenmesi, Mühendis ve Makina, Cilt: 50, Sayı: 590.R. Nicole, "Title of paper with only first word capitalized," J. Name Stand. Abbrev., in press.
[5] Özbakış, M. 2008. Debriyaj sistemlerinde kullanılan diyafram yayların karakteristiğinin incelenmesi ve optimizasyonu. Yüksek Lisans Tezi, DEÜ Fen Bilimleri Enstitüsü, Konstrüksiyon İmalat Anabilim Dalı, İzmirM. Young, The Technical Writer's Handbook. Mill Valley, CA: University Science, 1989.
[6] V.B. Bhandari, 2008. Design of machine elements, second edition, Tata Mc. Graw Hill Publishing Company.
[7] Panchal, N., & Patel, A. R. (2016). Design and Thermal analysis of clutch cover (pressure) plate. Technix International Journal for Engineering Research, 3(9), 101-105.
[8] Demir, C. (2020). Wear behaviour analysis of different metals by the finite element method (Doctoral dissertation, Institute of Science And Technology).
[9] Murat Haktanır1, Samet Kabacaoğlu1*, Oğuz Can Bargun1, Ahmet Merdan1 "Improvement of Distortion In 430 mm Diameter Clutch Cover Used In Heavy Commercial Vehicles" International Advanced Researches & Engineering Congress-2017 http://iarec.osmaniye.edu.tr/Osmaniye/TURKEY 16-18 November 2017

Debriyaj Rulmanının Taşıyıcı Parçasında Sıvama Bölgesinde Yapılan Tasarım Farklılığının Çekme Kuvvetine Etkisinin İncelenmesi

Investigation of the Effect of Design Variation in the Spinning Area of the Clutch Bearing Carrier Component on the Tensile Force

Ulaşcan KURT[*,1] Caner EŞ[1]

[*]u.kurt@donmezdebriyaj.com.tr, ORCID: 0000-0002-1280-7210
[1]*Ar&Ge ve Test Validasyon Mühendisi, Dönmez Debriyaj Sanayi ve Ticaret AŞ., İzmir, Türkiye*

Özet: Bu çalışmada, debriyaj sisteminin bileşenlerinden olan rulman komplesinin sıvama kanalındaki değişiminin çekme kuvvetine bağlı dayanımı gözlemlenmiş ve önemi anlatılmıştır. Debriyaj rulmanının katı modelleri NX8.0 üç boyutlu tasarım yazılımı, belirli parametreler kullanılarak oluşturulmuş ve Ansys Workbench analiz programı ile yapısal analizleri gerçekleştirilmiştir. Debriyaj sistemi düşük güçler ile yüksek atalet yüklerinin çalışmasına izin veren aktarma organıdır. Motor momentini şanzımana aktarmaktadır. Vites değiştirmeye yarayan mekanizma bütünüdür. Debriyaj sistemi üç ana, iki yardımcı parçadan oluşmaktadır. Bunlar sırasıyla debriyaj baskı komplesi, debriyaj disk komplesi, debriyaj rulman komplesi, volan ve debriyaj çatalıdır. Baskı komplesi, kafes, diyafram yay ve baskı plakasından oluşmaktadır. Baskı plakası, diyafram yayın mesnetlendiği ve kafese mesnet lamalarıyla bağlanan alt parçadır. Debriyaj diski için sürtünmeli yüzeyi oluşturmaktadır. Diyafram yay, baskı plakası tepe noktasında mesnetlenir baskı plakası üzerindeki yükün kalkmasını sağlayan alt parçadır. Debriyaj diski, volan ile baskı plakası arasında bulunur ve motor torkunu sürtünme yardımıyla aktaran alt parçadır. Debriyaj rulmanı, sistemin çalışması performasını etkileyen alt parçalardan biridir. Sürücünün pedala basması sonucunda uygulanan kuvveti debriyaj çatalı yardımıyla diyafram yaya iletir ve kavrama durumundaki debriyaj diskini boşa çıkartır. Debriyaj tipine göre artı ya da eksi yönde eksenel olarak kavrama ya da ayırma fonksiyonunu gerçekleştirmektedir. Üç alt parçadan oluşmaktadır. Rulman kafesi, tüm sistemi bir arada tutan ve koruyan alt parçadır. Rulman, sistemin dönmesini sağlamaktadır. Rulman taşıyıcı, çatal ile temaslı çalışır ve pedal yükünü iletmektedir. Çalışması sırasında meydana gelen ekseneler kuvvetler, rulman kafesinin rulman taşıyıcıdan sıyrılmasına neden olmaktadır. Rulman taşıyıcı üzerinde bulunan sıvama kanalında yapılan tasarım iyileştirmeleriyle kafesin eksenel yük dayanımı arttırılmıştır. Bu sayede kafesin rulmandan taşıyıcıdan sıyrılma probleminin önüne geçilmiştir.

Anahtar Kelimeler: *Debriyaj,Debriyaj Rulmanı, Eksenel Yükler,Sonlu Elemanlar Analizi*

Abstract: In this study, the resistance of the bearing assembly, which is one of the components of the clutch system, in the spinning groove due to the tensile force was observed and its importance was explained. Solid models of the clutch bearing were created using NX8.0 three-dimensional design software, certain parameters, and structural analyzes were performed with the Ansys Workbench analysis program. The clutch system is the driveline that allows low power and high inertia loads to work. It transfers the engine torque to the gearbox. It is the whole mechanism for changing gears. Clutch system consists of three main parts and two auxiliary parts. These are respectively the clutch pressure assembly, clutch disc assembly,

clutch bearing assembly, flywheel and clutch fork. Pressure assembly consists of cage, diaphragm spring and pressure plate. The pressure plate is the lower part on which the diaphragm spring is supported and connected to the cage with support blades. It forms the friction surface for the clutch disc. The diaphragm spring is supported at the apex of the pressure plate and is the lower part that allows the load on the pressure plate to be lifted. The clutch disc is located between the flywheel and the pressure plate and is the lower part that transmits the engine torque with the help of friction. Clutch bearing is one of the sub-parts that affect the operating performance of the system. The force applied as a result of the driver pressing the pedal transmits the diaphragm to the spring with the help of the clutch fork and releases the clutch disc in the clutch state. According to the clutch type, it performs the axial clutch or release function in the plus or minus direction. It consists of three sub-parts. The bearing cage is the lower part that holds and protects the entire system. The bearing provides the rotation of the system. The bearing carrier works in contact with the fork and transmits the pedal load. Axial forces that occur during its operation cause the bearing cage to peel off from the bearing carrier. The axial load resistance of the cage has been increased with the design improvements made in the spinning groove on the bearing carrier. In this way, the problem of peeling the cage from the bearing from the carrier is prevented.

***Keywords**: Clutch, Clutch Bearing, Axial Loads, Finite Element Analysis*

I. GİRİŞ

Debriyaj sistemi düşük güçler ile yüksek atalet yüklerinin çalışmasına izin veren, prizdirek mili ile krank milinin bağlanması için kullanılan bir aktarma organıdır. Motor momentini şanzımana aktarır. Taşıtların kavrama konumundan çıkmasını sağlayan ve vites değiştirmeye olanak sağlayan mekanizma bütünüdür.
Yaygın olarak kuru sürtünmeli kavrama kullanılan taşıtlarda üç ana alt parçadan oluşmaktadır. Bunlar,

- Debriyaj baskı komplesi
- Debriyaj diski ve
- Debriyaj rulmanı komplesidir.

A. Debriyaj Baskı Komplesi

Debriyaj kafesi, diyafram yay ve baskı plakasından oluşur. Rulman tarafından eksenel bir kuvvete maruz kalan diyafram yay baskı kuvvetini oluşturmaktadır. Baskı plakası yüzey alanı, sürtünme katsayısı ve baskı kuvveti aracın aktarabileceği tork miktarını direkt olarak etkilemektedir. Bu sebeple debriyaj baskısı sistemin olmazsa olmaz elemanlarındandır.



Şekil 1.Debriyaj Baskı Komplesi

B. Debriyaj Diski

Debriyaj diski, volan ve baskı plakası arasında bulunan, motor torkunu ve hareketini prizdirek miline sürtünme yardımıyla aktaran debriyaj sistemi elemanıdır. Debriyaj diskinde tork aktarımı sırasında gözlemlenen sürtünme ilk olarak balatalara uygulanır. Perçinler ile sisteme montajlanan balatalar anasac yüzeyinde bir gerilme oluşturur.[2]



Şekil 2. Debriyaj Diski

C. Debriyaj Rulman Komplesi

Debriyaj rulmanı debriyaj sisteminin performasını etkileyen alt parçalardan biridir. Kavrama sisteminde başlangıç elemanı olarak sürücü tarafından pedala basıldığında uygulanan kuvveti debriyaj çatalı ile debriyaj baskısında bulunan diyafram yaya iletir ve kavrama durumunda olan debriyaj diskindeki kuvveti boşa çıkaran sistemdir. Debriyaj tipine göre eksenel olarak (+) yönde ya da (-) yönde hareket esnasında kavrama fonksiyonunu ya da ayırma fonksiyonunu gerçekleştirebilmektedir.[1]

Üç alt parçadan oluşmaktadır.Rulman kafesi, tüm sistemi bir arada tutan ve koruyan alt parçadır.

Rulman taşıyıcı, debriyaj çatalı ile temaslı çalışarak pedal yükünü ileten alt parçadır. Rulman,sistemin dönmesine yardımcı olan alt parçadır.



Şekil3. Debriyaj Rulmanı

Rulman komplesi, rulman taşıyıcı, rulman kafesi ve rulmanın montajlanmasıyla meydana gelmektedir. Bu operasyonda rulman kafesi, rulman taşıyıcı üzerinde bulunan kanala sıvama operasyonuyla montajlanmaktadır. Bu sayede rulman taşıyıcı ve rulmanı bir arada tutar.

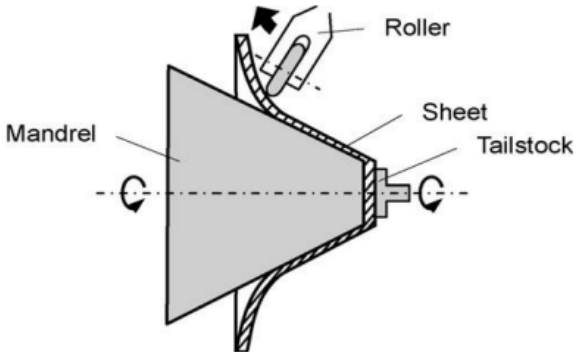
D. Sıvama Operasyonu

Rijit takımlarla ya da silindirler ile eksenel olarak simetrik olan parçalara şekil verme operasyonuna sıvama denir. Üç tip sıvama şekli bulunmaktadır. [5]

a) Geleneksel Dönerli Sıvama: Üretimi zor ve maliyetli konik işlemelerde kullanılır. Takım yardımıyla milde döndürülen sac levha şekillendirilmektedir.[5]

b) Kaymalı Döner Sıvama: parça çapı sabit kalır. Bundan dolayı eksenel ve ya eğrisel şekillendirmeler oluşuturulmada kullanılmaktadır.[5]

c) Boru Sıvama: Özel takımlar ile kalın azaltma gerçekleşirilir. İki tür yapılmaktadır, a.Dıştan b. İçten. Hacim değişmeden uzama sağlanır. Otomotiv sektöründe yaygın kullanılmaktadır.[5]



Şekil 3. Sıvama Operasyonu [3].

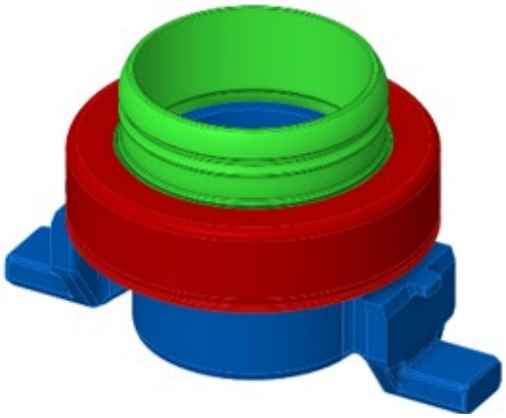
II.AMAÇ

Yapılan çalışmanın amacı, debriyaj alt parçası olan rulmanda meydana gelen sıyrılma problemlerinin azaltılmasına yönelik yapılan tasarım iyileştirme çalışmasıdır. Yapılan çalışmayla bu sıyrılma probleminin önüne geçilmesi hedeflenmektedir. Uygulanan tasarım değişikliği sıvama bağlantısının bulunduğu her alanda kullanılabilir olup literatüre katkı sağlayacağını düşünmekteyiz.

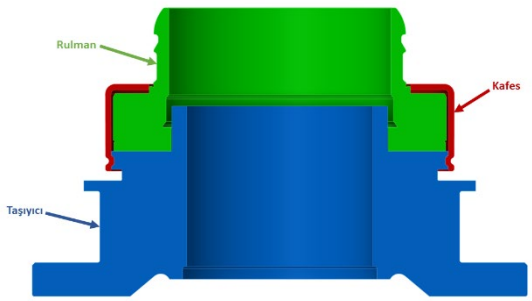
III.YÖNTEM

A. Debriyaj Rulmanının Üç Boyutlu Modellenmesi

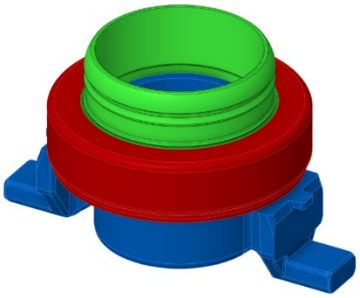
Farklı iki debriyaj rulmanının üç boyutlu modeli, Siemens NX 8.0 yazılımı kullanılarak yapılmıştır [Şekil 5 – 6]. Modelleme de ki kafeslerin sac kalınlığı 2 mm olarak belirlenmiştir. Kesitlerden anlaşılacağı üzere [Şekil 5.1-6.1] taşıyıcıda tasarım değiştirilmiştir. Şekil 6'da bu daha belirgin olarak gözükmektedir.



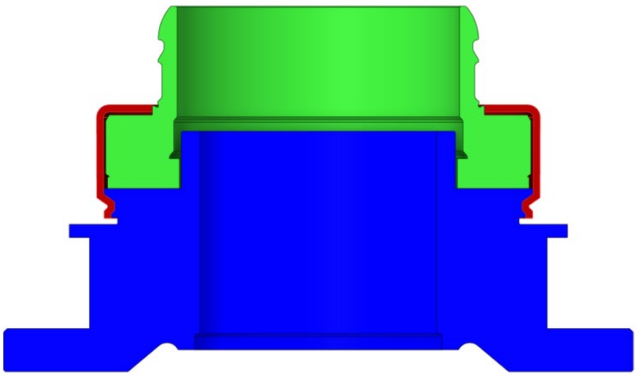
Şekil 5. Eski debriyaj rulman komplesi tasarımı.



Şekil 5.1. Eski debriyaj rulman komplesi tasarımının kesit görünümü.



Şekil 6. Yeni Debriyaj Rulman Komplesi tasarımı.



Şekil 6.1. Yeni debriyaj rulman komplesi tasarımının kesit görünümü.



Şekil 7. Eski &Yeni debriyaj rulman komplesi tasarımının kesit görünümü.

B. *Debriyaj Rulmanının Sonlu Elemanlar Modeli*

Tasarım hazırlandıktan sonra sonlu elemanlar yöntemi ile yeni ve eski kafes tasarımlarının taşıyıcıdan ayrılmadan dayanabileceği maksimum kuvvet değerinin bulunarak karşılaştırılması yapılacaktır.

Sonlu elemanlar yöntemi ile hesaplamalar yapabilmek için ANSYS 2023 R1 mühendislik yazılımında ki "Static Structural" modülü kullanılarak malzemelerin atanması, geometrilerin aktarılması ile birlikte ağ yapısı oluşturularak gerekli sınır şartlarının da tanımlanmasıyla sonuçlar incelenmiştir.

C. *Malzeme Bilgisinin Atanması*

Parçaların malzeme türleri olarak taşıyıcı için gri dökme demir, kafes için DD13 ve rulman için de yapısal çelik malzemesi kullanılmıştır.

Kullanılan malzemelerin mekanik özelliklerinin değerleri Tablo 1' de bulunmaktadır.

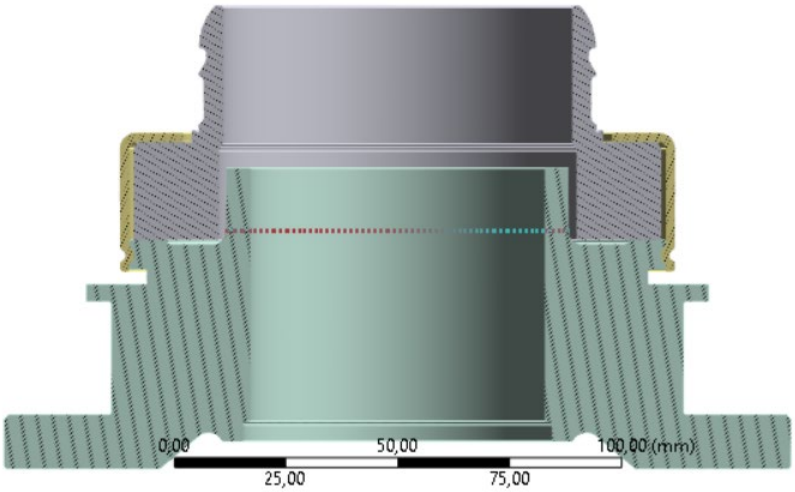
TABLO 1
DEBRIYAJ RULMANINDAKI PARÇALARIN MALZEME BILGILERI

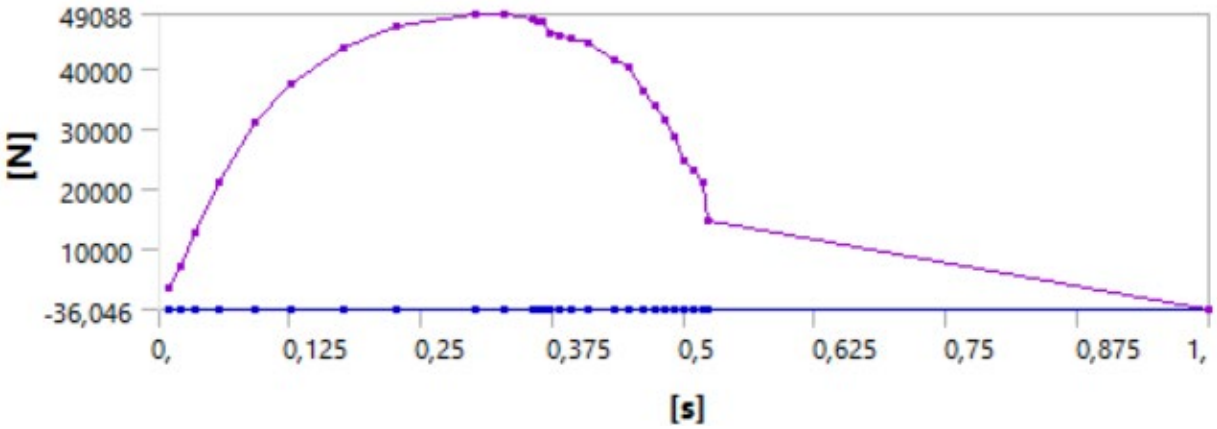
Özellikler	Yapısal Çelik	Gri dökme demir	DD - 13
Yoğunluk (kg/m3)	7850	7200	7800
Elastisite Modülü (Pa)	200000	110000	14430
Kayma Modülü (MPa)	7,69x10^4	4,29x10^4	5,5x10^4
Akma Dayanımı (Mpa)	2,5x10^2	2,4x10^2	1,7x10^2

kg = kilogram, m = metre, Pa = paskal, MPa = mega paskal.

IV.SONUÇLAR

Yapılan çalışmada rulman taşıyıcı üzerinde bulunan sıvama kanalında revizyon yapılmıştır. Aşağıda eski tasarıma ait kesit görüntüsü verilmiştir. Eski tasarıma yapılan analiz sonucunda, dikey yönde hareket ettirilmesiyle sıvamaya karşı tepki kuvveti aşağıdaki gibi verilmiştir;

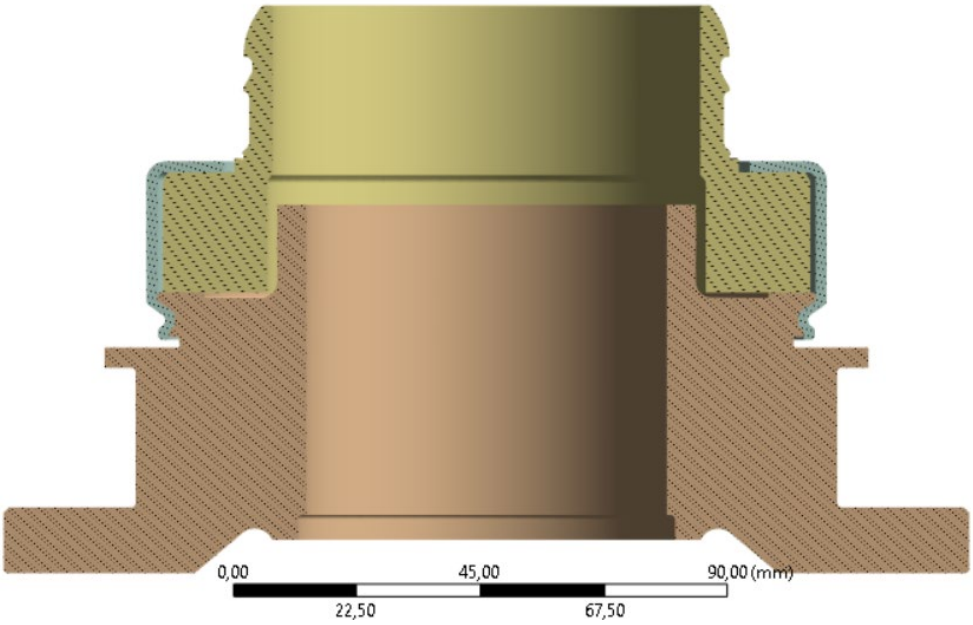




Grafik 1. Eski Sıvamada Sıvamadaki Zamana Bağlı Kuvvet Değişimi

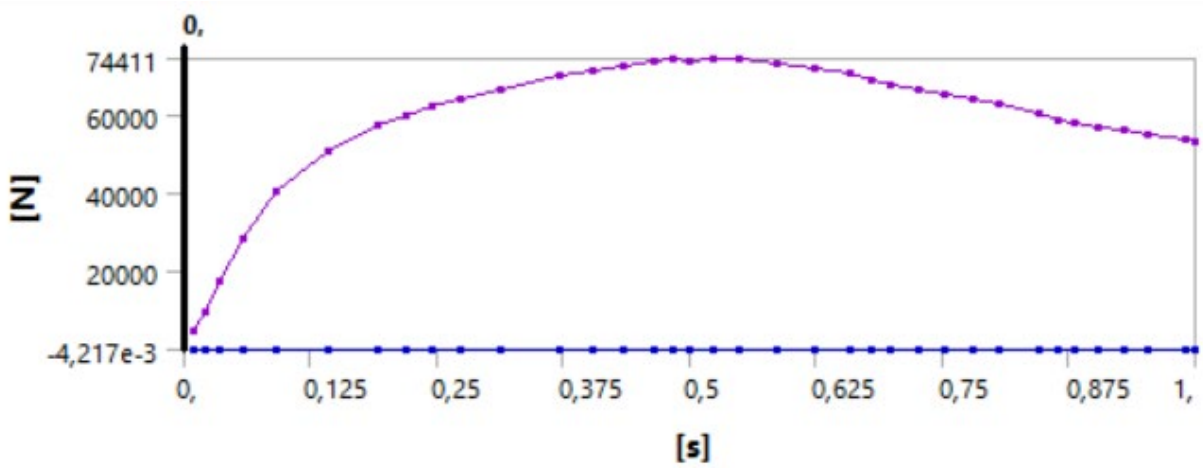
Yukarıda görülen grafikte eski tasarımımızın maksimum 49.088 N yük altında sıvama kanalından ayrılmakta ve rulman taşıyıcıdan sıyrılma meydana gelmektedir. Meydana gelen kopmalar araçlarda hasara yol açabilmektedir. Bu sebepten dolayı son kullanıcıda konforsuzluğuna mahal vermektedir.

Yeni yapılan tasarımda sıvama kanalının açısıyla ve genişliğiyle oynanmıştır. Rulman taşıyıcıda bulunan bu revizyon sayesinde rulman kafesi, taşıyıcının üzerine bulunan sıvama kanalına daha çok nüfus etmektedir. Yeni yapılan tasarımın kesit görünümü aşağıdaki gibidir.



Şekil 11. Yeni Sıvama Kesit Görünümü

Yapılan yeni sıvama kanalı analizinde Şekil 12 de görüldüğü üzere dikey yönde uygulanan kuvvet sonucunda 74.411 N kuvvete dayanım göstermiş ve sıyrılma meydana gelmiştir.



Grafik 2. Yeni Sıvamadaki Zamana Bağlı Kuvvet Değişimi

Tüm bunların sonucunda, yeni yapılan rulman sıvama kanalının dayanımı, eski tasarıma göre 1,5 kat arttırılmıştır. Bu artışla birlikte rulmanın sıyrılma probleminin azalacağı ön görülmüştür.

V. TARTIŞMA

Yapılan bu çalışmada hali hazırda üretilen debriyaj rulman komplesinde bulunan sıvama kanalından sıyrılma deformasyonu ele alınarak analizler yapılmıştır. Bu analizler sonucunda eski tasarım olarak adlandırdığımız tasarımda, maksimum 49.088 N eksenel yüke dayandığı görülmüştür. Simülasyon sonucunda bu eksenel kuvvette rulman kafesinin sıvama kanalından sıyrıldığı görülmüştür.

Yeni yapılan revizyonda ise sıvama kanalı genişletilmiş ve derinliği arttırılmıştır. Bu iyileştirme sonucunda rulman kafesi kanala daha çok nüfus etmiş ve simülasyon sonucunda eksenel kuvvet dayanımı 74.411 N olarak görülmüştür.

Bu yapılan çalışma, sıvama operasyonu yapılacak bölgenin nüfuziyeti arttıkça sıvanan parçanın (levha vb.) dayanacağı eksenel yükte iyileştirmeler yaratarak sıvama bölgesinde meydana gelecek deformasyonları azaltacaktır.

KAYNAKÇA

[1] Cakmak, S., Yildiz, Ö., Kurt, İ. C. K. U., & Eş, C. (2022). Alternatif Polimer Esaslı Malzemelerin Debriyaj Diski Stoperine Entegrasyonu.

[2] YILDIZ, Ö., Caner, E. Ş., AKBULUT, S., KAYMAZ, İ. C., Ulaşcan, K. U. R. T., & ÇAKILI, H. (2022). Debriyaj Diski Dış Ana Sac Batma Prosesinin Etkilerinin İncelenmesi. Düzce Üniversitesi Bilim ve Teknoloji Dergisi, 10(5), 127-136.

[3] O.C Bargun, A.Celik, U.O Yazici, A. Merdan "Improving The Spinning Operation of Various Clutch Release Bearings Used in The Clutch Systems of Heavy Commercial Vehicles With a New Spinning Geometry" International Journal of Advances on Automotive and Technology Promech Corp. Press, Istanbul, Turkey Vol.2, No. 1, pp. 53-60, January, 2018

[4] Özbakış, M. (2008). Debriyaj sistemlerinde kullanılan diyafram yayların karakteristiğinin incelenmesi ve optimizasyonu (Doctoral dissertation, DEÜ Fen Bilimleri Enstitüsü).

[5] Güler, H. (2008). İnce saçların desenleme yöntemi ile mukavemetinin arttırılması (Master's thesis, Uludağ Üniversitesi).

Tasarım Optimizasyonu ile DMF Ağırlık Azaltma Çalışması

Study On Weight Reduction of DMF Using Design Optimization

Ömer YILDIZ[*,1], Caner EŞ[1], Ulaşcan KURT[1]

[*]o.yildiz@donmezdebriyaj.com.tr, ORCID: 0000-0001-7851-3840
[1]*R&D Center, Dönmez Debriyaj San ve Tic A.Ş, İzmir, Turkiye*

Özet: Bu çalışmada içten yanmalı motorlarda oluşan mekanik titreşimlerin sönümlenmesinde ve şanzımana sağlıklı bir hareket aktarılmasını sağlayan çift kütleli volan (Dual Mass Flywheel) üzerinde tasarım optimizasyonu yapılmış ve sonuçları incelenmiştir. Çift kütleli volan kullanıcıya konforlu ve güvenli sürüşü mümkün kılan en önemli motor ve hareket aktarma parçalarından biridir. Çalışmada çift kütleli volan elemanlarından olan ana sac parçasında tasarım optimizasyonu yapılmış olup ağırlık azaltma sağlanmışır. Parça özelinde gerilmelerin ne yönde değiştiği, güvenlik katsayısının değişimi ve ağırlık değişimi incelenmiştir. Ağırlık azaltma yöntemi özellikle volan gibi enerji depolayan, dönen parçalarda her zaman, titreşim, dayanım, ses gibi kriterler için olumlu yönde etkilemese de çalışma sonucunda elde edilen veriler ile bu alanda çalışma yapan araştırmacılara parça üzerine etkiyen kuvvetler ve sonuçları konusunda fikir sahibi olmaları ya da ön görülü olmaları adına bu yönde yapılan çalışmaların literatüre katkısı tartışılmazdır.

Çalışma sonucunda %11.9 ağırlık azaltılmış olup ağırlık azaltmasının vektörel gerilmeleri az da olsa olumsuz etkilemesinin sonucunda eşdeğer gerilem değeri maksimum 54,17 Mpa seviyesinden 85,79 Mpa seviyesine çıkmıştır, fakat bu sonuç güvenli çalışma şartlarının altında kalmaktadır. Parça özelinde yaklaşık 86 gr ağırlık azaltması sağlanmış olup bu değer kullanıldığı araç üzerinde çok daha fazla etki gösterecektir.

Anahtar Kelimeler: *Çift Kütleli Volan, Optimizasyon, Tasarım, Titreşim*

Abstract: In this study, design optimization has been conducted on the dual-mass flywheel, which is an essential component for dampening mechanical vibrations in internal combustion engines and facilitating smooth motion transfer to the transmission. The dual-mass flywheel is one of the most crucial engine and powertrain parts that enable users to experience comfortable and safe driving. Within the study, design optimization has been performed specifically on the main plate component of the dual-mass flywheel, resulting in weight reduction. Changes in stress directions, variations in the safety factor, and loses in weight have been investigated at the component level. While weight reduction may not always have a positive impact on criteria such as vibration, durability, and noise, especially in parts like flywheels that store energy and involve rotational motion, the data obtained from this study undeniably contribute to the literature, providing valuable insights for researchers working in this field to gain an understanding of the forces influencing the component and its outcomes, or to be more predictive in their assessments.

As a result of the study, a weight reduction of 11.9% has been achieved. Although the weight reduction has a slight adverse effect on vectorial stresses, the equivalent stress value has increased from a maximum of 54,17 MPa to 85,79 MPa. However, it should be noted that this result remains below the safe operating conditions. Specifically for the main plate component,

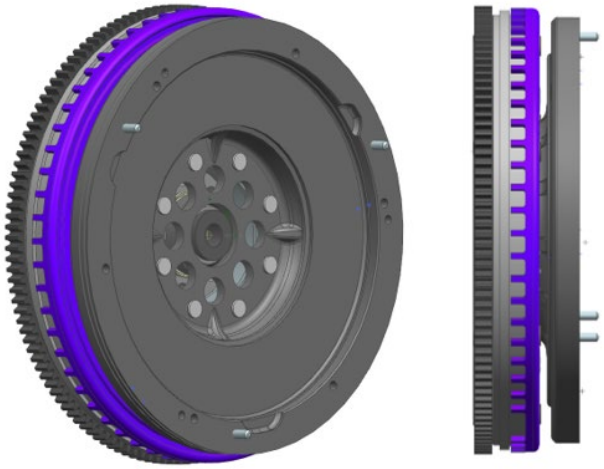
an approximate weight reduction of 86 grams has been accomplished. This reduction will have a much greater impact when applied to the used vehicle model.

Keywords: *Dual Mass Flywheel, Optimization, Design, Vibration*

I. GİRİŞ

A. Çift Kütleli Volan (DMF)

İÇTEN yanmalı motorlarda döngünün tamamlanması sırasında pistonlar, biyel kolları ve krank mili gibi parçaların her biri motor bütününde bir titreşim oluşturur. Bu titreşimler sürüş konforunu direkt olarak etkilemektedir. Salınım frekansı silindir sayısına ve açısal hıza bağlıdır, genliği ise yük koşullarından, hızdan, dönen kütlelerin ataletinden ve yanma prensibinden etkilenir [1]. Daha güçlü motor çıkış torku ve şu anda yaygın olarak kullanılan dizel motor yürüyen aksamlara gelen burulma titreşiminin daha iyi sönümlenmesi gerekmektedir [2]. Çift Kütleli Volan (DMF), burulma titreşimlerini neredeyse tamamen izole ettiği için aktarma organlarında bu burulma titreşimlerini sönümlemek için en sık kullanılan sistemlerden biridir. [3]. Çift kütleli volanın yapısı temelde motor tarafında bir birincil volan kütlesi ve şanzıman tarafında ataleti artıran ikincil bir volan kütlesinin bulunmasıdır. İki kütle bir yay/sönümleme sistemi aracılığıyla birbirine bağlanır ve serbest dönüşe izin vermek için bir yatak tarafından desteklenir. DMF, motor torku üretim düzensizliğini neredeyse tamamen sönümler ve sürüş esnasında artık rezonans oluşmaz. Birinci volan kütlesinin titreşimi sönümlediği ikincil volan tarafının ve dolayısıyla şanzıman giriş milinin daha düzgün çalışması nedeniyle dişli tıkırtısı oluşmasının önüne geçiyor. Diğer olumlu etkiler, sırasıyla motor düzensizliğinin azalmasına ve birincil volan kütlesinin azalmasına bağlı olarak şanzıman ve krank mili geriliminin giderilmesidir.



Şekil 1 Çift Kütleli Volan 3D Görünüm

B. Kütle-Titreşim İlişkisi

Çalışmamızda tasarım optimizasyonu ile ağırlık azaltımı gerçekleştirilecek ana sac birinci kütle içerisinde damper yaylarına yuva görevi görmesi adına bulunur. Birinci kütle motorda oluşan titreşimlerin sönümlendiği bölümdür. Piyasada birçok markanın farklı yay sayısı, kalınlıkları, konumlandırmaları ile tasarlanan birinci kütle titreşimi minimuma indirir ve göbek kısmındaki rulmanlı yatak ile montajlanmış ikinci kütleye hareketi aktarır.

Bu bölümde farklı devirlerde oluşacak farklı titreşim frekanslarını sönümlemek amacıyla farklı tel çaplarına, boylarına ve adım sayılarına sahip yaylar belirli açılarda konumlandırılır. 1. Kütle motora direkt olarak bağlı olan bölüm olması sebebiyle maksimum titreşime maruz kalan parçadır. Bir kütlenin ağırlığı doğal frekansını etkileyen faktörlerden başlıca

gelenlerindendir. Birinci kütlenin ağırlığının gereğinden fazla azalması doğal frekans ile motor tarafından oluşan titreşim frekanslarının çakışması sonucunda rezonans oluşumu meydana gelecektir.

C. *Uçaklarda Ağırlık ve Balans*

Uçaklarda kalkış anında en yüksek motor gücü talep edilir, bunun sebebi atmosfer basıncısının yüzeyde masimum seviyede olmasıdır. Büyük bir kütleyi havalandırmak için atmosfer basınıcının ağırlık kuvvetini yenmesi gerekir. Bu sebeple hava aracının olabildiğince hafif olması daha hızlı havalanma ve daha iyi yakıt tasarrufu açısından önemlidir.

Havacılık sektöründe taşıtlar uçuş sırasında 4 ayrı kuvvete maruz kalmaktadır. Bunlar;

- İtme
- Sürüklenme
- Kaldırma
- Yerçekimi (Ağırlık)

Bu kuvvetlerin dengelenmesi sonucunda düzgün bir uçuş performansı elde edilir. Kaldırma kuvveti yerçekimi kuvvetini, itme kuvveti sürtünme kuvvetini dengelemeli [4].

Uçaklar kanat yapıları ve kendi içerisindeki stabilite sebebiyle havada dengede durmalı. Havadaki hareketi ve süzülme durumu kanat tipleri, açıları ve sürtünme kuvvetlerine göre değişmektedir. Uçağın temel olarak dengede kalması ve balans ağırlıklarının konumu denge-moment ve bileşke moment ile bağıntılıdır [5].

Hem seri üretim sektörü olmayan hem de ağırlığının öneminin bir hayli önemli olduğu havacılık ve savunma sanayii mühendisleri ağırlık azaltma konusunda birçok çalışma yapmıştır. Topoloji ve tasarım optimizasyonları ile ağırlık azaltmanın yanı sıra kompleks, hafif ve dayanımlı parçalar üretmek için ise eklemeli imalat son derece uyum sağlamaktadır [6]

II. AMAÇ

Çalışmamızdaki amaç DMF ikinci kütle parçası olan anasac parçasına tasarım optimizasyonu uygulayarak ağırlık azaltımı elde etmektir. Bu işlem ağırlık azalmasını sağlarken ürünün dayanımını olumsuz anlamda etkilemeyecek şekilde bir ağırlık azaltma çalışmasıdır.

III. KAPSAM

DMF'nin piyasada aktif olarak kullanılmasının ardından yaklaşık 40 yılın ardınan DMF geliştirmesi ile ilgili birçok çalışma yapılmıştır. Deng ve Burde, motor yolverici karakteristikleri ile aktarma organları rezonans frekansı arasındaki ilişkiyi araştırdı [7]. ZF Company'den Schweinfurt, Simulink yazılımında girdi olarak tek frekanslı titreşimi kullanan DMF dinamik modeline dayalı olarak ikincil volanın açısal ivmesini analiz ederek DMF'nin sönümleme etkisini araştırdı [8]. Wang ve ark. farklı bağlantılı dişli çiftlerinde sürüş ve aşırı yük koşullarına dayalı DMF parametreleri eşleştirme ve tasarım yöntemini inceledi ve 3 aşamalı burulma sertliğine sahip bir DMF tasarlandı [9]. Chen ve ark. DMF-CS'nin (çevresel yaylı DMF) dinamik özelliklerini simüle etti. Sonuçlar, aktarma organı sisteminin başlatma ve durdurma koşullarında büyük titreşim taşıdığını gösterdi. DMF sönümlemesi artırılarak burulma titreşim genliğinin azaltılabileceği öne sürülmüştür [10]. Araştırmalar sonucunda yapılan yorumlar araç motoru ile aktarma organları üzerinde en çok titreşim ve rezonans durumu ilk hareket ve son hareket esnasında gerçekleştiği yönündedir. Bu sebeple bahsedilen aşamalar DMF tasarımda yay sertlikleri ve açıları hesaplanırken dikkat edilmesi gereken noktaların başında gelmelidir. Bunun yanında DMF'nin her iki kütlesi için de ağırlık

parametresinin atalet momentini etkilediği görülmüştür. İkincil kütlenin görevi titreşimleri sönümleyerek rezonans oluşmasını önlemek iken birincil kütle daha ağır bir yapıya sahiptir. Gerekli olan ataleti sağlaması için tasarlanır.

IV. YÖNTEM

Havacılık sektöründe kullanılan parçaların hafif olması gerekirken aynı zamanda dayanımı yüksek fakat maliyeti düşük malzemelerden üretilmesi gerekmektedir. Geçmişte blok malzemelerden talaşlı imalat ile işlenen birçok parça günümüzde topoloji optimizasyonu ile hafifletilmiş ve dayanımı simule edilmiş tasarımlar elde edilir. Ardından bu tasarımlar eklemeli imalat ile minimum talaş miktarı, maksimum hafiflik ve yeterli dayanımlarda ürünler elde edilmektedir.

Çalışmamızda NX unigraphics ticari yazılımında oluşturulan tasarım ANSYS 2021 R2 Ticari yazılımı ile sonlu elemanlar analizine tabii tutulmuştur. Çalışma sırasında görebileceği maksimum yüklemeler ve sınır şartlarına göre simüle edilmiştir. Bu analizde DMF birinci kütle ana sac parçasının önceki tasarımı ve optimizasyon yapılmış tasarım karşılaştırılacaktır. İki modele de hem maksimum devir hem de maksimum dönme açısı uygulanacaktır. Sonuç olarak yayların tepki kuvveti, eşdeğer gerilme ve vektörel gerilme sonuçları incelenecektir.

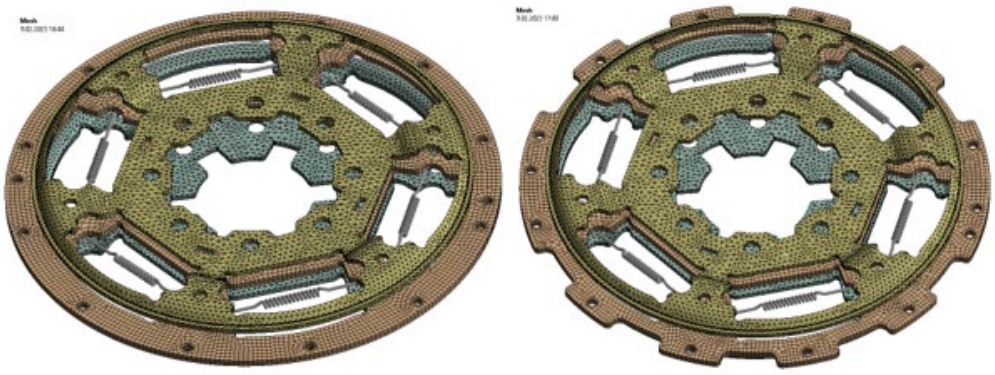
Öteyandan tasarım optimizasyonu ile anasac bütününde 0,086 kg ağırlık tasarrufu neticesinde bu konuda %11,9 gelişme kaydedilmiştir.

V. SONUÇ

DMF ana sacına uygulanan tasarım optimizasyonu, parçada ağırlık azalmasına gidilirken yapılan çalışmalar ile performansının da güvenli seviyelerde olduğunu doğrulamaktır. Tasarım optimizasyonundan önceki performansı ve tasarım değişikliğinden sonraki performansı karşılaştırılacak, çıkan sonuçlar yorumlanacaktır.

Her iki tasarımda da dmf anasacı sabit tutulup kapaklar 20 derece döndürülecektir. Bu sayede yay slotlarına tanımlanan yaylar sıkışacak ve yuva çeperlerine kuvvet uygulayacaktır. Analiz kurgusunun doğrulaması yayların tepki kuvvetinin matematiksel hesaplaması ve test cihazından gelen gerçek veriler ile yapılmıştır.

Öteyandan tasarım optimizasyonu ile anasac bütününde 0,086 kg ağırlık tasarrufu neticesinde bu konuda %11,9 gelişme kaydedilmiştir.

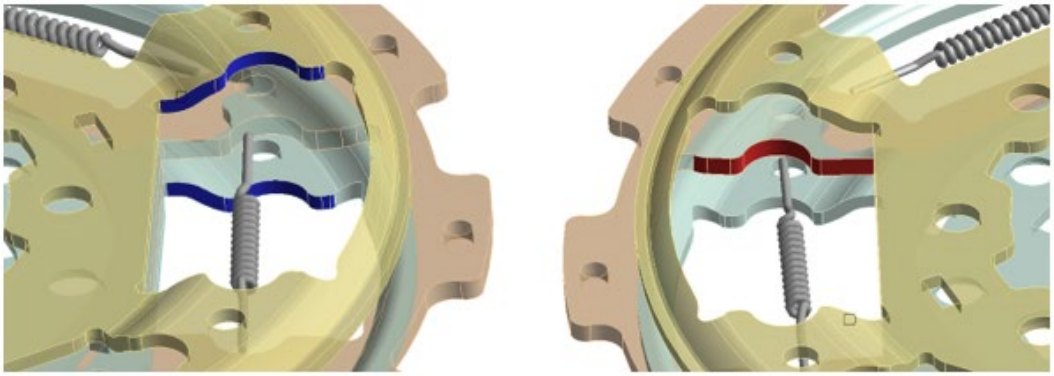


Şekil 2 1. ve 2.Tasarımların Mesh Yapısı

A. Yay Kuvveti

DMF damper yaylarının tanımlanması için gereken "reference" ve "mobile" yüzeyleri, yay stiffness'ının belirlenmesinin ardından 6 adet yay, kapaklar ve anasacdaki slotlara tanımlanmıştır. Max tork değeri 510 Nm olan bir araca takılacak DMF yayları bu değeri karşılamalıdır. Analiz sınır şartları ve yüklemelerin tanımlanmasının ardından spring probe ile alınan sonuçlar ile matematiksel hesaplamaların sonuçları birebir uyuştuğu görülmektedir.

ANSYS yazılımı yay kuvvetini hesaplamada arka planda aşağıdaki matematiksel işlem ile çözümlemektedir.



Şekil 3Ansys Yay Tanımlama Yüzeyleri

$$F = k\ x\ (D_{serbest} - D_{sıkışmış})$$

(1)

$F = Uygulanan\ kuvvet$

$k = Yay\ sabiti$

$D_{serbest}; = Serbest\ durumda\ yay\ uzunluğu$

$D_{sıkışmış} = Sıkışmış\ durumda\ yay\ uzunluğu$

$D_{serbest} - D_{sıkışmış} = Yer\ değiştirme$

$$F = 25{,}69\ x\ (69{,}91 - 39{,}38) = 784{,}28\ N$$

(2)

Analiz kurgusunda tanımlanan yayların herbiri 69,9 mm uzunluğa sahiptir, 20 dereceye kadar sıkıştırılan yayların yer değiştirmesi 30,53 olarak gözlemlenmiştir. 20 derecenin sonunda yayların her birinin 784,28 N ile tepki kuvveti verdiği görülmüştür. ANSYS mechanical modulünde yay tanımlamasında girdilerde bulunmayan yay ortalama çapı, tel çapı, çalışan sarım sayısı gibi parametrelerin de dahil olduğu başka bir matematiksel hesaplama ile bu sonuçları doğrulayacak olursak;

$$\frac{(D_{serbest} - D_{sıkışmış})x(78500\ x\ d^4)}{8\ x\ {d_{ort}}^3\ x\ I_f}$$

(3)

$d = Tel\ çapı$

$d_{ort} = Yay\ ortalama\ çapı$

$I_f = çalışan\ sarım\ sayısı$

$$\frac{(69{,}91 - 39{,}83)x(78500\ x\ 4.40^4)}{8\ x\ (30{,}8)^3\ x\ 4{,}9} = 784{,}276\ N$$

(4)

Bu sonuçlarla beraber DMF damper grubunu Dönmez Debriyaj Ar&Ge merkezi test laboratuvarı bünyesinde tork test cihazı ile teste tabii tuttuğumuzda bu sonucun 540 Nm olduğu görülmüştür. 784,28 N luk 6 adet yayın yarattığı tork 437,62 Nm olur iken yayların montajı esnasındaki yaklaşık 6 mm'lik bir ön gerilme kaynaklı fark ortaya çıkmaktadır. Bu etkenler de hesaba dahil edildiğinde çıkan tork miktarı 539,4 olarak hesaplanmıştır. Bu sonuç her iki tasarımda da geçerlidir.

Kapak çiftinin 20 derece döndürüldüğü durumda damper yaylarının kuvvet çıktılarının ve analiz kurgusunun doğru oluşturulduğu kanıtlanmış olmaktadır.

TABLO 1

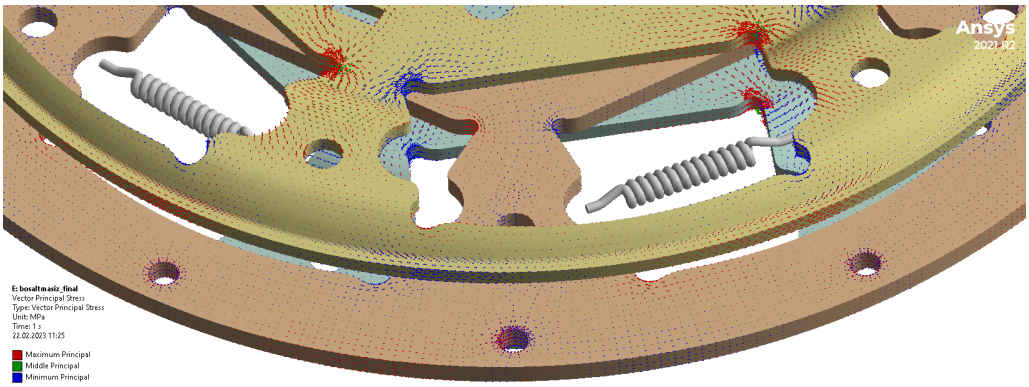
KUVVET SONUÇLARI	DMF YAY GRUBU
Matematiksel	4.705,606 N
ANSYS	4.705,68 N

TABLO 2

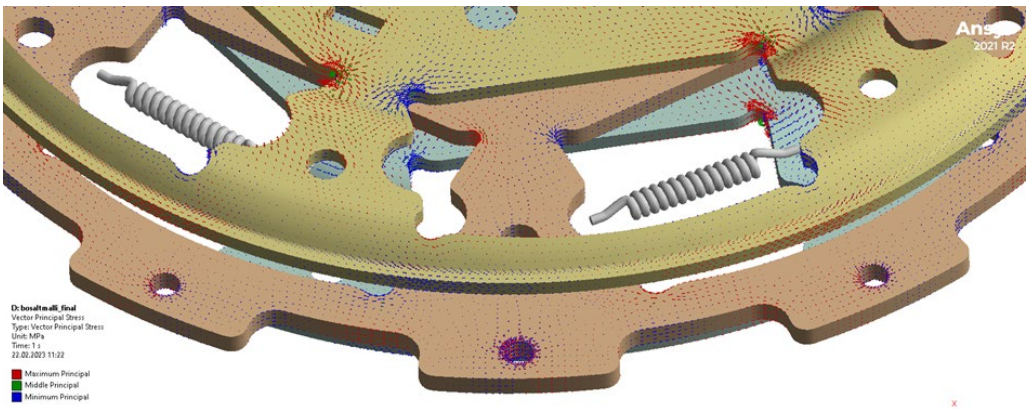
TORSİYONEL SONUÇLAR	DMF YAY GRUBU
Test Sonucu	540 Nm
ANSYS	437,62 Nm
Ön gerilme (6mm)	102,38 Nm

B. Vektörel Gerilim Dağılımları

Tasarım optimizasyonu ağırlık olarak tasarruf sağlanmasına rağmen geometride daha fazla form oluşturulması dolayısıyla gerilmelere müsait olabilir. Ayrıca et kalınlıklarının fazla azalması emniyeti de direkt olarak etkileyecektir. İki tasarıma da aynı sınır şartları, yüklemeler ve yay tanımlamaları yapılmasının ardından vektörel gerilmeler incelendiğinde yay slotlarında oluşan gerilme vektörlerine etkisinin olmadığı fakat ana sac dış çapı üzerindeki bası ve çeki gerilmelerinin etki alanlarını daralttığı ve delik bölgelerinde yoğunlaştığı gözlemlenmiştir. Bu etkinin sebebi boşaltma sonucunda fazladan köşeler oluşturularak gerilme yönlerinde düzensizlik oluşturmasıdır, bu sebeple eşdeğer gerilme değerinin artacağı tahmin edilmektedir.



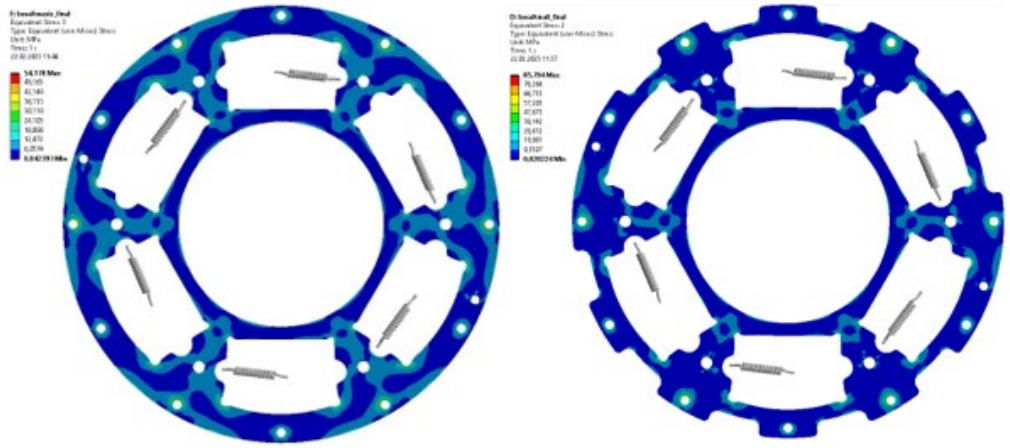
Şekil 4 1.Tasarım Gerilme Vektöreleri Dağılımı



Şekil 5 2.Tasarım Gerilme Vektörleri Dağılımı

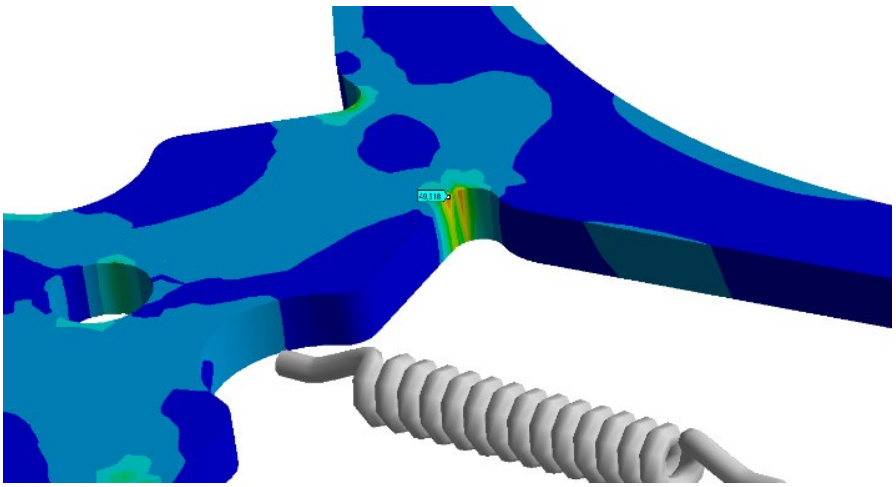
C. Eşdeğer Gerilme

Eşdeğer gerilme sonuçlarını incelediğimizde ağırlık azaltması uygulanmayan modelde 54,17 MPa olarak görülen değer ağırlık azaltmanın sonucunda 85,79 MPa değerine ulaşmıştır. Boşaltma uygulanan modelde %58,4'lük bir artış görülmüştür. Ana sac dış çapı üzerinde oluşturulan formlar ile 0,086 kg ağırlık tasarrufu ile %11,9 bir hafifleme kaydedilmiştir. Ana sac üzerindeki gerilmelerin artmasına rağmen güvenlik katsayısı sonuçlarını incelediğimizde parçanın güvenlik sınırları içerisinde olduğu görülmüştür. İlk tasarımın güvenlik katsayısı 3.69 olarak görülürken tasarım optimizasyonunun ardından bu sayı 2.33 olmuştur.



Şekil 6. 2 Farklı Tasarım İçin Eşdeğer Gerilme Dağılımları

Ana sac parçasının en kritik noktalarından biri yay slotu köşeleridir, yay slotları çevresi ince cidarlardan oluşmaktadır. İç çapa yakın köşelerde yayların daha çok sıkışmasından dolayı bu köşeler daha fazla kuvvete maruz kalmaktadır. Analiz sonuçlarımızda güvenlik bakımından uygun olmasının yanında, slot köşelerinde %42,6'lık bir artış görülmüştür.



Şekil 7 Maksimum Gerilmenin Görüldüğü Bölge

VI. ÇIKARIM

Çalışmamızda savunma sanayiinde kullanılan bir DMF ürünün ana sac parçası ele alınmıştır. Ana sac üzerinde bir tasarım optimizasyonu yaparak dış çapı üzerinde boşaltmalar gerçekleştirilmiştir. Bunun neticesinde %11,9 oranında bir ağırlık azaltması sağlanmıştır.

İki ürün arasındaki performans farklarını incelemek adına eşit yüklemeler ve sınır şartları ile sonlu elemanlar analizine tabii tutulmuştur. Motordan gelen titreşimleri sönümleyen damper grubunun yay tanımlamalarının yapılmasının ardından yayların sıkışmalarına göre matematiksel hesaplamalar ve ansys çıktıları karşılaştırılıp doğrulanmıştır.

Safety factor sonuçlarında tasarım optimizasyonu yapılmış modelde bu sayı düşmüş olsa da güvenli bölgede seyretmektedir. Gerilmelerin oluştuğu bölgeler beklenen bölgeler olup risk teşkil etmeyecek yükseklikte ve bölgelerde görülmüştür.

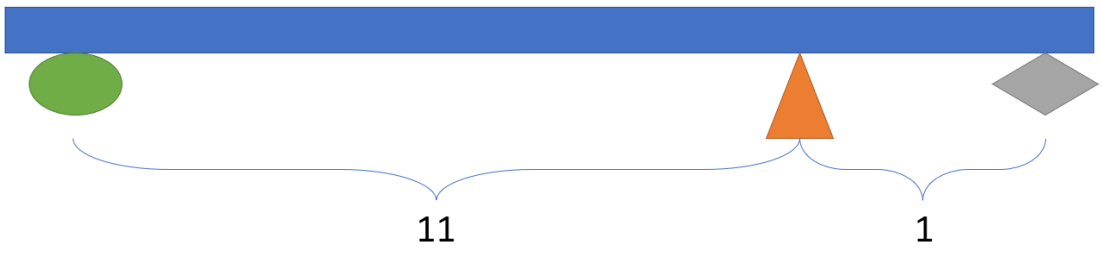
		1.TASARIM	2.TASARIM
AĞIRLIK	(KG)	0,723	0,637
GERİLME	(MPa)	54,17	85,79
GÜVENLİK KATSAYISI		3,69	2,33

Bu sonuçlarla beraber benzer torklarda çalışan DMF uygulamalarında anasac malzemesinin ve yay slot çeperlerinin geometrisine de bağlı olmak üzere, dış çap üzerinden ağırlık azaltmanın ürünün performansını etkilemeyeceği ve uygulamaya dökülebilir bir iyileştirme olduğu görülmüştür.

Ürün uygulamaya geçirileceği hava aracında DMF-ağırlık merkezi ve balans ağırlığı-ağırlık merkezi arasında 1-11 oranı vardır. Bu sebeple 0,086 KG lık ağırlık tasarrufu ile balanas ağırlığı da azalacağı için araç bütününde,

$$0{,}086\ x\ 11 = 0{,}946\ kg \tag{5}$$

Ağırlık azaltımına karşılık gelecektir.



TEŞEKKÜR

Çalışmada emeği geçen Dönmez Debriyaj A.Ş Ar&Ge merkezi çalışanları ve yöneticilerine teşekkürlerimizi sunarız.

REFERANSLAR

[1] Albers, A., Albrecht, M., Krüger, A., & Lux, R. (2001). *New methodology for power train development in the automotive engineering-integration of simulation, design and testing* (No. 2001-01-3303). SAE Technical Paper.

[2] Sun, W., Li, Y., & Huang, J. (2011). Nonlinear characteristics study and parameter optimization of DMF-RS. *SAE International Journal of Passenger Cars-Mechanical Systems*, *4*(2011-01-1550), 1050-1057.

[3] Reik, W., Seebacher, R., Kooy A., Dual Mass Flywheel, , 6th International Symposium, Baden- Baden: LuK Buhl, 1998, pp. 69

[4] Swatton, P. J. (2011). Principles of flight for pilots (Vol. 42). John Wiley & Sons.

[5] Başolun, S. (2010). Yük ve Denge.

[6] Cotteleer, M., & Joyce, J. (2014). 3D opportunity: Additive manufacturing paths to performance, innovation, and growth. Deloitte Review, 14(1), 3-19.

[7] Mohire, S., & Burde, R. (2010). Evaluation of interdependent behavior of dual mass flywheel (DMF) and engine starting system (No. 2010-01-0188). SAE Technical Paper.

[8] Bach, S. H. (2004). Systematic search for and vibratory assessment of new action principles for alternative rotary vibration decoupling systems in the passenger car driveline. Drive System Technique, 18(2), 3-12.

[9] Wang, Y., Qin, X., Huang, S., & Deng, S. (2016). Design and analysis of a multi-stage torsional stiffness dual mass flywheel based on vibration control. Applied Acoustics, 104, 172-181.

[10] Chen, Z. Y., Mao, Y., & Shi, W. K. (2016). Research on torsional vibration of powertrain with dual mass flywheel in start-stop conditions. Transactions of Beijing Institute of Technology, 36(1), 42-47.

Application of Metal-Organic Frameworks (MOFs) in Pipette-Tip Solid-Phase Extraction: A Mini Literature Review

Gamze OZCAKIR

gamze.ozcakir@bilecik.edu.tr , ORCID: 0000-0003-0357-4176
[1]*Bilecik Şeyh Edebali University, Faculty of Engineering, Department of Chemical Engineering, TR 11100, Bilecik, Turkiye*

Abstract: Among the several solid phase extraction techniques pipette tip solid phase extraction (PT-SPE) is mainly used for pharmaceutical and biological species. This technique is seen as simple to ap-plicate and high efficient. To obtain true results with this technique, it is necessary to work ad-sorbents which have high performance. One of these adsorbents is Metal Organic Frameworks (MOFs) as a new organic-inorganic hybrid material which compose of metal ions and organic linkers. MOFs has excellent features like very large porosity, high surface area, special topology. To the best of author's knowledge, PT-SPE with MOFs is a new topic in literature which can be studied since 2017. The aim of this study to show literature gap and novel studies about this topic.

Keywords: *Metal-Organic Framework; Pipette-Tip Solid-Phase Extraction; Pretreatment before analytical measurement; Purifying analyte*

I. INTRODUCTION

To reach a successful result, preparing analytes for chromatographic analysis is crucial. Extraction uses for this purpose. Thanks to extraction, analytes are separated from their components and enriched before their chromatographic detection. In solid phase extraction (SPE) as one type of extraction method, the aim is to catch the desired compound in an aqueous medium by using an immobilized phase. Then, the immobilized phase was washed by using an organic solvent to desorb the analyte. Bed sorbents for SPE can be in several forms like cartridge, disk, pipette tip, etc [1].

Metal-Organic Frameworks (MOFs) are porous polymeric materials. They investigated nearly twenty years ago. Previously, zeolites had been seen as the most popular porous materials. MOFs have a structure that includes interconnected metal ions with organic ligands. MOFs have crucial features such as large pores in their crystalline structure and high sorption capability [2]. MOFs generally have microporosity. However, difficult to use them in applications such as separation, drug delivery, and catalysis. Because their narrow pores can't let to attach large molecules. To solve this problem, researchers have developed novel types of MOFs that have mesoporosity. MIL-100(Cr) is one of them [3]. Another solution for this drawback in the application of MOFs has been found to support them with another material wide porous such as aerogels [4].

There are so many groups of MOFs in the scientific literature which are MIL, HKUST, LIC, ZIF, UiO, and so on. Metal ions of MOFs can be Fe, Cu, Co, Zn, etc. Organic ligands of MOFs can be polyamines, carboxylates, pyridyl and cyano groups, crown ethers, and phosphonates. Synthesis of MOFs can be made by using one of the approaches hydrothermal, solvothermal, mechanochemical and microwave-assisted, etc. In MOF synthesis, selecting accurate reaction

temperature, time, pressure, pH, and solvent is crucial to reach desired material properties. There are many application areas for MOFs in literature which are the adsorption of biological compounds, antibiotics, and toxic chemicals in aqueous medium; gas (CO_2, H_2S) adsorption; catalysis; sensing; electrochemical energy storage and drug delivery [5]. MOFs can be used as mass, optical, piezoresistive sensors. By this way, it is possible to detect gas molecules like propane, and organic solvents like toluene, pyridine, dichloromethane, methanol. In Fig 1, it can be seen chemical sensing behavior of a copper-based MOF. Besides that, MOFs have potential to be used as stationary material in chromatographic devices instead of traditional ones like zeolites, carbon, polystyrene. Because, MOFs have adjustible pore structure. Moreover, it can be possible to separate small molecules in MOF channels [6].

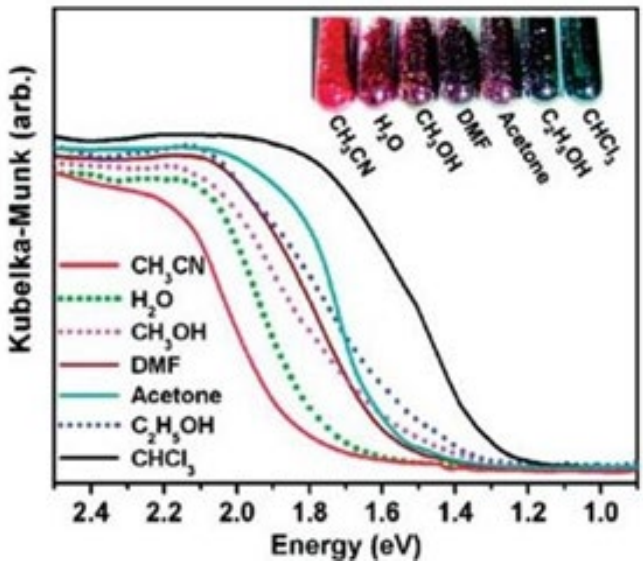


Fig. 1. Adsorbances for several solvents provided by MOFs chemical sensing property [7]

II. PIPETTE-TIP SOLID-PHASE EXTRACTION

Adsorbent-based extraction methods are used to separate analysts from a complex matrix before giving the samples to an analytical instrument. These methods have several advantages. The operation can occur easily in a short period. Besides that, during applying this method low amount of solvent is used compared to the liquid-liquid extraction method. Pipette-tip solid-phase extraction (PT-SPE) is one of the adsorbent-based extraction methods. This method can be applied for trace amounts of analyte [8]. Figure 2 shows general method for PT-SPE. First, pipette cuts to put adsorbent in it. Then, adsorbent packaging is carried out into the pipette. Cotton is used to prevent adsorbent losing. Adsorbent activation is made by using acetonitril and water solvents. Because the aim of study was Sulfonamide (SA) detection, SA sample solution was loaded to the pipette at the top. After filtering, the sample which was contained SAs analyzed via HPLC-UV. As seen in Fig 2, peaks after PT-SPE was clearer than directly injection without extracting the sample.

PT-SPE can be used for several samples such as polycyclic aromatic hydrocarbons, dyes, antibiotics, etc. For PT-SPE, the adsorbents such as Silica, MOFs, Covalent-Organic Frameworks (COFs), Polymers, Carbon Nanotubes, Graphene Oxide, and Molecularly Imprinted Polymers can be utilized. Inorganic adsorbents such as silica and carbon derivatives have good chemical stability and so they have been widely used. However, their selectivity is low. Besides that, sole organic adsorbents could not require desired functionality also. Because they have low chemical stability against basic, acidic, and organic solvents. Metal-Organic Frameworks have organic and inorganic features at the same time. And recently, they have applied several samples before their injections to high-performance liquid chromatography (HPLC) and gas chromatography [8].

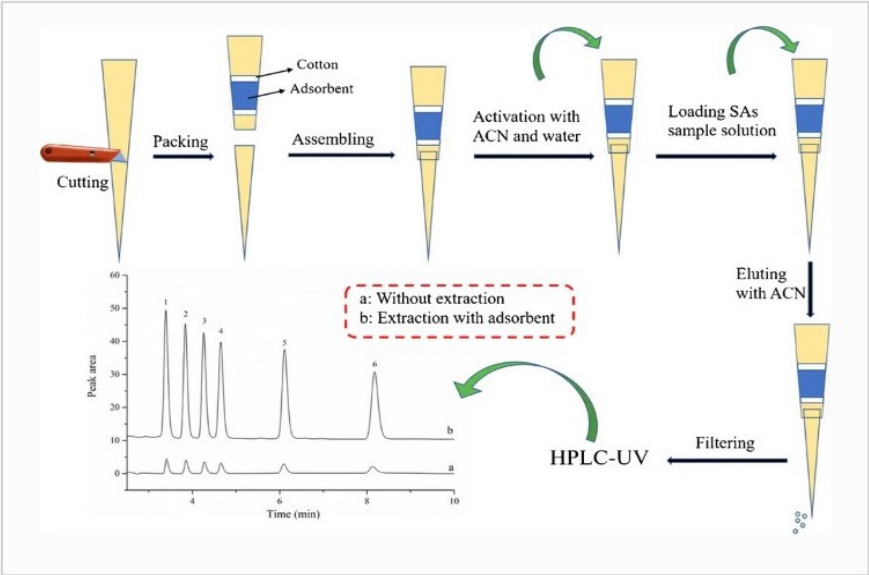


Fig. 2. General scheme of PT-SPE for preparation analyte [9]

III. METAL ORGANIC FRAMEWORKS (MOFS) IN PIPETTE-TIP SOLID-PHASE EXTRACTION

The method which is used to enrich the sample with analyte is easy. Generally, syn-thesized MOFs are loaded in a pipette-tip. The ends of this tip is covered with cottons to prevent losing MOFs. Then, sample which includes analyte are passed in this column. Finally, the sample is recovered from the adsorbents by using an organic solvent such as chloroform [10]. In Table 1, it was given some examples in recent literature about the topic.

TABLE I
CURRENT PT-SPE APPLICATIONS PUBLISHED IN THE LITERATURE FOR MOFS

Adsorbent	Analyte	Sample	Instrument	Reference
Co-MOF	Levofloxacin	Anti-biotic	HPLC-UV	[11]
PCN-222/MOF-545 (Zr-MOF)	Mercury	Fish	Cold vapor atomic absorption spectroscopy analysis (CVAAS)	[12]
Tantalum metal organic framework (Ta-MOF)	Nicotine	Wastewater	HPLC	[13]
Cr-MOF	Paraben	Wastewater	UV-VIS	[10]
Mg-metal organic framework composite electrospun nano fiber	Anti-cancer drugs, (Letrozole, Gefitinib)	Human biological fluids	HPLC-UV	[14]

IV. CONCLUSION

Before the analytical separation of samples via an instrument, it is crucial enriching the specimen with the analyte. Hence, the results can be more accurate after the instrumental analysis such as HPLC, UV, and GC. PT-SPE is a popular extraction method amongst others. Because it is possible to gain enriched analyte solutions in a breeze and a short period by using PT-SPE. Besides that, this method requires less solvent compared to liquid-liquid extraction. Metal-Organic Frameworks are porous crystalline materials that have so many crucial features. In this study, the aim was to draw attention to using MOFs in PT-SPE.

REFERENCES

[1] B. Buszewski, M. Szultka, "Past, present, and future of solid phase extraction: a review," Critical Reviews in Analytical Chemistry, vol. 42(3), pp. 198-21, 2012.

[2] S.L. James, "Metal-organic frameworks," Chemical Society Reviews, vol. 32(5), pp. 276-288, 2003.

[3] W. Xuan, C. Zhu, Y. Liu, Y. Cui, "Mesoporous metal–organic framework materials," Chemical Society Reviews, vol. 41(5), pp. 1677-1695, 2012.

[4] Z. Inonu, S. Keskin, C. Erkey, "An emerging family of hybrid nanomaterials: metal–organic framework/aerogel composites," ACS Applied Nano Materials, vol. 1(11), pp. 5959-5980, 2018.

[5] M. Safaei, M.M. Foroughi, N. Ebrahimpoor, S. Jahani, A. Omidi, M. Khatami, "A review on metal-organic frameworks: Synthesis and applications," TrAC Trends in Analytical Chemistry, vol. 118, pp. 401-425, 2019.

[6] B. Liu, "Metal–organic framework-based devices: separation and sensors," Journal of Materials Chemistry, vol. 22(20), pp. 10094-10101, 2012.

[7] Z.Z. Lu, R. Zhang, Y.Z. Li, Z.J. Guo, H.G. Zheng, "Solvatochromic behavior of a nanotubular metal− organic framework for sensing small molecules," Journal of the American Chemical Society, vol. 133(12), pp. 4172-4174, 2011.

[8] H. Sun, J. Feng, S. Han, X. Ji, C. Li, J. Feng, M. Sun, "Recent advances in micro-and nanomaterial-based adsorbents for pipette-tip solid-phase extraction," Microchimica Acta, vol. 188(6), pp. 189, 2021.

[9] Z. Chen, C. Yu, J. Xi, S. Tang, T. Bao, J. Zhang, "A hybrid material prepared by controlled growth of a covalent organic framework on amino-modified MIL-68 for pipette tip solid-phase extraction of sulfonamides prior to their determination by HPLC," Microchimica Acta, vol. 186, pp. 1-11, 2019.

[10] M. Kaykhaii, S.H. Hashemi, F. Andarz, A. Piri, G. Sargazi, "Chromium-based metal organic framework for pipette tip micro-solid phase extraction: an effective approach for determination of methyl and propyl parabens in wastewater and shampoo samples," BMC chemistry, vol. 15(1), pp. 60, 2021.

[11] M. Abbaszadehbezi, M.R.R. Kahkha, A. Khammar, M.M. Rabouri, "Application of pipette-tip solid-phase extraction tech-nique for fast determination of levofloxacin from wastewater sample using cobalt metal-organic framework," Analytical Methods in Environmental Chemistry Journal, vol. 5(02), pp. 51-59, 2022.

[12] M.R. Rezaei Kahkha, S. Daliran, A.R. Oveisi, M. Kaykhaii, Z. Sepehri, "The mesoporous porphyrinic zirconium metal-organic framework for pipette-tip solid-phase extraction of mercury from fish samples followed by cold vapor atomic absorption spectrometric determination," Food Analytical Methods, vol. 10, pp. 2175-2184, 2017.

[13] M.R.R. Kahkha, M. Kaykhaii, G. Sargazi, B.R. Kahkha, "Determination of nicotine in saliva, urine and wastewater samples using tantalum metal organic framework pipette tip micro-solid phase extraction," Analytical Methods, vol. 11(48), pp. 6168-6175, 2019.

[14] P. Khodayari, N. Jalilian, H. Ebrahimzadeh, S. Amini S. "Electrospun cellulose acetate/polyacrylonitrile/thymol/Mg-metal organic framework nanofibers as efficient sorbent for pipette-tip micro-solid phase extraction of anti-cancer drugs," Reactive and Functional Polymers, vol. 173, pp. 105217, 2022.

UV-VIS Detection of Algae Based Gold Nanoparticles: A Mini-Review

Gamze OZCAKIR

gamze.ozcakir@bilecik.edu.tr , ORCID: : 0000-0003-0357-4176
[1] *Bilecik Şeyh Edebali University, Faculty of Engineering, Department of Chemical Engineering, TR 11100, Bilecik, Turkiye*

Abstract: Gold (Au) is converted to nanoscale because of some reasons. First, it is possible to reach a high surface area per gram of Au. Second compared to bulk Au, nano-sized Au can be melted at lower temperatures. Several chemical and physical methods can be applied to synthesize Au Nanopar-ticles (AuNPs). However, these methods are hazardous to the environment and expensive. So, researchers have developed new green and cost-effective synthesis methods based on algae, bacteria, and yeast to create AuNPs. Because Au has biocompatibility, AuNPs have applications in medical imaging, catalysis, and biosensing. The method to synthesize AuNPs from algae is easy since it has not required high temperatures and pressures. It can be possible to reach 2-240 nm size range AuNPs to use different types of algae. UV-Vis spectrophotometry uses to see syn-thesized Au-NPs. The study aimed to display examples in scientific literature about the topic.

Keywords: *Biological synthesis of nanoparticles, Gold nanoparticles, Green chemistry*

I. INTRODUCTION

Currently, the term green chemistry has gained popularity. Green chemistry means developing environmental-friendly chemical processes. Hence, green chemistry aims to minimize using toxic chemicals and prevent the formation of hazardous by-products in any chemical processes. Besides that, obtaining maximum yield via minimum energy is crucial for green chemists. So, the researchers have developed three new strategies for reaching this purpose in their chemical reactions. One of the strategies is to create novel synthesis routes by using catalysts. The other one is to give up traditional solvents and face new solvents like supercritical CO_2. And the last one is replacing petroleum-based reagents with renewable ones [1].

Nanoparticles can be synthesized by utilizing three methods which are physical, chemical, and biological methods. Among these, biological routes have gained attention. Because the way coincides with the green chemistry approach. The method used plants, bacteria, microorganisms, yeast, and algae as biomass for nanoparticle synthesis [2]. Besides that, compared to physical and chemical routes biological method has many ad-vantages. This method is cost-effective. It does not require work under high temperatures and pressures. So, it is easy to scale up this process for industry [3].

Metallic nanoparticles are crucial materials concerning human life. The most studied metallic nanoparticles are Gold (Au), Silver (Ag), and Platinium (Pt) for this purpose. Besides that, researchers are worked on metallic nanoparticles to use in catalysis, polymer synthesis, sensing, and treatment and diagnosis of diseases [3]. AuNPs can be used as sensor to detect chemical and biological samples [4]. One of the biological compound that can be detected by AuNPs is Human Insulin [5]. In addition, AuNPs can used as sensor for methanol, acetone,

ethanol, and butanol [6-8]. Besides that, it can be possible to use AuNPs in transition metal sensing in organic medium. This is crucial development, because metal ions can be easily detecting after an industrial reaction [9].

This review paper aims to provide information about biological synthesis and applications of AuNPs. Specifically, literature information given for algae-based AuNPs and their characterization techniques.

II. BIOMASS BASED AU NANOPARTICLES (AUNPS): SYNTHESIS AND APPLICATIONS

It is known that gold has been utilized in several applications for nearly 400 years. Bringing gold as nano-sized has increased its application areas. Researchers started to work with these materials in several applications such as catalysis, biotechnology, elec-tronics, and electro-optical devices. At first, AuNPs were synthesized in chemical ways. Researchers noticed that Au could have different colors. These colors could be red, violet, or blue depending on their particle size and shape. However, these methods were expen-sive. Besides that, it needs to use hazardous chemicals. So, the researchers started to work on a biological route to synthesize AuNPs. Au(III) turned into its stable and reduced form in this route [10]. This process is called bioreduction. To date, so much biomass has been used to synthesize AuNPs. Used biomass types for AuNPs and their applications of them can be seen in previous research in Table I.

TABLE I
CURRENT BIOMASS BASED AUNPS AND ITS APPLICATIONS PUBLISHED IN THE LITERATURE

Biomass	Application	Reference
pineapple, orange, peanut	A dual-mode electrochemical sensor for carbendazim (CBD) detection	[11]
Lilium casa blanca petals	Methylene Blue (MB) degradation	[12]
Phoma sp. as an endophytic fungus isolated from peach trees	A new antimicrobial substance to control the pathogenic activity	[13]
rice husk	-degradation of industrial dyes (Methylene Blue and 4-Nitrophenol) - an anticancer material against human colon cancer	[14]
W. urticifolia flower	Photocatalytic degradation of Rhodamine-B	[15]

III. ALGAE BASED AU NANOPARTICLES (AUNPS): SYNTHESIS AND APPLICATIONS

Algae are defined as a single or multicellular organism that lives in marine or fresh-water. Researchers divided algae into two groups micro and macroalgae concerning their cell number. Algae can be used for several sectors such as agriculture, pharmaceuticals, medicine, cosmetics, and aquaculture. Besides that, it is possible to make natural dyes and biofuels from algae [16].

Nowadays, researchers have studied synthesizing algae-based nanoparticles [16]. This is not a surprising situation. Because algae have so many advantages. Algae are re-newable

feedstocks. And, their cultivation process is sustainable. Because they can be cul-tivated under sunlight. Besides that, they are used CO_2. Algae are biocompatible and non-hazardous. They can be synthesized in an open pond system. So, their synthesizing process is cheap. Their shape, size, and surface functionalities can be adjusted concerning their application field [16].

In Table II, it was given used types of algae for AuNPs and applications of them in previous researches.

TABLE II
CURRENT ALGAE BASED AUNPS AND ITS APPLICATIONS PUBLISHED IN THE LITERATURE

Family of algae	Application	Reference
Brown	an anticancer material against human colon cancer	[17]
Red	an antioxidant	[18]
Blue-Green	An antibacterial	[19]

IV. CHARACTERIZATION TECHNIQUES AND IMPORTANCE OF UV-VIS FOR ALGAE BASED AU NANOPARTICLES (AUNPS)

For algae-based synthesis of metal nanoparticles, it is important to investigate the ef-fect of reaction parameters such as temperature, pH, and stirring rate. Because these pa-rameters are responsible for the properties of the final nanoparticles which are size, mor-phology, and stability. For this purpose, researchers use several characterization equip-ments. Dynamic Light Scattering (DLS) and Transmission electron microscopy (TEM) is utilized to determine the mean diameter of AuNPs. TEM analysis is also beneficial for de-termining the morphology of synthesized AuNPs [20]. X-ray diffraction (XRD) analysis is applied to determine the crystal structure of AuNPs [21].

UV–visible spectrophotometry (UV-VIS) is another technique applied to detect stabil-ity and color changes in AuNPs. With the UV-VIS characterization technique, it is possible to decide whether AuNPs form or not in the solution. When Au3+ ions turn Au0, the color of the solution changes. With UV-VIS, it can be also determined the stability of AuNPs. If the surface plasmon resonance, λ i.e., of the solution remains the same after several months, this means that the particles conserve their stability [21].

Besides its characterization techniques, synthesized AuNPs tests for its application area. AuNPs have so many applications in the biomedical area. So, before its use in this area, the antimicrobial, antiviral, antioxidant, anticancer, antidiabetic, and bio-sensing properties of synthesized AuNPs are determined [22].

V. CONCLUSION AND SUGGESTIONS

Biological synthesis is a feasible way to synthesize metallic nanoparticles. Au, Pt, and Ag are crucial materials to use for human health applications. Algae are carbon-neutral biomass sources. So, using this feedstock to synthesize AuNPs is a good solution concerning sustainability and green chemistry approaches. There is an information scarcity in the literature about this topic. So, a literature gap has occurred in especially green synthesis of AuNPs via green micro and macro algae.

REFERENCES

[1] L. Soltys, O. Olkhovyy, T. Tatarchuk, M. Naushad, "Green synthesis of metal and metal

oxide nanoparticles: Principles of green chemistry and raw materials," Magnetochemistry, vol. 7(11), pp. 145, 2021.

[2] Y. A. M. Esa, N. Sapawe, "A short review on zinc metal nanoparticles synthesize by green chemistry via natural plant extracts," Materials Today: Proceedings, vol. 31, pp. 386-393, 2020.

[3] P. G. Jamkhande, N. W. Ghule, A. H. Bamer, M. G. Kalaskar, "Metal nanoparticles synthesis: An overview on methods of preparation, advantages and disadvantages, and applications," Journal of drug delivery science and technology, vol. 53, pp. 101174, 2019.

[4] C. C. Chang, C. P. Chen, T. H. Wu, C. H. Yang, C. W. Lin, C. Y. Chen, "Gold nanoparticle-based colorimetric strategies for chemical and biological sensing applications," Nanomaterials, vol. 9(6), pp. 861, 2019.

[5] K. Ge, Y. Peng, Y, Z. Lu, Y. Hu, G. Li, "Aptamer-gold nanoparticle doped covalent organic framework followed by matrix-assisted laser desorption/ionization time-of-flight mass spectrometry for selective enrichment and detection of human insulin," Journal of Chromatography A, vol. 1615, pp. 460741, 2020.

[6] M. Alsaiari, J. Ahmed, M. Faisal, F. A. Harraz, "Biomass-derived carbon decorated by gold nanoparticles as efficient methanol electrochemical sensor," Materials Science in Semiconductor Processing, vol. 146, pp. 106693, 2022.

[7] M. Geramilla, C. Muthukumaravel, U. Karunakaran, T. N. Sairam, "Gold nanoparticle decorated vertical graphene nanosheets composite/hybrid for acetone sensing at room temperature," Materials Science and Engineering: B, vol. 288, pp. 116211, 2023.

[8] S. Wang, Z. Lin, P. Fu, L. Liu, X. Zhang, "Preparation and gas-sensing properties of holey ZnO nanosheets doped by gold nanoparticles," Journal of Materials Science: Materials in Electronics," vol. 34(13), pp. 1109, 2023.

[9] M. Čonková, V. Montes-García, M. Konopka, A. Ciesielski, P. Samori, A. R. Stefankiewicz, "Schiff base capped gold nanoparticles for transition metal cation sensing in organic media," Chemical Communications vol. 58(38), pp. 5773-5776, 2022.

[10] V. Armendariz, I. Herrera, J. R. Peralta-Videa, M. Jose-Yacaman, H. Troiani, P. Santiago, J. L. Gardea-Torresdey, "Size controlled gold nanoparticle formation by Avena sativa biomass: use of plants in nanobiotechnology," Journal of nanoparticle research, vol. 6, pp. 377-382, 2004.

[11] T. Li, X. Zhang, X. Gao, J. Lin, F. Zhao, B. Zeng, "Sensitive dual-mode detection of carbendazim by molecularly imprinted electrochemical sensor based on biomass-derived carbon-loaded gold nanoparticles," Microchimica Acta, vol. 190(6), pp. 236, 2023.

[12] X. L. Cheng, T. R. Fu, D. F. Zhang, J. H. Xiong, W. Y. Yang, J. Du, "Biomass-assisted fabrication of rGO-AuNPs as surface-enhanced Raman scattering substrates for in-situ monitoring methylene blue degradation," Analytical Biochemistry, vol. 667, pp. 115087, 2023.

[13] M. Soltani Nejad, N. Samandari Najafabadi, S. Aghighi, E. Pakina, M. Zargar, "Evaluation of Phoma sp. biomass as an endophytic fungus for synthesis of extracellular gold nanoparticles with antibacterial and antifungal properties," Molecules, vol. 27(4), pp. 1181, 2022.

[14] A. G. Harby, O. M. El-Borady, M. El-Kemary, "The exploitation of rice husk biomass for the bio-inspired synthesis of gold nanoparticles as a multifunctional material for various biological and photocatalytic applications," Bioprocess and Biosystems Engineering, pp. 1-14, 2022.

[15] M. Y. Rather, M. Shincy, S. M. Sundarapandian, "Photocatalytic degradation of Rhodamine-B by phytosynthesized gold nanoparticles," International Journal of Environmental Science and Technology, vol. 20(4), pp. 4073-4084, 2023.

[16] M. Behera, P. R. Behera, P. P. Bhuyan, L. Singh, B. Pradhan, "Algal Nanoparticles and Their Antibacterial Activity: Current Research Status and Future Prospectives," Drugs and Drug Candidates, vol. 2(3), pp. 554-570, 2023.

[17] N. González-Ballesteros, S. Prado-López, J. B. Rodríguez-González, M. Lastra, M. Rodríguez-Argüelles, "Green synthesis of gold nanoparticles using brown algae Cystoseira baccata: Its activity in colon cancer cells," Colloids and Surfaces B: Biointerfaces, vol. 153, pp. 190-198, 2017.

[18] B. Sharma, D. D. Purkayastha, S. Hazra, M. Thajamanbi, C. R. Bhattacharjee, N. N. Ghosh, J. Rout, "Biosynthesis of fluorescent gold nanoparticles using an edible freshwater red alga, Lemanea fluviatilis (L.) C. Ag. and antioxidant activity of biomatrix loaded nanoparticles," Bioprocess and biosystems engineering, vol. 37, pp. 2559-2565, 2014.

[19] K. U. Suganya, K. Govindaraju, V. G. Kumar, T. S. Dhas, V. Karthick, G. Singaravelu, M. Elanchezhiyan, "Blue green alga mediated synthesis of gold nanoparticles and its antibacterial efficacy against Gram positive organisms," Materials Science and Engineering: C, vol. 47, pp. 351-356, 2015.

[20] L. H. Costa, J. V. Hemmer, E. H. Wanderlind, O. M. S. Gerlach, A. L. H. Santos, M. S. Tamanaha, G. I. Almerindo, "Green synthesis of gold nanoparticles obtained from algae Sargassum cymosum: optimization, characterization and stability," BioNanoScience, vol. 10, pp. 1049-1062, 2020.

[21] P. Senthilkumar, L. Surendran, B. Sudhagar, D. S. Ranjith Santhosh Kumar, "Facile green synthesis of gold nanoparticles from marine algae Gelidiella acerosa and evaluation of its biological Potential," SN Applied Sciences, vol. 1, pp. 1-12, 2019.

[22] E. O. Mikhailova, "Gold nanoparticles: biosynthesis and potential of biomedical application," Journal of Functional Biomaterials, vol. 12(4), pp. 70, 2021.

Enerji Verimliliğini Arttırarak Sürdürülebilirliği Sağlayan Merkezi Hidrolik Güç Ünitesi

Central Hydraulic Power Unit Ensuring Sustainability by Increasing Energy Efficiency

Mustafa Talha AKÇAY

talha.akcay@hidropar.com.tr, ORCID: 0009-0000-0568-4630
Tasarım ve Ar-Ge Merkezi, Hidropar İzmir, İzmir, Türkiye

Özet: Enerji verimliliği ürün ve hizmetlerin sağlanması için gereken enerji miktarını azaltma hedefidir. Bu sağlandığı taktirde ürün veya hizmetin ortaya çıkması için gereken işlemler daha az enerji ile gerçekleştirilebilir. Sınırlı kaynaklara sahip olduğumuzu bilerek, gelecek nesillerin kendi ihtiyaçlarını karşılama kabiliyetinden ödün vermeden kendi ihtiyaçlarımızı karşılamak günümüzün koşullarını ele aldığımızda ihtiyaçtan daha çok zorunluluk haline gelmiştir. Bu ihtiyaçları karşılamak sürdürülebilirliğin sağlanması için enerji verimliliğinin arttırılması büyük önem arz etmektedir. Böyle bir yeniliğe ihtiyaç olunmasının ana sebebi ise fabrikalardaki tüketilen enerjinin gereksiz denecek şekilde yüksek olması. Mevcut uygulamada, alüminyum döküm jant üretimi yapan fabrikalarda, bir holde yaklaşık 12 ile 15 adet arasında değişen, döküm tezgâhı bulunmaktadır. Her tezgâh 1 adet hidrolik güç ünitesi ile beslenmektedir. Tezgâhta 3 ana hidrolik eksen bulunur, yan maça pistonları + üst pleyt kapak pistonları ve itici pistonları. Sistemin çalışması; öncelikle yan maça pistonları kapanır, ardından üst pleyt kapak pistonu kapanır ve cevher kalıba alınır. Döküm tamamlandığında, üst pleyt kapak pistonu açılır, yan maça pistonları açılır ve itici pistonları jantı kalıptan çıkarır. Fabrikalarda her hol üzerinde bir güç ünitesi bulunmaktadır. Buradaki her ünite potansiyel bir arıza kaynağıdır ve üretim duruşlarına sebep olmaktadır. Tüketilen enerjinin yüksek olması, birim başına üretilen parça maliyetlerine olumsuz yansımaktadır. Bu çalışma kapsamında, otomotiv yan sanayisi, alüminyum jant fabrikalarında, jant üreten alçak döküm tezgahlarını tek kaynaktan beslemeye yarayan hidrolik sistem tasarımı incelenerek eski sisteme göre yapılan iyileştirmeler kalitatif ve kantitatif olarak açıklanacaktır. Yapılan iyileştirmelerin enerji verimliliğini önemli ölçüde artırdığını ve tüketilen enerji miktarında gözle görülür bir azalma sağladığı ortaya koyulacaktır. Bu yenilikçi yaklaşım, fabrikalardaki hidrolik güç ünitelerini entegre ederek, çok sayıda tezgâhta enerji tasarrufu sağlanmış ve bakım gereksinimlerini azaltmış olacaktır. Böylece, sürdürülebilir bir üretim süreci ve gelecek nesillere daha çevre dostu bir dünya bırakma hedefine katkıda bulunulacaktır. Bu çalışma, enerji verimliliği ve sürdürülebilirlik konularında ileriye dönük çözümler sunma açısından önemli bir adım olarak değerlendirilebilir.

AnahtarKelimeler: *Enerji Verimliliği, Sürdürülebilirlik, Hidrolik Sistem Tasarımı*

Abstract: Energy efficiency is the goal of reducing the amount of energy required to provide products and services. If this is achieved, the processes required to create the product or service can be realized with less energy. Knowing that we have limited resources, meeting our own needs without compromising the ability of future generations to meet their own needs has become a necessity rather than an obligation when we consider today's conditions. Increasing energy efficiency is of great importance in order to meet these needs and ensure sustainability.

The main reason for the need for such an innovation is that the energy consumed in the factories is unnecessarily high. In the current practice, there are approximately 12 to 15 Casting Benches in a hall in factories producing aluminum casting rims. Each bench is fed by 1 hydraulic power unit. One bench has 3 Main Hydraulic axes, side core pistons + top plate cover pistons and ejector pistons. The operation of the system; First of all, the side core pistons are closed, then the upper plate cover piston is closed and the ore is taken into the mold. When the casting is complete, the top plate lid piston opens, the side core pistons open and the pusher pistons remove the rim from the mold. There is a power unit on each hall in the factories. Every unit here is a potential source of failure and causes production downtime. The high consumption of energy has a negative impact on the cost of parts produced per unit. Within the scope of this study, the hydraulic system design, which is used to feed the low casting benches producing rims from a single source in the aluminum rim factories of the automotive supplier industry, will be examined and the improvements made according to the old system will be explained qualitatively and quantitatively. It will be revealed that the improvements made significantly increase the energy efficiency and provide a noticeable decrease in the amount of energy consumed. By integrating hydraulic power units in factories, this innovative approach will save energy and reduce maintenance requirements in many machines. Thus, it will contribute to the goal of leaving a sustainable production process and a more environmentally friendly world to future generations. This study can be considered as an important step in terms of providing forward-looking solutions on energy efficiency and sustainability.

Keywords: *Energy Efficiency, Sustainability, Hydraulic System Design*

I. GİRİŞ

Günümüzde sürdürülebilirlik kavramı neredeyse her alanda çok yaygın şekilde kullanılmaya ve gelecek nesillerin kendi ihtiyaçlarını karşılama kabiliyetinden ödün vermeden kendi ihtiyaçlarımızı karşılama esasına dayanmaktadır [1]. Kısaca açıklanması gerekirse; sınırlı kaynaklara sahip olduğumuzu bilmek anlamına gelir ve günümüzde git gide önemi artmaktadır. Rüzgâr, jeotermal, dalga, gelgit, güneş enerjisi gibi yenilenebilir enerji kaynaklarını kullanarak enerjinin devamlı olarak var olması yani tüketilememesini açıklayan kavrama sürdürülebilir enerji denir. Bu kaynaklar haricinde de enerji kullanımın verimliliğini arttırarak sürdürülebilirlik hedefi sağlanabilir. Enerji verimliliği ürün ve hizmetlerin sağlanması için gereken enerji miktarını azaltma hedefidir [2]. Enerji verimliliği ve yenilenebilir enerjinin sürdürülebilir enerji politikasının "ikiz sütunları" olduğu ve sürdürülebilir enerji hiyerarşisinin yüksek öncelikleri olduğu söylenmektedir [3]. Enerji kullanımının azaltılması, sera gazı emisyonlarının azaltılması sorununa da bir çözüm olarak görülmektedir. Uluslararası Enerji Ajansı'na göre, binalarda, endüstriyel süreçlerde ve ulaşımda iyileştirilmiş enerji verimliliği, 2050'de dünya enerji ihtiyaçlarını üçte bir oranında azaltabilir ve küresel sera gazı emisyonlarının kontrolüne yardımcı olabilir [4]. Enerji verimliliğini arttırmak amacıyla öncelikle enerji tüketiminin en yüksek olduğu alanlar incelenmelidir; bu alanların başında fabrikalar gelmektedir. Fabrikalardaki üretim istasyonlarında çok sayıda hidrolik pompa ve motor türü bulunmaktadır, genellikle tek bir hat için tek bir sistem kullanılmaktadır. Fabrikadan fabrikaya farklılık gösterse de döküm tezgâhları gibi sistemler genellikle hidrolik tabanlıdır.

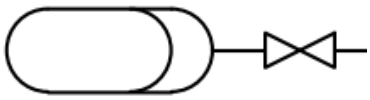
Bu çalışma kapsamında, otomotiv yan sanayisi, alüminyum jant fabrikalarında, jant üreten alçak döküm tezgahlarını tek kaynaktan beslemeye yarayan hidrolik sistem tasarımı incelenerek eski sisteme göre yapılan iyileştirmeler kalitatif ve kantitatif olarak açıklanacaktır.

II. LİTERATÜR ARAŞTIRMASI

Endüstriyel hidrolik sistemler, kuvvet ve gücün ön planda olduğu yerlerde kullanılırlar.

Hidrolik sistemlerde bahsedilen güç ve kuvvetin sağlanması için çeşitli avantajların yanında dezavantajları da bulunmaktadır. Avantajları; yüksek güç aktarımı, yüksek hassasiyet ve kontrol, ani basınç değişimlerine karşı güvenlidir, işletme maliyetlerini alternatiflerine nazaran düşürür, uzun ömürlü olmaları gibi birçok avantajı bulunmaktadır. Dezavantajları; Bakım gereksinimi (yağ temizliği ve filtre bakımı), sızıntı riskinin olması (yağ kaybı ve çevre kirliliğine sebep olabilir), ilk yatırım maliyetinin yüksek olması gibi dezavantajları vardır [5]. Bazı dezavantajların gerçekleştirilmesi sisteme avantaj da sağlayabilir. Örneğin sistemin uzun ömürlü olmasını istiyorsak bakım gereksinimlerinin iyi karşılanması gerekmektedir ya da işletme giderlerinin düşük olmasını istiyorsak ilk yatırım maliyetine katlanmamız gerekebilir.

Hidrolik sistemlerin avantajları ve dezavantajlarını gösterdikten sonra basit bir iki şema ile mevcut sistemlerde bulunan hidrolik ekipmanlar açıklanabilir. Hidrolik sistemler genellikle tank, elektrik motor, hidrolik pompa, basınç emniyet valfi, yön valfi, kısma valfi, akış kontrol valfi ve silindirden oluşur. Bunlar dışında sensör, gösterge, manometre, akümülatör, vana ve ara bağlantı elemanları gibi birçok ekipman sistemin ihtiyacına göre eklenebilir. Kısaca görevlerini açıklarsak; tank kısmında sistemi besleyen hidrolik yağ depolanır. Elektrik motor, elektrik enerjisini mekanik enerjiye dönüştüren cihazdır. Hidrolik pompa, mekanik enerjiyi hidrolik enerjiye dönüştürerek sistemdeki debi (bir kesitten birim zamanda akan sıvı hacmi) miktarının büyüklüğünün belirlenmesinde ana rol oynayan bir devre elemandır. Elektrik motor ve hidrolik pompa sistemde kaplin, kampana adı verilen parçalar ile entegrasyonu sağlanmaktadır. Basınç emniyet valfi, sistemin güvenliğini sağlamak amacıyla akışın belirli bir eşik değeri geçtiği anda tank hattını açarak geri dönüşünü sağlayan bir hidrolik sistem ekipmanıdır. Yön valfi; içerisindeki oda ve yön sayısına bağlı olarak farklı çeşitleri olsa da temel olarak akışın yönünü kontrol etmek için kullanılan valftir. Kısma valfi, bir sistemdeki akış hızını kontrol etmek için kullanılır. Akış kontrol valfi ise akışı tamamen kapatmak veya açmak için kullanılan bir valftir. İki valfin işlevi çok benzese de akış kontrol valfi; hassas bir şekilde kısma imkânı sağlar. Silindir (Şek. 2), hidrolik sistemlerde mekanik hareketin üretildiği ve kontrol edildiği önemli bir bileşendir. Bir piston ve bir silindir içindeki hidrolik yağın oluşturduğu basınç sayesinde ileri ve geri doğru hareket ederler. Akümülatör (Şek. 1), hidrolik sistemlerdeki enerji depolama ve ani basınç değişimlerini dengeleyerek sistem performansını optimize eden cihazlarıdır. Vana (Şek. 1), hidrolik hatlardaki akışın engellenmesi, yönünün değiştirilmesi ve deşarj işlemlerinde kullanılır, ayrıca herhangi bir valfi sökmek gerektiğinde bulunduğu hattaki yağı boşaltmaya gerek kalmaması için devrede kullanılabilir.



Şek. 1. Akümülatör ve vana şematik çizim

Bunlar gibi hidrolik sistemlerde çokça eleman bulunmaktadır, istenilen sisteme göre ekstra malzemeler de kullanılarak dizayn edilip tasarlanılabilir. Bahsedilen sistemin halka alanı (A_1), piston alanı (A_2), çalışma basınç (p), hacim (V) güç (P) ve debi (Q) hesabı silindirin strok uzunluğu (h), halka çapı (D), piston çapı (d), alan (A), verim (η), piston hızı (v) ve kuvvete (F) göre belirlenebilir [6]:

$$A_1 = \frac{\pi \, x \, D^2}{4} \quad (1)$$

$$A_2 = \frac{\pi \, x \, (D^2 - d^2)}{4} \quad (2)$$

$$p = \frac{F}{A} \quad (3)$$

$$V = A \, x \, h \quad (4)$$

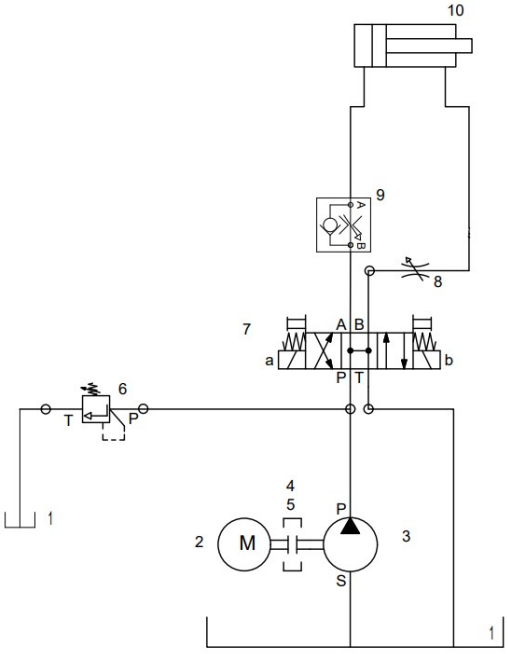
$$P = \frac{p\ x\ Q}{600\ x\ \eta} \tag{5}$$

$$Q = v\ x\ A \tag{6}$$

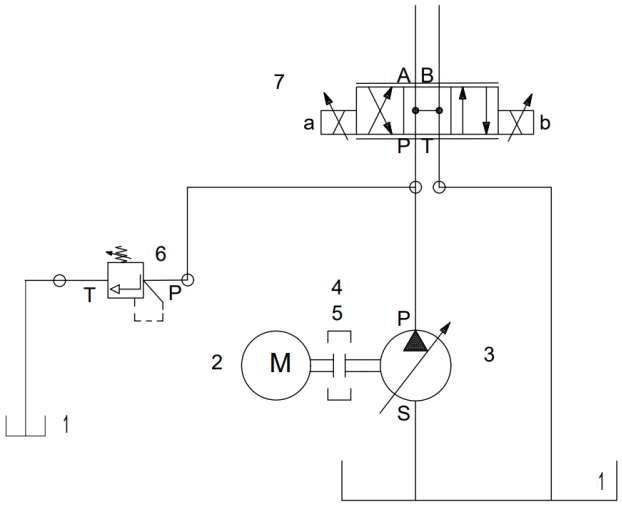


Şek. 2. Silindir şematik çizim

X hidrolik sistemi (Şek. 3) temel hidrolik bileşenlerden oluşan basit bir sistemdir. İçerisinde sırasıyla yağ depolama tankı, elektrik motor, hidrolik pompa, kaplin ve kampana, basınç emniyet valfi, yön valfi, kısma valfi, akış kontrol valfi ve silindir bulunmaktadır. Kontrol edilebilirlik açısından mevcut olan sistemin daha verimli versiyonu Y hidrolik sisteminde (Şek. 4) gösterilmiştir. Bu sistemin avantajı değişken debili pompa ve oransal valfi sayesinde olur. Değişken debili pompa, sabit debili pompalardan farklı olarak ihtiyaç duyulan akışın hızına göre debisini ayarlayabilir. Bu da hidrolik sistemlerin enerji verimliliğini artırır çünkü sadece gereken akış hızında çalışarak enerji tüketimini azaltır. Oransal valf, hidrolik sistemlerde akış hızını ve basıncını hassas bir şekilde kontrol etmek için kullanılır. Bunun sağladığı hassas kontrol, normal yön valflerine göre gereksiz bir enerji tüketimi sağladığı için pompanın aksine hidrolik sistemi daha verimsiz hale getirir fakat kontrol sistemini daha verimli çalışır. Bu iki sistemin gösterimindeki amaç; farklı gereksinimlerde farklı sistemlerin kurulabileceğini göstermektir.



Şek. 3. X hidrolik sistemi

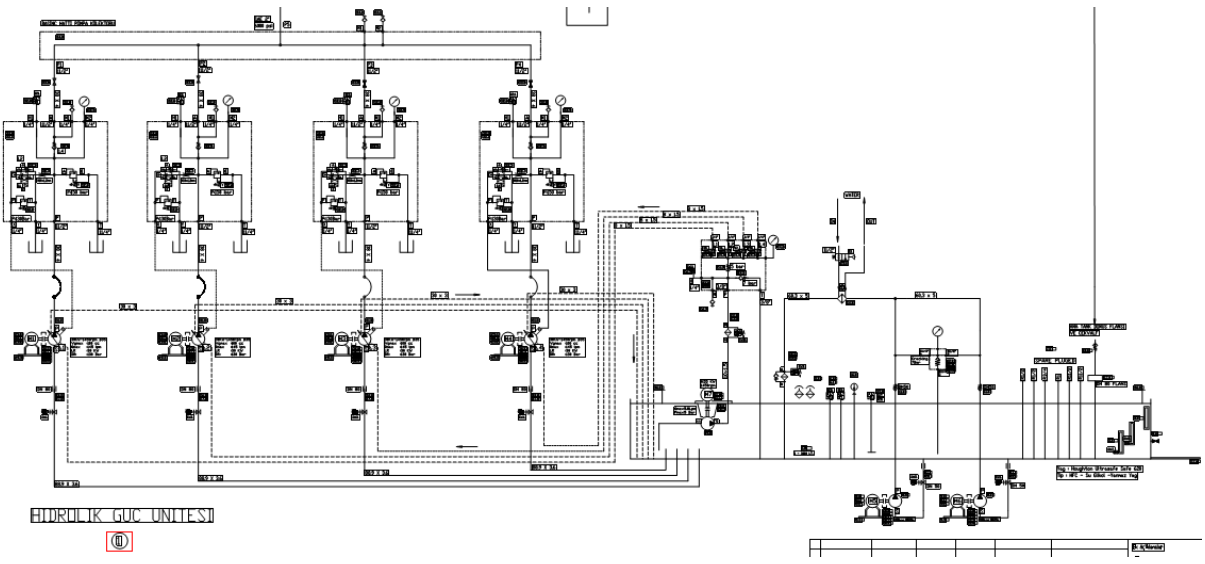


Şek. 4. Y hidrolik sistemi

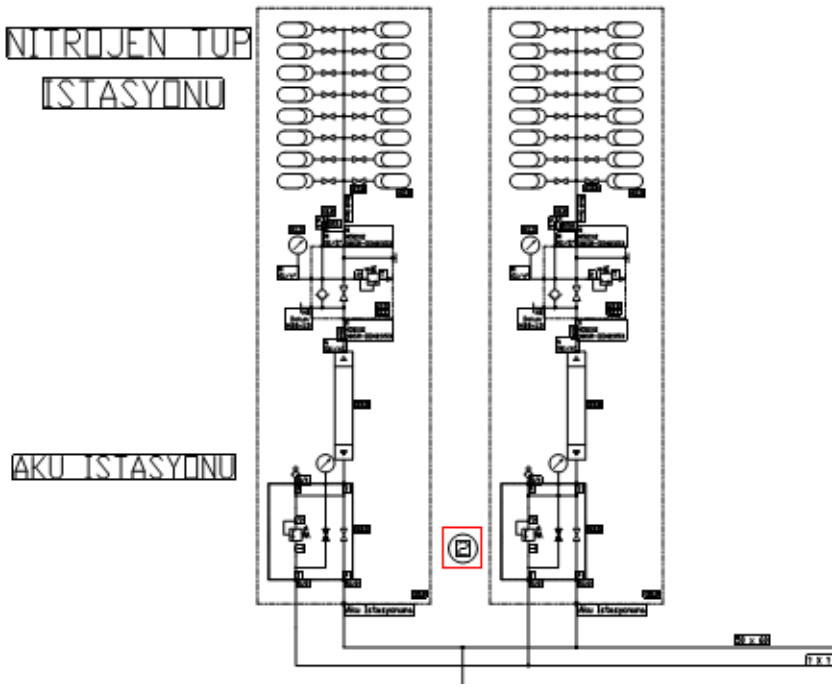
III. METOT VE YÖNTEM

Hidrolik sistemleri fabrika özeline indirip incelediğimizde mevcut uygulamada, her tezgâh bir adet 22 kilowatt (kW) Elektrik motoru x 145 litre/dakika (lt/dk) debi üreten pompa ile beslenir (Bu fabrika için geçerli verilerdir). Toplamda bir hatta/holde; 22kW X 15 ADET = 330 kW güç tüketilmektedir.

Tüketilen büyük enerjinin azaltılması için, tezgâh başına pistonların ihtiyaç duyduğu toplam debi miktarı hesaplanıp, aynı anda kaç tezgâhın birlikte çalışacağı da hesaba katılarak, ihtiyaç duyulan toplam debi miktarı bulunmuştur. Daha sonra kurulu gücün düşürülmesi ve enerji sarfiyatının azaltılması için istenen debi miktarının Akümülatörde biriktirilmesi fikri masaya yatırılmıştır. Böylece pompa sayısı düşecek, akümülatörde yağ biriktirilecektir. Pompa sayısının azalması, elektrik motoru sayını azaltacak kurulu gücü de düşürmektedir. Bu sayede enerji daha verimli bir şekilde kullanılmış olacaktır. 15 adet Tank/Güç ünitesi yerine 3000lt tek tank tüm tezgâhları besleyecek özellikte dizayn edilen merkezi hidrolik güç ünitesi (Şek. 5) ve mevcut uygulamada 15 adet pompa ile beslenen sistemin ihtiyaç duyduğu debi miktarını bünyesinde biriktiren akümülatör istasyonunun (Şek. 6) 2D teknik çizimleri sistemin büyük ama kompakt bir yapıda olduğunu efektif bir şekilde ifade etmektedir.

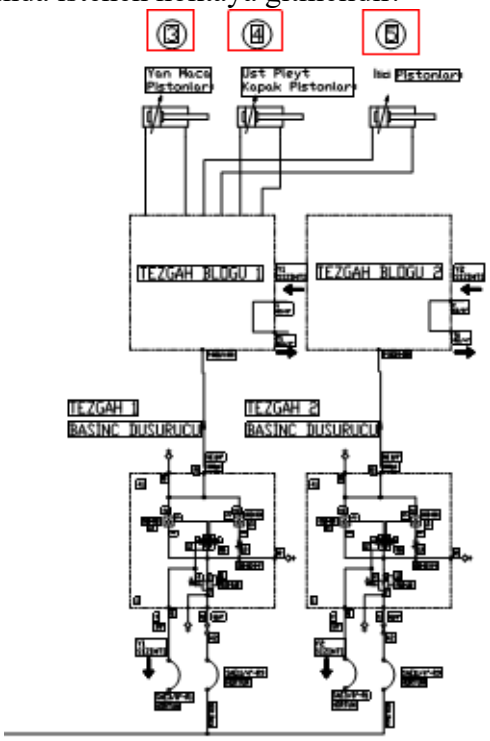


Şek. 5. Merkezi hidrolik güç ünitesi 2D şematik çizim



Şek. 6. Akümülatör istasyonu 2D şematik çizim

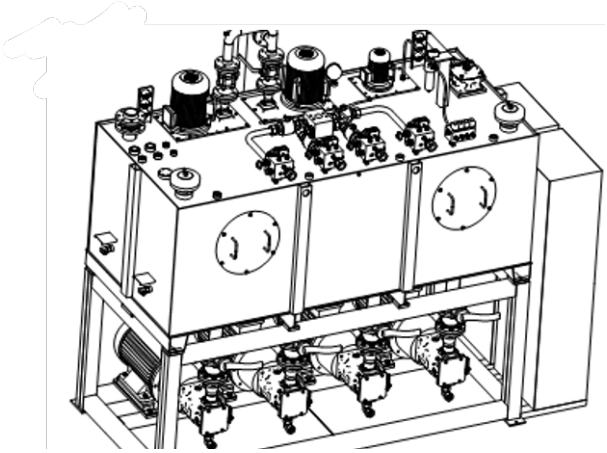
Alçak Döküm tezgahlarında çok hassas bir proses işlemektedir. Döküm haznesini açan kapatan Üst Pleyt Kapak Pistonu (Şek. 7), maça pistonlarını hareket ettiren (Şek. 7) ve Jantı kalıptan çıkaran itici pistonlar (Şek. 7) ardışık olarak belli harmoni içinde çalışmaktadır. Sistemde hareketler belli bir çevrim zamanı içinde ardışık olarak tamamlanmalı ve eksenler darbesiz olarak istenen zamanda istenen noktaya gitmelidir.



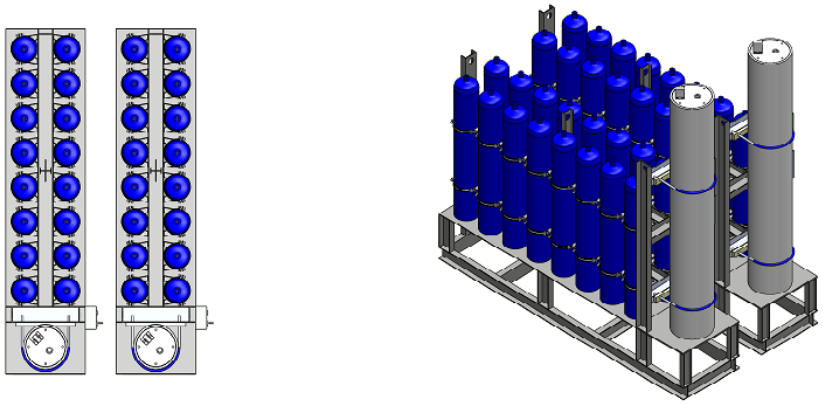
Şek. 7. Hidrolik pistonlar ve kontrol blokları

15 adet tezgâhta bu çevrimleri aynı anda sağlamasını garanti edecek hidrolik kaynak (Şek. 8), pompa debilerinden sağlanmamıştır. 400lt hacminde Pistonlu aküler standı (Şek. 9)

kullanılarak basınçlı yağ biriktirilecek, sistem ihtiyaç duyduğunda valf üzerinden eksenlere gönderilecektir. Hidrolik güç ünitesi, 4 adet 30kW elektrik motoru, 4 adet 145lt/dk pompadan oluşmaktadır. Sistemde 2 adet pompa aktif olarak çalışacak, diğer ikisi ihtiyaç olması durumunda, otomasyon yazılımında tanımlandığı şekilde devreye girebilecektir. Akülerde azalan yağ, pompalar ile takviye edilecektir. Bu durumda pompa sayımız alacak, kurulu gücümüz düşecektir. Sistem daha kompakt ve daha yalın bir hale gelecektir. Kurulu gücün azalması enerji maliyetlerini aşağı çekecek, maliyet azalması durumunda, birim maliyeti azalacak ve firmanın rekabet gücü artacaktır.



Şek. 8. Merkezi hidrolik güç ünitesi 3D genel görünümü



Şek. 9. Akümülatör standı 3D genel görünümü

IV. HESAPLAMALAR VE DEĞERLENDİRMELER

Mevcut uygulamada 22 kW güç sağlanmaktadır ve elektrik tüketimi (ET) 13,56 kilowatt saat (kWsa)'dir (enerji analizöründen ölçülen değer). Toplam üretim (1 tezgâh için) 12 parçadır. Çevrim süresi (ÇS):

$$ÇS = \frac{T}{N} = \frac{60\ (dakika)}{12\ (parça)} = 5\,\frac{dakika}{parça} \tag{7}$$

Bir parça için elektrik tüketimi (ET_1):

$$ET_1 = \frac{\sum(ET)}{TÜ} = \frac{13{,}56\ (kWsa)}{12} = 1.13\ kWsa \tag{8}$$

Yeni uygulanan sistemde merkezi ünite kurulu gücü 60 kW (15 tezgâh için) ve elektrik tüketimi 39 kWsa olarak ölçülmüştür. Çevrim süresi mevcut olan uygulama ile aynı olup 5 dk/parça'dır. Toplam üretim (15 tezgâh için) 180 parçadır. Bir parça için elektrik tüketimi (ET_2):

$$ET_2 = \frac{\sum(ET)}{TÜ} = \frac{39\ (kWsa)}{180} = 0{,}22\ kWsa \tag{9}$$

Mevcut olan ve yeni uygulan sistem arasındaki ET farkı:

$$ET = ET_1 - ET_2 = 1{,}13kWsa - 0{,}22kWsa = 0{,}91\ kWsa \quad (10)$$

Fabrikadaki 1 günde ortaya çıkan parça sayısı:

$$N = \frac{15\ (Tezgâh)}{(Hol)}\ x\ \frac{12\ (Parça)}{(Tezgâh)(Saat)}\ x\ \frac{24\ (Saat)}{(Gün)} = \frac{4320\ (Parça)}{(Hol)(Gün)} \quad (11)$$

Ortalama çıkan parça sayısına hata paylarını da göz önüne alarak 4300 parça/gün diyebiliriz. 1 yıl içerisinde 300 çalışma günü bulunmaktadır. Fabrikadaki 1 yılda ortaya çıkan parça sayısı:

$$N = \frac{4300\ (Parça)}{(Gün)}\ x\ \frac{300\ (Gün)}{(Yıl)} = \frac{1.290.000\ (Parça)}{(Yıl)} \quad (12)$$

Fabrikadaki 1 yılda mevcut olan ve yeni uygulan sistem arasındaki ET farkı:

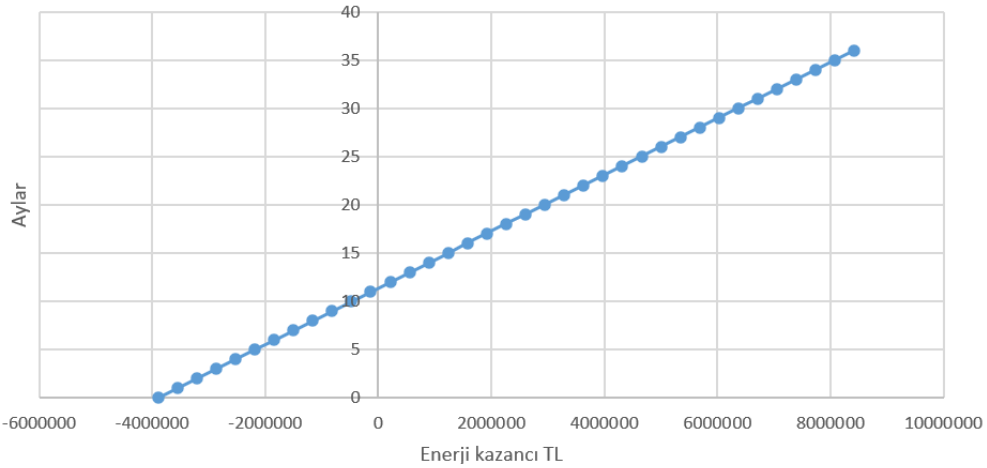
$$ET = \frac{1290000\ (Parça)}{(Yıl)}\ x\ \frac{0.91\ (kWsa)}{(Parça)} = \frac{1.173.900\ (kWsa)}{(Yıl)} \quad (13)$$

Bugünkü 1 kWsa enerji kullanımı için ödeme yapılan tutar yaklaşık 3,5 TL'dir [7]. Buna göre kâr miktarı:

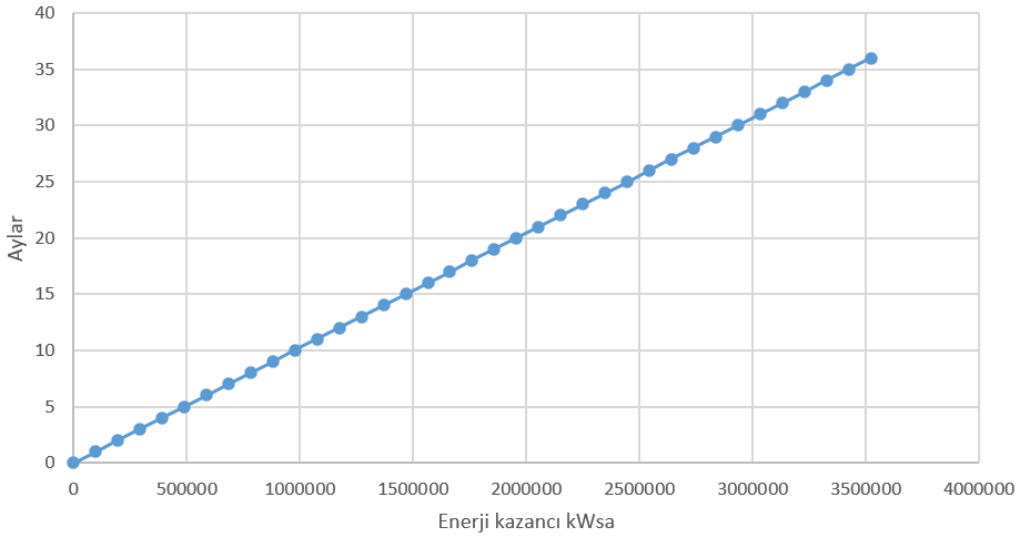
$$Kâr = \frac{1173900\ (kWsa)}{(Yıl)}\ x\ \frac{3{,}5\ (TL)}{(kWsa)} = \frac{4.108.650\ (TL)}{(Yıl)} \quad (15)$$

Malzeme ve işçilik maliyetleri tek bir maliyet olarak hesaplandığında yaklaşık 3.900.000 TL ediyor. Aylara göre enerji kazanç tablosuna (Şek. 10) bakıldığında 1 kWsa enerji kullanımı için ödeme yapılan tutar değişmediği sürece yapılan yatırımın 12 ay yani 1 yıl sonra başa baş noktasını (kâr ve zararın sıfır olduğu nokta) geçtiğini hesaplamaktayız. 36 ay içerisinde ise yapılan yatırım 2 katından daha fazla kâr edildiği görülmektedir. Elektrik tüketimi açısından aylara göre enerji kazanç tablosuna (Şek. 11) bakıldığında 1 parça için elektrik tüketimi değişmediği varsayılarak 12. Ayda 1.173.900 kWsa elektrik tüketiminden kâr edildiği hesaplanmıştır. 36. Ayda ise 3.521.700 kWsa daha az enerji harcandığını görülmektedir.

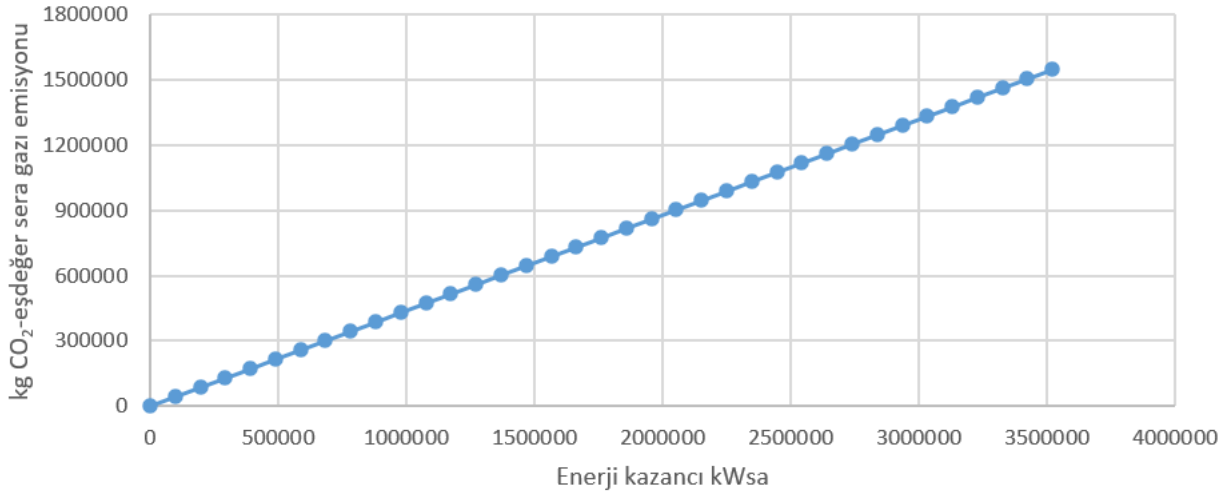
Hesaplamalara göre, Türkiye genelinde 1 kWsa (birim) net elektrik üretimi başına ortalama 0,44 kg CO_2-eşdeğer sera gazı emisyonu salınmaktadır [8]. Aylara göre elektrik üretimi başına salınmayan sera gazı emisyonu tablosuna (Şek. 12) bakıldığında başa baş noktasında (12. Ay) yaklaşık 473 bin kg CO_2-eşdeğer sera gazı emisyonu salınımı engellenebildiği hesaplanmıştır. 36 ay içerisinde ise yaklaşık 1,5 milyon kg CO_2-eşdeğer sera gazı emisyonu salınımı engellenebileceği görülmektedir.



Şek. 10. Aylara göre enerji kazanç tablosu (TL)



Şek. 11. Aylara göre enerji kazanç tablosu (kWsa)



Şek. 12. Aylara göre elektrik üretimi başına salınmayan sera gazı emisyonu tablosu

V. SONUÇLAR

Birleşmiş Milletler'in belirlediği 17 hedef doğrultusunda 2030'a kadar gerçekleştirilmesi amaçlanan sürdürülebilir hedefler doğrultusunda enerjinin sürdürülebilir olması istenmektedir. Sera gazı emisyonu azaltım hedefi doğrultusunda Türkiye'nin 2053'te net sıfır hedefine ulaşabilmesi için 2030'da en az %35 emisyon azaltımı gerçekleştirmesi gereklidir. Enerji verimliliği sağlandığında, enerji üretim ve tüketim süreçlerinde daha az fosil yakıt kullanılır ve bu da sera gazı emisyonlarının azalmasına yardımcı olur. Bu çalışmada, enerji verimliliği arttırılıp sürdürülebilir bir üretim aşaması sağlanması amacıyla gerçekleştirilen merkezi hidrolik güç ünitesinin karmaşık yapısı detaya çok inmemeye çalışılarak mevcut sisteme kıyasla olan avantajları ve dezavantajları, nicel ve nitel olarak incelenmiştir. Bu incelemelerin sonucunda ilk yatırım maliyeti yüksek ve kurulum için daha büyük bir alan gerekli olmasına rağmen kurulu gücün azaltılması ile maliyet ve enerji tüketimini de doğru orantılı olarak azalttığı görülmüştür. Ayrıca Türkiye'nin net sıfır hedefine ulaşma doğrultusunda sera gazı emisyonlarını azaltmaya katkısından dolayı uluslararası ilişkilerde de politik bir öneme sahiptir.

EK

Tablo. 1. Merkezi hidrolik güç ünitesi hesabı için birimler

Semb.	Büyüklük	SI birim sistemi
F	Kuvvet	1 F → 1 ton = 10.000 daN
p	Çalışma Basıncı	1 p → 1 bar = 100.000 pa
V	Hacim	1 V → 1 cm^3 = 0,001 dm^3
A	Alan	1 A → 1 cm^2 = 100 mm^2 = 0,0001 m^2
D	Piston halka çapı	1 D → 1 cm = 10 mm = 0,01 m
d	Piston kolu çapı	1 d → 1 cm = 10 mm = 0,01 m
v	Piston hızı	1 v → 1 cm/sn
h	Strok	1 h → 1 cm
Q	Debi	1 Q → 1 lt/dk
P	Tahrik gücü	1 P → 1 kW
η	Verim	
TÜ	Toplam üretim	1 TÜ → parça
ET	Elektrik tüketimi	1 ET → kWsa
W	Watt	1 W → 0.001 kW
ÇS	Çevrim süresi	1 ÇS → dk/parça
T	Toplam üretim süresi	1 T → dk
N	Üretilen parça sayısı	1 N→ parça

da=deka, N=newton, pa=pascal, dm=desimetre, m=metre , mm=milimetre, sn=saniye, cm=santimetre, lt=litre, sa=saat, k=kilo, dk = dakika.

REFERANSLAR

[1] Gedik Y., "Sosyal, Ekonomik Ve Çevresel Boyutlarla Sürdürülebilirlik Ve Sürdürülebilir Kalkinma" vol. III, International Journal of Economics, Politics, Humanities & Social Sciences, Yaz 2020, s. 2.

[2] Diesendorf, Mark (2007). Greenhouse Solutions with Sustainable Energy, UNSW Press, s. 86.

[3] Prindle, Bill and others (Mayıs 2007). The twin pillars of sustainable energy: synergies between energy efficiency and renewable energy technology and policy. Washington, DC, USA: American Council for an Energy-Efficient Economy (ACEEE). 18 Mart 2018.

[4] Sophie Hebden (22 Haziran 2006). "Invest in clean technology says IEA report". Scidev.net. 26 Eylül 2007.

[5] Karacan İ. (1987). "Endüstriyel Hidrolik". Teknik Eğitim Fakültesi Matbaası.

[6] TMMOB (2005). "Hidrolik Devre Elemanları ve Uygulama Teknikleri". MMO yayınları. Yayın No: 292.

[7] T.C. Enerji Piyasası Düzenleme Kurumu (1 Ağustos 2023). "Fatura Hesaplama Modülü".

[8] T.C. Enerji ve Tabii Kaynaklar Bakanlığı (9 Ağustos 2022). "Türkiye Elektrik Üretimi ve Elektrik Tüketim Noktası Emisyon Faktörleri".

Prediction of Diabetes Mellitus Using Tree-Based Machine Learning Algorithms: A Comparative Analysis

Serkan KARTAL

skartal@cu.edu.tr, ORCID: 0000-0001-9801-8986
Department of Computer Engineering, Cukurova University, Adana, Turkey

Abstract: Diabetes mellitus is a prevalent chronic disease that affects millions of individuals worldwide, with profound implications for public health. This condition is characterized by elevated blood sugar levels resulting from either insufficient insulin production or the body's ineffective use of insulin. Diabetes has multifactorial causes, encompassing genetic predisposition, lifestyle factors like diet and physical activity, as well as environmental influences. If left unmanaged, diabetes can precipitate a wide array of severe health complications, including cardiovascular diseases, kidney failure, blindness, neuropathy, and lower limb amputations. Consequently, the timely identification of individuals at risk of developing diabetes is imperative for effective prevention and management. In this study, the application of machine learning (ML) algorithms for diabetes prediction was investigated, with a specific focus on three widely-utilized tree-based ML algorithms: Random Forests (RF), Extreme Gradient Boosting (XGB), and Extremely Randomized Trees (ERT). To optimize the performance of these models, they were fine-tuned using the FLAML library, with each model allotted one hour for configuration. Model performance was evaluated using the standard accuracy metric. The results unequivocally demonstrated the effectiveness of ML algorithms in predicting the risk of diabetes mellitus. Among the algorithms studied, XGB emerged as the top-performing model, achieving an impressive accuracy rate of 79.22%. RF and ERT also exhibited commendable performance, with accuracy values of 78.57% and 77.27%, respectively. In conclusion, robust and effective tools for predicting diabetes mellitus are offered by tree-based ML algorithms, with XGB being identified as a particularly reliable choice. Great promise is held by these models in enhancing early risk identification and enabling personalized healthcare interventions. Future research directions may encompass the integration of additional clinical and genetic data to further enhance predictive accuracy and facilitate the development of user-friendly clinical decision support systems.

Keywords: *Machine Learning, Diabetes Mellitus, Random Forests, Extreme Gradient Boosting, Extremely Randomized Trees*

I. INTRODUCTION

Diabetes Mellitus, commonly referred to as diabetes, represents one of the most prevalent and challenging chronic diseases affecting communities worldwide [1]. It is a serious health issue characterized by uncontrolled sugar levels and is associated with a range of severe complications such as cardiovascular diseases, kidney failure, blindness, and lower limb amputations. This not only places a significant burden on affected individuals but also exerts immense pressure on healthcare systems globally.

While the primary cause of diabetes is sugar concentration, various factors like height, weight, genetic factors, and insulin play significant roles in influencing diabetes. Amidst these challenges, the early detection of individuals at risk of developing diabetes holds vital

importance for effective prevention and management. Early intervention has the potential to alter the course of diabetes, delay its onset, and reduce the risk of complications [2, 3, 4]. Consequently, there is a growing interest within medical and research communities in developing robust prediction models aimed at identifying high-risk individuals. In recent years, especially in the field of healthcare, advancements in machine learning (ML) have raised hopes for more effective predictive modelling and early risk identification. ML techniques possess the capacity to analyses large and complex datasets, revealing patterns and relationships that traditional statistical methods may overlook. This translates to the ability to make more precise predictions in healthcare, potentially revolutionizing disease prevention and management.

Li et al. [5] examined some ML models including Naive Bayes (NB), Support Vector Machines (SVM), and Artificial Neural Network (ANN) classifiers and proposed a new approach that combined these three classifiers for diagnosing diabetes. Their method adjusted classifier weights based on their historical performance and used a rule that blended majority voting and classifier weights. Experimental comparisons showed that their approach outperformed other methods in terms of sensitivity using the Pima Indians diabetes dataset. Kandhasamy et al. [6] assessed ML classifiers, including J48 Decision Tree (DT), K-Nearest Neighbours (knn), Random Forest (RF), and SVM, for early-stage diabetes prediction using datasets from the UCI ML data repository. Hasan et al. [7] dealt with the challenge of accurate diabetes prediction by proposing a robust framework that included outlier rejection, missing value handling, data standardization, feature selection, and the use of various ML classifiers (knn, DT, RF, AdaBoost, NB, and Extreme Gradient Boosting (XGB)). Additionally, they introduced a weighted ensembling approach based on the Area Under ROC Curve (AUC) to improve prediction accuracy. Yahyaoui et al. [8] proposed a Decision Support System for diabetes prediction using both conventional ML methods (SVM and RF) and deep learning approaches (Convolutional Neural Network). Their evaluation indicated that the RF method outperformed deep learning and SVM in terms of accuracy, achieving an accuracy rate of 83.67%.

Among the various branches of ML, tree-based algorithms have garnered attention. RF and XGB are well-established tree-based ML algorithms that have achieved significant success in this field. This study aims to investigate how three established tree-based ML algorithms, RF, XGB, and Extremely Randomized Trees (ERT), can be employed in the domain of diabetes prediction. Thus, this study aims to evaluate the performance of these algorithms and identify the most effective predictors of diabetes risk, contributing to ongoing efforts to improve early risk detection and ultimately facilitate more personalized health interventions in the context of diabetes.

II. DATASET

The data, sourced from the UCI repository is the Pima Indian Diabetes Dataset, contains information from 768 patients. The ninth attribute in this dataset serves as the class variable, with values of 0 indicating a negative outcome (no diabetes) and 1 indicating a positive outcome (diabetic). While constructing a diabetes prediction model, it's important to note that the dataset exhibits a slight class imbalance, with approximately 500 instances labelled as 0 (no diabetes) and 268 instances labelled as 1 (diabetic).

The dataset's primary goal is to develop a predictive model for diagnosing diabetes in female patients aged at least 21 years and of Pima Indian heritage. So, AI models' task is to determine whether a patient has diabetes (Outcome = 1) or does not have diabetes (Outcome = 0) based on various diagnostic measurements, including glucose level, blood pressure, skin thickness, insulin level, body mass index, diabetes pedigree function, and age. Attributes of the Dataset and their explanations are given in Table 1.

Table 1. Attributes of the dataset and their explanations

Att. No	Att. Name	Meaning
1	Pregnancies	Number of pregnancies
2	Glucose	Plasma glucose level in blood
3	Blood Pressure	Blood pressure measurement
4	Skin Thickness	Thickness of the skin
5	Insulin	Insulin level in blood
6	BMI	Body mass index
7	Diabetes Pedigree Function	Diabetes percentage
8	Age	Age
9	Outcome	Final result: 1 indicates that the individual has diabetes. 0 indicates that the individual does not have diabetes

III. METHODOLOGY

In this study, three distinct ML models—RF, XGB, and ERT—were employed for early diabetes prediction. Each of these algorithms has its own distinct methods for constructing and combining DTs, which contribute to their effectiveness across diverse ML and predictive analytics domains. These algorithms have demonstrated remarkable success in real-world applications due to their ability to handle complex relationships, mitigate overfitting, and deliver high-quality predictions. The details of the models are described below, respectively.

A. Random Forests (RF):

RF is an ensemble learning method based on DTs. It works by constructing a multiple DTs during training and then combines their predictions to make a more accurate and robust prediction. Each tree in the forest is generated using a random subset of the training data and a random subset of the features. This randomness helps prevent overfitting and enhances the generalization abilities of the model. When making predictions, RF aggregates the outputs of individual trees, typically using majority voting for classification or averaging for regression. RF is known for its versatility, ability to handle large datasets, and resistance to overfitting. More detailed information can be accessed from the original paper [9].

B. Extreme Gradient Boosting (XGB):

Extreme Gradient Boosting, often abbreviated as XGB, is a powerful and efficient gradient boosting framework that has gained popularity in ML competitions and real-world applications. XGB is an ensemble technique that sequentially creates DTs where each tree tries to correct the mistakes made by the previous ones. It focuses on reducing the model's prediction error by optimizing a specified loss function. XGB uses a number of regularization techniques to control overfitting and fine-tune model parameters via gradient descent. This approach typically results in highly accurate models that can handle complex relationships within the data while maintaining good generalization performance. Detailed information about the model and formulas can be found in the original paper [10].

C. Extremely Randomized Trees (ERT):

Extremely Randomized Trees, or Extra-Trees, is another ensemble learning method that builds multiple DTs like RF. However, ERT differs in the way it constructs each tree. In ERT, not only are random subsets of data used but also random thresholds for feature splitting are applied. This additional randomness makes ERT even more resistant to overfitting compared to RF. ERT is particularly useful when dealing with noisy or high-dimensional datasets, as it can reduce the variance of the model while maintaining predictive accuracy. Additionally, ERT

is computationally efficient, making it suitable for large-scale applications. Detailed information about the model can be found in the original paper [11].

IV. RESULTS AND DISCUSSIONS

In this study three well known ML models, namely RF, XGB, and ERT, were utilized for early diabetes prediction. The models rely on a range of hyperparameters, such as the number of trees and tree depth, which play a critical role in achieving accurate predictions. Optimizing all of these hyperparameters is essential for improving predictive performance. Typically, this involves time-consuming processes like random or grid searches, which can be resource-intensive, requiring powerful hardware. However, in this study, we utilized Microsoft's FLAML (Fast and Lightweight AutoML Library) as an alternative approach. Unlike traditional grid searches, FLAML takes the available computing time as an input and efficiently identifies the optimal hyperparameters. FLAML employs highly effective search strategies, allowing the model to make informed decisions regarding hyperparameters, sample size, and resampling strategy while considering both cost and error. In this particular study, each model underwent a fine-tuning process using FLAML, with a dedicated one-hour time limit for optimization. To evaluate the model, the data set is divided into training and test data sets. Accordingly, while 80% of the dataset was used for training purposes, 20% was used to evaluate the performance of the models. The models were evaluated based on their predictive accuracy. The results are given in Table 2.

Table 2. Prediction accuracy score of the used ML models.

Model Name	RF	XGB	ERT
Prediction Accuracy	78.57	79.22	77.27

The results show that each of these algorithms has shown prowess in handling complex relationships within datasets and mitigating overfitting, making them suitable for predictive analytics in healthcare. These results illustrate the effectiveness of ML algorithms in predicting the risk of diabetes mellitus. Among the algorithms investigated, XGB emerged as the top-performing model, boasting the highest accuracy. RF and ERT also performed commendably, contributing to the robustness of the predictive models.

As a result, this study demonstrates that tree-based ML algorithms offer effective tools for predicting diabetes mellitus. XGB, in particular, emerges as a robust choice with the highest accuracy among the models tested. These predictive models hold significant potential for improving early risk identification, which can lead to more personalized healthcare interventions. Future research directions may involve the integration of additional clinical and genetic data to further enhance predictive accuracy and enable the development of user-friendly clinical decision support systems

V. CONCLUSIONS

In conclusion, this study investigated the application of tree-based ML algorithms (RF, XB and ERT) for predicting diabetes mellitus. The results indicate that ML algorithms offer effective tools for diabetes prediction, with XGB emerging as the top-performing model with an accuracy of 79.22%. RF and ERT also demonstrated respectable performance with accuracies of 78.57% and 77.27%, respectively. Overall, tree-based ML algorithms show promise in the field of diabetes prediction, with XGB being a particularly robust choice. Future research directions may involve the incorporation of additional clinical and genetic data to further improve predictive accuracy and facilitate the development of user-friendly clinical

decision support systems. These advancements have the potential to revolutionize diabetes prevention and management, addressing a significant public health concern.

REFERENCES

[1] Kharroubi, A. T., & Darwish, H. M. (2015). Diabetes mellitus: The epidemic of the century. World journal of diabetes, 6(6), 850.

[2] Wang, N., & Kang, G. (2012, October). A monitoring system for type 2 diabetes mellitus. In 2012 IEEE 14th International Conference on e-Health Networking, Applications and Services (Healthcom) (pp. 62-67). IEEE.

[3] Sarwar, A., & Sharma, V. (2012). Intelligent Naïve Bayes approach to diagnose diabetes Type-2. International Journal of Computer Applications and Challenges in Networking, Intelligence and Computing Technologies, 3, 14-16.

[4] Vijayan, V., & Ravikumar, A. (2014). Study of data mining algorithms for prediction and diagnosis of diabetes mellitus. International journal of computer applications, 95(17).

[5] Li, L. (2014, November). Diagnosis of diabetes using a weight-adjusted voting approach. In 2014 IEEE International Conference on Bioinformatics and Bioengineering (pp. 320-324). IEEE.

[6] Kandhasamy, J. P., & Balamurali, S. J. P. C. S. (2015). Performance analysis of classifier models to predict diabetes mellitus. Procedia Computer Science, 47, 45-51.

[7] Hasan, M. K., Alam, M. A., Das, D., Hossain, E., & Hasan, M. (2020). Diabetes prediction using ensembling of different machine learning classifiers. IEEE Access, 8, 76516-76531.

[8] Yahyaoui, A., Jamil, A., Rasheed, J., & Yesiltepe, M. (2019, November). A decision support system for diabetes prediction using machine learning and deep learning techniques. In 2019 1st International informatics and software engineering conference (UBMYK) (pp. 1-4). IEEE.

[9] Breiman, L. (2001). Random forests. Machine learning, 45, 5-32.

[10] Chen, T., & Guestrin, C. (2016, August). Xgboost: A scalable tree boosting system. In Proceedings of the 22nd acm sigkdd international conference on knowledge discovery and data mining (pp. 785-794).

[11] Geurts, P., Ernst, D., & Wehenkel, L. (2006). Extremely randomized trees. Machine learning, 63, 3-42.

Kazık Gruplarının Oturması

Settlement of Pile Groups

Murat HAMDERİ

hamderi@tau.edu.tr, ORCID: 0000-0002-9167-8866
Mühendislik Fakültesi, İnşaat Mühendisliği Bölümü, Türk-Alman Üniversitesi, İstanbul, Türkiye

Özet: Geçmişte düşey yükler altında kazık gruplarının oturması kazık gruplarının bir blok gibi davrandığı kabul edilerek tahmin edilmiştir. Bu kabuller kazıkların çaplarını, aralıklarını, yanal sürtünme katsayılarını, dolaylı yoldan hesaba katmıştır. Bu yaklaşımlarda kazık oturmasında en etkili parametre olan zemin modülü en fazla 2 tabaka halinde girilmiştir. Son zamanlarda, 3 boyutlu yapı-zemin yazılımlarının gelişimi ile kazık gruplarının oturması daha hassas hesaplanabilir olmuştur. Bu bildiride 120 adet 3 boyutlu model ile meydana getirilen bir kazık grubu oturma formülü tanıtılacaktır. Bu formül, kazıklara bağlı radyenin ortasında ve kenarındaki oturmayı hesaplamaktadır. Formül 2 yönde kazık aralıklarının, kazık çapının, kazık boyunun, 5 adet zemin modülünün, kazık yanal ve uç direncinin, kazık elastisite modülünün, düşey yükün ve radye kalınlığının girilmesine izin vermektedir. Formül 3 boyutlu sonlu elemanlar programı sonuçlarına dayandığından hassas sonuçlar vermektedir. Formülün rahatça kullanımı için bir Android uygulaması mevcuttur.

Anahtar Kelimeler: *Kazık Grupları, Oturma, Radye Temel, Zemin-Yapı*

Abstract: In the past, the settlement of pile groups under vertical loads has been estimated using the assumption that the pile groups function as a block. These assumptions have indirectly taken into account the diameter, spacing and lateral friction coefficient of the piles. In such assumptions, the soil modulus, which is the most effective parameter for pile settlement, was included at most in 2 layers. Recently, with the development of 3D structure-soil software, the settlement of pile groups can be calculated more precisely. In this paper, a pile group settlement formula based on 120 3D models will be presented. This formula calculates the settlement at the center and edge of the raft connected to piles. The formula allows the input of pile spacing in 2 directions, pile diameter, pile length, 5 soil moduli, pile lateral and end resistance, pile modulus of elasticity, vertical load and raft thickness. Since the formula is based on the results of a 3D finite element program, it produces accurate results. An Android application is available for convenient use of the formula.

Keywords: *Pile Groups, Settlement, Raft Foundation, Soil-Structure*

I. GİRİŞ

ÇOK katlı binaların statik yüklerini zemine derinlik boyunca aktarmak için kazıklar kullanılır. Zayıf zeminler üzerinde yapılacak ağır yapılarda kazık ihtiyacı, öncelikle taşıma kapasitesinin yetersizliği ile başlar. Kazıklı tasarım ile taşıma kapasitesi sorunu giderildikten sonra tasarım, kazıklar üzerine oturan binanın oturma miktarını ayarlama problemine dönüşür. Kazıklı temellerin oturmasını tahmin etmek için geçmişte kullanılan yöntemler Dung ve diğerlerine göre dört grupta toplanabilir [1]: (1) Emprik veya yarı-empirik yaklaşımlar [2-3], (2) Eşdeğer radye veya kazık yaklaşımı [4-6], (3) Etkileşim faktörü yaklaşımı [7-8] ve (4) sayısal analiz yaklaşımı [9-10]. Dung ve diğ. bu metotların tahmin değerleri üzerinde yaptığı incelemelere göre, hesaplanan değerler arasındaki sapmanın yüzde 50 civarında olduğunu bildirmiştir.

Böyle bir sapma kullanılan yöntemlerde ciddi bir sıkıntıya işaret etmektedir. Son yıllarda gelişen bilgisayar işlem hızları ile, 3 boyutlu sonlu elemanlar programlarında hızlı sonuçlar alınmaya başlanmıştır. Böylece kazıklı temeller bilgisayar ortamında sıkça modellenir hale gelmiştir. Bilgisayar ortamında 120 adet değişik konfigürasyondaki kazıklı radye sistemi modelleyen Hamderi kazıklı radyenin oturmasını radyenin ortasında ve kenarında hesaplayan bir formül geliştirmiştir [11]. Bu formül dikdörtgen şekildeki kazıklı radyenin oturmasını hesaplarken kazıkların çaplarının (di), boylarını (le), aralıklarını (spx, spy), radyenin enini ve boyunu (wix, wiy), kalınlığını (th), radyeye etkiyen yayılı üniform yükü (ld), 5 tane zemin takasının zemin modülünü (E1, E2, E3, E4, E5), yanal kazık direncini (fr), kazık uç direncini (tr) hesaba katmaktadır. Hamderi kazıklı temel sonlu elemanlar modelini laboratuvar testiyle doğrulamış [11], formülün sonuçlarını 5 değişik vaka çalışmasının sonuçları ile karşılaştırmıştır. Bu bildiri kapsamında ise formülün kullanımı, formül için yazılmış Android uygulaması vasıtası ile tanıtılacaktır [12].

II. FORMÜL DETAYLARI

Hamderi, 2018 tarafından kazık radye temel oturması için önerilen oturma formülü aşağıda verilmektedirc [11]:

$$Oturma = S = S_b \left(\frac{sp_x + sp_y}{u_2}\right)^a . \left(\frac{l_e}{u_3}\right)^b . \left(\frac{di + u_4}{u_5}\right)^c . \left(\frac{wi_x . wi_y}{u_6}\right)^d .$$
$$\left(\frac{0.1E_1 + 0.2E_2 + 0.3E_3 + 0.4E_4 + u_7}{u_8}\right)^e . \left(\frac{E_5}{u_9}\right)^f . \left(\frac{ld}{u_{10}}\right)^g . \left(\frac{fr}{u_{11}}\right)^h . \left(\frac{tr}{u_{12}}\right)^i . \left(\frac{bed}{u_{13}}\right)^j . \left(\frac{th}{u_{14}}\right)^k . \left(\frac{Ec}{u_{15}}\right)^l$$

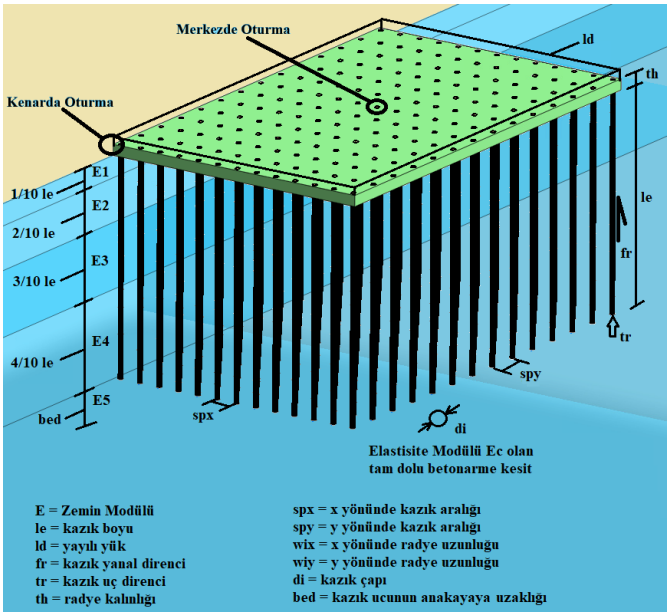
Burada spx, spy sırasıyla x ve y yönündeki kazık aralıklarını, le kazık uzunluğunu, di kazık çapını, wix ve wiy radyenin enini ve boyunu, E_1, E_2, E_3, E_4, E_5 tabakalara ait zemin modüllerini, ld radye üzerindeki yayılı yükü, fr kazığın yanal sürtünme direncini, tr kazığın uç direncini, bed kazıkların altı ile anakaya arasındaki mesafeyi, th radye kalınlığını, Ec kazık beton elastisite modülü ifade etmektedir. Bu girdi parametreleri ile ilgili detaylar Şekil 1'de verilmektedir. a, b, c, d, e, f, g, h, i, j, k, l birimsiz denklem katsayıları (Tablo 1), birim tutarlılığını sağlamak için S_b, $u_1 \ldots u_{15}$ birimli sabitler kullanılmaktadır (Tablo 2).

Tablo 1. Oturma formülünün birimsiz denklem katsayıları [11]

a	**b**	**c**	**d**	**e**	**f**
0.1406	-0.2999	-0.2274	0.5286	-0.4275	-0.6229
g	**h**	**i**	**j**	**k**	**l**
1.1082	-0.1025	-0.0267	0.1903	-0.1582	-0.0537

Tablo 2. Oturma formülünün birimli sabitleri [11]

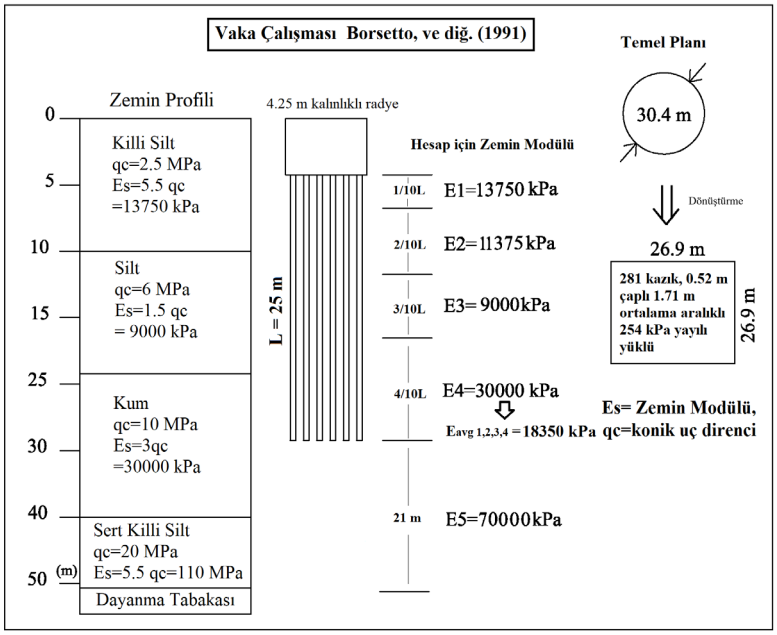
Sembol	Değer	Birim
S_b	0.3287	[m]
u_1, u_2, u_6	1	[m^2]
u_3, u_4, u_5	1	[m]
u_7	10000	[kN/m^2]
u_8, u_9, u_{10}	1	[kN/m^2]
u_{11}	500	[kN/m]
u_{12}	1000	[kN]
iu_{13}, u_{14}	1	[m]
u_{15}	25000	[MPa]



Şekil 1. Kazıklı radye oturma formülünün girdi parametreleri [11]

III. Bir Vaka Çalışmasının Andoroid Programı ile Çözümlenmesi

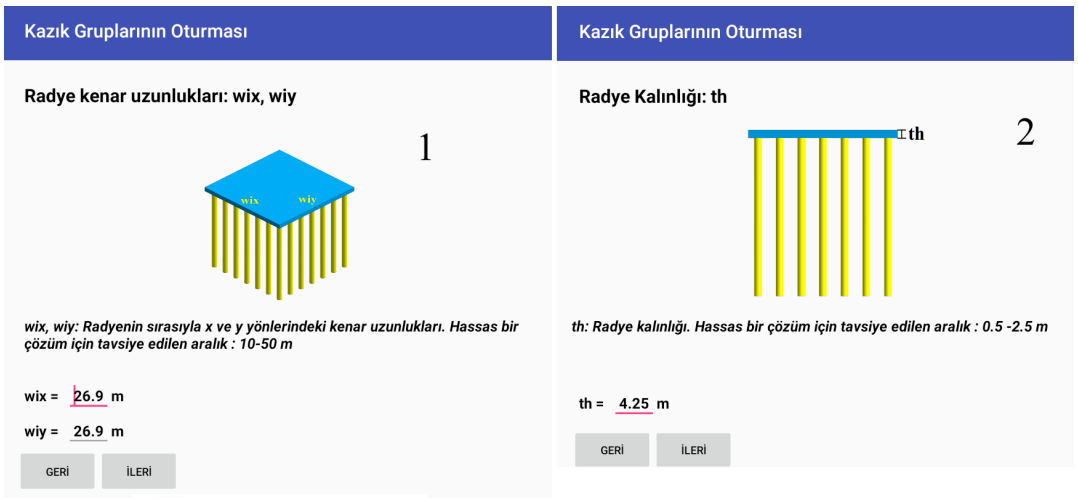
Borsetto ve diğ., İtalya'da Po Vadisindeki bir güç santralinin 200 m yüksekliğinde kazıklı temeller ile zemine oturan bacasının oturma ölçümleri bildirmiştir [13]. 281 adet 0.52 m çaplı 25 m uzunluğundaki Franki türü kazıklar, 30.4 m çapındaki ve 4.25 m kalınlığındaki radyeye oturmaktadır. Radye temele 184 MN yük etkimektedir. Şekil 2'de bu vakaya ait detaylar yer almaktadır.



Şekil 2. Borsetto ve diğ., tarafından bildirilen vakanın ayrıntıları [13]

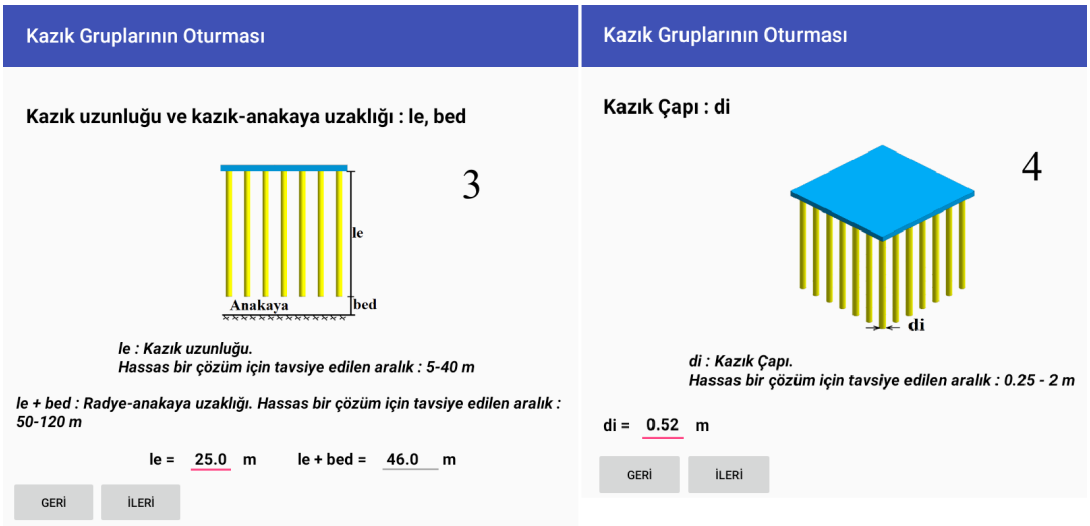
Söz konusu vaka analizideki kazıklı temelin oturması Hamderi, 2018 formülünü baz alan Hamderi, 2019 Android uygulaması ile hesaplanacaktır [10-11]. Vaka çalışmasında 30.4 m çaplı dairesel bir temel mevcuttur. Bu formüle 26.9 m kenar uzunluklu eşdeğer kare olarak

girilmiştir (wix, wiy, Şekil 3). Radye kalınlığı = 4.25 m değeri de bir sonraki ekrana girilmiştir (th, Şekil 3).



Şekil 3. Kazıklı radye oturma formülünün girdi parametreleri ekranı wix, wiy, th

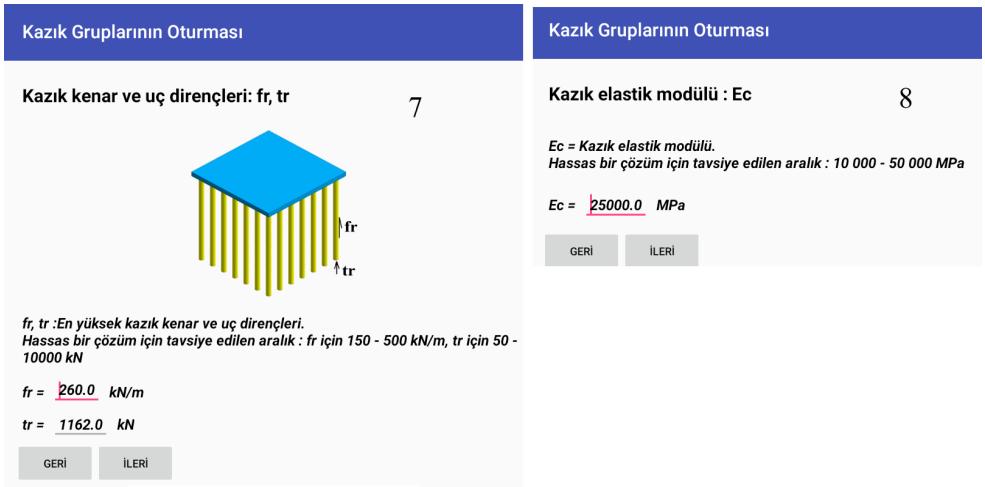
Kazık boyu = 25 m 3. ekrana girilmiştir (le, Şekil 4). Yüzeyle anakaya arasındaki uzaklık ise yine aynı ekrana girilmiştir (le+bed, Şekil 4). Kazık çapı = 0.52 m 4. ekrana girilmiştir (di, Şekil 4). Yatay ve düşey kazık aralıkları toplam kazık sayısını karesel alana eşit dağıtmak suretiyle 1.6 m olarak 5. ekrana girilmiştir (spx, spy, Şekil 5). Radyeye gelen ortalama yük 254 kPa 6. ekrana girilir (ld, Şekil 5). Kazık kenar ve uç dirençleri ise 7. Ekrana girilmiştir (fr, tr, Şekil 6). Kazık elastisite modülü 8. ekrana girilir (Ec, Şekil 6). Son olarak 5 tane tabakaya ait zemin modülleri 9. ekrana girilir (E1, E2, E3, E4, E5, Şekil 7). Burada dikkat edilmesi gereken tabaka kalınlıklarının 1/10 le, 2/10 le, 3/10 le, 4/10 le ve bed şeklinde ayarlanmasıdır. 10. ekranda ise bütün değerler bir arada görülebilir. Bu değerler istenirse önceki ekranlara gitmeden bu ekrandan değiştirilebilir. Hesapla butonuna basıldıktan sonra radyenin kenarında ve ortasındaki oturma ve ortalama sehim hesaplanır. Bu vaka çalışmasında merkezde ölçülen oturma 40 mm'dır. Hamderi, 2019 Android uygulaması ile bu 37 mm olarak hesaplanmıştır.



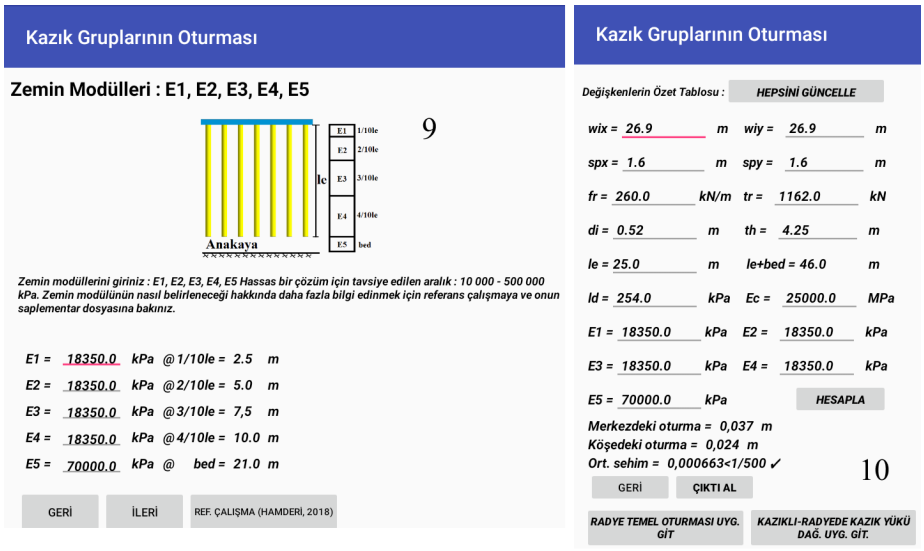
Şekil 4. Kazıklı radye oturma formülünün girdi parametreleri ekranı le, bed, di



Şekil 5. Kazıklı radye oturma formülünün girdi parametreleri ekranı spx, spy, ld



Şekil 6. Kazıklı radye oturma formülünün girdi parametreleri ekranı fr,tr, Ec



Şekil 7. Solda kazıklı radye oturma formülünün girdi parametreleri ekranı E1, E2, E3, E4, E5, sağda sonuç ekranı

IV. SONUÇLAR

- Bu bildiri kapsamında kazıklı radye temellerini ortasında ve kenarında meydana gelen oturmayı18 girdi parametresine göre hesaplayan bir formül tanıtılmıştır.
- Sonlu elemanlar programı tabanlı olması ve çok sayıda girdi parametresi ihtiva etmesinden dolayı formülün hassasiyet yüksektir.
- Formül bir vaka analizine uygulanmış, formülün bulduğu sonucun, ölçülen değere yaklaşık olduğu görülmüştür.
- Formülde kullanılan parametrelerin fazlalığı ve denklem katsayılarının karmaşık olması sebebiyle hesap yaparken bir Excel tablosu kullanılması gerekmektedir. Formülün kullanımı kolaylaştırmak için alternatif olarak bir ücretsiz Android uygulaması geliştirilmiştir. Android uygulamasına formülün girdi parametreleri kolayca girilmekte ve sonuçlar pdf formatında rapor olarak alınabilmektedir.

A. REFERENCES

[1] Dung, N.T., Chung, S.G., Kim, S.R. Settlement of large-scale piled foundations using equivalent raft approach, 2010, ICE Proceedings Geotechnical Engineering, 163

[2] Meyerhof, G.G.. Bearing capacity and settlement of pile foundations. J. Geotech. Eng., ASCE 102 (GT3), 1976, 195–228.

[3] Vesic, A.S. Design of pile foundations. National Cooperative Highway Research Program Synthesis of Practice No. 42. Transport Research Board, Washington, DC, 1977

[4] Terzaghi, K., Peck, R.B., 1967. Soil Mechanics and Foundation Engineering Practice. Wiley, New York.

[5] Fellenius, B.H. Pile Foundations. Foundation Engineering Handbook, 2nd ed. Chapman & Hall, New York, pp, 1991, 511–536.

[6] Poulos, HG. Settlement prediction for bored pile groups. Proceedings of the 2nd Geotechnical Seminar on Deep Foundations on Bored, 1993
and Auger Piles Ghent, 103–117.

[7] Poulos, H.G., Davis, E.H. Pile Foundation Analysis and Design. Wiley & Sons, New York, 1980

[8] Randolph, M.F., Wroth, C.P. An analysis of the vertical deformation of pile groups. Geotechnique, 1979, 29 (4), 423–439.

[9] Chow, Y.K. Analysis of vertically loaded pile groups. Int. J. Numer. Anal. Meth. Geomech.,1986, 10 (1), 59–72.

[10] Clancy, P., Randolph, M.F. Simple design tools for piled raft foundations. Geotechnique , 1996, 46 (2), 313–328.

[11] Hamderi, M. "Comprehensive group pile settlement formula based on 3D finite element analyses." Soils Found., 2018, 58 (1): 1–15. https://doi.org/10.1016/j.sandf.2017.11.012.

[12] Hamderi, M. 2019, Kazık Gruplarının Oturması Android Uygulaması https://play.google.com/store/apps/details?id=com.geo3dtech.setttlement&hl=en&gl=US

[13] Borsetto M, Barbera G, Colleselli F, Colombo P, Corti G, Failella D, Tripiciano L, Giuseppett G, Mazza G and Varagnolo P. Settlement analysis of main buildings in power plants by means of 2-D and 3-D models. Proceedings of the 10th European Conference on Soil Mechanics and Foundation Engineering, Florence, 1991 vol. 1, 323–328.

Etkileşimli Oyunlaştırılmış Fizyoterapi Uygulaması Örneği: Therapinno

An Example of Interactive Gamified Physiotherapy Application: Therapinno

Hakan YILMAZ

hakanyilmaz@karabuk.edu.tr, ORCID: 0000-0002-8553-388X
Tıp Mühendisliği, Karabük Üniversitesi, Karabük, Türkiye

Özet: Bu çalışma, fizyoterapi alanında oyunlaştırma konseptini kullanan "Therapinno" adlı uygulamanın geliştirilmesini kapsamakta ve bu uygulamanın amacını, yöntemini ve sonuçlarını özetlemektedir. Çalışmanın temel amacı, fiziksel rehabilitasyonun eğlenceli bir deneyim haline getirilmesini sağlayarak hastaların tedaviye daha fazla katılımını teşvik eden bir uygulama olan "Therapinno" uygulamasını geliştirmektir. Bu uygulama, bireylerin terapötik egzersizleri oyunlarla birleştirerek tedaviye daha istekli katılımlarını amaçlamaktadır. Uygulamanın geliştirilmesi için Unity oyun motoru ve C# programlama dili kullanılmıştır. Görüntü işleme ve yapay zekâ teknikleri kullanılarak, kullanıcının vücudu ve uzuvları gerçek zamanlı olarak tanınmakta ve belirli hareketleri doğru yapması durumunda oyun karakterinin hareket ettirilmesi sağlanmaktadır. Uygulama, doktorlar ve klinisyenlerle yapılan görüşmeler sonucunda belirlenen 4 farklı hareketi desteklemeyi amaçlamıştır. Bu hareketler şunlardır: servikal lateral fleksiyon, omuz abduksiyonu/adduksiyonu, lomber lateral fleksiyon ve denge egzersizi. Uygulama içerisinde "koşu oyunu", "kutu kırma oyunu" ve "elma toplama oyunu" olmak üzere üç farklı etkileşimli oyun tasarlanmıştır. Uygulamanın etkileşimli oyunlar aracılığıyla fizyoterapiyi daha eğlenceli hale getirmesi ve böylece hastaların tedaviye daha istekli katılmalarını teşvik edeceği düşünülmektedir. Uygulama, kullanıcının vücut hareketlerini doğru bir şekilde takip ederek oyun karakterini kontrol etmesine olanak tanımaktadır. Kullanıcıların doğru hareketleri gerçekleştirdikçe oyun içerisinde ilerlemeler kaydedebilmeleri, puan kazanmaları ve ödüller elde etmeleri, terapötik sürece katılım ve motivasyonu artırmaktadır. Uygulamanın düşük maliyetli olması ve özel donanıma ihtiyaç duymaması, farklı kullanıcı gruplarına hitap etme potansiyelini artırmaktadır. Uygulamanın daha fazla kullanıcı kitlesi tarafından kullanılabilmesi için mobil platformlara da uyarlanması ve kullanım kolaylığı sağlanması önerilmektedir. Ayrıca, yapay zekâ algoritmalarının daha fazla geliştirilerek farklı egzersizlerin tanınması ve desteklenmesi sağlanabilir. Gelecekteki çalışmalar, uygulamanın klinik etkinliğini daha ayrıntılı bir şekilde incelemeyi ve farklı fiziksel rehabilitasyon ihtiyaçlarına yönelik uyarlamalarını yapmayı amaçlamaktadır.

Anahtar kelimeler: *Oyunlaştırma, fizyoterapi, esenlik, etkileşimli fizyoterapi, oyunlaştırılmış terapi*

Abstract: This study covers the development of the application called "Therapinno", which uses the concept of gamification in physiotherapy, and summarizes the purpose, method and results of this application. The main purpose of the study is to develop the "Therapinno" application, which is an application that encourages more participation of patients in treatment by making physical rehabilitation an enjoyable experience. This application aims to make individuals more willing to participate in treatment by combining therapeutic exercises with

games. Unity game engine and C# programming language were used to develop the application. Using image processing and artificial intelligence techniques, the user's body and limbs are recognized in real time, and the game character can be moved if certain movements are made correctly. The application supports 4 different movements based on interviews with doctors and clinicians. These movements are: cervical lateral flexion, shoulder abduction/adduction, lumbar lateral flexion and balance exercise. Three different interactive games, namely "running game", "box breaking game" and "apple picking game" are designed within the application. It is thought that the application will make physiotherapy more fun through interactive games and thus encourage patients to participate more willingly in treatment. The application allows the user to control the game character by accurately tracking their body movements. The fact that users can make progress in the game, earn points and get rewards as they perform the right moves increases participation and motivation in the therapeutic process. The low cost of the application and the fact that it does not need special hardware increases its potential to appeal to different user groups. In order for the application to be used by more users, it is recommended to adapt it to mobile platforms and provide ease of use. In addition, artificial intelligence algorithms can be further developed to recognize and support different exercises. Future studies aim to examine the clinical efficacy of the practice in more detail and to adapt it for different physical rehabilitation needs.

Keywords: *Gamification, physiotherapy, well-being, interactive physiotherapy, gamified therapy*

I. GİRİŞ

Fiziksel rehabilitasyon; kazalar, yaralanmalar, cerrahi müdahaleler ve kronik sağlık sorunları sonucunda hareket kısıtlamaları yaşayan bireylerin fonksiyonel bağımsızlıklarını geri kazanmalarını amaçlayan bir sağlık alanıdır. Geleneksel fizyoterapi yöntemleri genellikle tekrarlayıcı egzersizlerden oluşmaktadırlar ve bazen hastalar için sıkıcı veya motive edici olmayan bir deneyim sunabilmektedir. Ancak son yıllarda, oyunlaştırma (gamification) konsepti, fizyoterapi uygulamalarında yenilikçi bir yaklaşım olarak öne çıkmıştır. Oyunlaştırılmış fizyoterapi, hastaların tedaviye daha fazla katılımını teşvik ederek hareket etmeyi eğlenceli hale getirmeyi amaçlar. Modern dünyamızda, sağlık ve esenlik (well-being) büyük ölçüde bireylerin sağlıkla ilgili davranışlarına dayalıdır. Motivasyon, sağlık davranışlarının değiştirilmesinde kritik bir etken olarak öne çıkar ve içsel olarak yönlendirilen davranış değişiklikleri sürdürülebilirdir [1].

Oyunlaştırma, öğrenmede motivasyonu ve katılımı teşvik etmek amacıyla oyun özelliklerinin, özellikle de video oyunu öğelerinin oyun dışı bağlamlara uygulanmasıdır [2], [3]. Fizyoterapide, oyunlaştırma yaklaşımı, hasta motivasyonunu artırma ve tedaviye daha fazla katılımı teşvik etme amacıyla kullanılır. Oyunlaştırılmış fizyoterapi, oyun dinamiklerini (örneğin puanlama, seviyeler, ödüller) fiziksel rehabilitasyon süreçlerine dahil ederek hastaların egzersizleri daha eğlenceli ve motive edici bulmalarını sağlar [1], [4].

Son çeyrek yüzyılda birçok alanda olduğu gibi sağlık davranışının iyileştirilmesinde de bilgisayar teknolojisinin yükseldiği görülmüştür. Bilgisayar tabanlı oyunlaştırma kişinin kendi sağlığını ve esenliğini izlemeye ve yönetmeye yönelik çeşitli uygulamaları içerir [5], [6]. Bu anlamda önemli alanlardan biri sağlıkla ilgili olumlu sonuçlar elde etmek için kullanılan sağlık oyunlarıdır. Bunların çoğunluğu "sağlık davranışı değiştirme oyunları" olarak nitelendirilebilir. Bu oyunlarla birlikte fiziksel aktivitenin artırılması ve fiziksel rehabilitasyon hedeflenmiştir [7]. Bu oyunlar görüntü işleme teknikleri, sanal gerçeklik, arttırılmış gerçeklik, insan bilgisayar etkileşimi gibi farklı teknikler kullanmaktadır [1], [8].

Bireyin sağlık ve esenlik seviyesinin arttırılması konusunda bilgisayar tabanlı oyunlaştırma birçok avantaj sunmaktadır. Bunlardan bazıları şöyle sıralanabilir:

- Katılım ve motivasyon: Bilgisayar oyunları dikkat çeken, ilgiyi sürdüren ve bireyleri

aktif katılıma motive eden doğal niteliklere sahiptir. Terapiye oyun öğelerinin dahil edilmesiyle terapi daha ilgi çekici ve eğlenceli hale gelir. Böylece bireyin terapötik sürece katılma ve devam etme motivasyonunu artırır [9].

- Beceri geliştirme ve çeşitli terapötik uygulamalar: Bilgisayar tabanlı oyunlaştırılmış terapi; bilişsel, fiziksel, duygusal veya sosyal beceriler gibi belirli terapötik hedeflere ulaşmak için tasarlanabilir. Bilgisayar tabanlı oyunlaştırılmış terapi; anksiyete bozuklukları, depresyon gibi zihinsel sorunların tedavisinde, motor becerilerin gelişimi ve ağrı yönetimi gibi fiziksel rehabilitasyonda, hafıza ve dikkat geliştirme gibi bilişsel eğitimde olmak üzere çeşitli alanlarda uygulanabilmektedir [1] .
- Duygusal ve davranışsal düzenleme: Bilgisayar tabanlı oyunlaştırılmış terapi, bireylerin duygusal ve davranışsal düzenleme becerilerini öğrenmelerine ve uygulamalarına yardımcı olabilir. Oyunlar, duyguları keşfetmek ve ifade etmek, başa çıkma stratejilerini öğrenmek ve öz düzenleme becerilerini geliştirmek için güvenli bir alan sağlayabilir. Kişinin davranışsal refahının arttırılmasına yardımcı olabilir [10]
- Kişiselleştirme ve ilerleme takibi: Bilgisayar oyunları, bireysel ihtiyaçlara ve yeteneklere göre uyarlanarak kişiselleştirilmiş deneyimlere olanak tanır. Veri izleme ve analiz yöntemleri sayesinde ilerleme izlenebilir ve hem terapiste hem de bireye geri bildirim sağlanabilir. Bu da terapi planının değerlendirilmesini ve ayarlanmasını kolaylaştırır [11].
- Sosyal etkileşim ve bağlantı: Çok oyunculu veya çevrimiçi oyunlar, bireyler arasında sosyal etkileşimi, iş birliğini ve bağlantıyı geliştirebilir, özellikle grup ortamlarını içeren terapiler için veya yüz yüze sosyal etkileşimlerde güçlük çeken kişiler için faydalı olabilir [12].
- Günlük yaşama uygunluk ve geniş ulaşılabilirlik: Bilgisayar tabanlı oyunlaştırılmış terapiler insanların hayatlarına özel zaman ve alan eklemeleri gereken terapilerin yerine bireylerin günlük programları içerisindeki aktivitelerle birlikte düzenlenebilir. Ayrıca bu oyunlara erişmek için genelde belirli bir yer (klinik, hastane vb.) şartı yoktur [11].

Masa başı çalışma, modern iş dünyasının temel bir gerçeğidir. Ancak, uzun saatler boyunca bilgisayar ekranlarının başında oturmak bazı sağlık sorunlarına yol açabilir. Masa başı çalışanlar, uzun süreli oturma nedeniyle boyun, sırt ve omuz bölgelerinde ağrılarla karşılaşabilirler. Ayrıca, yanlış postür alışkanlıkları da zamanla ciddi postür bozukluklarına neden olabilir [13]. Yanlış oturma düzeni, uygun olmayan masa yüksekliği ve bilgisayar ekranının göz seviyesinin altında olması gibi ergonomik faktörler, aynı pozisyonda uzun süre kalma ve sürekli bilgisayar kullanımı, kasların gerilmesine ve ağrılara yol açabilir. Bu da çalışanların esenliğini etkileyen ve uzun vadede fiziksel rahatsızlıklara ve verimlilik kaybına neden olabilecek bir durumdur. Bunun düzeltilmesi için ergonominin düzenlemeleriyle birlikte egzersiz ve esnemelerin de yapılması gerekmektedir. Oyunlaştırılmış terapi ile çalışanların eğlenceli vakit geçirerek terapi hareketlerini yapması sağlanabilir.

Bu çalışmada başta çocuklar ve çalışanlar olmak üzere fizyoterapinin oyunlaştırılarak yapılmasını sağlayacak uygulamanın geliştirilmesi amaçlanmıştır. Görüntü işleme ve yapay zekâ teknikleri kullanılarak bireyin vücudunun eş zamanlı olarak tanınması ve belirlenen hareketleri doğru yapması sonucu oyun karakterinin hareket ettirilmesi hedeflenmiştir.

II. MATERYAL VE METOT

A. Kullanılan Platformlar

Uygulamanın geliştirilmesi sırasında Unity oyun motoru ve C# programlama dili kullanılmıştır. Unity; bilgisayarlar, konsollar ve mobil cihazlar için video oyunları ve simülasyonları geliştirmek için kullanılan çapraz platform bir oyun motorudur [14]. Programlama sırasında C# kodlarının derlenebilmesi için Visual Studio 2022 tercih edilmiştir. Uygulamanın geliştirilmesi sırasında Intel i7 işlemcili 64 GB belleğe sahip, Windows işletim sistemi tabanlı bir bilgisayar kullanılmıştır.

B. Görüntünün Alınması ve Uzuvların Tespit Edilmesi

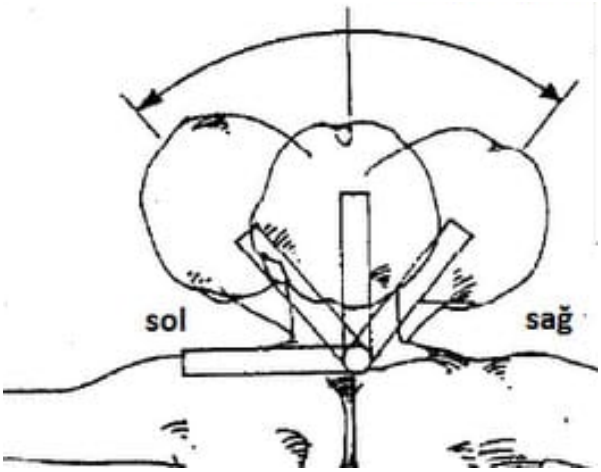
Çalışma kapsamında geliştirilen uygulamanın en önemli aşamalarından birisi görüntünün kamera aracılığıyla alınması ve vücudu oluşturan baş, kollar, bacaklar, gövde gibi uzuvların belirlenmesidir. Bu işlemin sağlanabilmesi için Google tarafından geliştirilip dağıtılan MediaPipe kullanılmıştır. MediaPipe, medya verilerinin işlenebilmesi için geliştirilmiş farklı platform ve programlama dilleriyle çalışabilen bir makine öğrenmesi çözümüdür. MediaPipe ile bir videodaki yüz, vücut, el gibi nesneler tespit edilebilir ve eş zamanlı olarak takip edilebilir [15]. Tam vücudun tespit edilmesi için bireyin kameradan 150-500 cm aralığındaki uzaklıkta olması gerekmektedir. Ancak boyun, el gibi vücudun belirli bir uzvu çalıştırılmak istendiğinde ilgili uzvun kamera açısında olması yeterlidir.

III. UYGULAMA VE ÖZELLİKLERİ

A. Desteklenen Hareketler

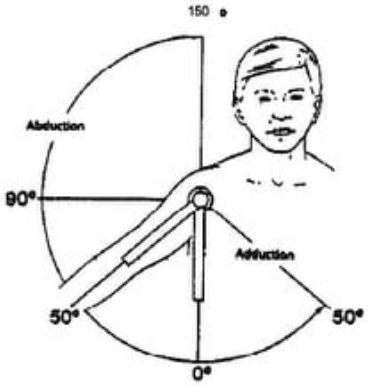
Therapinno uygulaması kapsamında fizik tedavi uzmanı doktorlar ve klinisyenlerle yapılan görüşmeler sonucunda, ilk olarak 4 farklı hareketin desteklenmesi hedeflenmiştir. Bu hareketler söyle sıralanabilir:

Servikal lateral fleksiyon: Bireyin otururak veya ayakta dik olarak durduğu zaman başını sağ ve sol taraflara eğerek gerçekleştiği harekettir. Bu hareketi yapan bir bireyin sağlıklı sayılabilmesi için başını 45° veya daha fazla sağa ve sola eğebilmesi gerekir [16]. Bu hareket Şekil 1'de gösterilmiştir.



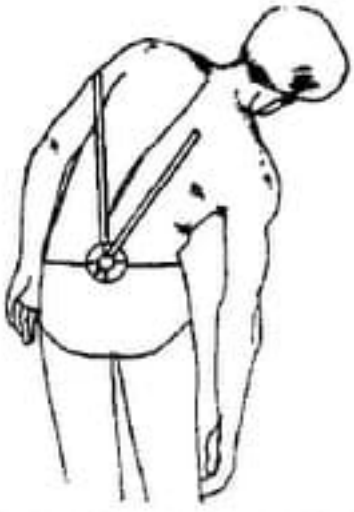
Şekil 1. Servikal lateral fleksiyon [17].

Omuz abduksiyonu/adduksiyonu: Avuç içleri bedene yapışık, kollar doğal konumdayken ve kol düzgünlüğü bozulmadan yana doğru kolun kaldırılmasıyla oluşan bir harekettir. Sağlıklı bireylerde bu hareket yapılırken kolun 150° ila 180° arasında kaldırılabilmesi gerekir [18]. Bu hareket Şekil 2'de gösterilmiştir.



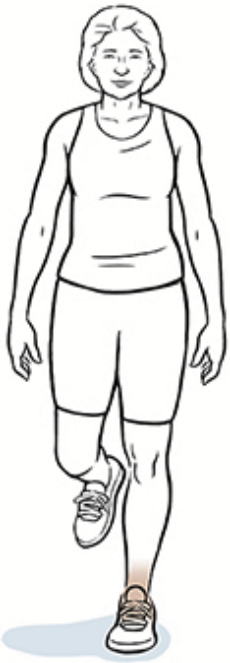
Şekil 2. Omuz abduksiyonu/adduksiyonu [17].

Lomber lateral fleksiyon: Birey ayakta, gövde, kollar ve bacaklar doğal pozisyonda iken vücudun bel kısmından sağa ve sola doğru eğilmesi ile gerçekleştirilen bir harekettir. Bu hareketi yapan bireyin sağlıklı sayılabilmesi için 35° civarında yana eğilebilmesi gerekmektedir [19]. Şekil 3'te bu hareket gösterilmiştir.



Şekil 3. Lomber lateral fleksiyon [17].

Denge egzersizi: Birçok yaralanma ve tıbbi durum dengeyi etkileyebilir. Örneğin bir ayak bileği burkulması, beyne denge girdisini taşıyan yumuşak dokudaki yırtılmalar nedeniyle denge bozuklukları yaşanabilir. Felç geçiren kişilerde sıklıkla yürümeyi zorlaştıran ciddi denge sorunları da görülür. Bu tür durumlarda denge egzersizleri önerilmektedir. Çalışma kapsamına alınan denge egzersizi Şekil 4'te gösterilmiştir.



Şekil 4. Denge egzersizi [20].

B. Tasarlanan Oyunlar

Bu çalışma kapsamında "koşu oyunu", "kutu kırma oyunu" ve "elma toplama oyunu" olmak üzere üç farklı etkileşimli oyun tasarlanmıştır.

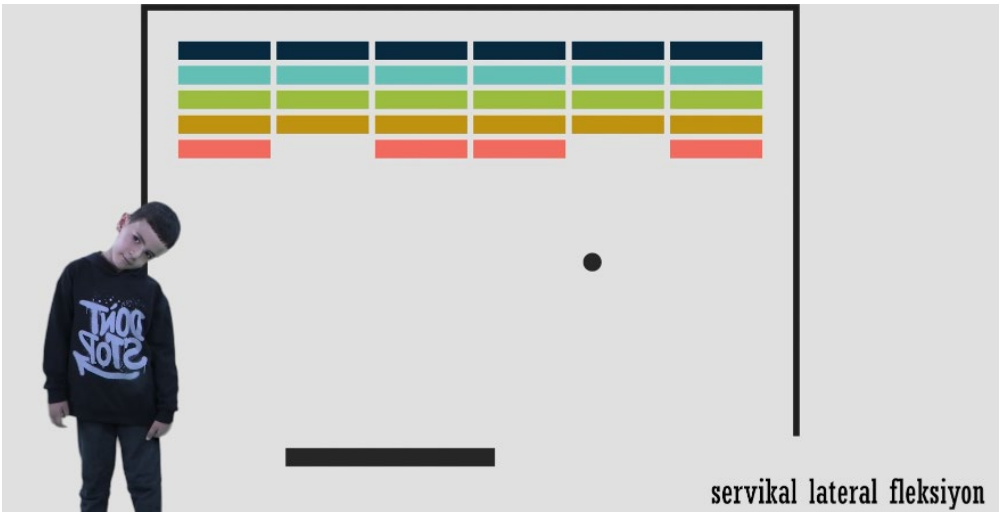
Koşu oyununda karakter yolda koşarken önüne farklı engeller ve ödüller çıkmaktadır.

Karakterin sağ-sol hareketleri ile ödülleri toplaması, engellerden ise kaçınması gerekmektedir. Bu oyunda omuz abduksiyonu/adduksiyonu, lomber lateral fleksiyon ve denge egzersizi olmak üzere üç farklı egzersiz desteklenmektedir (Şekil 5).



Şekil 5. Koşu oyunu görünümü.

Kutu kırma oyununda ise topun bir bar yardımı ile hareket ettirilmesi ve sahnede bulunan kutuların kırılması gerekmektedir. Bu oyun denge egzersizi, servikal lateral fleksiyon ve omuz abduksiyonu/adduksiyonu olmak üzere üç farklı egzersizi desteklemektedir (Şekil 6).



Şekil 6. Kutu kırma oyunu görünümü.

Elma toplama oyununda ise ağaçlardan düşen böcekler ve elmalar vardır. Sepeti hareket ettirerek elmaların toplanması, böceklerden ise kaçınılması gerekmektedir. Bu oyun da servikal lateral fleksiyon ve lomber lateral fleksiyon hareketi olmak üzere iki hareketi desteklemektedir (Şekil 7).



Şekil 7. Elma toplama oyunu görünümü.

C. Uygulamanın Çalışması ve Oyunların Oynanması

Therapinno uygulaması, görüntünün alınması, vücudun/uzuvların belirlenmesi ve uzuvların açılarının seçilen harekete göre hesaplanması, hareketin doğru olması durumuna göre (belirlenen açıların elde edilmesi) oyun karakterinin hareket ettirilmesi ve oyun karakterinin oyunda ilerlemesi (hediye ve elmaları toplama, kutuları kırma, yüksek puana erişme gibi) olmak üzere üç ana aşamadan oluşmaktadır. Therapinno uygulamasına ait iş akışı Şekil 8'de verilmiştir.



Şekil 8. Therapinno uygulaması iş akışı.

Görüntü, kamera aracılığı ile eş zamanlı alınarak kare kare işlenmektedir. Bu sırada herhangi bir gecikme yaşanmamakta ve ortalama olarak saniyede 20 kare alınmaktadır. Alınan görüntüler yapay zekâ tabanlı MediaPipe ile işlenerek vücudun ve uzuvların tespit edilmesi sağlanmaktadır. Şekil 9'da görüldüğü gibi uygulama için ihtiyaç olan baş, gövde, kollar, bel, bacaklar ve ayaklara ait koordinatlar sürekli olarak kaydedilmektedir.



Şekil 9. Alınan görüntüler üzerinden uzuvları belirlemek için gerekli koordinatların bulunması ve gösterilmesi.

Daha sonra seçilen hareketlere göre uzuv dereceleri (d) hesaplanmaktadır. Örneğin omuz adduksiyonu yapan bir birey için vücut doğal halindeyken omuzları ve dizleri oluşturan koordinatların x ekseninde (yatayda) ortalamaları alınarak (1)'e göre gövdenin eğimi hesaplanmaktadır. Daha sonra omuz, dirsek ve bilek koordinatları kullanılarak kolun eğimi (1) kullanılarak hesaplanır ve böylece omuz açısı elde edilmektedir. Eğer omuz açısı 150° derece ve üzerinde ise hareket doğru yapılmış kabul edilerek oyundaki karakterin yönlendirilmesi sağlanır. Böylece tüm hareketlerin kontrolü ve doğru yapılmasına göre oyun karakterinin puan kazanması sağlanır.

$$d = \tan^{-1}\left(\frac{y_2 - y_1}{x_2 - x_1}\right) * \frac{180}{\pi} \quad (1)$$

Tüm bu işlemler eş zamanlı olarak devam etmektedir ve görüntünün alınması, uzuvların belirlenmesi, ilgili uzuvlara ait açıların hesaplanması, hareket açısının doğruluk durumuna göre oyun karakterinin yönlendirilmesi yaklaşık 50 milisaniye içinde tamamlanmaktadır. Bu sayede herhangi bir gecikme olmadan oyun karakteri bireyin vücudu ile eş zamanlı olarak hareket etmektedir.

IV. SONUÇLAR VE ÖNERİLER

Bu çalışmada etkileşimli oyunlaştırılmış "Therapinno" isimli bir fizyoterapi uygulaması geliştirilmiştir. Therapinno uygulaması fizyoterapiyi eğlenceye dönüştürmeyi amaçlamaktadır. Böylece bireyler oyun oynarken terapilerini ve egzersizlerini tamamlayabilmektedir. Uygulama, eş zamanlı görüntüden vücudu analiz eder ve bireyin vücut boyutuna göre otomatik olarak kalibre olur. Yetişkinler ve çocuklar ek bir ayar gerekmeden uygulamayı kullanabilirler.

Uygulama, ayakta tüm vücut ile kullanılabileceği gibi sadece boyun hareketleri ile de kullanılabilir. Uygulama içerisinde dört farklı hareket desteklenmekte ve üç farklı oyun oynanabilmektedir. Bireyin vücudu ile eş zamanlı olarak oyun karakterleri yönetilmektedir. Standart bir web kamerası dışında başlık, el kumandası gibi herhangi bir ek donanıma ihtiyaç duymamaktadır. Bu da çoğu uygulama arasında öne çıkmasını ve düşük maliyetli olmasını sağlamaktadır. Ayrıca yeşil/mavi perde gibi özel arka planlara ihtiyaç duymadan yeterli ışığın olduğu her koşulda çalışabilmektedir. Desteklenen egzersiz hareketlerinin doğru yapılıp yapılmadıkları, kişinin terapiye ne kadar süre ayırdığı, hareketlerin ne kadarını doğru yaptığı gibi bilgiler kaydedilmektedir. Kurulan altyapı sayesinde farklı oyunlar ve hareketler de kolayca eklenebilir. Sadece fizyoterapi ihtiyacı olanlar değil uzun süre masa başı çalışanlar da uygulamayı kullanarak esneme/gevşeme yapabilirler.

Uygulamanın geliştirilerek daha kompakt hale getirilmesi planlanmaktadır. Ayrıca gelecek çalışmalarda yapay zekanın oyun karakterleri üzerinde de kullanılması, mobil platformlara uyarlanması ve farklı karakterlerin eklenmesi düşünülmektedir. Uygulamanın fizik tedavi kliniklerinde, araştırma merkezlerinde, rehabilitasyon merkezlerinde ve masa başı çalışanların yoğun olduğu ofislerde kullanılabileceği önerilmektedir. Uygulamanın klinik olarak da etkili olup olmadığının gösterilmesi için çalışmalar devam etmektedir.

V. REFERANSLAR

[1] D. Johnson, S. Deterding, K.-A. Kuhn, A. Staneva, S. Stoyanov, ve L. Hides, "Gamification for health and wellbeing: A systematic review of the literature", *Internet Interv*, c. 6, ss. 89-106, Kas. 2016, doi: 10.1016/j.invent.2016.10.002.

[2] K. Seaborn ve D. I. Fels, "Gamification in theory and action: A survey", *International Journal of Human-Computer Studies*, c. 74, ss. 14-31, Şub. 2015, doi: 10.1016/j.ijhcs.2014.09.006.

[3] R. S. Alsawaier, "The effect of gamification on motivation and engagement", *IJILT*, c. 35, sy 1, ss. 56-79, Oca. 2018, doi: 10.1108/IJILT-02-2017-0009.

[4] S. Rigby ve R. M. Ryan, *Glued to games: how video games draw us in and hold us spellbound*. içinde New directions in media. Santa Barbara, Calif: ABC-CLIO, 2011.

[5] R. A. Calvo ve D. Peters, *Positive computing: technology for wellbeing and human potential*. içinde The platform studies series. Cambridge, Massachusetts: The MIT Press, 2014.

[6] E. Knight, M. I. Stuckey, H. Prapavessis, ve R. J. Petrella, "Public health guidelines for physical activity: is there an app for that? A review of android and apple app stores", *JMIR Mhealth Uhealth*, c. 3, sy 2, s. e43, May. 2015, doi: 10.2196/mhealth.4003.

[7] H. Kharrazi, A. S. Lu, F. Gharghabi, ve W. Coleman, "A Scoping Review of Health Game Research: Past, Present, and Future", *Games Health J*, c. 1, sy 2, ss. 153-164, Nis. 2012, doi: 10.1089/g4h.2012.0011.

[8] B. Morschheuser, L. Hassan, K. Werder, ve J. Hamari, "How to design gamification? A method for engineering gamified software", *Information and Software Technology*, c. 95, ss. 219-237, Mar. 2018, doi: 10.1016/j.infsof.2017.10.015.

[9] S. Deterding, "The Lens of Intrinsic Skill Atoms: A Method for Gameful Design", *Human–Computer Interaction*, c. 30, sy 3-4, ss. 294-335, May. 2015, doi: 10.1080/07370024.2014.993471.

[10] D. Johnson, C. Jones, L. Scholes, ve M. Carras, "Videogames and wellbeing: A comprehensive review", 2013.

[11] S. P. Walz ve S. Deterding, Ed., *The Gameful World: Approaches, Issues, Applications*. The MIT Press, 2015. doi: 10.7551/mitpress/9788.001.0001.

[12] D. King, F. Greaves, C. Exeter, ve A. Darzi, "'Gamification': influencing health behaviours with games", *J R Soc Med*, c. 106, sy 3, ss. 76-78, Mar. 2013, doi: 10.1177/0141076813480996.

[13] A. Hedge, S. Morimoto, ve D. McCrobie, "Effects of keyboard tray geometry on upper body posture and comfort", *Ergonomics*, c. 42, sy 10, ss. 1333-1349, Eki. 1999, doi: 10.1080/001401399184983.
[14] "Unity Real-Time Development Platform | 3D, 2D, VR & AR Engine", *Unity*. https://unity.com (erişim 26 Ağustos 2023).
[15] "MediaPipe", *Google for Developers*. https://developers.google.com/mediapipe (erişim 26 Ağustos 2023).
[16] E. E. Swartz, R. T. Floyd, ve M. Cendoma, "Cervical spine functional anatomy and the biomechanics of injury due to compressive loading", *J Athl Train*, c. 40, sy 3, ss. 155-161, 2005.
[17] "Normal Eklem Hareket Açıklığı Ölçümü", *Fizyoo*, 27 Ocak 2018. https://fizyoo.com/normal-eklem-hareket-acikligi-olcumu/ (erişim 26 Ağustos 2023).
[18] "Shoulder Abduction". http://anatomyresources.hsc.wvu.edu/nm_deficits/Shoulder_Abduction.html (erişim 26 Ağustos 2023).
[19] A. H. McGregor, I. D. McCarthy, ve S. P. Hughes, "Motion Characteristics of the Lumbar Spine in the Normal Population", *Spine*, c. 20, sy 22, 1995, [Çevrimiçi]. Erişim adresi: https://journals.lww.com/spinejournal/fulltext/1995/11001/motion_characteristics_of_the_lumbar_spine_in_the.9.aspx
[20] "Single Leg Balance | Saint Luke's Health System". https://www.saintlukeskc.org/health-library/single-leg-balance (erişim 26 Ağustos 2023).

Tuning of the Controller Parameters Based on Equilibrium Optimizer Algorithm for Two Input Two Output Systems

Cagri Karakas[1], Tufan Dogruer[*,1]

cagri.karakas0422@gop.edu.tr
[*]tufan.dogruer@gop.edu.tr, ORCID: 0000-0002-0415-3042
[1]*Department of Electrical and Electronics Engineering, Tokat Gaziosmanpasa University, Tokat, Turkey*

Abstract: In this paper, controller design for two-input two-output systems (TITO), which is a part of multi-input multi-output systems (MIMO), is presented. Since TITO systems have a more complex structure than single-input single-output systems, it is more difficult to determine the controller parameters. For this reason, the researchers divided the TITO systems into sub-indexes in accordance with the decoupling techniques and determined the control parameters. In this study, an integer order TITO system is divided into two separate subsystems according to simplified and inverted decoupling methods. The PI control parameters of the reduced subsystems according to these decoupling techniques are determined using Equilibrium Optimizer (EO). The results obtained are compared with a study selected from the literature and the results are presented with figures. As a result, the PI controller parameters are successfully determined using the EO algorithm to control the TITO system.

Keywords: *TITO Systems, Controller Design, Simplified and Inverted Decoupling, Meta-heuristic Algorithms*

I. INTRODUCTION

One of the main objectives of control systems is to design controllers that ensure the desired operation of systems with specific characteristics. Therefore, researchers working on control systems have designed controllers of various types. Controllers of this type, which control systems by considering the values of proportional, integral, and derivative terms of the input, or their combinations, are commonly used in the forms of P, PI, PD, and PID. Due to the advantages of robust performance and simple structures, PID controllers are preferred more in the industry. While PID controllers are widely used in a high percentage, the practical applications often lead to the exclusion of the derivative component, resulting in the emergence of the PI controller structure [1]. The simplicity of the PI controller structure and its ability to yield satisfactory results for many systems have been the reasons for its utilization in this study.

Multi-input multi-output systems (MIMO) are defined as systems with multiple input and output variables. The most common model of MIMO systems widely used in the industry is the two-input two-output (TITO) system, which has two-inputs and two-outputs [2]. Designing controllers for MIMO systems is more challenging due to the interactions between the system's inputs and outputs [1]. Researchers have developed decoupling techniques to overcome this issue. Each decoupling technique has its own advantages and disadvantages. Therefore, the selection of an appropriate decoupling technique holds significant importance in controller design. Some researchers have taken the decoupling techniques as their subject and tried to get the best results by comparing them. For example, in a study, the ideal decoupling method and

the simplified decoupling method were compared, and when the results obtained were examined, it was observed that the simplified decoupling method gave better results than the ideal decoupling method [3]. In another study, ideal, simplified and inverted decoupling methods were compared and the results were observed [4]. The paper presented by Hajare and Patre [5] presents a decentralized PID controller design using the characteristic ratio assignment (CRA) method for two-input and two-output systems with time delay. In another study, the method suggested for developing a multivariable controller relies on an ideal decoupler *D(s)* and the optimization of a PID controller while considering limitations on robustness and sensitivity to measurement noise [6]. Another paper presents design approaches for decentralized PID controllers in the context of two-input two-output systems, employing decoupled subsystems as the basis for the methods [7]. The study conducted by Besta and Chidambaram [8] extends the application of the biggest log module tuning (BLT) method from designing decentralized proportional-integral controllers to the development of central PI controllers for two-input-two-output systems.

Controller parameters can be adjusted through various methods, and one of these approaches is the utilization of optimization methods. Optimization involves selecting the most optimal solution among the provided alternatives for solving a given problem [9]. First, decoupling methods will be applied to the TITO system considered in this study. By applying decoupling methods, two subsystems with single input and single output will be obtained. The controller parameters of these two subsystems will be found by a heuristic algorithm called equilibrium optimization. As a result of the optimization, the PI controller parameters of the TITO system will allow us to get the optimal values to control the system. Optimization methods are effective methods based on the minimization of the error signal and used to determine the control parameters. Criteria involving the integral of the error signal have been developed to find the optimum controller parameters considering the error in closed-loop control systems. Integral time absolute error (ITAE) performance index is used as the objective function to minimize the error while tuning the controller parameters with the EO algorithm.

In this study, the reduction of an integer-order TITO system into subsystems according to decoupling methods is presented. Unlike other studies, the PI controller parameters of the integer order system were determined using equilibrium optimization. During the optimization process, the integral of the time-dependent absolute value of the error signal was taken and the controller parameters to be found were ensured to be at the optimal value.

In the second part of this paper, the background of two-input two-output systems is given. The tuning of the controller parameters is explained in the third section. The fourth section introduces a simulation study aimed at assessing the effectiveness of the proposed method. In the last section, the obtained results are discussed.

II. BACKGROUND OF TWO INPUT TWO OUTPUT SYSTEMS

A. TITO System Structure

Since MIMO systems have multi-input and multi-output variables, they have a large number of loops. These loops cause the problem of interaction between each other. Decoupling methods have been developed to eliminate these interaction problems. Decoupling methods reduce MIMO systems to subsystems and transform the system into a simpler structure [10]. The block diagram of the TITO system is shown in Figure 1 [11].

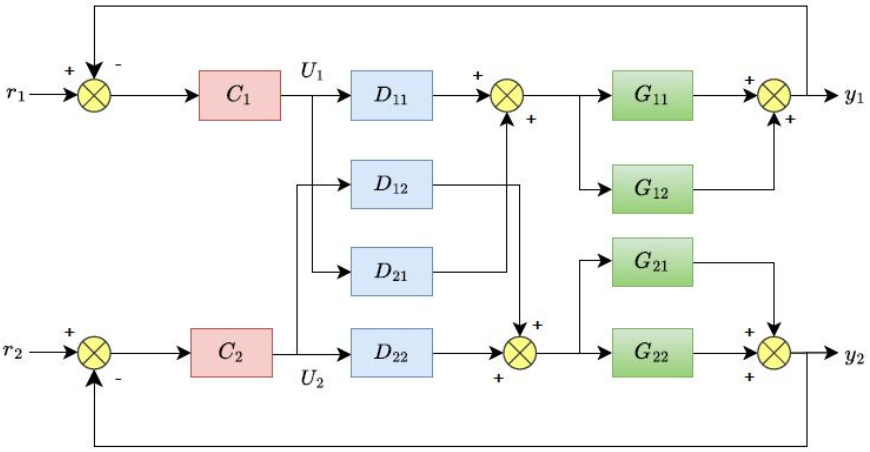


Fig. 1. TITO system block diagram.

The transfer function of the process of $G(s)$ in Figure 1 is given by matrix form,

$$G(s)=\begin{pmatrix} G_{11}(s) & G_{12}(s) \\ G_{21}(s) & G_{22}(s) \end{pmatrix} \tag{1}$$

The outputs of the process shown in Figure 1 can be expressed as follows [11].

$$y_1(s)=[D_{11}(s).G_{11}(s)+D_{21}(s)G_{12}(s)]U_1(s)+[D_{12}(s).G_{11}(s)+[D_{22}(s).G_{12}(s)]U_2(s) \tag{2}$$

$$y_2(s)=[D_{21}(s).G_{22}(s)+D_{11}(s)G_{21}(s)]U_1(s)+[D_{22}(s).G_{22}(s)+[D_{12}(s).G_{22}(s)]U_2(s) \tag{3}$$

In order to decoupling the $G(s)$ matrix of a TITO system, $D(s)$ decoupler transfer functions are needed. Let the decoupler transfer function $D(s)$ be defined as follows,

$$D(s)=\begin{pmatrix} D_{11}(s) & D_{12}(s) \\ D_{21}(s) & D_{22}(s) \end{pmatrix} \tag{4}$$

and from which the transfer functions $T(s)$ of the two decoupling subsystems are obtained.

$$T(s)=G(s).D(s)=\begin{pmatrix} T_1(s) & 0 \\ 0 & T_2(s) \end{pmatrix} \tag{5}$$

B. Simplified Decoupling Method

A simplified decoupling method block diagram for a TITO system is given in Figure 2 [11]. The variables $U_1(s)$ and $U_2(s)$ are controller outputs, y_1 and y_2 are system outputs [12]. Using Equations (1) and (4), the simplified decoupling method transfer functions are obtained. To facilitate the realization of the $D(s)$ matrix, the matrix is intended to be diagonal. Therefore, only blocks $D_{12}(s)$ and $D_{21}(s)$ are used in the simplified decoupling method [4].

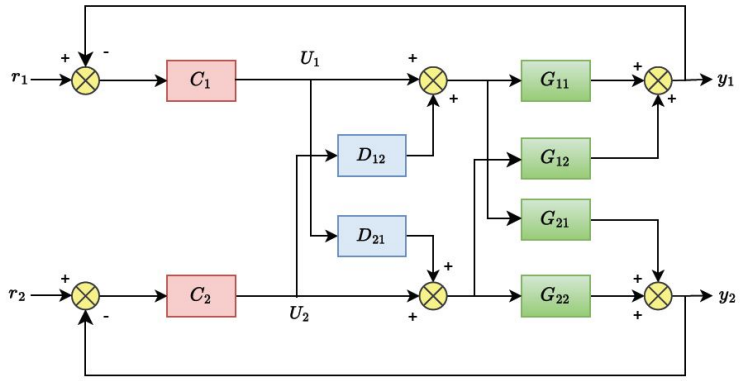


Fig. 2. Simplified decoupling block diagram.

$$D(s)=\begin{pmatrix} 1 & \dfrac{-G_{12}(s)}{G_{11}(s)} \\ \dfrac{-G_{21}(s)}{G_{22}(s)} & 1 \end{pmatrix} \tag{6}$$

Simplified decoupling transfer functions are obtained using Equations (1), (5) and (6).

$$T_1(s)=G_{11}(s)-\frac{G_{12}(s).G_{21}(s)}{G_{22}(s)} \tag{7}$$

$$T_2(s)=G_{22}(s)-\frac{G_{12}(s).G_{21}(s)}{G_{11}(s)} \tag{8}$$

C. *Inverted Decoupling Method*

The block diagram of the inverted decoupling method for a TITO system is given in Figure 3 [11]. The difference of this decoupling method from the simplified decoupling method is that the $D_{12}(s)$ and $D_{21}(s)$ blocks are connected inversely. The inverted decoupling transfer function $T(s)$ is expressed as Equation (9).

$$T(s)=\begin{pmatrix} T_1(s) & 0 \\ 0 & T_2(s) \end{pmatrix}=\begin{pmatrix} G_{11}(s) & 0 \\ 0 & G_{22}(s) \end{pmatrix} \tag{9}$$

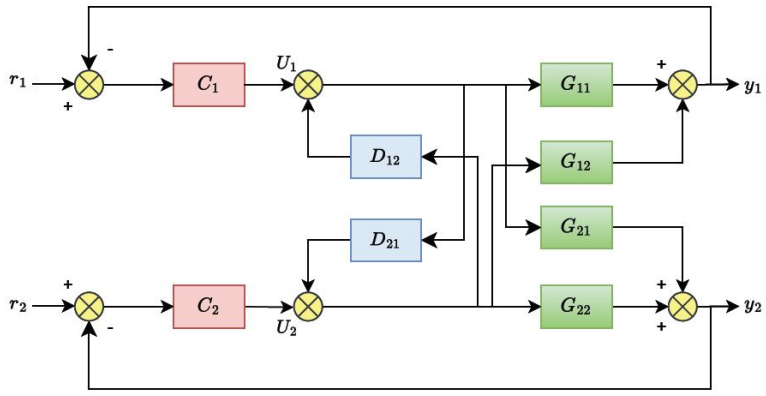


Fig. 3. Inverted decoupling block diagram.

III. TUNING OF THE CONTROLLER PARAMETERS

Optimization is the process that will provide the best solution to a problem among all the solutions determined under the given conditions for the problem. Any problem finding unknown parameter values that satisfy certain constraints is considered an optimization problem [13]. Heuristic algorithms are algorithms that use heuristic approaches to achieve a given goal [14]. Although heuristic algorithms do not guarantee an exact solution to problems, they can produce solutions close to the exact solution due to their convergence property.

An ideal control system is one in which the output signal follows the reference signal with zero error. But this is not possible in practice. Generally, when evaluating the performance of a control system, the transient and steady-state behavior of the system against a unit step response is examined. In particular, performance criteria such as the maximum percentage overshoot of the transient response, rise, settling and peak time are taken into account, and small values of these criteria are desirable. But it is difficult to design controllers according to these parameters. Therefore, integral performance criteria were developed to find the optimal controller parameters based on the error in the closed-loop control system. Thus, the use of integral performance criteria in controller design minimizes the error that may occur in the system to be controlled and enables the optimal controller parameters to be determined. Integral performance criteria are defined as objective functions in optimization processes and help to minimize the error. Integral performance criteria are expressed as IAE (integral of the absolute of the error), ISE (integral of the square of the error), ITAE (integral of the absolute of the time-weighted error), ITSE (integral of the square of the time-weighted error). In this study, ITAE criterion is used as an integral performance criterion for optimization and is expressed as in Equation (10). Thus, the error is minimized [15-17].

$$ITAE = \int_0^\infty t.|e(t)|.dt \tag{10}$$

The EO algorithm is a search algorithm developed by Faramarzi et al. based on the laws of physics [18]. The EO is inspired by volume mass balance control models used to predict both dynamic and equilibrium states. The mass balance equation is used to describe the concentration of a non-reactive component as a function of the various sources and leakage mechanism within the control volume.

In TITO systems, after decoupling processes, two single-loop subsystems that do not interact with each other are obtained. The controller design steps for these two single-loop subsystems apply separately. The block diagram of the system used in the design process is given in Figure 4. In the block diagram, the controller $C(s)$ is the PI controller and is expressed by Equation (11). Instead of $G(s)$, transfer functions obtained as a result of decoupling processes are used. The optimization algorithm becomes ready by including the objective function written according to the ITAE performance criteria into the EO algorithm and defining various parameter values in the algorithm.

$$C(s) = k_p + \frac{k_i}{s} \tag{11}$$

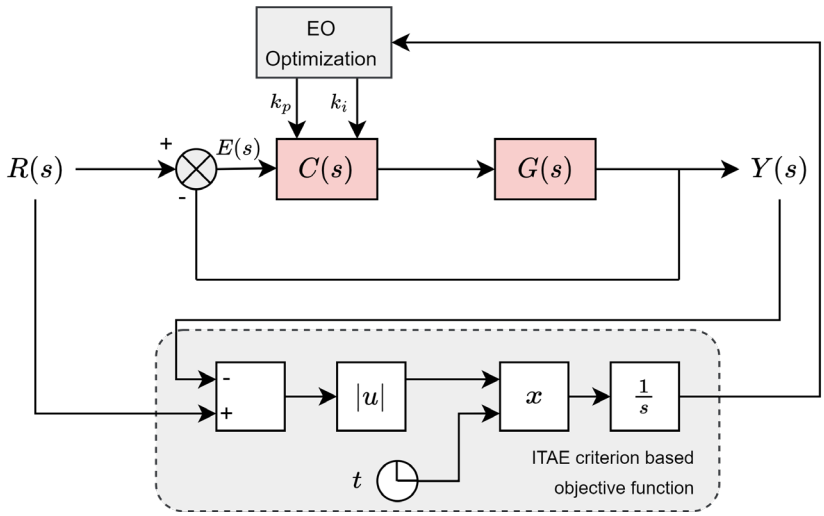


Fig. 4. Block diagram of proposed method.

IV. SIMULATION STUDY

Example: An integer-order TITO system is given as shown below [11]. The PI controller structure is used in the TITO system, which is decomposed by simplified and inverted decoupling methods, and the k_p and k_i parameters are found by EO Algorithm.

$$G(s)=\begin{pmatrix} \dfrac{s^2+2s+2}{s^4+3s^2+7.5s^2+5s+1} & \dfrac{1}{s^2+8s+3} \\ \dfrac{1}{s^2+6s+2} & \dfrac{s^2+2s+1}{s^4+3s^3+6s^2+4s+1} \end{pmatrix} \tag{12}$$

The system transfer functions for the inverted decoupling configuration are obtained as follows.

$$T_1(s)=\frac{s^2+2s+2}{s^4+3s^3+7.5s^2+5s+1} \quad \text{and} \quad T_2(s)=\frac{s^2+2s+1}{s^4+3s^3+6s^2+4s+1} \tag{13}$$

The decoupler transfer function matrices are the same for the simplified and inverted decoupling methods as given in Equation (14).

$$D_{12}(s)=\frac{-s^4-3s^3-7.5s^2-5s-1}{s^4+10s^3+21s^2+22s+6} \quad \text{and} \quad D_{21}(s)=\frac{-s^4-3s^3-6s^2-4s-1}{s^4+8s^3+15s^2+10s+2} \tag{14}$$

According to the method of Bulut and Deniz [11], the PI controller parameters for inverted decoupling are determined as k_{p1}=k_{p2}=7.6843 and k_{i1}=k_{i2}=7.8280. With the proposed method, PI controller parameters are determined as k_{p1}=4.9621, k_{i1}=1.2684, k_{p2}=3.4149, k_{i2}=1.003. By substituting the determined controller parameters in the block diagram, the unit step responses obtained from the y_1 and y_2 outputs of the TITO system are given in Figure 5 for inverted decoupling method. Figure 5 also includes unit step responses obtained by Bulut and Deniz [11]. When Figure 5 is examined, it is seen that the proposed method improves the time response properties of the system such as overshoot and settling time for both outputs. With the methods of Bulut and Deniz, an overshoot occurs over 50% in both outputs, while with the proposed method, the overshoot values decrease to approximately 18% for y_1 and 7% for y_2. Figure 6 shows the convergence curve of the best values obtained as a result of the EO

algorithm for y_1 and y_2. It is seen that the convergence curve for both outputs converges to its value at approximately the 15th iteration.

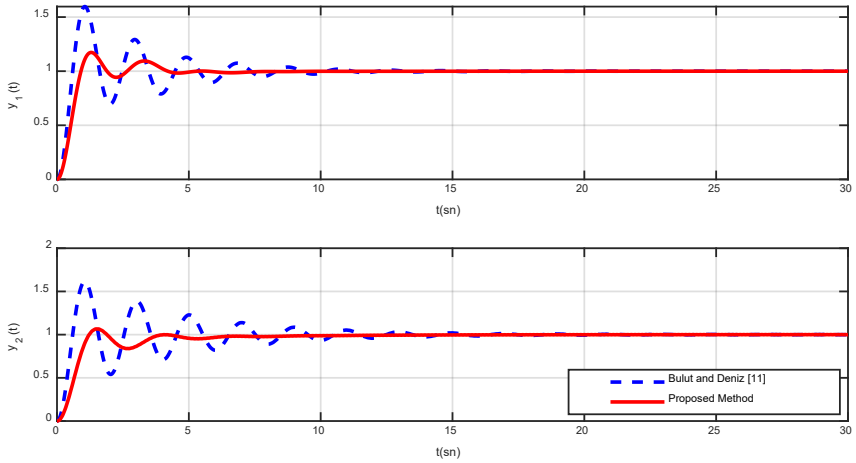


Fig. 5. Unit step responses based on inverted decoupling method for y_1 and y_2

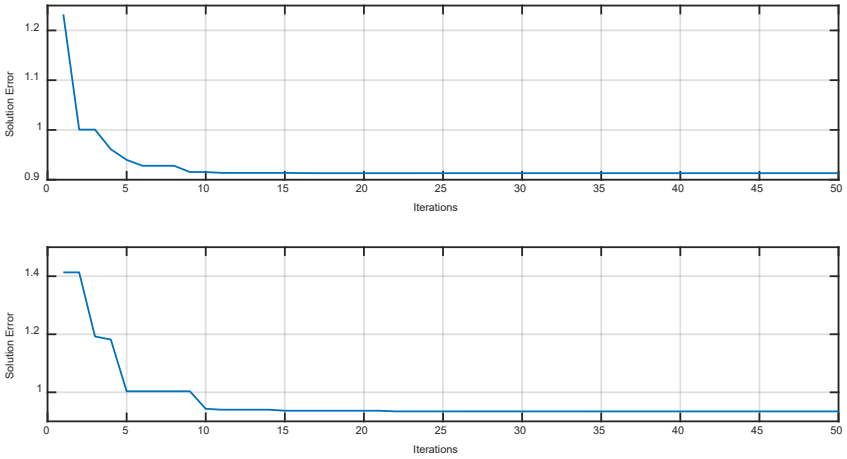


Fig. 6. Convergence curve based on inverted decoupling method for y_1 and y_2

For the same example, the study is repeated for simplified decoupling, and the transfer functions of the TITO system are obtained as in Equations (15) and (16).

$$T_1(s)=\frac{127s^7+93.5s^6+300.5s^5+525s^4+542s^3+318.5s^2+95s+11}{s^{10}+19s^9+137.5s^8+525s^7+1285s^6+2008s^5+1948.5s^4+1152s^3+402s^2+76s+6} \quad (15)$$

$$T_2(s)=\frac{127s^7+93.5s^6+300.5s^5+525s^4+542s^3+318.5s^2+95s+11}{s^{10}+19s^9+137s^8+517s^7+1247s^6+1976s^5+2087s^4+1404s^3+572s^2+128s+12} \quad (16)$$

In their study, Bulut and Deniz [11] are determined the PI controller parameters as k_{p1}=k_{p2}=9.2051 and k_{i1}=k_{i2}=5.9388. The PI controller parameters determined by the proposed method are as follows: k_{p1}=4.5137, k_{i1} =1.1584, k_{p2}=2.8065, and k_{i2}=1.3977. Figure 7 shows the unit step responses obtained according to the simplified decoupling method. It is seen from the figure that the proposed method improves the time response of the system in the simplified decoupling method as well as in the inverted decoupling method. Figure 8 shows the convergence curve of the best values obtained as a result of the EO algorithm for y_1 and y_2.

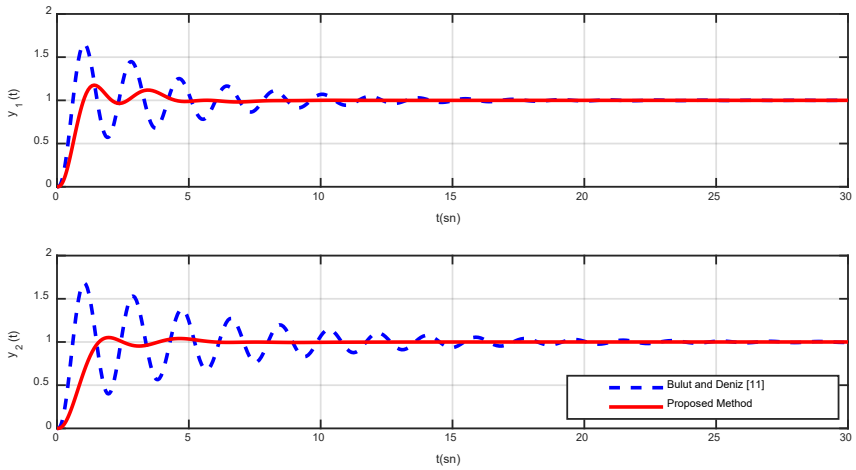


Fig. 7. Unit step responses based on simplified decoupling method for y_1 and y_2

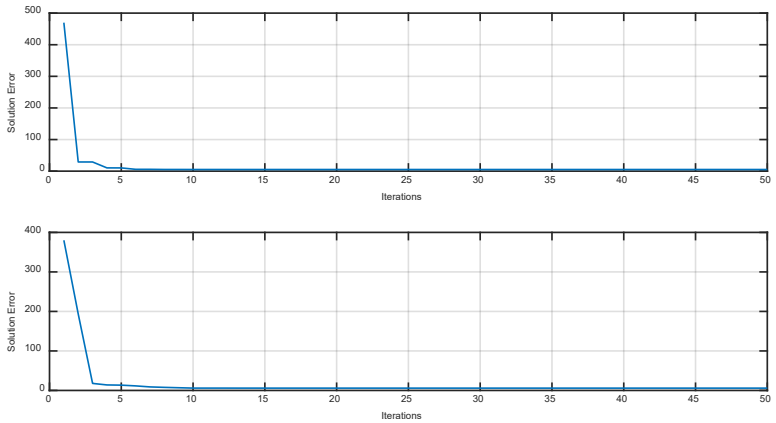


Fig. 8. Convergence curve based on simplified decoupling method for y_1 and y_2

In the analysis performed to evaluate the performances of the inverted and simplified decoupling methods, the unit step responses in Figure 9 are obtained for y_1 and y_2. For y_1, it is seen that the settling time of the response obtained by inverted decoupling is shorter, although the overshoot is almost the same for both decoupling methods. For y_2, the response obtained by the simplified decoupling method has slightly less overshoot than the response obtained by the inverted decoupling method. It has a shorter settling time in terms of settling time.

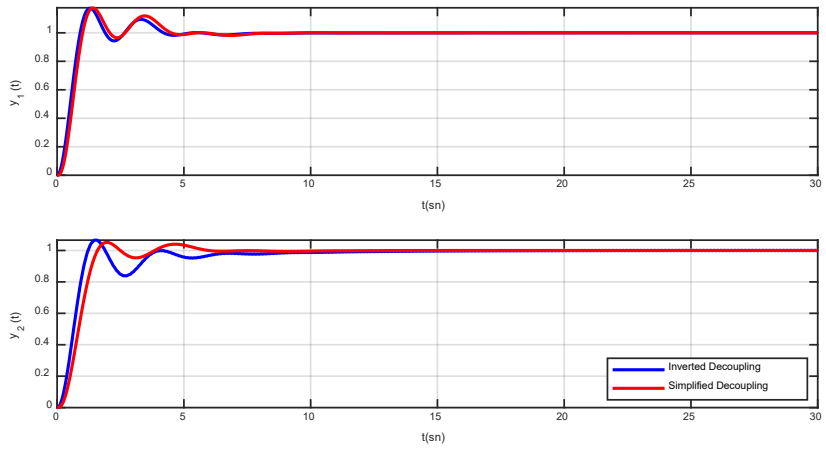


Fig. 9. Unit step responses obtained by inverted and simplified decoupling method for y_1 and y_2

V. CONCLUSIONS

This paper presents a tuning method for determining PI controller parameters in TITO systems. After the decoupling process, TITO systems are transformed into two single-loop control systems, thus simplifying the determination of controller parameters. The EO algorithm, where the ITAE performance criterion is integrated as the objective function, has been employed to tune PI controller parameters. In order to evaluate the effectiveness of the proposed technique, a simulation study was executed using a TITO system reported from the literature. In controller designs conducted for both simplified and inverted decoupling, it is evident that the proposed method yields both lower overshoot and shorter settling times. Additionally, comparisons were made between PI controller designs for systems obtained through simplified and inverted decoupling. It was observed that the results were nearly similar for y_1, while for y_2, simplified decoupling provided a better step response. In conclusion, it was observed that the proposed method can be employed to control TITO systems, yielding effective results.

REFERENCES

[1] K. J. Åström, K. H. Johansson, and Q.-G. Wang, "Design of decoupled PI controllers for two-by-two systems," *IEE Proceedings-Control Theory and Applications,* vol. 149, no. 1, pp. 74-81, 2002.

[2] S. Skogestad and I. Postlethwaite, *Multivariable feedback control: analysis and design*. john Wiley & sons, 2005.

[3] D. E. Seborg, T. F. Edgar, D. A. Mellichamp, and F. J. Doyle III, *Process dynamics and control*. John Wiley & Sons, 2016.

[4] E. Gagnon, A. Pomerleau, and A. Desbiens, "Simplified, ideal or inverted decoupling?," *ISA transactions,* vol. 37, no. 4, pp. 265-276, 1998.

[5] V. Hajare and B. Patre, "Decentralized PID controller for TITO systems using characteristic ratio assignment with an experimental application," *ISA transactions,* vol. 59, pp. 385-397, 2015.

[6] B. T. Jevtović and M. R. Mataušek, "PID controller design of TITO system based on ideal decoupler," *Journal of process control,* vol. 20, no. 7, pp. 869-876, 2010.

[7] D. Maghade and B. Patre, "Pole placement by PID controllers to achieve time domain specifications for TITO systems," *Transactions of the Institute of Measurement and Control,* vol. 36, no. 4, pp. 506-522, 2014.

[8] C. S. Besta and M. Chidambaram, "Tuning of multivariable PI controllers by BLT method for TITO systems," *Chemical engineering communications,* vol. 203, no. 4, pp. 527-538, 2016.

[9] K. G. Murty, "Optimization models for decision making: Volume," *University of Michigan, Ann Arbor,* 2003.

[10] L. Liu, S. Tian, D. Xue, T. Zhang, Y. Chen, and S. Zhang, "A review of industrial MIMO decoupling control," *International Journal of Control, Automation and Systems,* vol. 17, pp. 1246-1254, 2019.

[11] M. G. Bulut and F. N. Deniz, "Computation of stabilizing decentralized pi controllers for tito systems with simplified and inverted decoupling," in *2020 7th International Conference on Electrical and Electronics Engineering (ICEEE)*, 2020, pp. 294-298: IEEE.

[12] M. B. Hariz and F. Bouani, "Design of controllers for decoupled TITO systems using different decoupling techniques," in *2015 20th International Conference on Methods and Models in Automation and Robotics (MMAR)*, 2015, pp. 1116-1121: IEEE.

[13] H. J. Kadhum, K. Rajendran, and G. S. Murthy, "Optimization of surfactant addition in cellulosic ethanol process using integrated techno-economic and life cycle assessment

for bioprocess design," *ACS Sustainable Chemistry & Engineering,* vol. 6, no. 11, pp. 13687-13695, 2018.

[14] S. Akyol and B. Alataş, "Güncel sürü zekası optamizasyon algoritmaları," *Nevşehir Üniversitesi Fen Bilimleri Enstitüsü Dergisi,* vol. 1, no. 1, 2012.

[15] D. Atherton, *Control engineering*. Bookboon, 2009.

[16] M. S. Tavazoei, "Notes on integral performance indices in fractional-order control systems," *Journal of Process Control,* vol. 20, no. 3, pp. 285-291, 2010.

[17] M. Zhuang and D. Atherton, "Automatic tuning of optimum PID controllers," in *IEE Proceedings D (Control Theory and Applications)*, 1993, vol. 140, no. 3, pp. 216-224: IET.

[18] A. Faramarzi, M. Heidarinejad, B. Stephens, and S. Mirjalili, "Equilibrium optimizer: A novel optimization algorithm," *Knowledge-Based Systems,* vol. 191, p. 105190, 2020.

Effect of Additional Wire on Microstructure and Mechanical Properties of Weld Joints in Laser Welding

Ali YÜRÜK

alliyuruk@gmail.com, ORCID: 0000-0001-7160-9962
Kırka Eti Maden Mesleki ve Teknik Anadolu Lisesi, Eskişehir, Turkey

Abstract: Aluminum and its alloys are one of the most preferred metals in recent years due to their high corrosion resistance and good strength. However, in addition to these superior properties of aluminum, its high thermal conductivity, oxide layer on its surface and narrow solidification range cause various problems when joining with welding. Therefore, in this study, AA5754 H111 aluminum alloy and AA7075 T6 aluminum alloy were combined with wire and wireless fiber laser welding method and microstructure and mechanical properties investigation studies were carried out. As a result of the studies, it was seen that the sample produced using welding wire had a coarser grained microstructure. In addition, it was determined that the hardness of the sample produced using welding wire was lower than the hardness of the sample produced without using welding wire.

Keywords: *Laser welding, AA 5754,AA7075, Microstructure, Mechanical Properties*

I. INTRODUCTION

Aluminum and its alloys have recently started to be widely preferred both in terms of industrial and daily use. In addition, it is the second most used metal in the industry after steel [1]. The fact that aluminum is light, as well as having good strength properties is the most important reason for this, while its high corrosion resistance feature also contributes to its preference [2]. At the same time, the fact that the industry has a significant effect on the increase of greenhouse gas in the atmosphere in recent years has led to an increase in the use of aluminum in the industry [3]. Aluminum and its alloys have been widely used in the automotive, aircraft and ship industries, which aim to reduce exhaust emissions by lightening the vehicles they produce in order to reduce greenhouse gas emissions [4,5].

However, in addition to such good properties, there are problems in welding joints due to the properties of aluminum alloys such as the oxide layer on their surface, high thermal conductivity, and narrow solidification range. The most common problem during and after welding is weld deformation, known as hot cracking or hot tearing [6]. Aluminum alloys can be carry out by many welding methods such as GTAW (gas tungsten arc welding), MIG, laser welding, friction stir welding. Especially in recent years, laser welding has come to the fore in aluminum welding with its features such as narrow heat affected zone and low heat input.

The laser welding method is a non-contact high-energy welding [1]. When we compare laser welding with other arc welding techniques, laser beam can be obtained in a small spot after being centered by a lens, determining the correct welding position, high processing speed, good quality welding, predictable distortion due to low heat input and low cost features. [7]. These superior properties of laser welding have paved the way for its use in many areas from the automotive industry to the aerospace industry for joining ferrous and non-ferrous metals. Laser welding is used in many areas such as automotive industry, aircraft and space industry, electronics industry in which aluminum alloys are used extensively [8].

The increase in the usage areas of aluminum and its alloys and the fact that the problems experienced during welding have not been fully resolved have prompted academic circles to

conduct studies in this field. Here, an example of the work done with the welding of aluminum and its alloys is given. Kasman and Yenier joined AA5754 aluminum alloy and AA7075 aluminum alloy by friction stir welding method and stated that different defects occur at the bottom of the welds due to insufficient material flow and high heat input due to high friction velocity [9]. Prabhuraj et al., joined AA7075 aluminum alloy in sodium chloride solution by friction stir welding and stated that the weld metal contains equiaxed fine grains, while the grain size increases marginally in the TMHAZ region [10]. Kumar and Godwin joined AA7075 aluminum alloy and AA6061 aluminum alloy with TIG welding method and stated that the melting zone consists of a fine-grained microstructure depending on the cooling rate of TIG welding [11].

Laser welding method studies have focused on the joining of non-ferrous light metals and metals with different chemical and mechanical properties. Yu et al. In their study in which they joined 5A06 aluminum alloy with fiber laser welding method, they examined the causes of pore formation and as a result of this study, they said that gas gap formation is closely related to keyhole stability and fluctuation in the weld pool [12]. Hussien et al. They joined AISI 304 stainless steels with laser welding and reported that the weld penetration depth increased from 121 µm to 753 µm by increasing the laser power from 800 W to 1000 W [13]. Kawahito et al. They joined AISI 304 stainless steel and A 5052 aluminum alloy with fiber laser source and reported that the maximum penetration depths reached on the steel and aluminum sides were 13.1 and 15 mm, and the fusion zone on the AA 5052 aluminum side was more than twice that of the AISI 304 stainless steel side [14]. Liu et al. In their study in which they welded 1050 Al alloy with laser PET welding method, they reported that the ratio of the depths and widths of the grooves formed in the tissue has an effect on the tensile strength [15].

Due to the fact that the problems occurring in the welding of aluminum alloys have not been fully resolved, In this study, AA5754 and AA7075 aluminum alloys were joined by laser welding with and without welding wire, and microstructure and mechanical properties of the joints were investigated.

II. EXPERIMENTAL STUDY

II.I. MATERIAL

In this study, AA 5754 and AA 7075 aluminum alloys were made ready for welding after cutting with 200*100*2 mm guillotine shears and cleaning the foreign materials that might prevent welding on them by brushing and sanding. Joinings were carried out using an additional single and without using additional wire. While the chemical composition of AA 5754, AA7075 aluminum alloys and the ER5356 TIG welding wire used are given in Table 1, their mechanical properties are given in Table 2.

TABLE I
CHEMICAL COMPOSITION OF MATERIALS.

EN AW	Si	Fe	Cu	Mn	Mg	Cr	Zn	Ti	Diğer	Kalan
5754 H111	0,40	0,4	0,10	0,5	2,6-3,6	0,3	0,20	0,15		Al
7075 T6	0,5	0,5	1,2-2	0,3	2,1-2,9	0,18-0,28	0,25		0,15	Al
ER5356	0,50			0,50	5,0					Al

TABLE II
MECHANICAL PROPERTIES OF MATERIALS.

Alaşım Türü	Temper	Akma mukavemeti *(MPa)* min-max	Çekme Mukavemeti *(Mpa)* min-max	Uzama *(%50)* min-max	Sertlik *(Brinel)* min-max
AA5754	0/H111	80 -100	190 -240	24	50 -55
AA7075	T6	460-505	530-570	10	150
ER 5356		250	120	25	70

II.II. METHOD

AA 5754 and AA7075 aluminum alloys were joined face to face, leaving 1 mm weld gap between them, as in Figure 1. It was joined by fiber laser welding method using the welding parameters given in Table 3.

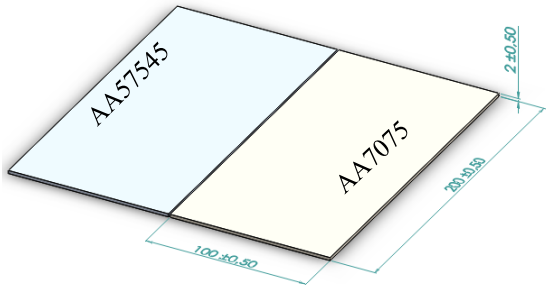


Fig. 1. Preparation for welding.

TABLE III
WELDING PARAMETERS.

Numune No	Güç (W)	Salınım Hızı (Hz)	Salınım Aralığı [mm]	Frekans (Hz)
L2	800	150	1	3000
TL2	800	150	1	3000

AA 5754 and AA7075 aluminum alloys were joined by fiber laser welding method with and without wire. After the joining process, metallographic and mechanical tests were performed on the samples. While microstructure studies were performed on the samples as metallographic test, hardness teste were performed on the samples as mechanical tests.

For macro and microstructural examinations of the produced samples, test samples were taken from the weld section perpendicular to the joining direction and after the samples were polished with standard methods, they were etched for 20 seconds with a keller etching reagent (2ml HF + 3ml HCl + 5ml HNO3 + 190ml Water). After etching, microstructure images were taken with a Metal Microscope and examined.

After taking the microstructure images on the same samples, as seen in Figure 2, from 1 point from the weld center and 2 points with 0.5 mm spacing towards both sides of the weld center, 0.5 mm from both sides of the IEB (the zone under the influence of heat). Hardness measurements were made from 3 points at each mm spacing and 2 points from the main materials, a total of 13 points. Then, using the obtained data, the hardness distribution graph was drawn.

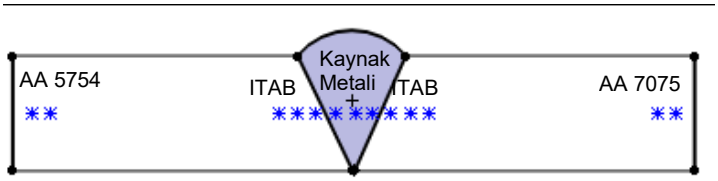


Fig. 2. Hardness measurement method.

III. SONUÇLAR VE TARTIŞMA

III.I. MIKROYAPI ÇALIŞMALARI

Microstructure studies were carried out to examine the effects of welding wire on the microstructure. Images of base metals from the images obtained as a result of microstructure studies are given in Figure 3, and images of welded joints are given in Figure 4.

The microstructure of the AA 5754 parent material was found to consist of equiaxed grains and homogeneously dispersed precipitates. Farzad et al., joined 5000 series aluminum alloys

with friction stir welding and stated that the base metal contains coaxial grains and precipitates [16]. It was observed that AA 7075 aluminum base metal exhibited flat shaped coarse grains elongating in the rolling direction. Similarly, Ma et al., in their study where they joined AA 7075 aluminum alloy with friction stir welding, stated that the AA7075 base material consists of coarse grains extending in the rolling direction, in the width direction and in the normal direction [17].

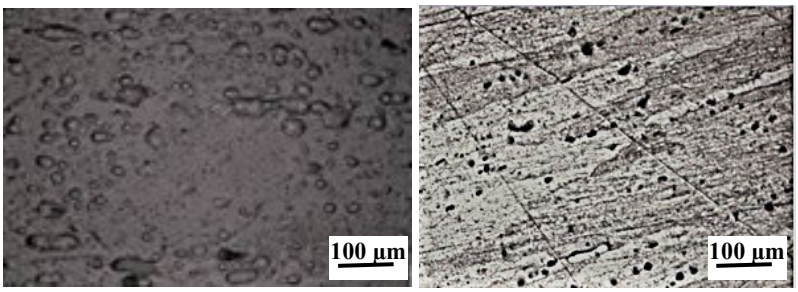


Fig. 3. Base metals.

When the microstructures of the welded joints produced with the base metal were compared, it was seen that the microstructure of the weld metal consisted of columnar grains. In addition, it has been determined that it contains smaller grains than base metals due to heat input and subsequent rapid cooling. Kumar and Godwin stated that the weld metal consists of fine grains due to rapid cooling in the study where they joined Al7075 and Al6061 aluminum alloys with TIG welding method [11]. In addition, it was determined that the microstructure of the weld metal consisted of elongated grains. Likewise, Sivashanmugam et al., in their study joined with GTAW and GMAW methods, stated that the microstructures of the samples joined with the GMAW method contain slightly elongated grains [18].

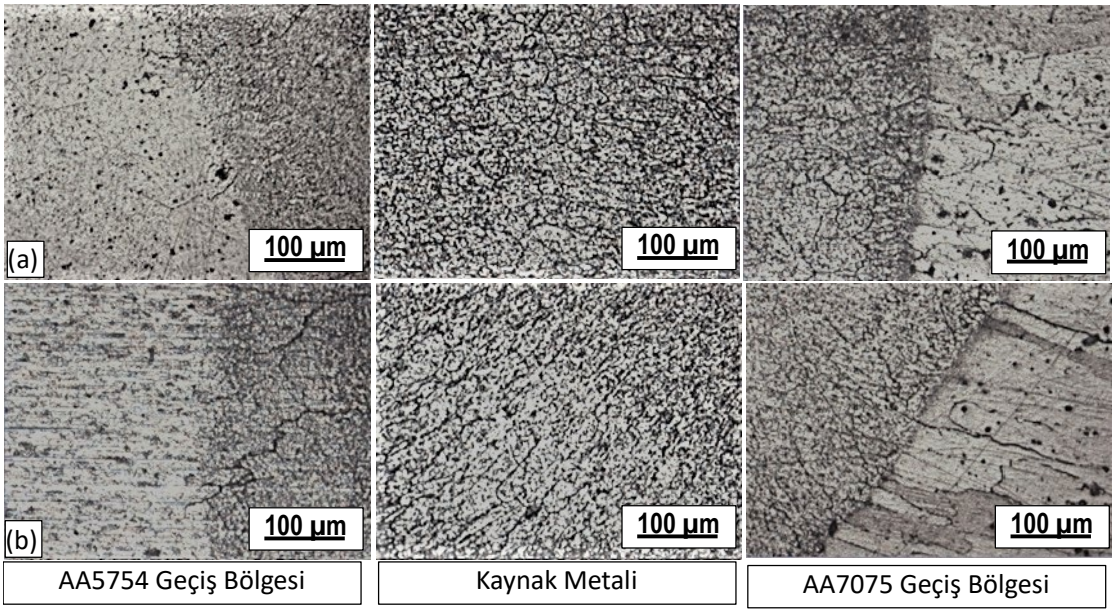


Fig. 4. Microstructure images a) L2 b) LT2.

When the effects of the welding wire on the microstructure were examined, it was observed that the microstructure of the joint produced using wire consisted of coarser grains than the microstructure of the joint produced without the use of wire. It is thought that the coarser grained microstructure of the joint produced by using additional wire is due to the mixture of the weld metal of the produced sample, AA 5754, AA7075 and the additional wire used, and the cooling process. Pujari and Patil stated that the properties of a weld metal depend on the composition of the base metals and the additional wire, and the solidification rate in their study in which they joined Al7075 aluminum with the GTAW welding method [19].

One of the most sensitive areas in a welded joint is the HAZ. When the weld structure of this region is examined, it is seen that the joint produced using additional wire contains larger grains than the joint produced without using additional wire. This is thought to be caused by the chemical composition of the additional wire used. This is thought to be due to the fact that the sample produced by using additional wire has a larger weld pool due to the use of wire and therefore produces more heat input.

III.II. MIKROSERTLIK

In order to investigate the effects of welding wire in addition to the hardness of the produced samples, hardness measurement processes were carried out. The hardness graph drawn by using the data obtained as a result of the studies carried out is given in Figure 5.

When the hardness measurement results were examined, it was determined that the hardness of AA7075 base metal was the hardest region in both welded joints, followed by AA7075 HAZ, weld metal, AA5754 HAZ and AA5754 base metal, respectively. Özsaraç et al., as a result of their study with AA5754 and AA7075 aluminum alloys, stated that the hardness of AA7075 aluminum alloy is higher than that of AA5754 aluminum alloy [4]. The highest hardness obtained in the HAZ on the AA7075 side was measured as 173.1 HV0.2 in the sample produced without using wire, while the highest hardness obtained in the weld metal was measured as 125 HV0.2 in the sample produced without using wire.

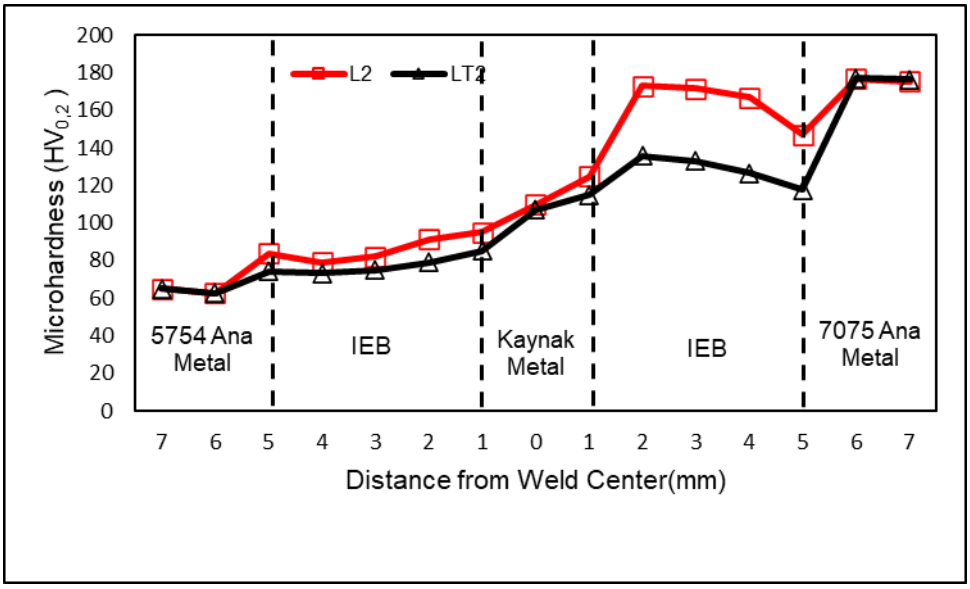


Fig. 5. Hardness measurement results.

When the effects of the welding wire on the hardness were examined, it was observed that the hardness of the sample produced using the welding wire was lower than the sample produced without the use of additional wire. It is thought that this change in hardness is caused by the chemical composition of the additional wire used.

IV. CONCLUSION

AA7075 and AA5754 aluminum alloys were successfully joined with and without welding wire, and the following results were obtained.

1. When the microstructures of the welded joints produced with the base metal were compared, it was seen that the microstructure of the weld metal consisted of columnar grains. In addition, it has been determined that it contains smaller grains than base metals due to heat input and subsequent rapid cooling.

2. It has been observed that the microstructure of the joint produced using wire consists of coarser particles compared to the microstructure of the joint produced without the use of wire.
3. Due to the chemical composition of the additional wire used, the hardness of the sample produced without wire was determined to be higher than the hardness of the sample produced using wire.

REFERENCES

[1] B. Çevik and B. Gülenç, "The effect of welding speed on mechanical and microstructural properties of 5754 Al (AlMg3) alloy joined by laser welding," Mater. Res. Express 2018, 5; 086520.

[2] A.Yürük, "6013-T6 Alüminyum Alaşımlarının Sürtünme Karıştırma Nokta Kaynağına Takım Bekleme Süresinin Etkisi," Politeknik 2021, pp.733-738.

[3] D. Wallerstein, A. Salminen, F. Lusquiños, R. Comesaña, J. Val García del, A. R. Rodríguez., A. Badaoui, and J. Pou, "Recent Developments in Laser Welding of Aluminum Alloys to Steel," Metals, 2021, 11; pp.2-32.

[4] U. Özsaraç, M. E. Unat, F. Varol, Ş. Işık, C. Özdemir and S. Aslanlar, "Investigation of Mechanical Properties of Aluminum 5754-7075 Alloys Joined by Cold Metal Transfer by Using Different Gas Pressures," International Journal of Computational and Experimental Science and Engineering (IJCESEN) 2017, 3(2); pp. 26-28.

[5] A.Yürük, Y. Ayan, B. Çevik and N. Kahraman,"Investigation of mechanical and microstructural properties of AA5754/AA6013 dissimilar aluminium alloys joined by GMAW and FSW methods," Kovove Mater., 2021, 59; pp. 245–256.

[6] H. S. Çubuk, G. Kurt and U. Çavdar, "Investigation of the Effects of Different Welding Methods Applied on Aluminum 7075 Material on the Mechanical and Microstructure Structure Properties of the Joint Zone," Turkish Journal of Engineering Research and Education, 2022, 1(2); pp. 120-128.

[7] Y. M. Baqer, S. Ramesh, F. Yusof, R. Mahmoodıan, S. Sıvakumar, T. Wu and C. Tan, " Fiber laser welding of similar and dissimilar aluminum alloys," Journal of Engineering Science and Technology, 2021, 16 (4), pp. 2950-2959.

[8] W. Tao, B. Han and Y. B. Chen, "Microstructural and mechanical characterization of aluminum-lithium alloy 2060 welded by fiber laser," Journal Of Laser Applıcatıons, 2016, 28(2), https://doi.org/10.2351/1.4944092.

[9] Ş. Kasman and Z. Yenier, "Analyzing dissimilar friction stir welding of AA5754/AA7075," Int J Adv Manuf Technol, 2014, 70; pp.145–156.

[10] P. Prabhuraj, S. Rajakumar and V. Balasubramanian, "Electro chemical response of stir zone in friction stir welded AA7075-T651 joint in sodium chloride solution," Materials Today: Proceedings, 2020, 22; pp. 546–550.

[11] S.Santhosh Kumar and G. Godwin, "An Enhancement of Properties on Al7075 and Al6061 Dissimilar Materials Welded by TIG Process," International Research Journal on Advanced Science Hub (IRJASH), 2020, 2: pp. 115-121.

[12] Y. Yu, C. Wang, X. Hu, J. Wang and S. Yu, "Porosity in fiber laser formation of 5A06 aluminum alloy," Journal of Mechanical Science and Technology,2010, 24 (5); pp.1077-1082.

[13] A. M. Hussien, A. El-Shabasy and B. Adel, Abd El-Ghany and Khalid M, "Evaluatıon of stainless steel 316l joınts welded by laser," Journal Of Al-Azhar University Engineering Sector, 2019, 14 (50), pp. 229-236.

[14] Y. Kawahito, N. Matsumoto, Y. Abe and S. Katayama, "Relationship of laser absorption to keyhole behavior in high power fiber laser welding of stainless steel and aluminum alloy," Journal of Materials Processing Technology, 2011, 211; pp. 1563–1568.

[15] J. Liu, Y. Dai, Y. Shi, W. Cui and T. Jiang, "Efect of Surface Texture on Tensile Shear Strength of 1060Al-PET Welding Joints," Chinese Journal of Mechanical Engineering, 2021, 34 (134), pp. 2-16.

[16] H. Farzad, A. Alireza and A. Mohammad, "Effects of processing parameters on microstructure and mechanical behaviors of underwater friction stir welding of Al5083 alloy," Journal of Manufacturing Processes, 2017, 25, pp. 77–84.

[17] Y. Ma, S. Niu, H. Liu, Y. Li, N. Ma, "Microstructural evolution in friction self-piercing riveted aluminum alloy AA7075-T6 joints," Journal of Materials Science & Technology, 2021, 82; pp 80–95.

[18] M. Sivashanmugam, C. Jothi Shanmugam, T. Kumar and M, Sathishkumar, "Investigation of Microstructure and Mechanical Properties of GTAW and GMAW Joints on AA7075 Aluminum Alloy," Osmangazi Universites, 2023, pp. 241-246.

[19] K. S. Pujari and D.V.Patil, "A Review on GTAW Technique for High Strength Aluminium Alloys (AA 7xxx series)," International Journal of Engineering Research & Technology (IJERT), 2013, 2(8); pp. 2477-2490.

Farklı Sinterleme Parametrelerinin Monolitik Alüminanın Yoğunluğuna Etkisinin İncelenmesi

Investigation of the Effect of Different Sintering Parameters on the Density of Monolithic Alumina

Samet YAVUZ[*,1], Mevlüt GÜRBÜZ[1]

[*]smtyvz4894@gmail.com, ORCID: 0000-0002-6912-279X
[1]*Makine Mühendisliği Bölümü, Ondokuz Mayıs Üniversitesi, Samsun, Türkiye*

Özet: Günümüz mühendislik çalışmalarında enerjinin verimliliği, yüksek dayanım, hafiflik ve düşük maliyet gibi malzeme özelliklerinin bir araya getirilerek yeni malzemelerin üretilmesi, endüstrinin temel geliştirme çalışmalarının başında gelmektedir. Bu geliştirme çalışmalarının hız kazandığı bir malzeme grubu olarak seramikler geçmişten günümüze kadar geniş bir çalışma alanı oluşturmuştur, yapılan geliştirmeler ile üretilen seramikler ileri teknoloji seramikler olarak tanımlanmaktadır. Son yıllarda ileri teknoloji seramikler grubunda yaygın olarak kullanılmakta olan alümina (Al_2O_3) yüksek mekanik özellikleri ile geleneksel olarak kullanılmakta olan metal ve alaşımlarının yerini almaktadır. Yüksek sertlik, yüksek aşınma dayanımı, düşük özgül ağırlık, yüksek ergime sıcaklığı ve korozyon direnci alüminanın üstün özelliklerinin başında gelmektedir. Bunların yanı sıra düşük kırılma tokluğu ise dezavantaj olarak öne çıkmaktadır. Yapılan bu çalışmada monolitik alüminanın toz metalurjisi ile üretilmesi ve işlem adımlarının incelenmesi ve optimum sinterleme parametrelerinin saptanması hedeflenmiştir. Bu amaçla farklı sinterleme sıcaklıklarında ve sürelerinde sinterleme işlemleri gerçekleştirilmiştir. Numunelerin sinterlenmesinde 1450 °C, 1550 °C işlem sıcaklıkları ve 2, 4 saat bekleme süresi uygulanarak elde edilen yoğunluk verileri sinterleme öncesi ve sonrası olarak her bir numune için karşılaştırılmış ve en iyi sonucu veren sinterleme parametresi tespit edilmiştir.

Anahtar Kelimeler: *Alümina, Sinterleme, Yoğunluk*

Abstract: In today's engineering studies, the production of new materials by combining material properties such as energy efficiency, high strength, lightness and low cost is one of the basic development studies of the industry. Ceramics, as a material group in which these development studies accelerated, has created a wide working area from past to present, ceramics produced with the improvements made are defined as advanced technology ceramics. Alumina (Al_2O_3), which has been widely used in the advanced technology ceramics group in recent years, replaces the traditionally used metals and alloys with its high mechanical properties. High hardness, high wear resistance, low specific gravity, high melting temperature and corrosion resistance are among the outstanding features of alumina. In addition to these, low fracture toughness stands out as a disadvantage. In this study, it was aimed to produce monolithic alumina by powder metallurgy, to examine the process steps and to determine the optimum sintering parameters. For this purpose, sintering processes were carried out at different sintering temperatures and times. The density data obtained by applying 1450 °C, 1550 °C processing temperatures and a waiting time of 2, 4 hours during the sintering of the samples were compared for each sample before and after sintering, and the sintering parameter that gave the best result was determined.

Keywords: *Alumina, Sintering, Density*

I. GİRİŞ

GÜNÜMÜZ mühendislik çalışmalarında enerji tasarrufu, yüksek dayanım ve düşük ağırlık gibi malzeme özelliklerinin bir araya getirilerek yeni malzemelerin geliştirilmesi ihtiyacı uzay, savunma ve otomotiv gibi endüstriler için oldukça önemlidir. Bu geliştirme çalışmaları neticesinde elde edilen kompozit malzemelerin üretimi mevcut mühendislik malzemelerinin yerini almaktadırlar. Kompozit malzemeler, birbirinden farklı iki veya daha fazla malzemenin bir araya gelmesiyle ile elde edilen bileşimindeki malzemelerin tek başına gösteremeyeceği çoğu özelliği gösterebilen yeni bir malzeme grubudur. Kompozitler, yüksek dayanım ve rijitlik gösteren bir malzemenin başka bir ana malzeme ile çevrelenmesi ile elde edilen malzeme olarak tanımlanabilir. [1]–[3]. Bu kompozitlerin üretiminde ise üstün özelliklerinden faydalanmak ve aynı zamanda gevrek yapısının sünek yapılı metal takviyeler ile geliştirildiği alümina matris malzemesi olarak yaygın olarak kullanılmaktadır.

Alümina yüksek termal kararlılık, yüksek aşınma dayanımı ve kimyasal kararlılık gibi özellikleri sebebiyle mekaniksel uygulamalarda yaygın olarak kullanılmaktadır. Fakat tokluğunun ve mukavemetinin yetersiz olması bu uygulamaları kısıtlamaktadır. Bu açıdan bakıldığında tekil fazlarla üretilen seramiklerin, metal takviyeli kompozitlerle karşılaştırıldığında tokluk ve mukavemet özelliklerini iyileştiği görülmektedir. Buradan hareketle havacılık ve otomotiv uygulamaları için malzemelerin performans gereksinimlerindeki sürekli artışlar, yapısal kompozit malzemelerin geliştirilmesinin önünü açmıştır. Ek olarak seramik-metal (sermet) yapılı kompozitlerin üretiminde oluşan ara yüzey reaksiyonlarının mukavemet ve toklukta düşüşe sebep oldukları göz önünde bulundurulmalıdır [4].

Alümina yüksek sertlik, düşük sürtünme katsayısı ve düşük aşınma oranı gibi özelliklere sahipken kırılma toklukları ve çekme dayanımları oldukça düşüktür. Bu sebeple gevrek olan Al_2O_3 matrise daha sünek olan ilave malzemelerin takviye edilmesi konusunda birçok çalışma yapılmış olup (Al, Ni, TiC), Ti ilavesi konusunda yapılan çalışmalarda son yıllarda hız kazanmıştır[5]–[7].

Önceki çalışmalar incelendiğinde, mikrodalga sinterleme yöntemiyle Al_2O_3 matrisli Ti(C,N) mikro-nano kompozit seramik uç malzemesinin hazırlanması ve özellikleri konusunda yapılan bir çalışmada sinterleme süresi ve bekleme sıcaklıklarının yoğunluk, mekanik özellikler ve mikro yapı üzerindeki etkilerini araştırmışlardır. Yapılan bu çalışmada kullanılan kompozisyon %61 α-Al_2O_3 (%99,99 saflıkta), %30 Ti(C,N) (%99,99 saflıkta) ve %9 Ni ve Mo (%99,99 saflıkta) şeklindedir. Sinterleme sıcaklık aralığı 1500 ºC -1650 ºC ve bekleme süresi 5-15 dk olarak belirlenmiştir. 1500 ºC de yapılan sinterleme işleminde tanelerin küçük ve porozitenin fazla olduğu bunun sonucunda ise yoğunluğun ve kırılma tokluğunun düşük olduğu rapor edilmiştir. Sinterleme sıcaklığı arttıkça 1550 ºC- 1600 ºC'lerde yoğunluğun arttığı mikro yapının daha homojen olduğu ve ince taneli yapının görüldüğü ve optimum değerlerin 1550 ºC' de yapılan sinterleme ile elde edildiği rapor edilmiştir. 1650 ºC'de yapılan sinterlemede ise tanelerin düşük sıcaklıklara nazaran daha büyük olduğu bununda dayanımı azaltacağı fakat tokluğu iyileştireceği bildirilmiştir Farklı bekleme sürelerinde ise yapılan incelemelerde 5 dk bekleme süresinde ince taneli yapının olduğu fakat yapı içerisinde porların çok miktarda kaldığı bununda kalıntı gerilemelerine ve tane sınırlarını zayıflattığı, 10 dk bekleme süresinin ince taneli yapı sağladığı ve optimal mekanik özellikleri sağladığı, 15 dk bekleme süresinin bürük porların ve büyük tanelerin oluşmasına sebep olduğu ve bununda yoğunluğun azalmasına ve ara yüzey yapışma mukavemetini düşürdüğünü belirtmişlerdir. Yapılan bu çalışmanın sonucunda kırılgan ve gevrek yapıda olan alüminanın kesici takım endüstrisinin ihtiyacı olan kırılma tokluğunun yükseltilmesi ihtiyacı, diğer parametrelere nazaran düşük sıcaklık ve düşük bekleme sürelerinde ince taneli, homojen mikro yapı ve düşük poroziteli yapıların eldesi ile mümkün olduğu rapor edilmiştir [8].

SPS yöntemiyle üretilen Al_2O_3/Ti kompozitlerinin mekanik özelliklerini incelemişlerdir. Yapılan bu çalışmada Ti oranı %0,20,40-60,80,100 olarak artırılarak numuneler elde edilmiştir. Farklı kompozisyonlarda alümina ve Ti ilavesi ile hazırlanan numunelerin yoğunlukları karşılaştırılmıştır en yüksek yoğunluğun monolitik alüminada 4,5

g/cm^{3}ölçüldüğü ve artan Ti oranıyla yoğunluğun azaldığı en düşük yoğunluğun 3,95 g/cm^3 olarak %100 Ti numunesinde ölçüldüğü tespit edilmiştir [5].

Başka bir çalışmada ise Al_2O_3/(W,Ti)C/grafen kompozit seramik kesici takım malzemesinin mikro yapı ve sertleştirme mekanizmalarını incelemişlerdir. Hazırlanan numunelere sabit kompozisyonlarda tutulan ana karışım malzemelerine ek olarak 0,2'lik artışlarla %0-0,8 oranların da grafen (GNPs) ilave edilerek, yapılan bu ilavenin mekanik özelliklere etkileri incelenmiştir. Bu çalışmada %0,2 lik grafen takviyesi yapılan numunenin yoğunluğunun en yüksek ölçüldüğü, grafen takviyesi olmayan numunenin yoğunluğunun ise artan diğer numunelerden daha yüksek yoğunluğunun elde edildiği bildirilmiştir[9].

Konvansiyonel sinterleme ile üretilen nikel ve titanyum katkılı $Al_2O_3/ZrO_2/CeO_2$ kompozitlerinin sentezi, mikro yapısı ve mekanik özelliklerini incelemişlerdir. Çalışma kapsamında hazırlanan numunelerin sinterleme sıcaklıkları ve bekleme süreleri ortak kullanılmıştır. Yapılan yoğunluk ölçümlerinde alümina seramiğin yoğunluğunun %94,2 ile en düşük gelirken, en yüksek %97 ile Al_2O_3-40ZrO_2-3Ni numunesinde hesaplandığı ve diğer numunelerin hepsinin saf alüminadan daha yüksek olduğu tespit edilmiştir. Gevrek ve kırılgan yapıda olan alüminanın, sünek yapılı olan Ni ilavesi ile tokluğunu artırmak amacıyla yapılan numunelerle saf alüminaya göre yüksek sonuçlar alınsa da, alümina matrise Ni yanında ZrO_2 veya CeO_2 ilavelerinin yapısının mekanik özelliklerini daha da iyileştirdikleri tespit edilmiştir. Şekil 7.5' de numunelerin yoğunluklarının karşılaştırmaları verilmiştir. Şekil 7.6' da ise numunelerin sertlik ve kırılma tokluklarının karşılaştırılması verilmiştir [10].

Yapılan önceki çalışmalar alüminanın yoğun olarak kullanıldığını ve sinterleme ile üretim işlemlerinde proses parametrelerinin yoğunluk başta olmak üzere mekanik ve mikroyapı üzerinde etkisinin olduğunu göstermektedir. Buradan hareketle monolitik alümina numunelerinin üretim ve sinterleme proses akışları ile elde edilen yoğunluk verileri ince taneli ve porozitenin az olduğu üretimin gerçekleştiği uygun parametrelerin seçildiğini göstermektedir. Bu amaçla genel olarak matris malzemesi olarak kullanılan alüminan yoğunluğuna sinterleme proses parametrelerinin etkileri incelenmiştir.

II. MATERYAL VE YÖNTEM

A. Materyal

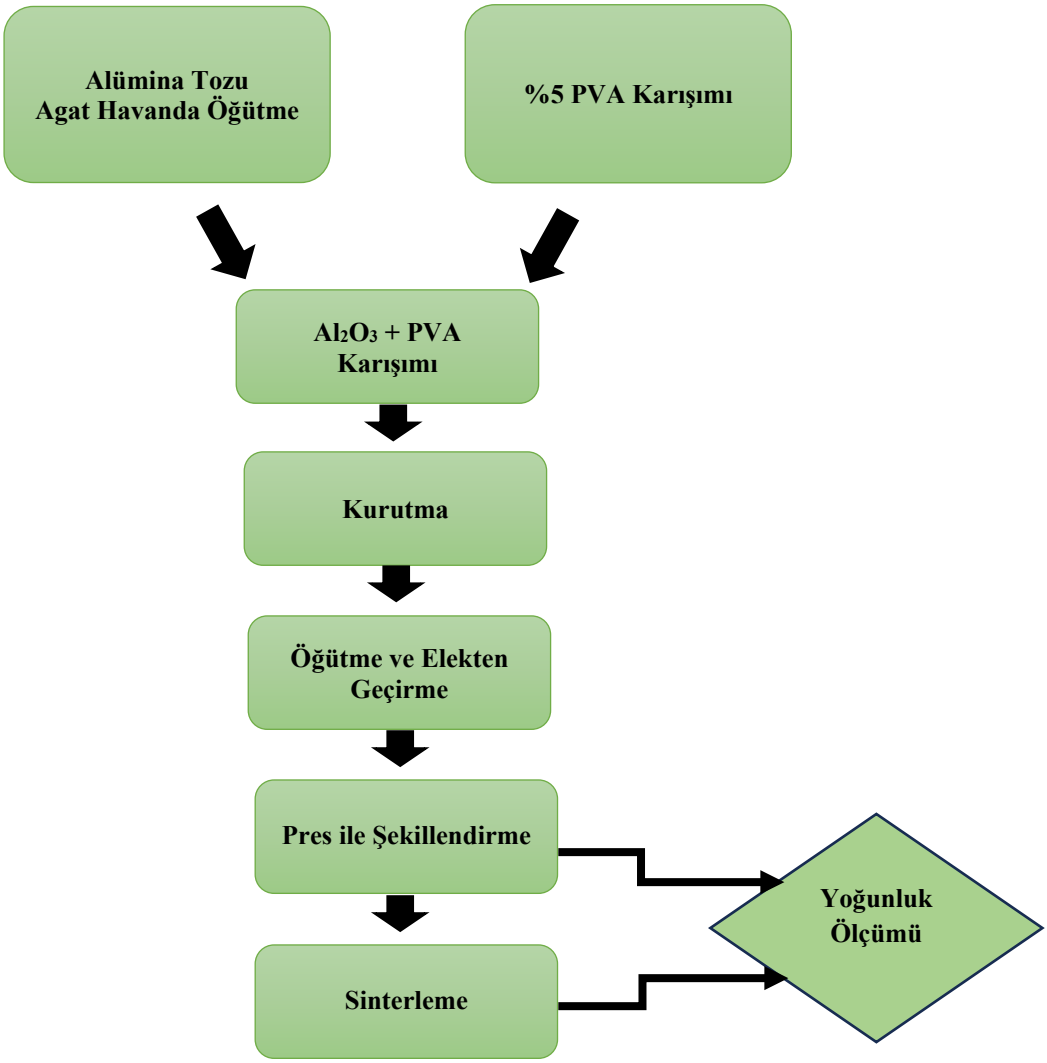
Alümina seramikleri düşük yoğunluk, yüksek sertlik, kimyasal kararlılık ve iyi yüksek sıcaklık özelliklerinin gerekli olduğu birçok özel uygulamada kullanılmaktadır. Al_2O_3'ün gevrek ve kırılgan yapıda olmasının getirdiği dezavantajın, yine Al_2O_3'ün yapısının daha sünek hale getirilmesi amacıyla takviye elemanları katkısı ile kompozitlerin üretimi ile gerçekleştirilebileceği literatürdeki araştırmalar göstermektedir. Yapılan bu çalışmada monolitik alüminanın yoğunluk değerleri üzerinde sinterleme parametrelerinin etkileri incelenecektir. Ayrıca şekillendirme işleminde uygulanan basıncın optimum sonucu vermesi için yapılan ön deneylerde elde edilen veriler karşılaştırmalı incelenecektir. Yapılacak incelemeler için numunelerin hazırlanmasında %99 saflıkta ve 70nm tane büyüklüğünde hazır olarak satın alınan Al_2O_3 tozu (Panadiye MR70 Kalsine Al_2O_3 Batch No:1270:83) kullanılmıştır.

B. Yöntem

Tozların Hazırlanması

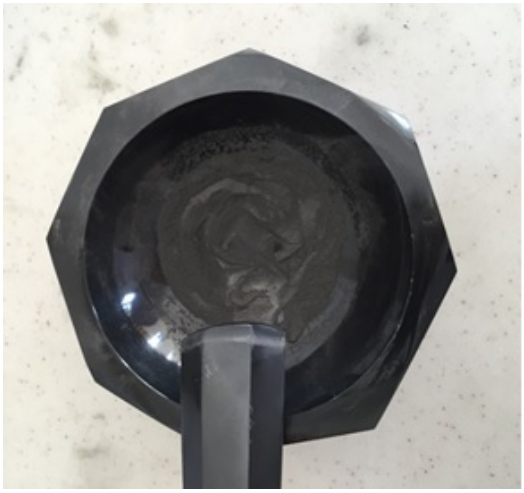
Numunelerin hazırlanması işlem basamakları alümina tozlarının öğütülüp, hazırlanan polivinil alkolün (PVA) eklenerek agat havanda karıştırılması ile başlayıp, sırasıyla kurutma, öğütme elekten geçirme, şekillendirme ve sinterleme işlemlerini kapsamaktadır. Al_2O_3 tozlarından numunelerin eldesi için yapılan işlemleler Şekil 1'de verilmiştir. Alüminaya eklenen PVA suda çözünebilme kabiliyeti yüksek olması ve bağlayıcılık özellikleri sebebi ile Al_2O_3 tozların şekillendirme öncesi hazırlanmasında ilave edilip tozların şekillendirme kabiliyetinin artması sağlanmıştır. Bezer şekilde alümina tozlarının hibrid olarak karışımının incelendiği bir çalışmada bağlayıcı olarak PVA kullanıldığını, hazırlanan PVA çözeltisinin

%80 deiyozine su + %20 PVA şeklinde olduğunu ve Al_2O_3 tozlarına %1 ağırlıkça oranında ilave edildiğini bildirmişlerdir[11]. Yapılan bu çalışmada ağırlıkça %5 PVA ilavesi yapılmıştır.



Şekil 1. Tozların hazırlanması işlem basamakları

Yapılan çalışmalarda kullanılan monolitik alümina tozu ilk olarak 12 cm çaplı agat havanda topaklanmalarının giderilmesi için öğütülmüştür. Öğütme ve karıştırma işlemlerinde kullanılan agat havanın görüntüsü Şekil 2'de verilmiştir.



Şekil 2. Tozların karıştırılmasında kullanılan agat havan

Öğütme işlemi ile paralel olarak ağırlıkça %5 PVA çözeltisi hazırlama işleminde 30 ml deiyonize su içerisinde çözündürme yapılmıştır. PVA ve deiyonize su ısıtma ve karıştırma cihazı ile çözülmüş olup aynı zamanda homojen karışım elde edilmiştir. PVA çözeltisinin hazırlanması işlemi Şekil 3'te verilmiştir. Elde edilen PVA karışımı öğütülen Al_2O_3'e ilave edilmiş ve bu işlem agat havanda karıştırılarak yapılmıştır. İşlem esnasında karışım sıcak hava akımı yardımıyla kurutulmuştur. Uygulanan kurutma ve karıştırma işlemi Şekil 4'te verilmiştir.



Şekil 3. Ağırlıkça %5 PVA karışımının hazırlanması



Şekil 4. Alümina ve PVA'nın agat havanda karıştırılması ve sıcak hava akımıyla kurutulması

Elde edilen Al_2O_3+PVA karışımı 24 süresince 70 ºC sıcaklıkta etüvde kurutulmuştur. Etüvde kurutma işleminin görüntüsü Şekil 5'te verilmiştir.



Şekil 5. Etüvde kurutma

Kurutulan Al_2O_3+PVA karışımı tekrar agat havanda öğütülüp, 200µm elekten geçirilerek şekillendirilmeye hazır Al_2O_3 tozu elde edilmiştir. İşlem sırasında kullanılan elek ve işlemin uygulanması Şekil 6'da verilmiştir.



Şekil 6. Kurutulan tozların şekillendirme öncesi agat havanda öğütülmesi ve 200 µm elekten geçirilmesi işlemi

Yapılan öğütme ve elekten geçirme işlemi ile şekillendirmeye hazır alümina tozu elde edilmiş ve numunelerin preslenerek şekillendirilmesi işlemine geçilmiştir.

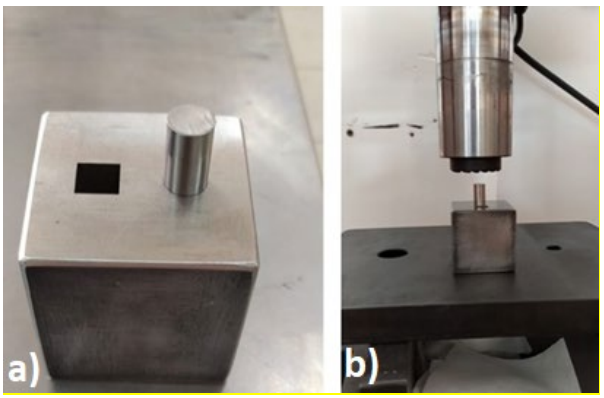
Şekillendirme İşlemi

Belirlenen toz hazırlama aşamalarından geçirilen tozlar, hidrolik pres ile uygun kalıp yardımıyla istenilen boyutlarda elde edilmektedir. Yapılan bu çalışmada da Al_2O_3 tozları presleme öncesi hassas terazide tartılıp, kalıba doldurma ve uygun basınç altında preslenerek şekillendirilmiştir. Şekillendirme aşamasında kullanılan hidrolik presin görüntüsü Şekil 7'de verilmiştir. Basınç saatinde uygun basınca kadar tozların sıkıştırılması yapılmaktadır.



Şekil 7. Şekillendirme işleminde kullanılan hidrolik pres

Presleme prosesi için Şekil 8'de görüntüsü verilen paslanmaz çelik kalıp kullanılmıştır Kullanılan kalıptaki delik çapı 10mm'dir. Presleme işlemi öncesi kalıbın hazırlanması önemli bir aşamadır. Tozların kalıba zarar vermemesi için önce bir yağlayıcı kullanılarak yağlanır. Yağlanarak hazırlanan kalıba alt aparat yerleştirildikten sonra önceden hassas terazide tartılan toz karışımı eklenip, son olarak kalıbın üst aparatı yerleştirildikten sonra presleme işlemine geçilir.



Şekil 8. a) Şekillendirme işleminde kullanılan kalıp, b) Presleme işlemi

Alümina matrisli kompozitlerin üretiminde tozların sıkıştırılması konusunda yapılan çalışmalarda; Al_2O_3 matrise Y_2O_3/Ti ilavesi yaptığı çalışmada uygulama basıncı olarak 30 MPa uyguladıklarını bildirmişlerdir[12]. Al_2O_3-Ti seramik kompozite grafen takviyesini inceldiği çalışmada 32 MPa uygulama basıncı kullanıldığı rapor etmiştir[13]. Al_2O_3-Ti seramik kompozite NiTi ilavesini inceledikleri çalışmada 32 MPa uygulama basıncı kullanıldığını bildirmişlerdir[14]. Al_2O_3 matrise Ti ilavesi yaptıkları çalışmada, karıştırma işleminden sonra 200 MPa basınç uygulandığını rapor etmişlerdir[8].

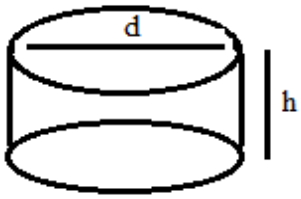
Sinterleme işleminde istenilen yoğunluğun ve mukavemetin elde edilmesi için oldukça önemli olan sıkıştırma ve şekillendirme işleminde seçilecek olan basıncın uygulanacak olan sinterleme yöntemine uygun olarak seçilmesinin oldukça önemli olduğu tespit edilmiştir. Bu amaçla yapılan bu çalışmada 80, 100, 120 bar basınçlarında numuneler hazırlanarak bu numunelerin yoğunlukları ölçülerek elde edilen veriler ışığında en uygun işlem parametresi belirlenmiştir.

Yoğunluk Ölçümü

Al_2O_3 numunelerinin ham teorik yoğunlukları mikrometre yardımıyla ölçümleri alınarak ρ_T=m/v formülünden faydalanılarak hesaplanmıştır. Ölçümlerin yapıldığı mikrometrenin ve numunenin görüntüsü Şekil 9'da verilmiştir. Elde edilen ham numunelerin boyutlarının şematik görünümü ve Şekil 10'da verilmektedir. Numunelerin yoğunluk hesaplamaları eşitlik (1) ve eşitlik (2)'de verilmiştir.



Şekil 9. Numunelerin mikrometre ile ölçümü



Şekil 10. Numunenin boyutlarının şematik gösterimi

Teorik yoğunluk (%) hesaplanırken aşağıdaki eşitlikler 4.1 ve 4.2'den yararlanılmaktadır.

$$\rho T = \frac{m}{V} \qquad (1)$$

Eşitlikteki, m ham numunenin ağırlığı, $V= \pi x r^2 x\ h$ denkleminden yararlanılarak hesaplanır.

$$\rho T(\%) = \frac{\rho T}{\rho Alümina} x100 \qquad (2)$$

Sinterleme

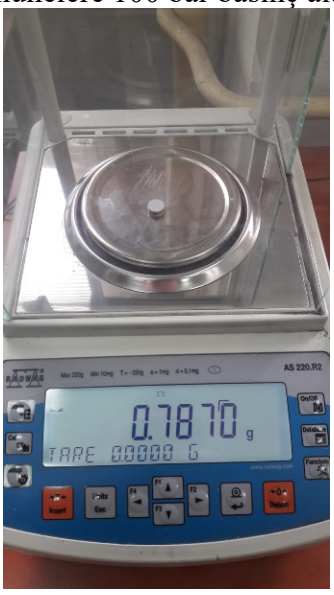
Bu çalışma kapsamında gerçekleştirilen sinterleme işlemleri önceki işlem basamakları tamamlanmış ve ham yoğunlukları ölçülmüş monolitik Al_2O_3 numunelerinin sinterleme sonrası yoğunluğuna etkisini incelemek amacıyla yapılmıştır. Numuneler önden yüklemeli karma fırınında (Nevola Thernevo Marka) sinterleme fırınında 1450°C ve 1550°C sıcaklıklarında, 2 saat ve 4 saat bekleme sürelerinde sinterlenerek elde edilen yoğunluk sonuçları karşılaştırılmış ve bu çalışması kapsamında uygulanacak olan optimum proses parametresi belirlenmiştir. Tüm sinterleme işlemlerinde ısıtma oranı 10 °C/dk sabit olarak tutulmuştur. Sinterleme işleminde kullanılan fırının görünümü Şekil 11'de verilmiştir.



Şekil 11. Sinterleme fırını

III. BULGULAR

Şekillendirme işlemi üç farklı basınçta gerçekleştirilmiş olup (80, 100, 120 bar) en uygun sonucu veren basınç ile tüm numunelere şekillendirilmiştir. Presleme sonrası elde edilen numunelerin görüntüleri Şekil 12'de verilmiştir. Elde edilen numunelere ayrı ayrı kodlar verilip ölçüm ve hassas terazide tartma işlemleri yapılmıştır Tablo 1'de ölçüm sonuçları verilen numunelerden elde edilen verilerden en yüksek yoğunluğun 100 bar basınç ile elde edildiği tespit edilmiş ve daha sonraki numunelere 100 bar basınç altında şekillendirilmiştir.

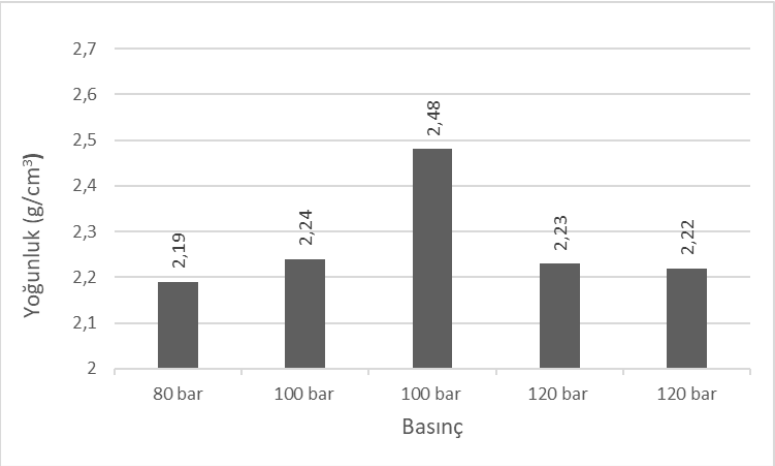


Şekil 12. Presleme sonrası elde edilen numuneler

TABLO I
FARKLI BASINÇLARDA YOĞUNLUKLARIN KARŞILAŞTIRILMASI

Uygulanan Basınç	80 bar	100 bar	100 bar	120 bar	120 bar
Numune Kodu	1 Nolu	1 Nolu	2 Nolu	1 Nolu	2 Nolu
Ağırlık (gr)	0,7897	0,7824	0,7974	0,7873	0,7888
Kalınlık (mm)	4,49	4,37	4,01	4,4	4,42
Çap (mm)	10,1	10,1	10,1	10,1	10,1
Yoğunluk (g/cm^3)	2,19	2,24	2,48	2,23	2,22

Tablo.1'de görüldüğü üzere en yüksek yoğunluğun eldesin de 100 bar basıncın uygulanması konusunda elde edilen verilerin grafik olarak gösterimi ise Şekil 13'de verilmiştir. Buradan da görüldüğü üzere 100 bar basınçta diğerlerine nazaran daha yüksek yoğunluk elde edilmiştir.



Şekil 13. Farklı basınçlar altında numunelerin yoğunluklarının karşılaştırılması

Sinterlenecek numunelerin sinterleme öncesi yoğunluk ölçümleri yapılmış ve elde edilen veriler Tablo 2'de verilmiştir. Bu işlemden sonra sinterleme aşamasına geçilmiştir.

TABLO II
NUMUNELERİN SİNTERLEME ÖNCESİ YOĞUNLUKLARI

Numune No	Ağırlık (gr)	Kalınlık (mm)	Çap (mm)	Yoğunluk (g/cm3)	Yoğunluk (%)
1	0,7824	4,37	10,1	2,24	56
2	0,7974	4,01	10,1	2,48	62
3	0,803	4,05	10,1	2,47	62
4	0,8011	4,41	10,1	2,26	57
5	0,7907	4,02	10,1	2,45	62

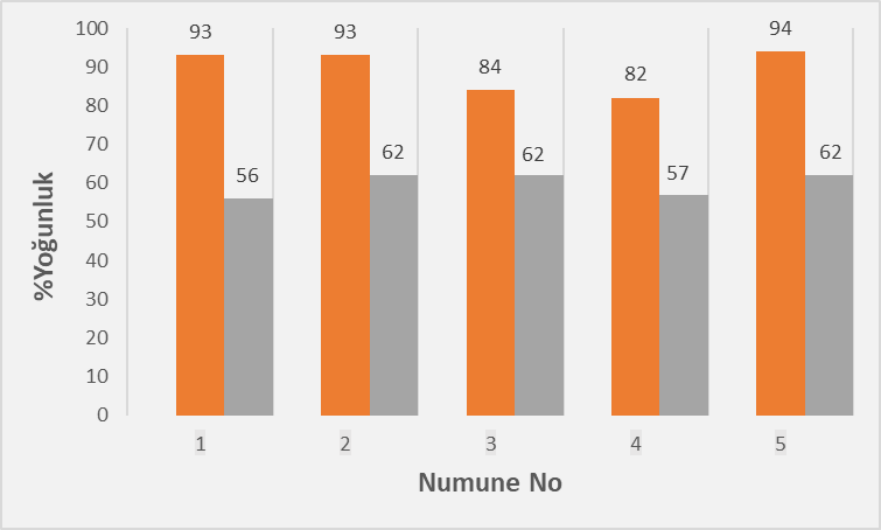
Proses parametrelerinin yoğunluk üzerindeki etkisini incelemek amacıyla farklı sıcaklık ve bekleme sürelerinde sinterlenen numunelerin sinterleme sonrası yoğunluklarının karşılaştırılması Tablo 3'te verilmiştir. Sinterleme işlemi için gerçekleştirilen çalışmalarda yapılan literatür araştırması sonucunda ısıtma oranı tüm numuneler için 10°C/dk olarak sabit tutulmuştur.

TABLO III
NUMUNELERİN SİNTERLEME SONRASI YOĞUNLUKLARI

Numune No	Sinterleme Sıcaklığı (°C)	Bekleme Süresi (sa)	Isıtma Oranı (°C /dk)	Ağırlık (gr)	Kalınlık (mm)	Çap (mm)	Yoğunluk (g/cm3)	Yoğunluk (%)
1	1550	2	10	0,7669	3,45	8,8	3,65	93
2	1550	2	10	0,7791	3,48	8,83	3,65	93
3	1450	2	10	0,7877	3,63	9,14	3,3	84
4	1450	2	10	0,783	3,62	9,21	3,24	82
5	1550	4	10	0,7735	3,46	8,77	3,7	94

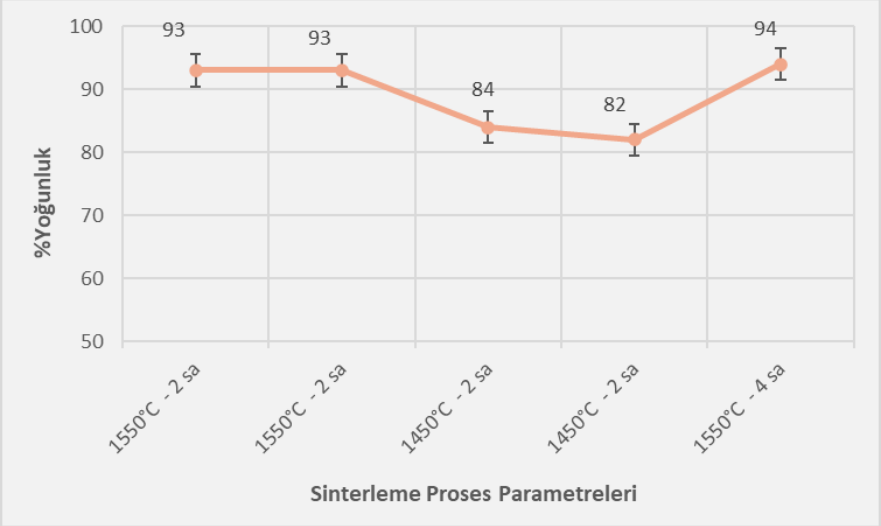
Tablo 2 ve Tablo 3'den elde edilen bulgular karşılaştırıldığında 1 ve 2 nolu numuneler 1550°C de 2 saat sinterlenmiş ve yoğunluklarının %31-37 arttığı tespit edilmiştir. 3 ve 4 nolu numuneler 1450°C'de 2 saat sinterlenmiş ve yoğunluklarının %20-22 arttığı tespit edilmiştir. 5 nolu numune 1550°C de 4 saat sinterlenmiş ve yoğunluğunun %32 arttığı tespit edilmiştir. Şekil 14'te sinterleme öncesi ve sonrası numunelerin karşılaştırmalı yoğunluk grafikleri

verilmiştir. Turuncu renk sinterleme sonrasını, gri renk sinterleme öncesi yoğunlukları göstermektedir.



Şekil 14. Numunelerin sinterleme öncesi ve sonrası yoğunluklarının karşılaştırılması

Şekil 15'de proses parametrelerine göre yoğunluk değişiminin karşılaştırılmasının grafiksel görüntüsü verilmiştir.



Şekil 15. Proses parametrelerinin yoğunluk yoğunluğa etkisi

Proses parametrelerinin etkileri daha önceki çalışmalara paralel olarak 1550 ºC sinterleme sıcaklığı, 2 saat bekleme süresi ve 10 ºC/dk ısıtma oranı en uygun değer olarak tespit edilmiştir. Yapılan bir çalışmada sinterleme parametrelerinin etkilerinin incelenmesi sonucunda 1550 ºC sıcaklık ve 10 ºC/dk ısıtma oranının optimal mekanik ve mikroyapı özelliklerinin elde edilmesini sağladığı bildirilmiştir [8]. Farklı bir çalışmada ise ısıtma oranının 5 ºC/dk sabit tutularak 1500 ºC sıcaklıkta 1, 2, 3 saat bekleme süresinde sinterleme yapıldıktan sonra, 1400 ºC, 1500 ºC ve 1600 ºC sıcaklıklarda 2 saat sinterlenme sonrası en iyi mekanik ve mikroyapı özelliklerinin 1500 ºC, 2 saat bekleme süresinde elde edildiği bildirilmiştir [15].

IV. SONUÇ

Yapılan şekillendirme işleminde uygulanan basıncının belirlenmesi amacıyla gerçekleştirilen deneylerde en yüksek yoğunluğu veren 100 bar basınç seçilmiştir. Bu çalışmada sinterleme işlemleri sonucunda sinterleme sıcaklığı arttıkça yoğunluğun arttığı bununla birlikte bekleme süresindeki artışında yoğunluğu artırdığı tespit edilmiştir. Elde edilen

verilerin karşılaştırmalı incelemeleri sonucunda sinterleme proses parametrelerinin yoğunluk üzerinde oldukça önemli etkisinin olduğu görülmüştür. Bu sebeple seçilecek olan proses parametrelerinde kullanılacak olan malzemeye uygun proses parametrelerinin seçimi istenilen mekanik ve mikroyapı özelliklerinin elde edilmesini sağlayacaktır. Bu çalışma kapsamında yoğunluğu %31-37 oranında artıran 1550 °C sıcaklık, 2 saat bekleme süresi ve 10°C/dk ısıtma oranının monolitik alüminanın sinterlenmesinde en uygun parametre olduğu tespit edilmiştir.

KAYNAKÇA

[1] M. Gürbüz ve T. Mutuk, "Karbon Esaslı Malzeme Takviyeli Titanyum Kompozitler ve Grafen Üzerine Yeni Eğilimler", *Mühendis ve Makina*, c. 60, sayı 695, ss. 101–118, 2019.

[2] T. Mutuk ve M. Gürbüz, "Grafen Takviyesi Miktarının Titanyum Matrisli Kompozitlerin Özelliklerine Etkisi", *Gaziosmanpaşa Bilim. Araştırma Derg.*, c. 6, ss. 1–9, 2017.

[3] E. Ayaş, "Al2O3-TiC/TiCN Kompozit Malzemelerin Üretim Yöntemleri", Anadolu Üniversitesi, 2003.

[4] G. Shi, Z. Wang, L. Liu, ve C. Wang, "Influence of Y2O3 addition on the Ti/Al2O3 cermets by hot pressing sintering", *J. Alloys Compd.*, c. 628, sayı 6, ss. 413–415, Nis. 2015, doi: 10.1016/j.jallcom.2014.12.014.

[5] S. Meir, S. Kalabukhov, N. Frage, ve S. Hayun, "Mechanical properties of Al2O3\Ti composites fabricated by spark plasma sintering", *Ceram. Int.*, c. 41, sayı 3, ss. 4637–4643, 2015, doi: 10.1016/j.ceramint.2014.12.008.

[6] M. Bahraminasab, S. Ghaffari, ve H. Eslami-Shahed, "Al2O3-Ti functionally graded material prepared by spark plasma sintering for orthopaedic applications", *J. Mech. Behav. Biomed. Mater.*, c. 72, sayı February, ss. 82–89, 2017, doi: 10.1016/j.jmbbm.2017.04.024.

[7] S. Shi, T. Sekino, S. Cho, ve T. Goto, "Ti and TiC co-toughened Al2O3 composites by in-situ synthesis from reaction of Ti and MWCNT", *Mater. Sci. Eng. A*, c. 777, sayı January, s. 139066, 2020, doi: 10.1016/j.msea.2020.139066.

[8] Z. Yin, J. Yuan, Z. Wang, H. Hu, Y. Cheng, ve X. Hu, "Preparation and properties of an Al2O3/Ti(C,N) micro-nano-composite ceramic tool material by microwave sintering", *Ceram. Int.*, c. 42, sayı 3, ss. 4099–4106, 2016, doi: 10.1016/j.ceramint.2015.11.082.

[9] E. Cui, J. Zhao, X. Wang, J. Sun, X. Huang, ve C. Wang, "Microstructure and toughening mechanisms of Al2O3/(W, Ti)C/graphene composite ceramic tool material", *Ceram. Int.*, c. 44, sayı 12, ss. 13538–13543, Ağu. 2018, doi: 10.1016/j.ceramint.2018.04.185.

[10] V. Verma ve M. B. V. Kumar, "Synthesis, Microstructure and Mechanical Properties of Al2O3/ZrO2/CeO2 Composites with Addition of Nickel and Titania Processed by Conventional Sintering", *Mater. Today Proc.*, c. 4, sayı 2, ss. 3062–3071, 2017, doi: 10.1016/j.matpr.2017.02.189.

[11] M. W. Khalid *vd.*, "Densification behavior of microwave hybrid sintered Al2O3 bimodal powder mixtures and comparison with 3D modeling and simulation", *Int. J. Refract. Met. Hard Mater.*, c. 99, s. 105586, 2021, doi: 10.1016/j.ijrmhm.2021.105586.

[12] S. Shi, S. Cho, T. Goto, T. Kusunose, ve T. Sekino, "Combinative effects of Y2O3 and Ti on Al2O3 ceramics for optimizing mechanical and electrical properties", *Ceram. Int.*, c. 44, sayı 15, ss. 18382–18388, 2018, doi: 10.1016/j.ceramint.2018.07.054.

[13] X. Wang, J. Zhao, E. Cui, H. Liu, Y. Dong, ve Z. Sun, "Effects of sintering parameters on microstructure, graphene structure stability and mechanical properties of graphene reinforced Al2O3-based composite ceramic tool material", *Ceram. Int.*, c. 45, sayı 17, ss. 23384–23392, 2019, doi: 10.1016/j.ceramint.2019.08.040.

[14] Z. Xiu, J. Laeng, X. Sun, Q. Li, S. K. Hur, ve Y. Liu, "Phase formation of Al2O3/Ti(C,N)-NiTi composite", *J. Alloys Compd.*, c. 458, sayı 1–2, ss. 398–404, 2008,

doi: 10.1016/j.jallcom.2007.03.116.
[15] S. J. Esparza-Vázquez, E. Rocha-Rangel, J. A. Rodríguez-García, ve C. A. Hernández-Bocanegra, "Strengthening of Alumina-Based Ceramics with Titanium Nanoparticles", *Mater. Sci. Appl.*, c. 05, sayı 07, ss. 467–474, 2014, doi: 10.4236/msa.2014.57050.

A Practical Implementation of Measurement System for QTF Sensing Applications

Shibo Cai

Shibo.Cai@setu.ie, ORCID: 0000-0003-3992-5687
Department of Engineering Technology, SETU, Waterford, Ireland

Abstract: In recent years, Quartz Tuning Fork (QTF) has gained much interest in developing sensor technology due to its excellent mechanical characteristics. Thus, a fully equipped and featured measurement system is essential for deploying the novel sensing technology. The traditional QTF sensing system configuration method is developed based on lock-in technology for advanced microscopy techniques. The implementation seeks the best sensitivity and functionality regardless of the complexity and cost. However, implementing the whole measurement system is relatively cumbersome and expensive. In addition, the equipment set-up is complicated, and the operation is tedious. This paper presents a practical implementation of a Quartz Tuning Fork (QTF) sensor-based measurement system, including sophisticated electronic hardware and advanced data processing software development. Implementing the high-speed data acquisition technique simplifies the system configuration compared to the traditional lock-in method. Fourier analysis combined with the nonlinear curve fitting technique improves the systematic characteristics of measurement, where the developed system minimises the computation requirement while overcoming the limitation of the quantisation interval of FFT at the same time, which allows determining the resonance frequency at the dynamic mode where a $10^{-3}Hz$ quantisation interval of resolution can be achieved.

Keywords: *Quartz Tuning Fork (QTF), Fast Fourier Transform (FFT), Curve Fitting, Qunatizaiton, Quantization Error, Resolution*

I. INTRODUCTION

RECENTLY, there has been much interest in the investigation of sensing technology based on the determination of the resonance frequency variation of a quartz tuning fork (QTF) [1] [2] [3] [4] [5]. QTF have ranged in size countable in millimetres scale, and materials have included aluminium nitride-coated silicon, lithium niobate, and quartz [6]. Millimetre-sized QTFs offer many advantages over microfabricated cantilevers in developing sensor technology. QTF has a relatively large active sensing area and is readily available as off-the-shelf items. Traditionally employed as frequency standards in wristwatches and microcontroller circuits, these double-pronged micro-machined devices exhibit a significant mechanical quality factor Q, a small spring constant k, and excellent thermal stability. Their well-defined mechanical characteristics have seen them deployed in a range of sensor applications [7] [8] [9] [10] [11] [12]. The proposed QTF sensor has various sizes, as shown in Table 1, and is commercially available in a cylindrical package. The rectangular cantilevers of QTF have mechanical coupling motion in a mirror fashion in resonance mode. As a result, the resonance frequency of QTF is sensitive to sensing environment changes. These changes can be in any parameters, i.e. mass, displacement, pressure, humidity, temperature, etc. Therefore, a specified modification process can optimise the response characteristics of the QTF that

allows QTF to be used for the target parameters' measurement. The previous research mainly focused on investigating sensor applications. This paper focused on systematic characterisation optimisation in developing the measurement system and treated the QTF as the sensing element to explore the sensing technique.

II. QTF SENSING THEORY

The resonance frequency of bare QTF in vacuum condition is given by:

$$f_0 = \frac{1}{2\pi}\sqrt{\frac{k}{m_{eff}}} \tag{1}$$

Where, m_{eff} is the effective mass of the tuning fork and relates to the actual mass of the tuning fork $m_{eff} = 0.2426\rho LTW$, the $\rho = 2649\, kg/m^3$ is density of quartz. k is the spring constant and depends on the dimension of QTF and given by:

$$k = \frac{EWT^3}{4L^3} \tag{2}$$

Where E is Young's modulus of quartz $7.87 \times 10^{10} Nm^{-2}$. Thickness T, length L, and width W along the direction of X, Y and Z axis, respectively, as shown in **Fig. 1.**

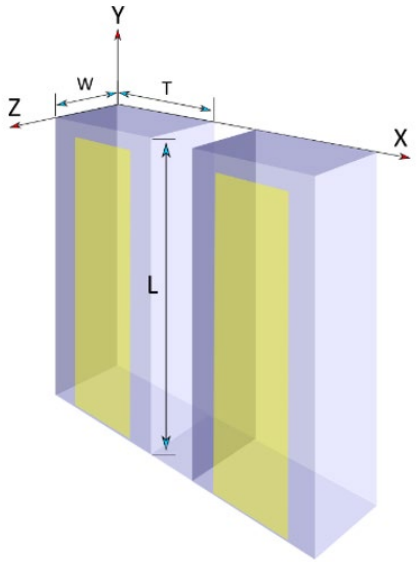


Fig. 1. Schematic of QTF orientation *X*, *Y* and *Z* axis are associated with the quartz crystal direction. The vibration of the rectangular cantilever beam along the *X*-axis. The golden area represents the metallic deposition of QTF for the piezoelectric signa.

The sensing environment changes will induce the changes of two parameters, k or m or both at the same time. The change in spring constant Δk is due to the sensing material-coated layer property has changed due to the sensing environment changes. However, the amount of variation can be neglected in most cases due to the changes is relatively too small compared to the k of quartz. In addition, the coated layer is usually considered as an infinity-thin layer [13]. Therefore, the mass changes become the primary sensing parameter. The resonance frequency changes when additional mass Δm load on the QTF sensor. The changed resonance frequency is given by:

$$f_1 = \frac{1}{2\pi}\sqrt{\frac{k}{m_{eff}+\Delta m_{eff}}} \tag{3}$$

Therefore, the resonance frequency changes due to the sensing environment change is given by:

$$\Delta f = f_0 - f_1 \tag{4}$$

In this case, the sensitivity S of QTF can be defined as the ratio of the resonance frequency shift to the input of the measurement system ΔI which the changes in the sensing environment:

$$S = \frac{\Delta f}{\Delta I} \tag{5}$$

III. QTF SENSING SYSTEM

A. QTF sensing system configuration

The primary measured value of QTF is the resonance frequency; therefore, the configuration of the system is based on the frequency determination method. Two types of configuration are commonly found for QTF measurement systems: the conventional configuration, which utilises the lock-in technique [3] [14] [15] [16]. The resonance frequency is determined by tracking the peak of QTF's sensing signal by the lock-in amplifier with a frequency sweep process provided by the signal generator. The advantage of this configuration is that when the system is deployed with an impedance analyser, the system is still able to measure the resonance response with a low-quality factor. It is usually used for high-viscosity sensing environment measurement. The alternative method is a high-speed data acquisition technique based [8] [17] [18]. The sensor is self-excitation, and sensing data acquisition and data processing is done by the developed software. The system has significantly improved the simplicity of the system configuration. The proposed system is implemented by the second method, the high-speed data acquisition configuration.

B. QTF sensing system structure

The principle of measurement system states that the purpose of using a measurement system is to obtain information from a process for the observer who requires the information [19]. Therefore, the output of the measurement system, i.e. measured value, presents information. In the proposed QTF sensor-based measurement system, the sensing In the proposed QTF sensor-based measurement system, the sensing element is the QTF sensor, and the resonance frequency of the QTF is the sensing element's output to present the process's information variable. The Signal conditioning element utilises the high-speed data acquisition technique that converts the resonance oscillation signal to digitalised data. Subsequently, the data processing element processes the data to numerical values by the Fourier transform analysis method. Finally, the observer can obtain the information from the value matrix or graphical diagram of the processed numerical value.

C. Proposed QTF sensing system

The schematic block diagram of the developed system is shown in **Fig. 2.** An array of QTF sensors sandwiched by dual high-speed multiplexers. The self-oscillation circuit generates an actuation signal to excite QTF sensors. The multiplexers are controlled by the logical instructions for selecting each QTF sensor. A voltage multiplier achieves the parasitic capacitance cancellation with an additional polar inversed capacitor. The signal level drifting issue due to the thermal noise is rectified by the offset circuit. Software routine based on the FFT and Levenberg-Marquardt (LM) algorithm is part of the program for the measurement data analysis to obtain the resonance frequency and frequency resolution enhancement.

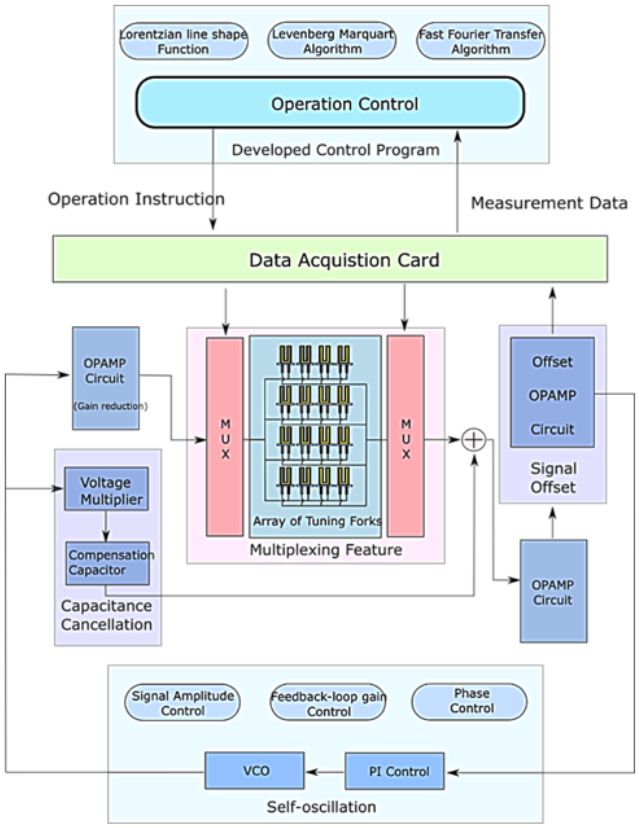


Fig. 2. Schematic of the implementation of QTF sensor-based measurement system

IV. FOURIER TRANSFORM TECHNIQUE

A. Fourier transform theory

The QTF sensing signal with oscillation frequency of f_q is sampled by the sampling interval of T_s, then the sensing signal can be represented by the function of $q(t)$:

$$q(t) = T_s \sum_{n=-\infty}^{n=+\infty} q_n \frac{\sin[2\pi f_q(t-nT_s)]}{\pi(t-nT_s)} \tag{6}$$

Where q_n represents samples of the sampled signal, t is time, and n is the integer. The acquired number of N data points can then be used to describe the sensing signal as Q_n in the frequency domain by using the Discrete Fourier Transform (DFT) $(k = 0, 1, 2, 3, \dots, N-1)$:

$$Q_n(f) = \sum_{k=0}^{N-1} q_k e^{2\pi ikn/N} \tag{7}$$

The direct computation of the Fourier Transform of the discrete type of data is time-consuming because of the complex component $e^{2\pi ikn/N}$ That necessitate complex multiplication of N^2. And the problem has been solved [20], resulting in the Fast Fourier Transform (FFT) algorithm becoming more popular. The FFT algorithm represents an approach that can reduce the order of complexity of the computation from N^2 to $N \log_2 N$. In addition, the use of binary computation with $N = 2^n$ is advantageous, as the entire calculation can be performed within the range of N data storage locations used for the given Fourier coefficients.

B. The challenge of Fourier transform implementation

From the measurement and instrumentation point of view, the resonance frequency is the output of the QTF sensor measurement system to indicate the information variable of the process. The numerical Fourier analysis determines the resonance frequency, which is the system's output. Therefore, the measurement resolution depends on the resolution of the Fourier analysis. The FFT resolution is proportional to the ratio of the sampling frequency and the number of data sampled, which creates a contradiction:

$$R_{FFT} = \frac{1}{T} = \frac{f_s}{N} \tag{8}$$

where R_{FFT} is the frequency resolution of the FFT, T is the sampling time, f_s is the sampling frequency, and N is the number of acquired samples.

Considering the Nyquist sampling theorem, the sampling rate f_s should be at least twice the highest frequency in the sampled signal. To obtain comprehensive information, the sampling frequency should be several times greater than the Nyquist sampling condition. Assuming N is constant, the faster the sampling rate will result in a large value fo the quantisation interval of FFT frequency resolution, which results in a poor resolution of the sensing measurement, and a significant quantisation error will occur. The alternative method is to increase the number of data points for the FFT computation. Assuming the value of the sampling frequency is constant, the larger number of data points requires a longer acquisition time and a larger data memory storage space. The issue is also found in previous research that adopted the Fourier analysis method [18]. The acquisition time of 96ms yields the 10Hz resolution of the FFT. The curve fitting technique was used to find the centre of the shape of the signal spectrum, and the resolution was optimised to the sub-Hz regime at roughly 0.1Hz.

V. CURVE FITTING TECHNIQUE

A. Least-square fitting

To improve the measurement quality and reduce the quantisation error, we have developed a curve fitting routine base on the mathematic fitting algorithm [21]. The algorithm used for fitting is dependent on the model of the data distribution. Suppose the measurement system generates a set of measurement data points. In that case, the least square fitting can indicate the minimisation of the sum of the squares of the errors between the data points and the system function. The least-square fitting is subject to the most likely maximum estimator fitting the parameters when the measurement error is independently random and shows a Gaussian distribution with a constant standard deviation from its true value. The probability density function, also known as the Gaussian distribution function for a discrete set, is shown below:

$$P = \prod_{i=1}^{N} \left\{ exp\left[-\frac{1}{2} \left(\frac{y_i - y(x_i)}{\sigma} \right)^2 \right] \Delta y \right\} \tag{9}$$

The probability of the measurement data is the product of the probability of each data point. In other words, the fitted data set is the product of each data point with the maximum probability that has the minimised sum of the square of the errors between the measured value against the true value. If each data point has its own standard deviation σ_i , then the maximum likelihood estimator of the model parameters can be obtained by minimising the quantity called the Chi-Square:

$$X^2 = \sum_{i=1}^{N} \left[\frac{y_i - y(x_i; a_1 \ldots a_n)}{\sigma_i} \right]^2 \tag{10}$$

Where the number of N data points is $(x_i, y_i) i = 1, \ldots, N$ and each data points has its own standard derviation σ_i.

B. Levenberg-Marquardt Algorithm

The proposed method can solve the problem using the nonlinear curve fitting technique. If the function of $y(x)$ is nonlinear, then it involves nonlinear least square curve fitting, with the popular method of the Levenberg-Marquardt algorithm. The nonlinear least square problem can be solved by the standard method that extends the nonlinear model to the Taylor series, where the elements of the series correct the function parameters through iteration on the assumption of the element of local linearity. K. Levenberg published his work on solving the nonlinear least square problem [22], which ensures an improvement of the initial solution through an extension of Newton's method. This improvement allowed the process to also apply to the simultaneous nonlinear equation. The next problem, however, is that the linear approximation approach to the correction of function parameters is extremely slow in obtaining the minimum value of the sum of the square of the errors than the initial solution. Later, D. W. Marquardt introduced the algorithm to combine the Taylor series method and the Gradient method [23]. The results have been extended to solve the problem of a set of nonlinear algebraic equations.

Therefore, the Levenberg-Marquardt algorithm combines two minimisation methods: The Newton method and the Gradient method. The Levenberg-Marquardt algorithm acts as the Newton method when the function parameter is close to the optimal value and where the reduction of the sum of the square error leads to the assumption that the least squares function is quadratic. In another situation, it acts like the Gradient method when the function parameter is far from the optimal value and where the sum of the square error is reduced by adjusting the parameter with the maximum likelihood to the greatest reduction of the least squares objective.

VI. EXPERIMENTAL EVALUATION

A. Evaluation of Fourier transform

Fast Fourier Transform (FFT) can rapidly convert a signal from the time domain to the frequency domain and obtain the signal's frequency. However, the resolution of the FFT conversion result is limited by the sampling rate and the number of data used in the FFT computation. The sampling rate of the used data acquisition card is 100kHz, and thus the frequency spectra of the acquired single data point is 100kHz, and the period of the single data point is $10\mu s$. A total of $131072 = 2^{17}$ data points were acquired and used for the FFT computation; therefore, the 0.76Hz resolution is obtained. The SRS synthesised function generator DS340 was used as the signal source to calibrate the FFT computation. The DS340 15MHz function generator is based on direct digital synthesis (DDS). It can output arbitrary waveforms up to 16,300 points long. The function generator outputs the frequency sweep signal, which increases frequency from 32760Hz to 32768Hz in the step of 1Hz. Therefore, the signal obtained from the function generator is considered as the true value of the process or the input of the developed measurement system, and the resolution is 1Hz.

The developed FFT Routine analysed the signal from the function generator. The analysis results are the measured value or output of the developed measurement system. The difference between the true value and the measured value is the quantisation error of the measurement process. The analysis result shows that the actual resolution of the FFT routine is equal to the calculated theoretical value of 0.76Hz. A quantisation error adjustment occurs every 3

quantisation intervals. This is shown in **Fig. 3.** The adjustment causes the quantisation error to have aperiodic distribution, which follows the trend line of the frequency increase.

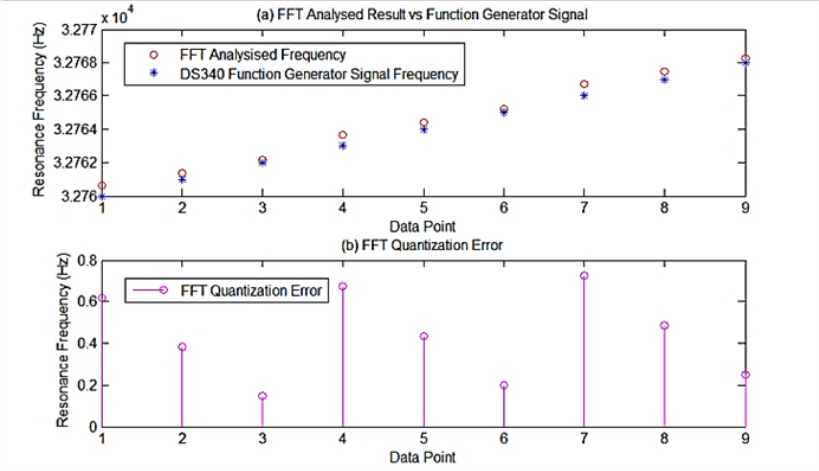


Fig. 3. (a) The measured value from the FFT analysis result vs the true value from the function generator; (b) the quantisation error between the two measured results.

B. Evaluation of Fourier curve fitting

The advantage of the curve fitting technique is that it allows us to improve the systematic characteristics of the measurement system without modifying the actual hardware and FFT algorithm-based software. Modern measurement and instrumentation theory states that error exists in all measurement results. Therefore, any measurement data always has a certain distortion. Fitting the measurement data will reduce this unwanted effect during the measurement process, making observation clearer and more precise. The curve fitting can also be used for constrained interpolation [18]. This is the main reason that curve fitting algorithm routines have been developed in this research for FFT resolution optimisation. In the previous discussion, the FFT had a limited resolution of 0.76Hz. Therefore, the measurement result shows a discrete distribution if the resonance frequency continues to increase or decrease variation more than a resolution interval. The curve fitting can interpolate the data points from the discrete type distribution into a continuous type distribution, allowing the measured value to be closer to the true value.

This evaluation experiment, as shown in Fig. 4, is part of developing a polymer-coated QTF sensor for volatile organic solvent (VOC) gas concentration sensing application. The developed system was used to observe gas concentration changes due to VOC volatilisation. Each measured data point takes about 20 seconds to be processed, and 100 data points were measured.

The QTF sensor was coated with one single layer of polylactic acid (PLA) by dip-coating. The coating solvent was made in 1:100 *g/ml* ratio. The resonance frequency was 32755.98349Hz before the coating and 32747.96063Hz after the coat- ing. The QTF sensors were exposed in an enclosed petri-dish to methanol (Sigma-Aldrich, Methanol anhydrous, 99.8%). Volumes of 30μl were measured by using a calibrated micropipette. The cover of the petri-dish was closed immediately once the methanol was injected into the petri-dish. The measurement was started at the same time.

The measured values show a 'bath-tub' type of characteristics consisting of three stages, as shown in **Fig. 5.** The resonance frequency of the QTF sensor decreased at the first stage, indicating the VOC vapour concentration increased due to the methanol volatilisation. In the second stage, the resonance frequency of the QTF sensor reaches the minimum value of the

monitoring process, indicating the VOC gas has the highest concentration. Finally, in the third stage is the recovery process, the resonance frequency resumes toward the initial value, indicating that the VOC vapour concentration decreased due to the leakage between the gap of petri-dish coverage. For further evaluation, the zoom-in view of the data point 60-70 of **Fig. 5**. is shown in **Fig. 6.**

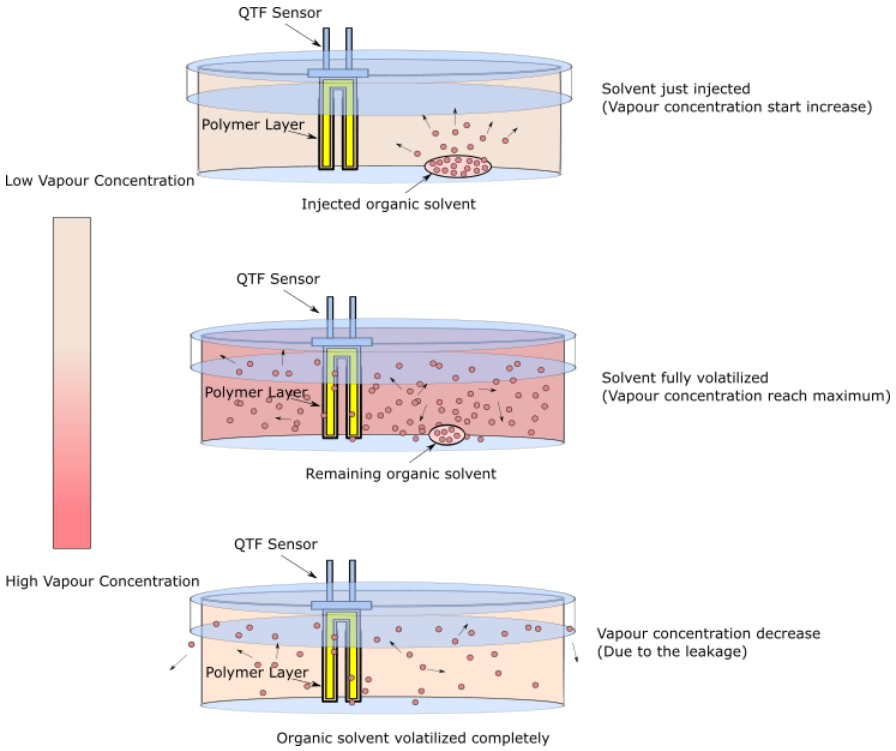


Fig. 4. The process of VOC volatilisation and concentration monitoring experiment

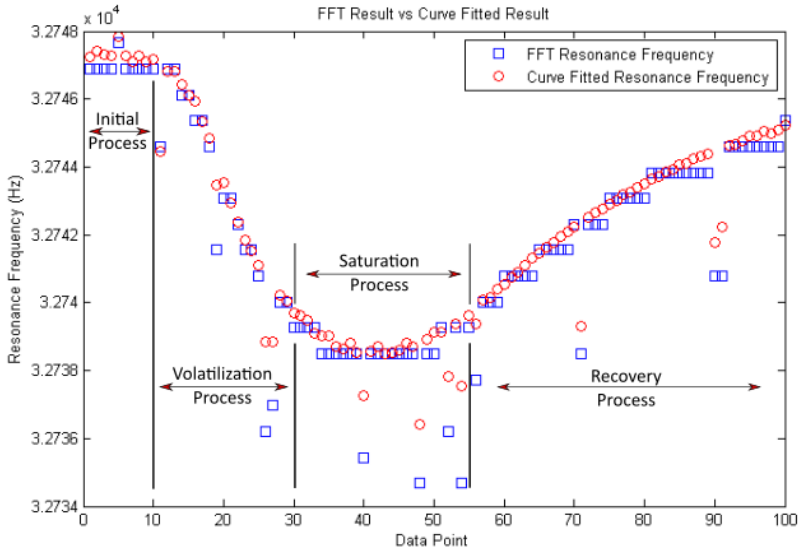


Fig. 5. FFT measured value (blue square) vs. the curve fitting algorithm result (red dot). The FFT resolution is 0.76Hz; the fitted quantisation interval is dynamic, and a minimum value of 0.0019Hz was observed.

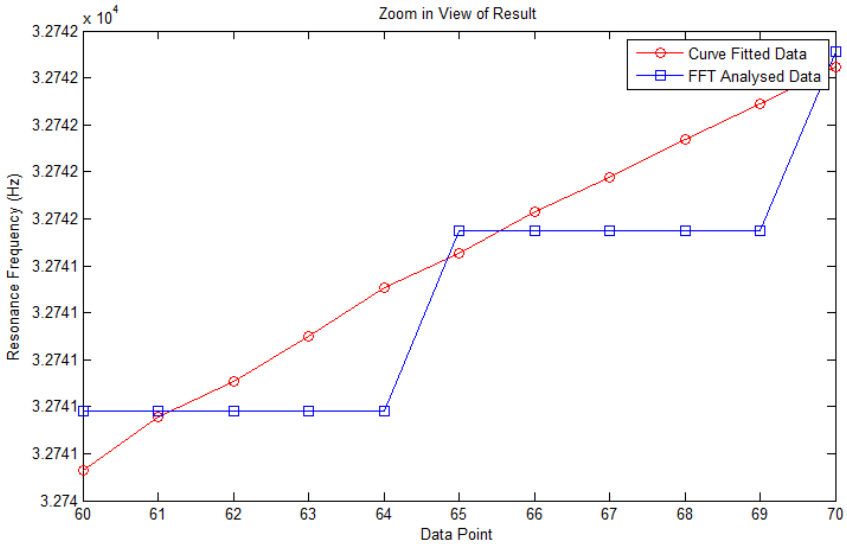


Fig. 6. Zoom-in view of data point 60-70 of FFT measured value (blue square) vs. curve fitting algorithm (red dot).

Based on the principle of the measurement system, the sensitivity of the polymer-coated QTF sensor for VOC gas concentration as the ratio between the variation of output (change of resonance frequency) to the variation of input (change of VOC gas concentration) and given by the equation of $S = \Delta f / \Delta \rho$. Where Δf is the induced frequency shift due to the vapour concentration changes $\Delta \rho$.

The evaluation results show that the resolution of the FFT measured value can be optimised by the curve fitting technique. The minimum of Δf that can be measured is 0.76Hz due to the limits of FFT resolution. When the sensor-induced changes in resonance frequency are less than 0.76Hz, the measurement value will round up or round down to the nearest quantisation level. Therefore, a quantisation error will occur. The Δf of the curve fitted result does not show a fixed value of the quantisation interval as shown in **Fig. 6.** Instead, much lower changes can be measured, i.e. 0.171Hz on average is achieved in evaluation, and the lowest 0.0019Hz was observed. The quantisation interval of the curve fitted result is dynamic and will be automatically adjusted based on the value of the value of the ΔI of the measurement input. If the ΔI has a significant change during the test trial period, then the quantisation interval will increase proportionally to the variation of ΔI. On the other hand, the quantisation interval will become a delicate value when the ΔI has a smooth change during the test trial period. Thus, the measured value always provides the corresponding information related to environmental changes.

VII. CONCLUSION

This paper presents a practical implementation of a measurement system for the QTF sensor application. The implementation is based on the high-speed data acquisition technique that offers simplicity in system configuration. The proposed curved fitting method provides a dynamic quantisation interval analysis result that solves the issue of quantisation error due to the limitation of FFT resolution.

ACKNOWLEDGMENT

This work was supported by the WINS project under the Ireland Wales INTERREG IVA 4A Programme

REFERENCES

[1] K. Karrai and R. D. Grober, "Piezoelectric tip-sample distance control for near field optica microscopes," *Appl. Phys. Lett,* vol. 66, no. 14, pp. 1842-1844, 1995.

[2] K Karrai and R. D. Grober, "Piezoelectric tuning fork tip-sample distance control for nea field optical microscopes," *Ultramicroscopy,* vol. 61, pp. 197-205, 1995.

[3] K Karrai and R. D. Grober, "Tip-sample distance control for near-field scanning optica microscopes," *SPIE,* vol. 2535, pp. 69-81, 1995.

[4] J. Zhang et al., "Determination of liquid denstiy with low frequency mechanical senso based on quartz tuning fork," *Sensor and Actuators B,* vol. 84, pp. 123-128, 2002.

[5] D Zeisel et al., "A precise and robust quartz sensor based on tuing fork technology fo (SF6)- gas density control," *Sensor and actuator A,* vol. 80, pp. 233-236, 2000.

[6] S. Lee, "Fabrication of an array of surface mount device 32,768kHz quartz tuning fork type crystals: photolithography and selective etching of an array of quartz tuning for resonators with subsequent photoresist spray coating," *Vacuum,* vol. 65, pp. 161-168 2002.

[7] J. Z. a. S. O'SHEA, "Tuning fork as micromechancial mass sensitive sensor for bio- o liquid detection," *Sensor and Actuator B,* vol. 94, pp. 65-72, 2003.

[8] X Zhou et al., "Humidity sensor based on quartz tuning fork coated with sol-gel-derive nanocrystalline zinc oxide thin film," *Sensor and Actuator B,* vol. 123, pp. 299-305, 2007

[9] B. Sun et al., "Comparative CO2-sensing characteristic studies of PEI and PEI/Starch thi film sensor," *Energy Procedia,* vol. 12, pp. 726-732, 2011.

[10] J. Change et al., "Quartz tuning fork enhanced photothermal spectroscopy gas detectio system with a novel QTF-self-difference technique," *Sensor and Actuators A: Physica* vol. 299, no. 111629, 2019.

[11] S. Datar et al., " Detection of binary and ternary mixtures of volatile organic compund using quartz tuning fork based sensor array," *Sensor and Actuators: A physical,* vol. 332 2021.

[12] M. Mutlu et al., "Development of mass sensitive sensor platform based on plasm polymerisation technique: Quartz tuning fork as transducer," *Applied surface science,* vo 540, no. 148360, 2021.

[13] G. G. Stoney, "The tension of metallic films deposited by electrolysis," *Proceeding of th Toyal Society of London,* vol. 82, no. 553, pp. 172-175, 1909.

[14] A Castellanos-Gomes et al., "Characterizaiton and optimisation of quartz tuning fork based force sensor for combined STM/AFM," *Scanning Probe Microscopy in Nanoscienc and Nanotechnology,* vol. 3, pp. 23-53, 2012.

[15] P. Patimisco et al., "Analysis fo the electro-elastic properties of custom quartz tuning fork for optoacoustic gas sensing," *Sensor and Actuator B,* vol. 227, pp. 539-546, 2016.

[16] R. Blaauwgeers et al., "Quartz tuning fork: thermometer, pressure- and viscometer fo helium liquids," *Journal of Low Temperature physics,* vol. 146, pp. 537-562, 2007.

[17] K. Waszczuk et al., "Application of piezoelectric tuning forks in liquid viscosity an density measurements," *Sensor and Actuators B,* vol. 160, pp. 517-523, 2011.

[18] R. P. Wali et al., "Fourier transform mechancial spectroscopy of micro-fabricate electromechanical resonators: A novel, information-rich pulse method for senso applications," *Sensor and Actuators B,* vol. 147, pp. 508-516, 2010.

[19] J. P. Bentely, "Principle of measurement system," in *The general measurement system* Pearson Education Ltd, 2005, pp. 3-7.

[20] a. J. W. T. J. W. Cooley, "An algorithm for the machine calculation of complex Fourie series," *Math. Comp,* vol. 19, pp. 297-301, 1965.

[21] K. Levenberg, "A method for the solution of certian nonlinear problems in least squares, *Quarterly of applied mathematics,* pp. 164-168, 1944.

[22] K. Levenberg, "A method for the solution of certian nonlinear problems in least squares, *Quarterly of applied mathematics,* pp. 164-168, 1944.

[23] D. W. Marquardt, "An algrithm for least-squares estimation of nonlinear parameters, *Journal of the society for industrial and applied mathematics,* pp. 431-441, 1963.

Polyamid Fırçalarda Biriken Tozların Elimine Edilebilmesi İçin Gerekli Ekipmanin Tasarım ve Analizi

Design and Analysis of the Equipment Required for the Elimination of Dust Accumulated in Polyamide Brushes

Öznur Bağ*[1,2], Lezgin Kaya[1], Samet Çalışkan[1]

*oznur.bag@serkonmakina.com, ORCID: 0000-0002-9944-8221
[1]*Serkon Tekstil Makina ve Ekipmanları Sanayi ve Ticaret Anonim Şirketi, İstanbul, Türkiye*
[2] *Tokat Gaziosmanapaşa Üniversitesi, Tokat, Türkiye*

Özet: Konfeksiyon sektöründe kesimhane bölümünde katlı kumaş kesimleri için kullanılan makineler arasında en fonksiyonel olanı CNC (bilgisayarlı numerik kontrol) otomatik kumaş kesim makinesidir. En basit anlamıyla CNC otomatik kumaş kesim makinesi kumaş yerleştirme, planlama, serme ve kesme işlemlerini içeren entegre bir sistemdir. Çok kat kumaşların istenilen kapasite ve kalitede kesim işleminin gerçekleştirilmesi için makine içerisinde kullanılan fırçalı kesim alanının temiz tutulması gerekmektedir. Aksi takdirde makinede kullanılan bıçaktaki hasarlar ve vakum sisteminin düzgün çalışmaması gibi nedenlerin etkisiyle kumaş katları doğru kesilememektedir. Bu durum firmalarda zaman ve maliyet açısından sorun teşkil etmektedir. Bu çalışmada CNC otomatik kesim makinelerinde kullanılmak üzere geliştirilen fırça temizleme sisteminde vibratör cihazının makine üzerinde bulunan alüminyum ray sistemine etkisi incelenmiştir. Ansys Workbench programı kullanılarak, makine şasesi ve fırçaların bulunduğu alüminyum rayın doğal frekansı modal analiz ile bulunup sonuçlar simüle edilmiştir. Statik ve harmonik analiz yöntemi ile makine üzerinde kullanılması gereken vibratörün özellikleri araştırılmıştır. Bu doğrultuda alüminyum raya hasar vermeyecek olan uygun vibratör cihazının çalışma frekans aralığı 96 Hz ve maksimum kuvvet 1038 N olarak belirlenmiş ve sonuçlar sunulmuştur.

Anahtar Kelimeler: *CNC Otomatik Kesim Makinesi, Fırça, Alüminyum Ray, Modal Analiz, Harmonik Analiz*

Abstract: CNC (computerized numerical control) automatic fabric cutting machine is the most functional among the machines used in the garment industry for ply fabric cutting in the cutting room section. In the simplest sense, CNC automatic fabric cutting machine is an integrated system that includes fabric placement, planning, laying and cutting processes. In order to realize the cutting process of multi-layer fabrics with the desired capacity and quality, the brush cutting area used in the machine must be kept clean. Otherwise, the fabric folds cannot be cut correctly due to reasons such as damage to the blade used in the machine and the vacuum system not working properly. This situation poses a problem for companies in terms of time and cost. In this study, the effect of the vibrator device on the aluminum rail system on the machine was examined in the brush cleaning system developed for use in CNC automatic cutting machines. Using Ansys Workbench program, the natural frequency of the machine frame and the aluminum rail where the brushes are located is found by modal analysis and the results are simulated. The properties of the vibrator that should be used on the machine were investigated by static and harmonic analysis method. In this direction, the operating frequency range of the appropriate vibrator device, which will not damage the aluminum rail, was

determined as 96 Hz and the maximum force was determined as 1038 N and the results were presented.

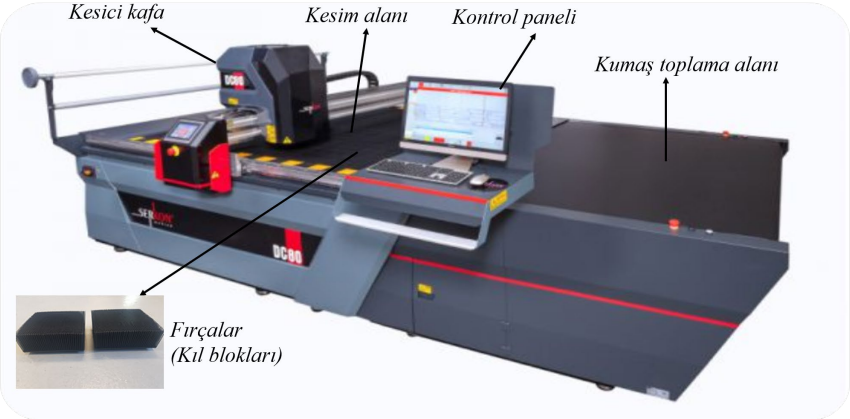
Keywords: *CNC Automatic Cutting Machine, Brush, Aluminum Rail, Modal Analysis, Harmonic Analysis*

I. GİRİŞ

Tekstil endüstrisi, daha kaliteli ürün üretimi için neredeyse her bölümde otomatik makinelerdeki teknolojik gelişimin görülebildiği, tüm dünyada yeniçağın en hızlı büyüyen imalat endüstrilerinden biridir. Daha fazla verimlilikle daha yüksek üretim, daha düşük işçilik maliyeti ve üretimin her bölümünde daha kaliteli ürünlerle en aza indirilmiş fire yüzdesi, firmaları rekabetçi pazarın ön saflarına taşıyabilmektedir [1, 2].

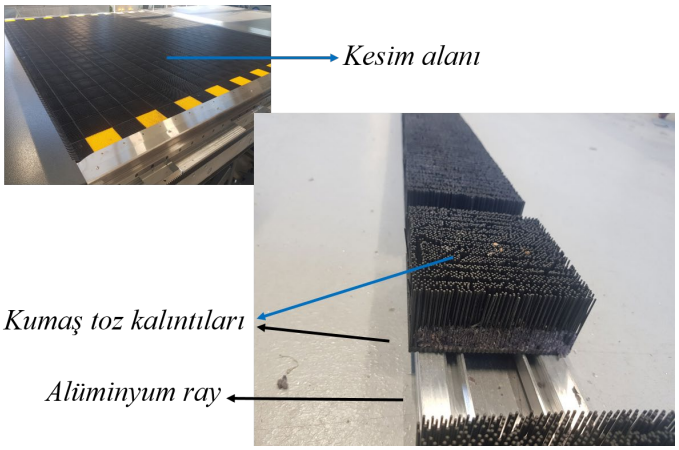
Tekstil endüstrisi içerisinde bulunan konfeksiyon, belirli ölçülere göre seri olarak üretilen, alıcının ölçülerine göre satılan hazır giyim eşyalarına ve bu konuyla ilgili sanayi dalına verilen isimdir [3]. Konfeksiyonda; kesimhane bölümü, teslim süresini ve zamanında sevkiyatı karşılamak için daha yüksek doğrulukta hassas kesimin sürdürülmesi gereken çok önemli bir bölümdür. Kesimhane, serim-kesim-tasnif işlemlerinden oluşmaktadır [4]. Kesim işlemi, fiziksel bir nesnenin keskin bir şekilde yönlendirilmiş bir kuvvet uygulanarak iki veya daha fazla parçaya ayrılmasıdır [5]. Kumaş kesimi, tekli veya çoklu kumaş katmanlarının kesilmiş parçalara dönüştürüldüğü örme ve dokumadan sonra giysi imalatında geri dönüşü olmayan süreçlerden biridir. Çoklu kumaş katmanlarını kesmek için farklı tipte kesme makineleri ve ekipmanları, ihtiyaca ve üretim hacmine göre kullanılan makineler mevcuttur. Bu doğrultuda kesme işlemi motorlu bıçaklar kullanılarak manuel olarak veya bilgisayar kontrollü sistemlerle otomatik olarak gerçekleştirilebilmektedir [6].

Yüksek hacimli giysilerin üretildiği yerlerde CNC otomatik kesim makineleri kullanılmaktadır [7]. Bu makineler kumaş katmanlarını bilgisayar sisteminde verilen komut doğrultusunda kesme işlemini gerçekleştirir [8]. Otomatik kesim, insan müdahalesini en aza indirerek ve üretim hatalarını önleyerek moda ürünlerinin kalitesinin yanı sıra üretkenliği de artırır. Otomatik kesimdeki sistem belli bir konfigürasyona sahiptir; bir kesme cihazı ve kesme cihazının sabitlendiği bir kafa, kesici kafayı kesme yüzeyi boyunca taşıyan bir enine kesme köprüsü (kiriş), fırçalarla kaplı bir konveyörlü masa (kesim alanı), kesme işlemini kontrol etmek için bir kontrol paneli ve kesici kontrol yazılımı bulunmaktadır. Şekil 1'de CNC otomatik kesim makinesi gösterilmektedir. Kesim işlemi konveyörlü kesim masalarında gerçekleştirilir ve alan uzunluğu 1800 mm, eni ise 1600-2400 mm (kesilen malzemeye göre değişken) uzunluğundadır. Konveyörlü masa, sürekli bir kesme işlemi ve artan üretkenlik sağlayan hareketli bir yüzeye sahiptir. Kesim masalarının çoğu, tüm kesim işlemi boyunca kumaş katlarını kesmek için kesici kafa ve üzerinde monteli bıçakla donatılmıştır ve kumaşlar CNC sisteminin kontrolü altında bıçakla kesilmektedir [9]. Kesici kafa, kesme tablasının genişliği ve enine kesme köprüsü boyunca hareket ederken, enine kesme köprüsü tablanın uzunluğu boyunca hareket eder. Bu hareketler, kesme cihazının kesim alanı üzerinde hareket etmesini sağlar ve bir kontrol ünitesi tarafından hassas bir şekilde yönetilir. Modern kesme cihazlarında, kesim masaları, malzemeyi aşağıda sabit tutmak ve kesme işlemi sırasında kesme hassasiyetini artırmak için bir vakum sistemi ile donatılmıştır [10]. Tekstil kumaşı gibi gözenekli malzemeler bu nedenle hava geçirmeyen film örtü ile kesilmektedir. Salınımlı bir bıçak, bıçak ilerledikçe yukarı ve aşağı hareket ederek kesme kabiliyetini en üst düzeye çıkarır. Bıçakla kesim, tek katlı ve çok katlı malzemede kaliteli kesim sağlar [11]. Bilgisayar kullanımı büyük yatırım gerektirir, ancak aynı zamanda avantajı; zamandan tasarruf etmesi, daha fazla verimlilik, seçenek ve doğruluk sağlamasıdır [10]. CNC otomatik kumaş kesme makinasında kesim 6-8 kat daha hızlı, kesim hatası yok denecek kadar azdır ve doğru kesim mümkündür [12]. Kesilen parçalar, konveyörlü sistem sayesinde kumaş toplama alanından geçer ve toplama alanında operatör tarafından toplanır.



Şekil 1. CNC otomatik kumaş kesim makinesi [13]

Bıçağın dikey hareketi ve doğru kesimin (en alt katlar için de) sağlanması gerekliliği nedeniyle, kesim alanı, bıçağın tüm kumaş katlarını yerinden oynatmadan veya herhangi bir hasara neden olmadan kolayca delmesini sağlayan fırçalarla (kıl bloğu) kaplıdır. CNC otomatik kesim makinelerinde ortalama 1000-1200 adet fırça bulunmaktadır. Kesim, bahsedildiği üzere, serilen kumaş katmanlarının vakumlanarak sabitlenmesini sağlayan fırçalı kesim alanında yapılır. Kesme işlemi boyunca kesici kafada bulunan bıçak tek tek kumaş parçalarını kesmek için fırçalar arasına daldırılır ve kumaş katmanları kesilir. Bu işlem sırasında kumaştan lif ve ip benzeri toz kalıntıları fırçalar arasına dökülür. Kullanılan vakum nedeniyle, bu toz kalıntıları fırça kılları arasına çekilir ve buraya yerleşerek fırçaların kirlenmesine sebep olur. Kirlenmiş fırçalar ve toz kalıntıları Şekil 2'de görülmektedir.



Şekil 2. Kesim alanında fırçalar üzerinde bulunan toz kalıntıları

Kesim alanında meydana gelen bu olumsuz durumla birlikte yatak boyunca vakum gücünün etkinliği azalarak hava akışı engellenir ve homojenlik azalır. Bu durum fırçaların esneme yeteneklerini kısıtlar ve normal kullanım sırasında bıçak tarafından kesilmeye daha yatkın hale gelerek fırçaların kıl ömrünü azaltır. Hatta vakum gücünün azalmasıyla kumaş sabit bir şekilde yerinde tutulamayabilir dolayısıyla bıçakta erken aşınma meydana gelerek kesici takımın verimli çalışmasına engel olabilir.

Bu çalışmada CNC otomatik kesim makinesinde kullanılmak üzere tasarlanan fırça temizleme sistemi için, makine şasesi ve üzerinde fırçaların bulunduğu alüminyum raylar göz önüne alınarak mukavemet açısından uygun vibratör seçimi yapılması amaçlanmıştır. Kullanılan vibratörün uyguladığı titreşim frekansından dolayı makine parçalarına özellikle hasar vermemesi, makinenin verimli çalışması için çok önemlidir. Bu nedenle makinenin yapısal güvenilirliğinin tasarımdaki en önemli göstergelerinden biri, fırçaların üzerinde

bulunduğu alüminyum ray ve makine şasesinde rezonansa veya yüksek titreşimlere sebep olabilecek frekansların bilinmesidir. Bu doğrultuda ray ve şasenin modal analizleri yapılarak doğal frekansları bulunmuştur. Ayrıca vibratörün belirli frekanslarda çalışması sırasında uyguladığı maksimum kuvvetin ray üzerinde meydana getirdiği gerilmelerin bulunması için ray üzerinde statik ve harmonik analiz yapılmıştır. Modal, statik ve harmonik analizler sonucunda vibratörün kullanılacağı sistemin kritik frekansları belirlenmiş olup vibratör seçiminde bu değerler göz önüne alınmıştır. Bunun yanı sıra harmonik analiz sonucuna göre güvenli sınırlar içerisinde vibratörün uygulayabileceği maksimum kuvvet belirlenmiştir.

II. MATERYAL-YÖNTEM

Ansys, karmaşık yapıdaki mühendislik problemlerini sayısal olarak çözmek için genel amaçlı bir sonlu eleman modelleme yöntemini kullanan bilgisayar destekli bir programdır [14, 15]. Bu program mekanik, yapısal analiz, hesaplamalı akışkanlar dinamiği ve ısı transferi gibi problemleri içerir. Öncelikle mevcut analizler için, Tablo 1'de gösterildiği gibi gerekli olan alüminyum rayın malzeme özellikleri incelenmiştir.

Tablo1. Alüminyum ray (EN-AW 6060-T6) malzeme özellikleri

Uzama (%)	15
Elastisite Modulü (MPa)	69000
Yoğunluk (g/cm³)	2,7
Akma Dayanımı (MPa)	226
Çekme Dayanımı (MPa)	250
Basma Dayanımı (MPa)	250

Vibratörün çalışma prensibi harmonik etkiye dayandığından alüminyum ray üzerinde Ansys Workbench programı kullanılarak harmonik analizler yapılmıştır. Harmonik analiz yapılabilmesi için öncesinde modal analiz yapılarak alüminyum ray ve makine şasesinin doğal frekansları tespit etmek gerekmektedir. Modal analiz, nesnelerin yapısal dinamiklerini, yapıları ve nasıl titreştiğini anlamak için önemli bir araçtır [16]. Modal analiz, yapının belirli bir frekans aralığı arasında rezonans yapmamasını sağlamak için temel olarak doğal frekansı belirler [17]. Bir cismin sadece esnekliğine ve kütlesine bağlı olan ve cismin o frekansta uyarılırsa yüksek genlikle ve sürekli olarak titreşeceği frekansa "doğal frekans" adı verilir. Doğal frekans hesabının temel formülü aşağıdaki şekildedir [14].

$$w = \sqrt{\frac{k}{m}}\ (rad/sn) \tag{1}$$

Denklem 1'de görüldüğü gibi doğal frekans eşitliğinde k parametresi yapıya özgü rijitliği (N/m), m parametresi yapıya özgü kütleyi (kg) ifade eder. Denklem 1'den doğal frekans,

$$f = \frac{1}{2\pi}\sqrt{\frac{k}{m}}\ (Hz) \tag{2}$$

Hz cinsinden elde edilir. Makine üzerinde kullanılabilecek olan vibratörlerin çalışma frekansları araştırılarak ilk altı doğal frekansın incelenmesinin uygulama için yeterli olduğu düşünülmüştür. Tablo 2'de modal analiz sonucunda belirlenen alüminyum ray ve şaseye ait ilk altı doğal frekans gösterilmektedir.

Tablo 2. Modal analiz sonucunda **(a)** Alüminyum ray doğal frekansı **(b)** Şase doğal frekansı

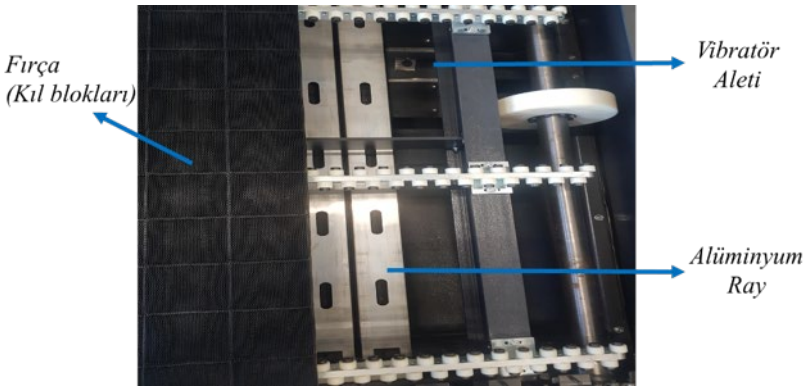
Mod	Frekans (Hz)
1	33,517
2	43,826
3	83,017
4	160,46
5	183,54
6	198,47

(a)

Mod	Frekans (Hz)
1	25,526
2	49,214
3	63,586
4	80,118
5	110,632
6	115,752

(b)

Şekil 3'te makine içerisinde vibratör cihazı, alüminyum ray ve fırçaların bulunduğu yerler görülmektedir. Sistemin zayıf noktası alüminyum ray olduğundan makine şasesi üzerinde harmonik analiz yapılmasına gerek duyulmamıştır. Vibratör alüminyum rayın sabitlenen noktalarına en uzak mesafe olan orta noktasına konulmuştur. Bu nokta alüminyum rayda titreşim genliğinin en yüksek olacağı kritik bölgedir. Vibratör seçiminde temel olarak iki parametre vardır. Bunlar kuvvet ve frekans değerleridir. Bu sebeple ilk adım olarak alüminyum rayın dayanabileceği maksimum statik kuvvet belirlenmiştir. Maksimum statik kuvvet belirlenirken ray üzerinde meydana gelen von Mises, çekme ve basma gerilmeleri dikkate alınmıştır.



Şekil 3. Makine içerisinde vibratör aleti, alüminyum ray ve fırçaların gösterimi

Statik analizler sonrasında ise elde edilen maksimum kuvvet kullanılarak harmonik analiz yapılmıştır. Harmonik analiz, zamanla sinüs (basit harmonik) dalgası olarak değişen yük altında lineer yapının kararlı durum yanıtını doğrulamak için kullanılan bir tür analiz yöntemidir. Harmonik analizin amacı, yapının çeşitli frekanslar altında nasıl tepki vereceğini belirlemektir. Bu yöntem sadece sabit zorlanmış titreşimi hesaplayabilmektedir. Böylece, sürekli dinamik özellikler tahmin edilebilir ve ayrıca sistemde rezonans oluşmayacağı doğrulanabilir [18].

Harmonik kuvvet altındaki sönümlü bir sistemin hareket denklemi aşağıdaki denklemden elde edilmektedir [19, 20, 21];

$$[M]\{X''\} + [B]\{X'\} + [K]\{X\} = \{F\}\sin(\theta t + \varphi) \quad (3)$$

Denklem 3'te F sistemin kuvvet vektörü, M kütle matrisi, B sönümleme matrisi, K ise rijitlik matrisidir. Sistemde X yerdeğiştirme vektörü, X' hız vektörü, X'' ise ivme vektörüdür. φ ise faz açısıdır.

Denklem 3'ün özel çözümünde harmonik olması beklenir ve çözümün aşağıdaki formda olduğu kabul edilebilir.

$$\{X\} = \{A\}\sin(\theta t + \varphi) \tag{4}$$

Denklem 4'te A, genlik vektörüdür.

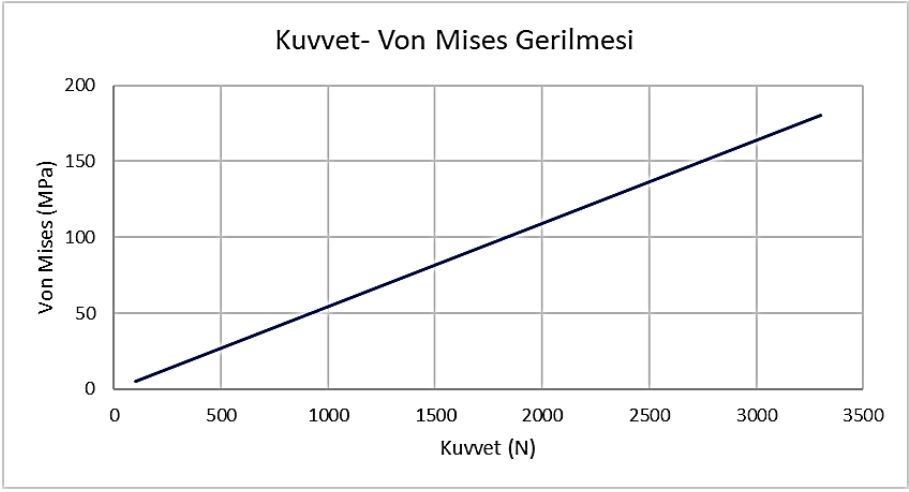
Denklem 4, Denklem 3'te yerine koyulursa, basitleştirdikten sonra aşağıdaki Denklem 5 elde edilir.

$$\{A\} = \{-[M]\theta^2 \sin(\theta t + \varphi) + [B]\theta \sin(\theta t + \varphi) + [K]\sin(\theta t + \varphi)\}^{-1}.[F]\sin(\theta t + \varphi) \tag{5}$$

Yukarıdaki teorik açıklamalara dayalı harmonik analizler sonucunda, frekansa bağlı olarak ray üzerinde meydana gelen gerilmeler detaylı incelenmiştir.

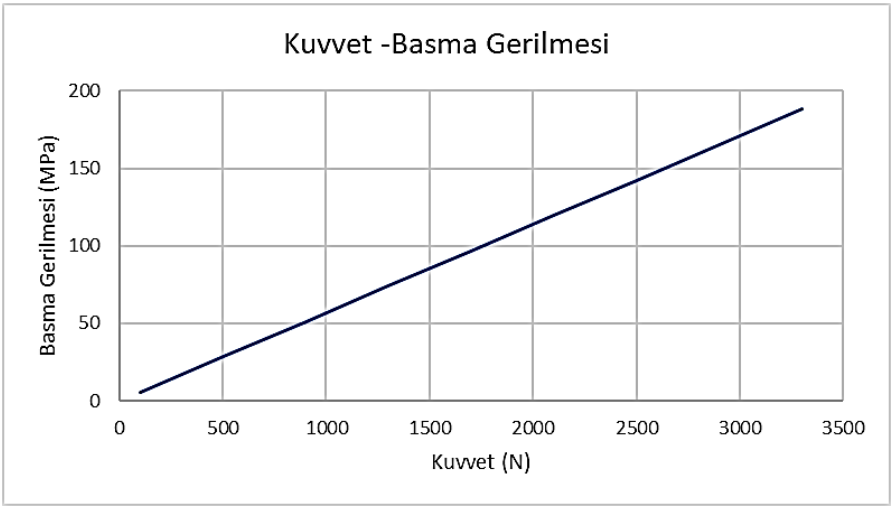
III. BULGULAR ve TARTIŞMA

Ansys Workbench programıyla yapılan statik analizler sonucunda Şekil 4'te alüminyum rayın kuvvet-von Mises gerilme grafiği gösterilmektedir. Grafiğe göre, 3000 N'dan sonra rayın emniyet faktörünün (akma değeri/ maksimum von Mises gerilmesi) oldukça azaldığı görülmektedir. Literatürde bahsedildiği gibi CNC makinelerde, dinamik yüklere maruz kalan makine parçaları için emniyet faktörünün (güvenlik katsayısı) 1,5 altına düşmesi tavsiye edilmemektedir [22]. Bu değerin altına düştüğü takdirde makine parçalarında hasarlar oluşabilmektedir. Bu sebeple 3000 N ve sonrası için alüminyum ray mukavemet açısından emniyetli görülmemektedir. Yani 3000 N veya daha yüksek değerde malzemenin plastik deformasyona uğrayacağı veya dayanım sınırına yaklaşacağı anlamına gelmektedir.



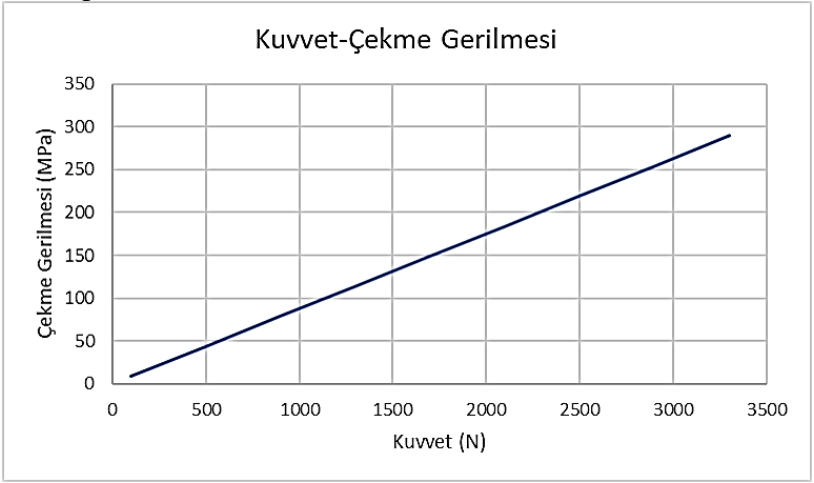
Şekil 4. Alüminyum rayın kuvvet-von Mises gerilmesi grafiği

Şekil 5'te alüminyum rayın kuvvet-basma gerilmesi grafiği görülmektedir. Grafiğe göre, 3000 N'dan sonra rayın basma dayanımı dikkate alındığında emniyet faktörünün azaldığı görülmektedir. Bu nedenle basma gerilmesi açısından uygulanabilecek maksimum kuvvet 3000 N'dur.



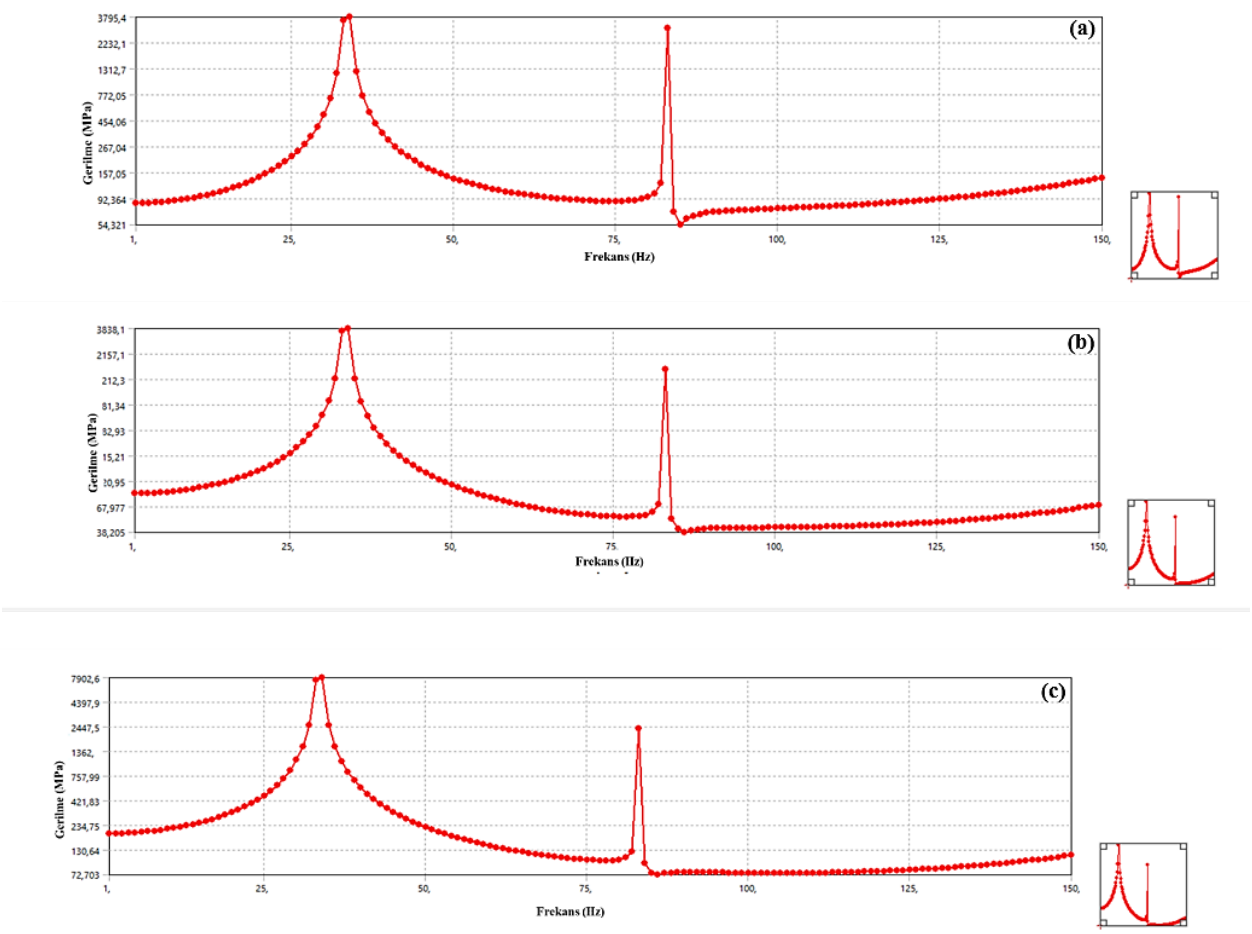
Şekil 5. Alüminyum rayın kuvvet-basma gerilmesi grafiği

Şekil 6'da alüminyum rayın kuvvet-çekme gerilmesi grafiği görülmektedir. Bu grafik incelendiğinde, 2000 N'dan sonra meydana gelen çekme gerilmesinin malzemenin çekme dayanımı göz önüne alınarak emniyetsiz olduğu görülmektedir. Yani 2000 N ve sonrasında, malzemenin belirli bir yük altında gerilmeye dayanamayabileceği, kalıcı deformasyona uğrayabileceği veya kırılabileceği anlamına gelmektedir. Von Mises gerilmesi çekme ve basma gerilmelerini içermediğinden rayın mukavemet kontrolü yapılırken meydana gelen maksimum çekme ile basma gerilmeleri de dikkate alınmalıdır. Bu gerilmeleri oluşturan kuvvetler içerisinde en küçük kuvvet değeri alüminyum raya uygulanabilecek maksimum kuvvet olarak belirlenmiştir. Bu sebeple dikkate alınan maksimum kuvvet 2000 N'dur.



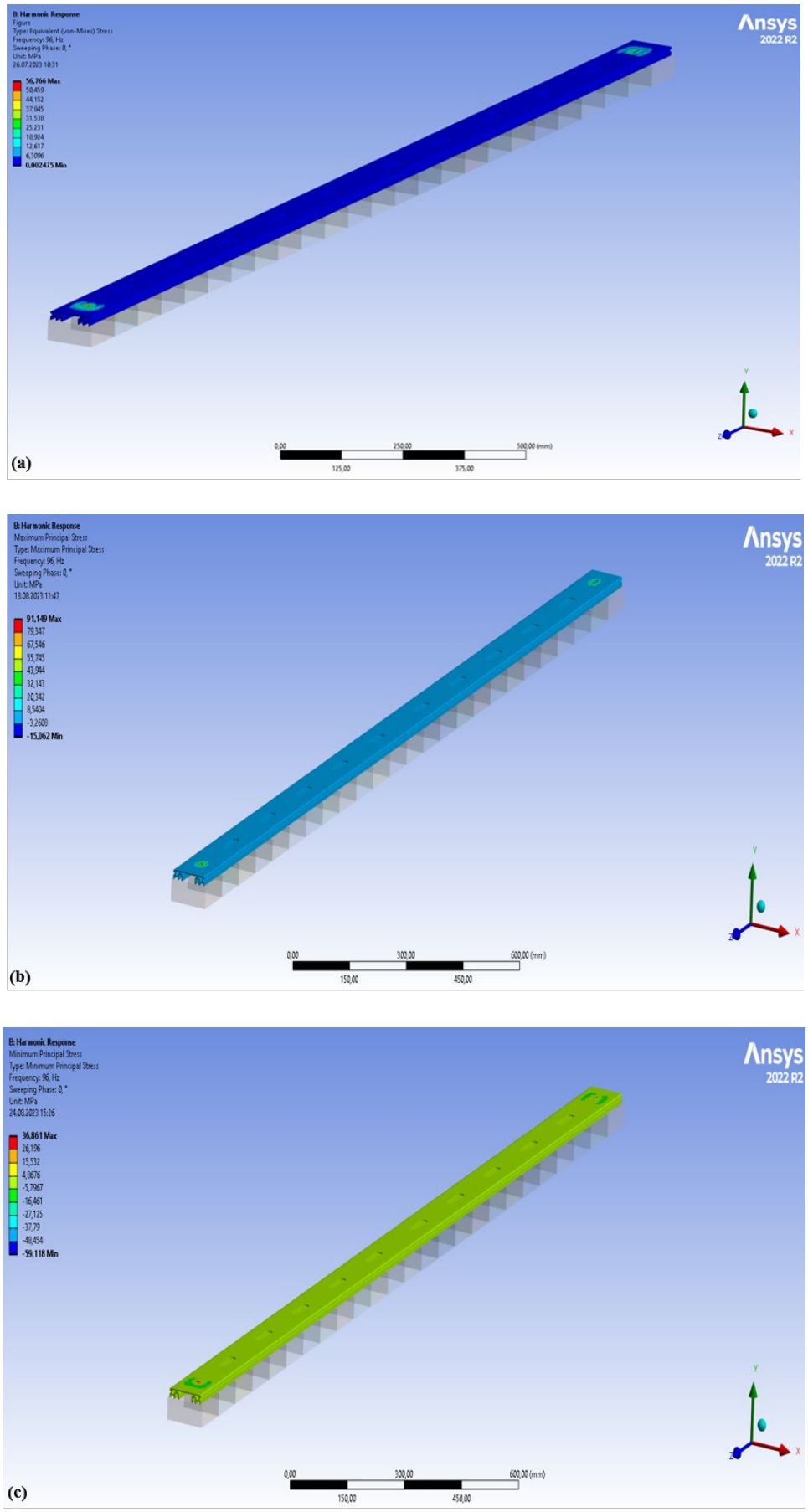
Şekil 6. Alüminyum rayın kuvvet-çekme gerilmesi grafiği

Ansys Workbench programıyla yapılan harmonik analizler sonucunda Şekil 7'de X, Y ve Z yönünde alüminyum ray üzerinde elde edilen normal gerilmelerin frekansa bağlı değişim grafikleri verilmiştir. Grafiklerde görülen pik noktalar alüminyum rayın doğal frekanslarındaki gerilmeleri göstermektedir. Vibratörün çalışma frekansı, grafiklerde görülen ve pik noktalarının oluştuğu frekans değerleriyle çakışır veya yakın olursa alüminyum rayda çok yüksek gerilmeler meydana gelir. Bu durumda ray hasar alır ve kullanılamaz hale gelir. Şekil 7'de 25-50 Hz ile 75-85 Hz aralığı kritik bölgeler olarak görülmektedir. Dolayısıyla seçilecek olan vibratör aletinin çalışma frekansı bu frekans aralıklarında olmamalıdır.



Şekil 7. Alüminyum ray üzerinde meydana gelen gerilme-frekans grafiği **(a)** X yönünde **(b)** Y yönünde **(c)** Z yönünde

Ansys Workbench programında modal, statik ve harmonik analizler sonucunda belirlenen vibratör özellikleri kullanılarak alüminyum rayda meydana gelen von Mises, çekme ve basma gerilmeleri Şekil 8'de görülmektedir. Alüminyum ray üzerinde maksimum von Mises gerilmesi 56,766 MPa, maksimum çekme gerilmesi 91,149 MPa ve maksimum basma gerilmesi 59,118 MPa olarak bulunmuştur. Rayın akma, çekme ve basma dayanımı göz önünde bulundurularak emniyet faktörü yaklaşık 4 olarak bulunmuştur [22]. Bu durum, alüminyum rayın, mevcut yükler altında herhangi bir hasar oluşmadan çalışabileceğini göstermektedir. Bu sonuca göre, alüminyum ray seçilen vibratörün çalışma koşullarında mukavemet açısından güvenlidir.



Şekil 8. Seçilen vibratöre göre alüminyum rayda meydana gelen **(a)** von Mises gerilmesi **(b)** çekme gerilmesi **(c)** basma gerilmesi

IV. SONUÇ

CNC otomatik kesim makinesinde kullanılması düşünülen vibratör aletinin seçimine dair Ansys Workbench programında yapılan modal, statik ve harmonik analizler sonucu vibratörün sahip olması gereken kuvvet ve frekans aralıkları elde edilmiştir. Bu sonuçlara göre, alüminyum ray üzerine monte edilecek olan vibratör için teorik bir temel oluşturulmuş ve makine üzerinde kullanılacak en verimli vibratör seçimi sağlanmıştır. Makine montaj kolaylığı da hesaba katılarak seçilen vibratörün uygulamış olduğu kuvvet 1038 N ve çalışma frekansı 96 Hz olarak belirlenmiştir. Bu özelliğe sahip vibratör aletinin alüminyum ray ve makine şasesi üzerinde herhangi bir probleme neden olmayacağı yapılan analizlerle gösterilmiştir.

KAYNAKÇA

[1] S. Mehrin, D. M. M. Hasan, M. L. R. Azad, M. M. R. Shahin, "Comparative Study on Automatic Fabric Cutting Machine and Straight Knife Cutting Machine," North American Academic Research, 5(5), 103-111, 2022. doi https://doi.org/10.5281/zenodo.6615342.

[2] S. Sahu ve A. K. Dey, "Automated Profile Cutting Machine Using PLC," International Conference on Advances in Human Machine Interaction, March 03-05, R. L. Jalappa Institute of Technology, Doddaballapur, Bangalore, India, 2016.

[3] H. Bilgiç, P. D. Baykal, "Konfeksiyonda Kalıp Sayısının Pastal Verimliliğine Etkisi," Ç.Ü Fen ve Mühendislik Bilimleri Dergisi, Cilt: 36-7, 2018.

[4] Z. Kumaş, E. C. Sabır, P. D. Baykal, "Konfeksiyon İşletmesinin Verimliliği için İş Etüdü Tekniği Kullanımı," Çukurova University Journal of the Faculty of Engineering and Architecture, 31(1), pp. 175-189, June, 2016.

[5] "Cutting Different Types of Fabric Cutting Machines Used in Garment Production," Online Clothing Study: https://www.onlineclothingstudy.com (accessed on 20-01-2021).

[6] "Requirements of Cutting Fabric," Textile Learner: https://textilelearner.blogspot.com (accessed on 20-01-2021).

[7] I. Vilumsone-Nemes, "Automation in spreading and cutting," Automation in Garment Manufacturing, The Textile Institute Book Series, Pages 139-16, 2018. http://dx.doi.org/10.1016/B978-0-08-101211-6.00006-9.

[8] P. Jungou, X. Xinping, C. Xiangqun, "An Arc Tangent Interpolation Algorithm Applying In CNC Cutting Machine," International Conference on Electric Information and Control Engineering, April, 2011. doi: 10.1109/ICEICE.2011.5778272.

[9] L. Guo-fu, H. Er-tian, "Design of Control System in CNC Clothes-Cutter Machine," Bulletin of Science and Technology, 21(6), 729-734, 2005.

[10] H. Er-tian, L. Guo-fu, "Structural Design of CNC Cloth-Cutting Machine," Mechanical &Electrical Magazine, 22(3), 51-54, 2005.

[11] I. Vilumsone-Nemes, "Industrial Cutting of Textile Materials," The Textile Institute Book Series (Second Edition), Pages 1-5, 2018. doi.org/10.1016/B978-0-08-102122-4.00001-9.

[12] "Computer Controlled Straight Knife Cutting Machine," Textile Learner. https://textilelearner.blogspot.com (accessed on 20-01-2021).

[13] Serkon Makina Ürün Broşürleri, www.serkonmakina.com, 01 Aralık 2022.

[14] S. A. Asiri, Dynamic, "Fatigue and Harmonic analysis of A Beam to Beam System with Various Cross-Sections Under Impact Load," Heliyon, 8, 2022. https://doi.org/10.1016/j.heliyon.2022.e10466.

[15] N. Kukreja, P. Singhal, "Design and Verify A Natural Frequency Using ANSYS Software," Materials Today: Proceedings 45, 3255–3258, 2021. https://doi.org/10.1016/j.matpr.2020.12.386

[16] M. L. Chandravanshi, A. K. Mukhopadhyay, "Modal Analysis of Structural Vibration," Proceedings of the International Mechanical Engineering Congress & Exposition, November, San Dıego, CA, 2013.

[17] L. Zuoshi, P. Jianyun, "Model analysis of vibrating screen's eccentric shaft based on ANSYS[J]," Mechanical, 37(2): 46-48, 2010.

[18] C. Baoming, J. Binfeng, Z. Hao, et., "Harmonic response analysis of banana screen based on ANSYS[J]," Mining & Processing Equipment, 40(10):96-100, 2012.

[19] L. Changling, C. Jianyi, L. Qingping, et., "Modal and Harmonic Response Analysis of Crankshaft of a Six Cylinders Compressor by ANSYS[J]," 40(8), 17-21, 2012.

[20] W. Xian, L. Junbi, "Assessment of Residual Strength flor Corroded Pipeline and Customized Development of ANSYS[J]," Pressure Vessel Technology, 29(1) :31-35, 2012.

[21] L. Jinkuan, L. Zaixin, Z. Dingli, L. Zhao, "Modal and Harmonic Response Analysis of Cutter Head of Juice Extractor," Seventh International Conference on Electronics and Information Engineering, edited by Xiyuan Chen, Proc. of SPIE, Vol. 10322, 103220E, 2017. doi: 10.1117/12.2265262.

[22] M.Rutheravan, "Summary of Safety Crıterıa in Design," Technical Report, 2016. doi: 10.13140/RG.2.1.1501.5285

A Multi-Scale Convolutional Neural Network and Empirical Mode Decomposition-Based Model for Electricity Price Forecasting

Ceyhun YILDIZ

ceyhun.yildiz@istiklal.edu.tr, ORCID: 0000-0002-5498-4127
Department of Electricity and Energy, Kahramanmaraş İstiklal University, Kahramanmaraş, Turkey

Abstract: Accurate electricity price forecasts play a vital role for energy generation companies and energy consumers in forming successful strategies for energy market operations. However, the inherent uncertainty and stochastic nature of electricity price data pose significant challenges to the forecasting process. In this study, a multi-scale convolutional neural network (CNN) and empirical mode decomposition (EMD)-based model was proposed to accurately forecast electricity prices. The EMD algorithm was utilized to extract features from the original electricity price signal. The multi-scale CNN was employed to capture multi-level spatial information from these extracted features. The model development and testing processes were realized using the dataset from the Turkish energy market. This dataset includes hourly recorded historical electricity price values. The min-max normalization was employed to normalize the dataset. The performance comparison tests were conducted to confirm the effectiveness of the proposed electricity price forecasting model. The obtained results from the proposed model were compared with the MLP- and EMD-MLP-based models. To validate the performance of the proposed and comparison models, a total of 20 experimental runs for each model were conducted. The performance metrics of mean absolute error (MAE), root mean squared error (RMSE), and correlation coefficient (R) were used to evaluate the results. The performance comparison tests revealed that the proposed model outperformed the comparison models with mean MAE, RMSE, and R values of 7.110, 9.527, and 93.498, respectively. The results of this study indicated that the proposed electricity price forecasting model has promising performance and can effectively be used for electricity market operations.

Keywords: *Convolutional Neural Network, Electricity Price, Empirical Mode Decomposition*

I. INTRODUCTION

WITH the liberalization of electricity markets, electricity price forecasts have become critical information for market participants. Accurate and reliable electricity price forecasts are of great importance for both energy generation companies and energy consumers. Energy generation companies employ price forecasts to effectively plan their generation schedules, optimize their generation mix, and mitigate financial risks. On the other hand, energy consumers utilize electricity price forecasts to organize their consumption patterns and effectively reduce electricity costs. Consequently, these forecasts have a substantial impact on how energy suppliers and consumers operate in the electricity market.

The researchers proposed numerous methods to address the issue of electricity price forecasting. These methods employed a range of approaches, including statistical analysis, machine learning, and deep learning. In addition, signal decomposition methods were also integrated into the methodologies to effectively extract meaningful features from the original dataset. In this study, the remarkable papers on electricity price forecasting are summarized,

providing an insightful overview of the advancements and breakthroughs achieved in this topic of research. One of those papers was [1], which introduced an interesting method for electricity price forecasting. The authors utilized a special type of artificial neural network (ANN) called adaptive wavelet ANN in their forecasting model. The dataset from the Spanish electricity market was used to conduct experimental studies. They stated that their model outperformed the benchmark models. Another method based on extreme learning machines (ELM) and bootstrapping was proposed in [2]. ELM and bootstrapping methods were utilized for modeling the electricity prices and uncertainties, respectively. The data from the Australian National Electricity Market was utilized to conduct both the model development and testing processes. [3] proposed distributional deep ANN for probabilistic electricity price forecasting. The realistic trading simulation with day-ahead electricity prices from the German market was performed to confirm the effectiveness of the proposed method. A comprehensive investigation was conducted in [4] to assess the performance of both statistical and machine learning algorithms in the context of electricity price forecasting. New Zealand electricity market data was used in the experimental studies. [5] introduced a two-stage model for electricity price forecasting. This model was a combination of the wavelet transform (WT) method and the autoregressive integrated moving average (ARIMA) model to forecast electricity prices. Authors stated that WT contributes to the forecasting performance. Electricity price data from the Spanish energy market was used to perform model development and testing studies. Another interesting approach was introduced in [6]. The authors proposed employing parametric and non-parametric methods to forecast both deterministic and stochastic components of the electricity price signal. The dataset from the Italian electricity market was used in the study. [7] proposed a hybrid model for day-ahead electricity price forecasting. This model includes linear regression, automatic relevance determination (ARD), and ensemble bagging extra tree regression (ETR) methods. The Nord Pool electricity market data was utilized to perform experimental studies. The papers reviewed above confirm the effectiveness of the machine learning algorithms in electricity price forecasting.

Moreover, it is widely acknowledged that deep learning-based methodologies have achieved remarkable success across various research domains. In alignment with this trend, researchers have introduced deep learning-based models for electricity price forecasting. [8] proposed a method that combines convolutional neural networks (CNN), sparse denoising auto-encoders, and signal decomposition to address the issue of electricity price forecasting. The experimental studies were conducted on a dataset from the Australian national electricity market. Another interesting deep learning based-model was introduced in [9]. The proposed model incorporates attention mechanism-based long short term memory (LSTM) and empirical WT. In addition, the crisscross optimization algorithm (CSO) was utilized to optimize hyperparameters of the network. The experimental studies were realized using the dataset from the Danish electricity market. Another deep network based on self-attention and CNN architecture was proposed in [10]. The dataset from the Ontario electricity market was utilized for model development and testing. These deep learning approaches achieved promising results. However, the literature on deep learning-based approaches for electricity price forecasting exhibits various gaps and limitations. Various deep learning architectures hold significant potential for achieving successful results in electricity price forecasting. Moreover, exploring these architectures across diverse datasets will contribute valuable insights to the existing body of literature.

In this study, a deep learning-based model was proposed for electricity price forecasting. This model incorporates a special CNN architecture that utilizes multi-scale kernels. The empirical mode decomposition (EMD) method was integrated to the network. The model development and testing processes were realized using the dataset from the Turkish electricity market. The contributions of the study are threefold:

1-The signal decomposition algorithm called EMD was employed to extract features from the original electricity price signal. EMD is particularly effective in decomposing non-linear and non-stationary signals, making it a suitable choice for handling complex signals such as electricity prices.

2- The special multi-scale CNN architecture was used to capture spatial patterns from extracted features. Multi-scale CNN offers the advantage of capturing diverse features at different resolutions, allowing it to robustly recognize information of varying sizes and contexts. This adaptability enhances localization accuracy, reduces overfitting, and improves performance.

3- Experimental studies were conducted using the dataset from the Turkish electricity market. Multiple performance tests were carried out to assess the effectiveness of both the proposed and the comparison models under the specific conditions of the Turkish electricity market.

The sections of this paper are organized as follows: The general perspective, related literature, and contributions of the study are summarized in this section. The theoretical background of the proposed model is introduced in the next section. The general architecture of the proposed model is explained in Section 3. The details of the experimental studies and the obtained results are summarized in Section 4. Finally, the study is concluded in Section 5.

II. THEORETICAL BACKGROUND

In this study, a multi-scale CNN-based model was developed to accurately forecast electricity prices. Absolutely, feature extraction in time series forecasting is essential for transforming raw data into informative features that enhance model performance. The effective signal decomposition algorithm, called EMD, was used to extract features from the original electricity price signal. The next subsection provides an explanation of the EMD algorithm.

A. Empirical Mode Decomposition

The signal processing technique EMD was introduced in [11] for decomposing nonlinear and non-stationary signals into a set of simpler components. These components, named intrinsic mode functions (Imfs), represent the original signal's inherent oscillatory modes at different time scales. Due to its ability to capture fundamental modes of complicated and non-stationary signals, EMD has found applications in a variety of fields, including finance, geophysics, and biomedical signal processing[12].

The pseudocode outlining the steps of the EMD algorithm is presented in Fig. 1. The algorithm starts with assigning the original signal (x) as the initial residue signal (r_i) and determining maximum number of the Imfs. Then the residue signal is stored in a temporary residue variable (r_i^{temp}) for the sifting operation. Sifting is the core of the EMD algorithm (steps 4-9). It extracts the candidate Imf signals (assigned as r_i^{cur}) from r_i^{temp}. r_i^{cur} is sifted until the predetermined maximum number of sifting is reached or the sift relative tolerance value calculated by the following equation is smaller than the threshold value.

$$sift\ relative\ tolerance \triangleq \frac{\left\| r_i^{temp} - r_i^{cur} \right\|_2^2}{\left\| r_i^{temp} \right\|_2^2} \tag{1}$$

The algorithm loops until the predefined maximum number of Imfs is reached.

EMD algorithm

Input: Original signal x
Output: $Imfs$ and a $residue$ signal
Initialization: $i \leftarrow 0$
$r_0 \leftarrow x$
$n \leftarrow$ number of $Imfs$
While $(i < n)$ **do**
  $r_i^{temp} \leftarrow r_i$ // store residue signal for sifting
  sifting
    //find the local minima and maxima points of r_i^{temp}
    //interpolate extremas to obtain upper and lower envelopes
    //obtain $mean$ of the envelopes
    $r_i^{cur} \leftarrow r_i^{temp} - mean$
  end
  If r_i^{cur} is Imf **then**
    $Imf_i \leftarrow r_i^{cur}$ // An Imf has been found
  else
    $r_i^{temp} \leftarrow r_i^{cur}$ **go to step 4**
  end
  $r_{i+1} \leftarrow r_i - r_i^{cur}$
  $i \leftarrow i + 1$
end

Fig. 1. The pseudocode of the EMD algorithm.

In this study, a Python-based EMD toolbox [13] was utilized to extract Imf and residue signals from the electricity price signal. Then the multi-scale CNN was used to capture information from these features. The next subsection provides detailed information regarding the concept of multi-scale CNN.

B. Multi-Scale Convolutional Neural Network

Recent research [14] has shown that multi-scale CNN architectures have a great potential in many different areas. The multi-scale (CNN) is a type of deep learning method that can gather information from data at various levels of detail. This is achieved by adding convolutional layers with different receptive fields or kernel sizes. The key idea is to allow the network to capture information at various degrees of depth, ranging from fine-grained small details to larger global patterns. This idea is especially useful in situations where patterns of interest may exist at different scales within the data. A multi-scale CNN in image analysis can recognize both small characteristics like edges and corners and larger structures like objects or sceneries. Similarly, it can discover both short-term variations and long-term trends in data in signal processing and time series analysis. In this study, multi-scale CNN layers were employed to capture spatial information from the components of the electricity price signal. The design of the proposed model is detailed in the following section.

III. THE PROPOSED MODEL ARCHITECTURE

In this study, an enhanced forecasting model that combines EMD and a multi-scale CNN was proposed to achieve accurate electricity price predictions. The model's architecture is presented in Fig. 2. In the initial phase, an efficient signal decomposition algorithm, EMD, was employed to extract features from historical electricity price data. These extracted features served as the input for the proposed multi-scale CNN network.

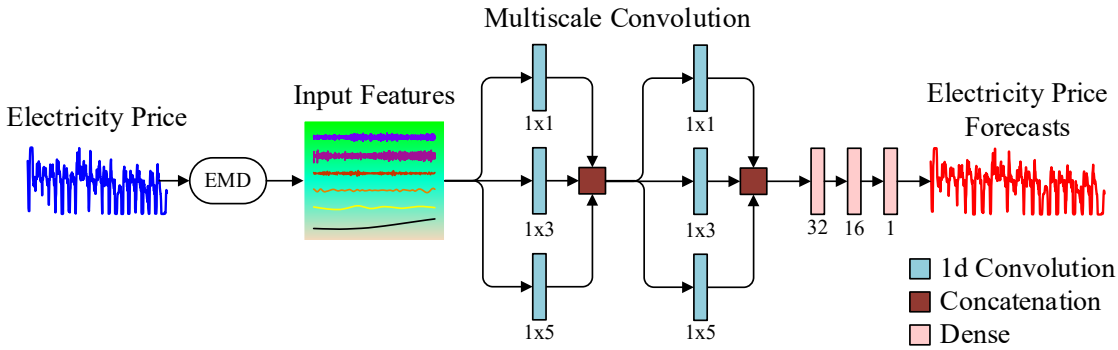


Fig. 2. The architecture of the proposed model.

Two CNN blocks were included in the multi-scale CNN architecture. For capturing multi-scale information, each block employed one-dimensional CNN layers with varying kernel sizes [1x1, 1x3, 1x5]. The outputs of these CNN layers were concatenated at the end of each CNN block. The output of these two CNN blocks was connected to three dense layers to obtain the final forecasts. The flow of the multi-scale CNN block can be formulated using the equations below.

$$\boldsymbol{Y}_{1x1} = f(\boldsymbol{W}_{1x1} * \boldsymbol{X} + b_{1x1}) \quad (2)$$

$$\boldsymbol{Y}_{1x3} = f(\boldsymbol{W}_{1x3} * \boldsymbol{X} + b_{1x3}) \quad (3)$$

$$\boldsymbol{Y}_{1x5} = f(\boldsymbol{W}_{1x5} * \boldsymbol{X} + b_{1x5}) \quad (4)$$

$$\boldsymbol{Y} = [\boldsymbol{Y}_{1x1}, \boldsymbol{Y}_{1x3}, \boldsymbol{Y}_{1x5}] \quad (5)$$

Where, $\boldsymbol{X}$ is the input of the block, $\boldsymbol{W}$ is the kernel matrix, and b is the bias. $\boldsymbol{Y}$ is the output of the block and $f(.)$ is an activation function. The details of the experimental study and results are summarized in the next section.

IV. EXPERIMENTAL STUDY AND RESULTS

A. Dataset Description

The experimental studies regarding the model development and testing processes were realized using the dataset from the Turkish energy market. This dataset includes hourly sampled total 4464 electricity price values, spanning from 01/02/2016 to 04/08/2016. Min-max normalization was employed to transform the electricity price data into a range between zero and one. The EMD algorithm was utilized to extract features from the original electricity price signal. This process yielded ten Imf signals, along with a residue signal. A visual representation of the original signal, the extracted Imf signals, and the residue signal is illustrated in Fig. 3. The statistical properties of the eleven extracted features are summarized in Table I. From the table, we can gather several insights about the extracted components obtained through the EMD process. The mean values of the components provide information about the central tendency of each component. Positive and negative mean values indicate whether the component tends to be above or below the overall mean of the dataset. For example, Imf 1 and Imf 3 have positive means, while Imf 2 and Imf 4 have negative means. The standard deviation values (Std.) give an indication of the spread or variability of values within each component. Larger standard deviations suggest greater variability, and smaller values suggest more consistent values. Components like Imf 3 and Imf 4 have relatively higher variability compared to others. The minimum and maximum values indicate the range of values spanned by each component. This helps understanding the range of values that each component covers. For example, Imf 1 has a wide range from -0.2769 to 0.2848, while Imf 8 has a narrower range from -0.0913 to 0.0966. The min and max values also provide insight into the amplitude of oscillations. Larger

differences between min and max values might suggest more oscillations. Overall, this table aids in understanding the statistical properties of the extracted components.

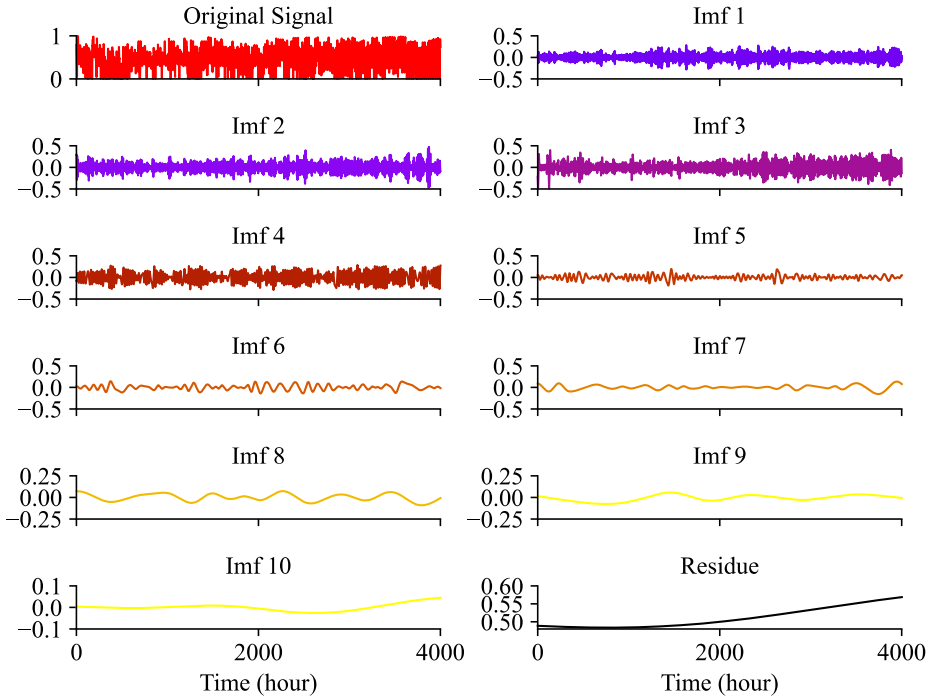


Fig. 3. The original electricity price signal and extracted features.

TABLE I
THE STATISTICAL PROPERTIES OF THE EXTRACTED SIGNALS

Property	Imf 1	Imf 2	Imf 3	Imf 4	Imf 5	Imf 6	Imf 7	Imf 8	Imf 9	Imf 10	Residue
mean	0.0014	-0.0005	0.0029	-0.0008	0.0006	0.0010	-0.0034	0.0063	-0.0092	0.0053	0.5173
Std.	0.0807	0.1053	0.1300	0.1202	0.0518	0.0562	0.0505	0.0466	0.0338	0.0214	0.0325
min	-0.2769	-0.4699	-0.4852	-0.291	-0.1898	-0.1414	-0.1541	-0.0913	-0.0762	-0.0259	0.4839
max	0.2848	0.4754	0.4081	0.2874	0.1963	0.1439	0.1357	0.0966	0.0570	0.0493	0.5812

B. Implementation Details

The first stage of the experimental study was the EMD-based feature extraction process. A Python-based EMD library [13] with default parameters was employed for this feature extraction process. The model input, a feature matrix, was then constructed using lagged features. These lagged features encompassed the values of various samples preceding the target hour. Specifically, they were selected as the feature values of the last 7 hours, the day before (24 hours prior), as well as 1, 2, and 3 weeks before the target hour (which correspond to 168, 336, and 504 hours prior, respectively). The lagged feature values were organized into a matrix with dimensions [11x11], where each row contained the lagged feature values.

The dataset was split into two distinct segments: 80% was allocated for model development, while the remaining 20% was dedicated to testing purposes. The model development phase included both model training and validation, ensuring that the model's performance was comprehensively assessed before being tested on the separate testing dataset. The experimental studies were conducted using the Python programming language, Python-based libraries, and the Google Colab environment. The powerful deep learning framework TensorFlow was utilized to develop a multi-scale CNN architecture. The Adam optimizer was utilized to train the network. The exponential learning rate decay was used to improve the stability of the training process. The details of the proposed multi-scale CNN architecture are summarized in Table II.

TABLE II
THE PARAMETERS OF THE PROPOSED MODEL

Layers	Parameters
Conv. 1x1	Input Shape:11x11 Number of kernels:32 Size of kernels:1x1 Padding: Same
Conv. 1x3	Input Shape: 11x11 Number of kernels:32 Size of kernels:1x3 Padding: Same
Conv. 1x5	Input Shape: 11x11 Number of kernels:32 Size of kernels:1x5 Padding: Same
Concat.	-
Conv. 1x1	Input Shape:11x96 Number of kernels:32 Size of kernels:1x1 Padding: Same
Conv. 1x3	Input Shape: 11x96 Number of kernels:32 Size of kernels:1x3 Padding: Same
Conv. 1x5	Input Shape: 11x96 Number of kernels:32 Size of kernels:1x5 Padding: Same
Concat.	-
Flatten	-
Dense	Number of nodes: 32
Dense	Number of nodes: 16
Dense	Number of nodes: 1

C. *Test Results*

To confirm the effectiveness of the proposed model, the obtained results were compared with the models based on MLP and EMD-MLP. The utilized MLP structure encompassed three dense layers with [32, 16, 1] nodes. The results from the proposed and caparison models are illustrated in Fig. 4.

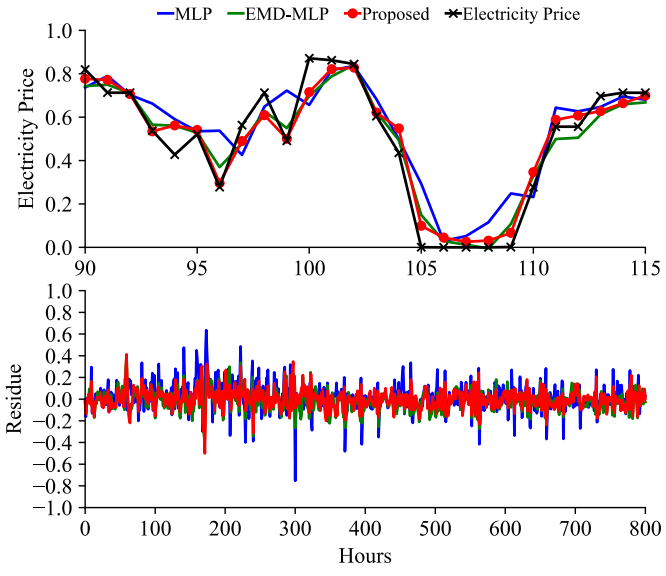


Fig. 4. The results for the proposed and comparison models.

The training and testing procedures were iterated 20 times to validate and ensure the consistency of the performances. The minimum, maximum, and mean performance metric values obtained for the proposed and comparison models are compared in Table III. It can be inferred from Fig. 4 and Table III that the proposed model achieved the best results when compared to the MLP-based and EMD-MLP-based models.

TABLE III
THE PERFORMANCE METRIC VALUES FOR MODELS

Metrics		MLP	EMD+MLP	Proposed
MAE	Min.	8.397	7.333	6.868
	Mean	8.704	7.808	7.110
	Max.	8.845	8.348	7.326
RMSE	Min.	12.301	9.672	9.134
	Mean	12.622	10.229	9.527
	Max.	12.838	10.765	9.957
R	Min.	87.555	92.126	92.708
	Mean	87.976	92.872	93.498
	Max.	88.634	93.423	94.158

V. CONCLUSION

An improved deep learning-based model was proposed in this study for accurately forecasting electricity prices. This model encompasses the EMD algorithm and a multi-scale CNN architecture. The EMD algorithm was utilized to effectively extract features from the electricity price signal. The proposed multi-scale CNN network was able to capture multi-level patterns from these features to forecast electricity. The dataset from the Turkish energy market was used to conduct experimental studies. The proposed model was compared with the MLP and EM-MLP models to confirm its effectiveness. The following conclusions are inferred from the findings of this study:

1-Extracting new features with the EMD algorithm contributes to the accuracy of the models.
2-The multi-scale CNN structure that captures multi-level patterns yields a substantial enhancement in the forecasting performance

The study's findings revealed that the proposed deep network architecture has promising performance. This model holds the potential to be efficiently employed in energy market operations. As a direction for further investigation, enhancing the design of the proposed model with comprehensive datasets containing diverse features like meteorological parameters and socio-economic indicators could be interesting research.

REFERENCES

[1] N. M. Pindoriya, S. N. Singh, and S. K. Singh, "An adaptive wavelet neural network-based energy price forecasting in electricity markets," *IEEE Trans. power Syst.*, vol. 23, no. 3, pp. 1423–1432, 2008.
[2] X. Chen, Z. Y. Dong, K. Meng, Y. Xu, K. P. Wong, and H. W. Ngan, "Electricity price forecasting with extreme learning machine and bootstrapping," *IEEE Trans. power Syst.*, vol. 27, no. 4, pp. 2055–2062, 2012.
[3] G. Marcjasz, M. Narajewski, R. Weron, and F. Ziel, "Distributional neural networks for electricity price forecasting," *Energy Econ.*, vol. 125, p. 106843, 2023.
[4] G. Kapoor and N. Wichitaksorn, "Electricity price forecasting in New Zealand: A comparative analysis of statistical and machine learning models with feature selection," *Appl. Energy*, vol. 347, p. 121446, 2023.

[5] A. J. Conejo, M. A. Plazas, R. Espinola, and A. B. Molina, "Day-ahead electricity price forecasting using the wavelet transform and ARIMA models," *IEEE Trans. power Syst.*, vol. 20, no. 2, pp. 1035–1042, 2005.

[6] I. Shah, H. Bibi, S. Ali, L. Wang, and Z. Yue, "Forecasting one-day-ahead electricity prices for italian electricity market using parametric and nonparametric approaches," *IEEE Access*, vol. 8, pp. 123104–123113, 2020.

[7] A. N. Alkawaz, A. Abdellatif, J. Kanesan, A. S. M. Khairuddin, and H. M. Gheni, "Day-ahead electricity price forecasting based on hybrid regression model," *IEEE Access*, vol. 10, pp. 108021–108033, 2022.

[8] Y. Q. Tan, Y. X. Shen, X. Y. Yu, and X. Lu, "Day-ahead electricity price forecasting employing a novel hybrid frame of deep learning methods: A case study in NSW, Australia," *Electr. Power Syst. Res.*, vol. 220, p. 109300, 2023.

[9] A. Meng *et al.*, "Electricity price forecasting with high penetration of renewable energy using attention-based LSTM network trained by crisscross optimization," *Energy*, vol. 254, p. 124212, 2022.

[10] A. Pourdaryaei *et al.*, "A new framework for electricity price forecasting via multi-head self-attention and CNN-based techniques in the competitive electricity market," *Expert Syst. Appl.*, p. 121207, 2023.

[11] N. E. Huang *et al.*, "The empirical mode decomposition and the Hilbert spectrum for nonlinear and non-stationary time series analysis," *Proc. R. Soc. London. Ser. A Math. Phys. Eng. Sci.*, vol. 454, no. 1971, pp. 903–995, 1998.

[12] H. Chaudhari, S. L. Nalbalwar, and R. Sheth, "A review on intrensic mode function of EMD," in *2016 International Conference on Electrical, Electronics, and Optimization Techniques (ICEEOT)*, 2016, pp. 2349–2352.

[13] D. Laszuk, "Python implementation of empirical mode decomposition algorithm," *GitHub Repos.*, 2017.

[14] E. Elizar, M. A. Zulkifley, R. Muharar, M. H. M. Zaman, and S. M. Mustaza, "A review on multiscale-deep-learning applications," *Sensors*, vol. 22, no. 19, p. 7384, 2022.

Enhancing Technical Drawing Education in Industrial Engineering through Architectural Approaches: An Educational Study

Erdem KÖYMEN

erdemkoymen@izu.edu.tr, ORCID: 0000-0002-6924-421X
S. Zaim University, Faculty of Engineering and Natural Sciences, Department of Architecture, Istanbul, Türkiye

Abstract: Engineering is a scientific discipline synonymous with providing practical solutions to issues in technical fields. In doing so, it consistently keeps variables such as optimal cost, human resources, material selection, and design at its forefront. Throughout this process, engineers are expected to mentally visualize developed systems within their respective fields and the parametric roadmap to achieving solutions. This cognitive agility and flow demand the presence or enhancement of a skillset, forming the foundation. In this context, disciplines such as industrial and mechanical engineering incorporate technical drawing courses aimed at fostering spatial thinking skills.

Architecture, partially akin to the realm of engineering, constitutes a three-dimensional virtual realm where the design of structures incorporating aesthetic and functional components occurs, thereby perpetually nurturing spatial acumen. Despite the diversification in accordance with traditional university approaches, architectural education centers around a systematic structure that places three-dimensional thinking at its core, running parallel to theoretical instruction.

This research aims to explore the inclination toward developing a new methodology by drawing on diverse approaches in architectural education to augment the content of technical drawing courses within the industrial engineering curriculum. Based on inspiration drawn from architectural projects and technical drawing courses, this study proposes a methodology encompassing feasibility analysis, collaborative design, 2D drafting, 3D modeling, material selection, physical production, pricing, and evaluation by a jury. The integration of this suggested methodology into technical drawing courses within industrial engineering education is significant in terms of enhancing students' spatial abilities and reinforcing design awareness within the production process.

As a result of a study conducted over one semester with 35 students, seven distinct industrial products were created, and based on surveys and expert assessments, the study was deemed successful across various educational outcomes. Additionally, the study culminated in the formulation of a lesson content framework for effective implementation of technical drawing courses in various engineering domains such as industrial engineering, contributing to the literature.

Keywords: *Technical drawing, Industrial Engineering, Architecture, Education, CAD*

I. INTRODUCTION

Throughout history, humans have employed visual representation to express and document the design methodologies of objects they used or created, alongside addressing their sheltering needs. Evolving over time with the infusion of technical conventions, the universally understood language of visual representation has transformed into a standalone expressive

form. Conceptually, technical drawing is a graphical representation created in adherence to predefined rules, elucidating the dimensions, forms, and attributes of an object or idea, with the intention of accurately and clearly conveying the desired replication [11]. In this context, even when sketched freehand onto a sheet of paper, the visualization of ideas is considered remarkably significant within the realm of engineering, which primarily centers on production and planning principles.

Scott Berkun from Microsoft suggests that unsuccessful ideas should surface not within the final product, but rather on sketch papers or prototypes, and emphasizes that this can only be achieved by expending energy to explore numerous concepts [4]. This approach proposes the identification and rectification of errors and deficiencies in the early stages of the product development process. As a result, the subsequent stages of product development can be carried out more successfully. The concerted effort shown in the early stages of production enables the development of an important strategy to enhance quality and optimize the design process in engineering.

Several studies underscore that while many new engineers are adept at computer-aided design (CAD), they exhibit deficiencies in fundamental knowledge, visualization, spatial skills, and freehand drawing abilities. A debate exists about whether this fundamental deficiency stems from the increasing prominence of CAD and the diminishing significance of manual drawing in foundational engineering graphics courses [14]. It has been observed that engineers trained solely in CAD tend to become proficient CAD operators, yet they struggle to develop an in-depth understanding of the core principles of engineering graphics. Particularly among engineers newly entering the profession, deficiencies have been identified in terms of their weak grasp of fundamental principles of drawing, lack of confidence in sketching, inadequate understanding of the necessity to adhere to rules, traditions, and standards, inability to visualize the three-dimensional form of an object based on two-dimensional drawings, struggles in interpreting 2D drawings with interconnected components, and weak spatial perception and reasoning abilities [16], [15].

In light of these studies and findings, the need for a new course content to enhance the efficiency and performance of technical drawing courses in engineering has been recognized. Thus, motivated by this, the current study has been developed with support from the discipline of architecture. To achieve this, students were divided into seven groups and tasked with creating an industrial design object. The projects were developed using AutoCAD and Sketchup training provided to the students, along with previous material and cost analyses. Completed designs were prototyped with the support of the university's material development laboratory. Finally, a jury was formed to evaluate the projects.

II. LITERATURE REVIEW

Technical drawing, a language constructed through specific drawing techniques, distinctive lines, symbols, and signs, serves as a common communication tool among architects, engineers, and other technical professionals. It forms an arrangement where professionals from various corners of the world can convey their ideas to each other, providing a universal framework. Technical drawing is employed throughout the entire process from the inception to the final form of a design. Design can be properly structured through geometry and accurately expressed through the rules of technical drawing [13]. The ability to visualize objects and situations in one's mind and manipulate these images is a cognitive skill of paramount importance, particularly in various fields that involve working with graphical images. Evidence demonstrates that well-developed spatial skills are critical for success in fields such as engineering, chemistry, computer science, mathematics, physics, medicine, dentistry, and many more. Various studies have extensively examined spatial abilities. According to research, advanced thinking, reasoning, and productive processes rely fundamentally on spatial abilities [12]. Spatial skills are widely regarded as fundamental

drivers of success in a broad range of scientific disciplines, playing a significant role in cognitive processes such as solving complex problems, conducting analysis, and creative thinking.

A study conducted on 141 engineers in both graduate and working positions delved into the significance of technical drawing courses in professional careers. The research indicates that these courses contribute to enhancing engineers' abstract and three-dimensional thinking skills and also impart abilities such as creating sections and views. The participants unanimously agreed on the necessity and importance of technical drawing courses; however, they expressed that the education in these courses was inadequate [3]. Another study conducted on first-year engineering students in Brazil underscored the importance of technical drawing in fostering students' spatial abilities and recommended improvements in teaching methodologies. The study emphasized that the relationship between spatial abilities and technical drawing performance has not been extensively studied, similar to studies in other academic performance domains. Nonetheless, in order to effectively plan the didactic process, it is essential to identify students who require more attention and support as early as possible [1].

For first-year engineering students, the use of Computer-Aided Design (CAD) software for their initial introduction to technical drawing offers numerous advantages. These students, accustomed to modern technologies such as the internet, 3D video games, smartphones, and the like, can easily adapt to these environments [7]. Additionally, this student cohort possesses a clear understanding of the necessity to learn CAD due to its alignment with their ability to keep up with the times, future career expectations, and efficient production of quality output [15].

When examining technical drawing education offered in undergraduate programs at universities, two distinct approaches are prevalent: traditional manual drawing and computer-aided design (CAD). However, there is no standardized approach among universities. In some Turkish universities, the inclusion of both fundamental technical drawing education and instruction on drawing software within the same course is viewed as an ineffective method. Instead, it's considered more suitable to separate technical drawing and computer-aided technical drawing courses, ensuring that while providing software training, the foundational skills of three-dimensional thinking, translating ideas into projects, and interpreting projects are not neglected [3].

In a study by [2], where spatial skills were tested against academic achievement levels in engineering education, the relationship between the two was found to be weak. While courses aimed at improving these skills are acknowledged to be important for engineering success, it's recommended that these courses be restructured with the support of modern technologies.

The difference between hand drawing and electronic drawing lies primarily in the drawing tool used. Apart from the ease and speed of electronic drawing, there should be no other significant distinction between hand-drawn and digitally drawn projects. Regardless of the chosen drawing method, the output should adhere to technical drawing standards. Furthermore, starting with hand drawing in education is believed to enhance design capabilities by engaging the brain and hand, promoting a collaborative effort between the two [5].

[6] present the development of a 3D interactive AR/VR teaching system using a design-based method to assist engineering and product design students in enhancing their technical drawing skills in critical and complex subjects. The research highlights the effectiveness of human-centered approaches in understanding student needs and demonstrates how international and interdisciplinary teams can facilitate the development of AR/VR technology applications for learning and teaching.

Studies indicate that engineering students often struggle to maintain focus throughout an entire class, and active learning approaches enhance students' learning capacity and attention spans [10]. Traditional methods tend to result in passive learning among students, lacking sufficient interaction between academic staff and students. Conversely, contemporary teaching

strategies employ methods developed based on cognitive science, presenting knowledge not merely as transmitted content but as an aid in the process of knowledge construction [9]. Modern engineering and design education strategies aim to integrate real-life concepts, experiences, technologies, and project-based work into a cohesive learning approach [8].

III. METHODOLOGY AND APPLICATION

Numerous professional fields utilize technical drawing for project design. Despite the underlying rules being the same, different perceptions of drawing styles specific to professions like mechanical engineering technical drawing, civil engineering technical drawing, and architectural technical drawing emerge due to the distinct subjects and products used in their respective fields. However, the differences are primarily due to the subjects of drawing being unique to each profession, while the fundamental rules remain consistent. For instance, mechanical engineering primarily involves drawing machine parts, while architecture focuses on drawing building and structural elements [5]. Considering this similarity in methods among different academic disciplines, an opportunity arises to transfer cross-disciplinary experiences and approaches into technical drawing education.

When examining architectural education, it becomes evident that architecture's planning and design core is facilitated through three key components: design studios/workshops, project supervisors/design instructors, and students/design aspirants. This education doesn't just involve the act of design but also encompasses theoretical courses. The aim is to cultivate individuals who can question, possess three-dimensional thinking and perception, critical thinking skills, and the ability to materialize ideas. Students are expected to create novel, unique, diverse, and innovative products. Education in this field involves not only the learning-teaching process but also different mental stages. Students learn through experiences, thinking, and drawing. Education occurs within a social interaction involving all students, rather than being limited to interactions between students and project supervisors. In this process, communication tools extend beyond verbal and numerical expressions; tools such as diagrams, sketches, and three-dimensional models come into play. Despite its initial complexity, this process is ultimately reduced to a single language through drawing rules and three-dimensional design skills, simplifying its complexity. At the end of the education process, no matter how innovative and successful a design is, conveying it in a language understandable by all is crucial. This language has been developed through drawing in architecture departments, and courses such as "Design Geometry and Technical Drawing" and "Perspective" are considered the most vital in developing the drawing language within architectural education [13]. The summarized architectural education's blend of social and technical depth could potentially be transferred to the field of industrial engineering, resulting in the following hypothesis (Table 1).

TABLE I

TRANSFER OF EDUCATIONAL APPROACHES FROM ARCHITECTURE TO INDUSTRIAL ENGINEERING FIELD

	Approaches in Architectural Education	**Transfer to Industrial Engineering Technical Drawing Course**
Social	Institution, building and fair visits	Industry visits and market research
	User interactions	Questioning the usage of objects
	Working with user scenarios	Generating scenarios for projects
	One-on-one sessions with project instructors	One-on-one work with instructors in all project stages
	Studio/workshop activities	Transferring studio culture from architecture education to classroom
	Group work	Encouraging group work among students
	Presentation skills and jury culture	Establishing end-of-term jury and conducting evaluations there
	Coordination training	Selection of group leaders and encouragement of task division
Technology	Technical expression enrichment through software	Training on 2D and 3D software
	Reducing errors in manufacturing through software	Pre-production checks with outputs from 3D modeling software

	Fundamental technology education	Sharing fundamentals of computer science within the course
Physical	Material knowledge	Sharing material research findings in the classroom
	Model making	Creating prototypes through physical production of projects
	On-site implementation	Complete production stages of physical models
	Project and construction site internships	Observing industrial visits and practical applications of manufacturing techniques
	Equipment and structural system training	Gaining experience in using technical tools throughout the process
Art	Aesthetic approach to products	Applying aesthetic approaches to project products with guidance from an instructor based in architectural education
	Art theories	
	Basic design and architectural movements	

The proposed methodology for transferring architectural education approaches to the industrial engineering technical drawing course has been implemented with 35 students at IZU Industrial Engineering department. Initially, the course structure was explained to the students. According to the structure, an industrial product would be designed and produced through group work. Students were given the freedom to form groups, allowing those with close collaboration opportunities to unite, resulting in 7 groups of 5 students each. Subsequently, students were taken on various industry visits and instructed to conduct research on materials and their applications. This helped develop students' familiarity with physical production materials. Building on this foundation, students were asked to suggest product ideas. Suggestions that involved material selection and production methods achievable through individual skills and basic tools were accepted. In the first third of the course, these topics were discussed and developed within the groups.

Concurrently, from the early weeks of the course, students were introduced to the principles of technical drawing using computer-aided design (CAD) software, specifically AutoCAD. As students learned AutoCAD commands, they were tasked with drawing various solid models' different views and sections as weekly applications. After gaining significant familiarity with AutoCAD commands, students were assigned to create technical drawings of their project products, encompassing plans, four views, and two sections. Additionally, they were required to draw technical details needed for production. Students' work up to this point was considered the midterm submission and graded accordingly.

Subsequently, students were taught how to use Sketchp software. Similar to the AutoCAD process, they were instructed to model various mechanical and architectural components. Any deficiencies or errors in the models were addressed by the instructor and rectified. Once the models were finalized, the industrial design projects, whose overall appearance had been refined through modeling and project development, were physically produced with the support of the school's material development laboratory and external manufacturing firms.

Following this stage, students were tasked with designing a poster illustrating all stages of their projects. Finally, a jury consisting of architects and industrial engineers was formed. Students were required to present their projects to the jury, explaining them from the conceptual phase to the production phase and showcasing their physical models. The jury members provided feedback and evaluations, and the students were subsequently asked to have the jury members score their performances based on criteria such as "originality," "aesthetics," "implementation," and "project planning" (Fig. 1), (Fig. 2).

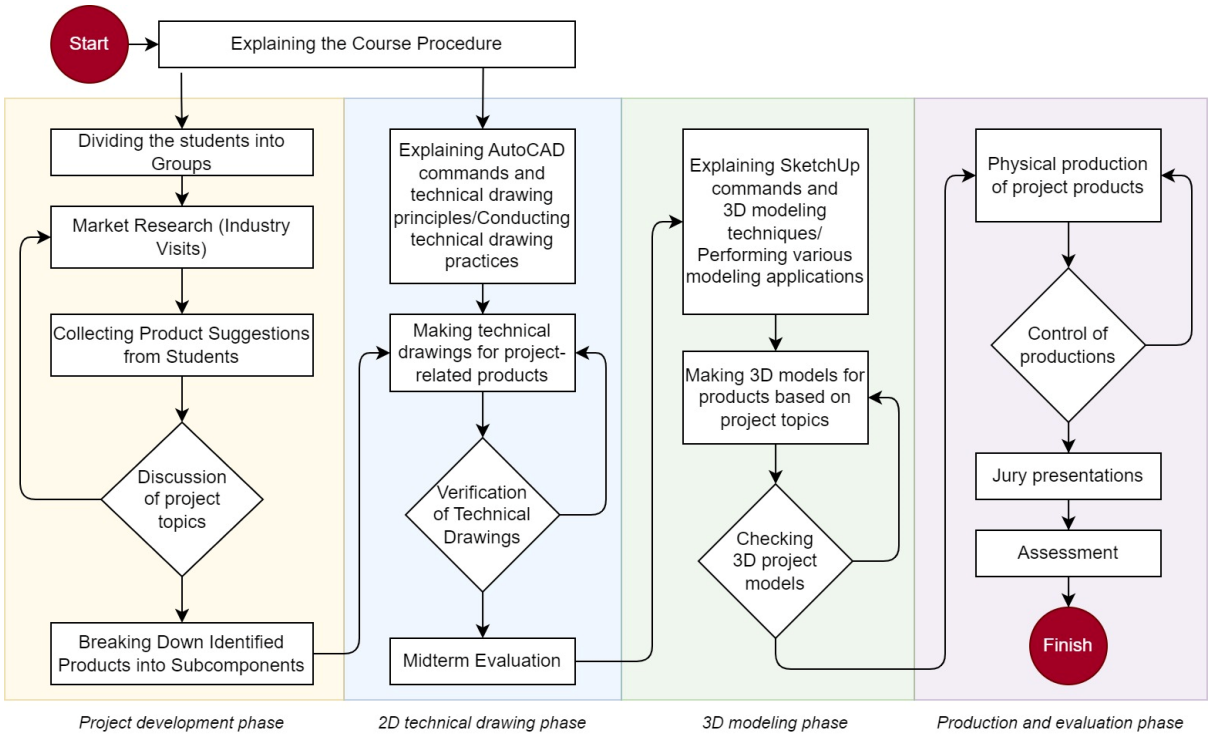


Figure 1. Flowchart of the course process.

As depicted in Figure 1, the course progressed through four phases. These phases include project development, 2D technical drawing, 3D modeling, and physical production and evaluation. Each phase is interconnected with the others. Following the project development phase, the ideas that became more distinct were then translated into 2D drawings and further modeled in 3D, leading to diverse achievements. These technical drawings aided in the production of physical prototypes of the products. As indicated in the figure, all these efforts culminated in a jury evaluation process.

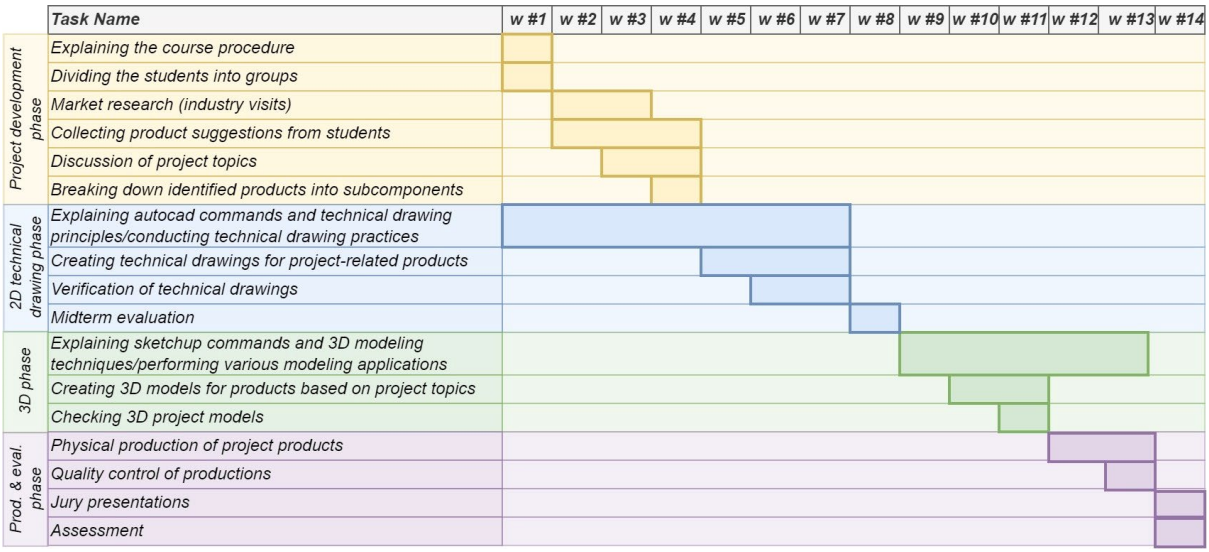


Figure 2. Representation of the course progress in a Gantt chart by weeks.

In Figure 2, a Gantt chart illustrates the course progression organized by weeks and actions. Upon interpreting the chart, it's evident that the initial 4 weeks are dedicated to project development. During these 4 weeks, close interaction was maintained with the students, and the insights they gathered from market and sector research were collectively evaluated within

the class. The materials brought in by students were examined, and technical assessments were conducted to ensure their suitability for the projects. At the end of this phase, the projects were refined, and the products to be produced were broken down into their components. This breakdown was intended to prepare the students for the technical drawings of their products. By doing so, students who were experiencing this process for the first time didn't get lost in the details but remained motivated and engaged.

As the chart shows, in parallel with these initial 4 weeks, the instruction of technical drawing principles and AutoCAD commands commenced right from the first week without delay. The reason for the urgency in this phase is due to the abundance of commands and the anticipation that more practice time would be needed for students to experiment with the drawings. This phase concluded with the collection of midterm submissions from students.

Over the next 5 weeks, the instruction shifted to teaching the Sketchup software. Alongside teaching fundamental commands, students were guided through practical applications of machine components and architectural details related to each command. While the instruction of commands continued, students were also given the opportunity throughout the course duration to model their own project concepts. This approach allowed for the rectification of modeling errors and ensured the progression of their projects. Due to the intensity of commands and approaches, this 3D modeling training continued into the subsequent manufacturing phase.

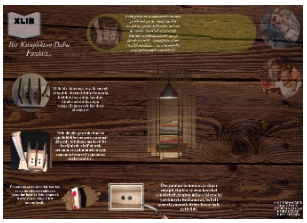
In the final manufacturing and evaluation phase, the project designs and developments from the preceding phases were translated into physical prototypes. This phase, spanning two weeks, involved continuous monitoring of student production with real-time interventions to ensure completion of the projects. The phase culminated with students presenting their projects to a jury, receiving feedback from jury members, and subsequently evaluating their achievements.

IV. PROJECT SUBMISSIONS AND EVALUATIONS

In this section, the posters of project works developed and pursued within the scope of the research methodology, detailed explanations of project and production methods, and jury evaluation notes are presented (Table 2).

TABLE II
STUDENT PROJECTS DEVELOPED WITHIN THE COURSE SCOPE AND JURY EVALUATIONS

Project Poster	Project and Production Method	Jury Evaluation
	**Group 1:** In this project named "Minimo," students created a miniature applique model of the "Şehitler Abidesi" monument located in Çanakkale, Türkiye. The production process involved laser cutting techniques. The model's components were calculated and designed in AutoCAD, and then virtually modeled and simulated using SketchUp. The project featured a creative concept where a lead figure representing the Çanakkale War was suspended in the air using a magnetic apparatus embedded within laser-cut wooden parts. When the apparatus was pulled down to the base, it triggered the illumination of a light, symbolizing the connection to the historical event of the Çanakkale War.	The product, deemed useful by the jury members, garnered appreciation for its intricate calculations despite its components. However, students' success in this aspect was commendable. The integration of technological components into the project was deemed successful; however, the project was evaluated as lacking originality in terms of aesthetics.
	**Group 2:** In the project named "Versatile" by the students, the goal was to combine the functions of a Bluetooth speaker and interior lighting. The project aimed to assemble 48 wooden cube blocks using a mechanism, enabling them to move mechanically similar to a Rubik's Cube logic. This design was intended to create different light dispersion	The project received praise for its original idea; however, the execution of assembling the wooden cubes to move in a Rubik's Cube-like manner was not achieved. Therefore, the project was criticized by the jury members in this aspect.

	patterns within the room using the light located in the center of the product..	
	**Group 3:** In the "Woo-Lap" project, students have designed a multifunctional laptop stand with both ergonomic and decorative features. The model incorporates a movable mechanism for ergonomic use, a laptop holder with cooling function, a cup holder, a section for a mouse pad, and a drawer. In this complex project consisting of intricate components and parts, students meticulously worked on precise measurements and careful laser cutting in the AutoCAD environment. Subsequently, the project was modeled and tested in the Sketchup environment.	The project received appreciation from both industrial and architectural department jury members and was considered a useful model. The jury members suggested that the project has potential for further development and encouraged the group members to take it to an industrial level.
	**Group 4:** In the project named "Book Support Lamp," students designed an adjustable head and mechanical holders for a book reading lamp. The product was constructed using wood materials and laser cutting techniques. Plastic supports were added to keep the book open. With the integrated power bank, the product can be used without a power outlet and can also charge mobile phones. The main components were drawn using AutoCAD in accordance with laser cutting techniques and were modeled in Sketchup to observe its appearance and functionality.	The project idea of the "Book Support Lamp" was not considered highly original by the jury members. The project was also evaluated as lacking in aesthetic appeal. However, the integration of a digital device into wooden components was appreciated for the applied skills and effort put into it.
	**Group 5:** In another project named "XLIB," students designed a book holder with an integrated lighting element aimed at promoting reading. In this project, the wooden parts of the book and lighting holder were created using laser cutting. The book holding section of the product was equipped with an Arduino Mini computer featuring a motion sensor, allowing the energy-efficient LED lights to illuminate only when the book is moved. This approach added a "conservation" themed aspect to the product's appearance.	The project named "XLIB" was positively evaluated by the jury members for its original idea, inclusion of additional software and hardware components, and received appreciation. However, it was criticized in terms of cost, usability, and aesthetics. In light of the feedback received, the project has been recommended for further development and industrialization to address the identified criticisms.
	**Group 6:** In another project with the theme "Into the Light with a Book," the group of students designed an illuminated decorative element inspired by the concept of a "book." This project features electronic switches within it that activate LED lights when its covers are opened. The design of the book-shaped covers was drawn using AutoCAD and then crafted using laser cutting on wood. Different cutting patterns were experimented with to achieve the ideal curvature of the spine. Additionally, the concept of folded paper from origami art was utilized to create the appearance of book pages.	Due to the presence of similar products in the market, the project was not considered as having an original idea by the jury members. Furthermore, the project received criticism for the limited utilization of significant outcomes of the course, such as 2D technical drawing and 3D modeling processes. However, the project team was praised for successfully implementing the idea and making the system functional.

	**Group 7:** In the spider-shaped lamp design project, the group of students initially created the drawings of the spider legs in the AutoCAD environment and then obtained these leg components through laser cutting on wood. Following that, they used a wood lathe to produce the body of the lamp, which would hold the socket, and attached these legs to the body. The project drew inspiration from the physical movements of a spider, aiming to capture the natural spider-like posture aesthetics on any surface through the mobility provided by the wooden leg forms.	Due to the uniqueness of the idea and the precision in execution, the project was deemed successful by the jury members. However, the limited utilization of technical drawing and modeling skills in this project raised concerns regarding the educational outcomes of the course. It was suggested that the project be further developed for industrialization.

V. CONCLUSION AND DISCUSSION

The research focuses on the journey of integrating architectural approaches into the technical drawing course with 35 first-year industrial engineering students. In this context, below are shared the gains, comments, critiques, and predictions related to the study:

It is emphasized that 3D thinking and perception hold significant value in engineering sciences, as observed in the literature [3], [14], [16], [15]. It is argued that teaching only basic technical drawing approaches falls short of providing substantial contributions to skill development. Consequently, the integration of 3D modeling techniques within the scope of the course has been deemed vital. The inclination toward teaching these 3D modeling techniques in the study is rooted in the idea that reflecting the continuity of design concepts in a 3D environment allows for an early-stage perception of the project's manifestation. The selection of Sketchup software for this purpose is due to the prior experience that highlights its intuitiveness and ease of learning among students. Furthermore, the study takes into account that students who are already accustomed to the digital realm can readily adapt to the virtual 3D environment and engage in the process of model development therein.

The motivation and incentivization of students in the first week of the course are presumed to be foundational. Based on past experiences, it is suggested that students should not become overwhelmed within the vast realm of research and application. Moreover, it is crucial to communicate the advanced benefits that students can gain from this exercise. Specifically, by highlighting the sectoral advancements made through technical drawing and modeling techniques in fields like production and planning, students can be provided with a forward-looking perspective.

Drawing inspiration from collaborative methods and group work emphasized in architectural education [13], the study was inspired to implement a similar approach. Allowing close friends to form groups facilitated more comfortable collaboration and better communication among students. However, it was observed that in some groups, there was an imbalance in the distribution of tasks, with more skilled and involved students taking on a larger role in technical drawing using AutoCAD and 3D modeling using Sketchup. This can be attributed to the tendency of close friends to group together. To counter this negative aspect, random group assignments could be considered.

Taking inspiration from architectural project courses that emphasize scenario-based design for each space, the study incorporated a similar approach. Students were required to develop user scenarios for their designed objects. This approach facilitated the shaping of products based on the scenarios created, providing a clear and functional foundation for design decisions.

Drawing from architectural science, which emphasizes the importance of suitable building materials in design, the study aimed to ensure that students do not lose sight of material and construction context while developing their projects. Although the design concept may be

brilliant, it cannot come to fruition without harmonious construction materials. Thus, efforts were made to keep students engaged with the material or medium aspect of design.

The study focused on instilling precision throughout the process, as the projects demanded meticulous accuracy. This precision was translated into the technical drawings, which required meticulous planning, sectioning, and detailing. When transitioning these drawings to the 3D environment, the same precision was sought to be maintained. The fact that many projects were manufactured using laser cutting added another layer of precision, prompting students to be mindful of balance and equilibrium in the manufacturing process, particularly at connection and transition points.

By virtually modeling projects, students were able to gain insights similar to those in architectural science, where project ideas are manifested even before they are realized. This perceptual aspect added depth to the study's outcomes.

Inspired by architectural science's practice of cost estimation, students were prompted to calculate production costs. This introduced the economic aspect into the design process, contributing to students' understanding of the economic implications of their designs.

The study was conducted with first-year industrial engineering students. Feedback from post-course surveys and interviews indicated that students believed this course would be more beneficial in subsequent years as they delve deeper into industrial engineering and gain a better understanding of its nuances.

The approach was carried out with a class of 35 industrial engineering students. To achieve broader results and outputs, the method should be tested with different student populations from diverse years and departments.

Borrowing from architectural education, students were provided the opportunity to present their projects in a jury defense. This experience contributed to their ability to prepare presentation materials, create visually appealing and convincing graphics, and confidently articulate their projects before an expert panel.

The feedback from the jury panel, composed of both architecture and industrial engineering experts, was mostly positive. Architecture professors stressed the need for aesthetic refinement in the produced objects and presentation materials. Moreover, several projects were recommended for industrialization and motivated for further development.

University workshops equipped with tools for physical production should be strengthened and opened for such educational purposes. Additionally, to enhance educational quality, joint workshops should be organized to foster interaction and knowledge exchange between architectural and industrial engineering disciplines. This would provide a platform for mutual enrichment and improved educational outcomes.

It was observed that after students became familiar with AutoCAD software and gained practical experience, they found Sketchup easier to learn compared to AutoCAD. This unique finding encourages experts in the field to conduct further research on this aspect of perceptual adaptation to digital environments.

In conclusion, the study explores the educational contribution of architectural science to industrial engineering and presents various outcomes through practical implementation. It also invites researchers in both fields to consider the potential benefits of cross-disciplinary collaboration, where architectural education could be enriched by the insights of industrial engineering and vice versa.

REFERENCES

[1] Adánez, G.P., & Velasco, A.D. (2002). Predicting academic success of engineering students in technical drawing from visualization test scores. Journal of Geometry and Graphics, 6(1), 99–109.

[2] Balak M. V., Kısa M. (2018) "Mühendislik Eğitiminde Uzamsal Görselleştirme Becerisinin Akademik Başarıya Etkisinin Araştırılması", Harran Üniversitesi Mühendislik Dergisi, 3(3): 234-242.
[3] Bayat, K. (2020). İnşaat Mühendisliğinde Teknik Resim Eğitiminin İncelenmesi. International Journal of Engineering Research and Development, 12 (2), 500-509. DOI: 10.29137/umagd.674242
[4] Berkun, S. (2020) "How Design Makes the World", Berkun Media LLC.
[5] Canbulat, T. (2018) "İç Mimarlıkta Teknik Resim", Remzi Kitabevi, İstanbul, 2018.
[6] Huerta, O., Unver, E., Arslan, R., Kus, A., & Allen, J. (2020). An approach to improve technical drawing using VR and AR tools. Computer-Aided Design & Applications Journal, 17(4), 836-849.
[7] La Verne, A. H. & Meyers, F.D. (2007) Engineering Design Graphics: Into the 21st Century. Engineering Design Graphics Journal, Vol. 71, No. 3, pp. 20–34.
[8] Merchant, Z. (2012) The Impact of Virtual Reality-based Learning Environment Design Features on Students' Academic Achievements, Ph.D. Thesis, Texas A&M University.
[9] Nepal, K.P. & Jenkins, G.A. (2011) Blending project-based learning and traditional lecture-tutorial based teaching approaches in engineering design courses, In Australasian Association for Engineering Education Conference 2011: Developing engineers for social justice: Community involvement, ethics & sustainability, Fremantle, Western Australia, 338.
[10] Prince, M. (2004) Does active learning work? A review of the research, Journal of Engineering Education, 93(3), 223-231. https://doi.org/10.1002/j.2168-9830.2004.tb00809.x
[11] Rubio, M. P., Vergara, D., & Rodríguez, S. (2020). Immersive Virtual Reality in Technical Drawing of Engineering Degrees. In Methodologies and Intelligent Systems for Technology Enhanced Learning, 9th International Conference (pp. 71-79). Springer International Publishing.
[12] Sorby, S., Drummer, T., Hungwe, K., & Charlesworth, P. (2005). Developing 3 D spatial visualization skills for non engineering students. In 2005 Annual Conference (pp. 10-428).
[13] Erten Bilgiç, D. & Konak, N. (2016). "Tasarı Geometri - Teknik Resim" ve "Perspektif" Derslerinin, Mimarlık Eğitimi Düşünsel Altyapısına Etkisi ve Prof. Dr. Yılmaz Morçöl. Mimarlık ve Yaşam, 1 (1), 1-11. DOI: 10.26835/my.257428.
[14] Metraglia, R., Baronio, G., & Villa, V. (2015). Issues in learning engineering graphics fundamentals: Shall we blame CAD?. In DS 80-10 Proceedings of the 20th International Conference on Engineering Design (ICED 15) Vol 10: Design Information and Knowledge Management Milan, Italy, 27-30.07. 15 (pp. 031-040).
[15] McLaren, S.V. (2008) Exploring perceptions and attitudes towards teaching and learning manual technical drawing in a digital age. International Journal of Technology and Design Education, Vol. 18, No. 2, pp. 167–188.
[16] Brown, P. (2009) CAD: Do Computers Aid the Design Process After All? Intersect: The Stanford Journal of Science, Technology and Society, Vol. 2, No. 1, pp. 52–66.

Design of a Novel Bubble Column Photobioreactor and Circular Illumination System for Microalgae Cultivation

Erdinç Aladağ[1*], Melih Onay[1], Alper Nuhoğlu[2]

[*]erdincaladag@gmail.com, ORCID: 0000-0003-1354-0930
[1]*Department of Environmental Engineering, Van Yüzüncü Yıl University, Van, Turkey*
[2]*Department of Environmental Engineering, Atatürk University, Erzurum, Turkey*

Abstract: Microalgae are promising potential feedstock candidates for many fields, including the pharmaceutical industry, food products and bioenergy. Especially recently, they have attracted more attention in biorefinery applications due to their relatively small land requirements, rapid growth and high valuable content. Microalgae are also very capable in environmental biotechnology applications such as carbon dioxide capture and advanced wastewater treatment. Light is among the most important environmental factors affecting biomass quality and photosynthetic efficiency in microalgae cultivation. The design of the light source and photobioreactor plays a key role in this process. In this study, a novel bubble column photobioreactor and a circularly illuminated LED-jacket were designed to enhance microalgal biomass production. The photobioreactor, which is aerated along its entire bottom, aims to prevent the formation of biofilm especially on the reactor wall and to reach the inner parts of the reactor, and the LED-jacket system with circular illumination aims to provide a more homogeneous light distribution by providing equal amount and equal angle of light to the outer surface of the reactor. As a result of the experiments conducted with the designed system in BBM medium at different light intensities using Chlorella zofingiensis, the highest biomass productivity and specific growth rate were obtained as 56 mg/L·day and 0.18 day^{-1} at 175 $\mu mol/m^2 \cdot s$ light intensity, respectively. It was found that biomass productivity increased up to 67% depending on the light intensity. The findings reveal that sustainable microalgal biomass production can be achieved with the innovative photobioreactor with whole bottom aeration and circular lighting system.

Keywords: *Microalgae, Photobioreactor, Illumination, Light intensity, Chlorella zofingiensis.*

I. INTRODUCTION

Microalgae have considerable potential in next generation biomass production. This is mainly because microalgae are a sustainable source of feedstock for many industries such as pharmaceuticals, cosmetics, dyes, food supplements, animal feed and biochemicals [1,2]. They also have many superiorities over terrestrial crops in the production of bioenergy such as biodiesel, bioethanol and biobutanol. These advantages include their growth quickly, resistance to seasonal variations, their lack of need for fertile soil and freshwater. In addition, they have a high CO_2 bio-fixation capacity and can live and grow in wastewater while simultaneously purifying effluents [3–5]. Therefore, researchers have recently shown particular interest in microalgae.

Microalgae convert light and carbon dioxide through photosynthesis into water and oxygen as well as biomass rich in value-added components such as proteins, pigments and lipids under photoautotrophic conditions [6]. Microalgae are cultivated outdoors in open ponds utilizing sunlight or in closed systems such as artificially illuminated photobioreactors. Photobioreactors are preferred over open ponds for microalgae cultivation due to low contamination risk as well

as more controllable growth conditions such as light intensity, temperature, nutrient and gas mixture [7]. An ideal photobioreactor would have adequate gas-liquid mass transfer for CO_2 uptake and O_2 release, excellent mixing of substrates with no dead zone, and low shear stress on the cells. Moreover, each photosynthetic cell inside the photobioreactor must have access to an optimal irradiance flux without shading [8]. However, in reality, these ideal conditions are mostly unattainable. Therefore, some conditions are optimized according to production capacity, product quality, targeted end-product, microalgal growth rate and bio-productivity. Until now, the development and design of photobioreactors as an important component of the algae industry has been widely researched. High nutrient removal and biomass production have been reported with an internally illuminated mirror flat-plate type photobioreactor by providing uniform light distribution in the culture medium [1]. In another air-lifted flat-plate photobioreactor utilizing municipal wastewater, efficient biomass productivity and high carbohydrate content were achieved [4]. Biomass productivity was improved in a periodically shaded tubular photobioreactor compared to a conventional tubular photobioreactor due to the controllability of the light:dark cycle [9]. Microalgae grown outdoors for long-term in a tubular photobioreactor showed an increase in antioxidant potential with nitrogen limitation [3]. Furthermore, various lighting systems were investigated to improve the efficiency of light utilization, which is crucial in microalgae cultivation. These include novel concepts such as hollow light guides placed inside the photobioreactor [7] and optical fibers immersed in the reactor that transmit the collected sunlight [10], LEDs powered by wireless energy transfer [6], high-frequency flashing light [2], and dynamic lighting systems that gradually increase depending on the biomass density [8]. However, the complexity, high energy costs, fouling and cleanup effort of these systems have limited their commercial viability. Therefore, there is a need for innovative perspectives in photobioreactor and illumination system design that ensure energy efficiency and high biomass production while minimizing biofouling. In this study, it was suggested to scrape the microalgae attached to the wall by air bubbles hitting the inner surface of the photobioreactor to prevent biofilm formation, and to provide homogeneous illumination along the periphery of the photobioreactor to illuminate partially light-deficient regions.

This work has three main objectives: (*i*) to design a novel well-mixed bubble column photobioreactor in which biofilm formation on the illuminated surface is minimized, (*ii*) to provide uniform illumination without dead zone along the periphery of the cylindrical reactor with a circular illumination system called LED-jacket, (*iii*) to study microalgal growth kinetics and biomass productivity at different light intensities using the novel photobioreactor and LED-jacket together. It is believed that the results obtained from this study will contribute to sustainable microalgal biomass production and shed light on innovative approaches in algae technology.

II. MATERIAL AND METHOD

A. Microalgae Cultures and Medium

The microalgae species *Chlorella zofingiensis* Dönz 1934 (CCALA 944) used in this study was obtained from the Czech Culture Collection of Autotrophic Organisms (CCALA). *Chlorella zofingiensis* were cultured in BBM medium [3] which contains: 250 mg $NaNO_3$; 75 mg K_2HPO_4; 175 mg KH_2PO_4; 75 mg $MgSO_4 \cdot 7H_2O$; 25 mg $CaCl_2 \cdot 2H_2O$; 4.98 mg $FeSO_4.7H_2O$; 50 mg EDTA; 31 mg KOH; 25 mg NaCl; 8.82 mg $ZnSO_4.7H_2O$; 1.44 mg $MnCl_2.4H_2O$; 1.57 mg $CuSO_4.5H_2O$; 0.49 mg $Co(NO_3)_2.6H_2O$; 11.42 mg H_3BO_3; 0.71 mg MoO_3 per liter. The pH was set to 7.0.

B. Microalgal Cultivation

Microalgae were pre-cultivated before the photobioreactor experiments. Fig. 4 shows images of *Chlorella zofingiensis* inoculated in petri dishes and flasks. In order to stock the purchased culture, it was firstly inoculated in a petri dish (Fig. 1a). The microalgae were then transferred

to flasks in BBM medium (Fig. 1b). Incubation was carried out in a JSR brand shaking incubator operating at 60 µmol/m^2·s light intensity, 16:8 light:dark ratio, 25±1 °C temperature and 100 rpm mixing speed. The biomass concentration was analyzed daily. Microalgae were inoculated in Erlenmeyer at 20% by volume and transferred to the photobioreactor at logarithmic growth phase (Fig. 1c).

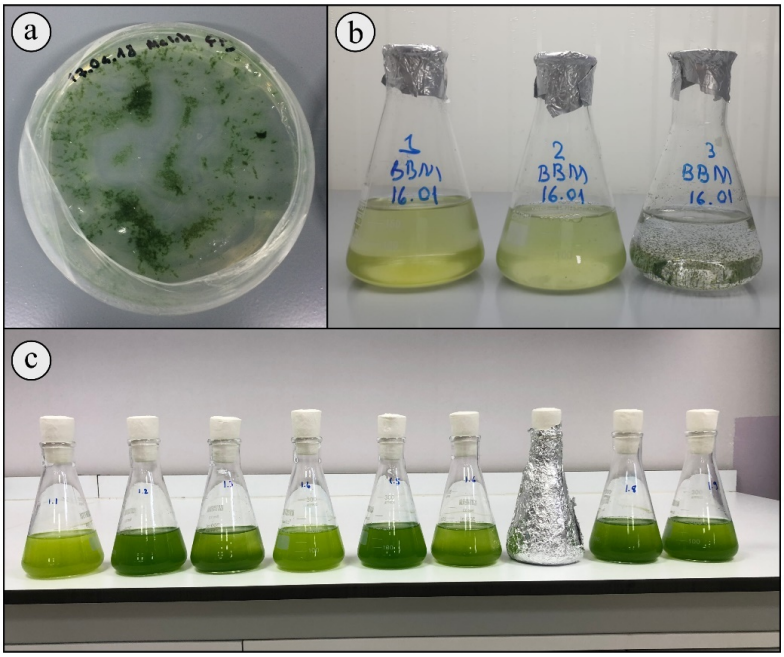


Fig. 1. Images of *Chlorella zofingiensis* inoculated in petri dishes and flasks.

C. Design of The Novel Bubble Column Photobioreactor

The photobioreactor was made of Poly(methyl methacrylate) (PMMA). PMMA, also known as plexiglas, is a synthetic polymer derived from methyl methacrylate. Plexiglass is a favored material for photobioreactor design because it is cheap, easily available, robust, heat resistant and has high light transmittance (Density: 1.19 gm/m^3, Refractive index: 1.49%) [8]. A transparent column with an inner diameter of 100 mm and a wall thickness of 5 mm was used. On the bottom of the reactor, a 100 mm diameter ceramic DURAN brand filter with a pore diameter between 40-100 µm (Por-2) was placed for air dispersion and bubble production. A pneumatic fitting was used for air to reach the reactor and a 25 cm × 25 cm plexiglass base was used for air collection [11]. A Kuletaş compressor was used for aeration and the air was continuously supplied to the system at 1 vvm to provide homogeneous distribution of light, temperature, nutrients, microalgae and carbon dioxide in the reactor. In order to keep constant the pH value in the medium, a JBL PROFLORA pH controller was used to dosing from a 99% pure CO2 cylinder at intervals. The reactor temperature was continuously measured with a WTW Multi 3420 multimeter. Fig. 2 shows images of the novel bubble column photobioreactor. Fig. 2a shows day one of the photobioreactor inoculated with *Chlorella zofingiensis*. Fig. 2b shows microalgal growth in the photobioreactor after two weeks of the cultivation. The photobioreactor has a total liquid height of 50 cm and a volume of approximately 4 liters. It was operated with a liquid height of about 46 cm and a volume of 3.6 liters, including air bubbles. The illuminated active surface area of the reactor was 0.16 m^2 and the surface area to volume ratio was 44.35 1/m. More details on the photobioreactor can be found in the Aladağ's PhD thesis [11].

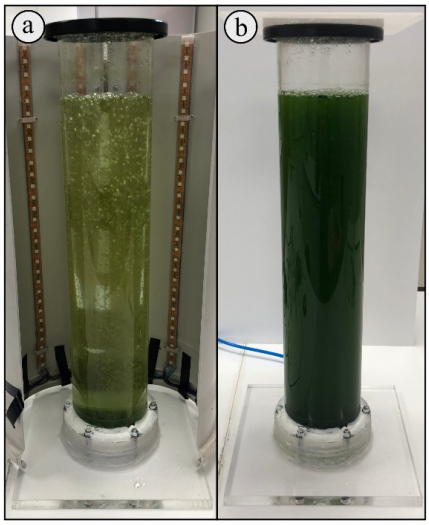


Fig. 2. Images of the novel bubble column photobioreactor.

D. Design of the LED-jacket

Light-emitting diode (LED) technology was used as the light source in the design of the circular lighting system. LED is preferred in microalgae cultivation due to its cheap, long life, small size, flexible, dimmable, low energy consumption and low heating [6]. A SMD 5050 type HI-LED brand RGB type LED (5.0 mm × 5.0 mm) was used to control the red, green and blue channels separately. For the jacket, a 50 cm long and 20 cm diameter light-proof PVC pipe was cut on both sides to form two half cylinders. On each of the half cylinders, 4 50 cm long LED strips were positioned at a 45° angle. A total of 240 LEDs was placed surrounding the reactor with 30 LEDs in each strip. The LEDs have a lens emitting 120° light. The distance between the LED-jacket and the photobioreactor is 40 mm [11]. Fig. 3 presents images of the LED-jacket with circular illumination and the photobioreactor. Fig. 3a, 3b and 3c are images of the overall LED jacket, right half cylinder and left half cylinder, respectively. Fig. 3d, 3e and 3f show images of the first, 7th and 14th day of microalgae cultivation, respectively. Light irradiance measurements were made at a total distance of 45 mm from the light source with an APOGEE brand light meter (MQ-200) attached to the inner wall of the photobioreactor. More details about the LED-jacket are in the Aladağ's PhD thesis [11].

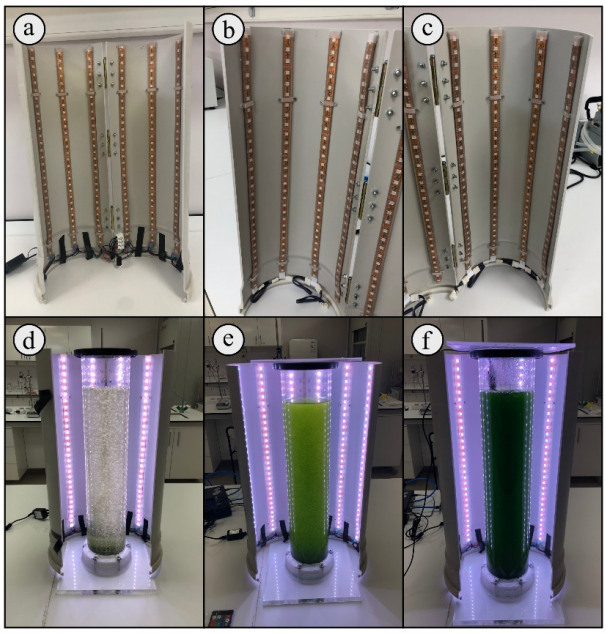


Fig. 3. Images of the LED-jacket with circular illumination and the photobioreactor

E. Measurement of Microalgae Growth

Optical density was determined by measuring the absorbance of 1 ml of microalgae sample at 680 nm wavelength with a spectrophotometer (Merck Prove 300). The relationship between measured optical density values and biomass concentrations is presented in Fig. 4. Equation (1) shows the calibration equation between optical density (Abs_{680}) and biomass (X) of *Chlorella zofingiensis*.

$$X = 817.37 \times Abs_{680} + 3.64 \ (R^2 = 0.993) \quad (1)$$

Where, X is the biomass concentration (mg/L) and Abs_{680} is the absorbance of the microalgae suspension measured at a wavelength of 680 nm.

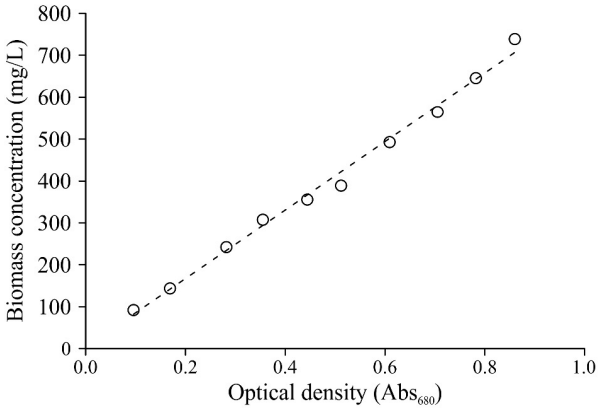


Fig. 4. Biomass and optical density calibration curve of *Chlorella zofingiensis*

Equations (2), (3) and (4) were used to calculate biomass productivity, specific growth rate and doubling time, respectively [4].

$$P = \frac{X_t - X_0}{t - t_0} \quad (2)$$

$$\mu = \frac{ln(X_0 - X_1)}{t - t_0} \quad (3)$$

$$t_d = \frac{ln(2)}{\mu} \quad (4)$$

Where P is biomass productivity (mg/L·day), μ is specific growth rate (day^{-1}), t_d is doubling time (day), X_t is microalgae concentration at time t (mg/L) and X_0 is initial microalgae concentration (mg/L).

III. RESULTS AND DISCUSSION

Light intensity is one of the most significant environmental factors for microalgae grown under phototrophic conditions. It can influence the cell growth and the metabolite production by directly affecting the photosynthetic kinetics of algal cells [2]. Therefore, the effectiveness of a novel designed bubble column photobioreactor and LED-jacket with circular illumination on microalgae cultivation was investigated with the light intensity. Fig. 5 illustrates the cell growth rate of *Chlorella zofingiensis* at light intensities of 60, 175, 300 and 450 µmol/m^2·s, respectively for 14 days. Samples were taken at 24-hour intervals from the culture grown under white LED light and 16:8 light:dark ratio. The reactor was operated at a temperature of 25±1 °C, pH 7 and air flow rate of 1 vvm. The pH value was kept constant with a pH controller via

CO_2. As can be seen in the figure, microalgal growth was lag until day 6. After day 6, growth shifted to the exponential phase. The highest biomass concentration reached 580 mg/L on day 14 at 175 µmol/m^2·s light intensity. The lowest biomass concentration was 382 mg/L at 450 µmol/m^2·s. At lighting intensities above the light saturation point, the photosynthetic rate is directly proportional to the light intensity. However, at higher light intensities, damage to the photosynthetic receptor system occurs and this is called photoinhibition [12]. In addition, although low light intensity is sufficient in the initial phase, the microalgal growth is limited in the later stages due to the self-shading effect of the cells [5].

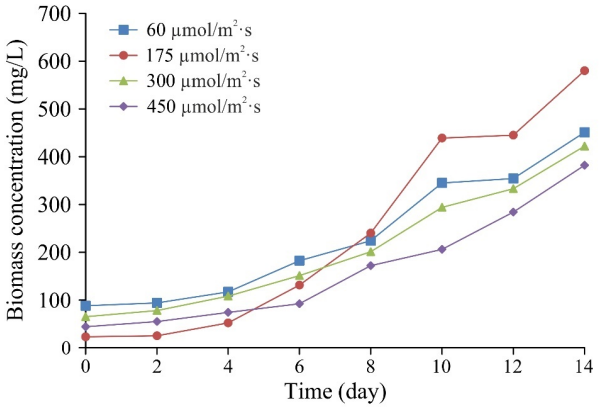


Fig. 5. Influence of light intensity on growth of *Chlorella zofingiensis*.

Table 1 summarizes the biomass productivity (P), doubling time (t_d) and specific growth rate (μ) of *Chlorella zofingiensis* grown at different light intensities. Biomass concentrations after the lag phase were taken into account when determining the microalgal growth coefficients. The highest biomass productivity and specific growth rate were calculated at 175 µmol/m^2·s light intensity, 56.12 mg/L·day and 0.18 day^{-1}, respectively. The lowest biomass production and specific growth rate were observed at 60 µmol/m^2·s. When the light intensity was increased from 60 to 175 mm, biomass production increased by approximately 67%. At higher light intensities, a significant decrease in biomass production was observed. It indicates that the light intensity has reached saturation for microalgal growth [11,12].

TABLE 1
SPECIFIC GROWTH RATE, DOUBLING TIME AND BIOMASS PRODUCTIVITY OF *CHLORELLA ZOFINGIENSIS* AT DIFFERENT LIGHT INTENSITIES

Light intensity (µmol/m^2·s)	Biomass productivity, P (mg/L·day)	Specific growth rate, μ (day^{-1})	Doubling time, t_d (day)
60	33.62	0.114	6.1
175	56.12	0.180	3.9
300	33.87	0.128	5.4
450	36.25	0.167	4.1

The optimum light intensity varies depending on the microalgae species as well as environmental conditions such as photobioreactor type, sizing, design, light source type, quality and placement. The largest biomass of 250 mg/L was achieved with an air-lift photobioreactor internally illuminated by optical fibers transmitting sunlight collected through a light collector. Due to the dimensions of the optical fibers, lower light intensity (13-30 µmol/m^2·s) was provided, resulting in a lower biomass concentration [10]. In a periodically shaded tubular photobioreactor continuously illuminated with fluorescent lamps, an increase

in biomass productivity up to about 22% was reported depending on the frequency of the light:dark cycle [9]. In a flat-plate photobioreactor using a mirror, the specific growth rate increased by 60%. Energy consumption was reduced by up to 10 times by recycling unutilized light by the algal cells through the mirror [1]. The biomass productivity was increased by over 23% in a flat-plate photobioreactor with hollow light guides designed for illumination. The enhanced biomass production was described by the homogeneous distribution of light along the PBR [7]. According to the comparison of the obtained results with the literature, in the photobioreactor with aeration along the bottom, both a more efficient mixing was achieved and algal biofilm formation was prevented on the illuminated surface of the reactor. In addition, a more uniform illumination was achieved by the circularly illuminated LED-jacket.

IV. CONCLUSION

In this study, a novel bubble column photobioreactor and a circularly illuminated LED-jacket were designed for microalgae cultivation. Microalgal growth was studied with *Chlorella zofingiensis* in BBM medium at different light intensities. The highest microalgal biomass production and specific growth rate were 56 mg/L·day and 0.18 day^{-1} at 175 µmol/m^2·s light intensity, respectively. Depending on the light intensity, biomass productivity increased up to 67%. The results obtained show that the novel photobioreactor and circular illumination system are suitable for sustainable microalgae cultivation.

ACKNOWLEDGMENT

This study was supported by The Scientific and Technological Research Council of Turkey (TÜBİTAK) under the project number 118Y477. This study is derived from part of Erdinç Aladağ's doctoral thesis (YÖK Thesis No. 600789), which was prepared under the supervision of Alper Nuhoğlu and co-advised by Melih Onay.

REFERENCES

[1] A.K. Ahangar, P. Yaqoubnejad, K. Divsalar, S. Mousavi, M. Taghavijeloudar, Design a novel internally illuminated mirror photobioreactor to improve microalgae production through homogeneous light distribution, Bioresource Technology. (2023) 129577.

[2] S. Wang, A.R. Stiles, C. Guo, C. Liu, Microalgae cultivation in photobioreactors: An overview of light characteristics, Engineering in Life Sciences. 14 (2014) 550–559.

[3] P.S. Corrêa, W.G. de M. Júnior, N.S. Caetano, Antioxidant potential of extracts of *Chromochloris zofingiensis* cultivated in pilot-scale outdoor tubular photobioreactors under nitrogen limitation, Algal Research. 67 (2022) 102859.

[4] M. Onay, E. Aladag, Production and use of *Scenedesmus acuminatus* biomass in synthetic municipal wastewater for integrated biorefineries, Environmental Science and Pollution Research. (2022) 1–13.

[5] B. Sajjadi, W.-Y. Chen, A.A.A. Raman, S. Ibrahim, Microalgae lipid and biomass for biofuel production: A comprehensive review on lipid enhancement strategies and their effects on fatty acid composition, Renewable and Sustainable Energy Reviews. 97 (2018) 200–232.

[6] M. Glemser, M. Heining, J. Schmidt, A. Becker, D. Garbe, R. Buchholz, T. Brück, Application of light-emitting diodes (LEDs) in cultivation of phototrophic microalgae: current state and perspectives, Applied Microbiology and Biotechnology. 100 (2016) 1077–1088.

[7] Y. Sun, Y. Huang, Q. Liao, Q. Fu, X. Zhu, Enhancement of microalgae production by embedding hollow light guides to a flat-plate photobioreactor, Bioresource Technology. 207 (2016) 31–38.

[8] P. Benner, L. Meier, A. Pfeffer, K. Krüger, J.E. Oropeza Vargas, D. Weuster-Botz, Lab-scale photobioreactor systems: Principles, applications, and scalability, Bioprocess and Biosystems Engineering. 45 (2022) 791–813.

[9] Q. Liao, L. Li, R. Chen, X. Zhu, A novel photobioreactor generating the light/dark cycle to improve microalgae cultivation, Bioresource Technology. 161 (2014) 186–191.

[10] S. Xue, Q. Zhang, X. Wu, C. Yan, W. Cong, A novel photobioreactor structure using optical fibers as inner light source to fulfill flashing light effects of microalgae, Bioresource Technology. 138 (2013) 141–147.

[11] E. Aladağ, Investigation of lipid production in bubble column photobioreactor by *Botryococcus braunii* and *Chlorella zofingiensis*, Atatürk University, Institute of Science and Technology, Department of Environmental Engineering, PhD Thesis, Erzurum, 2019.

[12] S. Wahidin, A. Idris, S.R.M. Shaleh, The influence of light intensity and photoperiod on the growth and lipid content of microalgae *Nannochloropsis sp.*, Bioresource Technology. 129 (2013) 7–11.

EAF Slag Detection System Development and Software

Elif MENDİ[1*], Ahmet SÖNMEZ[2], Halil ÖZTÜRK[2], Levent ÜNSAL[2], Doğan KAYA[2]

[*]elif.mendi@toscelik.com.tr,
[1]*Research and Development Center, Tosçelik Profile and Sheet Industry Co., Osmaniye, Turkey*
[2]*Meltshop , Tosçelik Profile and Sheet Industry Co., Osmaniye, Turkey*

Abstract: This study has been done to reduce slag that badly affects to good steel production by using Slag Detection Method in Steel Plant in Tosçelik Profile and Sheet Industry. We use Infrared Thermal Camera to detect slag and steel in this study .The temperature of steel that pouring from EAF is measured with the infrared thermal camera on measurement system. The molten steel and slag have a great difference emissivity. They could be distinguished according to their different emissivity and including. So, we has used image processing software to differ them by using infrared camera. There is the most important thing that a calibration for the temperature threshold that is used to distinguish the molten steel and slag in a certain environment. According to this information amount of slag is could be calculated in real-time. So, alarm level is arranged according to this calculation.

Keywords: *EAF Image Processing, Steel and Slag, Infrared Thermal Camera, Emissivity*

I.INTRODUCTION

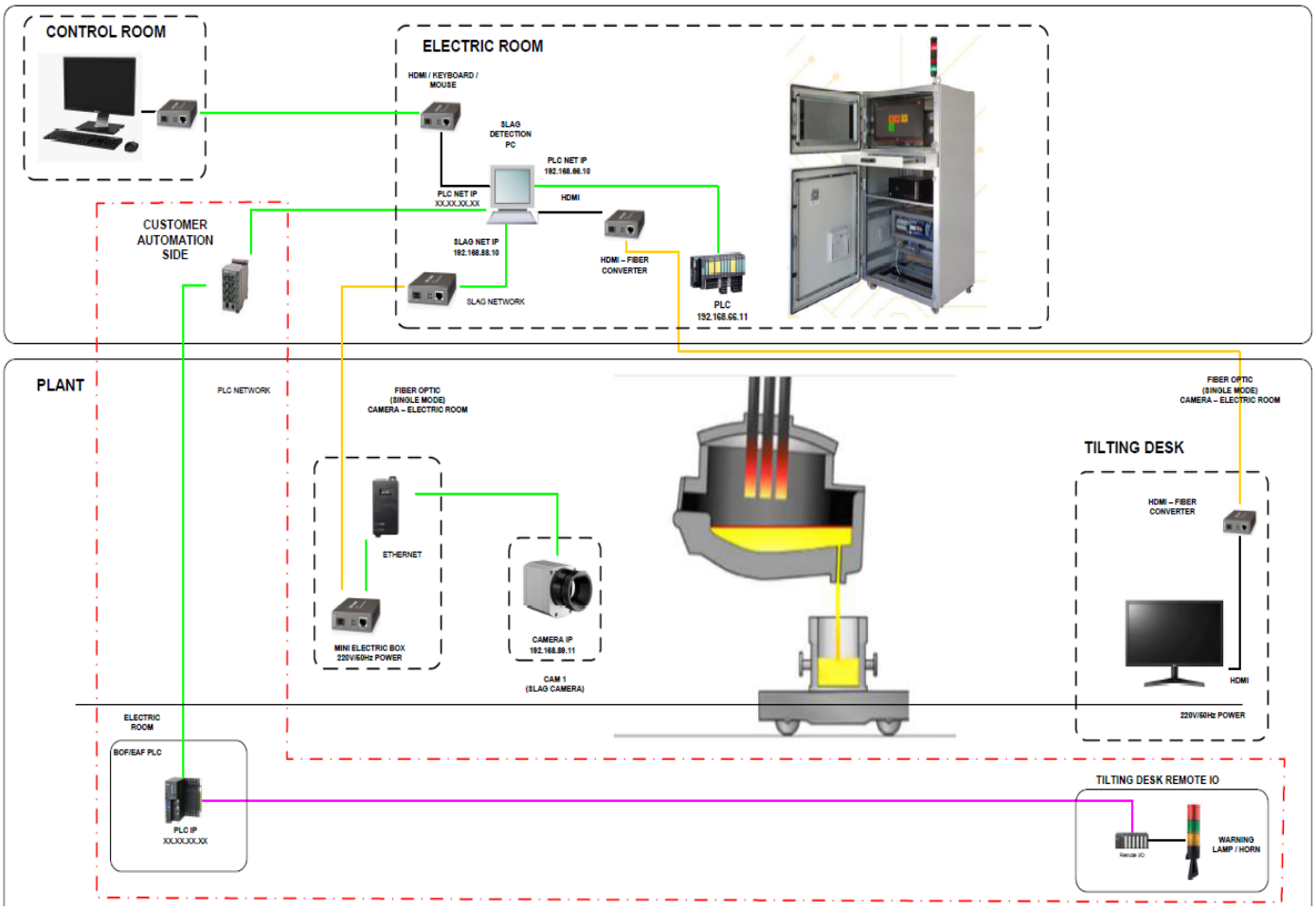
In his paper slag detection system has been mentioned. There is one Electric Arc Furnace in Tosçelik Profile ve Sac Industry Co. Fireplace generally, it charges 200 tons of scrap within its body. The hob also has six burners and an EBT hole is available. There are two main processes in the arc furnace: melting and smelting. Melting Smelting of the scrap is carried out at the stage. Scrap to be charged at this stage discharged into the furnace. The electrodes are immersed in the furnace, but not to the liquid metal. Care should be taken not to touch it. Otherwise, as soon as the electrodes touch the metal is broken. Lime or dolomite to form slag after energy withdrawal is added.

$$2P+5FeO+nCaO \leftrightarrow nCaO + P2O5 + 5Fe$$

Phosphorus in the form of slag is removed from the alloy by performing the reaction. To facilitate melting from the 'jet burners' on the walls of the furnace Combustion is provided by blowing natural gas and oxygen. In the smelting phase, after three charges, carbon and oxygen from the burners to the liquid metal phosphorus removal is done. With the help of oxygen, carbon and lime blown from the bottom slag is formed and raised to the surface of the liquid metal. This process is the last charge and melting. So, done after the process is completed. Smelting phosphorus removal It plays a very important role in steel production. Because phosphorus removal steel cannot be made at any other stage of production. After the smelting process, the slag removal process is started. Furnace angular one the slag formed on the surface by the movement is poured into the slag area from the slag door. slag gate If there is scrap in front of it, the door is opened using robot arms, if the slag caps are blocked, The lid mouth is opened using robot arms. After the slag removal process is completed, the furnace liquid steel discharge by tilting it in an angular movement (max $20^{o)}$, again in the opposite direction of its previous position. It is poured into the ladle from the pipe (EBT hole).At the same time, thermal

camera with imaging process software track to detect slag and clean steel stream. The amount of slag percent is higher than the limit, the alarm signal is output.

II.DETECTION PRECIPLE OF THE SYSTEM



When stream is taken from EAF to ladle the infrared thermal camera receives radiation emitted and detect slag and steel. The distance between Infrared thermal camera and stream is approximately 3 m.Slag and steel emissivity is calculated equation as:

$$\varepsilon = \left(\frac{Tr}{To}\right)^{n}$$

Tr is infrared radiation stream

To is the temperature of pouring stream.

Emissivity difference between slag ang steel is 8 – 12 µm far band. This difference is changeable according to environment condition and scrap ingredients

A. Figures and Tables



Fig. 1. Before tapping from EAF to ladle screen

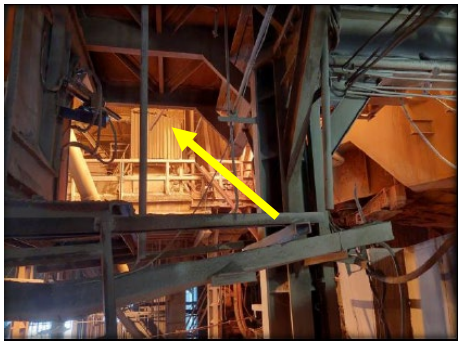


Fig. 2. Infrared Thermal Camera



Fig. 3. Tapping from EAF to ladle

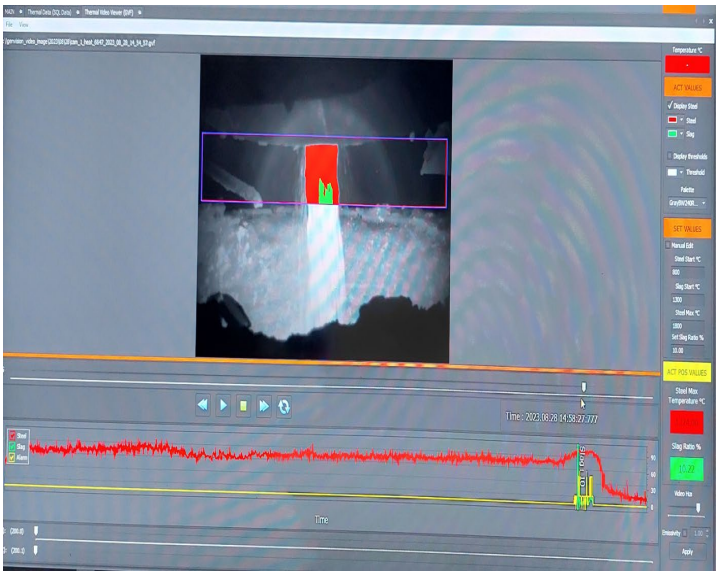


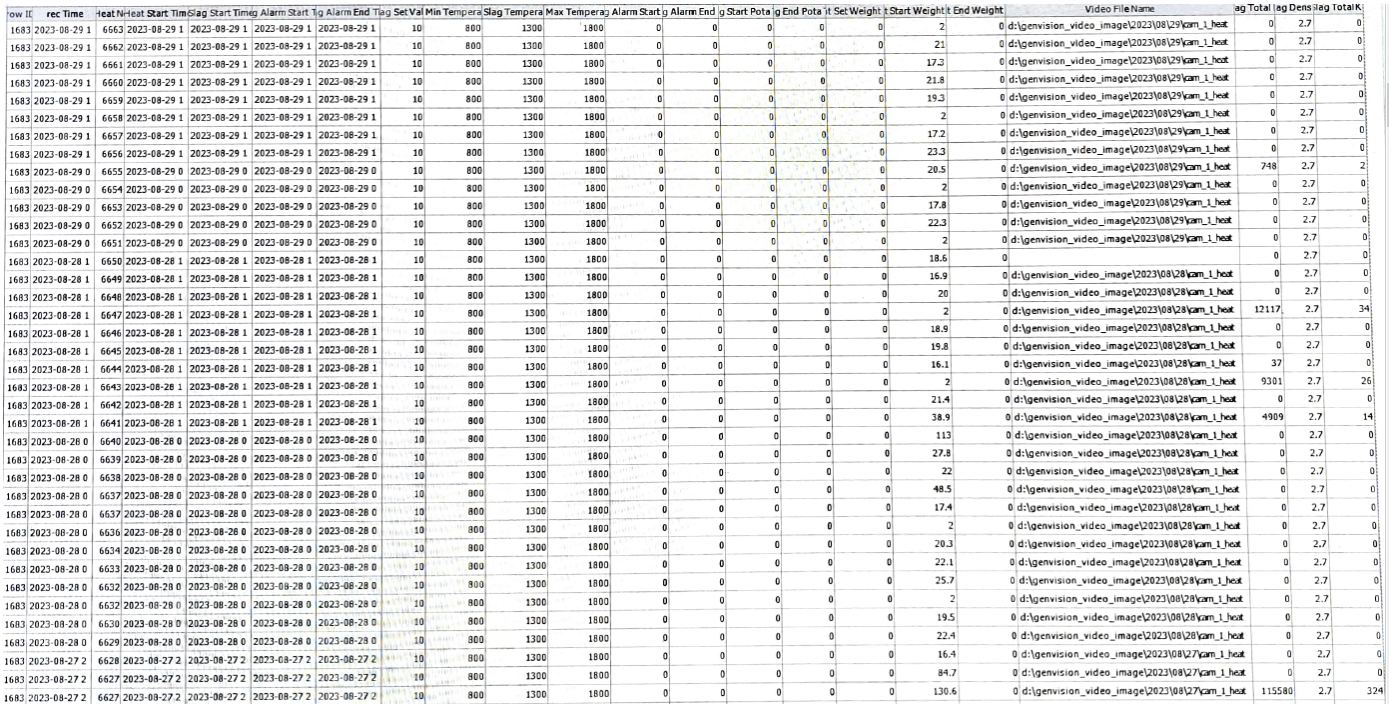
Fig. 4. Temperature difference slag and steel

The thermal camera track to pouring stream . The position of camera is stable. So the calculation of the interesting area (ROI) can not be higher than 18 percent of total area. ROI is express to rectangle of which top and bottom are set maually . Fig.4. is reperesented to ROI and is showed green and red color .Green color is slag and red color is steel.

The highest temperature of the steel and slag is calculated with some date.The first image was taken in the project on March 31, 2023. According to the number of EBT castings, 3 different recipes were prepared. The system has been working smoothly with the integrated recipe since May. According to the common quality material data of March and May, the slag removal rate from 15.46% was reduced to 12.32%. The reason for this situation is the process of getting used to the system and the situation of taking more steel into the ladle, and it is aimed that this rate will decrease further in the future. Based on this; The recovery table prepared according to the Ferroalloy material comparison given in March (before the system is commissioned) and May (after the system is put into operation) and calculated earnings material kilograms every good steel.

Table.1. Earning Ferroalyaj Materials

Earning Ferroalyaj Metarials	Kg /ts	$/kg	$/ts
FeSi	0,313	1,683	0,53
Lime	1,707	0,091	0,16
AF3	-0,02	0,535	-0,01
Alumium Wire	0,084	3,025	0,25
Granule Alumium	0,137	1,515	0,21
		Total ($/ts)	**1,13**



ow ID	rec Time	Heat N	Heat Start Tim	Slag Start Time	g Alarm Start	Tg Alarm End	Tlag Set Val	Min Tempera	Slag Tempera	Max Temperag	Alarm Start g	Alarm End g	Start Pota g	End Pota it	Set Weight t	Start Weight t	End Weight	Video File Name	ag Total	lag Dens	lag Total K
1683	2023-08-29 1	6663	2023-08-29 1	2023-08-29 1	2023-08-29 1	2023-08-29 1	10	800	1300	1800	0	0	0	0	0	2	0	d:\genvision_video_image\2023\08\29\cam_1_heat	0	2.7	0
1683	2023-08-29 1	6662	2023-08-29 1	2023-08-29 1	2023-08-29 1	2023-08-29 1	10	800	1300	1800	0	0	0	0	0	21	0	d:\genvision_video_image\2023\08\29\cam_1_heat	0	2.7	0
1683	2023-08-29 1	6661	2023-08-29 1	2023-08-29 1	2023-08-29 1	2023-08-29 1	10	800	1300	1800	0	0	0	0	0	17.3	0	d:\genvision_video_image\2023\08\29\cam_1_heat	0	2.7	0
1683	2023-08-29 1	6660	2023-08-29 1	2023-08-29 1	2023-08-29 1	2023-08-29 1	10	800	1300	1800	0	0	0	0	0	21.8	0	d:\genvision_video_image\2023\08\29\cam_1_heat	0	2.7	0
1683	2023-08-29 1	6659	2023-08-29 1	2023-08-29 1	2023-08-29 1	2023-08-29 1	10	800	1300	1800	0	0	0	0	0	19.3	0	d:\genvision_video_image\2023\08\29\cam_1_heat	0	2.7	0
1683	2023-08-29 1	6658	2023-08-29 1	2023-08-29 1	2023-08-29 1	2023-08-29 1	10	800	1300	1800	0	0	0	0	0	2	0	d:\genvision_video_image\2023\08\29\cam_1_heat	0	2.7	0
1683	2023-08-29 1	6657	2023-08-29 1	2023-08-29 1	2023-08-29 1	2023-08-29 1	10	800	1300	1800	0	0	0	0	0	17.2	0	d:\genvision_video_image\2023\08\29\cam_1_heat	0	2.7	0
1683	2023-08-29 1	6656	2023-08-29 1	2023-08-29 1	2023-08-29 1	2023-08-29 1	10	800	1300	1800	0	0	0	0	0	23.3	0	d:\genvision_video_image\2023\08\29\cam_1_heat	0	2.7	0
1683	2023-08-29 0	6655	2023-08-29 0	2023-08-29 0	2023-08-29 0	2023-08-29 0	10	800	1300	1800	0	0	0	0	0	20.5	0	d:\genvision_video_image\2023\08\29\cam_1_heat	748	2.7	2
1683	2023-08-29 0	6654	2023-08-29 0	2023-08-29 0	2023-08-29 0	2023-08-29 0	10	800	1300	1800	0	0	0	0	0	2	0	d:\genvision_video_image\2023\08\29\cam_1_heat	0	2.7	0
1683	2023-08-29 0	6653	2023-08-29 0	2023-08-29 0	2023-08-29 0	2023-08-29 0	10	800	1300	1800	0	0	0	0	0	17.8	0	d:\genvision_video_image\2023\08\29\cam_1_heat	0	2.7	0
1683	2023-08-29 0	6652	2023-08-29 0	2023-08-29 0	2023-08-29 0	2023-08-29 0	10	800	1300	1800	0	0	0	0	0	22.3	0	d:\genvision_video_image\2023\08\29\cam_1_heat	0	2.7	0
1683	2023-08-29 0	6651	2023-08-29 0	2023-08-29 0	2023-08-29 0	2023-08-29 0	10	800	1300	1800	0	0	0	0	0	2	0	d:\genvision_video_image\2023\08\29\cam_1_heat	0	2.7	0
1683	2023-08-28 1	6650	2023-08-28 1	2023-08-28 1	2023-08-28 1	2023-08-28 1	10	800	1300	1800	0	0	0	0	0	18.6	0		0	2.7	0
1683	2023-08-28 1	6649	2023-08-28 1	2023-08-28 1	2023-08-28 1	2023-08-28 1	10	800	1300	1800	0	0	0	0	0	16.9	0	d:\genvision_video_image\2023\08\28\cam_1_heat	0	2.7	0
1683	2023-08-28 1	6648	2023-08-28 1	2023-08-28 1	2023-08-28 1	2023-08-28 1	10	800	1300	1800	0	0	0	0	0	20	0	d:\genvision_video_image\2023\08\28\cam_1_heat	0	2.7	0
1683	2023-08-28 1	6647	2023-08-28 1	2023-08-28 1	2023-08-28 1	2023-08-28 1	10	800	1300	1800	0	0	0	0	0	2	0	d:\genvision_video_image\2023\08\28\cam_1_heat	12117	2.7	34
1683	2023-08-28 1	6646	2023-08-28 1	2023-08-28 1	2023-08-28 1	2023-08-28 1	10	800	1300	1800	0	0	0	0	0	18.9	0	d:\genvision_video_image\2023\08\28\cam_1_heat	0	2.7	0
1683	2023-08-28 1	6645	2023-08-28 1	2023-08-28 1	2023-08-28 1	2023-08-28 1	10	800	1300	1800	0	0	0	0	0	19.8	0	d:\genvision_video_image\2023\08\28\cam_1_heat	0	2.7	0
1683	2023-08-28 1	6644	2023-08-28 1	2023-08-28 1	2023-08-28 1	2023-08-28 1	10	800	1300	1800	0	0	0	0	0	16.1	0	d:\genvision_video_image\2023\08\28\cam_1_heat	37	2.7	0
1683	2023-08-28 1	6643	2023-08-28 1	2023-08-28 1	2023-08-28 1	2023-08-28 1	10	800	1300	1800	0	0	0	0	0	2	0	d:\genvision_video_image\2023\08\28\cam_1_heat	9301	2.7	26
1683	2023-08-28 1	6642	2023-08-28 1	2023-08-28 1	2023-08-28 1	2023-08-28 1	10	800	1300	1800	0	0	0	0	0	21.4	0	d:\genvision_video_image\2023\08\28\cam_1_heat	0	2.7	0
1683	2023-08-28 1	6641	2023-08-28 1	2023-08-28 1	2023-08-28 1	2023-08-28 1	10	800	1300	1800	0	0	0	0	0	38.9	0	d:\genvision_video_image\2023\08\28\cam_1_heat	4909	2.7	14
1683	2023-08-28 0	6640	2023-08-28 0	2023-08-28 0	2023-08-28 0	2023-08-28 0	10	800	1300	1800	0	0	0	0	0	113	0	d:\genvision_video_image\2023\08\28\cam_1_heat	0	2.7	0
1683	2023-08-28 0	6639	2023-08-28 0	2023-08-28 0	2023-08-28 0	2023-08-28 0	10	800	1300	1800	0	0	0	0	0	27.8	0	d:\genvision_video_image\2023\08\28\cam_1_heat	0	2.7	0
1683	2023-08-28 0	6638	2023-08-28 0	2023-08-28 0	2023-08-28 0	2023-08-28 0	10	800	1300	1800	0	0	0	0	0	22	0	d:\genvision_video_image\2023\08\28\cam_1_heat	0	2.7	0
1683	2023-08-28 0	6637	2023-08-28 0	2023-08-28 0	2023-08-28 0	2023-08-28 0	10	800	1300	1800	0	0	0	0	0	48.5	0	d:\genvision_video_image\2023\08\28\cam_1_heat	0	2.7	0
1683	2023-08-28 0	6637	2023-08-28 0	2023-08-28 0	2023-08-28 0	2023-08-28 0	10	800	1300	1800	0	0	0	0	0	17.4	0	d:\genvision_video_image\2023\08\28\cam_1_heat	0	2.7	0
1683	2023-08-28 0	6636	2023-08-28 0	2023-08-28 0	2023-08-28 0	2023-08-28 0	10	800	1300	1800	0	0	0	0	0	2	0	d:\genvision_video_image\2023\08\28\cam_1_heat	0	2.7	0
1683	2023-08-28 0	6634	2023-08-28 0	2023-08-28 0	2023-08-28 0	2023-08-28 0	10	800	1300	1800	0	0	0	0	0	20.3	0	d:\genvision_video_image\2023\08\28\cam_1_heat	0	2.7	0
1683	2023-08-28 0	6633	2023-08-28 0	2023-08-28 0	2023-08-28 0	2023-08-28 0	10	800	1300	1800	0	0	0	0	0	22.1	0	d:\genvision_video_image\2023\08\28\cam_1_heat	0	2.7	0
1683	2023-08-28 0	6632	2023-08-28 0	2023-08-28 0	2023-08-28 0	2023-08-28 0	10	800	1300	1800	0	0	0	0	0	25.7	0	d:\genvision_video_image\2023\08\28\cam_1_heat	0	2.7	0
1683	2023-08-28 0	6632	2023-08-28 0	2023-08-28 0	2023-08-28 0	2023-08-28 0	10	800	1300	1800	0	0	0	0	0	2	0	d:\genvision_video_image\2023\08\28\cam_1_heat	0	2.7	0
1683	2023-08-28 0	6630	2023-08-28 0	2023-08-28 0	2023-08-28 0	2023-08-28 0	10	800	1300	1800	0	0	0	0	0	19.5	0	d:\genvision_video_image\2023\08\28\cam_1_heat	0	2.7	0
1683	2023-08-28 0	6629	2023-08-28 0	2023-08-28 0	2023-08-28 0	2023-08-28 0	10	800	1300	1800	0	0	0	0	0	22.4	0	d:\genvision_video_image\2023\08\28\cam_1_heat	0	2.7	0
1683	2023-08-27 2	6628	2023-08-27 2	2023-08-27 2	2023-08-27 2	2023-08-27 2	10	800	1300	1800	0	0	0	0	0	16.4	0	d:\genvision_video_image\2023\08\27\cam_1_heat	0	2.7	0
1683	2023-08-27 2	6627	2023-08-27 2	2023-08-27 2	2023-08-27 2	2023-08-27 2	10	800	1300	1800	0	0	0	0	0	84.7	0	d:\genvision_video_image\2023\08\27\cam_1_heat	0	2.7	0
1683	2023-08-27 2	6627	2023-08-27 2	2023-08-27 2	2023-08-27 2	2023-08-27 2	10	800	1300	1800	0	0	0	0	0	130.6	0	d:\genvision_video_image\2023\08\27\cam_1_heat	115580	2.7	324

Fig.5. Thermal Data in Sofware

III.CONCLUSION

In this paper a slag detection system based on ınfrared thermal camera and image processing software. A set method for distinguish between slag and steel is important. To calculate the certain value has worked with 2 month data.After EAO Slag Detection System Development and Software is put into use , a profit of $1.13 is provided for each ton of steel production. In addition operator can see steel level as looking monitored and eliminated sequrity risk by preventing crucible overflows. It is aimed to use 1 ladle less per month that ıt is wear less and improve ladle performance.The studies prove that this system is so effective to control amount of slag in pouring stream. With thermal camera Image processing is useful application and software programme.

ACKNOWLEDGMENT

This studies was supported by Tosçelik Profile and Sheet Industry Co. and Research and Development Center**.** Thank you to Meltshop Manager Halil Öztürk, Meltshop Liquid Steel Chef Levent Ünsal, Meltshop Electrical Automation Chef Dogan Kaya, Meltshop Senior Business Engineer Ahmet Sönmez.Also, Thank you to Research and Development Manager İbrahim Dere, Research and Development Chef Anıl Agadangil .

REFERENCES

[1] E. Julius, W. Theissen, F.R. Block, Function and application of electromagneticlag detection system, World Steel Metal Working 8 (1) (1987) 56–61

[2] YU Hao, KANG Yong-lin, ZHAO Zheng-zhi, et al. Morphology and Precipitation Kinetics of MnS in Low-Carbon Steel During Thin Slab Continuous Casting Process [J]. Journal of Iron and Steel Research, International, 2006, 13(5): 30.

[3] Julius, W. Theissen, F.R. Block, Function and application of electromagneticlag detection system, World Steel Metal Working 8 (1) (1987) 56–61.

[4] QIU Dong-ming. A Study of Slag Detection System for Continuous Casting With 300 t Ladles [J]. Chinese Journal of Scientific Instrument, 1999, 19(1): 135 (in Chinese)

[5] M. Viale, O. Martin, F. Muratori, et al., Application of online infrared thermo-graphy in steel making industry, in: Proc. SPIE, 2007, p. 6541.

[6] D.V. Goldstein, A. Sharan, J.A. Stofannak, Infrared imaging for BOF slag detection, Iron Steelmaker 27 (7) (2000) 31–38.[4] G.R. Peacock, Thermal imaging of liquid steel and slag in a pouring stream, Proc.SPIE 4020 (2000) 50–60.

[7] Julius E. Electromagnetic Slag Detection in Metallurgical Vessels [J]. Stahl und Eisen, 1987, 107(9): 397 (in German).

[8] L.I. Jiang, J.-G. Zhou, Z. Zhong, et al., Application of infrared imaging technologyin 300t converter of Baosteel, Res. Iron Steel 5

[9] R. Usamentiaga, L. Perez, J. Molleda, D. Garcia, S. Huerta, Temperature measure-ment of streams of molten pig iron during pouring using infrared computervision, in: Proc. I2MTC, 2011, pp. 89–94

Realistic Robot Arm Energy Optimization with Using Torsional Springs

Furkan Cihangir[*,1], Ahmet Koyun[1]

[*]cihangir.fuurkan@gmail.com, ORCID: 0009-0007-6884-7012
[1]*Yıldız Technical University, Mechatronics Engineering Faculty, İstanbul, Turkey*

Abstract: Robot arms are highly used in today's world. Their precision, reliability and cost effectiveness make robot arms very useful. They are also safer and cheaper than human labor. However, researchers and engineers still spend a lot of times and effort to make these robot arms more energy optimized. Many solutions have been proposed and one of them is to use torsional springs, which note that they are passive elements. These torsional springs have two important parameters to be selected to optimize the system which they are spring constant and neutral angle. If correct values of spring constant and neutral angle is selected, energy spending can be reduced dramatically. However, when we make a literature search, we see that this energy optimization is made by using a simple equation of motion only. In reality, we use such controllers like PD, PID to ensure a stable reference tracking. And we know that selecting these P, I, D constants will change the actuator torques dramatically. Since in a real system, torques that actuators apply are these controller output torques, optimization should also be carried out using these controller output torques. In that way the optimization would be much more realistic and useful. In this study, we picked a 3 DOF robot arm, solved its direct and inverse kinematics, selected a trajectory, and designed an PD controller to ensure its stability. After that using two torsional springs, we made the system energy optimized. Optimization is carried out using controller output actuator torques to make the optimization more realistic and useful. Simulation results showed us that if we select correct springs, energy consumption can be dramatically reduced.

Keywords: *Robot Arm, Controller, Optimization, Energy*

I. INTRODUCTION

Since the industry met with robot technology, it is highly preferred due to its quality, high precision, reliability, and operation cost effectiveness. Even though robots, especially robot arms already dominated the industry, today control and optimization studies are still crucial. Researchers and engineers are still work on more precise, more cost-effective, less energy required robot arms.

One of the energy optimization techniques of a robot arm was to generate cost effective path trajectories, so to say, which path end-effector of the robot arm should follow so that robot arm can perform the task while the energy consumption is at minimum [1]. Other optimization technique is making robot arm optimum for a pre-planned, unchangeable trajectory. This can be achieved by selecting robot arm link dimensions [2] and/or using passive elements such as springs, pressurized air pistons or hybrid spring piston system [3].

Here in this study torsional springs are used to make robot arm energy optimum. Also, a control algorithm is designed so that precision is better. Such studies in this area are lack of a control algorithm. They don't have a controller therefore stability is poor under such uncertainties like friction, unexpected initial positions, and other disturbances. Previous studies in literature took the motor torques directly using equation of motion but torques

required with a controller differs much from torques required with just using equation of motion. Here, required input torque values -which is also going to be used for searching optimum point- for end effector to follow desired trajectory are directly taken from PD control algorithm so that while results are more realistic also the precision of the robot arm is ensured.

On upcoming sections, Literature will be summarized, Then the methodology will be introduced, and the method used for a specific application will be explained elaborately. Lastly the results going to be discussed and future works going to be explained.

II. LITERATURE SEARCH

Robot arm energy optimization is studied by many engineers and researchers. For a robot arm that has pre-planned given trajectory, the optimization is frequently made by springs. Both linear springs and torsional springs are used. Also, we can see such unique designs that made for same purpose.

When torsional springs are to be used for optimization, there are two parameters that is mostly considered which they are spring constant and neutral angle. Neutral angle is the angle of the joint where the torsional spring is completely unstretched. Selecting best duo to have minimum energy spending or minimum torque requirement is the aim.

We see in the literature that; optimization is made with using torques that comes out of equation of motion. However, in reality PD, PID controllers should be used to have stability, and changing these P, I, D constants will give much different torques. Such energy optimizations that use controller output actuator torques are lack in the literature.

III. METHODOLOGY

A. Robot Arm Geometry

To describe the translational and rotational relationships between adjacent links, Denavit and Hartenberg proposed a matrix method of systematically establishing a coordinate system (body-attached frame) to each link of an articulated chain. The D-H representation results in a 4 x 4 homogeneous transformation matrix representing each link's coordinate system at the joint with respect to the previous link's coordinate system. Thus, through sequential transformations, the end-effector expressed in the "hand coordinates" can be transformed and expressed in the "base coordinates," which make up the inertial frame of this dynamic system [4].

Methodology used to obtain kinematic diagram in Fig. 1 is explained elaborately by [4] Note that, to draw such kinematic diagram, key point is to set frames. Setting these frames are not unique. However, in order to obtain correct homogenous transformation matrices, these frames should be set according to rules that is explained in [4]

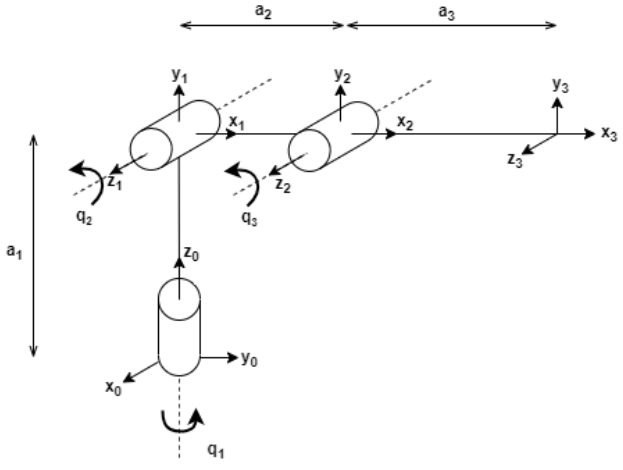


Fig. 1. Kinematic Diagram of Robot Arm

B. Robot Arm Direct Kinematics

Direct kinematics gives the end-effector position and orientation as output, while its input are joint angles.

To be able to obtain position and orientation of base of the robot arm and end-effector of robot arm relative to each other, relative position and orientation of adjacent joints should be governed first. The way of doing that is using transformation matrices.

Transformation matrices are matrices that has information of relative orientation and position between two frames. Transformation matrices between each adjacent joints are governed first. To govern these matrices denavit-hartenberg method is used.

$$H_{n-1}^{n} = \begin{bmatrix} cos(q_n) & -sin(q_n)cos(\alpha_n) & sin(q_n)sin(\alpha_n) & a_n cos(q_n) \\ sin(q_n) & cos(q_n)cos(\alpha_n) & -cos(q_n)sin(\alpha_n) & a_n sin(q_n) \\ 0 & sin(\alpha_n) & cos(\alpha_n) & d_n \\ 0 & 0 & 0 & 1 \end{bmatrix} \quad (1)$$

Equation (1) should be used to obtain transformation matrices between two adjacent links. Here n-1 is preceding frame and n is subsequent frame. However, $q_n, \alpha_n, a_n d_n$ values are needed. This values are taken from (1) which is structed by using rules in [4].

TABLE I
D-H TABLE

n	q	α	a	d
1	$q_1 + \pi/2$	$\pi/2$	0	a_1
2	q_2	0	a_2	0
3	q_3	0	a_3	0

Using D-H table and matrix formula above, adjacent frames transformation matrices are found as follows;

$$H_0^1 = \begin{bmatrix} -sin(q_1) & 0 & cos(q_1) & 0 \\ cos(q_1) & 0 & sin(q_1) & 0 \\ 0 & 1 & 0 & a_1 \\ 0 & 0 & 0 & 1 \end{bmatrix} \quad (2)$$

$$H_1^2 = \begin{bmatrix} cos(q_2) & -sin(q_2) & 0 & a_2 cos(q_2) \\ sin(q_2) & cos(q_2) & 0 & a_2 sin(q_2) \\ 0 & 0 & 1 & 0 \\ 0 & 0 & 0 & 1 \end{bmatrix} \quad (3)$$

$$H_2^3 = \begin{bmatrix} cos(q_3) & -sin(q_3) & 0 & a_3 cos(q_3) \\ sin(q_3) & cos(q_3) & 0 & a_3 sin(q_3) \\ 0 & 0 & 1 & 0 \\ 0 & 0 & 0 & 1 \end{bmatrix} \quad (4)$$

Now multiplying adjacent joint frames transformation matrices, the transformation matrix between base and end-effector is obtained as follows.

$$H_0^3 = H_0^1 H_1^2 H_2^3 \quad (5)$$

$$H_0^3 = \begin{bmatrix} -C_{23}S_1 & S_{23}S_1 & C_1 & -S_1(a_3C_{23} + a_2C_2) \\ C_{23}C_1 & -S_{23}C_1 & S_1 & C_1(a_3C_{23} + a_2C_2) \\ S_{23} & C_{23} & 0 & a_1 + a_3S_{23} + a_2S_2 \\ 0 & 0 & 0 & 1 \end{bmatrix} \quad (6)$$

In a 4x4 transformation matrix upper-left 3x3 matrix gives the relative orientation, 3x1 matrix on upper right side gives the relative P_x, P_y, P_z positions. This is illustrated at Fig. 2

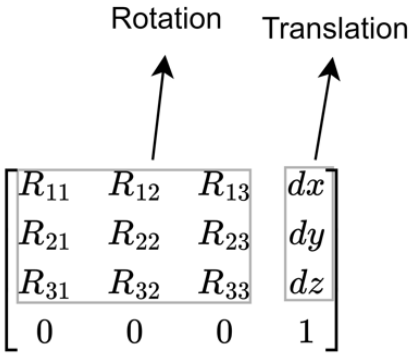


Fig. 2. Transformation matrix orientation and translation

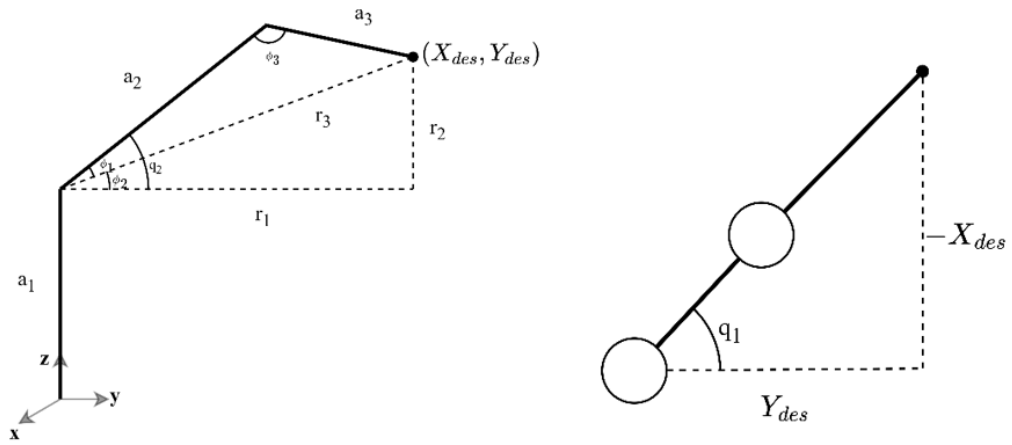
Now using H_0^3 transformation matrix, we can say that.

$$\begin{aligned} x_{des} &= -S_1(a_3C_{23} + a_2C_2) \\ y_{des} &= C_1(a_3C_{23} + a_2C_2) \\ z_{des} &= a_1 + a_3S_{23} + a_2S_2 \end{aligned} \quad (7)$$

Where x_{des}, y_{des}, z_{des} are desired end-effector coordinate space positions relative to base frame.

C. Robot Arm Inverse Kinematics

Inverse kinematics gives the joint angles as output, while its input are desired end-effector position and orientation. Here using the geometry, inverse kinematics are obtained as follows.



(a) (b)

Fig. 3. (a) Robot Arm Side View (b) Robot Arm Top View

Using side and top views given in Fig. 3 and Fig. 4, inverse kinematics are obtain as follows. Notice equations below should be carried out respectively so that desired joint angles can be obtained for a given desired coordinate space positions.

$$\tan q_1 = \frac{-x_{des}}{y_{des}} \tag{8}$$

$$q_1 = atan2(-x_{des}, x_{des}) \tag{9}$$

$$r_2 = x_{des} - a_1 \tag{10}$$

$$r_1 = \sqrt{{x_{des}}^2 + {y_{des}}^2} \tag{11}$$

$$r_3 = \sqrt{{r_1}^2 + {r_2}^2} \tag{12}$$

$$\emptyset_2 = atan2(r_2, r_1) \tag{13}$$

$${a_3}^2 = {a_2}^2 + {r_3}^2 - 2a_2 r_3 cos(\emptyset_1) \tag{14}$$

$$\emptyset_1 = cos^{-1}[({a_3}^2 - {a_2}^2 - {r_3}^2)/(-2a_2 r_3)] \tag{15}$$

$$q_2 = \emptyset_1 + \emptyset_2 \tag{16}$$

$${r_3}^2 = {a_2}^2 + {a_3}^2 - 2a_2 a_3 cos(\emptyset_3) \tag{17}$$

$$\emptyset_3 = cos^{-1}[({r_3}^2 - {a_2}^2 - {a_3}^2)/(-2a_2 a_3)] \tag{18}$$

$$q_3 = \emptyset_3 - \pi \tag{19}$$

D. Pre-planned Trajectory for a Defined Task

Here in this study, the robot arm that is aimed to be energy optimum is a sample pick-and-place robot arm. Therefore, the pre-planned trajectory is selected such that, robot arm picks the sample and then places it to the target position.

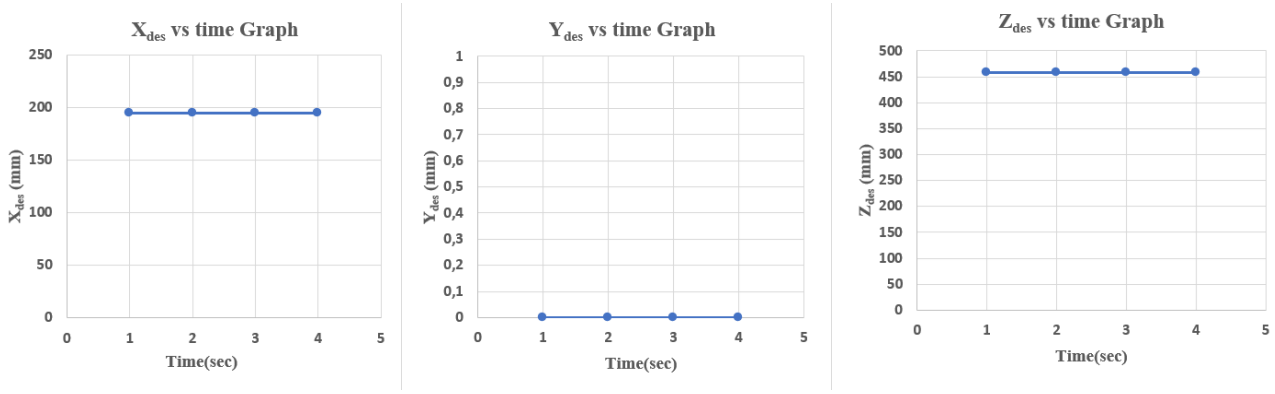
To be able to design a PD controller algorithm, joint-space trajectory equation is needed. Here in this section, it is explained how that trajectory equation is formulated. First, according to the task -which is picking and placing the sample- adjacent cartesian space points should be selected. Then using the inverse kinematics successive joint-space points are governed. Then using a polynomial fit with MATLAB, the joint-space trajectory equations are obtained.

The task is separated to four phase to have better fitted polynomials. Four phase makes a full cycle, so that at the end of the 4th phase, the end-effector arrives to the initial position for next cycle.

1. Picking phase.
2. Moving to the placing position.
3. Placing Phase
4. Moving to the picking position (initial position)

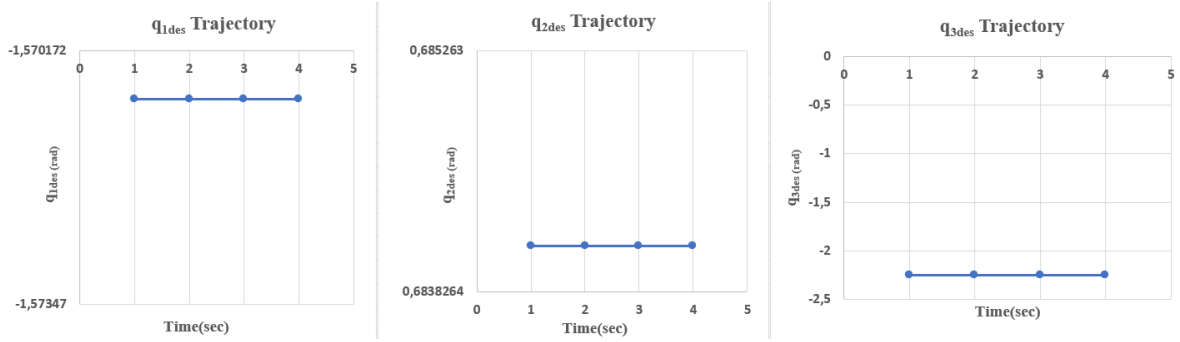
TABLE II
1ST OPERATION

Time[sec]	X_{des}	Y_{des}	Z_{des}	q_1	q_2	q_3
0	195	0	458	-1,5708	0,6841	-2,2486
1	195	0	458	-1,5708	0,6841	-2,2486
2	195	0	458	-1,5708	0,6841	-2,2486
3	195	0	458	-1,5708	0,6841	-2,2486



(a) (b) (c)

Fig. 4. 1st Operation (a) x Position (b) y Position (c) z position Time Graphs

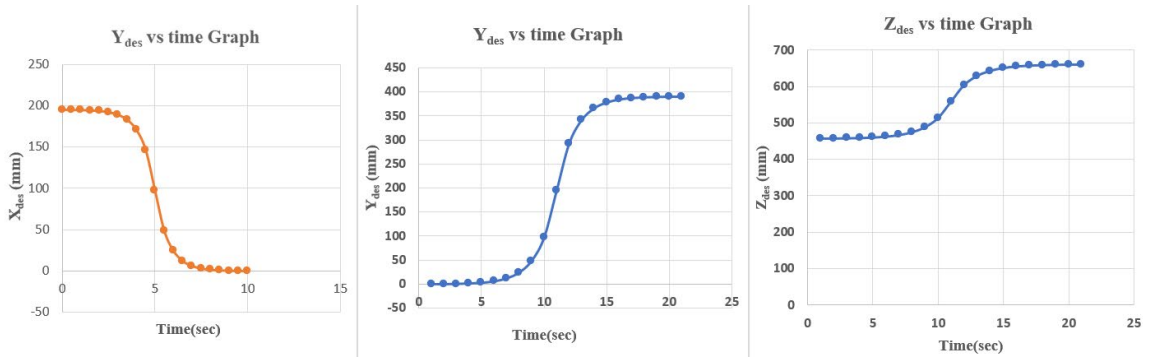


(a) (b) (c)

Fig. 5. 1st Operation Joint Space (a) q_1 (b) q_2 (c) q_3 Position-Time Graphs

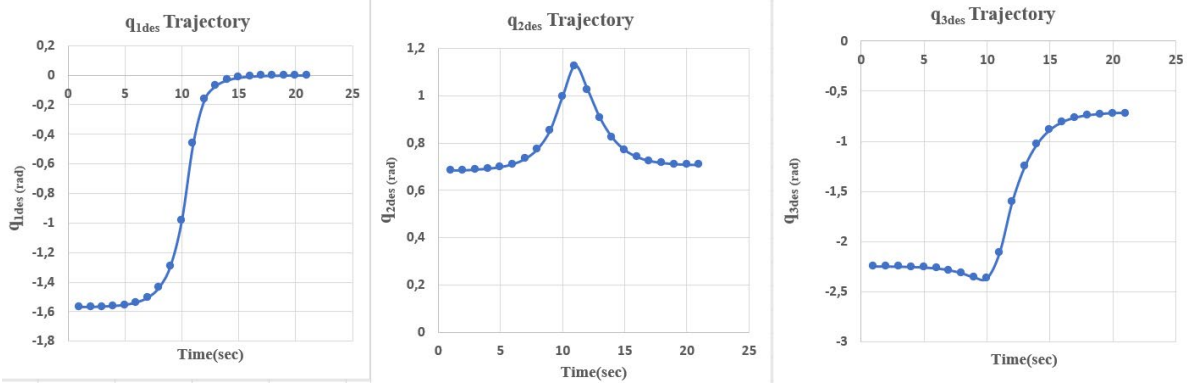
TABLE III
2ND OPERATION

Time[sec]	X_{des}	Y_{des}	Z_{des}	q_1	q_2	q_3
0	195	0	458	-1,5708	0,6841	-2,2486
0.5	195	0	458	-1,5708	0,6841	-2,2486
1	194,7141	0,571848	458,635	-1,5679	0,687	-2,2507
1.5	194,3288	1,334311	459,3707	-1,5639	0,6912	-2,253
2	193,5704	2,859238	460,6942	-1,556	0,6981	-2,2585
2.5	192,0455	5,909091	463,0765	-1,54	0,7105	-2,2682
3	188,9956	12,0088	467,3646	-1,5073	0,7333	-2,2859
3.5	182,8959	24,20821	475,0832	-1,4392	0,7754	-2,3164
4	170,6965	48,60704	488,9767	-1,2934	0,8543	-2,3586
4.5	146,2977	97,40469	513,985	-0,9834	0,9968	-2,3662
5	97,5	195	559	-0,4636	1,1262	-2,1117
5.5	48,70235	292,595	604,015	-0,1649	1,0264	-1,6078
6	24,30352	341,393	629,0233	-0,0711	0,9066	-1,2526
6.5	12,10411	365,7918	642,9168	-0,0331	0,8225	-1,0254
7	6,004399	377,9912	650,6354	-0,0159	0,7703	-0,8879
7.5	2,954545	384,0909	654,9235	-0,0077	0,7403	-0,8088
8	1,429619	387,1408	657,3058	-0,0037	0,7239	-0,7652
8.5	0,667155	388,6657	658,6293	-0,0017	0,7152	-0,7418
9	0,285924	389,4282	659,3646	-0,0007	0,7108	-0,7295
9.5	0	390	660	0	0,7074	-0,7197
10	0	390	660	0	0,7074	-0,7197



(a) (b) (c)

Fig. 6. 2nd Operation (a) x Position (b) y Position (c) z position Time Graphs



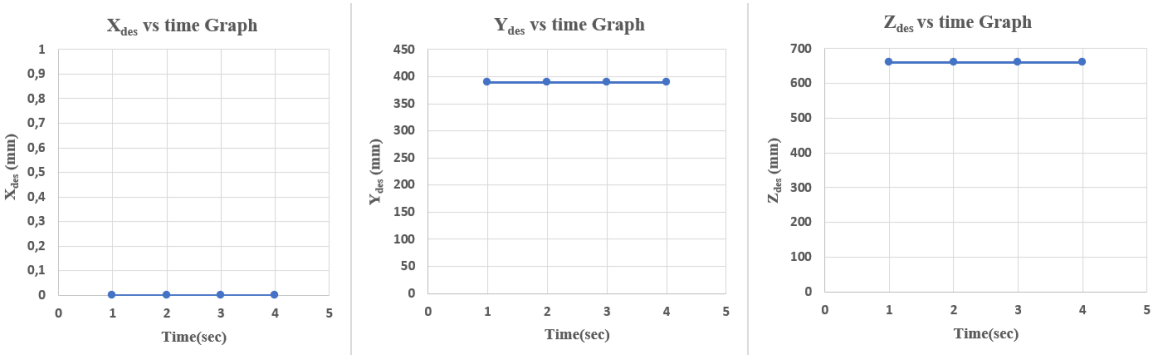
(a) (b) (c)

Fig. 7. 2nd Operation Joint Space (a) q_1 (b) q_2 (c) q_3 Position-Time Graphs

TABLE IV

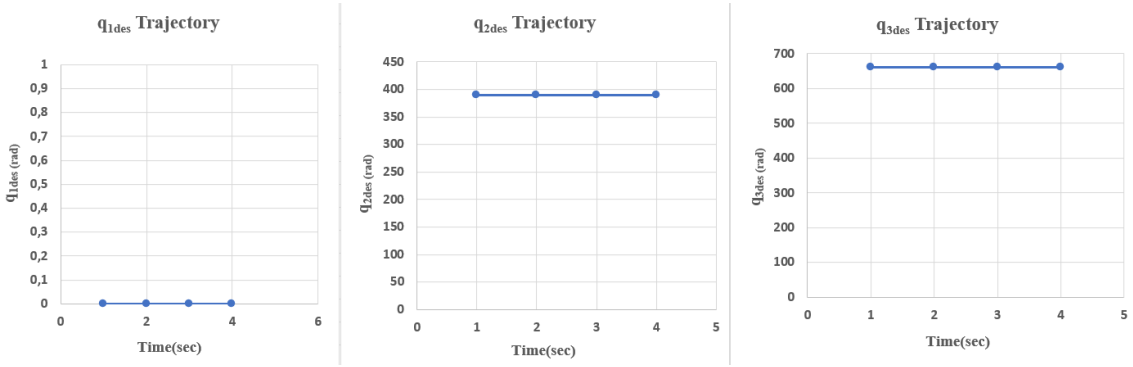
3TH OPERATION

Time[sec]	X_{des}	Y_{des}	Z_{des}	q_1	q_2	q_3
0	0	390	660	0	0,7074	-0,7197
1	0	390	660	0	0,7074	-0,7197
2	0	390	660	0	0,7074	-0,7197
3	0	390	660	0	0,7074	-0,7197



(a) (b) (c)

Fig. 8. 3th Operation (a) x Position (b) y Position (c) z position Time Graphs

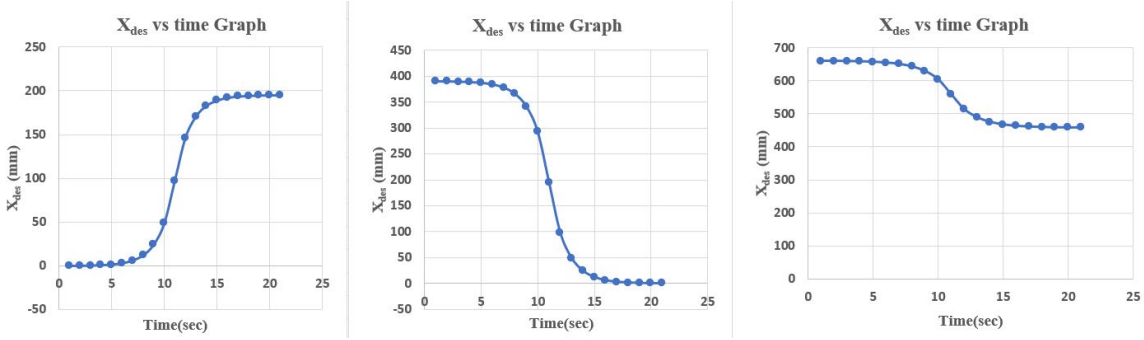


(a) (b) (c)

Fig. 9. 3th Operation Joint Space (a) q_1 (b) q_2 (c) q_3 Position-Time Graphs

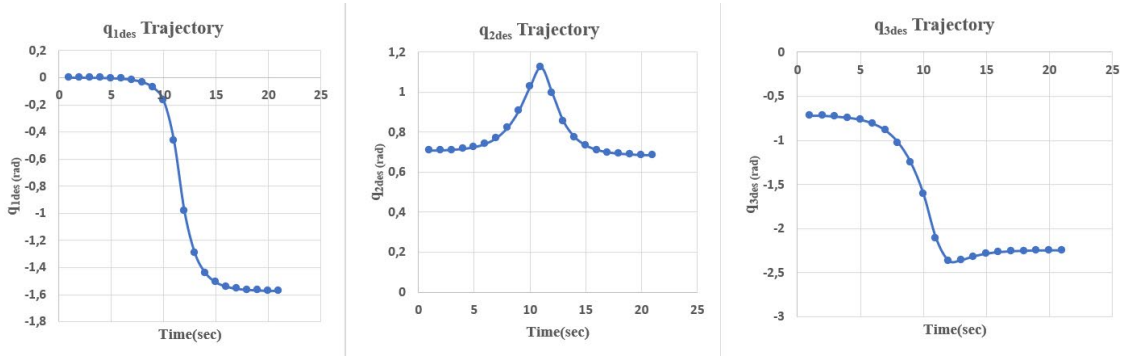
TABLE VI
4TH OPERATION

Time[sec]	X_{des}	Y_{des}	Z_{des}	q_1	q_2	q_3
0	0	390	660	0	0,7074	-0,7197
0.5	0	390	660	0	0,7074	-0,7197
1	0,285924	389,4282	659,3646	-0,0007	0,7108	-0,7295
1.5	0,667155	388,6657	658,6293	-0,0017	0,7152	-0,7418
2	1,429619	387,1408	657,3058	-0,0037	0,7239	-0,7652
2.5	2,954545	384,0909	654,9235	-0,0077	0,7403	-0,8088
3	6,004399	377,9912	650,6354	-0,0159	0,7703	-0,8879
3.5	12,10411	365,7918	642,9168	-0,0331	0,8225	-1,0254
4	24,30352	341,393	629,0233	-0,0711	0,9066	-1,2526
4.5	48,70235	292,5953	604,015	-0,1649	1,0264	-1,6078
5	97,5	195	559	-0,4636	1,1262	-2,1117
5.5	146,2977	97,40469	513,985	-0,9834	0,9968	-2,3662
6	170,6965	48,60704	488,9767	-1,2934	0,8543	-2,3586
6.5	182,8959	24,20821	475,0832	-1,4392	0,7754	-2,3164
7	188,9956	12,0088	467,3646	-1,5073	0,7333	-2,2859
7.5	192,0455	5,909091	463,0765	-1,54	0,7105	-2,2682
8	193,5704	2,859238	460,6942	-1,556	0,6981	-2,2585
8.5	194,3328	1,334311	459,3707	-1,5639	0,6912	-2,2534
9	194,7141	0,571848	458,6354	-1,5679	0,6874	-2,2507
9.5	195	0	458	-1,5708	0,6841	-2,2486
10	195	0	458	-1,5708	0,6841	-2,2486



(a) (b) (c)

Fig. 10. 4th Operation (a) x Position (b) y Position (c) z position Time Graphs



(a) (b) (c)

Fig. 11. 4th Operation Joint Space (a) q_1 (b) q_2 (c) q_3 Position-Time Graphs

E. Control Algorithm

E.A Lagrangian Method for Obtaining Equation of Motion

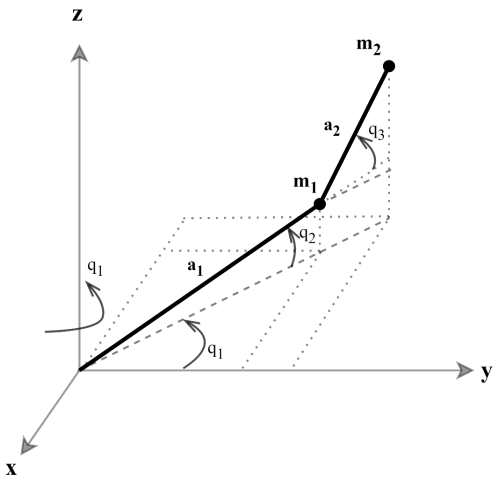


Fig. 12. Kinematic Diagram of the Robot Arm

Kinematic diagram of the robot arm is given in the Fig. 12 Using this figure following equations are obtained.

Lagrangian method is easier to use when it comes to derive equation of motion of such robot arm systems. Therefore, equation of motion of the pick-and-place robot arm is derived with this method and it is explained as follows;

$$\begin{aligned} x_1 &= -a_1(C_2S_1) \\ y_1 &= a_1(C_2C_1) \\ z_1 &= a_1(S_2) \end{aligned} \tag{20}$$

Where x_1, y_1, z_1 are coordinate space positions of point mass 1.

$$\begin{aligned} x_2 &= -a_1(C_2S_1) - a_2(C_{23}S_1) \\ y_2 &= a_1(C_2C_1) + a_2(C_{23}C_1) \\ z_2 &= a_1(S_2) + a_2S_{23} \end{aligned} \tag{21}$$

4

Where x_2, y_2, z_2 are coordinate space positions of point mass 2.

Velocities of the point masses can easily be derived with taking derivatives of its position.

$$\begin{aligned} V_{x1} &= -a_1(-\dot{q}_2S_2S_1 + \dot{q}_1C_2C_1) \\ V_{y1} &= a_1(-\dot{q}_2S_2C_1 - \dot{q}_1S_1C_2) \end{aligned} \tag{22}$$

$$V_{z1} = a_1(\dot{q}_2 C_2)$$

Where V_{x1}, V_{y1}, V_{z1} are x, y, z components of velocity of point mass 1.

$$\begin{aligned} V_{x2} &= -a_1(-\dot{q}_2 S_2 S_1 + \dot{q}_1 C_2 C_1) - a_2(-(\dot{q}_2 + \dot{q}_3) S_{23} S_1 + \dot{q}_1 C_{23} C_1) \\ V_{y2} &= a_1(-\dot{q}_2 S_2 C_1 - \dot{q}_1 S_1 C_2) + a_2(-(\dot{q}_2 + \dot{q}_3) S_{23} C_1 - \dot{q}_1 C_{23} S_1) \\ V_{z2} &= a_1(\dot{q}_2 C_2) + a_2(\dot{q}_2 + \dot{q}_3) C_{23} \end{aligned} \quad (23)$$

Where V_{x2}, V_{y2}, V_{z2} are x, y, z components of velocity of point mass 2.

Since the velocities of point masses have been derived kinetic energies can be derived.

$$V_{x2} = -a_1(-\dot{q}_2 S_2 S_1 + \dot{q}_1 C_2 C_1) - a_2(-(\dot{q}_2 + \dot{q}_3) S_{23} S_1 + \dot{q}_1 C_{23} C_1) \quad (24)$$

$$V_{y2} = a_1(-\dot{q}_2 S_2 C_1 - \dot{q}_1 S_1 C_2) + a_2(-(\dot{q}_2 + \dot{q}_3) S_{23} C_1 - \dot{q}_1 C_{23} S_1) \quad (25)$$

Where K_1 *and* K_2 are kinetic energies of mass 1 and mass 2.

Potential energies can be written as follows.

$$P_1 = m_1 g z_1 \quad (26)$$

$$P_2 = m_2 g z_2 \quad (27)$$

Where P_1 *and* P_2 are potential energies of mass 1 and mass 2.

Now that kinetic and potential energies of masses are derived, total kinetic and potential energy of the system can be written as follows.

$$K = K_1 + K_2 \quad (28)$$

$$P = P_1 + P_2 \quad (29)$$

Where K is total kinetic energy of the robot arm and P is total potential energy of robot arm.

To be able to apply Lagrangian equation of motion method, the Lagranian should be obtained first.

$$L = K - P \quad (30)$$

Where L is called lagrangian.

Since the Lagrangian is obtained, equation of motion can be found using following equation which is called Lagrange Equation.

$$\left(\frac{d}{dt}\right)\left(\frac{\partial L}{\partial \dot{\boldsymbol{q}}}\right) - \frac{\partial L}{\partial \boldsymbol{q}} = \boldsymbol{\tau} \quad (31)$$

Notice here, that bold terms are vectors, which they are as follows.

$$\boldsymbol{q} = \begin{bmatrix} q_1 \\ q_2 \\ q_3 \end{bmatrix} \quad (32)$$

$$\boldsymbol{\tau} = \begin{bmatrix} \tau_1 \\ \tau_2 \\ \tau_3 \end{bmatrix} \quad (33)$$

Where q_1, q_2, q_3 are joint angles τ_1, τ_2, τ_3 are joint torques, which later whey will be actuator inputs.

The robot arm equation of motion can be also written in such a compact, conventional form as follows.

$$\boldsymbol{M(q)\ddot{q} + V(q,\dot{q}) + F_r\dot{q} + G(q) = \tau} \tag{34}$$

Here, $\boldsymbol{G(q)}$ has gravitational terms, $\boldsymbol{F_r}$ has frictional terms, $\boldsymbol{V(q,\dot{q})}$ has velocity terms and $\boldsymbol{M(q)}$ has link and mass parameters. This form is going to be used for control algorithms. Elements of these matrices are found using (31)

E.B PID Controller Design

From robot arm equation motion state-space matrix can be defined as.

$$\boldsymbol{\ddot{q} = M^{-1}(\tau - V - G)} \tag{35}$$

And.

$$\boldsymbol{q_d} = \begin{bmatrix} q_{1d} \\ q_{2d} \\ q_{3d} \end{bmatrix} \tag{36}$$

Where $\boldsymbol{q_d}$ is desired joint angle vector and q_{1d}, q_{2d}, q_{3d} are desired joint angles.

Let an error vector be defined as.

$$\mathbf{e} = \boldsymbol{q - q_d} \tag{37}$$

Taking derivatives of both sides of (37) gives.

$$\boldsymbol{\ddot{e} = \ddot{q} - \ddot{q}_d} \tag{38}$$

Now using both equation (35) and (38) gives.

$$\boldsymbol{\ddot{e} = M^{-1}(\tau - V - G) - \ddot{q}_d} \tag{39}$$

Now let $\boldsymbol{\ddot{e}}$ be equated as follows.

$$\boldsymbol{\ddot{e} = -K_p e - K_d \dot{e} - K_i \int e} \tag{40}$$

Where, K_p, K_i, K_d are PID constants. This equation can be written as (41)

$$\begin{bmatrix} \boldsymbol{e} \\ \boldsymbol{\dot{e}} \\ \boldsymbol{\ddot{e}} \end{bmatrix} = \begin{bmatrix} 0 & 1 & 0 \\ 0 & 0 & 1 \\ -K_i & -K_p & -K_d \end{bmatrix} \begin{bmatrix} \int \boldsymbol{e} \\ \boldsymbol{e} \\ \boldsymbol{\dot{e}} \end{bmatrix} \tag{41}$$

Now, stability of the robot arm is assured if eigenvalues of (41) all are negative. Selecting such PID constants that ensures all eigenvalues are to be negative is a must.

Now, combining (39) and (40) gives (43)

$$\boldsymbol{M^{-1}(\tau - V - G) - \ddot{q}_d = -K_p e - K_d \dot{e} - K_i \int e} \tag{42}$$

Solving for $\boldsymbol{\tau}$ in (42) gives (43)

$$\boldsymbol{\tau} = \boldsymbol{M}(K_p\boldsymbol{e} + K_d\dot{\boldsymbol{e}} + K_i\int \boldsymbol{e} + \ddot{\boldsymbol{q}}_{\boldsymbol{d}}) + \boldsymbol{V} + \boldsymbol{G} \tag{43}$$

Using (43), input motor torques that makes end effector to follow desired trajectory can be found.

F. Adding Torsional Springs to The Joints

Joint 1 will not require higher torques since it has no job to overcome gravitational terms like joint 2 and join 3 have. So, there will be no need to add a torsional spring to joint 1.

The only thing differs when torsional springs are added is that a $\boldsymbol{\tau_{spring}}$ term is added to $\boldsymbol{\tau}$ in (43).

$$\boldsymbol{\tau} + \boldsymbol{\tau_{spring}} = \boldsymbol{M}(K_p\boldsymbol{e} + K_d\dot{\boldsymbol{e}} + K_i\int \boldsymbol{e} + \ddot{\boldsymbol{q}}_{\boldsymbol{d}}) + \boldsymbol{V} + \boldsymbol{G} \tag{44}$$

$$\boldsymbol{\tau_{spring}} = \boldsymbol{k}(\boldsymbol{\gamma} - \boldsymbol{q}) \tag{45}$$

Where $\boldsymbol{\gamma}$ is neutral angle vector and $\boldsymbol{k}$ is spring constant matrix. Which both are to be determined to make the robot arm energy optimized.

$$\boldsymbol{\gamma} = \begin{bmatrix} 0 \\ \gamma_2 \\ \gamma_3 \end{bmatrix} \tag{46}$$

$$\boldsymbol{k} = \begin{bmatrix} k_1 & 0 & 0 \\ 0 & k_2 & 0 \\ 0 & 0 & k_3 \end{bmatrix} \tag{47}$$

G. Energy Equation

$$\boldsymbol{E} = \int_0^t \boldsymbol{R}\,\boldsymbol{I}^2\,\boldsymbol{dt} \tag{48}$$

Spending energy can be found using (48). Where $\boldsymbol{R}$ is terminal resistance and $\boldsymbol{I}$ is current. However, we need such an Energy equation that involves torque.

$$\boldsymbol{I} = {}^{\boldsymbol{T}}/_{\boldsymbol{k_t}} \tag{49}$$

Using (49) and equation (48) we can have equation (50)

$$\boldsymbol{E} = \int_0^t \boldsymbol{R}\,({}^{\boldsymbol{T}}/_{\boldsymbol{k_t}})^2\,\boldsymbol{dt} \tag{50}$$

Since such controller systems are not continuous, we will use trapezoidal integral with help of MATLAB.

$$\boldsymbol{E} = \boldsymbol{trapz}(\boldsymbol{t}, \boldsymbol{R}({}^{\boldsymbol{T}}/_{\boldsymbol{k_t}})^2) \tag{51}$$

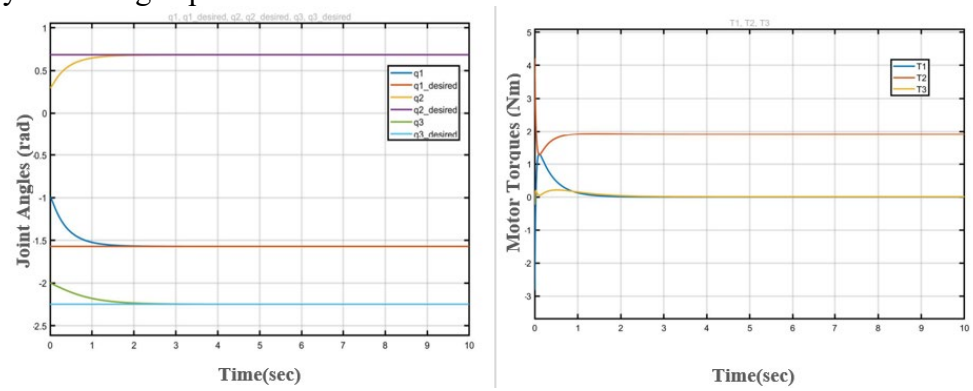
H. Optimization

Now that we have controller that gives us required actuator torques and an energy equation in terms of torques. We can start to think a strategy about how to make the energy optimization.

Since the system is not continuous due to controller, we can't use a direct method to solve optimum pairs of spring. Instead, we can use a simulation method to figure out the energy consumption for each $(k_1, \gamma_1), (k_2, \gamma_2)$ pair and note it. And then if we take the least energy consumption pair, those two springs are the springs that we should use to optimize the energy.

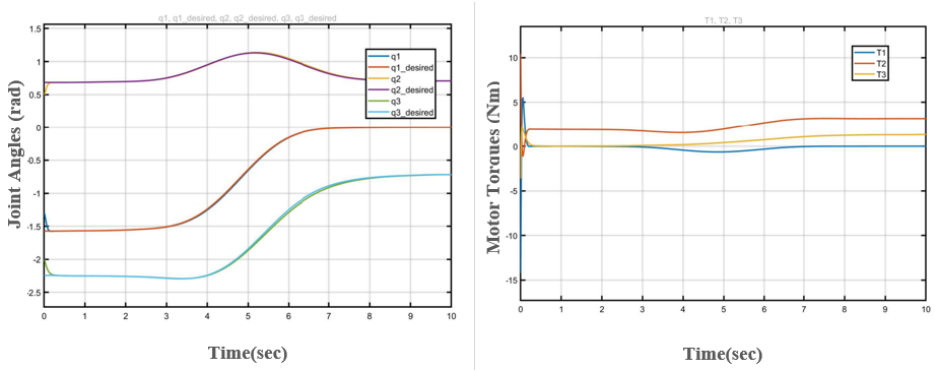
IV. Implementation and Simulation Results

In MATLAB environment reference trajectory tracking is simulated. As indicated before robot arm trajectory is sectioned to four parts. Therefore, performance of this four sections trajectory following is presented as follows.



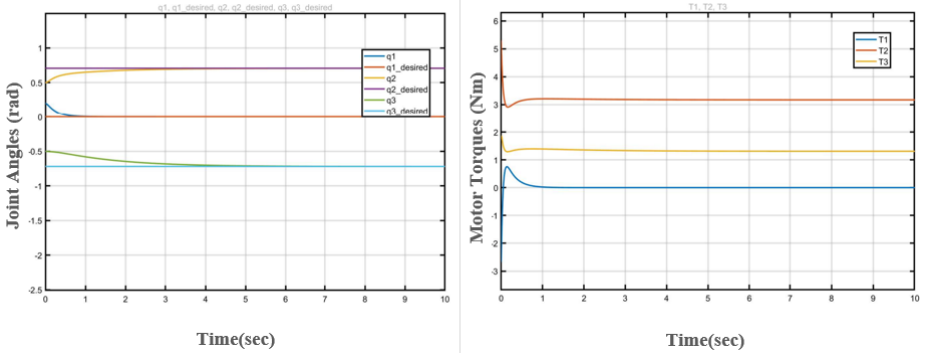
(a) (b)

Fig. 13. 1st Operation (a) Reference Trajectory Tracking (b) Motor Torques required



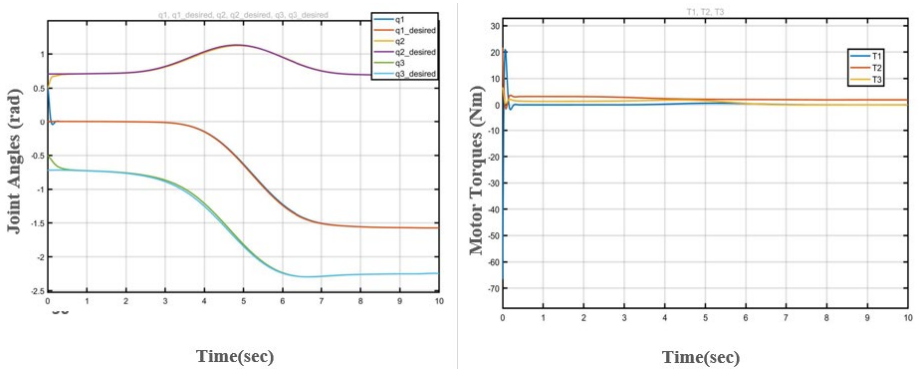
(a) (b)

Fig. 14. 2nd Operation (a) Reference Trajectory Tracking (b) Motor Torques required



(a) (b)

Fig. 15. 3rd Operation (a) Reference Trajectory Tracking (b) Motor Torques required



(a) (b)

Fig. 16. 4th Operation (a) Reference Trajectory Tracking (b) Motor Torques required

In MATLAB environment we took different spring pairs each time, then figured out how much energy system should spend to perform desired task. In Fig. 17 you can see first 23 pairs that is ran in the simulation. You can see the energy spending for each pair. Total number of 4453 pairs have been ran. You can see in Fig. 18 The optimum pair and its energy consumption.

	JOINT 2 VARIATIONS			JOINT 3 VARIATIONS		
Set Numarası	Neutral Angle(radians)	Spring Constant(Nm/radians)	Energy Spent (Joule)	Neutral Angle(radians)	Spring Constant(Nm/radians)	Energy Spent (Joule)
1	-3,141592654	0	34,77902275	-3,141592654	0	4,832514879
2	-3,141592654	0,5	107,132597	-3,141592654	0,5	17,28279091
3	-3,141592654	1	220,5762528	-3,141592654	1	38,04634586
4	-3,141592654	1,5	375,1100263	-3,141592654	1,5	67,1229752
5	-3,141592654	2	570,7338171	-3,141592654	2	104,5126887
6	-3,141592654	2,5	807,4477227	-3,141592654	2,5	150,2156792
7	-3,141592654	3	1085,251711	-3,141592654	3	204,2318485
8	-3,141592654	3,5	1404,14618	-3,141592654	3,5	266,5611644
9	-3,141592654	4	1764,130777	-3,141592654	4	337,2030888
10	-3,141592654	4,5	2165,204174	-3,141592654	4,5	416,1594292
11	-3,141592654	5	2607,368494	-3,141592654	5	503,4283138
12	-3,141592654	5,5	3090,622897	-3,141592654	5,5	599,0103771
13	-3,141592654	6	3614,967383	-3,141592654	6	702,9056265
14	-3,141592654	6,5	4180,403642	-3,141592654	6,5	815,1134474
15	-3,141592654	7	4786,926603	-3,141592654	7	935,6356401
16	-3,141592654	7,5	5434,543614	-3,141592654	7,5	1064,469605
17	-3,141592654	8	6123,246154	-3,141592654	8	1201,618386
18	-3,141592654	8,5	6853,041054	-3,141592654	8,5	1347,079523
19	-3,141592654	9	7623,929261	-3,141592654	9	1500,852653
20	-3,141592654	9,5	8435,901104	-3,141592654	9,5	1662,941321
21	-3,141592654	10	9288,966253	-3,141592654	10	1833,341994
22	-3,141592654	10,5	10183,12148	-3,141592654	10,5	2012,055845
23	-3,141592654	11	11118,3668	-3,141592654	11	2199,082876

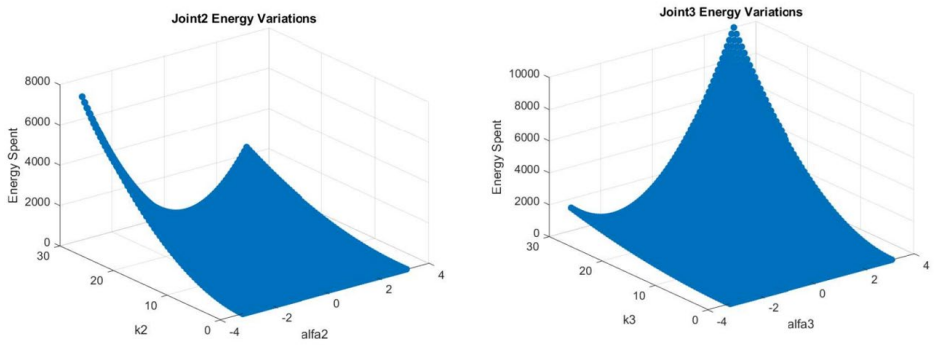
Fig. 17. First 23 pairs Energy Consumption List

	JOINT 2 VARIATIONS			JOINT 3 VARIATIONS		
Set Numarası	Neutral Angle(radians)	Spring Constant(Nm/radians)	Energy Spent (Joule)	Neutral Angle(radians)	Spring Constant(Nm/radians)	Energy Spent (Joule)
1	-3,141592654	0	34,77902275	-3,141592654	0	4,832514879
4389	3,054326191	28,5	21495,75356	3,054326191	28,5	94083,38458
4390	3,054326191	29	22286,49102	3,054326191	29	97428,46536
4391	3,054326191	29,5	23091,55057	3,054326191	29,5	100831,9681
4392	3,054326191	30	23910,85611	3,054326191	30	104293,9162
4393	3,141592654	0	34,77902275	3,141592654	0	4,832514879
4394	3,141592654	0,5	10,71434761	3,141592654	0,5	19,96036596
4395	3,141592654	1	2,037407904	3,141592654	1	95,70901694
4396	3,141592654	1,5	8,748203088	3,141592654	1,5	232,0784567
4397	3,141592654	2	30,84673381	3,141592654	2	429,0687045
4398	3,141592654	2,5	68,33299954	3,141592654	2,5	686,6797429
4399	3,141592654	3	121,2070005	3,141592654	3	1004,911578

Joint 2 İçin	Neutral Angle(radians)	Spring Constant(Nm/radians)	Energy Spent (Joule)
Dönel Yaysız Sistem	-3,141592654	0	34,77902275
Dönel Yaylı Enerji Optimum Sistem	3,141592654	1	2,037407904

Joint 3 İçin	Neutral Angle(radians)	Spring Constant(Nm/radians)	Energy Spent (Joule)
Dönel Yaysız Sistem	-3,141592654	0	4,832514879
Joint 3 İçin Kullanılan Herhangi Bir Yayın Enerji Tasarrufu Sağlamadığı Görüldü			

Fig. 18. Optimum Pair and its energy consumption



(a) (b)

Fig. 19. Nuetral angle, spring constant and total energy spending variations for (a) joint 2 (b) joint 3

You can see graphs of spring models and energy variations in Fig. 19. As we can see in Fig. 18, if there would be no torsional springs used for minimizing the energy consumption. Energy spent of joint 2 to perform the task is 34.78 Joules. But if we use the correct torsional spring for the joint, we see that energy spending is just 2.03 joules. We see lots of energy saving here in joint 2. However, for joint 3, even if use any spring, we see no energy saving at all. So, using a torsional spring here is unnecessary. Reason why we can't save any energy on joint 2 is uniqueness of robot geometry and the task. For example, if the task changes for the robot, even if the robot arm geometry is the same, we can see that we can save some energy spending using torsional spring on joint 3 too.

V. CONCLUSIONS

A robot arm kinematic and control design have been made. A trajectory has been designed according to a real task. Using torsional springs, we saw that energy optimization is valuable. Also, this optimization is not made just with equation of motion, The optimization includes effects of control algorithm, which it means that optimization we made is closer to the real applications.

REFERENCES

[1] A. Sengupta, T. Chakraborti, A. Konar, A. Nagar. "Energy Efficient Trajectory Planning by a Robot Arm using Invasive Weed Optimization Technique", 2011.

[2] J. Mostyn, D. Huczala, W. Moczulski, A. Timofiejczuk, "Dimensional Optimiziation of the Robotic Arm to Reduce Energy Consumption", 2020.

[3] W. Robert Brown and A. Galip Ulusoy, "A Passive-Assist Design Approach for Improved Reliability and Efficiency of Robot Arms", 2011.

[4] C.S. George Lee, University of Michigan,"Robot Arm Kinematics, Dynamics and Control",1982

YOLOv5 Deep Learning Model Approach for the Detection and Classification of Gunshot Residue Images

İlker KARA[*,1], Mehmet KASAP[2]

[*]ilkerkara@karatekin.edu.tr, ORCID: 0000-0002-9670-8964
[1]*Department of Medical Services and Techniques, Eldivan Medical Services Vocational School, Çankırı Karatekin University, 18000 Çankırı, Turkey*
[2]*Department of Physics, Faculty of Science, Gazi University, 06100 Ankara, Turkey*

Abstract: With the advancement of technology, forensic investigation has gained increasing significance as a field. Especially in incidents involving firearms, the detection and analysis of residues resulting from firearm discharges play a crucial role in crime scene examination and the clarification of forensic cases. For this purpose, the detection, analysis, and morphological classification of gunshot residues (GSR) can be achieved through methods that exceed traditional approaches by integrating morphological classifications and YOLOv5 deep learning techniques. This study aims to explore the utilization of morphological classifications and YOLOv5 deep learning techniques for the analysis of gunshot residues resulting from firearm use in the realm of digital forensic analysis. Given the limitations and complexity of traditional methods, this study aspires to offer a fresh perspective on the morphological analysis and detection of gunshot residues. The discussion will revolve around how features can be utilized in the detection of evidence through digital image analysis and how YOLOv5 deep learning techniques can be integrated. Throughout the study, a dataset comprising 4150 samples obtained from MKE brand cartridges was employed. For the analysis and morphological classification of gunshot residues in digital images, the fundamental deep learning method provided by YOLOv5 algorithm was employed. The proposed approach requires only 0.44 seconds on average for analysis. The results demonstrate the effectiveness of the proposed method in the detection, analysis, and morphological classification of gunshot residues.

Keywords: *Digital Forensic, Deep Learning, YOLOv5 algorithm, GSR.*

I. INTRODUCTION

In today's world, firearms are involved in 70% of the criminal incidents [1]. The accurate detection, analysis, and classification of residue particles resulting from firearm discharges play a critical role in crime scene interpretation and the comprehensive understanding of forensic scenarios [2]. At the crime scene, forensic experts collect GSR using adhesive carbon tape, which are then analyzed by scanning electron microscopy SEM. GSRs are micron-sized distinct particles with unique shapes, and certain characteristic features such as size are scanned using SEM. Through examinations conducted in forensic laboratories, it is conclusively determined whether the particles are gunshot residues using SEM (Figure 1). The SEM analysis, a labor-intensive and exhaustive process, is considered to be potentially replaced by an automated analysis method, offering easier and faster results.

Deep learning-based approaches are currently among the leading candidates for this purpose. Convolutional Neural Networks (CNN) are one of the most important Deep Learning (DL) models used in computer vision and image processing. Convolutional layers, which convolve the entire image, pooling layers, which reduce the spatial dimensions of the input data for the next convolutional layer, and fully connected layers, which are the high-level reasoning layers

of the neural network, are the three types of neural layers which make up a CNN [3].

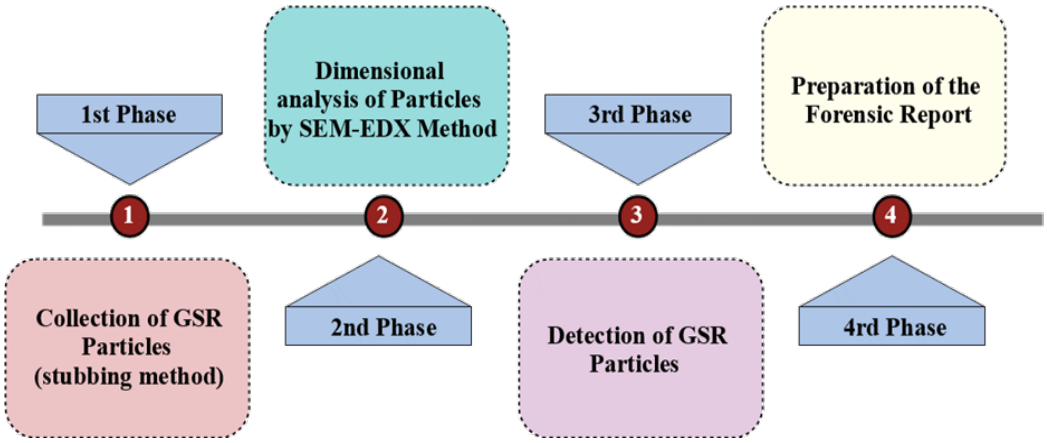


Fig. 1. The overall workflow of the detection of the GSR.

In order to handle categorization, localization, and object detection, CNN can be used to analyze, combine, and extract color, geometric, and texture data from images. A computer vision technique called object detection combines image classification and object localization [4]. The output of object detection is typically bounding boxes over the image, but some algorithms also produce semantic segmentation. R-CNN, Faster R-CNN, and Mask R-CNN are examples of region proposed object detection methods, while You Only Look Once (YOLO) [5] and Single Shot Detector (SSD) are examples of regression/classification-based models.

Jocher et al. from Ultralytics LLC (Los Angeles, CA - USA), a separate developer from the previous YOLO versions, released YOLOv5 in May 2020 [6]. Although there were some disagreements regarding the definition of the new YOLO version, the deep learning community embraced YOLOv5 [7].

In this study, the focus is on showcasing the potential of YOLOv5 deep learning algorithm as an alternative to traditional approaches for the detection and morphological classification of GSRs. Through the utilization of deep learning algorithms, the analysis of gunshot residues can be conducted faster, more accurately, and with greater reliability. With this objective in mind, the research has thoroughly examined how digital image analysis, feature extraction, and classification can be effectively employed in the context of GSRs.

The morphological structure of GSRs was analyzed in seven groups (Perfect Spheroid, Two Spherical with Bridge, Spongy, Elliptical, Hollow, Irregular, and Half-Spherical) [8]. The utilized dataset comprises 3320 training samples and a total of 830 test samples, reaching a total of 4150 samples. This dataset has been shared without any commercial concerns, enabling other researchers to utilize it (https://ilkerkara.karatekin.edu.tr/RequestDataset.html).

Furthermore, the study aims to highlight the application of deep learning methods in the field of forensic investigation, emphasizing the significance of innovative approaches in this domain for forensic scientists, criminalists, and other relevant experts. The outcomes of the research will underscore the growing importance of using deep learning techniques in the analysis of gunshot residues, accentuating the necessity for a more effective and efficient approach in forensic investigation practices.

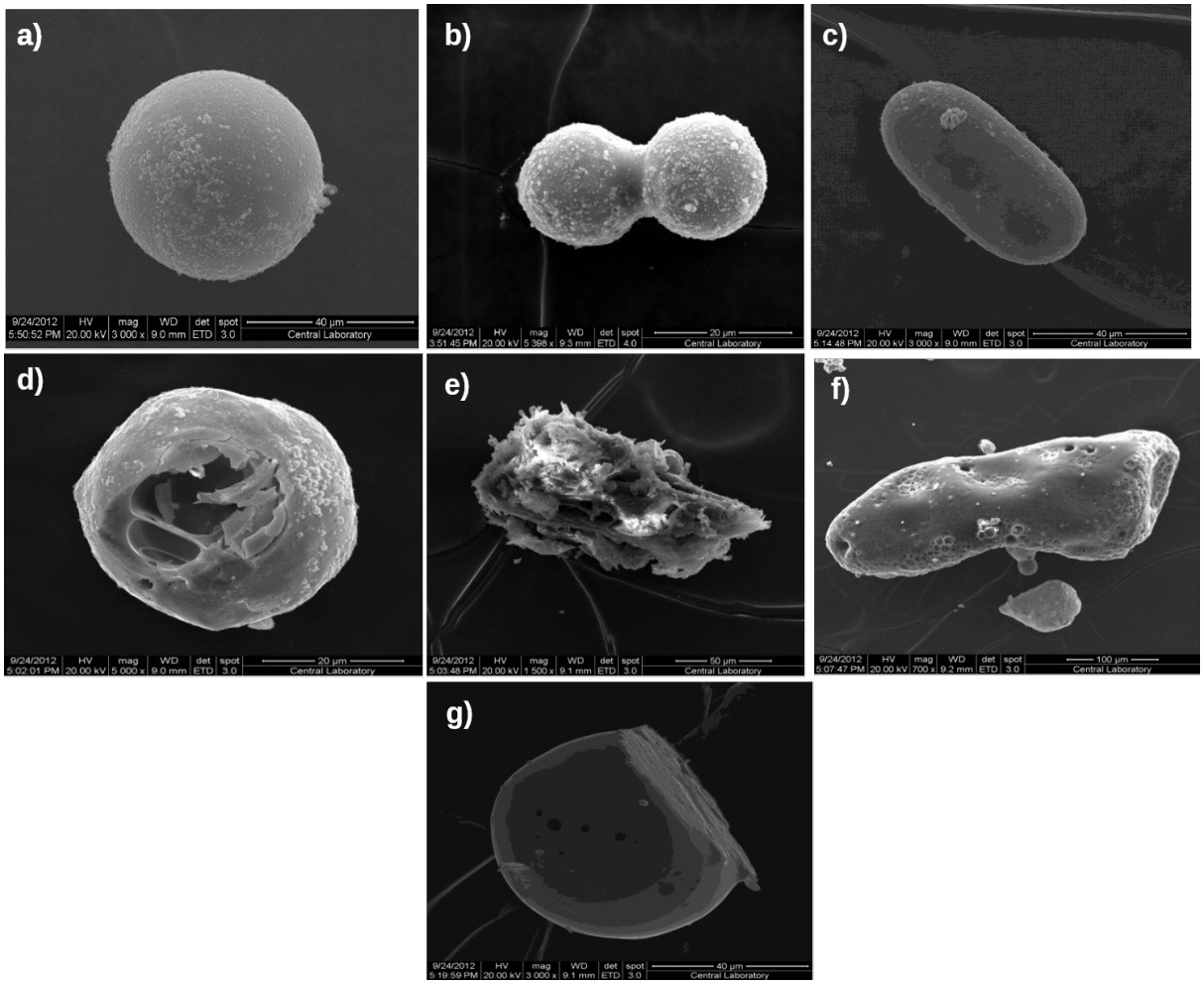


Fig. 2. Morphological class of GSR particles. (a)Perfect Spheroid, (b)Two Spherical with Bridge, (c)Spongy, (d)Elliptical, (e) Hollow, (f) Irregular, and (g)Half-Spherical [8].

II. RELATED WORK

The topic of morphological classification and detection of GSRs using deep learning in digital forensics has gained significant attention in recent years, alongside the technological advancements and growing popularity of digital analysis methods in forensic science. The notable advancements and relevant studies in this field aim to facilitate the more effective, rapid, and accurate analysis of gunshot residues, particularly considering the increasing volume of evidence in question.

In the study conducted by Brożek-Mucha, the number of GSR particles, their formation, and dimensional distributions were examined using the SEM/EDS method [9]. Swab samples obtained from various areas of the shooter (clothing, hair, and hands) were analyzed, thus this study is comprised of a small dataset due to the nature of the collected samples.

A study conducted by Kara et al. (2014) examined the morphological structure of gunshot residues, categorizing them into seven distinct groups: "Perfect Spheroid," "Two Spherical with Bridge," "Spongy," "Elliptical," "Hollow," "Irregular," and "Half-Spherical." This classification served as a fundamental step in comprehending the overall structure of gunshot residues [8].

In another study, Spathis (2017) examined the morphologies of GSR particles using the SEM/EDS method [10]. Interestingly, it was observed that structures of varying sizes and random morphologies coexisted with the classical spherical structure. Additionally, GSR

particles were categorized into seven distinct groups, where their morphologies were defined by their functionalities. However, it should be noted that this study was conducted with a limited dataset.

Similarly, Kara et al. (2022) addressed the critical role of morphological classification in the analysis of gunshot residues and evaluated the limitations of traditional methods [11]. This study represents one of the initial steps taken to explore the potential of machine learning methods in the analysis of gunshot residues.

In their study titled "Application of Hyperspectral Imaging and Machine Learning Methods for the Detection of Gunshot Residues," Głomb et al. (2018) investigated the application of a hyperspectral camera and two well-known Machine Learning algorithms to automatically detect potential GSR samples in a scene containing fabric [12]. The study involved collecting GSR samples of various fabric types to create a hyperspectral dataset. The obtained data led to the creation of two detection scenarios: unsupervised anomaly detection using the RX detector and supervised pixel classification using the SVM classifier. The results of the research revealed that accurate detection is possible in both scenarios, anomaly detection approach generally requiring image normalization, and the classifier not needing fabric-specific information. Additionally, hyperspectral imaging was found to generally outperform RGB imaging in terms of GSR detection accuracy [12].

Furthermore, Wang and Smith (2020) examined how machine learning methods can be utilized in the detection and classification of gunshot residues in digital forensic analysis [13]. Focusing on the potential of artificial neural networks and deep learning techniques, this study introduced novel approaches for more precise analysis of gunshot residues.

The study conducted by Wang and Smith (2020) stands out with its utilized methods and results. The presented idea demonstrates the substantial potential for the detection and classification of gunshot residues. To this end, we explored the capabilities of the YOLOv5 deep learning algorithm method for the analysis and morphological classification of gunshot residues, utilizing the dataset produced by Kara et al. (2014) in their doctoral thesis [8].

III. MATERIALS AND METHODS

In this section, first, the utilized dataset is introduced. Subsequently, the YOLOv5 deep learning algorithm used for the dimensional analysis of GSR morphological structures will be discussed.

A. DATASET

It is widely acknowledged that establishing the correct dataset is of paramount importance for data-focused studies. When reviewing the literature, it can be observed that there is a limited number of datasets available for GSR analyses [8, 12]. As a suitable dataset for our research, the dataset produced by Kara et al. (2014) in their doctoral thesis has been employed in this study [8]. The dataset utilized in the doctoral thesis by Kara et al. (2014) consists of 4150 SEM/EDS digital image samples of MKE brand 9x19 mm diameter full-metal jacket GSR particles.

B. THE APPROACH

In this section, the workflow and system of our entire approach are described in detail. The overall study comprises three stages (Figure 3).

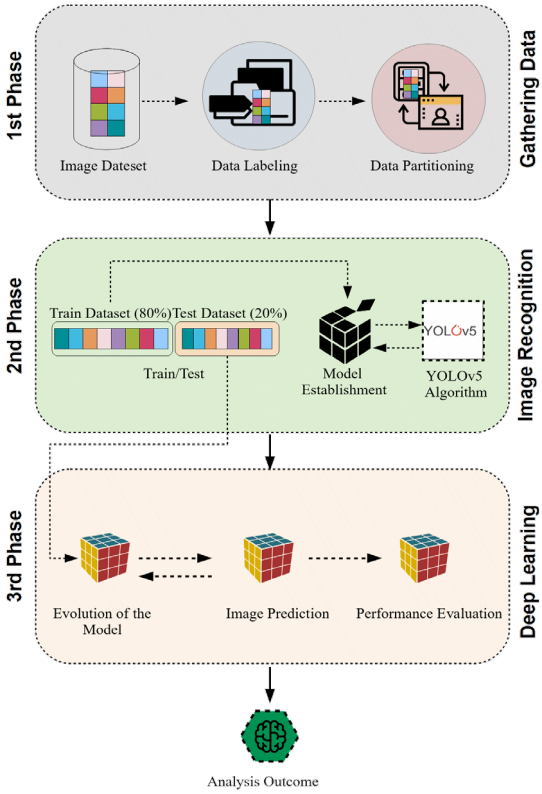


Fig. 3. The overall workflow of the proposed approach's.

Gathering Data: In the doctoral thesis study by Kara et al. (2014), the dataset consisted of 4150 SEM/EDS digital image samples of MKE brand 9x19mm diameter full-metal jacket GSR particles [8]. The data from seven classes were divided into 80% training data and 20% test data. The Makesense.ai platform was used to label the images in the dataset. The labeling type, consisting of three formats - VOC XML, YOLO, and .csv, was determined to be YOLO. Objects in the images were enclosed in bounding boxes, and their coordinates were defined. At the end of the labeling process, the coordinates of each image were exported as a text file.

Image Recognition: The images obtained through the SEM/EDS method are typically generated in two different formats: RGB (Red-Green-Blue) image format and Gray Scale image format. In RGB format, each pixel composing the image is represented with Red, Green, and Blue color values that can take values between 0 and 255. Gray scale, on the other hand, consists of values ranging from 0 to 255 obtained from images in the RGB color space. The dataset used in the study is in the gray scale image format.

The image files in the utilized dataset were analyzed at a resolution of 224x224 pixels and in an 8-bit grayscale format. Grayscale images lack color information [14, 15]. These images are stored on computers in an 8-bit luminance format [15]. Each pixel in the image is represented as an 8-bit binary code. In other words, since $2^8 = 256$, values range from 0 to 255. A value of 0 represents black, while 255 represents white [14].

Deep Learning: YOLO approaches object detection as a single regression issue, bypassing the pipeline of region proposal, classification, and duplication elimination, in contrast to other object detection algorithms that have been previously developed [16]. Images are reduced in size and resolution using YOLO techniques, which then run a single CNN on the images and output the detection results based on the model's confidence threshold. YOLO, introduced in 2016 by Joseph Redmon, Santosh Divvalai, Ross Girshick, and Ali Farhadi, is a member of the computer vision family. YOLO has gained the admiration of researchers [17]. Day by day, this network has been expanded by developers, and in these expansion stages, versions that can work at different speeds with different mathematical algorithms have been revealed. These versions have been named as YOLO, YOLOv2, YOLOv3, YOLOv4, YOLOv5, YOLOX, and

YOLOR, respectively. Due to their high success rates in current research, the most widely used versions are YOLOv3, YOLOv4, and YOLOv5 [18]. In this study, the YOLOv5 deep learning algorithm method was employed for the dimensional analysis of GSR morphological structures. In this study, the results obtained when the YOLOv5 algorithm was run with an "epochs" value of 200 are presented in Table 1.

TABLE I
TEST PERFORMANCE RESULTS OF THE YOLOV5 MODEL.

Class	Image	Instances	P	R	mAP50	mAP50-95:100%
(a)Perfect Spheroid	830	16	0.777	1	0.983	0.636
(b)Two Spherical with Bridge	830	2	1	1	0.638	0.468
(c)Spongy	830	27	0.948	1	0.468	0.752
(d)Elliptical	830	1	0.197	1	0.955	0.895
(e) Hollow	830	14	0.888	1	0.955	0.795
(f) Irregular	830	9	0.836	1	0.955	0.839
(g)Half-Spherical	830	17	0.81	1	0.955	0.769
All	830	86	0.78	0.857	0.942	0.736

The images of morphological classes of GSR particles under the headings (a) Perfect Spheroid, (b) Two Spherical with Bridge, (c) Spongy, (d) Elliptical, (e) Hollow, (f) Irregular, and (g) Half-Spherical resulting from the application of the YOLOv5 model are shown in Figure 4.

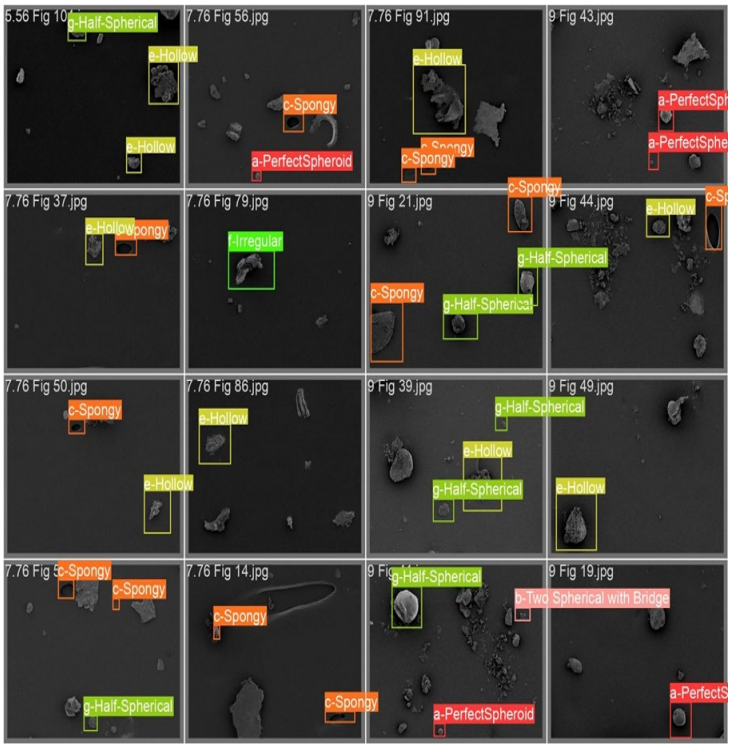


Fig. 4. The GSRs morphological classified under the headings (a) Perfect Spheroid, (b) Two Spherical with Bridge, (c) Spongy, (d) Elliptical, (e) Hollow, (f) Irregular, and (g) Half-Spherical resulting from the application of the YOLOv5 model.

The class distribution of the results of GSR particle classification using the YOLOv5 model is shown in Figure 5.

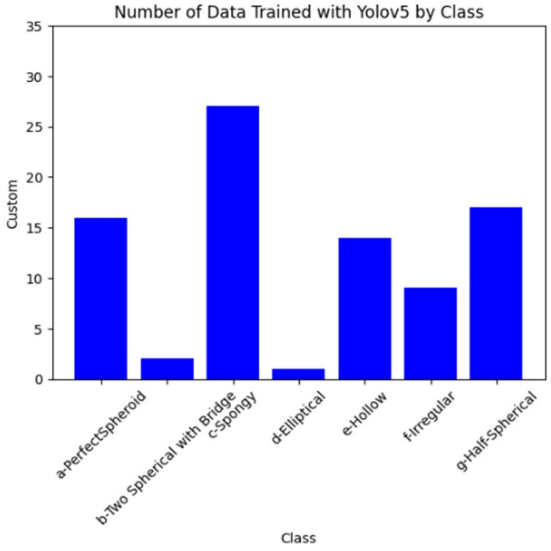


Fig. 5. The class distribution of particle classification results in the YOLOv5 model

The confusion matrix obtained from the implementation of the YOLOv5 model helps us understand the accuracy and performance of the classification model by comparing predicted classes with actual classes. The confusion matrix graph is shown in Figure 6.

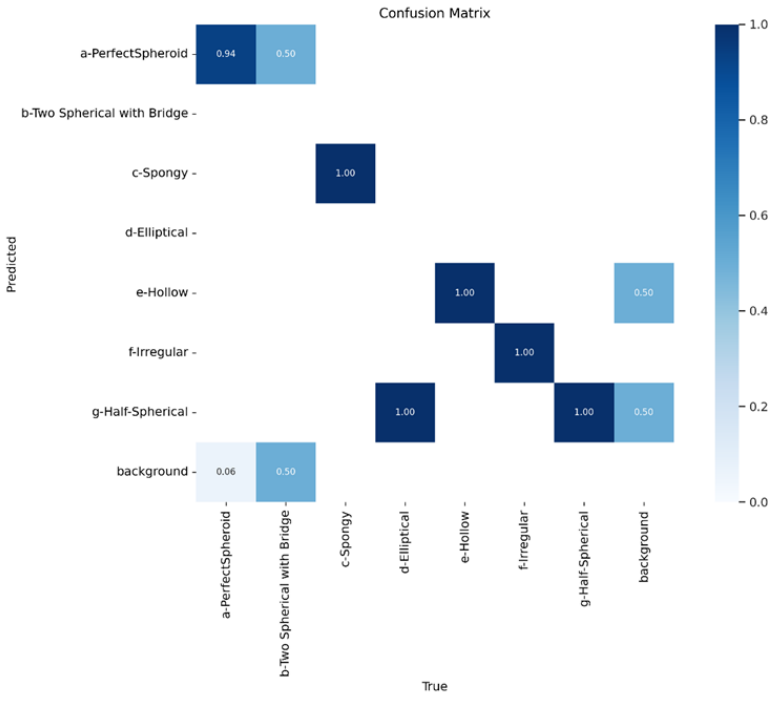


Fig. 6. The confusion matrix graph of the YOLOv5 model.

The data loss graphs obtained from the implementation of the YOLOv5 model are shown in Figure 7.

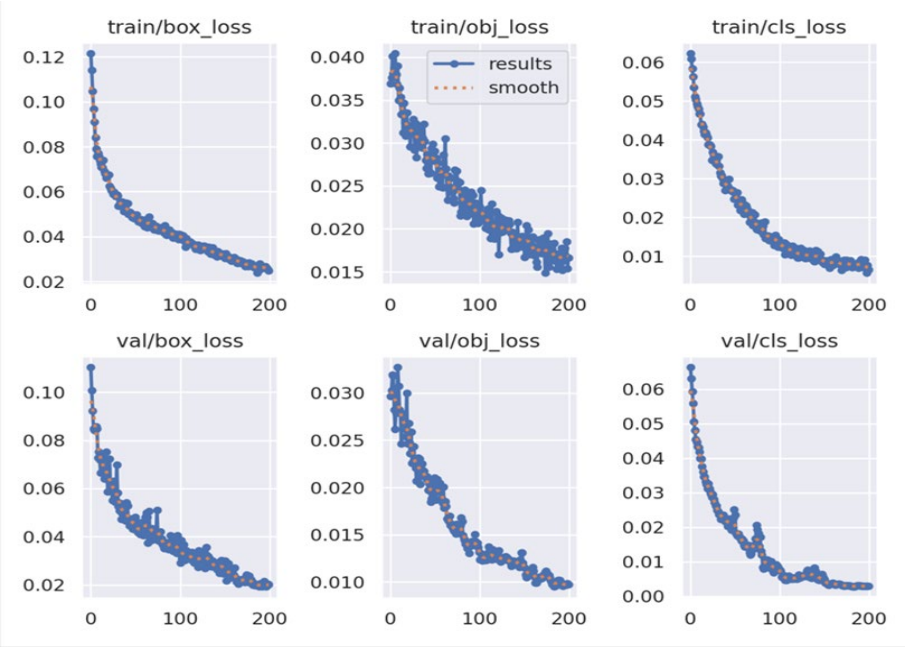


Fig. 7. The data loss graphs for the training dataset of the YOLOv5 model.

TABLE II
TRAINING PERFORMANCE RESULTS OF THE YOLOV5 MODEL.

Class	Image	Batch	epochs/num_steps	mAP50-95:100%
(a)Perfect Spheroid	3320	16	200	0.636
(b)Two Spherical with Bridge	3320	16	200	0.468
(c)Spongy	3320	16	200	0.752
(d)Elliptical	3320	16	200	0.895
(e) Hollow	3320	16	200	0.795
(f) Irregular	3320	16	200	0.839
(g)Half-Spherical	3320	16	200	0.769
YOLOv5	3320	16	200	0.736 (all)

IV. RESULT AND DISCUSSION

Similar to the study conducted by Głomb et al. (2018), our proposed framework primarily relies on the utilization of deep learning methods beyond traditional approaches for the detection, analysis, and morphological classification of GSR [12]. In the forensic examinations we address in this study, the investigated GSR serves as a source of information, offering two significant advantages: (1) morphological classification and categorization of images, and (2) expedited forensic examinations due to the increased volume of data.

On the other hand, the detection, analysis, and morphological classification of GSR entail certain challenges. First and foremost, the success rate of the analysis and morphological classification processes is influenced by various environmental parameters that are associated with GSR images. This situation consequently affects the overall accuracy. Furthermore, this

circumstance contributes to an increase in the total time required for forensic examinations.

In this study, we propose a novel strategy based on YOLOv5 deep learning method for the detection, analysis, and morphological classification of GSR within the scope of forensic examinations. The results of the study demonstrate that our approach does not introduce any bias in the analysis and morphological classification of digital images of GSR. However, it's important to note that our dataset is limited to 7 morphological classes, and we believe that larger datasets are necessary to further reinforce this argument in support of our experimental setups.

V. CONCLUSION

In this study, we have utilized the YOLOv5 deep learning method for the analysis and morphological classification of Gunshot Residue (GSR) digital images, which serve as a source of information in forensic examinations. In this regard, we have proposed an approach for the analysis and morphological classification, as well as categorization, of GSR digital images within the context of forensic investigations.

Experiments conducted using the YOLOv5 deep learning framework indicate that it is a suitable method for the analysis, morphological classification, and categorization of GSR digital images in forensic examinations. To support this study, we have prepared and released a publicly available dataset containing a total of 4150 image samples belonging to 7 different morphological classes, which were used in the study (https://ilkerkara.karatekin.edu.tr/RequestDataset.html).

In conclusion, the proposed approach demonstrates promising results with a reasonable detection time of 8 minutes and 56 seconds. Upon analyzing the obtained results, the morphological classification of GSR exhibits the highest accuracy of 0.895 for the Elliptical class and the lowest accuracy of 0.468 for the Two Spherical with Bridge class. These rates are anticipated to be enhanced based on the majority of particle class, clarity, and the epochs value in the trained GSR image data.

ACKNOWLEDGMENT

This study is produced from PhD thesis "ADLİ BİLİMLER AÇISINDAN ATIŞ ARTIKLARI ANALİZ TEKNİKLERİ VE KRİMİNAL UYGULAMALARI" prepared by İlker KARA in 2014 under the supervision of Prof. Dr. Mehmet KASAP.

REFERENCES

[1] M. Miller, W. Zhang D. Azrael. "Firearm purchasing during the COVID-19 pandemic: results from the 2021 National Firearms Survey," Annals of internal medicine, 2022, 175(2), pp. 219-225.

[2] M. Miller, I. D. Azrae, D. Hemen Way. "Rates of house Hold firearm owner ship and homicide across US regions and states, " 2022, pp. 1988-1997.

[3] A. Voulodimos, N. Doulamis, A. Doulamis, E. Protopapadakis. "Deep Learning for Computer Vision: A Brief Review. " Comput. Intell. Neurosci. 2018, pp. 7068349.

[4] Z.Q. Zhao, P. Zheng, S.T. Xu, X. Wu. "Object Detection with Deep Learning: A Review. IEEE Trans. Neural Netw. Learn. Syst. " 2019, 30, pp. 3212-3232.

[5] J. Redmon, S. Divvala, R. Girshick, A. Farhadi. "You only look once: Unified, real-time object detection. " In Proceedings of the IEEE Conference on Computer Vision and Pattern Recognition (CVPR), Las Vegas, NV, USA, 27-30 June 2016; IEEE Computer Society: Washington, DC, USA, 2016, pp. 779-788.

[6] G. Jocher, A. Stoken, J. Borovec, S.T.A.N. Christopher. "Laughing, L.C. ultralytics/yolov5: v4.0-nn.SiLU() activations, Weights & Biases logging, PyTorch Hub integration. " Zenodo 2021.

[7] R. Iyer, P. Shashikant Ringe, R. Varadharajan Iyer. "Prabhulal Bhensdadiya, K. Comparison of YOLOv3, YOLOv5s and MobileNet-SSD V2 for Real-Time Mask Detection. " Artic. Int. J. Res. Eng. Technol. 2021, 8, pp. 1156-1160.

[8] İ.Kara. "Adli Bilimler Açısından Atış Artıkları Analiz Teknikleri ve Kriminal Uygulamaları" Doktore Tezi, 2014. pp. 42-50.

[9] Z. Brożek-Mucha. "Chemical and morphological study of gunshot residues persisting on the shooter by means of scanning electron microscopy and energy dispersive X-ray spectrometry." Microscopy and Microanalysis, 2011, 17(6), pp.972-982

[10] V. Spathis. "Impact-disrupted gunshot residue: A sub-micron analysis using a novel collection protocol. Defence Technology," 2017, 13(3), pp. 143-149.

[11] I. Kara, E. Tahillioglu. "Digital image analysis of gunshot residue dimensional dispersion by computer vision method. Microscopy Research and Technique," 2022, 85(3), pp. 971-979.

[12] P. Głomb, M. Romaszewski, M. Cholewa, K. Domino. "Application of hyperspectral imaging and machine learning methods for the detection of gunshot residue patterns." Forensic science international, 2018, 290, pp. 227-237.

[13] T. Wang, N. Smith. "Firearms discharge residue analysis using deep learning-based image classification." Forensic Chemistry, 2020, 18, pp. 100215.

[14] M. Rahimzadeh, S. Parvin, E. Safi, M.R. Mohammadi, "Wise-SrNet: A Novel Architecture for Enhancing Image Classification by Learning Spatial Resolution of Feature Maps." arXiv preprint arXiv:2104.12294. 2021.

[15] S. Coulibaly, B. Kamsu-Foguem, D. Kamissoko, D. Traore, "Deep neural networks with transfer learning in millet crop images. Computers in Industry," 2019,108, pp. 115-120.

[16] M. T., Ağdaş, S. Gülseçen. "Güvenlik Kameralarında Otomatik Silah ve Bıçak Tespit Sistemi: Karşılaştırmalı YOLO Modelleri." Avrupa Bilim ve Teknoloji Dergisi, 2020, (41), pp. 16-22.

[17] J. Redmon, S. Divvala, R. Girshick, A. Farhadi. "You only look once: Unified, real-time object detection." In Proceedings of the IEEE conference on computer vision and pattern recognition 2016, pp. 779-788.

[18] W.R.W.M, Razin, T.S, Gunawan, M., Kartiwi, N.M. Yusoff. "Malaria Parasite Detection and Classification using CNN and YOLOv5 Architectures." In 2022 IEEE 8th International Conference on Smart Instrumentation, Measurement and Applications (ICSIMA) 2022, September, pp. 277-281. IEEE.

[19] Dateset,http://ilkerkara.karatekin.edu.tr/RequestDataset.htmlekle dataset, 2023.

Effect of CNT distribution on the dynamic behavior of carbon nanotube reinforced FGM shells

Zakia Hammou[*,1], Zakia Guezzen[2], Zouaoui Sereir[2], Yamna Hammou[3]

[*]z.hammou@yahoo.fr

[1]*Physical chemistry Department, Chemistry Faculty, University of Science and Technology of Oran, USTO, Oran, Algeria.*

[2]*Composite Structures and Innovative Materials Laboratory, Mechanical Engineering Faculty, University of Science and Technology of Oran, BP 1505 El M'naouer, USTO, Oran, Algeria.*

[3]*Maritime Sciences and Engineering Laboratory, Mechanical Engineering Faculty, University of Science and Technology of Oran, BP 1505 El M'naouer, USTO, Oran, Algeria*

Abstract: In the present paper an analytical model was developed to study the non-linear vibrations of Functionally Graded Carbon Nanotube (FG-CNT) reinforced doubly-curved shallow shells using the Multiple Scales Method (MSM). The nonlinear partial differential equations of motion are based on the FGM shallow shell hypothesis, the non-linear geometric Von-Karman relationships, and the Galerkin method to reduce the partial differential equations associated with simply supported boundary conditions. The novelty of the present model is the simultaneous prediction of the natural frequencies and their mode shapes for cylindrical curvatures and the different types of FG-CNTs. The results obtained show that the types of NTC distribution have considerable effects on the variation of the Dimensionless Fundamental Linear Frequency (DFLF). The frequency response of the shallow shells of the FG-CNTRC showed two types of nonlinear hardening and softening which are strongly influenced by the change in the fundamental vibration mode.

Keywords: *Galerkin method; Functionally Graded Carbon Nanotube; Fundamental Linear Frequency.*

I. INTRODUCTION

SHELL structures can be used in an efficient and economical way in different fields of engineering and architecture. Examples of such applications are shell roofs, silos, containment structures, pressure vessels, shell-type marine structures and space shuttles. Shell forms can be found abundantly in nature. Whatever the sector, due to their thinness, these structures are likely to present phenomena of structural instabilities or vibrations generated by static and dynamic stresses, which requires a good understanding of these weaknesses in order to avoid a bad sizing. The dynamic stress that such a structure can undergo during its operation can be complex and results most of the time from a combination of bending, torsion and shear vibrations.

The idea of improving the physical properties of polymers with carbon nanotube reinforcements is the subject of numerous studies. The interest in this type of composite is mainly due to the mastery of their manufacture on an industrial scale as well as their low cost. Studies by Cadek et al. [1] showed the improvement of the mechanical properties of Polymer/CNT composites. The latter observed an improvement in Young's modulus and hardness by respective factors of 1.8 and 1.6 for an inclusion of 1% by mass of MWNT. The same authors [2] observed a five-fold improvement in Young's modulus with this same composite, highlighting the role of polymer dispersion and crystallization in improving mechanical properties. Thus, an increase in hardness of 42% and tensile strength of 25% was

reported by Qian et al. [3], concerning a polymer composite based on polystyrene with an inclusion of 1% by mass of MWNT. Haggenmueller et al. [4] reported an increase in Young's modulus of about 450% for a polyethylene-based composite for 20% by mass of SWNT. This same team also observed an increase in the modulus of elasticity of approximately 162% for an inclusion of 2% by mass of SWNT, concerning a nylon-based composite [5].

In traditional nano-composites, the nanotubes are distributed uniformly or randomly so that the mechanical properties of the structure cannot be perfectly improved [3], [6]. To overcome this drawback, the functionally graded CRNTC in which the physical properties vary spatially according to a specific reinforcement phase distribution is generated. Using the concept of FGMs, Shen [7] studied the large amplitude bending of functional gradient CRNTC plates. He discerned that the bending behavior of plates can become better by using an FG distribution of CNTs in the matrix.

This pepper aims to develop a variational formulation to describe the vibrational behavior of functionally graded nano-composite material (FG-CRNTC). We predicted the properties of functionally graded materials from a mixture of SWNTs and the matrix using a unidirectional FG-UD configuration. We have developed the equations of motion for the shallow doubly curved hull for the simply supported boundary conditions. These equations were based on the low-curvature hull assumption of FGMs and on the nonlinear geometric relations of Von-Kármán, our system was reduced to a system of nonlinear partial differential equations [8]. The method of multiple scales was used for the determination of the effective non-linearity and the eigenmodes [9], [10]. By this method, we expressed the solution in terms of different time scales. This solution mainly gives us the effective non-linearity, the fundamental natural frequency which can be the source of the resonance phenomenon. To study the influence of the number of modes in the Galerkin approximation on the accuracy of the predicted response, we evaluated the effect of CNT distribution.

II. VIBRATION ANALYSIS

A. Material properties of FG-CNTRC Shell

As shown in Fig. 1a, the geometrical configuration of the FG-CNTRC shallow shell is depicted with the origin of the coordinate system was at the center of the left end of the shell. l_x, l_y and h represents the shell dimensions in the x, y and z directions, respectively. R_x and R_y represents, the radius of curvature along x and y directions respectively. As shown in Fig. 1b, five configurations of different distributions of the CNT were adopted. This is the uniform distribution (UD) or functionally graduated distributions (FG-Λ, FG-V, FG-O, FG-X) in the direction of the thickness of the shallow shell. The CNT volume fractions V_{cnt} of various types of the FG-CNTRC beam can be expressed as:

$$V_{cnt} = \begin{cases} 2\left(\dfrac{r - r_i}{r_0 - r_i}\right) V_{cnt}^{*} & \text{for FG-V CNTRC} \\ 2\left(\dfrac{r_0 - r}{r_0 - r_i}\right) V_{cnt}^{*} & \text{for FG-Λ CNTRC} \\ 4\left|\dfrac{r - r_m}{r_0 - r_i}\right| V_{cnt}^{*},\ r_m = \dfrac{r_i + r_0}{2} & \text{for FG-O CNTRC} \\ \left[2 - 4\left|\dfrac{r - r_m}{r_0 - r_i}\right|\right] V_{cnt}^{*}, r_m = \dfrac{r_i + r_0}{2} & \text{for FG-X CNTRC} \\ V_{cnt}^{*} & \text{for FG-U CNTRC} \end{cases} \quad (1)$$

Where, r_i and r_0 are the interior and exterior radius, respectively. Here, V_{cnt}^{*} depends on density and mass fractions of both matrix and CNT.

$$V_{cnt}^{*} = \frac{\rho^{m}}{\rho^{m} + \left(\rho^{cnt} / w^{cnt}\right) - \rho^{cnt}} \tag{2}$$

And wcnt is the mass fraction of the nanotube, and ρ^{cnt} and ρ^{m} are the densities of the carbon nanotube and of the matrix, respectively.

The effective material properties of FG-CNTRCs can be obtained by the extended rule of mixture based on the micromechanical model as follows [11], [12]:

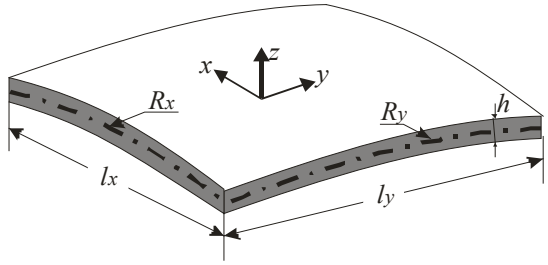
$$E_1 = \eta_1 V_{cnt} E_1^{cnt} + V_m E^{m} \tag{3}$$

$$\frac{\eta_2}{E_2} = \frac{V_{cnt}}{E_2^{cnt}} + \frac{V_m}{E^{m}} \tag{4}$$

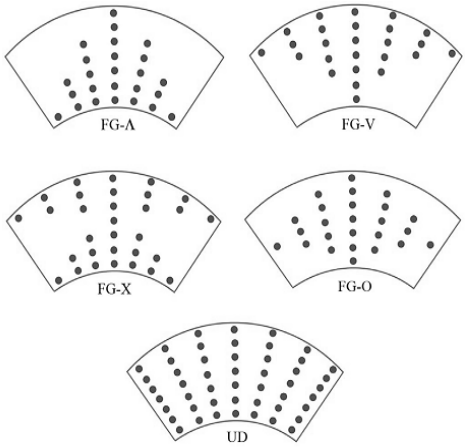
$$\frac{\eta_3}{G_{12}} = \frac{V_{cnt}}{G_{12}^{cnt}} + \frac{V_m}{G^{m}} \tag{5}$$

$$\upsilon_{ij} = V_{cnt} \upsilon_{ij}^{cnt} + V_m \upsilon^{m} \quad i, j = 1, 2, 3 \tag{6}$$

$$\rho = V_{cnt} \rho^{cnt} + V_m \rho^{m} \tag{7}$$



(a) Geometrical details of shallow shell.



(b) The five configurations of FG-CNTRC shallow shells.

Fig. 1. View of the FG-CNTRC shallow shell with different CNT distribution patterns.

Where E_1^{cnt}, E_2^{cnt}, G_{12}^{cnt}, υ_{cnt} and ρ^{cnt} denote the carbon nanotube, elastic modulus, shear modulus, Poisson's ratio and the density, respectively. E_m, G_m, υ_m and ρ^{m} denote the corresponding properties of matrix. V_{CN} and V_m signify the volume fractions of CNTs and matrix. η_j (j = 1, 2, 3) are the CNT efficiency parameters.

B. Governing equations

A shallow shell can be defined as a slightly curved plate or a shell whose smallest radius of curvature at each point is large compared to the greatest length measured along the middle surface of the hull. The study of the vibrational behavior of low-curvature FGM shells is based on Love's equations.

To obtain the modulation equations [8], an approximate solution for the governing equations (8) is reached using the MSM multiple scales method. When ε is small but nonzero, a correction must be added to the general solution of (8). We try a correction in the form of a power series of ε.

$$\ddot{W}_{\eta\nu} + 2\mu_{\eta\nu}\dot{W}_{\eta\nu} + \omega_{\eta\nu}^2 W_{\eta\nu} + \sum_{n,m=1}^{\infty}\sum_{l,j=1}^{\infty} P_{\eta\nu nmlj} W_{nm} W_{lj} + \sum_{n,m=1}^{\infty}\sum_{l,j=1}^{\infty}\sum_{p,q=1}^{\infty}\sum_{r,s=1}^{\infty} S_{\eta\nu nmljpqrs} W_{nm} W_{pq} W_{rs} = \frac{F_{\eta\nu}}{C4} cos(\Omega t) \quad (8)$$

For the fundamental mode (n=m=1), we express the transverse displacement W_{11} in terms of different time scales as :

$$W_{11}(t,\varepsilon) = \varepsilon W_{11}^{*}(t,\varepsilon^2 t) + \varepsilon^2 W_{11}^{**}(t,\varepsilon^2 t) + \varepsilon^3 W_{11}^{***}(t,\varepsilon^2 t) + \mathrm{L} \quad (9)$$

In general, we only need the three scales to have the sufficient solution. When n, m≠1 ;

$$W_{nm}(t,\varepsilon) = \varepsilon^2 W_{nm}^{**}(t,\varepsilon^2 t) + ... \quad (10)$$

After substituting the previous equations into each other and solving the differential equations, we obtain the following equation :

$$\begin{aligned} &\frac{\partial^2 W_{11}^{***}}{\partial t^2} + \omega_{11}^2 W_{11}^{***} = 2\omega_{11} a' \sin(\omega_{11} t + \beta) + 2\omega_{11} \\ &a\beta' \cos(\omega_{11} t + \beta) + 2a^3 \omega_{11} \left\{ \sum_{i,j}^{N,M} \left(P_{11ij11} + P_{1111ij} \right) \right. \\ &\left[\frac{P_{ij1111}}{8\omega_{11}\left(\omega_{ij}^2 - 4\omega_{11}^2\right)} + \frac{P_{ij1111}}{4\omega_{11}\omega_{ij}^2} \right] - \left. \sum_{i,j}^{N,M} \frac{3S_{1111ij1111}}{8\omega_{11}} \right\} \times \\ &\cos(\omega_{11} t + \beta) + 2a\mu_{11}\omega_{11} \sin(\omega_{11} t + \beta) + f_{11} \left[\cos(\omega_{11} t + \beta) \right. \\ &\left. \cos(\sigma\varepsilon^2 t - \beta) - \sin(\omega_{11} t + \beta) \sin(\sigma\varepsilon^2 t - \beta) \right] + NST \end{aligned} \quad (11)$$

Where NST stands for secular terms. Separating the variables from (11) gives us the modulation equations :

$$2\omega_{11} a' + 2\mu_{11}\omega_{11} a - f_{11} \sin(\sigma\varepsilon^2 t - \beta) = 0 \quad (12)$$

$$2\omega_{11} a\beta' + f_{11} \cos(\sigma\varepsilon^2 t - \beta) - 2\omega_{11}\alpha_e a^3 = 0 \quad (13)$$

This can be accomplished by introducing the effective nonlinearity α_e given by :

$$\alpha_e = -\sum_{i,j}^{N,M} \left(P_{11ij11} + P_{1111ij} \right) \left[\frac{P_{ij1111}}{8\omega_{11}\left(\omega_{ij}^2 - 4\omega_{11}^2\right)} + \frac{P_{ij1111}}{4\omega_{11}\omega_{ij}^2} \right] + \sum_{i,j}^{N,M} \frac{3S_{1111ij1111}}{8\omega_{11}} \quad (14)$$

It follows from (14) that $\alpha_e \to \infty$ when $\omega_{ij} \to 2\omega_{11}$, which corresponds to an internal resonance. The natural frequencies is given by :

$$\omega_{nm} = \sqrt{\frac{A1_{nm} C1_{nm} + C2_{nm} A2_{nm}}{C4 A1_{nm}}} \quad (15)$$

The vibration behavior of low curvature shells is described by the non-dimensional natural frequency :

$$\bar{\omega} = l_x^2 \omega \sqrt{\frac{\rho h}{D*}} \tag{16}$$

C. Model validation

In order to examine the effectiveness of this method, a double validation was carried out with other studies in terms of non-dimensional frequencies. First, the results of our model were compared to those presented by Alijani et al. [13] based on the nonlinear theory of shallow shells, Chorfi and Houmat [14] which developed the theory of first order shear strain and finally with Matsunaga [15] model based on the higher order two-dimensional (2D) theory. Table I shows that the values obtained are very close to the results of Alijani et al. [13] and Matsunaga [15]. It is seen that; they are not significantly different from the results of Chorfi and Houmat [14].

After the validation of the natural frequencies results, the nonlinear frequency-response results are also compared to those obtained analytically by Amabili et al. [16], Chen and Babcock [17], and Liu et al. [18]. By considering the same mechanical and geometrical properties of Chen and Babcock [17], Fig. 2 is plotted. This Fig. shows good agreements between the present results and those available in the literature.

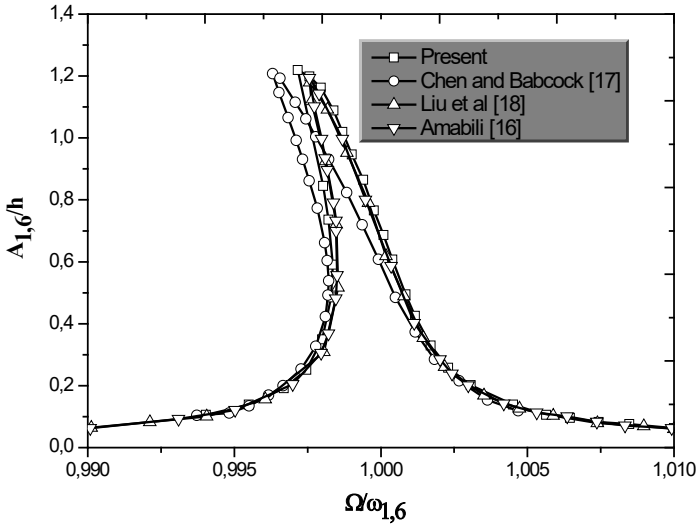


Fig. 2. Validation of the frequency–response curve with the literature results.

TABLE I

COMPARISON AMONG THE FUNDAMENTAL NATURAL OF SIMPLY SUPPORTED SQUARE Al/Al$_2$O$_3$ FG SHALLOW SHELLS (a/b=1, h/a=0.1).

	a.k$_x$	b.k$_y$	w$_{CN}$	Present	Alijani et al. [13]	Chorfi et al. [14]	Matsunaga [15]
Plate	0	0	0.0	0.05968	0.0597	0.0611	0.05777
			0.5	0.04796	0.0506	0.0519	0.04917
			1.0	0.04786	0.0456	0.0469	0.04427
			4.0	0.03677	0.0396	0.0406	0.03812
			10	0.03879	0.0380	0.0388	0.03640
Spherical	0.5	0.5	0.0	0.07582	0.0779	0.0814	0.07514
			0.5	0.06161	0.0676	0.0710	0.06570
			1.0	0.06114	0.0617	0.0649	0.06006
			4.0	0.04473	0.0519	0.0544	0.05035
			10	0.04286	0.0482	0.0502	0.04644
Cylindrical	0.5	0.0	0.0	0.06409	0.0648	0.0684	0.06224

			0.5	0.05171	0.0553	0.0588	0.05351
			1.0	0.04787	0.0501	0.0534	0.04846
			4.0	0.04473	0.0430	0.0455	0.04132
			10	0.03984	0.0408	0.0428	0.03898
Hyperbolic paraboloidal	0.5	-0.5	0.0	0.05968	0.0597	0.0678	0.05632
			0.5	0.04797	0.0506	0.0583	0.04794
			1.0	0.05263	0.0456	0.0529	0.04316
			4.0	0.03678	0.0396	0.0451	0.03717
			10	0.03879	0.0380	0.0425	0.03551

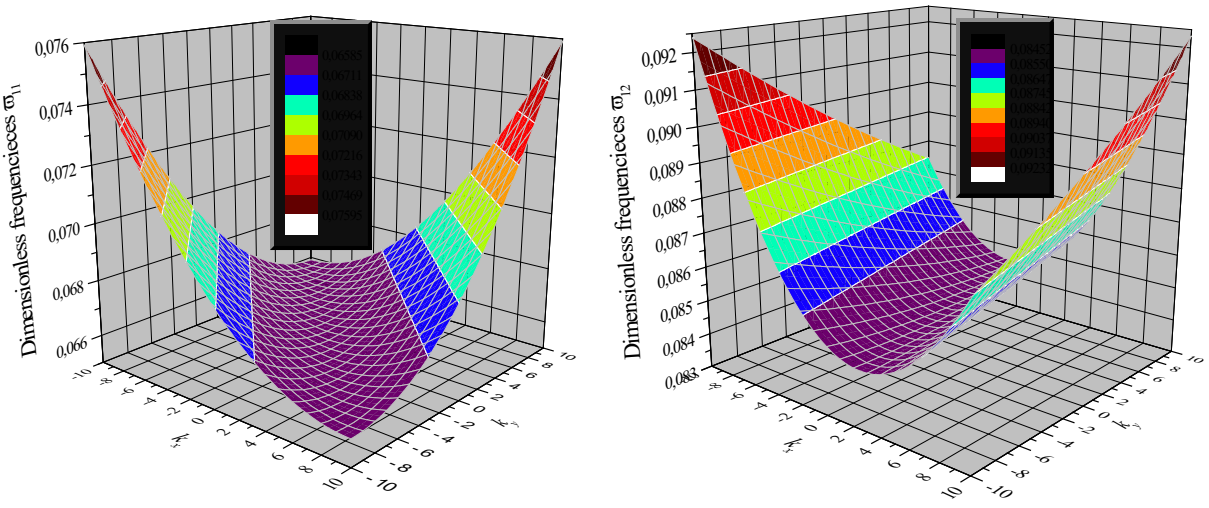
III. PARAMETRIC STUDY

In the following applications, the sallow shell is made by the poly methyl methacrylate (PMMA) matrix mixed with CNTs as fibers aligned in the axial direction [19]. PMMA is an isotropic material with E_m=2.5GPa, ρ_m=1150 kg/m^3 et υ_m=0.34. The SWCNT single-wall nanotube (10,10) are selected as reinforcements. The properties of the materials adopted for SWCNT are: $E_1^{cnt} = 5.6466$ TPa ; $E_2^{cnt} = 7.0800$ TPa ; $G_{12}^{cnt} = 1.9445$ TPa ; $\rho^{cnt} = 1400$ kg / m^3 et $\upsilon_{12}^{cnt} = 0.175$ [20], [21]. By matching the Young's modulus of and CNTRCs obtained by the extended mixing rule to those obtained by DM simulation [22] the efficiency parameter of CNT can be calculated (Table II).

Next, we used (12) and (13) to investigate the influence of the number of terms retained in the Galerkin approximation on the accuracy of the response calculated thus that the effect of the coefficients of curvatures k_x and k_y, on the dynamics behavior of simply supported shell. Where, the geometric characteristics of the single shallow shell and applied force are l_x=l_y=10 and f=10, respectively.

Table II
COMPARISON OF THE YOUNG'S MODULUS OF THE POLYMER/CNT REINFORCED BY (10,10) SWCNT AT T = 300K.

V_{CN}^*	CNTRC distribution	E_{11} (GPa)		E_{22} (GPa)	
		Han and Elliott [22]	Present	Han and Elliott [22]	Present
0.17	UD	138.9	138.680	4.9	4.899
	FG-V		140.042		4.980
	FG-Λ		137.318		4.959
	FG-X		138.680		4.971
	FG-O		138.680		4.971



(a) 1st Mode (b) 2end Mode

Fig. 3. 3D dimensionless frequencies plot for the FG-U CNTRC shallow shell with the curvatures k_x and k_y.

In Fig. 3, we show three-dimensional plots variation of the dimensionless frequencies for V^*_{CN}=0.17 and FG-U CNTRC shallow shell with the curvatures k_x and k_y. Clearly, the value of the dimensionless frequencies depends on the curvature values and the number of retained modes. For both modes, maximum values are observed for the doubly curved shallow shell; i.e, maximum k_y and minimum k_x. But minimum values are obtained when the two curvatures tend to zero (plate).

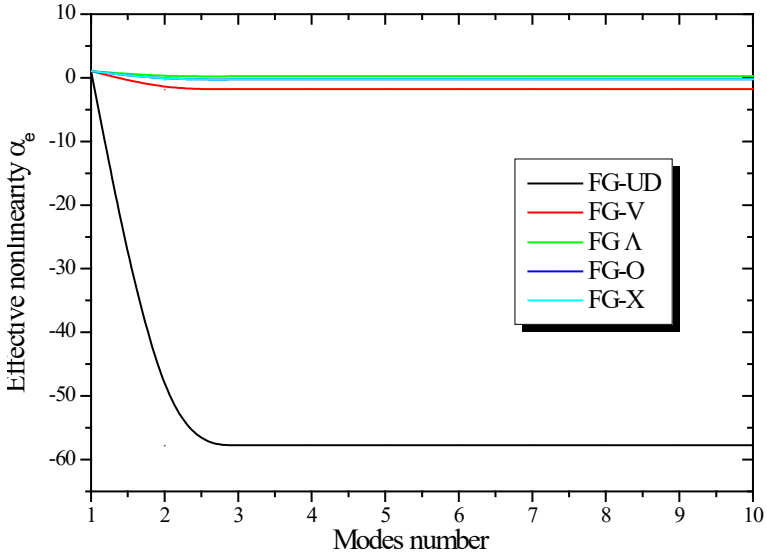
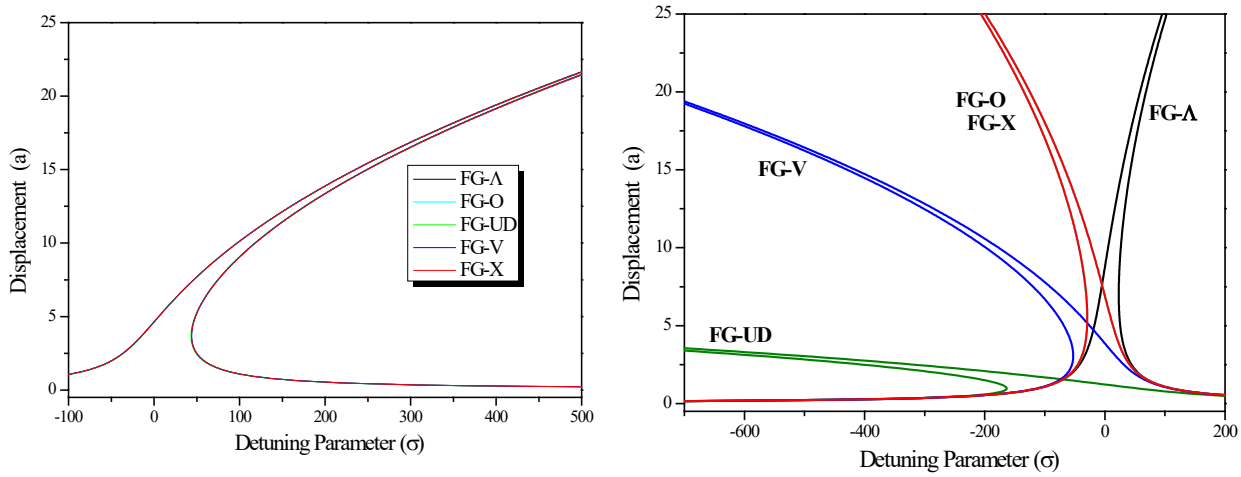


Fig. 4. The effective nonlinearity αe as a function of CNT distributions for k_x=5, k_y=0.

The results of the variation of the effective nonlinearity α_e as a function of the mode number N of the five CNT distributions (UD, V, Λ, O and X), for k_x =5, k_y =0 and V^*_{CN}=0.17 are represented in Fig. 4. We notice that the value corresponding to N = 1 ($\alpha_e \approx 1.074$) is almost the same for the five distributions studied. Increasing N from 1 to 2 results in a change of α_e from positive to negative values for all configurations (from hardening to softening) except for the CRNTC FG-Λ distribution which remains positive (Hardening).



(a) 1st Mode (b) 2end Mode

Fig. 5. Variation of the displacement versus the FG-CNTRC configuration and k_x=5, k_y=0.

Fig.5. Illustrate the variation of the frequency responses with respect to the displacement of the five FG-CNTRC distributions for the first and second modes. We notice in Fig 5a, that for a cylindrical curvature (k_x=5, k_y=0) with V^*_{CN}=0.17, fundamental modes (m = 1, n = 1) of the five considered CNT distributions, are all bent to the right with hardening nonlinearities. On the contrary, very distinctive curves are observed for the second shape mode (Fig.5b). The FG-Λ represents a hardening behavior, but, FG-O and FG-X gives softening behaviors with an important displacement. A very strongly softening is obtained for the FG-V and FG-UD distribution. For the Fig.5b, the change from the hardening to softening behavior is caused by the change of the displacement sign from the first to the second mode. This change is clearly observed for the FG-UD distribution because we have a uniform distribution of fibers. But the FG-Λ, FG-O and FG-X distributions tend to oppose changing the direction of the displacement due to the nature of the fiber's arrangement.

This time, we considered a cylindrical curvature k_x=10, k_y=0 for the volume fraction V^*_{CN}=0.17. The Fig.6. represents the variation of α_e as a function of N and the five distributions of CNT. We notice that the value α_e corresponding to N=1 is almost the same ($\alpha_e \approx 0.307$) for the five distributions studied. Increasing N from 1 to 2 results in a change of α_e from positive to negative values for CRNTC configurations FG-Λ, FG-O and FG-X. While for the CRNTC FG-UD and FG-V configurations the values of α_e are always positive (Hardening).

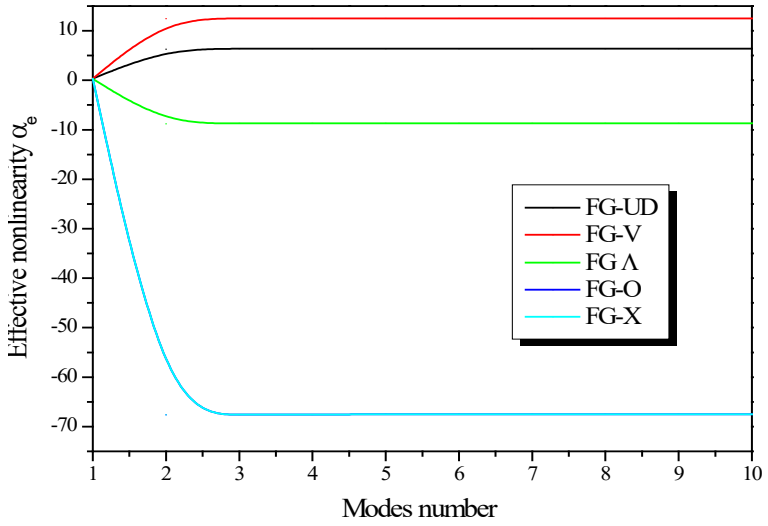
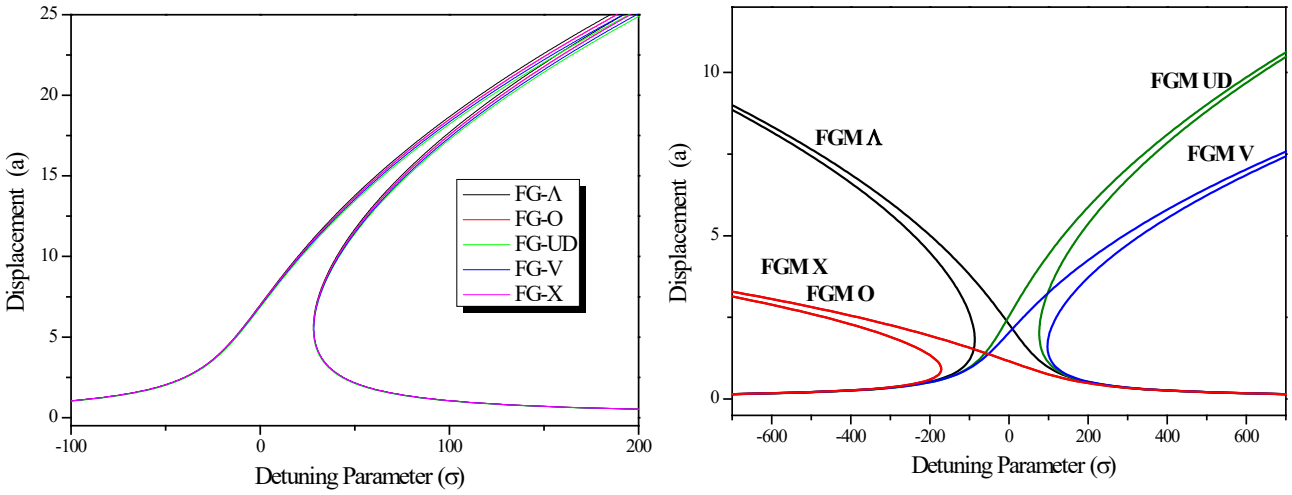


Fig. 6. The effective nonlinearity αe as a function of CNT distributions for k_x=10, k_y=0.

The variation of the frequency responses with respect to the shift of the five FG-CRNTC distributions for the first and second modes are shown in Fig. 7a and Fig.7b respectively. We notice in the Fig. 7a, that for a cylindrical curvature (k_x=10, k_y=0) with V^*_{CN}=0.17, the fundamental modes (n=1, m=1) of the five NTC distributions considered, are all oriented to the right with non-linearities of type stiffening. On the contrary, very distinctive curves which are observed for the second mode (Fig.7b), the distributions CRNTC FG-UD and FG-V represent a stiffening behavior but CRNTC FG-Λ gives a softening behavior with a significant displacement. A very strong relaxation is obtained for the CRNTC FG-O and FG-X distributions. We can see that the curves for the CRNTC FG-O and FG-X configurations are identical.



(a) 1st Mode (b) 2end Mode

Fig. 7. Variation of the displacement versus the FG-CNTRC configuration and k_x=10, k_y=0.

IV. CONCLUSION

This paper investigated the nonlinear vibration and design optimization of FG-CNT reinforced doubly-curved shallow shells using the simply supported boundary conditions. Using the Galerkin procedure, the governing dynamics equations are coupled nonlinear second order ordinary differential equations. An approximate solution of this set is then obtained by using the method of multiple scales for the case of primary resonance. Results are presented in figures and table to explore the effects of the CNT volume fraction, the CNT distribution type, and curvatures on the natural frequencies of the doubly-curved shallow shell. From this study, we can draw the following conclusions:

- The validation shows that the obtained are very close to the results of the literature.
- The three-dimensional plots have shown that the dimensionless frequencies depend on the values of the curvatures and on the number of modes retained.
- The FGΛ-CNTRC represents a hardening behavior, but, FGO-CNTRC and FGX-CNTRC gives softening behaviors with an important displacement.
- The harden and soften behavior of the shallow shell was clearly influenced by the number of modes and the different types of curvatures.

ACKNOWLEDGMENT

The authors would like to acknowledge financial support from the Algerian Ministry for Higher Education and Scientific Research (MESRS), especially the General Directorate of Scientific Research and Technological Development (DGRSDT).

REFERENCES

[1] M. Cadek, J.N. Coleman, V. Barron, K. Hedicke et W.J. Blau, "Morphological and mechanical properties of carbon-nanotube-reinforced semicrystalline and amorphous polymer composites", Applied Physics Letters, vol. 81, pp. 5123-5125, 2002.

[2] K.P. Ryan, M. Cadek, V. Nicolosi, S. Walker, M. Ruether, A. Fonseca, J.B. Nagy, W.J. Blau, and J.N.Coleman, "Multiwalled carbon nanotube nucleated crystallization and reinforcement in poly (vinyl alcohol) composites", Synthetic Metals, vol. 156, pp. 332-335, 2006.

[3] D. Qian, E.C. Dickey, R. Andrews, and T. Rantell, "Load transfer and deformation mechanisms in carbon nanotube-polystyrene composites", Applied Physics Letters, vol. 76, pp. 2868-2870, 2000.

[4] R. Haggenmueller, W. Zhou, J.E. Fischer and K.I. Winey, "Production and characterization of polymer nanocomposites with highly aligned single-walled carbon nanotubes", Journal of Nanoscience and Nanotechnology,vol. 3, pp. 105 – 110, 2003.

[5] R. Haggenmueller, F. Du, J.E. Fischer and K.I. Winey, "Interfacial in situ polymerization of single wall carbon nanotube/nylon 6, 6 nanocomposites", Polymer, vol. 47, pp. 2381-2388, 2006.

[6] G. D. Seidel and D. C. Lagoudas, "Micromechanical analysis of the effective elastic properties of carbon nanotube reinforced composites", Mechanics of Materials, vol. 38, pp. 884-907, 2006.

[7] H.S. Shen, "Nonlinear bending of functionally graded carbon nanotube-reinforced composite plates in thermal environments", Composite Structures, vol. 91, pp. 9-19, 2009.

[8] Z. Hammou, Z. Guezzen, F.Z. Zradni , Z. Sereir, A. Tounsi and Y. Hammou, "Vibration analysis and optimization of functionally graded carbon nanotube reinforced doubly-curved shallow shells", Steel and Composite Structures, vol. 44, No. 2, pp. 141-155, 2022.

[9] Z. Wu, Y. Zhang and G. Yao, "Nonlinear forced vibration of functionally graded carbon nanotube reinforced composite circular cylindrical shells", Acta Mech, vol. 231, pp. 2497-2519, 2020. http://dx.doi.org/10.1007/s00707-020-02650-6.

[10] H. Nayfeh, "Perturbation Methods", Wiley, New York, 1973.

[11] H.S. Shen, "Nonlinear bending of functionally graded carbon nanotube reinforced composite plates in thermal environments ", Compos Struct, vol. 91 (1), pp. 9-19, 2009. https://doi.org/10.1016/j.compstruct.2009.04.026.

[12] A. Farrokhian and R. Kolahchi, "Frequency and instability responses in nanocomposite plate assuming different distribution of CNTs", Structural Engineering and Mechanics, vol. 73(5), pp. 555-563, 2020. https://doi.org/10.12989/sem.2020.73.5.555.

[13] F. Alijani, M. Amabili, K. Karagiozis and F. Bakhtiari-Nejad, "Nonlinear vibrations of functionally graded doubly curved shallow shells", Journal of Sound and Vibration, vol. 330, pp. 1432-1454, 2011. https://doi.org/10.1016/j.jsv.2010.10.003.

[14] S. M. Chorfi and A. Houmat, "Non-linear free vibration of a functionally graded doubly-curved shallow shell of elliptical plan-form", Composite Structures, vol. 92, pp. 2573-2581, 2010. https://doi.org/10.1016/j.compstruct.2010.02.001.

[15] H. Matsunaga, "Free vibration and stability of functionally graded shallow shells according to a 2D higher-order deformation theory", Composite Structures, vol. 84, pp. 132-146, 2008. https://doi.org/10.1016/j.compstruct.2007.07.006.

[16] M. Amabili, F. Pellicano, M.P. Paidoussis, "Nonlinear vibrations of simply supported, circular cylindrical shells, coupled to quiescent fluid", J. Fluids. Struct., vol. 12, pp. 883-918, 1998. https://doi.org/10.1006/jfls.1998.0173.

[17] J.C. Chen, C.D. Babcock, "Non-linear vibration of cylindrical shells", AIAA J, vol. 13, pp. 868-876, 1975. https://doi.org/10.2514/3.60462.

[18] Y. Liu, Z. Qin, and F. Chu, "Nonlinear forced vibrations of functionally graded piezoelectric cylindrical shells under electric-thermo-mechanical loads", Int. J. Mech. Sci., vol. 201, pp. 106474,2021. https://doi:10.1016/j.ijmecsci.2021.106474.

[19] M.D. Rasool, F. Mehrdad and P. Aminallah, "Dynamic analysis of functionally graded nanocomposite cylinders reinforced by carbon nanotube by a mesh-free method", Materials and Design, vol. 44, pp. 256-266, 2013. https://doi.org/10.1016/j.matdes.2012.07.069.

[20] H.S. Shen, "Nonlinear bending of functionally graded carbon nanotube reinforced composite plates in thermal environments", Compos Struct, vol. 91 (1), pp. 9-19, 2009. https://doi.org/10.1016/j.compstruct.2009.04.026.

[21] H-S. Shen and Y. Xiang, (), "Nonlinear vibration of nanotube-reinforced composite cylindrical panels resting on elastic foundations in thermal environments", Composite Structures, vol. 111, pp. 291–300, 2014. https://doi.org/10.1016/j.compstruct.2014.01.010.

[22] Y. Han, J. Elliott, "Molecular dynamics simulations of the elastic properties of polymer/carbon nanotube composites", Comput Mater Sci, vol. 39, pp. 315–23, 2007.

A Case Study: Metallurgical Examination of Material Technical Requirements for M-50 Bearings in the Aerospace Industry

Nisa Yağmur Eren[*,1,2], Mehmet Erdoğan[3], Emrah Yalınız[2], Erdi Seçkin Habi[2]

nisayagmur.eren@tai.com.tr, ORCID: 0000-0001-5908-3814
[1]*Graduate School of Natural and Applied Sciences, Gazi University, Ankara, Turkey*
[2]*Special Processes Development and Verification Department, Helicopter Executive Vice Presidency, Turkish Aerospace Inc., Ankara, Turkey*
[3]*Department of Metallurgy and Materials Engineering, Gazi University, Ankara, Turkey*

Abstract: By means of microstructural observation, macro/microhardness, hardness profile and retained austenite tests were used to investigate the microstructure and mechanical properties of aerospace standard M50 bearing steel for ring and roller parts. The microstructural observation shows that the size of the carbides observed in the microstructure was found to average 6.18 microns in roller sample and 10.93 microns in ring sample. The results show that the general matrix structure is based mainly on tempered martensite with carbide alloys consisting of Mo, V and Cr carbides and a small amount of retained austenite. The mechanical characterization indicates that on average of the macrohardness value for the ring is 62.4 HRc while for the roller it is 61.3 HRc, on average of the microhardness value for the ring is 813.5 HV while for the roller it is 794 HV, respectively. The measurement results for roller hardness profile, the highest measurement is 826 HV and the lowest measurement is 769 HV. The measurement results for the ring hardness profile, the highest measurement is 845 HV and the lowest measurement is 761 HV. Microstructure analysis indicates that the maximum fraction of retained austenite in the specimen is 0.47 %. Taking the standard deviation as 0.15, the total range of retained austenite value is 0.32-0.59%. There is a consistent correlation between the results of the study and the data found in the literature.

Keywords: *M50, Bearing, Carbides, Microstructure, Hardness, Retained Austenite*

I. INTRODUCTION

Gas turbine engines in aircraft and bearings used in power transmission systems are one of the key components in the smooth operation of mechanical equipment. Bearings must meet technical requirements such as the requirement to operate at high speeds (approximately 2.4 million dN) relatively high temperature capability, aggressive lubrication conditions and a strength [1]- [4].

To meet the demands of higher operating temperatures, a family of molybdenum-based tool steels such as AISI M50 (AMS 6491) was introduced in the 1960s. Still today, through hardening M50 material is aerospace bearing steel used mainly for higher temperature applications [5], [6].

M50 steel is a molybdenum-based high temperature bearing steel and has extensive properties, including excellent high temperature hardness, high dimensional stability, excellent contact fatigue performance, good wear resistance and contact fatigue life. Due to these properties, it is widely used as the main production material for the main shaft bearings of engines in the aerospace industry and its related sectors [2], [7]-[9].

To ensure its dimensional stability at high temperatures (reaching about 300 ◦C), M50 steel

has traditionally been subjected to martensitic quenching followed by high temperature tempering (Q-T) to completely remove the retained austenite (RA). Thus, the microstructure consists mainly of tempered martensite, carbides, and a very small amount of retained austenite [3], [7], [8], [10].

The excellent performance expected from bearings is closely related to the bearing material. Considering the alloys and carbides found in M50 steel, it contains a large amount of alloying elements such as Cr, Mo and V elements, which are highly dependent on the secondary hardening effect of high temperature tempering. Therefore, carbides containing these alloys are formed in the structure [11]-[14].

In previous studies in the literature, results regarding the technical requirements of hardness and retained austenite were encountered. For example, in some sources, considering the operating temperature, the bearing hardness degree is specified that minimum hardness of Rockwell C 58 [15], [16]. In another study, it was stated that it can be hardened up to 60–64 HRC through the formation of finely dispersed carbide particles during tempering cycles at secondary hardening temperatures of 500–550 ◦C [17], Similarly, in another study, the hardness range at room temperature was shared as 60-63 HRC [10].

Another metallurgical technical requirement was determined as the residual austenite amount. Generally, it is known that during operation of a bearing, it causes dimensional instability and transforms into martensite under Hertz cycle stress conditions, even under no-load conditions. For this reason, it is stated in a National Aeronautics and Space Administration (NASA) source that 2-5 percent residual austenite is preferred especially in aviation bearing and gear applications. However, it has been emphasized that providing this technical hysteria with even lower residual austenite amount in critical applications will increase the reliability of the system [18]. Another bearing manufacturer shared the information that the residual austenite amount is kept at a maximum of 3 percent with the applied heat treatments [19].

The aim of present work is to obtain metallurgical data on ring and roller parts with M-50 material of an industrial bearing already used on a helicopter platform. Hardness, retained austenite and microstructure information of the specimens belonging to ring and roller components were examined. A comparison was made between the results obtained after the examination and the results in the literature. As the output of this study, metallurgical information about the M-50 material on an industrial basis for the aerospace sector was shared and technical requirements were clearly understood.

II. MATERIALS AND METHODOLOGY

The both ring and roller material cut in this study were M50 steel (AMS 6491). The percent weight information of the M50 chemical composition obtained from the supplier company are taken from Certificate of Conformity (CoC). The specific chemical composition was shown in Table I.

TABLE I.
THE SPESIFIC CHEMICAL COMPOSITION OF RING AND ROLLER MATERIAL

Element	C	Si	Mn	S	P	W	Cr	V	Ni	Mo	Co	Cu
Ring round bar (wt. %)	.83	.19	.23	.002	.005	.01	4.15	1.00	.08	4.31	.01	.06
Rollers round bar (wt. %)	.83	.20	.24	.001	.005	.01	4.14	1.00	.07	4.27	.01	.07

The test samples used in this study are Ø 40 x 11 mm in size. Figure 1 shows the schematic representation of the three main steps applied to obtain the samples to be examined.

First step: The bearing to be examined was divided into four parts by Electrical discharge

machining (EDM).

Second step: One of the the ring and roller are reserved for use.

Third step: The last step included sectioning, bakelite mounting, grinding and final polishing were carried out and the samples were etched in 3 vol.% nital solution for the phase characterization.

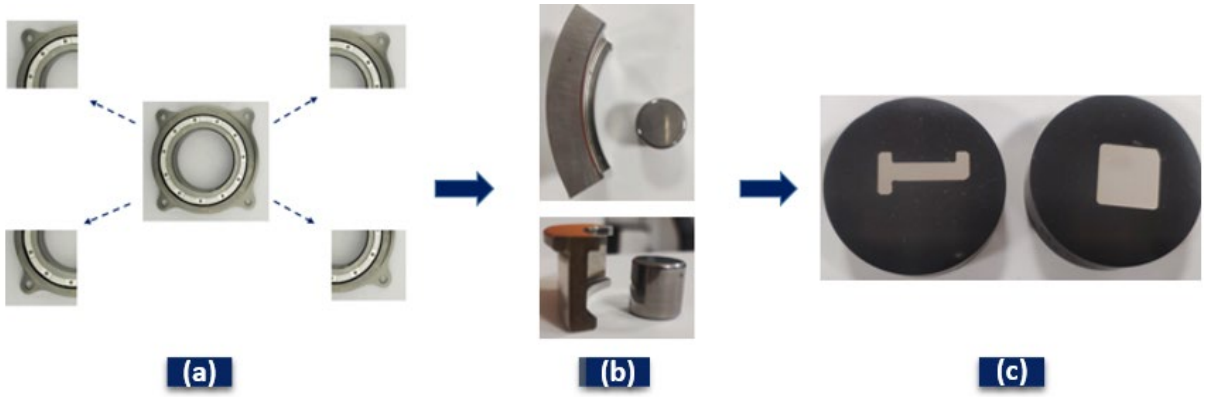


Fig. 1. The steps to obtain the samples (a) illustration of bearing divided into four parts (b) Top and side view of ring and roller parts (c) bakelite mounted samples

Optical microscope (OM) and field-emission scanning electron microscope (SEM) were used to observe the microstructure of the ring and roller. At the same time, element distribution maps were performed to analyze the main components in the samples by Energy dispersive x-ray spectroscopy (EDS) using the EDX detector on the SEM and to show the distribution of an element of interest on the sample.

The macrohardness test was carried out with a Rockwell hardness tester via method of Rockwell Superficial Hardness HR15N. The microhardness test and hardness profile of samples was carried out with Vickers hardness tester via method of HV 0,5 kg. As an output, in the both macrohardness and microhardness measurement, 2 points are taken on each sample, and the hardness value is the average value of the 2 points.

Furthermore, in order to scan the entire cross-section for the microhardness profile examination of the sample of the roller, 14 measurements were carried out in two series of plus 1 mm intervals. For the microhardness profile examination, three serial measurements were taken, in which the section thickness changed, in order to scan the entire section of the ring sample. Measurements were taken from 13 points in series 1, 8 points in series 2, and finally 19 points in series 3 with 0.5 mm intervals.

X-ray diffraction (XRD) method was employed to determine the volume fraction of retained austenite. Calculating principle is based on observing the scattered intensity of an X-ray beam hitting a sample as a function of incident and scattered angle, polarization, and wavelength or energy.

III. RESULTS AND DISCUSSION

A. Microstructural Observation

The microstructures of M50 steel ring under Optic Microscope are shown in Fig. 2(a)-(d). It is seen that the white structures in the microstructure are carbide. Additionally, as can be seen in Fig. 2(a)-(d), carbides are distributed in different shapes and sizes within the matrix structure.

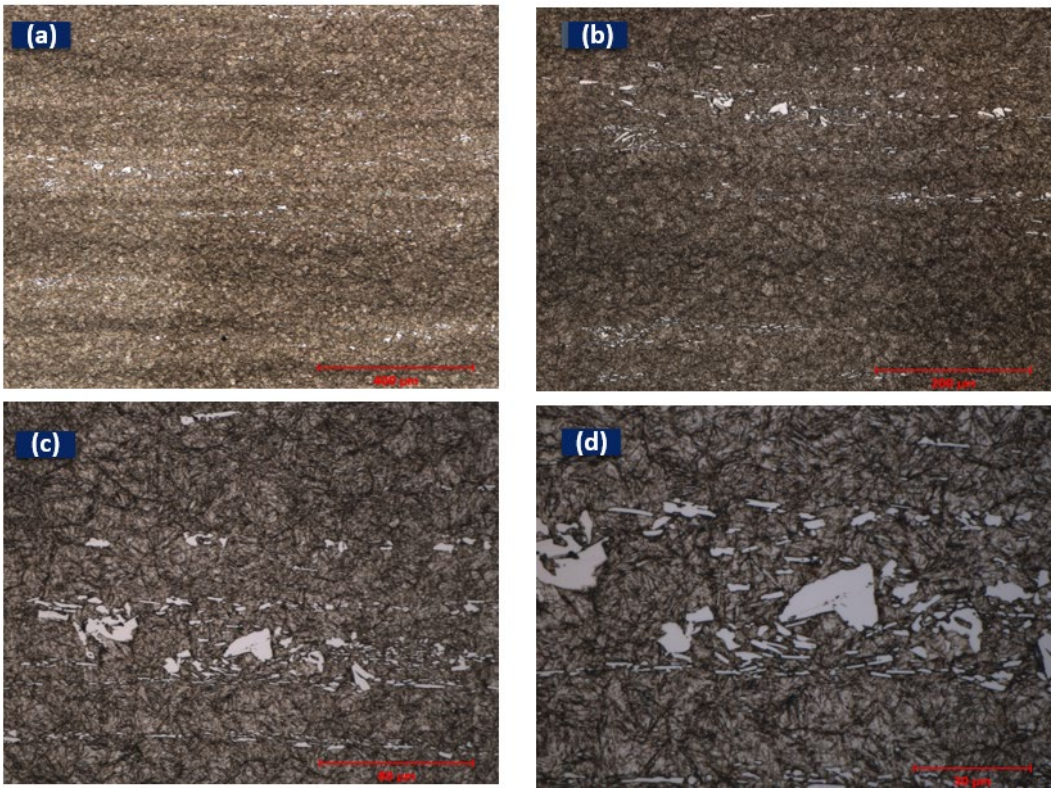


Fig. 2. Microstructure images of the ring sample at different magnifications (a) 100x, (b) 200x, (c) 500x, (d) 1000x

Fig. 3(a)-(d) show the microstructure of the M-50 steel of the roller specimen. Similar to the ring sample, it is seen that the white structures in the microstructure are carbide. As can be seen in Figures 3(a)-(d), the carbides are distributed in the matrix structure with different sizes, similar to the findings in the ring sample, but more uniformly.

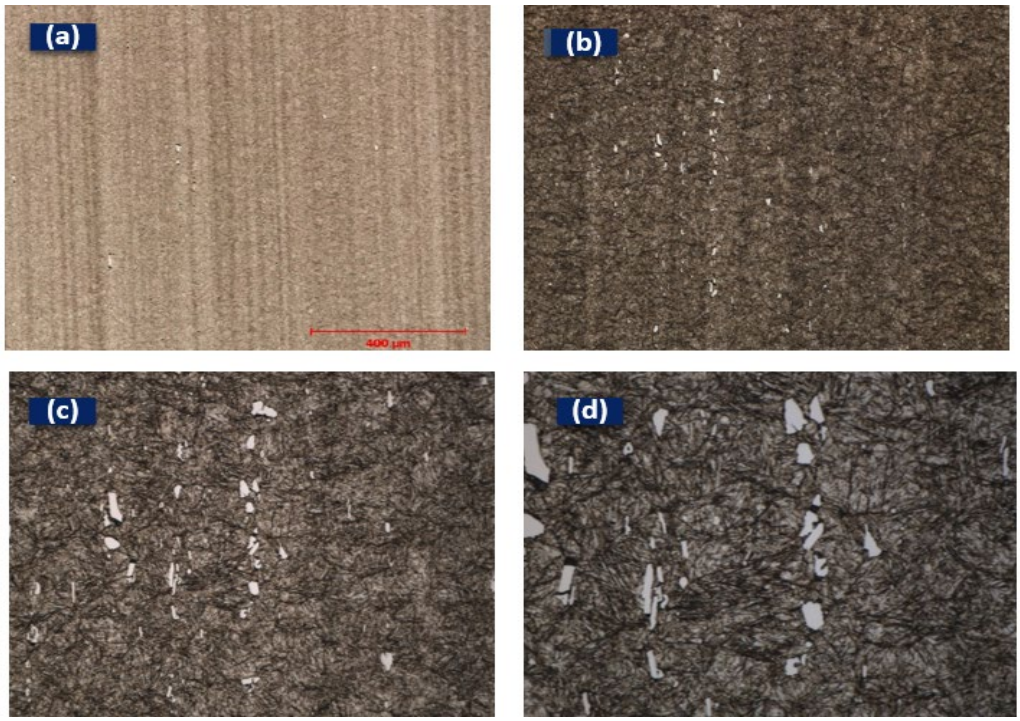


Fig. 3. Microstructure images of the roller sample at different magnifications (a) 100x, (b) 200x, (c) 500x, (d) 1000x

Fig. 4(a) shows the SEM image of the roller sample. A maximum carbide size of 11.7 microns was measured in the microstructure. Carbide sizes of the roller sample are generally below 10 microns. Fig. 4(b) shows the SEM image of the ring sample. A maximum carbide size of 19.7 microns was measured in the microstructure. Generally, the measurement results of the ring sample show that the carbide size is above 10 microns.

Figure 4(c) shows the size measurement and approximate average of eight randomly selected carbides. The average carbide size of the roller sample is 6.18 microns and the average carbide size of the ring sample is 10.93 microns. The bar graph also shows that the average carbide size for the roller sample is smaller than that of the ring sample.

Fig. 4(d) shows the EDS mapping of a sample within the microstructure. The overall matrix structure is mainly based on tempered martensite (Fe), which is purple in color. While large carbides appear to be Mo-based (blue color), some carbides appear to be V-based (yellow) and Cr-based (green). As a result, the carbide alloys consist of Mo, V, and Cr carbides.

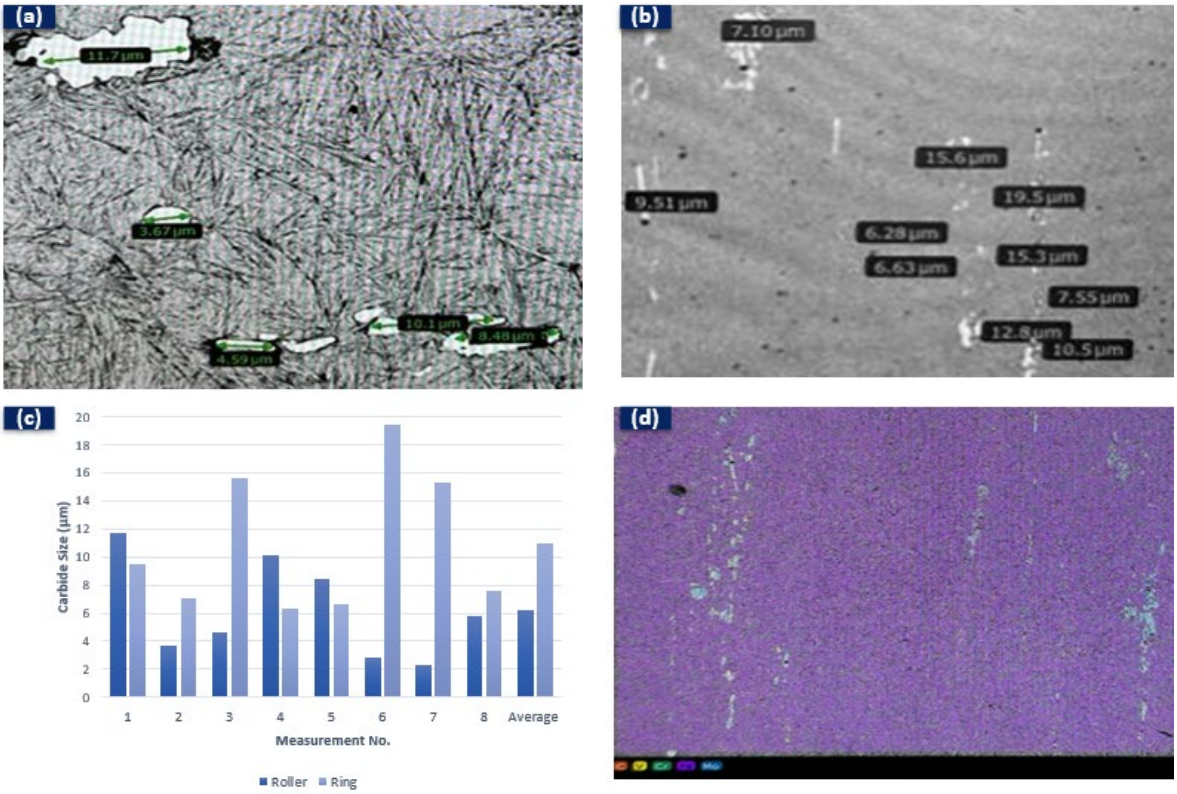


Fig .4. SEM results (a) carbide image of roller specimen (b) carbide image of ring specimen (c) Measured carbide sizes for ring and roller samples (d) The image of EDS mapping

B. Macro/Microhardness and Hardness Profile

Fig. 5(a) shows the Rockwell hardness results of the ring and roller specimens. All values for ring and roller specimens are higher than 61 HRc. On average, the macro hardness value for the ring is 62.4 HRc while for the roller it is 61.3 HRc.

Fig. 5(b) shows the Vickers hardness results of the ring and roller specimens. All values for ring and roller specimens are higher than 794 HV. On average, the microhardness value for the ring is 813.5 HV while for the cylinder it is 794 HV.

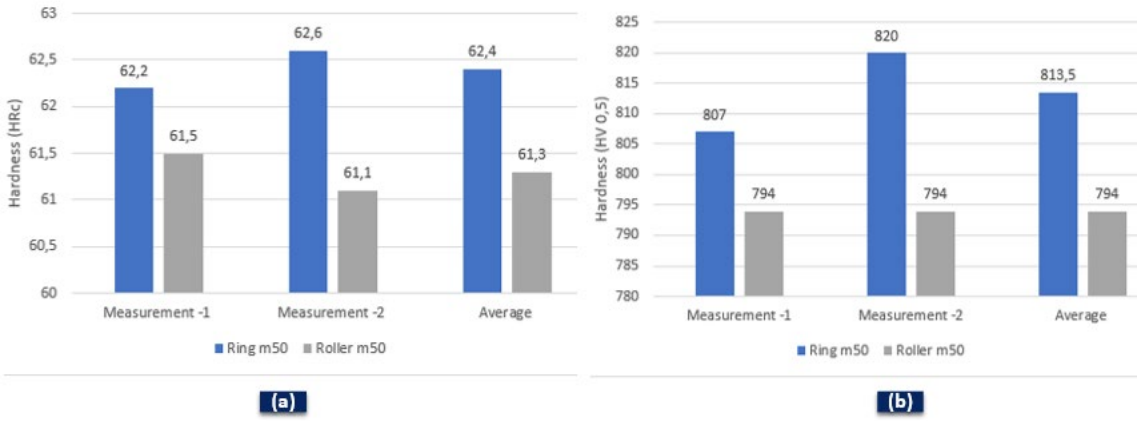


Fig. 5. Macrohardness and microhardness measurement results (a) Macrohardness Measurement (HR15N) (b) Microhardness Measurement (HV 0,5)

Fig. 6(a) shows the hardness profile path two series of the roller sample. The measurements in the two series show similar behavior and results. In Fig. 6(b) considering the measurement results of both series, the highest measurement is 826 HV and the lowest is 769 HV.

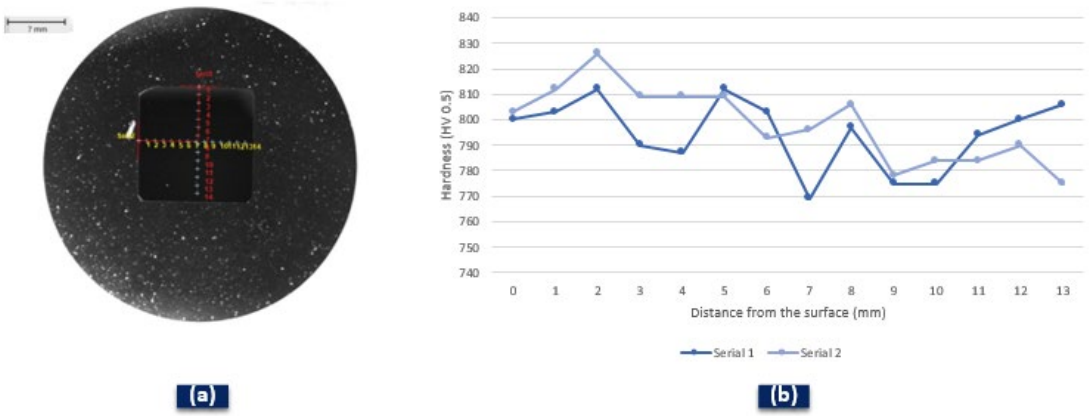


Fig. 6. Hardness profile of roller sample (a) two hardness profile series paths demonstration (b) the results of the two hardness profiles

Fig. 7(a) shows the hardness profile path three series of the ring sample. The measurements in the three series show similar behavior and results. In Fig. 7(b) considering the measurement results of the three series, the highest measurement is 845 HV and the lowest measurement is 761 HV.

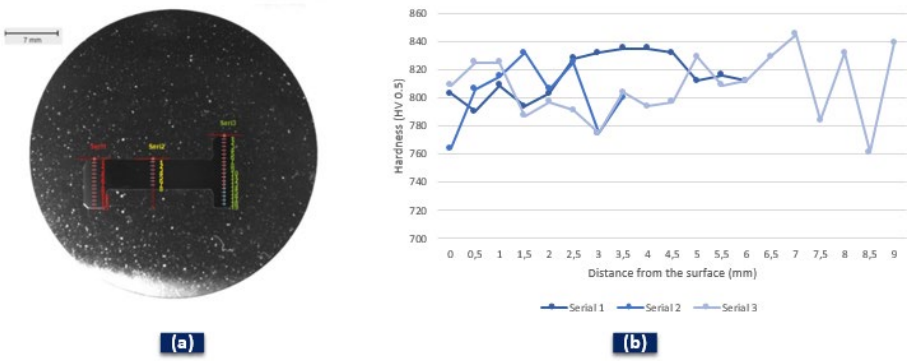


Fig. 7. Hardness profile of the ring sample (a) three hardness profile series paths demonstration (b) the results of the three hardness profiles

C. Retained Austenite

In this study the (200) α, (211) α, (220) γ and (200) γ peaks and their integrated intensities (I_α^{200}, I_α^{211}, I_γ^{220}, and I_γ^{200}) is calculated for the definition of the phases obtained. Software was used to determine the integrated intensities from the XRD patterns by calculating the area under the X-ray diffraction peaks. Integrated intensities and volume fractions of the RA result obtained as shown in Table X. As can be seen from Table X, the retained austenite value is measured as 0.47 percent by volume. Taking the standard deviation as 0.15, the overall range of the retained austenite value is 0.32-0.59 % .

TABLE II.
INTEGRATED INTENSITIES AND THE VOLUME FRACTIONS OF RETAINED AUSTENITE OBTAINED

I_α^{211}	I_γ^{220}	I_α^{200}	I_γ^{200}	V_α	RA. % Vol.	Standard Deviation
201.36	57.64	22.07	38.21	0.0047	0.47	0.15

The following table compares the data obtained from the study with that reported in the literature. According to the data in Table X, a consistent correlation exists between the results of the study and those found in the literature.

TABLE III.
COMPARISON TABLE OF THE RESULTS OF THE STUDY AND THE RESULTS FOUND IN THE LITERATURE

#	Source No.	Data in the Literature	Results of the Study
Microstructure	[3], [7], [8], [10]	The microstructure consists mainly of tempered martensite, carbides, and a very small amount of RA.	The general matrix structure is based mainly on tempered martensite with carbide alloys consisting of Mo, V and Cr carbides and a small amount of retained austenite.
Hardness	[15], [16], [17] [10],	min. Rockwell C 58 60–64 HRC 60-63 HRC	On average, the macrohardness value for the ring is 62.4 HRc while for the roller it is 61.3 HRc.
Retained Austenite	[18] [19]	2-5 % max. 3 %	The RA value is measured as 0.47 percent by volume. Taking the standard deviation as 0.15, the overall range of the retained austenite value is 0.32-0.59 % .

IV. CONCLUSION

In this study, the microstructural evaluation and mechanical properties of roller and ring final components made of M-50 steel has been investigated. The corresponding conclusions can be drawn as follows:

1) The size of the carbides observed in the microstructure was found to be 6.18 microns on average in roller samples and 10.93 microns in ring samples. Hence the average carbide size for the roller sample is smaller than that of the ring sample. The general matrix structure is based mainly on tempered martensite with carbide alloys consisting of Mo, V and Cr carbides and a small amount of retained austenite.
2) On average, the macrohardness value for the ring is 62.4 HRc while for the roller it is 61.3 HRc. On average, the microhardness value for the ring is 813.5 HV while for the roller it is 794 HV. Ring sample hardness is slightly higher than roller sample hardness.
3) Considering the measurement results for roller hardness profile, the highest measurement

is 826 HV and the lowest is 769 HV. The measurement results for ring hardness profile, the highest measurement is 845 HV and the lowest measurement is 761 HV.

4) The maximum fraction of retained austenite in the specimen is 0.47 %.

DECLARATION OF COMPETING INTEREST

The authors declare that they have no known competing financial interests or personal relationships that could have appeared to influence the work reported in this paper.

ACKNOWLEDGMENT

The opinions, interpretations, recommendations and conclusions are those of the authors.

REFERENCES

[1] T. &. K. M. Harris, "Chapter 13, Structural Materials of Bearings," in *Essential Concepts of Bearing Technology (5th ed.)*, CRC Press, https://doi.org/10.1201/9781420006599, 2006.

[2] S. Ooi and H. K. D. H. Bhadeshia, "Duplex Hardening of Steels for Aeroengine Bearings," in *ISIJ International*, 2012, Volume 52, Issue 11, Pages 1927-1934, https://doi.org/10.2355/isijinternational.52.1927.

[3] X. Yu, Y. Wei, . D. Zheng,, X. Shen, Y. Su, . Y. Xia and Y. Liu, "Effect of nano-bainite microstructure and residual stress on friction properties of M50 bearing steel," *Tribology International,* vol. 165, 2022, 107285, https://doi.org/10.1016/j.triboint.2021.107285..

[4] P. Gloeckner and C. Rodway, "The Evolution of Reliability and Efficiency of Aerospace Bearing Systems," *Engineering,* Vols. 9, No. 11, pp. 962-991, 2017 https://doi.org/10.4236/eng.2017.911058.

[5] C. A. K. Reddy, B. N. Rao and T. Srinivasan, "A review on heat treated bearing steels for aerospace applications," *Materials Today: Proceedings,* Vols. 68, , no. Part 6, pp. 2038-2040, 2022, ISSN 2214-7853, https://doi.org/10.1016/j.matpr.2022.08.356..

[6] F.-J. Ebert, "An Overview of Performance Characteristics, Experiences and Trends of Aerospace Engine Bearings Technologies," *Chinese Journal of Aeronautics,* vol. 20, no. 4, pp. 378-384, 2007, ISSN 1000-9361, https://doi.org/10.1016/S1000-9361(07)60058-2..

[7] F. Wang, Q. Sun, H. Ren , N. Cao, X. Song, S. Deng, D. Qian and M. Wu, "A novel quenching-electroshocking-tempering process for toughness improvement by microstructure refining and austenite stability tailoring in aviation bearing steel," *Materials Science and Engineering: A,* vol. 854, p. 143817, 2022 https://doi.org/10.1016/j.msea.2022.143817.

[8] F. Wang, Y. Du, D. Qian, N. Cao, L. Hua and M. Wu, "A novel route to improve the fatigue properties of aviation M50 steel via tailoring the bainite content and cold deformation," *Journal of Materials Research and Technology,* vol. 18, pp. 3857-3871, 2022, https://doi.org/10.1016/j.jmrt.2022.04.068.

[9] Y. Wei, X. Yu, Y. Su, X. Shen, Y. Xia and W. Yang, "Effect of residual stress and microstructure evolution on size stability of M50 bearing steel," *Journal of Materials Research and Technology,* Vols. 651-661, pp. 651-661, 2021 https://doi.org/10.1016/j.jmrt.2020.12.060.

[10] Y. Su, S. Yang, X. Yu, C. Zhou, Y. Liu, X. Feng, Q. Zhao, and J. Wu, "Effect of Austempering Temperature on Microstructure and Mechanical Properties of M50 Bearing

Steel," *Journal of Materials Research and Technology,* vol. 20, pp. 4576-4584, 2022, https://doi.org/10.1016/j.jmrt.2022.09.002.

[11] J. Guan, L. Wang, Z. Zhang, X. S. Shi and X. Ma, "Fatigue crack nucleation and propagation at clustered metallic carbides in M50 bearing steel," *Tribology International,* vol. 119, pp. 165-174, 2018, https://doi.org/10.1016/j.triboint.2017.10.016.

[12] N. Du, H. Liu, Y. Cao, P. Fu, C. Sun, H. Liu and D. Li, "Formation mechanism of MC and M2C primary carbides in as-cast M50 bearing steel," *Materials Characterization,* vol. 174, p. 111011, 2021, https://doi.org/10.1016/j.matchar.2021.111011.

[13] P. Wang, H. Guo, D. Wang, H. Duan, and Y. Zhang, "Microstructure and tribological performances of M50 bearing steel processed by ultrasonic surface rolling," *Tribology International,* vol. 175, p. 107818, 2022, https://doi.org/10.1016/j.triboint.2022.107818.

[14] L. Yang, W. Xue, S. Gao, H. Liu, Y. Cao, D. Duan, D. Li and S. Li, "Study on sliding friction and wear behavior of M50 bearing steel with rare earth addition," *Tribology International,* vol. 174, p. 107725, 2022, https://doi.org/10.1016/j.triboint.2022.107725.

[15] E. V. Zaretsky , "Rolling bearing steels – a technical and historical perspective," *Materials Science and Technology,* pp. 58-69, 2012, https://doi.org/10.1179/1743284711Y.0000000043.

[16] T. A. Harris, M. A. Ragen and R. F. Spitze, "The Effect of Hoop and Material Residual Stresses on the Fatigue Life of High Speed, Rolling Bearings," *Tribology Transactions,* pp. 194-198, 1992, https://doi.org/10.1080/10402009208982109.

[17] J. Yao, F. Yan, B. Chen, Y. Yang, Y. Xu, . M. Yan and Y. Zhang, "Dual-strengthening of steel surface and bulk via synergistic effect of plasma nitriding: A case study of M50 steel," *Surface and Coatings Technology,* vol. 409, p. 126910, 2021, https://doi.org/10.1016/j.surfcoat.2021.126910.

[18] E. V. Zaretsky, "Bearing and gear steels for aerospace applications," NASA Lewis Research Center Cleveland, OH, United States, 1990.

[19] TIMKEN, "Aerospace Design Guide," [Online]. Available: https://www.timken.com/resources/aerospace-design-guide-for-precision-metric-ball-and-cylindrical-roller-bearings/. [Accessed 27 August 2023].

Evaluating the Influence of Concrete Grade on the Performance of Reinforced Concrete Structures through Incremental Dynamic Analysis

İbrahim Baran KARAŞİN

baran.karasin@dicle.edu.tr, ORCID: 0000-0001-5990-1215
Department of Construction Technology, Diyarbakir, Vocational School of Technical Sciences, Dicle University,
Diyarbakır, Turkey

Abstract: The design of earthquake resistant structures is becoming increasingly important with the increasing number of devastating earthquake events. Earthquake is a natural phenomenon that occurs as a result of geological movements and can turn into a natural disaster depending on the behavior of the structures under the influence of this event. This study attempts to evaluate the performance levels of reinforced concrete structures depending on the class of concrete used. In particular, this research investigates the interaction between concrete class and structural behaviour in seismic events. To achieve this objective, the Incremental Dynamic Analysis (IDA) method is used, which provides a dynamic approach to evaluate the seismic performance of structures. The methodology involves subjecting a standardized 4-storey prototype building to IDA considering 2 different concrete classes for construction. This approach aims to demonstrate how different concrete grades affect the structural response under seismic loading. Storey drift limits are important parameters for assessing the resilience of buildings against earthquake loads. In this context, Hazus inter-storey drift ratio limit values are reasonably used as benchmarks to evaluate the structural behaviour. These predefined criteria provide a basic framework within which the structural integrity and performance of the structures under study are assessed. Thus, this study effectively emphasizes the concrete impact of concrete class on the overall performance of reinforced concrete structures.

Keywords: *Reinforced Concrete Structures; Concrete Grade; Dynamic Analysis*

I. INTRODUCTION

The imperative for designing earthquake-resistant structures has been accentuated in recent years owing to the escalating frequency of devastating seismic events. Earthquakes, inherently natural phenomena borne from geological forces, possess the potential to transform into catastrophic disasters contingent upon the response of constructed structures. The behavior of these structures during seismic events assumes paramount significance in mitigating the ensuing devastation.

When designing reinforced concrete buildings to withstand earthquakes, the main priorities are achieving sufficient stiffness, strength, and ductility. After an earthquake, damage to these structures is mostly caused by the strength of the materials used. As material strength increases, so does the stiffness of the building [1]. The most common culprit of damage to reinforced concrete buildings is earthquakes. Recent earthquakes have demonstrated that these structures can suffer damage due to various reasons after a moderate or severe seismic event, particularly if they were not designed and constructed with adequate care [2,3].

The likelihood of damage to such buildings depends on the magnitude of the earthquake.

This study aims to evaluate how different types of concrete affect the performance of reinforced concrete structures during seismic events. It focuses on the interaction between the grade of concrete and the structural behavior. The study uses the Incremental Dynamic Analysis (IDA) method to analyze the seismic performance of a standardized 4-storey prototype building constructed with two different classes of concrete. The goal is to uncover how the choice of concrete grades impacts the structural response under seismic loading.

The IDA analysis uses ground motion record from Kocaeli,1999 earthquake by using SeismoStruct software [4] to simulate the impact of earthquakes on buildings. These records are selected to represent a range of ground motion intensities and frequencies that structures may encounter in real-life seismic hazards. During the IDA procedure, the building is subjected to a series of ground motions that gradually increase in intensity. Nonlinear dynamic analysis is used to examine the building's response to each motion record. The primary output of this analysis is the inter-storey drift ratios, which are an important indicator of the building's performance during earthquakes. To evaluate the building's structural integrity and safety under seismic loading, predefined criteria known as Hazus inter-storey drift ratio limit values are used. These criteria are widely accepted in the field of seismic engineering and serve as benchmarks for assessing the building's performance. The results of the IDA analysis are analyzed and interpreted using statistical methods and comparative analyses. The focus is on identifying patterns and trends in the building's response, with a particular emphasis on the impact of the concrete class.

The study assesses the earthquake resistance of the structure using storey drift limits as a pivotal metric. The Hazus inter-storey drift ratio limits are used as benchmarks to measure structural behavior. These predefined criteria provide a foundational framework for evaluating the structural integrity and performance of the investigated structures.

II. MANUSCRIPT CONTENT

A. Incremental Dynamic Analysis (IDA)

In this study, the Incremental Dynamic Analysis (IDA) method to assess the seismic performance of a standardized 4-storey prototype building. IDA is a well-established dynamic analysis technique in earthquake engineering that allows for a comprehensive evaluation of a structure's performance under varying levels of ground motion intensity. It provides valuable insights into a structure's capacity and vulnerability across a range of seismic demands [5].

To investigate how concrete class affects structural behavior, we consider two different types: C20 and C25. These types represent a range of material properties commonly used in construction. Incremental dynamic analysis scales every earthquake record data in a row until the structure collapses [6,7].

IDA refers to a series of dynamic nonlinear analyses that are conducted using a scaled acceleration record. The selected intensity measures (IMs) cover the entire range from elastic to nonlinear and ultimately to the collapse of the structure. The objective is to record the damage measures (DMs) of the structural model at each IM level of the scaled ground motion. These values are then plotted as continuous curves that usually correspond to the intensity level (IM).

It is standard engineering practice for these graphs to appear "upside down" since the independent variable is the IM, which is likened to "force" and plotted on the vertical axis, similar to stress-strain, force-deformation, or static thrust analysis graphs. The results of an IDA study can be presented in various IDA curves, depending on the choice of IMs and DMs.

B. Description of Sample Building

The geometric and material properties for the mentioned building is represented in Table 1. The building model cases selected for analysis with respect to the concrete grades C20 and C25. The other parameters including dynamic parameters were considered as constant for all the analysis cases.

TABLE I
SPECIFICATIONS OF SAMPLE BUILDING

Parameter	Value	Parameter	Value
Concrete grade	C25&C20	Transverse reinforcement (Columns)	Φ10/100
Reinforcement grade	S420	Transverse reinforcement (beam)	Φ10/100
Beams	25*60 cm	Steel material model	Menegotto-Pinto
Height of floor	14 cm	Constraint type	Rigid diaphragm
Height of each story	300 cm	Local ground type	ZB
Cover thickness	3 cm	Longitudinal Reinforcement (columns)	8Φ16
Columns	50*40 cm	Permanent Load	5 kN/m

The sample building selected for analysis is a 4-story structure commonly found in rural areas. This choice was based on its familiarity and prevalence in those regions, making it a suitable candidate for study. Such buildings are considered representative of the construction in rural areas, making research on them applicable to practical scenarios in improving seismic resistance efforts. The 3-d view of the selected sample building is given in Figure 1.

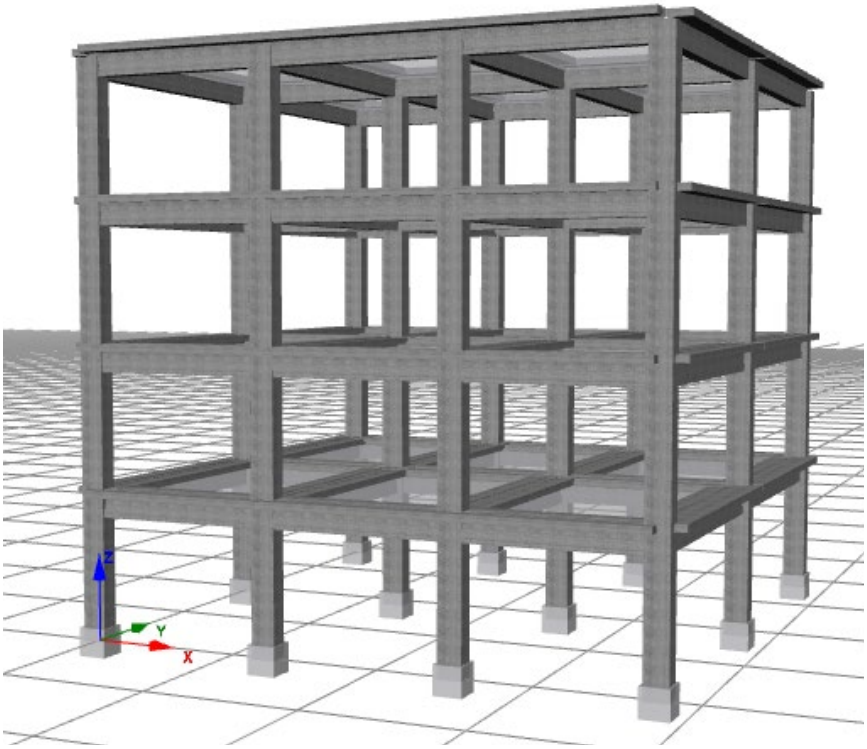


Figure1. 3D view of sample building

C. Results

An IDA analysis was conducted on a sample building using Kocaeli Earthquake (1999) ground motion data, with Intensity Measures (IM) ranging from 0.1g to 2g. The analysis used a scale factor that increased by 0.3g at each step. However, the analysis had to be halted when the building became unstable at an intensity measure of 1.3g, regardless of whether the structure was modelled with C20 or C25. To determine the damage states, values from HAZUS Earthquake Model Technical Manual (2022) [8] were consulted and used. These damage states are outlined in Table 2.

TABLE II
HAZUS DAMAGE STATES

HAZUS Slight	**HAZUS Moderate**	HAZUS **Extensive**
0.27%	0.43%	1.07%

The results of IDA analysis are given in Figure 2 comparatively for C20 and C25 concrete grades with damage limits of HAZUS 2022 code.

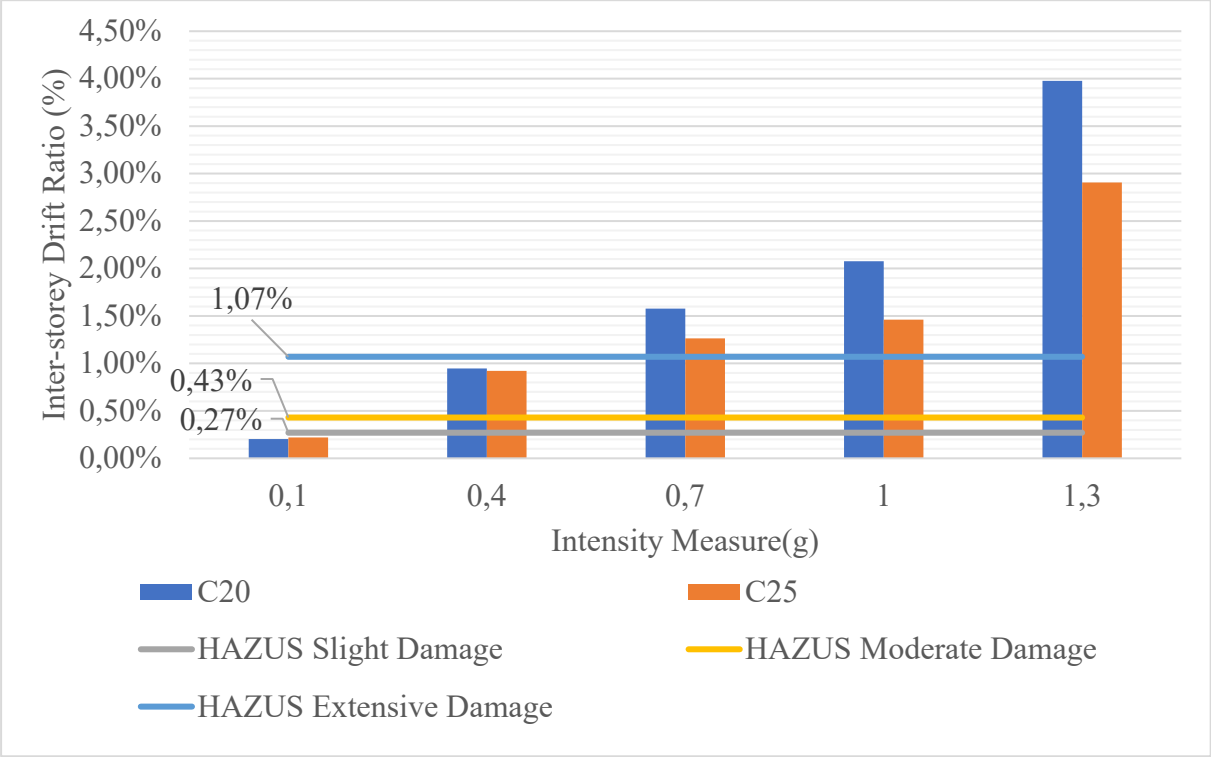


Figure 2. Comparison of Different Concrete Grades with Damage States

Upon examining Figure 2, it becomes evident that the inter-storey drift ratios (IDR) steadily increase with every analysis step. It is noteworthy to mention that the disparities between concrete grades become progressively more pronounced as the analysis proceeds.

III. CONCLUSION

By utilizing variables in this study, it was able to obtain analysis results from a software program and compare them. We found that the interstorey drift ratios has decreased as the concrete grade in each structural system increased. This highlights the importance of ensuring material strength during the application stage, as it directly affects the performance of the structure. Insufficient material strength is one of the primary causes of building damages, particularly in the event of earthquakes. Therefore, accurately determining material strength and ensuring it aligns with accepted values during the construction process is crucial for realistic behavior under loads.

This study showed that the C25 concrete class performed better than the structure modelled with C20 concrete class. When evaluating inter story drifts, it was observed that these values increased between the two concrete classes as the scale factor increased. Specifically, the maximum inter-storey drifts of C20 relative to C25 were 0.02% for 0.1g, 0.03% for 0.4g, 0.31% for 0.7g, 0.62% for 1g, and 1.07% for 1.3g, respectively, as the IM value increased from 0.1 to 1.3. Additionally, as the strength of the concrete used in the structure increased, the inter-storey drifts decreased significantly, illustrating the impact of concrete quality on the earthquake behaviour of structures.

ACKNOWLEDGMENT

Author, would like to express my appreciation to SeismoSoft company for granting me access to the academic license of their SismoStruct software.

REFERENCES

[1] Ülker, M., Işık, E., Bakır, D., Karaşin, İ.B., ''The Effects of Concrete Strength to Rigidity in RC Buildings'', International Conference on Natural Science and Engineering (ICNASE-2016), Kilis, Turkey. 2016.

[2] Celep, Z., Kumbasar, N., Deprem Mühendisliğine Giriş Ve Depreme Dayanıklı Yapı Tasarımı, Beta Dağıtım, İstanbul. 2007.

[3] Işık, E. , Yamaç, Ö. , Erçek, M. S. , Yamaç, İ. "Farklı Taşıyıcı Sistemlerdeki Yapılarda Malzeme Dayanımın Yapı Performansına Etkisi". Erciyes Üniversitesi Fen Bilimleri Enstitüsü Fen Bilimleri Dergisi 33 (2017): 33-40

[4] Seismosoft "SeismoStruct 2022 – A computer program for static and dynamic nonlinear analysis of framed structures", 2022. çevirim içi erişim: https://seismosoft.com

[5] Vamvatsikos, D., and Cornell, C. A., ''Incremental dynamic analysis'', Earthquake Engineering & Structural Dynamics, 31, 491–514. 2002. DOI: 10.1002/eqe.141

[6] Vamvatsikos, D., and Cornell, C. A. ''Applied incremental dynamic analysis'', Earthquake Spectra, 20, 523–553. 2004. https://doi.org/10.1193/1.1737737

[7] Işık, E., Kutanis M. ''Performance Based Assessment for Existing Residential Buildings in Lake Van Basin and Seismicity of the Region.'' Earthquakes and Structures, 9(4), 893-910. 2015.

[8] HAZUS 5.1 . ''Earthquake Model Technical Manual''. Federal Emergency Management Agency (FEMA), Washington, DC, USA. 2022.

Hybrid Approach for Link Prediction in The Networks Created from Turkish Literature

Ali Asghar[*,1], Emrah Özkaynak[*,2]
[*]aliasoo129@gmail.com, ORCID: 0000-0000-0000-0000
Department of Computer Engineering, Karabük University, Karabük, Turkey

Abstract: Link prediction, a vital aspect of network analysis, involves predicting future connections between nodes within a network. Its relevance spans diverse real-world networks, offering insights into latent connections and emerging relationships by scrutinizing existing network structures. This holds significance across domains such as global trade, air transport, social interactions, and scientific collaborations. This research focuses on constructing networks based on data pertaining to publishers, authors, and works in Turkey. The aim is to estimate connections for use in a recommendation system within these networks. To enhance the effectiveness of conventional similarity-based link prediction techniques, this study employs a hybrid approach, amalgamating machine learning methodologies. Hybrid models are synthesized through a fusion of Neighborhood-based methods, alongside algorithms like Random Forest, LightGBM, and SVM. Subsequently, the performance of these hybrid models is evaluated. The evaluation metric employed to gauge the models' efficacy is the Area Under the Curve (AUC). The traditional neighborhood-based link prediction methods yield a success rate of 74%. Through the integration of machine learning techniques to refine connection estimations, an impressive success rate of 99.12% is attained. These outcomes underscore the efficacy of the hybrid model within these networks, marking a substantial enhancement over traditional methodologies.

Keywords: *Link prediction; complex network; machine learning; similarity index; hybrid model.*

I. INTRODUCTION

In the ever-evolving world of academic research, link prediction has been taking up more and more space. Rooted in the quest to unearth latent connections, link prediction serves as a compass, guiding researchers through the vast maze of academic interrelations. A closer scrutiny of these connections, particularly within the milieu of scholarly collaborations, reveals a panorama of intricate relationships[1]. connections that not only define the past and present but also provide a roadmap to the future[2]. The world of social networks is becoming more complex as citation Networks, which track how research books cite each other, advance quickly. This challenges researchers to find real solutions for issues in this field, like connecting authors and publishers based on years and titles, forming what's called a citation Network [3][4].

Historically, the arena of link prediction has predominantly been navigated using traditional methods. These techniques, often rooted in basic similarity measures and statistical heuristics, served their purpose in a nascent stage [5]. However, as the scholarly network expanded and grew in complexity, the limitations of these traditional methods became starkly evident. They often fell short in capturing the nuanced relationships and predicting future collaborations with the desired accuracy.

To tackle these challenges and measure their solutions, Link Prediction becomes crucial. This involves predicting future links in the network. Various methods are used, such as looking at shared connections, similarities, and preferences between nodes in the network. These methods can be categorized into categories global and local. In this paper, we used local similarity indexes which are Common Neighbor, Jaccard Index, Preferential Attachment, Adamic-Adar Index, Resource Allocation Index, and Sorensen Index [6].

Making accurate Link Prediction measurements requires intelligent algorithms. This is where machine learning algorithms come in, helping these measurements work smartly and produce efficient results. These algorithms are skilled at handling the complexities of such intricate networks, making them a valuable tool in this evolving field. Machine learning is categorized into two main types: supervised and unsupervised learning. Supervised learning further branches into classification and regression. On the other hand, when there's no supervision, it's referred to as clustering. Each of these categories has its own unique set of algorithms tailored to its purpose [7].

This study focuses on enhancing link prediction within a complex network. Link prediction measurements were not only employed but also refined through classification algorithms utilized in supervised machine learning. A hybrid model was consequently developed to cater to the demands of this network. To construct the networks, data pertaining to publishers, authors, and literary works published in Turkey were utilized. The investigation extended to exploring the applicability of link estimation techniques in recommendation systems tailored to these networks, with subsequent evaluation of the attained results. Aiming to elevate the effectiveness of similarity-based link prediction methods, a hybrid model was meticulously crafted employing machine learning approaches. The performance of this model in predicting links was meticulously assessed.

In essence, the objective of this study is to construct a network model for link prediction, aimed at aiding authors and publishers in identifying optimal strategies for publishing their academic works in the upcoming years.

II. METHODS

In the realm of computational analysis and networking, the domain of link prediction has seen a surge of investigative endeavors. Numerous techniques, each underpinned by its unique algorithmic underbelly and theoretical framework, have been proposed. For a computer engineering scholar, wading through these multifaceted methodologies is akin to dissecting the intricacies of a highly sophisticated system.

A. Similarity-based methods

To decipher the labyrinthine intricacies of academic networks, local similarity indices are indispensable. These indices, pivotal in the domain of network theory, predicate on the belief that the proximate topological attributes around nodes can provide unparalleled foresight into impending connections.

1. The Common Neighbor (CN) Measure:

The formula for CN is defined as:

$$CN(u,v) = | N(u) \cap N(v) | \tag{1}$$

Where $N(u)$ and $N(v)$ are the neighborhood sets for nodes u and v respectively. The empirical analysis of the CN measure yielded a predictive accuracy of 74% on our dataset.

2. Jaccard Index (JC):

The Jaccard Index offers a predictive approach, rooted in the principles of data analytics[8]. The link likelihood between two specific nodes is ascertained by dividing the shared neighbors of the nodes by the aggregate number of neighbors[9]:

(2)

$$S_{xy} = \frac{| N(x) \cup N(y) |}{| N(x) \cap N(y) |}$$

3. Preferential Attachment (PA):

The Preferential Attachment index finds its application in expansive networks that aren't inherently scalable[8][10].The likelihood of establishing a new link to node X relates directly to $N(x)$. The link's chance between node x and y scales with $N(x) \times N(y)$. Nodes with a plethora of links are more likely to gain additional links in subsequent times. The link feasibility between two nodes resonates with the count of neighboring nodes in the system:

(3)

$$S_{xy} = N(x) \times N(y)$$

4. Adamic-Adar Index (AA):

This technique gauges common neighbors, placing amplified emphasis on nodes with fewer connections[8]. The term $N(x)$ defines the degree of a shared neighbor, denoted as node z, illustrating the number of nodes tethered to the said node[11].

(4)

$$AA(x, y) = \sum_{z \in N(x) \cap N(y)} \frac{1}{log | N(z) |}$$

Instead of merely counting common neighbors, AA weighs them inversely by their degrees, assuming that less connected neighbors contribute more than highly connected ones.

5. Resource Allocation Index (RA):

In intricate networks, the Resource Allocation Index discerns links between node pairs that aren't explicitly connected[8]. Despite the absence of a direct link, these nodes mediate transmission via mutual neighbors. Every intermediary node possesses a unit of resource, which it allocates uniformly amongst its neighbors. The nodes' similarity derives from the resources they mutually garner.

(5)

$$S_{xy} = \sum_{z \in (\Gamma(x) \cap \Gamma(y))} \frac{1}{k_z}$$

6. Sorensen Index (SI):

The Sorensen Index shares semblance with the Jaccard method. This index is determined by the quotient of twice the aggregate of common neighbors (x) and (y) and the combined total of $N(x)$ and $N(y)$[12].

(6)

$$S_{xy} = \frac{2|\Gamma(x) \cap \Gamma(y)|}{k_a + k_b}$$

B. Integration with Machine Learning Techniques

Incorporating machine learning amplifies the potency of the similarity indices. Various machine learning models were coupled with similarity metrics to ascertain the best synergy for prediction. Machine Learning Models Used:

- **Random Forest (RF):** is a versatile ensemble learning technique that excels in processing large and complex datasets. It works by creating multiple decision trees during the training process and combining their results to make predictions. Each tree is built using a random subset of the data and a random subset of features. By combining the predictions of individual trees, Random Forest delivers robust and accurate results, making it a useful tool in different machine learning tasks like classification and regression[13].
- **Gradient Boosting**: is a machine learning technique that enhances model predictions by repetitively filtering the model's performance. It accomplishes this by using the gradient descent algorithm to minimize prediction mistakes. During each repetition, a new model is trained to rectify the errors made by the former ones, gradually improving overall accuracy and predictive power[14].
- **Support Vector Machine (SVM)**: is an outstanding machine learning algorithm that excels in categorizing data points, specifically in spaces with a lot of dimensions. It recognizes a subspace that optimally separates different classes of data points, aiming to maximize the margin between them. SVMs are appropriate for cases where the data is complex and not linearly divisible, as they can change the data into a higher-dimensional space to find a separating hyperplane[15].
- **K-Nearest Neighbors (KNN):** a simple machine-learning algorithm that works by predicting results for new data points based on their closeness to known data points in the training set. It presumes that similar data points gravitate towards having similar labels, making it perfectly suitable for operations like classification and regression. KNN functions by calculating distances between the new data point and its neighbors and then working out the most common label among the k closest neighbors to make predictions[16].
- **LightGBM:** is a high-speed gradient boosting framework that stands out for its extraordinary speed and effectiveness in processing large volumes of datasets. It uses a histogram-based approach to build decision trees during the boosting process which results in faster training times all the while maintaining the quality of predictive accuracy. LightGBM is design and optimization make it a preferred choice for multiple machine-learning operations[17].

C. Hybrid Model Integration

A hybrid model synergizes the strengths of multiple individual methods to enhance link prediction accuracy[18].

(1) Combination of Local Indices and ML:

A method that might use features derived from similarity indices as input to machine learning models. For instance, values from the Adamic-Adar or Jaccard coefficients could serve as features for a Random Forest classifier.

(2) Ensemble methods:

These involve creating multiple models (of the same or different types) and combining their results for a final prediction. Techniques like stacking, bagging, and boosting are common ensemble strategies.

(3) LightGBM Integration:

In recent times, gradient-boosting frameworks like LightGBM have been effectively juxtaposed with traditional ML methods to harness their capability for processing large datasets, and categorical features, and improving prediction accuracy.
The local similarity indices were seamlessly merged with machine learning models, enhancing the precision of our predictions. This combination resulted in hybrid models, each tested for their respective accuracies. For example, integrating CN with Random Forest and LightGBM gave the best accuracy out of all the algorithms used. The results for all such combinations have been systematically arranged for comprehensive clarity.

III. EXPERIMENTAL STUDY

Link prediction methods are generally applied intensively on social networks and interaction networks. So, there are few studies that measure the performance of these methods in dynamic networks in for book publishers' relationship analysis, especially on the Turkish publishing dataset.

A. Dataset and Pre-processing

This dataset serves as a comprehensive compendium chronicling books in Turkey [19]. It spans a gamut of genres, encapsulating business, economics, psychology, academia, science, engineering, and literature, with the latter added in its third iteration (Version-3).
Each entry within this extensive compilation furnishes a plethora of details pertinent to each book. This includes vital data points like the book's title, its affiliated publisher, the author behind the masterpiece, a unique product code, the total number of pages the book comprises, its year of release, along other intricate details. Such an assemblage is an invaluable repository for a spectrum of users – from researchers and data analysts keen on dissecting the intricacies of the Turkish publishing world, to bibliophiles yearning to delve deeper into their passion.
Navigating such a vast ocean of historical data demanded an astute structural approach. To enhance usability and foster better understanding, the dataset was intricately carved into five distinct timeframes or epochs. Each of these epochs is a reservoir of unique nodes and edges. Nodes in this context represent key entities like the Author, Publisher, and Year of publication, whereas edges are synonymous with the Book Title.
To delineate the architecture further:

- The model is trained using the foundational year of 1922 to 2023. It's a behemoth with 148,447 nodes and a staggering 349,117 edges interlinking them.

This dataset is not just a mere collection of books; it's a well-structured, chronological anthology, serving as a goldmine for those intrigued by the Turkish literary and publishing landscape.

B. Creating Networks

In this context, a network was made to portray Turkish literature publications, as shown in Figure 1. We noticed that the higher the number of nodes, representing individual publications, increased, so did the number of links between said nodes within the network.
To enhance the visual clarity and comprehensibility of this complex network, the Gephi program was selected as the preferred tool. Gephi was selected due to its exceptional capacity to process large amounts of data. Furthermore, our choice was also due to Gephi's capability to transform written data into clear and comprehensible visual formats. [20].

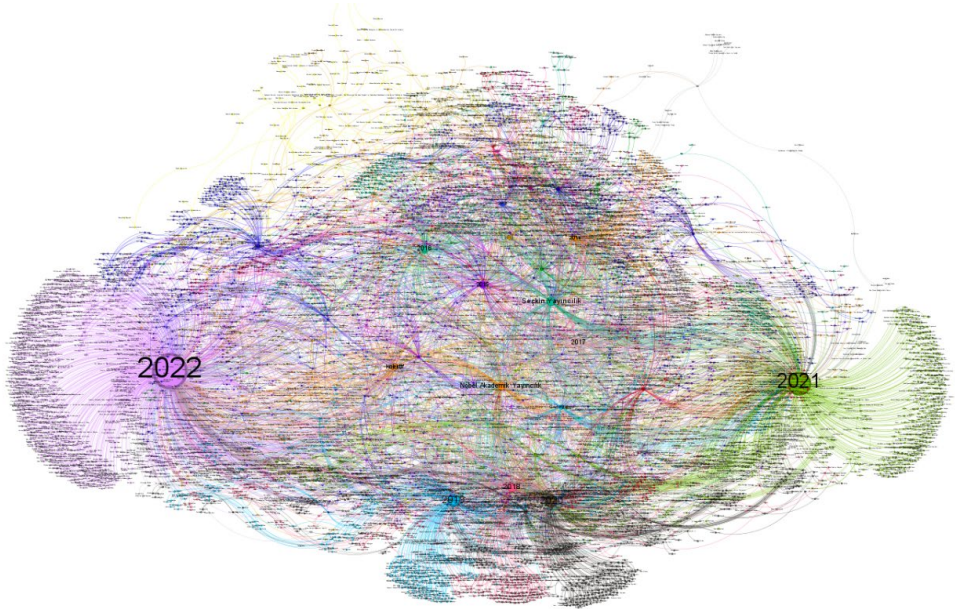


Fig.1. Integrated illustration of the network graph of book-author-publisher-year relations

C. Model Performance Analysis

The efficacy of both individual machine learning models and the hybrid models were rigorously scrutinized. Particular attention was paid to the model's resilience when a mere 0.08% of the dataset was utilized for both training and testing. This endeavor was to ensure the model's robustness across varied data sizes and complexities.

D. Link Prediction Network

In this scenario, nodes signify the Author, Publisher, and Year, while the edges are emblematic of the Book Title. This configuration empowers us not only to prognosticate potential collaborations but also to infer the probable nature (book titles) of these collaborations.

1. Primary Objectives:

Predict future collaborations between authors and publishers, emphasizing the propensity of publisher types for the impending years of 2021, 2022, and 2023.
Estimate the quantum of publishers likely to inaugurate collaborations with authors during 2021, 2022, and 2023.
The comprehensive results of the model's efficacy, in tandem with the data segmentation strategy, provide a holistic insight into the paradigms of academic collaborations, laying the foundation for future enhancements and refinements in the arena of link prediction.

IV. RESULTS AND DISCUSSION

In the multifaceted tapestry of network link prediction, our integrative approach, which seamlessly interweaves local similarity indices with potent machine learning models, has yielded profound insights. The chronicles of our experiments, buoyed by the exhaustive data segmentation and intricate hybrid modeling, have been delineated below.

A. Local Similarity Indices Evaluation

Understanding the nuances of a network often necessitates reliance on local topological features. We employed several such metrics, and their resultant accuracies are as follows:

A COMPARISON OF APPROACHES USING DIFFERENT SIMILARITY INDICES

Local similarity indices	Accuracy
Common Neighbor (CN):	74.00%
Jaccard Index (JC):	61.90%
Preferential Attachment (PA):	64.20%
Adamic-Adar Index (AA):	74.00%
Resource Allocation Index (RA):	73.90%
Resource Allocation Index (RA):	63.09%

It was evident that the Common Neighbor and Adamic-Adar Index were particularly adept at capturing the intricate relationships, with both achieving accuracies in the realm of 74%.

B. Machine Learning Modeling

In the paradigm of computational analysis, individual machine learning models, when aligned with local similarity metrics, demonstrated an intriguing array of results. Illustrated below is a cross-sectional analysis of our outcomes:

TABLE I

A COMPARISON OF DIFFERENT ML APPROACHES USING DIFFERENT SIMILARITY INDICES

Similarity Index	Random Forest	Gradient Boosting	SVM	KNN
Common Neighbor	99.00%	99.00%	93.00%	97.00%
Jaccard Index	92.00%	92.00%	88.00%	91.00%
Preferential Attach.	90.00%	90.00%	85.00%	89.00%
Adamic-Adar Index	91.00%	91.00%	86.00%	91.00%
Resource Alloc. Ind.	90.00%	90.00%	85.00%	89.00%
Sorensen Index	Data Unavailable	Data Unavailable	Data Unavailable	89.00%

C. Hybrid Modeling Synergy

A pivotal breakthrough in our explorations was the development of a hybrid modeling framework. This was accomplished by artfully juxtaposing the strengths of machine learning models and LightGBM. The encapsulated results showcase their prowess:

TABLE II

COMPARISON OF INDICES AND MODELS FUSION ACCURACY

INDICES & MODELS FUSION	ACCURACY
CN + SVM + LightGBM	94.77%
CN + Random Forest + LightGBM	99.12%
CN + Gradient Boosting + LightGBM	98.98%

D. Temporal Dataset Segmentation Outcomes

Upon dissecting our dataset temporally into distinct epochs, and subsequently implementing our modeling paradigms on them, we observed the following:

TABLE III
TEMPORAL DATASET SEGMENTATION OUTCOMES

STEP	TRAINING SPAN	TESTING YEARS	RANDOM FOREST ACCURACY	HYBRID MODEL (RF + LIGHTGBM) ACCURACY
1	1922-2003	2001-2003	89.00%	89.98%
2	1922-2008	2006-2008	95.00%	95.90%
3	1922-2013	2011-2013	98.00%	97.30%
4	1922-2018	2016-2018	98.90%	99.00%
5	1922-2022	2021-2023	99.00%	99.12%

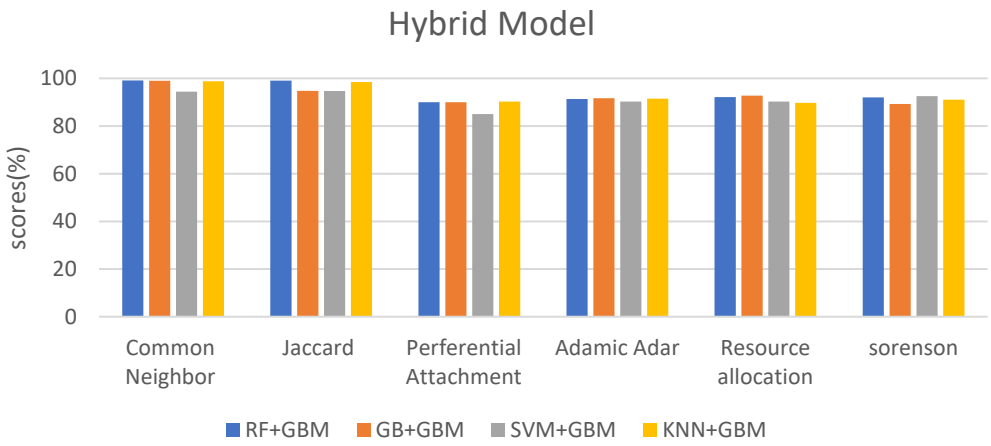


Fig.2. A demonstration for comparison of model accuracies over different testing years

For each segmented dataset, the Random Forest coupled with LightGBM showcased an ascendant trajectory in accuracy, culminating in a remarkable 99.12% for the years 2021-2023.

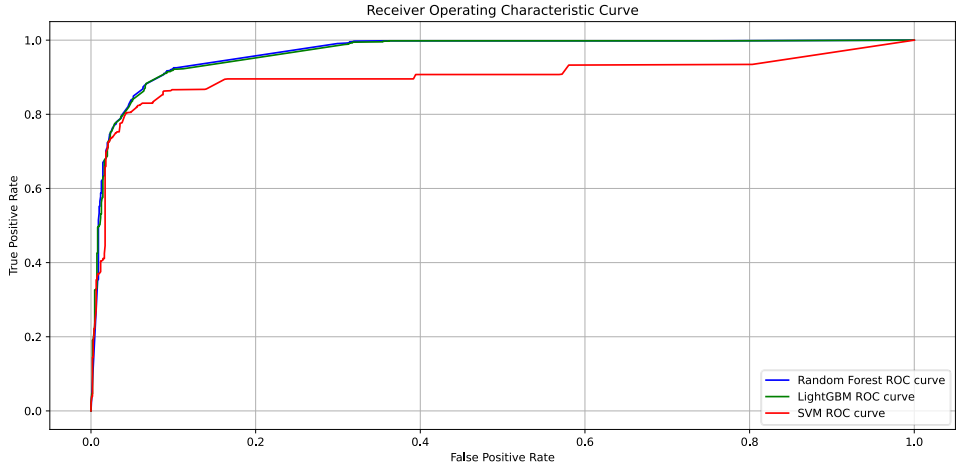


Fig.3. AUC-ROC (TP and FP rates) for Random Forest, LightGBM and SVM methods

Comprehensive exploration, spanning local similarity indices to intricate hybrid models, has underscored the potential and precision of using a collaborative approach in link prediction. The meticulous data segmentation, the robustness of individual models, and the synergistic

outcomes of hybrid models all converge to pave a promising trajectory for future network analysis endeavors.

E. Conclusive Reflections

This study is an exemplar of meticulous research, weaving the art of link prediction by merging local similarity indices with machine learning. By chronologically segmenting the dataset by considering variables like Author, Publisher, Year, and Book Title, the research achieves unparalleled contextual depth.

Additionally, our segmentation strategy offers invaluable glimpses into the changing landscape of academic liaisons over the decades. The resilience of the models, even when working with segmented data, reinforces the robustness and adaptability of our approach, holding promise for diverse future applications.

V. CONCLUSION AND FUTURE WORKS

This research successfully unveiled the latent potential of combining local similarity indices with machine learning paradigms for link prediction in academic networks. The data partition strategy, amalgamated with the hybrid modeling approach, establishes a solid foundation for predicting academic collaborations with high accuracy. In view of the promising results from our integrative approach to link prediction, several avenues deserve exploration in future endeavors. First of all, the consideration of global similarity indices, in addition to local indices, could provide a more comprehensive understanding of network behavior. With the rise of new machine learning architectures, especially deep learning models such as graph neural networks, the integration of these modern techniques could further bolster the accuracy and efficiency of predictions. In addition, studying the temporal evolution of the network might unearth dynamic patterns and critical inflection points in academic collaborations. Adding sentiment analysis on book titles might also help clarify evolving trends and interests in academic publishing. Lastly, adapting our methodologies to different datasets, such as online social networks and molecular structures, will determine the robustness and versatility of our developed models.

REFERENCES

[1] J. S. Rubin, "What Is the History of the History of Books?," *J. Am. Hist.*, vol. 90, no. 2, p. 555, 2003, doi: 10.2307/3659444.

[2] D. Lande, M. Fu, W. Guo, I. Balagura, I. Gorbov, and H. Yang, "Link prediction of scientific collaboration networks based on information retrieval," *World Wide Web*, vol. 23, Jul. 2020, doi: 10.1007/s11280-019-00768-9.

[3] X. Liu, "Full-Text Citation Analysis : A New Method to Enhance," *J. Am. Soc. Inf. Sci. Technol.*, vol. 64, no. July, pp. 1852–1863, 2013, doi: 10.1002/asi.

[4] M. Wei and A. Noroozi Chakoli, "Evaluating the relationship between the academic and social impact of open access books based on citation behaviors and social media attention," *Scientometrics*, vol. 125, no. 3, pp. 2401–2420, 2020, doi: 10.1007/s11192-020-03678-0.

[5] R. Guns and R. Rousseau, "Recommending research collaborations using link prediction and random forest classifiers," *Scientometrics*, vol. 101, no. 2, pp. 1461–1473, 2014, doi: 10.1007/s11192-013-1228-9.

[6] N. N. Daud, S. H. Ab Hamid, M. Saadoon, F. Sahran, and N. B. Anuar, "Applications of link prediction in social networks: A review," *J. Netw. Comput. Appl.*, vol. 166, p. 102716, 2020, doi: 10.1016/j.jnca.2020.102716.

[7] M. Batta, "Machine Learning Algorithms - A Review," *Int. J. Sci. Res.*, vol. 18, no. 8, pp. 381–386, 2018, doi: 10.21275/ART20203995.

[8] O. Findik and E. Özkaynak, "Link prediction on networks created from UEFA European

competitions," *Lect. Notes Inst. Comput. Sci. Soc. Telecommun. Eng. LNICST*, vol. 325 LNICST, pp. 207–217, 2020, doi: 10.1007/978-3-030-52856-0_16.

[9] L. da F. Costa, "Further Generalizations of the Jaccard Index," 2021, [Online]. Available: http://arxiv.org/abs/2110.09619

[10] D. S. M. Q. Taani, A. M. al-Wahadni, and M. al-Omari, "The effect of frequency of toothbrushing on oral health of 14-16 year olds.," *J. Ir. Dent. Assoc.*, vol. 49, no. 1, pp. 15–20, 2003.

[11] L. Wang, C. Chen, and H. Li, "Link Prediction of Complex Network Based on Eigenvector Centrality," *J. Phys. Conf. Ser.*, vol. 2337, no. 1, pp. 0–8, 2022, doi: 10.1088/1742-6596/2337/1/012018.

[12] F. Guo, W. Zhou, Z. Wang, C. Ju, S. Ji, and Q. Lu, "A link prediction method based on topological nearest-neighbors similarity in directed networks," *J. Comput. Sci.*, vol. 69, no. April 2022, p. 102002, 2023, doi: 10.1016/j.jocs.2023.102002.

[13] L. He, R. A. Levine, J. Fan, J. Beemer, and J. Stronach, "Random forest as a predictive analytics alternative to regression in institutional research," *Pract. Assessment, Res. Eval.*, vol. 23, no. 1, pp. 1–16, 2018.

[14] A. Natekin and A. Knoll, "Gradient boosting machines, a tutorial," *Front. Neurorobot.*, vol. 7, no. DEC, 2013, doi: 10.3389/fnbot.2013.00021.

[15] D. Srivastava and L. Bhambhu, "Data classification using support vector machine," *J. Theor. Appl. Inf. Technol.*, vol. 12, pp. 1–7, Feb. 2010.

[16] J. Tripathy, R. Dash, and B. K. Pattanayak, "A Case Study on Data Classification Approach Using K-Nearest Neighbor," *2021 Int. Conf. Adv. Power, Signal, Inf. Technol. APSIT 2021*, no. February 2022, 2021, doi: 10.1109/APSIT52773.2021.9641209.

[17] G. Ke *et al.*, "LightGBM: A highly efficient gradient boosting decision tree," *Adv. Neural Inf. Process. Syst.*, vol. 2017-Decem, no. Nips, pp. 3147–3155, 2017.

[18] P. Chuan, L. Son, M. Ali, K. Tran, H. Le, and N. Dey, "Link Prediction in Co-authorship Networks based on Hybrid Content Similarity Metric," *Appl. Intell.*, vol. 48, Aug. 2018, doi: 10.1007/s10489-017-1086-x.

[19]"Turkish_Book_Dataset"(2023)https://www.kaggle.com/datasets/ardaakdere16/turkish-book-dataset?group=bookmarked

[20] M. Bastian, S. Heymann, and M. Jacomy, "Gephi: An Open Source Software for Exploring and Manipulating Networks Visualization and Exploration of Large Graphs," *Proc., Int. AAAI Conf. Web Soc. Media*, pp. 361–362, 2009, [Online]. Available: www.aaai.org

Thermal And Forced Vibration of a Carbon Nanotube Incorporated in An Elastic Medium

Samir Belmahi[*,1,2], Yacine Bouzit [1], Abdelkader Bouziani [1], Mohamed Zidour[1,2]

[*]samir.belmahi@univ-tiaret.dz, ORCID:0000-0001-8424-2143
[1]*Department of Civil engineering, University of Tiaret, Algeria*
[2]*Laboratoire de Géomatique et Développement Durable, University of Tiaret, Algeria,*

Abstract: This article presents the study of the forced vibration under the effect of a thermal force of a carbon nanotube with single wall of zigzag type supposed to incorporate in an elastic medium of Winkler type. The model of beam considered is that of Euler-Bernoulli. The amplitudes and frequencies were determined using the theory of non-local elasticity which takes into account the small-scale effect e0a and the effect of elastic Van der Waals forces between the inner and outer tubes of the carbon nanotubes . The variation of temperature (T), geometric ratio (W=L/d) and stiffness of the elastic matrix (kw) were considered and discussed. The results showed the importance of their significant impact on the amplitudes and frequencies induced by the vibration of the carbon nanotube.

Keywords: *Carbon Nanotube, Vibration, Euler-Bernoulli, Winkler, Elasticity.*

I. INTRODUCTION

The carbon nanotube and since their discoveries by Sumio Iijima in 1991 [1] constitute a fundamental element of studies on nanotechnology and in materials science [2]. Carbon nanotubes have been used in many research activities, closely related to their extraordinary electrical, mechanical, thermal, physical and chemical properties [2,3]. they were used to make nanocomposites with a nanometric structure [4, 5] at a scale between 1 and 100 nm [6]. The cohesion of the nanocomposite is ensured by the matrix or the charge [7], while the carbon nanotube represents the reinforcement [8, 9] which is responsible for these mechanical performances and the overall stability [7]. CNTs are ultimate reinforcing agent, called nanofibers, in different matrix materials for the development of a new class of nanocomposites that are extremely strong and ultra-light [10]. Carbon nanotubes are currently of interest in several fields of mechanical , electrical and civil engineering. They are currently the basis of most composites materials, so their behavior in a matrix will be linked to this last and the results will be completely different. Several questions have been elaborated on this material, in particularly the free vibration, among which we quote some works on the linear and the non-linear vibration analysis of longitudinal vibration: By use and application of different theories [11], vibration of carbon nanotubes by variational iteration method [12], Nonlinear free vibration of a nanobeam based on non-local Euler-Bernoulli Beam theory [13] , Nonlinear finite element vibration analysis. Flexural free vibration and buckling analysis using different gradient elasticity theories [14, 15]. Analysis of nonlinear free vibration [16], embedded in viscoelastic medium [17]. For thermal studies we have studies on thermal stability of plates and functionally graded sandwich plates [18, 19, 20]. Thermal buckling [21, 22]. Hygro-thermo-mécanique [23, 24]. Thickness stretching effect for the flexure analysis of laminated composite plates [25]; stretching effect for thermomechanical bending 26]. We have seen that it is important to study a nanotube under the effect of a forced vibration, a thermal field and subject to the reaction of the Winkler type

elastic medium. The nanobeam is represented by the Euler-Bernoulli beam model and by application of the theory of nonlocal elasticity. The carbon nanotube considered in this work is of the single-walled type (SWCNT).

II. CALCULATION

Consider a simply supported single-layer carbon nanotube of length *L*, with a section *S*. the nanotube is integrated in an elastic medium of Winkler type, undergoes a reaction *Q* defined by the rigidity *kw* [27, 28] and subjected to a force thermal *Fth* [29] according to the following equations:

$$Q = -k_{w}.w \tag{1}$$

$$F_{th} = \alpha EST \tag{2}$$

With (α) is the thermal expansion coefficient in the direction of the (x) axis, (T) is the applied medium temperature, (E) is the Young's modulus of the nanotube, (S) is the section.

Based on the assumptions above, the displacement field is written as follows:

$$\begin{cases} u(x,z) = u_0(x) - z\dfrac{\partial w_0(x)}{\partial x} \\ w(x,z) = w_0(x) \end{cases} \tag{3}$$

Where:

u(x), w(x) are the axial and transverse displacement respectively,

$u(x), w(x)$ are the axial and transverse displacement respectively,

$z\dfrac{\partial w(x)}{\partial x}$, $\dfrac{\partial w(x)}{\partial x}$ are the axial displacement and the rotation due to bending respectively.

The "Hamilton" principle is used to derive the equations of motion. This principle can be stated in an analytical form [30].

$$\int_0^t (\partial U + \partial f + \partial V - \partial K)dt = 0 \tag{4}$$

Where:

δU is the virtual change in strain energy;

δf is the virtual variation of the potential energy,

δV is the virtual change in energy due to the external load,

δK is the virtual change in kinetic energy.

The change in strain energy of the beam can be expressed as:

$$\partial u = \int_0^l \int_S \sigma_{xx}\delta\varepsilon_{xx} + \tau_{xz}\delta\gamma_{xz})dSdx \tag{5}$$

The bending moment and axial deformations are given as follows:

$$\begin{cases} M = \int_S \sigma_{xx} z dS \\ \varepsilon_{xx} = \dfrac{\partial u}{\partial z} = -z \dfrac{\partial^2 w_0}{\partial^2 x} \\ \gamma_{xx} = \dfrac{\partial u}{\partial z} + \dfrac{\partial w}{\partial x} = 0 \end{cases} \tag{6}$$

Substituting equation (6) into equation (5) we get:

$$\partial u = \int_0^l \int_S (-M \frac{\partial^2 \delta w_0}{\partial^2 x}) dS dx \tag{7}$$

The typical elastic medium (Winkler) is used to model the interaction between the nanotube and the elastic medium thus, the virtual variation of the energy relating to the reaction of this elastic medium is given as follows:

$$\partial f = \int_0^l (k_w w \delta_w) dx \tag{8}$$

The virtual variation of kinetic energy is given as follows

$$\partial K = -\int_0^l \int_S \rho \frac{\delta^2 w}{\delta^2 t} \delta w \tag{9}$$

Where ρ is the density.

The virtual variation of energy due to the external load:

$$\partial K = -\int_0^l (Q + F_{th}) \delta w dx \tag{10}$$

Where Q is the load applied to create the forced vibration and F_{th} is the axial load which represents the thermal effect.

From Hamilton's principle and from equations (8, 9 and 10) we obtain the following balance equation:

$$\frac{\partial V}{\partial x} = K_w w - Q + F_{th} \frac{\partial^2 w}{\partial^2 x} + \rho S \frac{\partial^2 w}{\partial^2 t} \tag{11}$$

With V represents the shear force;
The relationship between the bending moment and the shear force:

$$\frac{\partial M}{\partial x} = -V \tag{12}$$

The non-local constitutive relation to present nano-beams can be estimated according to Hooke's law for a uni-axial state of the stress [27]:

$$\sigma(x) - e_{oa}{}^2 \frac{\partial^2 \sigma(x)}{\partial^2 x} = E\varepsilon(x) \tag{13}$$

Where: e_{0a} is the small scale ratio and I is the moment of inertia.

By using equations (6) and (13) we obtain:

$$M - {e_{0a}}^2 \frac{\partial^2 M}{\partial^2 x} = -EI \frac{\partial^2 w}{\partial^2 x} \tag{14}$$

Replacing equations (11) and (12) into equation (14) we obtain:

$$M = -EI \frac{\partial^2 w}{\partial^2 x} + {e_{0a}}^2 \left(k_w w - Q + F_{th} \frac{\partial^2 w}{\partial^2 x} + \rho S \frac{\partial^2 w}{\partial^2 t} \right) \tag{15}$$

By derivation of equation (15) we have:

$$V = -EI \frac{\partial^3 w}{\partial^3 x} + {e_{0a}}^2 \left(k_w \frac{\partial w}{\partial x} - \frac{\partial Q}{\partial x} + F_{TH} \frac{\partial^3 w}{\partial^3 x} + \rho S \frac{\partial^3 w}{\partial^2 t \partial x} \right) \tag{16}$$

Substituting the derivation of equation (16) into equation (11) we have:

$$-EI \frac{\partial^4 w}{\partial^4 x} + {e_{0a}}^2 \left(k_w \frac{\partial^2 w}{\partial^2 x} - \frac{\partial^2 Q}{\partial^2 x} + F_{th} \frac{\partial^4 w}{\partial^4 x} + \rho S \frac{\partial^4 w}{\partial^2 t \partial^2 x} \right) - k_w w + Q - F_{th} \frac{\partial^2 w}{\partial^2 x} - \rho S \frac{\partial^2 w}{\partial^2 t} = 0 \tag{17}$$

This is the general differential equation of the forced vibration of a single-layer carbon nanotube subject to a thermal effect according to the Euler-Bernoulli theory with:

The resolution of the latter with partial derivatives of order four is done by the technique of separation of the variables (x, and t). In fact, knowing that we are dealing with a vibration problem, we will assume that $w(x, t)$ and the loading $Q(x, t)$ are sinusoidal functions of pulsation ω. In the case of a simply supported single-layer carbon nanotube of length (L), the solutions are of the following form [28].

$$\begin{cases} w(x,t) = \overline{W} \sin \lambda x \sin \omega t \\ Q(x,t) = Q_0 \sin \lambda x \sin \omega t \\ \lambda = \dfrac{n\pi}{L} \end{cases} \tag{18}$$

Where $\overline{W}$ is the amplitude of deflection of the tube:

Substituting equation (18) into equation (17) we find:

$$\left(EI\lambda^4 + (1 + {e_{0a}}^2 \lambda^2) k_w - (1 + {e_{0a}}^2 \lambda^2) \rho S w^2 + (1 + {e_{0a}}^2 \lambda^2) F_{th} \lambda^2 \overline{W} - (1 + {e_{0a}}^2 \lambda^2) Q_0 = 0 \right. \tag{19}$$

The solution to equation (19) gives the amplitude in the nonlocal case $\overline{W}_{NL}$ as follows:

$$\overline{W}_{NL} = \frac{Q_0 L^4 K}{EI(\phi^4 + \dfrac{Y k_w L^4}{EI} - Y\Omega^2 + \dfrac{Y F_{th} \lambda^2 L^4}{EI}} \tag{20}$$

Where :

$$\begin{cases} \phi = \lambda L \\ Y = 1 + {e_{0a}}^2 \lambda^2 \\ \Omega^2 = \dfrac{\rho S w^2 L^4}{EI} \end{cases} \tag{21}$$

For the local case ($e_{0a}=0$) we conclude the local amplitude $\overline{W}_L$

From equation (19), for a free vibration ($Q=0$) of a carbon nanotube, without elastic medium (kw=0) and in the local case, We have:

$$EI\lambda^4 - \rho S\omega_n^2 = 0 \tag{23}$$

$$\omega_n^2 = \frac{EI\lambda^4}{\rho S} \tag{24}$$

$$\Omega^2 = \frac{\rho S w^2 L^4}{EI} = \frac{\rho S}{EI\lambda^4}(w^2 L^4 \lambda^4) = \frac{1}{w_n^2}(w^2 L^4 \lambda^4) = \phi^4 R^2 \tag{25}$$

With :

$$R^2 = \frac{\omega^2}{\omega_n^2} \tag{26}$$

$$\phi^4 = \lambda^4 L^4 \tag{27}$$

To study the effect of scaling parameters on the forced vibrations of a single-layer carbon nanotube (SWCNT), the results, including local and non-local parameters, are compared.

The ratio between the non-local amplitudes without and with the thermal medium is equal to:

$$\chi_{TH} = \frac{\overline{W_{NL}}}{\overline{W_{NL-th}}} = \frac{\phi^4(Y - YR^2) + Yk_w\psi}{\phi^4(Y - YR^2) + Y\psi(k_w F_{th}\lambda^2)} \tag{28}$$

With

$$\psi = \frac{L^4}{EI} \tag{29}$$

And ($\overline{W_{NL}}$,$\overline{W_L}$,$\overline{W_{NL-th}}$) are the amplitudes based on the nonlocal, local and nonlocal model with thermal medium respectively.

III. RESULTS

1. Effect of temperature and frequency ratio

The ratio of non-local amplitudes without and with the presence of a thermal force as a function of frequency ratio of carbon nanotube was calculated under the effect of increasing temperature ranges from 30 to 60°C, the results are shown in Table 1 and discussed in Figure 1.

TABLE 1.
RESULTATS DE RAPPORT DES AMPLITUDES χ_{TH} EN FONCTION DE RAPPORT DE FREQUENCES (R) POUR DIFFERENTS VALEURS DE TEMPERATURES.

R	*T = 20*	*T = 40*	*T = 60*
2	1,000010509	1,000021825	1,00003395
4	1,000002611	1,000005422	1,00000843
6	1,000001159	1,000002407	1,00000374
8	1,000000652	1,000001353	1,00000211
10	1,000000417	1,000000866	1,00000135
12	1,00000029	1,000000601	1,00000094
14	1,000000213	1,000000442	1,00000069
16	1,000000163	1,000000338	1,00000053
18	1,000000129	1,000000267	1,00000042
20	1,000000104	1,000000216	1,00000034

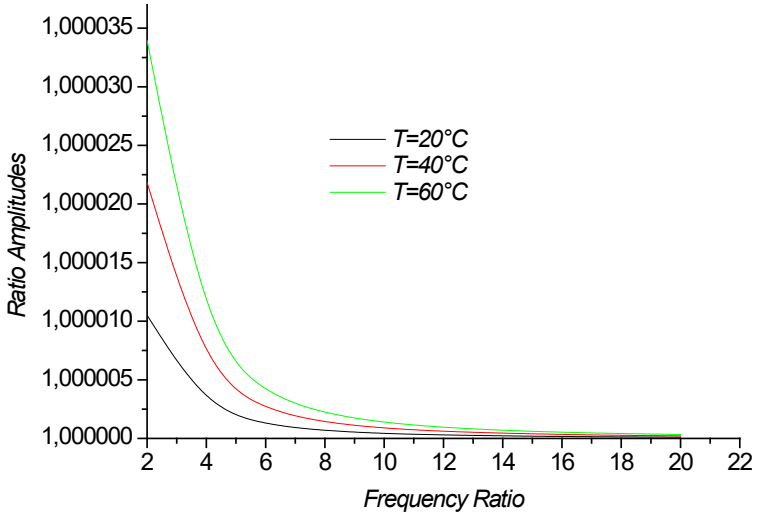


Fig. 1. Variation of amplitude ratio χ_{TH} as a function of frequency ratio (R) for different temperature values (T).

Figure 1 shows the variation in non-local amplitude ratio without and with the presence of a thermal force as a function of frequency ratio R. We notice that the intensity of this ratio is important for the lowest frequency ratios (less than 12 in our case); therefore beyond this value the ratio of the amplitudes tends towards 1 which explains that the temperature has no effect on the amplitudes. We also notice that the amplitudes increase as a function of temperature.

2. Effect of temperature and aspect ratio (L/d)

The ratio of amplitudes as a function of temperature T was calculated for different geometric ratios (L/d) according to Table 2.

TABLE 2.
RESULTS OF REPORTING AMPLITUDES χ_{TH} AS A FUNCTION OF TEMPERATURE *T* FOR DIFFERENT GEOMETRIC REPORT VALUES *L/D*.

T	*L/d=5*	*L/d=10*	*L/d=15*	*L/d=20*
0	1,000000000	1,000000000	1,0000000000	1,000000000
10	1,000007140	1,000029284	1,0000705320	1,000151318
20	1,000014560	1,000059718	1,0001438400	1,000308618
30	1,000022260	1,000091303	1,0002199260	1,000471907
40	1,000030240	1,000124039	1,0002987910	1,000641189
50	1,000038500	1,000157925	1,0003804360	1,000816472
60	1,000047040	1,000192962	1,0004648640	1,000997761
70	1,000055861	1,000229151	1,0005520730	1,001185063
80	1,000064962	1,000266491	1,0006420680	1,001378385
90	1,000074342	1,000304983	1,0007348480	1,001577732
100	1,000084003	1,000344627	1,0008304160	1,001783114

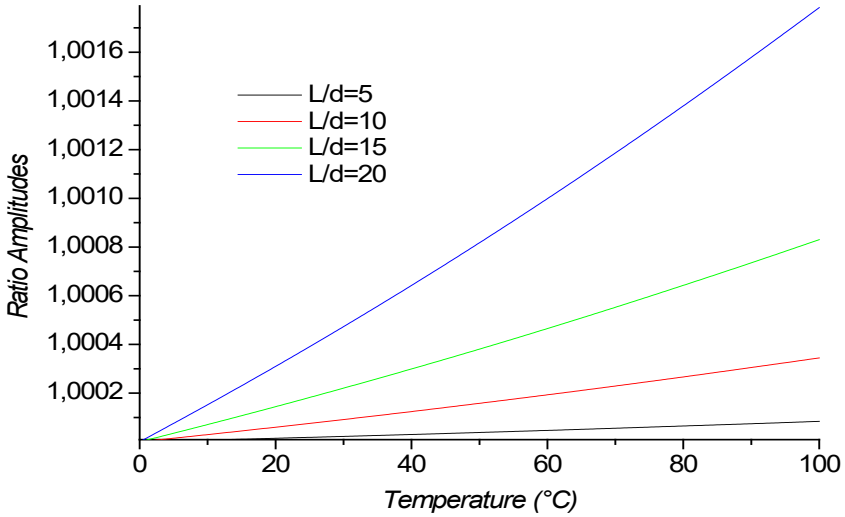


Fig. 2. Variation of amplitude ratio χ_{TH} as a function of temperature *T* for different geometric ratios (*L/d*).

Figure 2 shows the variation in the ratio of non-local amplitudes without and with the presence of a thermal force χ_{TH} as a function of the temperature *T* for different geometric ratios (*L/d*). It is always observed that the ratio of amplitudes increases as a function of temperature. Also, we can say that the longest nanotube gives the highest amplitude and opposite.

3. Effect of temperature and elastic medium *kw*.

TABLE.3

RESULTS OF RATIO OF AMPLITUDES χ_{TH} AS A FUNCTION OF TEMPERATURE T FOR DIFFERENT TYPES OF ELASTIC MATRIX OF RIGIDITY kw.

T	*Polyethylene* $kw= 0,9$	*Polycarbonate* $kw=2,2$	*epoxy Resin époxy* $kw=2,7$	*Polystyrene* $kw=3,2$
0	1,000000000	1,000000000	1,000000000	1,000000000
10	1,000029284	1,000029897	1,000030140	1,000030387
20	1,000059718	1,000060969	1,000061465	1,000061968
30	1,000091303	1,000093216	1,000093973	1,000094743
40	1,000124039	1,000126637	1,000127666	1,000128711
50	1,000157925	1,000161233	1,000162543	1,000163874
60	1,000192962	1,000197005	1,000198605	1,000200232
70	1,000229151	1,000233952	1,000235853	1,000237784
80	1,000266491	1,000272075	1,000274285	1,000276532
90	1,000304983	1,000311374	1,000313903	1,000316475
100	1,000344627	1,000351849	1,000354707	1,000357613

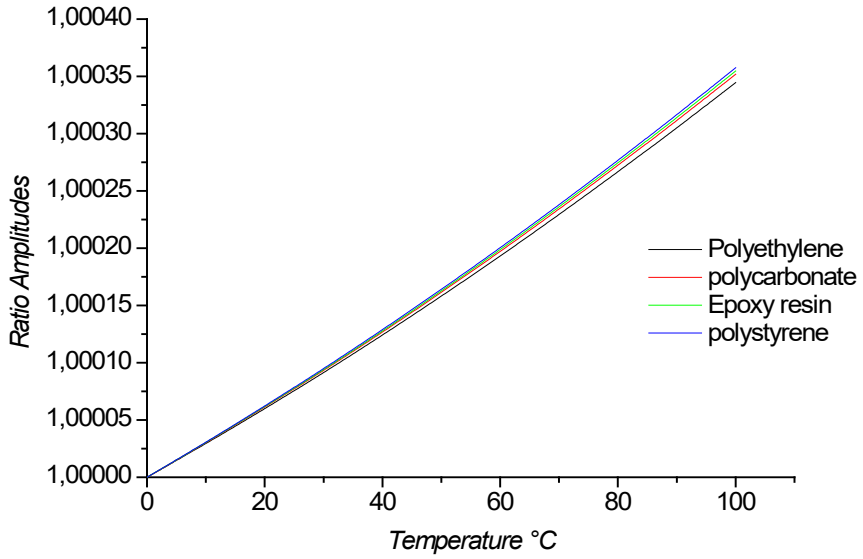


Fig. 3. Variation of amplitude ratio χ_{TH} as a function of temperature T for different types of elastic matrix of stiffness kw.

Figure 3 shows the variation in the ratio of non-local amplitudes without and with the presence of a thermal force as a function of temperature T for different types of matrix or rigidity. It is always observed that the ratio of the amplitudes increases as a function of temperature and that the rigidity increases the ratio of the amplitudes discussed. So a rigid matrix increases the amplitude unlike a flexible or less rigid matrix. This remark is more exact from the temperature T higher than 20°C according to our case.

IV. CONCLUSION

The ratio of the amplitudes of the forced vibration of a carbon nanotube in an elastic medium increases as a function of increasing the temperature, the length of the carbon nanotube and thus the rigidity of the matrix.

REFERENCES

[1] Iijima, S. (1991), "Helical microtubules of graphitic carbon", *Nature*, **354**(6348), 56-58.

[2] Ahmadi Asoor, A.A., Valipour, P. and Ghasemi, S.E. (2016), "Investigation on vibration of single-walled carbon nanotubes by variational iteration method", *Appl. Nanosci*., **6**(2), 243-249.

[3] Kiani, K. (2014), "Vibration and instability of a single-walled carbon nanotube in a three-dimensional magnetic field", *J. Phys. Chem. Solids*, **75**(1), 15-22.

[4] Acton, Q.A., (2013), *Issues in Hydrogen, Fuel Cell, Electrochemical, and Experimental Technologies*, Scholarly Edition, Atlanta, Georgia, U.S.A.

[5] Okpala, C.C. (2014), "The benefits and applications of nanocomposites", *J. Adv. Engg. Tech*., **5**(4), 12-18.

[6] Azeredo, H.M.C. (2009), "Nanocomposites for food packaging applications", *Food Res. Int*., **42**(9), 1240-1253.

[8] Okpala, C.C. (2013), "Nanocomposites: An overview", *J. Eng*., *Res. Develop*., **8**(11), 17-23.

[9] Öchsner, A. and Shokuhfar, A. (2013), *New Frontier of Nanoparticles and Nanocomposite Materials*, *Novel Principles and Techniques*, Springer, Germany.

[10] Kumar, D. and Srivastava, A. (2016), "Elastic properties of CNT-and graphene-reinforced nanocomposites using RVE", *Steel Compos. Struct*., **21**(5), 1085-1103.

[11] Ahmadi Asoor, A.A., Valipour, P. and Ghasemi, S.E. (2016), "Investigation on vibration of single-walled carbon nanotubes by variational iteration method", *Appl. Nanosci*., **6**(2), 243-249.

[12] Togun, N. and Bağdatlı, S.M. (2016), "Nonlinear vibration of a nanobeam on a pasternak elastic foundation based on non local Euler-Bernoulli beam theory", *Math. Comput. Appl*., **21**(3), 1-19.

[13] Ansari, R. and Hemmatnezhad, M. (2013), "Nonlinear finite element vibration analysis of double-walled carbon nanotubes based on Timoshenko beam theory", *J. Vib. Control*, **19**(1), 75-85.

[14] Karlicić, D., Kozić, P. and Pavlović, R. (2015), "Flexural vibration and buckling analysis of single-walled carbon nanotubes using different gradient elasticity theories based on reddy and huu-tai formulations", *J. Theor. Appl. Mech*., **53**(1), 217-233.

[15] Rakrak, K., Zidour, M., Heireche, H., Bousahla, A.A. and Chemi, A. (2016) "Free vibration analysis of chiral double-walled carbon nanotube using non-local elasticity theory", *Adv. Nano Res*., **4**(1), 31-44.

[16] Hajnayeb, A. and Khadem, S.E. (2015), "An analytical study on the nonlinear vibration of a doublewalled carbon nanotube", *Struct. Eng. Mech*., **54**(5), 987-998.

[17] Ali-Akbari, H.R. and Firouz Abadi, R.D. (2015), "Nonlinear free vibration of single-walled carbon nanotubes embedded in viscoelastic medium based on asymptotic perturbation method", *J. Sci. Eng*., **6** (2), 42-58.

[18] Bousahla, A.A., Benyoucef, S., Tounsi, A. and Mahmoud, S.R. (2016), "On thermal stability of plates with functionally graded coefficient of thermal expansion", *Struct. Eng. Mech*., **60**(2), 313-335.

[19] Bouderba, B., Houari, M.S.A., Tounsi, A. and Mahmoud, S.R. (2016), "Thermal stability of functionally graded sandwich plates using a simple shear deformation theory", *Struct. Eng. Mech*., **58**(3), 397-422.

[20] Menasria, A., Bouhadra, A., Tounsi, A., Bousahla, A.A. and Mahmoud, S.R. (2017), "A new and simple HSDT for thermal stability analysis of FG sandwich plates", *Steel Compos. Struct*., **25**(2), 157-175.

[21] El-Haina, F., Bakora, A., Bousahla, A.A., Tounsi, A. and Mahmoud, S.R. (2017), "A simple analytical approach for thermal buckling of thick functionally graded sandwich plates", *Struct. Eng. Mech.*, **63**(5), 585-595.

[22] Chikh, A., Tounsi, A., Hebali, H. and Mahmoud, S.R. (2017), "Thermal buckling analysis of cross-ply laminated plates using a simplified HSDT", *Smart Struct. Syst.*, **19**(3), 289-297.

[23] Beldjelili, Y., Tounsi, A. and Mahmoud, S.R. (2016), "Hygro-thermo-mechanical bending of S-FGM plates resting on variable elastic foundations using a four-variable trigonometric plate theory", *Smart Struct. Syst.*, **18**(4), 755-786.

[24] Zidi, M., Tounsi, A., Houari, M.S.A. and Bég, O.A. (2014), "Bending analysis of FGM plates under hygro- thermo-mechanical loading using a four variable refined plate theory", *Aerospace Sci. Tech.*, **34**, 24-34.

[25] Draiche, K., Tounsi, A. and Mahmoud, S.R. (2016), "A refined theory with stretching effect for the flexure analysis of laminated composite plates", *Geomech. Eng.*, **11**(5), 671-690.

[26] Hamidi, A., Houari, M.S.A., Mahmoud, S.R. and Tounsi, A. (2015), "A sinusoidal plate theory with 5-unknowns and stretching effect for thermomechanical bending of functionally graded sandwich plates", Steel Compos. Struct., 18(1), 235-253.

[27] Samir Belmahi, Mohamed Zidour, Mustapha Meradjah, Tayeb Bensattalah and Ahmed Dihaj.An alysis of boundary conditions effects on vibration of nanobeam in a polymeric matrix. Structural Engineering and Mechanics, Vol. 67, No. 5 (2018) 517-525.

[28] Samir Belmahi, Mohamed Zidour, Mustapha Meradjah. Small-scale effect on the forced vibration of a nano beam embedded an elastic medium using nonlocal elasticity theory. Advances in Aircraft and Spacecraft Science, Vol. 6, No. 1 (2019) 001-000 DOI:

[29] Riad HAMZA-CHERIF, Mustapha MERADJAH, Mohamed ZIDOUR,Abdelouahed TOUNSI, Samir BELMAHI and Tayeb BENSATTALAH. Vibration Analysis of Nano Beam Using Differential Transform Method Including Thermal Effect. Journal of Nano Research, Vol. 54, pp 1-14.

[30] Merdaci Slimane, Belmahi Samir, Belghoul Hakima, Hadj Mostefa Adda. Free Vibration Analysis of Functionally Graded Plates FG with Porosities. International Journal of Engineering Research & Technology (IJERT). Vol. 8 Issue 03, March-2019.

Classification Of Vocal Cord Diseases Using Wavelet Transforms in Multi-Class

Ecenur Aküren[*,1], Derya Yılmaz[2]

[*] ecenur.akuren@tubitak.gov.tr, ORCID: 0009-0002-7265-8197
[1]*Scientific and Research Council of Türkiye (TÜBİTAK), Ankara, Türkiye*
[2]*Department of Electrical and Electronics Engineering, Faculty of Engineering, Gazi University, Ankara, Türkiye,* deryayilmaz@gazi.edu.tr ORCID: 0000-0002-1903-7132

Abstract: Voice is a kind of energy that is shaped according to pressure changes, which is effective in the production of structures such as tongue, teeth, palate and larynx, as well as vocal cords. Voice, which has a variable dynamic in its nature, is also a unique identification tool for each person. The vocal folds produce the voice as vibrating by air passes through them during exhalation of air from the lungs. Some different deformation in these vocal tract components, especially vocal cords, which make up the voice in pathological cases are reflected in the voice, and the structure of the voice changes. Therefore, voice analyzes by using acoustics and traditional analysis techniques are frequently used in the assessment of vocal pathologies. In this study, healthy and three vocal cord pathologies such as cyst, polyp and sulcus were investigated by using wavelet transform and extracting features some of them come from nonlinear approaches which give useful especially findings in voice analysis. Feature selection algorithms of the Relief, one way Analysis of Variance (ANOVA) and Minimum Redundancy Maximum Relevance (MRMR) were performed to reduce the number of features by determining the importance of them. A four-class classifying procedure was realized by using two classifiers of Cosine K-Nearest Neighbor (KNN) and Neural Network to detection of voice disorders. Experimental results demonstrated that the multi-class classification test accuracies of 88.6 and 88.0 were achieved for Neural Network and KNN classifiers respectively and MRMR selection algorithm. The results provided promising classification accuracies in four-class classification to determination of voice diseases of vocal cord.

Keywords: *Voice disorders, KNN, Neural Network, Multi-Class Classification*

I. INTRODUCTION

Voice is produced by stimulating a dynamic vocal tract system consisting of various articulators, such as the lips, chin, and tongue, stimulated by a time-varying excitation signal. Disruptions in these organs cause the characteristics of the voice to change. It creates voice waves by vibrating the air flow with the vocal cords contained in the larynx, which is located in the upper part of the respiratory tract. The inefficacy of individuals to produce voice owing to functional or structural reasons is a symptom of voice disorders. There are many factors that can cause voice deficiencies. Chronic illnesses such as respiratory problems, gastric issues, allergies, hormonal imbalances, medical reasons such as thyroid surgery, intubation, heart surgery, and neurological disorders cause voice disorders. Voice pathologies can arise from infections, physiological and psychogenic factors, and may also be triggered by vocal misuse which is prevalent among professional groups such as teachers, singers and customer care representative (ccr) [1].

Diagnosis of voice disorders requires examination by experts and the use of medical equipment. Invasive techniques such as microsurgery, laryngeal frame surgery and vocal cord injection filling are utilized in the diagnosis of voice anomaly. However, these techniques pose risks for individuals as they require direct intervention to the vocal tract or respiratory system [2]. Therefore, non-invasive analysis methods utilizing computer-based voice analyzers in voice laboratories are preferred due to their lower risk, affordability, and comfort [3].

Acoustic voice analysis, which is a non-invasive method, helps experts as a complementary technique. Thus, contrary to the subjective measurement of voice quality based on expert experience, false results obtained in diagnosis are prevented. Due to the lack of a standardized method for voice disorder detection, research on non-invasive techniques is still ongoing.

In recent years, many studies have been carried out in the literature for the detection of voice disorders. Voice samples are processed by converting them into more useful features. Acoustic properties such as Mel-Frequency Cepstral Coefficients (MFCCs), pitch, shimmer, jitter, harmonic–noise ratio, noise energy were generally used in studies [4-9]. 11 features connected to the acoustic signal's the fundamental frequency, such as vibration, glow, and pitch, were used as features to detect healthy and pathological human voices with Spasmodic Dysphonia in [10], achieving 86% accuracy in distinguishing pathological voices. In [11], Five-Point Perturbation Division (PPQ), Divided by The Average Period (DDP), Harmonic to Noise Ratio (HNR), 3-Point Amplitude Perturbation Division (APQ3), Noise Harmonic Ratio (NHR), Correlation Dimension (D2) , Fundamental Frequency Variation (Spread1) and Pitch Period Entropy (PPE) have been extracted. In another study [18] which was utilized Saarbruecken Voice Database (SVD) which includes pathological data about distinct pathological problems and VD which includes Vocal Cyst (VC), Sulcus Vocalis (SV) and Vocal Fold Polyp (VFP) disorders, entropy, zero crossing rates (ZCR), MFCC, Kurtosis, Shimmer, Skewness and Jitter, largest area parameters (LAP), and two types of fusion models (Feature Level Fusion (FLF) and Decision Level Fusion (DLF)) by using artificial intelligence-based techniques (Convolutional Neural Network (CNN) and Long Short Term Memory Networks (LSTM)) were used for the detection of voice pathology. The best result 99.58% and 93.05% was obtained with DLF for VD and SVD, respectively.

Machine learning techniques are used in the detection of voice disorders because it takes less time and is inexpensive, and many studies have been done in this area [12-15]. The most widely used machine learning techniques are Decision Trees, Support Vector Machines (SVM), Artificial Neural Network (ANN), K-Nearest Neighbor (K-NN), CNN and LSTM. In [16], SVM, Decision Tree (DT), and a single-layer ANN were selected to estimate voice recordings of healthy subjects with hyperkinetic dysphonia, hypokinetic dysphonia, reflux laryngitis, and MFCC as features. Three classifiers were trained but not tested with a separate dataset. The highest classification accuracy (87.5%) is achieved by ANN classifier while SVM and DT performed 50% and 62.5% respectively. In [17], three different feature extraction approaches, wavelet transform, time/frequency, and cepstral, are compared. SVM (poly), SVM (core) and K-NN were chosen for classification. When used with SVM (poly) for cepstral features, an accuracy of around 80% was obtained [17].

It is seen that acoustic features, such as jimmer, jitter, fundamental frequencies, harmonics, and the change of voice energy over time, have been used in literature to make voice analysis and voice recognition. In the field of voice analysis, it is inevitable to encounter the limitations of traditional acoustic features. These limitations indicate that traditional acoustic features have some limitations on the full understanding and representation of complex audio data. The fundamental motivation of this study is to detect voice disorders related to the vocal cords by using multi-class classification and nonlinear properties of voice. In this study, the advantages of nonlinear features and their potential to provide an opportunity to develop new and effective

approaches in voice analysis. For this purpose, wavelet transforms, and some nonlinear features were used for analyzing the voice recordings obtained from three vocal cord problems and healthy case. Multi-class classification was implemented by using three feature selection algorithms and two classifiers for diagnosis voice disorders.

II. MATERIALS AND METHODS

The processes of this study were represented as a block diagram in Fig. 1. Voice recordings were taken from 57 people in the Department of Otorhinolaryngology, Faculty of Medicine, Sütçü İmam University. First of all, filtering is done to reduce and remove the noise in the raw signals. Normalization was applied to the signals. Three levels of denoising were performed. In denoising, Daubechies (db8) wavelet, heursure thresholding, which is an intuitive thresholding method, were used. A pre-emphasis filter was applied to normalize the energy losses at the beginning and end of the signal. Various features were obtained by performing the windowing process. In order to get better performance of the classification in the detection of voice disorders, feature selection was made and the performance analysis of the classification methods was made by applying machine learning techniques.

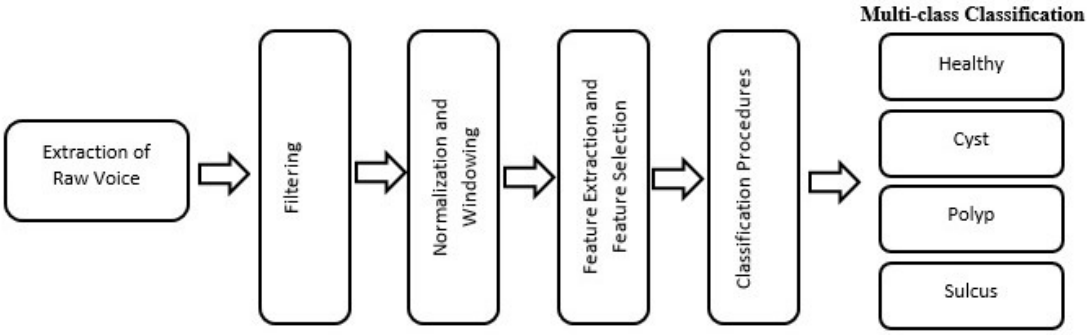


Fig. 1. Processing of voice signal.

A. Data

The data used in this study were obtained from the Department of Otorhinolaryngology, Faculty of Medicine, Sütçü İmam University. Data of 57 subjects (15-72 years old) from 15 healthy and 14, 15 and 13 patients with cyst, polyp and sulcus problems respectively, which was used in [18], were recorded. The information in relation to the database is given in Table 1. The recording was made in a quiet room with a background noise level of 45-60 dB(A), a sampling rate of 44100, and a 16-bit resolution level in single-channel pulse code modulation (PCM) format. /a/ audio was recorded for an average of 10 seconds. Signals from vocal fold disorders in this study are given as an example, in Fig. 2.

TABLE I
Pathological and Healthy Records of Voices

	# of males	**# of females**	**Total # of patients**
Healthy	8	7	15
Cyst	6	8	14
Polyp	6	9	15
Sulcus	5	8	13
Total			57

Before framing, 10000 segments from the beginning of the signal which have high energy and 30000 segments from the end of the signal which have low energy are subtracted. Then the resulting signal is divided into frames by choosing the window size of 40 ms with 20% overlap. In total 3445 samples for normal, 9154 samples for cyst, 7885 samples for polyp and 5966 samples for sulcus were obtained after framing. Among the samples obtained after framing, the samples with the least number of normal (229 samples×15), cyst (229 samples×14), polyp (229 samples×15) and sulcus (229 samples×13) were selected.

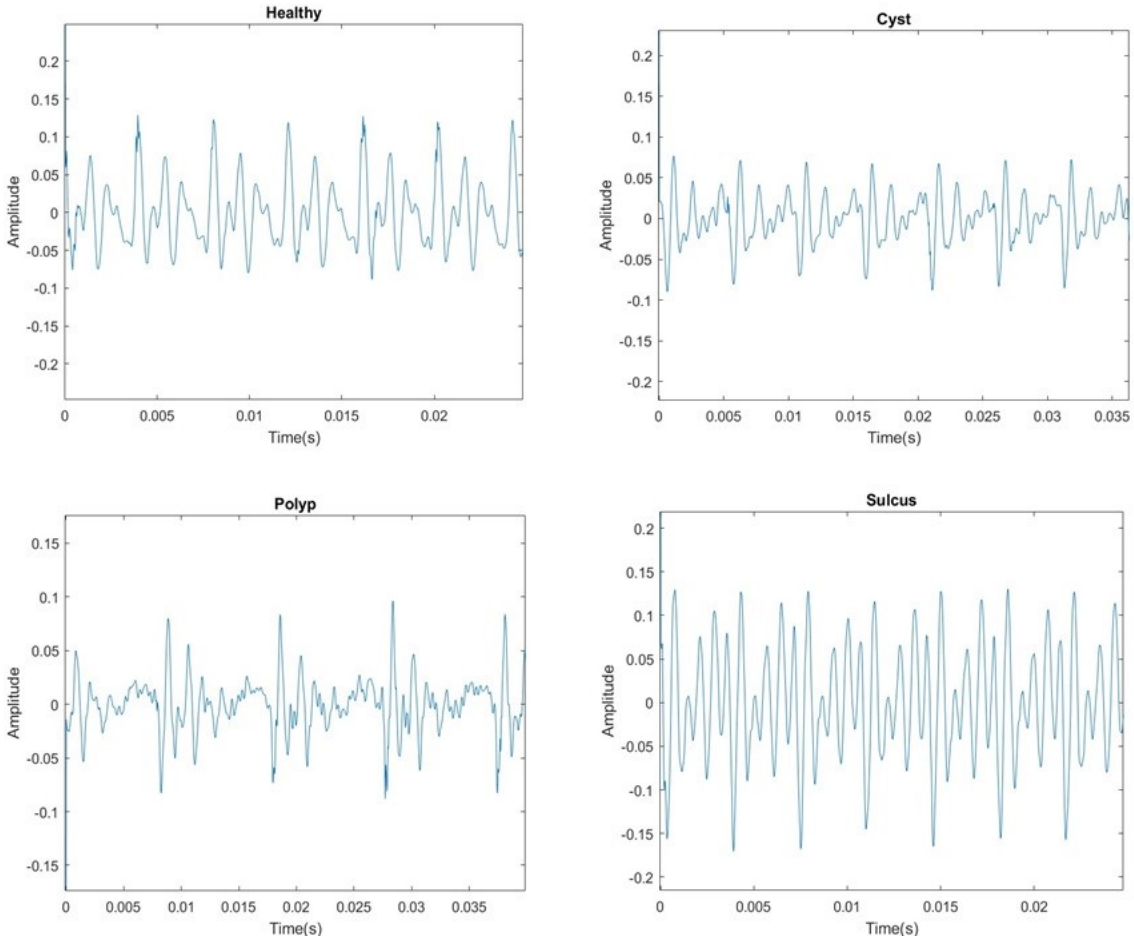


Fig. 2. Signals from vocal cord disorders.

B. Wavelet and Feature Extraction

Wavelet transform has the ability to analyze signals in both time and frequency domain. It differs from Fourier transform in which time and frequency are determined simultaneously. While the Fourier transform analyzes a signal at a fixed frequency, the wavelet transform can analyze how the signal changes over time and how different frequency components are related to time. This provides the ability to detect local changes over time. In feature extraction, wavelet transform is especially used in areas such as signal processing, image processing and time series analysis. The extraction of features in the dataset is accomplished by applying the wavelet transform at different scales (frequency and time resolution). This can help identify important structures and patterns within the data and then use those attributes for further analysis or modeling. In this paper, signal was decomposed into 6 levels and 178 features were calculated. The extracted features are given in Fig. 3, and their mathematical expressions are shown in Table II.

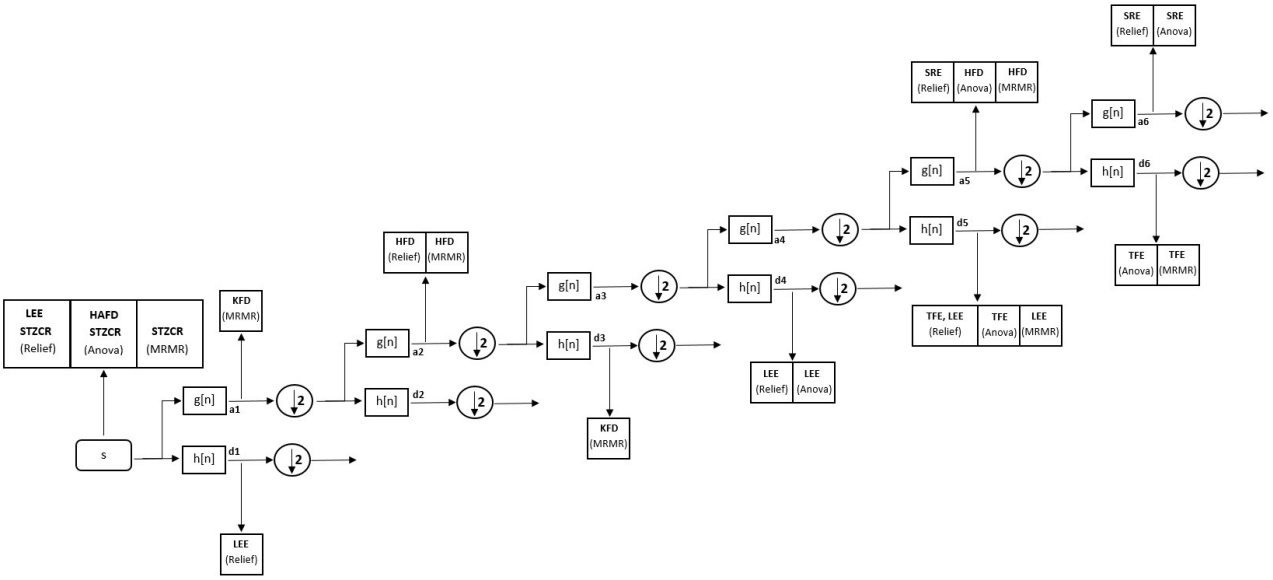


Fig. 3. Representation of wavelet transform and extracted features.

Square Root Energy (SRE): This feature represents the energy of the audio signal. The voice signal is an indication of pressure fluctuations that change over time. The audio signal energy is the time integral of the square of the amplitude of these fluctuations. SRE provides the square root of the energy values to spread over a wider range when calculating the energy. In this way, a more balanced and useful feature is obtained.

Time Frequency Entropy (TFE): It simultaneously analyzes the audio signal's the frequency and time properties. Entropy measures disorder or uncertainty of a signal. TFE provides information about the energy distribution and variability of the audio signal and shows the behavior of different frequency components over time.

Logarithmic Energy Entropy (LEE): It measures entropy, which is a disorder of the energy distribution of the audio signal. LEE is utilized to analyze the audio signal's the spectral contents and especially to evaluate the properties of the voice such as frequency distribution and voice intensity changes. It is particularly useful for understanding and representing the spectral characteristics of an audio signal in applications such as music analysis, speech recognition, voice effects extraction.

TABLE II
Extracted Features

Name of Features	**Features and Mathematical Expression**	
Square Root Energy (SRE)	$\sqrt{\frac{1}{N}\sum_{n=1}^{N} x(n)^2}$	(1)
Time Frequency Entropy (TFE)	$-\sum_t \sum_f \lvert S(t,f)\rvert^2 \ln \lvert S(t,f)\rvert^2$	(2)
Logarithmic Energy Entropy (LEE)	$-\sum_{i=1}^{N} (log_2(p_i))^2$	(3)
Short-Term Zero Crossing Rate (STZCR)	$\frac{1}{N-1}\sum_{i=1}^{N-1} \lvert sgn(x[i]) - sgn(x[i-1])\rvert$	(4)
Higuchi Fractal Dimension (HFD)	$\frac{1}{n}\sum_{m=1}^{n} L_m(n)$	(5)

Hausdorff Fractal Dimension (HAFD)	$\frac{log(N)}{log(r)}$	(6)
Katz Fractal Dimension (KFD)	$\frac{log(n)}{log(D/L) + log(n)}$	(7)

Entropy is calculated using the probability distribution of the energy spectrum values. Usually a logarithmic measurement is used because the energy spectrum values can vary over large ranges and the logarithmic scale reflects the irregularity.

Short-Term Zero Crossing Rate (STZCR): It measures how many times the audio signal crosses the zero line in time. It is used to capture the periodic properties and energy variations of the audio signal. A low crossing rate often indicates low-frequency voices, while a high crossing rate may indicate high-frequency voice.

Higuchi Fractal Dimension (HFD): It measures the fractal properties of the audio signal. Fractals can be thought of as mathematical structures composed of self-similar parts. HFD can determine the irregularity and complexity levels of the audio signal and reveal its time-series characteristics.

Hausdorff Fractal Dimension (HAFD): It is the feature type used especially in image processing and pattern recognition. HAFD is a metric used to measure the complexity or discrete nature of an object. The fractal dimension provides an indication of the object's complexity and discrete nature. A higher fractal dimension indicates that the object has a more complex and discrete nature. An object's HAFD is a metric that measures how that object is distributed in space. In the context of audio analysis, the HAFD is often used to understand how the audio signal changes with time and frequency. In this way, the complexity and structure of the voice can be accurately evaluated.

The Katz Fractal Dimension (KFD): It is an attribute used specifically to measure discrete or complex structures of objects. This feature, which is widely used in image processing and pattern recognition, is especially used to determine the degree of irregularity or fracture of objects. It can also be used in the context of audio analysis to evaluate the disorder or complexity of the audio signal. A higher KFD indicates that the voice has a more complex or disordered nature.

C. Feature Selection

Feature selection is an essential step aimed at understanding the relationship between the features in a dataset and a specific target variable, as well as improving model performance. Minimum Redundancy Maximum Relevance (MRMR), Relief and one way Analysis of Variance (ANOVA) were used as feature selection algorithm.

The Relief algorithm used in feature selection, is an effective method for classification problems. The Relief algorithm evaluates the contributions of features in the dataset to the classification performance, aiming to determine effective and important features. Particularly used in high-dimensional datasets, this method aims to reduce data dimensionality to achieve better performance. The Relief algorithm assigns weights to samples to determine effective features. These weights are calculated based on the differences in the feature values of neighbors of similar class and different class.

After updating the weights for all attributes, the attributes are prioritized using the resulting weights. Higher weighted features have more classification performance.

One way ANOVA is a statistical analysis method used to evaluate significant differences among different groups. This selection aims to identify the most important features to be used in the model and to bring down the negative impact of unnecessary or less effective features on the model.

The MRMR algorithm aims to select features that both maximize the relationship of features with the target variable and minimize the relationship between each other. Thus, more efficient features are obtained for classification models.

III. CLASSIFICATION METHODS

Neural Network and Cosine KNN were used to classify the groups. Health, cyst, polyp and sulcus groups consist of 15, 14, 15 and 13 subjects respectively. Two subjects from each group were separated for testing. The dataset was divided into two groups which were train (87%) and test (13%). In classifications, 5-k fold validation procedure was used.

A. K-Nearest Neighbours (KNN)

KNN, one of the supervised learning methods, aims to associate a data point with the classes of the nearest "K" neighbor data point around it. The KNN algorithm, which represents data points according to their positions in space, makes classification using similarity or distance criteria in space [19], [21]. The most commonly used distance criteria in the KNN algorithm are Euclidean (Euclidean), Minkowski, Hamming and Cosine Distances. Cosine KNN algorithm uses cosine similarity, which is a measure of similarity based on the angle between data points [20]. If the angle between the two vectors is 0 degrees, the cosine similarity approaches 1, indicating the highest similarity. Conversely, if the angle between the two vectors is 90 degrees, the cosine similarity approaches 0, indicating the lowest similarity.

B. Neural Network

The successful solution of classification problems is an important research topic in machine learning. Neural Network (NN) is neural network based classifier that consists of multiple layers and performs non-linear operations [22]. Trained with the backpropagation algorithm, NN has the capability to detect data patterns by adjusting the weights between layers. As a result, NN has achieved successful results in various domains, such as natural language processing, image recognition and speech detection [23].

Bilayered Neural Network (BNN) includes an input layer that receives the raw data and an output layer which provides the network's predictions. Thus, the computational complexity is reduced and quick decision making becomes easier. The working principle of the BNN is as follows: Input data is transmitted to the network by the input layer. Predictions based on learned relationships between the input and the desired output are generated by the output layer. Adjustment is made using optimization techniques such as gradient descent to minimize the error between the actual and predicted outputs. At each iteration, the network calculates the error and calculates the gradient of the error according to the weights. The weights are updated to this process and this process continues until the amount of network error is minimized.

BNN provides a compact and powerful solution for various machine learning processing. Its simple architecture is preferred in scenarios that require fast estimation.

IV. RESULTS AND DISCUSSION

The results obtained from the voice disorder classification are presented in this section. Features are selected Relief, ANOVA and MRMR. Pathology detection experiments were performed by using the Neural Network and Cosine KNN classifiers with the individual feature sets. In total, 7 features with Relief, 6 features with ANOVA and 7 features with MRMR are used. The most commonly used 3 features are as follows:

• STZCR - used on the non-decomposed signal for both the Relief algorithm and the ANOVA algorithm.

• HFD - used on the 5th degree approximation coefficient for both the Relief algorithm and the Anova algorithm.

• TFE - used on the 5th and 6th degree detail coefficients for the Relief algorithm and the MRMR algorithm.

These features are commonly used in audio signal analysis and represent different characteristics of the audio signal. In applications such as audio processing and recognition, these features help in better understanding, classifying, and processing audio data. For instance, these features are widely utilized in several fields such as speech recognition systems, music classification, voice effects, and speech analysis.

The nonlinear states of the groups can be analyzed by evaluating the values of the features given in Table III. As the LEE values are observed for all classes in Table III, it is seen that LEE increases from the healthy to the sulcus. For TFE and HFD values, a decreasing from the healthy to the sulcus was obtained, which means that the distribution of signal components is getting flatter.

The success rates were obtained with three different feature selection algorithms (Relief, ANOVA, MRMR) for two different classification methods, BNN and Cosine KNN. 5-fold cross validation process was used and 20 features selected from 178 features with Relief, ANOVA and MRMR. In the classifications performed using BNN and Cosine KNN, the classifier performance results are given in Table 4. As can be seen from Table 4 the best result was obtained with BNN in MRMR with 88.6% accuracy, 88.6% sensitivity and 96.2% specificity.

For Cosine KNN method, the highest success rate is achieved with the MRMR algorithm (88.0%) and confusion matrice of test is presented in Fig. 4. The success rates obtained with the other two feature selection algorithms are lower than MRMR (Relief: 52.5%, ANOVA: 61.0%).

The confusion matrice of the best classification test result obtained with the BNN for MRMR in Fig. 5. Most of the samples were placed in the correct class within 4 classes. 24 patient in polyp (2) were classified as healthy and 13 patients in healthy (0) were classified as cyst.

For BNN method, the highest success rate is achieved with the MRMR algorithm (88.0%). The success rates obtained with the other two feature selection algorithms are lower (Relief: 58.8%, ANOVA: 73.1%).

TABLE III
The Mean ± SD Values of Selected Features in Both Classification Procedures for Groups

Features	Healthy	Cyst	Polyp	Sulcus
SRE	0.9443±0.495	0.5264±0.334	0.5084±0.4957	0.6935±0.7005
TFE	0.5696±0.006	0.5685±0.0147	0.5656±0.0079	0.5651±0.0111
LEE	-20008.5±1168.21	-20728.38±3609.6	-21113.98 ±1800.92	-22618.05 ±2406.75
STZCR	0.0473±0.016	0.0418±0.0114	0.0352±0.0099	0.0369±0.0130
HFD	1.0572±0.031	1.0499±0.02	1.0425±0.016	1.0395±0.0156
HAFD	1.0168±5.92E-05	1.017±0.0006	1.0125± 8.63E-05	1.0189± 9.24E-05
KFD	1±1.43E-06	1±3.11E-06	1± 5.98E-07	1± 1.15E-06

TABLE IV
Classification Results of The Models

Feature Selection Algorithm	Classification Method	Accuracy (%)		Sensitivity (%)		Specificity (%)	
		Train	Test	Train	Test	Train	Test
Relief	Bilayered Neural Network	85.2	58.8	85.0	58.8	95.1	86.8
	Cosine KNN	89.5	52.5	89.3	52.3	96.5	84.2
ANOVA	Bilayered Neural Network	93.1	73.1	93	73.2	97.8	93.1
	Cosine KNN	89.4	61.0	89.1	61.3	97.0	86.2
MRMR	Bilayered Neural Network	**94.4**	**88.6**	**94.2**	**88.6**	**98.1**	**96.2**
	Cosine KNN	**94.5**	**88.0**	**94.4**	**88.05**	**98.2**	**96.0**

In[11], it was aimed to detect parkinson disease using ANN and KNN on voice disorders. In this experiment acoustic features were used. 84.34% correct classification rate was obtained by using ANN. So in our study, it is observed that results in a better performance with 88.6% accuracy using BNN. In [16], it is indicated that the best accuracy was 86.66% with Decision Tree (DT) comparing with SVM (80%) and KNN (81.66%) to compare healthy and pathological voices using Saarbruecken Voice Database. It is seen that better result is obtained both training and testing the data in our study than other results. In [24], pathological disorder of voice was detected performing VGG-16 CNN by using Respiratory Sound Database with 92.03% accuracy. Only the training process was done in this paper. Higher accuracy rates were obtained when only the training process was performed in our paper. But it is substantial to make classifying process separating the

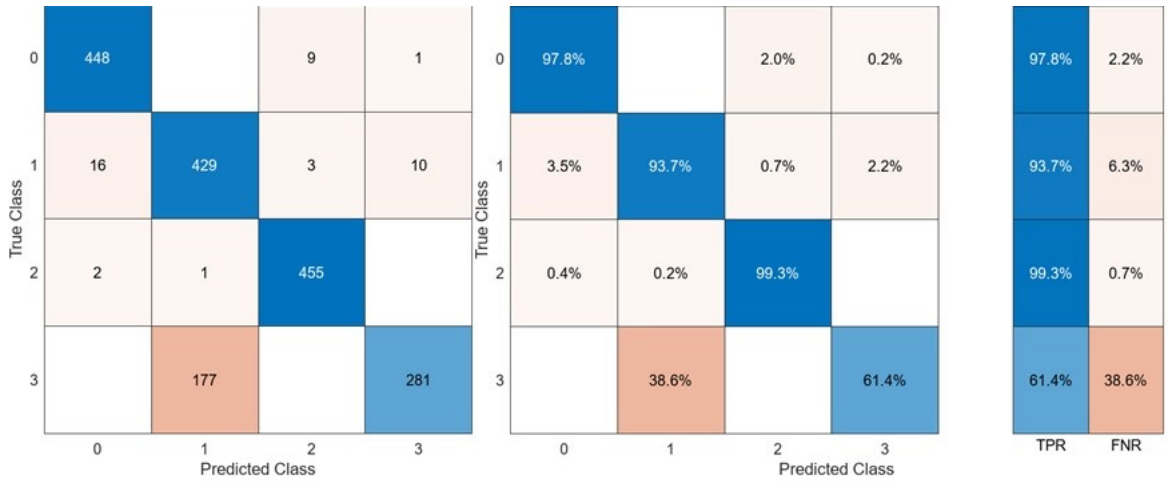


Fig. 4. The test confusion matrice of for multi-class with Cosine KNN and MRMR algorithm (0: healthy 1: cyst 2: polyp 3: sulcus) a) Number of observations. b) Decision percentages, TPR and false negative rate (FNR) values.

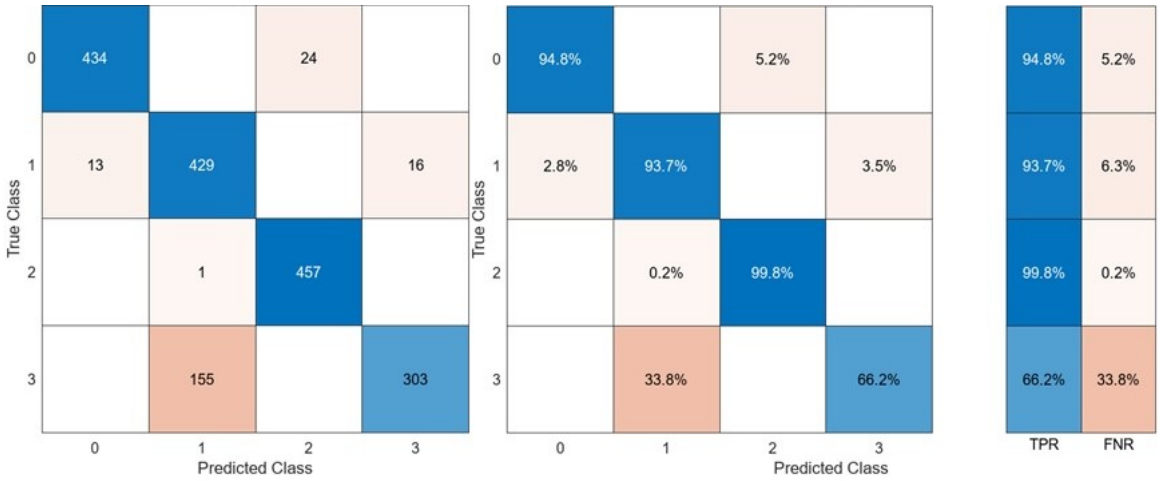


Fig. 5. The test confusion matrice of for multi-class with Bilayered Neural Network and MRMR algorithm (0: healthy 1: cyst 2: polyp 3: sulcus) a) Number of observations. b) Decision percentages, TPR and false negative rate (FNR) values.

database into training and test data to get correct results. In [18], 99.58% training accuracy as the best result was achieved with DLF for VD and the test procedure was not applied. The highest training accuracy we obtained in our study for VD was found to be 94.5% using MRMR algorithm performing BNN.

V. CONCLUSION

In this study, we investigated the performance of two essential components in voice disorder classification: the MRMR feature selection algorithm and BNN. Our dataset comprised 57 subjects, including 15 healthy individuals and 14, 15 and 13 patients with cyst, polyp, and sulcus problems respectively. Using Relief, ANOVA, and MRMR algorithms, we extracted the features from the audio signals. The results indicated that the MRMR algorithm consistently outperformed the other feature selection methods, exhibiting the highest accuracy for classification method BNN.

Moreover, our findings demonstrated the effectiveness of BNN as a classifier, yielding remarkable success rates in voice disorder classification. The BNN approach, which combines multiple different learning models, proved to be robust and stable in solving complex classification problems. By balancing the errors of various models, BNN achieved better generalizability and reliability in voice disorder diagnosis.

In conclusion, the combination of the MRMR feature selection algorithm and BNN provided a powerful and effective solution for voice disorder classification. These techniques hold significant potential for medical diagnosis and speech recognition systems. The results of this study shed light on the importance of feature selection algorithms and BNN in enhancing the accuracy and reliability of voice disorder classification, offering valuable insights for further research and development in this domain.

VI. ACKNOWLEDGMENT

The author would like to thank Prof. Dr. M. Akif Kılıç for sharing the database.

REFERENCES

[1] S. R. Kadiri, and P. Alku, "Analysis and Detection of Pathological Voice Using Glottal Source Features," IEEE Journal of Selected Topics in Signal Processing, vol. 14, no. 2, pp. 367, February 2020.

[2] H.R. Sharifzadeh, I.V. Mcloughlin, F. Ahmadi, "Speech Rehabilitation Methods for Larynegctomised Patients, " Springer, Amsterdam, The Netherlands, pp. 597–607, 2010.

[3] T. Zhang, Y. Wu, Y. Shao, M. Shi, Y. Geng and G. Liu, "A Pathological Multi-Vowels Recognition Algorithm Based on LSP Feature," IEEE Access, vol. 7, April 2019.

[4] Ö. Eskidere, A. Gürhanlı, "Voice Disorder Classification Based on Multitaper Mel Frequency Cepstral Coefficients Features," Hindawi Publishing Corporation Computational and Mathematical Methods in Medicine, June 2015

[5] K.H. Malki, "Voice disorders among Saudi teachers in Riyadh city," Saudi J. Otorhinolaryngol. Head Neck Surg. 12 (2) (2010) 189–199.

[6] B. Boyanov, S. Hadjitodorov, "Acoustic analysis of pathological voices. A voice analysis system for the screening of laryngeal diseases," IEEE Eng Med Biol Mag., vol.16, pp.74-82, August 1997.

[7] M. Chen, Y. Ma, J. Song, C. Lai, B. Hu, "Smart clothing: Connecting human with clouds and big data for sustainable health monitoring, " Mobile Netw. Appl., vol.21, pp.825–845, 2016.

[8] B.S. Atal, "Effectiveness of linear prediction characteristics of the speech wave for automatic speaker identification and verification", J. Acoust. Soc. Am., vol.55, pp.1304–1312, 1974.

[9] M. Chen, Y. Ma, Y. Li, D. Wu, Y. Zhang, C.-H. Youn, "Wearable 2.0: Enabling human-cloud integration in next-generation healthcare systems, " IEEE Communications Magazine, vol.55, pp.54–61, 2017.

[10] E. Hadjaidji, M. C. A. Korba, and K. Khelil, "Spasmodic Dysphonia Detection Using Machine Learning Classifiers," International Conference on Recent Advances in Mathematics and Informatics (ICRAMI), Septembet 2021.

[11] O. Asmae, S. Sara, R. Abdelhadi, K. Tajeddine, and C. Bouchaib, "Parkinson's Disease Identification using KNN and ANN Algorithms based on Voice Disorder," 1st International Conference on Innovative Research in Applied Science, Engineering and Technology (IRASET), April 2020.

[12] U. Cesari, G. De Pietro, E. Marciano, C. Niri, G. Sannino and L. Verde, "Voice disorder detection via an m-Health system: Design and results of a clinical study to evaluate Vox4Health," BioMed Research International, 2018.

[13] L. Verde, G. De Pietro and G. Sannino, "Voice disorder identification by using machine learning techniques, " IEEE Access, 2018.

[14] S.H. Fang, Y. Tsao, M.J. Hsiao, J.Y. Chen, Y.H. Lai, F.C. Lin, C.T. Wang, "Detection of pathological voice using cepstrum vectors: A deep learning approach," Journal of Voice, vol.33, pp 634-641, September 2019.

[15] H. Wu, J. Soraghan, A. Lowit and G. Di Caterina, "A Deep Learning Method for Pathological Voice Detection Using Convolutional Deep Belief Networks," Conference: Interspeech, 2018.

[16] M.G. Milani, M. Ramashini, and M. Krishani, "A real-time application to detect human voice disorders," International Conference on Decision Aid Sciences and Application (DASA), November 2020.

[17] R. Laila, L. Salwa, and R. Mohammed, "Detection of voice impairment for Parkinson's disease using machine learning tools", 10th International Symposium on Signal, Image, Video and Communications (ISIVC), April 2021.

[18] H. Ankışhan, and S. Ç. İnam, "Voice pathology detection by using the deep network architecture," Applied Soft Computing, vol. 106, July 2021.

[19] B. Nassih, N. Hmina and A. Amine, "Face Classification under Different Kernel Function Compared to KNN Classifier," 2016 13th International Conference Computer Graphics, Imaging and Visualization, May 2016.

[20] C. Chethana, "Prediction of Heart Disease using Different KNN Classifier," Proceedings of the Fifth International Conference on Intelligent Computing and Control Systems (ICICCS 2021), 2021.

[21] P. Ghadekar, S. Ingole and D. Sonone, "Handwritten Digit and Letter Recognition Using Hybrid DWT-DCT with KNN and SVM classifier," 2018 Fourth International Conference on Computing Communication Control and Automation (ICCUBEA), 2018.

[22] W. Jiang and S. G. Kong, "Block-Based Neural Networks for Personalized ECG Signal Classification," IEEE Transactions on Neural Networks, vol. 18, November 2007.

[23] Y. LeCun, Y. Bengio, and G. Hinton, "Deep learning, " Nature, vol. 521, pp.436-444, May 2015.

[24] A. B. Gumelar, E. M. Yuniarno, W. Anggraeni, I. Sugiarto, V. R. Mahindara, and M. H. Purnomo, "Enhancing Detection of Pathological Voice Disorder Based on Deep VGG-16 CNN," 3rd International Conference on Biomedical Engineering (IBIOMED), January 2020.

Sualtı Teknolojileri ile Elde Edilen Sonar Verilerine Dayalı Derin Öğrenme Tabanlı Mayın ve Kaya Ayırımının Tespiti

Deep Learning Based Mine and Rock Separation Detection Based on Sonar Data Obtained by Underwater Technologies

Ammar ASLAN[1], Tugay TELÇEKEN[2], Kubilay HAN[*,3]

[*]kubilayhan@subu.edu.tr, ORCID: 0000-0003-1472-2832
[1]*Bilgisayar Teknolojileri Bölümü Bilgisayar Teknolojisi Programı, Batman Üniversitesi, TÜRKİYE*
[2]*Destek Hizmet Müdürlüğü, Elazığ Belediyesi, TÜRKİYE*
[3]*Makine Mühendisliği / Lisansüstü Eğitim Enstitüsü, Sakarya Uygulamalı Bilimler Üniversitesi, TÜRKİYE*

Özet: Bir ülkenin deniz sınırlarını savunma amacıyla sıkça sualtı mayınları kullanılmakta ve bu mayınlar stratejik bir askeri araç olarak değerlendirilmektedir. Sualtı mayınlarının yapısına bakıldığında patlayıcı madde, tespit cihazı ve tetikleme mekanizmasından oluşan tam otonom cihazlar olduğu görülmektedir. Ancak eski tip mayınlar incelendiğinde aktif hale gele bilebilmeleri için (patlamayı gerçekleştirebilmek için) bir nesne ile fiziksel temas gerektirmektedir. Bu mayınların tespiti için genellikle sonar sistemler ve sualtı teknolojileri kullanılmaktadır. Sualtı teknolojileri günümüzde denizaltılar ve otonom cihazlar olarak karşımıza çıkmaktadır. Akustik navigasyon menzili olarak da bilinen sonar sistemleri ise su yüzeyinin üstünde veya altındaki nesnelerin keşfi, etkileşimi veya tespiti amacıyla ses dalgalarının kullanıldığı bir yöntem olarak bilinmektedir. Bu çalışma, denizaltı verilerinin frekans analizi yoluyla mayın ve kayaların sınıflandırılması amacıyla geliştirilen bir yapay sinir ağı modelini ele almaktadır. Çalışmada veri ön işleme adımları gerçekleştirilmiş, veri setindeki sayısal olmayan alanlar sayısal değerlerle eşleştirilmiş ve boş alanlar median kullanılarak doldurulmuştur. Veri setinin etkisiz verileri korelasyon analiziyle tespit edilmiş ve performans artırımı sağlamak için bu veriler kaldırılmıştır.
Oluşturulan yapay sinir ağı modeli, denizaltı verilerinin frekans bileşenlerini analiz ederek nesneleri (mayın veya kaya) sınıflandırmak üzere tasarlanmıştır. Modelin mimarisi tablo şeklinde verilmiş ve toplamda 3041 öğrenilebilir parametre içermektedir. Modelin eğitimi 1425 veri noktası kullanılarak yapılmış ve elde edilen sonuçlar yüzde 96 gibi yüksek bir başarı oranıyla değerlendirilmiştir. Ayrıca, modelin eğitim süreci görsellemelerle desteklenmiş ve doğrulama performansı da değerlendirilmiştir. Çalışmanın sonuçları, denizaltı verilerinin frekans analiziyle sınıflandırılmasının etkinliğini göstermiş ve yapay sinir ağlarının bu tür özelleşmiş uygulamalarda başarılı bir şekilde kullanılabileceğini vurgulamıştır. Frekans analizi gibi spesifik yöntemlerin, gerçek dünya uygulamalarında nasıl etkili sonuçlar doğurabileceği bu çalışma ile ortaya konulmuştur.

Anahtar Kelimeler: *Sualtı Teknolojileri, Mayın, Sonar Sitemler, Yapay Sinir Ağları*

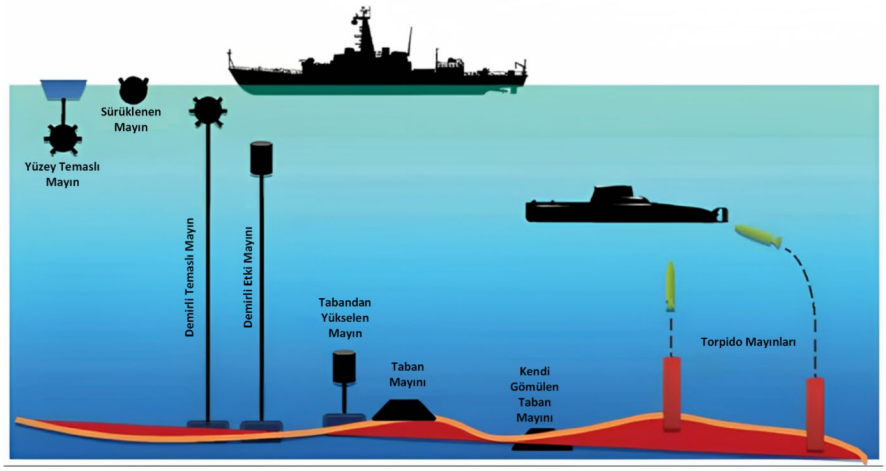
Abstract: Underwater mines are frequently used to defend a country's maritime borders and are considered a strategic military tool. When we look at the structure of underwater mines, we see that they are fully autonomous devices consisting of explosive material, a detection device, and a triggering mechanism. However, when old-type mines are examined, they require physical contact with an object in order to be activated (in order to realize the explosion). Sonar systems and underwater technologies are generally used to detect these mines. Underwater technologies are nowadays seen as submarines and autonomous devices. Sonar systems, also

known as acoustic navigation ranges, are a method that uses sound waves to explore, interact with, or detect objects above or below the water surface. This study deals with an artificial neural network model developed for the classification of mines and rocks through frequency analysis of submarine data. In the study, data preprocessing steps were performed, non-numeric fields in the data set were matched with numeric values, and empty fields were filled using the median. Ineffective data in the dataset was identified by correlation analysis and removed to improve performance. The neural network model is designed to classify objects (mines or rocks) by analyzing the frequency components of submarine data. The architecture of the model is given in tabular form and contains a total of 3041 learnable parameters. The model was trained using 1425 data points, and the results obtained were evaluated with a high success rate of 96 percent. In addition, the training process of the model was supported with visualizations, and the validation performance was also evaluated. The results of the study demonstrated the effectiveness of classification of undersea data using frequency analysis and emphasized that artificial neural networks can be successfully used in such specialized applications. This study demonstrates how specific methods, such as frequency analysis, can produce effective results in real-world applications.

Keywords: *Underwater Technologies, Mines, Sonar Systems, Artificial Neural Networks*

I. GİRİŞ

Bir ülkenin deniz sınırlarını korumak amacıyla genellikle sualtı mayınları kullanılır. Bu mayınlar stratejik bir askeri araç olarak kabul edilir. Sualtı mayınları yapısı incelendiğinde patlayıcı madde, algılama cihazı ve sigorta mekanizmasından oluşan tam otonom cihaz olarak karşımıza çıkmaktadır. Eski tip mayınlar patlamayı gerçekleştirebilmek için gemiyle fiziksel temas gerektirirken yeni nesil mayınlar ise genellikle akustik ve manyetik sinyallerin belli kombinasyonlarını tespit edebilen gelişmiş sensörlerle donatılmıştır. Aralarında yapay zekâ ile donatılmış akıllı mayınların da bulunduğu bazı türler yanıltıcı sinyaller yayarak tespiti zorlaştırmaktadır. Bu tür akıllı mayınlar gemilere ve denizaltılara büyük bir tehdit oluşturabilmektedirler [1]. Şekil 1'de su altında kullanılan mayın çeşitleri gösterilmiştir.



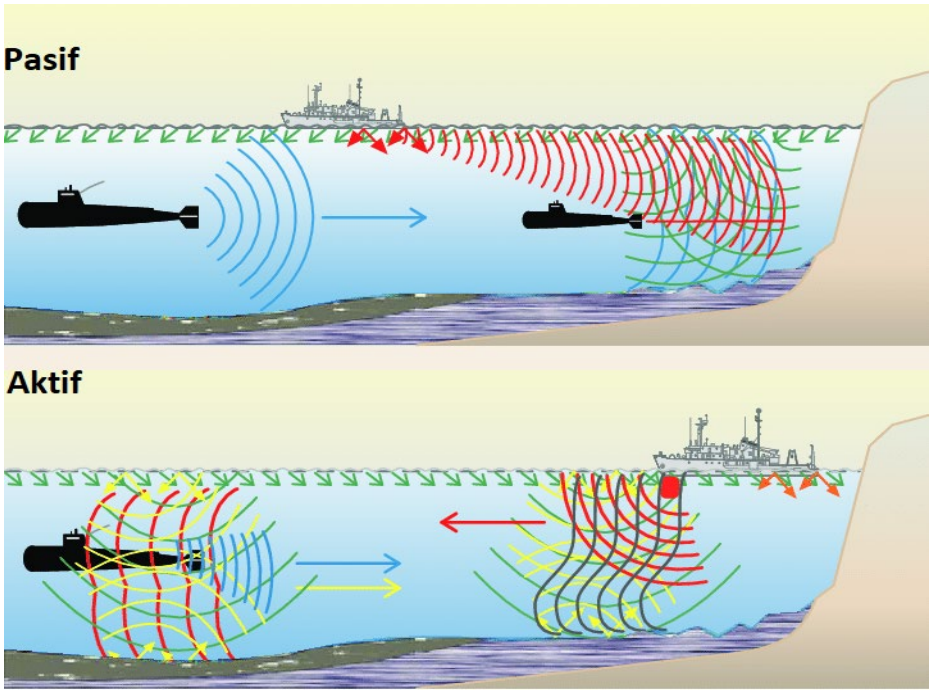
Şekil 1. Sınıflandırılmış deniz mayınları [2].

Sualtı mayınları, deniz kıta sahanlığının etkili bir şekilde savunulması ve güvenliğinin sağlama amacıyla yaygın olarak kullanılmaktadır. Bu tür mayınlar gelen gemi trafiğini kontrol etmek ve düşman denizaltılarına karşı önlem almak gibi önemli görevleri yerine getirmektedir. Ancak geleneksel tespit yöntemlerine karşı gelişen teknolojiyle birlikte sualtı mayınları da evrim geçirmiştir. Su altı mayınlarının tespiti için sonar sistemler kullanılmaktadır [3]. Sonar sistemleri bu alanda kaydedilen önemli bir ilerlemeyi temsil eder.

Sonar sistemleri su yüzeyi üzerindeki veya altındaki nesneleri tespit etmek veya onlarla iletişim kurmak için ses yayılımını kullanan bir tekniktir [4]. Sonar tespitinde aktif ve pasif

sonar teknolojileri olmak üzere iki temel prensip su altı ortamlarının keşfi amacıyla uzun yıllardır çalışılmaktadır. Pasif sonar, hedef unsurların yaydığı ses dalgalarını algılayarak hedeflerin konumunu ve diğer ilgili bilgileri elde etmekte kullanılır. Aktif sonar, su altındaki nesneleri tespit etmek için hidroakustik sinyaller gönderen bir cihaz olarak kullanılır. Bu teknoloji, resifler, gemi enkazları, okyanus derinlikleri ve ses emisyonu düşük denizaltılar gibi sabit ve düşük radyasyonlu gürültü yayan hedeflerin tespitinde etkilidir [5].

Sualtı hedeflerinin gizliliğine yönelik artan endişelerle birlikte, geleneksel monostatik sonarın performansı sınırlı hale gelmiştir. Ancak, çoklu platformların iş birliğiyle çalıştığı çok-tabanlı koordineli sonar teknolojisi, geniş tespit aralığı, esnek konfigürasyon ve parazite karşı üstünlük gibi avantajlar sunmaktadır [6]. Şekil 2' de pasif ve aktif olarak kullanılan sonar sistemleri gösterilmiştir.



Şekil 2. Aktif ve pasif denizaltı sonar sistemlerinin çalışma gösterimi [7].

Sonar sistemlerdeki verilerin birçoğu sualtı teknolojileri kullanılarak elde edilmektedir. Sualtı teknolojileri günümüzde çok ilerlemiş durumdadır. Bu teknolojilerin başında insansız su altı araçları gelmektedir. Bu otonom araçlar ile sualtı hareketlerinin gözlemlenmesi, okyanus tabanı sıcaklık haritalarının oluşturulması, gemi altı hasarlarının uzmanlık gerektiren incelemeleri, tehlikeli derinliklerden görüntü yakalama, batık araştırmaları, sahil güvenliğinin sağlanması, askeri operasyonların desteklenmesi, akarsuların denizlere ulaştığı noktalardaki su ortamlarının düzenli kirlilik analizleri ve kirlilik haritalarının çıkarılması gibi geniş bir yelpazeyi kapsar [8].

Makine öğrenimi, veri kümeleri kullanarak kalıpları sınıflandırma [9] ya da tahmin etmek [10] amacıyla kullanılan bir teknik olarak tanımlanabilir. Bu algılama ve tahminlerden önce denetimli veya denetimsiz bir öğrenme süreci gerçekleşir. Denetimli öğrenme durumunda sistemi eğitmek için giriş ve çıkış veri çiftleri kullanılmaktadır [11]. Denetimsiz öğrenmede ise sistem yalnızca giriş verilerini kullanarak kendini eğitmektedir. Her iki öğrenme tekniği içinde görüntüleme verilerinin yüksek çözünürlükte olması beklenir [12]. Bu durum ise genellikle düşük çözünürlüğe sahip sonar görüntülerinden ilgili özelliğin çıkarılması için büyük bir sorun teşkil eder.

Makine öğrenimi birçok alanda başarı ile uygulama alanı bulmuş nispeten yeni bir tekniktir [13]. Ancak makine öğrenimi teknikleri hala bazı zorluklarla karşılaşmaktadır. Model inşa edildikten sonra hedeflenen sonuçların bölünerek incelenmesi ve elde edilen sonuçların daha

sonra bir araya getirilmesi gerekmektedir. Bu işlemler ise karmaşık ve zorlu bir süreci içermektedir. Bunun yanı sıra makine öğrenimi yalnızca nesnenin özelliklerini ele alır ve genellikle tüm bağlam bilgilerini içermez. Bu nedenle verilerin tüm özelliklerinden faydalanamayabilir. Bu zorluklara şu an için yeni ve popüler bir teknik olan derin öğrenme yöntemlerinin kullanımı yardımıyla bu sorunların üstesinden gelinmesi mümkündür [14].

Derin öğrenme, makine öğrenimi alanının bir alt dalıdır. Beynin nöron bağlantılarının yapısından ilham alan yapay sinir ağları tabanlı algoritmaları içerir [15]. Bu yöntem verileri çeşitli soyutlama seviyelerinde işlemek için çok katmanlı hesaplamalı yapılar oluşturarak çalışır. Derin öğrenme hem yapılandırılmış hem de yapılandırılmamış verilerle başa çıkabilir ve otomatik özellik çıkarma süreçlerini gerçekleştirir [16]. Bu algoritmalar büyük miktarda veriyle etkileyici bir şekilde çalışabilir, verimli performans sergileyebilir ve yukarıda bahsedilen makine öğreniminin sınırlamalarını aşabilme yeteneğine sahiptir [17]. Bu durum derin öğrenmenin daha yüksek doğruluk oranlarına sahip olabilmesine ve diğer makine öğrenimi yöntemlerine kıyasla daha tercih edilebilir bir seçenek olduğunu işaret eder.

Derin öğrenme algoritmaları denetimli, yarı denetimli, denetimsiz ve takviyeli öğrenme olmak üzere dört ana kategoriye ayrılmaktadır. Denetimli öğrenme yaklaşımı verileri kategorilere ayrılmış etiketlerle eşleme işlevini tahmin etmek için kullanırken denetimsiz öğrenme ise etiketlenmemiş veri noktalarını içeren veri kümelerindeki kalıpları belirlemeye odaklanmaktadır. Yarı denetimli öğrenme ise sınırlı sayıda etiketli veriyi genişlemiş etiketlenmemiş veriyle birleştirmektedir. Son olarak takviyeli öğrenme etkileşimli bir ortamda kendi eylemlerinden ve deneyimlerinden elde ettiği geri bildirimleri kullanarak deneme yanılma yöntemiyle öğrenmeyi amaçlamaktadır [18].

Mayınların konumları ve özellikleriyle ilgili olarak kamuya açık veri kümelerinin eksikliği ve bu tür bilgilerin askeri bağlamdaki mahremiyet sorunları nedeniyle bu alanda kullanılabilir veri kümelerine tam anlamıyla ulaşmak mümkün değildir. Yapay sinir ağlarının eğitimi bu konuya özgü kısıtlamaları ve maliyetleri azaltma potansiyeline sahiptir [19.]

Ülkelerin sınır güvenliği ile ilişkili mayın bilgilerine açık platformlarda erişim sağlamak mevcut durumda mümkün değildir. Mevcut veri setleri mayın ayrımını etkili bir şekilde gerçekleştirmek için yeterli olmayabilir. Bu çalışmada özgün bir yapay sinir ağı modeli geliştirilmesi hedeflenmektedir. Bu model konuya özgü kısıtlamaları aşmayı ve maliyetleri düşürmeyi amaçlamaktadır. Bu çalışmada1425 farklı sonar frekansının tepkisini kullanarak kaya ve mayın arasındaki ayrımı tespit edebilme yeteneğine sahip bir makine öğrenme modeli geliştirmesi hedeflenmektedir.

II. MATERYAL VE YÖNTEM

A. Model Yapısı

Çalışmada verileri ön işleme çalışması yapılmıştır. Ön işlemede veri kümesi iyileştirilmeleri yapılmıştır. Veri kümesinde bulunan sayısal olmayan alanlar sayısal değerlerle eşleştirilmiş olup boş alanlar ise median yardımı ile doldurulmuştur. Ayrıca sonucu etkileyen faktörler göz önüne alınarak korelasyon hesaplaması yapılmıştır. Korelasyon sonucunda veri setinde etkili olmayan veriler veri setinden kaldırılarak hesaplamada performans artırımı gerçekleştirilmiştir. Veri kümesinin korelasyon sonuçları Tablo 1'de gösterildiği gibidir.

TABLO I
VERI SETININ KORELASYON DEĞERLERI

Parametre Adı	**Etkisi**
Sonuç	1.000000
Freq_11	0.432855
Freq_12	0.392245

Freq_49	0.351312
Freq_10	0.341142
***	***
Freq_37	-0.209055
Freq_35	-0.227670
Freq_36	-0.269151

Sonrasında oluşturulan veri kümesi düzenlenerek, modelin beslenmesi için kullanılmış ve tahmin işlemi için işleme tabi tutulmuştur. Toplamda 3041 parametre ile işlem yapılmıştır. Model yapısı Tablo 2'de verilmiştir.

TABLO II
MODEL YAPISI

Katman	Boyut	Parametre
Dense	10	1010
Dropout	10	0
Dense	10	1010
Dropout	10	0
Dense	2	1010
Dropout	10	0
Dense	1	11

B. Yapay Sinir Ağı

Yapay sinir ağları makine öğrenmesinin bir alt dalını oluşturmaktadır. Yapay sinir ağlarının katman sayılarının artırımıyla derin öğrenme yapısı ortaya çıkmıştır. Günümüzde birçok sorunu çözmek için derin öğrenme teknikleri kullanılmaktadır. Derin öğrenme yapay sinir ağları gibi belirli bir makine öğrenimi algoritmasının kullanıldığı, en az iki katmandan oluşan ve ön işlemleri gerektiren bir tekniktir.

Yapay sinir ağlarında, maliyet fonksiyonunu minimize etmek amacıyla çok sayıda katman bulunan yapay sinir ağları kullanılır. Yapay sinir ağları, finansal alan, bilgisayarlı görü, enerji tahmini gibi çeşitli alanlarda başarısını kanıtlamıştır [20, 21].

C. Veri Kümesi

Bu çalışmada kullanılan veri kümesi, bilinen bir mayın tarlasına ve kaya oluşumlarına uygulanan 1425 ayrı sonar frekansına dair yanıt ölçümlerini içermektedir [22]. Bu veriler, nesnenin kaya mı yoksa mayın mı olduğunu belirlemek amacıyla frekanslara göre tespit edilmiş sonuçları içermektedir. Denizaltı verileri analiz edilerek elde edilen bu sonuçlar, farklı frekans bileşenleri arasındaki ilişkileri kullanarak nesnenin doğasını ayırt etmeye yardımcı olmaktadır. Veri kümesi farklı veri sütunlarını barındırır; bu sütunlar denizaltı verilerini içermektedir. Son sütun ise bize veri setinde yer alan nesnenin kaya mı yoksa maden mi olduğunu belirtir. Hedef sütunu ise şunları içermektedir: R -> Kaya M -> Mayın. Veri kümesi çeşitli denizaltı verilerini içermekte olup, son sütunuyla birlikte nesnenin türünü belirlememize yardımcı olmaktadır. Bu sütunda yer alan 'R', kaya olduğunu; 'M', mayın olduğunu ifade etmektedir.

D. Geliştirme Ortamı

Google Colab, yaratıcılarını gelişmiş donanım olanaklarıyla buluşturan bir inovasyon ortamıdır ve Google tarafından sunulan bu platform, GPU (Grafik İşlemci Birimi) ve TPU (Tensor İşlem Birimi) gibi yüksek performanslı işlem birimlerini sağlayarak veri bilimi, makine öğrenimi ve yapay zeka çalışmalarına yeni boyutlar katmaktadır. Aynı zamanda, bu geliştirme ortamı Python ve R dillerini desteklemekte ve bu dilleri kullanarak geniş bir yelpazede geliştirme imkanı sunmaktadır. Google Colab, kullanıcılarına sadece dil çeşitliliği

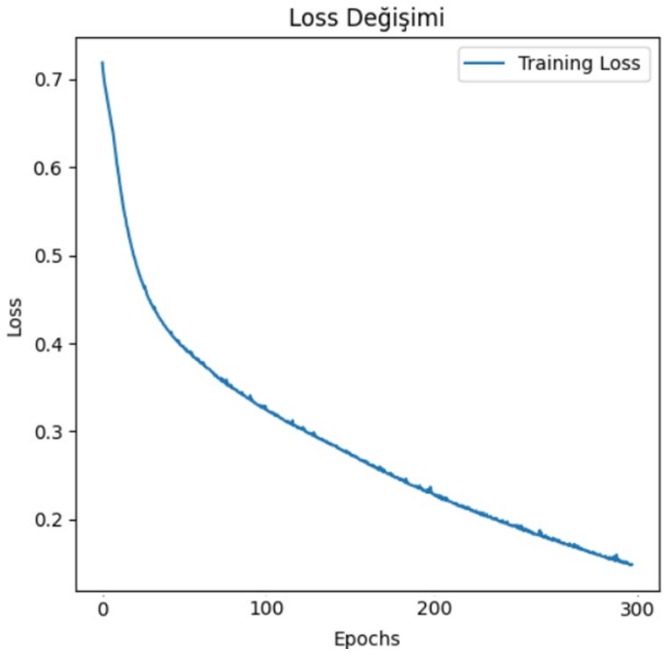
ve yüksek performanslı işlem birimleri sunmakla kalmayıp aynı zamanda esneklik sağlamak adına Google Drive entegrasyonu sunmaktadır. Bu entegrasyon sayesinde, projelerinizi kolayca yönetebilir, paylaşabilir ve istediğiniz cihazdan erişim sağlayabilirsiniz. Platform bağımsız bir yapıya sahiptir, böylece kullanıcılar farklı cihazlardan ve herhangi bir yerden projelerine kesintisiz erişebilirler. Google Colab, teknoloji meraklıları, araştırmacılar, öğrenciler ve profesyoneller için yenilikçi bir alan sunarak yaratıcılığı ve öğrenmeyi destekleyen bir geliştirme ve iş birliği platformu olarak öne çıkmaktadır [23].

III. BULGULAR

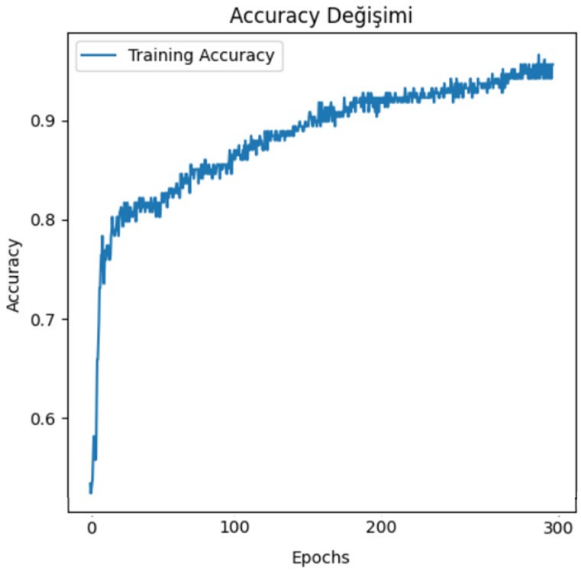
Bu çalışma, denizaltı verilerindeki frekansların kullanımıyla mayın ve kayaların tespit edilmesine yönelik bir yapay sinir ağı modelinin geliştirilmesi üzerine odaklanmaktadır. Model, yapay sinir ağı mimarisi üzerine inşa edilmiş olup, 3041 öğrenilebilir parametre içermektedir. Bu model, denizaltı verilerinin karmaşık frekans bileşenlerini analiz ederek ve bu bilgileri kullanarak mayın ve kaya türlerini başarıyla ayırt edebilmektedir. Elde edilen sonuçlar, modelin bu tür özelleşmiş denizaltı uygulamalarında yüksek bir başarı elde etme yeteneğini göstermektedir. Modelin performansı, yüzde 96 gibi yüksek bir doğruluk oranıyla ölçülmüş ve R2 değeri 0,92 olarak ölçülmüştür. Model toplam 1425 veri noktasıyla eğitilmiştir. Bu da geniş ve çeşitli bir veri kümesinin kullanıldığını işaret etmektedir. Eğitim sürecinin ilerleyişini görselleştirmek amacıyla Şekil 3'te eğitim kayıp (loss) fonksiyonu 300 adım boyunca değerlendirilmiştir. Ayrıca, modelin doğrulama performansını izlemek amacıyla Şekil 4'te eğitim doğrulama (accuracy) grafiği 300 adım boyunca gösterilmektedir.

Bu çalışmanın bir başka önemli yönü, istenilen bir alanla diğer parametreler arasındaki korelasyon değerleri karşılaştırılmaktadır. Bu analiz, modelin sonuçlarının ve performansının daha geniş bir bağlamda değerlendirilmesine yardımcı olmaktadır.

Sonuç olarak, bu çalışma denizaltı verilerinin frekans analizi yoluyla sınıflandırılmasının etkinliğini göstererek, yapay zeka ve denizaltı keşfi alanlarında önemli bir adım atmaktadır.



Şekil 3. Eğitim değişimi (Loss) 300 adım



Şekil 4. Eğitim başarım (Accuracy) 300 adım

IV. SONUÇ

Bu çalışmada, denizaltılarının frekansları yardımıyla mayın ve kaya tespit edebilen bir yapay sinir ağı modeli oluşturulmuştur. Bu analiz, 300 adım boyunca sürdürülen yoğun eğitim süreciyle desteklenmiştir. Veri kümesi, denizaltı verilerini içeren ve bu verilerin frekans bileşenlerini kullanarak nesneleri sınıflandırmayı amaçlayan bir yapıya sahiptir. Bu çalışmanın sonucunda elde edilen sonuçlar yüzde 96 gibi yüksek bir doğruluk oranına ulaşmıştır. Bu sonuçlar, yapay sinir ağlarının karmaşık sonar verilerini başarılı bir şekilde analiz edip öğrenebilme yeteneğini vurgulamaktadır. Mayın ve kayaların frekans özelliklerinin farklılıklarını tespit ederek, bu nesneleri ayırt etmekte ve yüksek bir başarı oranıyla sınıflandırmaktadır. Bu çalışma, yapay sinir ağlarının denizaltı verileri gibi gerçek dünya problemlerinde uygulamalarında potansiyelini göstermektedir. Aynı zamanda, frekans analizi gibi spesifik yöntemlerin kullanımının, bu tür özelleşmiş uygulamalarda nasıl etkili sonuçlar doğurabileceğine dair önemli bir örnek sunmaktadır.

KAYNAKLAR

[1] Hożyń, S., "A review of underwater mine detection and classification in sonar imagery. Electronics", 10(23), 2943. https://doi.org/10.3390/electronics10232943, 2021

[2] Szturomski, B., "The effect of an underwater explosion on a ship". Zeszyty Naukowe Akademii Marynarki Wojennej, 56(2 (201), 57-73., 2015

[3] Palomeras, N., Furfaro, T., Williams, D. P., Carreras, M., & Dugelay, S., "Automatic target recognition for mine countermeasure missions using forward-looking sonar data". IEEE Journal of Oceanic Engineering, 47(1), 141-161. https://doi.org/10.1109/JOE.2021.3103269., 2021

[4] Marszal, J., & Salamon, R., "Silent sonar for maritime security applications. In Proceedings of Meetings on Acoustics" (Vol. 17, No. 1). AIP Publishing. https://doi.org/10.1121/1.4792758, July 2012

[5] Wang, Y., Ji, Y., Woo, H., Tamura, Y., Tsuchiya, H., Yamashita, A., & Asama, H., "Acoustic camera-based pose graph slam for dense 3-d mapping in underwater environments". IEEE Journal of Oceanic Engineering, 46(3), 829-847. https://doi.org/10.1109/JOE.2020.3033036., 2020

[6] Avcioglu, A., Bereketli, A., & Bay, O. F., "Three Dimensional Volume Coverage in Multistatic Sonar Sensor Networks". IEEE Access, 10, 123560-123578. https://doi.org/10.1109/ACCESS.2022.3223714., 2022

[7] Kuperman, W., & Roux, P., "Underwater acoustics. Springer Handbook of Acoustics", 149-204. https://doi.org/ 10.1007/978-0-387-30425-0_5, 2007

[8] Yakut, M. , Yılmaz, S. , İnce, S. , Otçu, M. & Aygün, E., "Derinlik ve Yön Kontrol Uygulamaları için Sualtı Aracı Tasarımı". Gazi University Journal of Science Part C: Design and Technology, 3 (1) , 343-355 . Retrieved from https://dergipark.org.tr/en/pub/gujsc/issue/7466/98258, 2020

[9] Çelebi, S. B., & Emiroğlu, B. G., "A Novel Deep Dense Block-Based Model for Detecting Alzheimer's Disease. Applied Sciences", 13(15), 8686. https://doi.org/10.3390/app13158686, 2023

[10] Birecikli, B., Karaman, Ö. A., Çelebi, S. B., & Turgut, A., "Failure load prediction of adhesively bonded GFRP composite joints using artificial neural networks". Journal of Mechanical Science and Technology, 34, 4631-4640. https://doi.org/10.1007/s12206-020-1021-7, 2020

[11] Aslan, A., ve Çelebi, S. B., "Real Time Deep Learning Based Age and Gender Detection For Advertising and Marketing". In H. İş & İ. Demir (Eds.), Uluslararası Bilişim Kongresi (IIC 2022): bildiriler kitabı (pp. 10–16). Batman: https://hdl.handle.net/20.500.12402/4205, 2022

[12] Çelebi, S. B. & Emiroğlu, B. G., "Alzheimer Teşhisi için Derin Öğrenme Tabanlı Morfometrik Analiz". Journal of the Institute of Science and Technology , 13 (3) , 1454-1467 . https://doi.org/10.21597/jist.1275669, 2023

[13] Bharadiya, J., "Machine Learning in Cybersecurity: Techniques and Challenges". European Journal of Technology, 7(2), 1-14. https://doi.org/10.47672/ejt.1486, 2023

[14] Neupane, D., & Seok, J., "A review on deep learning-based approaches for automatic sonar target recognition". Electronics, 9(11), 1972. https://doi.org/10.3390/electronics9111972, 2020

[15] Han, K., Öztürk, G., & Aslan, A., "Yapay Sinir Ağları Kullanarak Yüzey Pürüzlülüğü Tespiti". International Conference on Pioneer and Innovative Studies, 1, 487–492. https://doi.org/10.59287/icpis.877, June 2023

[16] Zadgaonkar, A., & Agrawal, A. J., "An Approach for Analyzing Unstructured Text Data Using Topic Modeling Techniques for Efficient Information Extraction". New Generation Computing, 1-26. https://doi.org/10.1007/s00354-023-00230-5, 2023

[17] Çelebi, S.B., Emiroğlu, B.G., "Leveraging deep learning for enhanced detection of Alzheimer's disease through morphometric analysis of brain images". Traitement du Signal, Vol. 40, No. 4, pp. 1355-1365. https://doi.org/10.18280/ts.400405, 2023

[18] Albayati, M. G., Faraj, J., Thompson, A., Patil, P., Gorthala, R., & Rajasekaran, S., "Semi-supervised machine learning for fault detection and diagnosis of a rooftop unit". Big Data Mining and Analytics, 6(2), 170-184. https://doi.org/ 10.26599/BDMA.2022.9020015., 2023

[19] Cerqueira, R., Trocoli, T., Neves, G., Joyeux, S., Albiez, J., & Oliveira, L., "A novel GPU-based sonar simulator for real-time applications". Computers & Graphics, 68, 66-76. https://doi.org/10.1016/j.cag.2017.08.008, 2017

[20] Karaman, Ö. A., "Performance evaluation of seasonal solar irradiation models—case study": Karapınar town, Turkey. Case Studies in Thermal Engineering, 49, 103228. https://doi.org/10.1016/j.csite.2023.103228, 2023

[21] Aslan A, Ayayna F., Çalışkan A., "Akciğer Kanserinin Derin Öğrenme Yaklaşımları Kullanılarak Tespit Edilmesi" International Conference on Scientific and Academic Research (ICSAR'22), December 2022

[22] Sonar mine dataset. (n.d.). Sonar mine dataset. Kaggle. https://www.kaggle.com/datasets/mayurdalvi/sonar-mine-dataset. 28.07.2023 tarihinde erişildi.

[23] Google Colab. (n.d) https://research.google.com/colaboratory/ 30.07.2023 tarihinde erişildi.

Effect of Gelatin, Nano Gelatin, and Lyophilized Nano Gelatin on Swelling and Water Solubility Properties of Sodium Alginate Composite Films

Şevval Beyza BOZKURT*[1], Lalehan AKYÜZ*[2]

*: sevvalbeyzabozkurt1310@gmail.com, ORCID: ID: 0009-0008-8552-2428[1]:
[1]: *Aksaray University, Institute of Science, Department of Biotechnology and Molecular Biology, Aksaray, Turkey.*
[2]: *Aksaray University, Faculty of Science and Literature, Department of Molecular Biology and Genetics, Aksaray, Turkey.*

Abstract: Hydrogels are cross-linked hydrophilic networks with a high water retention capacity that are manufactured in gel or film form. Sodium alginate (SA) and gelatin (J) are commonly used combined in wound dressings due to their biocompatibility and biodegradability, as well as their ability to absorb wound exudate with their hydrogel qualities. Traditional wound dressings such as cotton and bandages are often only used as a passive barrier, creating a protective environment to shield the wound from external forces. However, they continue to be an issue since they do not offer the moist environment required for wound healing. As a result, the number of research into the creation of smart wound dressings has increased. With the development of the technology, nanoparticles have been used in smart wound dressings. Therefore, as a result, the swelling and water solubility characteristics of gelatin, nano gelatin, and lyophilized nano gelatin were examined in this work to investigate their suitability as wound dressings.

Nano gelatin solution was obtained from gelatin using a two-step desolvation method. The nano gelatin solution was lyophilized to form gelatin nanofibers. The gelatin nanofiber solution was obtained by dissolving the gelatin nanofibers in water. Gelatin, nano gelatin solution, and gelatin nanofiber solution containing equal amounts of gelatin were composited with SA and thin films were obtained. The gelatin-alginate film was used as a control and called SA/G. The nanocomposite film prepared from gelatin nanofibers solution was named SA/LGNP and the nanocomposite film prepared from nano gelatin solution was named SA/GNP. The SA/G, SA/LGNP and SA/GNP composite films were kept in $CaCl_2$ solution at different ratios (1%, 2%, 3%, 4%, and 5%) for 5 min. The solubility and swelling properties were examined in triplicate at pH 7.0 for 1, 5, 10, 15, 20, 30, and 40 min. It was observed that the swelling and water solubility properties of the composite films varied with the concentration of $CaCl_2$, the nano size of gelatin, and the use of lyophilized nano gelatin.

As a result, it was observed that hardening and breakage occurred in the films as the $CaCl_2$ concentration increased. Also, it was determined that the swelling and water solubility of SA/GNP were higher than the other films, while the water solubility capacity of SA/LGNP decreased with increasing time. In summary, it is predicted that the composite films can be used as a potential dressing material for biomedical applications by modifying them with different methods and concentrations in the future due to their high water retention capacity and moist environment.

Keywords: *Nanoparticles, Gelatin, Sodium Alginate, Wound Dressing, Hydrogel, Swelling Properties*

I. INTRODUCTION

The skin is the largest organ that protects the body from external influences and wounds occur when the skin opens or deteriorates due to biological, chemical, or physical causes [1]. Recently, wound dressings have been developed to be used in the treatment of wounds by covering the wound area and protecting the damaged tissue from external influences. Sponges, films, hydrogels, and foams produced by synthetic and natural polymers have been used in modern wound dressings [2]. Hydrogels have been frequently used in wound dressings due to their high water retention capacity and rapid swelling properties. They have been used in many fields such as controlled drug release, regenerative medicine, 3D support for tissue formation, tissue engineering, and tissue adhesives [3,4]. Compared to traditional wound dressings, hydrogels keep wounds moist and absorb exudate [5]. Natural polymers sodium alginate (SA) and gelatin (G) have been used in wound dressings due to their hydrogel properties. With the development of technology, smart wound dressings, which are different dimensions of wound dressings, have been developed. Especially nanoparticles are used in smart wound dressings.
Sodium alginate (alginic acid) is derived from brown algae. It is a negatively charged polysaccharide composed of β-D-mannuronic acid and α-L-guluronic acid units. Alginate has many applications in tissue engineering, drug delivery systems, wound healing, and heavy metal removal [6]. SA is generally used in composite form with gelatin. Alginates, due to their high liquid absorption capacity, turn into gel form when combined with wound exudate and ion exchange between calcium ions and sodium ions occurs, keeping the wound moist [7,8]. Gelatin is a water-soluble, digestible biopolymer that mimics the extracellular matrix (ECM). With its high water retention capacity, it is an ideal wound dressing for absorbing wound exudate [9]. Gelatin can be nanoparticulated and used in hydrogel form, in food, medicine, and drug delivery [10]. It has been determined that when the structure is nano-gelatin, the plasticizing property of gelatin is not lost, thus reducing the rupture in the films and increasing the strength [11].
Traditional wound dressings such as cotton and gauze often provide a passive barrier to protect the wound from external factors. However, their inability to provide the moist environment necessary for wound healing remains a problem. Some hydrogels degrade over time to prevent secondary damage during dressing changes. In order to prevent degradation, it has been observed that hydrogel structures containing different additives, crosslinkers, biomolecules and nanoparticles in hydrogel wound dressings increase the wound healing and skin regeneration potential [12]. In this study, the swelling and water solubility properties of gelatin, nano gelatin, and lyophilized nano gelatin, which were made into composite films with sodium alginate using the solvent casting method, were compared after crosslinking with polyethylene glycol (PEG) to investigate their usability as a biocompatible wound dressing.

II. MATERIALS AND METHOD

Materials

For SA/G blend film production, commercially available sodium alginate, PEG, and gelatin were purchased from Sigma Aldrich USA. To obtain nano gelatin, acetone, glutaraldehyde and hydrochloric acid were purchased from Merck. Glycerol (99.5 %) was obtained from TEKKIM Lot No: 211011516. Distilled water was used during all the experimental steps.

Preparation of Nano gelatin from Gelatin

To obtain nano gelatin, 1.25 g gelatin was dissolved in 25 mL of distilled water at 40 °C. Then 30 mL of acetone was added to the gelatin solution to precipitate the high molecular mass gelatin. The residue remaining after precipitation was again dissolved in 25 mL distilled water and adjusted to pH 2.5 with 1M HCl. To obtain nanoparticles, 40 mL acetone was added to the pH 2.5 solution. Cross-linking was performed by adding 1 mL of 8% glutaraldehyde solution. After 30/70% (v/v) acetone/water mixture was added to the solution, the residue was

removed by centrifugation 3 times. Finally, the acetone was evaporated in a water bath at 50 °C. The resulting solution includes gelatin nanoparticles [13]. The obtained nano gelatin solution was lyophilized at -80 °C for 24 hours to obtain nano gelatin fibers. The optical image of lyophilized nano gelatin fibers is given in Fig 1.

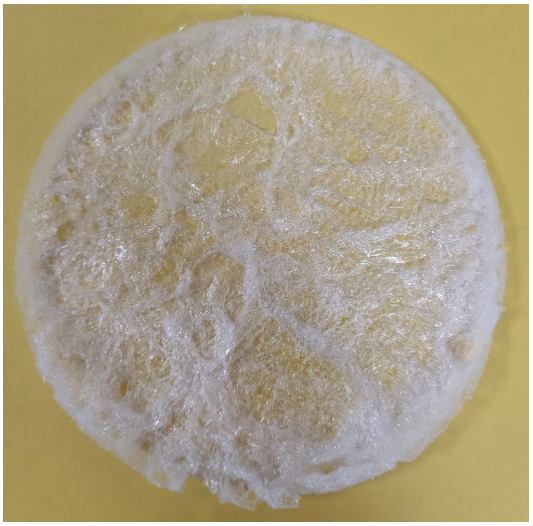


Fig.1. Lyophilized nano gelatin fibers

SA/G Film Preparation

For the SA/G film preparation, 0.37 g of sodium alginate was weighed and mixed in 15 mL distilled water at 300 rpm for 4 hours to obtain a homogeneous gel solution. 0.5 g of PEG was added into the alginate solution and stirred at 300 rpm for 1 hour until homogeneous. 0.67 g of gelatin was weighed and dissolved in 15 mL of water will be added. Then, a homogeneous solution was obtained by stirring at 300 rpm at 40 °C for 2 hours. The resulting solution was added to the alginate-PEG solution and mixed for 1 hour to obtain a homogeneous gel. Finally, glycerol (17 drops) was added to the homogeneous gel solution as a plasticizer and mixed with a homogenizer (10 min, 26,000 rpm) to form a film solution. The film solution was allowed to dry in a 12 mm petri dish at room temperature (25 °C) for 48 hours.

SA/GNP Film Preparation

For the SA/G film preparation, 0.37 g of sodium alginate was weighed and mixed in 15 mL distilled water at 300 rpm for 4 hours to obtain a homogeneous gel solution. 0.5 g of PEG was added into the alginate solution and stirred at 300 rpm for 1 hour until homogeneous. 15 mL nano gelatin solution containing 0.67 g gelatin was added to the alginate-PEG solution and mixed for 1 hour to obtain a homogeneous gel. Finally, glycerol (17 drops) was added to the homogeneous gel solution as a plasticizer and mixed with a homogenizer (10 min, 26,000 rpm) to form a film solution. The film solution was allowed to dry in a 12 mm petri dish at room temperature (25 °C) for 48 hours.

SA/LGNP Film Preparation

For the SA/G film preparation, 0.37 g of sodium alginate was weighed and mixed in 15 mL distilled water at 300 rpm for 4 hours to obtain a homogeneous gel solution. 0.5 g of PEG was added into the alginate solution and stirred at 300 rpm for 1 hour until homogeneous. 0.67 g of lyophilized nano gelatin fibers was dissolved in 15 mL distilled water and stirred at 300 rpm for 1 hour until homogeneous. This solution was added to the alginate-PEG solution and mixed for 1 hour to obtain a homogeneous gel. Finally, glycerol (17 drops) was added to the homogeneous gel solution as a plasticizer and mixed with a homogenizer (10 min, 26.000 rpm)

to form a film solution. The film solution was allowed to dry in a 12 mm petri dish at room temperature (25 °C) for 48 hours.

Preparation of Water Resistant Composite Films

In order to make the composite films water resistant, the method reported by Pavlath et al. (1999) and referred to as 'immersion film' was modified and applied [14]. The produced films 1x1mm were cut and kept inside 1%, 2%, 3%, 4%, and 5% $CaCl_2$ solution for 5 minutes. Finally, the obtained films were dried again in a 12 mm petri dish at room temperature (25 °C) for 72 hours.

Attenuated total reflectance infrared spectroscopy (ATR/ FT-IR)

FT-IR spectra were recorded for SA/G, SA/GNP, and SA/LGNP composite film samples using a PerkinElmer Spectrum Two FT-IR Spectrometer. The Spectra range was fixed between 450–4000 cm^{-1} with a resolution of 8 cm^{-1}.

Swelling behavior of composite films

To assess the swelling behavior of composite films, a few pieces of films were cut into and weighted as W_0, then they were immersed in water at 37 °C. After a certain number of minutes (1, 5, 10, 15, 20, 30, and 40 min), the films were dried and weighed as W_s. The experiment was repeated three times. The swelling ratio was calculated by the following equation:

$$Swelling\ (\%) = \left(\frac{w_s - w_0}{w_0}\right) \times 100 \qquad \text{(Eq.1)}$$

in which, W_o is the initial weight of the film and W_s is the weight of the film after treatment with deionized water (5 mL) [15].

Water solubility of composite films

Water solubility (WS) of the films was examined at 25±1 °C. SA/G, SA/GNP, and SA/LGNP composite films were cut into rectangular shapes (1x2 cm). The films were weighed and put into petri dishes. 20 mL of distilled water was added to the film samples. The films were checked at different time intervals. The experiment was completed after 24 hours and repeated three times. The water solubility was calculated by the following equation:

$$WS(\%) = \left(\frac{w_i - w_f}{w_i}\right) \times 100 \qquad \text{(Eq.2)}$$

where WS = weight loss, W_i = initially weight and W_f = finally weight [16].

RESULTS AND DISCUSSION

The optical images of SA/G, SA/GNP, and SA/LGNP composite films are shown in Fig. 2. As seen from the optical image, the SA/G film is transparent, the SA/GNP film is blurred and the SA/LGNP film is a fibrous structure.

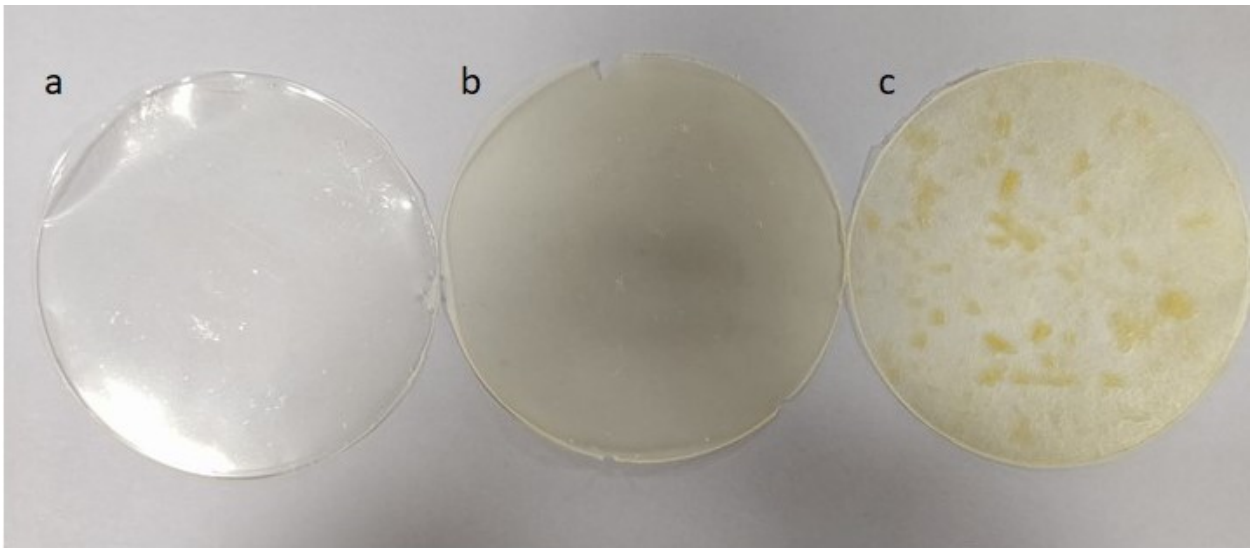


Fig. 2. The optical images of composite films a) SA/G b)SA/GNP and c) SA/LGNP

Attenuated total reflectance infrared spectroscopy (ATR/ FT-IR)

FT-IR analysis was carried out to determine the structural changes of the SA/G, SA/GNP, and SA/LGNP composite films. The spectra of the samples are given in Fig. 3. Since gelatin is a proteinaceous molecule, its existence is indicated by the stretching vibrations of the C, O, and NH bonds. Also, alginate contains carboxylate groups and similar peaks compared with gelatin. Since both gelatin and alginate contain similar functional groups such as carboxylate and hydroxy, comparable peaks are seen in the spectra [17]. Due to the presence of the carboxylate group, sodium alginate showed two infrared vibrations: an antisymmetric stretch at 1596 cm^{-1} and a symmetric stretch at 1412 cm^{-1} [18]. However, composite films obtained by casting from sodium alginate/gelatin and PEG solution yielded a spectrum where important significant changes in these bands were observed. While this peak is intense and is observed at 1632 cm^{-1} in the composite film obtained with standard gelatin, the intensity of the peak is less in the spectra obtained with nano gelatin. The carboxylate peaks were observed at 1607 and 1613 cm^{-1} in the SA/LGNP and SA/GNP spectra, respectively.

In the first spectrum, which belongs to the SA/G film, −OH bonds and C−H aliphatic stretching vibrations were observed at 3287 cm^{-1} and 2883 cm^{-1}, respectively. The sharp peak at 1632 cm^{-1} was attributed to the sodium COO^- (carboxylate) group in the alginate structure. N-H stretching and C-O stretching peaks of gelatin were observed at 1550 cm^{-1}, 1341 cm^{-1}, and 1113 cm^{-1}, respectively.

In the spectrum of SA/GNP, the observed broad peak at 3303 cm^{-1} is attributed to the H bond in the OH band. Aliphatic C-H stretching peaks were observed at 2883 cm^{-1}. Also, the sharp peak recorded at 1613 cm^{-1} was attributed to the carboxylate group of alginate. N-H stretching peaks were observed at 1551 cm^{-1} and 1341 cm^{-1}. The characteristic hexagonal ring peak of alginate was observed at 1028 cm^{-1} with the effect of the C-O-C group. The spectrum of SA/LGNP was similar to the SA/GNP spectrum.

Comparing the three spectra it was revealed that SA/G with regular gelatin differs from SA/GNP and SA/LGNP spectra, particularly in terms of sugar ring and carboxylate group. This difference may be due to the nano size of the gelatin and the use of glutaraldehyde in the synthesis of nano gelatin. Accordingly, nano gelatin and normal gelatin were successfully composited with alginate.

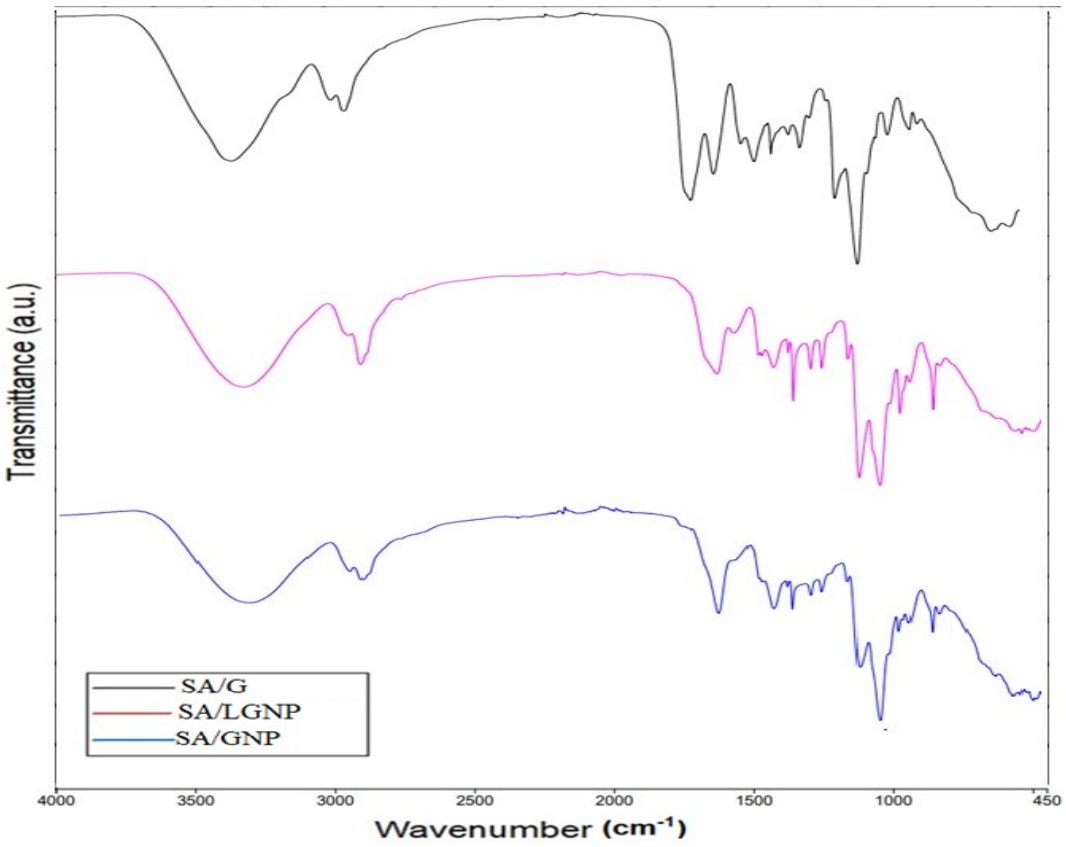


Fig.3. FT-IR spectra of the SA/G, SA/GNP, and SA/LGNP composite films

Percentage of Swelling of $CaCl_2$ Concentrations Versus Solubility Time

The swelling percentages of SA/G, SA/GNP, and SA/LGNP films in response to soaking time in different concentrations of $CaCl_2$ solution are shown in Figures 4 (a), (b), (c), (d), and (e). Accordingly, in Fig. 4 (a), the SA/LGNP composite film reached the maximum degree of swelling at $CaCl_2$ concentrations of 1%, 2%, and 3% compared to the other films due to nano gelatin fibers. In Figures 4 (d) and (e), the swelling rate of the LGNP composite film decreased with increasing time due to the collapse of the nano gelatin fibers after high water absorption. However, since the SA/GNP composite film is not lyophilized, the cross-links formed by Ca^{2+} ions increase the mechanical strength of the film, so it is thought that the swelling was at the maximum level. In general, the best swelling percentage was observed in SA/LGNP composite film at 1 min soaking time in 1% $CaCl_2$ solution. This was due to the lyophilization of the nano gelatin. In SA/LGNP composite film, it was thought that the intermolecular interaction increases as a result of the cross-linking of gelatin with $-NH_2$ groups, SA with Ca^{2+} ions and PEG with nano gelatin fibers.

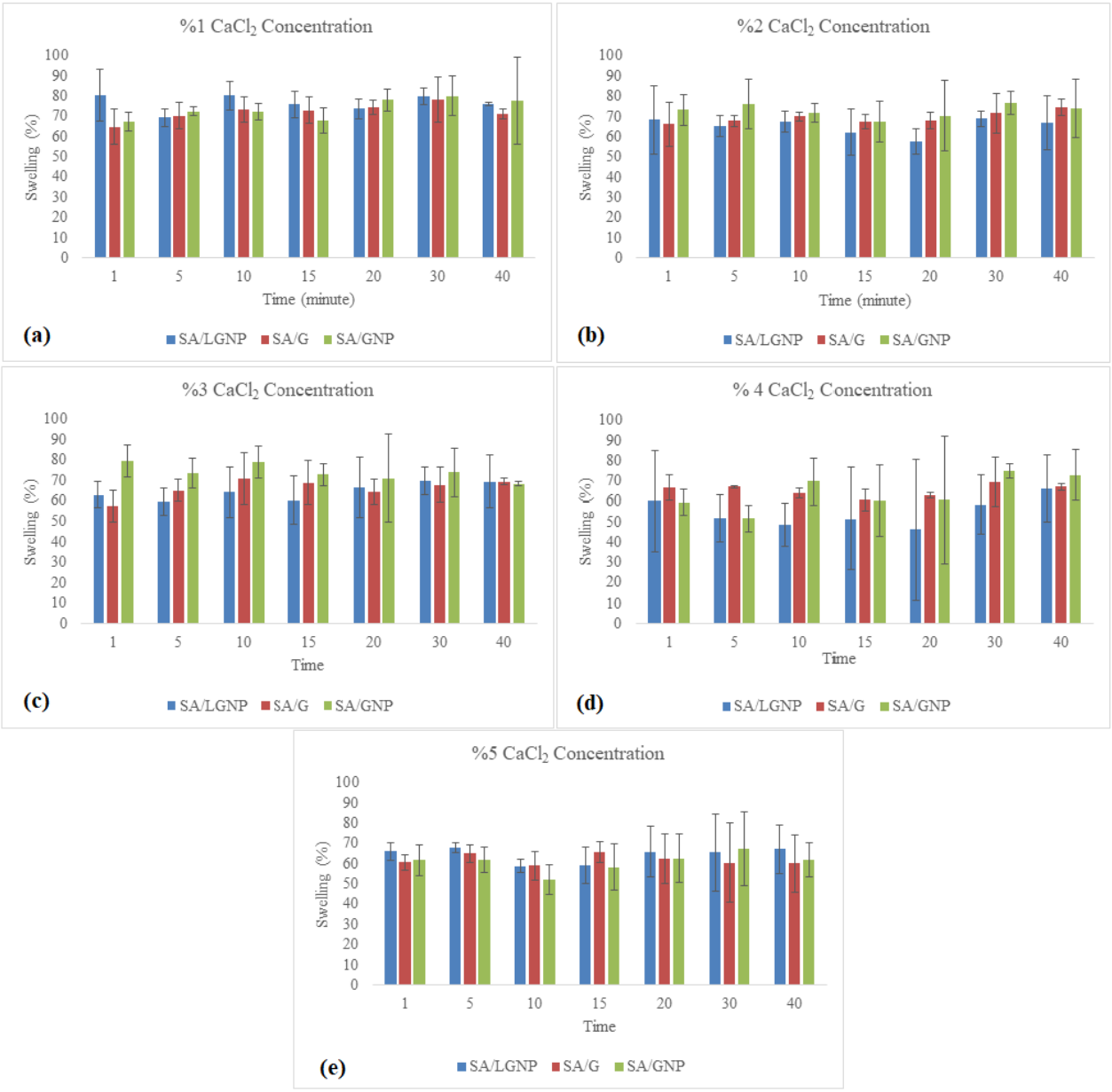


Fig.4. The swelling percentages of SA/G, SA/GNP, and SA/LGNP films in response to soaking time in different concentrations of $CaCl_2$ solution (a) $CaCl_2$ concentration of 1%, (b) $CaCl_2$ concentration of 2%, (c) $CaCl_2$ concentration of 3% (d) $CaCl_2$ concentration of 4%, (e) $CaCl_2$ concentration of 5%.

Water solubility of composite films

SA, gelatin, and PEG are water-soluble polymers. On the other hand, sodium alginate can be made insoluble in water by cross-linking with Ca^{2+} ions. However, the water solubility of the composite films obtained in this study was investigated without crosslinking with Ca^{2+} ions. The effect of nano gelatin on solubility in water was investigated. SA/G composite film was dissolved completely in water at 25 °C after resting for 1 h. But, SA/GNP and SA/LGNP film was insoluble in water at 25 °C after resting for 24 h. It was seen that the SA/LGNP film had a water solubility of 55% while the SA/GNP film had 79% solubility. It can be said that the NH_2 groups of nano gelatin in SA/GNP result from cross-linking with sodium alginate. In addition, it was observed that the solubility in water decreased because lyophilized nano gelatin was in fiber structure and cross-linking occurred.

IV. CONCLUSION

This study aimed to investigate the usability of gelatin, nano gelatin, and lyophilized nano gelatin made into composite films with sodium alginate as wound dressing materials. When the swelling behavior of the films was examined, it was observed that the water absorption capacity decreased as the crosslinking time increased. Increasing $CaCl_2$ concentration in the composite films caused hardness and brittleness in the films and thus the strength decreased. In general, the swelling ability of hydrogels was found to depend on the crosslinking concentration and time. In the results obtained, the best swelling percentage was determined to be in the SA/LGNP composite film.

In addition, when the water solubility was examined, it was determined that nano gelatin decreased the water solubility of the composite films without cross-linking. SA/LGNP showed the least solubility due to lyophilized nano gelatin fibers. Accordingly, it can be predicted that gelatin nanoparticles can be used in wound dressings with future detailed research.

REFERENCES

[1] J. Boateng and O. Cantanzano, Advanced threapeutic dressings for effective wound healing—a review, Journal of Pharmaceutical Sciences, vol. 104, no. 11, pp. 3653-3680, November 2015, doi: 10.1002/jps.24610.

[2] A. R. Ahmedy, K. Razmjooee, S. Saber-Samandari and D. Toghraie, Fabrication of chitosan-gelatin films incorporated with thymol-loaded alginate microparticles for controlled drug delivery, antibacterial activity and wound healing: In vitro- and in vivo studies, International Journal of Biological Macromolecules, vol. 223, pp. 567-582, December 2022, doi: 10.1016/j.ijbiomac.2022.10.249.

[3] H. Lei, C. Zhu and D. Fan, Optimization of human-like collogen composite polysaccharide hydrogel dressing preparation using response surface for burn repair, Carbohydrate Polymers, vol.239, January 2020, doi: 10.1016/j.carbpol.2020.116249.

[4] X. Xu, L. Che, L. Xu, D. Huang, J. Wu, Z. Du and others, Green preparation of anti-inflammation an injectable 3D porous hydrogel for speeding up deep second-degree scald wound healing, RSD Advances, no. 59, September 2020, doi: 10.1039/D0RA04990E.

[5] Y. Xu, Q. Hu, Z. Wei, Y. Ou, Y. Cao, H. Zhou and others, Advanced polymer hydrogels that promote diabetic ulcer healing: mechanisms, classifications, and medical applications, Biomaterials Research, vol.27, no. 36, pp. 2-48, April 2023, doi: 10.1186/s40824-023-00379-6.

[6] H. Ei-Thu and S. Fern-Ng, Gelatine enhances drug dispersion in alginate bilayer film via the formation of crystalline microaggregates, International Journal of Pharmaceutics, vol. 454, no. 1, pp. 99-156, September 2013, doi: 10.1016/j.ijpharm.2013.06.082.

[7] M. M-Sheir, M. M.A. Nasra and O. Y. Abdallah, Chitosan alginate nanoparticles as a platform fort he treatment of diabetic and non-diabetic pressure ulcers: Formulation and in vitro/in vivo evulation, International Journal of Pharmaceutics, vol. 607, September 2021, doi: 10.1016/j.ijpharm.2021.120963.

[8] Z. Azalea Sutirman, M. Marsin Sanagi and W. Ibrahim Wan Aini, Alginate-based adsorbents for removal of metal ions and radionuclides from aqueous solutions: A review, International Journal of Biological Macromolecules, vol. 174, pp. 216-228, March 2021, doi: 10.1016/j.ijbiomac.2021.01.150.

[9] B. Stubbe, A. Mignon, H. Declercg, S. Van Vlierberghe and P. Dubruel, Development of gelatin-alginate hydrogels for burn wound treatment, Macromolecular Bioscience, no. 8, pp .1-12, August 2019, doi: 10.1002/mabi.201900123.

[10] D. Suresh, A. Suresh and R. Kannan, Engineering biomolecular systems:Controlling the self-assembly of gelatin to form ultra-samll bioactive nanomaterials, Bioactive Materials, vol. 18, pp. 321-336, December 2022, doi: 10.1016/j.bioactmat.2022.02.035.

[11] M. Nuerjiang, X. Bai, L. Sun, Q. Wang, X. Xia and F. Li, Size effect of fish gelatin nanoparticles on the mechanical properties of collogen film based on its hierarchical structure, Food Hydrocolloids, vol. 144, November 2023, doi: 10.1016/j.foodhyd.2023.108931.

[12] M. Hadi Norahan, S. Cristina Pedroza-Gonzalez, M. Gabriela Sanchcez-Salaza, M. Moises Alvarez and G. Trujillo de Santiago, Structural and biological engineering of 3D hydrogels for wound healing, Bioactive Materials, vol. 24, pp. 197-235, June 2023, doi: 10.1016/j.bioactmat.2022.11.019.

[13] C. J. Coester, K. Langer, H. Von Briesen and J. Kreuter, Gelatin nanoparticles by two step desolvation-a new preparation method, surface modifications and cell uptake, Journal of Microencapsulation, vol. 17, no. 2, pp. 187-193, April 1999, doi: 10.1080/026520400288427.

[14] A. E. Pavlath, A. Voisin and G.H. Robertson, Pectin-based biodegradable water insolble films, Macromolecular Symposia, pp. 107-113, May 1999, doi: 10.1002/MASY.19991400112.

[15] H. Türe, Characterization of hydroxypattie-contaınıng alginate-gelatin composite films as a potential wound dressing, International Journal of Biological Macromolecules, vol. 123, pp. 878-888, February 2019, doi: 10.1016/j.ijbiomac.2018.11.143.

[16] L. Akyüz, B.Koç, S. Ilk, İ. Sargın, I. Akata, M. Kaya and others, Production and characterization of chitosan-fungal extract films, Food Bioscience, vol. 35, June 2020, doi:10.1016/j.fbio.2020.100545.

[17] A. Joshi, R. Keerthiprasad, R. D. Jayant and R. Srivastava, Nano-in-micro alginate based hybrid particles, Carbohydrate Polymers, vol. 81, no. 4, pp. 790-798, July 2010, doi: 10.1016/j.carbpol.2010.03.050.

[18] G. Lawrie, I. Keen, B. Drew, A. Chandler-Temple, L. Rintoul, P. Fredericks and others, Interactions between alginate and chitosan biopolymers characterized using FTIR and XPS, American Chemical Society Publications, vol. 8, no. 8, pp. 2533-2541, June 2007, doi: 10.1021/bm070014y.

A Review on Image Captioning Using Deep Learning Methodologies: Limitations, Datasets, Metrics, and Recommendations

Zainab Khalid[*,1], Nehad T.A Ramada[2]

[*]zeynepboyagci@gmail.com, ORCID: 0000-0000-0000-0000
[1] *Dept. of Computer Engineering, Karabuk University, Demir Celik Campus, 78050 Karabuk/Turkey –*
[2] *Dept. of Computer Engineering, Karabuk University, Demir Celik Campus, 78050 Karabuk/Turkey –*

Abstract: Image captioning is challenging since it combines natural language processing and computer vision to assign natural descriptions of visual content (scene or video). Image captioning task includes detecting image components, extracting their features, identifying their relationships, then training a natural language model to assign specific descriptions to the extracted features. Deep learning models achieved a considerable improvement in image captioning tasks, and they are developing day after day. However, the huge media size and their incredible development require high performance and more complex models. This paper presents a comprehensive study of image captioning methodologies, particularly focusing on deep learning approaches introduced in recent years. The paper discusses the state-of-art studies in terms of six principles: encoder-decoder-based, transformer-based, attention-based, GAN-based, Reinforcement based, and hybrid-based models. The studies are also compared regarding methodologies, utilized datasets, results, and limitations. The paper also discusses and compares the most used image captioning datasets and the most commonly used evaluation metrics. The discussion of this study can be used as a comprehensive guide for future studies in the field of image captioning since it lists the limitations and possible solutions for the forthcoming studies.

Keywords: *Image captioning, Deep learning, Natural language processing, Image description, BLEU, Encoder-decoder, attention mechanism, GAN, Transformer model.*

I. INTRODUCTION

Image captioning is one of the most challenging fields of computer vision (CV) that has received considerable attention from researchers in the last decade [1]. Image captioning aims to describe image content in a natural language. In order to achieve this mission, computer vision and natural language processing (NLP) are used together to analyze image components and describe them in a natural language [1] [2].

here are many applications for image captioning, including accessibility applications, content indexing, social media content creation, autonomous vehicle, education applications, etc. For accessibility applications, visual impairments people who are not able to see the surrounding world, image captioning applications can help them to explain their surrounding environment in an audible form after describing the scene in a natural language [3, 4].

In content indexing, image captioning is used to generate tags and labels of images allowing further operations to be performed like image retrieval [3-5]. Content creation can benefit from image captioning by generating descriptions for posts based on visual content. Such captioning can be used for marketing purposes. Image captioning systems can also be used to describe visual content for students, especially in online and interactive learning [6, 7].

With the development of deep learning neural networks, the image captioning task becomes more accurate and natural. Convolutional neural networks (CNN), which consist of many deep layers to extract different levels of image features [8], and Generative adversarial networks (GAN) [9] which allow for maximum likelihood estimation approximation and remove the need for Markov constraints or unrolled approximate inference networks, have achieved significant progress in the field of image captioning. On the other hand, attention-based models with encoder and decoder architecture are DL models that decide which part of features to be used in the captioning process, making the captioning process better and more accurate.

II. IMAGE CAPTIONING STEPS

The image captioning process consists of three main steps: feature representation, visual encoding, and language generation [10]. In the first step, a feature extraction-based model is used to get the best ***feature representation*** of the input image. Many possible deep models can be used in the feature representation step, including traditional CNN, Residual Nets (ResNet) [11], VGG [12], GAN [9], etc.

For the second step (***visual encoding***), the extracted features will be encoded using one of the features encoding models, including global representation, graph-based models, attention-based mechanisms, etc. This step aims to focus on the key features of the feature representations.

The third part of the captioning process is the ***language model*** generation which can be Recurrent Neural Networks (RNN), Long-Short Term Memory (LSTM) [13], Transformer models [14], etc. The language model is used to match each feature representation with the corresponding description.

III. RELATED WORK

In this section, the previous studies in the field of image captioning will be categorized into main categories, including the encoder-decoder-based, transformer-based, attention-based, GAN-based, and Reinforcement-based models. Each of these will be discussed, and the most recent studies in these categories will be listed, compared, and discussed in order to make a comprehensive review.

A. 3.1. Encoder-decoder simple captioning models

In the encoder-decoder architecture, the CNN architecture is used as an encoder in order to encode input images [15]. The encoding part transforms the image into an intermediate representation of visual and textual space. On the other hand, the decoder part is a language model (like RNN and LSTM) [16].

Sammani and Kyriazi [17] proposed an encoder-decoder architecture based on an iterative refinement captioning method. This model consisted of two parts; the EditNet, which is a language module with a copy-LSTM model supplied with a selective copy memory attention mechanism (SCMA). The second part was a DCNet which is an LSTM model of de-noising auto-encoder model. This part was used to de-noise previous captions. They obtained a BLEU-1 of 77.9 and a BLEU-4 of 38. The CIDEr-D and SPICE values obtained by their study were 1.2 and 21.2. The proposed methodology was tested using the MSCOCO dataset consisting of 82783 training images, 40504 validation images, and 40775 test images. Their proposed methodology is time-consuming due to the refinement process.

Khan et al. [30] utilized a multimodal architecture for an end-to-end image captioning process in their research. They combined a one-dimensional CNN to encode sequence information with a pre-trained ResNet-50 model. This image encoder was used to extract region-based visual features. The performance of their model was evaluated on the BanglaLekhaImageCaptions dataset (9000 images) using existing evaluation metrics and a

human evaluation for qualitative analysis. The language model used in their study was word embedding to extract linguistic information. The experiments demonstrate that the language encoder in this approach captures detailed information in the caption and generates accurate and varied captions when combined with the image features. The experiments applied on the selected dataset achieved scores of 0.651 on BLUE-1, 0.572 on CIDEr, 0.297 on METEOR, 0.434 on ROUGE, and 0.357 on SPICE. The main limitation of their study is that their model recognized only humans due to the used dataset.

Patwari and Naik [18] proposed an encoder-decoder architecture for image captioning based on both CNN and RNN models. The backbone of the CNN model (which is the encoder part) was the InceptionV3 model, while the RNN model (which is the decoder part) consisted of embedded word vectors with GRU units to build the description sentence. For experiments, they utilized the COCO caption dataset (which consists of 330000 images with 200000 annotated ones, and each of which is described by 5 sentences). Their model achieved a BLEU-1 of 70.6 and BLEU-4 of 24.3. They used a small subset of the dataset since they trained model on a limited hardware resource.

In their research, Mishra et al. [19] proposed a new image captioning model for images in Hindi. They utilized a dynamic convolution encoder model to capture image representations, while for the language model, they used the LSTM model as a decoder. To create a Hindi-based dataset manually based on the well-known MSCOCO dataset by translating English captioning sentences into Hindi. The experiments applied to the proposed model achieved a high BLEU score.

Poddar and Rani [20] proposed a multi-layered CNN and LSTM image captioning model. The input for their model was the input image and the description text file. The CNN model (Precisely the VGG-16 model) was used to extract visual features, while the LSTM model was used to generate captions. Meanwhile, text preprocessing steps were utilized. They applied their experiments to the Flickr8k Hindi dataset, consisting of 8000 training and 100 validation images, and achieved a BLEU score of 0.359 and 0.55 for Unigram and Bigram, respectively. The used dataset has a moderate size. In addition, the model was evaluated using only one metric, "BLEU".

B. 3.2. Transformer-based and attention-based captioning models

Although transformer models were mainly used for machine translation missions, many studies adopted them to accept their inputs as image parts and description sentences. Many studies introduced the idea of a vision transformer [21] [22] [23] or transformer-based image captioning models [24] [25].

He et al. [26] introduced the image transformer model for image captioning tasks. They modified the encoder part of the transformer model and used an implicit decoder part. They first used the R-CNN architecture to detect image parts. Then, the detected parts were fed up into a refinement spatial visual transformer model consisting of three stacks. The stack accepted the image parts obtained from the R-CNN detection algorithm. Each stack consisted of a multi-head dot product attention layer. The input image parts were transformed into features (queries, keys, and values), and the dot product attention was applied to them. After that, the output of each multi-head attention layer was added to the input, and the result was normalized. Finally, a decoder of LSTM stacks was used to generate the description sentence. The decoder took the output of the encoder besides the previous predicted word's embedded features. The experiments were applied to the MSCOCO dataset using 113287 images for training, 5000 for validation, and 5000 for testing. They discarded words with frequencies less than 4 times and got a vocabulary of 10369 words (each image was described by 5 sentences). They got a BLEU-1 value of 81.2 and a BLEU-4 value of 39.6.

Wang et al. [27] presented a Transformer-based model for end-to-end image captioning that replaces Faster R-CNN with SwinTransformer as the backbone encoder, which extracts the

grid-level features. Their proposed model included a refining encoder to acquire the intra-relationship between grid features and a decoder that generates captions word by word. To enhance the model's capability, they introduced a mean-pooled global feature that was refined along with grid features using the refining encoder, and a pre-fusion process that incorporates the refined global feature with generated words in the decoder. The proposed model was evaluated on the MSCOCO dataset (with 113287 training images, 5000 validation images and 5000 test images) and achieves state-of-the-art performance, with CIDEr scores of 138.2% (individual model) and 141.0% (ensemble model) on the 'Karpathy' offline test split, and 136.0% (c5) and 138.3% (c40) on the official online test server. They also got a BLEU-1 score of 82.8 (c5) and 96.5 (c40), and a BLEU-4 score of 41.4 (c5) and 74.1 (c40), respectively, where C5 and C40 are the used reference captioning.

Castro et al. [21] proposed a transformer-based image captioning model and studied the effect of using different hyperparameters on the performance of visual attention transformer models in image captioning task. They compared the performance of many transfer-learning models (ResNet101, ResNet152, ResNeXt-101 and MobileNetV3) with the Vision Transformer (ViT). In their experiments, they used the MSCOCO (2014 version) dataset with 328000 images. The experiments showed that the best performance was achieved using the Cross-entropy loss function with 73.09 TOP-5 and 20.1 BLEU. ResNet-152 achieved the best BLEU-4 value with a value of 20.2, while ResNeXt had the best Top-5 accuracy with a value of 73.128. ViT model achieved a BLEU-4 value of 32.07, 32.98, and 33.24 on three training processes. The main limitation of their study is that the hyperparameters were chosen manually without any optimization algorithm.

An attention-reinforced transformer was proposed by Wang et al. [28]. In their model, they implemented the feature attention block (FAB), which enhanced the image encoding process by detecting relationships between the image's parts. In training, they used the cross-entropy and contrastive loss functions, and used the MSCOCO 2014 dataset (they used 164062 images with 80% train, 10% validation and 10% test), and the 'Karpathy' test split online server and achieved BLEU-1 value of 81.2 and BLEU-4 value of 39.2. Some overhead may happen since the proposed methodology contains many additive architectures, like the FAB block.

Hu et al. [29] proposed a spatial enhanced attention model with a dual spatial encoder to extract geometric correlations between image parts. They also utilized the gated-normalized attention model (GNA), which corrected the inside attention model's distributions, minimized the redundant information, and smooth gradients. All those proposed modules were applied to the original transformer model. Their experiments were applied to the MSCOCO dataset and achieved 134 CIDEr on the original split and 134.8 CIDEr on the Karpathy online split.

Selivanov et al. [30] utilized image captioning in the medical domain based on generative pre-trained transformers (GPT). Their proposed methodology used two language models (GPT-3) and "Show-Attend-Tell" models. The produced textual summary includes crucial details regarding the pathologies detected, their location, and 2D heatmaps that pinpoint each pathology on the scans. The model underwent testing on two medical datasets, namely Open-I (7470 image pairs), MIMIC-CXR (377,110 images corresponding to 227,835 cases), as well as the general-purpose MS-COCO, and all images were resized into 224*224. They got BLEU-1 and BLEU-4 score of 0.725 and 0.418 on MIMIC-CXR dataset, 0.52 and 0.235 on the Open-I dataset, and 0.82 and 0.409 on the MSCOCO dataset. No state-of-art comparison between their study and others on the same medical datasets.

Sharma et al. [31] proposed the XGL-T transformer model for image captioning task. An encoder-decoder architecture was designed. The XGL-T model consists of four XGL attention layers in the encoder part, and Bilinear LSTM module in the decoder part. This mechanism extracted the semantic features, attributes, and other relationships between image components. They also used the Gaussian error linear unit (GELU) as an activation function to prevent the problem of vanishing gradient. Experiments were conducted on the MSCOC Karapathy test

split dataset. They achieved a BLEU-1 score of 81.5, a BLEU-4 score of 39.9, CIDEr score of 134, a METEOR score of 29.8 and ROUGE-L value of 59.9. However, their study did not compare the proposed XGL-Transformer model with other state-of-the-art image captioning models to demonstrate its superiority in a more comprehensive way.

Yang et al. [32] proposed a context-aware transformer model for image captioning. They called this model as "CATNet". Two main modules were implemented; the context augmented attention (CAA) in the encoder part to extract better features of image parts, taking into the communications between image multi-level features, and the dual way controller (DWC) in the decoder part, which enhanced the fusion of visual representations and language representations. The experiments were conducted on the MSCOCO dataset and obtained a BLEU-1 score of 81.8 and a BLEU-4 score of 40. The METEOR, ROUGE, and CIDEr were also computed and achieved scores of 29.4, 59.3, and 133, respectively. As with much other research, their model learned to represent the input image and caption text separately in two different representation spaces.

Padate et al. [33] utilized a dual attention-based model for image captioning. They first extracted image features using the well-known deep learning model (Inception V3). Then, the dual visual and text attention generation algorithm was proposed. Finally, the generation of image captions was done using the Bi-LSTM language model. Besides these techniques, the self-improved electric fish optimization algorithm was applied to get the best hyperparameters of the Bi-LSTM model. Their experiments were applied to the Flickr30k dataset and achieved a BLEU-1 score of 65.9 and a BLEU-4 score of 22. They did not combine visual and text attention.

C. 3.3. GAN-based and Reinforcement-based captioning models

The GAN model usually is not used for image captioning purposes; however, many studies used GAN-based models for this mission [34]. Reinforcement learning (RL) in the literature of image captioning usually appears with GAN-based models [35], so they are combined together in this paragraph.

The most influential research for GAN-based and RL-based models in Image Captioning is SeqGA [36], which solved the issue of generator differentiation by using gradient policy updates. Since the gradients of generated words are discrete, they cannot be back-propagated. The underlying idea of GAN-based image captioning is to transform RL rewards into policy gradients for backpropagation, allowing for the propagation of gradients through discrete word vectors. This is possible due to the generator and discriminator characteristics of the GAN. This approach greatly improves the naturalness and diversity of text generation in IC.

Chen et al. [37] introduced the idea of image captioning using the GAN model. They extended the traditional re-enforcement learning encoder-decoder methodology and designed a discriminator network to define if the generated caption of an image corresponds to human or machine-generated. For the generator part, they used both CNN and RNN models. The experiments were conducted on the MSCOCO dataset with 82,783, 40,504, and 40,775 images for training, validation, test splits, and five description sentences per image. They got the best result when using an ensemble of CNN-GAN and RNN-GAN models, with 81.9 as a BLEU-1 score and 39.6 as a BLEU-4 score. They also achieved a METEOR score of 28.7 and a CIDEr score of 123.1. However, their proposed methodology required higher computational time than other non-GAN-based methods.

Amirian et al. [38] utilized the Variational Autoencoder (VAE) for image captioning process. Their implementation was partially based on ATTEND-GAN, which consisted of two primary components: an attention-based caption generator that correlates various parts of an image with a caption, and an adversarial training mechanism (WGAN) that enhanced the

caption generator's ability to generate diverse stylistic components in the generated captions. By integrating VAE, WGAN, ATTEND-GAN, and sentiment analysis into the evaluation of the MSCOCO dataset, the aim was to generate more descriptive and meaningful descriptions for each image. The main problem of their methodology was that they did not validate their models.

A conditional GAN (SeqGAN) was proposed by Babavalian and Kiani [39]. They utilized the SeqGAN to learn distribution for video captioning based on two parts encoder and caption generator. The encoder part extracted temporal features, then the encoded vector was introduced as input for the SegGAN model using a spatial-temporal attention module. The LSTM model was used for the decoder part to generate captions of the encoded features. Experiments were applied to the MSVd and MSRVTT datasets. For the MSVD dataset, they got a BLEU-4 score of 54.82, METEOR of 35.9, Rouge of 71.6, and Cider of 83.4, while for the MSRVTT dataset, they obtained 44.76, 29.8, 61.7, and 52.7 scores for the same metrics, respectively. No object detection was performed, reducing the ability of the model to detect objects in the image.

Deepak et al. [40] introduced a residual attention GAN model named "RAGAN". The RAGAN model leverages feature maps to rapidly generate high-quality captions and enhance the variety of generated captions. This results in increased language metrics scores. The generator is structured as an unsupervised encoder-decoder mechanism with residual learning between them. The discriminator part had a language evaluation module, providing feed-forward to both the generator and discriminator to positively or negatively impact the image captioning process. Experiments were applied to Flickr30k (31783 images) and MSCOCO (28000 training, 1000 validation, and 1000 test images). The proposed model achieved a BLEU-1 score of 86 and a BLEU-4 score of 49. Although the high performance, the computational time was not evaluated in the paper, which may be significant due to the presence of many computationally intensive components.

Honda et al. [41] investigated the cause of this low discriminativeness and the fact that RL models tend to limit output words to high-frequency words, resulting in a limited vocabulary that hinders the model's ability to image caption beyond the vocabulary. Based on this bottleneck identification, they proposed a simpler task of encouraging low-frequency word generation. Drawing inspiration from long-tail classification and de-biasing methods, they introduced techniques to convert off-the-shelf RL models into discriminative ness-aware models with only one-epoch fine-tuning. Experiments were applied to the MSCOCO captioning dataset (precisely the Karpathy test splitting). Their proposed methodology achieved a CIDEr score of 119.0 and a SPICE score of 21, respectively. The discriminativeness analysis R@1, R@5, and R@10 scores were 21.6, 50.5, and 65.4 (R@1, R@5, and R@10 scores denote to the percentage of test images for which the correct caption is ranked in the top 1, 5, and 10 positions, respectively). The comparative study was conducted on three different models (Arr3in RL, UpDown RL, and Transformer RL). Experiments showed that the proposed methods improved discriminativeness without compromising the overall quality of the captions.

D. 3.4. Hybrid methods

The hybrid image captioning methods means using different technologies to generate captions, like attention mechanism with encoder-decoder parts and GAN architecture as in the study of Yan et al. [42]. They mainly proposed a hierarchical architecture consisting of two main parts; the CNN model for global feature representation and a local object feature extraction module. GAN network and enforcement learning were utilized to solve the problem of exposure bias in the supervised training of RNN-based architectures. The GAN architecture (discriminator) was also used to automatically measure the consistency between the predicted

captions and the original image caption (actual content). Experiments were applied using the MSCOCO 2014 version dataset. They got a BlEU-1 score of 72.611, a BLEU-4 score of 27.243, a METEOR score of 24.731, a CIDEr score of 88.14, and a ROUGE-L score of 56.048. However, their methodology required high computational time due to using a hierarchical model.

A Pyramid Attention mechanism that embeds relationship features into the global-local attention, enabling exploration of the internal visual and semantic relationships between different object regions, was proposed by Chen et al. [43]. In addition, the GAN model was utilized for sequence generation to address the exposure bias problem and improve the training process efficiency. A greedy decoding method was also employed to generate an efficient baseline reward for self-critical training. Their proposed model consisted of two main components: Pyramid Attention (PyAtt) and Self-critical GAN (SC-GAN). The PyAtt included both global attention and local-relation attention, which were used to derive the next word, probability p(yt). This probability was then passed on to SC-GAN, where the discriminator completed the generated sentence and updated the generator's parameters using a policy gradient method. Their proposed model was evaluated on the MSCOCO dataset, and the results demonstrated that it was capable of generating more accurate image captions. They achieved a BLEU-1 score of 78.3, a BLEU-4 score of 37.9, a METEOR score of 28.9, a CIDEr score of 119.6, and a ROUGE-L score of 58.5. Again, the proposed methodology contained high computational time.

The bi-LS-AttM model, which is a hybrid model of Bi-LSTM and attention model, was proposed by Xie et al. [44] for the image captioning process. The main idea of their approach is the ability to generate sentences that were essentially innovative in structure and significantly related to the image content. Besides this, they utilized the fast region-based CNN (Fast RCNN) model to detect features of image parts and objects instead of the entire image. The experiments were performed on the Flickr30k and MSCOCO datasets. Both datasets contained five sentences describing each image. Results showed that the Bi-LS-AttM outperformed the original Bi-LSTM model in terms of BLEU score. They got 64.5 and 20.2 of BLEU-1 and BLEU-4 in the case of the Bi-LS-AttM model, while the Bi-LSTM achieved 62.1 and 19.3, respectively. However, although this model's performance outperformed the original Bi-LSTM but was lower than other models like Hard attention mechanism [45] (which achieved 66.9 as BLEU-1 score on Flickr30k and 71.8 as BLEU-1 on MSCOCO dataset).

E. 3.5. Discussion of the related state-of-art

This section will compare the previously listed state-of-art studies and define the main key points, challenges, weak points and best performance. Table 1 includes a detailed comparison of the state-of-art image captioning studies.

Table 1. A detailed comparison of the state-of-art image captioning studies.

Researcher	Proposed Model	Dataset with its Specifications	Results	Limitations
Sammani & Kyriazi [17]	EditNet and DCNet	MSCOCO: 82,783 training images, 40,504 validation images, 40,775 test images	BLEU-1: 77.9, BLEU-4: 38, CIDEr-D: 1.2, SPICE: 21.2	Time-consuming due to the refinement process
Khan et al. [46]	1D-CNN and ResNet-50	BanglaLekhaImage Captions dataset (9000 images)	BLUE-1: 0.651, CIDEr: 0.572, METEOR: 0.297, ROUGE: 0.434, SPICE: 0.357	Model recognizes only humans

Researcher	Proposed Model	Dataset with its Specifications	Results	Limitations
Patwari & Naik [18]	InceptionV3 and GRU	COCO caption: 330,000 images with 200,000 annotated ones, each of which is described by 5 sentences	BLEU-1: 70.6, BLEU-4: 24.3	Used a small subset of the dataset due to hardware limits
Mishra et al. [19]	Dynamic convolution encoder and LSTM	Custom Hindi dataset based on MSCOCO	High BLEU score	Intended for Hindi language captions
Poddar & Rani [20]	Multi-layered CNN (VGG-16) and LSTM	Flickr8k Hindi: 8,000 training images, 100 validation images	BLEU score of 0.359 (Unigram), 0.55 (Bigram)	Moderate size of dataset and single evaluation metric
He et al. [26]	Image Transformer	MSCOCO	BLEU-1: 81.2, BLEU-4: 39.6	-
Wang et al. [27]	Transformer-based model with SwinTransformer and refining encoder	MSCOCO	BLEU-1: 82.8, BLEU-4: 41.4, CIDEr: 138.2% (individual model)	-
Castro et al. [21]	Transformer-based model with different transfer-learning models	MSCOCO	BLEU: 20.1, TOP-5: 73.09	Manual selection of hyperparameters
Fei [47]	Attention-aligned Transformer Model (A2)	MSCOCO	BLEU-1: 78.6, BLEU-4: 38.2	Need for manual selection of the image region features to perturb
Wang et al. [28]	Attention-reinforced Transformer with Feature Attention Block (FAB)	MSCOCO	BLEU-1: 81.2, BLEU-4: 39.2	Potential overhead due to additional architectures
Parvin et al. [48]	Transformer-based Local-global	Flickr30k, MSCOCO	For MSCOCO: BLEU-1: 86.1, BLEU-4: 37.8,	High computational cost

Researcher	Proposed Model	Dataset with its Specifications	Results	Limitations
	Guidance Image Captioning Model		METEOR: 39.2, CIDEr: 132.9	
Hu et al. [29]	Spatial Enhanced Attention Model with Dual Spatial Encoder and Gated-normalized Attention model (GNA)	MSCOCO	CIDEr: 134	-
Selivanov et al. [30]	GPT-based image captioning	Open-I, MIMIC-CXR, MSCOCO	For MSCOCO: BLEU-1: 0.82, BLEU-4: 0.409	No comparison with state-of-the art methods.
Sharma et al. [31]	XGL-T Transformer model	MSCOCO	BLEU-1: 81.5, BLEU-4: 39.9, CIDEr: 134, METEOR: 29.8, ROUGE-L: 59.9	Lack of comparison with other state-of-the-art models
Yang et al. [32]	Context-Aware Transformer Model (CATNet)	MSCOCO	BLEU-1: 81.8, BLEU-4: 40, METEOR: 29.4, ROUGE: 59.3, CIDEr: 133	Separate representation of image and text
Padate et al. [33]	Dual attention-based model with Inception V3 and Bi-LSTM language model	Flickr30k	BLEU-1: 0.659, BLEU-4: 0.22	Lack of visual and text attentions combination
Chen et al. [37]	GAN with CNN-RNN generator	MSCOCO: 82,783 training, 40,504 validation, 40,775 test images, 5 description sentences	BLEU-1: 81.9, BLEU-4: 39.6, METEOR: 28.7, CIDEr: 123.1	High computational time
Amirian et al. [38]	VAE with WGAN, ATTEND-GAN, and sentiment analysis	MSCOCO and SentiCap datasets	More descriptive and meaningful descriptions	Did not validate their models

Researcher	Proposed Model	Dataset with its Specifications	Results	Limitations
Babavalian & Kiani [39]	SeqGAN for video captioning	MSVd and MSRVTT datasets	BLEU-4: 54.82 (MSVD), 44.76 (MSRVTT), METEOR: 35.9 (MSVD), 29.8 (MSRVTT)	No object detection performed
Deepak et al. [40]	Residual attention GAN model (RAGAN)	Flickr30k: 31,783 images, MSCOCO: 28,000 training, 1,000 validation, 1,000 test	BLEU-1: 0.86, BLEU-4: 0.49	High computational time may be an issue
Honda et al. [41]	RL models with one-epoch fine-tuning	MSCOCO captioning dataset (Karpathy test splitting)	CIDEr: 119.0, SPICE: 21, R@1: 21.6, R@5: 50.5, R@10: 65.4	Not specified
Yan et al. [42]	Hierarchical GAN with an attention mechanism	MSCOCO 2014 version dataset	BLEU-1: 72.611, BLEU-4: 27.243, METEOR: 24.731, CIDEr: 88.14, ROUGE-L: 56.048	High computational time
Chen et al. [43]	Pyramid Attention and Self-critical GAN	MSCOCO dataset	BLEU-1: 78.3, BLEU-4: 37.9, METEOR: 28.9, CIDEr: 119.6, ROUGE-L: 58.5	High computational time
Xie et al. [44]	Bi-LS-AttM model	Flickr30k and MSCOCO datasets, 5 description sentences per image	BLEU-1: 64.5, BLEU-4: 20.2 (Bi-LS-AttM), BLEU-1: 62.1, BLEU-4: 19.3 (Bi-LSTM)	Performance lower than Hard attention mechanism

The studies on image captioning models have utilized different architectures, such as EditNet, 1D-CNN, InceptionV3, attention mechanism, and Transformer-based models, with several of them achieving high BLEU-1 and BLEU-4 scores. In terms of performance, the research by Parvin et al. [48] presented a Transformer-based Local-global Guidance Image Captioning Model, which achieved the highest BLEU-1 score of 86.1. However, the high computational cost was a noted limitation. Moreover, Patwari & Naik's [18] study utilized a smaller subset of the MSCOCO dataset due to hardware limits, thereby limiting the comprehensiveness of their model. A common challenge is the manual selection of hyperparameters and high computational time, as seen in a study by Castro et al. [21] and Fei [47].

Additionally, models such as the one by Khan et al. [46] were limited by their field, recognizing only humans. Other studies, like those by Selivanov et al. [30] and Sharma et al. [31], did not introduce a comparative analysis with other state-of-the-art studies. Utilizing GANs and attention mechanisms improved the image captioning performance but required a

high computational time. Overall, while achievements are being made in the field of image captioning, many challenges must be addressed, including overcoming computational limitations, enhancing model generalizability, and optimizing parameter selection processes.

F. 3.5. Image captioning performance metrics

For any image captioning or description system, the performance must be evaluated using specific evaluation metrics which are different from the known classification or segmentation metrics.
The image captioning evaluation metrics include the following:

1- Manual evaluation: this type of image captioning evaluation refers to relevance to the source image, fluency of expression, expression variety, etc. These metrics are accurate but require too much computation [35].

2- Rule-based evaluation metrics: these metrics compute the degree of correlation between the generated captions and the original description sentences and include the following metrics:
BLEU [49]: computes the degree of overlap between the generated captions and the original reference.
CIDEr [50]: calculates the correlation between a sentence generated by an image captioning model and a set of reference sentences.
METEOR [51]: assess the degree of coherence in the matched words of the generated description relative to the reference description.
ROUGE [35]: evaluates the text summarization models.

IV. CONCLUSION

In this study, a comprehensive review study of the most recent image captioning methods has been introduced. The study took into account related work in the last two years besides some of the essential studies in the last decade. The study also classified the previous work into many branches based on the utilized methodologies (encoder-decoder, transformer models, GAN models, Reinforcement learning models, attention-based models, and hybrid models). This study compared related work in terms of the utilized deep architectures, the used datasets, their main results, and the main limitations. The most commonly used evaluation metrics of image captioning and description were also explained. The results showed that the most used dataset in literature is the MSCOCO dataset, and the next one is the Flickr30k dataset. The best-registered score on the MSCOCO dataset corresponds to the study [48] with a BLEU-1 score of 86.1; similarly, the best BLEU-1 score on the Flickr32k dataset was also related to the study [33] with a score of 65.9. Some related studies evaluated their model's performance using specific metrics (which is insufficient since some metrics are affected by sentence length, like BLEU). Some studies utilized non-standard datasets, reducing their method's universality. Among previous studies, the transformer models appeared to be the best ones in terms of performance, especially with using supportive deep architectures like attention mechanisms. However, the basic encoder-decoder architecture is still the simplest method, but it lacks high performance, especially in the case of complex datasets. The current study recommends using highlight deep models with some efficient deep architecture (like attention models).

REFERENCES

[1] A. M. Rinaldi, C. Russo, and C. Tommasino, "Automatic image captioning combining natural language processing and deep neural networks," *Results in Engineering,* vol. 18, p. 101107, 2023.

[2] R. Marzouk *et al.*, "Natural Language Processing with Optimal Deep Learning-Enabled Intelligent Image Captioning System," *Computers, Materials & Continua,* vol. 74, no. 2, 2023.

[3] A. M. Hilal, F. Alrowais, F. N. Al-Wesabi, and R. Marzouk, "Red Deer Optimization with Artificial Intelligence Enabled Image Captioning System for Visually Impaired People," *Computer Systems Science & Engineering,* vol. 46, no. 2, 2023.

[4] A. Singh *et al.*, "Image Captioning Using Python," in *2023 International Conference on Power, Instrumentation, Energy and Control (PIECON)*, 2023: IEEE, pp. 1-5.

[5] Y. Feng, K. Maeda, T. Ogawa, and M. Haseyama, "Gaze-Dependent Image Re-Ranking Technique for Enhancing Content-Based Image Retrieval," *Applied Sciences,* vol. 13, no. 10, p. 5948, 2023.

[6] M. Gupta, P. Asthana, and P. Singh, "EDUVI: An Educational-Based Visual Question Answering and Image Captioning System for Enhancing the Knowledge of Primary Level Students," 2023.

[7] D. Gurari, Y. Zhao, M. Zhang, and N. Bhattacharya, "Captioning images taken by people who are blind," in *Computer Vision–ECCV 2020: 16th European Conference, Glasgow, UK, August 23–28, 2020, Proceedings, Part XVII 16*, 2020: Springer, pp. 417-434.

[8] S. A. Singh and K. Desai, "Automated surface defect detection framework using machine vision and convolutional neural networks," *Journal of Intelligent Manufacturing,* vol. 34, no. 4, pp. 1995-2011, 2023.

[9] I. Goodfellow *et al.*, "Generative adversarial nets," *Advances in neural information processing systems,* vol. 27, 2014.

[10] L. Xu, Q. Tang, J. Lv, B. Zheng, X. Zeng, and W. Li, "Deep Image Captioning: A Review of Methods, Trends and Future Challenges," *Neurocomputing,* p. 126287, 2023.

[11] K. He, Zhang, X., and S. Ren, & Sun, J, "Deep Residual Learning for Image Recognition," in *IEEE Conference on Computer Vision and Pattern Recognition (CVPR)*, 2016: IEEE, doi: https://doi.org/10.1109/CVPR.2016.90.

[12] K. Simonyan and A. Zisserman, "Very deep convolutional networks for large-scale image recognition," *arXiv preprint arXiv:1409.1556,* 2014.

[13] K. Thangavel *et al.*, "A novel method for image captioning using multimodal feature fusion employing mask RNN and LSTM models," *Soft Computing,* pp. 1-14, 2023.

[14] S. Dubey, F. Olimov, M. A. Rafique, J. Kim, and M. Jeon, "Label-attention transformer with geometrically coherent objects for image captioning," *Information Sciences,* vol. 623, pp. 812-831, 2023.

[15] M. A. Sabri, H. El Madhoune, C. Zouitni, and A. Aarab, "Image Captioning: An Understanding Study," in *International Conference on Digital Technologies and Applications*, 2023: Springer, pp. 482-491.

[16] K. R. Suresh, A. Jarapala, and P. Sudeep, "Image Captioning Encoder–Decoder Models Using CNN-RNN Architectures: A Comparative Study," *Circuits, Systems, and Signal Processing,* vol. 41, no. 10, pp. 5719-5742, 2022.

[17] F. Sammani and L. Melas-Kyriazi, "Show, edit and tell: a framework for editing image captions," in *Proceedings of the IEEE/CVF conference on computer vision and pattern recognition*, 2020, pp. 4808-4816.

[18] N. Patwari and D. Naik, "En-de-cap: An encoder decoder model for image captioning," in *2021 5th International Conference on Computing Methodologies and Communication (ICCMC)*, 2021: IEEE, pp. 1192-1196.

[19] S. K. Mishra, S. Sinha, S. Saha, and P. Bhattacharyya, "Dynamic Convolution-based Encoder-Decoder Framework for Image Captioning in Hindi," *ACM Transactions on*

Asian and Low-Resource Language Information Processing, vol. 22, no. 4, pp. 1-18, 2023.

[20] A. K. Poddar and R. Rani, "Hybrid Architecture using CNN and LSTM for Image Captioning in Hindi Language," *Procedia Computer Science,* vol. 218, pp. 686-696, 2023.

[21] R. Castro, I. Pineda, W. Lim, and M. E. Morocho-Cayamcela, "Deep learning approaches based on transformer architectures for image captioning tasks," *IEEE Access,* vol. 10, pp. 33679-33694, 2022.

[22] W. Liu, S. Chen, L. Guo, X. Zhu, and J. Liu, "Cptr: Full transformer network for image captioning," *arXiv preprint arXiv:2101.10804,* 2021.

[23] P. Zeng, H. Zhang, J. Song, and L. Gao, "S2 transformer for image captioning," in *Proceedings of the International Joint Conferences on Artificial Intelligence*, 2022, vol. 5.

[24] M. Cornia, M. Stefanini, L. Baraldi, and R. Cucchiara, "Meshed-memory transformer for image captioning," in *Proceedings of the IEEE/CVF conference on computer vision and pattern recognition*, 2020, pp. 10578-10587.

[25] S. Elbedwehy, T. Medhat, T. Hamza, and M. F. Alrahmawy, "Efficient Image Captioning Based on Vision Transformer Models," *Computers, Materials & Continua,* vol. 73, no. 1, 2022.

[26] S. He, W. Liao, H. R. Tavakoli, M. Yang, B. Rosenhahn, and N. Pugeault, "Image captioning through image transformer," in *Proceedings of the Asian conference on computer vision*, 2020.

[27] Y. Wang, J. Xu, and Y. Sun, "End-to-end transformer based model for image captioning," in *Proceedings of the AAAI Conference on Artificial Intelligence*, 2022, vol. 36, no. 3, pp. 2585-2594.

[28] Z. Wang, S. Shi, Z. Zhai, Y. Wu, and R. Yang, "ArCo: Attention-reinforced transformer with contrastive learning for image captioning," *Image and Vision Computing,* vol. 128, p. 104570, 2022.

[29] J. Hu, Y. Yang, Y. An, and L. Yao, "Dual-Spatial Normalized Transformer for image captioning," *Engineering Applications of Artificial Intelligence,* vol. 123, p. 106384, 2023.

[30] A. Selivanov, O. Y. Rogov, D. Chesakov, A. Shelmanov, I. Fedulova, and D. V. Dylov, "Medical image captioning via generative pretrained transformers," *Scientific Reports,* vol. 13, no. 1, p. 4171, 2023.

[31] D. Sharma, C. Dhiman, and D. Kumar, "XGL-T transformer model for intelligent image captioning," *Multimedia Tools and Applications,* pp. 1-22, 2023.

[32] X. Yang, Y. Wang, H. Chen, J. Li, and T. Huang, "Context-Aware Transformer for image captioning," *Neurocomputing,* p. 126440, 2023.

[33] R. Padate, A. Jain, M. Kalla, and A. Sharma, "Image caption generation using a dual attention mechanism," *Engineering Applications of Artificial Intelligence,* vol. 123, p. 106112, 2023.

[34] Y. Cao *et al.*, "A comprehensive survey of ai-generated content (aigc): A history of generative ai from gan to chatgpt," *arXiv preprint arXiv:2303.04226,* 2023.

[35] J. Jia *et al.*, "Image captioning based on scene graphs: A survey," *Expert Systems with Applications,* p. 120698, 2023.

[36] L. Yu, W. Zhang, J. Wang, and Y. Yu, "Seqgan: Sequence generative adversarial nets with policy gradient," in *Proceedings of the AAAI conference on artificial intelligence*, 2017, vol. 31, no. 1.

[37] C. Chen, S. Mu, W. Xiao, Z. Ye, L. Wu, and Q. Ju, "Improving image captioning with conditional generative adversarial nets," in *Proceedings of the AAAI conference on artificial intelligence*, 2019, vol. 33, no. 01, pp. 8142-8150.

[38] S. Amirian, K. Rasheed, T. R. Taha, and H. R. Arabnia, "Image captioning with generative adversarial network," in *2019 International Conference on Computational Science and Computational Intelligence (CSCI)*, 2019: IEEE, pp. 272-275.

[39] M. R. Babavalian and K. Kiani, "Learning distribution of video captions using conditional GAN," *Multimedia Tools and Applications,* pp. 1-23, 2023.

[40] G. Deepak, S. Gali, A. Sonker, B. C. Jos, K. Daya Sagar, and C. Singh, "Automatic image captioning system using a deep learning approach," *Soft Computing,* pp. 1-9, 2023.

[41] U. Honda, T. Watanabe, and Y. Matsumoto, "Switching to Discriminative Image Captioning by Relieving a Bottleneck of Reinforcement Learning," in *Proceedings of the IEEE/CVF Winter Conference on Applications of Computer Vision*, 2023, pp. 1124-1134.

[42] S. Yan, Y. Xie, F. Wu, J. S. Smith, W. Lu, and B. Zhang, "Image captioning via hierarchical attention mechanism and policy gradient optimization," *Signal Processing,* vol. 167, p. 107329, 2020.

[43] T. Chen, Z. Li, J. Wu, H. Ma, and B. Su, "Improving image captioning with Pyramid Attention and SC-GAN," *Image and Vision Computing,* vol. 117, p. 104340, 2022.

[44] T. Xie, W. Ding, J. Zhang, X. Wan, and J. Wang, "Bi-LS-AttM: A Bidirectional LSTM and Attention Mechanism Model for Improving Image Captioning," *Applied Sciences,* vol. 13, no. 13, p. 7916, 2023.

[45] K. Xu *et al.*, "Show, attend and tell: Neural image caption generation with visual attention," in *International conference on machine learning*, 2015: PMLR, pp. 2048-2057.

[46] F. Khan, S. M. S.-U.-R. Mohammad, and M. S. Islam, "Improved bengali **image captioning** via deep convolutional neural network based **encoder-decoder model**," presented at the International Joint Conference on Advances in Computational Intelligence: IJCACI Singapore, 2021.

[47] Z. Fei, "Attention-aligned transformer for image captioning," in *proceedings of the AAAI Conference on Artificial Intelligence*, 2022, vol. 36, no. 1, pp. 607-615.

[48] H. Parvin, A. R. Naghsh-Nilchi, and H. M. Mohammadi, "Transformer-based local-global guidance for image captioning," *Expert Systems with Applications,* vol. 223, p. 119774, 2023.

[49] K. Papineni, S. Roukos, T. Ward, and W.-J. Zhu, "Bleu: a method for automatic evaluation of machine translation," in *Proceedings of the 40th annual meeting of the Association for Computational Linguistics*, 2002, pp. 311-318.

[50] S. Liu, Z. Zhu, N. Ye, S. Guadarrama, and K. Murphy, "Improved image captioning via policy gradient optimization of spider," in *Proceedings of the IEEE international conference on computer vision*, 2017, pp. 873-881.

[51] S. Banerjee and A. Lavie, "METEOR: An automatic metric for MT evaluation with improved correlation with human judgments," in *Proceedings of the acl workshop on intrinsic and extrinsic evaluation measures for machine translation and/or summarization*, 2005, pp. 65-72.

Çok Kullanımlık Çantaların Üretiminde Verimlilik Artışını Sağlayan Bir Sistem

A System for Increasing Productivity in the Production of Reusable Bags

Sema IŞIK ÇALIŞKAN[*,1], Özge AVCI PAŞAOĞLU[1], Bülent CEYHAN[1], Serkan KAYA[1], Ali AVCI[1], Cüneyt YILMAZ[2]

[*]: arge@ultrapak.com.tr, ORCID: 0000-0001-6796-278X
[1]*Ar-Ge Departmanı, Ultrapak Makina San. ve Tic. A.Ş. , Istanbul, Türkiye*
[2]*Mekatronik Mühendisliği, Yıldız Teknik Üniversitesi, Istanbul, Türkiye*

Özet: Günümüzde çevre dostu yaklaşımı, sürdürülebilirlik ve kaynak-enerji tasarrufu farkındalıklarının artması ile birlikte plastik poşetlerin kullanımının azaltılmasına yönelik çabalar artmakta ve bu hususta çok sayıda yasal düzenlemeler getirilmektedir. Plastik atıkların büyük bir kısmını oluşturan tek kullanımlık poşetlerin yavaş çözünme süreleri nedeniyle, çevre dostu ve tekrar kullanılabilir çantaların tercih edilmesi teşvik edilmektedir. Perakende alışveriş, marketler, fuarlar, etkinlikler ve promosyon ürünleri gibi çeşitli kullanım alanları bulunan çok kullanımlık çantaların imalat sürecinin iyileştirilmesi amacıyla çalışmalar yapılmıştır.

Üretim hattındaki tüm istasyonlar yüksek önem arz etmektedir. Her bir istasyondaki bekleme süresi ve işlem adımları maliyetleri yüksek oranda etkilemektedir. Bu noktada mevcut üretim sisteminin analizi yapılmış, daha verimli bir sistem oluşturmak için literatür araştırmaları yapılmıştır. Araştırmalar neticesinde kesme ünitesinin geliştirilmesi gerektiği belirlenmiştir. Geliştirilmiş kesme ünitesinde, bıçak yapısı düz form yerine V formuna getirilmiş, alt destek yüzeyindeki döner plaka kaldırılmış, hidrolik sistemden pnömatik sisteme geçilmiş ve daha sağlıklı kesim gerçekleştirebilmek için kesme kanalı oluşturulmuştur.

Yapılan değişikler ile, bıçağın kullanım ömrü artırılarak tamir ve bakım maliyetleri düşürülmüş, alt destek yüzeyindeki mekanizmanın kaldırılmasıyla enerji sarfiyatının önüne geçilmiş, V formundaki bıçak yapısı ile kesme yüzeyi arıtılarak kullanım ömrü uzun olan bir yapı elde edilmiştir. Oluşturulmuş yeni sistemin; enerji tasarrufu, verimlilik, işgücü, fire ve malzeme maliyeti üzerindeki etkisi belirlenip eski sistem ile karşılaştırılmıştır. Bu kapsamda kapasite değerlerine göre elde edilecek yıllık ortalama kazançlar ortaya konulmuştur. Örneğin, tek bir makinada yıllık 47.598 USD'lik bir kaybın önleneceği ön görülmüştür. Ayrıca yeni sistemin potansiyel ihracat, yerlileşme vb. gibi makroekonomik etkileri analiz edilmiştir.

Anahtar Kelimeler: *Verimlilik, Fire Kaybı, Enerji Tasarrufu, Sürdürülebilir Üretim*

Abstract: Nowadays, efforts to reduce the use of plastic bags are increasing and many legal regulations have been introduced with the increase in awareness of environmentally friendly approach, sustainability and resource-energy saving. Due to the slow decomposition time of single-use bags, which constitute a large portion of plastic waste, the preference for environmentally friendly and reusable bags is encouraged. Efforts have been made to improve the manufacturing process of reusable bags, which have various uses such as retail shopping, markets, fairs, events and promotional products.

All stations in the production line are of high importance. The waiting time and process steps at each station have a high impact on costs. At this point, the existing production system was analyzed and literature research was conducted to create a more efficient system. As a result

of the research, it was determined that the cutting unit should be improved. In the improved cutting unit, the blade structure has been changed from flat to V-shaped, the rotating plate on the lower support surface has been removed, the hydraulic system has been switched to a pneumatic system and a cutting channel has been created in order to perform healthier cutting.

With the changes made, repair and maintenance costs were reduced by increasing the service life of the blade, energy consumption was prevented by removing the mechanism on the lower support surface, and a structure with a long service life was obtained by purifying the cutting surface with the V-shaped blade structure. The effects of the new system on energy saving, productivity, labor, waste and material costs were determined and compared with the old system. In this context, the average annual gains to be obtained according to capacity values were revealed. For example, it is predicted that a loss of 47.598 USD per year will be avoided in a single machine. In addition, the macroeconomic effects of the new system such as potential exports, localization, etc. were analyzed.

Keywords: *Productivity, Wastage Loss, Energy Efficiency, Sustainable Manufacturing*

I. GİRİŞ

Dünyamızda her geçen gün çevre duyarlılığı, sürdürülebilirlik ve enerji tasarrufu farkındalıkları artmaktadır. Türkiye dahil pek çok ülkede, çevre duyarlılığı ile ilgili olarak, tek kullanımlık çantaların kullanımlarının kısıtlanması ile ilgili girişimler yapılmıştır ve bu girişimler sayesinde çok kullanımlık çantaların kullanımları ve dolayısıyla üretimleri yaygınlaşmaya başlamıştır. Türkiye'de de bu çanta üretimleri alanında özgün çalışmalar yapılmakta ve uluslararası alanda yer almaya çalışılmaktadır. Ultrapak Makine, Türkiye'de bu alanda makine üretimi yaparak hizmet eden nadir firmalardan biridir. Üretilen makinaların daima daha verimlisinin tasarımı ve imalatı yoluna gidilmektedir. Her alanda olduğu gibi sürdürülebilirlik ve enerji tasarrufu her geçen gün daha da önem kazanmaktadır. Çanta üretiminde kullanılacak makinenin tasarımı da o anki şartlarda enerji, maliyet ve hammadde tasarrufu konuları göz önüne alınarak yapılmakta veya tasarım bu hedeflere yönelik olarak optimize edilmektedir.

Yapılan çalışma çok kullanımlık çantaların üretim sisteminde verimlilik artışını ve sürdürülebilir üretimi konu edindiği için bu bölümde yapılmış olan literatür araştırmasında, üretim sistemlerindeki verimlilik artırıcı uygulamalar ve sürdürülebilirlik üzerine daha önceden yapılmış olan çalışmalar incelenmiştir.

LİTERATÜR ARAŞTIRMASI

Farklı kumaş tiplerinde kesim parametrelerinin belirlenmesi üzerine yapılan bir araştırmada, kesim parametrelerindeki değişimin kesim süresi ve kesim niteliğine etkileri gözlemlenmiştir [1]. Kesim parametrelerine bağlı olarak, kesim veriminin ve kalitesinin artırılabileceği, olası hataların engellenebileceği belirlenmiştir. Kesim hızı ve dikey bıçak frekansının kesim kalitesini bozmadan mümkün olduğunca yüksek ayarlanması sonucuna varılmış, bileme sıklığının bıçak ömrünü ve kesim kalitesini doğrudan etkilediği saptanmıştır.

Bir tekstil fabrikasında enerji verimliliği uygulamalarına yönelik yapılan bir yüksek lisans tez çalışmasında, verimlilik artırımı üzerine yapılan faaliyetlerin fabrikaya olan etkisi ele almıştır [2]. Bu çalışma ile Türkiye'de bulunan farklı sektörlerdeki sanayi tesislerinde uygulanabilir çalışmaların gözler önüne serilmesi amaçlanmış, ilgili çalışmaların firmanın yıllık giderini azalttığı sonucuna varılmıştır.

Başka bir yüksek lisans tez çalışmasında, plastik ambalaj sektöründe endüstriyel kesici takım optimizasyonu ele alınmıştır [3]. Bu çalışmada, kesici takımda yeni bir tasarım yapılarak üretim sayısı ve verimliliğin artırılması amaçlanmıştır. Çalışmanın sonucunda üretim süresi düşürülmüş, kesici takım ömrü artırılmıştır. Maliyet çalışmaları ile de %60'lık bir maliyet düşüşünün gerçekleştirildiği gösterilmiştir.

Türkiye imalat sanayiinde yeşil imalatın uygulanabilirliğini göstermek için bir makine imalat sanayii örneği üzerine yapılan bir uzmanlık tez çalışmasında, yeşil üretimin tanımını yaparak Türkiye için yeni bir yaklaşım olan yeşil üretimin makina sanayinde uygulanabilirliği araştırılmıştır [4]. Ayrıca yeşil üretim ile kaynak tasarrufu yapılabileceğini, atıklarının bertarafının sağlanabileneceğini ve verimlilik artışıyla rekabet avantajı yaratılabileceğini vurgulamıştır.

Takım tezgahlarındaki enerji verimliliğini artırmak amacıyla yapılan bir çalışmada, tezgahın kesme gücü ve tahrik bileşenlerinin arasındaki güç kaybı ilişki modelleri oluşturulmuş, oluşturulan modellere dayanarak enerji tasarrufunun minimuma indirilebileceği, tasarruf değerlerinin takip edilebileceği sistemler kurulabileceği sonucuna varılmıştır [5].

Otomotiv sanayinde enerji verimliliği ve tasarruf olanakları ile ilgili yapılan bir çalışmada, çeşitli ve farklı uygulamalarla verimlilik artışının sağlanabileceği ve ilgili alandaki işletmelerin yıllık giderlerinin azaltılabileceği gösterilmiştir [6].

Yeşil teknoloji kullanımı üzerine yapılan bir çalışmada, çeşitli yeşil teknoloji örnekleri sunarak gelecekteki üretim sistemlerinin sürdürülebilir olmasını sağlamak için karşılaştırmalı araştırmalar yapılmış, IPAT denklemi, kaynak etkinliği ve verimliliği, sürecin iyileştirilmesi, sistemin iyileştirilmesi, kaldıraç sistemi gibi uygulamaların firmalara olumlu etkileri gösterilmiş ve sürdürülebilir üretimin önemi ortaya konulmuştur [7].

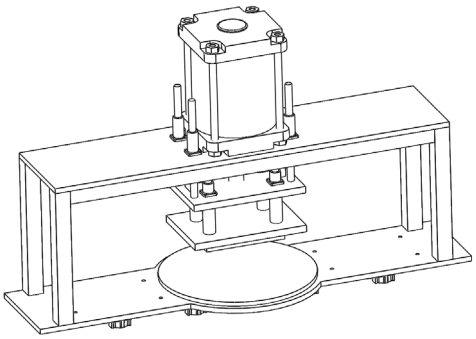
Tekstil sektöründeki makine ve üretim hatlarında kullanılan sistemler ile ilgili yayınlanmış makalelerin derlendiği kapsamlı bir kitapta, otomatik kesme sistemleri hakkında bilgi verilmekte [8], fakat kullanılan bıçakların profilinin önemi hakkında bilgiye ulaşılmamıştır. Genelde düz kesim bıçakları üzerinde durulmuştur.

Kumaş malzemelerin kesimi ile ilgili bir çalışmada, bıçak ucunun kumaşa girip kesmeye başladığı an, sonlu elemanlar yöntemi (FEM) ile teorik olarak incelenmiştir [9]. Kumaş malzemeye girmekte olan bıçağın kumaşa ne kadar nüfuz ettiğinin kesmeye etkisi ve aynı zamanda bıçak girişine karşı direnç kuvvetinin etkileri incelenmiştir. Ayrıca bu çalışmada, sürtünme faktörünün direnç kuvveti üzerindeki etkisinin bıçağın kumaşa nüfuz derinliğinin artması ile daha güçlü hale geldiği gösterilmiştir.

II. YÖNTEM

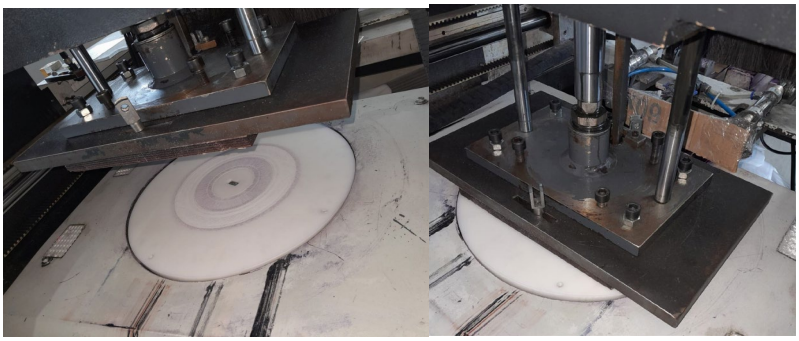
A. Bir Önceki Makinanın Yapısı ve İşleyişi

Atlet çanta olarak da adlandırılan market poşetlerinin formuna benzeyen çantaların nihai hali, üretim esnasında bıçak ünitesi ile kesim işlemi gerçekleştirilerek elde edilmektedir. Kesme işlemi hidrolik pres ile güç uygulanarak kestamit malzemeden imal edilen bir tabla üzerinde gerçekleştirilmektedir (Şekil 1). Bu işlemde kullanılan bıçak düz bir forma sahiptir, çantaların düzgün bir şekilde kesilebilmesi için bıçağın yapısı itibariyle yüksek bir kuvvet uygulanması gerekmektedir (Şekil 2). Bu yüksek kuvvete maruz kalan alt tabla üzerinde zamanla aşınmalar meydana gelmekte ve belli bir süre sonra kullanılamaz hale gelmektedir. Alt tabla üzerindeki deformasyonun en aza indirilmesi amacıyla mevcut sistemde her işlemin ardından tablaya belli bir açı ile dönme hareketi yaptırılmakta ve bu durum enerji kaybına neden olmaktadır.



Şekil 1. Eski sistemin üç boyutlu teknik resmi

Çanta üretimi yapan otomasyon sistemi dakikada 60 adet çanta üretmektedir. Makine yaklaşık 80.000 adet çantanın üretimini gerçekleştirdiğinde alt tablanın deformasyona uğraması ve bıçağın aşınması sebebiyle kesim işlemi düzgün yapılamamakta, makine fire vermektedir. Bu süreçte ortalama 100 adet çanta fireye ayrılmakta ardından makine durdurularak bakım gerçekleştirilmektedir. Alt tabla ve bıçak sistemden sökülerek bakım işlemi gerçekleştirilmekte fakat bu işlem maliyet kaybı oluşturmaktadır.



Şekil 2. Eski sistemde makinanın kesim anındaki görüntüsü

Alt tabla 5 defa işlem görmesinin ardından, Şekil 3'te bulunan kesici bıçak ise 550 saat kullanımın ardından tamamen kullanılamaz hale gelmektedir. Tüm bu hususlar, hammadde kaybına ve alet-teçhizat kaynaklarının verimli kullanılmasına engel olmaktadır.

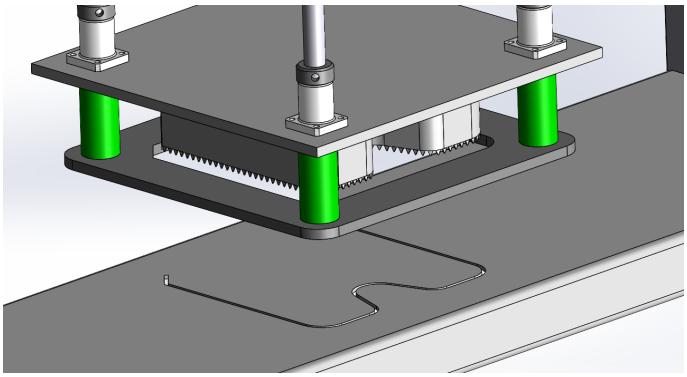


Şekil 3. Eski sistemde kesim ünitesinin alttan görünümü

İlgili sorunları aşmak amacıyla yeni bir ünite geliştirilip tasarlanmıştır.

B. Yeni (İyileştirilmiş) Makinanın Yapısı ve İşleyişi

Yeni sistemde, alt destek yüzeyinde bulunan döner plakanın dönme hareketi için herhangi bir mekanizmanın kullanılmadığı ve enerji sarfiyatının olmadığı bir yapı geliştirilmiştir (Şekil 4).

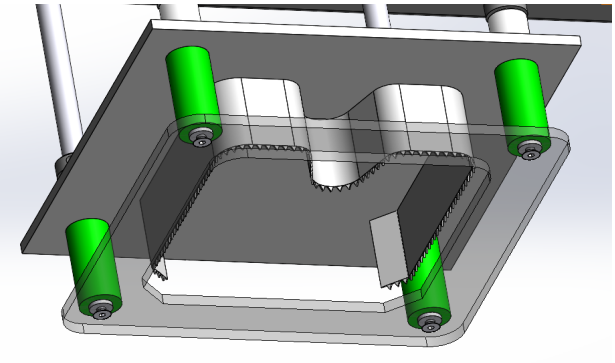


Şekil 4. Yeni sistemde kesme ünitesinin tasarımı

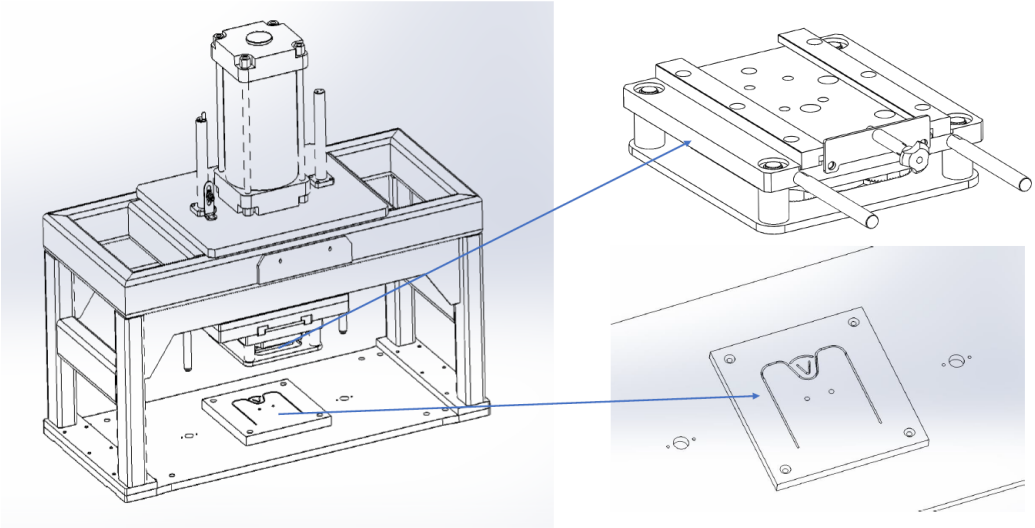
Kesme ekseninde kesici bıçakların sadece çanta ile temaslandırıldığı ve kesme ekseninde oluşturulan kesme kanalı vasıtasıyla kesici bıçakların kullanım ömrünün arttırıldığı ve daha sağlıklı bir kesmenin sağlandığı bir yapı ortaya konulmuştur (Şekil 5).

Kesici bıçaklar, önceki teknikteki düz yapılı yüzeyler yerine V formlu kesici yüzeyler içermektedir. Bu sayede kesme yüzeyinin arttırılarak açılı kesmenin sağlandığı kullanım ömrü uzun olan bir yapı sağlanmıştır (Şekil 5).

Ayrıca kesme bıçaklarının açılı yüzeyler içermesi ve bir kesme kanalında kesme gerçekleştirilmesi sebebiyle, kesme ekseninde yapılandırılmış olan düşey eksende baskı kuvveti uygulayan dikey tahrik elemanlarının daha az kuvvet uygulaması sağlanmış ve böylece, düşük enerji kullanımının sağlandığı bir yapı elde edilmiştir.



Şekil 5. Yeni sistemde kesme ünitesi tasarımının alttan görünümü



Şekil 6. Yeni kesme ünitesi tasarımının teknik resimleri

C. *Üretim ve Karşılaştırma Verisi*

Üretim firesi ile ilgili elde edilen veri Tablo I'de gösterilmektedir. Yeni sistemin eskiye göre fire kaybının 156 kat daha düşük olduğu ve sadece tek bir makine ile yıllık 2.325 dolarlık bir kaybın önleneceği görülmektedir. Burada yıllık maliyet kaybı hesabında tek çanta fire kaybı 0.075 dolar olarak alınmıştır.

Kestamit ve bıçak değişimi ile ilgili verimlilik verisi Tablo II'de gösterilmektedir. Yeni sistemin eskiye göre verimlilik kaybının 312 kat daha düşük olduğu ve sadece tek bir makine ile yıllık 27.990 dolarlık bir kaybın önleneceği görülmektedir. Burada dakikada 60 çanta üretildiği kabul edilerek 6 aylık ve yıllık toplam kayıp adedi elde edilmiş ve yine tek çanta kaybı 0.075 dolar alınarak toplam yıllık maliyet kaybı USD olarak hesaplanmıştır.

Tablo I. Tek bir Makine için Üretim Firesi Verisi ve Karşılaştırma Tablosu

	Eski Sistem	Yeni Sistem	Fark (Düşüş)
Kestamit Kaynaklı Çanta Firesi (adet/6 ay)	15000	0	-15000
Bıçak Kaynaklı Çanta Firesi (adet/6 ay)	600	100	-500
6 Aylık Toplam (adet)	15600	100	-15500
Yıllık Toplam Kayıp (adet)	31200	200	-31000
Yıllık Maliyet Kaybı (USD)	2.340,00	15,00	**-2.325,00**

Tablo II. Tek bir Makine için Verimlilik Kaybı Verisi ve Karşılaştırma Tablosu

	Eski Sistem	Yeni Sistem	Fark (Düşüş)
Kestamit Değişimi Kaynaklı Zaman Kaybı (dk/6 ay)	3000	0	-3000
Bıçak Değişimi Kaynaklı Zaman Kaybı (dk/6 ay)	120	10	-110
6 Aylık Toplam Kayıp (adet)	187200	600	-186600
Yıllık Toplam Kayıp (adet)	374400	1200	-373200
Yıllık Maliyet Kaybı (USD)	28080,00	90,00	**-27.990,00**

İşçilik kaybı verisi Tablo III'te gösterilmektedir. Yeni sistemin eskiye göre işçilik kaybının 154 kat daha düşük olduğu ve sadece tek bir makine ile yıllık 2.409 dolarlık bir işçilik kaybının önleneceği görülmektedir. Burada işçilik giderleri Tablo II'de verilen kestamit ve bıçak değişimlerinde harcanan zamana göre belirlenmiş değerlerdir.

Tablo III. Tek bir Makine için İşçilik Kaybı Verisi ve Karşılaştırma Tablosu

	Eski Sistem	Yeni Sistem	Fark (Düşüş)
Operatör Giderleri (TL/6 ay)	2750,00	18,00	-2.732,00
Bakım Personeli Giderleri (TL/6 ay)	3500,00	23,00	-3.477,00
Yönetim Personeli Giderleri (TL/6 ay)	18000,00	116,00	-17.884,00
6 Aylık Toplam Kayıp (TL)	24250,00	157,00	-24.093,00
Yıllık Maliyet Kaybı (TL)	48500,00	314,00	-48.186,00
Yıllık Maliyet Kaybı (USD)	2425,00	15,70	**-2.409,30**

Malzeme kaybı verisi Tablo IV'te gösterilmektedir. Yeni sistemin eskiye göre malzeme kaybının 63 kat daha düşük olduğu ve sadece tek bir makine ile yıllık 12.424 dolarlık bir malzeme kaybının önleneceği görülmektedir. Burada dolar kuru Ocak 2023 itibariyle yaklaşık 20 TL olarak alınarak yıllık maliyet kaybının USD değeri hesaplanmıştır.

Tablo IV. Tek bir Makine için Malzeme Kaybı Verisi ve Karşılaştırma Tablosu

	Eski Sistem	Yeni Sistem	Fark (Düşüş)
Kestamit Satın Alma (USD/6 ay)	36 adet x 137,00	0	-4932,00
Kestamit Tıraşlama (USD/6 ay)	180 adet x 6,00	0	-1080,00
Bıçak (USD/6 ay)	6 adet x 50,00	1 x 100,00	-200,00
6 Aylık Toplam Kayıp (USD)	6312,00	100,00	-6.212,00
Yıllık Maliyet Kaybı (USD)	12624,00	200,00	**-12.424,00**

Enerji kaybı verisi Tablo V'te gösterilmektedir. Yeni sistemin eskiye göre enerji kaybının 11 kat daha düşük olduğu ve sadece tek bir makine ile yıllık 2.450 dolarlık bir enerji kaybının önleneceği görülmektedir.

Tablo V. Tek bir Makine için Enerji Kaybı Verisi ve Karşılaştırma Tablosu

	Eski Sistem	Yeni Sistem	Fark (Düşüş)
Çanta Başına Enerji Tüketimi (TL)	0,00208	0,00019	-0,00189
60 çanta için Enerji Tüketimi (TL)	0,125	0,01158	-0,11342
6 Aylık Toplam (TL)	27000,02	2501,17	-24.498,85
Yıllık Maliyet Kaybı (TL)	54000,04	5002,34	-48.997,71
Yıllık Maliyet Kaybı (USD)	2700,00	250,12	**-2.449,89**

Tüm bu kayıplar toplandığında, yeni sistemin eski sisteme göre 84 kat daha az kayıp verdiği ve yeni sisteme sahip tek bir makina ile yıllık toplam 47.598 dolarlık bir kaybın önleneceği söylenebilir.

III. TARTIŞMA VE SONUÇ

Yapılan çalışmalar ile hedeflendiği üzere kesme bıçağının kullanım süresinin artırıldığı, tamir bakım maliyetlerinin düşürüldüğü, üretim süreçlerinin ve maliyetlerinin iyileştirildiği aynı zamanda enerji sarfiyatının azaltıldığı bir yapı geliştirilmiştir. Mevcut üretim hattına göre hammadde ve enerji verimliliği artmış, üretim kapasitesi arttırılarak makineyi kullanacak işletmelerin karlılığında artış sağlanmıştır. Ayrıca bu uygulama çevreyi de olumlu anlamda etkilemektedir.

Geliştirilen sistemin eski sisteme göre yaklaşık 84 kat daha az kayıp verdiği tespit edilmiştir. Bu kapsamda 20 makinaya sahip bir firma için yıllık kazancın 950.000 dolar seviyesinde olacağı öngörülmektedir.

Geliştirilen yerli kesme ünitesi ile yurt içindeki döviz kaybı ve ithalat azaltılıp cari açığın azalmasına katkı sağlanacaktır. Ardından yurt dışına ihracat yapabilecek potansiyele sahip ünitenin pazarlama faaliyetleri yapılacak, uluslararası arenada faaliyet gösterilecektir.

KAYNAKÇA

[1] Boz, S. ve Öndoğan, Z. (2011). An investigation on the cutting parameters for various types of fabric. Tekstil ve Konfeksiyon, 1(2012), 52-57.

[2] Cabak, B. (2018). Tekstil fabrikasında enerji verimliliği uygulamaları. Trakya Üniversitesi.

[3] Yavuz, M. (2019). Plastik ambalaj sektöründe endüstriyel kesici takım optimizasyonu. Sakarya Uygulamalı Bilimler Üniversitesi.

[4] Üstünışık, N. Z. (2014). Türkiye imalat sanayiinde yeşil imalatın uygulanabilirliği: makina imalat sanayii örneği. İktisadi Sektörler ve Koordinasyon Genel Müdürlüğü.

[5] Liu, P., Liu, F. ve Qiu, H. (2017). A novel approach for acquiring the real-time energy efficiency of machine tools. Energy, 121(2017), 524-532.

[6] Uylukçuoğlu, Ö. E. (2009). Otomotiv sanayinde enerji verimliliği ve enerji tasarruf olanaklarının belirlenmesi. İstanbul Teknik Üniversitesi.

[7] Dornfeld, D. A. (2014). Moving towards green and sustainable manufacturing. International Journal Of Precision Engineering And Manufacturing-Green Technology, 63(2014), 63-66.

[8] Nayak, R. ve Padhye, R. (2017). Automation in garment manufacturing. the textile ınstitute book series. Elsevier.

[9] Wang, L., Zhang, S., Gao, W. M., Wang, X. (2007). FEM Analysis of Knife Penetration through Woven Fabrics. CMES-Computer Modeling in Engineering & Sciences, 20(1), 11–20.

Sesaltı Rüzgar Tünelinde Naca0015 Kanat Profilinin Kuvvet Ve Akış Görüntüleme Yöntemi ile Analizi

Analysis of Naca0015 Airfoil in Subsonic Wind Tunnel by Force and Flow Imaging Method

Samet Giray TUNCA[*,1], Mustafa Arif ÖZGÜR[2]

[*]sgiray.tunca@dpu.edu.tr, ORCID: 0000-0002-7632-8745
[1]*Mühendislik Fakültesi Makine Mühendisliği, Kütahya Dumlupınar Üniversitesi, Kütahya, Türkiye*
[2]*Mühendislik Fakültesi Makine Mühendisliği, Kütahya Dumlupınar Üniversitesi, Kütahya, Türkiye*

Özet: Aerodinamik ölçümler kanat profillerinin karakteristik yapılarını belirlemek için yapılır. Bu ölçümler kanadın yapısını optimize etmek için kullanılır. Kanat profillerinin kalkış, uçuş ve iniş durumlarındaki durumunu incelemek için kaldırma katsayısı değerleri göz önünde bulundurulur.

Bu çalışmada kanat aerodinamiği çalışması ile sesaltı rüzgar tünelinin akış doğrulama çalışması yapılmıştır. Sesaltı rüzgar tünelinde NACA0015 kanat profili incelenmiştir. Test odasına kuvvet sensörü yerleştirilerek kanat profili analizi yapılmıştır. Sesaltı rüzgar tünelinde bal peteği, akış fileleri, daralma konisi, test bölmesi, difüzör ve emiş motoru bölümleri bulunmaktadır. Test bölmesi 50x50 cm olan sesaltı rüzgar tünelinde kullanılan model 3d yazıcı yöntemi ile imal edilmiştir. Kaldırma kuvveti ölçümleri $6x10^4$, $8x10^4$ ve $10x10^4$ Reynolds sayısı (Re) değerlerinde çalışılmıştır. Ölçümler hücum açısının 00 den başlayarak bir derecelik artışlarla analiz edilmiştir. Konumlamanın test odasının içinde olacak şekilde farklı Re sayılarında yapılan ölçümler neticesinde yaklaşık olarak 10 ve 11 derecelik açılarda tutunma kaybının başladığı gözlemlenmiştir. Kaldırma kuvveti katsayısında bağlantı elemanları nedeni ile kayıplar olduğu tespit edilmiştir. Kayıplar bağlantı iyileştirme çalışmaları ile en aza indirilmelidir.

Direnç teli ile yapılan akış görüntüleme sistemi rüzgar tüneli test bölmesinde duman akışı oluşturulmuştur ve akış ayrışması bu yöntem ile görüntülenmiştir. Akış görüntüleme deneyi 6 m/s hızda $6x10^4$ Re sayısında gerçekleştirilmiştir. Yüksek Re sayılarında akış görüntüleme deneylerinden sonuç almak için Re formülündeki değişkenleri düzenlemek gerekmektedir. Çalışılan kanadın kord uzunluğu değiştirildiğinde Re sayısı da değişecektir.

Yapılan çalışmalar neticesinde kaldırma kuvveti değerleri ve akış görüntüleme ile elde edilen duman görüntüsünde stall derecelerinin birbiri ile örtüştüğü anlaşılmıştır. Bu da sesaltı rüzgar tünelinde çalışılan Re sayılarında akışın laminer olduğu belirlenmiştir.

Anahtar Kelimeler: *Rüzgar tüneli, stall, kanat profili, kaldırma katsayısı, akış görüntüleme*

Abstract Aerodynamic measurements are made to determine the characteristic structures of airfoils. It is used to optimize the airfoil of these measurements. Continuous values are taken into account in order to understand the indicators of the wing profiles in take-off, flight and exit states.

With this wing aerodynamic study, the flow study of the subsonic wind tunnel was carried out. NACA0015 airfoil in subsonic wind tunnel. Airfoil analysis was performed by placing the test force sensor. The subsonic wind tunnel contains honeycomb, flow files, diffusion cone, test chamber, diffuser and suction engine sections. The model used in the 50x50 cm subsonic wind

tunnel in the test room was manufactured with the 3d printer method. Lifting force measurements are available at $6x10^4$, $8x10^4$, and $10x10^4$ Reynolds (Re). Measurements were analyzed in one-degree increments starting from 0^0 of the angle of attack. As a result of the measurements made at different Re numbers with the positioning inside the test room, it was observed that the stall started at approximately 10 and 11 degrees angles. Losses have been determined due to the fasteners in the structure of the lifting force. Losses should be minimized by connection work.
Drain monitoring system made with resistance wire smoke distribution system in wind tunnel test chamber and flow separation visualized by this method. The imaging flow experiment was performed at 6x104 re-presentations at a speed of 6 m/s. To work at high Re numbers, the variables in the Re formula need to be edited. When the cord length of the wing is changed, Re-number will also change.
As a result of the operations, it was understood that the lift force values and the stall degrees in the smoke image overlap with each other. This indicates that the flow is laminar in the Re numbers studied in the subsonic wind tunnel.

Keywords: *Wind tunnel, stall, airfoil, lift coefficient, flow display*

I. GİRİŞ

Aerodinamik ölçümler kanat profillerinin karakteristik yapılarını belirlemek için yapılır. Bu ölçümler kanadın yapısını optimize etmek için kullanılır. Kanat profillerinin kalkış, uçuş ve iniş durumlarındaki durumunu incelemek için kaldırma katsayısı değerleri göz önünde bulundurulur. Farklı açılarda yapılan çalışmalar ile karşılaştırmalar yapılarak kanat profil yapı değerlendirilir. Literatürde kanat profillerinin incelendiği bir çok aerodinamik ölçümler yapılan çalışmalar bulunmaktadır.
Duman teli ile akış görselleştirme deneyi rüzgar tünellerinde yaygın olarak kullanılan basit ve verimli bir yöntemdir[1,2]. Bu sistemde bir duman kaynağı (kanat önüne gerilmiş bir tel yardımıyla elde edilen dumandan veya duman jeneratörü) kullanılarak duman çizgilerinin yani çıkış çizgilerinin hareketi ile akış görsel olarak karakterize edilir. Dikkat edilmesi gereken en önemli husus duman kaynağının akışı bozmayacak yapıda olması gerekmektedir. Duman telinin akışa engel oluşturacak kalınlıkta olması akışımızın türbülanslı olmasına neden olacaktır[3,4,5].
Önen B. yaptığı çalışmada NACA 4412 kanat profilinin çeşitli hücum açılarında elde ettiği kaldırma ve sürükleme katsayısı sonuçlarını literatürle karşılaştırılmıştır. [6]. Kaya M. Tarafından yapılan çalışmada elde edilen sonuçların NACA gibi birçok araştırma birimi tarafından gerçekleştirilen rüzgâr tüneli deney sonuçları ile örtüştüğü tespit edildi [7]. Miklosevic düşük hızlı bir rüzgar tünelinde aerodinamik kuvvet hesaplamalarını 505.000 ve 520.000 aralığındaki Reynolds sayılarında ve -2˚ ile 20˚ aralığında değişen hücum açılarında çalışmıştır.[8].
CHANGE projesi ile kanat profilini farklı uçuş fazlarında sürekli olarak aerodinamik verimlilik sağlayabilmektir. [9].
H. Hamdani ve M. Sun (2000) NACA 0012 kanat profili ile yaptıkları çalışma gösteriyor ki düşük reynolds sayılarında kanat profilinin bir hızdan diğer bir hıza aniden hızlanması büyük aerodinamik kuvvetleri doğmasına sebep olduğunu göstermiştir [10].

M. A. Özdemir ve S. Onbaşıoğlu (2004), 0, 2, 4, 6 ve 8° lik hücum açılarında yaptıkları çalışmayı NACA (2003) tarafından rüzgar tünelleri kullanılarak elde edilen deneysel verilerle karşılaştırmışlar [11].

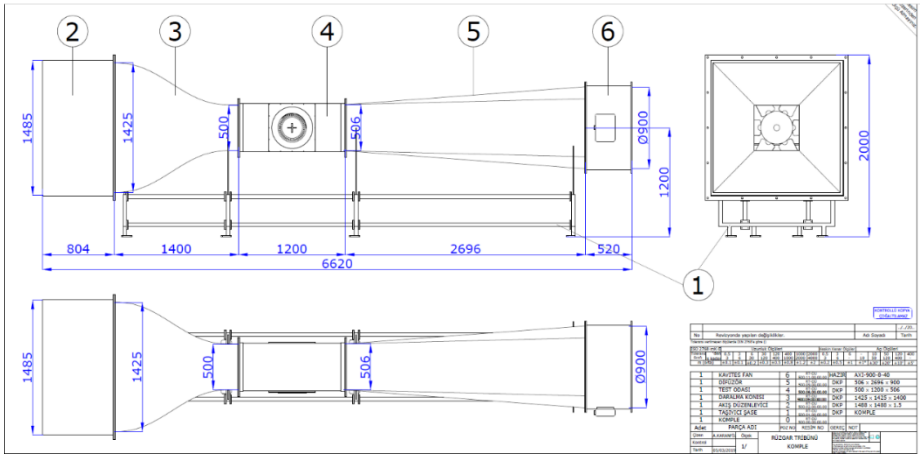
Göv İ., Doğru M.H. ve Korkmaz Ü çalışmalarında NACA 4412 kanat profili üzerinde çalışarak iki farklı kanat profili daha elde etmişlerdir. Çalışmalarında üç kanat yapısı için 0° ile 23° arasındaki hücum açılarında aerodinamik performans analizleri yapılmışlardır [12].
Kazemi ve diğerleri (Kazemi vd., 2016) ürettikleri kanat yapısının aerodinamik performanslarını sayısal ve deneysel olarak incelemişlerdir. Duman görüntüleme deneyleri, kanat yapısı üzerindeki ayrılma ve durma noktalarını belirlemek için küçük boyutlu bir rüzgâr tünelinde gerçekleştirilmiştir. Ürettikleri profil yapısına temel olarak kabul ettikleri NACA0021 kanat yapısına kıyasla kaldırma/sürükleme oranının yaklaşık olarak 2,9 kat yükseldiğini söylemişlerdir [3].

Tanürün H. E., Ata İ., Canlı M. E. ve Acır A çalışmalarında NACA0018 kanat yapısının aerodinamik performansı deneysel sonuçlarını yeni tasarladıkları iki kanat yapısı ile karşılaştırmışlardır. Yeni tasarlanan AR1 ve AR2 kanat yapılarının aerodinamik deneysel sonuçlarında CL değerlerinde %0,41 ve %2,71 oranında iyileşme sağlanmıştır[13].
Rubel I. ve arkadaşları yaptıkları çalışmada amaçları, deneysel ve sayısal yöntem için NACA 0015 kanat profilinin aerodinamik özelliklerinin sapmasını ve doğrulanmasını yapmaktadır. Reynolds sayı kaldırma katsayısının artmasıyla biraz artar ve belli bir noktadan sonra azalır. Azaldığı kısımda kanat profili üzerinde büyük negatif basınç oluşmaktadır. [14].

Yaptığımız çalışma ortam sıcaklığı 20^0C, havanın kinematik viskozitesi 1.5111 e^{-5} m^2/s kabul edilmiş ve olarak kanat profili kord uzunluğu 0,15 m.'dir. Testler 6 x 10^4 , 8 x 10^4 ve 10 x 10^4 Re sayılarında gerçekleştirilmiştir.

II. SİSTEMİN YAPISI VE DENEY ÇALIŞMALARI

Kütahya Dumlupınar Üniversitesi Makine Mühendisliği Laboratuvarında bulunan Sesaltı rüzgar tüneli açık sistem bir rüzgar tüneli olup 50x50 cm test bölmesine sahiptir. Çalışmamızda kaldırma kuvveti değerleri kuvvet cihazının test bölmesinin içine yerleştirilerek elde edilmiştir. Sistemimiz bal peteği, elekler, kollektör, test odası ve difüzör bölümlerinden oluşmaktadır.



Şekil.1. Sesaltı Rüzgar Tüneli Tasarımı



Şekil. 2. Sesaltı Rüzgar Tüneli

Sesaltı rüzgar tüneli kuvvet balans sistemi ile yapılan kaldırma kuvveti ölçümlerinde NACA0015 kanat profili kullanıldı. Kanat profili solidworks programında tasarımı yapılarak 3d yazıcıda test edilecek kanat yapısı elde edilmiştir. Kuvvet sistemi ile kanat profili arasında bağlantı elemanları da 3d yazıcı ile elde edilmiştir. Titreşim oluşmasından dolayı metal bağlantı elemanı da ölçümlerde denenmiştir.



Şekil. 3. Test bölmesinde kuvvet ölçüm cihazına bağlı olan 3d yöntemi ile baskısı alınan NACA0015 kanat profili

Şekil 3'te görüldüğü gibi rüzgar tüneli test bölmesinde kaldırma kuvveti değerleri alınmıştır. Çalışmalar 6, 8 ve 10 m/s hızlarda, 0^0 - 12^0 derece aralığında 10'lik artışlar yapılarak gerçekleştirilmiştir. Testlerde kullanılan NACA0015 kanat profili kord uzunluğu 150 mm. olarak imal edilmiştir.

Duman teli ile akış görüntüleme yöntemi kullanılmıştır. Düzenekte kullanılan direnç teline 30 V gerilim verilerek tel üzerine damlatılan parafinin yanması sağlanmıştır. Yanma sonucunda ortaya çıkan beyaz duman rüzgar tünelinin akış yönünde hareket etmiş ve kanat üzerinde hız sınır tabaka görüntüsü vermiştir.

A. Aerodinamik Yapının Matematiksel Modeli

Sesaltı terimi ise Mach sayısı ile ifade edilmektedir. Mach sayısı, akışkanlar mekaniğinde hareket halindeki bir kütlenin hızının, kütlenin bulunduğu şartlardaki ses hızına oranıdır. V (m/s) hareket halinde kütlenin hızını, c (m/s) ses hızını ifade etmektedir.

$$Ma=V/c$$

V (m/s) hareket halinde kütlenin hızını, c (m/s) ses hızını ifade etmektedir. Mach sayısı 0,8 değerinden küçük olduğu durumlar sesaltı olarak adlandırılır.

Kaldırma kuvveti akışa dik yönde cisme etkimektedir.

$$FL=CL\ 1/2\ \rho AV^2$$

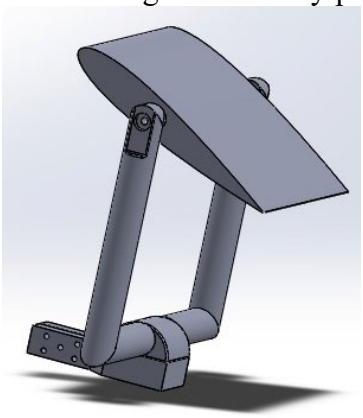
CL boyutsuz sürükleme kuvveti katsayısını, ρ (kg/m^3) havanın yoğunluğunu, A (m2) rüzgarın kanat üzerindeki etki alanını, V (m/s) rüzgar hızını ifade etmektedir.
Akışkanlar mekaniğinde Reynolds sayısı (Re), bir akışkanın, atalet kuvvetlerinin (v,d), viskozite kuvvetlerine (μ/ρ) olan oranıdır. Çalışmamızda üç farklı reynolds sayısında testler yapılmıştır.

$$Re=\frac{(v.d.\rho)}{\mu}$$

Kanat profilleri aerodinamik kuvvetler açısından incelendiğinde karşımıza stall kavramı çıkar. Kanat profili kaldırma kuvveti değerleri belli bir açıya kadar yükseldikten sonra kanadın üst yüzeyindeki sınır tabaka ayrılmaları ile değerler düşüşe geçer. Bu durum stall ile sonuçlanır.

B. Test Bölmesinin İçinde Alt Kısımdan Kuvvet Sensörü Bağlantısı

Bu çalışmada uygulanan yöntemde kuvvet cihazı test bölmesinin iç tabanına sabitlenmiştir. Şekil 4'de görüldüğü gibi kanat cihaz bağlantı tasarımı yapılmıştır. Bu yöntemle elde edilen kaldırma kuvveti katsayı verileri ve stall Tablo 1'de verilmiştir. Değerlerin literatür çalışmaları ile örtüşmesine rağmen kaldırma kuvveti değerlerinde kayıplar olduğu tespit edilmiştir.



Şekil 4. Kanat profilinin altına konumlandırılmış kuvvet cihazı, kanat modeli ve bağlantısı

C. Akış Görüntüleme Sistemi

Rüzgar tüneli test bölmesine akışın geldiği tarafta direnç üst ve alt noktalara sabitlenmiş bir direnç teli bağlanmıştır. Direnç teline üst kısımdan sıvı parafin damlatılmıştır. Sıvı parafin tel yüzeyini kapladığı anlaşıldığında güç kaynağından yaklaşık 30 volt elektrik gerilimi verilmiş ve tel yüzeyindeki parafin telin ısınması ile yanarak beyaz bir duman oluşturmuştur. Rüzgar tünelinin akış hızı yönünde duman ilerleyerek kanat profili üzerinde bir sınır tabaka meydana getirmiştir.
Rüzgar hızı 6 m/s ayarlanmıştır. Re sayısı yaklaşık 6 x 10^4 'te akış görüntüleme deneyi gerçekleştirilmiştir.

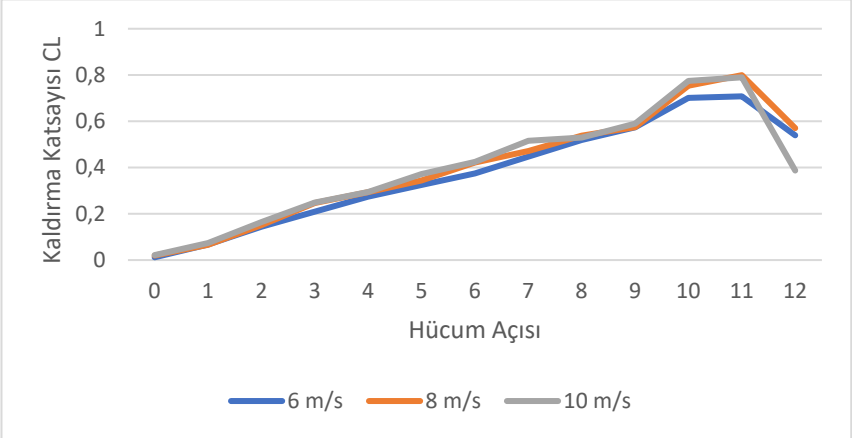
III. SONUÇLAR

Rüzgar tüneli test odası içinde modelin altından yapılan bağlantıda Şekil 5 de görüldüğü gibi stall tespit edilmiştir. Kaldırma kuvveti değerlerinde kayıplar olduğu literatür ile karşılaştırıldığında ortaya çıkmaktadır.
Tablo 1'de kaldırma katsayısı değerleri 0'dan 12^0 derecelik hücum açılarına kadar verilmiştir. Bu ölçümler 6,8 ve 10 m/s'lik hızlarda yapılmıştır.

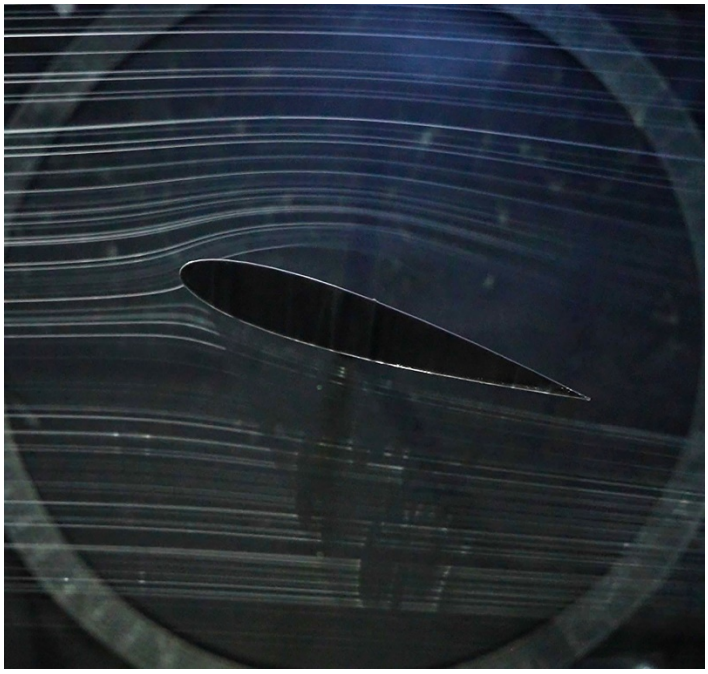
TABLO.1.
BELiRLENEN HIZLARDA KALDIRMA KATSAYISI (CL) DEĞERLERi

Kaldırma Katsayısı (CL)		Hız (m/s)		
		6	8	10
Hücum Açısı	0	0,009213	0,015078	0,016588
	1	0,051821	0,050776	0,056643
	2	0,110978	0,116389	0,126507
	3	0,160925	0,189557	0,191343
	4	0,210872	0,225804	0,22618
	5	0,249553	0,264769	0,286223
	6	0,288234	0,324067	0,326265
	7	0,343757	0,362659	0,396826
	8	0,39928	0,413702	0,407386
	9	0,441421	0,44204	0,453396
	10	0,539058	0,579669	0,595558
	11	0,544485	0,614894	0,607638
	12	0,414965	0,438963	0,297638

Şekil 6'da 10^0 'ye kadar lineer bir artış olduğu ve bu dereceden sonra kanat profilinin stallna maruz kaldığı görülmektedir. NACA0015 kanat profili ile yapılan çalışmalar incelendiğinde elde ettiğimiz katsayı değerlerinin %10 gibi bir oranda düşük olduğu tespit edilmiştir. Bu durumun bağlantı noktalarına kayan yüklerden kaynaklandığı düşünülmektedir.
Yapılan akış görüntüleme deneylerinde 10^0 ve 11^0 derece aralıklarında stall görülmüştür. Duman testlerindeki stall açısı ile kaldırma kuvveti testlerindeki stall açılarının örtüştüğü anlaşılmıştır. Bu deneyler neticesinde rüzgar tünelinin çalışılan hızlardaki akışının laminer bir akış olduğu belirlenmiştir.



Şekil 6. Kaldırma katsayısı (CL) ve Hücum açısı grafiği



Şekil. 7. Stall'un gerçekleştiği 10^0-11^0 derece aralığında 6 m/s hızda duman görüntüsü

IV.TARTIŞMALAR

Kaldırma katsayısı değerleri için kullanılan bağlantı yöntemin çalışılması gerektiği görülmektedir. Elde edilen sonuç üzerinden çalışmalar devam edilerek iyileştirme çalışmalarının gerekliliği tespit edilmiştir. Kuvvet kayıpları yeni bağlantı tasarımları ile giderilebilir.

Duman görüntüleme (akış görüntüleme) düzeneği iyileştirilerek daha ideal görüntüler elde edilebilir. 6 m/s hızların üzerinde duman görüntüsü almak mevcut sistemde zor olmasından dolayı, daha yoğun bir duman elde edilebilecek bir sistem tasarım çalışması yapılmalıdır. Kord uzunluğu değiştirilerek yüksek Re sayılarında çalışmaların yapılabileceği unutulmamalıdır.

TEŞEKKÜR

Bu çalışma, Dumlupınar Üniversitesi tarafından 2023 - 18 proje numarası ile desteklenmiştir.

KAYNAKÇA

[1] Kurç Ö., Uzol O., "Uzun Açıklıklı Köprü Kesitlerinin Rüzgar Altındaki Davranışının Analitik ve Deneysel İncelenmesi", Proje No: 110M799 Ankara (2012)

[2] Koca M.S.," Su Tünellerinde Model Hareket Kontrolü Ve Senkron Aerodinamik Kuvvet Ölçüm Sistemi Tasarımı", Başkent Üniversitesi Fen Bilimleri Ens., Yüksek Lisans Tezi (2019)

[3] Kazemi, S. A., Nili-Ahmadabadi, M., Sedaghat, A., Saghafian, M. (2016). Aerodynamic performance of a circulating airfoil section for Magnus systems via numerical simulation and flow visualization. Energy, 104, 1-15. (2016).

[4] Pope, A., Harper, J.J.,"Low-Speed Wind Tunnel Testing" Jhon Wiley & Soons, Inc, New York, USA (1984)

[5] Genç M., Serdar, M.,"Düz Flapli NACA0012 Kanat Profilinin Aerodinamik Performansının İncelenmesi", J. Of Thermal Science and Technology, 4: 271-285 (2008)

[6] Önen B.,"Bir Ses Altı Rüzgar Tünelinin Performansının Ve Bazı Modeller Üzerindeki Akışın Deneysel Ve Bilgisayar Destekli Analizi", Kocaeli Üniversitesi * Fen Bilimleri Enstitüsü, Yüksek Lisans Tezi, Kocaeli (2011)

[7] Kaya M., "Aırfoıl Yapının Yakın Çevresindeki Hız Ve Basınç Dağılımının Hesaplamalı Akışkanlar Dinamiği Yöntemi İle İncelenmesi", EÜFBED - Fen Bilimleri Enstitüsü Dergisi Cilt-Sayı: 4-1 59-69, (2011)

[8] Miklosovic D.S., Murray M.M., Howle L.E., Fish F.E., Leading-edge tubercles delay stall on humpback whale (Megaptera novaeangliae) flippers. Physics of Fluids, 2004, 16(5):L39-L42. DOI: 10.1063/1.1688341, (2004)

[9] Aslan P., Kalkan U., Tıraş H. Ve Diğerleri;"Bir Hibrit Firar Kenarı Kontrol Yüzeyinin Tasarımı Ve Analizi" TMMOB Makina Mühendisleri Odası VIII. Ulusal Uçak, Havacılık ve Uzay Mühendisliği Kurultayı 22-23 Mayıs 2015 / ESKİŞEHİR

[10] Hamdani, H. ve Sun, M., Aerodynamic Forces and Flow Structures of an Airfoil in Some Unsteady Motions at Small Reynolds Number, Acta Mechanica, 145, 173-187 (2000)

[11] Özdemir, M.A., Onbaşıoğlu, S., F-4 Phantom II Uçağının Etrafındaki Akışın H.A.D. Analizi Kısım 1: Kanat Kök Profili NACA 0006, Havacılık ve Uzay Teknolojileri Dergisi, 1, 4, 1-6, (2004)

[12] Göv İ., Doğru M.H. ve Korkmaz Ü.,"Improvement of the aerodynamic performance of NACA 4412 using the adjustable airfoil profile during the flight", Journal of the Faculty of Engineering and Architecture of Gazi University, (2019)

[13] Tanürün H. E., Ata İ., Canlı M. E. ve Acır A., "Farklı açıklık oranlarındaki NACA-0018 rüzgâr türbini kanat modeli performansının sayısal ve deneysel incelenmesi", Politeknik Dergisi, 23(2): 371-381, (2020)

[14] Rubel R.I , Kamal U, Zahidul I, M.D. Rokunuzzaman "Numerical and Experimental Investigation of Aerodynamics Characteristics of NACA 0015 Aerofoil", Internatıonal Journal Of Engıneerıng Technologıes, Vol 2 No 4 2016

Internet of Things Technology Combination with Smart Cities - Solution to Public Transportation

Deniz Dikbiyik

denizdikbiyik@gmail.com, ORCID: 0009-0008-5539-9182
Software Engineering, Bogazici University, Istanbul, Turkey

Abstract: The growth of the needs and the rise of technology brings beneficial implications to our lives in many areas. Especially smart city and Internet of Things concepts help us make the daily life easier with smart homes, tourism management, health check, environmental management, disaster mitigation and transportation management. There is still lack of studies to improve these areas. It can be seen in the literature that the studies about smart transportation are not sufficient or the existing projects are not applied by municipalities efficiently. Citizens complain about the traffic congestions and crowded public transportations. There are vehicle to vehicle or vehicle to road systems, car distribution applications, light synchronization, smart tickets, transit bus systems, and GPS-based buses to solve this problem. Our study suggests a different solution with the usage of transportation application system that can provide better route suggestion to the passengers. Users can register to the application, search according to their route and apply for the best-time vehicle with few people. Public transport ticket management and schedule of the vehicles can also be controlled there. Smart sensors can be integrated into the vehicles to detect the number of passengers on board so that the best route with the best time and the least number of passengers can be shown to the users. Technical infrastructure, middleware, development, microservice and network technologies are crucial for this implementation. Because the security of the application is also very important, big data and cloud management integrations are also recommended. The explanation of the need and the technological implementations are explained in this article. Our public transportation management system can be applied by municipalities, and further research can be done in future studies to improve the usage.

Keywords: *Transportation Application, Vehicle Sensors, Infrastructure Layer, Middleware, Security*

I. INTRODUCTION

The population of the world is growing, so the need for technological solutions is increasing. Many different devices are being used such as sensors, smart products, and digital devices, but they are mainly connected to each other through the Internet which brings the Internet of Things (IoT) concept [1]. The areas where these technological solutions are used are a wide range. Transportation, traffic management, buildings and home controls, energy consumption control, and pollution management have been the focuses of IoT, and smart city works for many years. Many private and public companies improve their businesses in these areas. Provincial municipalities especially try to solve the problems with the help of IoT-based projects. With this idea, the smart city concept with the implementation of IoT is becoming more important in life [2]. The smart city is an area where the existing platforms and tools are improved to reach a higher qualified and sustainable life of city operations. Information and Communication Technology (ICT) provides this combination of smart technologies with traditional city systems. They also argue that this occurs with the help of IoT and Big Data (BD) [3].

II. FIELDS WHERE SMART CITY TECHNOLOGIES ARE APPLIED

The smart city concept includes many different areas as explained in the introduction. There are still some gaps that need to be studied. Some example areas and their implementations are listed below. The gaps in the area are explained later.

A. Smart Homes

Home control can be achieved easily by smart city applications. Thanks to sensor implementations, waste from smart homes can be detected easily [4]. On the other hand, most of the devices that are used at home are intelligent and sensor-based machines, so life at home is getting more efficient and it can even be managed from a distant location. The people who are visiting the home can also be detected and classified with the help of smart city and IoT technologies. This detection provides proper services to individuals [5].

B. Tourism

Intelligent applications enable visitors to visit touristic areas while also obtaining information about them [5].

C. Health

Many people prefer to have smart watches especially to check their health reports. After doing exercise, they check the results from health control applications. Therefore, thanks to the sensors connected to mobile devices and providing personal health management, data collection is easier [5].

D. Environmental Management

In this section, various areas related to environmental control can be listed. For example, weather forecasts are provided by sensors in smart cities [4]. Consequently, temperature, precipitation probability, and speed of winds can be analyzed before they occur, and this makes efficient usage for their potential. Besides this, the greenhouse gases dispersion in the air can be detected with sensors in different areas of the city, then any unhealthy condition can be sent as information to the municipality as an alarm. Smart energy is another part of the environmental benefits of smart cities, so energy usage can be controlled from a distance via mobile phone applications which switch inefficient devices off [5].

E. Disaster Management

Disaster prediction and mitigation are also other important topics that municipalities focus on. Although earthquakes cannot be predicted exactly, emergency response to fire can be provided quickly by sensors in those areas. For this purpose, satellites are used to detect heat levels and call the firestation immediately [5].

F. Transportation and Smart Parking

Especially crowded cities face traffic problems very often. Forecasting applications make people's lives easier with the data collected via sensors. Besides that, the parking problem is also a time-consuming obstacle for people who live in crowded cities. With data collection systems connected to parking lots, and arrival data collection from the applications, parking lot areas can be controlled to provide drivers with a parking area when they arrive. This can be referred as car parking appointment system [4].

III. WHAT IS LACKING FOR CROWDED CITIES?

Even though the transportation systems are being improved, there are many other problems in that area. Municipality workers as well as city and region planners highlight that crowded

public transportation vehicles are a big problem and there is a need to solve it urgently. The government offers passengers to use public transport to solve traffic problems, but this creates another problem of crowded public transportation [6]. There are some studies on smart transportation systems and some also call them modern transportation systems. These studies offer many solutions to other parts of transportation such as dynamic passenger transport. There are modern applications that make passengers meet and continue the road together. BlaBlaCar is one of these examples for European countries and the other may be GoOpti from Slovenia. These applications make the vehicles take users from where they will start and to where they want to go. Even though this may decrease the number of people who use public transportation, it is not enough to solve this huge issue [7].

There is another study in China for smart transportation systems. While focusing on the vehicle-to-vehicle and vehicle-to-road systems with wireless technology, they plan to control the road network. With this study, they start managing road control, but they succeed in only emergency situations. As a result, when an accident occurs, they can reach the area easily [8].

As we basically know in real life, there is also a virtual traffic control system that provides information to the navigation applications. As an example, Google Maps uses this data to show the best option to its users. This system gets the distribution of cars data from navigation users and offers routes to other users accordingly. On the other hand, even though this virtual system has options for public transportation vehicles, it does not use the data efficiently for that part. It only explains the delays and if the vehicles are crowded but does not suggest a solution to that [7].

There is one more area that is traffic light synchronization, but again this is for all traffic on the road, not only for public transport [7].

The most relevant study to this problematic area comes with smart solutions including three components which are smart tickets, transit bus systems, and GPS-based buses. Their system is very similar to the transportation ticket system in Istanbul. The smart ticket system is like an Istanbul Card which can be loaded from an ATM and collects data to the municipality's database to be analyzed for further transportation system plans. The transit bus solution is also like Metrobus in Istanbul. In this system, if there is no passenger to get off the bus at a station, it continues the way without stopping. The smart GPS system is again the collection of time schedules and station points data. With the result of this collected data, Istanbul Electric Tram and Tunnel Operations (IETT) refreshes the information coming from the buses on their website and mobile app, so the users can predict how much time they will wait for the bus. Analyzing the deficiencies of solutions, because GPS-based buses are not connected to databases properly, the passengers wait at the stations with time-wasting, or they miss the bus. Transit buses are not working properly because usually there are too many passengers to get off at all the different stations. Smart ticket data is also analyzed and used later, but it can be used for the time it is taken [6].

IV. SOLUTION PROPOSAL AND BENEFITS

The solutions mentioned above can be improved with IoT and BD technologies. Firstly, the data taken from smart tickets can be synchronized with mobile applications on which users can give input about where they will get on public transport and where they will go. The system can collect all users' data together and manage existing public transportation vehicles' schedules accordingly. As a result, passengers can go to the station at the time offered to them and find the most convenient vehicle. As part of this solution, because passengers will be distributed accordingly, the vehicles will not be getting crowded. Most of the time, the two or three vehicles coming in a row are like the first one is too crowded, then the others are more empty. This is a time-wasting problem, but because users cannot be sure if an empty vehicle will come soon, they get on the one coming first even if it is crowded. This scheduling system will overcome this problem too. Secondly, some sensors can be embedded into the Metrobus vehicles as an example. Those will be both below the seats and on the ground of the bus. These

sensors will detect if the seats are full or empty and if there are many people standing on the bus. Thus, these data will be collected and shown in the app mentioned in the first solution. Eventually, either the municipality or passengers can reach the updated information about the crowded vehicles.

V. THE TECHNOLOGY AND CHALLENGES BEHIND THE SYSTEM

Some systems are already studied with the idea of IoT in the transportation area. One suggests the RERUM framework which is applicable to both smart transportation and environmental monitoring. They also claim to use this framework for traffic prediction with space and time conditions, so it has usage similarities with our solution. The difference is that the RERUM framework plans to combine sensors with mobile phone GPS. It is not compatible with our study because we need to collect the data from sensors on vehicles. The system cannot be sure if the vehicle is full of people without mobile phones [9].

In order to have a resilient system, it is suggested to have three layers which are infrastructure, middleware, and services. Our transportation sensor system should include these layers. Having sliced layers provides separated modules which are more reliable. In the cloud edge, including IoT gateways and services is important for critical applications. Many studies in the area suggest having such layers [10].

VI. INFRASTRUCTURE

This can be counted as the first or lowest layer for the IoT architecture. The infrastructure layer is comprised of real devices in our environment to integrate into the structure. These devices can send data to the system as they work like sensors. On the other hand, they also have limitations. To overcome their performance limitation, IoT gateways can be implemented [10]. Infrastructure devices can also be counted as monitoring, augmented reality using near-field communication, and environmental sensing tools. Gateways can be used here, but this time not for performance. Using gateways to connect the devices over the environment can be efficient. The infrastructure part can also include operational implementation. Hence, as the devices are connected in this layer, they can verify authentication, sending data between each other [11].

A. IoT Gateways

A routing protocol should be used to connect the devices with IoT gateways. In this idea, there are multiple paths to provide a resilient solution [10]. These IoT gateways are the programmable areas to provide more, and complex solutions and they are the network components. These devices can be embedded and integrated into the system as a computer [11].

VII. MIDDLEWARE AND DEVELOPMENT

Generally, the IoT framework is explained with two main slices which are infrastructure and services, but combining them with middleware makes them communicate properly, which affects the system to work more efficiently. The heterogeneity manager, communication manager, virtualized device manager, resilience manager, data collection and diffusion and knowledge database, and IoT service manager can be counted in the middleware layer of the IoT architecture. The heterogeneity manager is utilized for the standardization of communication, so each device mentioned previously is combined with this part to be converted into a common understandable language. For this conversion, cloud technology is useful to collect data in one place. There are also open-source projects in this area. Even if the heterogeneity manager is used to convert the devices' language, a communication manager is needed to transfer the information between them. This part works with four different areas to be compatible with different types of devices. Virtualized device manager is for managing all

connected devices. Operations such as name resolution, discovery and location, and placement and migration are provided by this part. All these parts are also useful for source management and consumption. Therefore, for an efficient and high-performance system, usage of all of them is highly recommended. On the other hand, having reliable systems is as important as how we manage them. Firstly, the main property of middleware is monitoring, so a resilience manager is the focus of it. To be able to protect the system and recover it when an error or a disaster occurs, monitoring and logging are beneficial components. Data is collected from the devices which are combined and managed by the areas explained above, but it also needs to be stored. Thus, data collection and diffusion as well as knowledge databases are crucial parts of a system as our architecture. Finally, the IoT service manager in the IoT middleware layer controls programmability. A system should have all the necessary components, but only coding and building a logical algorithm can make the architecture work properly. IoT services will be explained later in detail, but now big data and cloud integration will be introduced to show how the problem of large data can be solved [10].

A. Big Data and Cloud Integration

Cloud computing is becoming more popular these days because the storage capacities of everyday devices are not enough to collect all needed data and keep them in the devices. As we have sensors that provide a huge amount of data, our system needs a big data management system integration. Therefore, some offered softwares such as Cosm, or IDAS can be integrated. They check the storage frequently and are compatible with different or new types of devices. Generally, Amazon services and Microsoft Azure are preferred to work in such cloud areas because they are reliable and user-friendly. One of these cloud systems can be integrated with our architecture [11].

VIII. SERVICES

The smart city concept is mostly focused on this part because all the systems in smart areas can be counted as services to work in IoT architecture. Firstly, monitoring services are useful here. These services are mentioned before, but that time was not about working as sensors. Those monitoring systems were for performance and resource management. Now, to gather the data from sensors, monitoring services can be used. One example is environment monitoring which is put in the lightning systems. To analyze pollution as an example, they are also embedded to the municipality vehicles. This time, they can be integrated to analyze how crowded the vehicle is, so an already used service is a chance for our system to utilize with our purpose. Garden monitoring services are the other types which are for collecting a gardens' parameters. They are integrated with underground implementation. Thus, we need an underground extension to check the number of people in the station not for vehicles but for the stations. Participatory sensing service works for GPS data gathering, so the third recommendation for public transportation control structure can be participatory sensing. This service sends notifications and can be combined with an application in which passengers will be registered and directed to the possible transportation [11].

IX. MICROSERVICES

Microservices are like extensions of middleware layer components because they provide growing the system with different components, managing them with performance and resource control aspects, deployment and implementation of new devices. The availability of services and devices is important to make the system always work. Therefore, reactive microservices are used for this purpose. The components are IoT availability, data access, negotiation, health check, message channel, reactive broker and service discovery. IoT availability checks the communication between message channels and mapping services. It especially works for fault detection. Availability service also frequently checks the storage part if it is available or not. When there is a fault detected in these areas, IoT availability microservices show a detailed

message for the error to be solved. When the issue is solved, the problem message is closed successfully. Data access can be provided via a RESTful API. Asynchronous-type database systems like PostgreSQL can provide this. To make all these parts work, automated negotiation components can be integrated. After deciding on some conditions, this area checks the system if all conditions are provided like time and response type. Also, with past data, it is possible to check the situations which are not normal. As negotiation checks the stability and response times, the health check, on the other hand, checks if the microservices are up or down. The IoT message channel provides messages in bad situations. As a middleware service, it is possible to connect from a virtual server and get the messages in JSON format. There are some softwares to convert these messages to meaningful analysis, but for our system, these complicated integrations are not needed. They may later be used. A reactive broker is a helpful property for smart city integrations because it enables remote devices to be connected properly. It works with triggers, and as any command is taken, it handles it immediately. Service discovery is generally aimed at introducing the device to the outside. The name, location, and other needed data are provided from the device in this way. It can also be used for our transportation system, including registration, cancellation, searching, and applying to get possible routes [12].

X. NETWORK

There are some breakdowns in this section. Networks are huge areas of the world, but for IoT frameworks and smart cities, five points can be mentioned. They are the organization of the ZigBee network, address assignment, nodes entering or quitting the network, mobility of the nodes, and network workflow. Because the ZigBee network is beneficial for long-distance transmissions with high speed, it is useful for our transportation system. It costs a lot, but better with low energy consumption and high reliability. A wireless network can also be deployed with the TCP protocol that provides us with transmissions thanks to the packets. The ZigBee network will be used with coordination and connection via terminal nodes. When there is an upcoming signal, it is connected if there is an available node. According to signals or notifications that are coming from the coordinator, nodes are off or on. In the communication circle, the routes will be decided by address assignment. Then, nodes' final situations are managed by their entry or exit times with the connection of the network. When a node comes through, its location code is first generated, then the neighborhoods are listed, and they are directed to the related location with the code generated. Otherwise, if a node exits, its response connection is broken immediately. The mobility of the nodes is also related to this idea because while they are moving, their addresses are refreshed accordingly. Thus, our transportation system exactly needs one of these. The neighbor lists are also refreshed according to the mobility information. Finally, network workflow relates to an upper computer to check the addresses generated before. From this mother area, the system breaks down with the nodes. With the layer implementation, the management of this big system becomes easier [13].

XI. SECURITY

This part is important for both the network and IoT layer systems. The big data and cloud systems will be integrated with our system, so security issues should be considered carefully. There are some IoT systems that already use encryption for data protection such as healthcare, transportation, safety, and governance. [14]. We also need to apply encryption technology for data management systems in our architecture. Heterogeneity managers are explained previously. Now, some secure suggestions for heterogeneous systems are given. It is suggested that black networks can make the data secure. In the protocol linking time, these encrypt the data, so it is transmitted in a protected way. There are also trusted Software Defined Networking (SDN) controllers, unified registry, and key management ideas. SDN makes the connection of the nodes private. It divides packets from the flow and controls it with the on and off times properly. Therefore, this synchronization is applicable to our network system to be reliable. The unified registry can be connected at this time for the address creation. There

are a number of nodes and wireless connections in the system so that a unified registry controls the conversion between the connections. Within each layer, communication keys are crucial for all systems. Thus, the key management system finally generates keys for layer connections to be controlled properly [15].

XII. CONCLUSION

Even though there are many smart city architectures integrated with IoT, there is a huge lack of transportation systems solutions. Especially, when big and crowded cities are analyzed, it is seen that public transportation systems require better integration of new technologies because the management in this area is hard. As a consequence, a public transportation management structure is offered in this article. Besides having a brilliant idea, implementing it securely is also important. For that reason, the layer system and network suggestions are also given. The future studies in this area can be done about how to implement these suggestions in the real world.

REFERENCES

[1] S. Talari, M. Shafie-Khah, P. Siano, V. Loia, A. Tommasetti, and J.P. Catalão, "A review of smart cities based on the internet of things concept" Energies, vol. 10, no. 4, p. 421, 2017.

[2] R. Lea and M. Blackstock, "Smart cities: An iot-centric approach" In Proceedings of the 2014 international workshop on web intelligence and smart sensing, pp. 1-2, 2014.

[3] S.P. Mohanty, U. Choppali, and E. Kougianos, "Everything you wanted to know about smart cities: The internet of things is the backbone" IEEE Consumer Electronics Magazine, vol. 5, no. 3, pp. 60-70, 2016.

[4] H. Arasteh, V. Hosseinnezhad, V. Loia, A. Tommasetti, O. Troisi, M. Shafie-khah, and P. Siano, "Iot-based smart cities: A survey" In 2016 IEEE 16th International Conference on Environment and Electrical Engineering (EEEIC), pp. 1-6, 2016.

[5] N. Dlodlo, O. Gcaba, and A. Smith, "Internet of things technologies in smart cities" In 2016 IST-Africa Week Conference, pp. 1-7, 2016.

[6] D. Vakula and B. Raviteja, "Smart public transport for smart cities" In 2017 International Conference on Intelligent Sustainable Systems (ICISS), pp. 805-810, 2017.

[7] M. Pečar and G. Papa, "Transportation problems and their potential solutions in smart cities" In 2017 International Conference on Smart Systems and Technologies (SST), pp. 195-199, 2017.

[8] Z. Xiong, H. Sheng, W. Rong, and D.E. Cooper, "Intelligent transportation systems for smart cities: a progress review" Science China Information Sciences, vol. 55, no. 12, pp. 2908-2914, 2012.

[9] E.Z. Tragos, V. Angelakis, A. Fragkiadakis, D. Gundlegard, C.S. Nechifor, G. Oikonomou, H.C. Pöhls, and A. Gavras, "Enabling reliable and secure IoT-based smart city applications" In 2014 IEEE International Conference on Pervasive Computing and Communication Workshops (PERCOM WORKSHOPS), pp. 111-116, 2014.

[10] D.P. Abreu, K. Velasquez, M. Curado, and E. Monteiro, "A resilient Internet of Things architecture for smart cities" Annals of Telecommunications, vol. 72, no. 1-2, pp. 19-30, 2017.

[11] E. Theodoridis, G. Mylonas, and I. Chatzigiannakis, "Developing an iot smart city framework" In IISA 2013, pp. 1-6, 2013.

[12] C. Santana, L. Andrade, F.C. Delicato, and C. Prazeres, "Increasing the availability of IoT applications with reactive microservices" Service Oriented Computing and Applications, pp. 1-18, 2020.

[13] Z. Lv, B. Hu, and H. Lv, "Infrastructure monitoring and operation for smart cities based on IoT system" IEEE Transactions on Industrial Informatics, vol. 16, no. 3, pp. 1957-1962, 2019.

[14] S. Shukla, K. Balachandran, and V.S. Sumitha, "A framework for smart transportation using Big Data" In 2016 International Conference on ICT in Business Industry & Government (ICTBIG), pp. 1-3, 2016.

[15] S. Chakrabarty and D.W. Engels, "A secure IoT architecture for smart cities" In 2016 13th IEEE annual consumer communications & networking conference (CCNC), pp. 812-813, 2016.

Investigation of the Effects of Changes in Battery Components on Battery Performance Using Design of Experiments Approach

Akü Bileşenlerinde Yapılacak Değişikliklerin Akünün Performansına Etkilerinin Deneysel Tasarım Yöntemi ile İncelenmesi

İbrahim ÜLKE[*,1], Muhammed Ferhat ÖZTÜRK[1], Mustafa YURDAKUL[1]

[*]ibrahimulke@gazi.edu.tr, ORCID: 0000-0002-8927-0052
[1]*Makine Mühendisliği Bölümü, Gazi Üniversitesi, Ankara, Türkiye*

Abstract: Lead-acid batteries are the most widely used and widely used among many battery types today. In lead-acid batteries, discharging the battery to a certain DoD level and then fully charging it is called a "cycle". The "cycle life" of that battery is equal to the number of times the battery can be put into charge/discharge "cycles" so as to preserve up to 80% of its Ah capacity. Cycle life depends on grill thickness, grill material, plate dough chemistry, battery temperature. Capacity, on the other hand, depends on the surface areas of the plates, the internal resistance, the number of plates and the permeability of the separators used. In this study, it is aimed to improve the battery performance by changing the levels of the components of the battery.

Keywords: *Design of Experiment, Energy, Production Technologies*

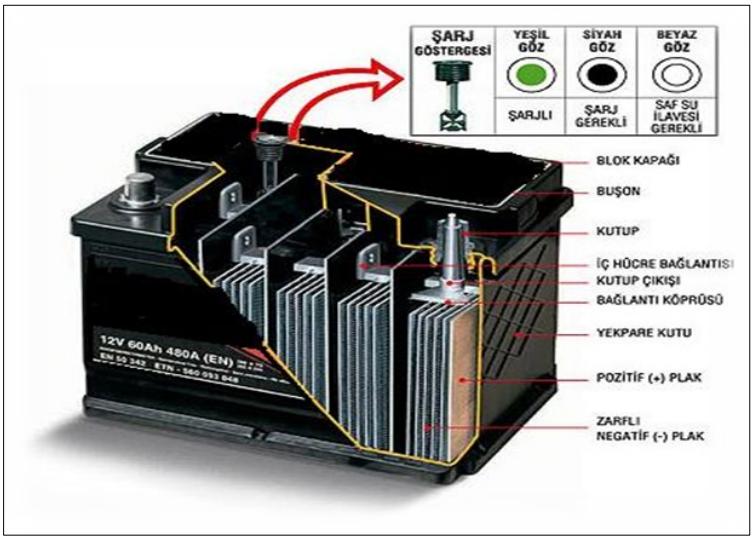
Özet Günümüzde birçok akü çeşidi arasından en çok kullanılanı ve kullanım alanı en geniş olanı kurşun-asit akülerdir. Kurşun-asit akülerde akünün belli bir DoD seviyesine kadar deşarj ve sonra tam şarj edilmesine bir "çevrim" denir. Akü Ah olarak belirtilen kapasitesini %80'e kadar koruyacak şekilde kaç kez şarj/deşarj "çevrimine" sokulabiliyor ise o akünün "çevrim ömrü" o sayıya eşittir. Çevrim ömrü, ızgara kalınlığına, ızgara malzemesine, plaka hamur kimyasalına, akü sıcaklığına bağlıdır. Kapasite ise, plakaların yüzey alanlarına, iç dirence, plaka sayılarına ve kullanılan seperatörlerin geçirgenliklerine bağlıdır. Bu çalışmada akünün bileşenlerinin seviyelerini değiştirerek akü performansının iyileştirilmesi amaçlanmaktadır.

Anahtar Kelimeler: *Deney Tasarımı, Enerji, Üretim Teknolojileri*

I. GİRİŞ

Akü kimyasal enerjiyi elektrik enerjisine ya da elektik enerjisini kimyasal enerjiye dönüşümlü olarak birçok sefer çevirebilen cihazlar olarak tanımlanır [1]. Akü araçta ateşleme, alternatörün yetersiz kaldığı durumlarda elektrik ihtiyacını karşılama ve elektrik sistemini dalgalanmalara karşı koruma gibi yaşamsal fonksiyonları gerçekleştiren bir cihazdır. Elektrolit tiplerine göre aküler; kuru ve sulu olarak sınıflandırılır. Elektrolit bir pasta haline getirilerek sabitlenmiş ise akü kuru akü, sıvı halde bulunuyorsa sulu akü adını alır. Kurşun-asit akümülatörlerinde plaka olarak kurşun ve kurşun oksitleri, elektrolit olarak da seyreltilmiş sülfürik asit kullanılmaktadır. Şarj olmuş bir aküde (+) artı plakada kurşun dioksit (PbO2), (-) eksi plakada ise süngerimsi gözenekli yapıya sahip kurşun (Pb) bulunur [2]. Deşarj işlemi sırasında kurşun dioksit ve kurşun, kurşun sülfata dönüşür. Geleneksel bir

akümülatörün parçaları ve kritik bileşenleri şunlardır;



Şekil 1. Geleneksel bir akünün şematik gösterimi

Plakalar: Bir akümülatörün enerji vermesini sağlayan en önemli parçalardır. Pozitif ve negatif olmak üzere iki çeşit plaka vardır. Plakaların iskeleti ızgaradır. Izgaranın üzerine pozitif veya negatif hamur sıvanarak plaka elde edilir. + plaka kapasiteyi, + ve – plakanın eşlenikleri aracı ilk çalıştırmak için gerekli olan marş basma gücünü gösterir. Pozitif plakalar akım veren plakalar oldukları için oksitlenme reaksiyonu bu plakalarda olur ve negatif plakaya göre daha kalın ve ağır üretilir. Pozitif plakanın aktif maddesi kurşun dioksit, negatif plakanın aktif maddesi yumuşak süngerimsi kurşundur [3].

Ayıraç (Seperatör): Pozitif ve negatif plakaların birbirine temas ederek kısa devre oluşturmasını engelleyen ve aynı zamanda da elektrik akımını taşıyan iyonların geçişine izin veren mikro gözeneklere sahip zarf veya levha şeklinde yapılardır.

Kutu ve Kapak: Kutu ve kapaklar polipropilenden üretilirler. Bunların görevi yeterli yalıtımı, sızdırmazlığı, uzun süreli dayanıklılığı sağlaması, mekanik ve kimyasal özellikleri korumasıdır.

Kutup Başları: Her kurşun-asit hücresi yaklaşık olarak 2V'tur. İstenilen akü voltajına bağlı olarak bunlar birbirlerine seri bağlanarak istenilen voltajda akü üretilir. Bunun sonucunda pozitif plakaların bağlı olduğu uç pozitif kutbu, negatif plakların bağlandığı uç negatif kutbu oluşturur. Kutupların üzerinde veya yanlarında (-) ve (+) işaretleri vardır.

Gaz Kapakları (Buşonlar): Akümülatörün üretiminde kullanılan alaşımın özelliğine bağlı olarak gaz çıkışları vardır, çıkan bu gazların hücre içindeki basıncı belirli bir seviyenin üzerine çıkarmaması gerekir, aksi takdirde aşırı basınç sonucu akü patlayabilir. Oluşan bu gazların bir kısmının dışarıya çıkmasını sağlayan delikli kapaklara buşon adı verilir.

Elektrolit: Plakaların içine batırıldığı, iyonların (+) kutuptan (-) kutuba taşınmasını sağlayan seyreltilmiş sülfirik asit çözeltisidir. Tam şarjlı aküde 27˚C'de 1,28gr/cm3 yoğunluktadır [4].

II. LİTERATÜR TARAMASI

Göçmen yaptığı çalışmada geliştirdiği pil paketinde dağıtıcı kanalın şeklinin akış homojenliğini nasıl etkilediği araştırmıştır. Bununla birlikte sıcaklık homojenliği için gerekli olan akış homojenliği koşulunu sağlamak için tasarım karmaşıklığını artırmıştır. Tasarım

değişikliğini, kapsamlı bir iteratif araştırma yaklaşımıyla yapısal tasarım metodolojisine dayalı olarak değiştirilmiştir. Çalışma sonunda ortaya çıkarılan tasarım, kanallar boyunca maksimum %0,81 hava debisi sapması ile homojen bir hava dağılımı sağlamıştır [5].

Celen ve Kaba hava akış yönlendirici kanatların kullanımının prizmatik lityum-iyon batarya sıcaklığı üzerine etkisinin farklı çalışma şartlarında deneysel ve sayısal olarak incelemişlerdir. Çalışmalarında elektrikli araçlarda kullanılan 20 Ah kapasiteye sahip torba tipi bir prizmatik lityum-iyon bataryanın termal yönetimi incelenmiştir. Akışkan olarak hava kullanılmış olup, akışkan giriş sıcaklığının (15°C, 25°C, 35°C), akışkan giriş hızının (0,5 m/s, 1 m/s, 1,5 m/s) ve deşarj hızının (2C, 3C, 4C) batarya yüzey sıcaklığına, batarya yüzey sıcaklık farkına ve ısı transfer hızına etkisi araştırılmıştır [6].

Çetin ve diğerleri ise çalışmalarında 18 adet silindirik lityum iyon pillerden oluşan batarya paketini, 1,5 mm et kalınlığındaki bakır plakalardan imal edilen S tipi bir sıvı soğutma kanalı içerisine yerleştirilerek sıvı soğutmalı batarya termal yönetim sisteminin soğutma performansı üzerinde etkisini araştırmışlardır. Batarya paketinin şarj ve deşarj deneylerinde, 15 °C, 25 °C ve 35 °C başlangıç sıvı giriş sıcaklıklarının, 475 ml/dk, 625 ml/dk ve 790 ml/dk sıvı akış hızlarındaki soğutma performansları incelenmiştir. Güç tüketimi ve soğutma performansı bir arada değerlendirildiğinde ise en verimli kombinasyonun 15 °C başlangıç sıvı giriş sıcaklığı ve 625 ml/dk sıvı akış hızı olduğu tespit edilmiştir [7].

Wu ve diğerleri PV akü sistemlerinde yaşam döngüsü maliyetini en aza indirmek için yaptıkları çalışmalarında iki katmanlı bir optimizasyon modeli geliştirerek en iyi batarya kapasitesini bulmaya çalışmışlardır [8].

Chen ve diğerleri ise akış düzeninin tasarlanması yoluyla hava soğutmalı akü termal yönetim sisteminin soğutma verimliliğinin iyileştirilmesi üzerine çalışmışlardır. Çalışmalarında giriş ve çıkış kanallarının simetrik olarak tasarlandığı hücrelerin en yüksek soğutma verimliliğini sağladığını tespit etmişlerdir [9].

Sezici, Çetin ve Polat ise Chen ve diğerlerinden farklı olarak silindirik yapıdaki 18 adet lityum iyon pil hücresinden oluşan pil takımı ve üç farklı modelin bir arada olduğu hava soğutmalı batarya kutusu tasarlanıp imal ederek hava soğutmalı batarya termal yönetim sisteminin soğutma deneylerini yapmışlardır [10].

III. MATERYAL VE YÖNTEM

Kurşun-asit akümülatörlerde kullanılan döküm ızgara alaşımları akümülatörün performansını etkileyen akümülatör üretiminin ilk basamağıdır. Akümülatör teknolojisinde kullanılan alaşımlar zaman içerisinde geliştirilerek üretilecek üründen beklenen özellikleri göre standardize edilmiştir. Saf kurşun çok yumuşak ve sünek olması ve kendi ağırlığını taşımada zorluk çekmesi nedeni ile alaşımlandırılmaktadır. Kurşun-Kalsiyum alaşımlı akümülatörlerde olması öngörülen korozyon pozitif ızgaralarda oluşur, negatif ızgaralar korozyonun asıl nedeni değildir. Buna ek olarak Kalsiyum alaşımlı kurşunlarda korozyon direncinin arttırılması için kalay, gümüş gibi elementler alaşıma eklenerek ürün performansı iyileştirilir. Ancak negatif ızgara alaşım içerikleri ve safsızlıkları elektolit ile etkileşimde bulunduğunda Hidrojen oluşumunu sağlayacak kimyasal reaksiyonlara neden olmaktadır ve böylelikle akümülatörde su kaybı artmaktadır.Izgara alaşımları çevrim ömrünü su kaybı, korozyon gibi fonksiyonel özellikleri nedeni ile direk etkilemektedir. Su kaybı yüksek, korozyon direnci düşük akümülatörler talep edilen aynı zaman standart gerekliliği olan çevrim ömürlerini sağlayamamaktadır. Bu nedenle geliştirilecek ızgara dizaynının su kaybı düşük, ızgara direnci yüksek böylelikle akümülatör ömrü uzun olmalıdır. Bu çalışmada Tablo 1'de verilen 10 farklı bağımsız değişkenin akü performansına etkileri incelenmiştir. Bağımsız değişkenler katkı maddesi özelliği, malzeme özelliği ve ızgara kalınlığı kategorilerinde belirlenmiştir.

Tablo 1. Bağımsız değişkenler

Katkı Maddesi Özelliği	Malzeme Özelliği	Izgara Kalınlığı
I. Sülyenli plaka	1. Antimuanlı ızgara (Sb)	a) 0.8 mm ızgara
II. Sülyensiz plaka	2. Kalsiyum alaşımlı ızgara (Ca)	b) 1.1 mm ızgara
III. 3BS tanecik yapılı		
IV. 4BS tanecik yapılı		
V. Kostikli asit kullanımı		
VI. Flux kaynak		

Çalışma kapsamında Tablo 2'de verilen 12 farklı kombinasyon incelenmiştir. Bu kombinasyonların kıyaslanmasında her kombinasyona ait akünün 12 ay sonunda voltaj ve iç direnç değerleri karşılaştırılmıştır. Karşılaştırma sonucunda en iyi değerleri veren grubun iç yapı özellikleri incelenmiştir.

Tablo 2. Deney grupları

Grup 1	Grup 2	Grup 3	Grup 4	Grup 5	Grup 6	Grup 7	Grup 8	Grup 9	Grup 10	Grup 11	Grup 12
1	2	1	1	1	1	1	1	1	1	1	1
a	a	a	b	a	a	a	a	a	a	a	a
II	II	II	II	I	II	I	I	I	I	I	I
III	III	III	III	III	III	III	IV	III	III	III	III
V	V	V	V	V	V	V	V	V	V	V	-
VI	VI	VI	VI	VI	VI	VI	VI	VI	-	VI	VI

IV. BULGULAR

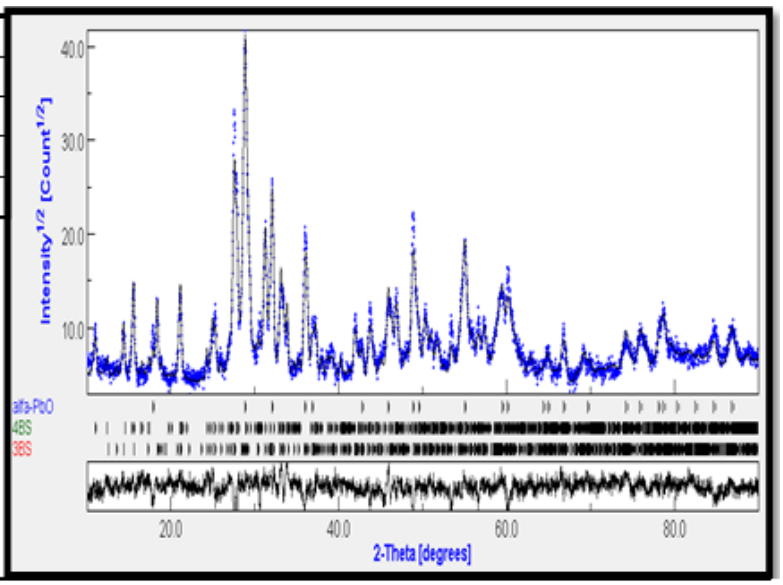
12 ay sonunda akülerden elde edilen voltaj ve iç direnç değerleri Tablo 3'te verilmiştir. Tablo incelendiğinde en yüksek voltaj ve en düşük iç direnç değerlerinin 8. Deney grubunundan elde edildiği görülmektedir. Çalışma devamında bu gruba ait akü bileşenlerinin iç yapıları incelenmiştir.

Tablo 3. 12 ay sonunda voltaj ve iç direnç değerleri

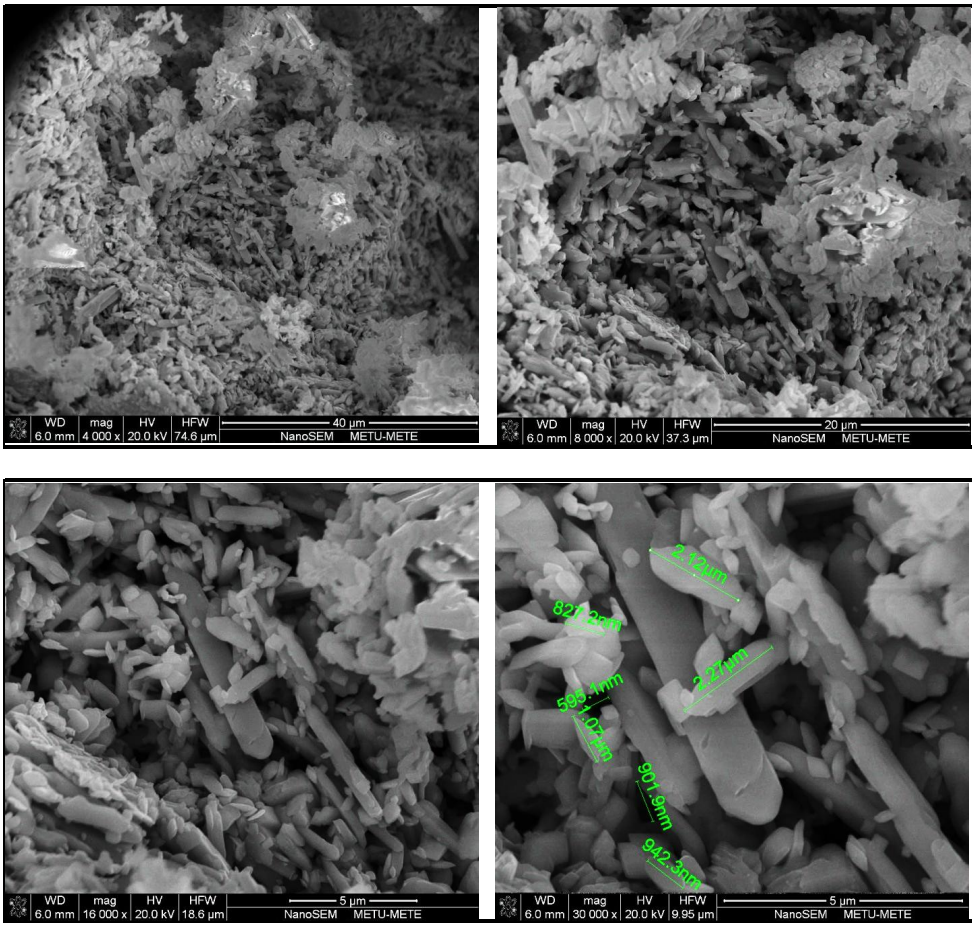
DENEY GRUPLARI	VOLTAJ (V)	İÇ DİRENÇ (mohm)
1	12,345	3,48
2	12,501	3,46
3	12,345	3,48
4	12,516	3,42
5	12,357	3,476
6	12,345	3,48
7	12,357	3,476
8	12,601	3,39
9	12,357	3,476
10	12,21	3,54
11	12,357	3,476
12	12,301	3,49

Çekirdekleştirme ajanı ile üretimi gerçekleştirilen ve düşük sıcaklıkta kürlenen 4BS Plaka Plakalar ile kür programının etkisini görmek amacı ile standart kürlenen 4BS Standart Plakalardan ve standart 3BS yapılı Plakalardan öncelikle oluşan fazları belirlemek için XRD, mikro yapıyı incelemek için SEM ve gözeneklilik oranını incelemek için civalı porozimetre analizleri yapılmıştır.

Rw	18,05	
	wt%	Vol %
Alfa-PbO	26,79	22,26
3BS	53,62	58,89
4BS	19,59	18,85



Şekil 2. En yüksek verimi veren gruba ait XRD sonuçları



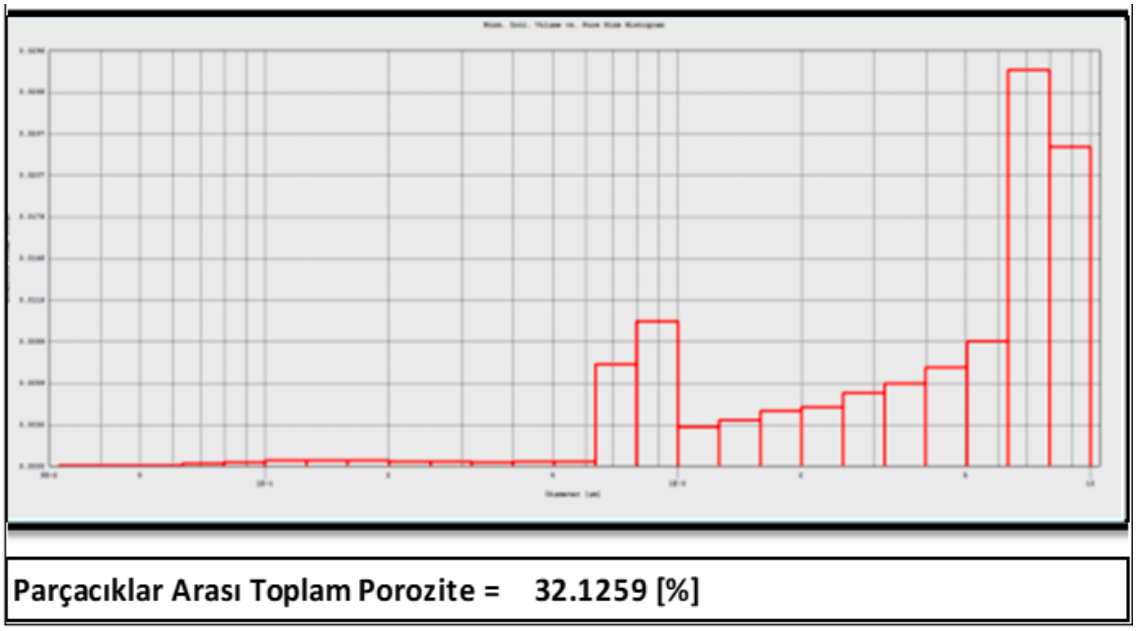
Şekil 3. 8. Gruba ait SEM görüntüleri

Çekirdekleştirme ajanı ile üretilen plakalar standart (3BS) kür programı ile kürlendiğinde ise 4BS faz oranının %72 civarında oluştuğu gözlenmiştir. SEM analizi incelendiğinde oluşan bazik sülfat taneciklerine ait boyut dağılımının ise 3,76 µm ile 8,65 µm aralığında olduğu gözlenmiştir. Tanecik boyutlarını B grubu Plakalara göre daha büyük olması (soft curing ile kürlenen 4BS içerikli plaklar), kür sıcaklığının tanecik büyümesi üzerinde etkili olduğunu göstermiştir.

Standart üretilen Plakaların 3BS faz içeriğinin ağırlıkça %53, hamur karma operasyonu sırasında gözlenebilecek bölgesel sıcaklık artışlarına bağlı olarak %19 oranında 4BS fazı içerdiği görülmüştür. SEM analizi incelendiğinde oluşan bazik sülfat taneciklerine ait boyut dağılımının 0,6 µm ile 2,27 µm aralığında olduğu gözlenmiştir. Bu durum literatürde 1 ile 4 µm aralığında değişen boyutlara sahip 3BS morfoloji özelliğine sahip üretimin gerçekleştirildiğini göstermektedir. Civa porozimetresi ile analiz edilen parçacıklar arası gözeneklilik oranı ise küçük tanecik yapısına bağlı olarak tanecikler arası boşluk oranı % 32,12 olarak gözlenmiştir.

Plaka Tipi ve Sayısı	Catalog Capasity (Ah)/CCA (A)	Hamur karaktesristiği (Kodlama)	Akü Adlandırması	Akü Dizayn Ağırlığı (kg) (±500 g)	Gerçekleşen Akü ağırlığı (kg)	1.C20 Kapasite (Ah)	CCA_1		2.C20 Kapasite (Ah)	CCA_2		3.C20 Kapasite (Ah)	CCA_3	
							In 10 s, V ≥ 7,5 V	6 V, t ≥ 90 s		In 10 s, V ≥ 7,5 V	6 V, t ≥ 90 s		In 10 s, V ≥ 7,5 V	6 V, t ≥ 90 s
5x5/115 EXP.TECK.	50/420	B grubu	Y Grubu	12,4	13,184	52,57	8,33	198	49,87	8,43	185	48,22	7,84	126
		B grubu			13,184	55,968	8,08	171	52,217	8,41	178	51,887	Çevrim Testine alındı ve testten kaldı	
		A Grubu	X Grubu		13,002	54,59	7,92	218	56,75	7,77	183	52,49	8,14	191

Şekil 4. X grubu (3bs) ve Y grubu (4bs) akülere ait fonksiyonel test sonuçları



Şekil 5. En yüksek verimi veren gruba ait civalı porozimetre sonuçları

V. SONUÇLAR

Akü bileşenlerinde yapılan değişikliklerin akünün performansına etkilerinin incelendiği bu çalışma kapsamında tribazik kurşun sülfatın, 1-4 mm uzunluğunda ve 0.2-0.8 mm çapında prizmatik kristaller oluşturduğu belirlenmiştir. Tetrabazik kurşun sülfatın ise 10-100 mm uzunluğunda ve 3-15 mm çapında prizmatik kristaller içerdiği görülmüştür. Çalışma sonunda ızgara kalınlığının, kalsiyumlu ızgaranın, sülyenli plakanın, kostikli plakanın ve 4bs plakanın aküdeki voltaj kaybının azalmasını sağladığı ve iç direncine olumlu etkileri olduğu bu sayede de akü ömrünün uzamasını sağladığı tespit edilmiştir.

KAYNAKLAR

[1] Cho, J., Jeong, S., & Kim, Y. (2015). Commercial and research battery technologies for electrical energy storage applications. Progress in Energy and Combustion Science, 48, 84-101.

[2] Jafari, H., & Rahimpour, M. R. (2020). Pb acid batteries. Rechargeable Batteries: History, Progress, and Applications, 17-39.

[3] Czerwiński, A., Wróbel, J., Lach, J., Wróbel, K., & Podsadni, P. (2018). The charging-discharging behavior of the lead-acid cell with electrodes based on carbon matrix. Journal of Solid State Electrochemistry, 22, 2703-2714.

[4] Akar, A. (2020). Otomobiller için yenilikçi bir akü koruma cihazı tasarımı (Master's thesis, Sakarya Uygulamalı Bilimler Üniversitesi).

[5] Göçmen, S. (2021). Numerical and experimental investigations of an air-cooled battery thermal management system (Master's thesis, Izmir Institute of Technology).

[6] CELEN, A., & KABA, M. Y. (2021). Elektrikli Araçlarda Kullanılan Silindirik Lityum İyon Bataryaların Soğutulmasının Parametrik İncelenmesi. Fırat Üniversitesi Mühendislik Bilimleri Dergisi, 33(1), 49-61.

[7] Çetin, İ., Sezici, E., Karabulut, M., Avci, E., & Polat, F. (2023). A comprehensive review of battery thermal management systems for electric vehicles. Proceedings of the Institution of Mechanical Engineers, Part E: Journal of Process Mechanical Engineering, 237(3), 989-1004.

[8] Wu, Y., Liu, Z., Liu, J., Xiao, H., Liu, R., & Zhang, L. (2022). Optimal battery capacity of grid-connected PV-battery systems considering battery degradation. Renewable Energy, 181, 10-23.

[9] Chen, K., Wu, W., Yuan, F., Chen, L., & Wang, S. (2019). Cooling efficiency improvement of air-cooled battery thermal management system through designing the flow pattern. Energy, 167, 781-790.

[10] Sezici, E., Cetin, I., & Polat, F. (2022). Design and Experimental Investigation of Air-Cooled Battery Thermal Management System for Electric Vehicles. Journal of Engineering Research and Applied Science, 11(2), 2062-2077.

Süreksiz Kolonlara Sahip Betonarme Binalarda Sehimlerin Analiz Yaklaşımlarına Göre İncelenmesi

Investigation of Deflections in Reinforced Concrete Buildings with Floating Columns According to Analysis Approaches

Musfir Ahmed*[1], Adem Doğangün**[1]

*: 502126011@ogr.uludag.edu.tr, ORCID: 0009-0003-6708-9767 ; ORCID**: 0000-0002-1867-7103
[1]: *İnşaat Mühendisliği Bölümü, Bursa Uludağ Üniversitesi, Bursa, Türkiye*

Özet: Süreksiz kolon olarak da adlandırılabilecek olan kirişe mesnetlenip altında herhangi bir kolon bulunmayan taşıyıcı sistemlerin yapılmasına düzensizlik olarak tanımlanarak izin verilmektedir. Bu çalışmada dikkate alınan süreksiz kolon alt ucundan her iki ucundan mesnetli bir kirişe oturan kolondur. Binaların analizlerinde genel olarak yapının tamamı modellenerek son durumu dikkate alınarak çalışmada geleneksel analiz yaklaşımı olarak tanımlanan yapısal analizlerle gerçekleştirilmektedir. Çalışmada geleneksel yaklaşımın yanında yapım aşamalarını da dikkate alan analizler gerçekleştirilmektedir. Bu çalışmanın amacı düşey düzensizliklerden taşıyıcı sistemde bulunmasına izin verilen süreksiz kolona sahip taşıyıcı sistemde oluşabilecek sehim değerlerinin belirlenmesinde kullanılan yapısal analiz yaklaşımlarından elde edilen sonuçları karşılaştırmalı olarak irdelemektir. Bu amaçla Türkiye Bina Deprem Yönetmeliği-2018'e göre kolon süreksizliği bulunan betonarme çerçevelerden oluşan 4 katlı bir bina dikkate alınmaktadır. Çalışma kapsamında dikkate alınan binanın analiz ve tasarımı ETABS yazılımı kullanılarak gerçekleştirilmiştir. Eğilme etkisindeki yapı elemanlarının sehim hesabı ise SAFE yazılımı ile ayrıca irdelenmiştir. Deprem etkisine göre hesapta, modal analiz yöntemlerinden biri olan tepki spektrumu analizi yöntemi kullanılarak lineer dinamik analizler gerçekleştirilmiştir. Geleneksel yaklaşım ve yapım aşamalarını dikkate alan yaklaşımlar ile oluşturulan bina modellerine göre gerçekleştirilen analizler sonucunda elde edilen yerdeğiştirmeler karşılaştırmalı olarak irdelenmektedir.

Anahtar Kelimeler: *Betonarme Yapılar, Yapım Aşamaları Dikkate Alan Analiz, Düşeyde Düzensizlik, Kolon Süreksizliği*

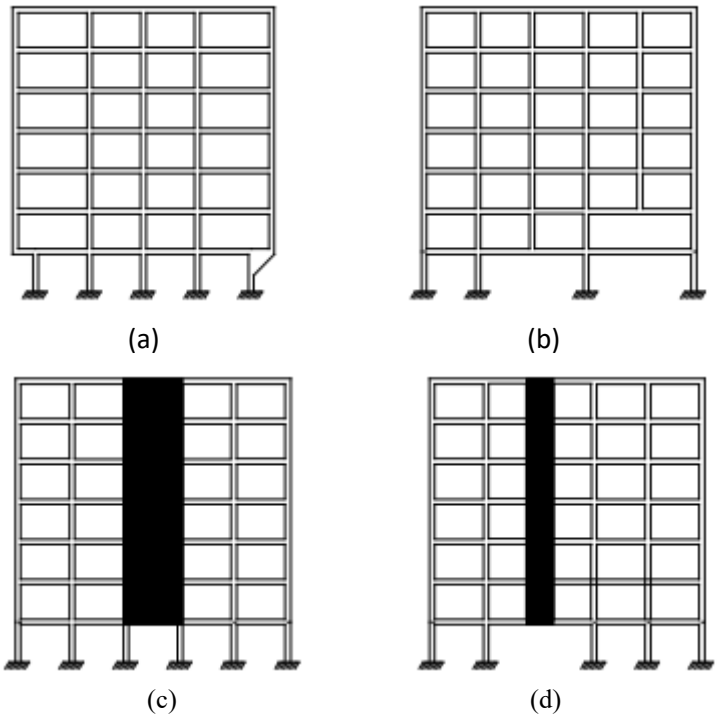
Abstract: It is allowed to construct structural systems that are supported on a beam, without any columns underneath, by defining it as irregularity. In this study the floating column considered is supported by a beam supported at both ends from the lower end. Structural analyses in buildings are generally performed by modeling the entire structure by considering its final state, which is defined as the conventional analysis approach in this study. In the study, in addition to the conventional approach, analyses that consider construction stages are also carried out. The aim of this study is to comparatively examine the results obtained from structural analysis approaches used to determine the deflection values that may occur in structural systems with discontinuous columns, where vertical irregularities are permitted in the structural system. For this purpose, a 4 story building consisting of reinforced concrete frames with a floating column is considered, according to the Turkish Building Earthquake Code-2018. The analysis and design of the building under consideration in this study were performed using the ETABS software. The deflection calculations for structural elements under flexural effects were separately examined using the SAFE software. In the calculation of earthquake effects,

linear dynamic analyses were performed using the response spectrum analysis method, one of the modal analysis methods. Displacements obtained from the analyses conducted based on both the traditional approach and approaches considering construction stages are examined comparatively.

Keywords: *Reinforced Concrete Structures, Construction Sequence Analysis, vertical irregularity, Column Discontinuity*

I. GİRİŞ

Türkiye Bina Deprem Yönetmeliğinde (TBDY 2018) 3'ü yatayda (A grubu) düzensizlikler ve 3 düşeyde (B grubu) düzensizlikler tanımlanmaktadır. Düşey düzensizliklerden birincisi yumuşak kat olarak adlandırılan düzensizliktir. İkincisi ise zayıf kat düzensizliği olarak adlandırılan düzensizliktir. Düşeyde düzensizliklerden üçüncüsü ise "B3 – Taşıyıcı Sistemin Düşey Elemanlarının Süreksizliği" düzensizliğidir. Binanın herhangi bir katında kolon ya da perdelerinin kaldırılarak kirişlerin veya guseli kolonların üstüne veya ucuna oturtulması ya da üst kattaki perdelerin altta kolonlara oturtulması durumudur. B3 düzensizliği için aşağıdaki Şekil 1'de sunulan 4 farklı düşey eleman düzensizliği tanımlanmaktadır. Bu 4 düzensizlikten 3 üne (Şekil 1a, c, ve d) müsaade edilmemektedir. Bunlardan sadece 1 tanesinin (Şekil 1b) taşıyıcı sistemde bulunmasına izin verilmekte ve bununla ilgili zorunlu hükümler getirilmektedir. Bu çalışmanın amacı düşey düzensizliklerden taşıyıcı sistemde bulunmasına izin verilen süreksiz kolona sahip taşıyıcı sistemde oluşabilecek sehim değerlerinin belirlenmesinde kullanılan yapısal analiz yaklaşımlarından elde edilen sonuçları karşılaştırmalı olarak irdelemektir.



Şekil 1. Taşıyıcı sistemin düşey elemanlarının süreksizliğinin düzensizliği (TBDY 2018).

Bu çalışmada gerçekleştirilen çalışmaya yakın konularda gerçekleştirilmiş çalışmalardan başlıcaları aşağıda sunulmaktadır:

[1] Bu çalışmada Deprem Bölgelerinde Yapılacak Binalar Hakkında Yönetmelik (DBYBHY-2007) esaslarına göre eşdeğer deprem yükü yöntemi ve zaman tanım alanında doğrusal olmayan analiz yöntemini kullanarak B3 düzensizliğin betonarme çerçevenin deprem davranışına olan etkisini irdelenmiştir. Kritik elemanlarının iç kuvvet değerlerinin % 50 arttırılması,

düzensizliğin yarattığı olumsuz etkinin önüne geçilmesi konusunda katkıda bulunduğu görülmüştür.

Deprem Bölgelerinde Yapılacak Binalar Hakkında Yönetmelik (DBYBHY-2007) dört farklı deprem bölgesi ve dört farklı zemin sınıfı için düzenli bir yapı ile zayıf kat düzensizliği, yumuşak kat düzensizliği ve kolon süreksizliği olan 4 farklı yapının dinamik davranışlarını değerlendirilmiştir [3].

[5] Çalışmalarında 11 katlı betonarme bir yapının geleneksel ve yapım aşamaları dikkate alan analizlerini ETABS programı yardımıyla yapmışlar. Yapılan çalışmada köşesinde ve içinde süreksiz kolon oluşturulan iki farklı binanın yerdeğiştirmeleri, kesme kuvvetleri ve eğilme momentleri kıyaslanarak incelenmiştir. Her iki bina için yapım aşamaları dikkate alan analizden elde edilen sonuçlar oldukça fazla olduğu görülmüştür. Ayrıca bu iki yöntemin analiz sonuçlarındaki fark, köşesinde süreksiz kolon oluşturulan binada daha da arttığı görülmüştür.

20 katlı betonarme bir yapının DBYBHY-2007 ve TBDY-2018' e göre doğrusal hesap yöntemlerini kullanarak tepkilerini incelenmiştir [6].

[7] Çalışmalarında kolon süreksizliği bulunan 30 katlı betonarme bir binanın malzemenin doğrusal olmayan davranışı ve P-Delta etkilerini hesaba katarak yapım aşamalarını dikkate alan analiz yapmışlar.

[8] Çalışmalarında ise yapısal parametreleri aynı olan 20 katlı, 45 katlı ve 68 katlı üç farklı yüksek yapının doğrusal olmayan dinamik analizlerini yapmışlar. İnşaat aşamaları analizde dikkate alındığında analiz sonuçlarında büyük bir artış görülmüştür. Geleneksel yöntemle bulunan süreksiz kolona mesnetlenen kirişlerin analiz sonuçları alt katlarda daha düşük alındığı, üst katlarda ise daha büyük alındığı sonucuna varılmıştır.

Düşeyde düzensiz olan 7 katlı betonarme bir binanın, DBYBHY-2007 ve TBDY-2018' göre doğrusal hesap yöntemleri yardımıyla deprem hesabını yaparak tasarlanmıştır [11].

5 katlı düzenli bir yapı ve bu yapıdan türetilmiş 3 ayrı düzensiz yapı için performans analizleri gerçekleştirerek kolon süreksizliğinin binanın deprem performansını olumsuz yönde etkilediğini vurgulanmıştır [14].

II. ÇALIŞMADA DİKKATE ALINAN BİNANIN VE DEPREMİN ÖZELLİKLERİ

Bu çalışmada deprem etkilerinin tamamının moment aktaran süneklik düzeyi yüksek betonarme çerçevelerle karşılandığı 4 katlı bir bina ele alınmaktadır. Zemin kat yüksekliği 4 m, normal kat yüksekliği 3m, yapının planda boyutları 24 × 24 m, döşeme sistemi ise iki doğrultuda çalışan kirişli plak döşeme sistemi olarak seçilmiştir. Transfer kirişinin boyutları 45 × 90 cm olarak seçilmiştir. Transfer kirişinin yüksekliği toplam sehimin izin verilen sınırın altında olmasını sağlayacak şekilde seçilmesine çalışılmıştır. Transfer kirişinin genişliğinin belirlenmesinde ise üstüne oturan kolonla en az aynı genişlikte olması gerektiği unutulmamalıdır. Bina malzeme bilgileri Tablo I'de yük özellikleri Tablo II'de, Taşıyıcı sistem elemanlarının boyutları ise Tablo III'de sunulmaktadır.

TABLO I
Malzeme özellikleri

Beton Sınıfı	C30
Beton Elastisite Modülü (Ec)	32000 MPa
Beton Poisson Oranı (V)	0.2
Beton Isı Genleşme Katsayısı (A_t)	$1 \times 10^{-5}/℃$
Donatı Sınıfı	B420C
Donatı Elastisite Modülü (Es)	200000 MPa
Donatı Isı Genleşme Katsayısı (A_t)	$1.2 \times 10^{-5}/℃$

TABLO II
Düşey yükler

Betonarme Birim Hacim Ağırlığı	25 kN/m^3
Zabit Yükler	1.5 kN/m^2
Duvar Yükü	7 kN/m
Parapet Duvar Yükü	3 kN/m
Hareketli Yük	2 kN/m^2
Çatı Hareketli Yük	1.5 kN/m^2
Kar Yükü	0.75 kN/m^2

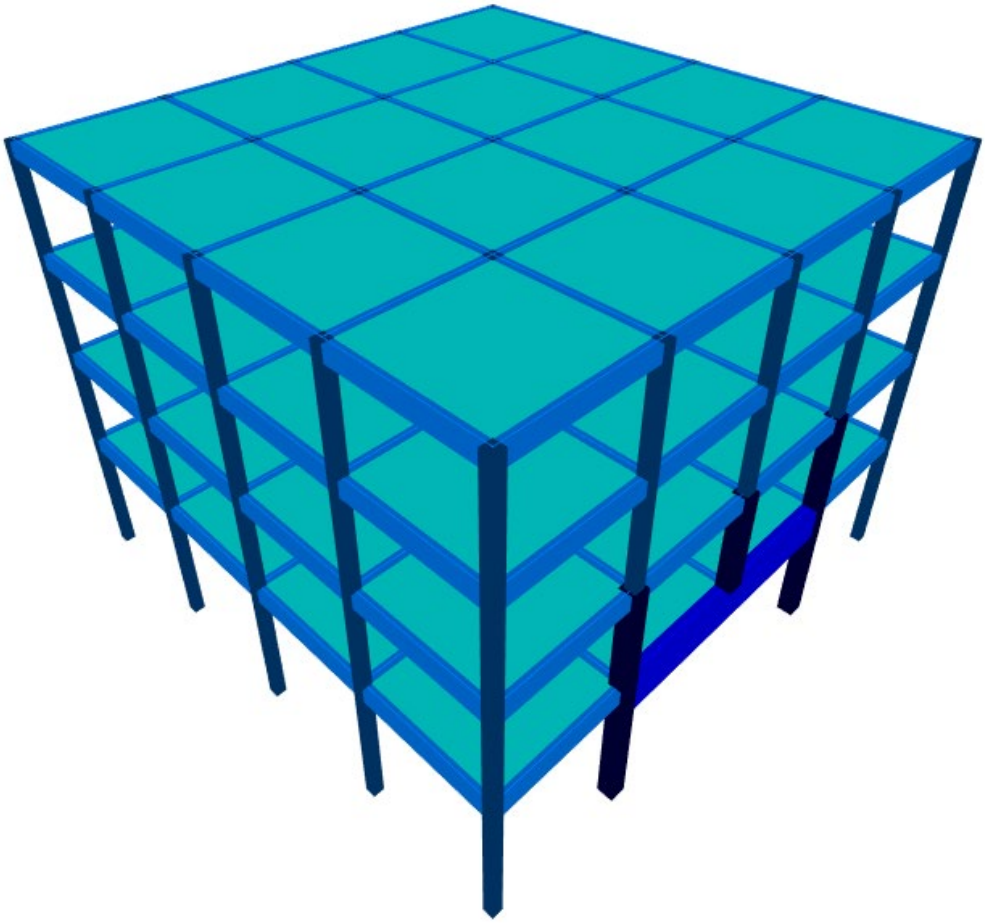
TABLO III
Taşıyıcı sistem elemanlarının boyutları

Taşıyıcı eleman	Kat	Kesit boyutları (mm)
Kolon (C2. C3. C4)	$1 \longrightarrow 2$	450×450
Kolon	$1 \longrightarrow 4$	300×300
Kiriş	$1 \longrightarrow 4$	250×400
Döşeme	$1 \longrightarrow 4$	120

TBDY-2018'de birbirine dik iki yatay doğrultudaki deprem etkilerinin geometrik ortalamasına karşı gelen harita spektral ivme katsayıları S_s ve S_1, referans zemin koşulu $(V_s)_{30} = 760\, m/s$ esas alınarak % 5 sönüm oranı için harita spektral ivmelerinin yerçekimi ivmesine bölünmüş şekilde Türkiye Deprem Tehlike Haritalarından https://tdth.afad.gov.tr/ adresli internet sitesinden yapının yapılacağı yerin koordinatları, yerel zemin sınıfı ve deprem yer hareketi düzeyine bağlı olarak elde edilmektedir. DTS = 1a olan örnek bina için enlem ve boylam koordinatı sırasıyla 40.217274 ; 28.976673, yerel zemin sınıfı ZB, deprem yer hareketi düzeyi ise DD-2 olarak seçilmiştir.

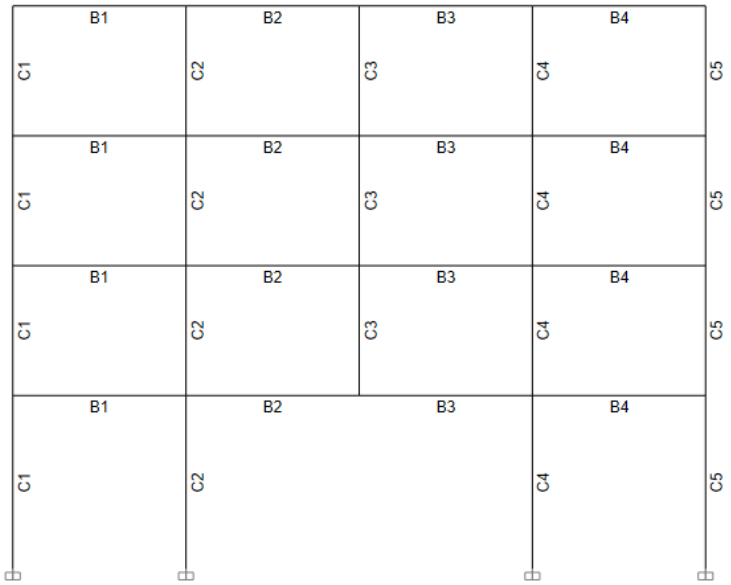
III. OLUŞTURULAN BİNA MODELİ

Çalışma kapsamında dikkate alınan betonarme binanın Şekil 2'de gösterilen modellenmede ETABS (2023) yazılımı kullanılmıştır. Eğilme etkisindeki yapı elemanlarının sehim hesabı ise SAFE (2023) yazılımı yardımıyla yapılmıştır. Yapısal analizlere tabi tutulacak olan binanın modellenmesinde döşemeler iki boyutlu kabuk sonlu elemanlarla (shell-thin) modellenmiştir. Böylelikle döşemelerde düşey ve yatay yükler altında döşemede düzlem içi ve düzlem dışı girilmelerin ve şekil değiştirmelerin oluşmasına imkan tanınmaktadır. Yük aktarımının doğru bir şekilde sağlanması için bu döşemelere (Default Floor Mesh) ataması yapılmıştır. Çubuk elemanlar otomatik (Auto Mesh) olarak atanarak her çubuk elemanın birleştiği diğer çubuk ve kabuk elemanlarla arasındaki etkileşim sağlanmıştır. Transfer kirişi olarak da adlandırılan süreksiz kolonun mesnetlendiği kirişte kolon-kiriş kesişim bölgesinde, iki çerçeve (çubuk) sonlu eleman dikkate alınarak kesit etkilerinin daha doğru bir şekilde temsil edilmesine çalışılmıştır.



Şekil 2. Dikkate alınan bina modelinin üç boyutlu görünümü.

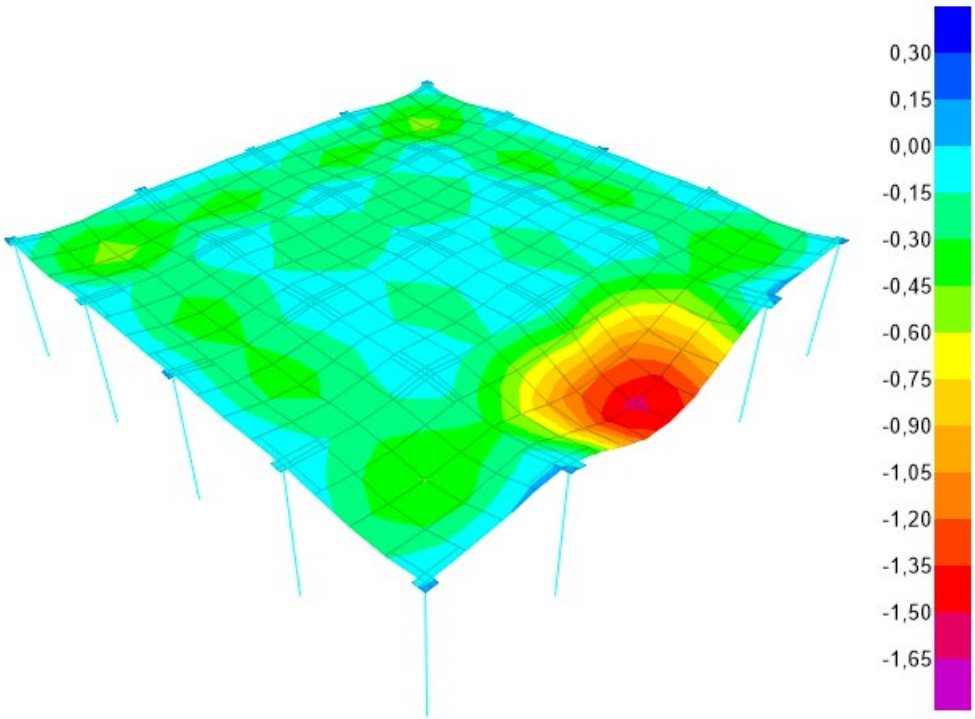
Çalışmada dikkate alınan binada süreksiz kolon üst katlarda devam etmekte ve zemin katta devam etmemektedir. Bu kolonun da bulunduğu çerçeve aksının düşey kesit görünümü Şekil 3'de sunulmaktadır.



Şekil 3. Süreksiz kolonun bulunduğu çerçevenin düşey kesit görünümü.

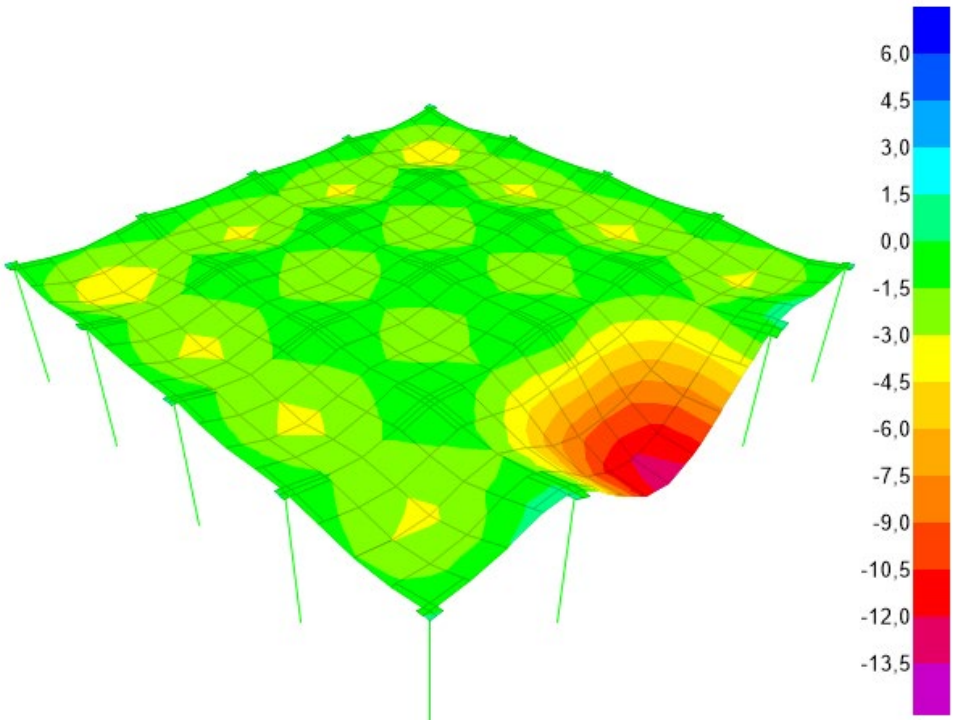
Binanın zemin katının tavanı ve süreksiz kolonun altından mesnetlendiği kirişin bulunduğu

kat döşeme ve kirişi için hesaplanan ani sehimler mm cinsinden Şekil 4'de görülmektedir.



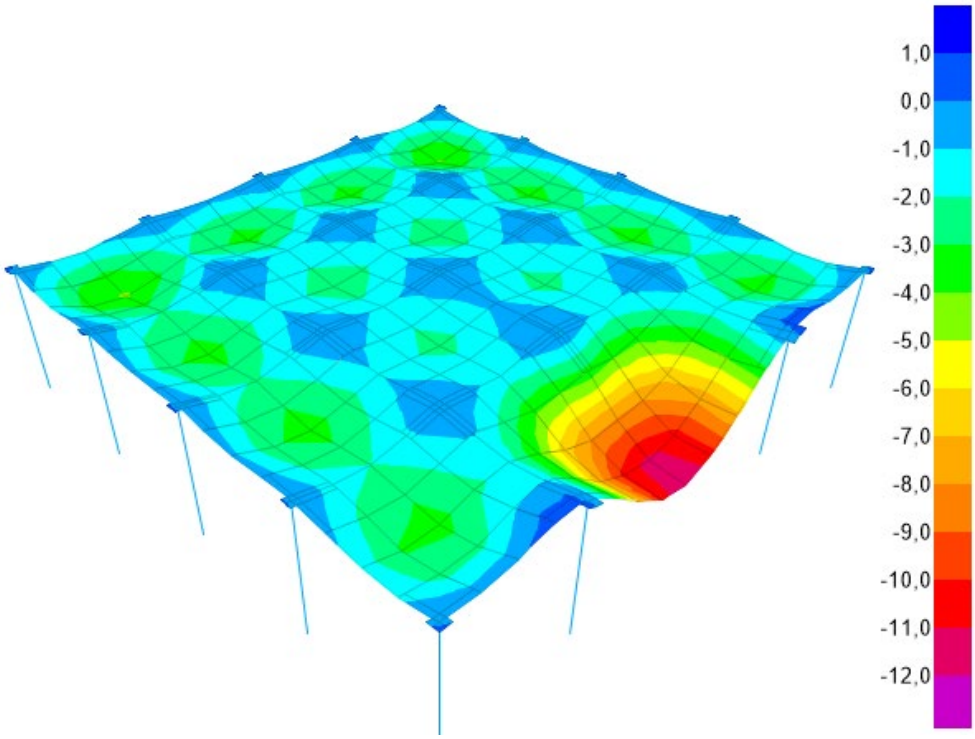
Şekil 4. Ani sehim

Çalışma kapsamında geleneksel analiz yöntemi olarak tanımlanan binanın tamamlandığı ve tüm yüklerin etkidiği analiz durumu için, binanın zemin katının tavanı ve süreksiz kolonun altından mesnetlendiği kirişin bulunduğu kat döşeme ve kirişi için hesaplanan toplam sehimler mm cinsinden Şekil 5'de görülmektedir.



Şekil 5. Geleneksel analiz sonucu bulunan toplam sehim

Çalışma kapsamında yapım aşamalarını dikkate alan analiz yaklaşımı olarak tanımlanan binanın inşaat aşamalarına göre maruz kaldığı yükleri dikkate alan analiz durumu için, binanın zemin katının tavanı ve süreksiz kolonun altından mesnetlendiği kirişin bulunduğu kat döşeme ve kirişi için hesaplanan toplam sehimler mm cinsinden Şekil 6'da görülmektedir.



Şekil 6. Yapım aşamalarını dikkate alan analiz sonucu bulunan toplam sehim

IV. SONUÇLAR

Çalışma kapsamında süreksiz kolon içeren B3 türü düzensizliğe sahip 4 katlı betonarme bir binanın taşıyıcı sistemi yapısal analizlere konu olmuştur. Bu binanın yapısal analizleri için iki yaklaşım kullanılmıştır. Birinci yaklaşım geleneksel analiz yaklaşımı olarak adlandırılan yaklaşım olup bu yaklaşımda yapının bütün ağırlığı ve yönetmelik gereği alınması gereken tüm yüklerin birlikte dikkate alındığı yaklaşımdır.

Geleneksel analiz yaklaşımıyla ve yapım aşamalarını dikkate alan analiz yaklaşımıyla bina analizlerinden elde edilen şekil değiştirme ve yer değiştirmeler karşılaştırıldığında hem değer olarak hem de bina içindeki dağılım açısından önemli farklar bulunmaktadır. Yapım aşamalarını dikkate alan yaklaşımla süreksiz kolonun alt ucunda bulunan transfer kirişinde elde edilen düşey yerdeğiştirme (sehim) değeri geleneksel analiz yaklaşımından elde edilenden daha büyük olmaktadır. Yapım aşamalarını dikkate alan yaklaşımla Transfer kirişindeki elde edilen toplam sehim değeri geleneksel analiz yaklaşımından elde edilene göre % 8.05 daha büyük olduğu tespit edilmiştir.

V. KAYNAKLAR

[1] A.O. Ateş, "Kolon Süreksizliğinin Taşıyıcı Sistem Deprem Davranışına Etkisi," (Yüksek Lisans Tezi). İstanbul Teknik Üniversitesi. Fen Bilimleri Enstitüsü. İstanbul, 2013.

[2] DBYBHY, Deprem Bölgelerinde Yapılacak Binalar Hakkında Yönetmelik, Bayındırlık ve İskân Bakanlığı, Resmi Gazete Tarihi: 14.07.2007 Resmi Gazete Sayısı: 26582, 2007.

[3] C. Ergin, "Düşeyde düzensiz yapıların dinamik davranışına deprem bölgelerinin ve zemin sınıflarının etkisinin incelenmesi," Bozok Üniversitesi. Fen Bilimleri Enstitüsü. Yozgat, 2016.
[4] ETABS, V20.0.0 - Extended Three Dimensional Analysis of Building Systems. Computer & Structures Inc., Available from www.csiamerica.com, 2023.
[5] A. Gujar, H.S. Jadhav, "Performance of multi-storey RC structure with floating column," Int Res Eng Technol, 2019.
[6] U.Ç. Koçluk, "Kolon süreksizliği bulunan betonarme bir binanın tasarımı ve deprem etkisi altındaki performansının değerlendirilmesi," (Yüksek Lisans Tezi). İstanbul Teknik Üniversitesi. Fen Bilimleri Enstitüsü. İstanbul, 2019.
[7] V. Kumar, B. Varghese, "Effect of construction sequence analysis along with p-delta and material non linearity on floating column structure," International Research Journal of Engineering and Technology. 4(05). 1946-1949, 2017.
[8] S. Panigrahi, V. Patil, H. Madan, S. Takkalaki, "Importance of Construction Sequence Analysis in design of High Rise Building," International Journal of Innovative Science. Engineering & Technology (IJISET), 2019.
[9] SAFE, Slab Analysis and Design Software. Computer & Structures Inc., Available from www.csiamerica.com, 2023.
[10] TBDY, Türkiye Bina Deprem Yönetmeliği, Çevre ve Şehircilik Bakanlığı. Yürürlük tarihi: Ocak 2019, 416 sayfa, 2018.
[11] M. Topaktaş, "Kolon süreksizliği bulunan betonarme bir binanın DBYBHY-2007 ve TBDY-2018 esaslarına göre incelenmesi," (Yüksek Lisans Tezi). İstanbul Teknik Üniversitesi. Fen Bilimleri Enstitüsü. İstanbul, 2019.
[12] TS498, Yapı Elemanlarının Boyutlandırılmasında Alınacak Yüklerin Hesap Değerleri. Türk Standartları Enstitüsü, 1997.
[13] TS500, Betonarme Yapıların Tasarım ve Yapım Kuralları. Türk Standartları Enstitüsü, 2000.
[14] R. Yaylalı, "Düşey Doğrultuda Süreksizlik ve Çerçeve Süreksizliği İçeren Binaların Deprem Performans Analizleri," (Yüksek Lisans Tezi). İstanbul Teknik Üniversitesi. Fen Bilimleri Enstitüsü. İstanbul, 2012.

The Investigation of The Effect of T6I6 Interrupted Aging on The Mechanical Properties of AA7075 Aluminum Alloy[1]

Rüçhan YILDIZ[1], Engin TAN[*,1]

[*] etan@pau.edu.tr, ORCID: 0000-0003-4441-3678
[1] *Department of Metallurgical and Materials Engineering, Pamukkale University, Denizli, Türkiye*

Abstract: AA7075 aluminum alloys are one of the essential materials of many important manufacturing sectors, such as the automotive, aerospace, and defense industries, with their high hardness, specific modulus of elasticity, and specific strength. The properties of these alloys can be improved by optimizing different heat treatment processes. In recent years, interrupted aging has been one of the heat treatment processes applied to improve properties. Unlike conventional aging processes, in the interrupted aging process, with the increase in strength and hardness, the alloys' forming ability can be improved. This study applied conventional T6 heat treatment and T6I6 interrupted aging process, one of the new generation aging processes, to commercially available AA7075 alloy at different temperatures and time parameters. T6 heat treatment optimization was carried out at two different solutionizing temperatures and times, at constant aging temperature and up to 24 hours. After T6 treatment, where the highest hardness value was obtained, T6I6 heat treatment (16 hours at 120°C + 700 hours at 65°C + 100-1000 hours at 100°C) was applied. The hardness of the samples was compared with the hardness measurements before and after the heat treatments. Optical microscope examinations were conducted to interpret the relationship between hardness changes and microstructure. As a result of the study, the hardness of the base sample without heat treatment (T0) was 77 $HV_{0.1}$, reaching 192.3 $HV_{0.1}$ after T6 treatment and 215.5 $HV_{0.1}$ after T6I6 treatment. The optical microscope examinations observed that the microstructure distribution and dimensions of the precipitate phases obtained as a result of T6 and T6I6 processes influenced the hardness change. It was determined that the secondary precipitate phases obtained at low temperatures by the T6I6 interrupted aging process were more densely and finely dispersed in the microstructure, as a result effectively obtaining the maximum hardness value.

Keywords: *AA7075, Interrupted Aging, T6I6, Hardness, Precipitate Phases*

I. INTRODUCTION

Aluminum alloys are one of the most widely used materials in technology and daily life. With their superior properties such as high specific strength (strength/density), deformability, and corrosion resistance, they are used in industries with high strength requirements, such as aerospace, automotive, and construction, as well as their attractive and bright appearance in areas such as art, building exterior coating, food packaging. It also allows it to be preferred [1, 2]. Some aluminum alloys can achieve mechanical properties superior to steel using different heat treatment processes. While the tensile strength of pure aluminum is about 70-140 MPa,

[1] This study was funded by Pamukkale University Scientific Research Projects Coordination Unit (PAUBAP), Project Number 2021FEBE067.

values up to 700 MPa can be obtained by alloying with various alloying elements and heat treatment. The place of aging heat treatment is significant in developing mechanical properties. Aluminum alloys take different names according to the alloying elements they contain. One of the most widely used aluminum alloys is AA7075 aluminum alloy. Zinc and magnesium, the main alloying elements of AA7075, directly affect the hardness increase during the aging process by forming the $MgZn_2$ precipitate. In addition, when hardened by the aging process with other elements, they form high-strength precipitates [$CuAl_2$, Mg_2Al_3, $Al_{32}(Mg, Zn)_{49}$] [3, 4].

Unique constructions with a high strength/density ratio in vehicle technology, aerospace, and especially in the aircraft industry can only be considered with aging alloys [5]. Strengthening by aging ensures the formation of homogeneously dispersed second-phase precipitates in the alloy in harmony with the main matrix. Since these precipitates have a structure compatible with the main matrix, they prevent dislocation movements in the form of an Orowan mechanism and contribute to the increase of the strength of the material. Thus, the mechanical properties of the material are improved. For the alloy to age, it must have an equilibrium diagram containing a solvus curve that dissolves at every rate in the liquid state [6]. AA7075 alloys generally contain GP regions and η′, η precipitates. During the aging heat treatment, the stable GP regions function as the nucleation centers of the semi-stable η′ ($MgZn_2$) phase, the strength-enhancing phase of the T6 temper [7]. T6 heat treatment increases the strength by increasing the aluminum alloy to a specific temperature according to its type, keeping it at this temperature for a specific time, cooling it quickly, and then aging it at a particular time and temperature according to the alloy type. T6 heat treatment is carried out in three steps: solutionizing, quenching, and aging [8].

Multistage aging processes have recently been developed for aluminum alloys to improve the hardening effect further. This heat treatment is called "interrupted" or "intermittent" aging. Secondary aging processes, called interrupted aging, are at the forefront of the heat treatment processes and are widely used as an alternative to the T6 process [9]. For specific conditions, this treatment has also been proven in previous studies to be very effective in further improving the strength levels achieved through a standard T6 treatment. Simultaneous strength and fracture toughness improvements are observed after interrupted aging applied to aluminum alloys [10]. Interrupted aging is generally the process of pre-aging the alloy at high temperatures for short periods, followed by secondary aging at low temperatures (up to 10.000 hours) to improve the microstructural properties [11, 12].

There are different temper classes depending on the application parameters of the interrupted aging process in the literature. T6I4 and T6I6 processes are the most widely used in industrial applications. T6, given in the first two rows in the notation, symbolizes the conventional aging process, and the letter I that follows represents the initial letter of the word Interrupted [13]. Fig. 1 shows the stages of the interrupted aging process [14], and Table I shows the variations of the interrupted aging process [15].

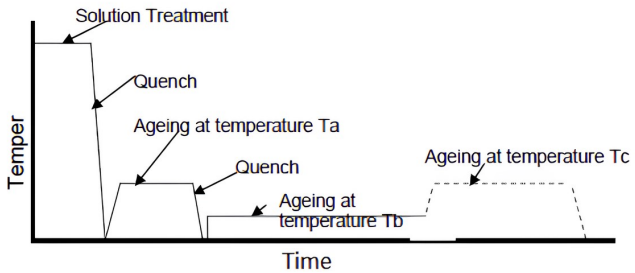


Fig.1. Application of interrupted (secondary) aging heat treatment [14]

TABLE I
INTERRUPTED AGING TEMPERS APPLIED TO ALUMINUM ALLOYS [15]

Temper	Process
T6I4	Solution treat, quench, underage at (Ta), quench, age at 25°C-65°C (T_b)
T6I6	Solution treat, quench, underage at (T_a), quench, age at 25°C-65°C (T_b), re-age at artificial ageing temperature (T_c), where $T_c \leq T_a$.
T6I7	Solution treat, quench, underage at (T_a), cool slowly (furnace cool or natural cool)
T6I76	Solution treat, quench, underage at T_a, quench, age at 25°C-65°C (T_b), re-age at artificial ageing temperature (T_c), where $T_c > T_a$.
T77I4	Solution treat, quench, age at (T_{a1}), age at temperature (T_{a2}), where $Ta_2 > Ta_1$,quench, age at 25-65°C (T_b)
T8I4	Solution treat, quench, cold work, underage at (T_a), quench, age at 25°C to 65°C (T_b)
T8I6	Solution treat, quench, cold work, underage at T_a, quench, age at 25°C-65°C (T_b), re-age at artificial ageing temperature (T_c), where $T_c \leq T_a$.
T9I4	Solution treat, quench, underage at (T_a), cold work, age at 25°C-65°C (T_b)
T9I6	Solution treat, quench, underage at T_a, cold work, age at 25°C-65°C (T_b), re-age at artificial ageing temperature (T_c), where $T_c \leq T_a$.

T6I6 interrupted heat treatment is carried out at temperatures equal to or lower than the T6 heat treatment temperature. The interrupted aging step at TB temperature aims to facilitate controlled secondary precipitation. It has been determined that the secondary precipitation during the interruption in the TB temperature changes the size, distribution, and proportions of the sediment phases, and subsequent T6I6 heat treatment results in higher mechanical properties and improvements in ductility, which is the opposite [16-18].

In this study, the relationship between hardness and microstructure was investigated with the new generation T6I6 interrupted aging process, which is an alternative to the conventional T6 heat treatment of AA7075 aluminum alloy, which is widely used in the industry, by optimizing the T6 heat treatment time and temperature parameters.

II. MATERIAL AND METHOD

AA7075 aluminum alloy was supplied from Seykoc Aluminum (Turkey) in sheet and bar forms, and T651 and T6 tempers, respectively, and test samples were prepared according to ASTM E8/E8M-09, TS EN ISO 7438-2021 and ASTM G99 standards [19-21]. The nominal chemical compositions (mass ratio, %) of the studied alloy are given in Table II.

TABLE II
CHEMICAL COMPOSITION OF ALLOY USED IN THE STUDY (%)

Alloy	Cu	Zn	Mg	Fe	Si	Mn	Cr	Ti	Al
7075 Bar	1.62	5.7	2.65	0.175	0.0526	0.046	0.237	0.0481	Bal.
7075 Sheet	1.5	5.8	2.5	0.14	0.07	0.06	0.18	0.02	Bal.

Since the test samples were supplied in different temper classes, T651 and T6, the homogenization heat treatment was kept at 500°C for 4 hours and slowly cooled in air. T6 heat treatment optimization was performed at two different solutionizing temperatures and times, at the same aging temperature and up to 24 hours of aging heat treatment (Table III).

TABLE III
TEMPERATURE-TIME PARAMETERS OF T6 HEAT TREATMENT OPTIMIZATION

Experiment Number	Alloy → Heat Treatment ↓	AA7075
1	**Solutionizing**	485°C 2 h
	Aging	120°C 4-8-12-16-20-24 h
2	**Solutionizing**	475°C 4 h
	Aging	120°C 4-8-12-16-20-24 h

T6I6 heat treatment was applied to AA7075 aluminum alloy after the temperature and time were determined after T6 heat treatment optimization. The T6I6 heat treatment temperature is determined as 100°C because it must be equal to or lower than the T6 heat treatment temperature. The graph of the applied heat treatments is given in Fig. 2. After T6 heat treatment and before T6I6 heat treatment, intermediate heat treatment was applied at 65°C for 700 hours.

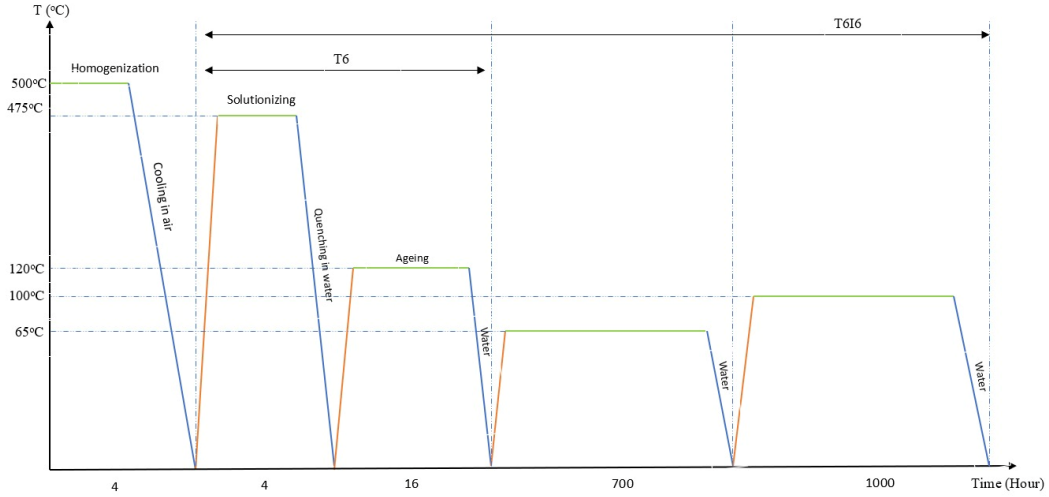


Fig.2. Heat treatment graph applied to AA7075 alloy

T6 and T6I6 heat treatments of AA7075 aluminum alloys were carried out in a heat treatment furnace with a capacity of 1200 °C and a fan oven with a temperature of up to 250 °C in the Heat Treatment and Casting Laboratory of the Faculty of Technology, Department of Metallurgy and Materials Engineering of PAU.

The hardness values of the samples subjected to T0, T6, and T6I6 heat treatments were measured as HV0,1 in the micro Vickers device in the Material Mechanics Laboratory of the PAU Technology Faculty Metallurgy and Materials Engineering Department. Hardness measurements were carried out by taking six measurements from the test samples. Thus, it is aimed to find the most accurate and homogeneous hardness values.

Metallographic processes were carried out to obtain optical images of the T0 sample and the samples with the highest hardness value after heat treatment. Sanding operations were carried out using 320-600-800-1200 mesh SiC sandpaper, and polishing was carried out using 1µ felt and 1µ diamond solution in Metkon Forcipol 1V brand automatic sanding-polishing device. The polished samples were etched with Keller etching solution with 2% HF + 3% HCl + 5% NHO_3 + 90% pure water content to carry out examinations under the optical microscope. Microstructure examinations were carried out using Nikon Eclipse LV150NL optical microscope in the Material Analysis Laboratory of the Faculty of Technology, Department of Metallurgical and Materials Engineering at PAU.

III. RESULTS

After the homogenization process was applied to AA7075 aluminum alloys (4 hours at 500°C + cooling in the air), the hardness value was measured as 77 $HV_{0.1}$. The hardness values measured due to the heat treatments performed with the T6 heat treatment parameters seen in Table II are given in Table III. As can be seen in Table III, the maximum hardness value after the measured hardness values were obtained at the 475°C hour solution temperature applied in experiment no.2 and the 16-hour aging period at 120°C for 4 hours. At longer aging times, there was a decrease in hardness due to excessive aging. The hardness, 77 $HV_{0.1}$ before the aging process, increased by 149.7% to 192.3 $HV_{0.1}$.

TABLE IV
HARDNESS RESULTS AFTER T6 HEAT TREATMENT OPTIMIZATION

Aging Time (Hour)	1st Experiment ($HV_{0,1}$)	2nd Experiment ($HV_{0,1}$)
0	94,3	96,5
4	152,6	147,4
8	159,2	165,2
12	164,3	176,9
16	171,5	192,3
20	172,6	185,3
24	185,6	173,9

7xxx series alloys tend to have high strength and hardness after T6 aging due to the precipitation of semi-consistent η′ non-equilibrium phases and a small number of η-equilibrium phases during aging [22]. This significant increase in hardness can be explained by the fact that second phases, such as $MgZn_2$ precipitated during aging, are dispersed in the structure, making dislocation movements more complex [23]. The hardness change after T6I6 heat treatment applied after T6 heat treatment is shown in Fig. 3.

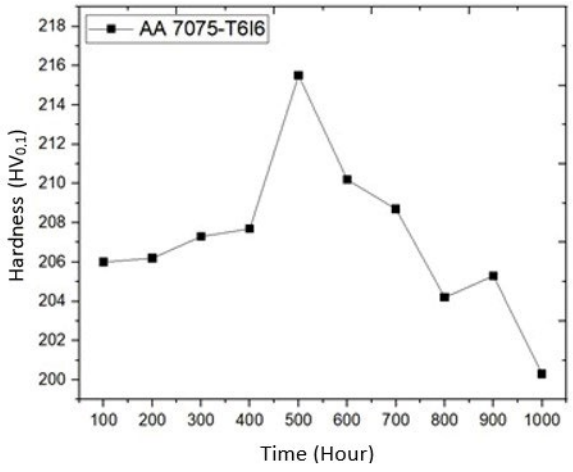


Fig. 3. Hardness change after T6I6 heat treatment applied to AA7075 alloy

As a result of the T6I6 heat treatment applied to the AA7075 alloy, the highest hardness was measured as 215.5 HV0.1 at the 500th hour, as seen in Fig. 3. An increase of 17% was observed compared to the T6 (192.3 $HV_{0.1}$) heat treatment.

The increase in hardness as a result of T6I6 interrupted aging results in a higher number of finer and more densely dispersed precipitates, and although some η′ precipitates grow and become somewhat more prominent during the T6I6 aging process, the final strength of AA7075-T6I6 alloy compared to AA7075-T6 alloy there is more complete precipitation rate

in its microstructure [24].

Optical images of AA7075 alloy after T6 and T6I6 heat treatments were examined. Optical images were taken at 100X magnification. Fig. 4 shows the microstructure changes due to the T6 and T6I6 heat treatments applied to the AA7075 alloy, and the optical images of the T0 sample are given.

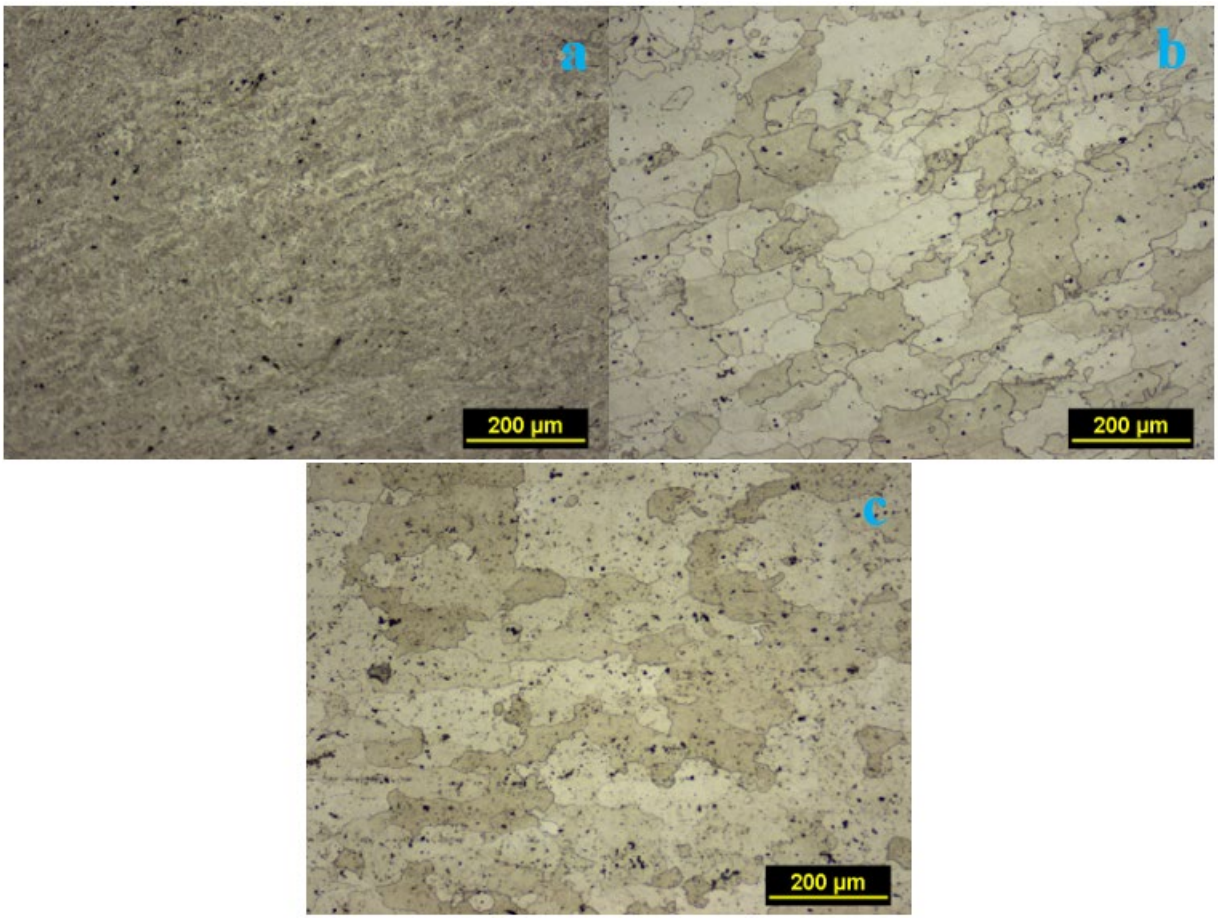


Fig. 4. Microstructure images of AA7075 alloy a) T0, b) T6, c) T6I6-500

The factors affecting the hardness increase are the precipitated secondary phase particles. When Fig. 4 is examined, it is seen that aging affects grain size as expected. The grains are coaxial in any direction. The visibility of the grains in the structure became more visible with increasing aging time [25].

As a result, higher hardness values can be achieved with interrupted aging heat treatment compared to T6 temper, meaning higher strength materials can be produced. This means reducing aluminum weight in at least half of current applications, particularly in vehicle manufacturing is possible [14].

IV. CONCLUSION

This study applied conventional T6 aging heat treatment and new generation T6I6 interrupted aging heat treatment of AA7075 alloy, which is widely used commercially. The effects of applied heat treatments on the hardness and microstructure of the alloys were determined. The results of the study are presented below in general:

- T6 peak hardness value was obtained after 475°C for 4 hours of cooling in water and 120°C for 16 hours of aging.
- The hardness, which was 192.3 $HV_{0.1}$ due to AA7075-T6 heat treatment, increased to 215.5 $HV_{0.1}$ with a 6% increase due to T6I6 heat treatment.

- After the T6I6 interrupted aging process, it was observed that the visibility of the grains and the density of the precipitates increased in the microstructure.

REFERENCES

[1] Ş.Y. Güven, ve Y. Delikanlı "AA 2024 Alüminyum Alaşımında Çökelme Sertleşmesinin Mekanik Özelliklere Etkisi", Teknik Bilimler Dergisi, vol. 2, pp. 13-20, 2012.

[2] H.I.A. AlSaadi, ve R.F. Tunay, " Suni Yaşlandırma İşleminin Alüminyum Alaşımının Sertliği Üzerine Etkisi", Journal of Engineering Sciences and Design, vol. 5(3), pp. 525-532, 2017.

[3] B. Akyuz ve S. Şenaysoy "Alüminyum Alaşımlarında Yaşlandırma İşleminin Mekanik Özellikler ve İşlenebilirlik Üzerindeki Etkisi" Bilecik Şeyh Edebali Üniversitesi Fen Bilimleri Dergisi, vol. 1, pp. 1-9, 2014.

[4] O. B. Tehinse, "Response of 7050 and 7075 Alloys to High Temperature Pre-Precipitation Heat Treatment", MsC. Thesis, University of Manitoba, Winnipeg, Canada. 2014.

[5] M. Esmailian, M. Shakouri, A. Mottahedi and S.G. Shabestari, "Effect of T6 and re-aging heat treatment on mechanical properties of 7055 aluminum alloy", International Journal of Chemical, Molecular, Nuclear, Materials and Metallurgical Engineering, vol. 9-11, pp. 1230-1233, 2015.

[6] M. Demir, "Alüminyum-7075 Dövme Alaşımlarının Dökülebilmesi ve T6 Yaşlandırma Isıl İşlemi İle Mekanik Özelliklerinin İyileştirilmesi" Sakarya Uygulamalı Bilimler Üniversitesi Yüksek Lisans Tezi, Sakarya, 2020.

[7] M. Y. Demirel ve İ. Karaağaç, "7075-T6 Alaşımının Mikroyapı ve Mekanik Özelliklerine Tavlama İşleminin Etkisinin Deneysel Olarak Araştırılması", Politeknik Dergisi, vol. 2, pp. 283-289, 2020.

[8] E. Tan, "Alüminyum alaşımlarında blister oluşumu", Doktora Tezi, Pamukkale Üniversitesi Fen Bilimleri Enstitüsü, Denizli, 2011.

[9] W. Haisheng, Y. Danqing, L. Huiqun and W. Bin, "Microstructure and Mechanical Properties of Interrupted Aged Cast Al–4.5Cu–3.5Zn–0.5 Mg Alloy", Materials Letters, Vol. 285, pp. 1-5, 2021.

[10] R.K.W. Marceau, G. Sha, R.N. Lumley and S.P. Ringer, "Evolution Of Solute Clustering In Al–Cu–Mg Alloys During Secondary Ageing", Acta Materialia vol. 58, pp. 1795–1805, 2010.

[11] J. Buha, R.N. Lumley, A.G. Crosky, "Secondary Ageing in An Aluminium Alloy 7050", Materials Science and Engineering A vol. 492, pp. 1–10, 2008.

[12] J.M. Tsai, "Study of interrupted aging in Al-Cu-Mg alloys", master's thesis, Colorado School of Mines, Colorado, 2013.

[13] R. Lumley, A.J. Morton, R.G. O'Donnell and I.J. Polmear, "New heat treatments for age-hardenable aluminum alloys" Heat Treating Progress, vol. 5, pp. 23-29, 2005.

[14] B. Baksan, I. Celikyürek, and O. Torun, "Influence of ıntermittent aging in aa7075 aluminum alloy", The Eurasia Proceedings of Science Technology Engineering and Mathematics, vol. 11, pp. 141-145, 2020.

[15] R.N. Lumley and A.J. Morton "Temper developments using secondary ageing", Materials Forum, vol. 28, pp. 85-95, 2004.

[16] R. G. O'Donnel, R.N. Lumley. and I.J. Polmear, "Observations of deformation in secondary aged aluminium alloys", Proceedings of the 9th International Conference on Aluminum Alloys, Brisbane, Australia, pp. 975–979, 2004.

[17] R. N. Lumley, I. J. Polmear, and A. J. Morton, "Interrupted aging and secondary precipitation in aluminium alloys", Materials Science and Technology, vol. 19, pp. 1483-1490, 2003.
[18] J. Buha, R.N. Lumley, A. Crosky, and H. Hono, "Secondary precipitation in an AlMgSiCu alloy", Acta Materialia, vol. 9, pp. 3015-3024, 2007.
[19] ASTM E8 / E8M-09, "Standard Test Methods For Tension Testing Of Metallic Materials", *ASTM International, West Conshohocken, PA*, 2009.
[20] ASTM G99-17, "Standard test method for wear testing with a pin-on-disk apparatus", *ASTM International, West Conshohocken, PA*,(2017.
[21] TS EN ISO 7438, Metallic Materials - Bend Test, Türk Standartları Enstitüsü,(2021).
[22] Y. Luo, Y. Zhuang, C. Li, S. Li, G. Bao, T. Wei, S. Sha, and X. Xu, "Microstructure and properties of T6I4 aged 700-MPa-grade aluminum alloy", Journal of Materials Engineering and Performance, vol. 31, pp. 9839-9849, 2022.
[23] A.D. Isadere, B. Aremo, M.O. Adeoye, O.J. Olawale, and M.D. Shittu, "Effect of heat treatment on some mechanical properties of 7075 aluminum alloy", Materials Research, vol. 16, pp. 190-194, 2013.
[24] J.F. Li, Z.W. Peng, C.X. Li, Z.Q. Jıa, W.J. Chen, and Z.Q. Zheng, "Mechanical properties, corrosion behaviors and microstructures of 7075 aluminium alloy with various aging treatments", Transactions of Nonferrous Metals Society of China, vol. 4, pp. 755-762, 2008.
[25] Ö. Kılıç, "Alüminyum Alaşımlarının Dökümünde Yörüngesel Çalkalamanın Mikroyapı ve Mekanik Özelliklere Etkisi", Yüksek Lisans Tezi, Yıldız Teknik Üniversitesi Fen Bilimleri Enstitüsü, İstanbul, 2020.

Detection of COVID-19 in X-Ray Images Using Image Processing and Machine Learning Methods

Emre Esef KILIÇDOĞAN[*,1], Mahmut BÜYÜKBAŞ[1], Bekir Hakan AKSEBZECİ[2]

[*]: emreesef.kilicdogan@agu.edu.tr, ORCID: 0009-0003-4138-416X
[1] *Department of Electrical & Electronics Engineering, School of Engineering, Abdullah Gül University, Kayseri, Turkey*
[2] *Department of Biomedical Engineering, School of Engineering, Abdullah Gül University, Kayseri, Turkey*

Abstract— The global repercussions of the COVID-19 pandemic have been profound and have comprehensively affected both human well-being and the world economy. The crisis underlined the critical importance of fast response time and manageable workloads for health workers, especially in a global context. Taking all these into account, it is understood that modern computer technologies can play an important role in reducing the burden on health workers in such crisis situations and acting quickly. The aim of this study is to develop an optimized, high-accuracy and fast algorithm by combining image processing techniques with a supervised machine learning model that can be trained quickly in a scenario with limited resources and data sets, such as COVID-19. It focuses on the use of a COVID-19 radiography dataset acquired from Kaggle, which contains a total of 33920 images. The dataset includes three classes: normal patient radiographs (10701 images), radiographs of non-COVID infected patients (11263 images), and COVID-19 infected people (11956 images). Furthermore, the dataset contains binary masks for lung segmentation alongside each image. However, the algorithm introduced in this study achieves lung segmentation autonomously through image processing methods. This approach strives to enhance the self-reliant accuracy of machine learning models by eliminating the manual mask annotation process during critical scenarios like the COVID-19 crisis. The first 999 of the COVID ones and the first 999 of the non-COVID ones of the images obtained from this dataset were selected for binary classification, which resulted in both a scenario with limited resources being created and the necessary time and computational cost for training. For the construction of the proposed algorithm in this study, at first it was enabled to perform automatic segmentation of the lungs with the image processing functions of OpenCV. A total of 111 different features were extracted from these segmented images and after that bi-directional and forward selection algorithms were applied. The optimal configuration involved using 20 features per image, which yielded the highest level of accuracy. Following this, various supervised machine learning algorithms were trained using the identical set of chosen features, subsequently. The algorithms obtained in their latest form process the raw images fed to them using image processing techniques and perform the segmentation of the lungs. From this segmentation, 20 predetermined features are taken as input and finally the patient's prediction of having COVID-19 or not is made. The XGBoost classifier outperformed other supervised machine learning methods used, achieving a classification accuracy rate of 96.44%.

Keywords: *COVID-19, Machine learning, Medical image processing, Feature extraction, Feature selection*

I. INTRODUCTION

The COVID-19 virus presents a significant pathogen that primarily targets the lungs of patients, resulting in a range of symptoms including respiratory difficulties, fever, and sore

throat [1]. Detection of this virus is accomplished through diagnostic methods such as Polymerase Chain Reaction (PCR) and antigen tests [2]. However, the PCR test requires a substantial amount of time for completion, while the antigen test offers quicker results within 15 to 30 minutes. Given these considerations, there has been a research effort focused on exploring image processing and machine learning techniques to develop a highly accurate predictive model.

Recent studies [3-5] have shown that the diagnosis of COVID-19 using deep learning models with chest X-ray images is possible with high accuracy. However, deep learning techniques, which are commonly used for this task, require large amounts of data to train and expensive GPUs to process. This problem can be solved by transfer learning methods and still high accuricies can be reached but deep learning algorithms do not have a clear workflow like traditional machine learning algorithms, which can make them inflexible for developers and hard to understand for researchers.

One study by Khuzani et al. [6] proposed a neural network classifier with three different class outputs (Normal, COVID-19, Pneumonia) for X-ray images to diagnose COVID-19. Their team focused on the extraction of properties such as textural properties, FFT, wavelet, GLCM, and GLDM methods. In this project, similar features are extracted from the image after masking. Another study by Zhang et al. [7] investigated the ResNet-18 classifier with three different classes, the same as Khuzani [6] et al.'s team. They achieved an accuracy of 92.49%.

For this project, we utilized advanced image processing techniques and created our own method for the lung segmentation. For this issue, another study [8] reported that they have used deep learning for the segmentation of the lungs which may results more accurate segmentations however, in our case we have limited time and data so that training another AI model would not be efficient.

We applied supervised machine learning models and evaluated them to determine the one that yielded the highest accuracy. Our primary objective was to identify the most effective method through comprehensive testing and evaluation. The selected approach, resulting from our meticulous investigation, is emphasized as a significant achievement in terms of accuracy and reliability because any part of our final model can be modified according to the needs of the future works.

II. METHODOLOGY

In this study, the COVID-19 Radiography Database from Kaggle is utilized [3]. The dataset contains a total of 33920 images which are 11956 COVID-19, 11263 non-COVID infections (Viral or Bacterial Pneumonia), and 10701 Normal, while inherently includes masks for each image. However, the proposed method in this paper employs an algorithmic approach to automatically generate masks. This adaptive algorithm enables the model to effectively process X-ray image datasets from various sources, eliminating the need for pre-existing masks.

The primary goal of this study is to develop a binary classifier model capable of determining the presence or absence of COVID-19 infection in patients by analyzing the radiographic images. Notably, this goal is pursued without resorting to complex deep learning classifier models. Instead, the performance of different machine learning classifiers is comprehensively evaluated and compared. Additionally, a concise set of features is employed for training the classifiers, optimizing the accuracy of the machine learning model while minimizing the complexity of features.

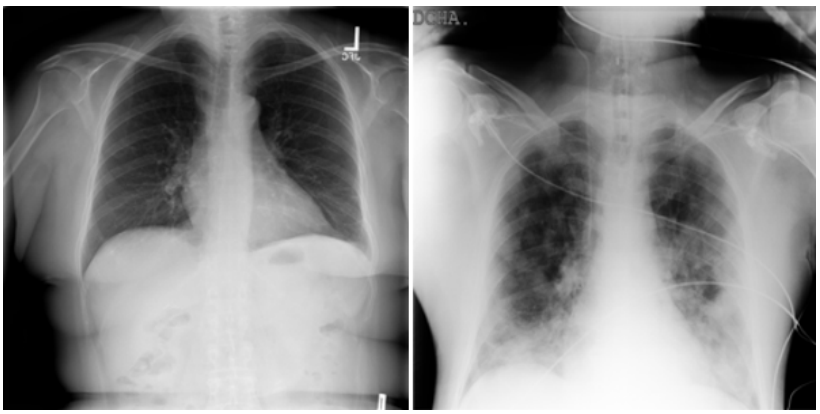


Fig. 1. X-ray images: COVID (left) and non-COVID (right)

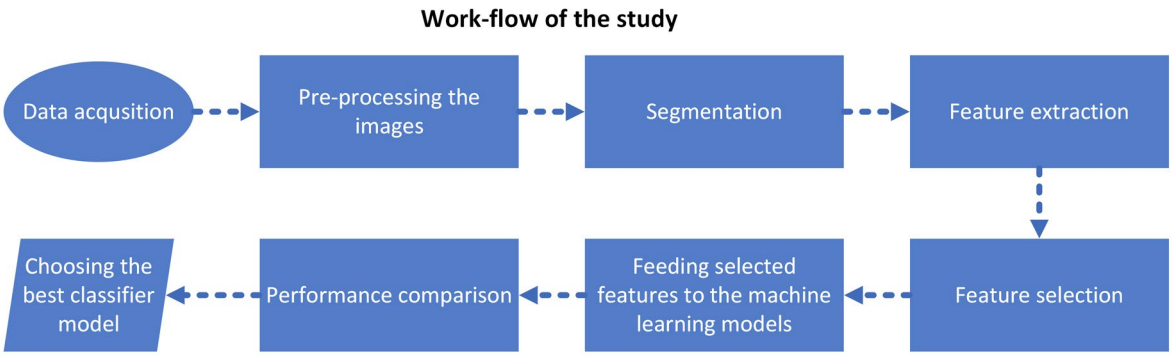


Fig. 2. Workflow of the study.

A. Pre-Processing the Data

In the dataset, all images were of equal size, yet certain images displayed larger lungs, arms, or necks, whereas others displayed very small lungs with no arms or neck present. Furthermore, some images contained superfluous elements, such as dates or numbers, which may have a minor impact on the machine learning model or image processing algorithms. For this reason, to improve the data quality, an optimal size was determined that matches all the image data, and each image in the specified data set was cropped at the same rate. This eliminated undesirable noise and brought the lung area closer. Figure 3 displays an example of the cropped image.

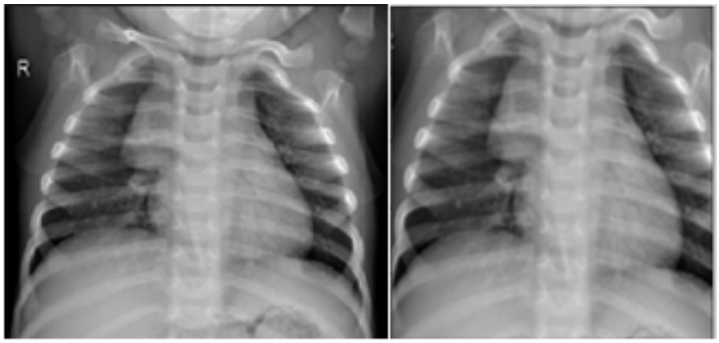


Fig. 3. X-ray images: Original image (left) and cropped image (right).

B. Detection of the Region of the Interest

The masks are essential to filter out the noise and exclude the irrelevant parts of the image in training machine learning models. The automated model for the mask creator is achieved by use of several image processing techniques, which will be described in this section. It is

important to note that the subsequent steps are exclusively employed for creating masks and not for enhancing image quality or refining the models' performance.

As a first step of the creation of the mask, Contrast Limited Adaptive Histogram Equalization (CLAHE) is applied to accentuate disparities in luminosity between lighter and darker regions within the images. This choice is motivated by the observation that the pulmonary features within the images exhibit relatively reduced intensities compared to other anatomical components. This adjustment of pixel intensity diversity is expected to result in an enhancement in the quality of the generated masks. Furthermore, it is pertinent to note the precedent established by Khuzani et al. [7], who previously incorporated adaptive histogram equalization as an initial step prior to feature extraction. In alignment with this prior practice, the current study incorporates CLAHE as an essential aspect of the mask creation process. Empirical investigations have confirmed that the imposition of contrast limitation during this procedure leads to a noticeably more effective outcome in terms of masking efficiency.

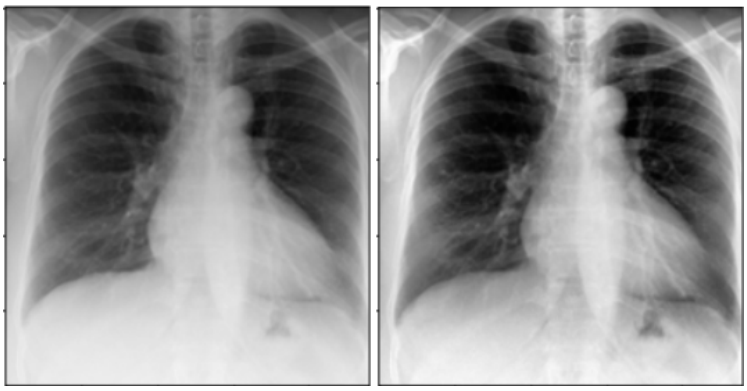


Fig. 3. X-ray images: Original image (left) and CLAHE applied image (right).

Subsequently, Gaussian blurring is implemented on the images to address extraneous noise within both the body and lung regions. Notably, empirical investigations conducted within the scope of this project revealed that the sequencing of Gaussian blurring after contrast limited adaptive histogram equalization yielded superior results in the context of mask generation. This strategic sequencing is pursued with the aim of enhancing.

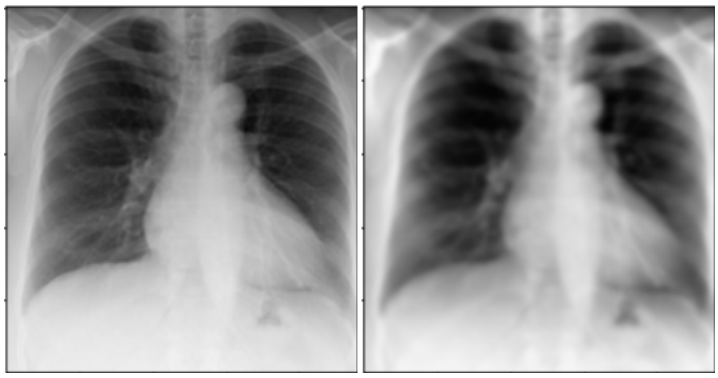


Fig. 5. X-ray images: Original image (left) and Gaussian blur applied image (right).

Proceeding further, Otsu's thresholding method is employed to generate an initial mask. The selection of the Otsu method is underpinned by its adoption as recommended within the OpenCV library documentation [11]. This method is chosen due to its capacity to identify an optimal threshold point situated between two prominent peaks discernible within the histogram of the images a principle well-suited for application within the context established through the procedural steps.

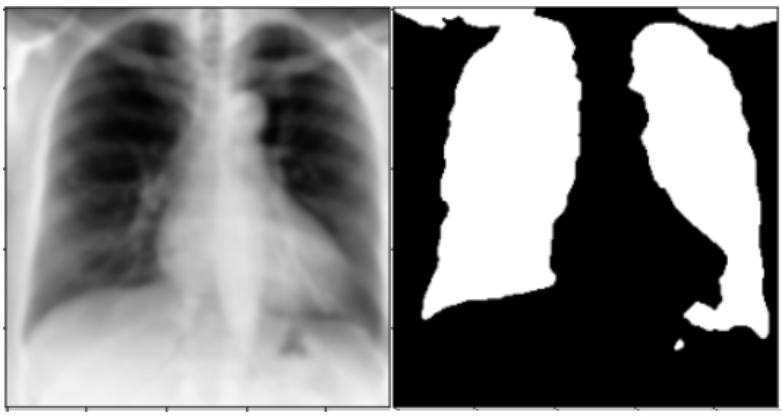


Fig. 6. Otsu's binarization method applied to create mask.

Finally, a morphological closing operation is implemented to enhance the quality of the mask. This operation serves the dual purpose of refining the mask quality and eliminating incidental small white regions that are extraneous to the lungs.



Fig. 4. Raw mask (left) and closing applied mask (right).

C. *Feature Extraction*

In the process of feature extraction, the Pyfeats library employes a crucial role by offering a variety of methods to extract distinctive characteristics from the data. This library's versatility empowers users to select from a broad spectrum of feature extraction techniques [9]. A notable aspect of this library is its reliance on masks, which are related to the original images. These masks automatically facilitate a process where images are prepared for feature extraction through masking. The objectives of enhancing efficiency and optimizing time utilization are central to this endeavor. This is achieved by selectively extracting features that carry significant relevance, effectively reducing the computational workload and saving processing time. It's important to highlight that the chosen features effectively capture the intrinsic qualities of the images being examined. In total, this process yields 111 distinct features for each individual image.
Textural Features that has been gathered using the library:

1- First order statistics/statistical features (FOS/SF):

The first-order statistics (FOS) encompass essential statistical features derived from the histogram information of the images. This histogram serves as an empirical probability density function, representing the distribution of individual pixel values within the image. These

statistical features offer insights into the basic characteristics of the pixel intensity distribution, playing a crucial role in image analysis and interpretation.

The outputs of the FOS are the following: Mean, standard deviation, median, mode, skewness, kurtosis, energy, entropy, minimal gray level, maximal gray level, coefficient of variation, percentiles (10, 25, 50, 75, 90) and histogram width.

2- Gray Level Co-occurance Matrix (GLCM):

Introduced by Haralick, the Gray Level Co-occurrence Matrix (GLCM) is a powerful method grounded in the estimation of second-order joint conditional probability density functions. This matrix serves as a comprehensive representation of the relationships between pairs of pixel values within an image. By capturing the frequency and spatial arrangement of these value pairs, GLCM provides valuable insights into texture patterns, spatial distribution, and the interplay of gray levels. This technique finds applications across various fields, offering a deeper understanding of the structural characteristics inherent in images.

The outputs of the GLCM is the following: Angular second moment, contrast, correlation, sum of squares: variance, inverse difference moment, sum average, sum variance, sum entropy, entropy, difference variance, difference entropy, information measures of correlation.

3- Local Binary Pattern (LBP):

Ojala is credited with pioneering the Local Binary Pattern (LBP), a robust and efficient method for characterizing textures. The LBP feature vector is generated using a straightforward algorithm: It starts by defining a circular neighborhood around each pixel. This circle, with a radius of R, encompasses P equidistant spots on its perimeter relative to the center pixel. These P spots are strategically selected. Depending on whether the gray value of each spot is greater or smaller than the gray value of the central pixel, a corresponding binary digit sequence of 0s and 1s is generated. This process effectively encapsulates local texture information, enabling the creation of feature vectors that capture texture patterns with exceptional efficacy. Ojala's innovation has found widespread use in diverse applications, facilitating advanced texture analysis with remarkable accuracy and efficiency.

The outputs of LBP is the following: 6 different scaled features including energy and entropy.

4- Gray Level Run Length Matrix (GLRLM):

A gray level run denotes a grouping of image points characterized by identical gray level values, arranged linearly in a sequence. The length of a run is determined by the count of image points it comprises. In other words, the run's length corresponds to the number of consecutive pixels sharing the same gray level value along the specified line. This concept plays a crucial role in image analysis, contributing to the characterization of various features and patterns within images based on their gray level distributions.

The outputs of GLRLM is the following: Short run emphasis, long run emphasis, gray level non uniformity, run length non-uniformity, run percentage, low gray level run emphasis, high gray level run emphasis, short low gray level emphasis, short run high gray level emphasis, long run low gray level emphasis, long run high level emphasis.

Histogram-Based Features:

1- Histogram (32 bins): This feature involves dividing the histogram into 32 distinct bins and using the value of each bin as a feature for the model.

The outputs of the Histogram feature are as follows: A 1x32 feature matrix is generated, encompassing information about each individual bin within it. This matrix effectively summarizes the distribution of pixel values across the entire spectrum, providing valuable insights into the image's intensity distribution.
Other Features:

1- Zernike's moments:

An image moment refers to a particular weighted average, or moment, calculated from the intensities of pixels within an image. This concept, extensively used in image processing, computer vision, and related domains, often involves functions derived from these moments. The selection of specific image moments is typically driven by their desirable characteristics or interpretations, enhancing their relevance in various applications. The kernel of a Zernike complete orthogonal polynomial, defined within the confines of the unit disc in polar coordinate space, forms a collection of Zernike complete orthogonal polynomials. These polynomials constitute a comprehensive set that possesses orthogonal properties, enabling them to be employed effectively in various mathematical and analytical contexts.

The outputs of Zernike's moments is the following: Orthogonal moments invariants with respect to translation.

2- Hu's moments:

Closely resembling Zernike's moments with minor distinctions, Hu's moments offer comparable characteristics in their calculation.

The outputs of Hu's moments encompass: Moment invariants that remain unchanged in the presence of translation, scaling, and rotation operations. These invariants are robust descriptors that facilitate reliable pattern recognition and analysis across diverse image transformations.

D. Feature selection

Feature selection plays a crucial role in today's field of data science and various machine-learning applications. When dealing with a set of data, not all the characteristics hold the same level of importance in relation to the outcomes and precision. In some datasets, there might be an excessive number of characteristics, which could lead to sluggish performance of machine learning models, or certain traits might guide the classification process in the wrong direction. This is why, in this study out of a total of 111 features extracted from each image, the top 20 features with the most significance were chosen. The selection of these 20 features was guided by the graphs obtained from the algorithms used for selecting the features. It was noted that once the set of 20 features was reached, any further addition did not bring about a significant change in the accuracy of the model.

The feature selection process utilized the Mlxtend (machine learning extensions) Python library [10]. This library was opted for as the feature selector because it has the ability to train a variety of classifier models, as desired by the users. It assesses the classifier's performance using K-fold cross validation with the individually selected features, thus evaluating each model's performance separately while determining the optimal features. This approach also contributes to the enhanced performance of each model individually during the final comparison of models.

In this project, two selection methods provided by the library were employed: sequential forward selection and bi-directional elimination [7]. These methods are also referred to as wrapper methods. Wrapper methods are anchored in a specific machine-learning algorithm that the user aims to apply to a given dataset. They explore all possible combinations of features and identify the most favorable ones for the designated machine-learning algorithm.

Forward Selection

The forward selection algorithm involves a step-by-step process for building regression models. To start, a certain confidence level, often 95%, is chosen. The algorithm then begins by creating simple regression models using each individual feature, selecting the one with the smallest p-value. Next, it expands the models by adding one more feature to the previously selected one(s). The new feature is chosen based on the lowest p-value. This process continues until adding more features doesn't significantly reduce the p-value below the chosen confidence level. At that point, the algorithm stops. This method helps identify the most influential features in predicting the outcome while considering statistical significance.

Bi-Directional Elimination (Stepwise Selection)

This method is akin to backward elimination, which is a technique used for refining regression models. Rather than introducing new features, it focuses on the significance of features that were previously included. If any of these features are deemed less important, they are eliminated. This step-by-step approach iteratively assesses the significance of existing features and trims away those that have a minor impact on the model's predictive power. The process continues until no more insignificant features are found, resulting in a streamlined model that retains only the most relevant predictors. This technique is particularly useful for simplifying complex models while preserving their accuracy.

E. Classification models and performance evaluation methods

In this paper, various classification models from the scikit-learn library [12] were implemented and evaluated. These models have different strengths and applications in machine learning. Logistic Regression is a method used to predict binary outcomes based on past data observations. It's commonly used when the outcome can be categorized into binary classes. Support Vector Machines (SVM) are used to create a separation between different classes in a dataset by mapping training examples to points in space. The goal is to maximize the gap between these classes, and new examples are classified based on which side of the gap they fall on. Random Forest is a versatile technique that improves predictive accuracy and prevents overfitting. It achieves this by building multiple decision tree classifiers on various subsets of the dataset and then averaging their predictions. Naive Bayes algorithms are built on the principles of Bayes' Theorem. These algorithms assume that the features being classified are independent of each other. Naive Bayes classifiers are useful for their simplicity and effectiveness in various applications. Extreme Gradient Boosting (XGBoost) is a powerful ensemble method that combines gradient boosting and classification. It creates a series of models, each correcting the errors of the previous one. This iterative learning process allows the model to progressively adapt and fit the data.

In the field of biomedical image classification, these computational models play a crucial role due to their unique characteristics and analytical abilities. Biomedical images, especially X-ray radiographs used to detect conditions like COVID-19, often show complex patterns and subtle details that need a strong classification method. Logistic Regression is handy for telling apart two outcomes, which suits well for distinguishing COVID-positive and COVID-negative cases. Support Vector Machines create smart boundaries between categories and work well for spotting structural differences that suggest viral infections in X-ray images. Random Forest is good at preventing overfitting and making accurate predictions, which is useful when working with limited biomedical data. Naive Bayes captures specific features in X-rays by assuming they're independent. Extreme Gradient Boosting, with its iterative learning, is promising for improving sensitivity in identifying complex conditions like COVID-19 in medical images.

Altogether, these models help experts quickly and precisely identify critical health issues in biomedical images.

Regarding performance evaluation, the initial step involves a comparison of accuracy scores. Nevertheless, relying solely on accuracy scores proves insufficient for a comprehensive assessment of a model's performance. To address this limitation, a comprehensive analysis is conducted, encompassing various metrics such as, accuracy, sensitivity, specificity, precision, Area Under the Curve (AUC) of Receiver Operating Characteristics (ROC) on 10-fold cross validation for all trained models. These metrics are subsequently deliberated upon in the forthcoming sections. Within the confines of this section, a succinct exposition of the rationale underpinning the chosen performance criteria is presented.

III. RESULTS

After completing the process of feature selection, each classification algorithm was individually trained using the specific features designated by the library for the respective model. At the same time, a thorough evaluation of these trained models' performance was conducted, and the results were meticulously documented in the forthcoming tables. It has been observed that after 20 features, the model performances do not change significantly. As a result, the optimal set of 20 features was selected to optimize the models. Additionally, for more comprehensive insights, the provided graphs elucidate the gradual increase in the number of features. This increase was achieved through the iterative implementation of both the bi-directional elimination and forward selection algorithms on the models. Within this iterative framework, the models underwent repeated training cycles. In each successive cycle, the training encompassed an expanded set of features, followed by the measurement of the corresponding performance scores.

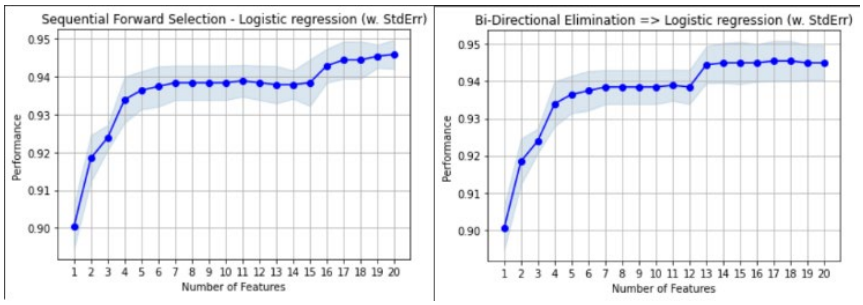


Fig. 8. The result of the sequential forward selection and bi-directional elimination algorithm for logistic regression model.

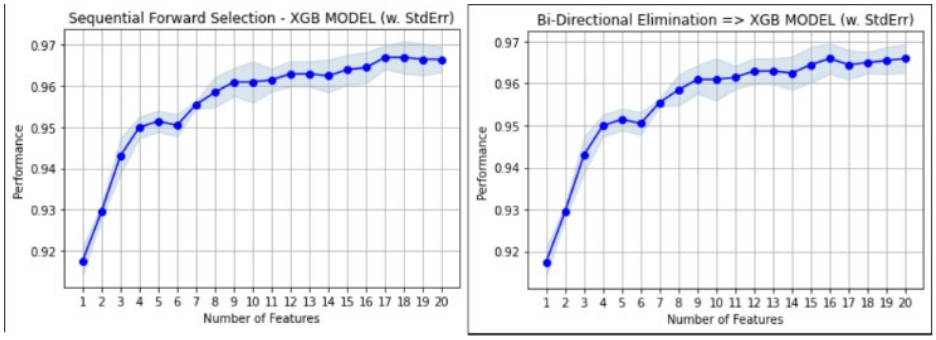


Fig. 9. The result of the forward selection and bi-directional elimination algorithm for XGB model

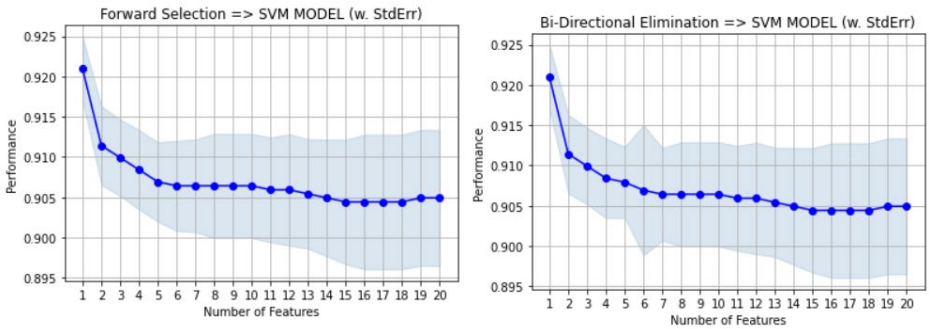


Fig. 10. The result of the forward selection and bi-directional elimination algorithm for SVM model

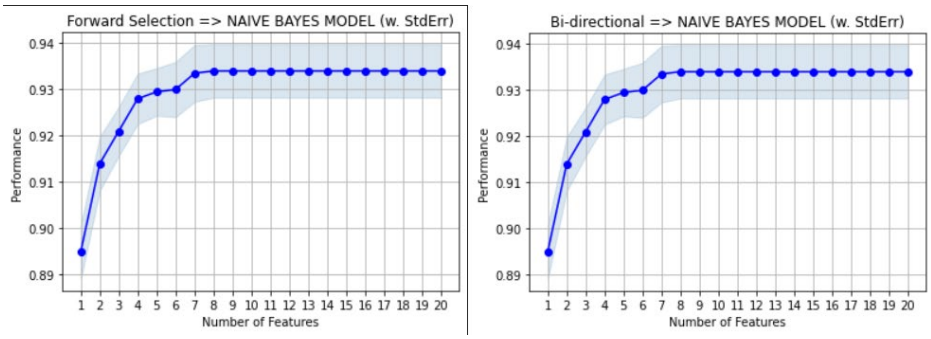


Fig. 11. The result of the forward selection and bi-directional elimination algorithm for naive bayes

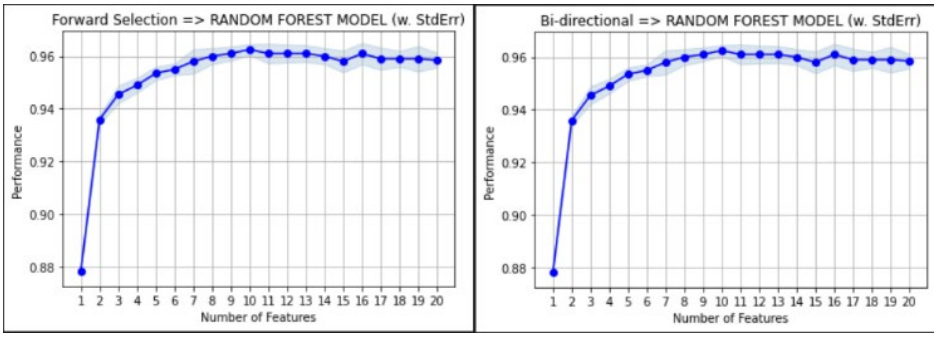


Fig. 12. The result of the forward selection and bi-directional elimination algorithm for random forest model

Furthermore, it is important to note that the results arising from the sequential and bidirectional application of selection algorithms consistently demonstrate a pattern where the first 5 most important features remain unchanged across all models. However, minor variations are observed in the subsequent rankings. Specifically, the consistently top-ranked features encompass GLRLM_LongRunEmphasis, FOS Distortion, Histogram box 8, GLCM_Correlation_Mean, and Hu moment 2.

s a result, the table below indicates the model performances which were trained that have been selected by the selection algorithms. The following models trained for the best 20 features that has been selected by the bi-directional selection algorithm because it has been observed that the features that has been selected by this algorithm performed better than sequential forward selection

BI-DIRECTIONAL SELECTION					
CLASSIFIER	ACCURACY	SENSITIVITY	SPECIFITY	PRECISION	AUC
LOGISTIC REGRESSION	0.9439	0.9123	0.966	0.9619	0.9391
NAIVE BAYES	0.9409	0.9072	0.966	0.9617	0.9366
SVM	0.9064	0.8556	0.966	0.9595	0.9108
RANDOM FOREST	0.9554	0.9536	0.9708	0.9685	0.9622
XGBOOST	0.9644	0.9484	0.9757	0.9735	0.962

Table. 1. Final results for all models and their performance evaluations

IV. DISCUSSION

The algorithm was able to achieve high accuracy using simple machine learning models even with a limited dataset of images. This suggests that the algorithm is robust and can be applied to other datasets with limited resources. The algorithm was also able to automatically segment the lungs from the chest X-ray images, which is a challenging task. This is a significant advantage of the algorithm, as it eliminates the need for manual segmentation, which can be time-consuming and error prone.

The most significant features that were selected were always from the textural features of the images and there were always histogram-related features selected for the algorithms. This situation was expected because textural features were also extracted in the related studies, which is explained at the background and related works section. As a result, these features are likely to be important for COVID-19 diagnosis.

The second-best algorithm was Random Forest which was also expected because Random Forest creates multiple decision trees to find the best fitting model inside of them. It is very similar to the neural network. However, the XGBoost algorithm was able to achieve slightly higher accuracy, suggesting that it may be a better choice for COVID-19 diagnosis.

The study has limitations that need to be addressed in future work. First, the algorithm was only tested on a limited dataset of chest X-ray images. A larger and more diverse dataset is needed to further validate the algorithm's performance. Second, the algorithm was only tested on COVID-19 and normal cases. It is important to test the algorithm on other diseases, such as pneumonia, to assess its generalizability.

Despite these limitations, the results of this study are very promising. The algorithm developed in this study is a valuable tool for COVID-19 diagnosis, and it has the potential to be used in a variety of settings to help improve patient care.

V. CONCLUSION

In conclusion, this study presents a novel algorithm for the diagnosis of COVID-19 using a combination of image processing and machine learning techniques. The algorithm attained an accuracy rate of 96.44%, which marks a substantial improvement over previous studies. These earlier researches have reported accuracy rates of about 90%. Additionally, the algorithm has various advantages. Firstly, this model can be trained rapidly, even with limited resources and datasets. Secondly, it automatically segments the lungs from the chest X-ray images, removing the need for manually drawn masks. Thirdly, its high accuracy makes it a valuable tool for COVID-19 diagnosis. These findings suggest that by combining image processing techniques with machine learning, algorithms for COVID-19 diagnosis can be swiftly developed with remarkable accuracy. This is a promising development that could help reduce the burden on health workers and speed up diagnosis in emergency situations. Further research can enhance the algorithm by employing a more extensive image dataset. The algorithm can also be used to diagnose other diseases, including pneumonia. Furthermore, analyzing the most critical selected features can provide deeper insights into COVID-19's underlying patterns in chest X-ray images.

REFERENCES

[1] "Symptoms of COVID-19," updated october 26. [Online]. Available: https://www.cdc.gov/coronavirus/2019-ncov/symptoms-testing/symptoms.html. [Accessed: 01-January-2022]

[2] "COVID-19 and PCR Testing," n.d. [Online]. Available: https://my.clevelandclinic.org/health/diagnostics/21462-COVID-19-and-pcr-testing. [Accessed: 01-January-2022]

[3] Rahman, T., Khandakar, A., Qiblawey, Y., Tahir, A., Kiranyaz, S., Kashem, S.B.A., Islam, M.T., Maadeed, S.A., Zughaier, S.M., Khan, M.S. and Chowdhury, M.E., 2020.

Exploring the Effect of Image Enhancement Techniques on COVID-19 Detection using Chest X-ray Images https://doi.org/10.1016/j.compbiomed.2021.104319.

[4] Chouhan, Vikash, Sanjay Kumar Singh, Aditya Khamparia, Deepak Gupta, Prayag Tiwari, Catarina Moreira, Robertas Damaševičius, and Victor Hugo C. de Albuquerque. 2020. "A Novel Transfer Learning Based Approach for Pneumonia Detection in Chest X-ray Images" Applied Sciences 10, no. 2: 559. https://doi.org/10.3390/app10020559

[5] M. E. H. Chowdhury et al., "Can AI Help in Screening Viral and COVID-19 Pneumonia?," in IEEE Access, vol. 8, pp. 132665-132676, 2020, doi: 10.1109/ACCESS.2020.3010287.

[6] Zargari Khuzani, A., Heidari, M., & Shariati, S. A. (2021). COVID-Classifier: an automated machine learning model to assist in the diagnosis of COVID-19 infection in chest X-ray images. Scientific reports, 11(1), 9887. https://doi.org/10.1038/s41598-021-88807-2

[7] Zhang, K., Liu, X., Shen, J., Li, Z., Sang, Y., Wu, X., Zha, Y., Liang, W., Wang, C., Wang, K., Ye, L., Gao, M., Zhou, Z., Li, L., Wang, J., Yang, Z., Cai, H., Xu, J., Yang, L., Cai, W., … Wang, G. (2020). Clinically Applicable AI System for Accurate Diagnosis, Quantitative Measurements, and Prognosis of COVID-19 Pneumonia Using Computed Tomography. Cell, 181(6), 1423–1433.e11. https://doi.org/10.1016/j.cell.2020.04.045

[8] Gite, S., Mishra, A. & Kotecha, K. Enhanced lung image segmentation using deep learning. Neural Comput & Applic (2022). https://doi.org/10.1007/s00521-021-06719-8

[9] PyFeats, "Open-source software for image feature extraction," n.d. [Online]. Available: https://pypi.org/project/pyfeats/. [Accessed: 01-March-2022]

[10] Mlxtend, "Mlxtend (machine learning extensions) is a Python library of useful tools for the day-to-day data science tasks," n.d. [Online]. Available: http://rasbt.github.io/mlxtend/. [Accessed: 01-March-2022]

[11] "Image Thresholding," n.d. [Online]. Available: https://docs.opencv.org/4.x/d7/d4d/tutorial_py_thresholding.html. [Accessed: 01-March-2022]

scikit-learn, "Machine Learning in Python," n.d. [Online]. Available: https://scikit-learn.org/stable. [Accessed: 01-March-2022]

Van İli Kuraklığının Yağış Anomali İndeksi (RAI) Yöntemi ile Belirlenmesi

Determination of Van Province Drought by Rainfall Anomaly Index (RAI) Method

Mahsum AYDIN

*maydin@yyu.edu.tr, ORCID: 0000-0001-9739-4066
[1]*İnşaat Mühendisliği, Van Yüzüncü Yıl Üniversitesi, Van, Türkiye*

Özet: Sanayi devrimi ile birlikte insan faaliyetleri nedeni ile artan fosil yakıt tüketimi ve yüksek oranlarda sera gazlarının salınımı nedeni ile son yıllarda kuraklık olaylarında bir artış meydana geldiği görülmektedir. Kuraklık nedeni ile yağış rejimlerinde ve miktarlarında anomaliler meydana gelebilmektedir. Bu nedenle çalışmada Van ilinin kuraklığının belirlenmesi amacıyla yağışlarda meydana gelen bu anomalilerin değerlendirilebileceği Yağış Anomali İndeksi (RAI) kullanılmıştır. Van ili sınırları içerisinde seçilen 5 adet meteoroloji gözlem istasyonu yağış verileri kullanılarak 1, 3, 6, 9 ve 12 aylık zaman periyotları için ayrı ayrı kuraklık değerleri hesaplanmıştır. Hesaplamalar sonucunda Van ili genelinin kısa dönemde çok kurak, uzun dönemde ise orta derece kurak bir bölge olduğu sonucuna varılmıştır. Ayrıca kuraklık olaylarının son yıllarda meydana gelme sayılarındaki artış nedeni ile tarım ürünlerini, su kaynaklarını ve canlı yaşamlarını koruyucu önlemler alınması önerilmiştir.

Anahtar Kelimeler: *Yağış Anomali İndeksi, Van İli, Kuraklık*

Abstract It is observed that there has been an increase in drought events in recent years due to the increasing consumption of fossil fuels and the release of greenhouse gases at high rates due to human activities with the industrial revolution. Anomalies in precipitation regimes and amounts may occur due to drought. Therefore, in this study, the Rainfall Anomaly Index (RAI) was used to evaluate these anomalies in precipitation to determine the drought of Van province. Using the precipitation data of 5 meteorological observation stations selected within the borders of Van province, drought values were calculated separately for 1, 3, 6, 9 and 12-month time periods. As a result of the calculations, it was concluded that Van province is a very arid region in the short term and a moderately arid region in the long term. In addition, due to the increase in the number of drought events in recent years, it is recommended to take measures to protect agricultural products, water resources and living life.

Keywords: *Rainfall Anomaly Index, Van Province, Drought*

I. GİRİŞ

Kuraklık insan ve canlı hayatını olumsuz etkileyen doğal felaketlerden biridir. Özellikle sanayi devrimi ile birlikte fosil yakıtların daha fazla kullanılmaya başlanması, kentleşme ve nüfus yoğunluğunun hızlı bir şekilde artması gibi sebepler ile iklim değişiklikleri meydana gelmektedir[1]. İklim değişiklikleri yağış rejimlerinin değişmesine ve ortalama sıcaklık değerlerinin zamanla artmasına sebebiyet vermektedir [2]. Bu değişiklikler ise kuraklığın etkisinin her geçen gün daha fazla hissedilmesine neden olmaktadır. Bu nedenle kuraklığın

büyüklüğünün belirlenmesi su kaynaklarının korunması ve canlı hayatına olan olumsuz etkilerinin ortadan kaldırılması için gerekli önlemlerin alınabilmesi açısından büyük önem arz etmektedir [3,4].

Kuraklık tanım olarak yağışların normalin altına düşmesi olarak ifade edilebilmektedir ve meteorolojik, hidrolojik, tarımsal ve sosyo-ekonomik olmak üzere 4 sınıfa ayrılabilir [5,6,7]. Ancak kuraklık karmaşık yapısından dolayı tahmin edilmesi zor bir doğal olaydır [8]. Literatürde meteorolojik kuraklığın belirlenebilmesi için birçok kuraklık indisi yöntemi geliştirilmiştir. Bu kuraklık indisi yöntemleri kullanılarak kuraklığın büyüklüğü ve şiddeti gibi özellikleri hesaplanmaya çalışılmaktadır. Literatürde en yaygın olarak kullanılan yöntemlerden biri Standart Yağış İndeksi (SPI) yöntemidir [9]. SPI yöntemi girdi olarak sadece yağış verisine ihtiyaç duyduğundan ve hesaplanması son derece pratik olduğundan dolayı sıklıkla tercih edilmektedir. Kuraklık indisi yöntemlerinden bir diğeri 1965 yılında Van-Rooy tarafından geliştirilen Yağış Anomali İndeksi (RAI)'dır [10]. RAI yöntemi de SPI yöntemine benzer şekilde girdi olarak sadece yağış verisine ihtiyaç duymaktadır, ancak eldeki yağış veri setinde eksik veri olmaması gerekmektedir. Bu nedenle SPI yöntemine göre uygulamada bazı zorlukları bulunsa da diğer kuraklık indisi yöntemlerine nazaran kullanımı kolay olan bir indeks olduğu bilinmektedir [11]. Literatürde RAI yöntemi ile ilgili yapılan çalışmalardan bazıları şu şekildedir;

Şener ve Davraz [12] tarafından 2021 yılında yapılan çalışmada Isparta ilinin meteorolojik kuraklığının belirlenmesi amacıyla SPI, RAI ve Normal Yağışın Yüzdesi (NYİ) yöntemleri kullanılarak farklı zaman periyotlarında analizler gerçekleştirilmiştir. Elde edilen sonuçlar incelendiğinde SPI yöntemi ile 24, RAI yöntemi ile 43, NYİ yöntemi ile 234 farklı zaman diliminde aşırı kurak dönem olduğu tespit edilmiştir. Kullanıla kuraklık indisi yöntemleri arasında pozitif yönde kuvvetli bir korelasyon olduğu ifade edilmiştir. Tüm elde edilen sonuçlar incelendiğinde ise her üç yöntemin de Isparta ili genelinde benzer sonuçlar verdiği değerlendirilmiştir.

Aryal vd. [13] 2022 yılında yaptıkları çalışmada Nepal'in kuraklığının belirlenmesi amacıyla SPI ve RAI yöntemlerini kullanmışlardır. Hesaplamalar için 1975-2015 yılları arası 41 yıllık günlük ortalama yağış verileri kullanılmıştır. Sonuçlar incelendiğinde Nepal'in kuzeybatı ve doğu bölgelerinde diğer bölgelere nazaran daha fazla kuraklık yaşandığı tespit edilmiştir. RAI ve SPI yöntemlerinin ülke genelinde benzer sonuçlar verdiği değerlendirilmiş ve her iki yöntemin de kuraklığın belirlenmesinde eşit şekilde kullanılabileceği sonucuna varılmıştır.

Sadiq vd. [14] 2020 yılında yaptıkları çalışmada yağış anomalilerinin Yola kenti ve çevresindeki mahsul üretimi üzerindeki etkilerini tahmin etmeyi amaçlamışlardır. Bu etkilerin belirlenmesi için kırk yıllık veri seti kullanılarak RAI yöntemi yardımı ile bölgede analizler yapılmıştır. Yapılan analizler sonucunda bölgenin 19 yıllık bir periyot boyunca nemli bir dönem geçirdiği, 6 yıllık bir periyot boyunca normal nemli bir dönem geçirdiği ve 15 yıllık bir periyot boyunca ise kurak bir dönem geçirdiği ve özellikle son yıllarda bu durumun tespit edildiği ifade edilmiştir. Bununla birlikte 2012 ve 2016 yıllarında ise tarım arazilerine zarar veren sel olaylarının şiddetlenmesine neden olabilecek aşırı yağışlı durumlar olduğu tespit edilmiştir. Gelişen kuraklık etkilerinden korunmak için bölgede kuraklığa dayanıklı mahsul üretiminin gerektiği ifade edilmiştir.

Costa ve Rodrigues [15] tarafından 2017 yılında yapılan çalışmada Birezilya'nın Ceará eyaletinde bulunan Salgado havzası için RAI'nın uzay-zaman dağılımının incelenmesi amaçlanmıştır. Bunun için 1974-2015 yılları arasında gözlenmiş günlük yağış verileri kullanılmıştır. Hesaplanan RAI değerleri kullanılarak mekânsal dağılım haritaları elde edilmiştir. Havza genelinde yağışlı dönemin Ocak-Nisan ayları arasında olduğu, yılın en kurak dönemlerinin ise Temmuz-Ekim arasında olduğu tespit edilmiştir. Havza içerisinde RAI

değerlerinin değiştiği tespit edilmiş, aşırı anomalilerin görüldüğü yıllarda bu anomalilerin deniz yüzey sıcaklık anomalisi olaylarıyla ilgili olduğu değerlendirilmiştir.

Hansel vd. [16] tarafından 2016 yılında yapılan çalışmada modifiye edilmiş Yağış Anomali İndeksi (mRAI) yönteminin gelecekteki ekstrem yağış özelliklerinin değerlendirilmesinde SPI yönteminin yerine kullanılabilirliğinin incelenmesi amaçlanmıştır. Gelecekteki yağış koşullarının değerlendirilmesinde SPI'ya alternatif olarak mRAI'nın uygunluğunun değerlendirilmesi için beş bölgesel iklim modelinden elde edilen on iki bölgesel iklim projeksiyonundan oluşan bir veri seti kullanılmıştır. Klimatolojik olarak Orta Doğu Avrupa'yı temsil eden bir test bölgesi için mRAI'nın frekans dağılımları ve eğilimleri SPI ile karşılaştırılmış ve test edilen tüm zaman ölçeklerinde birbiriyle yüksek oranda ilişkili olduğu ifade edilmiştir. İki yöntemin frekans dağılımlarında önemli bir fark olmadığı ancak mRAI'nın orta derecede kurak ila çok kurak sınıflarda biraz daha yüksek frekanslar gösterdiği gözlemlenmiştir. Sonuç olarak mRAI yönteminin gelecekteki yağış koşullarının değerlendirilmesinde güvenilir sonuçlar verdiği değerlendirilmiştir.

Bu çalışmada özellikle kurak iklim bölgesinde bulunan Van ilinde iklim değişiklikleri nedeni ile yağış rejimlerinde meydana gelen anomalilerin Yağış Anomali İndeksi (RAI) kullanılarak tespit edilmesi ve bölge için değerlendirme yapılması amaçlanmıştır.

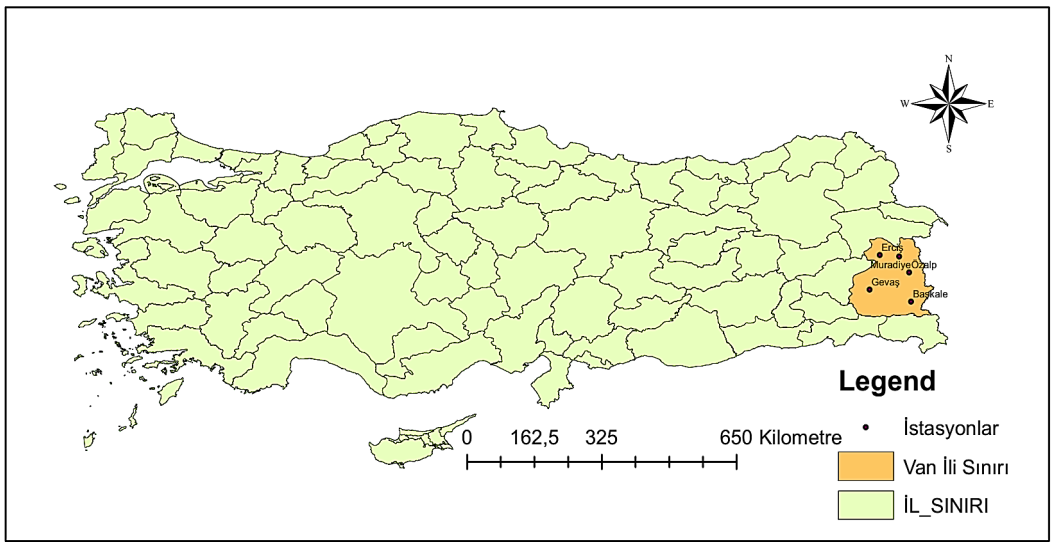
II. MATERYAL VE YÖNTEM

A. *Çalışma Alanı*

Van ili, Van Gölü kapalı havzası içerisinde yer alan ve bölgede en kalabalık nüfusa sahip olan illerden biridir. Kuzeyinde Ağrı, Batısında Bitlis, Güneyinde Hakkâri ve doğusunda ise İran ile çevrilidir. İl genelinde karasal iklim hâkimdir. Bu çalışmada Van ili sınırları içerisinde yer alan 5 adet meteoroloji gözlem istasyonuna ait 1982-2018 yılları arasında ölçülmüş olan aylık ortalama yağış verileri kullanılmıştır. Seçilen istasyonlara ait bazı istatistiki ve coğrafi bilgiler Tablo 1'de sunulmaktadır. İstasyonların coğrafi konumları Şekil 1'de gösterilmektedir.

TABLO I
SEÇİLEN İSTASYONLARA AİT BAZI İSTATİSTİKİ VE COĞRAFİ BİLGİLER

İstasyon Adı	Veri Aralığı	Ortalama	St. Sapma	Çarpıklık	Enlem	Boylam
Başkale	1982-2018	36.230	32.428	1.809	38.0435	44.0173
Erciş	1982-2018	34.320	28.275	1.017	39.0198	43.3386
Gevaş	1982-2018	41.930	33.892	0.936	38.2963	43.1197
Muradiye	1982-2018	46.760	37.064	1.504	38.9899	43.7630
Özalp	1982-2018	41.940	36.992	1.656	38.6573	43.9767



Şekil 1. Seçilen istasyonların coğrafi konumları

B. *Yağış Anomali İndeksi (RAI)*

Van-Rooy tarafından 1965 yılında geliştirilen Yağış Anomali İndeksi (RAI) pozitif ve negatif yağış anormalliklerine bir büyüklük atamak için sıralamaya dayalı bir kuraklık indeksidir [10, 17]. RAI indeksi Eşitlik 1 yardımıyla hesaplanabilir;

$$RAI = \pm 3 \frac{P_i - \bar{P}}{E - \bar{P}} \quad (1)$$

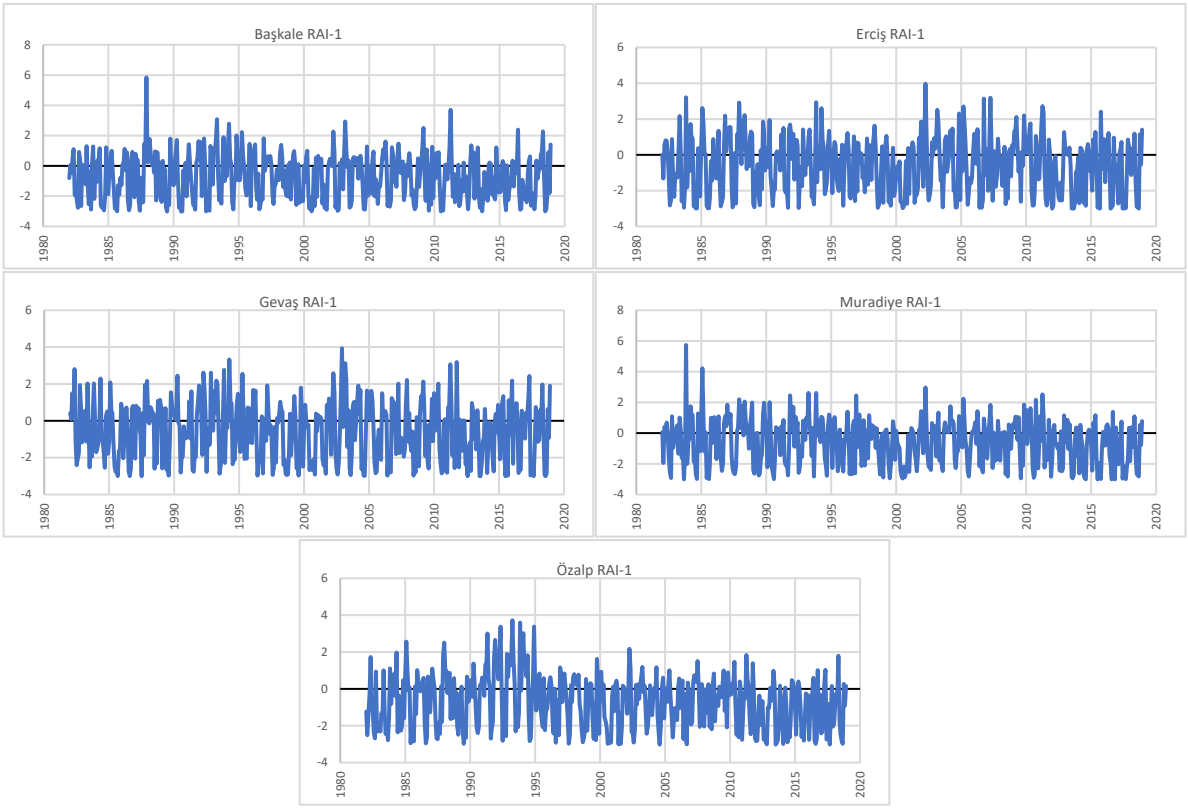
Burada, P_i i anında ölçülmüş olan yağış değeridir, $\bar{P}$ yağış değerlerinin ortalamasıdır, E değeri 10 ekstrem yağış değerinin ortalamasıdır (Pozitif değerler için en büyük 10 değer, negatif değerler için en küçük 10 değer), ± 3 ise $P_i - \bar{P} > 0$ ise +3 tersi durumda ise -3 olarak alınması gerektiğini ifade etmektedir [16, 17]. RAI indeksi farklı zaman periyotları için hesaplanabilmektedir. Hesaplanan değerlerin sınıflandırılması için Van-Rooy tarafından önerilen sınıflandırma Tablo 2'de sunulmaktadır.

TABLO II
RAI YÖNTEMİNE GÖRE KURAKLIK SINIFLARI

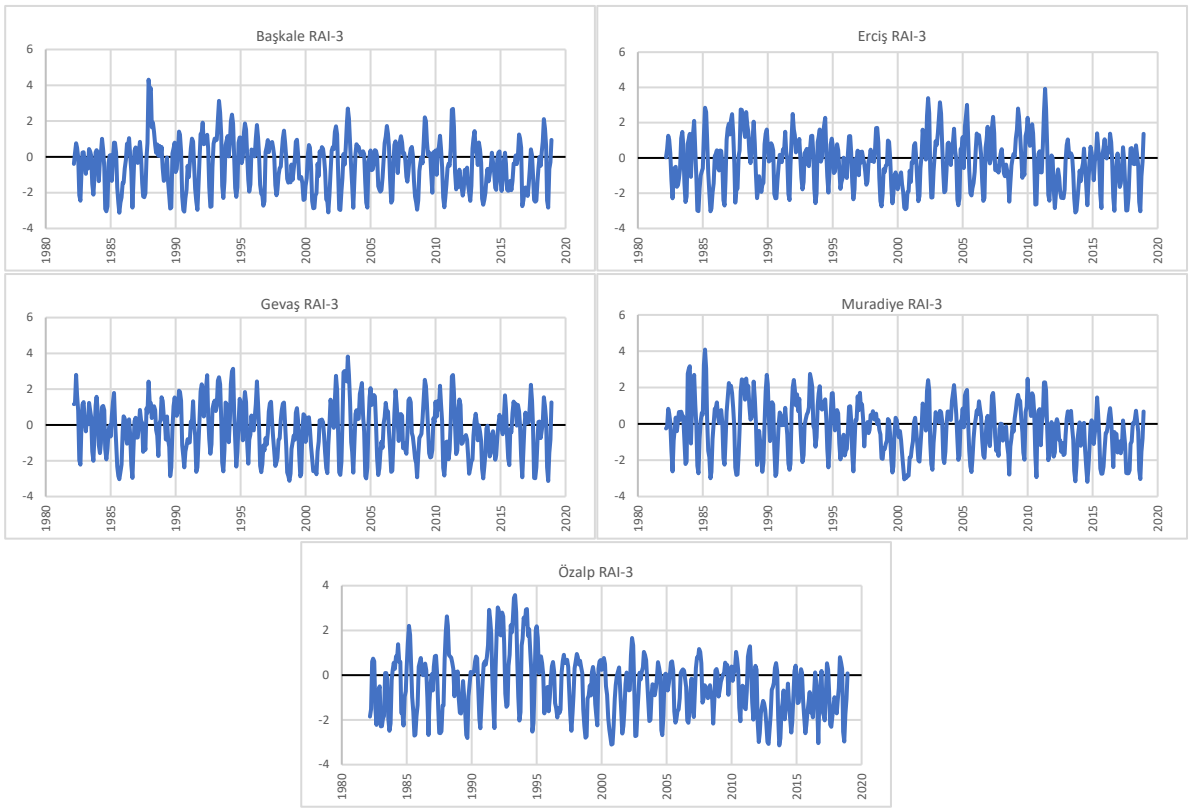
RAI değeri	**Sınıflandırma**
≥ 3.00	Aşırı Nemli
$2.00 - 2.99$	Çok Nemli
$1.00 - 1.99$	Orta Derece Nemli
$0.50 - 0.99$	Hafif Nemli
-0.49 – 0.49	Normale Yakın
-0.99 - -0.50	Hafif Kurak
-1.99 - -1.00	Orta Derece Kurak
-2.99 - -2.00	Çok Kurak
≤ -3.00	Aşırı Kurak

III. BULGULAR

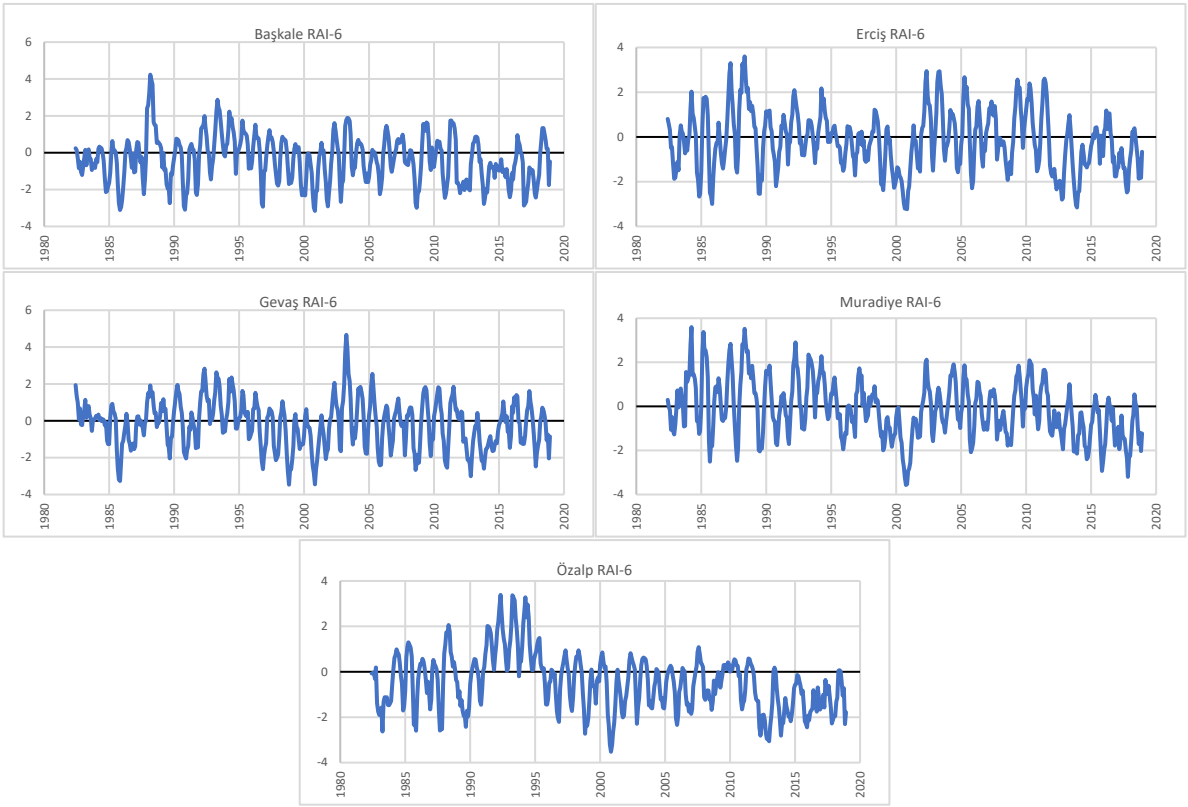
Van ili sınırları içerisinde seçilmiş olan 5 adet istasyona ait yağış verileri kullanılarak RAI yöntemi yardımıyla kuraklık değerleri 1, 3, 6, 9 ve 12 aylık zaman periyotları için ayrı ayrı hesaplanmıştır. Her bir zaman periyodunda tüm istasyonlar için hesaplanan kuraklık değerleri Şekil 2-6'da sunulmuştur.



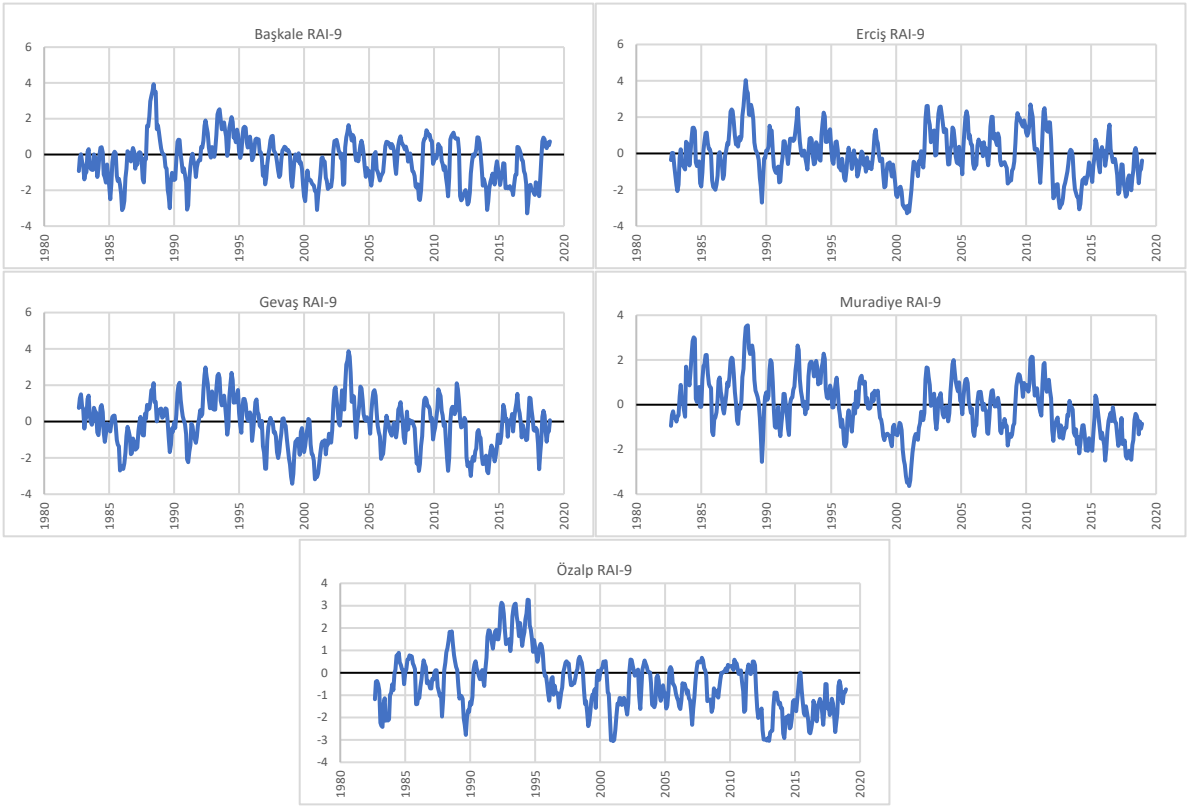
Şekil 2. Seçilen istasyonlar için hesaplanan 1 aylık RAI değerleri



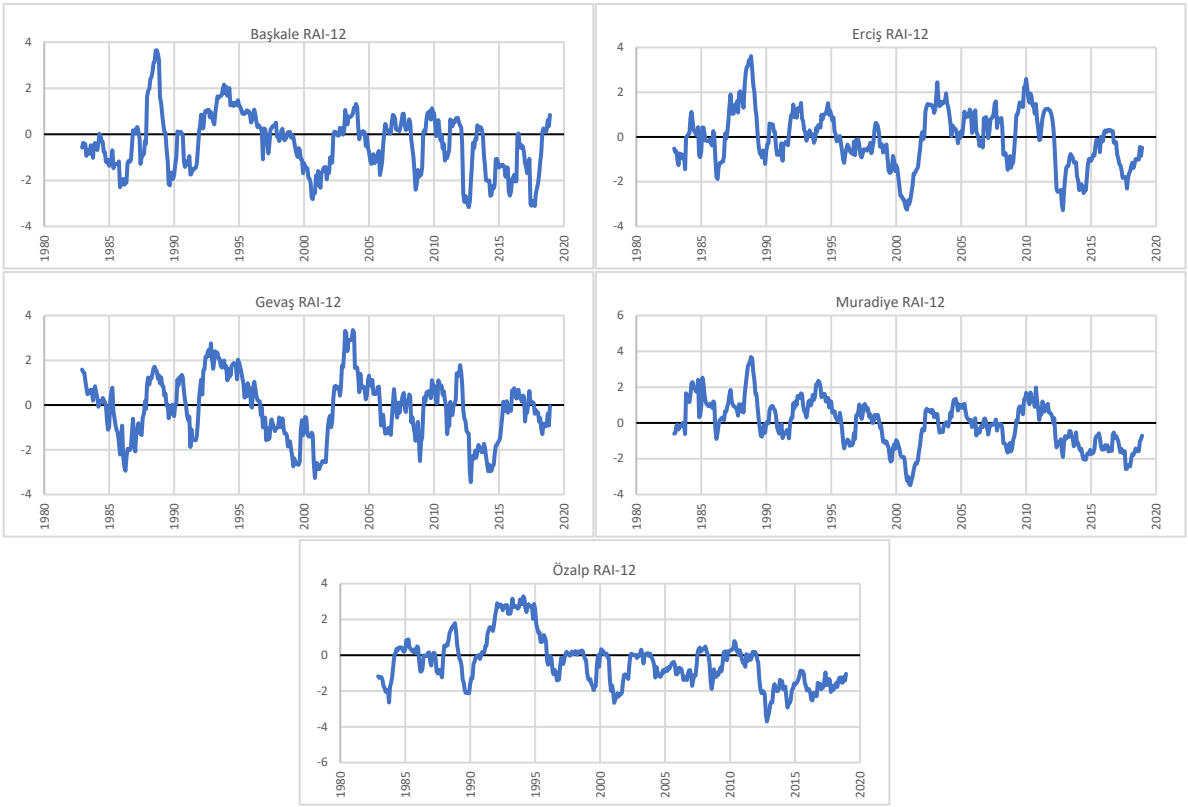
Şekil 3. Seçilen istasyonlar için hesaplanan 3 aylık RAI değerleri



Şekil 4. Seçilen istasyonlar için hesaplanan 6 aylık RAI değerleri



Şekil 5. Seçilen istasyonlar için hesaplanan 9 aylık RAI değerleri



Şekil 6. Seçilen istasyonlar için hesaplanan 12 aylık RAI değerleri

Van ili sınırları içerisinde seçilmiş olan 5 adet meteoroloji gözlem istasyonu için hesaplanan kuraklık değerleri kullanılarak elde edilen Şekil 2-6 incelendiğinde tüm zaman periyotları için kurak dönemlerin meydana gelme sayılarının nemli dönem meydana gelme sayılarından fazla olduğu ve bölgede kuraklığın etkisinin hissedildiği görülebilmektedir. Ayrıca şekiller incelendiğinde tüm istasyonlar için ve tüm zaman periyotlarında kurak dönem görülme sıklığının son yıllarda arttığı görülebilmektedir.



Şekil 7. Seçilen istasyonlar için hesaplanan kuraklık sınıfları ve meydana gelme sayıları

TABLO III
KURAKLIK SINIFLARI VE MEYDANA GELME SAYILARI

İstasyon Adı	Kuraklık Sınıfı	RAI-1	RAI-3	RAI-6	RAI-9	RAI-12
	Aşırı Kurak	5	4	3	5	5
	Çok Kurak	112	66	48	31	41
	Orta Derecede Kurak	74	86	86	104	104
	Hafif Kurak	34	39	64	44	43
Başkale	Normale Yakın	120	133	126	147	137
	Hafif Nemli	46	58	54	54	52
	Orta Derecede Nemli	42	43	47	40	39
	Çok Nemli	8	9	7	6	6
	Aşırı Nemli	3	4	4	5	6
	Aşırı Kurak	9	5	5	5	5
	Çok Kurak	102	56	30	28	24
	Orta Derecede Kurak	70	74	94	68	63
	Hafif Kurak	46	49	48	71	66
Erciş	Normale Yakın	97	120	130	126	133
	Hafif Nemli	50	48	44	49	48
	Orta Derecede Nemli	51	63	58	55	78
	Çok Nemli	15	23	27	30	10
	Aşırı Nemli	4	4	3	4	6
	Aşırı Kurak	7	3	5	5	3
	Çok Kurak	104	61	35	37	44
	Orta Derecede Kurak	69	71	87	69	75
	Hafif Kurak	36	57	37	58	52
Gevaş	Normale Yakın	100	104	139	136	112
	Hafif Nemli	57	42	57	55	61
	Orta Derecede Nemli	46	76	63	57	63
	Çok Nemli	20	25	13	15	19
	Aşırı Nemli	5	3	3	4	4
	Aşırı Kurak	5	4	4	5	5
	Çok Kurak	96	51	21	17	18
	Orta Derecede Kurak	71	79	94	85	86
	Hafif Kurak	40	41	66	64	50
Muradiye	Normale Yakın	128	133	114	123	117
	Hafif Nemli	45	56	49	61	65
	Orta Derecede Nemli	46	50	67	57	73
	Çok Nemli	11	23	21	20	14
	Aşırı Nemli	2	5	3	4	5
	Aşırı Kurak	6	5	4	4	4
	Çok Kurak	106	56	41	41	36
	Orta Derecede Kurak	78	100	117	114	119
	Hafif Kurak	39	53	47	62	45
Özalp	Normale Yakın	127	124	143	129	155
	Hafif Nemli	42	59	43	34	16
	Orta Derecede Nemli	36	25	27	36	20
	Çok Nemli	5	17	12	10	34
	Aşırı Nemli	5	3	5	6	4

Şekil 7 ve Tablo 3 incelendiğinde Van ili sınırları içerisinde seçilen meteoroloji istasyonlarının tamamına yakınında çok kurak ve orta derece kurak dönem sayılarının oldukça fazla olduğu, buna karşın nemli dönem meydana gelme sayılarının ise daha az olduğu görülmektedir. Özellikle 1 aylık zaman periyodu için tüm istasyonlarda çok kurak dönem meydana gelme sayılarının oldukça yüksek olduğu görülmektedir. 3,6,9 ve 12 aylık zaman periyotlarında ise tüm istasyonlarda orta derece kurak dönemin meydana gelme sayısının son derece yüksek olduğu görülebilmektedir. Erciş, Gevaş ve Muradiye istasyonlarında ise 12 aylık zaman periyodunda diğer istasyonlara göre orta derece nemli dönem meydana gelme sayısının daha fazla olduğu, ancak kurak dönem sınıflarının meydana gelme sayıları ile karşılaştırıldığında ise daha az nemli dönem görüldüğü tespit edilmiştir.

IV. TARTIŞMA VE SONUÇ

Çalışmada Van ili sınırları içerisinde yer alan 5 adet meteoroloji gözlem istasyonu yağış verileri kullanılarak Van ili kuraklığı RAI yöntemi yardımı ile 1, 3, 6, 9 ve 12 aylık zaman periyotları için ayrı ayrı belirlenmiş ve değerlendirilmiştir. Bölge için elde edilen veriler incelendiğinde, özellikle 1 aylık zaman periyodu için seçilen tüm istasyonlarda çok kurak dönem meydana gelme sayılarının oldukça fazla olduğu görülmüştür. 3, 6, 9 ve 12 aylık zaman periyotlarında ise yine tüm istasyonlarda orta derece kurak dönem meydana gelme sayısının oldukça fazla olduğu görülmüştür. Elde edilen kuraklık değerlerine göre seçilen tüm istasyonlarda kuraklığın görülme sıklığının son yıllarda arttığı ve bölgede kuraklığın etkisinin daha fazla hissedildiği söylenebilir. Bölge kısa dönem için çok kurak ve uzun dönem için ise orta derece kurak olarak değerlendirilebilir. Kuraklık ve iklim değişikliği kaynaklı olarak yağışlarda meydana gelen bu anomaliler sebebiyle bölgede üretilen tarım ürünleri, su kaynakları ve canlı hayatları üzerinde olumsuz etkiler meydana geleceği değerlendirilmektedir. Bu olumsuz etkileri en aza indirebilmek için bölgede kuraklık risk değerlendirmesi ve planlamalarının yapılması ve gerekli önlemlerin alınması ise son derece önemlidir. Alınabilecek önlemlerden bazıları şu şekilde sıralanabilir; çiftçiler kuraklığa dayanıklı ekin üretimi için teşvik edilmeli, daha az sulama suyuna ihtiyaç duyan ekinler tercih edilmeli, su kaynaklarını olumsuz etkilerden koruyacak önlemler alınmalı, bölge halkının daha bilinçli bir şekilde su tüketmesi için gerekli bilgilendirmeler yapılmalı ve önlemler alınmalı, şebeke sistemlerinde meydana gelen kayıplar tespit edilmeli ve en aza indirilmeli, bölgede kullanılan su kuyuları denetlenmeli ve izinsiz kuyu açılması ve kullanılmasının önüne geçilmelidir.

REFERENCES

[1] T. Öztürk, M. Türkeş and M. L. Kurnaz, "RegCM4. 3.5 iklim modeli benzetimleri kullanılarak Türkiye'nin gelecek hava sıcaklığı ve yağış klimatolojilerindeki değişikliklerin çözümlenmesi," Ege Coğrafya Dergisi, vol. 20, no. 1, pp. 17-27, 2011.

[2] M. Bahadır, "Türkiye'de iklim değişikliğinin iklim bölgelerine yansımasında kuzey-güney yönlü sıcaklık ve yağış değişim öngörüleri," Akademik Bakış Dergisi, vol. 26, pp. 1-18, 2011.

[3] S. Sırdaş and Z. Şen, "Meteorolojik kuraklık modellemesi ve Türkiye uygulaması," İTÜ Dergisi/d, vol.2, no. 2, pp. 95-103, 2010.

[4] S. Karaman and Z. Gökalp, "Küresel ısınma ve iklim değişikliğinin su kaynakları üzerine etkileri," Tarım Bilimleri Araştırma Dergisi, no.1, pp. 59-66, 2010.

[5] D. A. Wilhite and M. H. Glantz, "Understanding the drought phenomenon: The role of definitions," Water International, vol. 10, no. 3, pp. 111-120, 1985.

[6] M. Choi, J. M. Jacobs, M. C. Anderson and D. D. Bosch, "Evaluation of drought indices via remotely sensed data with hydrological variables," Journal of Hydrology, vol. 476, pp. 265-273, 2013.

[7] E. Şener and Ş. Şener, "SPI ve CZI kuraklık indislerinin CBS tabanlı zamansal ve konumsal karşılaştırması: Burdur Gölü Havzası örneği," Doğal Afetler ve Çevre Dergisi, vol. 7, no. 1, pp. 41-58, 2021.

[8] N. Beden, V. Demir and A. Ü. Keskin, "Samsun ilinde SPI ve PNI kuraklık indekslerinin eğilim analizi," Dokuz Eylül Üniversitesi Mühendislik Fakültesi Fen ve Mühendislik Dergisi, vol. 22, no. 64, pp. 107-116, 2020.

[9] L. Li, D. She, H. Zheng, P. Lin and Z. L. Yang, "Elucidating diverse drought characteristics from two meteorological drought indices (SPI and SPEI) in China," Journal of Hydrometeorology, vol. 21, no. 7, pp. 1513-1530, 2020.

[10] M. P. Van-Rooy, "A rainfall anomaly index (RAI), independent of the time and space," Notos, vol. 14, pp. 43–48, 1965.

[11] G. Wmo and G. Gwp, Handbook of drought indicators and indices. Geneva: World Meteorological Organization (WMO) and Global Water Partnership (GWP), 2016.

[12] E. Şener ve A. Davraz, "Yağış tabanlı farklı indisler kullanılarak meteorolojik kuraklık analizi: Isparta örneği," Mehmet Akif Ersoy Üniversitesi Fen Bilimleri Enstitüsü Dergisi, vol. 12, no. Ek (Suppl.) 1, pp. 404-418, 2021.

[13] A. Aryal, M. Maharjan, R. Talchabhadel and B. R. Thapa, "Characterizing meteorological droughts in Nepal: A comparative analysis of standardized precipitation ındex and rainfall anomaly ındex," Earth, vol. 3, no. 1, pp. 409-432, 2022.

[14] A. A. Sadiq, M. Suleman and U. Mohammed, "An estimation of rainfall anomaly index and its impact on crop production in Yola and environs," African Journal of Environment and Natural Science Research, vol. 3, no. 4, pp. 35-53, 2020.

[15] J. A. Costa and G. P. Rodrigues, "Space-time distribution of rainfall anomaly index (RAI) for the Salgado Basin, Ceará State-Brazil," Ciência e Natura, vol. 39, no. 3, pp. 627-634, 2017.

[16] S. Hänsel, A. Schucknecht and J. Matschullat, "The Modified Rainfall Anomaly Index (mRAI)—is this an alternative to the Standardised Precipitation Index (SPI) in evaluating future extreme precipitation characteristics?" Theoretical and Applied Climatology, vol. 123, pp. 827-844, 2016.

[17] T. Raziei, "Revisiting the rainfall anomaly index to serve as a simplified standardized precipitation index," Journal of Hydrology, vol. 602, pp. 1-24, 2021.

Evaluation of Recent Developments in Thermoelectric Generators

Perihan ÇULUN

pculun@bingol.edu.tr, ORCID: 0000-0002-1797-9695
Department of Mechanical Engineering, Faculty of Engineering and Architecture, Bingöl University, Bingöl, Turkey

Abstract: Thermo electricity generators are based on the production of electrical energy with the seeback effect by utilizing the temperature difference between an existing heat source and a relatively cold environment. These modules, which work opposite to the working principle of thermoelectric coolers are manufactured from different materials compared to thermoelectric coolers. In general, according to literature research, it is known that the efficiency of thermoelectric generators is between 15% and 20%. It is obvious that these modules, which have not received enough attention in the past due to their low efficiency, will make significant contributions to the country's economy, especially if they are used for the purpose of increasing the energy needs recently and due to this situation, especially for the evaluation of waste heat or a heat source we have. It is possible to benefit from these modules significantly in the long term, especially if waste heat is continuously and regularly evaluated or a continuous and regularly available heat source such as solar energy is evaluated. The improvement of the parameters affecting the efficiency in these modules undoubtedly depends on the materials used in the module structure and the conditions of use of the module. In this study, the efficiency gains of the modules were evaluated within the scope of national and international literature based on the usage conditions of the module. In line with the current studies, the properties, application areas and application methods of the modules used were evaluated and the change in their final efficiency was examined.

Keywords: *Heat transfer, Heat recovery, Thermoelectric generator, TEM, TEG, Energy management Exergy Efficiency*

I. INTRODUCTION

In order for countries to develop in the field of industry and to be promoted as humanity, it is undoubtedly necessary to gain their own energy and reduce their energy costs. In general, the struggles and wars on energy resources around the world are due to this reason. It is obvious that the search for energy resources is not limited to fossil resources, and that renewable and clean energy resources, which are alternatives to fossil resources, are gaining more importance today. The evaluation of solar energy, which has a wider area compared to other types of energy in terms of resources, is on the agenda in almost every country that receives sunlight. Hydrogen energy studies, which have a wide source like solar energy and promise great hope for the future, have also come a long way. Such important energy seeking studies are undoubtedly very important. However, internal combustion engines, aviation industry, metalworking, geothermal resources, flue gases, etc. In many application areas, a large amount of energy emerges as waste thermal energy. As the thermodynamic rules in engineering indicate, many combustion events operating with low thermal efficiency take place. In motor vehicles, 40% of the energy is spent on exhaust gases, 30% on engine cooling water, 5% on friction losses, while engine efficiency drops to 25%-30% [1; 2]. Due to the waste exhaust gases in the 400-

1000K temperature range, up to 400kW of energy is lost in the engine, depending on their capacity [3]. In addition, the efficiency of steam turbines is 40% and the heat is thrown to the outside at 60%. It is known that natural gas, solid fuel and liquid fuel boilers also cause significant waste heat. According to some studies, it is mentioned that 40% of the energy used in the industry is released to the external environment [4]. As can be seen from these examples, a high proportion of energy is thrown into nature as waste heat. However, it is possible to convert these heats into useful thermal energy, electrical or mechanical energy [5]. Recycling these waste heats can be easier, more practical and economical than obtaining new alternative energies. Considering the waste energy bill of such practices in the country and the world, it is understood that the evaluation of these waste energies should never be dropped from the agenda. As a matter of fact, the recycling of waste energies (Waste heat recovery (WHR)) will be more economical and more meaningful than the search for new energy sources.

Undoubtedly, there are many applications regarding the evaluation of waste thermal energies by various methods as thermal energy. For example, a waste flue gas is passed through another space that needs to be heated and the related space is heated, or the relevant flue gases are used in heat recovery units, or the same energy is used for heating a nearby greenhouse, or for heating domestic water, etc. many examples can be given. As can be seen, if thermal recycling of such waste thermal energy sources is possible, their conversion as thermal energy should be preferred. Because the recycling of the same type of energy will be more efficient. However, this is not possible in most applications and this energy is wasted. It is also possible to convert the thermal energy, which cannot be evaluated as a thermal source, into electrical energy by using thermoelectric generator modules (TEG) and to be given to the network or used as electrical energy in the relevant structure. However, these systems, whose research continues today, have unfortunately been put into the background for years due to their low efficiency. Currently, it is known that studies on generating electricity from this waste heat, especially waste flue gases and exhaust gases, are insufficient [6]. However, every effort to improve such systems, which can make a great contribution to the country's economy if they are used appropriately in many areas, is important. In this respect, if it is possible to convert waste thermal energy sources to other energy forms, it is essential to investigate and closely examine them, and to increase the efficiency of the said system. Such systems will be of great importance in terms of being more environmentally friendly in addition to efficiency. As a matter of fact, the increase in the use of fossil energy sources also causes environmental problems such as serious global warming, ozone layer depletion, greenhouse effect and climate change. However, while electricity is produced with the help of thermoelectric systems in high-temperature walls such as chimneys and exhaust, it is possible to reduce harmful gas side effects.

In this study, current studies on obtaining electrical energy using TEG from waste thermal energy sources were examined. The physical parameters used to increase TEG yields were evaluated. With our study, which aims to contribute to this field, it is aimed to contribute to the more efficient evaluation of waste thermal energies through TEG, especially in our own country and worldwide in general.

II. TERMOELECTRIC GENERATORS

Thermoelectric generators provide the generation of electrical energy from the electrical potential caused by two temperature differences. This effect was discovered by T. John Seebeck in 1821. Charles Athanese Peltier demonstrated in 1834 to achieve the opposite cooling effect. The production and active use of these modules started approximately 100 years later, and firstly, thermoelectric coolers (TEC), mostly for cooling purposes, were used. TEGs for electricity generation have become widespread recently. Both modules, whether TEG or TEC, consist of semiconductor material. Studies generally show that the use of Tellurium, Lead and Tin materials is predominant. It is known that Bi2Te3 and Sb2Te3 are the best

semiconductors in the current situation [7]. However, Ochieng et al. In his 2022 study, he also emphasizes that the efficiency remains around 5% in modules with bismuth tellurium material, since the temperature is limited at 260°C and the Z value does not exceed 1.2. Semiconductors are free charge carrier materials. If these free charges are positively charged, it is called P-type material, and if negatively charged, it is called N-type material[8]. The amount of voltage measured in a thermoelectric generator depends on the temperature difference ΔT between the hot and cold regions as in Eq. 2. The Seebeck coefficient of the material and the number of semiconductor pairs (n). The seebeck coefficient of the materials(Eq. 3) used in thermoelectric generators is at least 100μV/°C (Dalar, 2019). It is known that the Seebeck coefficient is different in different materials, but also changes with different temperature. Since the result of Equation 1 is in millivolt values, the voltage value can be increased by connecting more than one module electrically in series.

$$V = n\alpha\Delta T \tag{1}$$

$$\Delta T = T_2 - T_1 \tag{2}$$

$$\alpha = \alpha_2 - \alpha_1 \tag{3}$$

$$ZT = \frac{\alpha^2\sigma}{k}T \tag{4}$$

The thermoelectric effect also depends on the Thermoelectric Efficiency Coefficient (FOM-Figure of Merit) (ZT), also known as the material factor, which is the result of the electrical and thermal conductivity properties of the materials. According to the latest technology, the ZT <1 rule has been broken, and it has been understood that ZT can reach 2 and higher values [9]. As seen in Equation 4, it is understood that the ZT value is directly proportional to the square of the seebeck coefficient, electrical conductivity and average absolute temperature, and inversely proportional to the thermal conductivity (k). On the other hand, the dependence of the voltage measured in a thermoelectric generator on the temperature difference between the hot and cold regions, the seebeck coefficient of the semiconductor material used, and the number of semiconductor pairs have been expressed before. In addition, it is known that the amount of voltage can be increased with the serial connection of the N and P pairs in the thermoelectric modules, and the amount of current can be increased by the parallel connection of these pairs connected in series(Fig. 1).

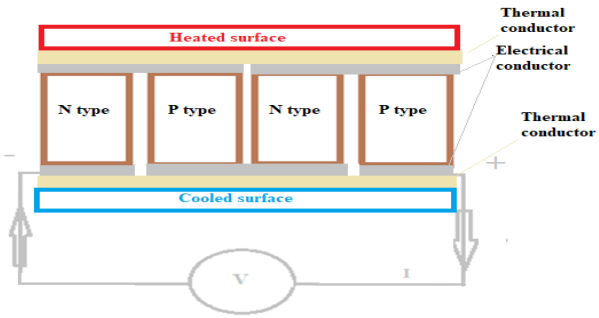


Fig. 1 . Seebeck effect

Thermoelectric generators have heat absorbed (from the hot side) and radiated (from the cold side). In order to provide high voltage and therefore high power, more heat should be absorbed on the heat-absorbed side and more heat should be dissipated on the heat-radiating side. In this sense, it is possible to increase the power by changing different parameters on the heat absorbing and heat radiating surface. As can be seen from the images taken from the Döşkaya

(2010) thesis in Fig. 2, the surface placed in the heat source environment can be called the heat absorbing surface (hot surface), and the other surface to which the heat is transferred can be called the heat emitting surface (cold surface)[10]. Acceleration of heat transfer on these two surfaces is important for power increase. In this respect, the development of heat absorber on the hot surface and the development of heat spreaders on cold surface are research subjects.

Table 1. Advantages and disadvantages of TEG modules

TEG Adventages	TEG Disadvantages
Obtaining electrical energy without intermediaries, All kinds of waste heat can be converted into electrical energy, They do not require maintenance for a long time, therefore their maintenance costs are low, They have a long life span of more than twenty years. Long-term use of high-temperature waste heat as electrical energy, No moving parts, noiseless and environmentally friendly, No emissions or waste.	They have low efficiency of around 15-20% with current technology. Since they are very small (average 40x40 mm), their voltage values are also small. In this respect, many uses are more meaningful.

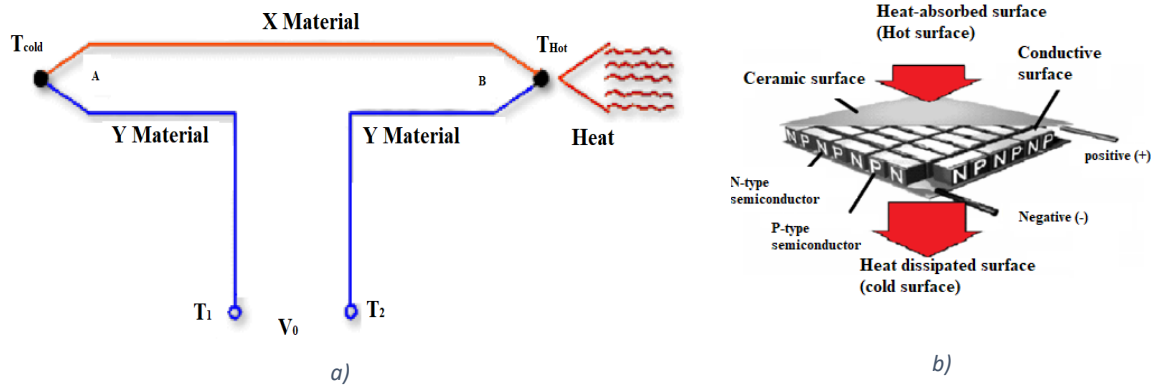


Fig. 2. Termoelectric generator hot and cold surfaces [10]

III. APPLICATION AREAS OF THERMOELECTRIC GENERATORS

Thermoelectric generator efficiencies are closely related to the temperature difference between the hot and cold source. In this regard, the usage areas of TEGs can be almost any place where heat losses occur (Figure 3). In the current situation, researches show that thermal energy is thrown into the environment as waste in the aviation sector, industry, automobiles, solar, etc. These modules can be used in applications. Also hot springs, hot rocks, hot soil etc. They can also be used for electricity generation from geothermal resources. Ochieng et al. (2022) study about the wide usage areas of TEGs is presented in Fig. 3[8].

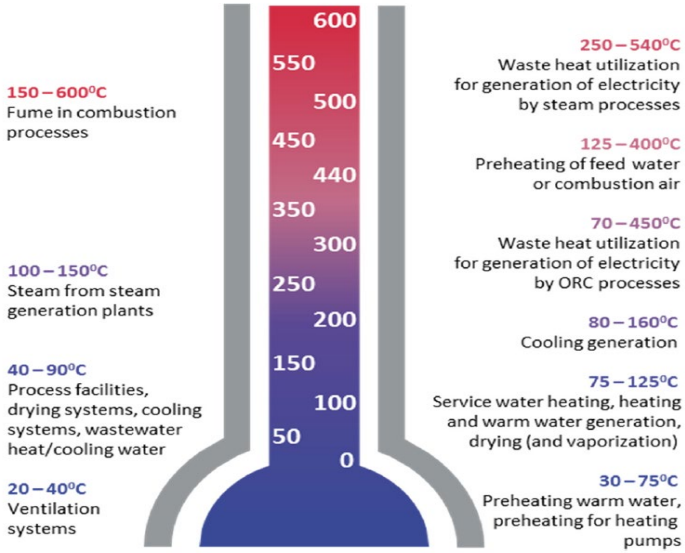


Fig. 3. Waste heat sources and their potential application [8]

In terms of the importance of high temperature gradient from TEG's, studies are also carried out to increase their high temperature resistance. In this sense, 15.3W electrical energy was produced in an area of 16cm^2 operating between 600°C hot and 100°C cold area (GMZ 2014). There are also studies promising to produce electricity up to 55W on the same area [9].

Kaya (2010) converted the exhaust gases into electrical energy by using TEG in his study and used it for charging the battery[11]. According to the related study, if an alternator is used to charge the vehicle battery, the vehicle must be run at a certain speed, whereas when TEG is used, there is no need for such a number of revolutions. However, the author mentions that with the current technology, many thermoelectric generators should be used in order to use thermoelectric generators instead of alternators in charging vehicle batteries, and this causes high costs. Therefore, he mentions that it would be more logical to use thermoelectric generators in vehicle electric-lighting components, which can be in the range of 30-35W at maximum, instead of charging batteries in the near future. However, considering the waste energy of exhaust gases, which can have temperatures up to 1000K, it is emphasized that thermoelectric generators can be used both in vehicle electrical equipment and vehicle charging system in the future, and in this case, fuel consumption and exhaust emissions will also decrease [12]. It has also been emphasized that the waste heat energy converted into electrical energy can also be used to operate the air conditioner [13].

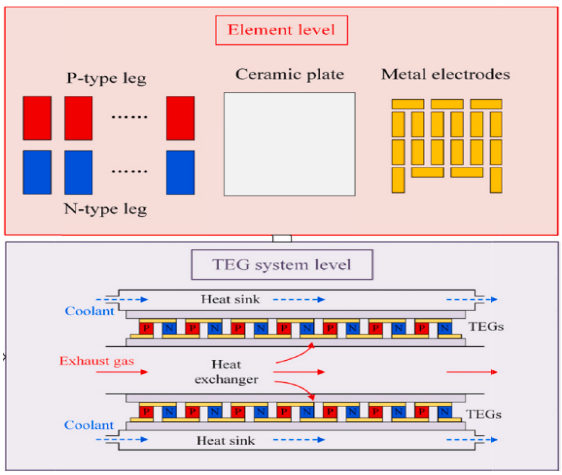
IV. CURRENT DEVELOPMENTS ON THERMOELECTRIC GENERATORS

According to the technological developments until 2019, electricity production up to 15-550W can be realized in TEG modules. It can be combined in electrical installations up to 5kW [9]. TEGs are devices that produce electrical energy up to 1-125W by combining different numbers of TEM modules. By increasing the number of TEMs, TEG powers can be increased up to 5kW [14].

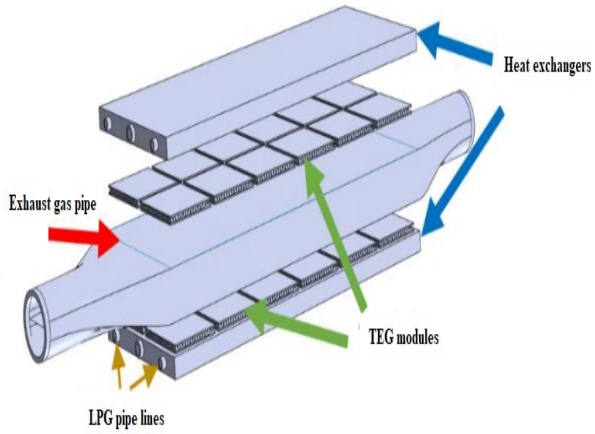
It is known that the exhaust gas temperatures in internal combustion engines are generally between 300-800°C [15,16]. Considering the use of TEM in vehicle exhaust gases, it is mentioned that module efficiency increases in hot-cold high temperature differences, high engine speeds and engine loads [17]. Ochieng et al. (2022), in his extensive literature research study, mentions that the hot side is generally fixed in TEG modules, that thermal improvements such as heat exchangers can only be applied to the cold side of the module, and presents some current numerical and experimental studies in this area.

In case TEG modules are used in exhaust gases, it is recommended to perform the cooling process with engine cooling water, as seen in Figure 4, in terms of being more appropriate and applicable [3, 18]. It has been understood from the numerical study[3] that the thermoelectric generator voltage and current values increase in direct proportion to the engine speed and engine load. In this study, it is mentioned that since 40 thermoelectric modules mounted on the exhaust generate 156,7W electricity at 3000 rpm and 100Nm load value, this electricity will keep the battery charged and electricity can be supplied to electrical components such as air conditioner heaters. In the related study, it is emphasized that good heating of the heated side and good and rapid cooling on the cooled side will play an important role in increasing the efficiency of these modules. In the same study, it is mentioned that using Bi2Te3 material and even at low engine load (25%) electricity generation above 1kW will be possible. Apart from this, there are other studies that produce 1 kW of energy by using TEG in the exhaust [19]. Indeed, Liu et. get. (2015) obtained a maximum output power of 944W in their study[20]. Aranguren et al. 2017 experimentally confirmed a previous numerical study with a 12% margin of error. In this study, 1 TEG consists of 32 TEMs of 40 x 40 mm2 size, model TG12-8-01L, which can be used at temperatures up to 230°C. In this study, in which serial and parallel connection were tried, higher power value (approximately 18kW) was obtained closer to the combustion chamber, and lower power value (11W) was obtained when it was farther from the combustion chamber. It has been determined that there is a decrease in the module power when the temperature and gas flow rate decrease[4]. In the case of using TEM in vehicle exhaust, it has been determined that the module electricity production increases with the increase in vehicle speed [21]. Ge et al. In the current experimental study of 2022, it has been determined that the TEG efficiency is closely related to the number of modules, temperature gradient and fluid flow. In the related study, the cooling of the modules with water is also seen in Fig. 4. Ochieng et al.(2022) in his study, he discussed TEG studies in the automotive and industrial fields from 2000 to 2021[8]. From the relevant literature study, it is understood that recent studies on the use of TEG modules in the recycling of waste heat energy in vehicle exhaust gases have increased approximately 4 times compared to 2008. This indicates the widespread use of TEG modules in automobiles in a short time.

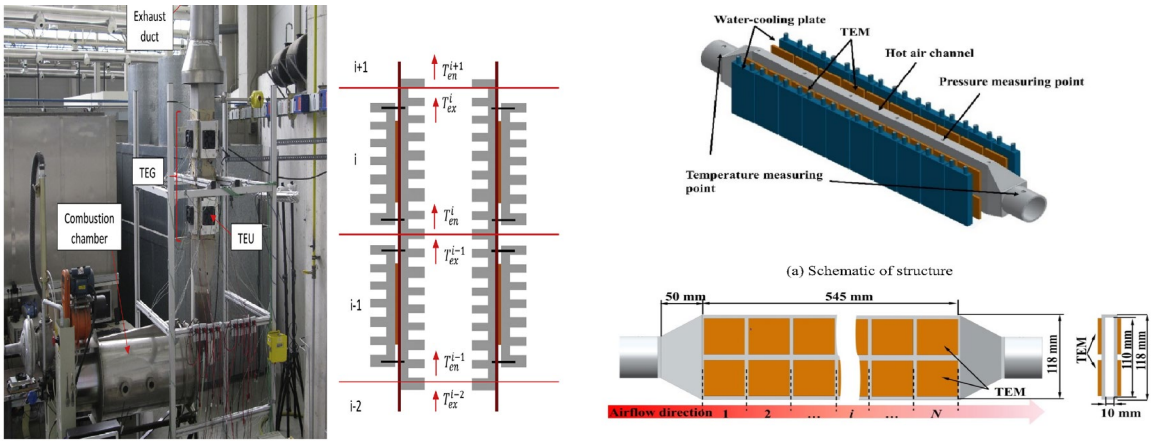
Thanks to TEG modules, it will be easier to heat fuels such as diesel, which have a waxy structure and whose fluidity decreases in the cold of winter, with hot exhaust gases. Akcay et al. (2020) in their study, the TEG module circulated the LPG fuel from the relevant surface for cooling purposes, both ensuring the heating of the fuel and increasing the ΔT temperature of the module. This case study also shows that in case of using TEG in fuel vehicles such as LPG or diesel, it is possible to increase engine efficiency by heating these fuels[22].



a)



b)



c) d)

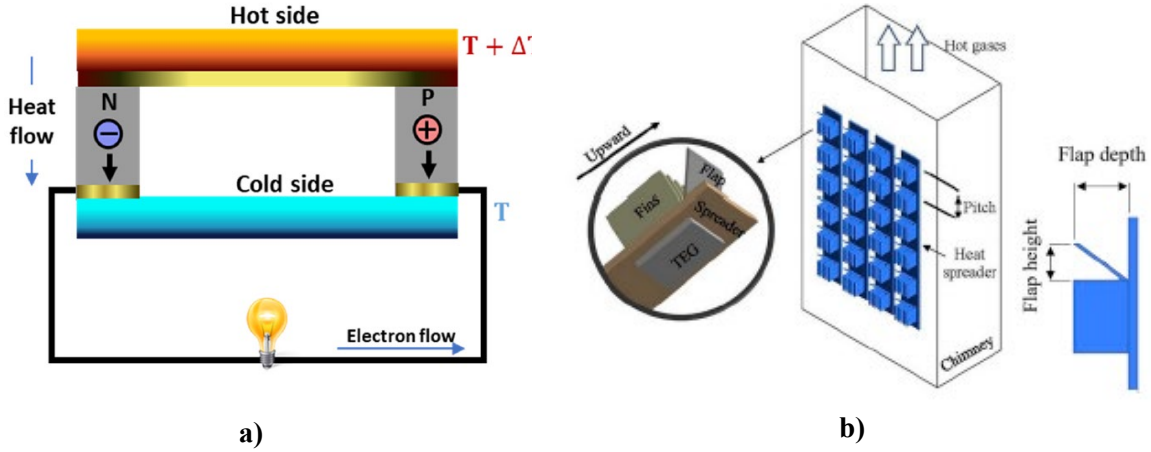
Fig. 4. Examples of current fin and heat exchanger structures used in TEG modules, a) [23], b)[22], c)[4], d) [18]

Studies show that if TEGs are used in exhaust gases, it will be extremely important in terms of fuel economy, reduction of emissions and high efficiency [3].

Undoubtedly, one of the important problems encountered in automobile vehicles is to reduce nitrogen gas (NO_x) emissions. As it is known, nitrogen gas emission is caused by the high temperature of the exhaust gases. Therefore, in order to reduce this gas, the temperature must be lowered. Reducing the internal combustion engine temperature is not a viable thing as it will reduce the engine efficiency. However, with the widespread use of TEG modules, it will be possible to reduce the exhaust gas temperatures and solve this problem.

V. STUDIES ON EFFICIENCY INCREASE IN THERMOELECTRIC GENERATORS

It is understood that the studies to increase the thermoelectric efficiency are mainly carried out on the physical regulation parameters such as the placement of materials and modules, increasing the temperature differences. Looking at the physical parameters, it is seen that the parameters that improve the heat transfer states on the hot and cold sides of the module have a significant effect on the efficiency. It has been stated that keeping the cold side of the module cold has a more significant effect on the efficiency. Because the modules are small in size (40x40 mm), the temperature effect on the hot side also spreads to the cold side. In addition, it is not easy to reduce the temperature of the cold side of such small modules or at least to maintain the same temperature [23]. One of these parameters is the velocity and interaction of the fluid in contact with the module in the hot and cold parts. In the studies conducted, there are studies showing that the module arrangements and their relative positions and chimney inclination angles in TEGs also have a significant effect on the output efficiencies [6, 25]. In the study of Khalil and Hassan (2020), Thermo electricity generators used heat sinks and heat emitters. Electricity generation of generators using heat emitters of 40x140 mm size is 17%-42%; In the case of using a 40x80mm spreader, it increased between 17% and 21%[25]. From this point of view, it is thought that the use of heat emitters of different sizes or the use of heat sinks can increase efficiency. Khalil and Hassan (2019), another study of the same author, mentions that the lateral flaps used in their study significantly increase generator efficiency (Fig.5)[24]. In the study, where the wing depth is between 14 - 50 mm and the height between 20 - 35 mm, there is a 129% increase in efficiency.



a) b)

Fig. 5. TEG module cold side and wing application, a) [8], b) [24]

Jang and Tsai (2013) emphasize that the energy density to be produced in TEG modules is closely related to optimum module placements. In the related study, the optimum distances of the modules and the optimum length and thickness of the emitter were investigated numerically(Fig. 6). According to the related study, it is mentioned that the power generation increases by 50% due to the fact that the thermal resistance will decrease compared to the emitterless situation with the adjustment of the appropriate emitter size. He also mentions that the convection coefficient of the hot gas affects the results more than the temperature gradient. In addition, the distance between the module (S) $40 < S < 300$ mm; he mentions that it would be appropriate to choose the emitter thickness (H) between $1 < H < 30$ mm[26].

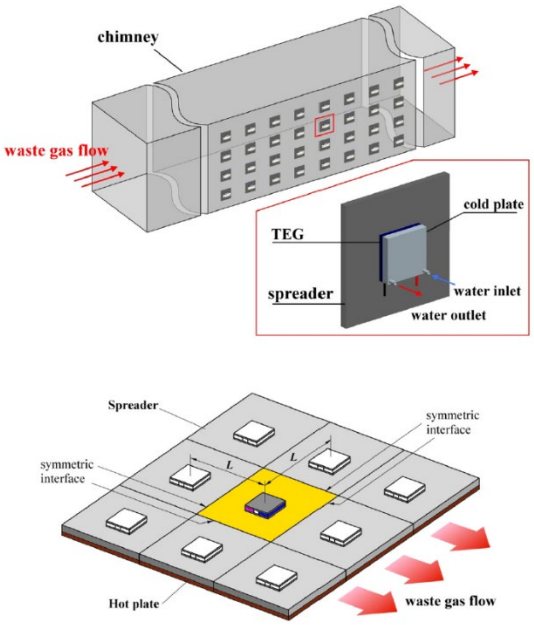


Fig. 6. Us of TEG in flue gas[26]

Demir and Dinçer (2017) numerically investigated the conversion of thermal energy to electrical energy by coating the heat exchanger pipes used in the vehicle exhaust gas recycling system with TEG(Fig. 7). In the study, two different materials $La_{1.98}Sr_{0.02}CuO_4$ and $GdCo_{0.95}Ni_{0.05}O_3$ were compared. It has been determined that the energy obtained from $GdCo_{0.95}Ni_{0.05}O_3$ is approximately 3 times higher than $La_{1.98}Sr_{0.02}CuO_4$. It was stated that the highest exergy efficiency was 0.9%, the highest energy efficiency was 0.6%, and the unit area energy density was 108.8W/m^2[27].

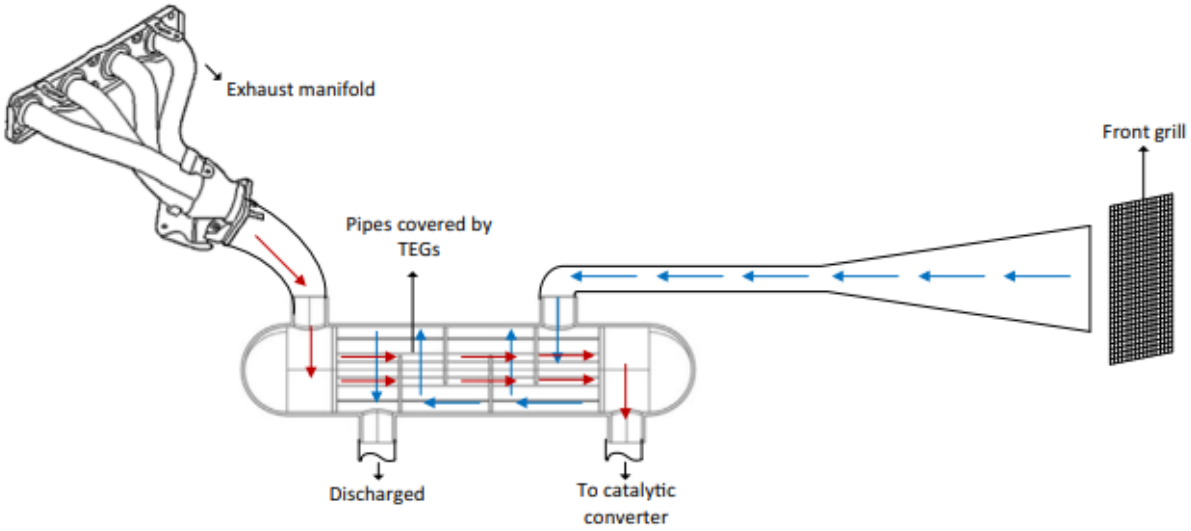


Fig. 7. Usage of TEGs in exhaust gases [27]

Astrain et al.(2010) in his numerical study, efficiency analysis was performed by using heat exchangers on both the hot and cold sides of TEG. According to the study, in the case of using a heat exchanger (finned plate) on the hot side, it is understood that the thermal resistance decreases, and as a result, the module temperature increases, and therefore the power increases. According to the numerical and experimental results, which are compatible with a maximum relative error rate of less than 5%, it is stated that it is possible to generate approximately 1 kW of power from 1 m chimney height. It is mentioned that 10% improvement in thermal resistance will provide an 8% increase in the power produced. In the related study, it is mentioned that although the efficiency of these modules is low, it is promising that the electricity production per unit square meter is higher than solar panels[28].

Improvements in heat transfer on both the hot and cold sides of thermoelectric generators contribute to the increase in efficiency. However, according to some studies, it is stated that the use of heat spreaders and fins, especially on the cold side, will increase power production by 129% and 42% [8,23]. Different TEG module placements, suitable design of heat transfer on the hot and cold side, together with the selection of the appropriate thermoelectricity for the application area, is thought to significantly increase the efficiency [29].

As can be seen, most of the important studies on efficiency increases in TEGs include heat exchanger applications that improve heat transfer in this area. Therefore, it would be appropriate to say that every parameter that affects the heat exchanger efficiency will also indirectly affect the TEG efficiency.

VI. THE FUTURE OF THERMOELECTRIC MODULES

Ge et al.(2022) in the study, they conducted a study on the use of TEGs in concentrated photovoltaic panels. In this study, which points to another important area for TEGs, higher electricity production was achieved by preventing the decrease in efficiency due to increasing temperature in photovoltaic panels[30]. As it is known, under normal conditions, the efficiency of photovoltaic panels is around 20%. However, as it is understood in this case study, when TEGs are used in PV panels, the total system has been increased to approximately 42% by both increasing the panel efficiency by removing unnecessary heat and providing extra electricity production by using the temperature gradient required for TEGs. Therefore, PV/TEG, PVT/TEG and their derivatives should be investigated closely.

Another interesting TEG study is Wang et al. (2023) is on the recycling of thermal energy in a supersonic vehicle. In this study, modules convert aerodynamic heat (or solar energy drawn by PV panel type materials to be placed on the wings of aircraft in the future) into electrical energy. It is seen that PCM material is used as a heat spreader [31].

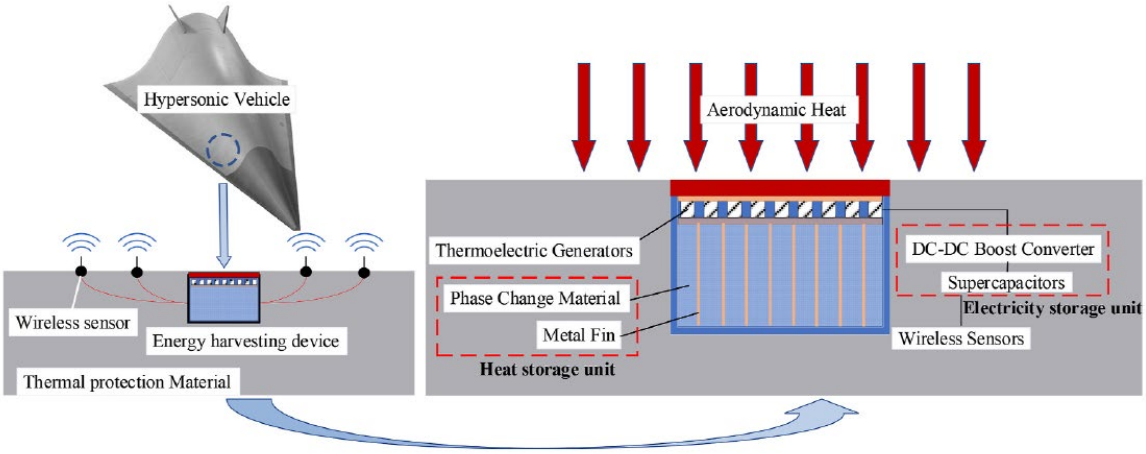


Fig. 8. Using of TEG in Hypersonic Vehicles

In Miao et al. (2022) study the validation of the numerical study was achieved using hot steel structures in an industrial setting. Based on this study, foundries etc. It can be concluded that working environments at high temperatures will also constitute important application areas of TEG modules[32].

VII. CONCLUSION

In this study, current studies on TEGs were examined and the current usage areas of TEGs and the parameters examined on yield increases were investigated. In this sense, important suggestions within the scope of the study are listed as follows:

1. It has been concluded that besides the material, important efficiency increase parameters in TEGs are related to thermal resistance, therefore different fin types or heat exchangers to be used in both heating and cooling sections need to be examined in more detail.

2. Due to the low efficiency disadvantage of TEGs in current technology, it is thought that it would be more appropriate to conduct these module studies in areas with high temperature gradients such as vehicle exhaust gases and boiler flue gases.

3. In the current situation, although the studies on vehicle exhaust gases in general have been intensified, many industrial application areas need to be investigated because 40% of industrial energy is waste heat. In short, it is clear that the areas with the highest thermal energy losses will form the application areas of TEG.

4. However, considering that they provide higher energy production per square meter area than PV panels, it is thought that TEGs will find wider usage areas in the near future, since they can also be used in areas with low temperature gradients such as computers.

5. Especially recently, it has been understood that there is little practice on the hybrid use of TEG modules in PV modules and that important studies can be done in this field. PVT/TEG, CPV/TEG, PVT/nanofluid/TEG, CPV/nanofluid/TEG etc. It is useful to examine the different parameters in detail in the systems.

6. In the aviation sector, the generation of electrical energy from solar energy with the help of TEG modules, by equipping both compressor turbine units and aircraft with PV type materials, can be among the topics that can be investigated. High temperatures in gas turbines pose a significant problem in the aviation industry. With the use of TEG modules in this area, it is possible to provide both cooling and electrical energy.

7. One of the issues mentioned in the literature as the most important problem in TEGs is the limited use of Bismuth tellurium (Bi2Te3) (260C), which is available in the market, preventing the use of this material in high temperature metalworking areas. New materials such as metal oxide semiconductors with high ZT values need to be investigated in this regard.

8. In addition, vertical, horizontal and angled positioning of TEG modules according to the heat source, the good adjustment of the distances of the modules to each other, the use of suitable heat emitters and heat sinks, appropriate heat exchanger designs, the use of phase change materials and nanomaterials for appropriate situations can be used to increase the efficiency of these modules.

9. In addition, it has been understood that the heat improvements on the cold side of the module will affect the efficiency more than the hot side. In this respect, since good cooling of the cold side will improve the efficiency, it will be more appropriate to apply applications with high convection / conduction coefficient for cooling purposes.

REFERENCES

[1] Champier, D., 2017. Thermoelectric generators: a review of applications. Energy Convers. Manage. 140, 167–181, http://dx.doi.org/10.1016/J.ENCONMAN.2017.02.070.

[2] Luo, D., Wang, R., Yu, W., Zhou, W., 2020. A numerical study on the performance of a converging thermoelectric generator system used for waste heat recovery. Appl. Energy 270, 115181. https://doi.org/10.1016/j.apenergy.2020.115181

[3] Temizer, İ., İlkılıç, C., & Cengiz, Ö. N. E. R. (2016). Dizel motor egzoz sistemi için termoelektrik jeneratör uygulaması ve akış analizi. Afyon Kocatepe Üniversitesi Fen ve Mühendislik Bilimleri Dergisi, 16(2), 431-445.

[4] Aranguren, P., Araiz, M., Astrain, D., & Martínez, A. (2017). Thermoelectric generators for waste heat harvesting: A computational and experimental approach. *Energy Conversion and Management*, *148*, 680-691.

[5] Castro Oliveira, M., Iten, M., Cruz, P. L., & Monteiro, H. (2020). Review on energy efficiency progresses, technologies and strategies in the ceramic sector focusing on waste heat recovery. Energies, 13(22), 6096.

[6] Khalil, H., & Hassan, H. (2019). 3D study of the impact of aspect ratio and tilt angle on the thermoelectric generator power for waste heat recovery from a chimney. Journal of Power Sources, 418, 98-111.

[7] Temizer,İ., (2012). Effects on vehicle systems of technology thermoelectric, Batman University International Participated Science And Culture Symposium, Batman University , Journal of Life Sciences.

[8] Ochieng, A. O., Megahed, T. F., Ookawara, S., & Hassan, H. (2022). Comprehensive review in waste heat recovery in different thermal energy-consuming processes using thermoelectric generators for electrical power generation. Process Safety and Environmental Protection, 162, 134-154.

[9] Dalar, U. (2019). Otomobil egzoz sistemlerinde Termoelektrik Jeneratörlü (TEJ) atık ısı geri kazanım sisteminin irdelenmesi (Master's thesis, Kütahya Dumlupınar Üniversitesi/Fen Bilimleri Enstitüsü).

10] Tugay, M. (2010). Dinamik yapılı parabolik yansıtıcı kullanılarak termoelektrik dönüştürücüler ile sağlanan elektrik enerjisinde optimum düzeyin elde edilmesi (Master's thesis, Kırıkkale Üniversitesi).

[11] Kaya, A. Y. (2010). Egzoz gazındaki ısı ile çalıştırılan termoelektrik sistemin deneysel incelenmesi (Doctoral dissertation, SDÜ Fen Bilimleri Enstitüsü).

[12] Topalcı, Ü., Gürbüz, H., Akçay, H., & Demirtürk, S. (2020). Buji Ateşlemeli Bir Motorda Egzoz Atık Isı Geri Kazanımı İçin Termoelektrik Jeneratör Modelinin Geliştirilmesi. Mühendislik Bilimleri Ve Tasarım Dergisi, 8(2), 582-596.

[13] Said, M.A., Hassan, H., 2021. Impact of energy storage of new hybrid system of phase change materials combined with air-conditioner on its heating and cooling performance. J. Energy Storage 36, 102400. https://doi.org/10.1016/j.est.2021.102400

[14] Mamur, H., Dilmaç, Ö. F., Begum, J., & Bhuiyan, M. R. A. (2021). Thermoelectric generators act as renewable energy sources. Cleaner Materials, 2, 100030.

[15] Patyk, A. (2013). Thermoelectric generators for efficiency improvement of power generation by motor generators–environmental and economic perspectives. Applied energy, 102, 1448-1457.

[16] Liang, X., Sun, X., Tian, H., Shu, G., Wang, Y., & Wang, X. (2014). Comparison and parameter optimization of a two-stage thermoelectric generator using high temperature exhaust of internal combustion engine. Applied energy, 130, 190-199.

[17] Kim, T. Y., Negash, A., & Cho, G. (2017). Experimental and numerical study of waste heat recovery characteristics of direct contact thermoelectric generator. Energy Conversion and Management, 140, 273-280.

[18] Ge M., Li, Z., Zhao, Y., Xuan, Z., Li, Y., & Zhao, Y. (2022). Experimental study of thermoelectric generator with different numbers of modules for waste heat recovery. Applied Energy, 322, 119523.

[19] Vale S, Heber L, Coelho PJ, Silva CM. Parametric study of a thermoelectric generator system for exhaust gas energy recovery in diesel road freight transportation. Energy Convers Manage 2017;133:167–77.

[20] Liu, X., Deng, Y. D., Li, Z., & Su, C. Q. (2015). Performance analysis of a waste heat recovery thermoelectric generation system for automotive application. Energy conversion and management, 90, 121-127.

[21] Zhang Y, Cleary M, Wang X, Kempf N, Schoensee L, Yang J, et al. High-temperature and high-power-density nanostructured thermoelectric generator for automotive waste heat recovery. Energy Convers Manage 2015;105:946–50.

[22] Akçay, H., Gürbüz, H., Demirtürk, S., & Topalcı, Ü. (2020). Tipik Bir Buji Ateşlemeli Motorda Egzoz Atık Isısı Enerjisinin Geri Kazanımı İçin Geliştirilen Termoelektrik Jeneratörün HAD Analizi. El-Cezeri, 7(3), 1088-1100.

[23] Luo, D., Liu, Z., Yan, Y., Li, Y., Wang, R., Zhang, L., & Yang, X. (2022). Recent advances in modeling and simulation of thermoelectric power generation. *Energy Conversion and Management*, *273*, 116389.

[24] Khalil, H., & Hassan, H. (2019). Enhancement thermoelectric generators output power from heat recovery of chimneys by using flaps. Journal of Power Sources, 443, 227266.

[25] Khalil, H., & Hassan, H. (2020). Enhancement of waste heat recovery from vertical chimney via thermoelectric generators by heat spreader. Process Safety and Environmental Protection, 140, 314-329.

[26] Jang, J. Y., & Tsai, Y. C. (2013). Optimization of thermoelectric generator module spacing and spreader thickness used in a waste heat recovery system. Applied thermal engineering, 51(1-2), 677-689.

[27] Demir, M. E., & Dincer, I. (2017). Performance assessment of a thermoelectric generator applied to exhaust waste heat recovery. Applied Thermal Engineering, 120, 694-707.

[28] Astrain, D., Vián, J. G., Martínez, A., & Rodríguez, A. (2010). Study of the influence of heat exchangers' thermal resistances on a thermoelectric generation system. Energy, 35(2), 602-610.

[29] Zheng, L.J., Lim, S., Kim, N.K., Kang, D.H., Youn, Y.J., Lee, W., Kang, H.W., 2020. Experimental study of a thin water-film evaporative cooling system to enhance the energy conversion efficiency of a thermoelectric device. Energy 211, 119040. https://doi.org/10.1016/j.energy.2020.119040

[30] Ge, M., Zhao, Y., Li, Y., He, W., Xie, L., & Zhao, Y. (2022). Structural optimization of thermoelectric modules in a concentration photovoltaic–thermoelectric hybrid system. Energy, 244, 123202.

[31] Wang, Y., Cheng, K., Dang, C., Wang, C., Qin, J., & Huang, H. (2023). Performance and experimental investigation for a novel heat storage based thermoelectric harvester for hypersonic vehicles. Energy, 263, 125885.

[32] Miao, Z., Meng, X., & Liu, L. (2022). Analyzing and optimizing the power generation performance of thermoelectric generators based on an industrial environment. Journal of Power Sources, 541, 231699.

Farklı çeliklerin Çift Taraflı TIG Kaynaklı birleşim özelliklerinin incelenmesi

Examination of Joint Properties of Double-Sided TIG Welded of Dissimilar Steels

Tanju TEKER [*1], Sinan AYDIN [2]

[*1]tanjuteker@cumhuriyet.edu.tr, ORCID: 0000-0001-7293-0723
[2]sinancan@cumhuriyet.edu.tr, ORCID: 0000-0003-2285-0906
[*1]*Sivas Cumhuriyet Üniversitesi, Teknoloji Fakültesi, İmalat Mühendisliği Bölümü, 58140, Sivas, Türkiye.*
[2]*Sivas Cumhuriyet Üniversitesi, Teknoloji Fakültesi, Mekatronik Mühendisliği Bölümü, 58140, Sivas, Türkiye*

Özet: İmalat sanayinde farklı alaşımlardaki kalın parçaların birleştirilmesi yaygın olarak yapılmaktadır. Bu çalışmada AISI 1040/AISI 304 kalite çelikler TIG-çift taraflı ark kaynağı (ÇTAK) ile ekstra tel kullanılmadan kaynaklanmıştır. Kaynaklı numunelerdeki mikroyapısal değişiklikler optik mikroskop (OM) ve mikrosertlik analizi ile incelenmiştir. Darbe enerjilerini absorbe etme yeteneği çentik testiyle belirlenmiştir. Kaynak akımı yoğunluğunun, kaynak bölgesi görünümünü büyük ölçüde değiştirmiştir. Mikroyapısal farklılıklar sertlikteki dalgalanmayı etkilemiştir. Kırılma yüzeyi farklı tipte çukurlardan oluşmuştur.

Anahtar Kelimeler: *ÇTAK, TIG, Sertlik, Darbe enerjisi*

Abstract The joining of thick different alloys is done a lot in the manufacturing industry. AISI 1040/AISI 304 grades were welded without extra wire by TIG- double side arc welding (DSAW). The microstructural changes in the welded samples were examined by optical microscopy (OM) and microhardness analysis. The ability to absorb impact energies was determined by the notch test. Welding current intensity changed the weld zone view drastically. Microstructure differences affected the fluctuation in hardness. The fracture surface consisted of different types of pits.

Keywords: *DSAW, TIG, Hardness, Impact energy*

I. GİRİŞ

Kaynak, endüstriyel büyümenin ayrılmaz bir üretim teknolojisidir. Mühendislik uygulamalarında ve metal üretiminin onarımında vazgeçilmez bir tekniktir. Benzer ve farklı malzemeler birleştirilebilir. Karbon çeliği ile paslanmaz çeliğin birleştirilmesi bir sorun teşkil etmektedir. Ergitme kaynak yöntemiyle yapılan farklı kaynakların birleştirilmesinde metalurjik uyumsuzluk ve metaller arası faz her zaman temel sorun olmuştur [1-3].

304 kalite çelik imalat sektöründe kolaylıkla bulunabilen ve şekillendirilebilen bir alaşımdır. 304 kalite paslanmaz çelik, dünya çapında en yaygın kullanılan paslanmaz çeliktir. Mekanik özellikler, kaynaklanabilirlik ve korozyon direncindeki iyi performanslarından dolayı endüstride tercih edilmektedir [4].

1040 serisi orta karbonlu bir çeliktir. Sünektir ve kolayca işlenir. Ana alaşım elementi karbondur. Mangan ve silisyum daha küçük miktarlarda bulunur. Taşıt otomobil bileşenlerinin imalatında kullanılır. AISI 1040 çeliğinin performansı, onu dünya çapında endüstriyel

ortamlarda en güvenilir alaşımlardan biri haline getirmiştir. Metalin bileşimindeki karbon kaynak metalini sertleştirir. Kaynakta çatlaklar ve kırılmalar meydana gelebilir. Günümüz endüstrisinde kullanılan malzeme çeşitleri giderek artmaktadır [5, 6]. Farklı alaşımların kaynaklanması malzeme maliyetlerini azaltır ve farklı alaşımların özelliklerini birleştirir. Kaynakta doğru metal seçimi, alaşımların aktif olarak buluşmasını sağlar ve korozyon nedenlerini azaltır [7, 8].

TIG-ÇTAK gaz ergitme kaynağıdır ve yaygın olarak uygulanır. Ekstra tel ve telsiz yapılabilir [9, 10]. Karbon çeliği ile paslanmaz çeliği farklı kimyasal işlemlerle birleştirmek zordur.

Peng ve ark. TIG kaynaklı 10CrNi3MoV çeliğin mikroyapısını ve performans özelliklerini araştırmış ve en yüksek darbe dayanıklılığı kısa ark mesafesinde olduğunu tespit etmişlerdir [11].

Bu çalışmada, AISI 1040/AISI 304 kaliteleri ekstra tel kullanılmadan TIG-ÇTAK kaynağı ile birleştirilmiştir. Birleşimlerdeki mikroyapı, sertlik ve darbe özellikleri açıklanmıştır.

II. MATERYAL VE YÖNTEM

60×50×10 mm ölçülerindeki AISI 1040-AISI 304 çelikler çift taraflı TIG kaynağı ile birleştirilmiştir. Çeliklerin kimyasal içerikleri Tablo 1'de listelenmiştir. Kaynak uygulamaları Ge-KA-Mak TIG cihazı ile yapılmıştır. Test çalışmalarının süreç parametresi Tablo 2'de açıklanmıştır.

Tablo. 1. Çeliklerin kimyasal içeriği

Malzeme	Fe	C	Cr	Si	Ni	Mn
AISI 1040	97.93	0.393	-	0.156	-	0.656
AISI 304	Bal.	0.066	18.180	0.4720	8.102	1.560

Tablo 2. Test çalışmalarının süreç parametresi

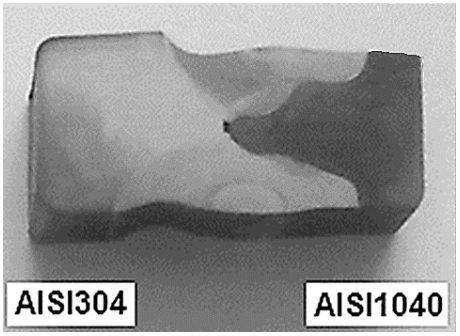
No	Akım (A)	Koruyucu gaz (l/min.)	Kaynak hızı (m/dak.)	Nozul çapı (mm)
S1	450	8	0.01	10
S2	430	8	0.01	10
S3	410	8	0.01	10

Numunelerin yüzeyi 80-1200 mesh zımpara kağıdı ile zımparalanmış ve 3 µm pasta ile parlatılmıştır. AISI 1040 tarafı Nital solüsyonu ile dağlanmıştır. AISI 304 tarafı %50 HNO_3 ve %50 alkol çözeltisi ile 30 saniye 3 V'da elektrolitik olarak dağlanmıştır. Kaynak bölgelerinin mikroyapısal farklılıkları LEICA DM750 optik mikroskobu ile incelenmiştir. Bağlantının mekanik performansı mikrosertlik ve darbe testleri kullanılarak değerlendirilmiştir. Darbe testi numuneleri 10x10x55 mm boyutlarında hazırlanmıştır. Mikrosertlik, QNESS Q10M cihazı ile 0,5 µm aralıklarla 200 g yük altında HV skalası ile belirlenmiştir. Darbe testi JB-300S darbe test cihazı ile gerçekleştirilmiştir. Kırık parçalar SEM kullanılarak incelenmiştir.

III. DENEYSEL SONUÇLAR

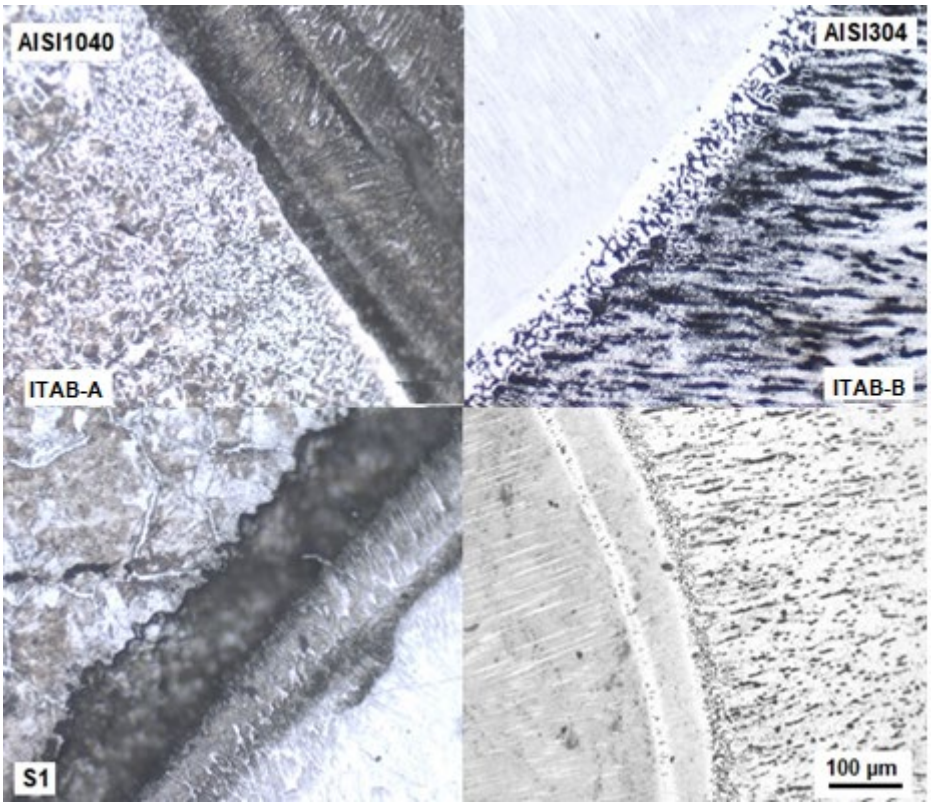
A. Dikiş ve birleştirmelerin değerlendirilmesi

S1 numunesinin kesit fotoğrafı Şekil 1'de verilmiştir. Birleştirme yüzeylerinde gözeneklik ve sıçrama kusurları gözlenmemiştir. İyi yayılma, düz ve pürüzsüz dikişler elde edilmiştir. Birleşim yerlerinin birleşim yerlerinde simetrik ve kum saati şeklinde profiller oluştu. Yüzey sıcaklığının artmasıyla birlikte üst ve alt taraftaki yayılma genişlikleri de artmıştır [12]. Daha düşük kaynak hızı, daha yüksek ısı girdisine ve artan yayılma genişliğine neden olmuştur.



Şekil 1. S1 birleştirmesinin kesiti.

S1 numunesinin optik fotoğrafları Şekil 2'de verilmiştir. Kaynakta ısı girdisi küçük bir alanda meydana gelirse, kaynak metali katılaşması da küçük bir alanda meydana gelmektedir. Böylece Isının tesiri altındaki bölge (ITAB) daralacaktır. Enerji girdisindeki artış ITAB'ı ve dikiş genişliğini artırmıştır. Ayrıca nüfuz derinliğini de artırmıştır. AISI1040-ITAB'ın kaba Widmanstatten ferrit, ferrit ve küçük perlit tanelerine sahip olduğu görülmüştür. Ana metale yakın bölgede ince ve yeniden kristalleşmiş taneler görülmüştür. AISI304'ün yapısı östenit tanelerinden oluşmuştur. Metaller arası oluşum, düşük ısı girdisi ve kaynak için koruma eksikliği ile kaynak havuzunun hızlı katılaşmasına neden olmuştur [13,14].



Şekil 2. S1 birleştirmesinin optik görüntüsü

B. Sertlik

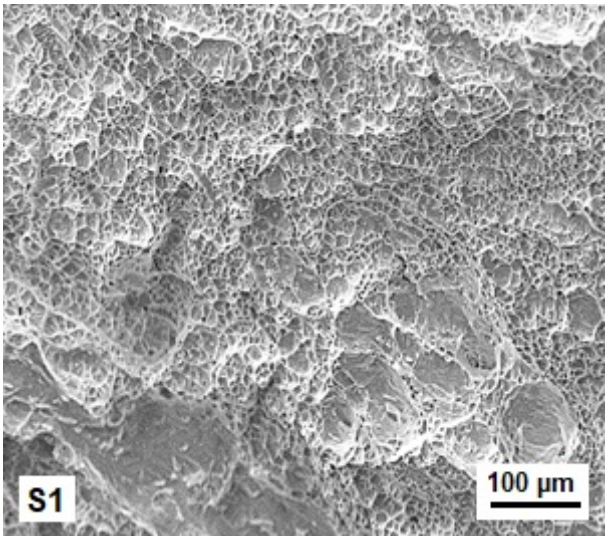
Birleşimlerin sertliği kaynak merkezinde en yüksek değere ulaşmıştır. Sertlik ana metale doğru azalmıştır. Birleşim yerlerindeki sertlik dağılımı eşit olmuştur. Birleşimlerin en yüksek sertliği S1, S2, S3 için 298, 295 ve 290 HV elde edilmiştir. Daha yüksek akım yoğunluklarında kaynak havuzunda daha yüksek sertlik meydana gelmiştir [15].

ITAB, toparlanma ve yeniden kristalleşme nedeniyle düşük sertlik oranı göstermiştir.

Mikroyapısal değişimler sertlikteki dalgalanmayı etkilemiştir. İri ferrit taneleri ITAB'ın sertliğini azaltmıştır. Isı girdisindeki artış ITAB'da tane irileşmesine neden olmuştur. İri taneli yapıların mukavemeti ince taneli yapılara göre daha azdır. İri taneli bölgede çeliklerin kırılma tokluğu düşüktür. Seçilen malzemelerin ve kaynak havuzunun kimyasal bileşimi bu bölgelerin dağılımını ve boyutunu belirlemiştir [13-15].

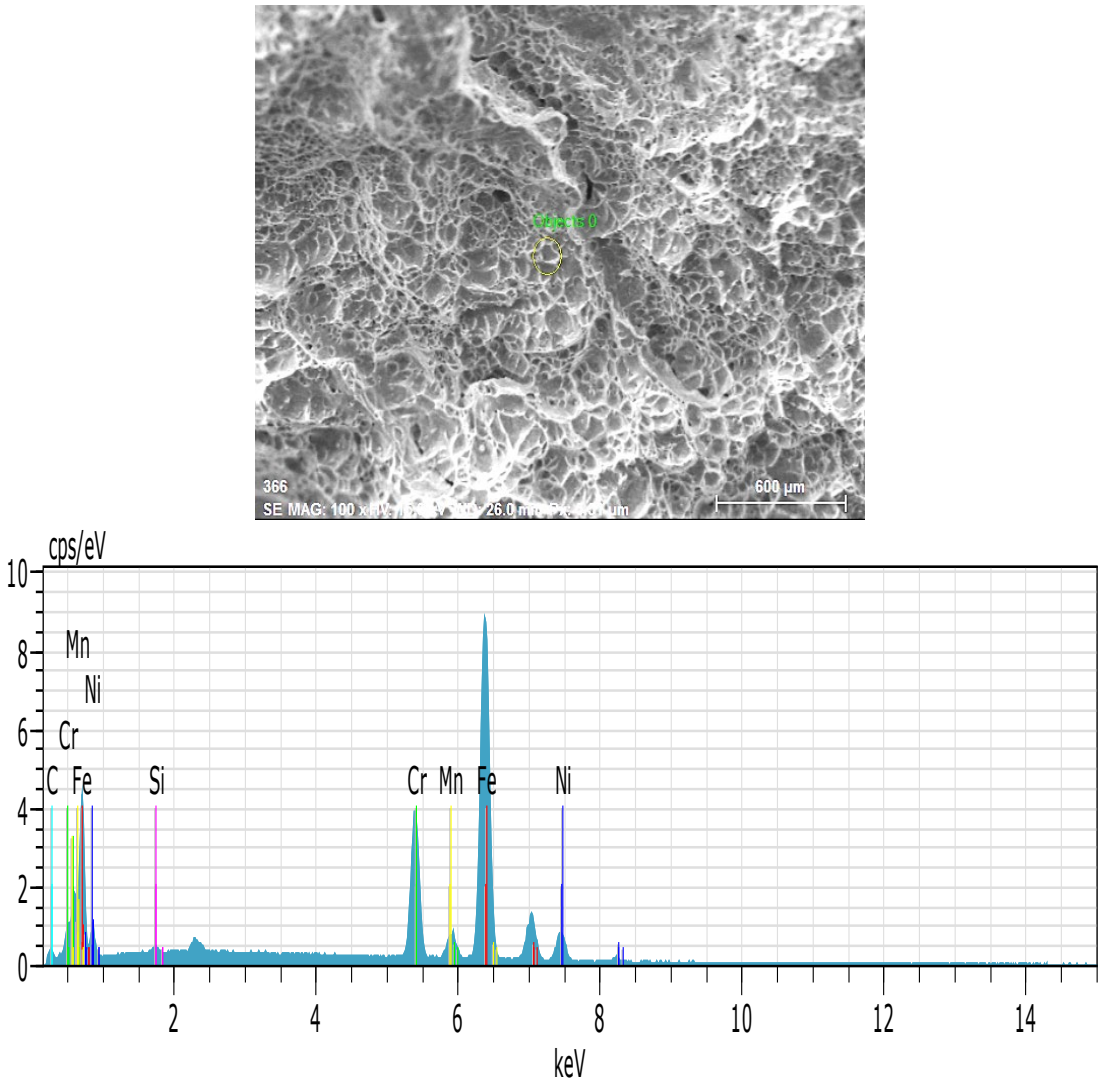
C. Darbe Testi

Birleştirmelerin darbe sonuçları Şekil 3'te gösterilmiştir. Kırılma enerjisi değerleri S1= 71.30 J, S2= 64.70 J ve S3= 42.60 J olarak belirlenmiştir. Artan enerji yoğunluğu penetrasyon derinliğini arttırmıştır. Bu nedenle birleştirmelerin kırılma enerjisi değerleri artmıştır. Kaynak metalindeki δ-ferrit miktarı arttıkça bağlantıların darbe tokluğu azalmıştır. Darbe yüklemesi altında, orijinal mevcut mikro çatlaklar ve yeni oluşan mikro çatlaklar, aralarındaki kesme geriliminin etkisi altında dağılmış ve birleşmiştir. Bu nedenle birleştirmeler daha düşük dirençle kırılmıştır. S1 birleştirmesinin kırılma modu, Şekil 4'te gösterilmiştir. Kaynakların kırılma modunda, transgranüler mikro boşluk birleşimi hâkimdir. Sünek kırılmanın nedeni, deformasyon uyumluluğunun zor olduğu, heterojen olarak çekirdeklenen çukurlardır. Kırılma yüzeyi farklı tipte çukurlardan oluşmuştur. Daha büyük çukurlar krom karbür çökeltilerinden kaynaklanmaktadır [16, 17]. Sünek kırılma, kırılmadan önce ve sonra mekanik enerjiyi dağıtan bir plastik deformasyon işlemidir.



Şekil 4. S1 birleştirmesinin kırılma modu

S1 bağlantısının kırılma yüzeyi EDS analizi Şekil 5'te açıklanmıştır. EDS analizi bağlantı havuzundaki Fe, C, Cr ve Ni kompozisyonunu ortaya koymuştur. Krom ve nikel paslanmaz çelikten AISI 1040 çeliğine, demir, karbon ise AISI 1040 çeliğinden paslanmaz çeliğe yayılmıştır. Karbon difüzyonu, 1040 çelik tarafında yumuşak bölge, paslanmaz çelik tarafında ise sert ve kırılgan karbürler oluşturmuştur. Kaynak metalinde krom, nikel, demir ve karbonca zenginleştirilmiş bir kaynak bölgesi oluşturmuştur.



Şekil. 5. S1 birleştirmesinin EDS analizi

IV. SONUÇLAR

TIG-ÇTAK ile farklı çelikler ekstra tel ve kaynak ağzı kullanılmadan tükenmez elektrotla birleştirilmiştir. Aşağıdaki önemli etkiler gözlenmiştir.

(1) Birleştirmelerde simetrik ve kum saati kaynak profili elde edilmiştir.
(2) Kaynak metalinde bölgesinde sertlik, ITAB'dan daha büyük elde edilmiştir.
(3) Kalın çelikler ekstra tel ve kaynak ağzı açmadan birleştirilmiştir.
(4) En iyi tokluk S1 numunesinde 71.30 J olarak gözlenmiştir.
(5) Bağlantı kırılmaları transgranüler mikro boşluklara neden olmuştur.

KAYNAKLAR

[1] J.C. Lippold and D.J. Kotecki, "Welding metallurgy and weldability of stainless steels'', A John Wiley Sons, Inc., Publication, 88-135, 2005.

[2] H.Y. Huang, S.W. Shyu, K.H. Tseng, and C.P. Chou, "Effects of the process parameters on austenitic stainless steel by TIG-flux welding'', J. Mater. Sci. Technol., 22(3), 367-373, 2008.

[3] C.C. Hsieh and W. Wu, "Phase transformation of δ→σ in multipass heat-affected and fusion zones of dissimilar stainless steels'', Met. Mater. Int., 17, 3375-3381, 2011.

[4] P. Sedeka, J. Brozda, L. Wang and P.J. Withers, "Residual stress relief in MAG welded joints of dissimilar steels'', Int. J. Pressure Vessels Pip., 80(10), 705-713, 2003.

[5] H. Naffakh, M. Shamanian, and F. Ashrafizadeh, "Weldability in dissimilar welds between Type 310 austenitic stainless steel and Alloy 657'', J. Mater. Sci., 43(15), 5300–5304, 2008.

[6] C. Jang, P.Y. Cho, M. Kim, S.J. Oh and J.S. Yang, "Effects of microstructure and residual stress on fatigue crack growth of stainless-steel narrow gap welds'', Mater. Des., 31(4), 1862-1870, 2010.

[7] M.M.A. Khana, L. Romolia, M. Fiaschib, G. Dinia and F. Sarri, "Laser beam welding of dissimilar stainless steels in a fillet joint configuration'', J. Mater. Process. Technol., 212(4), 856-867, 2012.

[8] S. Wang, Q. Ma and Y. Li, "Characterization of microstructure, mechanical properties and corrosion resistance of dissimilar welded joint between 2205 duplex stainless steel and 16MnR'', Mater. Des., 32(2), 831-837, 2011.

[9] K.H. Tseng and C.P. Chou, "The Effect of pulsed GTA welding on the residual stress of a stainless-steel weldment'', J. Mater. Process. Technol., 123(3), 346-353, 2002.

[10] D. Ananthapadmanaban, V.S. Rao, N. Abraham N and K.P. Rao, "A study of mechanical properties of friction welded mild steel to stainless steel joints'', Mater Des., 30(7), 2642–2646, 2009.

[11] K. Peng, C. Yang, C. Fan, S. Lin, Thermal processes, microstructure, and mechanical properties near weld toe in double-sided double gas tungsten arc backing welding joint of 10CrNi3MoV steel, J. Adv. Manuf. Tech., 96, 677–684, 2018.

[12] J.N. Dupont, S. W. Banovic, and A. R. Marder, "Microstructural evolution and weldability of dissimilar welds between a super austenitic stainless steel and nickel-based alloys'', Weld. J., 82(6), 2003.

[13] G. Karthik, "Comparative evaluation of mechanical properties and micro structural characteristics of 304 stainless steel weldments in TIG and SMAW welding processes'', Int. J. Curr. Eng. Technol., 2(2), 200–206, 2013.

[14] R. Rajeev, I. Samajdar, R. Raman, C.S. Harendranath and G.B. Kale, ''Origin of hard and soft zone formation during cladding of austenitic/duplex stainless steel on plain carbon steel'', Mater. Sci. Technol., 17(8), 1005–1011, 2001.

[15] P. Kang, C. Yang, C. Fan and S. Lin, "Thermal processes, microstructure, and mechanical properties near weld toe in double-sided double gas tungsten arc backing welding joint of 10CrNi3MoV steel'', Int. J. Adv. Manuf. Technol., 96(1-4), 677–684, 2018.

[16] C.D. Yang, H.J. Zhang, J.Y. Zhong, Y.X. Chen and S.B. Chen, "The effect of DSAW on preheating temperature in welding thick plate of high-strength low-alloy steel'', Int. J. Adv. Manuf. Technol., 71(1), 421–428, 2014.

[17] S.D. Bhole, J.B. Nemade, L. Collins, C. Liu, "Effect of nickel and molybdenum additions on weld metal toughness in a submerged arc welded HSLA line-pipe steel'', J. Mater. Process Technol., 173(1), 92–100, 2006.

Diagnosis of Coconut Tree Leaf and Bud Diseases using Deep Learning

Onursal ÇETİN

ocetin@bandirma.edu.tr, ORCID: 0000-0001-5220-3959
Bandirma Onyedi Eylul University, Electrical and Electronics Engineering Department, Balıkesir, Turkey

Abstract: Agriculture plays a key role in the economic development of many countries and is a critical sector for sustainable growth. Particularly in tropical regions, coconut is an important agricultural product with significant economic value. However, like other crops, coconut trees are threatened by a number of diseases that can lead to potential economic losses. Such diseases can cause significant yield losses and consequent economic setbacks. Early detection of these diseases can significantly reduce such economic losses, benefiting both farmers and the wider industry. This proactive approach can also improve the quality and quantity of coconut production. However, traditional methods of disease detection, which often involve labor-intensive laboratory testing or expert observation, can be time-consuming. Such methods inevitably limit the capacity for rapid and effective early diagnosis. Technological advances have brought automated detection methods to the forefront. The ability to automatically detect disease symptoms on coconut leaves and buds offers a rapid and effective approach suitable for large-scale applications. In this context, this study applies deep learning models using convolutional neural network and residual network architectures to detect diseases on coconut leaves and buds. Several performance metrics such as accuracy, specificity, sensitivity, precision, and F-score, were used to evaluate the proposed approach. The accuracy of 91.58% and 99.03% and an F-score of 91.91 and 99.38% were obtained for convolutional neural network and residual network models, respectively. Analysis of the performance metrics showed that both models performed very well, but ResNet-50 outperformed CNN on all metrics.

Keywords: *Deep Learning, Coconut Tree, Disease Diagnosis, Convolutional Neural Network, Residual Network*

I. INTRODUCTION

Agriculture is one of the cornerstones that plays a role in the economic development of a country. Various plant diseases and pests occurring in plants lead to yield loss in crops and agricultural products, adversely affecting the economy. The coconut tree is widespread in tropical and subtropical regions and holds critical importance for many economies in these areas. The products derived from this tree, ranging from the food industry to the cosmetics sector, have become indispensable in the modern world due to their extensive benefits [1]. However, the productivity and quality of the coconut tree are threatened by various diseases and pests [2]. Any disease affecting the yield of coconut plantations results in significant losses in production, eventually impacting the industries reliant on coconuts and the livelihoods of families dependent on the coconut economy [3]. Therefore, there is a strong need for close monitoring to prevent crops, plants and trees from being affected by diseases [1]. Coconut yield largely depends on healthy leaves, and common factors affecting the tree's productivity include pest attacks, as well as damage to leaves and buds. The primary diseases affecting coconut trees are bud rot, bud root dropping, gray leaf spot, leaf rot, and stem bleeding [4]. Traditional methods of detecting plant diseases, including those of the coconut tree, rely on determining

disease symptoms, which typically involves physical examination and laboratory testing. This process requires experts to closely inspect plants and trees, which is time consuming and labor-intensive. As a result, early disease detection becomes a challenge, increasing the risk of disease spread. In this context, the application of machine learning technologies promises revolutionary progress in disease detection. Computer vision and deep learning algorithms have made it possible to automatically detect disease symptoms in large datasets [1]. This is a critical factor for early diagnosis and intervention, thus controlling the spread of the disease.

Agricultural biodiversity is the basis for providing people with food and raw materials. However, factors such as temperature extremes, humidity fluctuations, pathogens, soil pH changes, etc. cause plant diseases and directly affect humans by reducing crop yield and quality. Traditionally, farmers detect plant diseases by eye, which is time consuming and often late [5]. To overcome this, the use of image processing, machine learning and deep learning techniques for plant disease detection has recently become widespread [2].

The methods used to analyze, enhance and transform images to solve a specific visual problem in order to obtain valuable information from images are called image processing. These methods consist of various stages such as image acquisition, image preprocessing, image segmentation, feature extraction and classification [5]. Thanks to technologies developed in the field of image processing [6], images of plant leaves can be used to identify diseases using appropriate, efficient and reliable image processing techniques [5]. Machine learning (ML) consists of algorithms designed for computer systems to automatically learn and improve a specific task based on data [7]. ML and image processing, two different branches of computer science, are used together in many modern applications. ML incorporates the concept of a loss function, which makes it more effective than image processing. The loss function makes it possible to determine how the proposed models will work by making predictions. ML methods have been used in various ways to develop new algorithms for early detection and classification of plant diseases.

In the literature, there are various studies using machine learning methods on different datasets. Chandy [8] proposed a deep learning-based system for pest and disease detection in coconut trees. The system uses Nvidia Tegra SoC with ARM architecture CPU and GPU integrated in the drone for image processing. The system also supports advanced machine learning algorithms. In the study, Region Proposal Network and Channel Spatial Attention model are used to find the regions affected by the disease. Nesarajan et al. [2] proposed deep learning architectures including EfficientNetBO, ResNet-50 and VGG16 and Support Vector Machine for disease detection in coconut trees. They found that EfficientNetBO CNN architecture works with high accuracy. In addition, the architecture recommends pesticides and fertilizers after completing the disease analysis. The proposed system uses OpenCV for image comparison. In the study, an Android application "Coconut DR System" is proposed to show the type of disease detected. In disease detection, 93.54% accuracy is achieved using SVM classifier and 93.72% accuracy is achieved using EfficientNetBO CNN architecture. Kaleem et al. [9] proposed a paper on disease detection on leaves using machine learning based SVM. Image processing is also used for disease detection. K-means clustering method is used for color based segmentation. Gray-level co-occurrence matrix is used for feature extraction using image segmentation. The classification of leaf diseases is done by SVM. In addition, the proposed system achieved an accuracy rate of 95.46% for leaf disease detection. Singh et al. [3] proposed a 2D CNN for coconut disease prediction using transfer learning methods. Pre-trained convolutional neural network models such as InceptionV3, VGG16, VGG19, DenseNet201, Xception, NASNetMobile, MobileNet and InceptionResNetV2 were used and MobileNet achieved high accuracy of 82.10%. In addition, while the CNN model achieved 85.63% accuracy with 2 convolution layers, it achieved 96.94% accuracy with 4 convolution layers by increasing the number of convolution layers.

This study aims to investigate the performance of CNN and ResNet-50 architectures, which are deep learning models used to detect leaf and bud diseases of coconut tree based on various parameters.

II. MATERIALS AND METHODS

Deep learning has achieved great success in recent years, especially in visual tasks such as image classification. In this study, CNN and ResNet-50 algorithms are used, which are deep learning methods capable of learning complex features in images, but differ in their architectures and training methods. The flowchart of the proposed method is shown in Fig. 1.

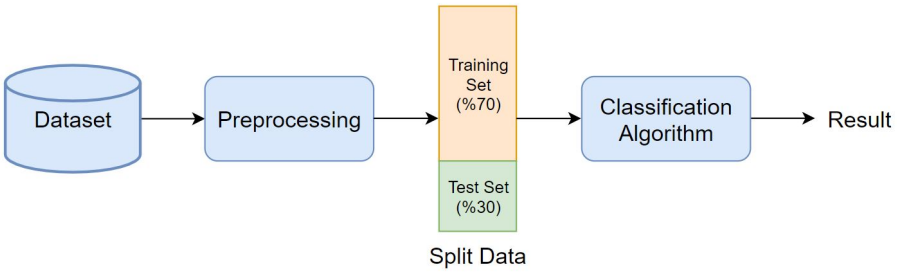


Fig. 1. Flow Chart of Coconut Tree Disease Detection

A. Convolutional Neural Network

CNN, a typical deep learning algorithm, is widely used in computer vision, speech recognition and natural language processing applications [10,11]. The basic working principle of CNN architectures can be summarized as extracting the features of the image from the input layer and classifying the extracted features in fully connected layers [6]. CNNs are very similar to feed-forward neural networks. However, the main difference between CNN-based machine learning models and traditional machine learning methods is that CNNs have convolutional layers that automatically extract features. CNN models basically consist of a convolution layer, a rectified linear unit (ReLU), a pooling layer, a flattening layer, a fully connected layer and a softmax classification layer [10].

The convolution layer is the main component used to learn features in the image. In the convolution layer, a small window in the form of a matrix shifts the input image to extract deep features consisting of edges, lines and corners. This window is called the "filter" or "kernel". ReLU is a widely used activation function in deep neural networks, including CNN. After the convolution layer, the ReLU activation function sets zero and negative values to zero and leaves positive values unchanged [12]. This function allows the model to learn more complex functions by providing the model with non-linearity. The pooling layer is an important component that increases the generalization ability of a CNN and thus provides more consistent results for different inputs. Typically, the maximum pooling method reduces the input size. This helps to reduce the size of the model and the computational load. In CNNs, the data coming from the convolutional and pooling layers is multi-dimensional. A smoothing layer is used to convert these multidimensional feature maps into a one-dimensional vector that can be fed into fully connected layers.

The fully connected layer is usually the last layer in a classification task and generates a probability value for each class using the learned features. These values are typically processed with a softmax activation function to produce the final classification result. Unlike convolution and pooling layers, which learn local and simple features, fully connected layers combine these simple features to learn more complex relationships and representations [12]. Particularly when trained on large datasets, the ability of CNNs to learn and generalize complex features is enhanced, and even challenging visual data processing tasks can be performed with high

success rates.

B. ResNet-50 Network

Deep learning has the ability to automatically learn features from complex data structures based on multi-layer neural networks. However, as the depth of these networks increases, the training process encounters some difficulties. Deep neural networks are very difficult to train due to vanishing/exploding gradients that prevent convergence [13]. Theoretically, the training error is expected to decrease as the depth of the network increases, but in reality the accuracy saturates and then decreases rapidly and the training error increases [13]. This is not due to overfitting but to a degradation/optimisation problem, showing that deeper models are not easy to optimize. To overcome this challenge, the Residual Network (ResNet) architecture was developed by Kaiming He et al. [14] A residual network consists of many "residual blocks". Each block contains one or more convolution operations, similar to a traditional neural network layer. However, at the output of the residual block, the original data entering the block is directly added. The basic component of the residual block is the "residual connection", which adds the original input to the output of the block. Explicitly created residual connections are used to train deep networks more consistently [14]. This allows the gradients to pass directly through the block, avoiding the loss of gradients during backpropagation. After the convolutions in the residual block, an activation function such as ReLU (Rectified Linear Unit) is usually applied. This allows the model to learn non-linear properties [14].

In some residual network designs, expansion or compression blocks are used to control the size of the network. These blocks can increase or decrease the size of the feature maps through convolutional layers. Many residual network designs use global average pooling instead of fully connected layers at the end of the network. This reduces the number of parameters in the model and limits the risk of overfitting. The methodology of residual networks aims to optimize the training process of deep learning models. If the information to be learned in a layer is the output of the previous layer, passing this information directly to the next layer can accelerate and stabilize the network's learning process. This approach allows even very deep networks to be trained effectively. Among the different versions of ResNets, the 50 layer ResNet-50 stands out for its balance between depth, computational efficiency and performance. This architecture has become one of the foundational models in deep learning, setting new benchmarks in various visual recognition tasks. The ResNet-50 architecture was used in this study due to its ability to learn rich hierarchical features while maintaining ease of training [14].

C. Dataset

The productivity and fruit quality of the coconut tree is constantly threatened by a number of diseases and pests. Among these diseases, bud root dropping severely affects the young buds, flowers and fruits of the coconut tree, resulting in significant yield loss. The symptoms of bud root dropping can be observed as paleness of young leaves, dropping of buds and early fruit loss of the tree. This disease, not associated with any specific pathogen, is generally considered a physiological disorder. Cultural practices like proper watering, balanced nutrition, and avoidance of stress factors play a critical role in preventing the disease [15].

Bud rot affects the terminal bud of the coconut tree. The rotting bud is covered with watery, dark-colored spots and the disease attacks the primary growth center of the tree, causing severe damage that can lead to the death of the tree. Fungicide applications and early diagnosis and isolation of infected trees are required to prevent the disease, which is caused by various fungal pathogens [15].

Gray leaf spot disease, one of the threats affecting coconut trees, is characterized by the formation of prominent grey spots on the surface of the leaves. The disease has the potential to spread rapidly and the spots spread over large areas of leaf tissue, reducing photosynthesis

capacity. Consequently, the overall health and productivity of the tree is adversely affected. The disease, caused by fungal pathogens, can be prevented by fungicide applications, cleaning of infected leaves, and proper watering [15].

Leaf rot disease is characterized by staining, yellowing, and ultimately rotting in the leaves of the coconut tree. This disease is typically caused by a number of biological factors caused by various pathogens. Pathogens infect trees, killing cells and reducing photosynthesis capacity. To control the disease, fungicide and bactericide applications, rapid removal of infected leaves and balanced nutrition of the tree are required [15].

In order to achieve high performance in the diagnosis of coconut tree diseases, a dataset containing a wide range of images is required [16]. The "Coconut Tree Disease Dataset" used in this study [17] is a comprehensive collection covering five different disease categories commonly found in coconut trees: bud root dropping, bud rot, gray leaf spot, leaf rot, and stem bleeding. In this study, four classes related to leaf and bud diseases were used, and for this purpose, the stem bleeding class was not included. As seen in Table 1, the dataset contains a total of 4792 labeled images of four different coconut diseases and there is no homogeneous distribution between the classes [17].

TABLE I. DATASET

Label	Name	Number of Samples
1	Bud Root Dropping	514
2	Bud Rot	470
3	Gray Leaf Spot	2135
4	Leaf Rot	1673

III. RESULT AND DISCUSSION

In this section, results are presented to illustrate the functionality of the models. 70% of the dataset was used for training and the remaining 30% for testing. That is, out of a total of 4792 images, 3354 sample images were used during the training phase of the model, while 1438 images were used during the testing phase. The performance metrics for the models were derived from their respective confusion matrices. Fig. 2 shows the confusion matrix for the CNN network.

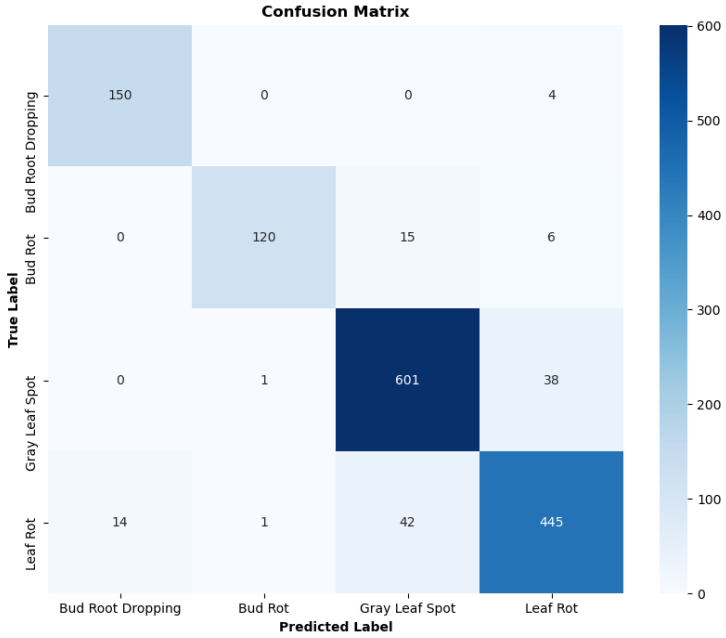


Fig. 2. Confusion matrix of CNN

According to the confusion matrix of the CNN algorithm, it's observed that the model classifies the bud root dropping disease quite well; it has only misclassified it as leaf rot disease in 4 cases. For bud rot disease, the model misclassified it for gray leaf spot disease in 15 cases and as leaf rot disease in 6 cases. This could indicate that the model has not fully learned the characteristics of the bud rot disease or that its characteristics are similar to the gray leaf spot and leaf rot diseases. The performance for the gray leaf spot disease is particularly high, with 601 cases correctly classified out of 640. The leaf rot disease is the class where the model made the most misclassifications. The model confused leaf rot disease with bud root dropping in 14 cases and gray leaf spot in 42 cases. This may indicate that the model hasn't fully learned the characteristics of leaf rot disease, or that its characteristics are similar to those of bud root dropping and gray leaf spot diseases.

Using the confusion matrix obtained, the performance metrics of the model were also calculated and the accuracy was found to be 91.58%. This indicates that the model has a high prediction success rate on the test dataset. The sensitivity rate, calculated for each disease class, was an average of 91.27%. This means that the ability of the model to correctly detect positive cases is quite high. The specificity value represents the model's ability to correctly classify negative cases accurately, and this rate averaged at 96.62%. The model's precision rate was calculated at 92.86% and the F-score at 91.91%. These metrics indicate that the model's classification ability is balanced, and it shows high performance for both classes (positive and negative). The training accuracy and error function graph for the training and testing phases of the CNN are shown in Fig. 3. Looking at the graphs, it can be seen that after an initial increase, the accuracy curve stabilizes and the error function decreases and reaches its minimum value.

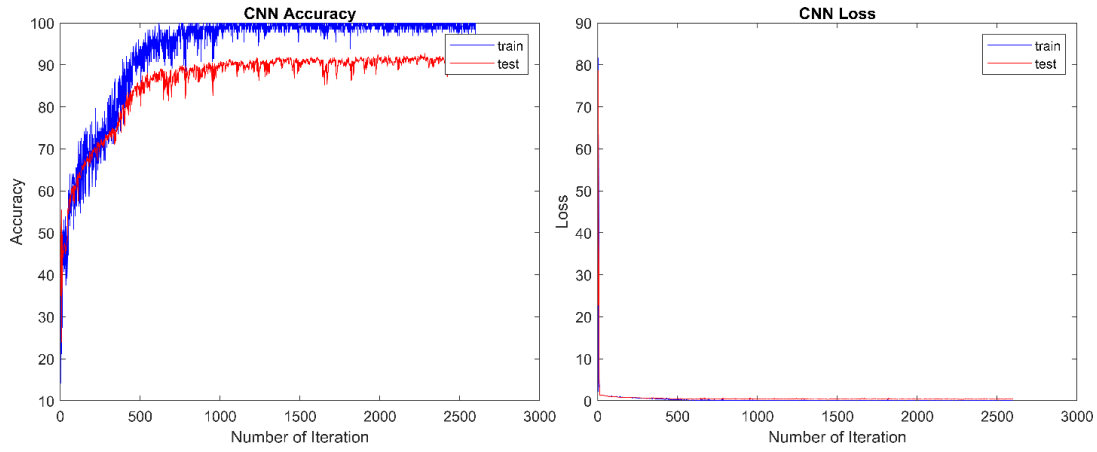


Fig. 3. Accuracy and loss function for training and testing of CNN model

The confusion matrix obtained for the ResNet-50 model, another deep learning algorithm used in the study, is shown in Fig. 4. According to the confusion matrix obtained with the ResNet-50 model, it can be observed that the model classifies both the bud root dropping and bud rot diseases with complete accuracy. This indicates that the ResNet-50 architecture has successfully learned the features of these two diseases. For the gray leaf spot disease, the model correctly classified 636 out of 640 cases and misclassified only 4 cases as leaf rot disease. For leaf rot disease, it's observed that the model correctly classified 492 out of 502 cases, but misclassified 10 cases as gray leaf spot disease. This suggests that the model is quite successful in classifying the gray leaf spot disease but may confuse it with the leaf rot disease in certain situations.

Looking at the performance values, it can be seen that the model generally classifies with an accuracy rate of over 99%. This confirms that the ResNet-50 architecture exhibits a very successful performance on the used dataset. However, a notable confusion between the gray

leaf spot and leaf rot diseases was observed. This could indicate that the two diseases may have similar features, or it could be due to sampling imbalance in the dataset. The training accuracy and error function graph for the ResNet-50's training and testing phases is shown in Fig. 5. When examining the graphs, it's noticeable for both the training and test phases, it's noticeable that after an initial increase, the accuracy curve stabilizes and the error function decreases until it reaches its minimum value.

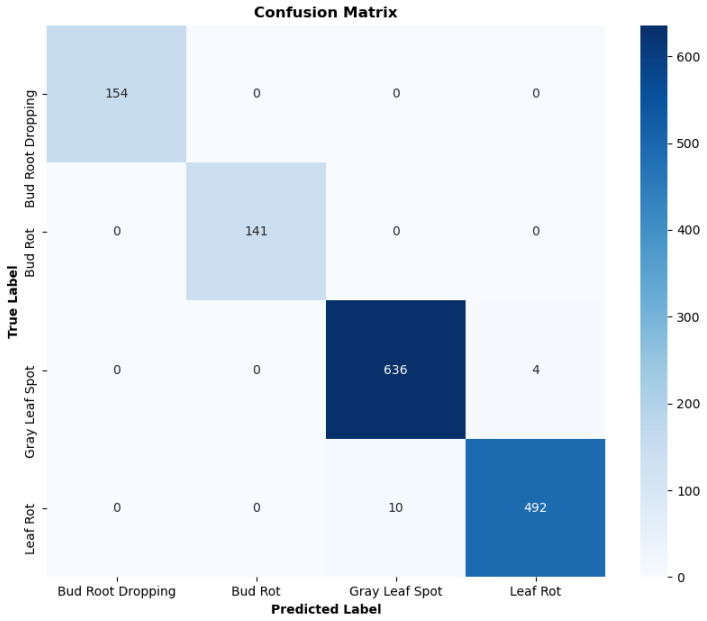


Fig. 4. Confusion matrix of ResNet-50

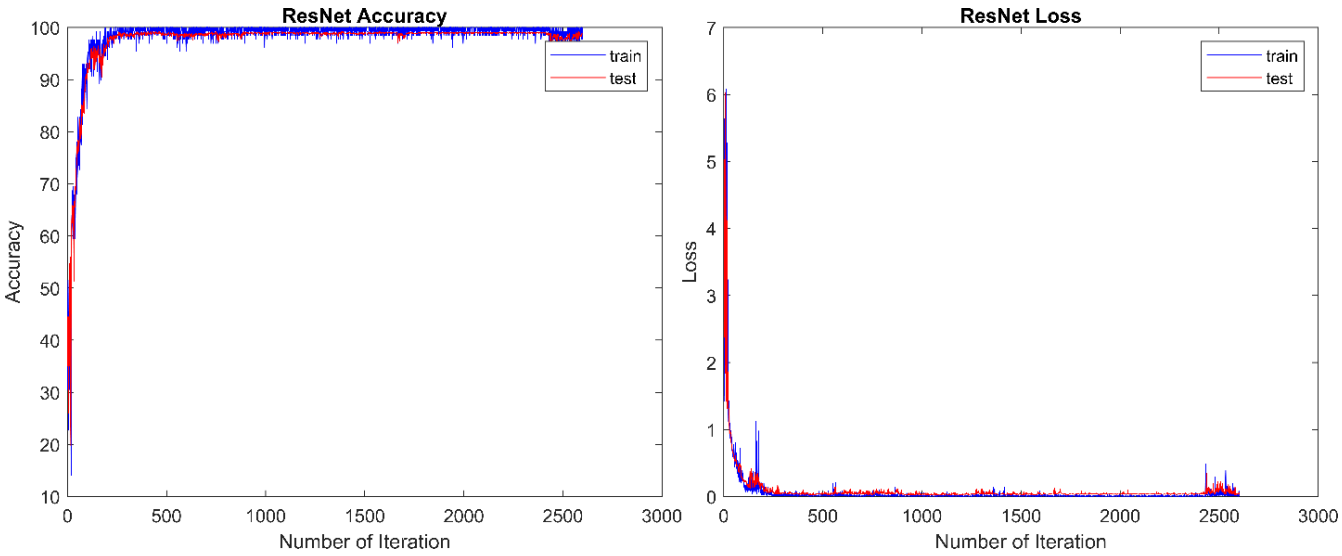


Fig. 5. Accuracy and loss function for training and testing of ResNet-50 model

In this study, the success of CNN and ResNet-50 architectures in classifying bud root dropping, bud rot, gray leaf spot and leaf rot diseases was investigated. The results are shown in Table 2.

TABLE II. RESULTS FOR CNN AND RESNET-50 MODELS

Model	Sensitivity	Specificity	Precision	F-score	Accuracy
CNN	0.9127	0.9662	0.9286	0.9191	0.9158
ResNet-50	0.9935	0.9958	0.9941	0.9938	0.9903

As a result of the analysis of the performance metrics, it was observed that both models gave very good results; however, ResNet-50 was found to be more successful than CNN in all metrics. The radar chart of the performance metrics of both methods is shown in Fig. 6.

The CNN model could not demonstrate high performance for all disease classes. Misclassifications between gray leaf spot and leaf rot can be interpreted as these two diseases may have similar features or that the dataset does not sufficiently highlight the differences between these two classes. This issue can be addressed by reviewing the training process of the model and collecting additional data.

The ResNet-50 algorithm generally showed better performance than the CNN. In particular, more successful results were obtained for the diseases bud root dropping and bud rot. Despite the same misclassifications observed in the CNN architecture between gray leaf spot and leaf rot, ResNet-50 distinguished these two classes better and generally made fewer errors.

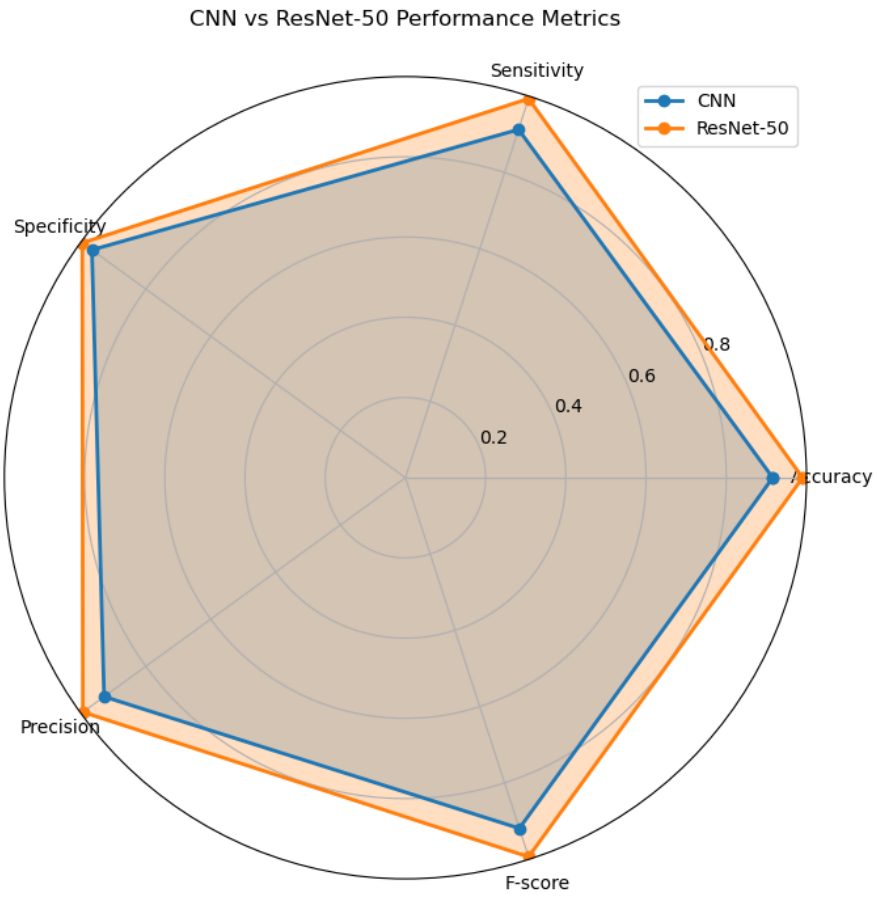


Fig. 6. Radar chart of the performance metrics of the models

IV. CONCLUSION

This study applies deep learning models using convolutional neural network and residual network architectures to detect diseases on coconut leaves and buds. In conclusion, the

importance of early detection of disease in coconut trees, a major agricultural commodity, cannot be underestimated in terms of its economic impact. Traditional diagnostic methods, while reliable, are often laborious and not well suited for rapid intervention. The advent of technology has ushered in automated detection systems that offer a timely and efficient alternative. This study has demonstrated the potential of using CNN and ResNet-50 models in automated detection systems. Notably, while both models demonstrated commendable performance, the ResNet-50 model outperformed in all metrics evaluated. In future studies, expanding the dataset, using data augmentation techniques, and testing different deep learning architectures could further improve these results.

REFERENCES

[1] N. T, P. Vijayalakshmi, J. Jaya, S. S, A Review on Coconut Tree and Plant Disease Detection using various Deep Learning and Convolutional Neural Network Models, in: 2022 Int. Conf. Smart Sustain. Technol. Energy Power Sect., IEEE, 2022: pp. 130–135. https://doi.org/10.1109/SSTEPS57475.2022.00042.

[2] D. Nesarajan, L. Kunalan, M. Logeswaran, S. Kasthuriarachchi, D. Lungalage, Coconut Disease Prediction System Using Image Processing and Deep Learning Techniques, in: 2020 IEEE 4th Int. Conf. Image Process. Appl. Syst., IEEE, 2020: pp. 212–217. https://doi.org/10.1109/IPAS50080.2020.9334934.

[3] P. Singh, A. Verma, J.S.R. Alex, Disease and pest infection detection in coconut tree through deep learning techniques, Comput. Electron. Agric. 182 (2021) 105986. https://doi.org/10.1016/j.compag.2021.105986.

[4] D. Michel, H. De Franqueville, M. Ducamp, Bud rot and other major diseases of coconut , a potential threat to oil palm, Exist. Emerg. Pests Dis. Oil Palm - Adv. Res. Manag. (2012) 13–14.

[5] Ramanjot, U. Mittal, A. Wadhawan, J. Singla, N.. Jhanjhi, R.M. Ghoniem, S.K. Ray, A. Abdelmaboud, Plant Disease Detection and Classification: A Systematic Literature Review, Sensors. 23 (2023) 4769. https://doi.org/10.3390/s23104769.

[6] O. Cetin, Accent Recognition Using a Spectrogram Image Feature-Based Convolutional Neural Network, Arab. J. Sci. Eng. 48 (2023) 1973–1990. https://doi.org/10.1007/s13369-022-07086-9.

[7] P. Mathur, Machine learning applications using python: Cases studies from healthcare, retail, and finance, 2018. https://doi.org/10.1007/978-1-4842-3787-8.

[8] A. Chandy, Pest Infestation Identification In Coconut Trees Using Deep Learning, J. Artif. Intell. Capsul. Networks. 01 (2019) 10–18. https://doi.org/10.36548/jaicn.2019.1.002.

[9] M.K. Kaleem, N. Purohit, K. Azezew, S. Asemie D A Assistant, A Modern Approach for Detection of Leaf Diseases Using Image Processing and ML Based SVM Classifier, Turkish J. Comput. Math. Educ. 12 (2021) 3340–3347.

[10] I. Ozer, O. Cetin, K. Gorur, F. Temurtas, Improved machine learning performances with transfer learning to predicting need for hospitalization in arboviral infections against the small dataset, Neural Comput. Appl. 33 (2021) 14975–14989. https://doi.org/10.1007/S00521-021-06133-0/TABLES/7.

[11] K. Gorur, M. Bozkurt, M. Bascil, F. Temurtas, GKP Signal Processing Using Deep CNN and SVM for Tongue-Machine Interface, Trait. Du Signal. 36 (2019) 319–329. https://doi.org/10.18280/ts.360404.

[12] K. KAPLAN, F. KUNCAN, Human Face Recognition Using Deep Neural Networks, Mühendislik Bilim. ve Araştırmaları Derg. 4 (2022) 189–198. https://doi.org/10.46387/bjesr.1139029.

[13] Y. Bengio, P. Simard, P. Frasconi, Learning long-term dependencies with gradient descent is difficult, IEEE Trans. Neural Networks. 5 (1994) 157–166.

https://doi.org/10.1109/72.279181.
[14] K. He, X. Zhang, S. Ren, J. Sun, Deep Residual Learning for Image Recognition, in: 2016 IEEE Conf. Comput. Vis. Pattern Recognit., IEEE, 2016: pp. 770–778. https://doi.org/10.1109/CVPR.2016.90.
[15] R. Rajendran, L. Rajendran, K. Gandhi, R. Thiruvengadam, Coconut (Cocos Nucifera Linn.) Diseases And Management Strategies, in: 2022: pp. 73–96. https://doi.org/10.1201/9781003160472-5.
[16] B. Anitha., S. Santhi., Disease Prediction in Coconut Leaves using Deep Learning, in: 2023 Int. Conf. Sustain. Comput. Data Commun. Syst., IEEE, 2023: pp. 258–264. https://doi.org/10.1109/ICSCDS56580.2023.10104940.
[17] Coconut Tree Disease Dataset, (n.d.). https://doi.org/10.17632/gh56wbsnj5.1.

Experimental Investigation of Mechanical Behavior of Household Gas Hob Glasses

Ayberk Salim MAYIL[*,1], Sezgin CIGA[1]

[*]: ayberk.mayil@haier-europe.com, ORCID: 0000-0002-6916-3487
[1]: *Haier Europe Research and Development Center, Eskisehir, TURKEY*

ABSTRACT

Gas hobs are essential in household appliance area. Hobs are used for cooking, operate with natural gas or LPG as a source and generally available in different size and shapes. However, it is important to consider certain technical factors for the safe and efficient operation of hobs. These factors include gas pressure, combustion efficiency, flame control, gas safety valve, material, and size of cooking grates. Another important factor is increasing the service life of hobs. In metal body gas hobs, there could be yellowness issue due to high temperature operating conditions. As an alternative, glass body can be used in gas hobs to prevent deformation as like metal body gas hobs. In built-in glass body gas hobs, suitability to furniture is critical. The glass on gas hobs forms the part that remains on the countertop and serves as the supporting part for the lower body. Therefore, its connection with the body must be able to withstand this force. The serigraphs applied to the glass are the communication interface between the user's desired function and the hobs. The tolerance accumulations that occur during the production and assembly of the glass should not cause incompatibility between the activating parts used to fulfill the hob's function and the reference lines that the user can adjust the correct function and level. These details should be common for all glasses. However, tempering control and behavior under load should be examined to determine the thickness of the glass. In this study, 6mm and 8mm glass samples are examined by experimentally and mechanical behaviors of samples are compared to specify the optimum material thickness of gas hob glass. For each sample, planarity, suitability, impact, and tempering are measured by experimentally methods. Based on the measurement, evaluation is carried out. Assessments show the optimum glass thickness for the built-in domestic gas hobs.

Keywords—*Gas Hobs; Domestic Appliance; Glass; Mechanical Behavior*

Fun Letters Collage from Music Notes with GAN Algorithm

Enes TOP

enes.top@outlook.com, ORCID: 0000-0001-8608-3756
Department of Electrical and Electronics Engineering, Karadeniz Technical University, Trabzon, Türkiye

ABSTRACT

Generative Adversarial Networks (GAN) are widely used in synthetic pattern producing applications. As this artificial intelligence algorithm makes it possible to generate nearly similar but actually unique patterns from original pattern libraries with pleasing achievement, variety of application designers such as in NFT market would keep demanding such and developed models.

In this study, it is find that GAN model is being highly interesting to create a personalized fun letters collage from music notes. The music notes patterns of dataset used to train the model so as the output it generates latent space of new musical notes symbols with highly rate of similarity and actual uniqueness.

Using Python abilities, both on web development and AI libraries, it is designed an artificial intelligence interface that interact with users. It is possible that entering any text alphabetically by the user in the designed artificial intelligence interface, their name and surname as an example. In the backend, after parsing the text to letters that comes from the user keys, GAN model that trained with 1-16 beats of music notes symbols starts to creates new synthetic patterns of notes in seconds. Small musical note symbols randomly selected and taken from the latent space and collaged to form the alphabetic characters in the seven rows and five columns matrix template.

The quality of pattern generation are important for future development onto this implementation, so some of the metrics used to calculate the success of the model. User can obtain the personalized unique fun letters collage from music notes, which can be a count as a kind of NFT, created by AI interface.

Keywords— *Music notes to letters; Generative Adversarial Networks (GAN); Personalised collage; NFT*

Effects of First Thinning on Stratification and Health in Sessile Oak

Muhammed Ali AYDIN[*,1], Derya EŞEN[1], Aytekin ERTAŞ[2]

[*]: muhammedali_aydin@ikc.edu.tr, ORCID: 0000-0002-4778-651X
[1]: *Izmir Katip Çelebi University, Faculty of Forestry, Izmir, Turkey*
[2]: *Istanbul University- Cerrahpaşa, Faculty of Forestry, Istanbul, Turkey*

ABSTRACT

Thinning enhances tree growth increment (diameter and height), stand stability, site conditions including soil resources, natural regeneration conditions, and forest aesthetics. Neglecting or insufficient levels of thinning bring on very high density and canopy closure in the stand, contributing to fierce within-stand competition. This study aimed to determine the effects of thinning intensities from none to moderate high thinning in sessile oak (*Quercus petraea* (Matt.) Liebl.) stands, to understand the effect of thinning intensity on stand canopy stratification and health. The study was carried out in four plots of a sessile oak stand of the pole development stage in compartment 113 of Istanbul Belgrad Forest. Over time, common hornbeam (*Carpinus betulus*) contributed to the mixture of upper canopy of the stand. The study used a completely randomized block design. In this context, four study plots, two control and two thinning plots. In 2017, The 0% (the control) and 15-20% (thinning) of the basal area were removed from the stand. Measurements were made on the sites following the thinnings and five years after treatment (YAT) (2022). The diameter at breast height (DBH) of trees was determined with a mechanical caliper. The canopy height of the stand was also determined by averaging the height of the four trees with the largest diameters for each plot. The upper, middle, and lower stratum boundaries were determined by dividing the upper length of the stand into three equal parts. For assessing tree health, scores of 1, 2, 3, and 4 assigned the completely healthy trees, trees with sparse water sprouts, trees with dense water sprouts and the 50% dead canopy, and finally trees with dense water sprouts and more than the 50% of the tree canopy dead. Dead trees were not included in the study, yet their number was recorded.

Five YAT, the percentage of sessile oaks in the dominant layer of the canopy of the moderately thinned stands decreased a little, from 96% to 92%. The decrease was yet more pronounced (from 84% to 59%) on the control sites for this oak species. Common hornbeam was heavily crowded (99%) the lower canopy of the moderately thinned stands. However, the percentage of this broadleaved tree species in the mixture decreased from 97% to 84% in the control plots. On the other hand, five YAT, common hornbeam substantially increased their abundance (from 3% to 16%) in the upper canopy layer of the control stands. 350 stems per ha were in total killed as the result of the natural stem exclusion process on the control sites whereas this rate was significantly less than 75 individuals per ha in the moderately thinned stands five YAT. In 2017, the percentage of healthy trees (groups 1 and 2) in the dominant canopy layer of the thinned stands decreased from 84% to 78%. For the control stands, the health status of the individuals in the dominant layer decreased more, from 66% to 45% over the five years. When tree health is evaluated for the intermediate canopy strata; stand health decreased from 38% to 32% for the moderately thinned stands and from 32% to 23% for the control stands. In general, tree health is greater for the trees of the intermediate and upper canopy layers in the thinned stands. In conclusion, reducing competition among trees for light

and soil resources to a certain extent appears to be necessary for the dominant and the overtopped layers of the stand canopy, to preserve sessile oak, a typical light-demanding tree. Moderate and timely high thinning at the pole stage when competition within the stand is high is therefore critical. Also, it should be noted that delayed thinning may result in the loss of the gains by thinning operations and revert a stand to the status of unthinned.

Keywords— *Thinning, Sessile oak, Stand dynamics, Stratification, Vitality*

Adsorption Properties of Red Mud, Bauxite and Red Soils in Seydişehir (Konya)-Akseki (Antalya) Region

Muazzez Çelik Karakaya[*,1], Necati Karakaya [1], Aydın Ruşen[2], Derya Ölçer[3], Serpil Edebali[3]

[*]: mckarakaya@ktun.edu.tr, ORCID: 0000-0003-1104-2110

[1]: *Department of Geological Engineering, Engineering and Natural Sciences Faculty, Konya Technical University, Konya, Türkiye*

[2]: *Metallurgical and Materials Engineering Department, Karamanoğlu Mehmetbey Üniversity Engineering Faculty, Karaman, Türkiye*

[3]: *Department of Chemical Engineering, Engineering and Natural Sciences Faculty, Konya Technical University, Konya, Türkiye*

ABSTRACT

Examined samples were taken from the red mud pool, some bauxite and red soil deposits in the region. Since the 1970s in the Seydişehir region, red mud, which is the waste generated after alumina production from various bauxite deposits, has stored in the waste pool in the region. In the research, it is aimed to enrich rare earth elements (REE) and some critical/strategic elements e.g., Sc, Ga, Ti, etc from the materials. For this purpose, the critical element contents were determined and the relationship between these element contents and the adsorption capacities of the materials was investigated.

Before examining the adsorption properties of the samples, besides the determination of some physical properties, especially mineral compositions and main and trace element contents were determined by X-ray diffraction (XRD) and X-ray fluorescence (XRF) and Inductive Copule Plasma-Mass Spectrometry (ICP-MS). In order to determine N2 absorption/desorption, red mud, bauxite and red soil samples were kept at 150 ºC for one hour, then at 200 ºC for 2 hours to obtain a constant weight in degas. After the degas treatment, N2 adsorption at -198 ºC and other properties were determined in the BET device. The surface area, pore size, pore volume and adsorption capacity of the samples were measured by using P/Po in the range of 0.06 to 0.30 in isotherms and in desorption of isotherms after degassing.

In the red mud and bauxite samples, the most common Al-hydroxide minerals are diaspore and partially boehmite, while in the red soil samples the most common alumina mineral is boehmite and a small amount of gibbsite. Hematite is the most abundant iron oxide mineral after alumina minerals in the first two mineral groups. Quartz, feldspar and kaolinite are silicate minerals that are more abundant in red soil samples than in other sample groups. Significant differences in the mineralogical composition and element contents of the examined materials were determined between material types and within the same material type. It was determined that the REE content of red mud, bauxite and red soils varied from 437 to 1161, 161 to 4072 and 187 to 1274 ppm, respectively.

No significant difference was observed in the adsorption properties of the examined samples after degassing at these two different temperatures or only 200 ºC. For this reason, all samples were degassed at 200 ºC. It was determined that the BET value of the red mud samples varied from 11.60 to 16.08, while the bauxite was between 6.80 and 19.68 m^2/g. The adsorption capacities varied between 3.20 and 4.40 and between 1.90 and 5.40 cm^3/g, respectively. These two properties of red soil samples are slightly higher than the first two sample groups (average 28.68 m^2/g and 11.36 cm^3/g), probably related to the higher clay mineral content of this group.

A strong positive correlation was determined between these determined properties of all samples.

The strong positive correlation (R^2=0.94) may explain that the adsorbing capacity of these samples increased with the increase in the surface area of the samples, and possibly some elements were present in the material in the form of adsorption. However, the low surface area and adsorption capacity may indicate that the REE content may be in the form of a single mineral rather than being present in the material as adsorption.

Keywords— *Adsorbsion, bauxite, BET, red mud, red soil*

Rare Earth Element Contents of Bauxites in Seydişehir (Konya) Region

Muazzez Çelik Karakaya[*,1], Aydın Ruşen[2], Necati Karakaya[1]

[*]: mckarakaya@ktun.edu.tr, ORCID: 0000-0003-1104-2110
[1]: *Department of Geological Engineering, Engineering and Natural Sciences Faculty, Konya Technical University, Konya, Türkiye*
[2]: *Metallurgical and Materials Engineering Department, Karamanoğlu Mehmetbey Üniversity Engineering Faculty, Karaman, Türkiye*

ABSTRACT

In the Seydişehir (Konya) and Akseki (Antalya) regions, Turkey's most important bauxite deposits are found in various reserves, grades and features. From the aforementioned bauxite deposits, especially in the Seydişehir region, operations have been carried out to obtain alumina since 1970. In the literature, researches on the enrichment/recovery of REE elements from red mud have been conducted. However, there is no research on the enrichment of these elements from bauxite, which is the raw material of red mud. For this reason, it is aimed to determine the rare earth elements (REE) contents of the bauxite deposits and the REE-rich mineral in samples with high content of these elements.

Seventeen bauxite samples from six different bauxite deposits in the region were taken from different bauxite types in different parts of the deposits. Before determining NE-content and NT-enrich minerals of the bauxite of some physical properties of the samples were investigated. Mineralogical compositions and main and trace element contents were determined by X-ray diffraction (XRD), X-ray fluorescence (XRF) and Inductive Couple Plasma-Mass Spectrometry (ICP-MS), respectively. Microprobe analyzes were performed to determine REE-containing minerals in bauxites.

Mineralogical composition of the bauxites is partially homogeneous. The most common Al-hydroxide minerals are diaspore and partially boehmite. Hematite is the most abundant iron oxide mineral and goethite is rarely found as Fe-hydroxide mineral. Quartz, feldspar and kaolinite are silicate minerals that are rarely determined in some bauxites, except massive bauxite. The REE content of the bauxites varied from 161 to 4072. It has been determined that the REE contents of massive bauxites are generally higher than other type bauxites. Thin sections of the bauxite samples with REE content of more than 1000 ppm were polished and microprobe analyzes were carried out to detect REE-rich minerals and content of the elements.

After microprobe analysis, it was determined that the elements with the highest REE oxide contents were La (31.51%), Pr (8.53%), Nd (5.42%) and rarely Ce (2.80%) and Gd (1.48) elements, respectively. When the La and other detected elements were evaluated, it was thought that the composition was partially similar to bastnäsite and perisite, especially determined in karstic bauxites, due to the very low Ce content, and the high Pr and Nd content could be a different mineral or modification.

Keywords— *Bauxite, alumina, red mud, REE, Seydişehir*

Recovery of Lanthanum (La) from A Bauxide Residue (Red Mud) Solution by Sorption Process with A Strong Acid Cation Exchange Resin and A Microcapsule

Derya Ölçer[*,1], Serpil Edebali[1], Muazzez Çelik Karakaya[2]

[*]: deryailker@yahoo.com, ORCID: 0000-0001-8159-3415
[1]: *Chemical Engineering Department, Konya Technical University, Konya, Turkey*
[2]: *Geological Engineering Department, Konya Technical University, Konya, Turkey*

ABSTRACT

For the recovery of a light rare earth element, lanthanum (La) from a aqueus solution, both a commercially available resin, Lewatit MonoPlus SP 112 and a microcapsule prepared by using chitosan and a clay mineral, Palygorskite was used. The recovery was acquired from the solution obtained by water leaching from bauxite residue (red mud). Batch adsorption processes were carried out as a function of time, adsorbent dosage, concentration, pH and temperature to evaluate the performance of the adsorbents.

Lewatit MonoPlus SP 112 is a strongly acidic, macroporous cation exchange resin with Sulfonic acid functional group, and Palygorskite is a clay mineral characterized by a microfibrous morphology, low surface charge, high magnesium content, and high specific surface area. In order to improve the adsorption capacity of Palygorskite, another very effective non-toxic and bioactive adsorbent, chitosan is used by preparing microcapsules.

To evaluate the experimental data, Langmuir, Freundlich, D-R and Scatchard isotherm models were used. The experimental data were well fitted to the Langmuir and Scatchard isotherm models for Lewatit MonoPlus SP 112, and Langmuir isotherm model for Palygorskite-Chitosan Microcapsule, with a correlation coefficient of 1.0 and 0.996 for Lewatit MonoPlus SP 112 and 0.8397 for Palygorskite-Chitosan Microcapsule respectively. The adsorption kinetics can be described by pseudo second-order model for Lewatit® MonoPlus SP 112 and pseudo first-order model for Palygorskite-Chitosan Microcapsule.

The optimum pH for La adsorption was found as 6.0 for both of the adsorbents. It was found that more than 99% recovery was achieved under optimal conditions. The maximum adsorption capacities are 0.104 and 0.022 mmol/g of Lewatit® MonoPlus SP 112 and Palygorskite-Chitosan Microcapsule, respectively.

Keywords— *Bauxide Residue, Adsorption, Rare Earth Elements, Lanthanum, Lewatit MonoPlus SP 112, Palygorskite, Chitosan, Microcapsule*

Recovery Of Lanthanum (La) From A Bauxide Solution by Sorption Process with A Weak Acid Cation Exchange Resin and A Microcapsule

Derya Ölçer[*,1], Serpil Edebali[1], Muazzez Çelik Karakaya[2]

[*]: deryailker@yahoo.com, ORCID: 0000-0001-8159-3415
[1]: *Chemical Engineering Department, Konya Technical University, Konya, Turkey*
[2]: *Geological Engineering Department, Konya Technical University, Konya, Turkey*

ABSTRACT

For the recovery of a light rare earth element, lanthanum (La) from a aqueus solution, both a commercially available resin, Lewatit TP 260 and a microcapsule prepared by using chitosan and a naturally abundant zeolite, Chabazite was used. The recovery was acquired from the solution obtained by water leaching from bauxite. Batch adsorption processes were carried out as a function of time, adsorbent dosage, concentration, pH and temperature to evaluate the performance of the adsorbents.

Lewatit TP 260 is weakly acidic, macroporous cation exchange resin with chelating amino methyl phosphonic acid groups, whereas Chabazite, a tectosilicate mineral of the zeolite group, is one of the most porous natural zeolites and, having a high surface area. In order to improve the adsorption capacity of chabazite, another very effective non-toxic and bioactive adsorbent, chitosan is used by preparing microcapsules.

To evaluate the experimental data, Langmuir, Freundlich, D-R and Scatchard isotherm models were used. The experimental data were well fitted to the Langmuir and Scatchard isotherm models for both Lewatit TP 260 and Chabazite-Chitosan Microcapsule, with a correlation coefficient of 0.9959 and 0,9988 for Lewatit TP 260 and 0,9474 and 1,0 for Chabazite-Chitosan Microcapsule respectively. The adsorption kinetics can be described by pseudo second-order model for both of the adsorbents.

The optimum pH for La adsorption was found as 2.6 for both of the adsorbents. It was found that more than 99% recovery was achieved under optimal conditions. The maximum adsorption capacities are 2.895 and 0.578 mmol/g of Lewatit TP 260 and Chabazite-Chitosan Microcapsule, respectively.

Keywords—*Bauxide, Adsorption, Rare Earth Elements, Lanthanum, Lewatit TP 260, Chabazite, Chitosan, Microcapsule*

Investigation Of Roasting Parameters on Rare Earth Elements Recovery from Bauxite

Aydın RÜŞEN[*,1], Mahmut Sami ALKAN[1], Hanae CHOUBİ[1], Muazzez ÇELİK KARAKAYA[2]
Necati KARAKAYA[2]

[*]: aydinrusen@kmu.edu.tr, ORCID: 0000-0002-8953-314X
[1]: *Department of Metallurgy and Materials Engineering, Karamanoğlu Mehmetbey University, Karaman, Türkiye*
[2]: *Department of Geological Engineering, Konya Teknik University, Konya, Türkiye*

ABSTRACT

Bauxite, the main ore in aluminum metal production, is a lateritic rock and may contain significant amounts of rare earth elements (REEs). Therefore, chemical, mineralogical, and thermal analysis of bauxite rocks obtained from deposits in the Seydişehir region were firstly carried out. Result of chemical analysis reveals that the REEs concentration in the sample ranges between 1000 - 2000 ppm. According to mineralogical analysis of the examined bauxite deposit, boehmite is the most common alumina mineral of the Al-hydroxide phases and hematite is the second most abundant mineral. Anatase and kaolinite were also detected in the bauxite sample as the titanium mineral and a clay mineral, respectively.

In the experimental study, pyro-hydrometallurgical method (sulfation – roasting - leaching) was preferred for the recovery of REEs determined in bauxite rocks obtained from deposits in the Seydişehir region. Instead of leaching the bauxite directly with sulfuric acid, the basic principle is to mix the bauxite at a certain rate and keep it for a period of time at 120 °C, so that the oxidized elements in the structure turn into sulfated structures as much as possible, then roasting at a temperature that will preserve the sulfated structure of the REEs. Finally, it is aimed to take sulphate REEs with soluble properties into solution by water leaching. In this study, in order to determine the most important parameters (roasting temperature and duration) affecting the recovery efficiency of REEs, roasting processes were carried out at different temperatures (700-800°C) and for different times (1-4 hours). According to the results, it has been observed that some REE recovery rates approached 70% after water leaching.

Keywords—*Roasting; Rare Earth Elements; Recovery; Bauxite*

Rare Earth Elements Recovery from Red Mud with Hydrochloric Acid Using Taguchi Method

Aydın RÜŞEN[*,1], Mahmut Sami ALKAN[1], Muazzez ÇELİK KARAKAYA[2], Necati KARAKAYA[2]

[*]: aydinrusen@kmu.edu.tr, ORCID: 0000-0002-8953-314X
[1]: *Department of Metallurgy and Materials Engineering, Karamanoğlu Mehmetbey University, Karaman, Türkiye*
[2]: *Department of Geological Engineering, Konya Teknik University, Konya, Türkiye*

ABSTRACT

In this study, it was aimed to recover rare earth elements and critical raw materials (REE/CRM: Ce, La, Nd, Y, Pr, Sm, Ga, Sc) by hydrometallurgical method from red mud, which is one of the important wastes of the aluminum industry, using the Taguchi method. This method is an experimental design method recommended to produce high quality and low-cost products with fewer experiments. In the experimental studies, the experimental series designed according to the Taguchi Method (L16) orthogonal arrays were applied and the optimum conditions were determined by considering the effects of the selected parameters on the leaching efficiency. Technical grade hydrochloric acid (HCl 37%) was chosen as the leaching reagent, and experiments were carried out under following parameters; 1M-4M HCl concentrations, in the temperature range of 25 °C - 95 °C, at 1/40 - 1/10 solid/liquid ratios and at different times (60 - 480 min.). After the analyzes based on the results obtained, as the common optimum test condition for the selected REE/CRMs; 4 M HCl concentration, 75 °C temperature, 480 min. time and 1/30 solid/liquid ratio were determined. In the verification test performed with optimal conditions of the process parameters to demonstrate the effectiveness of the Taguchi method, a recovery of over 90% was obtained for the selected rare earth elements such as La, Ce, Y, Pr, Nd, Sm and critical metal (Sc). Results of the experiments indicate that Taguchi optimization method is very applicable way to optimize the REEs/CRM recovery efficiency from red mud in hydrochloric acid media.

Keywords—*Hydrometallurgy; Rare Earth Elements; Recovery; Red Mud; Taguchi Method*

Application Of Hybrid Particle Swarm Optimization for Energy Demand Prediction in Türkiye

Merve KAYACI ÇODUR

merve.codur@erzurum.edu.tr, ORCID: 0000-0003-1459-9678
Industrial Engineering Department, Erzurum Technical University, Erzurum, Türkiye

ABSTRACT

Energy plays an indispensable role in the development and functioning of countries and various aspects of daily life. It drives economic growth, improves living standards, supports social services, enhances national security, and contributes to environmental sustainability. Ensuring reliable, affordable, and sustainable energy access is essential for a country's overall development and progress. Türkiye's energy consumption has undergone notable changes and expansion. As a rapidly developing country, Türkiye has experienced a substantial increase in energy demand due to population growth, urbanization, industrialization, and economic development. The country's energy sources encompass a blend of fossil fuels, renewable sources, and imports. Particularly, electricity consumption holds a significant share in Türkiye's overall energy usage. Nevertheless, despite the remarkable rise in energy consumption, Türkiye's energy production remains comparatively modest. Therefore, the development of energy policies and the estimation of energy demand are a most important priority for developed and developing countries.

The goal of this study is to propose a Hybrid Particle Swarm Optimization (H-PSO) algorithm for optimizing coefficients to predict energy demand based on several predictor variables including GDP, population, imports, and exports in Türkiye. Linear and exponential forms of mathematical expressions were employed for energy demand estimations. Historical data spanning 43 years, from 1979 to 2021, was utilized for the training and testing stages of the models. Four different measurement metrics were utilized to evaluate the performance of the models. This study aims to achieve more accurate models and results, formulate better plans for managing future energy demand in Türkiye, and contribute to the development of alternative technologies. The expectation is that this research holds the potential to formulate highly effective and relevant strategies concerning energy policies.

Keywords—*Energy; Machine Learning; Particle Swarm Optimization*

Drone Arm Optimization Using Genetic Algorithm

Özlem AKÇAY[*,1], Medeni SÖMER[2]

[*1]:ozlemakcay044@gmail.com, ORCID: 0009-0002-2316-6540
[1]: Automotive engineering of technology faculty, Fırat University, Elazığ, Türkiye
[2]: Automotive Program, Department of Motor Vehicles and Transport Technology, İstanbul Nişantaşı Vocational High School, İstanbul Nişantaşı University, İstanbul, Türkiye

ABSTRACT

Weight reduction studies are being carried out in many industries today. Weight reduction is one of the most important factors, especially in the aviation industry. For this reason, optimization methods are widely used for weight reduction studies. Optimization is the process of transporting a problem to an ideal solution under certain loads and boundary conditions. Optimization methods are divided into 3 in terms of size, shape, and topology. In the dimension optimization method, the goal is to optimize the structure by adjusting the dimensions of the subcomponents. Chamfers, radii can be changed in the shape optimization method. In the topology optimization method, it is tried to choose the best structure with certain constraints and loads applied to the design area. The method chosen during an optimization study is one of the most important factors in achieving an optimal part. In this context, it is very important to choose a method that contributes to the correct and rapid progression of the problem to the best result in the solution space. In addition, by combining the selected methods with artificial intelligence, better results are obtained in weight reduction studies. In this study, the optimal dimensions of a drone arm were determined first by using the topology optimization method, then by using the shape optimization method. Genetic algorithm, one of the artificial intelligence optimization techniques, was used for shape optimization. In this context, the first solid first model of the part was created by using the computer-aided design program first. Static analyses of the first model created later were performed using the finite element program. As a result of the analysis, the maximum displacement value is 0.468 mm, the maximum stress value is 4.28 MPa and the weight is 12.38 grams. After static analysis, topology optimization was applied. As a result of topology optimization, 25 iterations have been obtained. A new model was created and analyzed with reference to these iterations. According to the analysis data, the maximum displacement value of the new model is 0.503 mm, the maximum stress value is 4.55 MPa and the weight is 11.10 grams. Although the stress value increases, this value is within the safety stress range of the material. Here, a weight reduction of 10.5% has been achieved together with topology optimization. Subsequently, shape optimization was performed on the part using a genetic algorithm. As a result of the optimization performed with the genetic algorithm, the optimal weight of the part was determined to be 10.2 grams, and an additional weight reduction of about 8% was made compared to the topology optimization. As a result of the topology and shape optimization, approximately 18% weight reduction has been made compared to the main model.

Keywords— *Drone arm, Genetic algorithm, Topology optimization, Shape optimization*

A Software System Design for Data-Driven Automotive Spare Parts Management

Selçuk Bayracı[1], Bilal Sedef [1], Guven Yuceturk[2], Gokhan Akgun[2], Buket Doğan[*,3]

[*]: buketb@marmara.edu.tr, ORCID: 0000-0003-1062-2439
[1]: *Dept. of Data Analytics, Borusan Otomotiv İthalat A.Ş, Avcılar, İstanbul, Turkey*
[2]: *Dept. of Data Science, Oredata Yazilim Limited Sirketi, Esenler, Istanbul, Turkey*
[3]: *Marmara Üniversitesi, Teknoloji Fakültesi, Bilgisayar Mühendisliği Bölümü, İstanbul, Turkey*

ABSTRACT

Reasons such as the uncertainties of customer demands and economic indicators may force businesses to keep excess spare parts stocks. Particularly the automotive spare parts management with a large commercial volume and mobility is integrated with many industrial areas that requires fast logistics service. However, excessive spare parts stock has an effect on businesses as ineffective management of financial resources and storage costs. For this reason, keeping an optimum stock is an important issue for businesses to gain a place in the market and maintain their competitiveness. It is possible to analyze historical customer demand data by machine learning methods and use these analysis results for the management of spare parts. In this study, a software system design that performs data-driven stock management processes of vehicles spare part demand forecasting such as Jaguar, Land Rover and BMW for Borusan Automotive which is one of the leading companies of the automotive industry is presented. There are many parts in the company that have low consumption amount and product variety which causes difficulties in stock management. It is aimed to create a software system that will determine the optimum amount of stock to be kept for these parts, provide decision support for its management, and generate the analysis results of historical sales data on a piece basis. The first stage of this design work, which will be prepared under the leadership of the business requirement document determined by the interviews with the field experts, includes the stage of taking the data tables from the SAP systems used by the company and combining them in the AZURE SQL database. This system will be integrated into a pipeline on Azure ML Studio and will be developed using the Python programming language on Azure Python SDK. A pipeline structure will be created in the Azure Data Factory environment to retrieve and save existing data and access stored procedures in the SQL server environment. After the data preprocessing phase, data mining models that perform stock prediction will be created with LightGBM Regression, XGBoost Classification and Prophet Time Series methods. Data analysis outputs resulting from ML pipeline will be transferred from Azure Blob Storage to SQL database. This system can be configured parametrically according to the needs of field experts and will be enabled to operate in a cloud-based scalable structure with distributed processing capability. By keeping the software system in the Atlassian Confluence environment, it will be possible to create a corporate project memory. Throughout the software development process, development and test teams will be able to work together with Atlassian Jira software and the status of each requirement in the system will be systematically followed by the project team and stakeholders.

Keywords—*Spare Parts Management; Regression; Classification; Time Series Data Analysis*

Firefly and Artificial Bee Colony Metaheuristic Algorithms for Enhanced Neural Network Prediction Modeling of Sediment Load in Çoruh River

Okan Mert KATİPOĞLU

okatipoglu@erzincan.edu.tr, ORCID: 0000-0001-6421-6087
Civil Engineeering, Erzincan Binali Yıldırım University, Erzincan, Türkiye

ABSTRACT

The amount of sediment load (SL) is important for determining the service life of the downstream dam, river hydraulics, waterworks construction, and reservoir management. The importance of Artificial Intelligence (AI) and nature-based optimization algorithms is increasing in solving water resources problems, such as SL estimation. This study combines the artificial neural network (ANN) algorithm with Firefly (FF) and artificial bee colony (ABC) optimization techniques for the estimation of monthly SL values in the Çoruh River in Northeastern Turkey. The estimation of SL values can only be achieved with the inputs of previous SL and streamflow values, which are provided to the models. The relationship between actual and predicted sediment values was visually compared using scatter diagrams and time series comparison charts. The accuracy of the established hybrid approaches was evaluated according to various statistical metrics such as root means squared error (RMSE), mean absolute error (MAE), mean absolute percentage error (MAPE), determination coefficient (R^2), and mean bias error, mean absolute percentage error (MAPE), bias factor (BF), kling gupta efficiency (KGE). As a result of the analyzes, it was determined that the ABC-ANN hybrid approach outperformed the others in SL estimation. As a result of the analyzes, it was determined that the combination of Q(t), Q(t-1) models and ABC-ANN algorithm with (R^2:0.905, RMSE:1406.730, MAE:769.545, MAPE:5.861, MBE: -251.090, BF: -4.457, KGE:0.737) had the highest estimation. In addition, since FF and ABC optimization techniques enable the parameters of the ANN model to be optimized, higher accuracy prediction outputs were obtained than the single ANN model.

Keywords— *Artificial neural network, Sediment load, Streamflow, Firefly optimization, Artificial bee colony optimization, Çoruh River*

Fabrication Of Graded Al_2O_3-SiC Composites by Spark Plasma Sintering

Ali ÇELIK[*,1], Yasemin ÇELIK[1]

[*]: acelik@eskisehir.edu.tr, ORCID: 0000-0001-6206-1587
[1]: *Department of Materials Science and Engineering, Eskişehir Technical University, Eskişehir, Turkey*

ABSTRACT

Ceramics with outstanding thermal stability, wear resistance and mechanical strength are the most appropriate materials for various functional and structural applications, such as cutting tools for metal machining, parts for aero-engines, capacitors, components for transportation and energy storage, and bio-implants. Alumina (Al_2O_3) is the most well-known material among the oxide ceramics and is utilized for applications in which combination of high chemical and mechanical resistance is required. However, Al_2O_3 ceramics are susceptible to fracture due to their strong ionic and directional covalent bonds which makes them vulnerable to impacts and internal defects. Since many applications require Al_2O_3-based ceramics with superior mechanical properties, as well as reliability, toughening of these ceramics by different methods, such as secondary particle toughening, transformation toughening, whisker-fiber toughening, creating graded (layered) composites, is applied to improve their performance. The graded composite fabrication is a promising approach to improve fracture resistance by creating residual compressive forces on the surface layer of the bulk ceramic thanks to slight differences in the composition of each layer that make up the composite. In this study, it was aimed to increase fracture toughness of Al_2O_3 without sacrificing its surface hardness. For this purpose, graded Al_2O_3 ceramics reinforced with SiC particles were manufactured by spark plasma sintering (SPS) method. SiC powders with different amounts (5-10 vol.%) were added into the Al_2O_3 matrix and loaded into the mold layer by layer and sintered. The microstructural properties, phase development, physical and mechanical properties of the obtained composites will be discussed in this presentation.

Keywords— *Alumina; Al_2O_3; SiC; Layered-composite; Fracture toughness*

Modelling and Analyses of Collection Process of an Insurance Company via "Business Process Modelling and Simulation"

Beyza Sultan KORKMAZ[*,1], Adil BAYKASOĞLU[1]

[*]: korkmaz.beyza@outlook.com, ORCID: 0009-0006-9085-4190
[1] *Department of Industrial Engineering / The Graduate School of Natural and Applied Sciences, Dokuz Eylül University, Izmir, Turkey*

ABSTRACT

In an environment where competition between companies increases, customer experience gains importance and directly affects companies' revenue; it is of great importance for companies to analyze and manage their processes that touches customers. Especially in companies, which have multi-stakeholder and complex processes, good analysis and effective management of processes can both increase customer satisfaction and reduce costs with improvements to be made in processes. In this study, the concepts of business process management and process modeling are explained, studies in the literature were searched and the collection process of an insurance company was modeled with the Process Simulator software via Microsoft Office Visio. The process modeled in discrete event-based simulation software was simulated repetitively. The causes of the problems in business processes were investigated by evaluating the model results. In order to eliminate these problems, changes and improvement suggestions that need to be made in the process are presented. Alternative solution scenarios were determined, alternative processes were modeled and simulated in discrete event-based simulation software. A decision-making study was applied to make a choice between the existing process and alternative processes. Suggestions for changes and improvements to be made in the process in order to eliminate these problems were presented.

As a result of this study, the importance of BPM approach has been understood for companies to be successful in today's competitive environment. In future Discrete-Event-Based process modeling studies, it has been seen that companies using Microsoft Office Visio software for process modeling can model and simulate their processes quickly and easily with the Process Simulator software, and it has been understood how processes can be improved with the Process Simulator software.

Keywords— *Business process management; process modelling; process analyzing; modelling software; Process Simulator*

Derin Öğrenme Algoritmalarının Gelecekteki Potansiyel Gelişme Alanlarının Değerlendirilmesi

Evaluation of Potential Future Development Areas of Deep Learning Algorithms

Hüseyin VURAL

hvural@adiyaman.edu.tr, ORCID: 0000-0001-9260-6317
Bilgisayar Mühendisliği, Adıyaman Üniversitesi, Adıyaman, Türkiye

ÖZET

Makine Öğrenmesinin bir dalı olan ve Yapay Sinir Ağları mimarisi temel alınarak geliştirilen Derin Öğrenme algoritmalarının son yıllarda Görüntü Tanıma, Sağlık, Doğal Dil İşleme, Siber Güvenlik ve daha birçok alandaki problemlerin çözümünde başarılı sonuçlar elde etmesi nedeniyle, birçok araştırmacı çalışmalarını Derin Öğrenme alanında yoğunlaştırmıştır. Derin Öğrenme üzerinde yapılan çalışmaların artışı, bu alanın gelecekte ilerleyebileceği potansiyel gelişmeleri önemli kılmaktadır. Bu nedenle, çalışmamızda bu potansiyel gelişmelerin neler olabileceği değerlendirilmektedir.

Bir problemin çözümünde kullanılacak büyük miktardaki ham veriler günümüz uygulamalarında manuel olarak sınıflandırılmakta ve etiketlenmektedir. Bunun yerine bu işlemleri otomatik olarak yapabilecek bir yöntemin geliştirilmesi zaman ve insan kaynağı konusunda avantaj sağlayacaktır. Bundan dolayı, bu alanın Derin Öğrenmenin potansiyel gelişim alanlarından biri olacağı değerlendirilmektedir. Veri kalitesinin arttırılması amacıyla geliştirilecek bir veri ön-işleme yöntemide yine potansiyel bir gelişim alanı olarak öngörülmektedir çünkü derin öğrenme algoritmalarında başarı oranı; veri seyrekliğine sahip, karışık değerler taşıyan, ilgisiz özellikler içeren, veri uyumsuzluğuna sahip veri setlerinde düşmektedir. Derin öğrenme algoritmalarında modeldeki düğümlerin ve katmanların sayısı, parametrelerin değerleri, eşik ayarları gibi bir çok özellik ile modelin yapısı oluşturulmaktadır. Manuel olarak oluşturulan modellerde başarı oranları ve performans modeli oluşturan kişinin bilgisine ve tecrübesine bağlı olarak değişmektedir. Bunun yerine, veriye dayalı olarak modelin otomatik olarak oluşturulacağı bir yöntemin geliştirilmesi başarı oranının ve performansın maksimize edilmesinde etkili olabilecektir bu nedenle bu alan potansiyel bir gelişim alanı olarak değerlendirilmektedir. Derin öğrenme algoritmaları alanındaki çalışmaların artışına bağlı olarak geliştirilen modellerin sayısında da artış yaşanmaktadır. Geliştirilen algoritmaların hangi problem üzerinde uygulanacağı; performans, başarı oranı, uygulanabilirlik ve benzeri açılardan önem taşımaktadır. Bu nedenle problem-algoritma seçiminin doğru bir şekilde belirleyecek bir yöntemin geliştirilmesi potansiyel gelişim alanlarından bir tanesi olarak değerlendirilmektedir. Bu çalışmada bahsedilen yöntemlerin uygulamalarda kullanılması ile Derin Öğrenme algoritmalarının gelecekteki potansiyel gelişim alanları değerlendirilecektir.

Anahtar Kelimeler—*Derin Öğrenme*; *Veri Önişleme*; *Model Belirleme*; *Otomatik Model Oluşturulması*; *Problem Algoritma Seçimi*

ABSTRACT

Many researchers have focused their studies on Deep Learning, as Deep Learning algorithms, which is a branch of Machine Learning and developed based on Artificial Neural Networks architecture, have achieved successful results in solving problems in Image Recognition, Health, Natural Language Processing, Cyber Security and many more in recent years. The increase in studies on Deep Learning makes the potential developments in this field important in the future. Therefore, in our study, what these potential developments might be is evaluated.

Large amounts of raw data to be used in solving a problem are manually classified and labeled in today's applications. Instead, the development of a method that can perform these operations automatically will provide advantages in terms of time and human resources. Therefore, it is considered that this area will be one of the potential development areas of Deep Learning. A data preprocessing method to be developed in order to increase data quality is also foreseen as a potential development area because the success rate in deep learning algorithms decreases in data sets with data sparsity, mixed values, unrelated features, and data incompatibility. In deep learning algorithms, the structure of the model is created with many features such as the number of nodes and layers in the model, the values of the parameters, and the threshold settings. Success rates and performance in manually created models vary depending on the knowledge and experience of the model creator. Instead, the development of a method in which the model will be automatically created based on the data may be effective in maximizing the success rate and performance, so this area is considered as a potential improvement area. Depending on the increase in the studies in the field of deep learning algorithms, there is an increase in the number of models developed. On which problem the developed algorithms will be applied; It is important in terms of performance, success rate and applicability. For this reason, the development of a method that will accurately determine the problem-algorithm selection is considered as one of the potential development areas. The potential development areas of Deep Learning algorithms will be evaluated by using the methods mentioned in this study in applications.

Keywords—*Deep Learning*; *Data Preprocessing*; *Model Detection*; *Automatic Model Creation*; *Problem Algorithm Selection*

Investigation The Utilization of Rice Husk Ash in The Production of Ceramic Coating Materials

İlker ÖZKAN[*,1], Esra DOKUMACI ALKAN[2]

[*] ilker.ozkan@deu.edu.tr, ORCID: 0000-0002-7506-5795
[1]: *Industrial Glass and Ceramics Department, Torbali Vocational School, Dokuz Eylül University, Izmir, Turkey*
[2]: *Metallurgical and Materials Engineering Department, Faculty of Engineering, Dokuz Eylül University, İzmir, Turkey*

ABSTRACT

The investigations on the usage of the alternative raw materials have been always popular in the ceramic industry. Manufacturers have been interested in this subject for both increasing product quality and decreasing production costs.

The aim of this study is to provide the recycling of rice husk, which is the waste material of rice, produced abundantly in the world and in our country. Thus, it is aimed to prevent the environment and stock area problems. With this purpose, studies have been carried out to use rice husk ash in the production of ceramic coating material. Rice husk ash is obtained by applying heat treatment to the rice husk. The ash obtained under suitable combustion conditions contains a high amount of silica and the ash has a high specific surface area value. Quartz is used as a source of silica in ceramic coating materials. In this study, the use of rice husk ash instead of quartz was studied in ceramic coating materials due to its high silica content.

The aim of this study is to investigate the usability of rice husk ash in the production of ceramic coating material. In this context, rice husk ash samples were characterized by XRD, SEM and chemical analyses. Utilization of rice husk ash in raw glaze compositions have been carried out. Color changes of the fired glazes were observed by color measuring device. Sodium borosilicate glass production studies were carried out by using rice husk. The samples were fused at 1000°C and 1100°C. The metal surface coating studies were carried out by using sodium borosilicates obtained from rice husk ash. The obtained glasses were ground, mixed with water and applied on 304 stainless steel plates. The samples were fired at 900°C and 950°C as two separate groups. It was observed that glassy structures were developed on the metal surfaces.

As a result of these studies, it has been observed that rice husk ash is an alternative raw material that can be used instead of quartz in the production of ceramic coating material.

Keywords—*Rice Husk Ash; Ceramic Coating; Glaze; Sodium Borosilicate; Characterization*

Establishing an Urban Mobility Index within the Scope of Sustainable and Smart Mobility

Yunus Emre AYÖZEN

ayozenyunusemre@gmail.com, ORCID: 0009-0007-6933-0699
Ministry of Transport and Infrastructure, Ankara, Türkiye.

ABSTRACT

The transportation area, one of the critical infrastructures of cities, provides mobility for the urban population to access services. In this study, the mobility indexes of the cities in Turkey are discussed. The urban mobility index is calculated for each city by using sub-indicators such as public transportation management, traffic management, demographic structure, cost, and investments, which are covered by the leading indicators such as manageability, safety and security, technology and innovation, financial management, accessibility in transportation, mobility, and sustainability. It is expressed as the mobility score calculated for Mobility indexes calculated by considering different parameters such as transportation, population structure, accessibility, sustainability, environment, and cost. Thus, it is ensured that the mobility index score of each city is formed as a result of the indicator taken into consideration. As a result, by using the indicator values to be calculated in the future periods of the cities, it will be ensured that this study analyzes the developments of the provinces in the fields of sustainable and smart mobility for the relevant period. In addition, with a developed model, it will be possible to calculate index scores and create an automatic system by using up-to-date data from cities.

Keywords—*Mobility; Mobility Index; Transportation; Indicators; Sustainability*

Banka Müşterilerinin Dijital Bankacılığa İlişkin Yaklaşımlarının Veri Madenciliği Teknikleri ile İncelenmesi

Examination of Bank Customers' Approaches to Digital Banking with Data Mining Techniques

Rabia KARAHAN[*,1], Ayşenur BUDAK[1]

r.karahan2021@gtu.edu.tr
Endüstri Mühendisliği, Gebze Teknik Üniversitesi, Kocaeli, Gebze

ÖZET

Bu çalışmanın amacı, dijital bankacılık kavramının, bu alanda yapılan çalışmaların ve gelinen aşamanın incelenmesi ve banka müşterilerinin dijital bankacılığa ilişkin yaklaşımlarının tespit edilmesidir. Çalışmada dijital bankacılıkta gelinen aşamanın tespiti için resmi kurumların kaynaklarına ve akademik çalışmalara başvurarak bir literatür araştırması yapılmıştır. Bu araştırma sonucunda dijital bankacılık kavramı, kapsamı, gelinen aşama ve Türkiye'deki dijital bankacılık kullanım oranları tespit edilmiştir. Bu bilgiler doğrultusunda banka müşterilerinin eğilimlerini ölçmek amacıyla ilk 6 sorusu demografik bilgilerden kalan 17 sorusu da dijital ortam ve bankacılık kullanım bilgilerinden oluşan 23 soruluk bir anket hazırlanmıştır. Dijital ortamda farklı yaş grupları ve bölgelere dağılımı yapılan anket sonucunda bir veri seti elde edilmiştir. Bu veri setini analiz etmek için veri madeciliği teknikleri ve araçları incelenmiştir.
Yapılan araştırmalar sonucunda açık kaynaklı bir veri madenciliği, makine öğrenimi ve veri görselleştirme programı olan Orange kullanılmıştır. Öncelikle veri seti bu programa yüklenerek veri setindeki değişkenlerin istatistikleri grafikler ile incelenmiştir. Dijital bankacılık kullanan ve kullanmayan müşterilerin profilleri ayrıntılı olarak incelenmiştir. Bu istatistiki veriler Orange ile görselleştirilmiştir. Bir sonraki aşamada birliktelik kuralları analizi ile modeller üretilerek müşterilerin dijital bankacılık kullanımına ilişkin yaklaşımları belirlenmeye çalışılmıştır. Çalışmada kümeleme analizi ile müşteriler kümelere ayrıştırılmış ve müşterilerin demografik özelliklerinin her küme üzerindeki etkileri ayrı ayrı incelenmiştir. Yapılan bu çalışmalar ile dijital bankacılığı kullanan ve kullanmayan müşteri profilleri incelendiğinde müşteriler arasındaki farklar tespit edilebilmektedir. Dijital bankacılığı kullanan veri kümelerinin yüksek oranda kullandıkları dijital bankacılık ürünleri çeşitli kampanyalarda kullanılabilcek şekilde tespit edilebilebilmektedir. Dijital bankacılığı kullanmayan müşterilerin kullanmama nedenleri tespit edilebilmektedir. Dijital ve geleneksel bankacılığın zaman için de geleceği nokta hakkında tahminler yapılabilmektedir. Sonuç olarak dijital bankaların sayısında son yıllarda ciddi oranda artış meydana gelmiştir. dijital bankacılığı kullanan müşteri sayısıda bu doğrultu da giderek artmaktadır. Gelecekte geleneksel bankacılığın yerini dijital bankacılığın alacağı anket sonuçları ve araştırmalara dayanarak yüksek olasılıktadır. Anket verileri kullanılarak yapılan analiz sonuçlarına göre birlikte ürün kullanımları ile ilgili kampanyalar yapılabilecektir. Dijital bankacılığın kullanmayan müşterilerinde kullanmama nedeni yaş kriteri değişkeninin öne çıkarak yüksek oranda güven ve bilgi eksikliğidir.

Keywords— *Veri Madenciliği; Birliktelik Kuralları Analizi; Dijital Bankacılık*

ABSTRACT

The purpose of this study is to examine the concept of digital banking, the existing research in this field, and the current stage of development, as well as to identify bank customers' attitudes towards digital banking. In this study, a literature review was conducted by referring to official sources and academic studies to determine the stage of development in digital banking. As a result of this research, the concept and scope of digital banking, the current stage of development, and the usage rates of digital banking in Turkey were identified. Based on this information, a 23-question survey was prepared, with the first 6 questions focused on demographic information and the remaining 17 questions related to digital usage and banking behavior, in order to measure the tendencies of bank customers. The survey was distributed online across different age groups and regions to collect a dataset. Data mining techniques and tools were explored for analyzing this dataset. Upon conducting the research, an open-source data mining, machine learning, and data visualization program called Orange was employed. Initially, the dataset was loaded into this program to examine the statistics of the variables and visualize them through graphs. The profiles of customers who use and do not use digital banking were analyzed in detail, and these statistical findings were visualized using Orange.
In the subsequent phase, association rule analysis was conducted to generate models aiming to determine customers' approaches to using digital banking. Through clustering analysis, customers were segmented into groups, and the impacts of demographic characteristics on each cluster were individually examined. These analyses allowed for the identification of differences among customer profiles who use and do not use digital banking. The specific digital banking products preferred by user clusters that engage in digital banking were identified for potential use in various campaigns. The reasons for non-usage of digital banking among certain customers were also identified. Insights were drawn to speculate on the future of digital and traditional banking over time. In conclusion, there has been a significant increase in the number of digital banks in recent years, and the number of customers using digital banking has been consistently rising. Based on the results of surveys and research, it is highly likely that digital banking will largely replace traditional banking in the future. The analysis results from the survey data can be utilized to design campaigns related to bundled product usage. Additionally, the survey revealed that the primary reason for non-usage of digital banking among certain customers is the age criterion, mainly due to concerns related to trust and lack of information.

Keywords— *Data Mining; Association Rule Analysis; Digital Banking*

An Experimental Investigation of a New Tensile Strength Test Method for Concrete

Ayşegül DURMUŞ DEMİR[*,1], Hatice SÜLEYMANOĞLU[1]

[*]: aysegul@ktu.edu.tr, ORCID: *0000-0003-1302-7838*
[1]: *Department of Civil Engineering, Karadeniz Technical University, Trabzon, Turkey*

ABSTRACT

Concrete stands as the most extensively used construction material worldwide. Despite its extensive use as a structural material in the construction industry, concrete is a highly complex substance, and its properties are not easily assessed. It is well-established that concrete exhibits a significantly lower tensile strength compared to its compressive strength. This inherent weakness in tension has led to the predominant use of concrete as a material for the compressive members in the construction of most concrete structures. However, the tensile strength of concrete plays a crucial role in various applications, including water-retaining structures, nuclear plants, pre-stressed concrete elements, resistance to bond and shear failure in reinforced concrete members, and prevention of cracking of mass concrete works.

Concrete is commonly evaluated based on its compressive strength, but the significance of its tensile strength in design, analysis, and modeling should not be underestimated. Existing methods to measure tensile strength have limitations, leading to inaccuracies. To address this, a new method was developed using a hollow block-shaped specimen and a specialized loading apparatus. The Hollow Block Test (HBT) was conducted alongside the Direct Tension Test (DTT) to validate the results of the proposed method.

A block was specifically designed with dimensions of 200 mm in length, 100 mm in width, and 300 mm in height. This design allows for the formation of a hollow with 100mm in diameter and 100 mm in height which serves two essential purposes. Firstly, it allows for the application of tensile force to the specimen. Secondly, the hollow shape facilitates the examination of any defects present in the concrete specimen during the test. Additionally a pull by push apparatus was designed to subject the proposed hollow block specimen to a tensile load by utilizing a uniaxial compression machine.

Within the scope of the study, three different test methods were used: Compression Test (CT), Direct Tension Test, and Hollow Block Test (HBT). The dimensions of the cylindrical specimens used for the CT and DTT are, respectively, 150 mm in diameter and 300 mm in height, and 75 mm in diameter and 150 mm in height. The specimens under examination consisted of plain concrete, comprising aggregates, cement, and water. The proportions of these materials were determined based on their respective weights. According to the available commercial gradation, two types of aggregates were used: coarse aggregates (5-15mm) and fine aggregates (0-5mm). The densest combination of both fine and coarse aggregates was decided as 2 to 3, respectively. Trabzon-Sistaş basalt sand and Gümüşhane-Şahkar crushed limestone with specific gravity of 2650kg/m3 and 2700kg/m3 were used as aggregates. Two different mix design were determined after several experimental trials. The cement used in the mix design was Portland cement (CEM I 42.5 R), a product of the Trabzon Aşkale Cement Factory, with a dosage of 250 kg and 330 kg. Municipial drinking water was used in the concrete mixes with a ratio relative to cement: W/C=0.63 and 0.48.

A total of 36 samples were produced, with 6 specimens for each test method in each concrete

mix. According to the standard curing conditions, the concrete specimens are cured in water at a temperature of 20±2°C after being removed from the molds. At the age of 28 days, the concrete specimens were tested.

In order to determine the relationship between compressive strength and tensile strength, CT is performed on specimens in cylindrical shapes with diameter of 150mm and height of 300 mm according to EN 12390-3 standard.

In conclusion, a new tensile test method Hollow Block Test (HBT) that eliminates the holding and gluing problems of Direct Tension Test (DTT) and allows using uniaxial compression machine was proposed. The experimental results are quite encouraging, indicating a close similarity between the results of the HBT and the DTT. In light of the results from this experimental investigation, it is advisable to pursue additional research concerning the HBT test to improve its efficiency and establish it as a commonly utilized technique for assessing concrete's tensile strength.

Keywords—*Tensile Strength; Concrete; Direct Tension Test; Hollow Block Test*

Synthesis and Piezoresistive Characterization of Pressure-Sensitive MWCNTS Decorated Electrospun MWCNTS/TPU Nanofibrous Structures

Ihsan Fatih Ertas*[,1], Abdulkadir Sanli[2], Muhammet Uzun[3]

ihsanfatihertas@gmail.com

[1]: *Department of Textile Engineering, Institute of Pure and Applied Sciences, Marmara University, Istanbul, Turkey*

[2]: *Department of Mechatronics Engineering, Turkish-German University, Istanbul, Turkey*

[3]*Department of Textile Engineering, Marmara University, Istanbul, Turkey*

ABSTRACT

Pressure sensors are widely used in electronic wearables and medical devices to detect small physical movements and mechanical deformation. However, producing desirable, comfortable-wearing, highly sensitive and responsive sensors to capture the physiological signs of the human body still remains a challenge. To solve this problem, a new capacitive flexible pressure sensor was made using thermoplastic polyurethane elastomer rubber (TPU) electrospinned nanofiber membranes, which have a stretchable polymeric structure with the inclusion of silver nanowires (AgNWs) to form a nanofiber dielectric layer. coated with carbon nanotubes (CNTs) as flexible electrodes on TPU membranes to maintain its breathability. This flexible pressure sensor, which is desired to be produced, can detect even small body marks. At the same time, for other sensing such as pulse and speech recognition, different conductive nanofibers should be produced for a flexible pressure sensor with high sensitivity and stability under different strain levels.

In this study, homogeneous CNT:TPU:DMF and TPU:DMF solutions were prepared and the cut pieces of nanofiber structures obtained by electrospinning were placed in ethanol and carbon nanotube (CNT) solution prepared at 1% concentration and sonicated for 1 hour to fabricate conductive fibrous structures.We focus on the detection performance of flexible pressure sensors with different conductive networks at different weights by dipping CNT:TPU:DMF and TPU:DMF-based nanomaterials in different concentrations, produced by electrospinning method, into a 1% CNT:Ethanol solution. Although the purpose of doing this was previously using different materials to bring CNTs in CNT-based nanofiber structures to the surface, advances were made in this study by dipping into CNT: Ethanol-based solution for the first time. At the same time, the produced nanofiber sensors have a porous, perfectly breathable structure. It is designed to monitor various movements of various parts of the human body (fingers, wrists, elbows and leg bends). The swelling and degradation behaviors of the bond-like scaffolds were studied in vitro for 7 days. Scanning electron microscopy proved the geometry of scaffolds suitable for connective-like tissue. FT/IR analysis was carried out in order not to observe the spectral absorption peaks occurring in the chemical bonds in the structure and to have an idea about the characterization of the raw materials

Keywords—*carbon nanotube, thermoplastic polyurethane electrospinning, piezoresistivity, nanofiber*

Reversing Process of Zoning's Plan The 18th Article Implementation Which is Annulment by a Justice Decision

Yargı Kararıyla İptal Edilen İmar Planı 18'inci madde Uygulamasının Geri Dönüş Süreci

Yaşar İNCEYOL

yinceyol@adiyaman.edu.tr, ORCID: 0000-0001-7455-2869
Department of Construction, School of Technical Sciences, Adiyaman University, Adiyaman, Turkey.

ABSTRACT

Zoning plans have an important effect on the creation of a sustainable environment and physical living conditions in cities. However, this effect depends on the production of viable development plans, experienced technical staff and the vision of local administrations. In the implementation of the zoning plans for local administrations, "18th article implementation" or "land readjustment" is an important tool. Land arrangement aims to prepare enough lands for the construction of housing, which is required by the cities, and to form the settlements in accordance with the plan, science, health and environmental conditions for the formation of planned and regular settlement. In this implementation, a readjustment area is determined according to the needs and planning priority within the boundaries of the zoning plan. After the plot and lands within this readjustment area were combined by the local administration and included in the zoning plan, roads, green areas, schools, public buildings, etc. after the lands required for shared public spaces are reserved, the remaining parts are given to their former owners. The areas reserved for shared public spaces are called "development readjustment share (DOP)". DOP, which was determined as 45% according to the latest legal regulations made in 2019, is brought to the public in return for the "value increase due to the Land arrangement". Local administrations can create common public areas such as roads, parks, green areas, health facilities and schools in the zoning plans without paying any expropriation fee. In this context, unique opportunities are offered to local administrations. In addition, this application; due to the increasing population, it has an important potential to provide enough zoned parcel to meet the increasing housing needs of middle and low-income groups. For this reason, it is indispensable for local administrations to apply this method and make the zoning plans implementation. However, the implementation steps of the land readjustment are generally not performed properly as expected. This situation mostly occurs as a violation of the relevant legal legislation. Legal and technical mistakes made in this process are intensely brought to administrative judiciary by the landowners, whose expectations from this practice cannot be met sufficiently. These lawsuits filed in the administrative judiciary often result in stay of execution for justified reasons, cancelled of 18th article implementation and reversing decisions. The lack of clarity in the legislation regarding the cancellation of the application and how the reversing decisions will be implemented causes some serious problems related to property. This study; It aims to eliminate the hesitations of practitioners regarding the reversing process by defining the problems encountered in practice related to the reversing processes.

Keywords—*Zoning Plan; Land Readjustment; The 18th Article Implementation; Reversing; Reversing Process*

ÖZET

Kentlerde sürdürülebilir bir çevre ve fiziksel yaşam koşullarının oluşmasında imar planları önemli bir etkiye sahiptir. Ancak bu etki uygulanabilir imar planlarının üretilmesine, deneyimli teknik elemanlara ve yerel idarelerin vizyonuna bağlıdır. Yerel idareler için imar planlarının uygulanmasında "18. Madde uygulamaları" veya diğer adıyla "arazi ve arsa düzenlemesi" önemli bir araçtır. Arazi ve arsa düzenlemesi, kentlerin gereksinmesi olan yeteri kadar arsayı konut yapımına hazır duruma getirmeyi, planlı ve düzenli yerleşmenin oluşması için yapılaşmaların plan, fen, sağlık ve çevre koşullarına uygun bir şekilde oluşmasını amaçlamaktadır. Bu uygulamada öncelikle imar planı sınırları içerisinde ihtiyaçlara ve planlama önceliğine göre bir düzenleme sahası belirlenir. Bu düzenleme sahası içindeki arsa ve araziler, yerel idare tarafından birleştirildikten ve imar planında yol, yeşil alan, okul, kamu binaları vb. ortak kamusal alanlar için gereken araziler ayrıldıktan sonra artan kısımlar eski sahiplerine verilir. Ortak kamusal alanlar için ayrılan alanlar "düzenleme ortaklık payı (DOP)" olarak isimlendirilir. 2019 yılında yapılan son yasal düzenlemelere göre %45 olarak belirlenen DOP, "imar düzenlemesinden kaynaklı değer artışı" karşılığı olarak kamuya kazandırılmaktadır. Yerel idareler imar planlarındaki yol, park, yeşil alan, sağlık tesisleri, okul gibi ortak kamusal alanları herhangi bir kamulaştırma bedeli ödemeden oluşturabilmektedir. Bu kapsamda yerel idarelere eşsiz imkanlar sunulmaktadır. Ayrıca bu uygulama; artan nüfusa bağlı olarak orta ve düşük gelirli grupların artan konut ihtiyacını karşılamak için yeterli imarlı arsa arzını sağlayacak önemli bir potansiyele sahiptir. Bu nedenle yerel idareler için bu yöntemin uygulanması ile imar planlarının uygulanabilir kılınması vazgeçilemez bir öneme sahiptir. Ancak arazi ve arsa düzenlemesinin uygulama adımları genellikle beklenen şekilde düzgün olarak gerçekleştirilememektedir. Bu durum çoğunlukla ilgili yasal mevzuat hükümlerine aykırılık şeklinde ortaya çıkmaktadır. Bu süreçte yapılan hukuki ve teknik hatalar, bu uygulamadan beklentileri yeterince karşılanamayan arazi sahipleri tarafından yoğun bir şekilde idari yargıya götürülmektedir. İdari yargıda açılan bu davalar, çoğunlukla haklı gerekçelerle yürütmenin durdurulması, 18. Madde uygulamalarının iptal edilmesi ve geri dönüş kararları ile sonuçlanmaktadır. Uygulamanın iptal edilmesi ve geri dönüş kararlarının nasıl uygulanacağı ile ilgili yasal mevzuatta yeterince bir açıklık olmaması, mülkiyetle ilgili ciddi bazı sorunlara neden olmaktadır. Bu çalışma; geri dönüş işlemleri ile ilgili uygulamada karşılaşılan sorunları tanımlayarak, geri dönüş süreci ile ilgili uygulayıcılar açısından oluşan tereddütleri ortadan kaldırmayı amaçlamaktadır.

Anahtar Kelimeler—*İmar Planı; Arazi ve Arsa Düzenlemesi; 18. Madde Uygulaması; Geri Dönüş; Geri Dönüş Süreci*

Pervious Concrete - Sustainable Solution for Low Traffic Areas

Ivana Barišić[*,1], Ivanka Netinger Grubeša

[*]: ivana@gfos.hr, ORCID: 0000-0002-8680-977X
[1]: *Faculty of Civil Engineering and Architecture Osijek, University of Osijek, Osijek, Croatia*
[2]: *Department for Civil Engineering, University North, Varaždin, Croatia*

ABSTRACT

In order to address the demand for waste accumulation and environmental footprint reduction in the domain of road building, this research aims to introduce novel environmentally friendly paving materials for low traffic areas. Pervious concrete is a type of a concrete designed and installed to have high porosity. However, the mechanical properties of pervious concrete are diminished by the concrete's high porosity achieved during design and installation. But this high porosity also contributes to its most advantageous feature, outstanding drainage capabilities that make it a viable green pavement solution for specific traffic areas, especially bicycle and pedestrian infrastructure.

Despite the 40 years of intensive research on pervious concrete, there are still no European guidelines for its testing and installation. International researchers are primarily focused on improving the composition of pervious concrete and its mechanical qualities for use as concrete slabs or monolithically formed concrete pavement surfaces. Within this research, we present possibility of incorporating all advantages and disadvantages of pervious concrete by its properly selected application. For the purpose of producing and installing pervious concrete paving flags, experimental research on the qualities of pervious concrete will be discussed in this study. Testing for standard mechanical characteristics such as weathering resistance using a water absorption measurement, bending strength, abrasion resistance and drainage were done on pervious concrete paving flags made in a laboratory. Also, some specific characteristics important for low traffic areas will be presented and discussed.

Various pervious concrete paving flag solutions will be presented as sustainable paving solution: made with waste materials and waste water purification effect and with architecturally appealing design. The specifics of the production and installation of these materials as well as the results of the test field observation will also be presented.

Keywords—*Pervious concrete; Paving flag; Pedestrian area; Bicycle area; Sustainability*

Effect of Construction and Demolition Waste Substitution on the Compressive Strength of Cement Mortars

İsmail Raci Bayer

rbayercsb@gmail.com, ORCID: 0000-0003-0827-9168
Ministry of Environment, Urbanization and Climate Change, 06510, Ankara, Türkiye

ABSTRACT

A high amount of construction and demolition waste (CDW), which accounts for approximately 40% of the total solid waste, is generated as a result of earthquakes, maintenance activities, construction and demolition operations. While some of these waste materials are used in applications such as road filling, a significant portion ends up being stored in clean disposal areas. Given the growing population and the constant need for urbanization, the construction industry has a high demand for raw materials. Thus, evaluating CDW by reclassifying it from waste to reusable resources within the construction sector could lead to notable environmental and economic benefits. This research focuses on the utilization of CDW-based materials, including hollow brick (HB), roof tile (RT), red clay brick (RCB), concrete (C), and glass (G) wastes, in cement mortar mixtures. In the first stage, CDW-based materials were collected from demolition sites and subjected to crushing and grinding processes. The d(0.9) fineness values of the HB, RT, RCB, C and G after the same crushing-grinding process were found to be 36.2, 43.6, 32.1, 48.6 and 61.2, respectively. According to the chemical content analysis, the ratios of SiO_2, Al_2O_3, and CaO in HB are 54.3%, 14.5%, and 5.1%; in RT are 52.6%, 15.1%, and 4.9%; in RCB are 57.1%, 14.8% and 4.7%, in C are 33.2%, 7.5%, and 25.7%; and in G are 68.6%, 0.87%, and 7.96%, respectively. Subsequently, each CDW-based material was included in a total of five cement mortar mixtures alongside a reference mixture entirely composed of cement. The cement mortar mixtures were designed as 1:0.5:3 for cement-water-sand composition. In mixtures containing CDW, the mass of CDW was set at 25% based on the total binder material quantity, while the cement content was adjusted to 75%. Specimens were kept under water curing until the testing age to assess their compressive strengths at 7 and 28 days. According to the results, the 7-day compressive strength of the fully Portland cement-based reference mortar was found to be 26.9 MPa. The 7-day compressive strengths of mortars containing 25% replacement of Portland cement with HB, RT, RCB, C, and G were determined as 22.2 MPa, 21.5 MPa, 23.1 MPa, 21.6 MPa, and 20.3 MPa, respectively. The 28-day compressive strength results show that the reference mixture achieved 31.3 MPa, whereas mortars with replacements of HB, RT, RCB, C, and G resulted in compressive strengths of 26.1 MPa, 25.3 MPa, 27.8 MPa, 24.8 MPa, and 23.1 MPa, respectively. According to the results, the compressive strength performance of CDW-based materials is significantly influenced by their fineness and chemical composition. Among the materials, RCB, which has the finest particle size distribution, exhibited the highest compressive strength. On the other hand, HB, with the second finest particle size, showed higher compressive strength compared to the others. The fine nature of the materials enhances their pozzolanic activity, increasing the degree of reaction with calcium hydroxide, a secondary hydration product of cement. This, in turn, positively contributes to the compressive strength. Furthermore, the high SiO_2 and Al_2O_3 content in RCB also significantly contributes to the compressive strength. The elevated SiO_2 and Al_2O_3 content aids in the

formation of the C-S-H gel, responsible for the compressive strength in the matrix due to pozzolanic activity, thereby enhancing the compressive strength. This assertion is confirmed by the fact that G, which has relatively coarse particles and low Al_2O_3 content, exhibits the lowest compressive strength. Additionally, when comparing the 7-day and 28-day results, it can be observed that as the age of CDW-replaced mixtures increases, their compressive strength improves more rapidly. This indicates that these materials possess pozzolanic activity, particularly in later ages, which positively influences compressive strength. These results suggest that CDW-based materials can be used as cement substitutes in the construction industry, thus reducing raw material requirements and offering environmental and economic advantages through waste utilization.

Keywords—*Construction and Demolition waste; Cement substitution; Compressive strength; Pozzolanic activity*

High Strength Special Octagon Profile Production

Aytekin ÖZGÜVEN[*,1] Meliha RİGAN[1]

[*]: aytekin.ozguven@toscelik.com.tr, ORCID: 0000-0000-0000-0000
[1]: *Tosyalı Holding, Ar-Ge Merkezi, Osmaniye, Türkiye*

ABSTRACT

In this study, it is aimed to give an octagonal form to the profile by designing new printing rollers. The coils arriving at Tosçelik Profile and Sheet Erw facilities are slitting into tapes in slitting machines according to the requirements of the product to be produced. The tapes are fed into the flops of the pipe machines. Pipe or profile production can be made from the bands. While pipes and profiles can be produced in conventional machines, universal machines are special machines designed only for profile production. In the Tosçelik ERW facility, profile production in conventional machines is carried out by pressing and forming the material coming from the form group as pipes with the help of Turkish heads. It is aimed to give the profile an octagonal form by designing printing rollers instead of this form group. While the octagonal profile has many uses, it is generally used as a flagpole and is demanded from both domestic and foreign markets. Ninety-degree bends are made in the production of four-cornered profiles from the tape, which adversely affects the strength of the material as a result of the accumulation of material defects called dislocations at the corner points in the material. As a result of the study, the design of which was completed, the bending angles of the material were reduced from ninety degrees to forty-five degrees, and since the bending was made from eight points instead of four points, the accumulation of dislocations at the corners was reduced and the overall strength of the material was increased. Thus, with the work carried out, profile production with a different form than conventional pipe-profile production machines were achieved and a more durable profile was obtained from profiles with the same wall thickness and a product suitable for high strength and low weight requirements was produced. Since the wall thickness of the octagonal profile will decrease by 10% compared to the pipes, this change has decreased depending on the length of the profile. Thanks to this study, it will be seen that products in different forms can be produced from conventional pipe-profile machines, and the way for different forms will be opened.

Keywords: *Octagonal Profile, Turkish Head, Plastic Forming, Forming*

Silajlık Mısır Tarımı ve Sürdürülebilirlik: Kiraz/İzmir Örneği

Silage Corn Farming and Sustainability: The Case of Kiraz/Izmir

Hatice İLHAN ACAR*,[1], Hakan GEREN[1]

* ilhanhatic@gmail.com, ORCID: 0000-0000-0000-0000
[1]*Ziraat Fakültesi, Ege Üniversitesi, İzmir, Türkiye*

ÖZET

Küresel ısınma, su kaynaklarının azalması ve iklim değişikliği gibi çeşitli nedenlerle "sürdürülebilirlik" kavramı günümüzde gittikçe önem kazanmaktadır. Sürdürülebilir tarım, küresel gıda talebinin yeterli ve kaliteli olarak uygun maliyetler ile üretimi sağlanırken, doğanın ve kaynakların gelecek nesillere sorunsuz bir şekilde miras bırakılmasını göz önünde bulundurur. Bu bağlamda hem akademik literatürde hem de sektörel çalışmalarda, tarım ve gıda üretiminde sürdürülebilir süreçlerin nasıl olması gerektiği sıklıkla tartışılmaktadır.

Hayvancılık sektörü özelinde silaj olarak ülkemizde genellikle mısır (Zea mays) bitkisi kullanılmaktadır. Hayvancılığın yoğun olarak yapıldığı İzmir Küçük Menderes havzası, süt üretimi açısından olduğu kadar tarım faaliyetleri bakımından da yoğun bir yerdir. Küçük Menderes bölgesinin önemli tarım merkezlerinden biri olan Kiraz ilçesi son yıllarda hayvan sayısı ve mısır üretimi bakımından öne çıkmaktadır. Bu çalışmada, Kiraz/İzmir ekolojik koşullarında yetiştirilen çeşitli mısır genotiplerinin bazı verim unsurlarının belirlenmesi amacıyla bir deneme yürütülmüştür. Araştırmada bitkisel materyal olarak olum süresi 75, 90 ve 120 gün olan üç mısır genotipi araştırılmıştır. Çalışmada kullanılan farklı bitki çeşitleri seçilirken, bölgede hayvancılıkla uğraşan çiftçiler tarafından sıklıkla ekimi yapılan silajlık mısır türleri göz önünde bulundurulmuştur. Denemede; bitki boyu, bin tane ağırlığı, biyolojik ve tane verimi ve hasat indeksi özellikleri test edilmiştir.

Araştırma, tek faktörlü tesadüf blokları deneme desenine göre 3 tekerrürlü olarak yürütülmüştür. Elde edilen sonuçlara göre olgunlaşma zamanının artması ile bitki boyu, bin tane ağırlığı, tane verimi ve hasat indeksinin arttığı gözlemlenmiştir. Sonuç olarak, tipik Akdeniz ikliminin görüldüğü Kiraz/İzmir koşullarında her kriter için olgunlaşma süresinin 120 gün olduğu mısır türü en verimli çeşit olmuştur. Bölgede silajlık mısır ekimi için yoğun sulama ve ekipman kullanımı dikakte alındığında, sürdürülebilirlik hayvancılık için silajlık mısırda verimin ne kadar önemli daha iyi anlaşılacaktır. Bununla birlikte, ilerleyen çalışmalarda, aynı türlerin iki yıl üst üste ekimi yapılarak sonuçların karşılaştırılması daha farklı sonuçlara ulaşılmasını sağlayabilir.

Anahtar Kelimeler—*Mısır, Sürdürülebilirlik, Hayvancılık*

ABSTRACT

The concept of "sustainability" is gaining importance due to various reasons such as global warming, decrease in water resources and climate change. Sustainable agriculture takes into account the seamless inheritance of nature and resources to future generations, while ensuring the production of sufficient and high quality food at affordable costs. In this context, it is

frequently discussed how sustainable processes should be in agriculture and food production, both in the academic literature and in sectoral studies.

In our country, corn (Zea mays) is generally used as silage in the livestock sector. İzmir Küçük Menderes area is an intense place in terms of agricultural activities as well as milk production. Kiraz district, which is one of the important agricultural centers of Küçük Menderes region, has come to the fore in recent years in terms of animal numbers and corn production. In this study, an experiment was conducted to determine some yield components of various corn genotypes grown in Kiraz/İzmir ecological conditions. In the research, three maize genotypes with 75, 90 and 120 days of maturity were investigated as plant material. While choosing the different corn varieties used in the study, the silage corn types that are frequently planted by the farmers in the region. In the study; plant height, thousand grain weight, biological and grain yield and harvest index properties were tested.

The research was carried out according to the randomized blocks design with three replications. According to the results obtained, it was observed that plant height, thousand grain weight, grain yield and harvest index increased with the increase in maturity time. As a result, under the typical Mediterranean climate of Kiraz/İzmir conditions, corn with a maturation period of 120 days for each criterion is the most productive variety. Considering the use of intensive irrigation and equipment for silage corn cultivation in the region, it will be better understood how important the yield of silage corn for sustainability livestock is. However, in future studies, comparing the results by planting the same species for two consecutive years may lead to different results.

Keywords—*Corn, Sustainability, Livestock*

Eczacıbaşı Yapı Gereçleri Sipariş Verileri ile Birliktelik Kuralı Analizi

Association Rule Mining Analysis with Eczacıbaşı Building Products Inc. Order Data

Cansu Aktaş Dinçel [1], Ömer Sevinçtekin [2], Buket Doğan[*,3]

[*]: buketb@marmara.edu.tr, ORCID: 0000-0003-1062-2439
[1]:, *Eczacıbaşı Bilişim A.Ş.,İstanbul, Turkey*
[2]:, *Eczacıbaşı Yapı Gereçleri , İstanbul,Turkey*
[3]: *Marmara Üniversitesi, Teknoloji Fakültesi, Bilgisayar Mühendisliği Bölümü, İstanbul, Turkey*

ÖZET

Bilgi ve iletişim teknolojilerindeki yeni gelişmeler, farklı alışveriş kanalları ve yönelimleri birçok sektörde rekabetin artmasına neden olmuştur. Bu nedenle firmalar müşterilerinin tercihlerini ve alışkanlıklarına eldeki veriden yapılacak veri madenciliği analizleri ile ortaya koymakta ve buna göre satış yöntemlerini, promosyonlarını ve satış kanallarını geliştirmektedirler. Bu noktada bir veri kümesinde birlikte sık görülen öğeleri ve bu öğeler arasındaki ilişkileri/örüntüleri etkili bir şekilde keşfetmek için birliktelik kuralı analizi yöntemi kullanılabilmektedir. Keşfedilen örüntüler, sık birlikte gözlenen öğeler ya da kurallar olarak firmaların satış ve pazarlama kararlarına yön verebilmektedir. Bu çalışmada Eczacıbaşı Yapı Gereçleri'nin ERP sisteminde yer alan mağazacılık kanallarından gelen sipariş verileri ve siparişlerdeki ürünlerin nitelikleri üzerinden birliktelik kurallarını gösterecek bir veri analiz yazılımı oluşturulmuştur. Analiz edilen verideki ilk sonuçlar Nisan 2022 – Nisan 2023 tarihleri arasındaki perakende satış kanalından yapılan alışverişleri içermektedir. Bu verilerde ürün bazında filtreleme sonrası malzeme üzerinde kukla değişkenler oluşturulup karakter kodlaması yöntemi ile bir önişleme çalışması yapılarak öncelikle mevcut veri analize hazır hale getirilmiştir. Birliktelik kuralı analizi için kullanılan Apriori algoritması Python programlama ortamında Pandas, Numpy, Mlxtend.Frequent_Patterns -Apriori, Mlxtend.Frequent_Patterns -Association_Rules ve datetime kütüphaneleri kullanılarak oluşturulmuştur. Oluşturulan analiz yazılımı doğrudan ERP sistemine bağlantı kurarak verilere erişim sağlamaktadır. Gerçekleştirilen yazılım, Apriori yöntemi ile birlikte alınan ana ürün ve tamamlayıcı ürün düzeyindeki birliktelik kurallarını bularak görüntüleyebilmektedir. Öncül ve sonuç ürünlerin ilişki ve sonuçları destek, güven ve tesir metrikleri üzerinden sıralanarak satış ve pazarlama ekiplerine her hafta güncellenerek sunulmaktadır. Haftalık çalışan sistemde oluşturulan birliktelik kuralları analizlerinin sonuçlarının satış ve pazarlama birimleri tarafından kullanılması ile hem mağazacılık hem de e-ticaret kanalında sepet büyüklüğü ve çapraz satışların artırılması, sepet tamamlayıcı ürünler ve ana ürünler arasındaki ilişkilere bağlı olarak müşterilere doğru ürün önerisi yapılması mümkün olacaktır. Bu analiz ile müşteriye doğru ürünün sunulması, uygun pazarlama ve satış stratejilerinin belirlenmesi ve müşteri memnuniyeti sağlanacaktır.

Anahtar Kelimeler—*Apriori; Birliktelik Kuralları; Pazarlama;*

ABSTRACT

As a result of new developments in information and communication technologies, different shopping channels and orientations have increased competition in many sectors. For this reason, companies use data mining analyzes with existing data to discover the preferences and mindset of their customers and develop their sales methods, promotions and sales channels accordingly. At this point, association rule mining analysis can be used to explore the items that are frequently seen together in a dataset and the relationships/patterns between these items effectively. Discovered patterns can guide the sales and marketing decisions of companies as frequently observed items or rules. In this study, a data analysis software that performs association rule analysis with order data coming from retailing channels in Eczacıbaşı Building Products' ERP system and the attributes of the products in the orders was created. The first results in the analyzed data include the purchases made through the retail sales channel between April 2022 and April 2023. In these data, after filtering on the basis of the product, dummy variables were created on the material and a preprocessing study was carried out with the character coding method, and the existing data was first made ready for analysis. Apriori algorithm used for association rule mining was created in Python programming environment by using Pandas, Numpy, Mlxtend.Frequent_Patterns -Apriori, Mlxtend.Frequent_Patterns -Association_Rules and datetime libraries. The implemented software accesses the data by establishing a direct connection with the ERP system. Our system can find and display the association rules at the level of the main product and supplementary product found with the Apriori method. Association rule results of antecedent and consequential products; are presented to the sales and marketing teams by updating them every week by ranking over support, confidence and lift metrics. By using the results of the association rules analyzes created in the weekly system by the sales and marketing units, it will be possible to increase the basket size and cross sales in both the retail and e-commerce channels, and to make the right product recommendation to the customers depending on the relations between the basket complementary products and the main products. With this analysis; presenting the right product to the customer, determining the appropriate marketing and sales strategies and customer satisfaction will be ensured.

Keywords—*Apriori; Association Rules; Marketing;*

Dye Sensitive Solar Cells and Their Applications

Fatma Nur Yıldırım[*,1], İsmail Arsel[2], Emel Ece[2]

[*]: erz_ant_2507@outlook.com, ORCID: 0000-0002-9976-9535
[1]: *Karamanoğlu Mehmetbey University, Institute of Science, Department of Physics, Karaman, Türkiye.*
[2]: *Karamanoğlu Mehmetbey University, Kamil Özdağ Faculty of Science, Department of Physics, Karaman, Türkiye.*

ABSTRACT

Among all renewable energy technologies, photovoltaic technology is particularly attractive for directly converting sunlight into high-quality electricity. Studies in the field of energy have intensified around the keywords cheap, clean, and renewable. Among all renewable energy technologies, photovoltaic technology is particularly attractive for directly converting sunlight into high-quality electricity and with many positive properties solar energy plays a key role in the clean energy transition. Photovoltaic cells (solar cells) have been divided into four groups according to their historical development. These; are named first-generation solar cells, second-generation solar cells, third-generation solar cells, and fourth-generation solar cells. The third generation solar cell, the Dye Sensitive Solar Cell (DSSC), is the one receiving the most interest. This is owing, in part, to its low production costs, stability, environmental friendliness, ease of application, and wide application regions because of its thin structure. As can be expected such advantages have so far sparked a lot of research interest and commercialization activity.

This study aims to explore advanced approaches and research trends in this promising technology. In order to achieve this purpose, studies on DSSC and their usage areas in the last 20 years have been examined from the perspective of device modeling, cutting-edge methodologies, and unique device topologies.

Keywords—*Photovoltaic; Solar cells; Third generation solar cells; Dye sensitive solar cell*

Investigation of different Structures of Perovskites as the Absorber layers in the Solar Cells from the Perspective of COMSOL Simulation

Nagihan Delibaş[*,1], Aya Khachnaoui[1], Aligholi Niaei[1,2]

[*]: caylak@sakarya.edu.tr, 0000-0001-5752-062X
[1]: *Department of Physics, Faculty of Science, University of Sakarya, Sakarya, Turkey*
[2]: *Department of Chemical Engineering, University of Tabriz, Tabriz, Iran*

ABSTRACT

In the realm of solar cell research, our focus lies in discovering cost-effective materials that exhibit optimal performance. Our particular interest revolves around materials with the dual ability to efficiently absorb light and facilitate the movement of electrical charges. This study delves into the realm of perovskite materials, aiming to assess their viability for employment in solar cells. To achieve this, we employ the computational prowess of the COMSOL program, a versatile tool enabling us to scrutinize the behavior of perovskites across diverse scenarios. Our investigation centers on simulating various structures of perovskite solar cells (PSCs) using the aforementioned COMSOL simulation package.

A typical PSC configuration encompasses three distinct active layers: the light-absorbing perovskite layer, the electron transporting materials (ETM), and the hole transporting materials (HTM). These active layers can manifest in diverse organic or inorganic compositions. Through systematic simulations, we explore a range of PSC structures formed by combining these different compositions.

The outcomes of study are presented in Tables, providing a comprehensive depiction of the PSC structures' performance. Visual aids in the form of overlapped figures facilitate direct comparisons between various PSC configurations. This aids in discerning which PSC materials exhibit superior performance characteristics. Our comprehensive analysis reveals that perovskites based on methylammonium exhibit notably enhanced performance attributes. These findings underscore the potential of methylammonium-based perovskites as promising candidates for advancing the field of solar cell technology. In sum, this study not only contributes to the broader understanding of perovskite materials but also sheds light on their applicability in pushing the boundaries of solar cell efficiency.

Keywords— *Perovskite; Comsol*

PV Sistemler için Artan İletkenlik ve Değiştir-Gözle Yöntemlerinin Yapay Sinir Ağı ve PID Kontrolör Kullanılarak İyileştirilmesi

Improvement of Incremental Conductance and Perturb&Observer Methods for PV Systems using Artificial Neural Network and PID Controller

Zedan Saeed Murad MURAD[1], Mehmet Serhat CAN[*,1]

[*]: mehmetserhat.can@gop.edu.tr, ORCID: 0000-0003-2356-9921
[1]: *Tokat Gaziosmanpaşa Üniversitesi, Mühendislik ve Mimarlık Fakültesi, Elektrik-Elektronik Mühendisliği Bölümü, Tokat.*

ÖZET

Dolaylı çevre zararları tartışılmakla birlikte, fotovoltaik (FV) prensiple elektrik üretiminin fosil enerji kaynaklarına bağlı elektrik üretimine göre daha çok çevre dostu olduğu genel bir kanıdır. Ayrıca FV prensiple elektrik üretiminin kaynağı olan güneş, öngörülere göre oldukça uzun bir süre için varlığını sürdürebilecektir. Bu sebeple önemli bir yenilebilir enerji kaynağıdır. Çevre dostu olması, yenilenebilir olması, hareketli mekanik bileşenler içermemesi, montaj kolaylığı ve bakım maliyetinin düşük olması gibi nedenlerle popülerlik kazanmış ve bu popülerliğini devam ettirmektedir. Bir FV sistemden elde edilen elektrik enerjisi güneş ışınımına ve FV sistemdeki modüllerin sıcaklığına bağlıdır. Değişen güneş ışınımın ve sıcaklığın değişimi ile birlikte FV sistemden elde edilen güç ve dolayısıyla enerji değişmektedir. Anlık güneş ışınım ve sıcaklığa göre FV sistemin üretebileceği en yüksek güç miktarı Maksimum Güç Noktası (MGN) olarak adlandırılmaktadır. Her farklı güneş ışınımı ve sıcaklık değeri için MGN nin tespiti ve takibi için kullanılan yöntemler Maksimum Güç Noktası İzleme (MGNİ) başlığında toplanmaktadır.

Artan İletkenlik (Aİ) ve Değiştir-Gözle (DG) basit olmaları sebebiyle çokça kullanılan iki yöntemdir. Artan İletkenlik algoritmasında FV modülün güç-gerilim (P-V) eğrisi dikkate alınır. MGN de FV gücündeki değişim miktarının FV gerilimdeki değişim miktarına oranı sıfır olmaktadır. Buradan yola çıkarak FV panelin iletkenliği ve iletkenlik artışı dikkate alınarak kontrol işareti güncellenir. Aİ yönteminin bir dezavantajı parçalı gölgelenme durumlarında gerçek MGN yi izleyememesidir. Ayrıca MGN de salınım olmaktadır. Değiştir-Gözle algoritmasında ise FV panelin çıkış gerilimi bir kontrolör referans işareti ile değiştirilir ve bu değişime karşılık FV çıkış gücünün artma veya azalma eğilimi gözlenir. Çıkış gücünün değişim yönüne göre kontrol referansı güncellenir. DG yöntemi hızlı değişen atmosferik durumlarda MGN den sapmalara sebep olmaktadır. Bu yöntemde de MGN de ciddi salınımlar görülmektedir. Geleneksel Aİ ve DG yöntemlerinde MGN de gözlemlenen salınım miktarı, kontrol sinyalindeki değişim oranının küçük tutulması ile kısmen azaltılabilmektedir. Fakat bu durumda MGN yi yakalama hızı düşmektedir.

Bu bildiri çalışmasında, geleneksel Aİ ve DG yöntemlerinde bir problem olan MGN deki salınımların azaltılması için Yapay Sinir Ağı (YSA) ve Oransal-İntegral-Türevsel (PID) kontrolöre dayanan bir yöntem önerilmektedir. Önerilen bu yöntemde, geleneksel Aİ ve DG yöntemlerinde sabit değerli olarak kullanılan kontrol işareti değiştirme oranı YSA ve PID

kontrolör ile değişen atmosferik durumlara göre adaptif olarak ayarlanmaktadır. Böylece değişen çevre şartlarında MGN de oluşan salınımlar önemli seviyede düşürülebilmiştir. Çalışma Matlab/Simulink üzerinde benzetim çalışması şeklinde gerçekleştirilmiştir.

Anahtar Kelimeler—*FV sistem; MGNİ; YSA; PID; Artan İletkenlik; Değştir-Gözle.*

ABSTRACT

Although indirect environmental damage is discussed, it is a general opinion that electricity generation with the photovoltaic (PV) principle is more environmentally friendly than electricity generation based on fossil energy sources. In addition, the sun, which is the source of electricity production with the PV principle, will continue to exist for a very long time according to the predictions. For this reason, it is an important renewable energy source. It has gained popularity and continues to be popular for reasons such as being environmentally friendly, renewable, free of moving mechanical components, ease of assembly and low maintenance cost. The electrical energy obtained from a PV system depends on solar radiation and the temperature of the modules in the PV system. With the change in solar radiation and temperature, the power obtained from the PV system, and therefore the energy, changes. The maximum amount of power that the PV system can produce according to the instantaneous solar radiation and temperature is called the Maximum Power Point (MPP). The methods used for the detection and tracking of MPP for each different solar radiation and temperature value are collected under the title of Maximum Power Point Tracking (MPPT).

Incremental Conductance (IC) and Perturb&Observe (PO) are two methods that are widely used due to their simplicity. In the Incremental Conductance algorithm, the power-voltage (P-V) curve of the PV module is taken into account. The ratio of the amount of change in PV power to the amount of change in PV voltage in MPP becomes zero. Based on this, the control sign is updated considering the conductivity of the PV panel and the increase in conductivity. A disadvantage of the IC method is that it cannot track the real MPP in partial shadowing situations. In addition, MPP also oscillates. In the Perturb&Observe algorithm, the output voltage of the PV panel is changed with a controller reference signal, and the PV output power tends to increase or decrease in response to this change. The control reference is updated according to the change direction of the output power. The PO method causes deviations from the MPP in rapidly changing atmospheric conditions. In this method, serious oscillations are seen in the MPP. In traditional IC and PO methods, the amount of oscillation observed in MPP can be partially reduced by keeping the rate of change in the control signal small. But in this case, the rate of catching MPP decreases.

In this paper, a method based on Artificial Neural Network (ANN) and Proportional-Integral-Derivative (PID) controller is proposed to reduce oscillations in MPP, which is a problem in traditional IC and PO methods. In this proposed method, the control signal switching rate, which is used as a fixed value in traditional IC and PO methods, is adjusted adaptively according to the changing atmospheric conditions with ANN and PID controllers. Thus, the oscillations in the MPP under changing environmental conditions have been significantly reduced. The study was carried out as a simulation study on Matlab / Simulink.

Keywords—*PV system; MPPT; ANN; PID; Incremental Conductance; Perturb&Observe.*

Characterization of Hydrochar Product from Pistachio Shell

Zeynep YILDIZ UZUN

zyildiz@sinop.edu.tr, ORCID: 0000-0001-6280-1215
Department of Chemistry and Chemical Processing Technologies, Sinop University, Sinop, Turkey

ABSTRACT

Biomass is known as an important energy source that can be found naturally and produced in large quantities. Examples of biomass types are agricultural waste, forest residue and industrial waste. Biomass can be converted into more valuable solid products with higher fuel quality using conversion techniques such as pyrolysis, gasification and combustion. In this study, solid product (hydrochar) was obtained from pistachio shell biomass by hydrothermal carbonization (HTC) method. Techniques such as Thermogravimetric Analysis (TGA), proximate analysis (%Volatile matter, ash and fixed carbon), ultimate analysis (% C, H, N, S and O) and Fourier Transform Infrared Spectroscopy (FTIR) analysis were used for the characterization of the raw material. After characterization of the raw material, the hydrochar product was produced at 220 °C with a residence time of 90 minutes. The biomass water ratio was taken as 1:10. Techniques such as proximate and ultimate analysis, FT-IR analysis and Scanning Electron Microscopy (SEM) analysis were used for the characterization of the hydrochar product. FT-IR analysis technique was used to determine the functional groups in the structure of raw samples and hydrochar products. SEM analysis was performed to examine the surface morphology of the hydrochar product. In addition, the fuel properties (high heating value, energy and mass yield and energy densification ratio) of raw pistachio shell and hydrochar product were investigated. According to the ultimate analysis results, compared to the raw material, the hydrochar product has a higher calorific value. As a result, it has been shown that the hydrochar product produced from the pistachio shell by the hydrothermal carbonization method can be used as a biofuel.

Keywords— *Hydrothermal carbonization; hydrochar; pistachio shell*

Convertible Wheel/Track Design for Robots

Robotlar için Dönüşebilen Tekerlek/Palet Ayak Tasarımı

Tuğba BOZKURT*[1], Ertuğrul ÇETİNSOY*[2]

tugbabozkurt@marun.edu.tr, ORCID: 0000-0003-4718-5586
[1]: *Marmara University, Institute of Science, Mechatronic Engineering, Istanbul, TURKIYE*
[2]: *Marmara University, Institute of Science, Mechatronic Engineering, Istanbul, TURKIYE*

ABSTRACT

Autonomous and semi-autonomous robots are used today for material handling in the factory, capable of moving both in the field and on the road to transport ammunition and wounded soldiers in the military, mobilization of patients with physical disabilities and patients after surgery, transport of the wounded, transport of dead and material during search and rescue operations, and regional scanning missions. These robots have the potential to become widespread, preferred as wheeled or tracked according to road conditions. Although the track provides safety against slipping and sinking in heavy terrain conditions, it causes high energy consumption. Although the wheel offers fast travel and low energy consumption, it does not move well except on hard ground. Hybrid drive system designs combining track and wheel are an important research topic as they have the potential to offer the most efficient cruising under all targeted conditions. Within the scope of this project, a track/wheel hybrid drive system that can be used in mobile robots has been developed. This proposed system is formed by combining 4 quadrants with end-to-end joints. When it is broken and flattened from these 4-quarter joints, it turns into a track, and when it is most open, it turns into a wheel.

The drive shaft coming out of the robot body rotates the sun gear in the center of the system. When the mechanism is in track mode, the sun gear rotates the 4 gear wheels that are constantly clamped to it, allowing the band to move forward. This tape acts as a track, transferring the movement to the floor. When the mechanism is in wheel mode, the frame that carries the tension wheels and which has teeth as the counterpart of the sun gear is clamped to the sun gear. In this way, it starts to rotate with the open 4 quarter sun gear, which is a full circle. In this case, the tape acts as a fixed coating to the surface, forming the tire outer surface of the wheel. This design does not require a deformable (elongating or shortening) belt seen in most examples in the literature. Therefore, thanks to this newly designed belt life and reliability are increased.

The transition between the flattening of the 4 quadrants and the open state is provided by the wire drawing mechanism, which takes the pulling force from the engine mounted on the robot body and has the same design as the propeller pitch changing mechanism in aircraft. As long as the wheel/track mechanism is in wheel mode, there must be tension on the wire to keep the 4 quadrants open without being crushed. To switch to track mode, the system is placed in an angular position where folding can occur and the tension on the wire is relieved. Support channels have been added between the quarter circles so that the belt does not come out of the slot in wheeled and tracked mode. Silicon hose was added to the middle part of the belt to prevent the belt from sliding left and right. Plastic teeth are formed to fit between all gears for the transmission of movement.

Keywords— *Wheel/Track Drive System; Hybrid Mechanical System; Robotics*

ÖZET

Fabrikalarda malzeme, askeri alanda mühimmat ve yaralı askerlerin transferi alanlarında hem saha hem de yol koşullarında ilerleyebilen, ameliyat sonrası bedensel engelli ve hastaların mobilizasyonu, yaralıların taşınması, arama kurtarma operasyonlarında ölü ve malzeme taramaları ve bölgesel tarama görevleri için otonom ve yarı otonom robotların kullanılması günümüzde yaygınlaşma potansiyeline sahiptir. Bu robotlar yol şartlarına göre tekerlekli veya paletli olarak tercih edilmektedir. Palet ağır arazi koşullarında kayma ve batmaya karşı güvenlik sağlasa da yüksek enerji tüketimine neden olur. Tekerlek hızlı yolculuk ve düşük enerji tüketimi sunsa da sert zemin dışında iyi ilerleyemez. Palet ve tekerleği birleştiren hibrit tahrik sistemi tasarımları, hedeflenen tüm koşullar altında en etkin seyiri sunma potansiyeli taşıma bakımından önemli bir araştırma konusudur. Bu proje kapsamında mobil robotlarda kullanılabilecek bir palet/tekerlek hibrit tahrik sistemi geliştirilmiştir. Önerilen bu sistem 4 çeyrek dairenin uç uca eklemlerle birleştirilmesiyle oluşturulmuştur. Bu 4 çeyreklik birleşim yerlerinden kırılıp düzleştirildiğinde palete, en açık hale geldiğinde ise tekerleğe dönüşür.

Robot gövdesinden çıkan tahrik mili sistemin merkezinde bulunan güneş dişlisini döndürür. Mekanizma palet modunda iken, güneş dişlisi kendisine sürekli kenetli durumdaki 4 adet dişli çarkı döndürerek bandın ilerlemesini sağlar. Bu bant palet olarak görev yapar, hareketi zemine aktarır. Mekanizma tekerlek modundayken, gergi çarklarını taşıyan ve üzerinde güneş dişlisinin karşılığı olarak dişler bulunan çerçeve güneş dişlisine kenetlenir. Bu sayede tam daire olmuş açık 4 çeyrek güneş dişlisi ile birlikte dönmeye başlar. Bu durumda, bant yüzeye sabit bir kaplama görevi görür, tekerleğin lastik dış yüzünü oluşturur. Bu tasarımda literatürdeki çoğu örnekte görülen ve dayanıklılığı büyük ölçüde azaltan deforme olabilen (uzayan veya kısalan) bir kayışa gerek olmadığı için ömür ve güvenilirlik artmıştır.

4 çeyreğin kırılarak düzleşmesi ile açık durum arasındaki geçiş, robot gövdesi üzerine monte edilmiş motordan çekme kuvvetini alan ve hava araçlarındaki pervane hatvesi değiştirme mekanizmasıyla aynı tasarıma sahip olan tel çekme mekanizması ile sağlanmaktadır. Tekerlek/palet mekanizması tekerlek modunda olduğu sürece, 4 çeyreğin ezilmeden açık kalması için telin üzerinde gerilim olması gerekir. Palet moduna geçiş için sistem katlanmanın gerçekleşebileceği açısal konuma getirilir ve telin üstündeki gerilim boşaltılır. Böylece sistemin üzerindeki yükün baskısıyla katlanma gerçekleşir, palet ayak moduna geçilir. Tekerlekli ve paletli modda bandın yuvasından çıkmaması için çeyrek dairelerin arasına destek kanalları eklenmiştir, tüm dişlilerin ortasında yarık bulundurulmuş ve enleme yönüne orta hizasına silikon hortumdan bir çıkıntı olan özel bir bant geliştirilmiş ve üretilmiştir.

Anahtar Kelimeler— *Tekerlek/Palet Tahrik Sistemi; Hibrit Mekanik Sistem, Robotik*

Calculation of bulk modulus as a function of pressure in a perovskite-like framework of $[(C_3H_7)_4N]$ $[Mn(N(CN)_2)_3]$

Sedat AVCI[*,1], Mustafa KURT[2]

[1]: sedat.avci@comu.edu.tr, ORCID: 0000-0001-8971-0575
[1]: *Department of Energy Management, Faculty of Applied Sciences, Çanakkale Onsekiz Mart University, Çanakkale, TURKEY*
[2]: *Department of Electronic Engineering, Engineering Faculty, Çanakkale Onsekiz Mart University, Çanakkale, TURKEY*

ABSTRACT

Perovskite materials are described as a compound exhibiting a crystal structure, formulated as ABX_3. The first discovery of this structure was made in the form of a mineral known as perovskite, composed of calcium titanium oxide (CaTiO3) by Gustav Rose in 1839. Last quarter, perovskite materials exhibit ferroelectric and electric properties have been great attention by the scientists, because of potential in electronic and optoelectronic applications. Recent studies related to explore of perovskite materials in literature have demonstrated perovskite-like molecules such as [(C3H7)4N][Mn(N(CN)2)3] (shortly; [TPrA][Mn(dca)3]) having properties such as various properties, including magnetism, ferroelectricity, luminescence, switchable dielectric behavior, multiferroic behavior and non-linear optical, as perovskites, as in perovskites. The crystal structures and properties of molecular perovskites are influenced by various parameters, including the molecular linker's length and flexibility, as well as the organic cation's size, shape, and its capacity to establish hydrogen bonds with the metal linker framework. Molecular crystals as perovskites and perovskite-like framework exhibit structural phase transitions by changing the molecular order with increasing pressure. The application potential of [TPrA][Mn(dca)3] can be significantly enhanced by the structural phase transition under varying pressure conditions in the production processes. [TPrA][Mn(dca)3] shows two structural phase transition with pressure; first is from tetragonal phase (Cmc21) to orthorhombic phase (Pcnb) at 0.3 GPa, second is from orthorhombic phase (Pcnb) to monoclinic phase (P21/n) at 2.8 GPa in room temperature. While existing literature related to pressure-induced structural phase transitions, there are currently a lack of comprehensive studies that sufficiently explain the micro dynamics of the phase transition in [TPrA][Mn(dca)3]. In this work, we conducted an analysis to ascertain the isothermal compressibility in relation to pressure by examining the measured wavenumber for Raman modes and volume data in [TPrA][Mn(dca)3], both above and below the phase transition. This analysis was performed using theoretical methods. Subsequently, the Bulk modulus values (10 GPa for the Pcnb -phase and 36 GPa for the P21/n -phase) were determined by using up of predicted isothermal compressibility values for each relative phase. These results show that perovskite-like framework of [TPrA][Mn(dca)3] can be modified for some application with pressure. This study is supported by Çanakkale Onsekiz Mart University the Scientific Research Coordination Unit, (Project number: FDK-2021-3591).

Keywords—*perovskite-like materials; Phase Transition; Bulk Modulus; Compressibility*

Örnek Bir Bina İçin Yapısal Performans ile Maliyet Arasındaki İlişkinin İncelenmesi

Investigation of Relationship between Structural Performance and Cost for a Sample Building

Serkan Sağıroğlu[*,1], Ali Haj Hamad[1]

[*]: serkansagiroglu@uludag.edu.tr, ORCID: 0000-0001-7248-3409
[1]: *İnşaat Mühendisliği Bölümü, Bursa Uludağ Ünivesitesi, Bursa, Türkiye*

ÖZET

Yeni binaların tasarımında kullanılan yönetmelikler, konut yapılarının beklenen tasarım depremi altında "Can Güvenliği" veya "Kontrollü Hasar" olarak adlandırılan performans seviyelerini karşılamasını gerektirmektedir. Bu performans düzeyleri farklı mevzuatlarda benzer şekilde tanımlanmaktadır. Bu seviyeyi karşılayan binalarda yapısal ve yapısal olmayan bileşenlerde büyük hasar görülebilir ancak yapının çökmemesi gerekir. Ayrıca tehlikeli yapısal olmayan hasarlar da sınırlıdır. Ancak insanların binayı tekrar kullanabilmesi için onarım yapılması gerekebilir. Bu performans seviyesine uyan binalarda can güvenliği riski düşüktür. Genel bir kural ve anlayış olarak, yönetmeliklerin asgari gereksinimleri belirlediği ve tasarımcının, bina sahibinin veya bina kullanıcılarının talepleri doğrultusunda yönetmeliklerin gerektirdiğinden daha iyi bir performans düzeyi sağlayacak şekilde binayı tasarlayabileceği söylenebilir. Elbette daha iyi bir performans ek bir maliyet getirecektir.

Bu çalışmada binanın performans düzeyi ile maliyeti arasındaki ilişkinin araştırılması amaçlanmaktadır. Bu amaçla taban alanı 225 m2 olan 5 katlı örnek bina seçilmiştir. Bu bina, Türkiye Bina Deprem Yönetmeliği (TBDY-2018) ve Betonarme Yapıların Tasarım ve Yapım Kuralları (TS-500) yönetmeliğine uygun olarak tasarlanmıştır. Daha sonra performans analizi yapılmış ve yapının performansının beklendiği gibi "Can Güvenliği (Kontrollü Hasar)" düzeyinde olduğu görülmüştür. Daha sonra yapı elemanlarının ve donatıların boyutları iteratif olarak artırılarak her iterasyonda performans analizi yapılmıştır. "Sınırlı Hasar" performans seviyesine ulaşıldığında iterasyon durdurulmuştur. Ayrıca daha kötü bir performans düzeyiyle kıyaslama yapılabilmesi için eleman boyutları ve donatılar azaltılarak "Göçme" performans seviyesiyle sonuçlanan bir tasarım da çalışmada sunulmuştur. Farklı performans seviyelerindeki tasarımların metrajları (beton, donatı ve kalıp) hesaplanmış ve karşılaştırılmıştır. Tasarlanan örnek binanın performans seviyesinin "Kontrollü Hasar" seviyesinden "Sınırlı Hasar" performans seviyesine çıkması durumunda beton miktarında %54, kalıp miktarında %17 ve donatı miktarında %125 oranında artış meydana gelmektedir. Performans düzeyi "Göçme" seviyesinde olan binanın beton, kalıp ve donatı miktarları "Can Güvenliği" performans seviyesindeki binaya göre sırasıyla %3, %2 ve %7 daha azdır.

Beton, kalıp ve donatı maliyetinin binanın toplam maliyetine oranının yaklaşık %40 olduğu dikkate alındığında, performans düzeyinde "Kontrollü Hasar" seviyesinden "Sınırlı Hasar" seviyesine doğru iyileşme, maliyette yaklaşık %26 lık bir artışa, öte yandan performans düzeyinde "Kontrollü Hasar" seviyesinden "Göçme" seviyesine geçiş, maliyette yaklaşık %2'lik bir düşüşe karşılık gelmektedir.

Anahtar Kelimeler— *Performansa dayalı tasarım; Betonarme; Maliyet; Performans analizi*

ABSTRACT

The codes and regulations used in the design of new buildings require residential buildings to meet performance levels called "Life Safety" or "Controlled Damage" under the expected design earthquake. These performance levels are defined similarly in the regulations. Extensive damage to structural and nonstructural components could be seen in the buildings meeting this level, but the structure should not collapse. In addition hazardous nonstructural damage is controlled. However, repairs may be required before people can use the building again. The risk to life safety in the buildings complying this performance level is low. As a general rule and understanding, it can be said that the regulations set the minimum requirements and the designer can design the building in line with the demands of the building owner or building users to provide a better performance level than the one what regulations require. Of course, a better performance will bring an additional cost.

In this study, it is aimed to investigate the relationship between the building performance level and its cost. For this purpose, a 5-storey sample building with a floor area of 225 m^2 was chosen. This building was designed in accordance with the Turkish Building Earthquake Code (TBDY-2018) and the Requirements for Design and Construction of Reinforced Concrete Structures (TS-500) regulations. Then, the performance analysis was performed and the performance of the structure was found to be "Life Safety (Controlled Damage)" level as expected. Then, the dimensions of the structural elements and reinforcements were increased in an iterative manner and performance analysis was performed at each iteration. Iteration was stopped when "Immediate Occupancy" performance level is achieved. In addition, in order to be able to compare with a worse performance level, element dimensions and reinforcements were reduced, and a design that result in "Collapse" performance level was also presented in the study. Quantities (concrete, reinforcement and formwork) of designs with different performance levels were calculated and compared. If the performance level of the designed sample building increases from the "Life Safety" level to the "Immediate Occupancy" performance level, an increase of 54% in the concrete quantity, 17% in the formwork quantity and 125% in the reinforcement quantity occur. The concrete, formwork and reinforcement quantities of the building whose performance level is at the "Collapse" level are 3%, 2% and 7% less, respectively, compared to the building with the "Life Safety" performance level.

Considering that the ratio of the cost of concrete, formwork and reinforcement to the total cost of the building is approximately 40%, the improvement from the "Life Safety" level to the "Immediate Occupancy" level in the performance level corresponds to an increase of approximately 26% in the cost. On the other hand, a change in performance level from "Life Safety" to "Collapse" corresponds to a decrease of approximately 2% in cost.

Keywords—*Perfromance based design; Reinforced concrete; Cost; Perfromance Analysis*

Evaluation of Critical Factors in Mechanically Extrusion Based Syringe Driver System Design for 3D Bioprinters

Bünyamin ÖZTÜRK[*,1], Sezcan YILMAZ[1]

[*]: bunyamin.ozturk@ogu.edu.tr, ORCID: 0000-0002-3923-4256
[1]: *Department of Mechanical Engineering, Eskişehir Osmangazi University, Eskişehir, Türkiye*

ABSTRACT

With the developments in the field of biomedical, 3D bioprinting technology has become of great importance. This technology includes many different methods that allow the production of complex biological structures. Extrusion-based bioprinting, one of these methods, aims to create desired structures by extruding material using pressure. Extrusion-based bioprinting is a promising technique with the potential to create biomimetic structures of tissues and organs. It offers great potential, especially for the production of complex structures. This technique enables the creation of various textural structures with the use of different hydrogel inks. However, appropriate conditions must be provided for cell survival and functionality during printing.One of the most critical components of extrusion-based bioprinting is the syringe drive system, which allows the bioink to flow at the flow rate desired by the user. Syringe drive systems used in these structures are generally divided into three groups: pneumatic, piston and screw. Pneumatic propulsion syringes are widely used because they do not require extra equipment and allow working with a constant pressure. However, an externally sourced compressed air unit is needed for pneumatic propulsion. When it is desired to make a syringe drive system that works only with electrical energy, piston or screw systems are preferred. Screw propulsion systems have a much simpler structure than piston ones. However, if there is a fluid containing living tissue in the syringe, the screw mechanism's rate of damaging living tissue is higher than other propulsion systems. Although piston propulsion systems have a much more complex structure than others, they can be preferred because they can operate independently and allow very precise control with their electric motor.When designing this structure, syringe chamber diameter, needle exit diameter, fluid viscosity and fluid outlet flow rate values should be taken into consideration. Although there are many different designs for the piston drive system, the structure that provides the propulsion generally consists of stepper motor, reducer and screw driven linear guide components. In order to obtain biomaterial output at the desired flow rate via syringe, these structural elements must be selected and sized appropriately. The rheological behavior of hydrogels is a critical factor affecting print quality. Hydrogels are generally non-Newtonian fluids, meaning their viscosity varies with shear rate. This means that a balance must be achieved between the viscosity of the bioink and the shear stress generated during printing. The pressure used during extrusion printing can affect the cell morphology and function of the biomaterial.Choosing a motor with too much power and torque may damage the biomaterial due to the high pressure that occurs when there is a blockage in the syringe needle or when the fluid is tried to be removed at a high flow rate. If an appropriate reduction ratio is not selected, the biomaterial output flow rate may not be controlled. In this case, the first stage of the design should be to determine the maximum pressure that the fluid biomaterial can withstand without deterioration and the minimum pressure values needed to achieve the desired flow rate. Then, depending on these values, the propulsion force and speed limits of the syringe piston should be calculated according to the maximum and minimum fluid

output flow rates desired to be obtained from the syringe needle, taking into account the syringe chamber diameter and needle diameter. Once the propulsion force and speed limits of the piston are determined, the power of the engine to be used can be calculated based on these values. After the motor is selected, the reduction ratio is calculated depending on the output torque and speed values of the motor and the force and speed values required for propulsion on the syringe piston. In this study, it was examined how the critical factors that should be taken into account in the design of piston syringe systems used in 3D bioprinters should be used in determining modeling parameters. In this context, a mathematical model has been created that reveals the operating dynamics of the system. In conclusion, the extrusion-based bioprinting method has significant potential, which is expected to play a major role in biomedical applications in the future. Further development and optimization of this method may enable more precise, high-resolution and cell-friendly prints to be obtained. In this context, discussing the features of the design of the mechanical syringe driver may also contribute to the overall effectiveness and applicability of the method.

Keywords— *3D bioprinter; Syringe; Piston-driven propulsion*

Possible Problems with Multi-DOF Force/Torque Sensor Designed and Built Using Cost-Effective Load Cells

Bünyamin ÖZTÜRK[*,1], Sezcan YILMAZ[1]

[*]: bunyamin.ozturk@ogu.edu.tr, ORCID: 0000-0002-3923-4256
[1]: *Department of Mechanical Engineering, Eskişehir Osmangazi University, Eskişehir, Türkiye*

ABSTRACT

Force and torque measurement holds fundamental importance in various applications. These measurements are commonly performed based on the principle of measuring the change in surface tension that occurs when objects are subjected to a force. Strain gauge sensors, whose resistance changes under stress, are used to measure surface tension. These sensors are mechanically attached in a specific arrangement to structures designed to measure force and/or torque based on surface tension. Additionally, for accurate measurement and easy calibration, they are connected to amplifiers using electrical Wheatstone bridge connections. This setup allows the creation of single or multiple degrees of freedom (DOF) measurement equipment for various applications. Today, there are a wide variety of force and torque sensors commercially available in a wide variety of types, sizes, and features. The most commonly used among these sensors are load cells designed to measure a force effect in a single axis, such as tension, compression, pressure, or torque. They are ideal due to their high accuracy, versatility, and cost-effectiveness. These sensors offer suitable and effective solutions for many applications. However, customized measurement system designs may still be required for certain applications. Customized measurement systems can be created by attaching strain gauge sensors in a specific arrangement to structural bodies or by combining load cells in different configurations. Careful planning and implementation of both the mechanical design and the electronic components are required when constructing such structures. This study aims to highlight potential problems encountered in the design of multi-degree-of-freedom force/torque measurement systems created using cost-effective load cells. One of the initial challenges in creating such systems is related to designing the mechanical structure accurately. In applications where force or torque measurement is required along different axes, appropriate load cells can be rigidly connected to each other. However, in applications using customized load cells designed specifically for force measurement, rigid connections can hinder accurate measurements when both force and torque need to be measured simultaneously. In such applications, load cells should be considered as part of a mechanism, and the structure should be designed accordingly to position the load cells to measure forces only in the directions they are capable of measuring. Moreover, some mechanical designs may lead to cost-inefficiencies due to their requirement for highly precise manufacturing. In such cases, solutions created by directly attaching strain gauge sensors can be much more cost-effective. Another problem to consider is that cost-effective load cell bodies are often made of aluminum. Aluminum-bodied load cells have longer response times compared to steel-bodied ones. Therefore, in applications requiring dynamic force/torque measurement, steel-bodied load cells should be preferred. When selecting amplifiers and analog-to-digital converters (ADCs), the operating frequency and response time required for the application should be taken into account. Electronic system costs increase dramatically as the required operating frequency grows and the response time becomes shorter. To achieve a cost-effective solution, the optimum operating frequency and

response time should be determined. In this study, solutions to possible problems that may be encountered in the creation of a cost-effective multi-degree-of-freedom force/torque sensor are presented.

Keywords— *Force sensor; Torque sensor; Load cell; Multi-DOF system; Strain gauge*

Evaluation of Liquefaction Potential of Alluvial Deposits in Canakkale Settlement Area by using Shear Wave Velocity

Mehmet Celal TUNUSLUOGLU

ctunus@comu.edu.tr, ORCID: 0000-0002-2421-6864
[1]*Department of Geological Engineering, Canakkale Onsekiz Mart University, Terzioglu Campus, 17020 Canakkale, Turkey*

ABSTRACT

Liquefaction is one of the most important problems in geotechnical engineering. If the settlements built on alluvial deposits where the groundwater level is close to the surface are located in a seismically active region, the possibility of liquefaction-induced damage to the structures is high. Canakkale settlement area is located between the Saros-Gazikoy Fault and the Yenice-Gonen Fault. These faults form the central and southern branches of the North Anatolian Fault Zone (NAFZ). The aim of this study is to determine the sensitivity of the alluvial deposits on which Canakkale settlement area is located against liquefaction by the shear wave velocity (V_s) method. For this purpose, the liquefaction potential of the alluvium deposits was investigated by using liquefaction analysis based on shear wave velocity using the data obtained from seismic refraction measurements and MASW studies. In addition, the liquefaction susceptibility map made by Tunusluoglu and Karaca (2018) using the standard penetration test (SPT) method in the Canakkale settlement area and the liquefaction susceptibility map created as a result of this study were also compared.

Within the scope of microzonation studies carried out in Canakkale settlemet area, it was determined that two-thirds of the settlement area was construct on an alluvial deposits. A total of 131 geotechnical boreholes and 82 seismic refraction measurement point studies were carried out on the alluvial deposit. Soil mechanics tests such as moisture content, unit volume weight, particle size distribution, Atterberg limits were carried out on alluvial samples taken from boreholes. Considering an earthquake scenario with a magnitude of M_w=7.5 in the study area, liquefaction analyzes were performed with shear wave velocity data. Then, liquefaction severity index (L_s) values were found by using shear wave velocity (V_s) data and liquefaction severity maps were created. As result of the study, according to Vs, the liquefaction severity index (L_s) values of the Quaternary alluvial deposits in the study area were determined %5 as very high and 29% as high. In the study conducted by Tunusluoglu and Karaca (2018), according to SPT-N, the liquefaction severity index (L_s) were found to be very high in 19% and high in 60%, respectively.

Considering these results, it has emerged that it is extremely important to determine the geotechnical properties of liquefiable soils for suitable foundation designs in the part of Canakkale settlement area located on Quaternary alluvial deposits.

Keywords—*Liquefaction; Shear wave velocity; Liquefaction severity index; Canakkale*

Multiple Sclerosis Lesion Prediction using CNN-LSTM

Zahra ELMI

zahra.elmi@izu.edu.tr, ORCID: 0000-0003-1487-8570
Department of Computer Engineering, Istanbul Sabahattin Zaim university of organization1, Istanbul, Turkey

ABSTRACT

Multiple sclerosis (MS) is a chronic and progressive autoimmune disease affecting the brain and spinal cord. The disease causes various potential symptoms, including vision problems, problems with arm or leg movement, and emotional problems. As a result of this disease, multiple areas of scar tissue called sclerosis may appear. MS is most diagnosed in people between 20 and 30 but can occur at any age. Women suffer from this disease 2-3 times more often than men. MRI imaging is a complementary initial examination for the monitoring and diagnosing of MS and provides significant information to doctors. Classification of multiple sclerosis MS lesions from MRI brain images is essential in diagnosing this disease, and diagnosis and analysis of these lesions from MRI brain images is usually time-consuming and expensive. Therefore, automatic and semi-automatic methods are recommended for segmenting MS lesions. The main aim of this paper is to present a new approach based on the combination of convolutional neural networks (CNN) and long short-term memory networks (LSTM) (CNN-LSTM). The experimental result of the proposed method is compared to multi-layer perceptron and VGG19 along with CNN. Accuracy, precision, recall, and F1-score are utilized as the most common metrics for classification performance. The results obtained by the proposed model have the best performance.

Keywords— *Multiple sclerosis; convolutional neural network; long short-term memory networks; Deep learning; Machine learing.*

The Usability of Hazelnut Shell Agricultural Waste as Filler in Polymer Composites

Sami DURSUN

samidursunn@ktun.edu.tr, ORCID: 0000-0002-4581-4900
Department of Metallurgical and Materials Engineering, Konya Technical University, Konya, Turkey

ABSTRACT

Water is indispensable for living things to survive. While the demand for water is increasing day by day, usable water in our world is decreasing day by day. In addition, various types of pollution directly or indirectly pollute existing water resources. Polluted water can cause many diseases and even death. Precipitation, adsorption, ion exchange, oxidation, and membrane filtration are some of the methods used to remove impurities from water. The adsorption method is highly preferred due to its ease of use, large capacity and low cost. Hydrogels are cross-linked networks containing functional polymers and are widely used in the treatment of polluted waters. Recently, studies have been conducted on the construction of semi-interpreting polymer networks produced by integrating two or more polymers to improve the properties of hydrogels, such as adsorption capacity, mechanical stability and chemical stability. Also, the incorporation of certain fillers into the structure of this polymer helps to further improve the properties of the materials. In particular, bio-fillers are highly preferred because they are environmentally friendly, low-cost, easily available, and biodegradable. Hazelnut shell (HS) is one of the filling materials that can be added to the structure of semi-interpreting polymer networks. Therefore, by using HS as a filling material, less waste can be generated and biocomposite materials can be produced at lower costs. In this study, the usability of HS agricultural wastes as a filler in polymer composites was investigated. HS bio-filling material was used together with several polymers and a new biocomposite polymer was produced. During the production process, HS was first cleaned with water. After the cleaned and dried HS was crushed, it was sieved with the help of a sieve to obtain homogeneous dimensions. Boiling was then carried out to remove impurities. Obtained micro particles were reacted using APS initiators in the presence of PVA, PAA, and NMBA precursors. After the necessary purification and drying processes of the obtained product, a polymer composite with filler material was produced. The structural and morphological properties of this HS-filled polymer composite were characterized by FT-IR, TGA, DSC, FE-SEM, and EDX measurements, and the production mechanism is discussed.

Keywords—*Biocomposite; Hazelnut shell;polymer; Bio-filler*

Arbitrary Amplitude Dust-Acoustic Solitary Structures in Thermally Degenerate Plasmas

Muhammad Asaduzzaman
azaman@phy.kuet.ac.bd, ORCID: 0009-0002-7632-045X
Department of Physics, Khulna University of Engineering and Technology, Khulna-9203, Bangladesh

ABSTRACT

The basic features of arbitrary amplitude dust-acoustic solitary structures (associated with the self-gravitational field), which are found to exist in a multi-nucleus unmagnetized dusty plasma system containing inertial charged dust fluid, non-inertial warm light as well as heavy nucleus species and non-inertial thermally degenerate electron species, have been investigated by employing the pseudo-potential approach, which is valid for nonlinear structures with arbitrary amplitudes. It is found from the nonlinear analysis (both weakly and highly) that the thermally degenerate dusty plasma model can support solitary waves only with negative potential. The subsonic and supersonic dust-acoustic solitary structures (DASSs) along with their fundamental properties are identified. It has been found that the fundamental properties of these subsonic and supersonic DASSs are significantly modified by the effects of ultra-relativistic as well as non-relativistic degenerate electron species, dynamics of dust fluids, dynamics of heavy nucleus species, temperatures of light and heavy nuclear species, temperature of dust fluids, number densities, etc. The electron species, heavy nucleus species, and dust fluids are responsible for the formation of subsonic DASSs. The possibility of the formation of subsonic DASSs is reduces due to the effect of electron degeneracy as well as the temperatures of dust, heavy nucleus and light nucleus. When the temperature of light as well as heavy nucleus species and dust fluids increases the amplitude (width) of the subsonic and supersonic DASSs decreases (increases). On the contrary, the amplitude (width) of the subsonic and supersonic DASSs increases with the increase of number density of dust and the number density of light and heavy nucleus species. The implications of our results to some astrophysical and space plasma systems, especially to planetary ring-systems and cometary tails, are briefly mentioned.

Keywords: *Pseudo-potential, Dust-acoustic solitary structures, Self-gravitational perturbation, Nonlinearity, Degenerate pressure, Relativity, Compact objects*

Self-Gravitational Potential Structures in Dusty Quantum Plasmas

Muhammad Asaduzzaman
azaman@phy.kuet.ac.bd, ORCID: 0009-0002-7632-045X
Department of Physics, Khulna University of Engineering and Technology, Khulna-9203, Bangladesh

ABSTRACT

A rigorous theoretical investigation has been made on the propagation of self-gravitational potential structures in both unmagnetized and magnetized, self-gravitating, super dense dusty quantum plasma system consisting of inertial extremely massive dust fluid, non-inertial thermally degenerate heavy nuclear species (heavy nuclei/element) and non-inertial thermally degenerate ultra-relativistic electron species. The nonlinear behaviors for these potential structures (associated with the self-gravitational field) in planar geometry has been examined. The standard reductive perturbation technique, which is valid for small but finite amplitude potential structures, has been employed in order to derive the Korteweg-de Vries (K-dV) and modified K-dV (mK-dV) type equations. The nonlinear equations derived here have been solved to obtain stationary localized solutions and their numerical analysis. The parametric regimes for the existence of solitary self-gravitational potential structures (SGPS) and their basic properties (amplitude, width, etc.) have also been examined. It has been found that (i) the nonlinear dynamics of the SGPS is governed by the mK-dV type equation, which gives periodic U-shaped potential structures; (ii) the static external magnetic field converts the periodic U-shaped potential structures represented by secant square function into solitary self-gravitational potential structures represented by hyperbolic secant square function; (iii) the basic properties (viz., amplitude, width, speed, etc.) of the solitary SGPS are found to be significantly modified by the effect of static external magnetic field and obliqueness and also by the combined effects of dust component and self-gravitational field; (iv) the fundamental properties of the SGPS are influenced in the ultra-relativistic limit. The applications of the present investigation in different space dusty plasma environments and laboratory dusty plasma devices are briefly discussed.

Keywords: *Self-gravitational perturbation, Solitary waves, Nonlinearity, Degenerate pressure, Relativity, Compact objects.*

Investigation of Practical Use of Infill Walls with Flexible Connections

Alper CUMHUR

alper.cumhur@yalova.edu.tr, ORCID: 0000-0003-3664-3545
Department of Civil Engineering, Faculty of Engineering, Yalova University, Yalova, Turkey

ABSTRACT

Infill walls are non-structural elements applied to fill gaps in the structural system and to create partitions in the building area. Commonly used infill wall types are bricks and aerated concrete. Although infill walls exhibit positive behaviors under earthquake effects, they are often not incorporated in the design calculations. Infill walls can display both in-plane and out-of-plane behaviors under earthquakes. As a result of these behaviors, significant damages like corner crushing, diagonal cracking, shear cracking, and out-of-plane collapse can be observed in infill walls. This situation has, in the past, resulted in loss of life and property in the past earthquakes.

Turkish Building Earthquake Code (TBDY 2018) has introduced certain amendments and has set limitations on inter-story drifts for infill walls. The code outlines two different practices for infill walls: closely integrated with the reinforced concrete frame (jointless adjacent) and those separate from the frame (joint-separated). The allowable relative storey drift is twice as high for joint-separated infill walls compared to jointless adjacent walls. However, in this case, TBDY 2018 mandates the use of infill walls with flexible connections. While the example of flexible connections for infill walls provided in TBDY 2018 Information Annex 4C is intended to be informative and practical, it lacks sufficient applicability for all structures. Additionally, due to the limited number of experimental studies on flexibly connected infill walls, there are insufficient practical examples.

This study aimed at reducing infill wall damages under earthquake effects, identifying the parameters that are effective during the design phase of flexibly connected infill walls envisaged in TBDY 2018, and determining simple and cost-effective infill wall flexible connection details that are easy to implement. This study primarily examined the damages and causes of infill wall damages caused by earthquakes in Türkiye. Accordingly, sample applications that provide harmony between the design complying with TBDY 2018 and the actual implementation were examined to mitigate infill wall damages.

The findings revealed that in flexibly connected infill wall applications, the type of infill wall (brick, aerated concrete, briquette, etc.), flexible infill material, flexible joint spacing, type of connection (wall connection components), and number of connections (dowels, anchors, etc.) were found to be effective on the behavior of the structure (relative storey drifts). Furthermore, to ensure that the use of a flexibly connected infill wall aligns with the constraints outlined in TBDY 2018, these parameters should be identified and implemented based on experimental studies and considering the structure's characteristics during the design phase.

Keywords—*Earthquakes; Infill wall damages; Infill walls with flexible connections; Relative storey drifts*

Investigating The Effects of Chemical Waterproofing Agent Application Techniques on The Permeability of Concrete Specimens

Oğuzhan ŞAHİN

oguzhan.sahin@ankara.edu.tr, ORCID: 0000-0003-2104-5761
Department of Civil Engineering, Ankara University, Ankara, Turkiye

ABSTRACT

Concrete permeability is a critical factor that can significantly affect the durability and engineering performance of concrete structures. High permeability can lead to ingress of water and other harmful substances, which in turn may cause corrosion of reinforcing steel, deterioration of concrete, and other structural issues. Therefore, mitigating the permeability of concrete is of paramount importance in the construction applications. By considering this, this study investigated the effects of chemical waterproofing agent application techniques on the permeability of concrete specimens. To do this, a series of concrete specimens were fabricated using a specifically designed concrete mixture with a compressive strength of 25 MPa. Two distinct chemical waterproofing agent application techniques were employed in this study: (i) direct brushing method and (ii) pre-application method. The direct brushing method involved applying the chemical waterproofing agent directly onto the concrete specimen's surface via brushing, while the pre-application method entailed applying the agent to the mold surface before the concrete mixture was poured. Following the applications, a series of permeability tests were conducted on the concrete specimens to evaluate the chemical waterproofing agent's effectiveness in preventing water ingress under pressure. The results of the study revealed that the choice of chemical waterproofing agent application techniques has a notable impact on the performance of the chemical waterproofing agent. According to the results of the experimental tests, although both application techniques demonstrated the potential of the chemical waterproofing agent to enhance the concrete's resistance to water permeability, the pre-application method exhibited more remarkable effectiveness in substantially enhancing the impermeability of concrete.

Keywords—*Permeability; Chemical waterproofing agent; Concrete; Application techniques; Brushing*

Lung Tumor Detection and Localization on CT scans Using a Deep Learning Algorithm

Raşit ÖZTOPÇU*[1], Muhammet Üsame ÖZİÇ[1]

*: roztopcu19@posta.pau.edu.tr, ORCID: 0009-0005-4834-929X
[1]: *Department of Biomedical Engineering, Faculty of Technology, Denizli, TURKEY*

ABSTRACT

Lung tumors are anomalies that result from the irregular growth of cells in lung tissues. These tumors can occur as both benign and malignant, eventually spreading to other organs through metastasis. The disease can negatively impact an individual's daily life with symptoms such as chest pain, blood in sputum, excessive coughing, fatigue, weight loss, and loss of appetite. Smoking is identified as the largest risk factor. According to the World Health Organization's 2020 data, 1.8 million individuals lose their lives to lung cancer every year, with 2.2 million new cases diagnosed annually. Lung tumors are diagnosed and monitored using Computed Tomography (CT), an X-ray-based imaging technique. Images taken as cross-sections from the chest area are transformed into three-dimensional image forms using specialized software. This allows for the determination of various morphological and distinctive features of the tumor, such as its shape, size, spread, location, type, and stage. In recent years, deep learning models have become increasingly popular for disease detection, classification, segmentation, and object detection in medical images. This has enabled the design of clinical decision support systems that can assist doctors in diagnosis. In this study, the YOLO deep learning model, which performs object detection, was used to detect and localize tumors in CT images. The CT lung images used in this study were obtained from publicly available data in the Medical Segmentation Decathlon provided by The Cancer Imaging Archive. These data consist of 96 thin-sliced 3D volumes with slice thicknesses smaller than 1.5 mm. The data includes masks of regions marked as lung tumors by expert chest radiologists using the OsiriX program. In the study, raw CT images were overlaid, color-coded, and saved in PNG format using the MRIcro program to create masks. This allowed for annotation using the open-source browser-based makesense application for drawing bounding boxes. Slices, where lung tumors were not visible, were removed from the dataset to ensure that training was conducted only with relevant data. The resulting labeled dataset of 1420 two-dimensional images was divided into 70% training, 20% validation, and 10% testing subsets. Training and testing processes were conducted using the YOLOv8 deep learning model on the Linux-based Google COLAB cloud platform. Results were evaluated using performance metrics including precision, recall, F1-score, and mean average precision. The evaluation of test data showed that the YOLOv8 model achieved high performance, with precision, recall, and F1-score all exceeding 90% for detecting and localizing lung tumors in CT images obtained from the chest.

Keywords— *Computed Tomography; Deep Learning; Lung Tumor; YOLOv8.*

Examining The Effects of Centrifugal Fan Body Design Changes on Air Flow Rate and Pressure Through Computational Fluid Dynamics

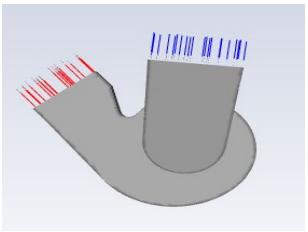
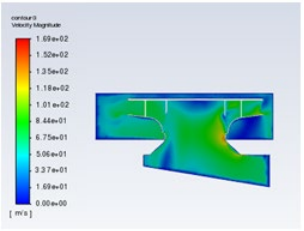
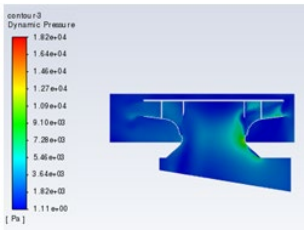
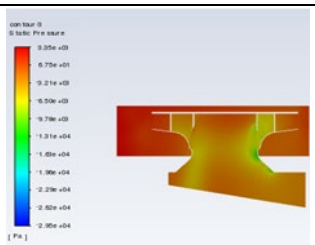
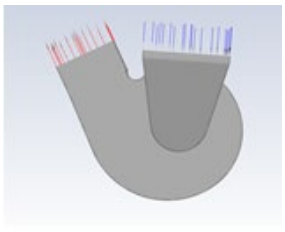
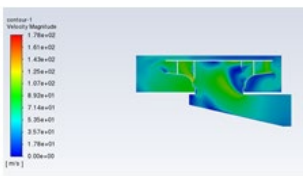
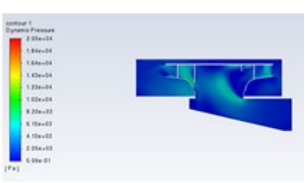
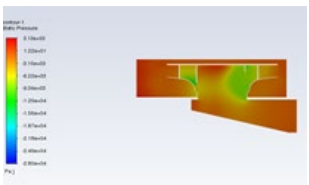
Vedat FETULLAHOĞLU[*1], H. Atakan BAYTAŞ[1], Gökhan KOCA[1]

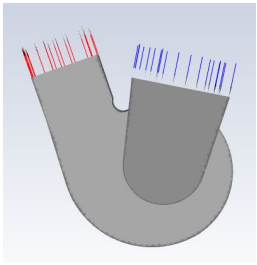
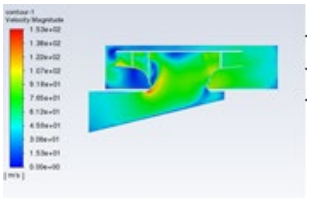
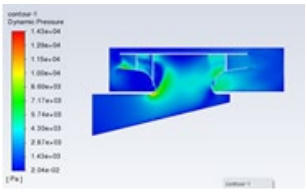
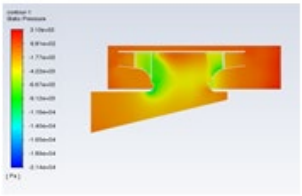
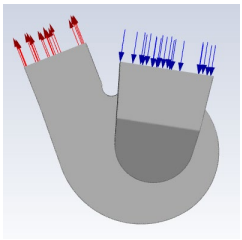
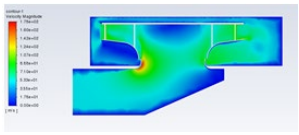
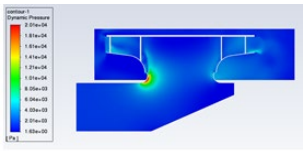
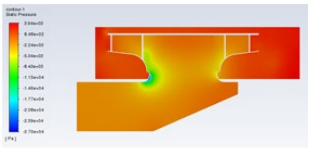
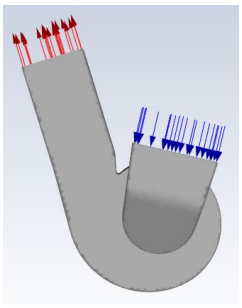
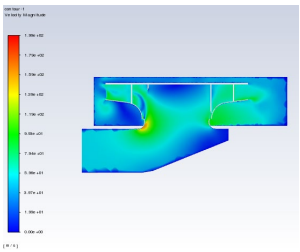
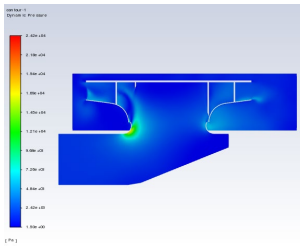
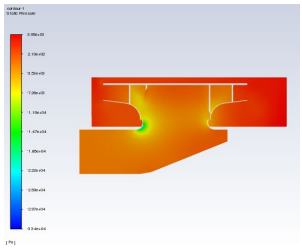
[*]: vedat.fetullahoglu@koluman.com, ORCID: 0009-0000-5551-6707
[1]: *Koluman Otomotiv Endüstri A.Ş., Mersin, Turkiye*

ABSTRACT

In this study, centrifugal fan body dimensions that have specific geometry have been changed according to CFD analysis results. Five trials have been done with same conditions and results are examined in scope of flow characteristics such as pressure difference, velocity of flow. In order to compare the results, the previous model was accepted as the initial condition at first step. In the second step, diameter of inlet box was decreased in order to delivery air flow to directly impeller. Additionally, distance between inlet box and scroll housing is decreased Because of the pressure decrease, second step is canceled and will not apply to design. In the third step, diameter of the inlet box increased from than first condition and distance between inlet box and scroll housing is same with second condition. So, at the end of the third step, pressure difference increase has been observed. In the fourth step, cross-section of inlet box is increased and the middle of the front wall is bent. At the end of the fourth step, air velocity and pressure difference increase has been observed eventually. In the fifth step, in order to scroll housing design parameter, radius of volute tongue is decreased. As result, pressure difference and air velocity values are increased if we compare with initial condition.

Keywords—*Centrifugal Fan, Computational Fluid Dynamics, Blower, ANSYS.*

1		 ***V=45,5 m/s***	 ***V=45,5 m/s***	 ***ΔP=317,079 mmH₂O***
2		 ***V=36,4 m/s***	 ***V=36,4 m/s***	 ***ΔP=196,290 mmH₂O***

3		 V=38,7 m/s	 V=36,4 m/s	 $\Delta P=254,112\ mmH_2O$
4		 V=45,25 m/s	 V=45,25 m/s	 $\Delta P=352,923\ mmH_2O$
5		 V=52,20 m/s	 V=52,20 m/s	 $\Delta P=419,5\ mmH_2O$